

J. Ping Liu
Eric Fullerton
Oliver Gutfleisch
David J. Sellmyer
Editors

Nanoscale Magnetic Materials and Applications

Foreword by Peter Grünberg

 Springer

Nanoscale Magnetic Materials and Applications

J. Ping Liu
Eric Fullerton
Oliver Gutfleisch
David J. Sellmyer
Editors

Nanoscale Magnetic Materials and Applications

Foreword by Peter Grünberg

 Springer

Editors

J. Ping Liu
University of Texas, Arlington
Department of Physics
502 Yates Street
Arlington, TX 76019
USA
pliu@uta.edu

Eric Fullerton
University of California, San Diego
Center for Magnetic Recording Research
9500 Gilman Drive
La Jolla, CA 92093-0401
USA
efullerton@ucsd.edu

Oliver Gutfleisch
Leibniz Institute for Solid State
and Materials Research
(IFW Dresden)
Institute of Metallic Materials
Helmholtzstr. 20
D-01069 Dresden
Germany
o.gutfleisch@ifw-dresden.de

David J. Sellmyer
Department of Physics and Astronomy
and Nebraska Center for Materials
and Nanoscience
University of Nebraska
Lincoln, NE 68588-0113
USA
dsellmyer@unl.edu

ISBN 978-0-387-85598-1 e-ISBN 978-0-387-85600-1

DOI 10.1007/978-0-387-85600-1

Springer Dordrecht Heidelberg London New York

Library of Congress Control Number: 2008943510

© Springer Science+Business Media, LLC 2009

All rights reserved. This work may not be translated or copied in whole or in part without the written permission of the publisher (Springer Science+Business Media, LLC, 233 Spring Street, New York, NY 10013, USA), except for brief excerpts in connection with reviews or scholarly analysis. Use in connection with any form of information storage and retrieval, electronic adaptation, computer software, or by similar or dissimilar methodology now known or hereafter developed is forbidden.

The use in this publication of trade names, trademarks, service marks, and similar terms, even if they are not identified as such, is not to be taken as an expression of opinion as to whether or not they are subject to proprietary rights.

Printed on acid-free paper

Springer is part of Springer Science+Business Media (www.springer.com)

Foreword

The appearance of materials with dimensions on the nanoscale has brought new stimulus also to magnetism. The discoveries of giant magnetoresistance and tunnel magnetoresistance can be seen as a result of this development.

Generally, magnetism tends to become weaker or even disappears when the geometrical dimensions of samples are decreased. In thin films used for data storage in magnetic recording, for example, this can lead to instability of stored information.

However, this trend is not always to the disadvantage of possible applications. In small nanoscale particles, for example, the occurrence of superparamagnetism leads to hysteresis-free magnetization curves with vanishing remanence. This is useful when the magnetic response should be given as much as possible by an external field rather than by the “magnetic history” of the material. There are numerous examples for this in medical applications as described in this volume. On the other hand – to dwell a little further on the mentioned problem in data storage – new interactions have also been discovered, which are operative on the nanoscale and can be used to solve a given problem. Such an interaction is the interlayer exchange coupling, which is employed in antiferromagnetically coupled (AFC) media to enhance the stability of stored information.

Magnetic surfaces and interfaces represent further special classes of nanoscale materials. Uncompensated spins at the surface of an antiferromagnet, for instance, give rise to a phenomenon called “exchange bias”, which is applied in magnetic field sensors to tailor the response curve.

For magnetic structures on the nanoscale there is also a new possibility to affect their magnetic order by means of electrical currents. This phenomenon called “current-induced magnetization dynamics” is foreseen to be used for writing information. It is currently one of the most active fields of research on nanoscale magnetism and also offers a new method of microwave generation by the current-driven precession of the magnetization.

Hence, a variety of new phenomena operative on the nanoscale is available to render nanomagnetism an interesting research field and to generate the potential for new applications. What are the systems, in which these phenomena can occur? We mentioned already layered magnetic structures and nanoparticles. Other classes of materials are magnetic nanowires and dots, either lithographically defined or

realized by assembling molecules and atoms such as fullerenes filled with magnetic materials.

The field of nanomagnetism is rich indeed both from a fundamental scientific viewpoint and with respect to applications and new devices.

Peter Grünberg
2007 Nobel Prize in Physics

Preface

This book has its genesis in the 2007 Materials Research Society (MRS) Fall Meeting where we organized the symposium “Nanoscale Magnetic Materials and Applications”. This symposium, with more than 200 submissions of presentations and 30 invited talks, was one of the most successful meetings in magnetic materials research in recent years. Ms. Elaine Tham from Springer suggested us to edit a book based on the topics presented in this symposium. We invited a number of presenters in the symposium to be the authors of this book which shares the title of the symposium. Moreover, we have extended the scope of the book to other topics as well that were not covered in the symposium.

Magnetic materials have a long history. People have been using compasses for thousands of years. However, new magnetic materials and applications are emerging and are proving indispensable in our daily lives and modern industries. One example is that there are already over a billion giant magnetoresistance sensors produced for information technology and other related applications. Hard and soft magnetic materials are key for efficient energy conversion, especially for converting electric energy to mechanical energy so that they are important to meet the challenges of the depletion of fossil fuels, climate change, and global warming.

Nanotechnology is one of the most important developments in science and technology in our generation, and it has brought revolutionary progress in materials processing and characterization. Current magnetic nanotechnologies have their roots in the development of bulk materials, such as permanent magnets where the functionality is derived from a complex nanoscale multi-phase morphology. Nanotechnology has offered a coupling of synthesis, theory, and characterization of materials at the nanoscale that enables materials design to evolve beyond earlier Edisonian approaches. By its very nature, magnetic materials are a class of nanoscale materials. Although early researchers did not explicitly work on the nanoscale, theoretical research revealed some time ago that nanoscale correlations exist in magnetic materials and control their properties. Several important characteristic dimensions in magnetism are in the nanoscale range such as the magnetic domain wall thickness and the “exchange length” in hard magnetic phases. This highlights why the research and development of new nanoscale magnetic materials are important and will lead to enhanced performance and new functionality. Some recent examples highlighted in this book include patterned magnetic recording

media and exchange-coupled nanocomposite magnets, where intense worldwide efforts are underway to significantly improve the areal density of data storage and the energy product of permanent magnets, respectively.

This book covers many of the exciting areas in nanoscale magnetic materials and applications. Readers will find topics in the book including theoretical work on novel magnetic structures, characterization of magnetic structures, single-phase materials and nanocomposite magnets, spintronic materials, domain structure and domain wall motion, magnetic nanoparticles and patterned magnetic recording media, magnetocaloric effect, and shape memory effect. The book also covers the most important emerging applications of advanced materials. The applications include new devices based on domain wall motion driven by current or fields, new magnetic sensors based on giant magnetoresistance and tunneling magnetoresistance, soft and hard magnetic materials for specific applications, thin-film applications in micro-electro-mechanical systems, and nanoparticle applications in biomedicine. We hope that this new book provides a comprehensive view of recent progress in all the related fields.

While attempting to present the most exciting developments in materials research and device applications, discussions in depth about the novel phenomena and emerging new materials are also presented in the book, such as the controllable exchange bias and inter-phase exchange interactions. Though more work is needed to understand the issues, we hope that this book gives a good introduction to future advancement.

We thank Prof. Peter Grünberg, the 2007 Nobel Laureate in Physics, for giving his insightful and visionary foreword to this book. We thank Ms. Elaine Tham and Ms. Lauren Danahy from Springer who initiated this book and did a great deal of work to bring it to completion. Mrs. Grace Liu has worked hard in collecting all the manuscripts, figures, and related paperwork. Finally, we thank all of our authors who contributed their very informative and in-depth chapters which made this new book a reality.

Arlington, TX, USA
La Jolla, CA, USA
Dresden, Germany
Lincoln, NE, USA

J. Ping Liu
Eric Fullerton
Oliver Gutfleisch
David J. Sellmyer

Contents

1 Spin Dynamics: Fast Switching of Macro-spins	1
X.R. Wang, Z.Z. Sun, and J. Lu	
1.1 Introduction	1
1.2 Spin and Its Kinetics and Dynamics	3
1.2.1 Basic Concepts of Spin	3
1.2.2 Kinetics of Spin: Spin Current	4
1.2.3 Dynamics of Spin: Bloch Equation, Landau–Lifshitz Equation, and Landau– Lifshitz–Gilbert Equation	5
1.3 Macro-spin Reversal with a Static Magnetic Field	9
1.3.1 A Nonlinear Dynamics Picture of Magnetization Reversal	9
1.3.2 The Exactness of SW-Limit at Infinitely Large Dissipation	11
1.3.3 Critical Value of Damping Constant	13
1.3.4 Ballistic Reversal	15
1.4 Macro-spin Reversal with a Time-Dependent Magnetic Field	17
1.4.1 Strategy I: Field Following the Magnetization Motion	18
1.4.2 Strategy II: Synchronizing the Magnetization Motion with a Circularly Polarized Microwave	21
1.4.3 Theoretical Limits of Switching Field/Current and Optimal Reversal Pulses	25
1.5 Summary	32
References	32
2 Core–Shell Magnetic Nanoclusters	35
Jinlan Wang and X.C. Zeng	
2.1 Introduction	35
2.2 Experimental Studies of Core–Shell Magnetic Clusters	37
2.2.1 Iron-Based (Fe@Au) Core–Shell Nanoclusters	38
2.2.2 Cobalt-Based Core–Shell Nanoclusters	44
2.2.3 Ni-Based Core–Shell Nanoclusters	50

2.3	Theoretical Studies of Bimetallic Magnetic Core–Shell Nanoclusters	51
2.3.1	Iron-Based (Fe@Au) Core–Shell Nanoclusters	51
2.3.2	Cobalt-Based Core–Shell Nanoclusters	53
2.3.3	Mn-Based Core–Shell Nanoclusters: [Mn ₁₃ @Au ₂₀] [−]	59
2.4	Summary	60
	References	62
3	Designed Magnetic Nanostructures	67
	A. Enders, R. Skomski, and D.J. Sellmyer	
3.1	Introduction	67
3.2	Structure, Chemistry, and Geometry	70
3.2.1	Synthesis of Supported Nanostructures	71
3.2.2	Case Study: Fe Clusters on Pt Surfaces	73
3.2.3	Structure of Embedded Clusters	75
3.2.4	Case Study: FePt Clusters in a Carbon Matrix	78
3.3	Anisotropy and Hysteresis	79
3.3.1	Surface and Interface Anisotropies	80
3.3.2	Hysteresis of Fe Clusters on Pt	81
3.3.3	Role of Heavy Transition Metals	83
3.3.4	Proteresis	85
3.4	Quantum-Mechanical Effects	86
3.4.1	Embedding from a Quantum-Mechanical Point of View	86
3.4.2	Exchange Interactions	87
3.4.3	Preasymptotic Coupling	90
3.4.4	Kondo Effect	92
3.4.5	Entanglement	93
3.5	Concluding Remarks	95
	References	95
4	Superconductivity and Magnetism in Silicon and Germanium Clathrates	105
	Joseph H. Ross Jr. and Yang Li	
4.1	Introduction	106
4.2	Superconductivity in Si ₄₆ Clathrates	108
4.3	Rattler Atoms and Narrow Bands	109
4.4	Superconducting Mechanism	111
4.5	Zintl Concept and Vacancies	115
4.6	Superconductivity in Other Clathrates	117
4.7	Magnetism	117
4.8	Conclusions	119
	References	119

5	Neutron Scattering of Magnetic Materials	123
	Olivier Isnard	
5.1	Introduction	123
5.2	Interaction of Neutrons and Materials: A Brief Presentation	124
5.3	Crystal Structure Investigation	126
	5.3.1 Powder Diffraction	126
	5.3.2 Single Crystal Diffraction	126
5.4	In Situ Neutron Diffraction	128
	5.4.1 Thermodiffraction: Crystallization of Amorphous Materials	128
	5.4.2 In Situ Investigation of the Synthesis and Ordering of nanocrystalline FePt Alloys	129
	5.4.3 Time-Resolved Neutron Diffraction Studies	130
5.5	Magnetic Structure Determination	133
5.6	Magnetic Phase Transition	135
	5.6.1 Magnetic Phase Transitions Studied by Powder Diffraction	135
	5.6.2 Magnetic Phase Transitions Studied by Single Crystal Diffraction	137
5.7	Polarized Neutron Techniques	138
	5.7.1 Uniaxial Polarization Analysis	138
	5.7.2 Spherical Neutron Polarimetry	141
5.8	Small-Angle Neutron Scattering	141
5.9	Neutron Scattering on Magnetic Surfaces	144
5.10	Magnetic Excitations	146
5.11	Neutron Scattering Under Extreme Conditions	148
5.12	Conclusions	150
	References	150
6	Tunable Exchange Bias Effects	159
	Ch. Binek	
6.1	Introduction	160
6.2	Electrically Tuned Exchange Bias	165
	6.2.1 Electrically Tuned Exchange Bias with Magnetoelectrics	165
	6.2.2 Electrically Tuned Exchange Bias with Multiferroics	168
	6.2.3 Piezomagnetically and Piezoelectrically Tuned Exchange Bias	169
6.3	Magnetic Field Control of Exchange Bias	170
6.4	Training Effect in Exchange-Coupled Bilayers	174
	6.4.1 Physical Background of Training Effects in Various Systems	174

6.4.2	Tuning the Training Effect	178
6.5	Conclusion	179
	References	179
7	Dynamics of Domain Wall Motion in Wires with Perpendicular Anisotropy	185
	Dafiné Ravelosona	
7.1	Introduction	185
7.2	Basics of Field-Induced DW Motion in Pt/Co/Pt Ultra-Thin Films	187
7.2.1	Mechanisms of Magnetization Reversal in Pt/Co/Pt Trilayers	188
7.2.2	Different Regimes of DW Motion: The Role of Defects	189
7.3	Control and Detection of Single DW Motion in Magnetic Wires	192
7.3.1	Wires Nanofabrication and Injection of a Single Domain Wall	193
7.3.2	Electrical Methods to Detect DW Motion Along Tracks	194
7.4	Field-Induced DW Motion Along Wires: Role of Structural Defects	196
7.4.1	The Role of Edge Roughness on the Creep Regime in Co/Pt Films	196
7.4.2	The Role of Intrinsic Defects in Co/Ni Films	201
7.5	Control of the Pinning Potential	203
7.5.1	Ion Irradiation of Co/Pt Films: A Way to Reduce Intrinsic Structural Defects	204
7.5.2	A DW Propagating in a Hall Cross: An Artificial Pinning Potential	207
7.6	Current Induced DW Depinning	208
7.7	Conclusion	213
	References	214
8	Magnetic Nanowires for Domain Wall Logic and Ultrahigh Density Data Storage	219
	R.P. Cowburn	
8.1	Domain Wall Propagation and Nucleation	219
8.2	Domain Wall Conduits	221
8.3	The NOT Gate and Shift Register Element	223
8.4	Data Input–Output	226
8.5	Using the Chirality of the Transverse Domain Wall	228
8.6	Potential Applications of Domain Wall Logic	233
8.7	Conclusion	234
	References	235

9 Bit-Patterned Magnetic Recording: Nanoscale Magnetic Islands for Data Storage	237
Thomas R. Albrecht, Olav Hellwing, Ricardo Ruiz, Manfred E. Schabes, Bruce D. Terris, and Xiao Z. Wu	
9.1 Introduction	238
9.2 Theoretical Perspective of Bit-Patterned Recording	240
9.2.1 Island Addressability in Bit-Patterned Recording	240
9.2.2 Fabrication Tolerances of BPM	242
9.2.3 Thermal Constraints	243
9.2.4 Magnetostatic Interaction Fields Between Islands	245
9.2.5 BPM Designs for Tb/in ² Densities	246
9.3 Optimization of the Magnetic Materials	248
9.3.1 Magnetic Characterization	249
9.3.2 Magnetic Switching-Field Distribution	252
9.3.3 Laminated Magnetic Media	254
9.3.4 Magnetic Trench Noise Reduction	255
9.4 Fabrication of Bit-Patterned Media	256
9.5 Generation of Master Patterns Beyond 1Tbit/in ² via Guided Self-Assembly of Block Copolymer Domain Arrays	259
9.5.1 Ordering, Size Distribution, and Scalability: Patterned Media Requirements vs. Block Copolymer Fundamental Limitations	260
9.5.2 Approaches to Long-Range Orientational and Translational Order in Block Copolymer Templates	262
9.6 Write Synchronization	265
9.6.1 Requirements for Write Synchronization	265
9.6.2 Options to Achieve Write Synchronization	265
9.6.3 Timing Variations Observed in a Conventional Drive	266
9.6.4 Implementation of a Sector Synchronization System	268
9.7 Conclusion	270
References	271
10 The Magnetic Microstructure of Nanostructured Materials	275
Rudolf Schäfer	
10.1 Overview	275
10.2 Coarse-Grained Material and Amorphous Ribbons	277
10.3 Domains in Nanocrystalline Ribbons	282
10.3.1 Random Anisotropy Model	283
10.3.2 Interplay of Random and Uniaxial Anisotropies	287
10.3.3 Magnetization Process	292
10.4 Domains in Nanocrystalline Magnetic Films	296

10.5	Domains in Fine- and Nanostructured Permanent Magnets . . .	301
10.6	Summary	304
	References	304
11	Exchange-Coupled Nanocomposite Permanent Magnets	309
	J.P. Liu	
11.1	Introduction	309
11.2	Fundamental Aspects	311
	11.2.1 The Early Models	311
	11.2.2 The Soft Phase Effects	313
	11.2.3 The Interface Effects	314
	11.2.4 Coercivity Mechanisms	316
	11.2.5 Characterization of Inter-phase Exchange Coupling	316
11.3	Experimental Approaches	321
	11.3.1 The Early Approaches	321
	11.3.2 Nanoparticle Approaches	322
	11.3.3 Fabrication of Nanocomposite Bulk Magnets	327
11.4	Work Toward Anisotropic Nanocomposite Magnets	331
	References	332
12	High-Temperature Samarium Cobalt Permanent Magnets	337
	Oliver Gutfleisch	
12.1	Introduction	337
12.2	Physical Metallurgy and Crystal Structures	339
12.3	Coercivity Mechanism and the Development of High-Temperature 2:17-Type Magnets	343
	12.3.1 The $\text{Sm}(\text{CoCu})_5$ Cell Boundary Phase	343
	12.3.2 Alloy Optimization	344
	12.3.3 Stability at Operating Temperature	348
12.4	Microchemistry and Pinning Behavior in $\text{Sm}_2\text{Co}_{17}$ -Type Magnets	349
	12.4.1 Redistribution of Cu and Slow Cooling	349
	12.4.2 Stability of Microchemistry	352
	12.4.3 “Anomalous” Coercivity Behavior	355
12.5	Magnetic Domains and Coercivity	357
	12.5.1 Analysis of Magnetic Microstructure	357
	12.5.2 Domains and Processing Parameters	358
12.6	Non-equilibrium Processing Routes	362
	12.6.1 Rapidly Quenched $\text{SmCo}_5/\text{Sm}_2\text{Co}_{17}$ Magnets	362
	12.6.2 Mechanically Alloyed $\text{SmCo}_5/\text{Sm}_2\text{Co}_{17}$ Magnets	363
	12.6.3 Hydrogen Disproportionated SmCo_5 and $\text{Sm}_2\text{Co}_{17}$ Alloys	364
	References	367

13 Nanostructured Soft Magnetic Materials	373
Matthew A. Willard and Maria Daniil	
13.1 Introduction	373
13.2 Materials Development	376
13.2.1 Alloy Processing and Design	377
13.2.2 Phase Transformations	378
13.2.3 Annealing Techniques	381
13.3 Magnetic Performance	382
13.3.1 Exchange-Averaged Anisotropy	383
13.3.2 Intrinsic Magnetic Properties	384
13.3.3 Domain Structure	385
13.3.4 Hysteretic Losses	386
13.3.5 AC Properties	388
13.3.6 Thermomagnetism	389
13.4 Applications	390
13.4.1 Power Applications	391
13.4.2 Electromagnetic Interference Applications	392
13.4.3 Sensor Applications	393
13.5 Summary	393
References	394
14 Magnetic Shape Memory Phenomena	399
Oleg Heczko, Nils Scheerbaum, and Oliver Gutfleisch	
14.1 Introduction	399
14.2 Martensitic Transformation and Twinning	401
14.3 Modes of Magnetic Field-Induced Strain	403
14.3.1 Magnetostriction	403
14.3.2 Magnetic Field-Induced Phase Transformation	404
14.4 Magnetically Induced Structure Reorientation	405
14.5 The Ni–Mn–Ga System	408
14.5.1 Compositional Dependence of Structure and Transformation	408
14.5.2 Martensitic Phases in Ni–Mn–Ga	410
14.5.3 Magnetic Properties of Ni–Mn–Ga	412
14.6 Twin Boundary Mobility	416
14.7 Energy Model for MIR	418
14.8 Angular Dependence	421
14.9 Reversible and Irreversible MIR Strain	422
14.10 Temperature Dependence of MIR	426
14.11 MIR in Polycrystals, Composites, and Films	427
14.12 Other Applications Based on MSM Alloys	430
14.13 Conclusion	430
Further Reading	431
References	431

15 Magnetocaloric Effect and Materials	441
J.R. Sun, B.G. Shen, and F.X. Hu	
15.1 Introduction	441
15.2 Theoretical Description of Magnetocaloric Effect	443
15.3 Experimental Determination of Magnetocaloric Effect	446
15.3.1 Direct Measurement of Adiabatic Temperature Change	446
15.3.2 Indirect Measurement of Entropy and Adiabatic Temperature Changes	446
15.4 Magnetocaloric Effect Associated with First-Order Phase Transition	447
15.4.1 MCE Due to an Idealized First-Order Transition	447
15.4.2 MCE Due to a Non-Idealized First-Order Phase Transition	448
15.5 Typical Materials with Giant Magnetocaloric Effect	451
15.5.1 $\text{LaFe}_{3-x}\text{M}_x$ ($\text{M} = \text{Al}, \text{Si}$) Intermetallics	452
15.5.2 $\text{Gd}_5(\text{Ge},\text{Si})_4$ and Related Compounds	472
15.5.3 Mn-Based Heusler Alloys	476
15.5.4 Mn–As-Based Compounds	478
15.6 Concluding Remarks	479
References	479
16 Spintronics and Novel Magnetic Materials for Advanced Spintronics	485
Jiwei Lu, Kevin G. West, Jiani Yu, Wenjing Yin, David M. Kirkwood, Li He, Robert Hull, Stuart A. Wolf, and Daryl M. Treger	
16.1 Introduction to Spintronics	485
16.2 Novel Magnetic Oxide Thin Films by Reactive Bias Target Ion Beam Deposition	489
16.2.1 Reactive Bias Target Ion Beam Deposition (RBTIBD)	490
16.2.2 $\text{Cr}_x\text{V}_{1-x}\text{O}_2$ Thin Films	491
16.2.3 $\text{Co}_x\text{Ti}_{1-x}\text{O}_2$ Thin Films	496
16.3 Diluted Ferromagnetic $\text{Ge}_{1-x}\text{Mn}_x$ by Ion Implantation	500
Additional Reading on Spintronics	507
References	507
17 Growth and Properties of Epitaxial Chromium Dioxide (CrO_2) Thin Films and Heterostructures	511
Guo-Xing Miao and Arunava Gupta	
17.1 Density of States (DOS) of Half-Metallic CrO_2 and the Double Exchange Mechanism	511
17.2 Intrinsic Properties of Epitaxial CrO_2 Films	513

17.3	Influence of Strain on the Magnetic Properties of CrO ₂ Thin Films	517
17.3.1	Film Growth on Atomically Smooth TiO ₂ Substrates	517
17.3.2	Films Grown on As-Polished TiO ₂ Substrates	521
17.4	CrO ₂ -Based Heterostructures	523
17.4.1	Epitaxial SnO ₂ Barrier Layer	525
17.4.2	Epitaxial RuO ₂ Barrier Layer	528
17.4.3	VO ₂ Barrier Layer	530
17.4.4	TiO ₂ Barrier Layer	531
17.4.5	Cr ₂ O ₃ Barrier Layer	532
	References	535
18	FePt and Related Nanoparticles	537
	J.W. Harrell, Shishou Kang, David E. Nikles, Gregory B. Thompson, Shifan Shi, and Chandan Srivastava	
18.1	Introduction	538
18.2	Thermal Effects in Magnetic Nanoparticles	538
18.3	Magnetic Recording and the Superparamagnetic Limit	541
18.4	Chemical Synthesis and Shape Control of FePt and Related Nanoparticles	541
18.4.1	Synthesis	541
18.4.2	Shape Control	544
18.5	Prevention of Sintered Grain Growth During Annealing	545
18.5.1	FePt/MnO Core/Shell Nanoparticles	546
18.5.2	FePt/SiO ₂ Core/Shell Nanoparticles	547
18.5.3	Salt Matrix Annealing	548
18.5.4	Flash Annealing	549
18.6	Effect of Metal Additives on Chemical Ordering and Sintered Grain Growth	550
18.7	Easy-Axis Orientation	552
18.7.1	Model of Easy-Axis Orientation	552
18.7.2	Easy-Axis Orientation Measurements	553
18.8	Composition Distribution	554
18.9	Anisotropy Distribution	556
18.10	Size Effect on Chemical Ordering	556
18.11	Summary and Conclusions	557
	References	558
19	Magnetic Manipulation of Colloidal Particles	563
	Randall M. Erb and Benjamin B. Yellen	
19.1	Introduction	563
19.2	Magnetic Manipulation of Particles	565
19.2.1	Deterministic and Brownian-Dominated Particle Systems	565
19.2.2	Material Properties	565

19.2.3	Magnetic Force	568
19.3	Deterministic Particle Manipulation	570
19.3.1	Substrate-Based Self-Assembly of Particles	570
19.3.2	Substrate-Based Transport and Separation	571
19.4	Brownian-Influenced Particle Manipulation	573
19.4.1	Magnetic and Nonmagnetic Particle Chains	573
19.4.2	Magnetic and Nonmagnetic Mixed Assemblies in Ferrofluid	576
19.4.3	Anisotropic Particle Alignment	576
19.5	Brownian-Dominated Manipulation of Particle Populations	579
19.5.1	Modeling Thermal Diffusion	579
19.5.2	Magnetic Particle Concentration	581
19.5.3	Nonmagnetic Particle Concentrations	584
19.5.4	Applications of Concentration Gradients	586
19.6	Conclusions and Outlook	587
	References	588
20	Applications of Magnetic Nanoparticles in Biomedicine	591
	Carlos Bárcena, Amandeep K. Sra, and Jinming Gao	
20.1	Introduction	591
20.2	Nanoparticle Classification	592
20.3	Syntheses of SPIO Nanoparticles	593
20.3.1	Co-precipitation	593
20.3.2	Microemulsion	594
20.3.3	Thermal Decomposition	595
20.3.4	Alternative Methods	596
20.4	Surface Modifications of Magnetic Nanoparticles	596
20.4.1	Organic and Polymeric Stabilizers	597
20.4.2	Inorganic Molecules	598
20.5	Pharmacokinetics and Toxicology	600
20.6	Biomedical Applications of Magnetic Nanoparticles	603
20.6.1	Magnetic Resonance Imaging	603
20.6.2	Therapeutic Applications	612
20.7	Conclusion	616
	Abbreviations	616
	References	618
21	Nano-Magnetophotonics	627
	Mitsuteru Inoue, Alexander Khanikaev, and Alexander Baryshev	
21.1	Introduction	627
21.2	Magnetophotonic Crystals	628
21.2.1	1D MPCs Composed of Alternating Magnetic and Dielectric Layers	629
21.2.2	Microcavity-Type 1D MPCs	633
21.2.3	Photonic Band Structure and Eigenmodes of 2D MPCs	635

21.2.4	Faraday Rotation of Three-Dimensional Magnetophotonic Crystals	637
21.2.5	Nonlinear Optical and Magneto-Optical Properties	640
21.2.6	Conclusion	641
21.3	Magnetorefractive Effect in Nanostructures	641
21.3.1	Magnetorefractive Effect in Nanostructures and Manganites	642
21.3.2	Enhancement of the MRE in Magnetophotonic Crystals	644
21.3.3	Conclusion	647
21.4	Plasmon-Enhanced Magneto-Optical Responses	647
21.4.1	Garnet-Noble Metal Nanocomposites	648
21.4.2	Metal-Garnet Structures Supporting Transmission Resonances	651
21.4.3	Conclusion	653
	References	653
22	Hard Magnetic Materials for MEMS Applications	661
	Nora M. Dempsey	
22.1	An Introduction to MEMS	661
22.1.1	What Are MEMS?	661
22.1.2	How Are MEMS Made?	662
22.2	Magnetic MEMS	662
22.2.1	Downscaling Magnetic Systems	663
22.2.2	Prototype Magnetic MEMS	665
22.3	Permanent Magnets	666
22.4	Fabrication of μ -Magnets: Top-Down Routes	667
22.4.1	Bulk Processed Magnets	668
22.4.2	Bulk Processed Hard Magnetic Powders	669
22.5	Fabrication of Thick Hard Magnetic Films	671
22.5.1	Electrodeposition	672
22.5.2	Sputtering	672
22.5.3	Pulsed Laser Deposition (PLD)	675
22.6	Micro-Patterning of Thick Hard Magnetic Films	676
22.6.1	Topographically Patterned Films	676
22.6.2	Crystallographically Patterned Films	679
22.7	Conclusions and Perspectives	680
	References	680
23	Solid-State Magnetic Sensors for Bioapplications	685
	Goran Mihajlović and Stephan von Molnár	
23.1	Introduction	685
23.2	Magnetic Sensors Based on GMR Effect	687
23.2.1	GMR Sensors	689
23.2.2	Spin Valve Sensors	693

- 23.2.3 GMR and Spin Valve Sensors for Detection of Nanoparticles 695
- 23.3 MTJ Sensors 697
- 23.4 Sensors Based on AMR Effect 700
 - 23.4.1 AMR Ring Sensors 700
 - 23.4.2 Planar Hall Effect Sensors 700
- 23.5 Hall Effect Sensors 702
- 23.6 GMI Sensors 706
- 23.7 Conclusions 707
- References 708
- Index** 711

Contributors

Thomas R. Albrecht Hitachi Global Storage Technologies, San Jose Research Center, San Jose, CA 95123, USA, Thomas.Albrecht@hitachigst.com

Carlos Bárcena Harold C. Simmons Comprehensive Cancer Center, University of Texas Southwestern Medical Center at Dallas, Dallas, TX 75390; Department of Chemistry, University of Texas at Dallas, Richardson, TX 75080, USA

Alexander Baryshev Toyohashi University of Technology, Toyohashi, Aichi, Japan; Ioffe Physico-Technical Institute, 194021 St. Petersburg, Russia

Ch. Binek Department of Physics and Astronomy, Nebraska Center for Materials and Nanoscience, University of Nebraska, Lincoln, NE 68588, USA, cbinek2@unlnotes.unl.edu

R.P. Cowburn Blackett Physics Laboratory, Imperial College London, Prince Consort Road, London SW7 2BW, UK, r.cowburn@imperial.ac.uk

Maria Daniil US Naval Research Laboratory, Washington, DC, USA

Nora M. Dempsey Institut Néel, CNRS-UJF, 25 rue des Martyrs, 38042, Grenoble, France, nora.dempsey@grenoble.cnrs.fr

A. Enders Department of Physics and Astronomy and Nebraska Center for Materials and Nanoscience, University of Nebraska, Lincoln, NE 68508, USA, axel@unl.edu

Randall M. Erb Department of Mechanical Engineering and Materials Science, Center for Biologically Inspired Materials and Material Systems, Duke University, Durham, NC 27708, USA, randall.erb@duke.edu

Jinming Gao Harold C. Simmons Comprehensive Cancer Center, University of Texas Southwestern Medical Center at Dallas, Dallas, TX 75390; Department of Chemistry, University of Texas at Dallas, Richardson, TX 75080, USA, Jinming.Gao@UTSouthwestern.edu

Arunava Gupta Center for Materials for Information Technology (MINT), The University of Alabama, Tuscaloosa, AL 35487, USA, agupta@mint.ua.edu

Oliver Gutfleisch Leibniz Institute for Solid State and Materials Research (IFW Dresden), Institute for Metallic Materials, Helmholtzstr. 20, 01069 Dresden, Germany, o.gutfleisch@ifw-dresden.de

J.W. Harrell Department of Physics, Center for Materials for Information Technology, The University of Alabama, Tuscaloosa, AL 35487-0209, USA, jharrell@bama.ua.edu

Li He Department of Materials Science and Engineering, University of Virginia, Charlottesville, VA, 22904, USA

Oleg Heczko Leibniz Institute for Solid State and Materials Research (IFW Dresden), Institute for Metallic Materials, Helmholtzstr. 20, 01069 Dresden, Germany, Institute of Physics, Academy of Sciences, Czech Republic Na Slovance 2, CZ-182 21 Praha 8, Czech Rep., heczko@fzu.cz

Olav Hellwig Hitachi Global Storage Technologies, San Jose Research Center, San Jose, CA 95123, USA

F.X. Hu State Key Laboratory for Magnetism, Institute of Physics, Chinese Academy of Sciences, Beijing 100080, Peoples' Republic of China

Robert Hull Department of Materials Science and Engineering, University of Virginia, Charlottesville, VA, 22904, USA

Mitsuteru Inoue Toyohashi University of Technology, Toyohashi, Aichi, Japan, inoue_mitsuteru@eee.tut.ac.jp

Olivier Isnard Institut Néel, CNRS, Boîte F, BP166, F-38042 Grenoble, Cédex 9, France, olivier.isnard@grenoble.cnrs.fr

Shishou Kang Center for Materials for Information Technology, The University of Alabama, Tuscaloosa, Alabama 35487-0209, USA, skang@mint.ua.edu

Alexander Khanikaev Toyohashi University of Technology, Toyohashi, Aichi, Japan

David M. Kirkwood Department of Materials Science and Engineering, University of Virginia, Charlottesville, VA, 22904, USA

Yang Li Department of Engineering Science and Materials, University of Puerto Rico at Mayaguez, Mayaguez, PR 00681-9044

J.P. Liu Department of Physics, University of Texas at Arlington, Arlington, TX 76019, USA, pliu@uta.edu

Jiwei Lu Department of Materials Science and Engineering, University of Virginia, Charlottesville, VA, 22904, USA

J. Lu Physics Department, The Hong Kong University of Science and Technology, Clear Water Bay, Hong Kong SAR, China

Guo-Xing Miao Center for Materials for Information Technology (MINT), The University of Alabama, Tuscaloosa, AL 35487, USA

Goran Mihajlović Materials Science Division, Argonne National Laboratory, Argonne, IL 60439, mihajlovic@anl.gov

David E. Nikles Department of Chemistry, Center for Materials for Information Technology, The University of Alabama, Tuscaloosa, Alabama 35487-0209, USA, dnikles@mint.ua.edu

Dafiné Ravelosona Institut d'Electronique Fondamentale, UMR CNRS 8622, Université Paris Sud, 91405 Orsay, France, dafine.ravelosona@u-psud.fr

Joseph H. Ross, Jr Department of Physics, Texas A&M University, College Station, TX 77843-4242, USA, ross@physics.tamu.edu

Ricardo Ruiz Hitachi Global Storage Technologies, San Jose Research Center, San Jose, CA 95123, USA

Manfred E. Schabes Hitachi Global Storage Technologies, San Jose Research Center, San Jose, CA 95123, USA

Rudolf Schäfer Leibniz Institute for Solid State and Materials Research (IFW Dresden), Institute for Metallic Materials, Helmholtzstr. 20, 01069 Dresden, Germany, r.schaefer@ifw-dresden.de

Nils Scheerbaum Leibniz Institute for Solid State and Materials Research (IFW Dresden), Institute for Metallic Materials, Helmholtzstr. 20, 01069 Dresden, Germany

David. J. Sellmyer Department of Physics and Astronomy and Nebraska Center for Materials and Nanoscience, University of Nebraska, Lincoln, NE 68508, USA

B.G. Shen State Key Laboratory for Magnetism, Institute of Physics, Chinese Academy of Sciences, Beijing 100080, Peoples' Republic of China

Shifan Shi Department of Physics, Center for Materials for Information Technology, The University of Alabama, Tuscaloosa, Alabama 35487-0209, USA, shi004@bama.ua.edu

R. Skomski Department of Physics and Astronomy and Nebraska Center for Materials and Nanoscience, University of Nebraska, Lincoln, NE 68508, USA, rskomski@neb.rr.com

Amandeep K. Sra Harold C. Simmons Comprehensive Cancer Center, University of Texas Southwestern Medical Center at Dallas, Dallas, TX 75390, USA

Chandan Srivastava Department of Metallurgical and Materials Engineering, Center for Materials for Information Technology, The University of Alabama, Tuscaloosa, Alabama 35487-0209, USA, sriva001@bama.ua.edu

Z.Z. Sun Physics Department, The Hong Kong University of Science and Technology, Clear Water Bay, Hong Kong SAR, China

J.R. Sun State Key Laboratory for Magnetism, Institute of Physics, Chinese Academy of Sciences, Beijing 100080, Peoples' Republic of China, jrsun@g203.iphy.ac.cn

Bruce D. Terris Hitachi Global Storage Technologies, San Jose Research Center, San Jose, CA 95123, USA

Gregory B. Thompson Department of Metallurgical and Materials Engineering, Center for Materials for Information Technology, The University of Alabama, Tuscaloosa, Alabama 35487-0209, USA, gthompson@coe.eng.ua.edu

Daryl M. Treger Strategic Analysis, Arlington, VA 22203, USA

Stephan von Molnár MARTECH and Department of Physics, Florida State University, Tallahassee, FL 32306, USA

Jinlan Wang Department of Physics, Southeast University, Nanjing, 211189, P. R. China

X.R. Wang Physics Department, The Hong Kong University of Science and Technology, Clear Water Bay, Hong Kong SAR, China, phxwan@ust.hk

Kevin G. West Department of Materials Science and Engineering, University of Virginia, Charlottesville, VA, 22904, USA

Matthew A. Willard US Naval Research Laboratory, Washington, DC, USA, willard@anvil.nrl.navy.mil

Stuart A. Wolf Department of Materials Science and Engineering, University of Virginia, Charlottesville, VA, 22904, USA, saw6b@Virginia.EDU

Xiao Z. Wu Hitachi Global Storage Technologies, San Jose Research Center, San Jose, CA 95123, USA

Benjamin B. Yellen Department of Mechanical Engineering and Materials Science, Center for Biologically Inspired Materials and Material Systems, Duke University, Durham, NC 27708, USA, yellen@duke.edu

Wenjing Yin Department of Materials Science and Engineering, University of Virginia, Charlottesville, VA, 22904, USA

Jiani Yu Department of Materials Science and Engineering, University of Virginia, Charlottesville, VA, 22904, USA

X.C. Zeng Department of Chemistry and Nebraska Center for Materials and Nanoscience, University of Nebraska, Lincoln, Nebraska 68588, USA, xzengl@unl.edu

Chapter 1

Spin Dynamics: Fast Switching of Macro-spins

X.R. Wang, Z.Z. Sun, and J. Lu

Abstract Recent progress on the theoretical studies of fast magnetization reversal of Stoner particles is reviewed. The following results are discussed: (1) The Stoner–Wohlfarth (SW) limit becomes exact when the damping constant is infinitely large. Under the limit, magnetization moves along the steepest energy descent path. (2) For a given magnetic anisotropy, there is a critical damping constant, above which the minimal switching field is the same as that of the SW-limit. (3) The field of a ballistic magnetization reversal should be along a certain direction window in the presence of energy dissipation. (4) Since a time-dependent magnetic field can be an energy source, two new reversal strategies are possible. One is to use a field following magnetization motion, and the other is to use a circularly polarized microwave near the ferromagnetic resonance frequency. The critical switching fields of both strategies are substantially lower than that of precessional reversal for realistic materials. (5) The theoretical limits for both field-induced and current-induced magnetization reversal are presented for uniaxial Stoner particles.

1.1 Introduction

Spin dynamics is an old and important subject rooted in magnetism and the nuclear/electron-spin/ferromagnetic resonances that have wide applications in physics, information processing, chemistry, biology, and medicine [1–5]. In the field of magnetic data storage [4], magnetization reversal has received a lot of attention because data input and output involve switching the magnetization of magnetic storage cells that are important components of modern computers. The typical switching time with currently used technology is of the order of nanoseconds. If one wants to have a faster computer (modern electronic computers are working at a clock speed

X.R.Wang (✉)
Physics Department, The Hong Kong University of Science and Technology, Clear Water Bay,
Hong Kong SAR, China
e-mail: phxwan@ust.hk

of the order of GHz) with magnetic random access memory (MRAM), the conventional magnetization reversal method shall be a bottleneck. Thus, fast magnetization switching shall be of great importance for future development of high-speed information industry.

Magnetization reversal is a very complicated problem in bulk material [5] because it can be achieved in many different ways. For example, magnetization reversal can go through bucking and curling modes, coherent rotation, and/or domain nucleation and domain wall propagation. Recent technological advances allow us to fabricate magnetic nano-particles [6] that are believed to be useful for high-density information storage [7–10]. For a magnetic nano-particle, strong exchange interactions keep the magnetic moments of atoms rigid, creating just a single magnetic domain, such that the constituent spins rotate in unison. Such a nano-particle is often called a Stoner–Wohlfarth (SW) or Stoner particle. The understanding of magnetization reversal of a Stoner particle should be relatively simple in comparison with that of a bulk system, yet important in nano-technologies [4] as a consequence of the miniaturization into the nano-meter scale.

Magnetization reversal of macro-spins (of Stoner particles) is known as the SW problem because it was first studied by Stoner and Wohlfarth in 1948 [11]. One current topic in nanomagnetism is the control and manipulation of the magnetization of Stoner particles, and magnetization reversal is one of the basic operations. Magnetization state can be manipulated by a magnetic field [11–22], or by a spin-polarized electric current [23–28] through so-called spin-transfer torque (STT), or by a laser light [30]. In terms of applications, manipulation by a magnetic field and/or a spin-polarized electric current dominates and will continue to dominate the information storage industry. Examples are field-driven and current-driven MRAM. Important issues in applications are scalability, power consumption, and speed. These issues relate to the problems of lowering the critical field/current required to reverse a magnetization [4], as well as to the problems of designing a field/current pulse such that the magnetization can be switched from one state to another extremely quickly [21, 29].

Regarding the issue of minimal switching field, Stoner and Wohlfarth [11] showed that a static field larger than the so-called SW-limit can switch a magnetization from its initial state to the target one. The idea is to make the target state to be the only energy minimum. Thus the system rolls down to the target state. However, the system can only gradually dissipate its energy during a precessional motion so that the magnetization moves around the precession axis many times (ringing phenomenon or ringing mode) [12–16, 21, 22] before reaching the target state. As a result, it takes typically nanoseconds to switch a magnetization at a field of teslas. Subsequent theoretical and experimental studies [14, 15] have shown that the minimal switching field can be smaller than the SW-limit. The energy consideration alone in the SW theory is not adequate, and one has to take into account magnetization dynamics. The magnetization dynamics of a nano-structure is governed by the so-called Landau–Lifshitz–Gilbert (LLG) equation that does not have a general analytical solution. Most theoretical work in the field has relied on numerical calculations, and most reversal schemes [21, 27, 28] have

been proposed on a hunch. Ideas include thermal assistance [27] and sample designs [28].

Regarding the issue of switching time, picoseconds magnetization switching has been observed recently in experiments [14, 15] by using pulsed magnetic fields. This approach has received much theoretical attention [12, 17–19]. Numerical investigations [12] showed that the switching time can be substantially reduced because ringing effect is avoided so that the magnetization moves along a so-called ballistic trajectory [19]. The precessional magnetization reversal provides not only a shorter time but also a lower switching field (well below the SW-limit), as found in the early numerical calculations [12]. In the absence of energy dissipation, precessional magnetization switching can also be investigated analytically. Analytical results for the minimal field were obtained by Porter [20].

There are already many nice reviews and books on the general subject of spin dynamics, and we shall not try to make a thorough review on the subject. Instead, we concentrate on the recent theoretical progress on two issues of the SW problem. One is how to make magnetization reversal fast, and the other is how to lower the switching field/current. For those readers who want to know more about many other aspects of spin dynamics, they may read several nice books [1–4] on the subject. The outline of this chapter is as follows. A brief introduction of spin and its kinetics and dynamics subjected to different interactions are given in Section 1.2. These include the dynamics of an isolated spin (without damping) and the dynamics of a macro-spin in contact with the environments (with damping through spin relaxation and spin decoherence). Spin current as a result of spin kinetics is also discussed. Section 1.3 is about magnetization reversal by a static magnetic field. The existence of a critical damping constant, above which the SW theory predicts correctly the switching field, is discussed, and a direction window for ballistic reversal is explained. Section 1.4 is about the macro-spin reversal by a time-dependent magnetic field. The fundamental difference between a static magnetic field and a time-dependent magnetic field is revealed. Based on the fact that a time-dependent magnetic field can be an energy source, two strategies with substantial lower (than the precessional one) critical switching field are discussed. The theoretical limits of the critical switching field or current out of all possible designs, together with the optimal reversal trajectory, are also given. Section 1.5 is a short summary.

1.2 Spin and Its Kinetics and Dynamics

1.2.1 Basic Concepts of Spin

Like electric charge, spin and the associated magnetic moment are fundamental properties (intrinsic quantum numbers) of elementary particles. The spin quantum number relates to many phenomena in elementary particle physics as well as in nuclear, atomic, solid state, and statistical physics. Spin is one type of angular momentum which does not have a classical analogy, but one may tentatively view

a spin coming from a spinning motion of a particle. From the symmetry transformation viewpoint, spin is one class of generators of spatial rotation transformations, while electric charge is the generator of so-called U(1) gauge symmetry transformations. Spin has three components, s_1 , s_2 , and s_3 that generate rotations around x-, y-, and z-axis. Unlike electric charge being a scalar, the expectation value of a spin operator \vec{s} is a vector. According to quantum mechanics, spin operators \vec{s} satisfies the following fundamental commutation relations

$$[s_j, s_k] = i\hbar\varepsilon_{jkl}s_l, \quad (1.1)$$

where ε_{jkl} is an antisymmetric tensor on three indices, for which $\varepsilon_{jkl} = 0$ except for $\varepsilon_{123} = \varepsilon_{231} = \varepsilon_{312} = 1$ and $\varepsilon_{321} = \varepsilon_{213} = \varepsilon_{132} = -1$. This symmetry viewpoint explains well why spin is a good quantum number of an elementary particle that has an intrinsic rotational symmetry. From quantum mechanics, it is known that a spin can take only integers or half-integers values of \hbar .

Following classical electrodynamics, the magnetic moment of a charged particle moving in a circular orbit is given by

$$\vec{M} = \frac{q}{2m_e}\vec{L}, \quad \vec{L} = \vec{r} \times \vec{p}, \quad (1.2)$$

where q and m_e are the charge and the mass of the particle, respectively. \vec{L} is the orbital angular momentum of a particle at position \vec{r} with momentum \vec{p} . Although the magnetic moments of elementary particles and their spins do not follow exactly the above equation, they are related to each other by

$$\vec{M} = g\frac{q}{2m_e}\vec{s} \quad (1.3)$$

with g a fundamental parameter for a given particle.

1.2.2 Kinetics of Spin: Spin Current

Just as the flow of charge generates electric current, so the flow of spin in space creates a spin current. Different from the electric current density which is a vector, spin current density is a rank-2 tensor because of the vector nature of spin. As mentioned earlier, spin is only one type of angular momenta. All particles can have orbital angular momentums besides spins. An electron can exchange its spin with its orbital angular momentum through spin-orbit interaction or exchange its spin angular momentum with the angular momenta of other electrons and/or particles through particle-particle interactions. As a result, spin current is very fragile, not continuous, and does not even conserve because the spin state of an electron is seldom stationary. To see why the spin current behaves like this, it may be helpful to understand why an electric current reaches easily the continuity condition. The

reason is not only due to the charge conservation (otherwise, the spin current should also be very robust) but also because of both charge quantization and large Coulomb interaction. Each type of particle carries only a fixed number of charges. For example, all electrons have one negative charge. Large Coulomb interaction prevents any real material from either absorbing or releasing excessive charges. In comparison, an electron can be in any innumerable number of possible spin states, and there is no interaction to prevent angular momentum accumulation and transformation from one object to another.

The differences in the electric current and spin current make the study of spin current much more challenging than that of electric current. In fact, even the issue of a proper definition of the spin current has been an active issue of debate recently in the spintronics community [31–33]. Interested readers are referred to the literature [31–33] for a full discussion.

1.2.3 Dynamics of Spin: Bloch Equation, Landau–Lifshitz Equation, and Landau–Lifshitz–Gilbert Equation

Consider a spin \vec{s} under the influence of its Hamiltonian $W(\vec{s})$. The dynamics of \vec{s} is governed by the Heisenberg equation if \vec{s} can be regarded as a closed system

$$\frac{d\vec{s}}{dt} = \frac{1}{i\hbar} [\vec{s}, W(\vec{s})]. \quad (1.4)$$

It is straightforward to evaluate the commutator, and Eq. (1.4) becomes

$$\frac{d\vec{s}}{dt} = \gamma \vec{s} \times \vec{H}_t, \quad (1.5)$$

where $\gamma = 2.21 \times 10^5 (\text{rad/s})/(\text{A/m})$ is the gyromagnetic ratio, and the effective field $\vec{H}_t = -\nabla_{\vec{s}} W(\vec{s})/\gamma$ comes from external magnetic fields and from various magnetic anisotropy energies [5]. If one takes the expectation value of the above equation with respect to the spin state, and assumes $\langle -\gamma \vec{s} \times \vec{H}_t \rangle = -\gamma \langle \vec{s} \rangle \times \langle \vec{H}_t \rangle$, then the magnetization of an isolated spin, $\vec{M} \equiv \gamma \langle \vec{s} \rangle$, satisfies the following dynamic equation

$$\frac{d\vec{M}}{dt} = -\gamma \vec{M} \times \vec{H}_t. \quad (1.6)$$

Classically, $\vec{H}_t = -\nabla_{\vec{M}} W(\vec{M})/\mu_0$, where $\mu_0 = 4\pi \times 10^{-7} \text{N/A}^2$ is the vacuum magnetic permeability, and $W(\vec{M})$ is the classical magnetic energy density.

1.2.3.1 Bloch Equation

Equation (1.6) is called the Bloch equation of an isolated spin by the nuclear magnetic resonance (NMR) and quantum optics scientific community because of the critical contributions of F. Bloch on these subjects. It is also known as the Landau–Lifshitz equation without dissipation in magnetism. Equation (1.6) is correct only for isolated spins, which is not the case for most realistic systems. Spins in a sample made up by condensed matter experience various interactions with other dynamical degree of freedoms of the sample and its environment. These interactions create internal magnetic fields. Due to the dynamical nature of the environments, these internal fields not only contribute an averaged field to the total magnetic field \vec{H}_t but also exert residual fluctuating fields on the spins. These fluctuating fields, originated in the infinite number of degrees of freedom of the environment as well as their thermal and the quantum fluctuations, can lead to both spin relaxation and spin decoherence, meaning that the spin magnetization will approach to a preferred equilibrium value M_{z0} along the z-axis which is selected by either external magnetic field or sample anisotropy. The physics is as what was explicitly demonstrated in Reference [34]: A random field perpendicular to the z-axis, which produces an off-diagonal term in the Hamiltonian, can induce transitions between different spin states. The randomness in the transitions and the spontaneous decay of quantum fluctuations leads the spin magnetization to take an equilibrium statistical value. The fluctuating field along the z-direction makes the spin precession random, which gives rise to spin decoherence.

If one takes into account spin relaxation and spin decoherence in the spin dynamics, the proper way to describe the magnetization dynamics is the so-called Bloch equation with spin relaxation and spin decoherence.

$$\begin{aligned}
 \frac{dM_z}{dt} &= -\gamma(M_x H_{ty} - M_y H_{tx}) - \frac{M_z - M_{z0}}{T_1} \\
 \frac{dM_x}{dt} &= -\gamma(M_y H_{tz} - M_z H_{ty}) - \frac{M_x}{T_2} \\
 \frac{dM_y}{dt} &= -\gamma(M_z H_{tx} - M_x H_{tz}) - \frac{M_y}{T_2}
 \end{aligned} \tag{1.7}$$

where T_1 and T_2 are called spin relaxation time and spin decoherence time, respectively. T_1 is the typical time for an initial non-equilibrium M_z to reach the equilibrium value M_{z0} , and T_2 is the typical time for a magnetization to lose the memory of its initial precession position. The above equation is the starting point of usual NMR analysis because the NMR signal is related to the average magnetization \vec{M} of an ensemble of spins.

1.2.3.2 Landau–Lifshitz Equation and Landau–Lifshitz–Gilbert Equation

The Bloch equation describes well the magnetization dynamics of an ensemble of non-interacting or weakly interacting spins, but it does not capture the proper

physics of a strongly interacting spin system such as a piece of magnet. This is because the magnetization magnitude of a magnet shall not change with time, and Eq. (1.7) does not preserve the magnitude of the magnetization. To take into account the dissipative effect of the environment, Landau and Lifshitz [35] introduced a phenomenological term, $\alpha\gamma\vec{m} \times (\vec{M} \times \vec{H}_t)$, where α is a dimensionless phenomenological parameter measuring the damping strength, and \vec{m} is the unit vector of \vec{M} . Equation (1.6) with this damping term becomes

$$\frac{d\vec{M}}{dt} = -\gamma\vec{M} \times \vec{H}_t - \alpha\gamma\vec{m} \times (\vec{M} \times \vec{H}_t). \quad (1.8)$$

Equation (1.8) is called the Landau–Lifshitz (LL) equation.

Later Gilbert [36] proposed an alternative way to include dissipation. Similar to Ohm’s law in electron transport, Gilbert assumed a friction field of $-\alpha(d\vec{m}/dt)$ on a moving magnetization due to the dissipation. This friction field generates a torque on the magnetization. Thus Eq. (1.6) should be modified as

$$\frac{d\vec{M}}{dt} = -\gamma\vec{M} \times \vec{H}_t + \alpha\vec{M} \times \frac{d\vec{m}}{dt}. \quad (1.9)$$

This equation is called the Landau–Lifshitz–Gilbert (LLG) equation that can also be written as

$$(1 + \alpha^2)\frac{d\vec{M}}{dt} = -\gamma\vec{M} \times \vec{H}_t - \alpha\gamma\vec{m} \times (\vec{M} \times \vec{H}_t). \quad (1.10)$$

Although Eqs. (1.10) and (1.8) have the same mathematical form, the two approaches to the dissipation are fundamentally different. According to Eq. (1.10), the change rate of the magnetization goes to zero as $\alpha \rightarrow \infty$, and the magnetization shall move along the dissipation direction of $-\vec{m} \times (\vec{M} \times \vec{H}_t)$ when $\alpha \rightarrow \infty$. However, Eq. (1.8) says that the rate change of the magnetization becomes infinity at infinite damping, and it does not make any sense. Thus LL’s approach to dissipation is not physical! It is generally accepted that LLG equation is the right description of magnetization dynamics for a magnet, and it is the starting point in our discussion of magnetization reversal of Stoner particles.

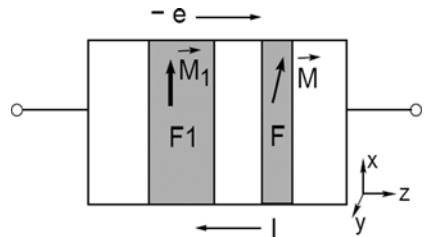


Fig. 1.1 An STT structure. Note that the direction of the electrical current is opposite to that of electron flow

Equation (1.9) contains only a torque from a magnetic field. To include the interaction between a spin-polarized electric current and the magnetization, one needs to add the so-called spin-transfer torque (STT) to Eq. (1.10). The idea of STT was independently suggested [23] by Slonczewski and Berger in 1996, and it was verified by several experiments [26]. In order to see the origin of the STT, consider a magnetic multilayer structure of nano-meter scale as illustrated in Fig. 1.1. It consists of two ferromagnets sandwiched in three nonmagnetic metallic layers. Electrons flow along the \hat{z} direction (from the left to the right) in the sample (the current I is in the opposite direction, $-\hat{z}$, as shown in Fig. 1.1). The first ferromagnet F1 is usually very thick so that the current does not affect its magnetization \vec{M}_1 . Electrons are polarized along \vec{M}_1 after they pass through F1 and retain their polarizations before entering the second ferromagnet F when the thickness of the spacer layer between F1 and F is much smaller than the spin diffusion length. The polarized electrons transfer their spin angular momentums to F, resulting in so-called STT [23]. This STT can affect the dynamics of magnetization \vec{M} of F when it is thin enough. Theoretical studies [23–25] show that the STT Γ is proportional to the current with the following form

$$\Gamma \equiv \left[\frac{d(\vec{M}V)}{dt} \right]_{STT} = \frac{\gamma \hbar I}{\mu_0 e} g(P, \vec{m} \cdot \hat{s}) \vec{m} \times (\vec{m} \times \hat{s}), \quad (1.11)$$

where \hat{s} is the unit vector of the current polarization direction (along \vec{M}_1). V and e denote the volume of F and the electron charge, respectively. The exact microscopic formulation of the STT is still a subject of study and debate [24, 25]. Different theories differ themselves in different expressions of the function g that depends on the degree of the current polarization P and relative angle between \vec{m} and \hat{s} . All experimental investigations [26] so far are consistent with the result of Slonczewski [23], which will be used throughout this study,

$$g(P, \vec{m} \cdot \hat{s}) = \frac{4P^{3/2}}{(1+P)^3(3+\vec{m} \cdot \hat{s}) - 16P^{3/2}}. \quad (1.12)$$

Equation (1.9) including the STT becomes the following generalized LLG equation

$$\frac{d\vec{M}}{dt} = -\gamma \vec{M} \times \vec{H}_t + \alpha \vec{M} \times \frac{d\vec{m}}{dt} + \gamma a_I \vec{M} \times (\vec{M} \times \hat{s}), \quad (1.13)$$

where $a_I = \hbar I g / (\mu_0 e M^2 V)$ is a dimensionless parameter. This equation is the starting point of most studies of magnetization dynamics of Stoner particles in the presence of both a magnetic field and a spin-polarized electric current. Because the magnitude of \vec{M} does not change with time, \vec{M} can be described by the polar

angle θ and the azimuthal angle ϕ in spherical coordinates, and Eq. (1.13) can be rewritten in a dimensionless form

$$(1 + \alpha^2) \frac{d\vec{m}}{dt} = -\vec{m} \times \vec{h}_1 - \vec{m} \times (\vec{m} \times \vec{h}_2), \quad (1.14)$$

where

$$\begin{aligned} \vec{h}_1 &= \vec{h}_t + \alpha a_I \hat{s}, \\ \vec{h}_2 &= \alpha \vec{h}_t - a_I \hat{s}, \end{aligned}$$

and t in Eq. (1.14) is measured in units of $(\gamma M)^{-1}$. The magnetization and the magnetic field are in the units of M . The total field $\vec{h}_t = \vec{h} + \vec{h}_i$ includes both applied magnetic field \vec{h} and internal field \vec{h}_i due to the magnetic anisotropy energy density $w(\vec{m})$ (which is in unit of $\mu_0 M^2$), $\vec{h}_i = -\nabla_{\vec{m}} w(\vec{m})$. Different particles are characterized by different magnetic anisotropy. Let \hat{e}_r , \hat{e}_θ , and \hat{e}_ϕ be the three spherical unit vectors of \vec{m} . In terms of θ and ϕ , Eq. (1.14) can be written as

$$\begin{aligned} (1 + \alpha^2) \dot{\theta} &= h_{t,\phi} + \alpha h_{t,\theta} + a_I (\alpha s_\phi - s_\theta), \\ (1 + \alpha^2) \sin \theta \dot{\phi} &= \alpha h_{t,\phi} - h_{t,\theta} - a_I (\alpha s_\theta + s_\phi). \end{aligned} \quad (1.15)$$

Here $h_{t,\theta}$, $h_{t,\phi}$ and s_θ , s_ϕ , s_r are the \hat{e}_θ , \hat{e}_ϕ , and \hat{e}_r components of \vec{h}_t and \hat{s} , respectively.

Both LL and LLG equations are semi-classical. The description should be inadequate when quantum effects become important. This may occur for extremely small particles, or in the case that spin wave excitation can affect spin dynamics. So far, a quantum version of the LLG equation is still missing.

1.3 Macro-spin Reversal with a Static Magnetic Field

This section is about the magnetization reversal of a uniaxial particle by a static magnetic field in the absence of an electric current. Thus, there is no STT, $a_I = 0$. A uniaxial model of $w(m_x) = -k_2 m_x^2 / 2 - k_4 m_x^4 / 4 - h_x m_x - h_z m_z$ will be used to illustrate the results whenever a detailed magnetic anisotropy is needed. In the model, k_2 and k_4 are model parameters characterizing the potential barrier and the shape of the potential landscape. Two parameters are needed to model different uniaxial Stoner particles since one of the parameters can be eliminated by choosing a proper time scale in Eq. (1.14).

1.3.1 A Nonlinear Dynamics Picture of Magnetization Reversal

The magnetization reversal of Stoner particles can be conveniently described by the terminology of nonlinear dynamics. The phase space related to the magnetization is a two-dimensional (2D) plane of polar angle θ and azimuthal angle ϕ , shown

in Fig. 1.2a. In the $\theta - \phi$ plane, each point corresponds to a particular state of the magnetization. A magnetization state will in general move to new states due to its dynamics. Its motion can be described by a trajectory in the phase plane, called phase flow. The phase flow for a dissipative system ends at a few types of destinies (attractors), including fixed points, limit cycles, or strange attractors. They correspond to stable states and periodic, aperiodic, and chaotic motions [38]. In a 2D phase plane, however, the strange attractor solution is not allowed.

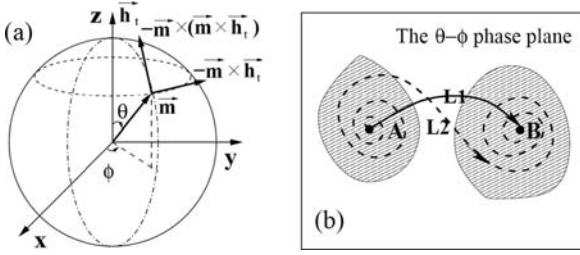


Fig. 1.2 (a) z-axis is along the total magnetic field \vec{h}_t . $-\vec{m} \times \vec{h}_t$ points to the precession direction, and $-\vec{m} \times (\vec{m} \times \vec{h}_t)$ decides the dissipation direction. (b) The $\theta - \phi$ phase plane for the magnetization of a Stoner particle. Points A and B represent the initial and the target state, respectively. Two shadowed areas denote schematically basins of two stable fixed points A and B. The solid curve L1 and dashed curve L2 illustrate two different phase flows from A to B

The only attractor relevant to the magnetization reversal of Stoner particles under a static field is fixed points. The magnetization reversal problem is as follows: Before applying an external magnetic field, there are two stable fixed points (denoted by A and B in Fig. 1.2b), corresponding to magnetizations, say \vec{m}_0 (point A) and $-\vec{m}_0$ (point B), along its easy axis. The phase plane can be divided into two parts, called basins of attractors. One is around A and the other around B, denoted by shadowed areas in Fig. 1.2b. The system in basin A(B) will end up at state A(B). Initially, the magnetization is \vec{m}_0 , and the goal is to apply a small external field to switch the magnetization to $-\vec{m}_0$ fast.

The conventional magnetization switching is based on a damping mechanism. From the viewpoint of nonlinear dynamics, the idea behind the method is to construct the external magnetic field in such a way that the target state is the only stable fixed point. In other words, basin A (Fig. 1.2b) is reduced to zero and the whole (except probably a few isolated points) phase plane is the target state basin (basin B). The minimal reversal field (SW-limit) is the one at which basin A shrinks to a point. Since the initial and the target states have very large energy difference, the extra energy must be dumped into the lattice during a spiral motion before the system reaches the final state. The system first spirals out of A, and then spirals toward B, denoted by phase flow L2 in Fig. 1.2b. This spiral motion is often referred [19] to as ringing effect. The reversal time is largely determined by the effectiveness of energy dissipation – *damping is good!*

In the precessional magnetization reversal, one applies a short magnetic field pulse perpendicular to the magnetization such that both initial and final states are not fixed points, and system will start to flow in the phase plane. In order to switch the magnetization, one needs to let the system to reach the basin of the final state (basin B) such that the system will flow to the target state after the pulse field is switched off. Ideally, one wants both initial and target states on its precessional path. This is a non-damping method, and the reversal time does not rely on the spin relaxation time. There are several ways with different control precisions to move the system to the desired state. One way is to apply a perpendicular pulse field to “kick” the system to basin B. In comparison with the conventional method, the spiral motion out of the initial state is replaced by a ballistic [19] motion. However, the system relies on ringing effect to reach the final state. It was shown [12] that the switching time can be reduced substantially, but it is still hundreds of picoseconds for a normal magnetic particle due to the ringing effect in the last stage of magnetization reversal. More efficient reversal is the so-called ballistic reversal in which both the initial and the target states are on the same phase flow trajectory as schematically illustrated by the solid line L1 connecting points A and B with an arrow in Fig. 1.2b. The typical time for a precession of 180° in a field of teslas is on the order of picoseconds for usual magnetic materials so a picoseconds magnetic field pulse is required in this method. The *damping is bad* in this approach, and a precise control of the pulse duration is required.

From the computational point of view, the magnetization reversal time can be evaluated as soon as the phase flow connecting the initial and the target states is found. Since the time for the magnetization to travel a small section dl of the trajectory equals dl divided by the phase velocity $\sqrt{\dot{\theta}^2 + \dot{\phi}^2}$, the reversal time is

$$t = \int_A^B \frac{dl(\theta, \phi)}{\sqrt{\dot{\theta}^2 + \dot{\phi}^2}}. \quad (1.16)$$

In the language of nonlinear dynamics, an external field modifies the dynamics by changing the phase velocity field. This velocity field is in general a continuous function of the external field. A phase flow between the initial and target states could only be set up when the external field is strong enough because the initial and final states are two stable fixed points with equally large basins at the beginning. The minimal switching field is the critical one at which such a flow is created.

1.3.2 The Exactness of SW-Limit at Infinitely Large Dissipation

The conventional method is based on damping. Its classical result is the so-called SW-limit. For a uniaxial model with the easy axis along the x-axis and magnetic field in the xz-plane, the SW-limit is obtained by assuming that the magnetization

moves in the xz -plane during its reversal. The minimal switching field is given by [11]

$$dw/dm_x = 0, \quad (1.17)$$

$$d^2w/dm_x^2 = 0, \quad (1.18)$$

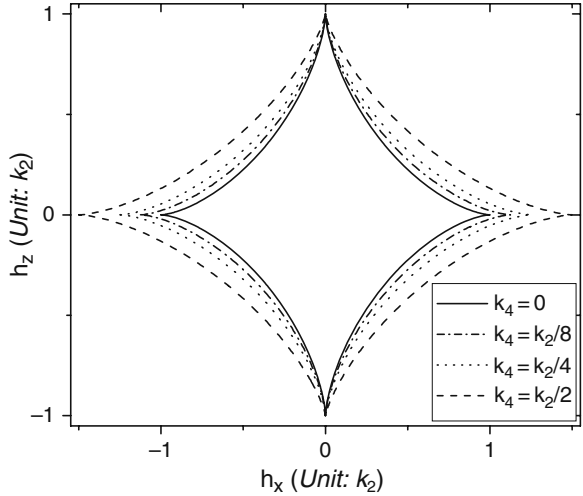
with $m_x^2 + m_z^2 = 1$. The SW-limit[11] for $k_2 \neq 0$ and $k_4 = 0$ is

$$(h_x/k_2)^{2/3} + (h_z/k_2)^{2/3} = 1, \quad (1.19)$$

corresponding to the solid line in Fig. 1.3. The SW-limits for various choices of k_4 are also plotted in Fig. 1.3.

Fig. 1.3 The SW-limit for various choices of k_2, k_4 .

Solid curve: $k_4 = 0$;
dash-dot curve: $k_4 = k_2/8$;
dotted curve: $k_4 = k_2/4$;
dashed curve: $k_4 = k_2/2$



The original SW-limit was derived in the static case [11]. As shown in the dynamical Eq. (1.10), the first term on the right hand side (RHS) will lift the magnetization away from the xz -plane. Thus the assumption of the SW-limit that the magnetization moves in the xz -plane is only true when this term can be neglected. This will happen when the damping constant becomes infinite ($\alpha \rightarrow \infty$). In this case, the magnetization will move toward the total field as denoted by the big circle (dot-dash) passing through the north-south poles in Fig. 1.2a. This is the steepest energy descent path for the magnetization. Thus, the minimal switching field in the SW-limit corresponds to the one at which there is only one minimum in the energy landscape.

1.3.3 Critical Value of Damping Constant

In a realistic system, as damping constant is not infinitely large, the magnetization does not need to move along the steepest energy descent path. As a result, a system may still move from the initial state to the local minimum located near the target state even when an external field is smaller than the SW-limit. Thus, after the external field is removed, the system will move toward the target state through a ringing mode, achieving the magnetization switching. As it was shown in many previous studies [12, 20], the minimal switching field can be smaller than the SW-limit. Numerical calculations [12] show that when the damping constant $\alpha < 1$, magnetization switching can occur well below the SW-limit. While $\alpha \geq 1$, the minimal switching field is the SW-limit. Thus, it implies a critical α_c exists, above which the minimal switching field is given by the SW-limit. In Reference [12], $\alpha_c = 1$. It can be shown [21] that there is indeed a critical damping constant for a given magnetic anisotropy. But this critical value can be different for different anisotropy, and $\alpha = 1$ is not special.

To understand the origin of α_c , let us consider energy landscape under different external field. As it was mentioned in the previous section, there is only one stable fixed point when $h > h_{SW}$. Asymptotically, the system shall always end up at the fixed point for any non-zero damping. Thus, if one switches off the field after it reaches the fixed point, the system will surely move to the target state (state B). There is also a $h_1 (< h_{SW})$ at which the initial state energy equals that at the saddle point between two stable fixed points. Thus there is no way to switch the magnetization when $h < h_1$ because the initial energy of the system is too low to climb over the potential barrier. h_1 can be determined from the following equations

$$dw/dm_x = 0, \quad (1.20)$$

$$w(m_x) = w_A, \quad (1.21)$$

where w_A is the energy of the initial state ($m_x = 1$). For a field h between h_1 and h_{SW} , $h_1 < h < h_{SW}$, there exist two stable fixed points. Furthermore, the energy of the initial state is higher than that of the saddle point. Figure 1.4 is a schematic 3D plot of the energy landscape for the case of $h_1 < h < h_{SW}$. Point A denotes the initial state whose energy is supposed to be higher than that of the saddle point (SP). The flow starting from A will eventually end at either of two fixed points, depending on the value of α . When α is infinity, the system will evolve into the minimum, near the initial state along the steepest descent path, as shown by line R1. For the opposite extreme of zero damping ($\alpha = 0$), the system will move along an equal potential contour (line R4) surrounding the two minima (fixed points). For small α , the magnetization can make many turns around the two local minima before it falls into either one. So there is a special $\alpha = \alpha_i$ with which the system just touches the saddle point (SP) when it rolls down from A, denoted by dotted line R3. For $\alpha > \alpha_i$, energy damping is too strong for the system to “climb” over the

saddle point, denoted by line R2. Value α_i depends obviously on the magnetic field, and critical damping α_c is the value of α_i at $h = h_{SW}$.

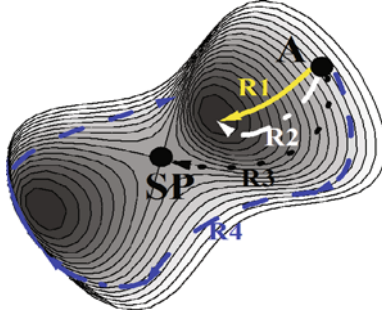


Fig. 1.4 The schematic 3D energy landscape plot of the case $h_1 < h < h_{SW}$. Point A denotes the initial state, whose energy is supposed to be higher than that of the saddle point (SP). Lines R1, R2, R3, and R4 show schematically four typical evolution trajectories for $\alpha = \infty, > \alpha_i, \alpha_i,$ and 0, respectively

One may also understand the result from Fig. 1.5 of trajectories of various α in the energy contour plot at $h = h_{SW}$ along 135° to $+x$ -axis. The result in the figure is for the uniaxial model with $k_2 = 2$ and $k_4 = 0$. As mentioned early, the saddle point and one minimum merge together at h_{SW} to form an inflexion point denoted by T in Fig. 1.5. It is clear that all trajectories with $\alpha > \alpha_c$ pass through T while all those with $\alpha < \alpha_c$ do not. All curves of $\alpha > \alpha_c$ terminate at T because the system shall not move at a saddle point. But any small fluctuation will result in the system to leave T and to end up in FP.

In order to demonstrate the correctness of our reasoning for α_c , and the dependence of the value of α_c on the magnetic anisotropy, we carried out numerical calculations on the uniaxial magnetic anisotropy model with different ratio

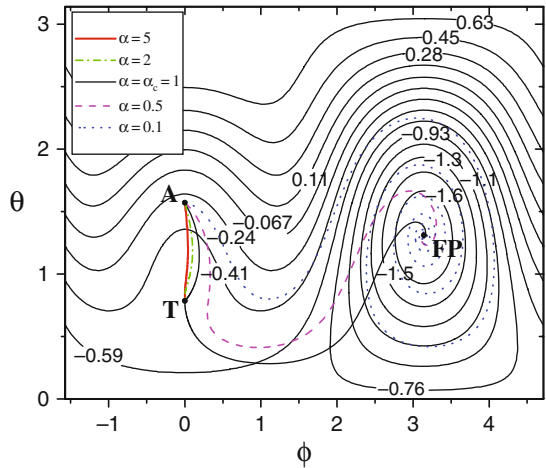
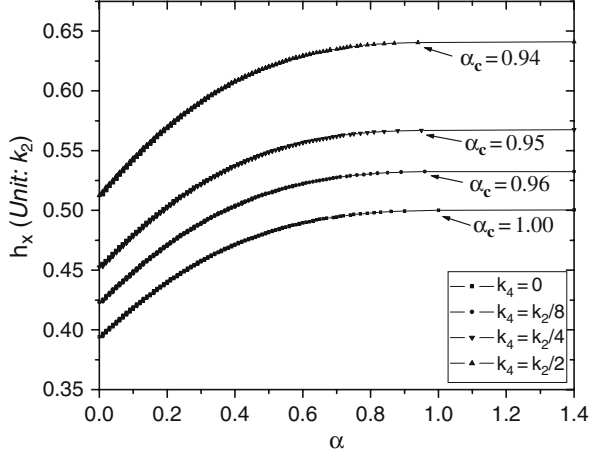


Fig. 1.5 The contour plot of $w(\phi, \theta)$ at $h = h_{SW}$ for the uniaxial magnetic anisotropy model with $k_2 = 2$ and $k_4 = 0$. The field is along $3\pi/4$ to $+x$ -axis. Point A is the initial point. FP denotes the stable fixed point. T denotes the inflexion point. All flow trajectories of $\alpha \geq \alpha_c$ touch T while those with $\alpha < \alpha_c$ do not

of k_4/k_2 . Figure 1.6 is α dependence of the minimal switching field for $k_4/k_2 = 0; 1/8; 1/4; 1/2$, respectively. Indeed, all curves (depend only on the ratio of k_4/k_2) saturate to their corresponding SW-limit values h_{SW} after α is greater than certain values α_c . Furthermore, α_c varies from $\alpha_c = 1$ for $k_4 = 0$ to $\alpha_c = 0.94$ for $k_4 = k_2/2$. Thus, $\alpha_c = 1$ is not special at all!

Fig. 1.6 The minimal switching field vs. damping constant α . The field is along $3\pi/4$ to $+x$ axis. Curves (from bottom to top) correspond to $k_4/k_2 = 0; \frac{1}{8}; \frac{1}{4};$ and $\frac{1}{2}$



1.3.4 Ballistic Reversal

We would like to discuss the field direction in a ballistic reversal. Without dissipation, LLG equation is a conservative system. A phase flow is an equal potential curve. As it was pointed out in Reference [22], only a perpendicular field is possible to connect the initial and the target states ballistically. Different from the conservative case [22], the system starting from A will never pass through the target state B in the presence of dissipation. Even under an infinitely large field, the energy loss during a 180° precession is not negligible. Although 180° precession time τ decreases as inverse of magnetic field, $\tau \sim \pi(1 + \alpha^2)/h$ when $h \gg 1$ and $\alpha \ll 1$, the energy dissipation rate goes as $dw/dt = -\frac{\alpha}{1+\alpha^2} |\vec{m} \times \vec{h}_t|^2 \propto h^2$, thus the energy loss during τ is proportional to field h [21]! In order to connect A and B ballistically, one has to create a small energy difference between A and B such that the energy dissipated on its way from A to B equals the energy difference.

On the other hand, Eq. (1.14) can be solved exactly in the absence of magnetic anisotropy ($k_2 = k_4 = 0$) [37] with solution $\phi = ht/(1 + \alpha^2)$ and $\cos \theta = [(1 + \cos \theta_0)e^{2\alpha ht/(1+\alpha^2)} - 1 + \cos \theta_0]/[(1 + \cos \theta_0)e^{2\alpha ht/(1+\alpha^2)} + 1 - \cos \theta_0]$, where θ_0 is the initial angle between the field and the magnetization (we assume the field is along the z-axis). Thus the field in a ballistic reversal should be along direction θ satisfying $-\cos \theta = [(1 + \cos \theta_0)e^{2\alpha \pi} - 1 +$

$\cos \theta] / [(1 + \cos \theta)e^{2\alpha\pi} + 1 - \cos \theta]$. It is interesting to notice that the solution is unique and the angle is $\tan(\theta/2) = e^{\alpha\pi/2}$.

Given a damping constant α and magnetic anisotropy, a 180° -precession time $\tau(h, \beta)$ is a function of field strength $h \equiv \sqrt{h_x^2 + h_z^2}$ and its angle β to the z -axis (β relates to θ by $\theta = \pi/2 + \beta$). Thus the energy dissipated $\Delta\varepsilon(h, \beta) = \int_0^\tau \frac{dw}{dt} dt$ during τ is also a function of h and β . For $h \gg 1$, the above isotropic solution is good because the magnetic anisotropy can be neglected. Under the limit, $\Delta\varepsilon$ is $2h\{1/[1 + \tan^2(\beta/2 + \pi/4)e^{-2\alpha\pi}] - 1/[1 + \tan^2(\beta/2 + \pi/4)]\}$. The energy difference $\Delta E(h, \beta)$ between A and B is $2h \sin \beta$. Therefore, a ballistic path must satisfy $\Delta\varepsilon = \Delta E$ (a necessary condition but not a sufficient one). Due to the symmetric reason, one needs to consider only $\beta \in (0, \pi/2)$. Without energy dissipation, the only solution is $\beta = 0$ and any h larger than certain minimal value. With large field ($h \gg 1$) and energy dissipation ($\alpha \neq 0$), the approximate solution is $\tan(\beta/2 + \pi/4) = e^{\alpha\pi/2}$, the same as the isotropic solution $\tan(\theta/2) = e^{\alpha\pi/2}$. For $\alpha \neq 0$ and $k_2 \neq 0$, we cannot solve $\Delta\varepsilon = \Delta E$ analytically. The field configuration of the ballistic connection between A and B was found numerically. The results were displayed as in Fig. 1.7.

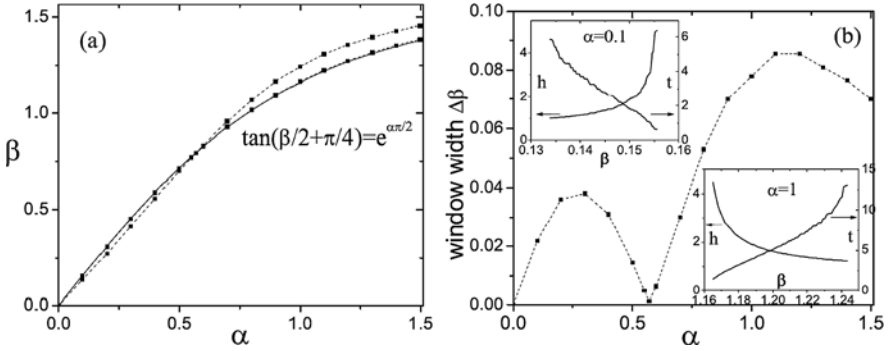


Fig. 1.7 Ballistic reversal for magnetic anisotropy $k_2 = 2$ and $k_4 = 0$. (a) The upper and lower bounds of β as a function of damping constant α . The solid line is $\tan(\beta/2 + \pi/4) = e^{\alpha\pi/2}$. (b) The window width $\Delta\beta$ vs. α . Insets: The magnetic field and the corresponding reversal time as a function of β in the ballistic direction window. $\beta \in (0.134, 0.156)$ for $\alpha = 0.1$ (upper left), $\beta \in (1.165, 1.243)$ for $\alpha = 1$ (lower right). The dashed lines are used to guide eyes

Surprisingly, the field can be applied in a range of direction, i.e., a direction window. Given β in this direction window, h is uniquely determined. Both the lower and the upper bounds of this β -window increase with the damping constant. Figure 1.7a is the plot of the upper and the lower bounds of β as a function of α . The solid line is $\tan(\beta/2 + \pi/4) = e^{\alpha\pi/2}$, which is indeed one bound of the window. The width of the window depends both on the damping constant and the magnetic anisotropy. At the zero and the infinite damping constant, the width is zero. The width is also zero in the absence of magnetic anisotropy as indicated by the exact solution given earlier. Thus, the width is expected to oscillate with α for a given

magnetic anisotropy. This oscillation was indeed observed in numerical calculations as shown in Fig. 1.7b for $k_2 = 2, k_4 = 0$. The upper-left inset of Fig. 1.7b is the field and the corresponding reversal time in the direction window for $\alpha = 0.1$ and $k_2 = 2, k_4 = 0$. In this particular case, β is between 0.134 and 0.156. One sees that h increases while the reversal time decreases with β . The similar plot for $\alpha = 1$ is shown in the lower-right inset of Fig. 1.7b. Opposite to the case of small $\alpha (= 0.1)$, h decreases and the reversal time increases with β . Thus one should compare the lower bound for $\alpha < 0.57$ and the upper bound for $\alpha > 0.57$ with $\tan(\beta/2 + \pi/4) = e^{\alpha\pi/2}$ since it is expected to be exact for $h \rightarrow \infty$ when the magnetic anisotropy can be neglected. An excellent agreement was shown in Fig. 1.7a. Figure 1.7b is the window width $\Delta\beta$ as a function of α . Our numerical results indicate that the perpendicular configuration employed in the current experiments [14, 15] cannot achieve a fully ballistic reversal. It should be pointed out that the above results are for the precise ballistic magnetization reversal. As we mentioned early, other field can also switch magnetization if one will also like to use the ringing effect at certain stages during the reversal process.

1.4 Macro-spin Reversal with a Time-Dependent Magnetic Field

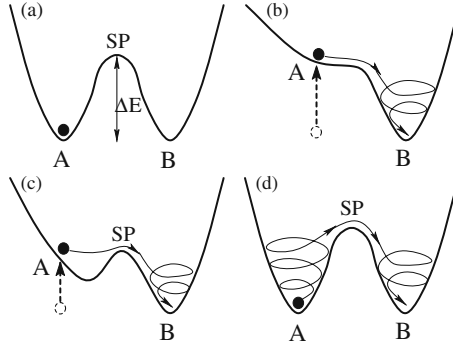


Fig. 1.8 Energy surface of a uniaxial magnetic particle in various schemes. *SP* denotes the saddle point between two minima. **(a)** In the absence of magnetic fields: *A* and *B* are the two minima, separated by a potential barrier ΔE . **(b)** At the SW-limit: Target state *B* is the only minimum. **(c)** Precessional magnetization reversal: The particle energy at *A* is higher than that at *B* so that it can pass through *SP* so that it can pass through *SP* under its own dynamics. **(d)** New strategy: Time-dependent fields pump the energy into a Stoner particle so that the particle climbs over the potential barrier to reverse its magnetization

In order to show that the magnetization reversal by a time-depeneent external magnetic field is qualitatively different from that by a constant field, it is useful to consider the energy change rate when $a_l = 0$. From Eq. (1.13), one on show [21]

$$\frac{dw}{dt} = -\frac{\alpha}{1 + \alpha^2} \left| \vec{m} \times \vec{h}_t \right|^2 - \vec{m} \cdot \dot{\vec{h}}, \quad (1.22)$$

where $\dot{\vec{h}}$ is the time derivative of \vec{h} . If the external field is time independent, the second term on the RHS vanishes, and hence the energy will always decrease. In other words, a constant field cannot be energy source. Conversely, a time-dependent field could supply energy to a particle. According to Eq. (1.22), the second term on the RHS can be either positive or negative depending on the relative direction of \vec{m} and $\dot{\vec{h}}$. This second term can even be larger than the first one so that the particle's energy increases during its motion. In other words, a time-dependent magnetic field can be an energy source such that the particle can constantly obtain energy from the field and reach its target state. This provides new ways to reverse a magnetization. Pictorially, one can view different reversal strategies in Fig. 1.8. In the absence of magnetic fields, two energy minima (points *A* and *B* in Fig. 1.8a), separated by a potential barrier ΔE , are along the easy axis of a magnetic particle. At the SW-limit, the original minimum near the initial state *A* disappears (Fig. 1.8b), and the particle will end up at its unique minimum near the target state *B*. In the precessional reversal as illustrated in Fig. 1.8c, magnetization reversal may occur when the particle energy at *A* is higher than the saddle point *SP*. New strategies are to pump energy into a Stoner particle so that the particle can climb over the potential barrier to reverse its magnetization as illustrated in Fig. 1.8d.

1.4.1 Strategy I: Field Following the Magnetization Motion

$-\vec{m} \cdot \dot{\vec{h}}$ is a maximum when \vec{m} and $\dot{\vec{h}}$ are in the opposite direction. From $|\vec{m}| = 1$, it is known that \vec{m} and $\dot{\vec{m}}$ are orthogonal to each other, which leads to $\vec{m} \cdot \dot{\vec{m}} = -\dot{\vec{m}} \cdot \vec{m}$. The second term on the RHS of Eq. (1.22) is the maximum when $\vec{h} = h_0 \dot{\vec{m}} / |\dot{\vec{m}}|$ for a fixed h_0 . Then, from Eqs. (1.13) to (1.22), the maximal rate of energy increase is

$$\frac{dw}{dt} = \frac{|\vec{m} \times \vec{h}_t|}{\sqrt{1 + \alpha^2}} \left(h_0 - \frac{\alpha}{\sqrt{1 + \alpha^2}} |\vec{m} \times \vec{h}_t| \right). \quad (1.23)$$

It should be highlighted that $\dot{\vec{h}}$ is only well defined when $\dot{\vec{m}} \neq 0$. Thus, in a numerical calculation, some numerical difficulties will exist when the system is near the extremes or the saddle points. Special care must be taken at these points.

The field of magnitude h_0 noncollinear with the magnetization was applied to drive the system out of its initial minimum. Fluctuations may also drive the system out of the minimum, but fluctuations are inefficient. When the system is out of the minimum and $\dot{\vec{m}} \neq 0$, a time-dependent field $\vec{h} = h_0 \dot{\vec{m}} / |\dot{\vec{m}}|$ is applied such that $\dot{w} > 0$. The system will climb the energy landscape from the bottom. When the system energy is very close to the saddle point, the field of magnitude h_0 can be rotated to noncollinear with the magnetization, say $\pi/4$ to the direction of the target state so that problems of $\dot{\vec{m}} = 0$ are avoided and the system can move closer to the target state. When the system has overcome the potential barrier between the initial and target state and stays inside the basin of the target state, the field can be turned off or applied in the opposite direction to the motion of the magnetization,

i.e., $\vec{h} = -h_0 \dot{\vec{m}} / |\dot{\vec{m}}|$. In the first case, the system will reach the target state through the ringing motion caused by the energy dissipation, often due to the spin–lattice relaxation. In the second case, the system will move faster toward the target state because both terms on the RHS of Eq. (1.22) will be negative, resulting in a faster energy release from the particle.

This strategy is schematically illustrated in Fig. 1.8d. The particle first spins out of its initial minimum by extracting energy from the field, and then spins into the target state by both energy dissipation and energy release (to the field). Since the energy gain from the field is partially compensated by the energy dissipation during the spinning-out process while both the field and the damping consume energy in the spinning-in motion, the particle moves out of its initial minimum slowly in comparison with its motion toward the target state.

For simplicity, consider the case of a uniaxial magnetic anisotropy with the easy axis lying along the x-axis whose magnetic anisotropy is $w(\vec{m}, \vec{h})$,

$$w(\vec{m}, \vec{h}) = -\frac{1}{2}km_x^2 - m_x h_x - m_y h_y - m_z h_z, \quad (1.24)$$

where h_x , h_y , and h_z are the applied magnetic fields along x-, y-, and z-axis, respectively. $k > 0$ is the parameter measuring the strength of the anisotropy. To find the minimal switching field for the uniaxial anisotropy of Eq. (1.24), one notes from Eq. (1.14) (with $a_I = 0$) that $\dot{\vec{m}}$ is linear in the magnetic field, and each field generates two motions for \vec{m} . The first one is a precession around the field, and the second one toward the field. Under the influence of the internal field (along the x-axis) and of the applied field $\vec{h} = h_0 \dot{\vec{m}} / |\dot{\vec{m}}|$, the system evolves into a steady precession state for a small h_0 because the precession motion due to the applied field can exactly cancel the damping motion due to the internal field. The net motion (sum of precession around the internal field and damping motion due to the applied field) is a precession around the x-axis (easy axis). In this motion, the energy loss due to damping and the energy gain from the time-dependent external field are equal. The balance equation is

$$h_0 - k\alpha \cos \eta \sin \eta = 0, \quad (1.25)$$

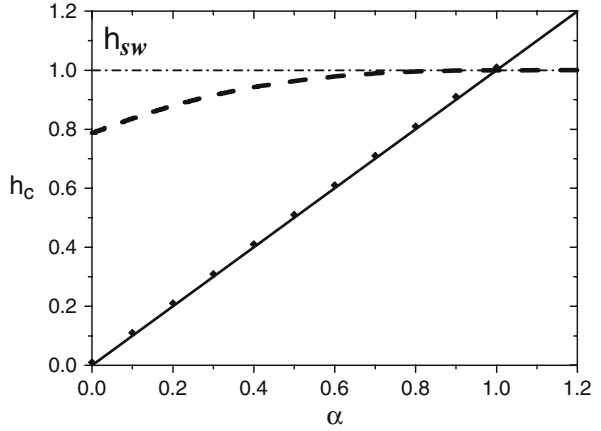
where η is the angle between the magnetization and the x-axis. The initial state is around $\eta = 0$, any stable precession motion must be destroyed in order to push the system over the saddle point at $\eta = \pi/2$. Since Eq. (1.25) has solutions only for $h_0 \leq \alpha k/2$, the critical field is

$$h_c = \alpha k/2. \quad (1.26)$$

It is of interest to note that the minimal reversal field is proportional to the damping constant, and approach zero when the damping constant goes to zero irrespective

of how large the magnetic anisotropy. For an arbitrary magnetic anisotropy, it may not be possible to find the analytical expression for the minimal reversal field and should thus use numerical calculations. To demonstrate that this can indeed be done numerically, a calculation for the magnetic anisotropy of Eq. (1.24) has been performed. The result of the minimal reversal field vs. damping constant α is plotted in Fig. 1.9. For comparison, the minimal reversal field for a time-independent magnetic field laying at 135° from the x-axis has been plotted. As it was explained in Reference [21], the minimal reversal field is smaller than the SW-limit for a small damping constant $\alpha < \alpha_c$ (which is 1 for the model given by Eq. (1.24)) and equals to the SW-limit for $\alpha > \alpha_c$. It is clear that the new strategy is superior to that of SW or precessional reversal scheme only for $\alpha < 1$, and it is worse for larger α .

Fig. 1.9 The minimal reversal field (in unit $k/2$) vs. the damping constant. The diamond symbols are the numerical results of the new strategy for the uniaxial model of Eq. (1.24). The solid curve is the analytical results. For comparison, the dashed line is the minimal reversal field under a constant field 135° to the x-axis for the same magnetic anisotropy



To see the type of field to be used in this new strategy, the trajectory of the system is numerically calculated and the time-dependent magnetic field is recorded. The results for $k = 2$, $\alpha = 0.1$, and $h_0 = 0.11 > h_c$ are given in Fig. 1.10. Figure 1.10a is the phase flow of the system starting from a point very close to the left minimum. As explained early, the particle moves many turns in the left half of the phase plane before it crosses the potential barrier (the saddle point on the middle line), while it moves toward the right minimum (the target state) much faster (with fewer turns). Figure 10(b–d) are the corresponding time dependence of x-, y-, and z-components of the magnetic field. The oscillatory nature of h_y and h_z reflects the spinning motion around minima. In general the spinning periods along different paths vary. Thus the time-dependent magnetic field contains many different frequencies as can be seen from the Fourier transform of $h_i(t)$, $i = x, y, z$ shown in the insets of Fig. 1.10(b–d). For Co-film parameters of $M_S = 1.36 \times 10^6 \text{ A/m}$ [14], the time unit is approximately $(\gamma M_S)^{-1} = 3.33 \text{ ps}$. Correspondingly, the field consists of circularly polarized microwaves of about 100 GHz .

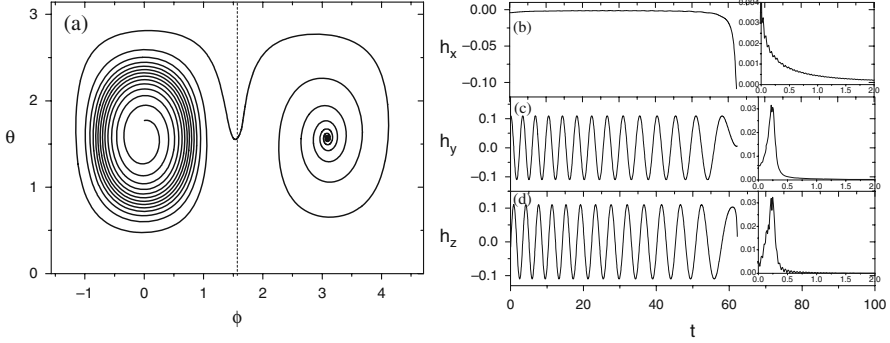


Fig. 1.10 (a) The phase flow under the new strategy with $k = 2$, $\alpha = 0.1$, and $h_0 = 0.11$. Just as illustrated in Fig. 1.8(d), the phase flow shows a slow spin-out motion near the initial state and a fast spin-in motion near the target state. (b–d) The time-dependent reversal field with the same parameter as that in (a). Insets: The corresponding Fourier transforms

1.4.2 Strategy II: Synchronizing the Magnetization Motion with a Circularly Polarized Microwave

Another way to utilize Eq. (1.22) is to *synchronize* the magnetization motion with a circularly polarized microwave. *Synchronization* is a general phenomenon in nonlinear dynamics [39]. Since a magnetization in the absence of a damping will precess around its easy axis, the magnetization motion should be easily synchronized with a circularly polarized microwave near the FMR frequency and propagating along the easy axis. After the synchronization, the magnetization starting from its initial minimum obtains energy from the microwave. The magnetization reversal is achieved if the synchronized state can go over the saddle point and into the basin of the target state. A nonlinear dynamic system under an external periodic field may undergo a non-periodic motion other than synchronization [39]. In general, the reversal criterion is *The magnetization is reversed if the system can cross the saddle point.*

For the uniaxial particle of Eq. (1.24), one can use $k/2$ as the field scale (set to 1). Under a circularly polarized microwave of amplitude h_0 and frequency ω

$$\vec{h}(t) = h_0[\cos(\omega t)\hat{y} + \sin(\omega t)\hat{z}], \quad (1.27)$$

synchronized motion is

$$\vec{m}(t) = \cos \eta \hat{x} + \sin \eta [\cos(\omega t + \varphi)\hat{y} + \sin(\omega t + \varphi)\hat{z}], \quad (1.28)$$

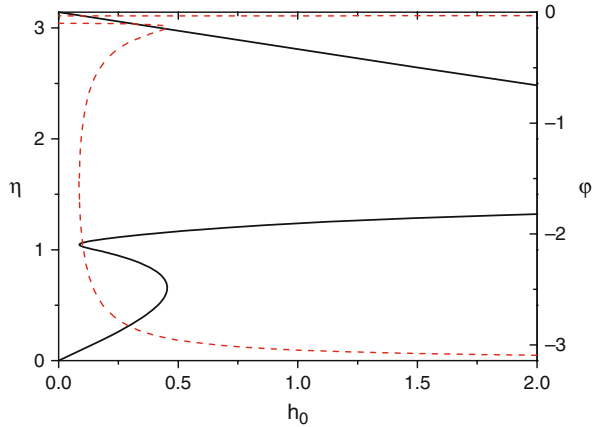
where η is the precessional angle between \vec{m} and the x-axis. φ is the *locking phase* in the synchronized motion. Substitute Eqs. (1.24), (1.27), and (1.28) into Eq. (1.14) with $a_I = 0$, η and φ satisfy

$$\sin \eta \sqrt{\alpha^2 \omega^2 + (2 - \omega / \cos \eta)^2} = h_0, \quad (1.29)$$

$$\sin \varphi = -\alpha \omega \sin \eta / h_0, \quad (1.30)$$

where $\eta \in [0, \pi]$. For fixed (h_0, ω, α) , η and φ may have multiple solutions. As illustrated in Fig. 1.11, the solutions of η (solid lines) are plotted as a function of h_0 for $\omega = 1$ and $\alpha = 0.1$. The dashed lines denote the corresponding φ . Multiple solutions of η, φ are evident. For example, there are four solutions of η when $h_0 \in [0.09, 0.45]$. Numerically, it can be shown that two solutions around $\eta = 1$ are unstable, while the other two near $\eta = 0, \pi$ are stable. Thus, the system shall eventually end up at one of the two stable solutions. Which one the system will choose depends on the initial condition. For a given initial condition, the system picks the solution near $\eta = \pi$ (magnetization reversed) when h_0 is larger than a critical value called the minimal switching field.

Fig. 1.11 Graphic demonstration of multiple synchronization solutions. The solid lines are from Eq. (1.29) and the dashed lines are from Eq. (1.30). The graph is plotted at $\alpha = 0.1$ and $\omega = 1$



A nonlinear dynamic system under an external periodic field may undergo a non-synchronized motion. Unfortunately, a non-synchronized motion is, in general, hard to define analytically. Usually, reliance must be placed on the numerical method. In terms of the LLG equation under a circularly polarized microwave of Eq. (1.15), it is straight forward [21] to calculate numerically $\vec{m}(t)$ starting from $\vec{m}(0) = \hat{x}$. The upper inset of Fig. 1.12 is the trajectory of $\vec{m}(t)$ after long time in $m_x m_y m_z$ space for $h_0 = 0.35$, $\omega = 1$, and $\alpha = 0.1$. A simple closed loop in a plane parallel to the yz-plane indicates that this is a synchronized motion. Alternatively, the lower right inset of Fig. 1.12 is the long-time trajectory of $\vec{m}(t)$ for $h_0 = 0.35$, $\omega = 1.2$, and $\alpha = 0.1$. Its motion is very complicated, corresponding to a non-synchronized

motion. It is found that whether the motion is synchronized or not is sensitive to the microwave frequency. For example, all motions for $\omega = 1$ are synchronized while both synchronized and non-synchronized motions are possible for $\omega = 1.2$. The motion is non-synchronized for h_0 in the range of $[0.27, 0.42]$ while it is synchronized for other values of h_0 . Figure 1.12 is m_x of synchronized motions as a function of h_0 for $\omega = 1$ and 1.2.

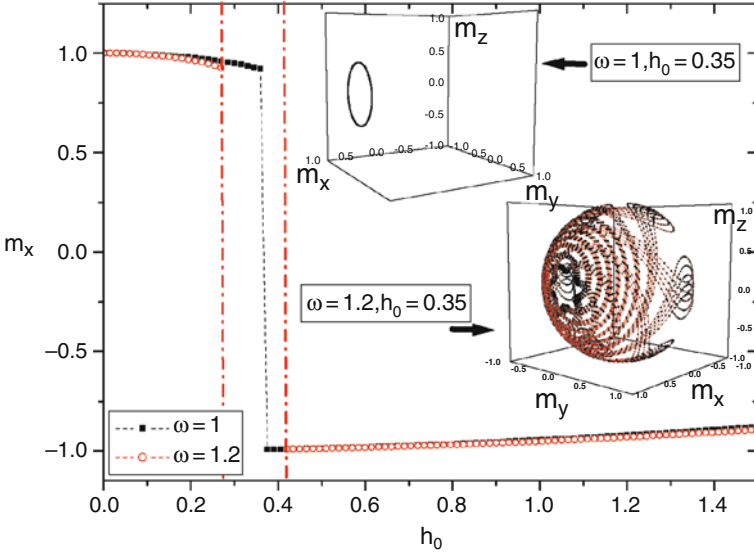


Fig. 1.12 m_x of synchronized motion vs. h_0 for $\alpha = 0.1$ and $\omega = 1$ (filled squares); 1.2 (open circles). Non-synchronized motion when $h_0 \in [0.27, 0.42]$ (between two dash-dotted lines) is found for $\omega = 1.2$. Upper inset: Long-time trajectory of $\vec{m}(t)$ for $\omega = 1$ and $h_0 = 0.35$. Lower inset: Long-time trajectory of $\vec{m}(t)$ for $\omega = 1.2$ and $h_0 = 0.35$

Using the reversal criterion given earlier, the minimal switching field h_c in Fig. 1.12 is about 0.375 for $\omega = 1$ because m_x in the synchronized motion is negative when $h_0 > 0.375$. For $\omega = 1.2$, the minimal switching field takes a value at which the magnetization undergoes a non-synchronized motion. Numerically, it can be shown that \vec{m} crosses the yz -plane when $h_0 \geq 0.285$. Thus, the minimal switching field is determined as $h_c = 0.285$ for $\omega = 1.2$. The reason that the value of the minimal switching field is so sensitive to the microwave frequency is because a switching field, as illustrated in Fig. 1.8d, needs to overcome the dissipation which is related to the motion of the magnetization. To reveal the frequency dependence of the minimal switching field, Fig. 1.13 shows the minimal switching field h_c vs. the microwave frequency ω for various $\alpha = 0, 0.001, 0.1, 1, \text{ and } 1.5$. $\omega = 0$ corresponds to the case of a static field along the y -axis. The curve of $\alpha = 0$ intersects the h_c -axis at $h_c = 1$ which agrees with the exact minimal switching field $h_c = 1$ [21]. The intersections of all other curves of $\alpha \neq 0$ are the same as those with a static field [12,21]. When $\alpha \geq 1$, it becomes the SW-limit $h_c = 2$. For a given α , Fig. 1.13 shows the existence

of an optimal microwave frequency, ω_c , at which the minimal switching field is the smallest. Far from the optimal frequency, the minimal switching field can be larger than the SW-limit. The inset of Fig. 1.13 is ω_c vs. α . The optimal frequency is near the natural precessional frequency at which the dissipation is a maximum.

Fig. 1.13 The minimal switching field h_c vs. ω for various damping constant $\alpha = 0; 0.001; 0.1; 1; \text{ and } 1.5$. Inset: The optimal frequency ω_c vs. α

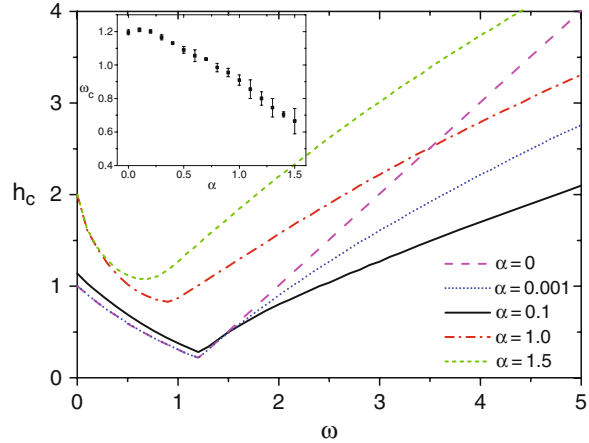
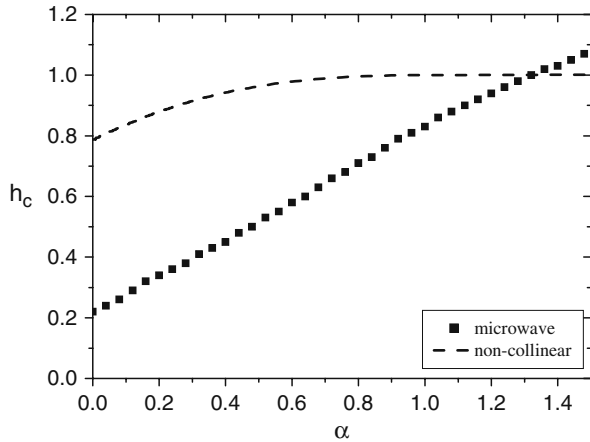


Fig. 1.14 h_c vs. α for the uniaxial model of Eq. (1.24) under different reversal schemes. Square symbols are the numerical results of h_c at the optimal frequency in the present strategy with a circularly polarized microwave. The dashed line is h_c under a non-collinear static field of 135° to the easy axis. It saturates to the SW-limit beyond $\alpha = 1$ [21]



The minimal switching field is lowest at the optimal frequency ω_c . The square symbols in Fig. 1.14 are the minimal switching fields at ω_c . They are approximately linear in α , $h_c \approx 0.23 + 0.58\alpha$. This approximate linear relation is related to the fact that the damping (field) is proportional to α . For comparisons, the minimal switching fields of a precessional magnetization reversal under a static magnetic field and the SW-limit are also plotted in Fig. 1.14. It can be seen that for small

damping, the smallest (at the optimal frequency) minimal switching field can be much smaller than that in the precessional magnetization reversal.

1.4.3 Theoretical Limits of Switching Field/Current and Optimal Reversal Pulses

After examining the above two strategies based on Eq. (1.22), it is natural to ask the question whether there exists a theoretical limit in the critical switching field out of all possible reversal magnetic field pulses. There are infinite number of paths that connect the initial and the target states. Each of these paths could be used as a magnetization reversal path. We shall show, at least for the uniaxial Stoner particles, that there exists [29] indeed an optimal path along which the critical switching field is the smallest. Let $\vec{h}^{L,s}(t)$ be the magnetic field pulse of design s along magnetization reversal route L . We can define the following quantities.

Definition of switching field $H^{L,s}$: The switching field $H^{L,s}$ of design s along route L is defined to be the largest magnitude of $\vec{h}^{L,s}(t)$ for all t , i.e., $H^{L,s} = \max \left\{ \left| \vec{h}^{L,s}(t) \right|; \forall t \right\}$.

Definition of minimal switching field H^L on reversal route L : The minimal switching field H^L along route L is defined to be the smallest value of $H^{L,s}$ for all possible designs s that will force the magnetization to move along L , i.e., $H^L = \min \{ H^{L,s}; \forall s \}$.

Definition of theoretical limit of minimal switching field H_c : The switching field limit H_c is defined as the smallest value of H^L out of all possible routes, i.e., $H_c = \min \{ H^L; \forall L \}$.

Claim 1: For a given uniaxial magnetic anisotropy of $w(\cos \theta)$, the theoretical limit of the minimal switching field is given by $H_c = \frac{\alpha}{\sqrt{1+\alpha^2}} Q$, where $Q = \max \{ f(\cos \theta) \sin \theta \}$, $\theta \in [0, \pi]$ and $f(\cos \theta) = -\frac{\partial w(\cos \theta)}{\partial (\cos \theta)}$.

Proof: To find the lowest possible switching field, it should be noticed that field along the radius direction h_r of an external field does not appear in Eq. (1.15) when $a_l = 0$. Thus one can lower the switching field by setting $h_r = 0$, and the magnitude of the external field is $h = \sqrt{h_\theta^2 + h_\phi^2}$. $\dot{\theta}$ and $\dot{\phi}$ are fully determined by h_θ and h_ϕ and vice versa. It can be shown that h^2 can be expressed in terms of θ , ϕ , $\dot{\theta}$, and $\dot{\phi}$.

$$g \equiv h^2 = (1 + \alpha^2)\dot{\theta}^2 + 2\alpha f(\cos \theta) \sin \theta \dot{\theta} + (\alpha \sin \theta \dot{\phi})^2 + \sin^2 \theta [\dot{\phi} - f(\cos \theta)]^2. \quad (1.31)$$

Here $g(\dot{\theta}, \theta, \dot{\phi})$ does not depend explicitly on ϕ for a uniaxial model.

In order to find the minimum of g , it can be shown that ϕ must obey the following equation:

$$\dot{\phi} = f(\cos \theta)/(1 + \alpha^2), \quad (1.32)$$

which is from $(\partial g / \partial \dot{\phi})|_{(\dot{\theta}, \theta)} = 0$ and $(\partial^2 g / \partial \dot{\phi}^2)|_{(\dot{\theta}, \theta)} > 0$.

Equation (1.32) is a necessary condition for the smallest minimal switching field. This can be understood as follows. Assume H_c is the minimal switching field along reversal path L described by $\theta(t) = \theta_1(t)$ and $\phi(t) = \phi_1(t)$ (i.e., H_c is the maximum magnitude of the external field that generates the motion of $\theta_1(t)$ and $\phi_1(t)$). If $\phi_1(t)$ does not satisfy Eq. (1.32), then one can construct another reversal path L^* specified by $\theta(t) = \theta_1(t)$ and $\phi(t) = \phi_2(t)$, where $\phi_2(t)$ satisfies Eq. (1.32). Because $\theta(t)$ and $\dot{\theta}$ are exactly the same on both paths L and L^* at an arbitrary time t , the values of $g(t)$ shall be smaller on L^* than those on L at any t . Thus, the maximum $g^* = (H_c^*)^2$ of g on L^* will be also smaller than that $(H_c^c)^2$ on L , i.e., $H_c^* < H_c$. But this is in contradiction with the assumption that H_c is the theoretical limit of the minimal switching field. Hence, $\phi(t)$ must obey Eq. (1.32) on the optimal path that generates the smallest switching field, H_c .

Substituting Eq. (1.32) into Eq. (1.31), we have

$$h^2 = \left[\sqrt{1 + \alpha^2} \dot{\theta} + \frac{\alpha f(\cos \theta) \sin \theta}{\sqrt{1 + \alpha^2}} \right]^2. \quad (1.33)$$

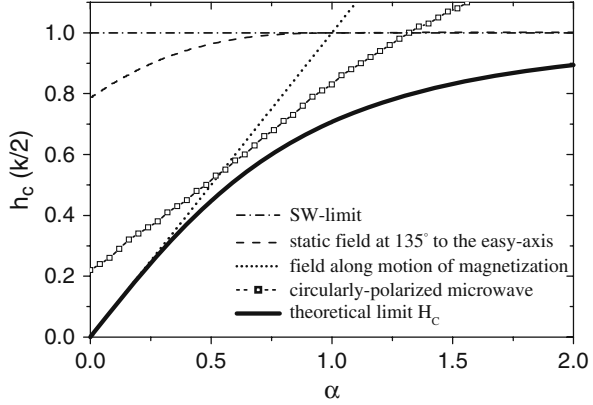
In order to complete a magnetization reversal, the trajectory must pass through all values of $0 \leq \theta \leq \pi$. In particular, it must pass through whatever value of θ in that range maximizes $f(\cos \theta) \sin \theta$ on that range. At that maximizing value of θ , the trajectory must be such that θ is non-decreasing, that is, $\dot{\theta} \geq 0$, so that the trajectory is proceeding in the correct direction. Substituting these constraints into Eq. (1.5), we see that at that point in the trajectory, h must be at least $\alpha Q / \sqrt{1 + \alpha^2}$, where $Q = \max \{ f(\cos \theta) \sin \theta \}$, $\theta \in [0, \pi]$ **Q.E.D.**

To have a better picture about what this theoretical limit H_c is, we consider a well-studied uniaxial model, $w(\vec{m}) = -km_z^2/2$, or $f = k \cos \theta$. It is easy to show that the largest h is at $\theta = \pi/4$ so that $Q = k/2$, and

$$H_c = \frac{\alpha}{\sqrt{1 + \alpha^2}} \frac{k}{2}. \quad (1.34)$$

At small damping, H_c is proportional to the damping constant that is what we obtained in strategy I. At the large damping, H_c approaches the SW-limit [21] when a non-collinear static switching field is 135° from the easy axis. The solid curve in Fig. 1.15 is H_c vs. α . For comparison, the minimal switching fields from other reversal schemes are also plotted. The dotted line is the minimal switching field of strategy I when the applied field is always parallel to the motion of the magnetization [29]. The curve in square symbols is the minimal switching field when a circularly polarized microwave at optimal frequencies is applied [29]. The dashed line is minimal switching field under a non-collinear static field of 135° to the easy axis. It saturates to the SW field beyond α_c [12, 21].

Fig. 1.15 The switching field h_c vs. damping constant α under different reversal schemes



Although the theoretical limit of the switching field is academically important because it provides a low bound to the switching field so that one can use the theorem to evaluate the quality of one particular strategy, a design using a field at the theoretical limit would not be interesting from a practical point of view because the switching time would be infinite long. Thus, it is more important to design a reversal path and a field pulse such that the reversal time is the shortest when the field magnitude H ($H > H_c$) is given. An exact result is given by the following theorem.

Claim 2: Suppose a field magnitude H does not depend on time and $H > H_c$. The optimal reversal path (connects $\theta = 0$ and $\theta = \pi$) that gives the shortest switching time is the magnetization trajectory generated by the following field pulse $\vec{h}(t)$,

$$\begin{aligned} h_r(t) &= 0, \\ h_\theta(t) &= \alpha H / \sqrt{1 + \alpha^2}, \\ h_\phi(t) &= H / \sqrt{1 + \alpha^2} = h_\theta / \alpha. \end{aligned} \quad (1.35)$$

Proof: The reversal time from A to B (Fig. 1.2b) is $T \equiv \int_0^\pi d\theta / \dot{\theta}$. According to Eq. (1.15), one needs $(h_\phi + \alpha h_\theta)$ to be as large as possible in order to make $\dot{\theta}$ maximal at an arbitrary θ . Since $H^2 = h_r^2 + h_\theta^2 + h_\phi^2$, one has the following identity:

$$(1 + \alpha^2)H^2 = (1 + \alpha^2)h_r^2 + (h_\phi + \alpha h_\theta)^2 + (h_\theta - \alpha h_\phi)^2. \quad (1.36)$$

Thus, $(h_\phi + \alpha h_\theta)$ reaches the maximum of $\sqrt{1 + \alpha^2}H$ when $h_r = 0$ and $h_\theta = \alpha h_\phi$, which lead to Eq. (1.35). **Q.E.D.**

Under the optimal design of (1.35), $\phi(t)$ and $\theta(t)$ satisfy, respectively, Eq. (1.32) and

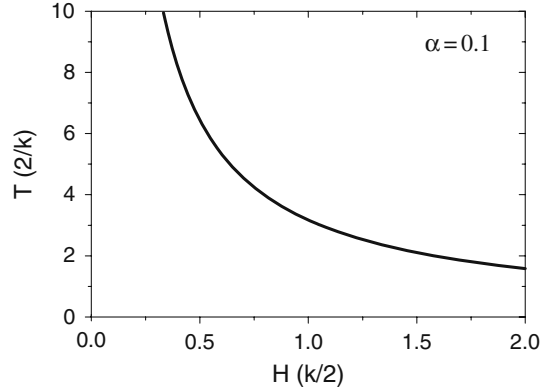
$$\dot{\theta} = H / \sqrt{1 + \alpha^2} - \alpha f(\cos \theta) \sin \theta / (1 + \alpha^2). \quad (1.37)$$

For uniaxial magnetic anisotropy $w(\vec{m}) = -km_z^2/2$, it is straightforward to integrate Eq. (1.37) and to find the reversal time T ,

$$T = \frac{2}{k} \frac{(1 + \alpha^2)\pi}{\sqrt{4(1 + \alpha^2)H^2/k^2 - \alpha^2}}. \quad (1.38)$$

In the weak damping limit $\alpha \rightarrow 0$, $T \approx \pi/H$ while in the large damping limit $\alpha \rightarrow \infty$, $T \approx \frac{\alpha\pi}{\sqrt{H^2 - k^2/4}} \rightarrow \infty$. For the large field $H \rightarrow \infty$, $T \approx \sqrt{1 + \alpha^2}\pi/H$, inversely proportional to the field strength. Thus, it is better to make α as small as possible. Then the critical field is low, and the speed is fast ($T \sim \pi/H$). Figure 1.16 shows the field dependence of the switching time for $\alpha = 0.1$, where T and H are in the units of $2/k$ and $k/2$, respectively.

Fig. 1.16 The field dependence of T under the optimal field pulse Eq. (1.35) for $\alpha = 0.1$. The field is in the unit of $k/2$, and the unit for time is $2/k$



The above results can also be generalized to the current-induced magnetization reversal where $a_I \neq 0$ and $\vec{h} = 0$. Assume $C^{L,q}(t)\hat{s}(t)$ be the polarized electric current pulse of design q along magnetization reversal route L and $C^{L,q}(t)$ be the current amplitude, similar to the field case, three interesting quantities can be defined:

Switching current $I^{L,q}$: The switching current $I^{L,q}$ of design q along route L is defined to be the maximum of $|C^{L,q}(t)|$ for all t , i.e., $I^{L,q} = \max \{|C^{L,q}(t)|; \forall t\}$.

Critical current I^L of reversal route L : The critical current I^L along route L is defined to be the smallest value of $I^{L,q}$ for all possible designs q that will force the magnetization to move along L , i.e., $I^L = \min \{I^{L,q}; \forall q\}$.

Theoretical limit of critical currents I_c : The critical current limit I_c is defined as the smallest value of I^L out of all possible routes, i.e., $I_c = \min \{I^L; \forall L\}$.

Claim 3: Under the constraint of the constant current magnitude and constant polarization degree P , the optimal time-dependent polarization direction of the current for a uniaxial particle of $w(\cos \theta)$ is

$$\begin{aligned} s_r^* &= \frac{(1+P)^3}{16P^{3/2}-3(1+P)^3} \\ s_\phi^* &= -\alpha s_\theta^* = \frac{\alpha}{\sqrt{1+\alpha^2}} \sqrt{1-s_r^{*2}} \end{aligned} \quad (1.39)$$

such that the reversal time from $\theta = 0$ to $\theta = \pi$ is the shortest.

Proof: According to Eq. (1.15), different $\hat{s}(t)$ generates different angular velocities for θ and ϕ , and the magnetization reversal time from $\theta = 0$ to $\theta = \pi$ is given by $T \equiv \int_0^\pi d\theta / \dot{\theta}$. In order to find the optimal $\hat{s}(t)$ that minimizes T , one only needs $a_I(\alpha s_\phi - s_\theta)$ or $g(P, s_r)(\alpha s_\phi - s_\theta)$ to be maximum such that $\dot{\theta}$, according to Eq. (1.15), will be the largest at any θ . This observation is important, and it can be applied to other function forms of g . Because $s_r^2 + s_\theta^2 + s_\phi^2 = 1$, the maximum of $g(P, s_r)(\alpha s_\phi - s_\theta)$ can be obtained from the standard Lagrange multiplier method in which one introduces $F \equiv g(P, s_r)(\alpha s_\phi - s_\theta) - \lambda(s_r^2 + s_\theta^2 + s_\phi^2)$. By setting the partial derivatives of F with respect to s_i ($i = r, \theta, \phi$) to zeros, the maximum of $g(P, s_r)(\alpha s_\phi - s_\theta)$ is

$$\left[g(P, s_r)(\alpha s_\phi - s_\theta) \right]_{\max} = \sqrt{1 + \alpha^2} G(P), \quad (1.40)$$

where

$$G(P) = g(P, s_r^*) \sqrt{1 - s_r^{*2}} \quad (1.41)$$

and the optimal \hat{s}^* is given by Eq. (1.39). **Q.E.D.**

Claim 4: The theoretical limit of critical currents is

$$I_c = \frac{\mu_0 e M^2 V}{\hbar G(P)} \frac{\alpha}{\sqrt{1 + \alpha^2}} Q. \quad (1.42)$$

Here $Q \equiv \max \{ f(\cos \theta) \sin \theta \}$ for $\theta \in [0, \pi]$, $f(\cos \theta) = -\frac{\partial w(\cos \theta)}{\partial (\cos \theta)}$, and $G(P)$ is given by Eqs. (1.41) and (1.39).

Proof: Under the optimal design of Eq. (1.39), $\theta(t)$ and $\phi(t)$ satisfy, respectively,

$$\dot{\theta} = \frac{\hbar I}{\mu_0 e M^2 V} \frac{G(P)}{\sqrt{1 + \alpha^2}} - \frac{\alpha f(\cos \theta) \sin \theta}{1 + \alpha^2} \quad (1.43)$$

and

$$\dot{\phi} = f(\cos \theta) / (1 + \alpha^2). \quad (1.44)$$

For the uniaxial model, the limit I_c of critical current is the smallest value of I making $\dot{\theta}$ (Eq. (1.43)) zero for certain θ . This is because $\dot{\theta}$ cannot be negative if the

magnetization of a uniaxial particle moves from $\theta = 0$ to $\theta = \pi$. The first term in Eq. (1.43) must exceed the second term due to magnetic anisotropy for all $\theta \in [0, \pi]$ in a reversal. Since Eq. (1.43) is the largest possible velocity, one has $I_c = \frac{\mu_0 e M^2 V}{\hbar G(P)} \frac{\alpha}{\sqrt{1+\alpha^2}} \max \{f(\cos \theta) \sin \theta\}$. **Q.E.D.**

It is proper to make a few remarks here. (1) According to Eq. (1.39), $s_r^* = -1$ and $s_\theta^* = s_\phi^* = 0$ when $P = 1$. Then it seems that $\dot{\theta} = 0$ at $\theta = 0$ and π according to Eq. (1.15). But this is not correct since a_I diverges at $s_r = -1$ for $P = 1$. In fact, $\dot{\theta}$ diverges under the limit of $s_r \rightarrow -1$ at $P = 1$. This peculiar feature of Slonczewski's formula (Eq. (1.12)) may be an artifact which is a subject of debate [25]. (2) The relative direction of the current polarization and the magnetization in an optimal pulse does not change with time. (3) Although the optimal \hat{s}^* appears to depend only on damping constant α and P , not on $f(\cos \theta)$, it is in fact time dependent because \hat{s} is expressed in a moving frame whose coordinate units $\hat{e}_r, \hat{e}_\theta, \hat{e}_\phi$ vary with the time. (4) From Eqs. (1.43) and (1.44), the optimal reversal route is given by

$$\frac{d\theta}{d\phi} = \frac{\alpha Q}{f(\cos \theta)} [I/I_c - f(\cos \theta) \sin \theta / Q].$$

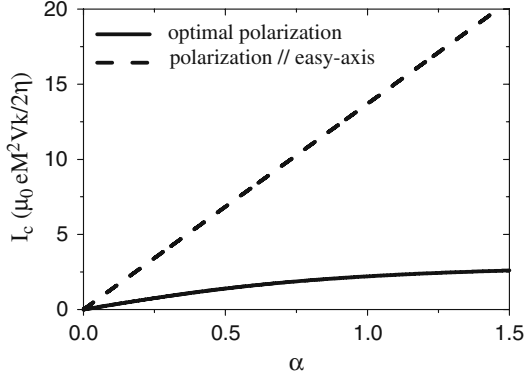
Thus, a solution passing through $\theta = 0$ and π simultaneously exists when and only when $I > I_c$. For $I < I_c$, the system undergoes a stable precession motion [24] (θ satisfies $I/I_c = f(\cos \theta) \sin \theta / Q$) even under a pulse of Eq. (1.39). The evolution of \vec{m} under the optimal polarization pulse (meaningful only for $I > I_c$) is determined by $\dot{\theta} = \alpha Q [I/I_c - f(\cos \theta) \sin \theta / Q] / (1 + \alpha^2)$ and $\dot{\phi} = f(\cos \theta) / (1 + \alpha^2)$. It is clear that magnetic anisotropy $f(\cos \theta)$ shall influence the evolution of \vec{m} which in turn influences the time dependence of \hat{s}^* . Thus, if they were to change $f(\cos \theta)$ and nothing else, the time-dependent \hat{s}^* would be different.

One notices that the derivation of I_c (Eq. (1.42)) does not require constant I and P . The result should be the same even for the time-dependent I and P as long as STT is proportional to I and g . To see how far that the best value of critical currents is from the theoretical limit in the most advanced strategy where the current polarization direction is fixed [28], let us compare it with the critical current limit of Eq. (1.42) for $w(\vec{m}) = -km_z^2/2$. The theoretical limit of critical currents from Eq. (1.42) is $I_c = \frac{\mu_0 e M^2 V}{2\hbar G(P)} \frac{\alpha k}{\sqrt{1+\alpha^2}}$. It is known [28] that the critical current for the polarization direction \hat{s} parallel to the easy axis of \vec{m} (parallel configuration) is smaller than that when \hat{s} is perpendicular to the easy axis (perpendicular configuration). The critical current in the parallel configuration for the same magnetic anisotropy is [23,28]

$$I_c = \frac{\mu_0 e M^2 V}{\hbar g(P, 1)} \alpha k. \quad (1.45)$$

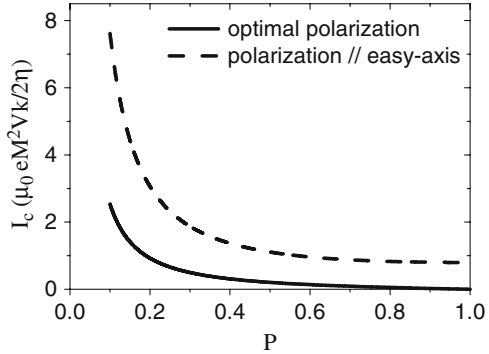
Figure 1.17 is the plot of I_c vs. damping constant α for $P = 0.4$ which is a realistic value for magnetic materials. The dashed line is of Eq. (1.45), and the solid line is the theoretical limit of the critical current which saturates to a constant at

Fig. 1.17 I_c vs. α for $P = 0.4$ and a uniaxial model of $w(\vec{m}) = -km^2/2$



large α limit. At $\alpha = 0.1$, critical current limit I_c is about one fourth of that given by Eq. (1.45), showing a large room for the improvement. The difference between Eqs. (1.42) and (1.45) depends on the degree of polarization P . Figure 1.18 is I_c vs. P at $\alpha = 0.1$. It should be pointed out that zero I_c in Eq. (1.42) at $P = 1$ is an artificial result originated from the divergence of $g(1, x)$ at $x = -1$ in the Slonczewski's theory [23]. This divergence is removed in other formulations of g [25].

Fig. 1.18 I_c vs. P at $\alpha = 0.1$. The rest of system parameters are the same as that of Fig. 1.17



The reversal time T is obtained by integrating Eq. (1.43) from $\theta = 0$ to $\theta = \pi$ (I_c is given in Eq. (1.42)),

$$T = \frac{2}{k} \frac{(1 + \alpha^2)\pi}{\alpha \sqrt{(I/I_c)^2 - 1}}. \quad (I > I_c) \quad (1.46)$$

In the weak damping limit ($\alpha \rightarrow 0$) or large current limit ($I \rightarrow \infty$), $T \propto \pi/I$. To have an idea about the order of magnitudes for the critical current limit and the time scale considered here in a realistic set-up, let us consider a Co nano-structure [28] of 3 nm thick and lateral dimension of $30 \times 60 (nm)^2$. Other parameters [28]

are $\alpha = 0.01$, $M = 1.4 \times 10^6 \text{ A/m}$, $k = 7 \times 10^4 \text{ J/m}^3$, and $P = 0.4$. Then, the theoretical limit of critical currents is about $I_c \approx 18 \mu\text{A}$ (current density of about 10^6 A/(cm)^2) compared with $80 \mu\text{A}$ from Eq. (1.45). The optimal switching time is about 360 ps for $I = 1.8 \text{ mA} > I_c$ (current density of 10^8 A/(cm)^2). This switching time is shorter than the typical experimental value of order of several nano-seconds [26, 28].

1.5 Summary

In summary, we discussed several theoretical results obtained on the fast magnetization reversal of Stoner particles. For the reversal by a static magnetic field, SW-theory is the special solution of the LLG equation in the infinite damping limit. The existence of a critical damping constant above which the SW-limit is exact is explained. In terms of ballistic reversal, the existence of a direction window is proposed. For the reversal by a time-dependent magnetic field, two new strategies were proposed based on the fact that a time-dependent magnetic field can be an energy source. One strategy is to use a field following the magnetization motion, and the other one is to use a circularly polarized microwave near the FMR frequency to synchronize the magnetization motion. Both strategies can substantially reduce the critical switching field. Furthermore, theoretical limits on the switching field, switching current, and switching time were obtained for uniaxial Stoner particles. The limits could be used as a benchmark to evaluate different reversal scheme besides other possible usages.

Acknowledgments This work is supported by UGC, Hong Kong, through RGC CERG grants #603007, 603106, 603508, and RPC07/08.SC03. We would also like to thank APS for granting us permission to use some materials in our early publications in APS journals.

References

1. W. W. Paudler, *Nuclear magnetic resonance: general concepts and applications*, (Wiley, New York, 1987).
2. R. Kitamaru, *Nuclear magnetic resonance: principles and theory*, (Elsevier, Amsterdam/New York, 1990).
3. M. H. Levitt, *Spin dynamics: basics of nuclear magnetic resonance*, (John Wiley & Sons, New York, 2001).
4. B. Hillebrands and K. Ounadjela, eds., *Spin Dynamics in Confined Magnetic Structures I & II*, (Springer-Verlag, Berlin, 2001); B. Hillebrands and A. Thiaville, eds., *Spin Dynamics in Confined Magnetic Structures III*, (Springer-Verlag, Berlin, 2006).
5. R. C. O'handley, *Modern Magnetic Materials: Principles and Applications*, (John Wiley & Sons, New York, 2000).
6. Y. Hou, S. H. Sun, C. Rong, J. P. Liu, *Appl. Phys. Lett.* 91, 153117 (2007); Y. I. Wang, Y. Li, C. Rong, and J. P. Liu, *Nanotechnology* 18, 465701 (2007); Y. Hou, Z. Xu, S. Peng, C. Rong, J. P. Liu, and S. Su, *Adv. Mater.* 19, 3349 (2007).
7. S. H. Sun, C. B. Murray, D. Weller, L. Folks, and A. Moser, *Science* **287**, 1989 (2000).
8. C. T. Black, C. B. Murray, R. L. Sandstrom, and S. H. Sun, *Science* **290**, 1131 (2000).

9. S. I. Woods, J. R. Kirtley, S. H. Sun, and R. H. Koch, *Phys. Rev. Lett.* **87**, 137205 (2001).
10. D. Zitoun, M. Respaud, M.-C. Fromen, M. J. Casanove, P. Lecante, C. Amiens, and B. Chaudret, *Phys. Rev. Lett.* **89**, 037203 (2002).
11. E. C. Stoner and E. P. Wohlfarth, *Phil. Trans. Roy. Soc. London* **A240**, 599 (1948), reprinted in *IEEE Trans. Magn.* **27**, 3475 (1991).
12. L. He, W. D. Doyle, and H. Fujiwara, *IEEE. Trans. Magn.* **30**, 4086 (1994); L. He and W. D. Doyle, *J. Appl. Phys.* **79**, 6489 (1996).
13. W. K. Hiebert, A. Stankiewicz, and M. R. Freeman, *Phys. Rev. Lett.* **79**, 1134 (1997).
14. C. H. Back, D. Weller, J. Heidmann, D. Mauri, D. Guarisco, E. L. Garwin, and H. C. Siegmann, *Phys. Rev. Lett.* **81**, 3251 (1998); C. H. Back, R. Allenspach, W. Weber, S. S. P. Parkin, D. Weller, E. L. Garwin, and H. C. Siegmann, *Science* **285**, 864 (1999). Y. Acremann, C. H. Back, M. Buess, O. Portmann, A. Vaterlaus, D. Pescia, and H. Melchior, *Science* **290**, 492 (2000).
15. H. W. Schumacher, C. Chappert, P. Crozat, R. C. Sousa, P. P. Freitas, J. Miltat, J. Fassbender, and B. Hillebrands, *Phys. Rev. Lett.* **90**, 017201 (2003).
16. T. M. Crawford, T. J. Silva, C. W. Teplin, and C. T. Rogers, *Appl. Phys. Lett.* **74**, 3386 (1999).
17. M. Bauer, J. Fassbender, B. Hillebrands, and R. L. Stamps, *Phys. Rev. B* **61**, 3410 (2000).
18. Y. Acremann, C. H. Back, M. Buess, D. Pescia, and V. Pokrovsky, *Appl. Phys. Lett.* **79**, 2228 (2001).
19. J. Miltat, G. Albuquerque, and A. Thiaville, in *Spin Dynamics in Confined Magnetic Structures I*, edited by B. Hillebrands and K. Ounadjela (Springer-Verlag, Berlin, 2001).
20. D. G. Porter, *IEEE. Trans. Magn.* **34**, 1663 (1998).
21. Z. Z. Sun, and X. R. Wang, *Phys. Rev. B* **71**, 174430 (2005); **73**, 092416 (2006); **74**, 132401 (2006); *Phys. Rev. Lett.* **97**, 077205 (2006).
22. D. Xiao, M. Tsoi, and Q. Niu, *J. Appl. Phys.* **99**, 013903 (2006).
23. J. Slonczewski, *J. Magn. Magn. Mater.* **159**, L1 (1996); L. Berger, *Phys. Rev. B* **54**, 9353 (1996).
24. J. Z. Sun, *Phys. Rev. B* **62**, 570 (2000); Z. Li and S. Zhang, *ibid.* **68**, 024404 (2003); Y. B. Bazaliy, B. A. Jones, and S. C. Zhang, *ibid.* **57**, R3213 (1998); **69**, 094421 (2004).
25. A. Brataas, Y. V. Nazarov, and G. E. W. Bauer, *Phys. Rev. Lett.* **84**, 2481 (2000); X. Waintal, E. B. Myers, P. W. Brouwer, and D. C. Ralph, *Phys. Rev. B* **62**, 12317 (2000); M. D. Stiles and A. Zangwill, *ibid.* **66**, 014407 (2002).
26. M. Tsoi, A. G. M. Jansen, J. Bass, W.-C. Chiang, M. Seck, V. Tsoi, and P. Wyder, *Phys. Rev. Lett.* **80**, 4281 (1998); E. B. Myers, D. C. Ralph, J. A. Katine, R. N. Louie, and R. A. Buhrman, *Science* **285**, 867 (1999); J. A. Katine, F. J. Albert, R. A. Buhrman, E. B. Myers, and D. C. Ralph, *Phys. Rev. Lett.* **84**, 3149 (2000).
27. Z. Li and S. Zhang, *Phys. Rev. B* **69**, 134416 (2004); W. Wetzels, G. E. W. Bauer, and O. N. Jouravlev, *Phys. Rev. Lett.* **96**, 127203 (2006).
28. J. Sun, *J. Magn. Magn. Mater.* **202**, 157 (1999); *Nature* **425**, 359 (2003); K. J. Lee, O. Redon, and B. Dieny, *Appl. Phys. Lett.* **86**, 022505 (2005); J. Manschot, A. Brataas, and G. E. W. Bauer, *ibid.* **85**, 3250 (2004); A. D. Kent, B. Ozyilmaz, and E. del Barco, *ibid.* **84**, 3897 (2004).
29. X. R. Wang and Z. Z. Sun, *Phys. Rev. Lett.* **98**, 077201 (2007).
30. M. Vomir, L. H. F. Andrade, L. Guidoni, E. Beaurepaire, and J.-Y. Bigot, *Phys. Rev. Lett.* **94**, 237601 (2005).
31. S. Murakami, N. Nagaosa, and S.-C. Zhang, *Phys. Rev. B* **69**, 235206 (2004).
32. S. Zhang and Z. Yang, *Phys. Rev. Lett.* **94**, 066602 (2005).
33. J. Shi, P. Zhang, D. Xiao, and Q. Niu, *Phys. Rev. Lett.* **96**, 076604 (2006).
34. X. R. Wang, Y. S. Zheng, and S. Yin, *Phys. Rev. B* **72**, R121303 (2005).
35. L. Landau and E. Lifshitz, *Phys. Z. Sowjetunion* **8**, 153 (1953).
36. T. L. Gilbert, *Phys. Rev.* **100**, 1243 (1955).
37. R. Kikuchi, *J. Appl. Phys.* **27**, 1352 (1956).

38. Textbooks on nonlinear physics, such as, S. H. Strogatz, *Nonlinear Dynamics and Chaos*, (Addison-Wesley, 1994).
39. Z. Z. Sun, H. T. He, J. N. Wang, S. D. Wang, and X. R. Wang, *Phys. Rev. B* **69**, 045315 (2004); X. R. Wang, J. N. Wang, B. Q. Sun, and D. S. Jiang, *Phys. Rev. B* **61**, 7261 (2000); X. R. Wang and Q. Niu, *Phys. Rev. B*, **59**, R12755 (1999).
40. P. R. Gillette and K. Oshima, *J. Appl. Phys.* **29**, 529 (1958).

Chapter 2

Core–Shell Magnetic Nanoclusters

Jinlan Wang and X.C. Zeng

Abstract Nanoclusters, aggregates of a few tens to millions of atoms or molecules, have been extensively studied over the past decades. Core–shell nanoclusters have received increasing attention because of their tunable physical and chemical properties through controlling chemical composition and relative sizes of core and shell. The magnetic core–shell nanoclusters are of particular interests because these heterogeneous nanostructures offer opportunities for developing devices and cluster-assembled materials with new functions for magnetic recording, bio, and medical applications.

The purpose of this review is to report latest progress in the experimental and theoretical studies of bimetallic magnetic core–shell nanoclusters (e.g., at least one component of the constitution is magnetic). Due to page limit, a concise survey of synthetic techniques and main experimental characterizations for magnetic properties is presented. A more detailed overview is given to previous theoretical work.

2.1 Introduction

Nanoclusters (or nanoparticles), aggregates of a few tens to millions of atoms or molecules, have attracted enormous interest from either basic science or application point of view in the past decades. From basic science point of view, nanoclusters are species intermediate in size between microscopic atoms or molecules and macroscopic bulk matter, and these may be considered as new forms of matter or superatoms that display properties very different from their molecular and bulk counterparts. Small nanoclusters can show strongly size-dependent characteristics, for example, their structures can vary dramatically with size. Among others, manifestation of this strong-size dependence includes behavior of “magic number” clusters,

X.C. Zeng (✉)

Department of Chemistry and Nebraska Center for Materials and Nanoscience, University of Nebraska, Lincoln, Nebraska 68588, USA
e-mail: xzengl@unl.edu

metal–nonmetal transition, nonmagnetic–magnetic transition, red or blue shift of optical gap, and selective catalysis [1, 11, 12, 24, 31, 42, 60]. The intriguing properties of nanoclusters stem from their finite size, large surface-to-volume ratio, and quantum effect. From application point of view, highly stable nanoclusters can serve as building blocks for assembly of new materials and for design of nano-devices. Size-dependent characteristics also open a possibility for tailoring properties of nanoclusters by precisely controlling the formation process.

Nanoclusters are usually produced from mass-selective cluster beams and can be studied in the gas phase, or within an inert matrix, or adsorbed onto a surface. Many technologies such as mass spectrometry; ion mobility spectrometry; photo- and collision-induced dissociation; photoionization, photoelectron, and infrared spectroscopies; electron paramagnetic resonance; Stern–Galach molecular-beam deflection; and optical spectroscopy have been advanced to measure the energy, ionization potential, electron affinity, magnetic moment, and optical absorption of nanoclusters.

Theoretical computations have also played a key role in the cluster science since certain properties of nanoclusters are difficult to measure, and many conventional theories developed for treatment of atomic/molecular systems or bulk matter are inapplicable to nanoscale systems. Common computational tools include empirical potential methods such as molecular dynamics and Monte Carlo simulation, semi-empirical methods such as tight-binding approximation, and first-principles methods or *ab initio* electronic structure calculations such as density functional theory and molecular orbital methods. In particular, the density functional theory has become a *de facto* tool for the study of nanoclusters with more than a few tens of atoms.

Current investigations in cluster science can be loosely categorized into two main areas. One is to understand how the structures and properties of the matter evolve from isolated atom or molecule to nanoparticle and to the bulk as the size increases. Another is to explore new cluster-assembled materials for practical applications, such as novel electronic and optical devices, chemical sensors, and efficient and selective catalysts.

Core–shell nanoclusters have recently received considerable attention owing to their physical and chemical properties that are strongly dependent on the structure of the core, shell, and interface. This structure dependence opens possibility for tuning properties by controlling their chemical composition and relative size of the core and shell. The core–shell magnetic nanoclusters are of special interests since the heterogeneous nanostructures offer opportunities for developing devices and cluster-assembled materials with new functions for magnetic recording, bio, and medical applications. In fact, superparamagnetic nanoparticles with suitable biocompatible coatings have important implications in biology, biotechnology, and other biomedical disciplines [36, 44, 35].

The purpose of this review is to survey most recent studies on bimetallic magnetic core–shell nanoclusters. Toward this end, we will mainly focus on core–shell nanoclusters with at least one component of the constitution being magnetic. Other fascinating topics – for example, binary clusters and nanoalloys, whose structures

are neither core–shell nor magnetic – are completely left out for space reasons. The metal-oxide core–shell clusters are also not discussed in this chapter, although these species can be magnetic. Readers interested in these topics are referred to [8, 10, 17, 41, 43]. Nevertheless, even on the topics that we are focusing we do not claim to be exhaustive. If some contributions are left out, we apologize in advance. We will review previous experimental and theoretical studies: On the experimental part, we present a brief summary of known synthetic technology and measured magnetic properties. On the theoretical part, we provide more detailed review since much less theoretical work has been published in the literature.

The review is organized as follows. In Section 2.2, we give a short description of the experimental techniques for the fabrication of core–shell nanoclusters, as well as a survey of previous analysis and characterization of clusters' structures, components, size, and magnetic properties. In Section 2.3, we summarize previous theoretical work on the core–shell clusters and discuss their structural, electronic, and magnetic properties with different core and shell. Specifically, magnetic systems including iron-, cobalt-, nickel-, manganese-based core–shell clusters are discussed in detail. In Section 2.4, we conclude by providing an outlook for future research about core–shell nanoclusters.

2.2 Experimental Studies of Core–Shell Magnetic Clusters

In this section, we survey the recent progress in fabrication and characterization of magnetic core–shell nanoclusters. The main focuses are placed on three prototype magnetic core/shell nanoclusters, i.e., iron-, cobalt-, nickel-core-based nanoclusters. A list of previous experimental and theoretical studies on the core/shell magnetic nanoclusters is presented in Table 2.1.

Table 2.1 Summary of the recent experimental and theoretical studies on the core–shell magnetic nanoclusters

Clusters	References
Fe@Au	[2, 48, 15, 13, 14, 63, 64, 40, 16, 20, 7, 62, 57, 45]
Co@Au	[48, 3, 4, 5, 6, 39, 61, 9, 58]
Co@Ag	[50, 29, 56, 26, 32, 51, 25, 27, 65, 57]
Co@Cu	[29, 39, 30, 27, 65]
Co@Pt	[46, 47, 39, 34]
Co@Pd	[3, 4, 5, 6, 39]
Ni@Au	[3, 4, 5, 6, 18]
Ni@Ag	[3, 4, 5, 6, 53, 28, 19, 38, 18]
Ni@Pd	[53]
Pt@Co	[54]
Mn@Au	[58]

2.2.1 Iron-Based ($Fe@Au$) Core–Shell Nanoclusters

Nanometer-sized magnetic particles of iron show promise for practical applications in catalysis, magnetic recording, magnetic fluids, and biomedical applications. However, pure iron nanoparticles are chemically unstable in the air and easily oxidized, which limits their utility. To protect the particles from oxidation, one way is to coat the particles with another inert layer, namely, making a core–shell structure. The core–shell structure is capable of maintaining favorable magnetic properties of metal iron while preventing the nanoparticles from oxidation. Materials such as metal-oxide (iron oxide), inorganic compound (SiO_2), and noble metal (gold and silver) are commonly used as the coating for iron nanoparticles.

Gold has been one of the popular coating materials owing to its chemical inertness, bio-compatibility, non-toxic, and diverse cluster geometries such as planar sheets, cages, and tubes [49, 33, 59, 37]. Indeed, it has been found that gold-coated nanoparticles are more resistant to oxidation and corrosion, compared to the uncoated particles. The gold coating (shell) tends to distribute more uniformly on the spherical particles than on the acicular ones. More importantly, the gold coating is capable of retaining many favorable magnetic properties (such as coercivity or blocking temperature) of the core. The iron-core gold-shell $Fe@Au$ nanoparticles are of particular importance owing to their potential biondiagnostic applications, such as rapid magnetic separation and concentration of biomaterials.

Paulus et al. [48] has fabricated $Fe@Au$ colloidal particles (stabilized by organic ligands) with average sizes of 2 nm and 5.1 nm. They found that the $Fe@Au$ nanoparticles are superparamagnetic at room temperature with the blocking temperature $T_B \sim 40$ K. The magnetic anisotropy of $Fe@Au$ is larger than the bulk, which might be caused by the formation of inhomogeneous Fe/Au alloy.

Lin et al. [40] have developed a unique reverse-micelle method to synthesize gold-coated iron ($Fe@Au$) nanoparticles as illustrated in Fig. 2.1. The average size of $Fe@Au$ nanoparticles is about 10 nm. These nanoparticles are characterized by a combination of transmission electron microscopy (TEM), energy dispersive spectroscopy (EDS), X-ray diffraction (XRD), ultraviolet-visible spectroscopy (UV/vis), and quantum design superconducting quantum interference device (SQUID) magnetometry. The absence of oxygen and iron oxide, based on the EDS and XRD measurements, confirms a complete coating of the iron core by the gold shell. The authors have also found that a red shift and broadening occurs in the absorption band of the $Fe@Au$ colloid as compared to that of pure gold particles.

Particularly interesting is that these $Fe@Au$ nanoparticles are superparamagnetic with $T_B \sim 42$ K. At 300 K, no coercivity (H_c) and remanence (M_r) are observed, while they are 728 Oe and 4.12 emu/g at 2 K, respectively (see Fig. 2.2).

The authors have also investigated self-assembly of the $Fe@Au$ nanoparticles in a magnetic field for potential biomedical applications. The $Fe@Au$ nanoparticles formed parallel chains with length ranging from 5 to 30 nm, and each chain can be considered as a single magnetic domain. Under the influence of the external

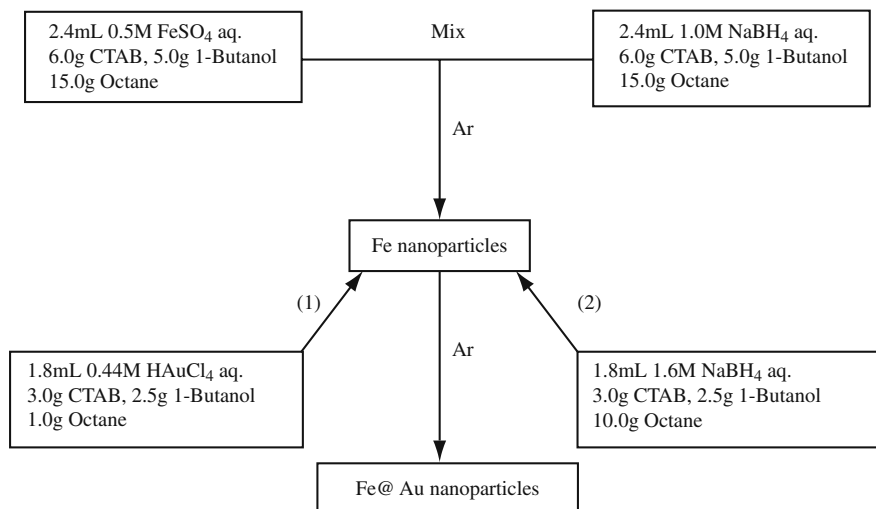


Fig. 2.1 Schematic diagram showing the reverse-micelle method for preparation of Fe@Au nanoparticles. Reproduced with permission from J. Solid State Chem. **159**, 26–31 (2001) Copyright 2001 Elsevier

magnetic field, these single domains are aligned along the direction of the magnetic field to form even longer parallel chains.

Other researchers [15, 13, 14, 63, 64, 16, 45] have also successfully fabricated different sized Fe@Au nanoparticles using the same method and characterized them with XRD, UV/vis, and TEM techniques. Zhou et al. [63] obtained the average particle size of the core–shell structure about 8 nm, with about 6 nm diameter core and 1–2 nm thick shell. Carpenter [16] synthesized nanoparticles with a 7 nm core in diameter and a 1 nm thick shell. These Fe@Au nanoparticles are found to be air stable, and their magnetic properties are enhanced.

Chen et al. [20] have synthesized gold-coated acicular and spherical iron-based nanoparticles by using a mild chemical reduction process. Iron core nanoparticles are synthesized by simultaneous thermal decomposition of Fe(CO)₅ and polyol reduction of Co(acac)₃ in dioctyl ether before coating. The acicular iron particles are coated with gold from the gentle chemical reduction of an organo-gold compound in nonaqueous solvents. TEM and alternative gradient magnetometry studies indicate that the small particles have relatively uniform coatings, while for the larger particles, many gold surfaces have been decorated. Compared with uncoated particles, gold-coated commercial iron particles show good corrosion resistance even in a 1.03 M HCl solution at 80°C for 12 h. Additionally, although the Fe@Au particles possess a very small coercivity because of slight oxidation, the magnetic moment is still larger than that of pure iron oxide.

Ban et al. [7] have successfully synthesized Fe@Au nanoparticles (about 11 nm core of Fe and 2.5 nm shell of Au) by the partial replacement reaction in a polar aprotic solvent. High-resolution transmission electron microscopy (HRTEM) studies

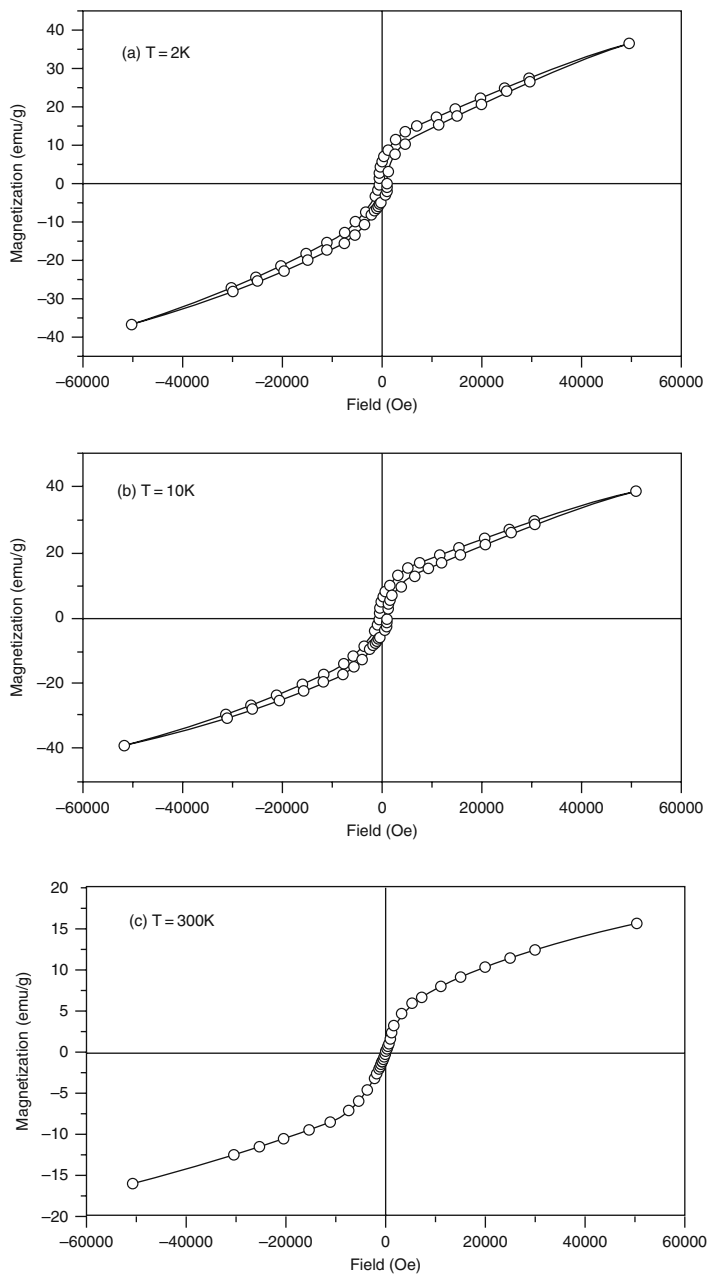


Fig. 2.2 Magnetization of Fe@Au nanoparticles vs. the magnetic field at (a) 2 K (b) 10 K, and (c) 300 K. Reproduced with permission from J. Solid State Chem. **159**, 26–31 (2001) Copyright 2001 Elsevier

confirm the core–shell structures with different crystal lattices: Fe (110 and 200 lattice planes) and Au (111 and 200 lattice planes). SQUID magnetometry reveals that particle magnetic properties are not significantly affected by the thickness of Au shell. The produced Fe@Au nanoparticles exhibit a red shift in absorption band as compared to pure gold nanoparticles, due to the surface plasmon resonance. Interestingly, the Fe@Au nanoparticles are ferromagnetic at room temperature.

Cho et al. [23] have reported chemical synthesis of Fe@Au nanoparticles using a reverse-micelle method through the reduction of an aqueous solution. The blocking temperature of the particles T_B is about 150 K, which is much higher than that of 50 K obtained by O'Connor group. A negative giant magnetoresistance effect has been observed, and the particles are metallic, which imply a metallic α -Fe core. However, the Mössbauer studies on the samples a month later have confirmed the occurrence of oxidation over time, which indicates that the Fe core is not fully covered by the Au shell or that the Au shell is permeable to oxygen. Therefore, the authors have proposed that the formation of α -Fe core Au-shell structure and subsequently the Fe core oxidizes.

Later, however, the authors have found that the structure of Fe@Au nanoparticles might be not as simple as reported earlier. To investigate the growth mechanisms and oxidation-resistant characteristics of the Fe@Au core–shell structure, Cho et al. [21] used the same synthetic method to fabricate a large enough Fe core coated with gold shell (about 19 nm). TEM, EDX, XRD, Mössbauer spectroscopy, and inductively coupled plasma studies demonstrated the Fe@Au core–shell structures and the presence of the Fe and Au phases. From atomic-resolution Z-contrast imaging and electron energy loss spectroscopy (EELS) in a scanning transmission electron microscope (STEM) studies, the Au shell grows by nucleating at selected site on the surface of the Fe core before coalescing, and the surface is rough. The authors further found that the magnetic moments of the nanoparticles, in the loose powder form, decrease over time due to oxidation (see Fig. 2.3). On the other hand,

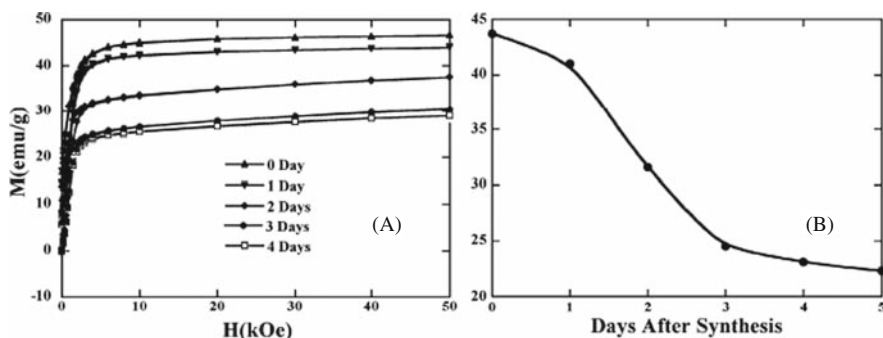


Fig. 2.3 (A) First quadrant of the magnetic hysteresis loop at 5 K. From the top, each curve indicates the measurement with a 1-day interval, right after synthesis. (B) Decay of saturation magnetization of exposed Fe/Au nanoparticles over time. Reproduced with permission from Chem. Mater., 17, 3181–3186 (2005). Copyright 2005 American Chemical Society

electrical transport measurements showed that the particles in the pressed pellet form are fairly stable for the resistance, and magnetoresistance does not change over time.

Cho et al. [22] have further investigated the Fe@Au nanoparticles using both the conventional- and synchrotron-based X-ray diffraction and the magnetic and Mössbauer spectral techniques. The powder X-ray diffraction patterns indicate the presence of crystalline α -iron and gold and the absence of any crystalline iron oxides or other crystalline products. However, the Mössbauer spectra of both uncoated iron nanoparticles and the Fe@Au nanoparticles showed that three major iron-containing components are found (see Fig. 2.4). Of the iron components, 16% and 40% are represented by the expected α -iron phase in the uncoated and gold-coated iron nanoparticles, respectively. The other byproducts are an amorphous $\text{Fe}_{1-x}\text{B}_x$ alloy and Fe(III) oxide as well as paramagnetic Fe(II) and Fe(III) components. These results indicate that the produced Fe@Au nanoparticles through reverse micelles are far more complicated than had been believed.

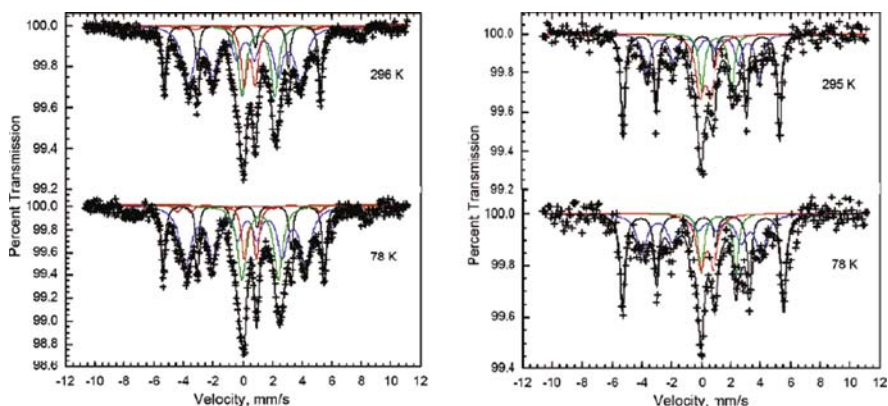


Fig. 2.4 Mössbauer spectra of the iron (*left panel*) and the Fe@Au (*right panel*) nanoparticles prepared in a reverse micelle. The Fe(II), Fe(III), R-iron, and $\text{Fe}_{0.73}\text{B}_{0.27}$ components are shown in different colors (see original article). They are obtained within a week and approximately 2 weeks after synthesis for gold-coated and uncoated iron particles. Reproduced with permission from Chem. Mater. **18**, 960–967 (2006). Copyright 2006 American Chemical Society

Zhang et al. [62] have exploited a laser ablation technique to synthesize the Fe@Au core-shell nanoparticles. This technique includes three steps. The first step is to make both the Fe core and the Au shell by using the laser ablation method separately. The second step is to prepare the Fe core through a wet chemistry method and to be subsequently coated with Au shell by laser ablation of Au powder. The third step is magnetic extraction/acid washing for sample purification. The main advantage of this fabrication technique is the second step, which provides a higher overall yield and better control of the size of the magnetic core. Their studies indicate that although the effect of irradiation is complicated, the most possible coating

process is that Au particles are fragmented into small Au clusters and deposited onto the iron core through repeated heating and melting. The laser-irradiated mixture Fe-containing nanoparticles were separated by magnetic extraction techniques, and the uncoated or incompletely Au-coated nanoparticles were washed away through acid washing. The detailed synthesized process is illustrated in Fig. 2.5.

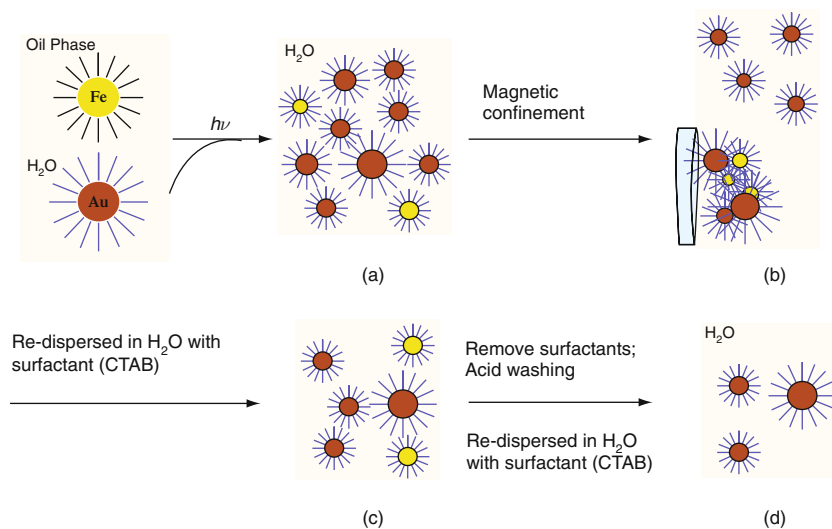


Fig. 2.5 Experimental process for fabrication of Fe@Au magnetic core–shell nanoparticles. Reproduced with permission from *J. Phys. Chem. B.* **110**, 7122–7128 (2006). Copyright 2006 American Chemical Society

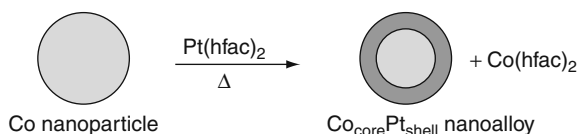
The samples have been characterized during and up to several months after synthesis by HRTEM, HAADF STEM, EDX, XRD, UV-vis, inductively coupled plasma atomic emission spectroscopy, and SQUID magnetometry. The red-shifted and much broadened spectra are observed in the absorption band structure of the Fe@Au nanoparticles due to the surface plasmon resonance, a reflection of the shell-thickness effect. The Au shell is about 3-nm diameter with fcc structure and the lattice interplanar distance of 2.36 Å. The core is about 18-nm diameter bcc Fe single domain with the lattice interplanar distance of 2.03 Å. The nanoparticles are superparamagnetic at 300 K with a high blocking temperature T_B of 170 K and exhibit excellent long-term oxidation resistance. After 4 months of shelf storage in normal laboratory conditions, high-saturation magnetization is found (210 emu/g), which is about 96% of the Fe bulk value.

As discussed above, the Fe@Au nanoparticles have some unique advantages: first, they can be easily prepared in either aqueous or organic medium. Second, the particles often have high saturation magnetization, as compared with iron oxide and other magnetic material. Third, because of diverse surface functionality of gold, gold-coated iron nanoparticles have increased functionality.

2.2.2 Cobalt-Based Core–Shell Nanoclusters

2.2.2.1 Co@Pt Core–Shell Nanoalloys

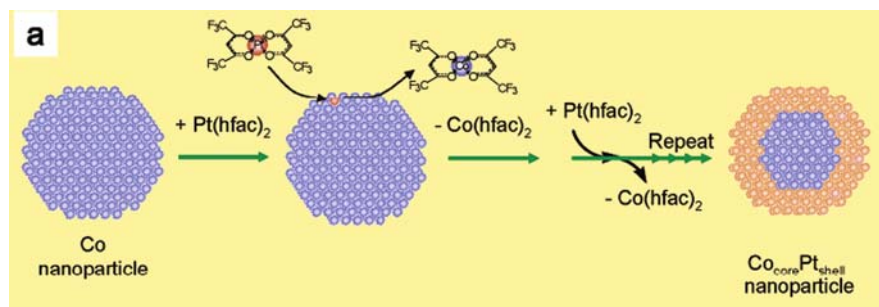
Park et al. [46] have exploited redox transmetalation reaction techniques for the first time to synthesize $\text{Co}_{\text{core}}\text{Pt}_{\text{shell}}$ nanoalloys under 10 nm. As shown in Scheme 2.1, first, the Co nanoparticles are prepared from the thermolysis of $\text{Co}_2(\text{CO})_8$ in toluene solution. Next, the $\text{Co}_{\text{core}}\text{Pt}_{\text{shell}}$ nanoparticles are synthesized by refluxing 6.33 nm Co nanoparticle colloids (0.5 mmol) and $\text{Pt}(\text{hfac})_2$ (0.25 mmol) in a nonane solution containing 0.06 mL of $\text{C}_{12}\text{H}_{25}\text{NC}$ as a stabilizer. After 8 h of reflux, the core–shell nanoparticles are isolated from the dark red–black solution in powder form after adding ethanol and centrifugation. Last, reaction byproduct $\text{Co}(\text{hfac})_2$ is separated from the core–shell nanoparticles.



Scheme 2.1 Synthetic route of core–shell nanoalloys via modified redox transmetalation reaction. Reproduced with permission from J. Am. Chem. Soc. **123**, 5743–5746 (2001). Copyright 2001 American Chemical Society

Magnetic studies of the $\text{Co}_{\text{core}}\text{Pt}_{\text{shell}}$ nanoparticles indicate that they retain most magnetic properties of pure Co core and are not significantly affected by the Pt shell. The block temperature of this sample is about 15 K and a coercivity is 330 Oe at 5 K, which are less than the pure Co nanoparticles but are close to those of nanoparticles with similar size to the Co_{core} .

Later, Park et al. [47] have exploited a similar redox transmetalation reaction technique to fabricate similar-sized $\text{Co}_{\text{core}}\text{Pt}_{\text{shell}}$ nanostructures (Scheme 2.2) and studied their magnetic properties and thermally induced dynamic phase transition behavior.



Scheme 2.2 Synthetic routes of $\text{Co}_{\text{core}}\text{Pt}_{\text{shell}}$ nanoalloys via modified redox transmetalation reaction. Reproduced with permission from J. Am. Chem. Soc. **126**, 9072–9078 (2004). Copyright 2004 American Chemical Society

The $\text{Co}_{\text{core}}\text{Pt}_{\text{shell}}$ nanoparticles are superparamagnetic with zero magnetic coercivity (H_c) at room temperature, and 330 Oe at 5 K. In particular, the H_c is considerably improved to 1300 and to 7000 after the $\text{Co}_{\text{core}}\text{Pt}_{\text{shell}}$ nanoparticles are annealed at 600 and 700 °C for 12 h. Moreover, the particle annealed at 700 °C shows ferromagnetism with an H_c of 5300 Oe at room temperature (Fig. 2.6).

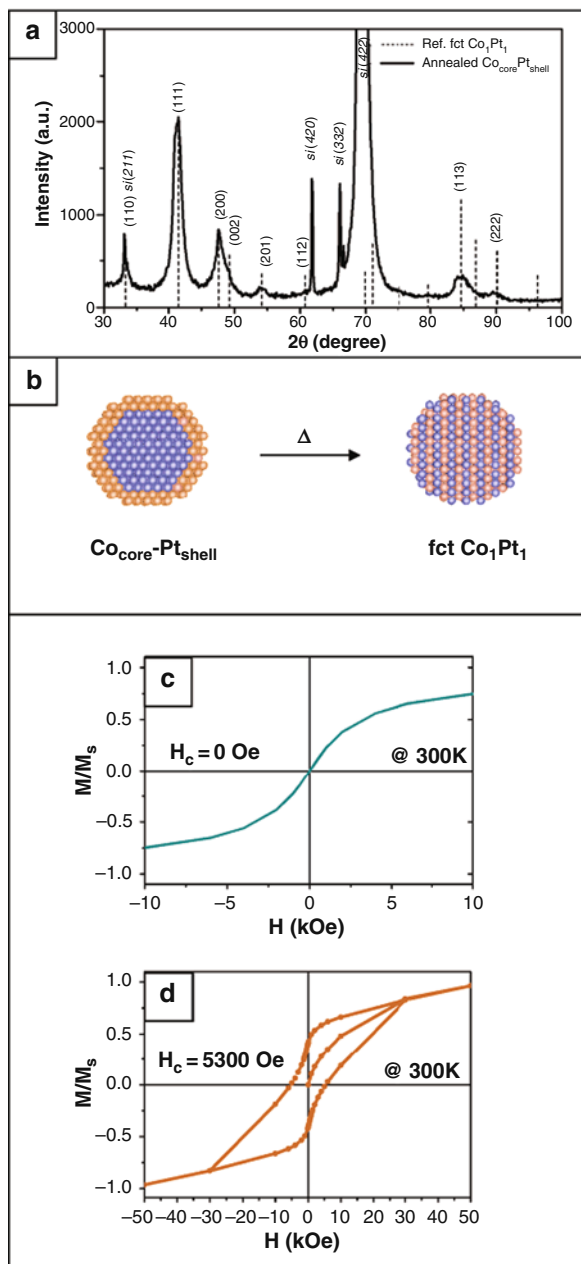


Fig. 2.6 XRD analysis and magnetic properties of $\text{Co}_{\text{core}}\text{Pt}_{\text{shell}}$ nanoparticles. (a) XRD pattern of $\text{Co}_{\text{core}}\text{Pt}_{\text{shell}}$ nanoparticles annealed at 700 °C for 12 h. All peaks are well matched to reference fct Co_1Pt_1 alloys (dashed line). (b) Thermal alloying of $\text{Co}_{\text{core}}\text{Pt}_{\text{shell}}$ nanoparticles to anisotropic fct structure. Hysteresis loops of $\text{Co}_{\text{core}}\text{Pt}_{\text{shell}}$ nanoparticles measured at 300 K (c) before and (d) after the annealing process at 700 °C. The magnetic coercivity of the nanoparticles is significantly enhanced from 0 to 5300 Oe, exhibiting room-temperature ferromagnetism. Reproduced with permission from J. Am. Chem. Soc. **126**, 9072–9078 (2004). Copyright 2004 American Chemical Society

Jun et al. [34] have demonstrated Co@Pt core-shell nanoparticles can be effectively served as a bifunctional nanoplatform for the hydrogenation of a number of unsaturated organic molecules under mild conditions, and also for the magnetic separation and recycling ability. They also prepared Co@Pt nanoparticles via the redox transmetalation reaction process between Pt(hfac)₂ and cobalt particles. The platinum shell surface is stabilized by dodecyl isocyanide capping molecules (Fig. 2.7). The average particle size is 6.4 nm, while the diameter of a cobalt core is 4.6 nm; the overall stoichiometry is Co_{0.45}Pt_{0.55}. Elemental analysis and HRTEM study indicate that the thickness of the Pt layer is about ~0.9 nm, corresponding to ~4 layers of Pt. The core-shell nanoparticles exhibit superparamagnetic behavior at room temperature with the blocking temperature $T_B \sim 15$ K and a coercivity $H_c \sim 660$ Oe at 5 K

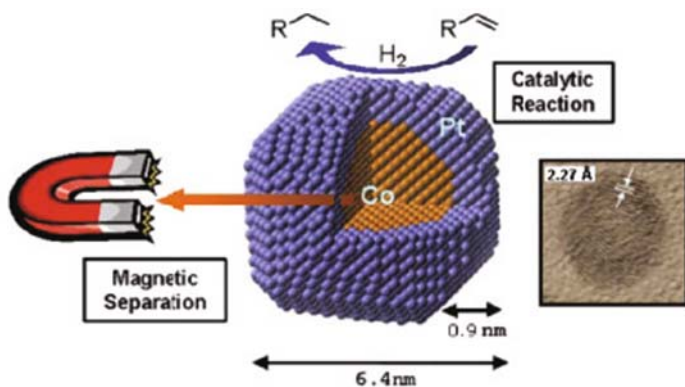
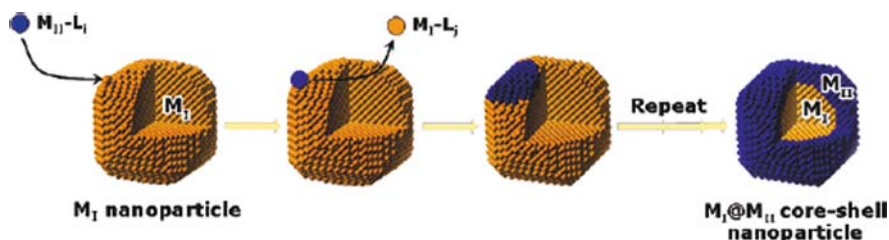


Fig. 2.7 The dual functionality of Co@Pt core-shell nanoparticles. Insert: The HRTEM image of a single nanoparticle. The 2.27 Å represents the lattice constant of the Pt shell. [35] – *Reproduced by permission of The Royal Society of Chemistry*

2.2.2.2 Co@Au, Co@Pd, Co@Pt, and Co@Cu Nanoparticles

Lee et al. [39] have successfully fabricated Co@Au, Co@Pd, Co@Pt, and Co@Cu core-shell nanostructures by using the redox transmetalation reaction technique. During the transmetalation processes, metal ions M_{II} ($M_{II} = Au^{3+}$, Pd^{2+} , Pt^{2+} , or Cu^{2+}) of the reactant metal complexes ($M_{II} - Li$) are reduced on the surface of M_I ($M_I = Co$ in this work) nanoparticles, while neutral $M_I(Co)$ atoms are oxidized to $M_I^{y+}(Co^{2+})$ accompanying the formation of a Co-ligand complex ($M_I - L_j$) as a resultant reaction byproduct (Scheme 2.3). Repeating this process leads to a complete covering of Co core by M_{II} shell layers. The advantage of this technique is that the original Co nanoparticles are retained because of shell layer formation and core metal consumption occur simultaneously.

EDS studies indicate that the nanoparticle is estimated to have a 5.7 nm Co core and 0.4 nm Au shell with Co/Au ratio of 79:21 for Co@Au; 4.9 nm Co core and



Scheme 2.3 Schematic of core–shell nanoparticle formation via redox transmetalation processes. Reproduced with permission from J. Am. Chem. Soc. 127, 16090–16097 (2005). Copyright 2005 American Chemical Society

0.9 nm Pd shell with Co/Pd ratio of 47:53 for Co@Pd; the Co/Pt ratio of 45:55 with 4.6 nm Co core and 0.9 nm Pt shell for Co@Pt; and 5.2 nm Co core shell and 0.7 nm Cu shell with the ratio of 54:46 for Co@Cu nanostructure. The HRTEM studies further confirm the formation of the shell of Au, Pd, Pt, and Cu on Co nanoparticles by their good coincidence with the corresponding lattice parameters for their fcc (111) plane.

SQUID magnetometer measurements are performed on these core–shell structures and show coercivity (H_c) of 2090 Oe for pure Co nanoparticles, 1310 Oe for Co@Au, 840 Oe for Co@Cu, 660 Oe for Co@Pt, and 740 Oe for Co@Pd core–shell nanoparticles, respectively (Fig. 2.8). Taking into account that average diameter of cobalt for Co, Co@Au, Co@Cu, Co@Pt, and Co@Pd is estimated to be 6.5, 5.7, 5.2, 4.7, and 4.9 nm, respectively, the H_c trend suggests that core–shell nanoparticles with larger Co core sizes have higher coercivity. Therefore, the magnetism of the core–shell nanoparticles mainly stems from the magnetic core while the noble metal shell layer has little effect on it. Superparamagnetic behavior is observed for all of these nanoparticles at room temperature.

2.2.2.3 Pt@Co Core–Shell Nanoclusters

Sobal et al. [54] have developed a new two-stage route to synthesize monodisperse, controllable Pt@Co core–shell structures. The first step is to prepare definite diameter pure platinum particles. The second step involves thermal decomposition of cobalt carbonyl on the Pt seeds. The thickness of the Co shell can be controlled by varying the amount of dicobalt dicarbonyl. For the ratio Pt:Co₂(CO)₈ 1:4, the average diameter of the spherical bimetallic particles is 7.5 nm with the maximum thickness of Co (2.3±0.2 nm). In the case of Pt/Co₂(CO)₈ 1:5, incomplete coverage was observed due to cobalt island formation on the platinum surface. The particles exhibit superparamagnetic behavior at room temperature, and the blocking temperature T_B is between 175 and 225 K.

2.2.2.4 Co@Cu Core–Shell Nanoclusters

Guo et al. [30] have fabricated Co@Cu core–shell nanoparticles by using a displacement method in aqueous solution at room temperature. The nanoparticles

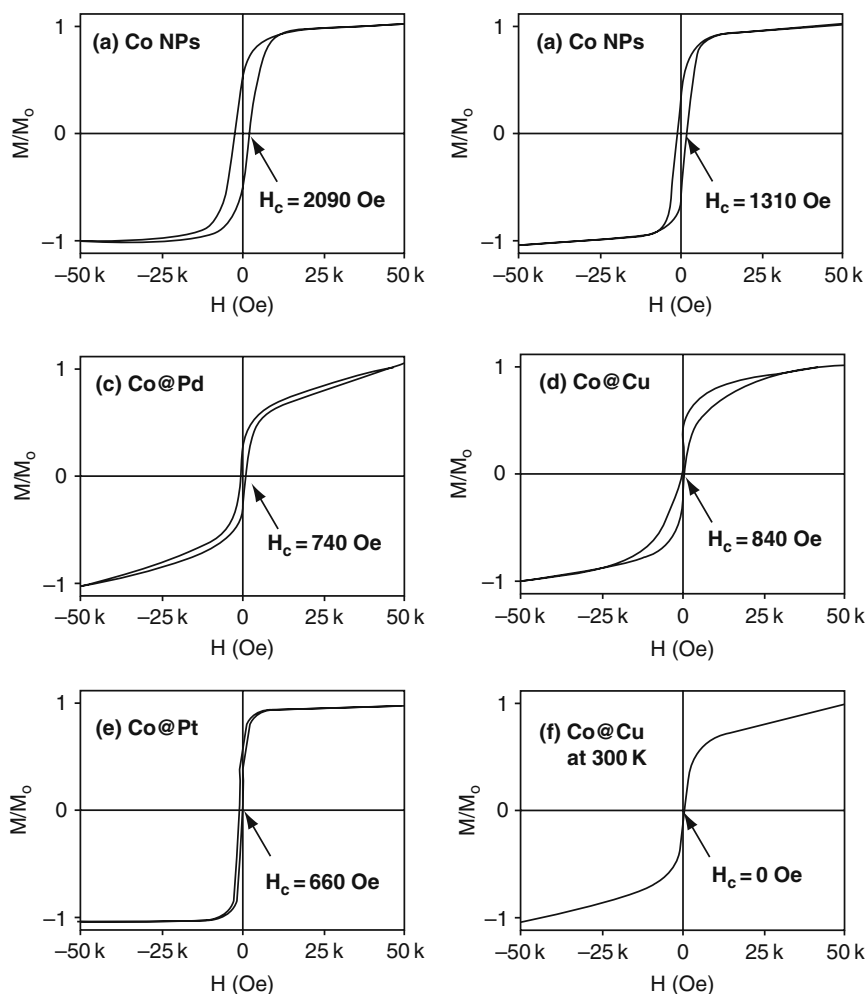


Fig. 2.8 Hysteresis loops of (a) Co nanoparticles and core-shell nanoparticles (b) Co@Au, (c) Co@Pd, (d) Co@Cu, and (e) Co@Pt at 5 K on a SQUID magnetometer. (f) Hysteresis loop of Co@Cu nanoparticles at 300 K shows superparamagnetism. Reproduced with permission from *J. Am. Chem. Soc.* 127, 16090–16097 (2005). Copyright 2005 American Chemical Society

were fabricated through a wet chemical scheme by using the surfactant sulfobetaine, dodecyltrimethyl (3-sulfopropyl) ammonium hydroxide (98%) in tetrahydrofuran. Cobalt oxide was not present in the nanoparticles upon exposure to air through X-ray absorption near-edge structure analysis. The relative high blocking temperature ($T_B \sim 235$ K) was found for the Co@Cu nanoparticles, indicating the coating enhanced the magnetic properties of the nanoparticles.

2.2.2.5 Co@Ag Core/Shell Nanoclusters

Sobal et al. [54] have fabricated monodisperse bimetallic Ag@Co core–shell nanoparticles by using colloid chemistry methods. These nanoparticles exhibit optical and magnetic behavior significantly different from that of pure Ag and Co metals. In addition, the presence of a noble metal appears to improve the stability of nanosized Co against oxidation.

Rivasa et al. [50] have prepared Co@Ag nanoparticles through a microemulsion method in an inert atmosphere. The size of the nanoparticles is controlled by the water droplets of the microemulsions. This whole procedure can be divided to two steps. The first step is to produce the magnetic core by mixing two water-in-oil microemulsions containing the reactants dissolved in the aqueous phase. The second step is to coat the core with Ag through successive reactions in microemulsions. The reaction takes place inside the droplets, which controls the final size of the particles. Subsequently, silver ions are adsorbed onto these particles and finally are reduced to produce a silver shell. The produced samples contain 3.3–40.5 vol% Co, and the average size of the particles is about 15–60 nm.

The authors have also investigated the temperature dependence of the magnetization and found that the magnetic properties are strongly dependent on the annealing temperature. The study shows coercive fields as high as $H_c = 600$ Oe at room temperature after thermal treatments ($T_A \approx 500$ deg C).

Later, Rivasa et al. [51] have synthesized Co@Ag core–shell nanoparticles with the same technique and explored magnetic behavior vs. heat treatment. This study confirms that under the experimental conditions, the size of the Co nuclei is determined by the reactant concentration, whereas microemulsion droplet size controls the Ag covering.

2.2.2.6 Co@Au Core–Shell Nanoclusters

Paulus et al. [48] have presented a detailed experimental study of Co colloidal particles stabilized by organic ligands with and without gold coating. The magnetic anisotropy of the Co@Au particles was found to be highly reduced, to a value very close to the bulk.

Xu and Wang [61] have fabricated Co@Au core–shell nanoparticles directly from gas phase by using a physical-vapor-deposition-based nanocluster deposition technique. The synthesized Co–Au nanoparticles are Co_{82.7}Au_{17.3} at.% with the size ranging from 5 to 15 nm in diameter and an average size of about 12 nm. The composition ratio in the particles can be adjusted by changing the ratio of sputtered areas of Co and Au in the target. The advantage of this method is that it can precisely control conditions for particle formation, thus good control of phase, size, and size distribution of particles.

Low-temperature and room-temperature hysteresis loops show that the Co–Au nanoparticles retain the magnetic properties of pure Co core. At room temperature, the Co–Au nanoparticles show superparamagnetic behavior with a very high blocking temperature $T_B \sim 290$ K. A field-cooled low-temperature hysteresis loop

of Co–Au nanoparticles at 50 K indicates the existence of oxide, and Au shell does not fully cover the Co core.

To avoid the formation of the interface between the core and the shell in the redox transmetalation reaction process, Bao et al. [9] have synthesized Co–Au core–shell nanoparticles by using an organo-gold compound as precursor in a nonpolar solvent. No diffraction pattern of cobalt oxide was observed in XRD, which confirmed that these produced Co–Au core–shell nanoparticles are stable in organic solution and last up to several months. However, their stabilities are reduced in aqueous solution, which are mainly caused by the reaction of cobalt and thiol groups.

TEM, HRTEM, and Z-contrast imaging studies show that the core–shell structure is about 9 nm and a single-crystal Co core is surrounded by multiple gold grains, forming a raspberry structure, and the core diameter is 5–6 nm, close to the size of the cobalt seeds used during synthesis, and the shell is roughly 1.5–2.0 nm thick. The particles are superparamagnetic at room temperature and the blocking temperature T_B is about 55 K. The UV-visible absorption spectra of these nanoparticles show a red shift to 680 nm because of the surface plasmon resonance enhanced absorption.

2.2.3 Ni-Based Core–Shell Nanoclusters

2.2.3.1 Ni@Pd Core–Shell Nanoclusters

Sao-Joao et al. [53] have successfully fabricated Pd–Ni core–shell nanoparticles with the average size (5–7 nm) through decomposition of metalorganic compounds. TEM, EDS, HRTEM, energy-filtered microscopy (EFTEM), and XPS studies indicate that the physical and chemical properties of the Pd shell are sensitively dependent on its electronic properties, which are influenced by the presence of the Ni core and by the deformation in the Pd lattice. The catalytic properties of the pure metal and the bimetallic particles, toward CO oxidation, have been investigated. The core–shell clusters show similar catalytic activities toward the CO oxidation as the case of pure Pd clusters, i.e., no increase of reactivity is observed on the Ni@Pd core–shell structure, which might be caused by the presence of edges in the small particles.

2.2.3.2 Ni@Ag Core–Shell Nanoclusters

Chen et al. [19, 38] have successfully fabricated Ni@Ag core–shell nanoparticles by successive hydrazine reduction of metal salts in ethylene glycol without the addition of protective agents. To prohibit the particles from coalescing, the appropriate nickel concentration for the coating of Ag nanoshells should be less than 1.0 mm. The TEM and XPS on surface composition studies indicated that Ni cores are fully covered by Ag nanoshells, and the shell thickness could be controlled by the silver nitrate concentration. The EDP and XRD analyses reveal that both Ni cores and Ag shells have an fcc structure.

Later, Chen et al. [38] have further developed this synthetic technique by using polyethyleneimine (PEI) as a protective agent to fabricate Ni-core/Ag-shell

(Ni@Ag) nanoparticles. The produced Ni@Ag nanoparticles are monodisperse, and the core is about 6.2 nm in diameter, and the shell thickness is about 0.85 nm. In the nickel concentration of 0.25–25 mM, the size of the Ni@Ag nanoparticles shows no significant change for different thickness of Ag coating. X-ray photoelectron spectroscopy indicates both Ni cores and Ag shells have an fcc structure, and the Ni cores are fully covered by Ag shells. Moreover, a peak was observed at 430 nm in the absorption band of the Ni@Ag nanoparticles, which is consistent with the characteristic spectra of Ag nanoparticles. The sample is nearly superparamagnetic. The saturation magnetization (M_s), remanent magnetization (M_r), and coercivity H_c are 17.2 emu g⁻¹, 4.0 emu g⁻¹, and 81 Oe, respectively, based on the weight of Ni cores. The coating of Ag shells leads to a decrease of M_s and M_r , which indicates that the formed Ni–Ag interface plays a quenching role on the magnetic moment. The thermal and XRD analyses indicate that the Ag shells provide a better anti-oxidation protection to Ni@Ag nanoparticles as compared to the case of pure Ni nanoparticles.

2.2.3.3 Ni@Au Core–Shell Nanoclusters

Chen et al. [18] have developed a redox transmetalation method by combining with a reverse-microemulsion technique to synthesize Ni–Au core–shell nanoparticles. The obtained size of the nanoparticles ranges from 15 to 30 nm in diameters, with 5–10 nm core diameters and 5–10 nm shell thickness. A red-shift absorption to 590 nm was observed in this core–shell structure as compared to pure gold nanoparticles due to the enhanced surface plasmon resonance absorption. The blocking temperature of the nanoparticles is 16 K, and the superparamagnetic behavior was detected at room temperature. The saturation magnetization, remanent magnetization, and coercivity at 5 K are 9.0 emu/g, 4.1 emu/g, and 2 kOe, respectively, which are dramatically smaller than that of 55 emu/g at 300 K for bulk nickel metal. This reduction in moment might stem from the small size effect, the oxidation of the Ni cores, the increased surface of the nanoparticles, the crystal lattice defects, etc.

2.3 Theoretical Studies of Bimetallic Magnetic Core–Shell Nanoclusters

In contrast to extensive experimental studies of bimetallic core/shell nanostructures, theoretical studies are much less (Table 2.1). In this section, we will give a more detailed survey on previously reported theoretical results.

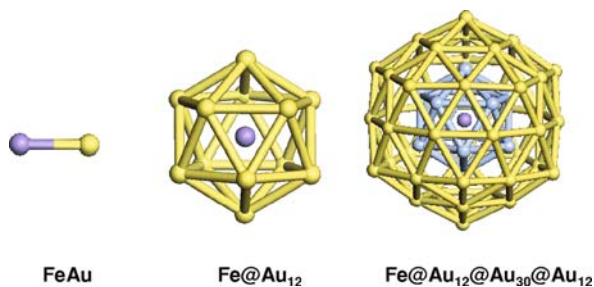
2.3.1 Iron-Based (Fe@Au) Core–Shell Nanoclusters

Sun et al. [56] have reported the first theoretical study of gold-coated iron nanoclusters using a gradient-corrected density functional theory (DFT). Specifically,

the authors used a combination of the Becke exchange functional and the Perdew–Wang correlation functional (BPW91), and a plane-wave basis set with the projector augmented plane-wave (PAW) method. The authors focused on the effect of gold coating on the structural and magnetic properties of the iron core of various sizes, as well as chemical reaction of uncoated and coated iron clusters with oxygen.

Calculated magnetic moments of clusters $\text{Fe}_1@Au_1$, $\text{Fe}_1@Au_{12}$, and $\text{Fe}_1@Au_{12}@Au_{30}@Au_{12}$ (Fig. 2.9) are 3.44, 3.0, and 3.0 μ_B , respectively. These values are all greater than the bulk value of 2.2 μ_B/atom , indicating that the gold shells provide an enhancement effect on the magnetism of iron atom.

Fig. 2.9 Geometries of Fe atom enclosed in gold shells. Reproduced from [57]. Copyright (2006) by the American Physical Society



The authors have also examined whether a Fe_{13} core can remain magnetic with a gold shell of two different thicknesses, namely, $\text{Fe}_{13}@Au_{42}$ and $\text{Fe}_{13}@Au_{134}$. Main results of their calculation for Fe_{13} , $\text{Fe}_{13}@Au_{42}$, and $\text{Fe}_{13}@Au_{134}$ are given in Table 2.2. For $\text{Fe}_{13}@Au_{42}$, the lowest-energy structure is an icosahedron with I_h symmetry, although bare Fe_{13} itself is a distorted icosahedron, which indicates that the gold coating results in a structural change of the iron core. Meanwhile, the magnetic moment of the Fe_{13} core is more or less preserved even though the Fe–Fe bond length is expanded by 3.2% with the gold coating. Covering additional gold shells to $\text{Fe}_{13}@Au_{42}$ has little effect on the bond length and magnetic moment of the Fe_{13} core. The induced magnetic moment within the Au shell is mainly at the Au/Fe interfacial layer, and the outermost Au layer shows no magnetic moment. Hence, the thickness of the gold shell has a negligible effect on the magnetic moment of the Fe_{13} core and little influence on the induced moment within the gold coating.

Sun et al. have also studied the oxidation of Fe_{13} and $\text{Fe}_{13}@Au_{42}$ nanoclusters and found that O_2 dissociates and the atomic O binds strongly with the outer Fe atoms with a binding energy of 8.04 eV. The total magnetic moment of Fe_{13}O_2 is 38 μ_B , less than that of the pure Fe_{13} . As for $\text{Fe}_{13}@Au_{42}$, oxygen remains molecular, and the adsorption energy of O_2 to the cluster is small (< 0.25 eV), indicating that gold coating prevents the iron core from oxidation.

Table 2.2 Bond lengths (in Å) and magnetic moment (in μ_B) of Fe_{13} and the Fe@Au core–shell nanoclusters. Reproduced from [56]. Copyright (2006) by the American Physical Society

	Fe_{13}	$\text{Fe}_{13}@Au_{30}@Au_{12}$	$\text{Fe}_{13}@Au_{30}@Au_{12}@Au_{60}@Au_{12}$
μ_{Fe1}	2.32	2.384	2.357
μ_{Fe2}	3.00	2.923	2.801
μ_{Au}		0.018 (1st shell)	0.015 (1st shell)
		0.014 (2nd shell)	0.012 (2nd shell)
			0.010 (3rd shell)
			0.007 (4th shell)
			0.003 (5th shell)
R_{Fe1}	2.390	2.457	2.438
R_{Fe2}	2.512	2.594	2.543
$R_{\text{Fe-Au}}$		2.830	2.820

2.3.2 Cobalt-Based Core–Shell Nanoclusters

2.3.2.1 Co@Cu, Co@Ag Core–Shell Nanoclusters

Guevara et al. [29] have explored electronic and magnetic properties of Co cluster coated with Cu and Ag ($C_{O_N}X_M$, $X = \text{Cu, Ag}$, and $N + M$ up to 405) using a parametrized tight-binding Hamiltonian method. The noble-metal coating has the structure of an fcc lattice. In the case of Co@Cu clusters, both the average and the total magnetic moments show an oscillatory behavior as a function of coating thickness, as shown in Fig. 2.10. Because of hybridization with the Cu atoms, the moment of the core–shell cluster is attenuated in comparison with the bare Co_{13} cluster. For some special coatings, Cu is antiferromagnetic (AFM) to Co and thus yields smaller magnetic moment per Co atom, and in some cases even smaller than that of bulk Co. They also found that a rather open or corrugated cluster surface induces a ferromagnetic polarization.

For the Co@Ag core–shell clusters, the total magnetic moment depends not only on the number of Co atoms but also on the number of surrounding Ag atoms as well as the shape of the Ag shell, as shown in Fig. 2.11. Moreover, Guevara et al. have found that the spin on Ag is antiparallel to that on Co for various coatings, thereby giving smaller total magnetic moment of the core–shell clusters than that of pure Co clusters. In contrast to the Cu coating, the magnetization of Co core per atom within the Ag coating is larger than that of bulk Co value. A few cases of ferromagnetic polarization are also identified and these are due to a corrugated outer Ag shell with several poorly coordinated Ag atoms (spikes).

Fig. 2.10 Magnetic moment per Co atom vs. increasing number of Cu atoms for $\text{Co}_{13}\text{Cu}_M$ clusters. \circ corresponds to the total magnetic moment, \bullet to the magnetic moment of the Co core. Reproduced from [29]. Copyright (1998) by the American Physical Society

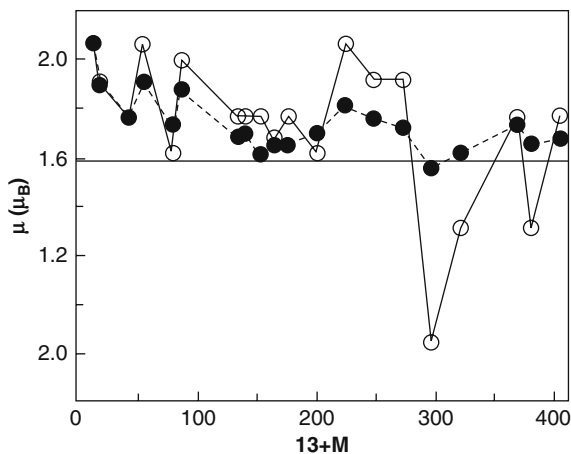
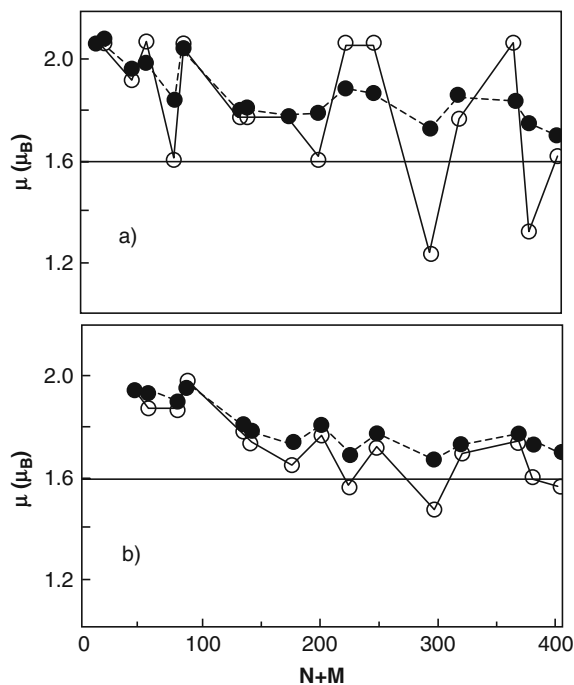


Fig. 2.11 Same as Fig. 2.10 for (a) $\text{Co}_{13}\text{Ag}_M$ and (b) $\text{Co}_{43}\text{Ag}_M$ clusters. Reproduced from [29]. Copyright (1998) by the American Physical Society



2.3.2.2 Pd@Ag, Ni@Ag, Ni@Au, Co@Au Core-Shell Nanoclusters

Baletto et al. [3–6] have investigated the growth of Pd@Ag and Ni@Ag core-shell structures using molecular dynamics simulation and empirical many-body potentials derived within the second-moment approximation to the tight-binding model. Their

studies suggest that very stable core–shell structures can form over a wide range of temperatures. A novel multi-shell $A-B-A$ structure can also form by inverse deposition of B atoms above A cores. The growth of $A-B-A$ structures depends on the structure of the initial A core and the temperature. If the initial A core is an fcc cluster, the $A-B-A$ multi-shell structures can be achieved for all three bimetallic systems (Ni/Ag and Pd/Ag) in different temperature ranges. On the contrary, the $A-B-A$ structures cannot form by deposition on the I_h cores, where normal core–shell structures grow instead. The growth of the intermediate B shell is triggered by the fact that the most favorable positions for isolated B impurities inside A clusters are located just one layer beneath the cluster surface.

Rossi et al. [52, 28] have identified a new family of magic-number polyicosahedral core–shell clusters, Ni@Ag, by using a genetic algorithm coupled with DFT calculation (Fig. 2.12). The authors have demonstrated that these core–shell clusters are very stable on basis of energetic, electronic energy gap, and thermodynamic information. More interestingly, these core–shell clusters can have higher melting points than the corresponding pure clusters.

Several other theoretical studies have shown that Ag–Co, Au–Ni, and Au–Co particles tend to form core–shell structures, while Ag–Pd and Au–Cu tend to mix in

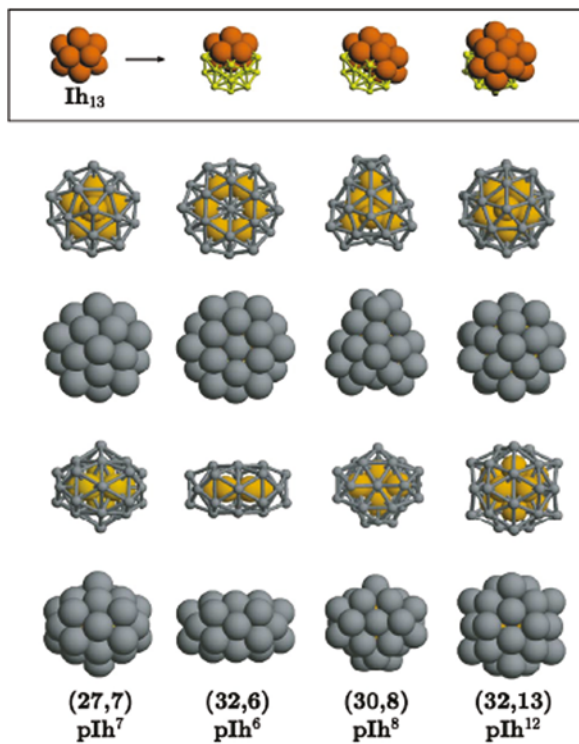


Fig. 2.12 Magic-number core–shell pI_h clusters. Reproduced from [52]. Copyright (2004) by the American Physical Society

bulk alloy phases. Many calculations have also shown that magnetic effects destabilize the core-shell arrangement of Ag-Co and Au-Co bimetallic clusters.

Hoof et al. [32] have employed Metropolis Monte Carlo and molecular mechanics methods and embedded atom potentials to study the structural and thermodynamic equilibrium states of isolated Ag-Co nanoparticles with the size ranging from 200 to 3000 atoms and temperature ranging from 0 to 1500 K. The authors have obtained a lower and an upper limit to the Co concentration for the occurrence of core-shell structure. The lower limit is determined from the balance between Co-Co binding interaction and the stress of the Ag lattice. The upper limit is associated with the wetting of the Co core by Ag shell. In the core-shell structure, the Co core expands within 2% while the Ag lattice contracts. The Co core melts at a temperature < 1500 K, and the melting is insensitive to the thickness of the Ag shell. Since the melting temperature of the Ag shell is fairly lower than that of the Co core, a solid core covered by a liquid shell can be observed. The coexistence of a liquid layer and a solid center is found within the Co core, and the thickness of the liquid layer increases with increasing the temperature. As the temperature is increased, the Ag shell may undergo a crystal to amorphous transition followed by an amorphous to liquid transition, depending on its thickness. A detailed melting process is shown in Fig. 2.13, where the disordering of the core starts at the interface and proceeds toward the center as the temperature is increased.

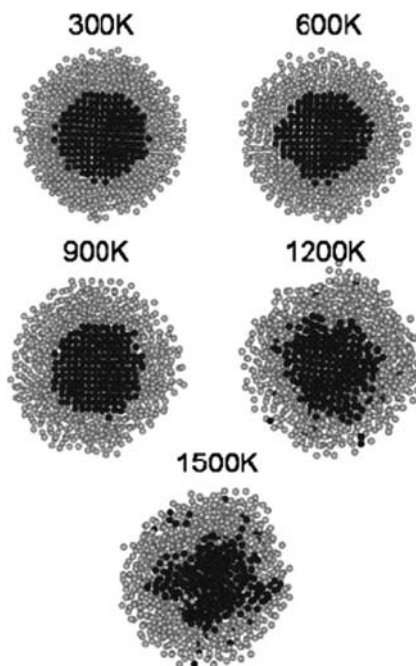


Fig. 2.13 Cuts through equilibrium $\text{Ag}_{2250}\text{Co}_{750}$ cluster configurations at several temperatures. Dark spheres: Co atoms; light spheres: Ag atoms. Reproduced from [32]. Copyright (2005) by the American Physical Society

Hou and coworkers [27, 65] have shown that the equilibrium atomic configurations of Ag–Co and Cu–Co are determined by the binding and interfacial configuration energies. Thermal vibrational entropy plays an important role in the balance of energy contributions to thermodynamic equilibrium. Core–shell Ag–Co and “onionlike” Cu–Co equilibrium configurations were observed, which can be altered by adjusting composition and temperature.

Hou and coworkers [26, 57] have also explored the slowing down process (deposition) of $\text{Co}_{285}\text{Ag}_{301}$ nanoclusters on an Ag (100) substrate using classical molecular dynamics simulation. The kinetic energies of the nanoclusters range from 0.25 eV to 1.5 eV per atom to mimic the low-energy cluster beam deposition and aerosol-focused beam techniques. Initial $\text{Co}_{285}\text{Ag}_{301}$ has a core–shell structure with one complete Ag monolayer covering the Co core. The cluster undergoes partial accommodation and partially retains a “memory” of its initial morphology. As a result of the impact, the substrate undergoes significant damage, while the degree of damage depends on the slowing down energy.

Using the same simulation methods, the authors extended their study to clusters with no special morphology when deposited on the Ag (100) surface. The effect of size and deposition energy was systematically examined. The authors have found that the interface formed between the Ag matrix and the core–shell Co@Ag nanoclusters is no more than a few atomic layers thick and that both the cobalt core and the silver shell display limited epitaxy with the substrate. The effect is not much energy dependent but is strong for the Ag shell than for the Co core.

Dorfbauer et al. [25] have explored structures of $\text{Co}_x\text{Ag}_{1-x}$ nanoparticles (864 atoms, 2.8 nm) by using molecular dynamics simulation with an embedded atom potential. Starting from a completely random distribution of Co and Ag atoms, the clusters are heated up to 1300 K and then cooled down to form Co core and Ag shell structures. Radial distribution function (RDF) analysis suggests the coexistence of both hcp-like and fcc-like stackings in the Co core.

We [58] have recently explored the structure and magnetic properties of gold-coated Co_{13} icosahedral anionic clusters $[\text{Co}_{13}\text{@Au}_{20}]^-$ using a gradient-corrected DFT. First, we searched for the lowest-energy states of the uncoated Co_{13}^- and gold-coated $[\text{Co}_{13}\text{@Au}_{20}]^-$ clusters over a broad range of total spin magnetic moment S_z values, from 2 to 38 μ_B . Main results are summarized as follows: The $[\text{Co}_{13}\text{@Au}_{20}]^-$ anion cluster is a perfect I_h structure (Fig. 2.14). The Co–Co,

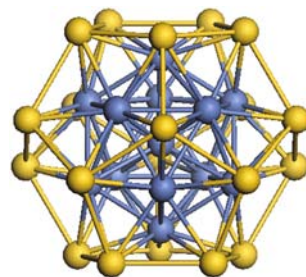


Fig. 2.14 Optimized geometry of $[\text{TM}_{13}\text{@Au}_{20}]^-$, TM=Mn and Co. Dark color represents the TM core, while light color depicts the gold shell

Co–Au, and Au–Au bond lengths in the lowest-energy structure are 2.45, 2.61, and 2.89 Å, respectively. These bond lengths can vary, depending on the total magnetic moment. In general, the Co–Co and Au–Au bond lengths increase as the magnetic moment increases, while the Co–Au bond lengths display a complicated variation pattern although in the higher magnetic states the bond lengths are usually longer.

More interestingly, the magnetic moment of $[\text{Co}_{13}@\text{Au}_{20}]^-$ is significantly reduced compared to the bare Co_{13}^- , that is, from 30 to 20 μ_{B} with the gold coating, 33% less than the optimal value (30 μ_{B}) of the bare Co_{13}^- (see Fig. 2.15). This result indicates that the gold coating can have an attenuation effect on the magnetism of strongly magnetic clusters. Paulus et al. [48] have also found the magnetic anisotropy of the Co@Au particles being greatly reduced, to a value very close to the bulk.

Mulliken population analysis on Co_{13}^- and $[\text{Co}_{13}@\text{Au}_{20}]^-$ confirms that the main magnetic moment of $[\text{Co}_{13}@\text{Au}_{20}]^-$ originates from the contribution of Co

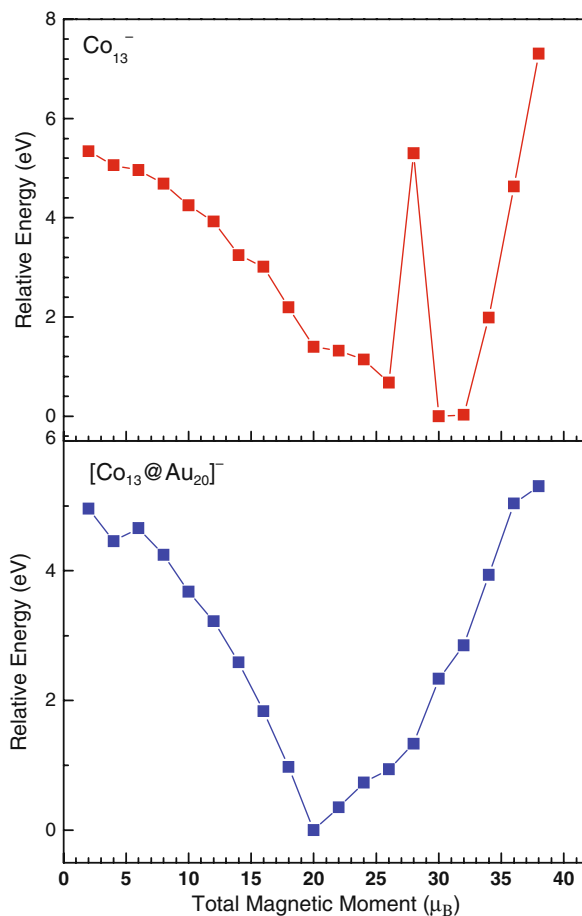


Fig. 2.15 Energies of Co_{13}^- and $[\text{Co}_{13}@\text{Au}_{20}]^-$ in different spin states referred to the respective lowest-energy states

atoms. The local atomic spins on each Au atom are nearly zero, but close to $2.0 \mu_B$ on each Co atom. The Co atoms are ferromagnetically ordered in both uncoated and gold-coated Co_{13}^- , although the moment S_z in the uncoated cluster is larger (2.33 vs. $1.59 \mu_B$ for surface Co atoms, and 2.06 vs. $1.89 \mu_B$ for the central Co atom). Another source for the reduction of the total S_z of $[\text{Co}_{13}@\text{Au}_{20}]^-$ is the antiparallel ordering of the spin moments of all Au atoms ($0.05 \mu_B$ per Au) with respect to the moment of the Co_{13}^- core.

2.3.3 Mn-Based Core–Shell Nanoclusters: $[\text{Mn}_{13}@\text{Au}_{20}]^-$

Using the same computational scheme [58], we have also studied the structure and magnetic properties of gold-coated Mn_{13} anionic cluster $[\text{Mn}_{13}@\text{Au}_{20}]^-$. The lowest-energy configuration of $[\text{Mn}_{13}@\text{Au}_{20}]^-$ is a slightly distorted icosahedral structure (C_s) with a very large total S_z of $44 \mu_B$ (see Fig. 2.16). The low spin state with the total S_z of $2 \mu_B$ at the same symmetry (C_s) is the second lowest-energy

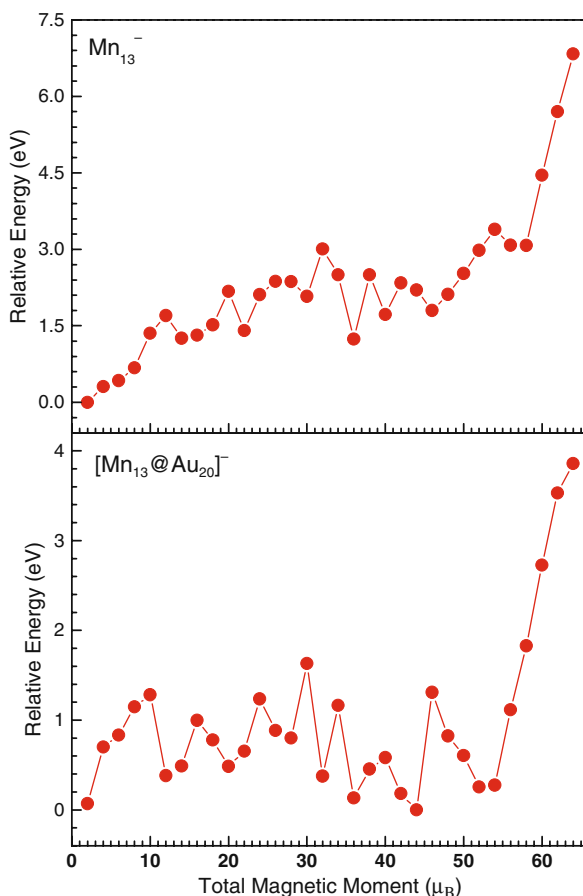


Fig. 2.16 Energies of Mn_{13}^- and $[\text{Mn}_{13}@\text{Au}_{20}]^-$ in different spin states referred to the respective lowest-energy states

configuration whose energy is only 0.071 eV higher. Other high spin states such as $S_z = 36, 42, 52, 54 \mu_B$ are found as deep local minima whose energy is 0.133, 0.182, 0.253, 0.277 eV higher, respectively, than the lowest-energy state (Fig. 2.16).

The average bond lengths of Mn–Mn, Mn–Au, and Au–Au in the lowest-energy configuration are 2.76, 2.61, and 2.95 Å, respectively. Different spin-correlated behavior for the bond lengths of Mn–Mn, Mn–Au, and Au–Au are observed. The Mn–Mn bond lengths are more spin-sensitive at high spin states, while the Au–Au bond lengths are more spin-sensitive at the low spin states. The Mn–Au bond lengths are very sensitive to the spin states in general, and they decrease as the magnetic moments increase from 2.635 to 2.602 Å.

Mulliken population analysis on $[\text{Mn}_{13}@\text{Au}_{20}]^-$ shows that the local atomic spins on each Au atom vary from -0.24 to $0.20 \mu_B$, and most are nearly zero, while they are around $4.0 \mu_B$ on every Mn atom.

Most interestingly, $[\text{Mn}_{13}@\text{Au}_{20}]^-$ exhibits a giant magnetic moment ($44 \mu_B$), whose corresponding lowest-energy state has a ferrimagnetic arrangement where one surface Mn atom is antiparallel to the rest eleven surface atoms with the local moment of -3.877 and $3.949 \mu_B$, respectively, and the core Mn atom possesses a local moment of $2.679 \mu_B$. For the state of $S_z = 2\mu_B$, six surface Mn atoms are antiparallel to the rest six surface atoms with the atomic moment of 3.927 and $-4.104 \mu_B$, respectively. The core Mn atom possesses a small moment of $3.066 \mu_B$. In the case of $S_z = 36 \mu_B$, two symmetric apex Mn atoms are antiparalleled ($-3.770 \mu_B$) to the rest eleven Mn atoms ($3.981 \mu_B$ for the surface atoms and $2.575 \mu_B$ for the core atom). In the case of $S_z = 52$ and $54 \mu_B$, all the Mn atoms are paralleled, and the local moment of Mn atoms is around $4.0 \mu_B$. In contrast, the bare Mn_{13}^- favors a ferrimagnetic ordering with a net total moment of $2 \mu_B$, where six surface Mn atoms have antiparallel spin arrangements ($-3.63 \mu_B$) to the rest six surface Mn atoms ($3.85 \mu_B$), and the core atom possesses $1.09 \mu_B$. The ferromagnetic state of Mn_{13}^- has a total S_z of $52 \mu_B$, while the core Mn atom possesses $0.94 \mu_B$ and the twelve surface Mn atoms have the atomic moment of 3.72 – $4.59 \mu_B$ (Fig. 2.17).

2.4 Summary

As summarized in previous sections, the core–shell magnetic clusters often exhibit new physical and chemical properties compared to their single-component counterparts. In many cases, the noble metal coating not only can enhance magnetic properties with large coercivity and high blocking temperature but also can provide sufficient resistance to the oxidation of the magnetic core. These added values in core–shell clusters pave the way for the applications of the magnetic nanoparticles in future information and biological technologies such as information storage, magnetic sensors, bioseparation, and drug delivery. Although a variety of physical and chemical techniques have been employed for their fabrication, challenges in producing uniformly coated and highly stable core–shell nanoparticles (e.g., without

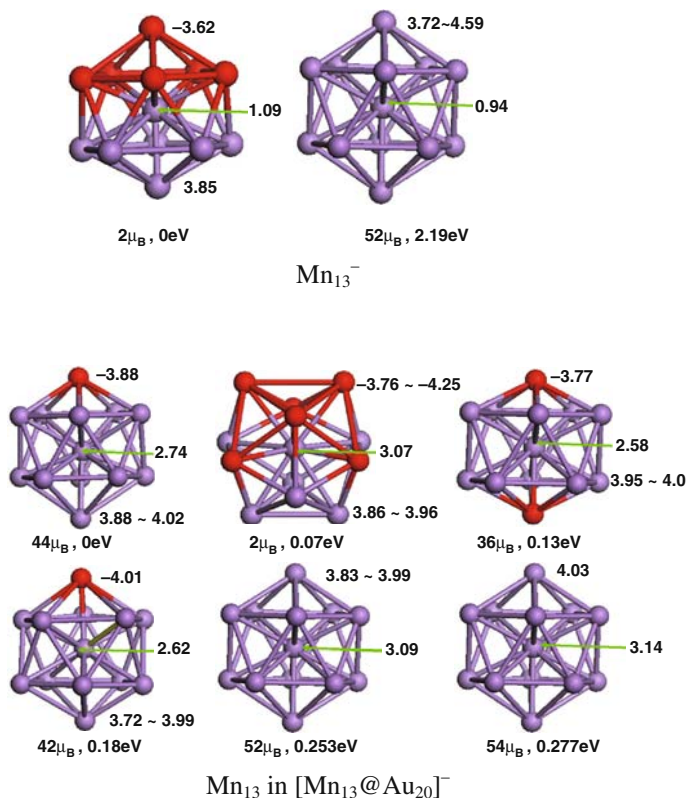


Fig. 2.17 Local spin on bare and coated Mn_{13}^- clusters in different spin states Mn_{13}^- Mn_{13} in $[\text{Mn}_{13}@\text{Au}_{20}]^-$

aggregation associated with their production) have limited wide application of the core–shell nanoclusters (or nanoparticles).

On the other hand, compared to the large amount of literature in fabrication and characterization of core–shell magnetic nanoclusters, theoretical work on the core–shell clusters is considerably less in the literature, especially on the study of nanomagnetism based on first-principles theory. Better understanding of core–shell magnetic clusters, including their structures (morphology), growth mechanics, magnetic, electronic, and optical properties are greatly needed and will definitely benefit both basic science and application. Another issue that limits extensive first-principles studies is that the core–shell nanoclusters produced in most experiments are a few to a few tens nanometers in sizes, which are beyond computational capability for the first-principles studies in most researchers' laboratory. However, the gap between the two sides is narrowing as smaller-sized core–shell clusters can be produced and characterized more routinely, and more efficient computational methodologies as well as more powerful computers are under development. We are optimistic that a

great surge in joint theoretical/experimental studies will come up in the near future, which undoubtedly will expedite our understanding and utilizing this novel form of matter.

Acknowledgement The work was supported by the National Nature Science Foundation of China (No. 10604013, 20873019), the Program for New Century Excellent Talents in the University of China (NCET-06-0470), Qinglan Project in the University of Jiangsu Province, and the Teaching and Research Foundation for the Outstanding Young Faculty of Southeast University (JW), and partly by the Office of Basic Energy Sciences (DE-FG02-04ER46164), National Science Foundation (CHE-0427746 and DMR-0820521), the Nebraska Research Initiative, and the UNL Research Computing Facility (XCZ).

References

1. Alonso, J.A.: Electronic and atomic structure, and magnetism of transition-metal clusters. *Chem. Rev.* **100**, 637–678 (2000).
2. Ravel, B., Carpenter, E.E., Harris, V.G.: Oxidation of iron in iron/gold core/shell nanoparticles. *J. Appl. Phys.* **91**, 8195–8197 (2002).
3. Baletto, F., Mottet, C., Ferrando, R.: Growth of three-shell onionlike bimetallic nanoparticles. *Phys. Rev. Lett.* **90**, 135504–135507 (2003).
4. Baletto, F., Mottet, C., Ferrando, R.: Growth simulations of silver shells on copper and palladium nanoclusters. *Phys. Rev. B* **66**, 155420–155430 (2002).
5. Baletto, F., Mottet, C., Ferrando, R.: Time evolution of Ag–Cu and Ag–Pd core–shell nanoclusters. *Eur. Phys. J. D* **24**, 233–236 (2003).
6. Baletto, F., Mottet, C., Rapallo, A.: Growth and energetic stability of AgNi core–shell clusters. *Surf. Sci.* **566–568**, 192–196 (2004).
7. Ban, Z.B., Barnakov, Y.A., Li, F., Golub, V.O., O’Connor, C.J.: The synthesis of core–shell iron@gold nanoparticles and their characterization. *J. Mater. Chem.* **15**, 4660–4662 (2005).
8. Bansmann, J., Baker, S.H., Binns, C., Blackman, J.A., Bucher, J.-P., orantes-Dávila, J., Dupuis, V., Favre, L., Kechrakos, D., Kleibert, A., Meiwes-Broer, K.-H., Pastor, G.M., Perez, A., Toulemonde, O., Trohidou, K.N., Tuillon, J., Xie, Y.: Magnetic and structural properties of isolated and assembled clusters. *Surf. Sci. Rep.* **56**, 189–275 (2005).
9. Bao, Y., Calderon, H., Krishnan, K.M.: Synthesis and characterization of magnetic–optical Co–Au core–shell nanoparticles. *J. Phys. Chem. C* **111**, 1941–1944 (2007).
10. Binns, C., Trohidou, K.N., Bansmann, J., Baker, S.H., Blackman, J.A., Bucher, J.-P., Kechrakos, D., Kleibert, A., Louch, S., Meiwes-Broer, K.-H., Pastor, G.M., Perez, A., Xie, Y.: The behaviour of nanostructured magnetic materials produced by depositing gas-phase nanoparticles. *J. Phys. D: Appl. Phys.* **38**, R357–R379 (2005).
11. Bloomfield, L. A., Deng, J., Zhang, H., Emmert, J.W.: in *Proc. International Symposium on Cluster and Nanostructure Interfaces*, edited by P. Jena, S. N. Khanna, and B. K. Rao, World Publishers, Singapore, 2000, p. 131.
12. Brack, M.: The physics of simple metal clusters: self-consistent jellium model and semiclassical approaches. *Rev. Mod. Phys.* **65**, 677–732 (1993).
13. Carpenter, E., Kumbhar, A., Wiemann, J., Srikanth, H., Wiggins, J., Zhou, W., O’Connor, C.: Synthesis and magnetic properties of gold–iron–gold nanocomposites. *Mater. Sci. Eng. A* **286**, 81–86 (2000).
14. Carpenter, E., Sims, J., Wienmann, J., Zhou, W., O’Connor, C.J.: Magnetic properties of iron and iron platinum alloys synthesized via microemulsion techniques. *J. Appl. Phys.* **87**, 5615–5617 (2000).
15. Carpenter, E.E., Sangregono, C., O’Connor, C.J.: Effects of shell thickness on blocking temperature of nanocomposites of metal particles with gold shells. *IEEE Tran. Magn.* **35**, 3496–3498 (1999).

16. Carpenter, E.E.: Iron nanoparticles as potential magnetic carriers. *J. Magn. Magn. Mater.* **225**, 17–20 (2001).
17. Caruso, F.: Nanoengineering of particle surfaces. *Adv. Mater.* **13**, 11–22 (2001).
18. Chen, D., Li, J., Shi, C., Du, X., Zhao, N., Sheng, J., Liu, S.: Properties of core–shell Ni–Au nanoparticles synthesized through a redox-transmetalation method in reverse microemulsion. *Chem. Mater.* **19**, 3399–3405 (2007).
19. Chen, D., Wang, S.: Protective agent-free synthesis of Ni–Ag core–shell nanoparticles. *Mater. Chem. Phys.* **100**, 468–471 (2006).
20. Chen, M., Yamamuro, S., Farrell, D., Majetich, S.A.: Gold-coated iron nanoparticles for biomedical applications. *J. Appl. Phys.* **93**, 7551–7553 (2003).
21. Cho, S.J., Idrobo, J.C., Olamit, J., Liu, K., Browning, N.B., Kauzlarich, S.M.: Growth mechanisms and oxidation resistance of gold-coated iron nanoparticles. *Chem. Mater.* **17**, 3181–3186 (2005).
22. Cho, S.J., Shahin, A.M., Long, G.J., Davies, J.E., Liu, K., Grandjean, F., Kauzlarich, S.M.: Magnetic and mössbauer spectral study of core/shell structured Fe/Au nanoparticles. *Chem. Mater.* **18**, 960–967 (2006).
23. Cho, S.J., Kauzlarich, S.M., Olamit, J., Liu, K., Grandjean, F., Rebbouh, L., Long, G. J.: Characterization and magnetic properties of core–shell structured Fe–Au nanoparticles. *J. Appl. Phys.* **95**, 6803–6806 (2004).
24. de Heer, W.A.: The physics of simple metal clusters: experimental aspects and simple models. *Rev. Mod. Phys.* **65**, 611–676 (1993).
25. Dorfbauer, F., Schrefl, T.: Nanostructure calculation of CoAg core–shell clusters. *J. Appl. Phys.* **99**, 08G706 (2006).
26. Dzhurakhalov, A., Rasulov, A., Van Hoof, T., Hou, M.: Ag–Co clusters deposition on Ag(100): an atomic scale study. *Eur. Phys. J. D* **31**, 53–61 (2004).
27. Dzhurakhalov, A.A., Hou, M.: Equilibrium properties of binary and ternary metallic immiscible nanoclusters. *Phys. Rev. B* **76**, 045429–045438 (2007).
28. Ferrando, R., Fortunelli, A., Rossi, G.: Quantum effects on the structure of pure and binary metallic nanoclusters. *Phys. Rev. B* **72**, 085449–085457 (2005).
29. Guevara, J., Llois, A.M., Weissmann, M.: Large variations in the magnetization of Co clusters induced by noble-metal coating. *Phys. Rev. Lett.* **81**, 5306–5309 (1998).
30. Guo, Z.H., Kumar, C.S.S.R., Henry, L.L., Doomes, E.E., Hormes, J., Podlaha, E.J.: Displacement synthesis of Cu shells surrounding Co nanoparticles. *J. Electrochem. Soc.* **152** D1–D5 (2005).
31. Haberland, H. (ed.), *Clusters of Atoms and Molecules I: Theory, experimental methods in: Cluster of atoms and molecules*. Springer-Verlag, Berlin (1994).
32. Hoof, T.V., Hou M.: Structural and thermodynamic properties of Ag–Co nanoclusters. *Phys. Rev. B* **72**, 115434–115445 (2005).
33. Johansson, M.P., Sundholm, D., Vaara, J.: Au₃₂: A 24-carat golden fullerene. *Angew. Chem. Int. Ed.* **43**, 2678–2681 (2004).
34. Jun, C.H., Park, Y.J., Yeon, Y.R., Choi, J.R., Lee, W.R., Ko, S.J., Cheon, J.: Demonstration of a magnetic and catalytic Co@Pt nanoparticle as a dual-function nanoplatfrom. *Chem. Commun.* **15**, 1619–1621 (2006).
35. Jun, Y.K., Choi, J., Cheon, J.W.: Heterostructured magnetic nanoparticles: their versatility and high performance capabilities. *Chem. Commun.* 1203–1214 (2007).
36. Kim, D. K., Zhang, Y., Kehr, J., Klason, T., Bjelke, B., Muhammed, M.: Characterization and MRI study of surfactant-coated superparamagnetic nanoparticles administered into the rat brain. *J. Magn. Magn. Mater.* **225**, 256–261 (2001).
37. Kondo, Y., Takayanagi, K.: Synthesis and characterization of helical multi-shell gold nanowires. *Science*. **289**, 606–608 (2000).
38. Lee, C., Chen, D.: Large-scale synthesis of Ni–Ag core–shell nanoparticles with magnetic, optical and anti-oxidation properties. *Nanotechnology* **17**, 3094–3099 (2006).

39. Lee, W.-R., Kim, M.G., Choi, J.-R., Park, J.-I., Ko, S.J., Oh, S.J., Cheon, J.: Redox-transmetalation process as a generalized synthetic strategy for core-shell magnetic nanoparticles. *J. Am. Chem. Soc.* **127**, 16090–16097 (2005).
40. Lin, J., Zhou, W.L., Kumbhar, A., Wiemann, J., Fang, J., Carpenter, E. E., O'Connor, C. J.: Gold-coated iron (Fe@Au) nanoparticles: synthesis, characterization, and magnetic field-induced self-assembly. *J. Solid State Chem.* **159**, 26–31(2001).
41. Liz-Marzán, L.M., Mulvaney, P.: The assembly of coated nanocrystals. *J. Phys. Chem. B* **107**, 7312–7326 (2003).
42. Moskovits, M.: Metal clusters. *Annu. Rev. Phys. Chem.* **42**, 465–499 (1991).
43. Murray, C.B., Kagan, C.R., Bawendi, M.G.: synthesis and characterization of monodisperse nanocrystals and close-packed nanocrystal assemblies. *Annu. Rev. Mater. Res.* **30**, 545–610 (2000).
44. Niemeyer, C.M.: Nanoparticles, proteins, and nucleic acids: biotechnology meets materials science. *Angew. Chem., Int. Ed.* **40**, 4128–4158 (2001).
45. O'Connor, C.J., Kolesnichenko, V., Carpenter, E., Sangregorio, C., Zhou, W., Kumbhar, A., Sims, J., Agnoli, F.: Fabrication and properties of magnetic particles with nanometer dimensions. *Synth. Met.* **122**, 547–557 (2001).
46. Park, J.-I., Cheon, J.: Synthesis of “solid solution” and “core-shell” type cobalt–platinum magnetic nanoparticles via transmetalation reactions. *J. Am. Chem. Soc.* **123**, 5743–5746 (2001).
47. Park, J.-I., Kim, M. G., Jun, Y.-W., Lee, J.S., Lee, W.-R., Cheon, J.: Characterization of superparamagnetic “core-shell” nanoparticles and monitoring their anisotropic phase transition to ferromagnetic “solid solution” nanoalloys. *J. Am. Chem. Soc.* **126**, 9072–9078 (2004).
48. Paulus, P.M., B'onnemann, H., van der Kraan, A.M., Luis, F., Sinzig, J., de Jongh, L.J.: Magnetic properties of nanosized transition metal colloids: the influence of noble metal coating. *Eur. Phys. J. D* **9**, 501–504 (1999).
49. Pyykkö, P.: Theoretical chemistry of gold. *Angew. Chem. Int. Ed.* **43**, 4412–4456 (2004).
50. Rivas, J., Sanchez, R.D., Fondado, A., Izco, C., Garca-Bastida, A.J., Garca-Otero, J., Mira, J., Baldomir, D., Gonzalez, A., Lado, I., Lopez- Quintela, M.A., Oserov, S.B.: Structural and magnetic characterization of Co particles coated with Ag. *J. Appl. Phys.* **76**, 6564–6566 (1994).
51. Rivas, J., Garcia-Bastida, A.J., Lopez-Quintela, M.A., Ramos, C.: Magnetic properties of Co/Ag core/shell nanoparticles prepared by successive reactions in microemulsions. *J. Magn. Mater.* **300**, 185–191 (2006).
52. Rossi, G., Rapallo, A., Mottet, C., Fortunelli, A., Baletto, F., Ferrando, R.: Magic polyicosahedral core-shell clusters. *Phys. Rev. Lett.* **93**, 105503–105506 (2004).
53. Sao-Joao, S., Giorgio, S., Penisson, J.M., Chapon, C., Bourgeois, S., Henry, C.: Structure and deformations of Pd–Ni core-shell nanoparticles. *J. Phys. Chem. B* **109**, 342–347 (2005)
54. Sobal, N.S., Ebels, U., Mohwald, H., Giersig, M.: Synthesis of core-shell PtCo nanocrystals. *J. Phys. Chem. B.* **107**, 7351–7354 (2003).
55. Sobal, N.S., Hilgendorff, M., Mohwald, H., Giersig, M., Spasova, M., Radetic, T., Farle, M.: Synthesis and structure of colloidal bimetallic nanocrystals: the non-alloying system Ag/Co. *Nano Lett.* **2**, 621–624 (2002).
56. Sun, Q., Kandalam, A. K., Wang, Q., Jena, P., Kawazoe, Y., Marquez, M.: Effect of Au coating on the magnetic and structural properties of Fe nanoclusters for use in biomedical applications: A density-functional theory study. *Phys. Rev. B* **73**, 134409–134414 (2006).
57. Van Hoof, T., Dzhurakhalov, A., Hou, M.: Interface formation by low energy deposition of core-shell Ag–Co nanoclusters on Ag(100). *Eur. Phys. J. D* **43**: 159–163 (2007).

58. Wang, J., Bai, J., Jellinek, J., Zeng, X.C.: Gold-coated transition-metal anion $[\text{Mn}_{13}@\text{Au}_{20}]$ -with ultrahigh magnetic moment. *J. Am. Chem. Soc.* **129**, 4110–4111 (2007).
59. Wang, J., Jellinek, J., Zhao, J., Chen, Z., King, R.B., von Rague Schleyer, P.: Hollow cages versus space-filling structures for medium-sized gold clusters: the spherical aromaticity of the Au_{50} cage. *J. Phys. Chem. A* **109**, 9265–9269 (2005).
60. Wilcoxon, J.P., Abram, B.L.: Synthesis, structure and properties of metal nanoclusters. *Chem. Soc. Rev.* **35**, 1162–1194 (2006).
61. Xu, Y.H., Wang, J.P.: Magnetic properties of heterostructured Co–Au nanoparticles direct-synthesized from gas phase. *IEEE Tran. Magn.* **43**, 3109–3111 (2007).
62. Zhang, J., Post, M., Veres, T., Jakubek, Z. J., Guan, J.W., Wang, D., Normandin, F., Deslandes, Y., Simard, B.: Laser-assisted synthesis of superparamagnetic $\text{Fe}@\text{Au}$ core–shell nanoparticles. *J. Phys. Chem. B* **110**, 7122–7128 (2006).
63. Zhou, W., Carpenter, E., Kumbhar, A., Sims, J., O’Connor, C.: Nanophase and nanocomposite materials III. *J. Mater. Res. Soc. Symp. Proc.* **581**, 107–112(2000).
64. Zhou, W.L., Carpenter, E.E., Lin, J., Kumbhar, A., Sims, J., O’Connor, C.J.: Nanostructures of gold coated iron core–shell nanoparticles and the nanobands assembled under magnetic field. *Eur. Phys. J. D* **16**, 289–292 (2001).
65. Zhurkin, E.E., Hoof, T.V., Hou, M.: Nanoscale alloys and core–shell materials: Model predictions of the nanostructure and mechanical properties. *Phys. Rev. B* **75**, 224102–224116 (2007).

Chapter 3

Designed Magnetic Nanostructures

A. Enders, R. Skomski, and D.J. Sellmyer

Abstract The fabrication, structure, and magnetism of a variety of designed nanostructures are reviewed, from self-assembled thin-film structures and magnetic surface alloys to core–shell nanoparticles and clusters embedded in bulk matrices. The integration of clusters and other nanoscale building blocks in complex two- and three-dimensional nanostructures leads to new physics and new applications. Some explicitly discussed examples are interactions of surface-supported or embedded impurities and clusters, the behavior of quantum states in free and embedded clusters, the preasymptotic coupling of transition-metal dots through substrates, inverted hysteresis loops (proteresis) in core–shell nanoparticles, and nanoscale entanglement of anisotropic magnetic nanodots for future quantum information processing.

3.1 Introduction

Magnetic nanostructures form a broad range of geometries, chemical compositions, and internal structures, with intriguing physical properties and important applications [1–6]. Aside from thin films and multilayers, which are often considered as a separate field, there are natural or artificial dots, antidots, wires, and rings. Some examples of more complex nanostructures are core–shell particles [7, 8], including encapsulated transition-metal atoms or cluster-assembled solids such as CrSi_{12} [9], various types of thin films [5, 10–16], doped clusters [17], and nanotubes [18]. Some bulk magnets may also be considered as embedded nanostructures, as exemplified by Sm–Co permanent magnets [3, 19, 20]. The structural features are on length scales ranging from less than 1 nm to several 100 nm [3, 18], and the involved magnetic substances range from magnetic elements (Fe, Co, Ni) and alloys (such as

A. Enders (✉)

Department of Physics and Astronomy and Nebraska Center for Materials and Nanoscience,
University of Nebraska, Lincoln, NE 68508, USA
e-mail: axel@unl.edu

permalloy, $L1_0$ alloys, and rare-earth transition-metal intermetallics) to oxides and complicated compounds.

Non-interacting structures are interesting research subjects [21] and have important applications. For example, FePt nanoparticles with sizes down to 3 nm are of interest in permanent magnetism [22] but require coating by a thin shell or embedding in a matrix. A large volume fraction of the particles is necessary, because, the key figure of merit in permanent magnetism is the energy product, which scales as the square of the saturation magnetization $M_s = m/V$ in sufficiently hard magnets [23]. Another example is catalysis, which is usually realized by non-magnetic transition-metal surfaces [7]. The catalytic activity of a material [24] reflects subtle details of the electronic structure, which is easily modified by nanostructuring [25]. The confinement of electrons on a length scale of the order of 10 nm makes the electronic band-structure quasi-continuous, with level spacings and shifts sufficiently large to potentially interfere with the catalytic performance or the magnetic properties [26]. Other applications involving non-interacting nanoparticles are in optics, biomedicine [27], and magnetic recording (bit-patterned media) [28]. In the last case, a high-areal density of magnetic elements is required, and the suppression or management of the inter-particle interactions is an important, yet nontrivial task [4, 16, 29]. Figure 3.1 shows some elementary nanostructures, which can be produced in various homogeneous and inhomogeneous chemical compositions.

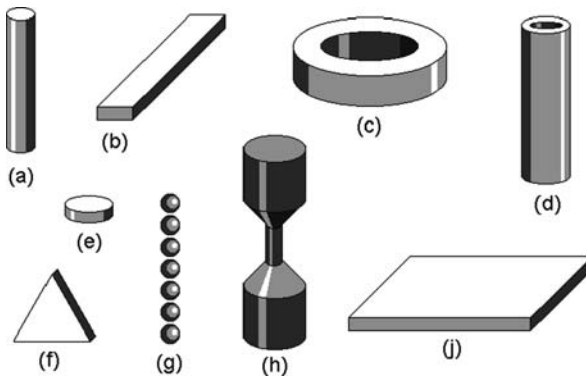


Fig. 3.1 This cartoon shows some simple nanostructures: (a,b) nanowires, (c) nanorings, (d) nanotube, (e,f) nanoparticles, (g) nanoparticle chain, (h) nanojunction, and (j) thin film. Chains of magnetite nanoparticles (g) naturally occur in the brains of animal such as bees and doves, where they may contribute to the spatial orientation during migration

The magnetic properties of the nanostructures in Fig. 3.1 are strongly influenced by their particular shape. But if the size of a metallic structure is decreased to only a few nanometers, then coordination effects become observable and exploitable. The reduced coordination results in an electronic structure different from that of bulk or single atoms. Fundamental magnetic properties, such as spin and orbital moments or magnetic anisotropy, are thus found to depend on the sample size and shape. For instance, clusters of Fe, Ni and Co in the gas phase show enhanced magnetic

moments per atom [30, 31], the magnetic anisotropy of clusters strongly depends on the number of atoms forming it [32, 33], and a magnetic moment is found in ultrathin layers of Rh, which is non-magnetic in the bulk [34]. But not only new magnetic and electronic properties emerge; also the structure [35], the reactivity [36] or thermal properties can deviate drastically from bulk behavior.

For surface-supported or embedded nanostructures, the mere size and shape are only among many other quantities that determine their properties. Also, mutual interactions [37], interactions with the substrate [38] or with ligands, capping layers, etc. influence their magnetic and electronic behavior, offering a wealth of possibilities to manipulate their magnetic properties. The desire emerges to use them in future devices such as patterned storage media, calling for the further study of nanoscale clusters deposited on surfaces. First experiments addressing the magnetic and structural cluster properties after deposition have been performed with rather large clusters consisting of $N > 100$ atoms [39, 40]. It turns out that size effects in the spin and orbital magnetic moments or the anisotropy energy become only observable in clusters of a few atoms in size. In fact, nanomagnetism is intermediate between atomic-scale magnetism and macroscopic magnetism (Maxwell's equations) but cannot be considered as a superposition of the two limits [3]. Not only the size but also their areal density [41], the interaction with the substrate or a cover layer [42, 43], and the electronic exchange and hybridization during alloy formation decisively determine the magnetic cluster properties.

One aspect of the quest for new structures, new physics, and new applications is the development of *complex* nanostructures. Such structures can be used for logic operations [44, 45], exchange spring and other composite media for magnetic recording [23, 46–53], multiferroics [54], and can be rather exotic, such as three-dimensional arrays and hybrids involving living cells and magnetic nanostructures. The ultimate goal is the creation of complicated three-dimensional objects from nanoscale building blocks, and the hope is that complex structure and chemical composition results in complex interactions, and ultimately in useful properties or additional functionality. The achievable level of complexity of nanostructures depends on advances in fabrication and synthesis [55]. Intriguingly, new structures are often discovered in other areas of nanotechnology [56] but then develop into magnetic structures with very different physical properties, such as magnetic nanotubes [18].

The length scales considered in this review range from less than 1 nm to several 100 nm, although in most cases the feature size are 5–20 nm. A natural length scale is $a_0/\alpha = 7.2$ nm [3, 57, 58], where a is Bohr's hydrogen radius and $\alpha = 1/137$ is Sommerfeld's fine-structure constant. Basically, this length scale determines the range of magnetic interactions and distinguishes nanostructures from macroscopic magnets.

The thermal stability of the magnetization direction in nanostructures is a critical for applications as magnetic recording media [46, 59]. For a small particle of volume V and anisotropy K , the relaxation time $\tau = \tau_0 \exp(KV/k_B T)$, where $\tau_0 \sim 10^{-10}$ s. The particle volume is usually limited, so that room temperature thermal stability requires the control and enhancement of the anisotropy, including surface and

interface anisotropy contributions [3]. Quantum-mechanical effects such as entanglement are even more demanding and require temperatures of 4.2 K or below. Thermally stable hard-magnetic nanoparticles can now be produced down to 3 nm [22], but some of the other nanostructures discussed here are of the low-temperature type.

In this chapter, we review synthesis strategies with prospect of success for the fabrication of moderately complex nanometer- and sub-nanometer scale structures and discuss relevant interactions and effects that determine the magnetic behavior of such structures as a result of their complexity.

3.2 Structure, Chemistry, and Geometry

Some nanostructures occur naturally—in minerals and biological systems—or are easily produced by bulk-processing methods. However, in most cases the structures are produced artificially, by using methods such as pulsed laser deposition (PLD), cluster deposition [60, 64], lithography [5], patterning using nanomasks and templates such as porous alumina [61], focused ion-beam milling (FIB) [45, 62], molecular-beam epitaxy (MBE), ball milling, STM deposition [63], melt spinning, lithography, and chemical vapor deposition (CVD). More recently, supramolecular chemistry [66] and self-assembly [65] have attracted special attention, as they allow for the fabrication of complex surface-supported structures with nearly atomic precision.

There is a crucial distinction between top-down and bottom-up methods. Top-down methods start from relatively big structural units and use methods such as cutting and milling to *decrease* the structure size. Examples of top-down methods are traditional microfabrication and lithography. By contrast, bottom-up methods start from very small units like atoms, molecules, or small clusters and implement concepts such as self-assembly and ‘lock-and-key’ type molecular recognition, with the goal to *increase* the structure size. It is anticipated that devices based on functional self-assembled structures will become available by combining both top-down and bottom-up fabrication steps [55]. A summary of all available techniques would go far beyond the scope of this chapter, but a few methods will be described as we go along.

The processing, analysis, or application of nanostructures requires their deposition on a surface, embedding in a matrix (Fig. 3.2), or incorporation into a more complicated structure (Fig. 3.3). Nanoscale embedding is characterized by interface-specific features that go beyond the short-range atomic order observed in many intermetallic compounds. The collective ferromagnetic behavior of Fe nanodots on Cu surfaces [38] or the canted uniaxial anisotropy of Fe or Co atoms at Pt step edges [67, 68] is direct consequences of embedding, i.e., the interaction of the nanostructure with the supporting host. A counter-example is rare-earth transition-metal alloys, where the relatively big rare-earth atoms tend to be surrounded by a large number of transition-metal atoms. These groups of atoms look like clusters—and some properties, such as the rare-earth anisotropy, can be interpreted as cluster

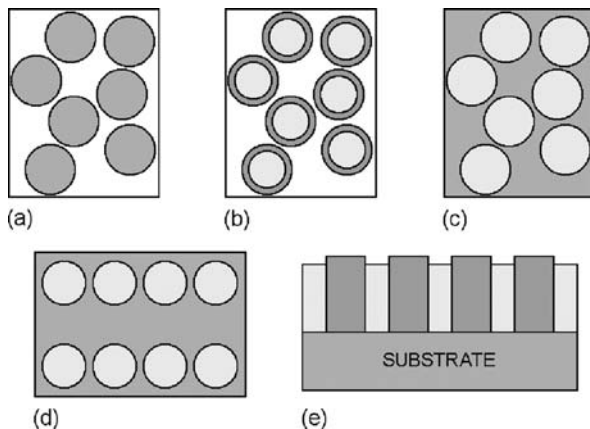


Fig. 3.2 Some types of embedding: (a) free isolated clusters, (b) free coated clusters, (c) randomly distributed clusters on a substrate (top view), (d) ordered nanoparticles on a substrate, and (e) simplified side view of a high-density recording medium

properties [69]—but the electronic structure of these units is very different from that of true clusters (Section 3.1).

An important practical point is the packing fraction of the clusters, which is roughly proportional to the magnetization M . Figures of merit of magnetic materials depend on M , as exemplified by the energy product of permanent magnets, which is quadratic in M . The packing also affects the hysteresis, especially via the demagnetizing factor [70]. Magnetic recording requires high-areal densities [29], but interactions between particles lead to harmful cooperative effects [4]. However, while we consider interactions, a detailed discussion of packing and compression issues goes beyond the scope of this chapter.

3.2.1 Synthesis of Supported Nanostructures

All bottom-up strategies for the fabrication of metallic nanostructures at surfaces are essentially based on growth phenomena. Atoms or molecules are deposited on the substrate in vacuum and nanoscale structures evolve as the result of a multitude of atomistic processes. Key processes during *epitaxial growth* are the surface diffusion of single adatoms, including diffusion on terraces, over steps, along edges, and across corners. Each diffusion step is thermally activated, with the respective rate depending exponentially on corresponding potential energy barrier. The shape and size of nanostructures are largely determined by the competition of active diffusion processes, and the growth temperature is the key for shaping the growing aggregates. The control over the epitaxial growth can be further increased by exploiting structured surfaces, such as stepped, reconstructed, or corrugated surfaces, as nanotemplates. Such surfaces offer predefined nucleation sites and the position of

each nanostructure is hence exactly defined by the template with nanometer accuracy (recent overview in [65]). However, surface free energies, lattice mismatch, or structural imperfections set limits to the epitaxial growth and most of the growth strategies work only for a few model systems.

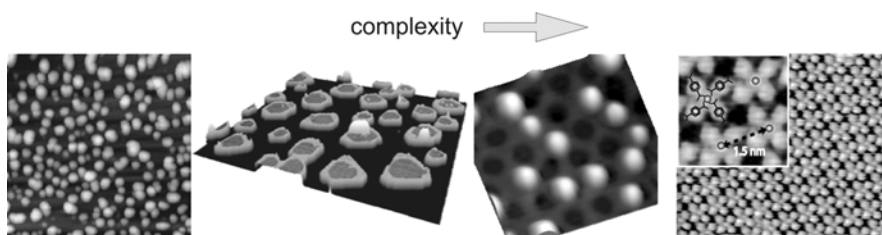


Fig. 3.3 STM images of surface-supported nanostructures of increasing complexity. From left: Fe clusters on Pt [71]; 2D core-shell particles of Fe cores (*grey*) with Pt shell (*bright*) on Pt substrate (*dark*) [72]; Co clusters, deposited on corrugated boron nitride template surface [73]; and Mononuclear $\text{Fe}(\text{TPA})_4$ clover-leaf compounds from Fe-directed assembly of terephthalate organized in regular superlattices on $\text{Cu}(100)$ [74, 75]

The complications associated with epitaxy can be overcome with *cluster deposition* methods, to fabricate cluster layers or cluster-assembled nanocomposites [64]. Here, the clusters are formed *before* they make contact with the surface. Mainly two techniques are established, which are soft-landing of clusters formed in the gas phase [76] and buffer-layer-assisted cluster growth (BLAG) [77–79]. Both techniques are, in principle, suitable to form clusters of almost any material on any substrate [80]. Advantages of BLAG are that (i) no experimental equipment beyond the standard molecular-beam epitaxy tools are required, (ii) it can be used to deposit clusters on nanotemplate surfaces, such as stepped substrates [81] or corrugated boron nitride monolayers ([82] and Fig. 3.3), to achieve controlled, ordered cluster arrangements, and (iii) the cluster formation is a parallel process and high cluster coverage can be achieved during a short preparation step. In contrast, the flux of dedicated cluster sources is limited by the mass filtering, but they usually give clusters with much narrower size distribution. Recent overviews over fabrication and properties of surface-supported clusters can be found in Refs. [83, 84]. A direct comparison between deposited and epitaxial Fe clusters illustrates best the effect of direct overlayer-substrate interaction during preparation and can be found, for instance, in Ref. [85].

Buffer-layer-assisted cluster fabrication requires pre-coating the substrate by a noble gas layer, such as Xe, at low temperature. Metal deposited on this buffer layer is mobile enough already at such low temperatures to form small clusters [79]. Warming up the substrate to 90 K causes evaporation of the Xe layer. The clusters coalesce during the Xe sublimation and thus grow in size, until making contact with the surface. The final cluster size and the size distribution depend mainly on the initial thickness of the Xe layer and on the metal coverage. Still on the Xe layer the cluster structure can partly relax. Figure 3.4 indicates that the site occupancy depends on size of the embedded particles. The corresponding statistical mechanics

is nontrivial and similar to the description of Krypton on graphite by the $q = 3$ Potts model [86]. We will return to these methods in the context of Fe–Pt thin-film nanostructures (Section 3.2.2).

Molecular self-assembly on metal surfaces is a powerful means to realize structurally complex nanosystems [55, 66, 87, 88]. Molecular networks are formed during the deposition of specific organic molecules on single crystalline metal surfaces under ultrahigh vacuum. Desired architectures can be obtained by controlling non-covalent interactions, such as hydrogen bonding, ionic bonding, and metal–ligand interactions, with the functional groups of the molecules. A particular class of network structures, the so-called metal–organic coordination systems (see Fig.3.3, right), is obtained by the co-deposition of functionalized organic molecules and metal atoms. The self-assembly depends here on coordination bondings between the two species. Metal–organic systems represent a fascinating form of magnetic material, as they are a lattice of metal centers with the lattice spacings defined by the molecules and interactions mediated by molecules and the surface. The symmetry of the networks can be controlled in a wide range by the design of the molecules and the preparation conditions [89–93].

3.2.2 Case Study: Fe Clusters on Pt Surfaces

The clusters of Fe, shown in the STM images in Fig. 3.4, have been produced by buffer-layer-assisted growth on pristine metal surfaces [71]. The cluster size and areal density are controlled during BLAG mainly by two parameters, namely by the thickness of the Xe buffer layer and by the coverage of the cluster material. The smallest clusters in Fig. 3.4, of less than 2 nm diameter, can be formed with 0.05 monolayers (ML) Fe and 2 ML Xe (a). For the images (b–d), 2 ML Fe and buffer layers of varied thickness between 5 and 45 ML have been used. We see that higher Xe layer thicknesses or higher Fe coverages result in larger clusters. The cluster density can also be controlled via both the Fe and the Xe coverage, and higher cluster densities are achieved with thin Xe layers and comparatively large Fe coverage (Fig. 3.4b). The diameter of the clusters of flattened hemispherical shape increases from 2.0 ± 1.0 to 9.9 ± 7.6 nm, from (a) to (d). Since STM tends to

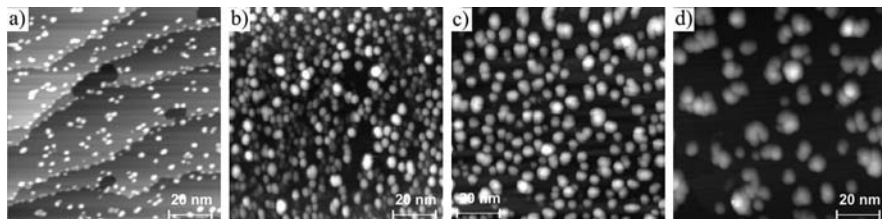


Fig. 3.4 Scanning tunneling microscopy (STM) pictures of Fe clusters fabricated by buffer-layer-assisted growth. (a) 0.05 ML Fe on Ag(111) using 2 ML Xe, (b–d) 2 ML Fe on Pt(997) using Xe buffer layers of 5, 18, and 45 ML thickness

overestimate the cluster size due to well-known tip convolution effects, the quoted cluster sizes are an upper limit. Without the Xe layer, the Fe is found to grow in the Volmer–Weber mode at substrate temperatures of 300 K and below [85]. Rough Fe films are obtained in this case with an average island size depending on the nominal Fe coverage.

Fe and Pt are known to form structurally and magnetically interesting phases in the bulk, such as Fe₃Pt (cubic Cu₃Au structure) and FePt (tetragonal *L*₁₀ structure). The latter has a rather high magnetic anisotropy of about 5 MJ/m³, which makes it suitable for ultrahigh-density magnetic recording [3, 94]. *L*₁₀-ordered FePt can also be produced in thin-film form, although stacking sequences different from the original ABAB stacking yield modified electronic properties. However, supported growth offers completely new possibilities to form also other Fe–Pt structures of different stoichiometry, geometry, and coordination. Fe–Pt sub-nanostructures can be realized, for instance, on flat Pt(111) or the vicinal Pt(997) Pt surfaces, by exploiting simple rules of epitaxial growth [65]. By controlling only the growth temperature and the Fe coverage, low-coordinated atoms, dots, and wires of Fe on the Pt, as well as ordered or disordered FePt surface alloys can be formed (Fig. 3.5) [95]. The local atomic environment in all these structures is different from bulk alloys. The iron partially spin polarizes the Pt, which then exhibits spin, orbital moment, and magnetic anisotropy and contributes to, if not dictates, the magnetism of the Fe [96, 97].

In a thermodynamic sense, zero- and one-dimensional structures (dots and long wires) do not exhibit long-range ferromagnetic order but are *paramagnetic*. However, the interaction between wires and dots, realized by the Pt atoms, can make the system ferromagnetic. A very simple example is one fcc(111) monolayer of Fe atoms where every second monatomic row is replaced by Pt atoms, similar to the surface alloy in the right part of Fig. 3.5. Denoting the respective Fe–Fe and Fe–Pt exchange interactions by J and $J^* \ll J$ yields the mean-field Curie temperature

$$T_c = 2(J + J^{*2}/J)/k_B \quad (3.1)$$

It can be shown that the corrections to the mean-field approximation are comparable to the mean-field result itself [99], which makes even the simplest surface alloys quite intriguing.

A nontrivial question is the onset of ferromagnetism in low-dimensional systems. It can be shown exactly that one-dimensional ‘ferromagnets’ are actually paramagnetic [100–102]. The proof for thin-film stripes of width w and thickness t is similar to the argumentation for the Ising model [100], except that the Ising bonds J must be replaced by effective exchange bonds scaling as $J_{\text{eff}} = 4tw(AK_{\text{eff}})^{1/2}$, where A and K_{eff} are the exchange stiffness and effective anisotropy, respectively [3] of the film. Kinetic barriers to reaching equilibrium, as considered in [67], are irrelevant to the problem, because ferromagnetism is defined as an equilibrium property. A slow approach toward equilibrium may mimic ferromagnetic order. The kinetics merely decides how long it takes to establish equilibrium [102] and structures larger than 1 or 2 nm behave bulk like.

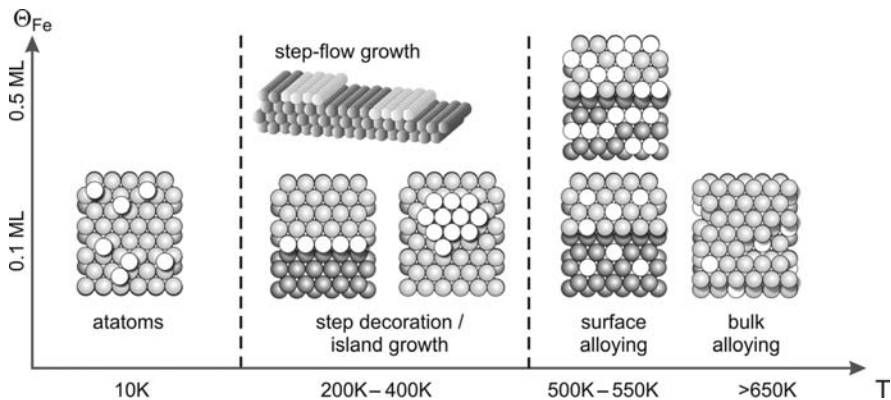


Fig. 3.5 Top-view on magnetic Fe–Pt surface structures (schematic). The brightest colors represent Fe atoms and darker colors represent Pt atoms in different layers. A variety of different Fe–Pt nanostructures can be fabricated by controlling only the substrate temperature during Fe deposition (T) and the Fe coverage (θ_{Fe}). The increased mobility at higher temperatures promotes chain or stripe formation on Pt(997) or compact cluster formation on Pt(111), and eventually surface and bulk alloying [98]

3.2.3 Structure of Embedded Clusters

Let us now discuss the structure and properties of clusters that are embedded in a matrix. Such cluster systems, for example Fe–Pt, Co–O, Mn–Au and Ti–O, can be produced by cluster deposition (Sect. 3.2.1) and other methods. The formation of clusters in a solid matrix can often be considered as an addition of substitutional or interstitial atoms. Figure 3.6 shows that here is a major distinction between coherently embedded and precipitated clusters. In dilute magnetic oxides and other systems, there may be segregated phases with distinct lattice parameters and structures (d), or coherent clustering with some lattice strain but without topological disruption of the lattice (c). This phenomenon applies to both substitutional and interstitial atoms and has many parallels in other areas of magnetism (C in Fe, N in $\text{Sm}_2\text{Fe}_{17}\text{N}_3$). It is related to *spinodal decomposition* and involves phenomena such as negative diffusion constants (see below). In many cases, the site occupancy is random (not shown in Fig. 3.6), and there is a general trend toward randomness above a structural ordering temperature T_c . The mean-field description of this transition is known as the Gorský–Bragg–Williams model and predicts that T_c is proportional to the interatomic interaction strength.

The model is actually very similar to the spin-1/2 Ising mean-field model, except that the average spin variables $s_i = \pm 1$ (or \uparrow and \downarrow) are replaced by the concentration $c_i = 0$ (A-atom) and $c_i = 1$ (B-atom). The relation between c_i and s_i is therefore $c_i = (1 + s_i)/2$, and the mean-field equation

$$\langle s \rangle = \tanh \left(\frac{zJ \langle s \rangle + h}{k_B T} \right) \quad (3.2a)$$

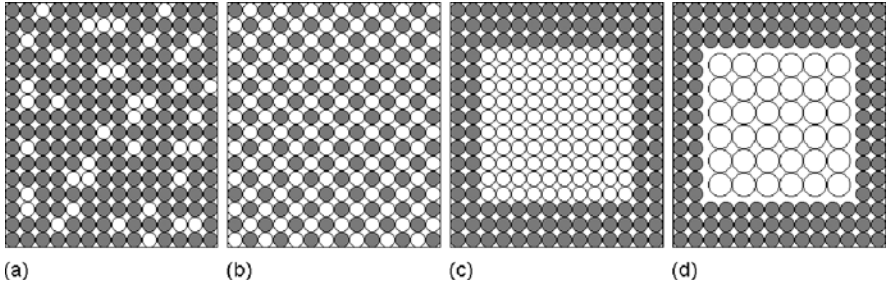


Fig. 3.6 Embedding of atoms in a matrix: (a) solid solution, (b) alloy, (c) coherent embedding, and (d) incoherent embedding or precipitation. These mechanisms are realized in a variety of nanostructures, including dilute magnetic semiconductors

becomes

$$\langle c \rangle = \frac{1}{1 + \exp\left(\frac{4zJ \langle c \rangle + h - 2zJ}{k_B T}\right)} \quad (3.2b)$$

In the latter equation, J is a (non-magnetic) net interaction energy between A and B atoms. The external field (or force) variable h has the character of a chemical potential and fixes the total numbers of A and B atoms [103]. In both cases, z is the number of nearest neighbors ($z = 4$ in the simplified model of Fig. 3.6b), and the mean-field ordering temperature $T_c = z|J|/k_B$. Above T_c , the structures of (b) and (c) are destroyed.

Treating the dynamics of the structures on a mean-field level amounts to the introduction of an effective diffusion constant [105, 206],

$$D = D_o \left(1 - 4c(1 - c) \frac{T_c}{T}\right) \quad (3.3)$$

where D_o is the interaction-free diffusivity and $c = \langle c \rangle$ is the concentration of the impurity atoms. An important special case is spinodal decomposition, that is, the transition from Fig. 3.6a to c.

A striking feature of (3.3) is the prediction of negative diffusion constants D . Ordinary diffusion means that initial concentration gradients are smoothed, whereas negative diffusion constants lead to the enhancement of pre-existing concentration inhomogeneities. Figure 3.7 illustrates this point by showing the evolution of a concentration inhomogeneity for $D < 0$, eventually leading to phase segregation, Fig. 3.6c. Interestingly, there are three cases where the diffusivity is concentration independent. First, for small concentrations ($c \sim 0$), we obtain the trivial limit $D = D_o$, roughly corresponding to Fig. 3.6a. Second, for high concentrations ($c \sim 1$), one obtains $D = D_o$, meaning that dense systems behave like diluted systems. This is a diffusion analogy to dense electron gases, which behave like non-interacting

particles. The underlying physics is the division of the phase space into cells, namely crystal sites in diffusive systems and k -space cells in electron gases. Then, the hard-core repulsion of the atoms and the Pauli principle, respectively, reduce the importance of interactions. Alternatively, one may consider diffusing holes rather than diffusing particles. The third exception is the limit of high temperatures: since $c(1-c) \leq 1/4$, negative diffusion coefficients are limited to $T \leq T_c$ and $D = D_0$ for $T = \infty$.

The role of attractive interactions between A (or B) atoms is seen from the ideal-gas analogy. A non-interacting hard-core gas can be compressed to a relatively dense random packing fraction of about 64%, but it never becomes a fluid with different high and low-density phases. The interactions between diffusing atoms are largely elastic [103, 104]. The electronic interactions determine the solubility, parameterized by h in (1b), and ensure the hard-core repulsion between atoms, but their contribution to J is negligible. Due to the size difference between A and B atoms, Fig. 3.6c is elastically more favorable than Fig. 3.6c, so that spinodal decomposition is a very common phenomenon, especially for interstitial impurities. However, some alloys have strong A - B interactions, and the resulting structure is similar to Fig. 3.6b. Examples are $L1_0$ alloys, such as FePt, where the light and heavy transition-metal atoms form layers, and the surface alloys discussed in the following subsection.

An interesting point is that the mean-field approximation works well for impurity atoms if the summation $zJ = \sum_j J_{ij}$ includes more distant atoms. This is different from the magnetic Ising model, where the critical exponents become incorrect in fewer than four dimensions [104, 105]. Note that the elastic energy of Fig. 3.6c is smaller than that of (a), but a global minimum of the elastic energy is achieved by incoherent phase segregation, Fig. 3.6d. For large atomic-size differences, the incoherent state is the only one that can be realized in practice. Experimentally, (d) yields two well-separated x-ray diffraction peaks, but (a-c) are more difficult to distinguish.

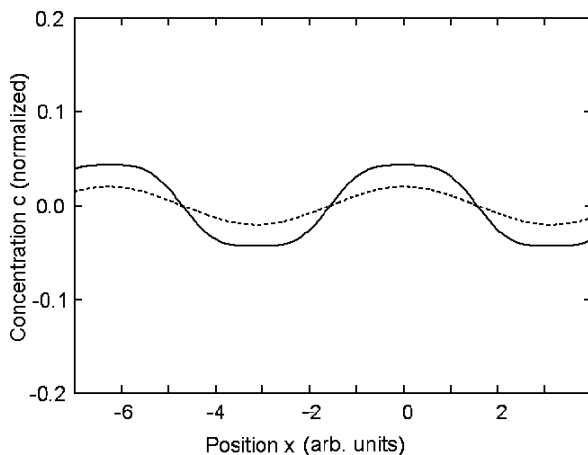


Fig. 3.7 Effect of negative diffusion constants during spinodal decomposition. In contrast to ordinary diffusion, initial concentration gradients (*dotted line*) are enhanced during the diffusion (*solid line*)

3.2.4 Case Study: FePt Clusters in a Carbon Matrix

Recently, interest in films based on magnetic nanoclusters has grown enormously with increasing attention devoted to the extension of the magnetic recording areal density to 1 terabit/in² and beyond. This depends on the development of high-anisotropy films with uniform size clusters or grains below 10 nm that are exchange decoupled or weakly coupled [29, 106, 107]. The Equiatomic FePt nanoclusters with $L1_0$ phase are a promising candidate for such media, because of their large anisotropy constant K of about $\sim 7 \times 10^7$ erg/cm [107, 108], which helps to meet the requirement for both high signal-to-noise ratio and thermal stability of the media.

While many efforts have been made to fabricate oriented $L1_0$ FePt nanoparticle or nanograin films with some exchange coupling [109, 110], understanding the magnetic properties of a collection of well-isolated clusters is of similar high interest for exploring FePt clusters as a potential media for extremely high-density recording. Xu et al. [111] have prepared FePt nanoclusters with small average cluster size ($d \sim 4$ nm) using a gas-aggregation technique [112]. The FePt clusters are nearly monodispersed with a narrow Gaussian size distribution (standard deviation $\sigma / d \sim 0.09$). Dilute FePt:C nanocluster films have been prepared, in which the FePt volume fraction ranged from 5 to 30%. Carbon was used as the matrix for isolating the FePt clusters to decrease the exchange interaction and to reduce the cluster growth during high-temperature annealing.

Fig. 3.8 TEM image of FePt:C cluster film with 5 vol% FePt annealed at 700°C for 10 min

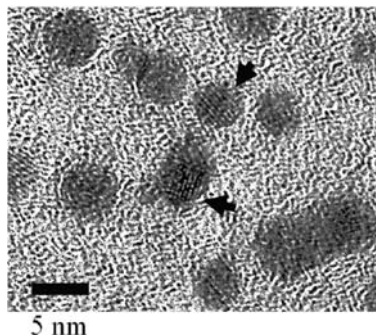


Figure 3.8 shows a TEM image of FePt:C cluster film with 5 vol% FePt annealed at 700°C for 10 min. Well-isolated clusters with single crystal $L1_0$ structure are observed. The arrows indicate the clusters with lattice fringe observable, suggesting single crystalline clusters.

Figure 3.9a shows the in-plane and perpendicular hysteresis loops of the FePt:C film with 5 vol% FePt annealed at 700°C for 60 min, measured at 10 K. Both in-plane and perpendicular loops are similar, indicating that the easy axes of the FePt clusters are distributed randomly, which is in agreement with the XRD measurement. A perpendicular coercivity of about 29 kOe at room temperature and 40 kOe at 10 K are achieved. This result indicates the high degree of $L1_0$ ordering after annealing for a relatively long time (> 10 min). The loops are not saturated at an applied

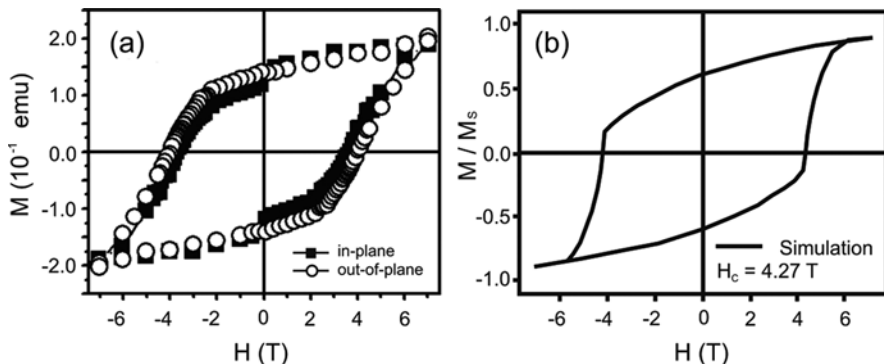


Fig. 3.9 In-plane and perpendicular hysteresis loops of FePt:C cluster films with 5 vol% FePt annealed at 700°C for 60 min: (a) at 10 K; (b) hysteresis loop obtained by numerical simulation based on Landau–Lifshitz–Gilbert equation

field of 70 kOe. Assuming these isolated clusters are non-interacting and the formula $H_c = 0.48 H_k$ can be applied [113], an anisotropy field $H_k = 2K/\mu_0 M_s$ of 8.3 T [83 kOe] is obtained. This estimate is confirmed by a numerical simulation using the NIST OOMMF code based on Landau–Lifshitz–Gilbert equation.¹ The simulation assumes $L1_0$ FePt spheres of diameter of 4.5 nm. The spheres occupy 5% of the total volume and are randomly oriented in a non-magnetic matrix, without intergranular exchange interactions. The chosen parameters are the anisotropy constant $K = 4 \text{ MJ/m}^3$ and the saturation magnetization $M_s = 1.13 \text{ T}$ [900 emu/cm³], corresponding to $H_k = 8.9 \text{ T}$, as well the exchange stiffness $A = 10 \text{ pJ/m}$. The simulated hysteresis loop, Fig. 3.9b, is essentially a Stoner–Wohlfarth loop for randomly oriented particles, and its coercivity of 4.27 T is close to the experimental value of 4 T at 10 K. This confirms that the 5 vol% of FePt clusters in the C matrix behave like non-interacting Stoner–Wohlfarth particles. Such a system may show useful and more interesting nanomagnetism if the orientation of the clusters can be controlled, which needs to be further investigated.

3.3 Anisotropy and Hysteresis

The control of anisotropy and hysteresis is one of the key aims of magnetic nanostructuring. Anisotropy means that the magnetic energy depends on the angle between magnetization and crystal (or nanostructure) axes. In contrast, interatomic exchange refers to the *relative* orientation of neighboring atomic spins. Magnetic hysteresis and coercivity reflect energy barriers caused by magnetic anisotropy, although the barriers depend on the exchange, too. Both anisotropy and hysteresis are real-structure dependent. The real-structure dependence of the anisotropy is

¹<http://math.nist.gov/oommf/>

epitomized by surface and interface anisotropies, whereas hysteresis and coercivity are often affected by seemingly small imperfections. For example, tiny additions of N or C may enhance the coercivity of pure iron by several orders of magnitude [69, 114].

The practical importance of anisotropy and coercivity cannot be overestimated. In soft magnets, low coercivity is desired and achieved by embedding of Fe–Si nanoparticles of random-anisotropy in a three-dimensional matrix [115, 116]. Permanent magnets are usually characterized by high anisotropies and coercivities, whereas ultrahigh-density recording media combine well-defined hysteresis loops with sufficient anisotropy and reasonably low writing fields. The focus of this section is on some aspects of the anisotropy of *embedded* nanostructures. There is a rich literature on specific magnetization-reversal mechanisms [3, 58, 117–121] and the resulting hysteresis loops in various systems, such as soft magnets [116], permanent magnets [23, 69, 122–124], and recording media [47, 49].

A long-standing challenge in nanomagnetism is the thermal stability of the magnetization direction. For a small particle of volume V and anisotropy K , the relaxation time

$$\tau = \tau_0 \exp(KV/k_B T) \quad (3.4)$$

where $\tau_0 \sim 10^{-10}$ s. The particle volume is usually limited, so that room temperature thermal stability requires the control and enhancement of the anisotropy, including surface and interface anisotropy contributions. Thermally stable hard-magnetic Fe–Pt nanoparticles can now be produced down to 3 nm [22], and much work is presently being done to understand and exploit the lower end of these length scales, especially in ultrahigh-density magnetic recording. Based on present-day bulk materials (SmCo_5), stable room temperature ferromagnetism is possible down to particle sizes of slightly less than 2 nm. SmCo_5 is quite corrosive and therefore not suitable as traditional recording material. However, future recording may be realized by sealed drives, partially for tribological reasons, which could put SmCo_5 in the spotlight again.

3.3.1 Surface and Interface Anisotropies

Magnetostatic contributions, such as shape anisotropy, are important in some materials. However, the leading anisotropy contribution is usually magnetocrystalline and reflects the interplay between crystal–field interaction (including hopping) and spin–orbit interaction. This includes not only bulk anisotropies but also surface, interface, and magneto-elastic anisotropies. The magnetic surface anisotropy adds to the total anisotropy [3, 125, 126].

In a nutshell, magnetocrystalline anisotropy reflects aspherical current loops (orbital moments) created by the spin–orbit coupling. These orbital-moment electron clouds interact with the atomic environment (crystal field), resulting in a directional dependence of their orientation which is observed as magnetocrystalline

anisotropy. It is important to keep in mind that symmetry breaking at surfaces and interfaces is a necessary but not sufficient condition for magnetic anisotropy. For example, the Heisenberg model (Section 3.1) is intrinsically *isotropic*, that is, the exchange energy does not depend on the angle between magnetization direction and bond axis $\mathbf{r}_i - \mathbf{r}_j$. A challenge is that surface anisotropy is closely linked to the *indexing* of the surface [3, 121, 133], which makes the frequently assumed normal anisotropy $-K(\mathbf{s} \cdot \mathbf{n})^2$ [126, 205] a very crude approximation.

The calculation of the anisotropy is often complicated [127, 128], but there exist simple models for a variety of limiting cases [69, 120, 129, 130]. For example, rare-earth anisotropy is characterized by a spin-orbit coupling much larger than the crystal-field interaction. This leads to a rigid Hund's-rules coupling between spin and orbital moments and means that the anisotropy energy is essentially equal to the electrostatic interaction energy between the rare-earth 4f shells and the crystal field [69, 120]. Most rare-earth shells are aspherical and yield large anisotropy contributions, but gadolinium (Gd) has a half-filled 4f shell ($4f^7$) with spherical symmetry and zero magnetocrystalline anisotropy.

The crystal-field character of the anisotropy is seen, for example, from the possibility of changing the magnetization direction of Ni due to reversible absorption of H on Ni/Cu(001) [131]. A similar mechanism, namely the interstitial absorption of N, can be used to turn the soft magnetic material $\text{Sm}_2\text{Fe}_{17}$ into hard-magnetic $\text{Sm}_2\text{Fe}_{17}\text{N}_3$ [105]. In itinerant 3d metals, the electron density $\psi^*(\mathbf{r})\psi(\mathbf{r})$ is largely determined by the interatomic hopping (band structure), and the spin-orbit coupling is a small perturbation [132]. The relation between crystal-field (hopping) and anisotropy can no longer be mapped onto a simple electrostatic interactions [120, 129, 133], but it remains possible to postulate rules for limiting cases, such as nearly filled 3d shells (Section 4.3)

An unusual surface magnetic anisotropy occurs in MnO nanoparticles. Mn^{2+} has a half-filled shell ($3d^5$) and should be isotropic in any environment, similar to the role of Gd in the rare-earth series. The anisotropy of bulk MnO is indeed very small, but there is a striking anisotropy enhancement in nanoparticles [134]. This is explained in terms of a high-spin-low-spin transition created by the strong crystal-field interaction at the surface. The crystal field causes majority 3d electrons to jump to low-lying minority states and creates anisotropy in the Mn atoms [134].

3.3.2 Hysteresis of Fe Clusters on Pt

Let us now return to the Fe/Pt system introduced in Section 3.2.2. Figure 3.10 shows Kerr-effect (MOKE) hysteresis loops for an epitaxially grown Fe layer of nominally deposited 2 ML of Fe (left), and cluster ensembles formed from the same amount of Fe on Xe layers of the indicated thickness (see STM images in Fig. 3.4). For the clusters, preferential in-plane magnetization is found, in contrast to the perpendicular anisotropy found for the epitaxial Fe layer. The increase of the average cluster size with Xe buffer layer thickness enhances the total magnetic signal. Due to a

distribution of the cluster size and orientation, the loops are not saturated at the maximum available field.

For all samples shown in Fig. 3.4, the magnetic anisotropy is significantly enhanced with respect to bulk Fe [71]. This is the result of the large Fe–Pt interface anisotropy caused by the hybridization of iron-series 3d and heavy transition metal 4d/5d electrons (Section 3.3.3). By choosing suitable combinations of substrate and clusters, it is possible to tune the magnetic anisotropy of the clusters, and values of up to 0.9 meV/atom and 9 meV/atom have been reported for smallest Fe and Co clusters on Pt [135]. In addition, STM images reveal the presence of significant strain in epitaxial Fe islands on Pt(117) due to the lattice mismatch. The corresponding magneto-elastic contribution to the anisotropy energy is sufficient to overcome the shape anisotropy, thus favoring perpendicular magnetization [85].

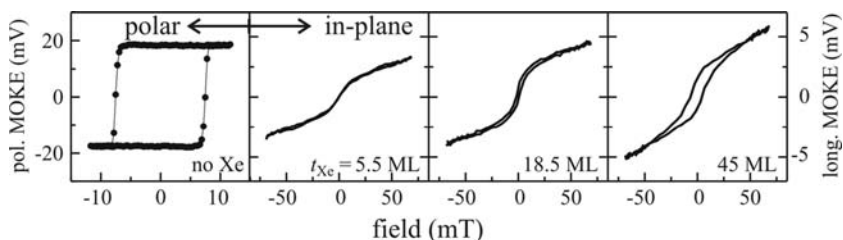


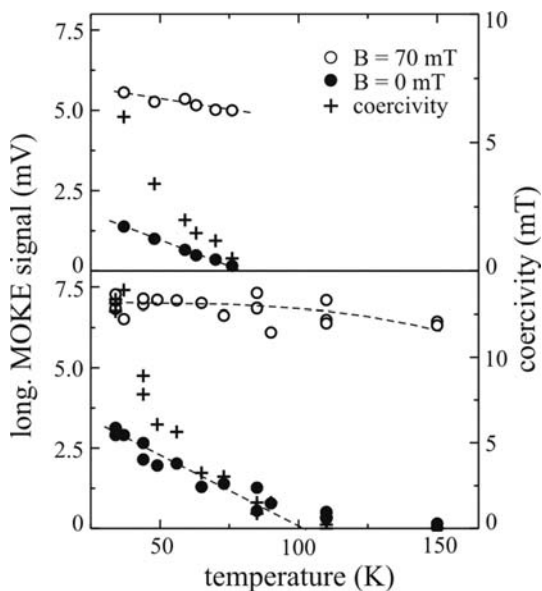
Fig. 3.10 MOKE hysteresis loops of 2 ML Fe on Pt(997) prepared on Xe buffer layers of varying thickness between 0 and 45 ML. Without Xe, Fe grows epitaxially in Vollmer–Weber mode [68], while the Xe layer promotes the formation of partially relaxed Fe clusters. The cluster size increases with the Xe thickness, see Fig. 3.4

The evaluation of experimental hysteresis loops and the determination of the anisotropy are complicated by the unknown moment of the clusters. In fact, the surface enhancement of the magnetic moment in clusters can even exceed the moments found in monolayer thin film or in metallic surfaces [136]. Ignoring interactions, the deposited particles are superparamagnetic, and their anisotropies can be estimated from the superparamagnetic blocking temperature T_B , which can be determined experimentally from temperature-dependent MOKE measurements (Fig. 3.11). Taking the average cluster volume from STM images and putting $\tau \sim 100$ s in (3.4) gives an estimate for the anisotropy of the clusters, which is $K = 13 \mu\text{eV}$ per atom for clusters of 2 ML Fe and 45 ML Xe (compare to bulk Fe: $4 \mu\text{eV}$ per atom). The anisotropy energy per atom in the cluster might actually be larger since STM tends to overestimate the cluster volume. The importance of finite-temperature effects is also seen from Fig. 3.11; the pronounced decrease of magnetization and coercivity is a consequence of Eq. (3.4).

The net magnetization of clusters can be stabilized by inter-particle and particle–substrate interactions [37, 38, 137, 138]. In the present case, the dominant contribution to the magnetic anisotropy is expected to come from the interaction of the clusters with the substrate. The clusters hybridize with the underlying substrate, thus producing a cloud of magnetic polarization in the Pt [139, 140]. Although the

contact to the substrate somewhat reduces the average spin moment per atom in the cluster, it introduces a moment in the d-band of the substrate, which might even be extended beyond the region of physical contact [141]. Hence, the effective magnetic volume as well as the anisotropy is increased, which stabilizes the overall magnetization, increases the blocking temperature, and ties the cluster magnetization to the substrate lattice. However, this leads to cooperative magnetization reversal [3] and goes at the expense of the effective cluster size, eventually reducing the areal density in magnetic recording. Furthermore, (3.4) is limited to very *small* particles [59]. In large particles, incoherent magnetization processes and thermal excitations reduce the volume V to some effective volumes $V_{\text{eff}} < V$. For example, magnetization reversal in long and highly anisotropic wires requires a thermal energy of $4\pi R^2(AK)^{1/2}$, corresponding to $V_{\text{eff}} = 4\delta_B R^2$, where R is the wire radius and $\delta_B = \pi(A/K)^{1/2}$ is the Bloch-wall width of the wire. In other words, making wires very long yields large values of KV but no proportional increase in thermal stability.

Fig. 3.11 Temperature dependence of the coercivity (+), the longitudinal MOKE signal at remanence (●), and in a field of 70 mT (○) for 2 ML Fe/45 ML Xe/Pt(997) (*top*) and 4 ML Fe/18 ML Xe/Pt(997) (*bottom*). The blocking temperature increases with the cluster size. The MOKE measurements have been done after Xe desorption at 100 K



3.3.3 Role of Heavy Transition Metals

The spin polarization of exchange-enhanced Pauli paramagnets in compound structures affects not only the magnetic moment but also the anisotropy. This is because the 4d and 5d elements are much heavier than the 3d elements and exhibit a more pronounced spin-orbit coupling. This explains the pronounced anisotropy of $L1_0$ -ordered 3d/4d and 3d/5d magnets, such as the FePt, CoPt, and FePd [94], as well as the 'giant' [135] anisotropy of various thin-film structures. Since a single late 3d

atom can spin polarize several 4d or 5d atoms, the anisotropies per 3d atom can actually be huge, for example, 9 meV for one Co atom on Pt(111) [135]. In thin-film nanostructures, such as those shown in Fig. 3.3 or Fig. 3.5, the effect strongly depends on the chemical nature and indexing of the substrate, on the structure and shape of the clusters, on the lattice mismatch (strain), and on the reduced coordination.

However, the main contribution to the anisotropy comes from the heavy transition metals, and the anisotropy per Pt atom is relatively large but not surprising. In fact, even larger values can be achieved in 5f compounds, but as in the Co/Pt(111) system, these high values are limited to low temperatures [130]. Incidentally, the temperature dependence of these structures is quite intriguing, with substantial deviations from the popular Callen-and-Callen theory [142–144].

The spin polarization also affects the *dynamics* of thin-film structures, because spin–orbit coupling is a major source of damping. The effect is also known as spin pumping [145], although it is somewhat different from the spin pumping usually considered in magneto-transport. Figure 3.12 shows a typical geometry. As in other inhomogeneous nanostructures [146–148], the magnetization modes are localized, and the damping comes from the regions where both the magnetization and the spin–orbit coupling (λ) are large. Physically, iron-series 3d electrons hop onto Pt sites, where they give rise to damping via the spin–orbit interaction of the Pt 5d electrons. Since the Co ensures a significant spin polarization in the Pt, the effect is large in Fig. 3.12a. In (b), the Ni is essentially unable to spin polarize the Pt and may actually become paramagnetic at the interface. This means that the damping is larger in the Co/Pt systems than in the Ni/Pt system. The effect can be investigated experimentally, by using optical pump-probe techniques [209] or FMR [145].

An idea related to the magnetic anisotropy of 3d/4d and 3d/5d thin-film nanostructures is the exploitation of heavy transition metals such as W in permanent magnetism and ultrahigh-density magnetic recording. One example is the Fe–W system [149]. In fact, there are many ferro- and antiferromagnetic $L1_0$ -type compounds [96, 150–154], and many alloys exhibit easy-axis anisotropy along the c -axis, especially those containing Pt and Pd, whereas MnRh has in-plane anisotropy [96]. This reflects the orientation of the easy axis to the bond axis of itinerant magnets [129].

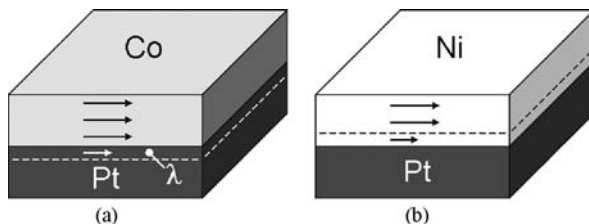


Fig. 3.12 Damping at Co–Pt and Ni–Pt interfaces. The damping is much larger in Co–Pt, because the Co yields a substantial spin polarization in adjacent Pt atoms, which then realize damping via the strong spin–orbit coupling (λ) of the Pt 5d electrons

Aside from binary $L1_0$ compounds, one can consider alloys with the general composition $A_xB_yC_z$, where $A = \text{Fe, Co}$, $B = \text{Pd, Pt}$, $C = \text{Mn, Ni, Cu, W, Rh, Ir}$, and x , y , and z are compatible with the stoichiometry and solid-solution range [152–154] of the tetragonal $L1_0$ phase. Similar considerations apply to materials crystallizing in the hexagonal NiAs structure, especially MnBi and PtBi. Based on these materials, two-phase nanostructuring can be used to tailor the magnetic anisotropy. Anisotropy is an atomic quantity, but the ferromagnetic exchange ensures an anisotropy averaging over a few nanometers, in contrast to the absence of nanoscale Curie temperature averaging [120, 155]. In particular, the intriguing temperature dependence of the anisotropy of many alloys [130, 144] opens the door for the creation of temperature-dependent anisotropy zeros, with a useful write-field reduction in magnetic recording. On an atomic scale, a similar effect is well known to occur in alloys such as Fe–Co–Tb–Dy but limited to a relatively narrow range of rare-earth transition-metal intermetallics [156]. Nanostructuring offers a way to greatly extend the range of these materials.

3.3.4 Proteresis

Nanoscale embedding may yield properties and phenomena not encountered in bulk magnets and single-phase nanostructures. One example is the occurrence of inverted hysteresis loops (or proteresis) in CoO/Co core–shell nanostructures. The effect was originally discovered in granular nanocomposites and means that the hysteresis loop is cycled clockwise rather than anticlockwise [157]. The phenomenon is counterintuitive, because it means that magnetostatic energy is created rather than dissipated. The basic explanation [157] involves an energy transfer between magnetic and exchange energies, so that the net energy is well behaved.

Proteresis has recently been observed in ultrasmall Co:CoO core–shell nanoclusters [8]. The structures, produced by cluster-beam deposition, have Co core sizes ranging from 1 to 7 nm and a common CoO shell thickness of about 3 nm. Figure 3.13 shows that the proteretic behavior reflects a subtle interplay between various anisotropies and exchange interactions in the Co and CoO phases and at the Co–CoO interface. A striking feature is the existence of proteretic (clockwise) rather than hysteretic loops in a relatively narrow core size range from 3 to 4 nm—smaller and larger particles exhibit ordinary hysteresis loops.

The size dependence is explained by first considering a very small soft-magnetic core in a hard matrix. The hard and soft regions are then strongly exchange-coupled, and the core–shell cluster rigidly rotates in a magnetic field, and the loop is hysteretic. In the opposite limit of large core–shell clusters, the system behaves like a superposition of two phases, both hysteretic. Only on a length scale of a few nanometers, where the interactions shown in Fig. 3.13b–c are comparable, proteresis is observed.

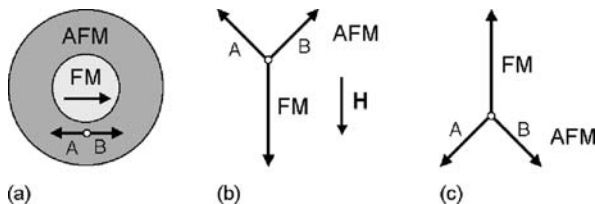


Fig. 3.13 Proteresis in Co:CoO core-shell nanoparticles: (a) structure and sublattice magnetizations, (b) initial spin structure and (c) final spin structure. In (b), the magnetic field acts on the sublattices A and B of the AFM CoO, but not on the FM magnetization of the core

3.4 Quantum-Mechanical Effects

Both free and embedded nanostructures exhibit interesting quantum effects [21, 158], although the relative importance of those effects tends to decrease with increasing feature size and is often difficult to distinguish from classical real-structure effects [159]. According to quantum mechanics, electrons behave like waves, and the embedding of an atom or cluster in a bigger unit tends to mix the wave functions both in the cluster and in the matrix. The range of those interaction is rarely much larger than 1 nm, but this is sufficient to create major changes.

A crude way of gauging of the effect of nanostructuring on the anisotropy is to compare the spin-orbit coupling λ (about 0.05 eV for the late 3d metals) with the 3d band width of about 5 eV. This means that minor structural changes may have a strong impact on the anisotropy, and depending on the individual energy levels near the Fermi level, the effect may extend over several nanometers. Anisotropy rules for itinerant ferromagnets are therefore more difficult to establish than for rare-earth magnets.

3.4.1 Embedding from a Quantum-Mechanical Point of View

How do the quantum states change when an isolated cluster is embedded in a matrix? A conceptually simple—though practically often demanding—procedure is the mapping of the complex states onto simpler wave functions, such as hybridized atomic states or extended orbitals. The corresponding procedure is known as *down-folding* [160–162] and goes back to a perturbation approach by Löwdin [163]. The idea is to divide the quantum states $|\psi\rangle$ of the full system into arbitrary classes, which yields a relatively simple formula describing the interaction between sub-systems. In solids, downfolding is used to simplify Hamiltonians and to introduce physically transparent extended orbitals (including third-nearest neighbors). This method was successfully applied, for example, to high-temperature superconductors [162].

In the present case, it is natural to choose the quantum states $|\phi\rangle$ of the embedded cluster or nanostructure as the first class and the quantum states $|\chi\rangle$ of the

embedding matrix as the second class. The Schrödinger equation $H|\psi\rangle = E|\psi\rangle$ can then be written as

$$H_{\text{cluster}}|\phi\rangle + V|\chi\rangle = E|\phi\rangle \quad (3.5a)$$

and

$$V^+|\phi\rangle + H_{\text{matrix}}|\chi\rangle = E|\chi\rangle \quad (3.5b)$$

where V describes the interaction between cluster and matrix. Substitution of $|\chi\rangle$ into 3.5(a) yields

$$H_{\text{cluster}}|\phi\rangle + V \frac{1}{E - H_{\text{matrix}}} V^+|\phi\rangle = E|\phi\rangle \quad (3.6)$$

This equation is the type $H_{\text{eff}}|\phi\rangle = E|\phi\rangle$, where H_{eff} is an effective interaction and may be solved by various methods. For example, one can first diagonalize H_{matrix} and label the eigenvalues by k , so that $1/(E - H_{\text{matrix}})$ becomes $1/(E - E_k)$. As a special case, (3.6) yields ordinary perturbation theory [163].

Equation (3.6) is remarkable, because it does not contain the unknown wave function $|\chi\rangle$ of the matrix but yields the exact energy eigenvalues. The downside and practical challenge is the energy dependence $H_{\text{eff}}(E)$ of the effective Hamiltonian. Consider, for example, a single impurity level $|\phi\rangle$ in a solid. If H_{eff} was independent of E , then the energy would be given by $E = \langle\phi|H_{\text{cluster}}|\phi\rangle + \langle\phi|H_{\text{eff}}|\phi\rangle$. However, for each eigenstate of H_{cluster} , the E in the denominator of (3.6) creates additional roots of the secular equation. The corrections are particularly large when the eigenvalues of the clusters (E) are comparable to those of the matrix (H_{matrix}). This is particularly common in metals, where the bulk states form rather broad bands and easily hybridize with the discrete states of the embedded objects if they have comparable energies.

3.4.2 Exchange Interactions

The Curie temperature and many other magnetic properties, such as the temperature dependence of the anisotropy, reflect interatomic exchange. On a one-electron level, exchange is obtained by making the potential spin dependent, as in the Stoner model and in LSDA calculations. On a many-electron level, there are correlation corrections, with the Heisenberg model as an extreme limit (Section 3.3). Here, we focus on a simplified model, namely on the Ruderman–Kittel–Kasuya–Yosida (or RKKY) model [164]. The idea is to model two spins S and S' at \mathbf{r} and \mathbf{r}' , respectively, by a point-like interaction J with conduction electrons s_n . The effect of the S and S' can then be described perturbatively, by equating the conduction electron Hamiltonian with H_{matrix} in (3.6) and applying perturbation theory.

A key feature of the free-electron RKKY exchange [164] is its long-range oscillatory behavior, which is caused by the sharp Fermi surface and described by $J_{ij} = \sim \cos(2k_F r)/r^3$, where k_F is the Fermi wave vector and $r = |\mathbf{r}_i - \mathbf{r}_j|$ is the distance between the spins. The oscillations means that spatial features smaller than about $1/k_F$ cannot be resolved with the available zero-temperature wave functions. Interestingly, net RKKY interactions do not average to zero but actually *increase* when embedded atoms are replaced by embedded nanoparticles, although the size-dependent increase is less pronounced than of the magnetostatic energy [165].

While traditional RKKY theory considers conduction electrons, the same approach can be used to treat tightly bound electrons [166] and electron orbitals localized around impurities [167]. The latter is of interest for dilute magnetic semiconductors [168–174], where structures similar to Fig. 3.6a yield ferromagnetism at and above room temperature.

Let us assume that the exchange between the two localized 3d spins is mediated by s electron (or hole) states from shallow donors or acceptors, which hybridize and may or may not form a narrow band. The calculation of the exchange amounts to the evaluation of the total energy for parallel and antiparallel spin orientations $S_i = \pm S_j$. The corresponding energies are

$$E_{\pm} = \Sigma_{\mu} \frac{|\langle \Psi_{\mu} | V(S_i) \pm V(S_j) | \Psi_0 \rangle|^2}{E_{\mu} - E_0} \quad (3.7)$$

where $|\Psi_{\mu}\rangle$ describes the mediating electrons and the interaction potential V is of the s-d type

$$V_i(\mathbf{r}) = \pm J_0 S_i \delta(\mathbf{r} - \mathbf{r}_i) \quad (3.8)$$

Here, the sign indicates whether the mediating electron is \uparrow or \downarrow . When both localized (3d) spins are located in one single-occupied shallow orbital, then the exchange is ferromagnetic, irrespective of the sign of J_0 , because both 3d spins are parallel (or antiparallel) to the spin of the shallow electron. With increasing impurity concentration, the shallow orbitals overlap and eventually percolate. Since the shallow orbitals have a radius of the order of 1 nm, this happens at very low concentrations.

Consider the exchange mediated by two overlapping shallow orbitals located at \mathbf{R}_1 and \mathbf{R}_2 . The hybridized wave functions have the character of (anti)bonding states whose level splitting is determined by the hopping integral t , and (3.7) yields the exchange [167]

$$J_{ij} = -\frac{J_0^2}{8t} (\rho(r_i - R_1) - \rho(r_i - R_2)) (\rho(r_j - R_1) - \rho(r_j - R_2)) \quad (3.9)$$

where ρ denotes the hydrogen-like density $\Psi^* \Psi$ of the shallow electrons. Here the involvement of J_0^2 reflects the second-order perturbation character of the theory, whereas the level splitting $E_{\mu} - E_0 \sim t$ originates from the denominator in Eq. (3.2a,b).

Equation 3.9 is separable and can be interpreted in terms of Fig. 3.14: the exchange is ferromagnetic (FM) if the magnetic ions are located in the same shallow s-orbital (a) and antiferromagnetic (AFM) if they are in different s-orbitals (b). The dashed line in the figure provides an alternative explanation: spins on the same side of the line exhibit FM coupling, whereas spins separated by the dashed line exhibit AFM coupling.

In contrast to the free-electron RKKY exchange J_{ij} , equation (3.9) cannot be reduced to a function of $\mathbf{r}_i - \mathbf{r}_j$ and also depends on \mathbf{R}_1 and \mathbf{R}_2 . The present model does not yield RKKY interactions in a proper sense, because shallow orbitals do not correspond to a sharp Fermi surface. However, aside from band-filling effects, the RKKY oscillation period π/k_F is essentially given by the interatomic distance. In the present model, the exchange changes sign in a very similar way, on a length scale given by the average distance between the donor and the acceptors.

The above mechanism is independent of whether the shallow orbitals form isolated clusters or percolate. In other words, it does not matter whether one considers dilute magnetic semiconductors or ‘dilute magnetic dielectrics’ [174]. However, the magnetic phase transition (critical temperature T_c) requires separate consideration. For localized spin-1/2 systems, the corresponding mean-field equation are

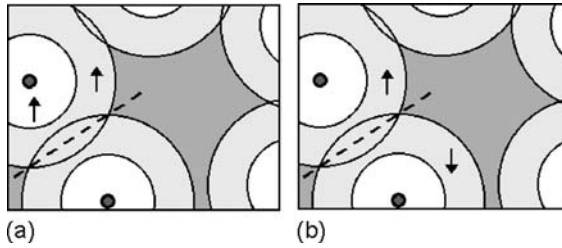


Fig. 3.14 Exchange mediated by two shallow orbitals: (a) ferromagnetic and (b) antiferromagnetic exchange. The *dark small circles* are the shallow donors or acceptors, whereas the *arrows* show the (fixed) positions of the localized 3d spins

$$m_i = \tanh \left(\frac{\sum_j J_{ij} m_j + \mu_o \mu_g H m_i}{k_B T} \right) \quad (3.10)$$

where $m_i = \langle S_i \rangle$. At the critical point, the zero-field magnetization vanishes ($m_i = 0$) so that (6) can be linearized and $m_i = \sum_j J_{ij} m_j / k_B T$. This equation can also be written in secular form, $\sum_j (J_{ij} - k_B T \delta_{ij}) = 0$, indicating that the critical temperature is basically an eigenvalue of the matrix J_{ij} . In more detail, $k_B T_c = J_{\max}$, where J_{\max} is the largest eigenvalue of J_{ij} .² This procedure, applies to a wide range of materials, including ferro-, ferri-, and antiferromagnets [210]; spin glasses [183]; magnetic nanostructures [155]; and magnetic semiconductors [212]. The reliability

²The other eigenvalues have no transparent physical meaning, because $|m_i| > 0$ below T_c and the approximation $m_i = 0$ are no longer valid.

of the mean-field predictions depends on the dimensionality of the structure [155, 211] and on the range of the interactions, similar to the well-known critical behavior of homogenous magnets [86].

From a quantum-mechanical point of view, the RKKY theory is a fairly crude approximation. In particular, (3.7) ignores spin–orbit coupling, which affects the anisotropy and—to a lesser extent—the magnetization [207, 208]. Dilute magnetic semiconductors are often anisotropic, exhibiting not only a preferential magnetization direction but also a direction dependence of the magnetic moment, for example, in the film plane of V-doped SnO₂ [175].

3.4.3 Preasymptotic Coupling

Moment formation and interatomic exchange in itinerant magnets such as Fe, Co, and many of their alloys is very different from the coupling between stable local moments, as represented by the RKKY mechanism. Itinerant moments are strongly band-structure dependent, as epitomized by the Stoner criterion $ID(E_F) \geq 1$, where $I \sim 1 \text{ eV}$ is the Stoner parameter and $D(E_F)$ is the density of states (DOS) at the Fermi level. Small band widths $W \sim 1/D(E_F)$ favor ferromagnetism, because the intra-atomic interactions responsible for moment formation (I) compete against hybridization energies of order W .

Strongly exchange-enhanced Pauli paramagnets such as Pd and Pt, which nearly satisfy the Stoner criterion, are easily spin polarized by neighboring Fe or Co atoms. Examples are $L1_0$ magnets [176], Fe/Pt thin films [177], spin-glass-type dilute alloys [183], and various magnetic nanostructures [31, 135]. Some other elements such as V exhibit moderate exchange enhancement, whereas elements such as Cu and Ag can be considered as non-interacting metals [178]. The *spatial* aspect of exchange-enhanced Pauli paramagnetism is described by the wave-vector-dependent susceptibility [179]

$$\chi(k) = \frac{\chi_o(k)}{1 - U \chi_o(k)/2\mu_o\mu_B^2} \quad (3.11)$$

where $\chi_o(k)$ is the non-interacting or Pauli susceptibility:

$$\chi_o(k) = \chi_h(1 - k^2/12k_F^2 + O(k^2)) \quad (3.12)$$

The higher-order terms in this equation exhibit a complicated behavior with a singularity at $k = 2k_F$, which is the origin of the RKKY oscillations [164, 179]. However, when the Stoner criterion is nearly satisfied, the quadratic term is strongly enhanced in (3.11), and Fourier transformation yields a pronounced exponential decay with a decay length $1/\kappa$. The decay is preasymptotic, that is, for long distances there remains an oscillating tail [180]. For Pd thin films, the transition from exponential to power-law behavior occurs at about 10–12 monolayers [180]. The range of the preasymptotic decay scales as $1/(1 - UD)^{1/2}$. It is rarely larger than about 2 Å but

sufficient to spin polarize a significant neighborhood of atoms such as Pt or Pd. Figure 3.15 illustrates the geometry of the polarization cloud for small transition-metal dots on a 4d/5d surface.

For semiquantitative calculation of polarization-cloud and interdot exchange coupling (Fig. 3.15), it is convenient to start from the energy density [181, 182]

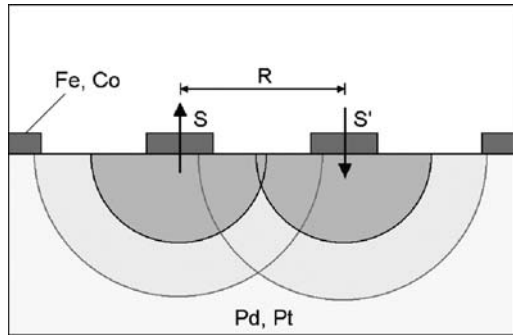
$$\eta = \frac{1}{48k_F^2 D} (\nabla m)^2 + \frac{1}{4} \left(\frac{1}{D} - U \right) m^2 \quad (3.13)$$

By Fourier transformation, it is straightforward to show that this equation corresponds to the quadratic limit of (3.11). Minimization of (3.13) yields the Yukawa-type equation $\nabla^2 m + \kappa^2 m = 0$. Let us first consider a spherical Fe or Co particle of radius R_0 in a Pt or Pd matrix. In this case, the Yukawa equation with the well-known spherical solution $m_s(r) = c \exp(-\kappa r)/4\pi r$, where r is the distance from the center of the cluster. Next, we integrate $m(\mathbf{r})$ over $4\pi r^2 dr$, taking into account that the magnetization at the cluster surface is equal to that of the Fe or Co, $m(R) = m_0$, and that the moment of the Fe particle $\mu_0 = 4\pi R_0^3 m_0/3$. This yields the moment

$$\mu = 3\mu_0 \frac{1 + \kappa R_0}{\kappa^2 R_0^2} \quad (3.14)$$

Taking a single Co atom of moment $\mu_0 = 1.73 \mu_B$ and radius $R = 1.24 \text{ \AA}$, we obtain theoretical polarization-cloud predictions of about $3.5 \mu_B$ for Pt and $7.3 \mu_B$ for Pd. Moments of this order of magnitude are indeed observed, for example, in dilute alloys [183].

Fig. 3.15 Coupling between two Fe or Co clusters on a Pt surface (schematic). The exchange is estimated by volume integration of the energy density (3.13), thereby ignoring surface-state contributions



The interdot exchange $J = -(E_+ - E_-)$ is obtained by putting $m_{\pm}(\mathbf{r}) \sim m_s(|\mathbf{r} - \mathbf{R}_1|) \pm m_s(|\mathbf{r} - \mathbf{R}_2|)$ into (3.13) and evaluating the total energies $E_{\pm} = \int \eta(m_{\pm}) dV$. Here the sign corresponds to ferromagnetic (+) and antiferromagnetic (−) exchange, and the calculation requires careful bookkeeping, including the boundary condition $m_{\pm}(\mathbf{r}) = m_0$ at the cluster–matrix interface and the consideration of the semi-infinite character of the problem [99] and yields in lowest order

$$J = \frac{J_{\text{at}}}{2} \frac{R_0^2}{R_{\text{at}}^2} \exp(-\kappa R) \quad (3.15)$$

Equation (3.15) shows that the exchange increases quadratically with the radius R of the clusters but is rapidly outweighed by the exponential term. This is different from the RKKY interaction between nanoparticles [165], which exhibits a power-law dependence on the particle or cluster separation. Taking $R_0 = 1 \text{ nm}$ and $R = 3 \text{ nm}$ yields an effective preasymptotic interaction of about 5 mK, corresponding to an interaction field of order $15 \mu\text{T}$. By comparison, magnetostatic interaction fields are typically of the order of a few mT. In other words, for cluster sizes and separations exceeding about 1 nm, intercluster interactions are weaker than magnetostatic dipole interactions and the RKKY tail interactions through the substrate.

3.4.4 Kondo Effect

The Kondo effect arises when electrons of a spatially confined system with discrete energy levels interact with the conduction electrons of an otherwise non-magnetic metal. Such systems can be ferromagnetic impurities in strongly diluted alloys, or magnetic adatoms, clusters, magnetic molecules, or artificial quantum structures on metal surfaces (recent reviews in [184, 185]). Requirements for the Kondo effect to occur are that the defects are magnetic, that is, they have a nonzero total spin, and that the metal is cooled to temperatures below the Kondo temperature, T_K . At the origin of the Kondo effect are correlated electron exchange processes between the discrete and continuum states that effectively flip the spin of the impurity, while simultaneously creating a spin excitation in the Fermi sea (see Fig. 3.16). The involved electrons form a many-electron ground state, the Kondo state. The Kondo temperature can be thought of as the binding energy of this correlated state and is typically of the order of 0–400 K. The spin polarization of the impurity and the host are opposite to each other, hence, the conduction electrons effectively screen the impurity's spin.

The Kondo effect has two profound experimental consequences: (i) the magnetization is reduced below the free-moment value due to the screening, and (ii) the electron scattering cross-section of the impurity is strongly enhanced, resulting in anomalies in transport measurements near and below T_K . The Kondo resonance is experimentally observable on surface-supported atoms or nanostructures with low-temperature scanning tunneling microscopy (STM), where it shows up as a Fano resonance in the differential conductance of the tunneling contact dI/dV at the lateral adatom position [186–189].

Progress in nanotechnology has made it possible to construct spatially confined nanostructures with pronounced discretization of electronic states, in which the Kondo physics is clearly displayed [190–192]. The Kondo effect is thus by no means limited to single impurity atoms but is a phenomenon generally associated

with magnetic nanoscale systems with discrete electronic states and non-zero net spin. However, the Kondo temperature is rapidly suppressed as the size of the cluster increases and goes to zero exponentially with increasing cluster size [193]. The Kondo effect is of fundamental importance for the study of magnetism in nanoscale systems, as it can serve as a local probe to determine the exchange interaction in sub-nanometer clusters. For instance, the magnetic ground state of spin-frustrated Cr trimers [194] and the exchange interaction between single Ni or Co atoms [195, 196] could be determined from measurements of the Kondo state the clusters form with the substrate. Recent experiments have demonstrated that the Kondo effect can be manipulated by tuning the interaction with the bulk-state electrons via local coordination, chemical bonding, or quantum size effects [197–199].

Potential applications for the Kondo effect might arise in spintronics and quantum information processing, as it permits, for example, to transport information in systems which are too small for conventional wiring [191].

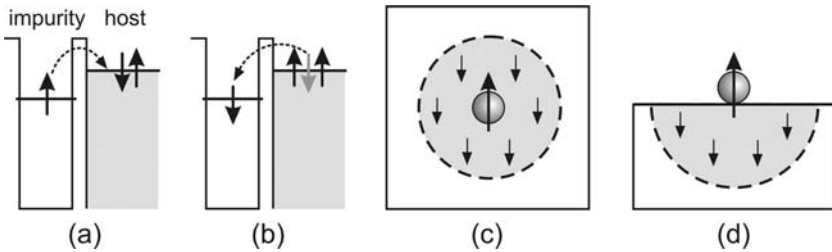


Fig. 3.16 Electronic (spin-flip) exchange between the discrete energy levels of an impurity and the delocalized states of a host metal, leading to the Kondo effect. An electron tunnels into an empty state near the Fermi energy of the host (a), and the hole is filled with an electron of opposite spin from the host (b). The so-induced spin polarization of the delocalized electrons around the impurity is effectively screening the magnetic moment of the impurity. (c) Screening cloud around an impurity in a bulk matrix and (d) on a metal surface

3.4.5 Entanglement

Entanglement is a key consideration in quantum information processing systems [200–203], including magnetic nanostructures [158]. It has been shown theoretically that and how quantum entanglement arises in interacting magnetic nanodots [158]. The thermal stability of the entangled states increases with the magnetic anisotropy of the dots, which reaches substantial values for some noncubic intermetallic compounds. This is of potential importance for future quantum computing above 4.2 K.

An example of an entangled state is the wave function $|\Phi\rangle = |\alpha\rangle |\beta\rangle + |\beta\rangle |\alpha\rangle$, which cannot be written as a product of one-electron states. Entanglement between magnetic nanodots of total spin S can be realized by using the macrospin wave functions of the type $|\alpha\rangle = |S\rangle$ and $|\beta\rangle = |S - 1\rangle$. Another approach is

to exploit those wave functions such as $|\Phi\rangle$, which naturally occur in Heisenberg magnets. Fig. 3.17 shows a simple example, namely the AFM spin-1/2 Heisenberg square. The square is described by the transparent Hamiltonian

$$H = -J(\mathbf{s}_1 \cdot \mathbf{s}_2 + \mathbf{s}_2 \cdot \mathbf{s}_3 + \mathbf{s}_3 \cdot \mathbf{s}_4 + \mathbf{s}_4 \cdot \mathbf{s}_1) \quad (3.16)$$

where $J > 0$. The quantum states of the square may be manipulated by an inhomogeneous magnetic field and/or by interactions with neighboring dots.

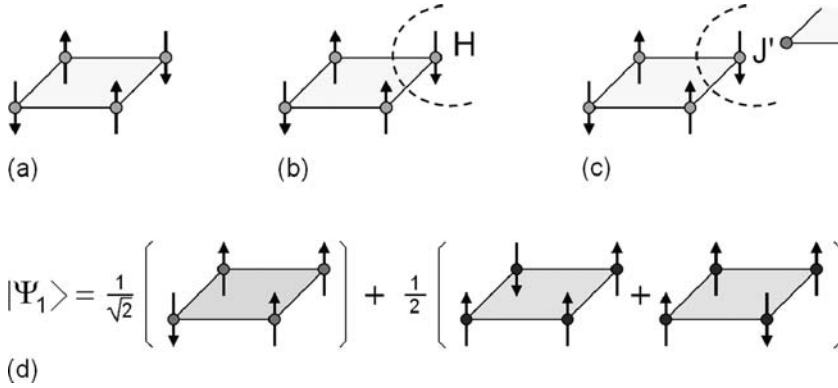


Fig. 3.17 Interactions and entanglement in small-scale nanostructures: (a) free square, (b) local interaction field, (c) exchange interaction with neighboring atoms, and (d) entangled wave function in the limit of strong interactions. For simplicity, only the ground state is shown in (d)

In spite of its simplicity, the model exhibits a substantial degree of complexity, even in the ground state. In the absence of a magnetic field, the classical ground state is shown in Fig. 3.17a, meaning that neighboring spins minimize the energy by forming pairs with antiparallel spins. The quantum-mechanical ground state is of the many-electron type but easily obtained by diagonalizing the 16×16 Hamiltonian matrix (3.4). Aside from the classical ground-state configurations, Fig. 3.17a, there is a substantial admixture of states that have two parallel bonds, as in Fig. 3.17b. These states do not appear in the classical ground state, because they cost exchange energy, but in the quantum-mechanical case, they reduce the total energy by realizing hybridization between degenerate classical ground-state configurations.

From a quantum-mechanical point of view, Heisenberg spin structures are highly complicated and poorly described by one-electron approaches, including LSDA+U and SIC. A particular effect is spin-charge separation, meaning that the low-lying excitations are magnetic and rather unrelated to the interatomic hopping of the electrons [179, 204]. In more detail, the Heisenberg model assumes that the four spin-carrying electrons are localized at the corners of the square but the spins are free to switch. The electron's interatomic hopping (hopping integral t) is important in itinerant and RKKY systems but enters the Heisenberg model only indirectly by determining the exchange [179].

3.5 Concluding Remarks

In summary, we have investigated how nanoscale proximity effects change the properties of magnetic nanostructures. Progress in fabrication and deposition techniques has made it possible to produce an unprecedented range of structures, from embedded and coated clusters to nanotubes and complex thin films, including magnetic surface alloys. The structures offer new physics on length scales of more than a few interatomic distances, making it different from typical atomic-environment effects in alloys and at surfaces. Focus has been on the relation between classical and quantum effects. Some quantum effects, such as RKKY interactions between nanoparticles, but many nanoscale effects are of the micromagnetic type, where interatomic exchange ensures a coherent spin orientation over several nanometers. An example of the latter is proteresis in core-shell nanoparticles, which is counter-intuitive from a magnetostatic point of view but explained by the involvement of nanoscale exchange interactions between noncollinear magnetic sublattices. While future research is necessary in various directions, including, for example, the fabrication of monodisperse metal clusters on substrates with good control over size, density, orientation, and anisotropy, the structures will have potential applications in many areas of nanotechnology, from biomagnetism and sensors to materials for bulk applications and structures for quantum and classical information processing. It will be fascinating to monitor and accompany this development in the years to come.

Acknowledgments The contribution of A.E. to this work was supported by NSF CAREER (DMR-0747704), that of R.S. by DoE, and D.J.S. by NSF-MRSEC and INSIC. The authors have benefited from discussions with X.-H. Wei, R. D. Kirby, S. A. Michalski, S. Enders, J. Zhang, R. Zhang, J. Zhou (Nebraska), and J. Honolka, J. Zhang, V. Sessi, I. Brihuega, and K. Kern (Stuttgart).

References

1. Feynman, R. P.: There's plenty of room at the bottom. *Eng. Sci.* **23**, 22 (1960)
2. Solzi, M., et al.: Macroscopic Magnetic Properties of Nanostructured and Nanocomposites Systems. In H. S. Nalwa (Ed.), *Magnetic nanostructures*, pp. 123–201. American Scientific, Stephenson Ranch (2002)
3. Skomski, R.: Nanomagnetism. *J. Phys.: Condens. Matter* **15**, R841 (2003)
4. Sellmyer, D. J. and Skomski, R. (Eds.): *Advanced Magnetic Nanostructures*. Springer, Berlin (2006)
5. Terris, B. D., et al.: Ion-beam patterning of magnetic films using stencil masks. *Appl. Phys. Lett.* **75**, 403 (1999)
6. Coehoorn, R., et al.: Meltspun permanent magnet materials containing Fe₃B as the main phase. *J. Magn. Magn. Mater.* **80**, 101 (1989)
7. Tushima, N., et al.: Novel synthesis, structure and catalysis of inverted core/shell structured Pd/Pt bimetallic nanoclusters. *Eur. Phys. J. D* **16**, 209 (2001)
8. Wei, X.-H., et al.: Proteresis in Co:CoO core-shell nanoclusters. *J. Appl. Phys.* **103**, 07D514-1-3 (2008)
9. Khanna, S. N., et al.: Magic numbers in metallo-inorganic clusters: chromium encapsulated in silicon cages. *Phys. Rev. Lett.* **89**, 016803-1-4 (2002)

10. Bland, J. A. C. and Heinrich, B. (Eds.): *Ultrathin Magnetic Structures I*. Springer, Berlin (2005)
11. Himpfel, F. J., et al.: Magnetic nanostructures. *Adv. Phys.* **47**, 511 (1998)
12. Sawicki, M., et al.: Exchange springs in antiferromagnetically coupled DyFe₂-YFe₂ superlattices. *Phys. Rev. B* **62**, 5817 (2000)
13. Al-Omari, A. and Sellmyer, D. J.: Magnetic properties of nanostructured CoSm/FeCo films. *Phys. Rev. B* **52**, 3441 (1995)
14. Sellmyer, D. J.: Applied physics: strong magnets by self-assembly. *Nature* **420**, 374 (2002)
15. Zeng, H., et al.: Curie temperature of FePt:B₂O₃ nanocomposite films. *Phys. Rev. B* **66**, 184425 (2002)
16. Sellmyer, D. J., et al.: Nanoscale design of films for extremely high density magnetic recording. *Phys. Low-Dim. Struct.* **1–2**, 155 (1998)
17. Rao, B. K. and Jena, P.: Giant magnetic moments of nitrogen-doped Mn clusters and their relevance to ferromagnetism in Mn-Doped GaN. *Phys. Rev. Lett.* **89**, 185504 (2002)
18. Sui, Y. C., et al.: Nanotube magnetism. *Appl. Phys. Lett.* **84**, 1525 (2004)
19. Kumar, K.: RETM₅ and RE₂TM₁₇ permanent magnets development. *J. Appl. Phys.* **63**, R13–57 (1988)
20. Zhou, J., et al.: Sm-Co-Ti high-temperature permanent magnets. *Appl. Phys. Lett.* **77**, 1514 (2000)
21. Wernsdorfer, W., et al.: Macroscopic quantum tunneling of magnetization of single ferromagnetic nanoparticles of barium ferrite. *Phys. Rev. Lett.* **79**, 4014 (1997)
22. Rong, Ch.-B., et al.: Structural phase transition and ferromagnetism in monodisperse 3 nm FePt particles. *J. Appl. Phys.* **101**, 043913-1-4 (2007)
23. Skomski, R. and Coey, J. M. D.: Giant energy product in nanostructured two-phase magnets. *Phys. Rev. B* **48**, 15812 (1993)
24. Samorjai, G. A.: *Introduction to Surface Chemistry and Catalysis*. Wiley, New York (1994)
25. Wieckowski, A., Savinova, E. R. and Constantinos, V. G. (Eds.): *Catalysis and Electrocatalysis at Nanoparticle Surfaces*. Marcel Dekker, New York (2003)
26. Skomski, R. and Sellmyer, D. J.: Magnetic impurities in magic-number clusters.
27. Pankhurst, Q. A., et al.: *J. Phys. D: Appl. Phys.* **36**, R167–R181 (2003).
28. Sun, S., et al.: Monodisperse FePt nanoparticles and ferromagnetic FePt nanocrystal superlattices. *Science* **287**, 1989 (2000)
29. Weller, D., et al.: High Ku materials approach to 100 Gbits/in². *IEEE Trans. Magn.* **36**, 10 (2000)
30. Billas, I. M. L., et al.: Magnetism from the atom to the bulk in Iron, Cobalt, and Nickel clusters. *Science* **265**, 1682 (1994)
31. Stepanyuk, V. S., et al.: Magnetism of 3d, 4d, and 5d transition-metal impurities on Pd(001) and Pt(001) surfaces. *Phys. Rev. B* **53**, 2121 (1996)
32. Pastor, M., et al.: Magnetic anisotropy of 3d transition-metal clusters. *Phys. Rev. Lett.* **75**, 2, 326 (1995)
33. Nonas, B., et al.: Strongly enhanced orbital moments and anisotropies of adatoms on the Ag(001) surface. *Phys. Rev. Lett.* **86**, 10, 2146 (2001)
34. Goldoni, A., et al.: Experimental evidence of magnetic ordering at the Rh(100) surface. *Phys. Rev. Lett.* **82**, 15, 3156 (1999)
35. Martin, T. P.: Shells of atoms. *Phys. Rept.* **273**, 199 (1996)
36. Heiz, U., et al.: Size-dependent molecular dissociation on mass-selected, supported metal clusters. *J. Am. Chem. Soc.* **120**, 9668 (1998)
37. Lee, H. K., et al.: Monte Carlo simulations of interacting magnetic nanoparticles. *J. Appl. Phys.* **91**, 10, 6926 (2002)
38. Pierce, J. B., et al.: Ferromagnetic stability in Fe nanodot assemblies on Cu(111) induced by indirect coupling through the substrate. *Phys. Rev. Lett.* **92**, 23, 237201 (2004)
39. Dürr, H. A., et al.: Spin and orbital magnetization in self-assembled Co clusters on Au(111). *Phys. Rev. B* **59**, 2, R701 (1999)

40. Fruchart, O., et al.: Enhanced coercivity in submicrometer-sized ultrathin epitaxial dots with in-plane magnetization. *Phys. Rev. Lett.* **82**, 6, 1305 (1999)
41. Edmonds, K. W., et al.: Doubling of the orbital magnetic moment in nanoscale Fe clusters. *Phys. Rev. B* **60**, 1, 472 (1999)
42. Guevara, J., et al.: Large variations in the magnetization of Co clusters induced by noble-metal coating. *Phys. Rev. Lett.* **81**, 24, 5306 (1998)
43. Redinger, J., et al.: Ferromagnetism of 4d and 5d transition-metal monolayers on Ag(111). *Phys. Rev. B* **51**, 19, 13852 (1995)
44. Allwood, D. A., et al.: Nanoscale magnetics magnetic domain wall logic. *Science* **309**, 1688 (2005)
45. Sorge, K. D., et al.: Interactions and switching behavior of anisotropic magnetic dots. *J. Appl. Phys.* **95**, 7414 (2004)
46. Weller, D. and Moser, A.: Thermal effect limits in ultrahigh density magnetic recording. *IEEE Trans. Magn.* **35**, 4423 (1999)
47. Suess, D., et al.: Exchange spring media for perpendicular recording. *Appl. Phys. Lett.* **87**, 012504 (2005)
48. Suess, D.: Multilayer exchange spring media for magnetic recording. *Appl. Phys. Lett.* **89**, 113105-1-3 (2006)
49. Victora, R. H. and Shen, X.: Composite media for perpendicular magnetic recording. *IEEE Trans. Magn.* **41**, 537 (2005)
50. Sellmyer, D. J., et al.: High-anisotropy nanocomposite films for magnetic recording. *IEEE Trans. Magn.* **37**, 1286 (2001)
51. Wang, J.-P., et al.: Composite media (dynamic tilted media) for magnetic recording. *Appl. Phys. Lett.* **86**, 142504-1-3 (2005)
52. Goodman, S. J., et al.: Micromagnetics of hysteresis loops in CGC perpendicular media. *IEEE Trans. Magn.* **39**, 2329 (2003)
53. Dobin, A. Yu., et al.: Domain wall assisted magnetic recording. *Appl. Phys. Lett.* **89**, 062512-1-3 (2006)
54. Baettig, P., et al.: Ab initio prediction of a multiferroic with large polarization and magnetization. *Appl. Phys. Lett.* **86**, 012505-1-3 (2005)
55. Barth, J. V., et al.: Engineering atomic and molecular nanostructures at surfaces. *Nature* **437**, 671 (2005)
56. Wang, F. and Lakhtakia, A. (Eds.): *Selected Papers on Nanotechnology—Theory and Modeling, Milestone Series 182*. SPIE Press, Bellingham (2006)
57. Skomski, R., et al.: Micromagnetics of ultrathin films with perpendicular magnetic anisotropy. *Phys. Rev. B* **58**, 3223 (1998)
58. Skomski, R.: Nanomagnetic scaling. *J. Magn. Magn. Mater.* **272–276**, 1476–1481 (2004)
59. Skomski, R.: Role of thermodynamic fluctuations in magnetic recording. *J. Appl. Phys.* **101**, 09B104-1-6 (2007)
60. Qiang, Y., et al.: Magnetism of Co nanocluster films. *Phys. Rev. B* **66**, 064404 (2002)
61. Sellmyer, D. J., et al.: Magnetism of Fe, Co and Ni nanowires in self-assembled arrays. *J. Phys.: Condens. Matter* **13**, R433–R460 (2001)
62. Liou, S. H. and Yao, Y. D.: Development of high coercivity magnetic force microscopy tips. *J. Magn. Magn. Mater.* **190**, 130 (1998)
63. Kent, A. D., et al.: Properties and measurement of scanning tunneling microscope fabricated ferromagnetic particle arrays. *J. Appl. Phys.* **76**, 6656 (1994)
64. Xu, Y. F., et al.: Cluster-Assembled Nanocomposites. In D. J. Sellmyer and R. Skomski (Eds.), *Advanced magnetic nanostructures*, ch. 8, pp. 207–238. Springer, Berlin (2006)
65. Enders, A., et al.: Magnetism of low-dimensional metallic structures. In H. Kronmüller and S. Parkin (Eds.), *The handbook of magnetism and advanced magnetic materials*, Vol. 1: Fundamentals and theory, pp. 577–598. Chichester, UK: John Wiley & Sons Ltd. (2006)
66. Barth, J. V.: Molecular architectonic on metal surfaces. *Annu. Rev. Phys. Chem.* **58**, 375 (2007)

67. Gambardella, P., et al.: Ferromagnetism in one-dimensional monatomic metal chains. *Nature* **416**, 301 (2002)
68. Repetto, D., et al.: Structure and magnetism of atomically thin Fe layers on flat and vicinal Pt surfaces. *Phys. Rev. B* **74**, 054408 (2006)
69. Skomski, R. and Coey, J. M. D.: *Permanent Magnetism*. Institute of Physics, Bristol (1999)
70. Skomski, R., et al.: Effective Demagnetizing Factors of Complicated Particle Mixtures. *IEEE Trans. Magn.* **43**, (6), 2956 (2007)
71. Zhang, J., et al.: Magnetism of Fe clusters formed by buffer-layer assisted growth on Pt(997). *Eur. Phys. J. D* **45**, 515 (2007)
72. Rusponi, S., et al.: The Remarkable Difference Between Surface and Step Atoms in the Magnetic Anisotropy of Two-Dimensional Nanostructures. *Nature Mat.* **2**, 546 (2003)
73. Brihuega, I., et al.: Electronic decoupling and templating of Co nanocluster arrays on the boron nitride nanomesh. *Surf. Sci. Letters* **602**(14) (2008) L95–L99.
74. Lingenfelder, M., et al.: Towards surface-supported supramolecular architectures: tailored coordination assembly of 1,4-benzenedicarboxylate and Fe on Cu(100). *Chem. Eur. J.* **10**, 1913 (2004)
75. Dmitriev, A., et al.: Design of extended surface-supported chiral metal-organic arrays comprising mononuclear iron centers. *Langmuir* **41**, 4799 (2004)
76. Bromann, K., et al.: Controlled deposition of size-selected Silver nanoclusters. *Science* **274**, 956 (1996)
77. Weaver, J. and Waddill, G.: Cluster assembly of interfaces: Nanoscale Engineering. *Science* **251**, 1444 (1991), G. Kerner and M. Asscher, "Laser patterning of metallic films via buffer layer", *ibid.*
78. Huang, L., et al.: Buffer-layer-assisted growth of nanocrystals: Ag-Xe-Si(111). *Phys. Rev. Lett.* **80**, 18, 4095 (1998)
79. Haley, C. and Weaver, J.: Buffer-layer-assisted nanostructure growth via two-dimensional cluster-cluster aggregation. *Surf. Sci.* **518**, 243 (2002)
80. Weaver, J. and Antonov, V. N.: Synthesis and patterning of nanostructures of (almost) anything on anything. *Surf. Sci.* **557**, 1 (2004)
81. Hahn, E., et al.: Orientational instability of vicinal Pt surfaces close to (111). *Phys. Rev. Lett.*, **72** 3378 (1994)
82. Corso, M., et al.: Boron nitride nanomesh. *Science* **303**, 217 (2004)
83. Bansmann, J., et al.: Magnetic and structural properties of isolated and assembled clusters. *Surf. Sci. Repts.* **56**, 189 (2005)
84. Shen, J., et al.: The effect of spatial confinement on magnetism: films, stripes and dots of Fe on Cu(111). *J. Phys.: Cond. Mat.* **15**, R1 (2003)
85. Repetto, D., et al.: Magnetism of Fe clusters and islands on Pt surfaces. *Appl. Phys. A* **82**, 109 (2006)
86. Yeomans, J. M.: *Statistical Mechanics of Phase Transitions*. University Press, Oxford (1992)
87. Yokoyama, T., et al.: Selective assembly on a surface of supramolecular aggregates with controlled size and shape. *Nature* **413**, 619 (2001)
88. Grill, L., et al.: Nano-architectures by covalent assembly of molecular building blocks. *Nat. Nanotech.* **2**, 687 (2007)
89. Dmitriev, A., et al.: Modular assembly of two-dimensional metal-organic coordination networks at a metal surface. *Angew. Chem. Int. Ed.* **42**, 2670 (2003)
90. Stepanow, S., et al.: Steering molecular organization and host-guest interactions using two-dimensional nanoporous coordination systems. *Nat. Mater.* **3**, 229 (2004)
91. Ruben, M., et al.: 2D supramolecular assemblies of Benzene 1,3,5-tri-yl Tribenzoic Acid: Temperature-induced phase transformations and hierarchical organization with macrocyclic molecules. *J. Am. Chem. Soc.* **128**, 15644 (2006)
92. Hauschild, A., et al.: Molecular distortions and chemical bonding of a large π -conjugated molecule on a metal surface. *Phys. Rev. Lett.* **94**, 036106 (2005)

93. Boehringer, M., et al.: Two-dimensional self-assembly of supramolecular clusters and chains. *Phys. Rev. Lett.* **83**, 324 (1999)
94. Klemmer, T., et al.: Magnetic hardening and coercivity in $L1_0$ Ordered FePd ferromagnets. *Scripta Met. Mater.* **33**, 1793 (1995)
95. T.-Lee, et. al.: Growth and surface alloying of Fe on Pt(997). *Surf. Sci.* **600**, 3266 (2006)
96. Ravindran, P., et al.: Large magnetocrystalline anisotropy in bilayer transition metal phases from first-principles full-potential calculations *Phys. Rev. B* **63**, 144409-1-18 (2001)
97. Komelj, M., et al.: Influence of the substrate on the magnetic anisotropy of monatomic nanowires. *Phys. Rev. B* **73**, 134428 (2006)
98. Lee, T.-Y., et al.: Growth and surface alloying of Fe on Pt(997). *Surf. Sci.* **600** (16) 3266 (2006)
99. Skomski, R., et al.: Substrate-controlled growth and magnetism of nanosize Fe clusters on Pt. *J. Appl. Phys.* **103**, 07D519-1-3 (2008)
100. Ising E.: Beitrag zur Theorie des Ferromagnetismus. *Z. Phys.* **31**, 253 (1925)
101. De Jongh, L. J. and Miedema, A. R.: Experiments on simple magnetic model systems. *Advan. Phys.* **23**, 1 (1974)
102. Shen, J., et al.: Magnetism in one dimension: Fe on Cu(111). *Phys. Rev. B* **56**, 2340 (1997)
103. Alefeld, G.: Wasserstoff in Metallen als Beispiel für ein Gittergas mit Phasenumwandlungen. *Phys. stat. sol.* **32**, 67 (1969)
104. Wagner, H. and Horner, H.: Elastic interaction and the phase transition in coherent metal-hydrogen system. *Adv. Phys.* **23**, 587 (1974)
105. Skomski, R.: Interstitial Modification, In J. M. D. Coey (Ed.), *Rare-earth—iron permanent magnets*, pp. 178–217. University Press, Oxford (1996)
106. Wood, R.: The feasibility of magnetic recording at 1 Terabit per square inch. *IEEE Trans. Magn.* **36**, 36 (2000)
107. Sellmyer, D. J., et al.: High-anisotropy nanocomposite films for magnetic recording. *IEEE Trans. Magn.* **37**, 1286 (2001)
108. McCurrie, R. A. and Gaunt, P.: The magnetic properties of platinum-cobalt near the equiatomic composition. I. The experimental data. *Philos. Mag.* **13**, 567 (1966)
109. Zeng, H., et al.: Orientation-controlled nonepitaxial $L1_0$ CoPt and FePt films. *Appl. Phys. Lett.* **80**, 2350 (2002)
110. Yan, M. L. et al.: Fabrication of nonepitaxially grown double-layered FePt:C/FeCoNi thin films for perpendicular recording. *Appl. Phys. Lett.* **83**, 3332 (2003)
111. Xu, Y., et al.: Magnetic properties of dilute FePt:C nanocluster films. *J. Appl. Phys.* **97**, 10J320 (2005)
112. Xu, Y., et al.: Magnetic properties of $L1_0$ FePt and FePt:Ag nanocluster films. *J. Appl. Phys.* **93**, 10 (2003) 8289
113. Stoner, E. C. and Wohlfarth, E. P.: A mechanism of magnetic hysteresis in heterogeneous alloys. *Philos. Trans. R. Soc. London, Ser. A* **240**, 599 (1948); reprinted by *IEEE Trans. Magn.* **27**, 3475 (1991)
114. Kersten, M.: Zur Theorie der ferromagnetischen Hysterese und der Anfangspermeabilität. *Z. Phys.* **44**, 63 (1943)
115. Yoshizawa, Y., et al.: New Fe-based soft magnetic alloys composed of ultrafine grain structure. *J. Appl. Phys.* **64**, 6044 (1988)
116. Herzer, G.: Nanocrystalline soft magnetic materials. *J. Magn. Magn. Mater.* **112**, 258 (1992)
117. Chikazumi, S., *Physics of ferromagnetism*, Second edition. Oxford University Press, (1997)
118. Kittel, Ch.: Theory of the structure of ferromagnetic domains in films and small particles. *Phys. Rev.* **70**, 965 (1946)
119. Kronmüller, H. and Schrefl, T.: Interactive and cooperative magnetization processes in hard magnetic materials. *J. Magn. Magn. Mater.* **129**, 66 (1994)
120. Skomski, R.: *Simple Models of Magnetism*. University Press, Oxford (2008)

121. Skomski, R., et al.: Magnetization reversal in cubic nanoparticles with uniaxial surface anisotropy. *IEEE Trans. Magn.* **43**, (6), 2890 (2007)
122. Kronmüller, H.: Theory of nucleation fields in inhomogeneous ferromagnets. *Phys. Stat. Sol. (b)* **144**, 385 (1987)
123. Nieber, S. and Kronmüller, H.: Nucleation fields in periodic multilayer's. *Phys. Stat. Sol. (b)* **153**, 367 (1989)
124. Kneller, E. F. and Hawig, R.: The exchange-spring magnet: a new material principle for permanent magnets. *IEEE Trans. Magn.* **27**, 3588 (1991)
125. Gradmann, U.: In *Handbook of Magnetic Materials* Vol. 7, In K. H. J. Buschow (Ed.), Elsevier Science Publishers B. V., New York, (1993)
126. Kachkachi, H. and Bonet, E.: Surface-induced cubic anisotropy in nanomagnets. *Phys. Rev. B* **73**, 224402-1-7 (2006)
127. Komelj, M., et al.: From the bulk to monatomic wires: An ab initio study of magnetism in Co systems with various dimensionality. *Phys. Rev. B* **66**, 140407-1-4 (2002)
128. Daalderop, G. H. O., et al.: First-principles calculation of the magnetic anisotropy energy of (Co)n/(X)m multilayers. *Phys. Rev. B* **42**, 11, 7270 (1990)
129. Wang, D.-Sh., et al.: First-principles theory of surface magnetocrystalline anisotropy and the diatomic-pair model. *Phys. Rev. B* **47**, 14932 (1993)
130. Skomski, R.: Exchange-Controlled Magnetic Anisotropy. *J. Appl. Phys.* **91**, 8489 (2002)
131. Sander, D., et al.: Reversible H-induced switching of the magnetic easy axis in Ni/Cu(001) thin films. *Phys. Rev. Lett.* **93**, 247203-1-4 (2004)
132. Brooks, H.: Ferromagnetic anisotropy and the itinerant electron model. *Phys. Rev.* **58**, 909 (1940)
133. Sander, D., et al.: Film stress and domain wall pinning in sesquilayer iron films on W(110). *Phys. Rev. Lett.* **77**, 2566 (1996)
134. Morales, M. A., et al.: Surface anisotropy and magnetic freezing of MnO nanoparticles. *Phys. Rev. B* **75**, 134423 (1–5) (2007)
135. Gambardella, P., et al.: Giant magnetic anisotropy of single cobalt atoms and nanoparticles. *Science* **300**, 1130 (2003)
136. Šipr, O., et al.: Magnetic structure of free iron clusters compared to iron crystal surfaces. *Phys. Rev. B* **70**, 174423 (2004)
137. Kechrakos, D. and Trohidou, K.: Magnetic properties of dipolar interacting single-domain particles. *Phys. Rev. B* **58**, 12169 (1998)
138. Novosad, V., et al.: Effect of interdot magnetostatic interaction on magnetization reversal in circular dot arrays. *Phys. Rev. B* **65**, 60402 (2002)
139. Stepanyuk, V. S., et al.: Magnetism of 3d, 4d, and 5d transition-metal impurities on Pd(001) and Pt(001) surfaces. *Phys. Rev. B* **53**, 2121(1996)
140. Ederer, C., et al.: Magnetism in systems with various dimensionalities: A comparison between Fe and Co. *Phys. Rev. B* **68**, 52402 (2003)
141. Garibay-Alonso, R. and López-Sandoval, R.: Ground-state spin local magnetic moments of deposited Fe clusters *Solid State Comm.* **134**, 503 (2005)
142. Skomski, R., et al.: Finite-temperature anisotropy of PtCo magnets. *IEEE Trans. Magn.* **39**, 2917 (2003)
143. Mryasov, O. N., et al.: Temperature-dependent magnetic properties of FePt: Effective spin Hamiltonian model. *Europhys. Lett.* **69**, 805 (2005)
144. Skomski, R., et al.: Finite-temperature anisotropy of magnetic alloys. *J. Appl. Phys.* **99**, 08E916-1-4 (2006)
145. Tserkovnyak, Y., et al.: Enhanced Gilbert damping in thin ferromagnetic films. *Phys. Rev. Lett.* **88**, 117601-1-4 (2002)
146. Chipara, M. I., et al.: Magnetic modes in Ni nanowires. *J. Magn. Magn. Mater.* **249**, 246 (2002)
147. Skomski, R., et al.: Incoherent magnetization reversal in nanowires. *J. Magn. Magn. Mater.* **249**, 175 (2002)

148. McMichael, R. D., et al.: Localized ferromagnetic resonance in inhomogeneous thin films. *Phys. Rev. Lett.* **90**, 227601-1-4 (2003)
149. Andersen, T., et al.: Substrate effects on surface magnetism of Fe/W(110) from first principles. *Phys. Rev. B* **74**, 184415-1-8 (2006)
150. Kashyap, A., et al.: Magnetism of $L1_0$ compounds with the composition MT ($M = \text{Rh, Pd, Pt, Ir}$ and $T = \text{Mn, Fe, Co, Ni}$). *J. Appl. Phys.* **95**, 7480 (2004)
151. Umetsu, R. Y., et al.: Magnetic anisotropy energy of antiferromagnetic $L1_0$ -type equiatomic Mn alloys. *Appl. Phys. Lett.* **89**, 052504-1-3 (2006)
152. Willoughby, S., et al.: Electronic, Magnetic and Structural Properties of $L1_0$ $\text{FePt}_x\text{Pd}_{1-x}$ Alloys. *J. Appl. Phys.* **91**, 8822 (2002)
153. McHenry, M. E., et al.: First principles calculations of the electronic structure of $\text{Fe}_{1-x}\text{Co}_x\text{Pt}$ *IEEE Trans. Mag.* **37**, 1277 (2001)
154. Skomski, R.: Phase formation in $L1_0$ magnets. *J. Appl. Phys.* **101**, 09N517-1-3 (2007)
155. Skomski, R. and Sellmyer, D.J.: Curie Temperature of Multiphase Nanostructures. *J. Appl. Phys.* **87**, 4756 (2000)
156. Evetts, J. E. (Ed.): Concise Encyclopedia of Magnetic and Superconducting Materials, Pergamon, Oxford, (1992)
157. O'Shea, M. J. and Al-Sharif, A. L.: Inverted hysteresis in magnetic systems with interface exchange. *J. Appl. Phys.* **75**, 6673 (1994)
158. Skomski, R., et al.: Quantum entanglement of anisotropic magnetic nanodots. *Phys. Rev. A* **70**, Art. No. 062307-1-4 (2004)
159. Tejada, J., et al.: Macroscopic resonant tunneling of magnetization in ferritin. *Phys. Rev. Lett.* **79**, 1754 (1997);
160. Lambrecht, W. R. L. and Andersen, O. K.: Minimal basis sets in the linear muffin-tin orbital method: Application to the diamond-structure crystals C, Si, and Ge. *Phys. Rev. B* **34**, 2439 (1986)
161. Tank, R. W. and Arcangeli, C.: An introduction to the third-generation LMTO method. *Phys. Stat. Sol. (b)* **217**, 89 (2000)
162. Andersen, O. K., et al.: Muffin-tin orbitals of arbitrary order. *Phys. Rev. B* **62**, R16219–R16222 (2000)
163. Löwdin, P.-O.: A note on the Quantum-Mechanical Perturbation Theory. *J. Chem. Phys.* **19**, 1396 (1951)
164. Ashcroft, N. W. and Mermin, N. D.: Solid State Physics. Saunders, Philadelphia (1976)
165. Skomski, R.: RKKY Interactions between nanomagnets of arbitrary shape. *Europhys. Lett.* **48**, 455 (1999)
166. Mattis, D. C.: Theory of Magnetism. Harper and Row, New York, (1965)
167. Skomski, R., et al.: Indirect exchange in dilute magnetic semiconductors. *J. Appl. Phys.* **99**, 08D504-1-3 (2006)
168. Dietl, T., et al.: Zener model description of ferromagnetism in zinc-blende magnetic semiconductors. *Science* **287**, 1019 (2000)
169. Priour Jr., D. J., et al.: A disordered RKKY lattice mean field theory for ferromagnetism in diluted magnetic semiconductors. *Phys. Rev. Lett.* **92**, 117201 (2004)
170. Coey, J. M. D., et al.: Ferromagnetism in Fe-doped SnO_2 thin films. *APL* **84**, 1332 (2004)
171. Das Pemmaraju, Ch. and Sanvito, S.: Ferromagnetism driven by intrinsic point defects in HfO_2 . *Phys. Rev. Lett.* **94**, 217205, 1–4 (2005)
172. Venkatesan, M., et al.: Unexpected magnetism in a dielectric oxide. *Nature* **430**, 630 (2004)
173. Coey, J. M. D., et al.: Donor impurity band exchange in dilute ferromagnetic oxides. *Nat. Mater.* **4**, 173 (2005)
174. Griffin, K. A., et al.: Intrinsic ferromagnetism in insulating cobalt doped anatase TiO_2 . *Phys. Rev. Lett.* **94**, 157204-1-4 (2005)
175. Zhang, J., et al.: Temperature-dependent orbital-moment anisotropy in dilute magnetic oxides. *Phys. Rev. B* **75**, 214417-1-5 (2007)

177. Antel, Jr, W. J., et al.: Induced ferromagnetism and anisotropy of Pt layers in Fe/Pt(001) multilayers. *Phys. Rev. B* **60**, 12933 (1999)
178. Janak, J. F.: Uniform susceptibilities of metallic elements. *Phys. Rev. B* **16**, 255 (1977)
179. Fulde, P.: *Electron Correlations in Molecules and Solids*. Springer, Berlin (1991)
180. Celinski, Z. and Heinrich, B.: Exchange coupling through Fe/Cu, Pd, Ag, Au/Fe Trilayers. *J. Magn. Magn. Mater.* **99**, L25 (1991)
181. Qi, Q.-N., et al., Strong ferromagnets: Curie temperature and density of states. *J. Phys.: Condens. Matter* **6**, 3245 (1994)
182. Mohn, P.: *Magnetism in the Solid State*. Springer, Berlin (2003)
183. Fischer, K.-H. and Hertz, A. J.: *Spin Glasses*. University Press, Cambridge (1991)
184. Kouwenhoven, L. and Glazman, L.: Revival of the Kondo effect. *Phys. World*, Jan., 33 (2001)
185. Kondo, J.: Sticking to my bush. *J. Phys. Soc. Jpn.* **74**, 1 (2005)
186. Madhavan, V., et al.: Tunneling into a Single Magnetic Atom: Spectroscopic Evidence of the Kondo Resonance. *Science* **280**, 567 (1998)
187. Li, J., et al.: Kondo scattering observed at a single magnetic impurity. *Phys. Rev. Lett.* **80**, 2893 (1998)
188. Újsághy, O., et al.: Theory of the fano resonance in the STM tunneling density of states due to a single kondo impurity. *Phys. Rev. Lett.* **85**, 2557 (2000)
189. Plihal, M. and Gadzuk, J.: Nonequilibrium theory of scanning tunneling spectroscopy via adsorbate resonances: Nonmagnetic and Kondo impurities. *Phys. Rev. B* **63**, 085404 (2001)
190. Cronenwett, S. M., et al.: A tunable Kondo effect in quantum dots. *Science* **281**, 540 (1998)
191. Manoharan, H. C., et al.: Quantum mirages formed by coherent projection of electronic structure. *Nature* **403**, 512 (2000)
192. Nilius, N., et al.: Tailoring electronic properties of atomic chains assembled by STM. *Appl. Phys. A* **80**, 951 (2005)
193. Giete, G. A., et al.: Kondo effect and STM spectra through ferromagnetic nanoclusters. *Phys. Rev. B* **66**, 024431 (2002)
194. Jamneala, T., et al.: Kondo Response of a single antiferromagnetic Chromium trimer. *Phys. Rev. Lett.* **87**, 25, 256804 (2001)
195. Madhavan, V., et al.: Observation of spectral evolution during the formation of a Ni₂ Kondo molecule. *Phys. Rev. B* **66**, 212411 (2002)
196. Wahl, P., et al.: Exchange interaction between single magnetic atoms. *Phys. Rev. Lett.* **98**, 056601(2007)
197. Schneider, M. A., et al.: Kondo state of Co impurities at noble metal surfaces. *Appl. Phys. A* **80**, 937 (2005)
198. Zhao, A., et al.: Controlling the Kondo effect on an adsorbed magnetic ion through its chemical bonding. *Science* **309**, 1542 (2005)
199. Fu, Y.-S., et al.: Manipulating the Kondo resonance through quantum size effects. *Phys. Rev. Lett.* **99**, 256601 (2007)
200. Nielsen, M. A. and Chuang, I. L.: *Quantum computation and quantum information*. University Press, Cambridge (2000)
201. Burkard, G., et al.: Coupled quantum dots as quantum gates. *Phys. Rev. B* **59**, 2070 (1999)
202. Yao, W., et al.: Nanodot-Cavity quantum electrodynamics and photon entanglement. *Phys. Rev. Lett.* **92**, 217402 (2004)
203. Reimann, S. M. and Manninen, M.: Electronic structure of quantum dots. *Rev. Mod. Phys.* **74**, 1283 (2002)
204. Schofield, A. J.: Non-Fermi liquids. *Contemporary Phys.* **40**, 95 (1999)
205. Aharoni, A.: *Introduction to the Theory of Ferromagnetism*. University Press, Oxford (1996)
206. Kutner, R., et al.: Diffusion in concentrated lattice gases. II. Particles with attractive nearest-neighbor interaction on three-dimensional lattices. *Phys. Rev. B* **26**, 2967 (1982)
207. Skomski, R., et al: Ruderman-Kittel-Kasuya-Yosida interactions between spin distributions of arbitrary shape. *J. Appl. Phys.* **85**, 5890 (2000)

208. Mahadevan, P., et al.: Unusual directional dependence of exchange energies in GaAs diluted with Mn: Is the RKKY description relevant? *Phys. Rev. Lett.* **93**, 177201-1-4 (2004)
209. Michalski, S. A. and Kirby, R. D. unpublished (2007)
210. Smart, J. S.: *Effective field theories of magnetism*. Sanders, Philadelphia (1966)
211. Skomski, R., et al.: Superparamagnetic ultrathin films. *J. Appl. Phys.* **81**, 4710 (1997)
212. Das Sarma, S., et al.: Temperature-dependent magnetization in diluted magnetic semiconductors. *Phys. Rev. B* **67**, 155201 (2003)

Chapter 4

Superconductivity and Magnetism in Silicon and Germanium Clathrates

Joseph H. Ross Jr. and Yang Li

Abstract Clathrates are materials containing closed polyhedral cages stacked to form crystalline frameworks. With Si, Ge, and Sn atoms populating these frameworks, a wide variety of electronic and vibrational properties can be produced in these materials, by substitution upon framework sites or through incorporation of ions in cage-center positions. Commonly formed structures include the type I, type II, and chiral clathrate types, whose properties will be described here. $\text{Ba}_8\text{Si}_{46}$ with the type-I structure has been found to exhibit superconductivity with T_c as high as 9 K. The enhanced T_c in this compound has been shown to arise predominantly from very sharp features in the electronic densities of states associated with the extended sp^3 -bonded framework. Atomic substitution can tailor these electronic properties; however, the associated disorder has been found to inevitably lower the T_c due to the disrupted continuity of the framework. Efforts to produce analogous Ge-based superconductors have not been successful, due to the appearance of spontaneous vacancies, which also serve to disrupt the frameworks. The formation of these vacancies is driven by the Zintl mechanism, which plays a much more significant role for the structural stability of the Ge clathrates. The sharp density of states features in these extended framework materials may also lead to enhanced magnetic features, due to conduction electron-mediated coupling of substituted magnetic ions. This has led to magnetic ordering in Fe- and Mn-substituted clathrates. The largest number of clathrates exhibiting magnetic behavior has been produced by substitution of Eu on cage-center sites, with a ferromagnetic T_c as high as 38 K observed in such materials.

J.H. Ross (✉)

Department of Physics, Texas A&M University, College Station TX 77843-4242, USA
e-mail: ross@physics.tamu.edu

4.1 Introduction

Clathrates containing crystalline frameworks of group-IV semiconductors have attracted considerable interest in recent years for their variety of electronic and vibrational properties. Like carbon-based fullerenes, silicon, germanium, and tin also form polyhedral cage structures. However, unlike fullerenes, the heavier group-IV elements form sp^3 -bonded connected structures periodic in three dimensions. Intermediate between the disconnected fullerenes and the tetrahedral diamond structure, these materials have a number of unique properties. In this chapter, we discuss the electronic and vibrational properties of these framework materials, specifically as they relate to the appearance of superconductivity and magnetism.

While closed-cage materials of all types can be denoted as clathrates, the class of group-IV clathrates generally refers to the set of materials that share a common structure with the hydrate clathrates. The latter are crystalline materials such as methane hydrate, $8\text{CH}_4 \cdot 46\text{H}_2\text{O}$, in which the water molecules form a framework enclosing individual methane molecules in a regular array. Methane clathrate is naturally occurring when natural gas combines with seawater at pressures of the ocean floor. The potential for useful energy reserves or of greenhouse gas emissions from such formations is one of the reasons for intensive interest in such materials. Several recent reviews [1–4] describe the features of the hydrate clathrates.

Jeffrey [5] developed a naming convention for the hydrate clathrates; by this labeling scheme “type I” and “type II” are the most commonly observed structures. These are illustrated in Figs. 4.1 and 4.2. These structures feature three-dimensional tessellations that completely fill spaces with polyhedral cages, such as the dodecahedron and tetrakaidecahedron that make up the type-I structure shown in Fig. 4.1. In the hydrate clathrates, the vertices of these polyhedra are water oxygens, while small molecules fill the closed cages. Figures 4.1 and 4.2 show silicon clathrates for

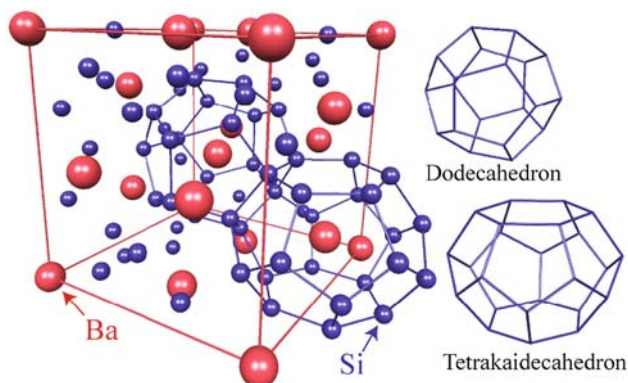


Fig. 4.1 Type-I clathrate structure, with Si and Ba atoms labeled according to the $\text{Ba}_8\text{Si}_{46}$ composition. Also shown are the two basic cages forming the Si_{46} framework for the structure (space group $\text{Pm}\bar{3}m$, #223), along with the cubic unit cell. The Si_{46} framework is a closed network involving all Si sites; only two of the polyhedra are shown connected for clarity

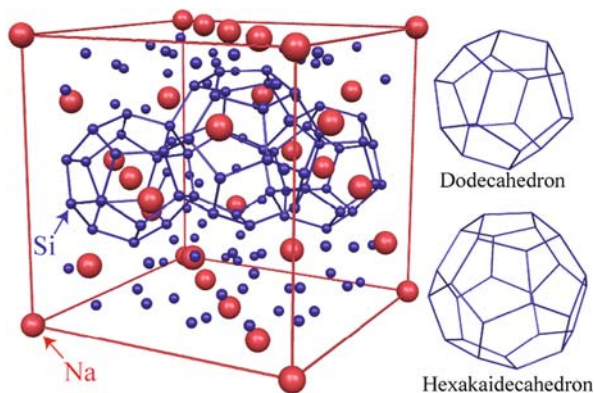


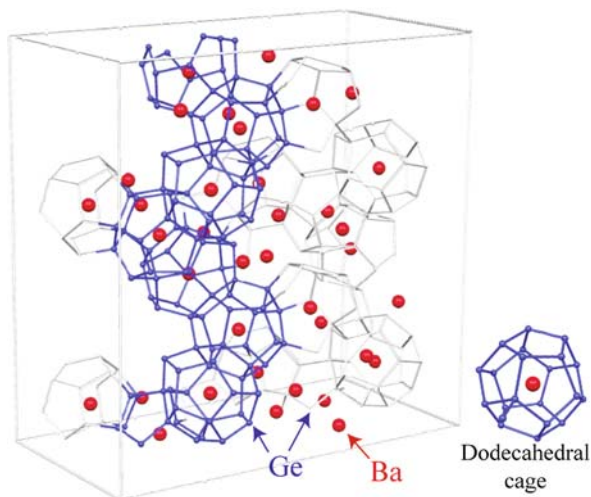
Fig. 4.2 Type-II clathrate structure, illustrated along with the two cages that make up the closed network. Inside the cubic unit cell, a central hexakaidecahedron is shown connected to two of its neighboring dodecahedra. Atom labels correspond to $\text{Na}_{16}\text{Si}_{136}$; $8b$, the large cage-filling site, is shown unoccupied. Space group is $Fd\bar{3}m$ (#227)

which the framework is a fourfold-bonded Si-atom network. Another set of materials sharing identical structural characteristics is the clathrasils [6], in which the crystalline framework is constructed of SiO_2 , rather than H_2O .

The silicon clathrates were first synthesized in 1965 [7], when type-I $\text{Na}_8\text{Si}_{46}$ and type-II $\text{Na}_x\text{Si}_{136}$ were prepared. A large number of related compositions have since been synthesized, including those with frameworks of Ge and Sn, and cage-filling atoms including Na, K, Rb, Sr, Ba, Te, Cl, Br, I, Eu, H_2 . Aside from column-IV elements, the framework may be substituted from columns II through VI, a few examples being type-I $\text{Sr}_8\text{Al}_{16}\text{Ge}_{30}$ [8], $\text{Ba}_8\text{Ga}_{18}\text{Sb}_2\text{Ge}_{26}$ [9], $\text{Te}_8(\text{Si}_{38}\text{Te}_8)$ [10], and $\text{Cs}_8\text{Zn}_4\text{Sn}_{42}$ [11], or type-II $\text{Ba}_{16}\text{Ga}_{32}\text{Sn}_{104}$ [12]. Furthermore, several late transition metal elements have been substituted on the Si and Ge frameworks [13], while Si and Ge type-II clathrates can also be formed as empty frameworks [14, 15], by driving Na out of the filled cages or out of an intermediate product, respectively.

Closely related structural types not observed among the hydrate clathrates include the low-temperature stable structure found in $\alpha\text{-Ba}_8\text{Ga}_{16}\text{Sn}_{30}$ [8] and $\alpha\text{-Eu}_8\text{Ga}_{16}\text{Ge}_{30}$ [16], a cubic structure closely related to the type-I structure stable at high temperatures in both of these materials (type I corresponding to the β -phases). This structure has also been called “clathrate VIII,” as an addition to the seven structure types originally identified among hydrate clathrates. The chiral clathrate structure, originally discovered as the structure of $\text{Ba}_6\text{In}_4\text{Ge}_{21}$ [17], has been identified to form several silicon and germanium compounds, generally in combination with barium, as in the binaries $\text{Ba}_6\text{Si}_{25}$ [18] and $\text{Ba}_6\text{Ge}_{25}$ [19]. Tin-based chiral clathrates can be formed with alkali metals, for example, K_6Sn_{25} [20]. A member of the chiral space group #213 ($P4_123$), the chiral clathrate structure, features polyhedral cages arranged in a three-dimensional network of interlinked helices (Fig. 4.3). Aside from the single type of closed cage, which encloses the cation occupying the $8c$ site, the structure also features two additional cation sites in open regions of the

Fig. 4.3 Chiral clathrate structure, as observed in $\text{Ba}_8\text{Ge}_{25}$ [18]. A $2 \times 2 \times 1$ raft of cubic cells is illustrated. Large spheres are Ba, with connected framework composed of Ge atoms. One helical grouping of framework cages has been highlighted for clarity; however, all cages are identical, forming somewhat irregular dodecahedra



cell. In addition, two of the six framework sites (representing 8 of the 25 framework atoms per formula unit) are only threefold coordinated to other framework atoms, as opposed to the fourfold coordination uniformly observed in all other clathrates discussed here. At times this structure has been termed type IX or type III (although a different hydrate clathrate structure also has been labeled type III); here the designation “chiral clathrate” will be used.

4.2 Superconductivity in Si_{46} Clathrates

Roy [21] initially searched for superconductivity in type-I and type-II Na–Si clathrates; however, these original silicon clathrates were found not to be superconducting. A few years later the type-I composition $\text{Na}_{2.9}\text{Ba}_{4.5}\text{Si}_{46}$ was prepared and shown to be superconducting with T_c near 4 K [22]. Similarly, the K- and Ba-filled analog was found to have $T_c = 3.2$ K [23]. Advances in synthesis, in particular high-pressure methods, led to the preparation of $\text{Ba}_8\text{Si}_{46}$ for which the alkali metals were replaced completely by Ba [24]. This composition achieves a superconducting $T_c = 8$ K. $\text{Ba}_8\text{Si}_{46}$ prepared with a slight deficit of Ba was found to have T_c as high as 9.0 K [25], which is a high-water mark for superconducting transition temperatures among sp^3 -bonded clathrates.

Further advances in synthesis have included the production of single crystals of $\text{Ba}_{7.6}\text{Si}_{46}$ [26], however, with no increase in T_c of this material. Single crystals of the $\text{Na}_2\text{Ba}_6\text{Si}_{46}$ clathrate have also been produced, and a crystallographic study has confirmed the ordered structure of this material, with Na ions occupying the smaller dodecahedral cages and Ba ions the larger tetrakaidecahedral cages, surrounded by a fully populated Si_{46} framework [27].

4.3 Rattler Atoms and Narrow Bands

Among the distinctive features commonly observed in the clathrates is low-frequency Einstein-like phonon modes. Generally associated with ions loosely held within their encapsulating cages, such modes can be observed by various techniques, including Raman scattering [28] or detection of the displacements of the encapsulated ions via x-ray [29] or neutron [30] crystallography. Einstein modes with energies corresponding to approximately 80 K have been reported for $\text{Ba}_8\text{Si}_{46}$ [31], between 30 and 60 K for type-I $\text{Eu}_8\text{Ga}_{16}\text{Ge}_{30}$, $\text{Sr}_8\text{Ga}_{16}\text{Ge}_{30}$ and $\text{Ba}_8\text{Ga}_{16}\text{Ge}_{30}$ [30], and 45–60 K in type-I $\text{Cs}_8\text{Ga}_8\text{Sn}_{38}$ [32], with similar small values obtained for many other clathrate materials.

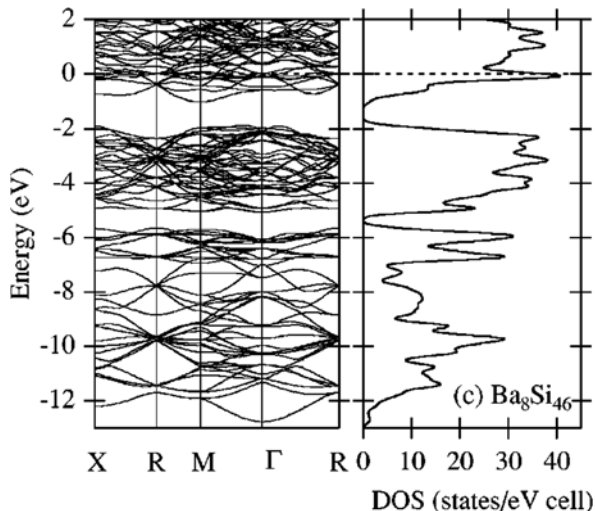
Slack [33] originally suggested the idea that the “rattling” of encapsulated ions may contribute to low observed thermal conductivities, a feature of great current interest due to potential thermoelectric applications for semiconducting compositions of these materials. Similar behavior is observed in other cage-type materials, particularly the skutterudites [34]. Much effort has been devoted to understanding such behavior in type-I materials in particular, for which the larger tetrakaidecahedral cages afford room for smaller ions to displace to off-center positions within the cage. A recent work [35] gave direct evidence for a very low-frequency (450 MHz \sim 20 mK) mode attributed to tunneling between such off-center positions in $\text{Eu}_8\text{Ga}_{16}\text{Ge}_{30}$. Furthermore, glass-like thermal conductivity with T^2 temperature dependence has been observed in $\text{Eu}_8\text{Ga}_{16}\text{Ge}_{30}$ and $\text{Sr}_8\text{Ga}_{16}\text{Ge}_{30}$ [36], at temperatures of the order of a few kelvins. The standard explanation for such behavior is phonon tunnel centers spread over a wide range of energies. The source of this energy spread is not entirely clear; however, there is additional spectroscopic evidence for distributed behavior [37, 38], which may be related to intrinsic framework-site disorder due to mixed atomic occupation in the alloyed clathrates such as $\text{Sr}_8\text{Ga}_{16}\text{Ge}_{30}$.

Note that other mechanisms may also affect the thermal conductivity; in particular, a large electron–phonon coupling parameter has been argued to be important in the Ba–Ge type-I clathrates [39, 40]. However, it is clear that there is a large density of phonon modes at low frequencies, which can potentially affect the superconducting behavior in these systems. Some of the observed behavior may relate to the mixed site occupancy in alloyed clathrates; however, even in $\text{Na}_8\text{Si}_{46}$, amorphous-like thermal conductivity has been observed at low temperatures [41].

The electronic properties of the superconducting silicon clathrates feature sharp electron density of states peaks at or near the Fermi energy (E_F). This is illustrated in Fig. 4.4 [42], where a particularly sharp peak can be seen in the calculated density of states at the position of E_F for $\text{Ba}_8\text{Si}_{46}$. It was noted in the original report [22, 43] that a similar behavior may hold for $\text{Na}_2\text{Ba}_6\text{Si}_{46}$. Photoemission [44] and NMR [45] experiments have confirmed the large $g(E_F)$ in these cases.

Aside from the behavior near E_F , it is also a general feature of the silicon and germanium clathrates that the bands are narrowed, and $g(E)$ enhanced, compared to the corresponding diamond-structure semiconductors. Figure 4.5 shows a comparison of calculated electronic structures for empty silicon and germanium clathrates

Fig. 4.4 Band structure and electron density of states for type-I $\text{Ba}_8\text{Si}_{46}$, calculated using an ab initio pseudopotential method, from [42]. Horizontal *dashed line* represents E_F . States are measured per cell, which contains the standard formula unit $\text{Ba}_8\text{Si}_{46}$. © 2000 American Physical Society



[46]. These feature larger band gaps than diamond-structure silicon or germanium. This result follows the general expectation of expanded structure leading to reduced hybridization and hence a smaller bandwidth. This mechanism is demonstrated in A_3C_{60} fullerides ($A =$ alkali metal atom), for which $g(E_F)$ increases monotonically with cell size as the cation is changed, decreasing the overlap between

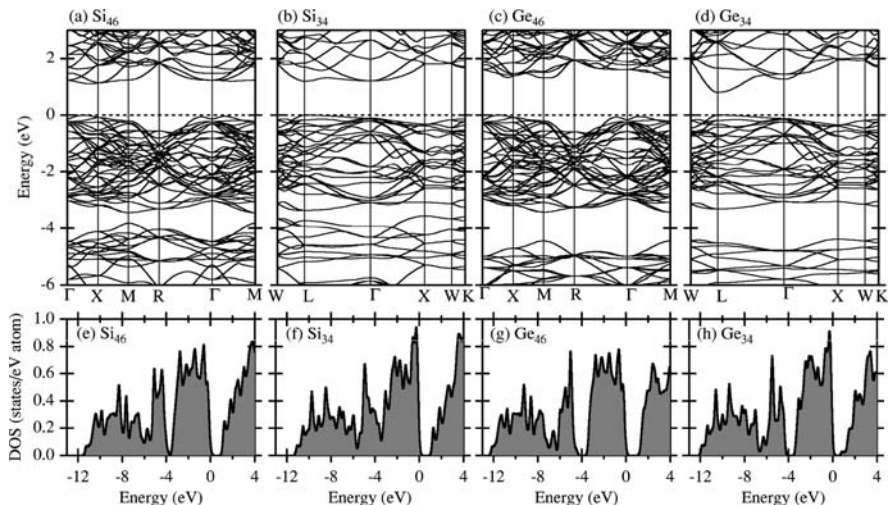
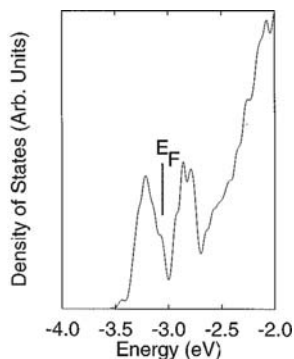


Fig. 4.5 Band structures and electron densities of states calculated for empty Si and Ge clathrates [46], using an ab initio pseudopotential method. Si_{34} and Ge_{34} are type-II clathrates. Si_{46} and Ge_{46} are hypothetical empty type-I frameworks. © 2000 American Physical Society

fullerene molecules. An increase in superconducting T_c that is also monotonic in cell size tracks the $g(E_F)$ increase [47]. For example, in $\text{Rb}_2\text{CsC}_{60}$, $T_c = 31$ K, while $g(E_F)$ is 24 states/eV per C_{60} molecule, comparable to the height of the peak seen in Fig. 4.4.

In contrast to the fullerenes, however, the cage-center guest ions in group-IV clathrates hybridize relatively strongly with the framework ions. Calculations for superconducting Si_{46} clathrates reveal significant Na and Ba contributions [43] modifying the conduction band, so that the large $g(E_F)$ can be attributed in part to states of these ions. Similarly in semiconducting $\text{Ba}_8\text{Ga}_{16}\text{Ge}_{30}$, and analogs centered by Sr and Eu, guest-ion d -states appear to participate strongly in the conduction band [48]. In type-II $\text{Na}_x\text{Si}_{136}$ clathrates, ^{27}Na NMR shifts have been found to be strongly temperature dependent, indicating the presence of Na-based electron states at E_F [49]. Figure 4.6 shows a theoretical $g(E)$ for this situation; E_F appears at a sharp dip in this case rather than the sharp peak as in the type-I case. From the strong presence of Na states in the band edge one may make the case that conductivity in $\text{Na}_x\text{Si}_{136}$ proceeds via an impurity band, as originally invoked to explain the metal–insulator behavior observed in this material [50]. However, this picture seems less apt for the type-I clathrates, for which hybridization between cage-center and framework atoms are generally stronger and band calculations have generally been successful in modeling the electrical transport behavior.

Fig. 4.6 Calculated density of states for type-II $\text{Na}_8\text{Si}_{136}$ from [49]. E_F appears at an energy just above a strong band of Na-dominated states.
© 1998 American Physical Society



4.4 Superconducting Mechanism

The observation of superconductivity in $\text{Ba}_8\text{Si}_{46}$ has led to significant interest in the reason for the relatively large T_c in this material. One of the challenges has been the range of reported transition temperatures due to the difficulty of preparing single-phase $\text{Ba}_8\text{Si}_{46}$. A study of silicon isotope-substituted samples of $\text{Ba}_8\text{Si}_{46}$ [51], however, showed an isotope effect corresponding to the range of expected values for the BCS theory, indicating that a phonon mechanism is responsible for the superconducting state. In addition, by matching the changes in T_c due to applied pressure to

ab initio calculations [52], a further measure was obtained for the parameters driving superconductivity in the material. In the McMillan theory [53], T_c can be expressed as

$$T_c = \frac{\Theta_D}{1.45} \exp\left(\frac{-1.04(1 + \lambda_{ep})}{\lambda_{ep} - \mu^*(1 + 0.62\lambda_{ep})}\right), \quad (4.1)$$

where Θ_D is the Debye temperature, and λ_{ep} and μ^* are the electron–phonon coupling constant and repulsive interaction, respectively. For $\text{Ba}_8\text{Si}_{46}$, λ_{ep} was found to be about 1.05, and μ^* to be 0.24. The parameter λ_{ep} is a product of $g(E_F)$ and the electron pairing interaction, V_{ep} . By comparison with theoretically calculated values [52], it appears that $g(E_F)$ is the most important parameter determining T_c .

Further information has been obtained by changing the composition through substitution of framework or cage-center atoms. Table 4.1 summarizes the reported changes in T_c for such materials. In some cases only the end member of a series is given in this table, for example, in Fig. 4.7 the susceptibility for a series $\text{Ba}_{8-x}\text{Sr}_x\text{Si}_{46}$ [54], showing the progressive change in T_c , is shown.

Framework substitutions by fourth-row Ge, Ga, and Cu have a progressively larger effect on T_c , as might be expected from the increasing differences in electronic character relative to Si. A calculated series of electron densities of states [57] (Fig. 4.8) indicates a nearly rigid-band change in the region near E_F upon going from $\text{Ba}_8\text{Si}_{46}$ to $\text{Ba}_8\text{Ga}_6\text{Si}_{40}$. The observed change in T_c for $\text{Ba}_8\text{Ga}_6\text{Si}_{40}$ is consistent with a reduction of λ_{ep} to 0.78, attributable to a reduction in $g(E_F)$ of this magnitude, combined with a modest reduction in V_{ep} [57]. Thus, it appears that relatively

Table 4.1 Superconducting transition temperatures as reported in type-I silicon clathrates

Molecular	T_c	Reference
$\text{Ba}_8\text{Si}_{46}$	8	[24]
$\text{Ba}_{7.76}\text{Si}_{46}$	9	[25]
$\text{Na}_{0.2}\text{Ba}_6\text{Si}_{46}$	4.8	[55]
$\text{Na}_{0.2}\text{Ba}_{5.6}\text{Si}_{46}$	3.5	[56]
$\text{Na}_{0.3}\text{Ba}_{6.2}\text{Si}_{46}$	4	[55]
$\text{Na}_{1.5}\text{Ba}_6\text{Si}_{46}$	2.6	[55]
$\text{Na}_{2.9}\text{Ba}_{4.5}\text{Si}_{46}$	4	[22]
$\text{Na}_8\text{Si}_{46}$	0	[56]
$\text{K}_{2.9}\text{Ba}_{4.9}\text{Si}_{46}$	3.2	[56]
K_7Si_{46}	0	[56]
$\text{Ba}_2\text{Sr}_6\text{Si}_{46}$	4.1	[54]
$\text{Ba}_8\text{Si}_{40}\text{Ga}_6$	3.3	[57]
$\text{Ba}_8\text{Si}_{23}\text{Ge}_{23}$	2.3	[26]
$\text{Ba}_8\text{Cu}_{0.5}\text{Si}_{45.5}$	6.3	[58]
$\text{Ba}_8\text{Cu}_4\text{Si}_{42}$	2.9	[59]
$\text{Ba}_8\text{Ag}_{0.5}\text{Si}_{45.5}$	6.1	[58]
$\text{Ba}_8\text{Au}_1\text{Si}_{45}$	5.8	[58]

Fig. 4.7 Magnetic susceptibility for $\text{Ba}_{8-x}\text{Sr}_x\text{Si}_{46}$ alloys [54], showing the progressive change in T_c . © 2005 American Physical Society

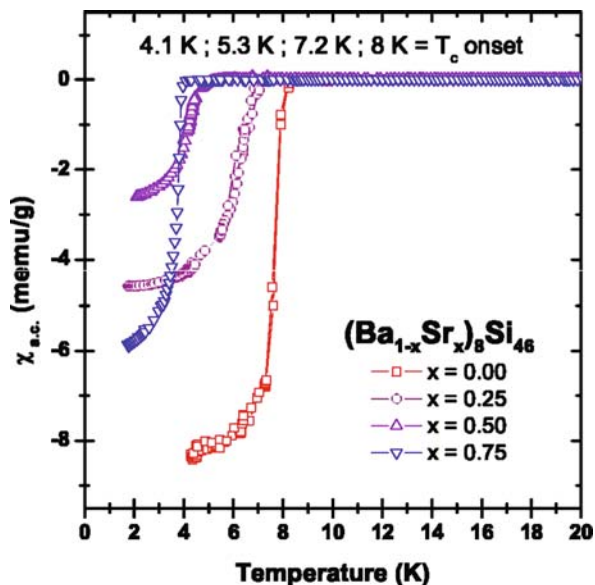
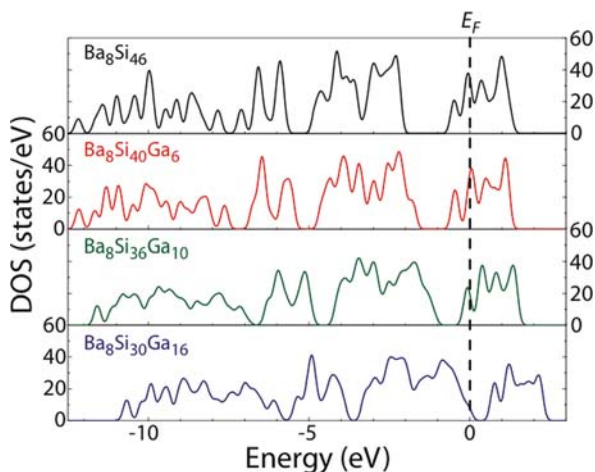


Fig. 4.8 Calculated electron densities of states for Ga-substituted $\text{Ba}_8\text{Si}_{46}$ [57]. © 2007 American Physical Society



low substitution of Ga preserves the sp^3 character of the Si clathrate network. By contrast, a calculated set of electron bands for $\text{Ba}_8\text{Cu}_6\text{Si}_{40}$, and the corresponding density of states (Fig. 4.9, left), shows a much larger change [59], clearly not rigid-band in character near E_F .

Additional information can be obtained from valence-electron density plots, as in the left panels of Fig. 4.10, for $\text{Ba}_8\text{Ga}_x\text{Si}_{46-x}$ [57]. Near the top and bottom these

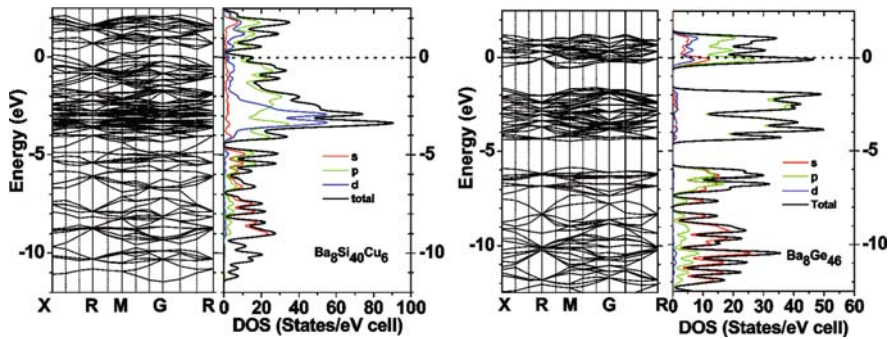


Fig. 4.9 Calculated electron bands and densities of states for $\text{Ba}_8\text{Cu}_6\text{Si}_{40}$ (left) and hypothetical $\text{Ba}_8\text{Ge}_{46}$ [59]

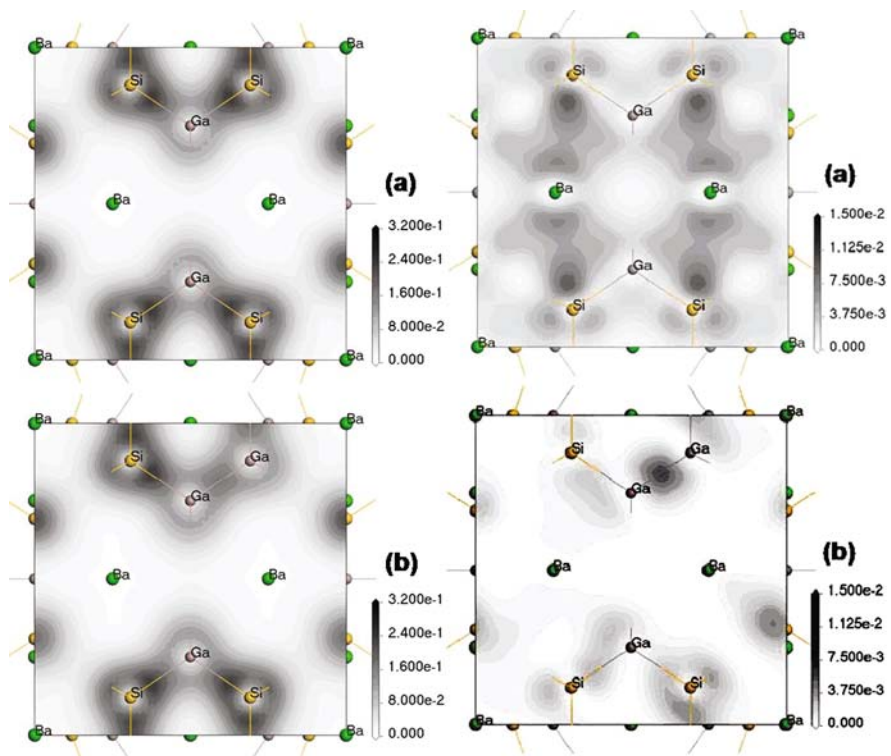


Fig. 4.10 Contour maps of valence-electron densities (left) and Fermi-level-resolved electron densities (right) for (a) $\text{Ba}_8\text{Ga}_6\text{Si}_{40}$ and (b) $\text{Ba}_8\text{Ga}_{16}\text{Si}_{30}$ [57]. © 2007 American Physical Society

sections cut through Si–Ga–Si and Si–Ga–Ga bond sequences, showing that the hybridization of the framework is maintained. The left panels illustrate the Fermi-level resolved states, responsible for the superconductivity, which maintain their integrity for the case $\text{Ba}_8\text{Ga}_6\text{Si}_{40}$, but become much less well connected for the more highly substituted case.

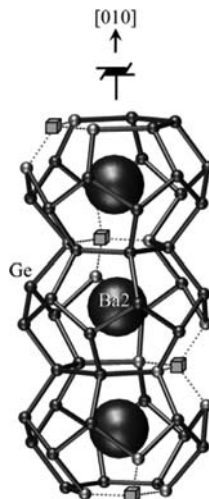
Calculations for Ge-based type-I clathrates (Fig. 4.9, right) indicate an electronic structure for $\text{Ba}_8\text{Ge}_{46}$ rather similar to that of $\text{Ba}_8\text{Si}_{46}$ [57]; the lack of superconductivity in the former material is due to vacancy formation, as shown below. However, there is also likely an increase in V_{ep} going up the periodic table; calculations for a hypothetical type-I carbon clathrate [52] have indicated a significant increase over that observed in silicon clathrates, indicating potentially large increases in T_c if such materials could be formed. Among germanium clathrates, there has been only one report of superconductivity, in $\text{Ba}_8\text{Ga}_{16}\text{Ge}_{30}$ [60]; however, most samples of this composition do not show such behavior, which must not be a general property of the material [30].

4.5 Zintl Concept and Vacancies

The Zintl phases [61] are a class of compounds featuring cations from the first or second column combined with more weakly ionic anions from the carbon group or later. In these materials, the anions combine to form clusters or connected networks. The combination of electron transfer from the cations and anion–anion hybridization can be viewed as leading to closed-shell configurations in these materials, and hence enhanced stability. The clathrates include classic examples of Zintl phases. For example, in the type-I structure, each framework atom has four framework neighbors. In a localized-bond picture, the hypothetical empty type-I clathrate Si_{46} would have a closed shell of four bonds per atom, Si having a valence of 4. In $\text{Ba}_8\text{Ga}_{16}\text{Si}_{30}$, the presence of 16 valence-3 Ga atoms implies a deficit of 16 bonding electrons per cell. The electron transfer from 8 Ba atoms, each in a nominal 2^+ state, can thus achieve a completed bond network. This simplified model has predictive power, and indeed $\text{Ba}_8\text{Ga}_{16}\text{Si}_{30}$ is a stable material synthesized more easily than, for example, $\text{Ba}_8\text{Si}_{46}$, which has excess framework electrons when viewed in a Zintl picture. Furthermore, the $A_8B_{16}\text{Ge}_{30}$ and $A_8B_{16}\text{Si}_{30}$ materials ($A = \text{Sr}, \text{Ba}, \text{Eu}$; $B = \text{Al}, \text{Ga}$) are semiconductors, a hallmark of the Zintl phases, or at most they are very weakly metallic, indicating proximity to a filled-band situation.

$\text{Ba}_8\text{Si}_{46}$ exhibits an unbroken framework, as established through crystallography and NMR [27, 62]. However, its analog $\text{Ba}_8\text{Ge}_{46}$ does not form a fully populated framework, instead favoring spontaneous vacancy formation [63, 64], with the configuration $\text{Ba}_8\text{Ge}_{43}\square_3$, \square denoting the vacancies, with a superstructure as shown in Fig. 4.11. According to a Zintl picture 4 vacancies, with 4 electrons each, might be expected to accept the 16 electrons from Ba^{2+} , completing a network of filled

Fig. 4.11 View of the large cages in $\text{Ba}_8\text{Ge}_{43}$, with structure based on the type-I structure [64]. Small cubes are vacancies, forming a helical superstructure as shown. © 2004 Wiley-VCH



bonds. The observed vacancy count of three may indicate incomplete charge transfer from ionized Ba, or the limitations of the Zintl concept. Type-I alkali metal–tin clathrates exhibit the composition $\text{A}_8\text{Sn}_{44}\square_2$, in this case precisely satisfying the Zintl criterion [65–67], as does $\text{K}_8\text{Ge}_{44}\square_2$ [68].

Germanium and tin clathrates commonly adhere closely to Zintl stability conditions, forming vacancies as needed. For example, the type-I compound initially reported as $\text{Ba}_8\text{Cu}_6\text{Ge}_{40}$ was found instead to form a composition close to $\text{Ba}_8\text{Cu}_{5.3}\text{Ge}_{40.7}$, satisfying the Zintl criterion [69], with Cu treated as a simple *s-p* substituent having a valence of 1. On the other hand, silicon-based $\text{Ba}_8\text{Cu}_x\text{Si}_{46-x}$ forms with varying composition not keeping to Zintl rules [59, 70]. Other germanium and tin clathrates obeying Zintl criteria are $\text{Ba}_8\text{Al}_{16-x}\text{Ge}_{30+y}$, which forms vacancies when $x \neq 0$ to maintain a Zintl composition [71], and $\text{I}_8\text{Te}_{5.3}\text{Ge}_{40}$ [72], $\text{Sn}_{24}\text{P}_{19.3}\text{I}_{8-y}\text{Cl}_y$ [73], and $\text{Sn}_{14}\text{In}_{10}\text{P}_{21.2}\text{I}_8$ [74], all exhibiting spontaneous vacancies. $\text{Ba}_8\text{Ga}_{10}\text{Si}_{36}$ is the only silicon-based clathrate thus far reported to exhibit spontaneous vacancy formation [70, 75]. On the other hand, $\text{Ba}_8\text{Ga}_6\text{Si}_{40}$, a composition further from the Zintl phase $\text{Ba}_8\text{Ga}_{16}\text{Si}_{30}$, is a bulk superconductor as described above [57], and thus most likely features an unbroken framework. Typically the Si–Si bond strength makes vacancy formation less common in silicon-based systems, and although the electronic structures would appear to favor superconductivity in germanium and tin clathrates [59] the tendency of these compounds to form vacancies rather than high-electron compositions explains the lack of superconductivity observed in such materials. It is possible that a high-pressure synthesis technique might stabilize a vacancy-free germanium clathrate, but the relatively weak Ge–Ge bond may make this difficult.

4.6 Superconductivity in Other Clathrates

There are no reports of superconductivity in type-II clathrates, although these materials feature complete sp^3 -bonded frameworks similar to the type-I structure. In part this is because far fewer compositions are found to be stable in the type-II structure. For example, there is only one report of a Ba–Si type-II clathrate: $\text{Na}_{16}\text{Ba}_8\text{Si}_{136}$ contains Ba in the larger cage [76]; however, there has been no superconductivity observed in this compound above 2 K. Among Sn clathrates $\text{Ba}_{16}\text{Ga}_{32}\text{Sn}_{104}$ can be formed with a larger concentration of second-column ions [77, 78], although this is a likely Zintl phase with a corresponding low carrier concentration.

By contrast, chiral clathrates have been reported to exhibit superconductivity, for silicon-based and also for germanium-based materials. $\text{Na}_2\text{Ba}_4\text{Ge}_{25}$ was found to have $T_c = 0.84$ K, and $\text{Ba}_6\text{Ge}_{25}$ $T_c = 0.24$ K, under ambient conditions [79]. However, with applied high pressure an increase was observed for $\text{Ba}_6\text{Ge}_{25}$ up to $T_c = 3.8$ K in 2.7 GPa [79]. $\text{Ba}_6\text{Ge}_{25}$ is not a Zintl semiconductor; however, the eight sp^2 -bonded framework sites per formula unit can formally be regarded to possess lone pairs acting as electron acceptors, so that a Zintl-type charge transfer from Ba ions to the framework may be regarded as explaining in part its stability [80]. This material exhibits two structural changes under ambient conditions [81] involving shifts of both Ge and Ba atoms. The structural distortions induced under high-pressure conditions have been found to be associated with a large increase in $g(E_F)$, which has been identified to be largely responsible for the enhanced T_c [82].

Recent reports have also shown that $\text{Ba}_6\text{Si}_{25}$ is a superconductor [83, 84], with T_c as high as 1.55 K [83]. There is no large pressure-induced change in $\text{Ba}_6\text{Si}_{25}$, as observed for $\text{Ba}_6\text{Ge}_{25}$, and the complex sequence of structural transitions at ambient conditions is also not present. Thus this material can be compared directly to the corresponding type-I superconductor Ba_8S_{46} . It is not yet entirely clear why such a large difference is observed between T_c for the chiral and type-I Ba–Si clathrates. The presence of sp^2 -bonded sites in the sp^3 framework has been invoked as reducing the electron–phonon coupling [83], as have a significant difference in low-frequency vibrational properties [40]. Further study will be needed to resolve this question.

4.7 Magnetism

The narrow peak in $g(E_F)$ evidenced in $\text{Ba}_8\text{Si}_{46}$ might be expected to favor magnetism as well as superconductivity, similar to the $A_3\text{C}_{60}$ materials, which are close to a Mott–Hubbard transition. However, in both cases, superconductivity is generally preferred. It has been argued that the sp^2 orbital degeneracy of the fullerenes stabilizes the expanded C_{60} materials against a metal–insulator transition [85]; similarly the sp^3 configuration for Si and Ge clathrates may also help to stabilize the superconducting state. As described above, superconductivity in $\text{Ba}_8\text{Si}_{46}$ is uniformly suppressed by substitution of transition metals. However, this effect has generally been shown to be attributable to the broadening of the $g(E_F)$ peak rather than the competing appearance of a magnetic moment.

Ready substitution of transition metals onto the clathrate framework has only been exhibited for late transition elements, starting with Ni. These late transition metals exhibit filled d -bands when substituted on the silicon and germanium clathrates, shown for example by the formal valence of 1 for Cu atoms in the germanium type-I clathrate [69]. The earlier transition metals would be expected to induce magnetic moments, similar to observations in doped III–V and related semiconductors [86, 87]. The difficulty of substituting earlier transition metals is consistent with diamond-structure silicon, for which the Fe-group atoms are most commonly interstitial rather than substitutional [88]. In addition, there are many competing binary phases among the silicides and germanides. Two examples of substituted magnetic clathrates have been found thus far: type-I $\text{Ba}_8\text{Mn}_2\text{Ge}_{44}$ [89] and chiral $\text{Ba}_6\text{Fe}_3\text{Ge}_{22}$ [90]. However, these materials are difficult to prepare, for example, $\text{Ba}_6\text{Fe}_3\text{Ge}_{22}$ is apparently stable only at intermediate temperatures. Complicated interrelationships control the stability of such materials [91]; it may be that further advances will be made in this direction, for example, through stabilization with vacancies.

The largest class of magnetic materials based on the silicon and germanium clathrates occurs with Eu ions occupying cage-filling positions in type-I compounds. In these cases, Eu^{2+} carries a large local moment, leading to a ferromagnetic transition temperature as high as 38 K for $\text{Eu}_2\text{Ba}_6\text{Ga}_8\text{Si}_{36}$ [92]. The coupling between europium-based magnetic moments is apparently due to an RKKY interaction in all cases, with even the nominally semiconducting Zintl phases having a sufficient residual electron density to allow carrier-intermediated interactions as specified by the RKKY model. It will be interesting to see if the magnetic behavior can be tailored by modifying the carrier concentrations in some of these compounds. The properties of these materials will not be reviewed here, but in Table 4.2, we have summarized the compositions reported to exhibit ferromagnetic behavior, along with the reported transition temperatures.

Table 4.2 Eu-containing magnetic clathrates along with reported magnetic transition temperatures. All have type-I structure except for type-VIII $\alpha\text{-Eu}_8\text{Ga}_{16}\text{Ge}_{30}$

Material	T_c (K)	Reference
$\text{Eu}_2\text{Ba}_6\text{Ga}_8\text{Si}_{36}$	38	[92]
$\alpha\text{-Eu}_8\text{Ga}_{16}\text{Ge}_{30}$	36	[16]
$\text{Eu}_2\text{Ba}_6\text{Al}_8\text{Si}_{36}$	32	[70]
$\text{Eu}_6\text{Sr}_2\text{Ga}_{16}\text{Ge}_{30}$	20	[93]
$\text{Eu}_4\text{Sr}_4\text{Ga}_{16}\text{Ge}_{30}$	15	[93]
$\beta\text{-Eu}_8\text{Ga}_{16}\text{Ge}_{30}$	10.5	[16]
$\text{K}_6\text{Eu}_2\text{Cd}_5\text{Ge}_{41}$	9.3	[94]
$\text{Eu}_2\text{Ba}_6\text{Cu}_4\text{Si}_{42}$	5	[70]
$\text{Eu}_2\text{Ba}_6\text{Cu}_4\text{Si}_{38}\text{Ga}_4$	4	[70]
$\text{K}_6\text{Eu}_2\text{Zn}_5\text{Ge}_{41}$	4	[94]
$\text{K}_6\text{Eu}_2\text{Ga}_{10}\text{Ge}_{36}$	3.8	[94]

4.8 Conclusions

Group-IV clathrates are expanded cage-structured materials akin to the fullerenes. However, the presence of the extended sp^3 networks in these materials, as well as the vibrational behavior and Zintl behavior, leads to a number of properties unique to these materials. Here, we have discussed the superconducting behavior and shown that the enhanced superconductivity can be regarded as related most strongly to the electronic features of the sp^3 framework. Charge transfer between the cage-center atoms and the framework enhances the stability of these materials, but the Zintl mechanism also limits the ability to design high-carrier density composition, for example, promoting spontaneous vacancy formation. In addition because of significant hybridization, the cage-center ions participate much more actively in the electronic properties, as compared to carbon-based fullerenes. Magnetism has been observed in a number of cases where framework or cage-center positions can be substituted by magnetic ions.

Acknowledgments This work was supported in part by the Robert A. Welch Foundation (Grant No. A-1526) and the NSF (Grant No. DMR-0821284).

References

1. E. D. Sloan Jr. and C. Koh. *Clathrate Hydrates of Natural Gases*, 3rd ed. CRC Press (2007).
2. E. D. Sloan Jr. *Nature* **426**, 353 (2003).
3. A. V. Milkov, *Earth-Sci. Rev.* **66**, 183 (2004).
4. J. S. Loveday and R. J. Nelmes. *Phys. Chem. Chem. Phys.* **10**, 937 (2008).
5. G. A. Jeffrey. Hydrate Inclusion Compounds In *Inclusion Compounds*, vol. 1, J. L. Atwood, J. E. D. Davies, and D. D. MacNicol (eds.) Academic, London, p. 135 (1984).
6. H. Gies. Clathrasils and zeosils: inclusion compounds with silica host frameworks In *Inclusion Compounds*, vol. 5, J. L. Atwood, J. E. D. Davies, and D. D. MacNicol (eds.) Oxford, p. 1 (1991).
7. J. S. Kasper, P. Hagenmüller, M. Pouchard, and C. Cros. *Science* **150**, 1713 (1965).
8. B. Eisenmann, H. Schafer, and R. Zagler. *J. Less-Common Met.* **118**, 43–55 (1986).
9. S. Lattner, X. Bu, N. P. Blake, H. Metiu, and G. D. Stucky. *J. Solid State Chem.* **151**, 61–64 (2000).
10. N. Jaussaud, P. Toulemonde, M. Pouchard, A. San Miguel, P. Gravereau, S. Pechev, G. Goglio, and C. Cros. *Solid State Sci.* **6**, 401–411 2004.
11. G. S. Nolas, T. J. R. Weakley, and J. L. Cohn. *Chem. Mater.* **11**, 2470–2473 (1999).
12. R. Kroner, R. Nesper and H. G. von Schnering, *Z. Kristallogr. NCS* **186**, 172 (1989).
13. G. Cordier and P. Woll. *J. Less-Common Met.* **169**, 291–302 (1991).
14. J. Gryko, P. F. McMillan, R. F. Marzke, G. K. Ramachandran, D. Patton, S. K. Deb, and O. F. Sankey. *Phys. Rev. B* **62**, R7707–R7710 (2000).
15. A. M. Guloy, R. Ramlau, Z. Tang, W. Schnelle, M. Baitinger, and Y. Grin. *Nature* **443**, 320–323 (2006).
16. S. Paschen, W. Carrillo-Cabrera, A. Bentien, V. H. Tran, M. Baenitz, Yu. Grin, and F. Steglich. *Phys. Rev. B* **64**, 214404 (2001).
17. R. Kroener, R. Nesper and H. G. von Schnering, *Z. Kristallogr. NCS* **182**, 164–165 (1988).
18. H. Fukuoka, K. Ueno, and S. Yamanaka. *J. Organomet. Chem.* **611**, 543–546 (2000).
19. S. J. Kim, S. Q. Hu, C. Uher, T. Hogan, B. Huang, J. D. Corbett, and M. G. Kanatzidis. *J. Solid State Chem.* **153**, 321–329 (2000); H. Fukuoka, K. Iwai, S. Yamanaka, H. Abe, K. Yoza, and

- L. Häming. *J. Solid State Chem.* **151**, 117–121 (2000); W. Carrillo-Cabrera, J. Curda, H. G. von Schnering, S. Paschen and Y. Grin. *Z. Kristallogr. NCS* **216**, 172–172 (2001).
20. T. F. Fässler and C. Kronseder. *Z. Anorg. Allg. Chem.* **624**, 561 (1998).
 21. S. B. Roy, K. E. Sim, and A. D. Caplin. *Philos. Mag. B* **65**, 1445–50 (1992).
 22. H. Kawaji, H. Horie, S. Yamanaka, and M. Ishikawa. *Phys. Rev. Lett.* **74**, 1427–1429 (1995).
 23. S. Yamanaka, H. Horie, and H. Kawaji. *Eur. J. Solid State Inorg. Chem.* **32**, 799–807 (1995).
 24. M. Imai, T. Hirano, T. Kikegawa, and O. Shimomura. *Phys. Rev. B* **58**, 11922–11926 (1998).
 25. H. Fukuoka, J. Kiyoto, and S. Yamanaka. *Inorg. Chem.* **42**, 2933–2937 (2003).
 26. H. Fukuoka, J. Kiyoto, and S. Yamanaka. *J. Solid State Chem.* **175**, 237–244 (2003).
 27. M. Baitinger, H. G. von Schnering, J. H. Chang, K. Peters, and Y. Grin. *Z. Kristallogr. NCS* **222**, 87–88 (2007).
 28. G. S. Nolas and C. A. Kendziora. *Phys. Rev. B* **62**, 7157 (2000).
 29. B. C. Sales, B. C. Chakoumakos, D. Mandrus, and J. W. Sharp. *J. Solid State Chem.* **146**, 528–532 (1999).
 30. B. C. Sales, B. C. Chakoumakos, R. Jin, J. R. Thompson, and D. Mandrus. *Phys. Rev. B* **63**, 245113 (2001).
 31. R. Viennois, P. Toulemonde, M. Koza, H. Mutka, A. San Miguel, and R. Lortz. *J. Phys.: Conf. Ser.* **92**, 012121 (2007).
 32. C. W. Myles, J. Dong, O. F. Sankey, C. A. Kendziora, and G. S. Nolas. *Phys. Rev. B* **65**, 235208 (2002).
 33. G. A. Slack. *MRS Symp. Proc.* **478**, 47–54 (1997).
 34. V. Keppens, D. Mandrus, B. C. Sales, B. C. Chakoumakos, P. Dai, R. Coldea, M. B. Maple, D. A. Gajewski, E. J. Freeman, and S. Bennington. *Nature* **395**, 876–878 (1998).
 35. R. P. Hermann, V. Keppens, P. Bonville, G. S. Nolas, F. Grandjean, G. J. Long, H. M. Christen, B. C. Chakoumakos, B. C. Sales, and D. Mandrus. *Phys. Rev. Lett.* **97**, 017401 (2006).
 36. J. L. Cohn, G. S. Nolas, V. Fessatidis, T. H. Metcalf, and G. A. Slack. *Phys. Rev. Lett.* **82**, 779–782 (1999).
 37. W. Gou, Y. Li, J. Chi, J. H. Ross Jr., M. Beekman, and G. S. Nolas. *Phys. Rev. B* **71**, 174307 (2005).
 38. R. Baumbach, F. Bridges, L. Downard, D. Cao, P. Chesler, and B. Sales. *Phys. Rev. B* **71**, 024202 (2005).
 39. A. Bentien, M. Christensen, J. D. Bryan, A. Sanchez, S. Paschen, F. Steglich, G. D. Stucky, and B. B. Iversen. *Phys. Rev. B* **69**, 045107 (2004).
 40. J. S. Tse, T. Iitaka, and K. Parlinski. *Europhys. Lett.* **75**, 153–159 (2006).
 41. J. S. Tse, K. Uehara, R. Rousseau, A. Ker, C. I. Ratcliffe, M. A. White, and G. MacKay. *Phys. Rev. Lett.* **85**, 114 (2000).
 42. K. Moriguchi, M. Yonemura, A. Shintani, and S. Yamanaka. *Phys. Rev. B* **61**, 9859–9862 (2000).
 43. S. Saito and A. Oshiyama. *Phys. Rev. B* **51**, 2628–2631 (1995).
 44. T. Yokoya, A. Fukushima, T. Kiss, K. Kobayashi, S. Shin, K. Moriguchi, A. Shintani, H. Fukuoka, and S. Yamanaka. *Phys. Rev. B* **64**, 172504 (2001).
 45. H. Sakamoto, H. Tou, H. Ishii, Y. Maniwa, E. A. Reny, and S. Yamanaka. *Physica C* **341**, 2135–2136 (2000).
 46. K. Moriguchi, S. Munetoh, and A. Shintani. *Phys. Rev. B* **62**, 7138–7143 (2000).
 47. R. M. Fleming, A. P. Ramirez, M. J. Rosseinsky, D. W. Murphy, R. C. Haddon, S. M. Zahurak, and A. V. Makhija. *Nature* **352**, 787 (1991).
 48. G. K. H. Madsen, K. Schwarz, P. Blaha, and D. J. Singh. *Phys. Rev. B* **68**, 125212 (2003).
 49. J. Gryko, P. F. McMillan, R. F. Marzke, A. P. Dodokin, A. A. Demkov, and O. F. Sankey. *Phys. Rev. B* **57**, 4172 (1998).
 50. N. F. Mott. *J. Solid State Chem.* **6**, 348–351 (1973).
 51. K. Tanigaki, T. Shimizu, K. M. Itoh, J. Teraoka, Y. Moritomo, and S. Yamanaka. *Nat. Mater.* **2**, 653–655 (2003).

52. D. Connétable, V. Timoshevskii, B. Masenelli, J. Beille, J. Marcus, B. Barbara, A. M. Saitta, G.-M. Rignanese, P. Mélinon, S. Yamanaka, and X. Blase, *Phys. Rev. Lett.* **91**, 247001 (2003).
53. W. L. McMillan. *Phys. Rev.* **167**, 331 (1968).
54. P. Toulemonde, C. Adessi, X. Blase, A. San Miguel, and J. L. Tholence. *Phys. Rev. B* **71**, 094504 (2005).
55. H. Kawaji, K. Iwai, and S. Yamanaka. *Solid State Commun.* **100**, 393–395 (1996).
56. S. L. Fang, L. Grigorian, P. C. Eklund, G. Dresselhaus, M. S. Dresselhaus, H. Kawaji, and S. Yamanaka. *Phys. Rev. B* **57**, 7686–7693 (1998).
57. Y. Li, R. Zhang, Y. Liu, N. Chen, Z. P. Luo, X. Ma, G. Cao, Z. S. Feng, C.-R. Hu, and J. H. Ross Jr. *Phys. Rev. B* **75**, 054513 (2007).
58. R. F. W. Herrmann, K. Tanigaki, S. Kuroshima, and S. Kuroshima. *Chem. Phys. Lett.* **283**, 29 (1998).
59. Y. Li, Y. Liu, N. Chen, G. Cao, Z. Feng, J. H. Ross Jr. *Phys. Lett. A* **345**, 398 (2005).
60. J. D. Bryan, V. I. Srdanov, G. D. Stucky, and D. Schmidt. *Phys. Rev. B* **60**, 3064–7 (1999).
61. S. M. Kauzlarich, ed., *Chemistry, structure, and bonding of Zintl phases and ions*. VCH, New York (1996).
62. G. K. Ramachandran, P. F. McMillan, J. Diefenbacher, J. Gryko, J. Dong, and O. F. Sankey. *Phys. Rev. B* **60**, 12294–12298 (1999).
63. R. F. W. Herrmann, K. Tanigaki, T. Kawaguchi, S. Kuroshima, and O. Zhou. *Phys. Rev. B* **60**, 13245 (1999).
64. W. Carrillo-Cabrera, S. Budnyk, Y. Prots, and Y. Grin. *Z. Anorg. Allg. Chem.* **630**, 2267 (2004).
65. J.-T. Zhao and J. D. Corbett. *Inorg. Chem.* **33**, 5721 (1994).
66. F. Dubois and T. F. Fässler. *J. Am. Chem. Soc.* **127**, 3264–3265 (2005).
67. A. Kaltzoglou, S. D. Hoffmann, and T. F. Fässler. *Eur. J. Inorg. Chem.* **2007**, 4162–4167 (2007).
68. G. K. Ramachandran and P. F. McMillan. *J. Solid State Chem.* **154**, 626–634 (2000).
69. Y. Li, J. Chi, W. Gou, S. Khandekar, and J. H. Ross Jr. *J. Phys.: Condens. Matter* **15**, 5535 (2003).
70. Y. Mudryk, P. Rogl, C. Paul, S. Berger, E. Bauer, G. Hilscher, C. Godart, and H. Noel. *J. Phys.: Condens. Matter* **14**, 7991–8004 (2002).
71. C. L. Condon, S. M. Kauzlarich, F. Gascoin, and G. J. Snyder. *Chem. Mater.* **18**, 4939–4945 (2006).
72. K. A. Kovnir, N. S. Abramchuk, J. V. Zaikina, M. Baitinger, U. Burkhardt, W. Schnelle, A. V. Olenov, O. I. Lebedev, G. Van Tendeloo, E. V. Dikarev, and A. V. Shevelkov. *Z. Krist.* **221**, 527–532 (2006).
73. J. V. Zaikina, W. Schnelle, K. A. Kovnir, A. V. Olenov, Y. Grin, and A. V. Shevelkov. *Solid State Sci.* **9**, 664 (2007).
74. M. M. Shatruk, K. A. Kovnir, M. Lindsjö, I. A. Presniakov, L. A. Kloo, and A. V. Shevelkov. *J. Solid State Chem.* **161**, 233–242 (2001).
75. D. Nataraj and J. Nagao. *J. Solid State Chem.* **177**, 1905–1911 (2004).
76. T. Rachi, K. Tanigaki, R. Kumashiro, J. Winter, and H. Kuzmany. *Chem. Phys. Lett.* **409**, 48–51 (2005).
77. A. Czybulka, B. Kuhl, and H.-U. Schuster. *Z. Anorg. Allg. Chem.* **594**, 23–28 (1991).
78. R. Kroner, K. Peters, H. G. von Schnering, and R. Nesper. *Z. Kristallogr. NCS* **213**, 664 (1998).
79. F. M. Grosche, H. Q. Yuan, W. Carrillo-Cabrera, S. Paschen, C. Langhammer, F. Kromer, G. Sparr, M. Baenitz, Yu. Grin, and F. Steglich. *Phys. Rev. Lett.* **87**, 247003 (2001).
80. H. G. von Schnering, A. Zurn, J. H. Chang, M. Baitinger, and Y. Grin. *Z. Anorg. Allg. Chem.* **633**, 1147–1153 (2007).
81. W. Carrillo-Cabrera, H. Borrmann, S. Paschen, M. Baenitz, F. Steglich, and Y. Grin. *J. Solid State Chem.* **178**, 715–728 (2005).

82. H. Q. Yuan, F. M. Grosche, W. Carrillo-Cabrera, V. Pacheco, G. Sparn, M. Baenitz, U. Schwarz, Y. Grin, and F. Steglich. *Phys. Rev. B* **70**, 174512 (2004).
83. R. Viennois, P. Toulemonde, C. Paulsen, and A. San-Miguel. *J. Phys.: Condens. Matter* **17**, L311–L319 (2005).
84. T. Rachi, H. Yoshino, R. Kumashiro, M. Kitajima, K. Kobayashi, K. Yokogawa, K. Murata, N. Kimura, H. Aoki, H. Fukuoka, S. Yamanaka, H. Shimotani, T. Takenobu, Y. Iwasa, T. Sasaki, N. Kobayashi, Y. Miyazaki, K. Saito, F. Z. Guo, K. Kobayashi, K. Osaka, K. Kato, M. Takata, and K. Tanigaki. *Phys. Rev. B* **72**, 144504 (2005).
85. P. Durand, G. R. Darling, Y. Dubitsky, A. Zaopo, and M. J. Rosseinsky. *Nature Mater.* **2**, 605 (2003).
86. S. Picozzi. *Nature Mater.* **3**, 349 (2004).
87. T. Jungwirth, J. Sinova, J. Mašek, J. Kučera, and A. H. MacDonald. *Rev. Mod. Phys.* **78**, 809 (2006).
88. K. A. Kikoin and V. N. Fleurov. *Transition Metal Impurities in Semiconductors*. World Scientific, Singapore (1994).
89. T. Kawaguchi, K. Tanigaki, and M. Yasukawa. *Appl. Phys. Lett.* **77**, 3438 (2000).
90. Y. Li and J. H. Ross Jr. *Appl. Phys. Lett.* **83**, 2868 (2003).
91. P. Mahadevan and A. Zunger. *Phys. Rev. Lett.* **88**, 047205 (2002).
92. Y. Mudryk, P. Rogl, C. Paul, S. Berger, E. Bauer, G. Hilscher, C. Godart, H. Noel, A. Saccone, and R. Ferro. *Physica B* **328**, 44 (2003).
93. G. T. Woods, J. Martin, M. Beekman, R. P. Hermann, F. Grandjean, V. Keppens, O. Leupold, G. J. Long, and G. S. Nolas. *Phys. Rev. B* **73**, 174403 (2006).
94. S. Paschen, S. Budnyk, U. Kohler, Y. Prots, K. Hiebl, F. Steglich, and Y. Grin. *Physica B* **383**, 89 (2006).

Chapter 5

Neutron Scattering of Magnetic Materials

Olivier Isnard

Abstract Neutron scattering is a comprehensive tool for condensed matter research. After a brief description of the interaction of neutrons with matter, the usefulness of neutrons to probe the physical properties of magnetic materials is illustrated using examples taken from different research areas. Then a description of the crystal structure investigation, including in situ and time-resolved studies is given. The use of polarized or unpolarized neutrons to study magnetic structures or magnetic phase transition is also illustrated. The potential of techniques such as small-angle neutron scattering or neutron scattering on magnetic surfaces is presented showing that neutron scattering now offers a wide range of useful techniques to probe the structural and magnetic properties of magnetic materials whatever their state: polycrystalline, single crystal, amorphous, bulk, or thin films. Examples are taken from a wide range of research fields: hard magnetic materials, nanocomposite soft magnets, multilayers, superlattices, geometrically frustrated magnetic materials, etc. The experimental aspects are not covered in detail but relevant references are given throughout the chapter.

5.1 Introduction

Since the discovery of neutrons in 1932 by Chadwick [1, 2] and the following studies in nuclear physics, scattering of neutrons on crystals has become a powerful technique to study the properties of condensed matter. As a consequence several books and reviews have been devoted in the past to neutron scattering and diffraction studies among which one can cite [3–8]. The last few years have been the occasion of numerous technical developments of both neutron sources on the one hand with increasing performances of spallation sources and neutron scattering instruments on the other hand. Many neutron scattering techniques are now available for scientists

O. Isnard (✉)
Institut Néel, CNRS, Boîte F, BP166, F-38042 Grenoble, Cédex 9, France
e-mail: olivier.isnard@grenoble.cnrs.fr

and engineers to perform investigations of materials with neutrons. This experimental progress has significantly widened the field of research that can be undertaken by neutron scattering techniques. The present article is confined to magnetic materials; we will present here some essential aspects of the use of neutron scattering for nanoscale magnetic materials and their applications. A description of magnetic neutron scattering is even too broad to be treated in the limited space of this chapter. For further information, the readers are advised to consult books especially devoted to magnetic neutron scattering such as [9, 10].

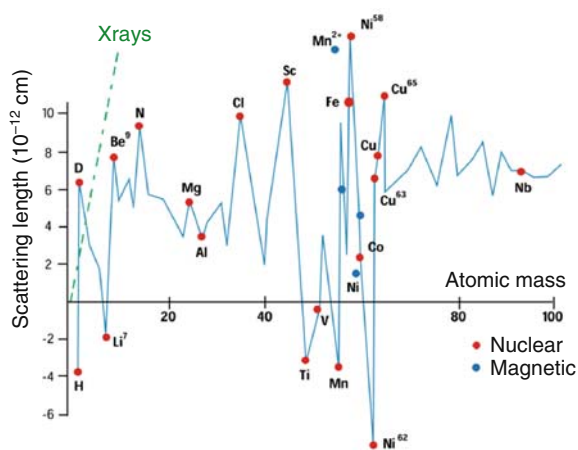
If the idea of magnetic neutron scattering originates from Bloch [11], Shull and Smart [12] provided the first experimental demonstration of the existence of antiferromagnetism predicted theoretically by Néel [13, 14]. To illustrate the potential of neutrons, we will present examples of scattering studies taken from different fields of research. The instruments used and the more technical parts are not discussed here, for more details the reader is referred to the following references [9, 15, 16]. This article is organized as follows the next section gives a brief description of the basics of interaction of neutron with materials. Then Section 5.3 presents the use of the neutron diffraction to investigate crystal structure on either polycrystalline or single crystal samples. In situ and time-resolved studies by neutron diffraction are illustrated in Section 5.4 with a few examples showing the usefulness of such techniques to investigate synthesis, processes, or kinetics of phase transformations. The study of magnetic structures is treated in Section 5.5, followed by examples of magnetic phase transition studies. Polarized neutron techniques are discussed in Section 5.7 with an emphasis on diffraction techniques. Small-angle neutron scattering and neutron scattering on magnetic surfaces are presented in Sections 5.8 and 5.9, respectively. Magnetic excitations as probed by inelastic neutron scattering are illustrated in Section 5.10. The possibility of performing neutron scattering investigations under extreme conditions of pressure, temperature, and magnetic field is addressed in Section 5.11.

5.2 Interaction of Neutrons and Materials: A Brief Presentation

Unlike neutrons inside the nucleus which are stable, a free neutron is unstable and decays. Consequently, neutron diffraction experiments must be carried out with neutrons from either a nuclear reactor or a spallation source [17]. For most neutron scattering studies, the high kinetic energy of the produced neutrons must be reduced, i.e., the neutrons must be thermalized, through collisions with a moderator such as light or heavy water. The resulting thermal neutrons have energy of ca. 10^{-1} to 10^{-3} eV or a wavelength, corresponding to ca. 1–5 Å. Thus, thermal neutrons have wavelengths appropriate for diffraction by an atomic or molecular lattice. As a consequence, neutron diffraction is closely related to x-ray diffraction, and typically neutron diffraction studies are preceded by x-ray diffraction structural studies. Neutron diffraction does, however, have certain advantages over x-ray diffraction, advantages which will be discussed herein. Neutrons interact with matter in a variety of ways which make neutron diffraction both similar to and yet different from x-ray diffraction.

The fundamental aspects of neutron diffraction and its use in the study of materials have been covered in detail in several excellent books which should be consulted for details [3–10, 15–18]. It is worth to note also that the range of energy of the neutrons matches very well the typical energy range of excitations in the matter: solid, liquid, or gas. Consequently neutrons are excellent tools to probe the diffusion of atoms in solid or liquid, or to investigate the vibrations in materials either atomic or collective (phonons) or rotation. Finally, a neutron has a spin magnetic moment so that it is very sensitive to the presence of a magnetic field in general and to the atomic magnetic moments in particular. Neutron scattering is thus the ideal tool to investigate magnetic materials both for their magnetic structure and to analyze magnetic excitations such as spin waves [6, 9, 16]. This is now an intensive field of research since polarized neutrons can be produced leading to even better sensitivity to magnetism. Thus, the advantages of neutrons versus electrons or x-rays include the magnetic scattering which can be very useful, particularly in conjunction with polarized neutron scattering studies, in determining the magnetic structure of an ordered material. Further, because of the very different neutron scattering lengths – see Fig. 5.1 – it is usually possible to both accurately locate light atoms, such as hydrogen, deuterium, or lithium, even in the presence of heavy atoms, and distinguish between atoms with similar atomic numbers, such as nitrogen and oxygen or cobalt and iron. In both cases, the analogous x-ray studies are either impossible or very difficult. Thanks to the sensitivity of neutrons to most of the nuclide, a wide range of materials can be investigated with the same efficiency from polymers to inorganic materials or even metals and alloys. Another advantage of neutrons is that because the neutron is uncharged it can easily approach the point-like atomic nuclei found in a material before that *nuclear* scattering occurs. The rather weak interaction of neutrons with materials enables them to penetrate much deeper into the material than either electrons or x-rays. This is particularly useful to know the bulk properties of a material and is more and more often used by materials science engineers [19, 20].

Fig. 5.1 Atomic coherent scattering length for thermal neutrons, a dash line shows the corresponding trend for x-ray scattering. A much smaller contrast is observed from one atom to the following atom in the periodic table using x-rays



5.3 Crystal Structure Investigation

Crystallographic studies by neutron diffraction can be performed by different techniques such as powder diffraction, single crystal diffraction using a poly, or monochromatic beam [21, 22].

5.3.1 Powder Diffraction

The applications of powder neutron diffraction have been greatly expanded by the use of the Rietveld line profile analysis technique [21], a technique which permits a detailed analysis of the intensity of the individual powder diffraction lines in terms of a refinement from a proposed structure. In many cases, this information is available and the Rietveld method will, for instance, permit the determination of the occupancy of a given metal crystallographic site by, say, manganese and/or iron. This can be useful to determine the preferential substitution scheme of magnetic phases and understand the composition dependence of the magnetic properties in a solid solution. Examples of such neutron diffraction type studies can be found in [23–25].

As mentioned above, one of the main advantages of neutrons versus x-rays for crystallography is the possibility to locate very accurately light elements in the vicinity of heavier ones. This has been particularly useful for the study of the influence of interstitial elements on the physical properties of magnetic materials containing rare-earth and transition metal elements. Indeed it has been found to be possible to insert interstitial elements like H, C, or N in the crystal lattice of the R_2Fe_{17} phases (R being a rare-earth element) [26–28]. Tremendous change of the magnetic properties have been observed after insertion of light elements such as H, C, or N in the crystal structure of binary or ternary intermetallic phases.

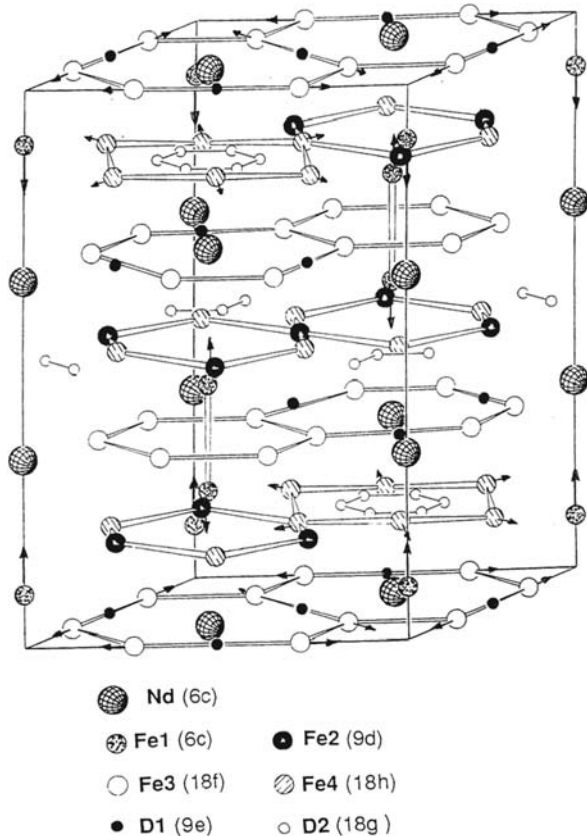
In the case of hydrogen in Nd_2Fe_{17} , two inequivalent interstitial sites have been found to accommodate H atoms in the crystal structure: an octahedral site and a tetrahedral site referred to as D_1 and D_2 , respectively [26, 29], see Fig. 5.2. Unlike hydrogen, larger atoms like N or C have been found to be exclusively located on the octahedral site [27, 30], thus clarifying that the upper carbon or nitrogen content that can be accommodated in the structure is 3 atoms/ f.u. compared to 5 atoms/f.u. for hydrogen.

In addition to the determination of the crystal structure and the study of its temperature dependence, neutron scattering can provide much more information in particular concerning the dynamics of the interstitial atoms. This has, for example, been performed using inelastic neutron scattering on the $Pr_2Fe_{17}H_x$ isotope compounds [31–33].

5.3.2 Single Crystal Diffraction

Four circle diffractometry is the most precise technique to determine the crystal structure by neutron diffraction and it requires a single crystal of typically 1 mm in diameter. Indeed, since the interaction of neutrons with matter is weak with

Fig. 5.2 Crystal structure of the $\text{Nd}_2\text{Fe}_{17}\text{H}_5$ compound showing the atomic position (D1 and D2) of the hydrogen atoms as revealed by powder neutron diffraction investigation [26, 31]. The arrows indicate the local atomic displacements induced by hydrogen insertion in the interstitial sites



respect to that of electron or x-rays, large quantities of material are usually needed to obtain good statistics in reasonable counting times and good signal/background ratio. The improvement of instruments and neutron flux these last years has permitted to decrease significantly the sample size. In some cases, set-ups are now available to use powder or single crystal with volumes as small as 0.001 mm^3 . Single crystal diffraction can be performed with an unpolarized neutron beam giving access to the crystal structure (atomic location and interatomic distances) as well as to the magnetic structure (size and orientation of the atomic magnetic moments in the ordered state). Four circle diffractometry is usually based on the use of constant wavelength and the sequential acquisition of the set of (hkl) Bragg reflection intensities. Precise crystallographic investigation can also be carried out by Laue diffractometry [34, 35], such a polychromatic technique is particularly useful to investigate phase transitions occurring in matter. Indeed the use of a polychromatic beam enables to perform diffraction by several (hkl) families of plane at the same time and the use of large-angle detectors permit to obtain fast acquisition. An example of such a polychromatic diffraction pattern is given in Fig. 5.3, in the case of FeTa_2O_6 [36].

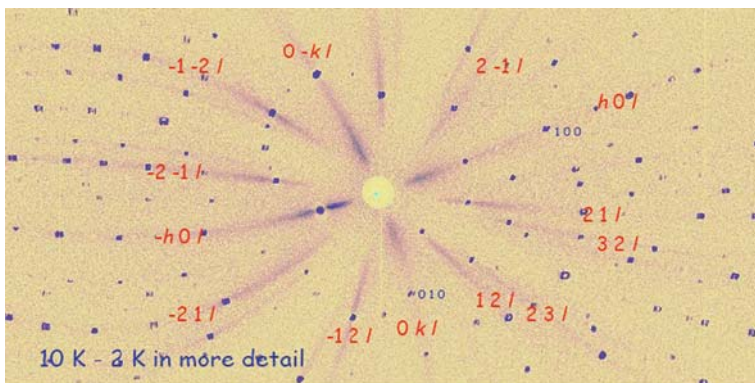


Fig. 5.3 Typical single crystal diffraction pattern recorded on the quasi Laue neutron diffractometer VIVALDI FeTa_2O_6 [36]. The figure presents the difference between the patterns recorded at 10 and 2 K in order to better observe the pure magnetic Bragg reflections

5.4 In Situ Neutron Diffraction

5.4.1 Thermodiffraction: Crystallization of Amorphous Materials

In situ neutron diffraction investigation is now widely used to investigate the crystallization steps of amorphous materials such as metallic glasses [37, 38]. This enables to determine the stability domain of metallic glasses, as well as to identify the phases produced by the transformation of the glass, including metastable or transitory phases. An example of such an application is given in Fig. 5.4, where the diffraction pattern has been recorded every 5 min during a temperature ramp performed at $2^\circ/\text{min}$, meaning that between two spectra the temperature has changed by 10°C . As can be seen from Fig. 5.4, the as synthesized sample is vitreous and the diffraction pattern only shows a broad bump characteristic of the amorphous state. This bump remains up to 520°C , due to the large penetration depths of the neutrons, this proves that the bulk metallic sample stays amorphous in the whole volume. On heating, the Fe–Ni–Co–Si–B alloy transforms irreversibly around 900 K to stable and metastable crystalline phases according to in situ neutron diffraction experiment. The main peaks appearing can be associated to a simple cubic phase with lattice parameter close to that of Fe. Several other crystallization processes occur such as the formation of Fe_2B , FeSi , and Co_3B_2 . At 656°C , the simple cubic Fe phase disappears and transforms into a cubic centered phase close to $\gamma(\text{Fe})$. More details of the present example can be found in reference [37, 38]. This type of information is very useful and can be combined with other techniques such as DSC measurements [39, 40] or magnetic measurements [37, 38], thus leading to a deeper understanding of the behavior of amorphous or glass materials. Neutron scattering is also a very useful technique for time-resolved reaction processes inside materials. In situ neutron diffraction has been widely developed at the high neutron flux sources. Many

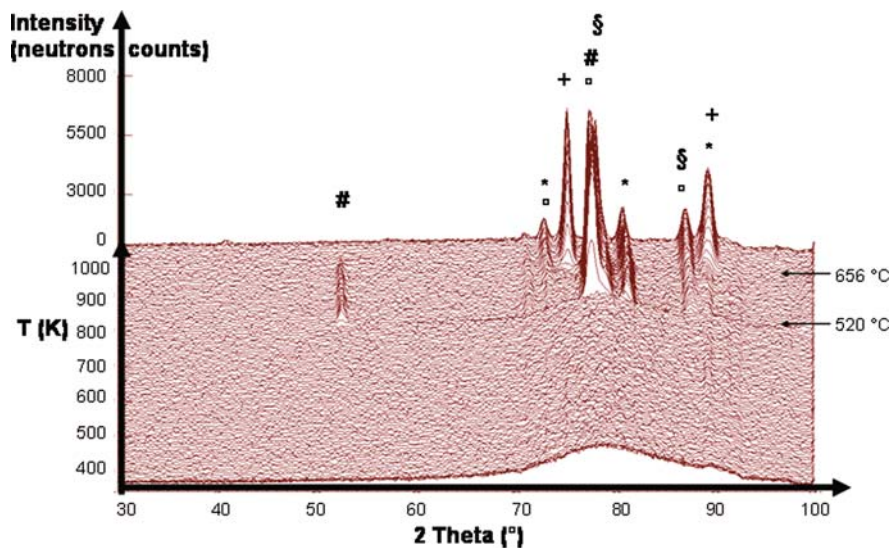


Fig. 5.4 Thermal evolution of the powder neutron diffraction pattern recorded upon heating an amorphous alloy of Fe–Ni–Co–Si–B type. The symbols +, #, °, *, and § indicate the Bragg peaks corresponding to the FCC (Fe,Ni,Co), simple cubic (Fe,Ni,Co), Fe_2B , Co_3B_2 FeSi phases, respectively [37, 38]

examples including time-resolved neutron diffraction investigations can be found in the following references [41, 42].

5.4.2 In Situ Investigation of the Synthesis and Ordering of nanocrystalline FePt Alloys

The excellent magnetic properties of the Fe–Pt alloys have been studied for decades. The FePt alloys have attracted considerable attention during the past few years since they are considered as candidates for ultrahigh-density magnetic storage media (as thin films or nanoparticles) and as materials for special permanent magnet applications such as magnetic micro-electromechanical systems. In this context, it is necessary to prepare both nanocrystalline and well-ordered Fe–Pt alloys in order to combine a high magnetocrystalline anisotropy and a small grain size required for example for high-density data storage. The excellent magnetic properties of these alloys are associated with the ordered $L1_0$ structure of the FePt phase see Fig. 5.5. Both experimental data and theoretical calculations have indicated a correlation between the degree of order within the $L1_0$ phase and the intrinsic properties, such as magnetocrystalline anisotropy and Curie temperature. The knowledge of the ordering process is thus of prime importance in order to optimize the magnetic properties of such compounds. A recent example of thermodiffraction is the ordering of nanocrystalline Fe–Pt alloys [43] obtained by mechanical alloying. Figure 5.5

presents the thermal evolution of the neutron diffraction pattern for Fe₅₀Pt₅₀ powders obtained by mechanical alloying after 4 h of milling. The typical acquisition time for such a diffraction pattern was about 3–5 min. The in situ investigation [43] has shown the coexistence of several phases during the thermal treatment. The formation of the tetragonal ordered L₁₀ phase results from the combination of the Fe and Pt elements into a disordered face centered cubic phase labeled A1 in Fig. 5.5. But other off stoichiometric phases such as Fe₃Pt and FePt₃ have been found to be formed as well depending on the operating conditions. The Rietveld analysis of all the diffraction patterns recorded allows us to determine quantitatively the volume fraction of each phase as well as its temperature dependence [43]. The comparison of the diffraction patterns recorded for different milling conditions [43, 44] is thus very useful to both better understand and optimize the ordering process and the magnetic properties. The reader is referred to Figs. 3–7 of reference [43] for more details. Depending upon the starting composition, it is also possible to characterize the synthesis experimental condition of nanocomposite systems consisting of a mixture of hard and soft phases for exchange coupled nanocomposite bulk magnets. Furthermore, while cooling down an ordered L₁₀ phase and recording the thermal evolution of the neutron diffraction pattern, one can follow the progressive magnetic ordering and quantify the magnetic moments by recording the thermal evolution of the neutron diffraction pattern. This has been undertaken successfully and was recently published in [44]. Further examples of magnetic studies can be found elsewhere [45–48].

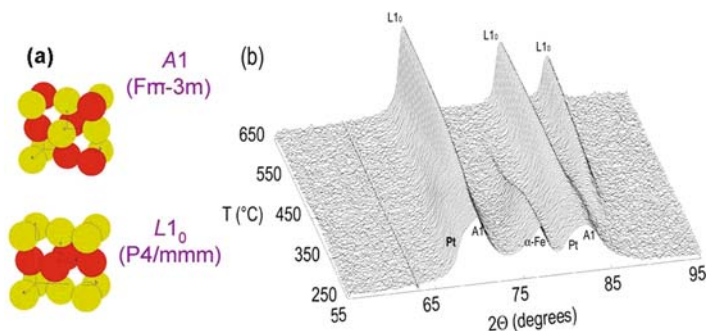


Fig. 5.5 (a) The atomic arrangement of the Fe₅₀Pt₅₀ alloys are schematically presented for the disordered A₁ (left) and ordered L₁₀ phase. The colors present the different nature of Fe or Pt atoms. (b) Thermal evolution of the neutron powder diffraction patterns recorded at a heating rate of 0.8 K/min during the formation of the ordered L₁₀ phase from a Fe₅₀Pt₅₀ powder milled for 4 h at liquid nitrogen temperature [43]. The diffraction peaks corresponding to the phases observed are indicated

5.4.3 Time-Resolved Neutron Diffraction Studies

Thanks to the increasing neutron flux available and the use of large angular detectors, it is now possible to investigate not only in situ but also time-resolved physical

or chemical processes over several time scales ranging from hours to a few milliseconds. Several recent examples have been reported in different fields of research: physics, magnetism, chemistry, and metallurgy. In addition to powder neutron diffraction, among the scattering techniques that can be used to perform in situ or time-resolved experiments one can cite small-angle neutron scattering and neutron radiography. A review of in situ and/or time resolved neutron scattering can be found elsewhere [41] as well as in references [42, 49]. In order to illustrate the investigation of irreversible processes, we will describe two examples.

5.4.3.1 Decomposition of $\text{Nd}_2\text{Fe}_{14}\text{B}$ Under Hydrogen Atmosphere

Materials design on the nanoscale can be used to improve a magnet's performance. The high-performance Nd–Fe–B permanent magnets are made of microstructures controlled at the nanoscale. One of the more efficient routes to make coercive powder for magnets is the so called hydrogen-disproportionation–desorption–recombination (HDDR) process [50–54]. Among other techniques neutron diffraction has been carried out in situ to investigate the mechanisms involved in this process [55, 56]. The use of neutron has proved to be very useful from both the fundamental and the applications point of view.

This process first requires the disproportionation of the $\text{Nd}_2\text{Fe}_{14}\text{B}$ phase under hydrogen atmosphere to better control the recombination reaction under vacuum to form $\text{Nd}_2\text{Fe}_{14}\text{B}$. The key point is to control the recombination process in order to form very fine grains of $\text{Nd}_2\text{Fe}_{14}\text{B}$ required for high coercivity of the powder. The two first steps of the process: HD are presented in Fig. 5.6. The powder has been decomposed in situ under 0.8 bar of deuterium gas (this isotope has been preferred to hydrogen in order to reduce the neutron diffraction background). The temperature profile used is plotted in Fig. 5.6. It consists of a heating rate of $400^\circ/\text{h}$ up to 720°C , followed by a plateau for 1 h at 720°C . The starting neutron diffraction pattern is characteristic of the presence of the tetragonal $\text{Nd}_2\text{Fe}_{14}\text{B}$ majority phase together with an additional phase of the $\text{Nd}_{1+x}\text{Fe}_4\text{B}_4$ ($x = 0, 0.1$) type. Starting at 600°C , the $\text{Nd}_2\text{Fe}_{14}\text{B}$ begins to disappear. Simultaneously one can observe the appearance of iron and of a neodymium hydride NdD_x . After 1 hour at 720°C , the $\text{Nd}_2\text{Fe}_{14}\text{B}$ has completely disappeared. The refinement of each of the recorded diffraction patterns permits to determine the relative quantity of the different phases present at each step of the process. A comparison of the reaction of $\text{Nd}_2\text{Fe}_{14}\text{B}$ and D_2 gas at different experimental conditions has thus been derived in Fig. 5.6. It is clearly shown that the decomposition is soon accomplished after the start of the plateau at 720°C , on the contrary, the HD process is not complete after 1 h at 680°C and a temperature of 600°C is too low to initiate the decomposition of the $\text{Nd}_2\text{Fe}_{14}\text{B}$ phase under hydrogen atmosphere. Since the acquisition of the diffraction pattern is time resolved, it is also possible to access the kinetics of the decomposition process. A comparison of the different decomposition kinetics is given in Fig. 5.6 for different operating conditions. It has thus been shown that the kinetics of iron formation in the HD process can be slowed down by adjusting the temperature of the plateau [55–56]. This is very useful in terms of permanent magnetic properties since soft particles like

Fe have to be avoided to optimize the performance of the hard magnetic material. Since a small fraction of the hard $\text{Nd}_2\text{Fe}_{14}\text{B}$ phase is not decomposed after the heat treatment at 680°C , adjusting the reaction temperature can be used to keep some $\text{Nd}_2\text{Fe}_{14}\text{B}$ germs which will favor the next step of the process: recrystallization. Following the evolution of the lattice parameters during the reaction process can give further structural information such as the quantity of hydrogen atoms inserted in the $\text{Nd}_2\text{Fe}_{14}\text{B}$ structure before decomposition, provided that the determination of the hydrogen atom localization has been performed previously by high-resolution neutron diffraction [57].

This example shows that high neutron flux instruments available nowadays enable to investigate complex physical and chemical processes such as the HDDR used industrially to produce coercive magnetic powders.

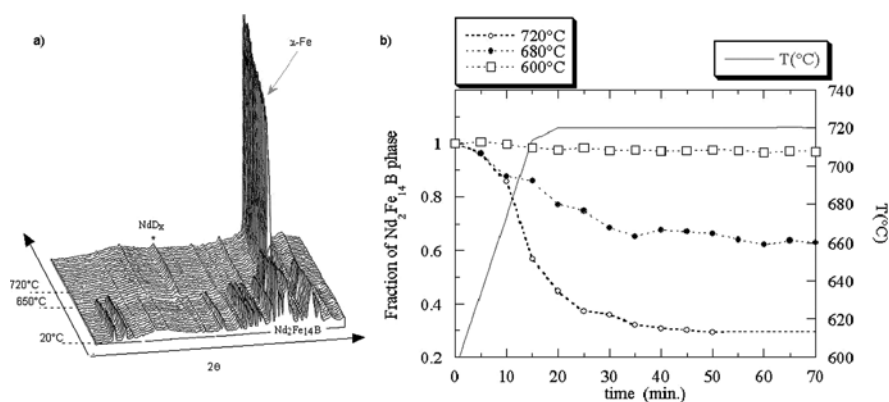


Fig. 5.6 (a) Thermodiffraction pattern recorded during the decomposition of the $\text{Nd}_2\text{Fe}_{14}\text{B}(\text{D})_x$ (plateau at 720°C for 1 h). (b) Time evolution of the quantity of $\text{Nd}_2\text{Fe}_{14}\text{B}$ phase during the decomposition step of an HDDR process performed at the indicated temperature 720, 680, and 600°C . The temperature profile used is indicated for the plateau at 720°C [55]

5.4.3.2 Kinetics of Photoinduced Transformation

The field of molecular magnetism can also be probed by neutron scattering and even in situ. Some compounds offer the possibility to externally control their magnetic, optical, or electronic properties and are potential candidates as switchable materials for information storage or optical switching. Recently, Goujon et al. have reported a structural study during the photoinduced transformation of the $[\text{Fe}(1-n\text{-propyltetrazole})_6](\text{BF}_4)_2$ switchable compound from low-spin to high-spin state [58, 59]. Two neutron diffraction studies have been carried out on single crystals one by polarized neutron diffraction and more recently by time-resolved Laue diffraction techniques using an unpolarized beam. For these experiments, a dedicated set-up has been developed in order to perform the photoexcitation of the single crystal in situ in the cryostat and to study the crystal structure in situ by neutron diffraction in the low-spin state, the high-spin state or to investigate the kinetics of the photoinduced

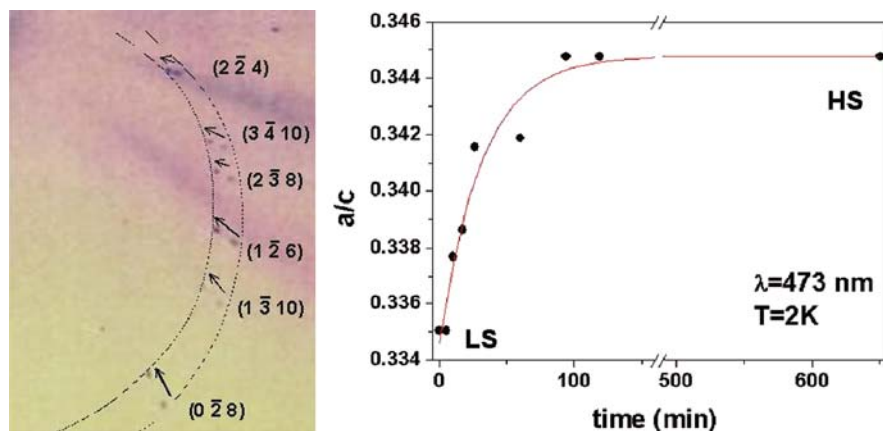


Fig. 5.7 The *arrows* on the *left* part of the figure indicate the change of position of the Bragg peak when going from the low-spin state to the high-spin state of the $\text{Fe}(1-n\text{-propyltetrazole})_6(\text{BF}_4)_2$ compound [59]. The part on the *right* shows the relative evolution of the lattice parameters as a fingerprint of the photo-conversion. At 2 K the conversion of the single crystal can be performed in about an hour. The photon wavelength used was $\lambda = 473\text{ nm}$ [58]

transition to the metastable high-spin state. Figure 5.7 indicates the evolution of the Bragg peak positions between the two spin states as recorded on the Laue VIVALDI spectrometer [34]. Such investigations have clearly demonstrated the continuous character of the photoinduced transition [58, 59]. The right part of Fig. 5.7 illustrates the lattice parameter change during the structural transition. The kinetics of the photoexcitation can easily be studied and the irradiation time required for a complete conversion determined. A precise structural study has been undertaken evidencing the main structural changes occurring during the transition from the low-spin Fe^{II} state to the high spin one, in particular the increase of Fe–N distances from 1.97 to 2.18 Å [58].

5.5 Magnetic Structure Determination

Neutron-diffraction is a unique method for the determination of magnetic structures. It has first revealed the existence of antiferromagnetic order in MnO [12]. When Shull and Smart saw for the first time, the magnetic order in a MnO powder neutron diagram, there was no ambiguity: new diffraction peaks had grown indicating the doubling of the magnetic unit cell. Magnetic neutron scattering was born with a large impact on magnetism.

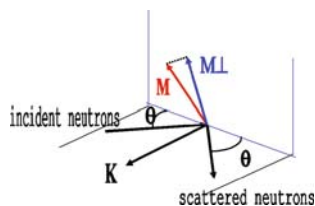
The magnetic interaction of neutrons is due to the coupling of the neutron spin with the magnetic field, arising from unpaired electrons. There are two origins one coming from the classical dipolar interaction due to the spin of electrons, whereas the other arises from the orbital motion. The full theory of neutron scattering by magnetic materials can be found elsewhere [3, 4, 7, 9, 10, 60].

The magnetic scattering amplitude a_m can be written as:

$$a_m(\mathbf{K}) = b\mu_n f(\mathbf{K})\mathbf{M} \quad (5.1)$$

where the product $b\mu_n$ is a constant equal to $0.2696 \cdot 10^{-12}$ cm. μ_n and σ being the magnetic moment of the neutron and a unit vector along the neutron magnetic moment, respectively, $f(\mathbf{K})$ being the form factor of the magnetic ion and \mathbf{M} being the projection of the magnetization onto the plane perpendicular to the scattering vector \mathbf{K} . See Fig. 5.8. This angular dependence of the scattering amplitude allows to determine both the amplitude and the direction of the magnetic moment. So in the general case the magnetic amplitude depends upon the relative direction of the magnetic moment \mathbf{M} and the scattering vector. This amplitude is maximum when the magnetic moment \mathbf{M} is perpendicular to the diffusion vector \mathbf{K} and null when both are collinear. It is worth to note that the magnetic scattered intensity can be of the same magnetic order or even larger than the intensity of scattering nuclear origin.

Fig. 5.8 Geometry of neutron scattering by magnetic materials



Since the birth of magnetic neutron diffraction techniques, many different kinds of complex magnetic orders including conical, spiral, and sinusoidal structure have been observed. A more general background on this subject can be found in a number of previous reviews and books [3, 4, 9, 10, 61, 62]. The systematic use of symmetry and group theory arguments has led to a good deal of progress in the interpretation of neutron diffraction patterns. The majority of neutron diffraction investigations have been made on polycrystalline samples first because of the simplicity of the method and second because single crystal neutron diffraction requires the use typically millimeter-sized sample. The improvement of neutron diffraction techniques together with the gain of flux obtained at both spallation and reactor sources now enables experiments on single crystals of much smaller size.

In cases of high symmetry structures, it is frequently impossible to get unambiguous results from powder diffraction alone. Then the use of single crystal diffraction is necessary. Single crystal neutron diffraction techniques is a wide field of research and depending on the complexity of the problem to be solved the user can use either an unpolarized neutron beam [9] or polarized neutron techniques [7, 9, 63] or even of so called polarimetry technique [9, 64, 65]. The specificity of the different techniques will be addressed below.

Geometrically frustrated magnets are a class of systems where the lattice geometry prevents all magnetic interactions to be satisfied simultaneously. A famous example is that of antiferromagnetic moments on a triangle, where all moments want to

be antiparallel to each other. In three dimensions, the pyrochlore lattice with corner-linked tetrahedra is frustrated. $\text{Tb}_2\text{Sn}_2\text{O}_7$ is such a geometrically frustrated magnet, where magnetic interactions cannot be satisfied because of the lattice symmetry [66]. Magnetic order settles in two steps, with a smeared transition at 1.3(1) K, then an abrupt transition at 0.87(2) K. A new magnetic structure is observed, akin to an ordered spin ice, with both ferromagnetic and antiferromagnetic characters.

By neutron diffraction, the onset of a new magnetic structure has been observed below 1.3 K. With decreasing temperature, a spin liquid phase is shown to transform into a new type of ordered phase, not predicted by theory, which could be called an “ordered spin ice.” When temperature decreases the broad liquid peak narrows and slightly shifts from its theoretical value, as an intense signal grows at low angles, showing the onset of ferromagnetic correlations (Fig. 5.9). Just above the transition, an abnormal change in the spin correlations shows the influence of dipolar interactions. At still lower temperatures, magnetic Bragg peaks appear showing that the spin liquid transforms into an ordered phase. Refinement of the magnetic structure shows that the local spin structure is very close to that of a spin ice. But in contrast with the true spin ices, all individual tetrahedra are identical, yielding the magnetic Bragg peaks. This new magnetic phase has been called an “ordered spin ice”. Actually, the magnetic moments remain correlated at the scale of about 20 nm only, even at 0.10 K.

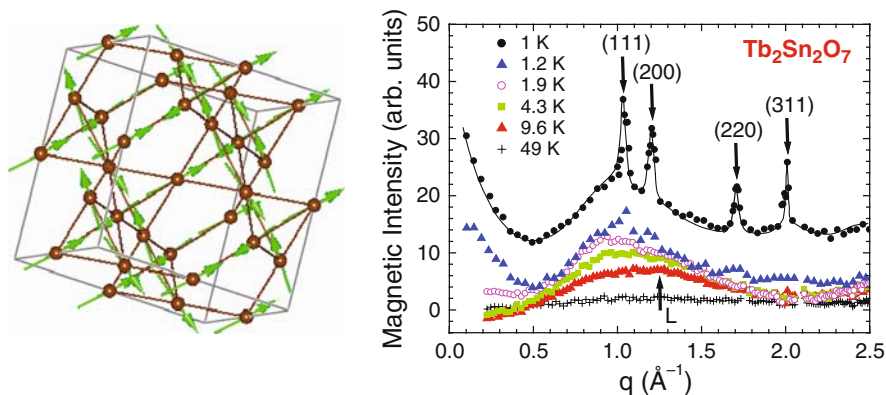


Fig. 5.9 (left) Ordered spin ice magnetic structure, (right) magnetic intensity of $\text{Tb}_2\text{Sn}_2\text{O}_7$ versus the scattering vector $q = 4\pi \sin\theta/\lambda$. A spectrum at 100 K was subtracted. Arrows show the position of the Bragg peaks and liquid peak (L) [66]

5.6 Magnetic Phase Transition

5.6.1 Magnetic Phase Transitions Studied by Powder Diffraction

Thanks to its spin, the neutron is very sensitive to the presence of magnetic fields in matter, and thus magnetic phase transitions can be studied by neutron diffraction

[9, 45, 46, 23, 24]. Any magnetic order (ferromagnetic, antiferromagnetic, helimagnetic, etc.) occurring in the matter leads to a characteristic diffraction pattern. The use of neutron powder diffraction is thus a direct way to measure the temperature at which the magnetic orders occur and to determine the corresponding arrangement of the magnetic moments. Consequently neutron thermodiffraction has become the most used technique to follow the change of magnetic structures.

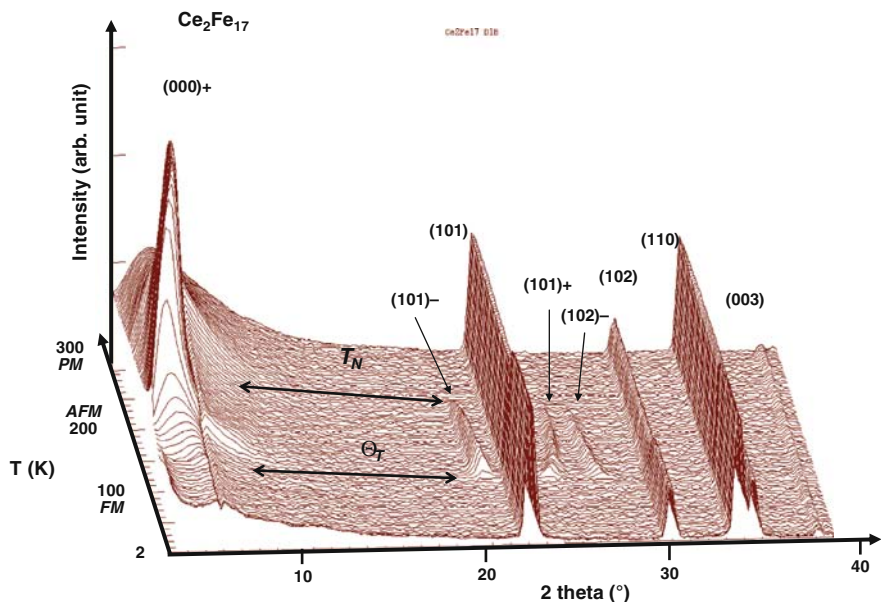


Fig. 5.10 Thermal dependence of the low-angle part of the diffraction pattern of $\text{Ce}_2\text{Fe}_{17}$ showing the three different magnetic phases, ferromagnetic *FM* up to Θ_T , antiferromagnetic *AFM*, and finally paramagnetic *PM* above T_N

An example is given for the case of $\text{Ce}_2\text{Fe}_{17}$ compounds which have been studied for decades [45–46, 67–71] before solving the complexity of the magnetic structures involved in the magnetic phase diagram. Figure 5.10 shows the thermal evolution of the neutron diffraction pattern of $\text{Ce}_2\text{Fe}_{17}$ at ambient pressure in the form of a three-dimensional plot. Above 210 K, a high-temperature paramagnetic state noted *PM* in Figs. 5.10–5.11 is observed since only the diffraction peaks corresponding to rhombohedral $\text{Ce}_2\text{Fe}_{17}$ are found. The presence of a very broad peak at low angles ($2\theta \approx 5^\circ$) indicates, however, that some short-range magnetic order exists even at high temperatures. Below 210 K the peak at $2\theta \approx 5^\circ$ increases abruptly and additional superlattice reflections appear. These peaks correspond to the antiferromagnetic structure which exists down to about 90 K where the increase of intensities of the (101) and (102) nuclear peaks reflects the onset of ferromagnetism. These results are in excellent agreement with the macroscopic magnetic measurements presented as an inset in Fig. 5.10. The antiferromagnetic phase is characterized by the observation of purely magnetic satellites peaks around the nuclear peaks referred

to as $(hkl)_{+/-}$ in Fig. 5.10. These satellites can be indexed using an incommensurate wave vector [45]. Since only first-order satellite reflections were detected, the presence of a simple helimagnetic spiral structure was assumed [45]. It is worth to mention that such type of thermodiffractionometry can be also undertaken in situ under special environment, such as in a pressure cell thus enabling to determine complete magnetic phase diagrams as a function of temperature and pressure see Fig. 5.11 [45]. In the case of Ce_2Fe_{17} , the application of high pressures leads to significant changes of the magnetic structure. The ferromagnetic phase is suppressed down to 2 K by pressures higher than 3 kbar and gets substituted by a new and more complex incommensurate antiferromagnetic phase. More details on the incommensurate helical magnetic structure, its thermal evolution or pressure dependence can be found in the following references [45, 46]. When substituting Mn for Fe in the $Ce_2Fe_{17-x}Mn_x$ compounds, the magnetic interactions are changed thus leading to modification of the magnetic order. The evolution of the corresponding magnetic phase diagram (T , P , x) has been studied as a function of temperature at different pressure [45, 70] thus leading to the results presented in Fig. 5.11.

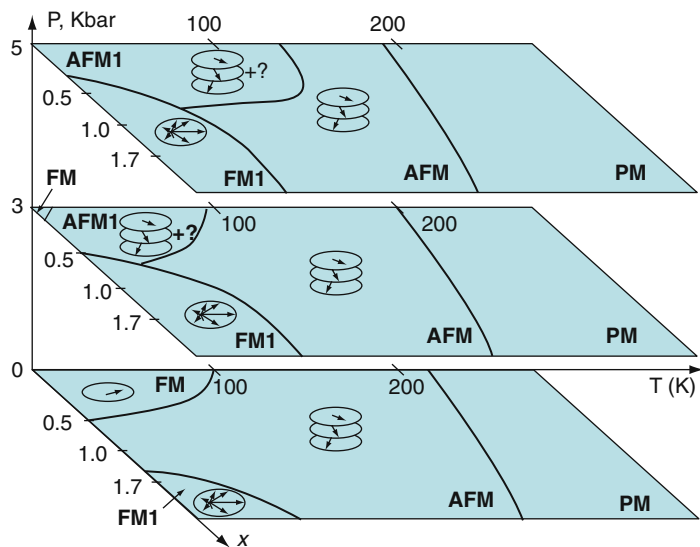


Fig. 5.11 Magnetic phase diagram (T , P , x) of the $Ce_2Fe_{17-x}Mn_x$ compounds as obtained from thermodiffraction studies at different pressures [45, 46, 70]. Three different types of magnetic phases are referred to ferromagnetic FM , antiferromagnetic AFM , and PM state above T_N

5.6.2 Magnetic Phase Transitions Studied by Single Crystal Diffraction

The thermodiffractionometry studies devoted to investigate magnetic phase transitions have for a long time been rather limited to powder neutron diffraction, but

the development of two-dimensional detectors has extended this to single crystal diffractometry. Indeed instrument such as the quasi Laue diffractometer recently developed at the ILL (instrument VIVALDI or LADI) enables a wide part of the reciprocal lattice to be recorded in a short time of about one to a few minutes. Thanks to the image plate detectors, it is thus possible to investigate the evolution of the magnetic diffraction pattern by recording a set of diagrams at different temperature on a single crystal [36]. For example, a typical diffraction pattern of a FeTa_2O_6 single crystal has been presented in Fig. 5.3. This compound has been found to order antiferromagnetically at 8 K and to exhibit a quasi two-dimensional antiferromagnetic behavior above T_N . More generally the $(\text{Fe}_{1-x}\text{Co}_x)\text{Ta}_2\text{O}_6$ series of compounds have been found to exhibit peculiar magnetic behavior as reported elsewhere [47].

5.7 Polarized Neutron Techniques

5.7.1 Uniaxial Polarization Analysis

Because the neutron has a magnetic moment of spin $1/2$ which can be in one of two states, $+1/2$ or $-1/2$, this leads to the possibility of generating polarized beams with all neutrons in one spin state can be generated. Polarization analysis was first introduced by Moon, Riste and Khoeler [72] and consists in analyzing the initial and final polarization component parallel to the applied magnetic field. By measuring spin-flip and spin-non-flip scattering cross sections in more than one direction, it can separate the various spin-dependent interactions. It can be implemented on different neutron spectrometers, thus enabling the performance of a wide range of investigations among which one can cite polarized neutron diffraction on single crystals to study magnetic structure [62], it has also been proved to be useful to study paramagnetic scattering [9, 73–75], it can easily show non-collinear components in ferromagnetic arrangements [76], contribute to separating the magnon and phonon peaks in case of ambiguity, or is also very useful to investigate the magnetism of thin films and layers.

The field of polarized beam techniques has significantly expanded these last years and powerful tools are now available to study the microscopic magnetic properties of condensed matter and especially of spin densities in crystals. By using polarized neutrons, one has a much more sensitive tool for magnetic studies. Keeping in mind that there is coherence between nuclear and magnetic Bragg scattering: instead of having the total intensity as follows (case of unpolarized neutrons):

$$I = I_N + I_M \quad (5.2)$$

with $I_N \sim |F_N|^2$ and $I_M \sim |F_M|^2$, one has in the simple case where neutron polarization is unity:

$$I^\pm = |F_N \pm F_M|^2 \quad (5.3)$$

The + and – sign corresponding to the parallel or antiparallel orientation of the neutron spins relative to the magnetization direction of the crystal. Lets take the following example: if F_M is 10% of F_N The sensitivity gain is obvious, in an unpolarized neutron study, the magnetic intensity I_M is only 1% of the nuclear one. Using a polarized neutron beam, the ratio of intensities measured with the two neutron spin states (+ or –) is

$$\frac{I^+}{I^-} = \left(\frac{F_N + F_M}{F_N - F_M} \right)^2 \approx 1 + 4 \frac{F_M}{F_N} \text{ for small } \frac{F_M}{F_N} \quad (5.4)$$

for the chosen case the ratio amounts to 40%.

Without going further in the description of the features of the polarized neutron techniques, we will describe a few examples of applications of such techniques. For more details on the neutron techniques using polarization, we refer to references [7, 77, 78] and [9, 62] for the theoretical and experimental aspect, respectively.

One of the key roles of polarized neutrons in studying magnetism is that it permits to determine the magnetization density distributions. This has been extensively used to investigate single crystalline magnetically ordered materials such as soft or hard magnetic materials, but has also been shown to be very useful for the study of molecular magnetism since the emergence of this research field [79]. This technique applies to single crystals which are magnetized by an applied field and scatter a beam of polarized neutrons. The polarization of the beam is either parallel to the magnetic field or reversed.

To illustrate the potential of polarized neutron diffraction, Fig. 5.12 presents the example of the magnetization density in the YCo_5 unit cell as revealed by polarized neutron diffraction on a single crystal [80]. The regions in red show the region carrying negative polarization due to the polarization of the conduction electrons by the magnetic Co atoms. In particular, one can note a negative magnetic moment on the edges of the hexagonal cell corresponding to the location of Y atoms. Such negative polarization first evidenced experimentally by neutron diffraction has been confirmed since then by band structure calculations [81]. The analysis of the two inequivalent Co sites in YCo_5 has shown that they exhibit large localized magnetic moment of $1.77(2)\mu_B$ and $1.72(2)\mu_B$, a result that bears witness to the accuracy of this neutron polarimetry technique. In addition it is possible to quantify the orbital and spin contribution to the magnetic moment on each Co site and determine the wave function occupations on the different orbitals [80]. This has been successfully done on YCo_5 and other isotype compounds [82–84]. For YCo_5 , the spin contribution to the magnetic form factor has been determined to be 74 and 84% for the two inequivalent sites, respectively, thus demonstrating the large contribution of the orbital magnetic moment. The discovery of this large unquenched orbital moment on the Co site has been very useful to explain the huge magnetocrystalline anisotropy of YCo_5 . This particularly high orbital moment on one Co site has been attributed to its peculiar and asymmetric local environment.

Such polarized neutron techniques are very sensitive, and low magnitude magnetic moments can be determined accurately, this is particularly useful in the case of

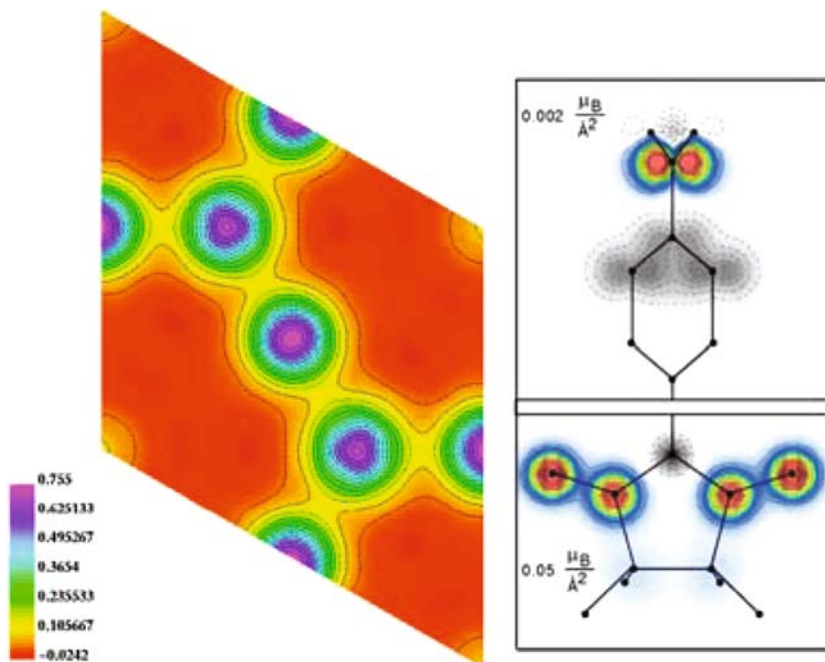


Fig. 5.12 *Left:* The unit cell and the magnetization density projected along the c -axis of YCo_5 as obtained by maximum entropy from the magnetic contribution to the diffracted neutron polarized intensity, the scale is given in $\mu_B/\text{\AA}^2$ [80]. *Right:* Projection onto the nitroxide mean plane of the spin density of the free radical paratitrophenyl nitronyl nitroxide [85]. High level contour step $0.002 \mu_B/\text{\AA}^2$ top and $0.05 \mu_B/\text{\AA}^2$ bottom

molecular magnetism. An illustration is given in Fig. 5.12 which presents the projection onto the nitroxide mean plane of the spin density of the free radical paratitrophenyl nitronyl nitroxide. Note that the level contour is given in steps of $0.002 \mu_B/\text{\AA}^2$ in the upper part showing the extreme sensitivity of this technique. This compound was the first purely organic molecular magnet reported in the literature. The density map shows that the spin is mostly localized on the two NO group of the radical. A negative contribution (dashed part) is observed on the central carbon, a result which has been attributed to a spin polarized effect. The polarized neutron study was also very efficient in revealing the important role played by the N atom. This atom is located between the two neighboring molecules and carries a significant spin contribution, thus demonstrating the importance of this atom in the transmission of the super-exchange like interaction between the molecules.

Other examples of the application of polarized neutron diffraction can be found in the following references for ferromagnetic materials $Y_2Fe_{14}B$, $Nd_2Fe_{14}B$ [86], $ThCo_5$ [83, 84], or molecular magnetism [87].

At this point, it is worth to underline that polarized neutron techniques are no longer restricted to the investigation of single crystals but have been extended to the field of thin films and multilayers [88, 89] as well as recently to powder diffraction

[90]. This emerging technique benefits from the combination of wide angle neutron polarizers and large position sensitive detectors which enable a reduction in the data acquisition time while maintaining the accuracy of neutron polarization methods.

5.7.2 Spherical Neutron Polarimetry

Without going into the details of the technique, it is worth to mention the recent development of spherical neutron polarimetry. This is a very precise technique which requires the independent measurement of the three components in both the incident and the scattered neutron polarization. Consequently, the method exploits the maximum information one can get from magnetic neutron scattering. It has been shown that spherical neutron polarimetry can be very useful in the case of antiferromagnetic structures and their domain population, for example [91]. For more details on this technique, the reader is referred to [9, 64, 76].

To conclude, polarized neutron diffraction has proved to be a very sensitive tool to experimentally probe magnetization distributions at the sub-atomic scale in condensed matter.

5.8 Small-Angle Neutron Scattering

Small-Angle Neutron Scattering (SANS) is an ideal tool for studying the structure of materials in the mesoscopic size range between 1 and about 100 nm. One of the main advantages of SANS is that this is a non-destructive method and that it provides information with high statistical accuracy due to the averaging over a macroscopic sample volume. This is consequently a complementary technique to other investigation techniques at the mesoscopic scale. Among these one can cite atomic force microscopy which is mostly surface sensitive or transmission electron microscopy which provides a direct image of the specimen.

The basics of small-angle scattering can be found in classical text books [92, 93, 94], whereas examples of this techniques in materials science can be found in the following articles [95, 96]. It is worth to remember that in many cases, neutron and x-ray small-angle scattering are complementary techniques both having their merits. SANS also offers the particular interest of being sensitive to the magnetic spin. A full description of the different scattering amplitudes for the different polarizations can be found in the article of Moon, Riste and Koehler [72]. Even if the incident beam is unpolarized, the magnetic neutron–target interaction may be useful in identifying and separating structural and magnetic inhomogeneities. A simple case to consider is the magnetic saturation with M parallel to the applied field H , it can be shown [95] that in this case, the scattered intensity is

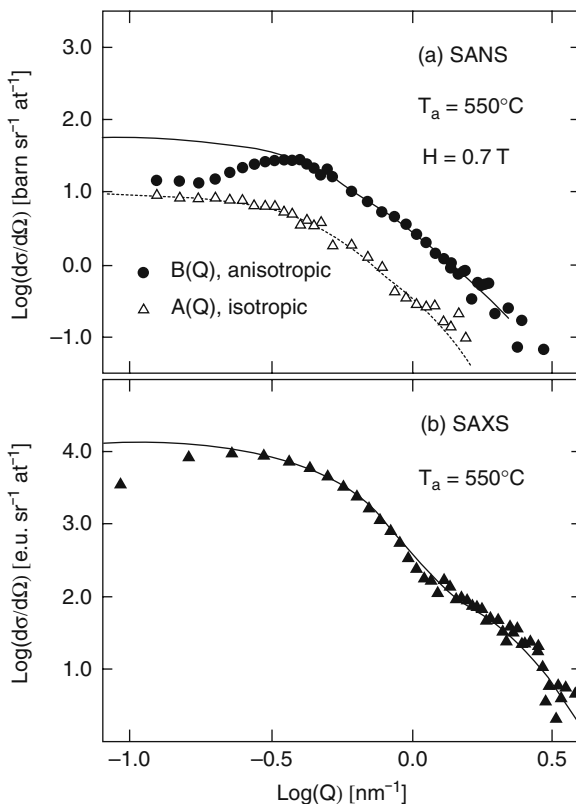
$$I^{\perp//} = |F_{(Q)} \pm M_{(Q)}|^2 \quad (5.5)$$

If the scattering vector Q is perpendicular to H . Where $F_{(Q)}$ and $M_{(Q)}$ refer to the scattering amplitude of the system and the magnetic scattering amplitude, respectively. But no magnetic scattered intensity occurs for Q parallel to H . Consequently, for an unpolarized neutron beam, one can rewrite the previous equation as $I^\perp = |F_{(Q)}|^2 + |M_{(Q)}|^2$ or $I^\parallel = |F_{(Q)}|^2$ depending upon the field direction respect to the scattering vector. \perp and \parallel stands for the perpendicular and parallel geometry, respectively. Because the scattering intensity measured along the direction parallel to the magnetic field includes only the nuclear component, the magnetic component can be extracted by subtracting this nuclear component from the scattering intensity measured along the direction perpendicular to the magnetic field.

Making use of the magnetic scattering cross section for neutrons, it is possible to study magnetic clusters or precipitates by SANS, some applications are discussed in [94–96]. On the basis of a few examples, we will illustrate some use of SANS in the field of magnetic materials. Many useful applications are possible, a simple case is that of a magnetic phase embedded in a non-magnetic matrix or vice versa which will result in a contrast of neutron scattering. This has been done to demonstrate the presence of non-magnetic Ni_3Al particles of about 5 nm diameter in an homogeneous matrix of $Ni-Al$ alloys, by measuring at the temperature where the matrix is completely ferromagnetic. In general, measurements of SANS in zero field on bulk ferromagnetic materials are not often performed if domain walls are present, as they introduce multiple refraction. Nevertheless domain walls and grain boundaries in $Nd-Fe-B$ hard magnets have been examined by SANS experiments for different heat treatments of the sintered permanent magnets [97]. This study has used both magnetized and demagnetized sintered samples and also different orientation of the magnetization versus the scattering vectors. This enabled the domain walls thickness to be evaluated to be 70 Å. The domain walls appearing as magnetic contrast precipitates. In addition, thin layer-like precipitates along the grains boundaries with thickness varying from 60 to 40 Å depending on the heat treatment have been evidenced due to nuclear scattering contrast of these precipitates, a contrast resulting from the difference in composition with respect to the $Nd_2Fe_{14}B$ matrix. This last result has been correlated to the coercive field increase occurring versus the heat treatment.

SANS can also give valuable information on nanocomposite soft magnets. SANS can also be performed under an applied magnetic field, this has been undertaken to investigate the spin disorder in nanoperm-type nanocomposite ferromagnets [98]. Such investigations can also be performed in situ to study the effect of magnetic field annealing on the soft magnetic properties of nanocrystalline materials [99]. Using unpolarized and polarized neutrons in a saturating field of 0.7 T, the nuclear and magnetic contribution to SANS from a magnetically soft amorphous alloy (FINEMET) have been compared by Kohlbrecher et al. [100]. The corresponding results are presented in Fig. 5.13 [100]. The difference between the two contributions permits to investigate the features of the nanocrystalline inclusions that have been formed by the heat treatment at 550°C. In addition to the determination of the volume fraction and size of the two different phases involved in the soft composites, SANS can provide unique information on the characteristic magnetic

Fig. 5.13 Small-angle neutron scattering (SANS) on Fe_{73.5}Si_{15.5}B₇Cu₁Nb₃ annealed for 1 h at 550°C at saturation under 0.7T. The isotropic A(Q) signal is assigned to nuclear scattering only of the Fe₃Si crystallites whereas B(Q) represents the magnetic scattering contribution. The corresponding small-angle x-ray scattering (SAXS) is given below for comparison [100]



length scales and local anisotropies at the nanoscale in nanocomposite ferromagnets. The current trend is to reduce the grain size of ferromagnets below the ferromagnetic exchange correlation length (about 30 nm for Fe) in order to dramatically diminish the magnetocrystalline anisotropy of the soft nanocomposite. Such composites are usually made of two-phase ferromagnets consisting of crystalline magnetic particles that are exchange coupled to an amorphous magnetic matrix. SANS is now routinely used to probe the nanocrystalline particles in a matrix to determine their shape size and difference in compositions. This has been, for example, performed to study Fe₃Si or Fe particles in amorphous FeSiBCuNb or nanocrystalline alloy matrix [101, 102]. A comprehensive presentation of the analysis of SANS from nanocrystalline ferromagnets can be found in [103]. Using both magnetic and nuclear scattering contributions, this investigation has shown that in these rapidly quenched samples, the Fe₃Si particles are surrounded by a diffusion zone of about 3–4 nm thickness. SANS is the only known method which can unambiguously resolve spin disorder at the nanoscale inside the bulk of a nanocomposite ferromagnet, since static variations of the magnetization on the scale of a few nanometers to a hundred of nanometers give rise to intense elastic magnetic scattering [103].

Ferrofluids are a special category of smart nanomaterials, in particular magnetically controllable nanofluids [104]. They consist of suspensions of monodomain ferromagnetic particles in non-magnetic and insulating fluids. The size, shape, distribution, composition, structure, and magnetic correlations can be studied by SANS [105, 106, 94]. Unpolarized as well as polarized neutron diffraction are now commonly used to probe the properties of ferrofluids leading to a better understanding of the influences of the different characteristics of the magnetic particles (density, composition, shape, etc.), the surfactant, or the fluids. Recent reviews on these applications of SANS can be found in [94, 104].

More generally the SANS technique can nowadays be applied to investigate a wide range of systems among which one can cite: study of the assemblies of disordered crystalline iron nanoparticles [107], measurement of magnetic flux line lattices in superconductors [108]. Finally it is worth mentioning that the SANS technique can now also be applied using grazing incident angle in order to investigate magnetic nanostructures on surfaces [109].

5.9 Neutron Scattering on Magnetic Surfaces

The magnetic interaction of neutrons with ordered spins in a superlattice provides the opportunity to study magnetic spin configurations and the range of coherence of the involved magnetism [110–112]. This has been used to probe the propagation of magnetic coupling and phase information from a magnetically ordered layer (e.g., Er or Dy) across an intervening non-magnetic layer (e.g., Y or Lu) to additional ordered layers. In addition to the structural information that can be obtained from the wide-angle diffraction from the superlattice, extra peaks of solely magnetic origin can be observed below the ordering temperature. In case of incommensurate magnetic order such as found in Dy or Er, this leads to peaks whose position is dictated by the propagation vector. The study of such magnetic diffraction permits the investigation of exchange coupling across the non-magnetic layers. This has been extensively examined to determine the exchange coupling dependence on (a) the direction of the spin alignment (basal plane or *c*-axis), (b) the type of spin structure (ferromagnetic or periodic antiferromagnetic), (c) the growth direction of the superlattice, and (d) the nature and thickness of the non-magnetic interlayers. The study of Dy/Fe superlattices has demonstrated the loss of coherence as the spacer thickness is increased [113] as well as the occurrence of ferromagnetic coupling across the spacer layers. For Lu layers greater than 10 atomic planes thick antiparallel alignment of the Dy layers is always observed [113]. Looking at the diffuse scattering about the nuclear peak positions, characteristic of short-range ferromagnetic correlations, the coherence range of about 24 Å has been extracted for Dy/Sc multilayers. These examples illustrate the usefulness of neutrons to probe the magnetic exchange coupling between magnetic layers. In this context, the discovery of Giant Magnetoresistance [114] in layer structures has triggered a wide range of studies of the magnetic structures and interactions in surfaces, such as exchange bias between ferro and antiferromagnetic layers, multilayers, or superlattices. To go deeper into

the analysis of such systems, neutron spectrometers using polarized neutron beams have been developed. This has given rise to emergent techniques such as neutron polarized reflectometry which has emerged as a routine tool for characterization of magnetic heterostructures. The fundamental theory of neutron reflectometry as well as further examples can be found in the following references [88, 115–118].

Polarized neutron reflectivity has been used to investigate the structure and magnetism of $\text{Fe}_{1-x}\text{Co}_x/\text{Mn}/\text{Fe}_{1-x}\text{Co}_x$ trilayers, and especially to study the magnetic structure of $\delta\text{-Mn}$ (bcc with two atoms per cell) which can be stabilized in the form of thin films by molecular beam epitaxy on the (001) surface of bcc $\text{Fe}_{1-x}\text{Co}_x$ ($x = 0\text{--}0.75$) up to thicknesses of 3 nm. Polarized neutron reflectivity performed at room temperature (see Fig. 5.14) has indicated a net magnetization of $0.8 \mu_{\text{B}}/\text{at}$ to be present in the Mn layer in $\text{Fe}_{0.5}\text{Co}_{0.5}/\text{Mn}/\text{Fe}_{0.5}\text{Co}_{0.5}$ and no net magnetization in the Mn layer in $\text{Fe}/\text{Mn}/\text{Fe}$ [118, 119]. Fitting the neutron reflectivity curves recorded at low field (1.2 mT), with a Mn magnetization parallel to the applied field has led to the determination of the angle between the direction of magnetizations of the $\text{Fe}_{0.5}\text{Co}_{0.5}$ layers to be $90 \pm 5^\circ$, both being tilted at 45° with respect to the applied field (see Fig. 5.14).

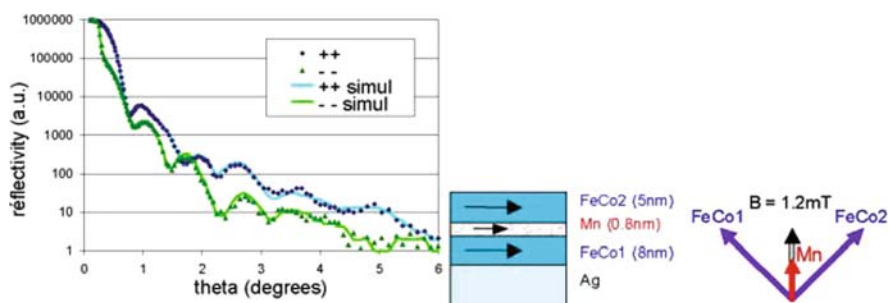


Fig. 5.14 *Left*: Reflectivity for two different neutron polarization states of a $\text{Fe}_{0.5}\text{Co}_{0.5}$ (8 nm)/Mn(0.8 nm)/ $\text{Fe}_{0.5}\text{Co}_{0.5}$ (5 nm)/Ag trilayer in a saturating field of 0.5 T. *Right*: Magnetic configuration deduced from the fit of the polarized neutron reflectivity of this trilayer system in a low magnetic field (1.2 mT) [118, 119]

In addition to classical reflectometry to probe the sample along its depth only, the technique of off-specular scattering has been developed, a technique which is particularly useful to investigate the roughness since it permits one to probe in plane structures ranging from 50 down to $0.5 \mu\text{m}$. This can be used to determine the size of magnetic domains in multilayers. This has been performed on different Fe/Cr or Co/Cu superlattices [120–122]. The last technique which has emerged is the grazing incident scattering which can now be used to probe magnetic thin films [123, 124], nanodots [125], or stripes [123, 126]. A review on magnetic neutron scattering investigations of magnetic nanostructures has recently been published [94] with an emphasis on polarized neutrons.

As has been discussed above, neutron scattering provides a wide range of experimental techniques useful to investigate magnetic surfaces, layers, and nanostructures. No doubt the increasing interest for magnetic heterostructures for

high tech applications like Magnetic RAMs and Giant Magneto Resistive systems will continue to push further the development of these neutron scattering techniques to investigate magnetic surfaces.

5.10 Magnetic Excitations

Neutron inelastic scattering can provide much useful information about magnetic materials. This is probably the most established and direct experimental method to determine spin wave energies in magnetic solids, as well as both crystal electric field and exchange interactions in rare-earth-containing compounds. Indeed, it turns out that the energy range over which the magnetic excitations occurs is very well suited to neutron scattering. Depending on the neutron energy range used, it is thus possible to investigate transitions within 4f element multiplets, or even between the low-lying multiplets of the rare-earth ions. Crystal electric field excitations have energies which are typically in the range 1–100 meV so that they can easily be probed by cold or thermal neutron spectrometers. In addition, the use of high-energy neutron spectroscopy >0.1 eV has been developed these last years, thus enabling to investigate, among others using high-energy excitations, spin orbit excitations transition between the $J = 5/2$ and the $J = 7/2$ of Sm^{3+} such as in SmPd_3 [127]. Inelastic neutron scattering can be used in many systems ranging from hard magnetic materials to valence fluctuation and heavy fermion 4f systems. Of particular interest are metals and intermetallic systems, since in these systems the optical spectroscopy is generally extremely difficult. A detailed description of the inelastic neutron scattering theory can be found in the following references [6, 9, 128, 129], whereas experimental details are described in [9, 130]. Several review articles or book chapters have been devoted to the use of INS: concerning magnetic excitations in crystal-field split 4f systems, the review by Fulde and Loewenhaupt [131] gives a comprehensive survey of the use of neutron inelastic scattering features. For neutron scattering, investigations of anomalous 4f behavior such as valence fluctuation and heavy fermion 4f systems, the reader is referred to the excellent specialized review articles such as [132, 133]. Crystal electric field effects as studied by inelastic neutron scattering in intermetallic compounds have been reviewed by Moze [134]. The book edited by Chatterji give comprehensive illustrations of the study of spin waves in pure metals (Ni, Fe) as well as in manganites [9].

Below, among all the different applications of inelastic neutron scattering to investigate magnetic materials, we will describe two examples, one of the analysis of the crystal electric field scheme and one of the determination of exchange interactions. For other examples, the reader is referred to the following references [9, 130, 132–136]

In general, performing neutron scattering experiments with energy transfers of up to hundred of millivolts or so leads to investigate the manifold of states split by the crystal electric field from the $(2J+1)$ -fold degenerate ground state of a rare-earth element in compounds. Indeed, for an understanding of the magnetic properties at a microscopic scale, knowledge of the crystalline electric field (CEF) interaction

is indispensable. Thus, one should see peaks at the neutron energy transfers corresponding to the splitting within a multiplet, broadened by instrumental resolution and also by other effects such as thermal broadening or exchange broadening. In order to identify the states between which the transitions are occurring, it is often necessary to measure the temperature dependence of the various lines or the relative intensities for up and down scattering. Then, the level scheme can be measured. An example of such a study on $\text{Nd}_2\text{Pd}_2\text{Al}_3$ [137] is given in Fig. 5.15. One can notice that the intensities of the CEF transitions are decreasing with increasing scattering vector due to the form factor, and their temperature dependence is governed by Boltzmann statistics. As shown in Fig. 5.15, the ten-fold degenerated ground state multiplet $^4I_{9/2}$ of Nd^{3+} in $\text{Nd}_2\text{Pd}_2\text{Al}_3$ has been shown to be decomposed into five doublets (Γ_7 , $\Gamma_8^{(1)}$, $\Gamma_8^{(2)}$, $\Gamma_9^{(1)}$, $\Gamma_9^{(2)}$). The inelastic energy spectra of paramagnetic $\text{Nd}_2\text{Pd}_2\text{Al}_3$ shown in Fig. 5.15 exhibit three inelastic lines, which appear for neutron energy loss (noted A, B, and C) and for energy gain (A' , B'). Such investigations by neutron crystal-field spectroscopy has been performed on many systems and the reader can find further examples in the following references [138, 139] for the $\text{RNi}_2\text{B}_2\text{C}$ and $\text{R}_2\text{Fe}_{14}\text{B}$ series, respectively.

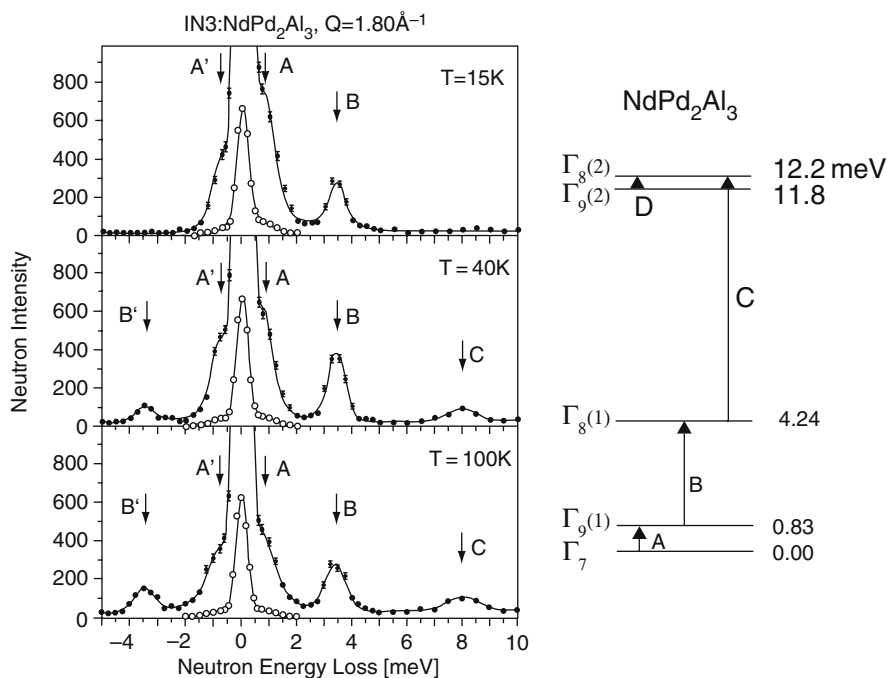


Fig. 5.15 Inelastic neutron scattering spectra (*left*) and the corresponding energy level scheme (*right*) deduced from polycrystalline hexagonal $\text{Nd}_2\text{Pd}_2\text{Al}_3$. The *arrows* indicate the dipolar transitions observed by inelastic neutron scattering [137]

The magnetic inter-sublattice exchange coupling of rare-earth transition metal hydride (or deuteride) has been directly probed by inelastic neutron scattering on a high energy time of flight spectrometer installed at the Isis spallation source [140–142]. Inelastic neutron scattering experiments on Gd compounds have the advantage that the energy transfers of the dispersionless spin wave mode (flat mode) are a direct measure of the exchange fields B_{ex} experienced by the Gd spins in the various types of Gd intermetallics [143–145]. As already observed for other interstitial elements such as C or N, D insertion reduces the exchange field B_{ex} at the Gd site. B_{ex} is found to decrease from 285 T for $\text{Gd}_2\text{Fe}_{17}$ to 247 T for $\text{Gd}_2\text{Fe}_{17}\text{D}_5$. It is noteworthy that although it is well known that the permanent magnet properties of D-doped samples are considerably better than those of the pure compound $\text{Gd}_2\text{Fe}_{17}$, there is a reduction in the Gd–Fe exchange field. The influence of deuterium insertion on the exchange interactions between the Gd and the Fe sublattices has been compared to that of nitrogen (N) or carbon (C). The C and N atoms are found to be more efficient in reducing the inter-sublattice coupling. This has been related to the much smaller increase of the unit cell volume by D insertion in comparison to that of C or N. In spite of a significantly larger overall iron magnetic moment in $\text{Gd}_2\text{Fe}_{17}\text{D}_5$ compared to $\text{Gd}_2\text{Fe}_{17}$, an important decrease of the exchange interactions experienced at the Gd site is observed. The determination of the J^{ex} exchange coupling constant for different compositions has revealed that the insertion of D atoms in the octahedral interstitial sites D (noted D1 on Fig. 5.1) has almost no influence on J^{ex} , whereas when the tetrahedral interstitial sites (noted D2 on Fig. 5.1) are filled the J^{ex} value drops significantly.

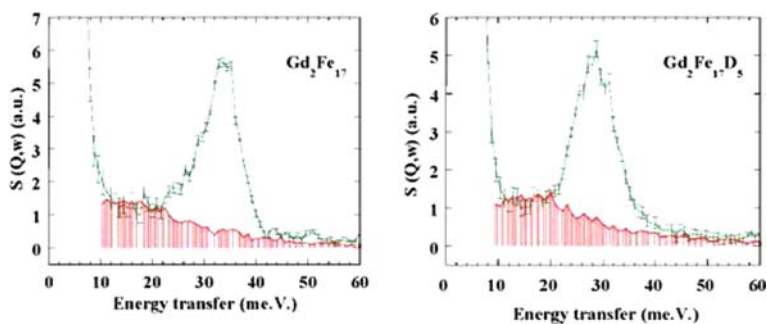


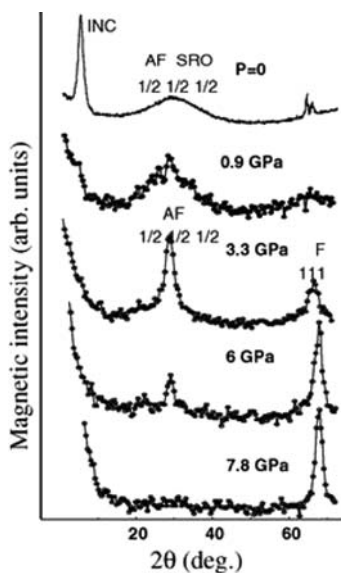
Fig. 5.16 Inelastic neutron spectra of $\text{Gd}_2\text{Fe}_{17}\text{D}_x$ $x = 0$ (left) and 5 (right) at $T = 15$ K. The shaded area indicates the non-magnetic inelastic intensity as deduced from the spectrum at high Q values. The incident neutron energy was 250 meV taken from [140]

5.11 Neutron Scattering Under Extreme Conditions

Thanks to the ability of neutrons to penetrate deep into matter, ancillary equipment can be used to perform experiments under extreme conditions such as very low temperatures, high pressure, under magnetic field, or a combination of these. Neutron

scattering can thus provide useful information on matter in technical conditions difficult to explore. Medium pressures ranging from 0 to 35 kbar are now widely used in neutron research centers and high pressure is also available at some centers (up to 50 GPa). Details on the experimental setup and examples of neutron studies under pressure can be found in the following recent references [146–148], whereas the evolution of high-pressure neutron scattering over time is described in [149]. Many pressure induced phenomena exist in condensed matter sciences, among which one can cite valence transitions, hybridization of magnetic moments, and magnetic transitions induced by structural transitions. Since the 1980s [150], instrumental development has demonstrated the feasibility of performing neutron diffraction in diamond and sapphire anvil cells. Some specialized spectrometers are now dedicated to the pressure studies on reactor sources [151] as well as on spallation sources [152] example of which are the G61 and PEARL instrument at Laboratoire Léon Brillouin and ISIS, respectively. An example is shown in Fig. 5.17, where an unusual succession of magnetic phases have been investigated up to high pressure by neutron powder diffraction studies on the Laves type $\text{Ho}(\text{Mn}_{0.9}\text{Al}_{0.1})_2$ phase [153]. It has been shown that the main effect of Al for Mn substitution is lattice expansion, expansion which can be reversed by applied pressure. Under pressure, the magnetic order changes since the atomic Mn–Mn distances are modified thus leading to pass the critical distance 2.67 \AA when the Mn moment starts to be unstable. As can be seen from Fig. 5.17, depending upon the applied pressure, short-range anti-ferromagnetic correlations are observed according to the broad SRO signal, whereas antiferromagnetic order and ferromagnetic order are observed at higher pressures, respectively [153]. The succession of the magnetic phases results from an energy balance between the dominant Mn–Mn interactions, frustrated by the Mn lattice to

Fig. 5.17 Magnetic neutron diffraction patterns obtained at 15 K and at the indicated pressures for $\text{Ho}(\text{Mn}_{0.9}\text{Al}_{0.1})_2$. The spectra in the paramagnetic state have been subtracted. A short-range order (SRO) of antiferromagnetic (AF) origin is observed at ambient pressure coexisting with an incommensurate magnetic phase (INC). A long-range order appears progressively upon increasing the applied pressure first of antiferromagnetic (AF) type evolving toward a ferromagnetic type order (F) at higher pressure



competing R–Mn and R–R ones. In the meantime, the nature of the Mn magnetism changes, under pressure, from localized to an induced and then to a non-magnetic state.

High-pressure cells can also be useful for inelastic neutron scattering measurements and a review on such experiments can be found in [154, 155, 148]. The investigation of the pressure dependence of phonon or even magnons is also possible [156].

In terms of low temperature measurements, temperatures as low as down to 50 mK are now becoming feasible in many neutron facilities, this range of temperature can be even confined with magnetic field (up to 7 T) and high pressures (up to 50 GPa) offering a wide playground for in material scientists. In fact, very low temperature phenomenon can be studied by neutron scattering. Typical examples are the investigations of nuclear order in noble metals [157]. Neutron is a unique tool to determine the magnetic structure of the nuclei. A study has been carried out by neutron experiments on antiferromagnetic nuclear order in silver at picokelvin temperatures [158]. Another unusual magnetic property has been investigated: the magnetic behavior of the solid oxygen which is the only elementary molecular magnet. Indeed the magnetic phase diagram has been investigated up to 9.5 GPa [159, 160]. Several neutron institutes are already equipped with superconducting coils to perform neutron scattering up to 20 T and projects are in progress to develop neutron spectrometers operating up to 30 T. Due to the specific shape of the coils, the spectrometer will be of time of flight type.

5.12 Conclusions

Neutron scattering is a comprehensive tool for the investigation of condensed matter in general and magnetic materials in particular. Even if the incident beam is unpolarized, the magnetic neutron–target interaction may be useful for obtaining structural and magnetic information. As has been discussed above, neutron scattering offers a wide range of useful techniques to probe the structural and magnetic properties of magnetic materials whatever their state: polycrystalline, single crystal, amorphous, bulk, or thin films. At this point, it is worth remembering that in addition to neutron scattering, other techniques, in particular local probes such as x-ray scattering, Mössbauer spectroscopy, NMR studies, etc. can provide valuable complementary information on the properties of materials. The recent improvement of neutron sources and spectrometers offers new perspectives to investigate magnetic materials and a description of some of these possibilities has been recently reviewed in [9, 161, 162].

References

1. Chadwick J.: Possible existence of a neutron. *Nature (London)* **129** 312 (1932).
2. Chadwick J.: Existence of a neutron. *Proc. Roy. Soc. London Ser. A* **136** 692–708 (1932).
3. Bacon G. E.: *Neutron Diffraction*. Clarendon Press, Oxford (1975).

4. Bacon G. E.: Fifty Years of Neutron Diffraction: the Advent of Neutron Scattering. Adam Hilger, Bristol (1986).
5. Lovesey S. W., Springer T.: Dynamic of Solids and Liquids by Neutron Scattering, Topics in Current Physics, Vol. 3. Springer-Verlag, Berlin (1977).
6. Squires G. L.: Introduction to the Theory of Thermal Neutron Scattering. Cambridge University Press, Cambridge (1978).
7. Williams, W. G.: Polarized Neutrons. Clarendon Press: Oxford (1988).
8. Willis B. T.: Chemical Application of Thermal Neutron Scattering. Oxford University Press, Oxford (1973).
9. Chatterji T.: Neutron Scattering from Magnetic Materials. Elsevier B.V., Amsterdam (2006).
10. Izyumov Yu. A., Naish V. E., Ozerov R. P.: Neutron Diffraction of Magnetic Materials. Consultant Bureau, Plenum Pub. New York (1991).
11. Bloch F.: On the Magnetic Scattering of Neutrons. Phys. Rev. B **50** 259 (1936).
12. Schull C. G., Smart J. S.: Detection of Antiferromagnetism by Neutron Diffraction. Phys. Rev. **76** 1256–1 (1949).
13. Néel L.: Influence des fluctuations du champ moléculaire sur les propriétés magnétique des corps. Ann. Phys. (Paris) **17** 5–105 (1932).
14. Néel L.: Propriétés magnétiques des ferrites ferrimagnétisme et Antiferromagétisme. Ann. Phys. (Paris) **3** 137–198 (1948).
15. Baruchel J., Hodeau J. L., Lehmann M. S., Regnard J. R., Schlenker C.: Neutron and Synchrotron Radiation for Condensed Matter Studies, Vol. I: Theory, Instruments and Methods. Springer-Verlag, Berlin (1993).
16. Baruchel J., Hodeau J. L., Lehmann M. S., Regnard J. R., Schlenker C.: Theory, Instruments and Methods, Vol. II: Applications to Solid State Physics and Chemistry. Springer-Verlag, Berlin (1994).
17. Scherm R., Fak B.: Neutrons in Baruchel. J. Hodeau, J. L. Lehmann, M. S. Regnard, J. R. Schlenker (eds.) Neutron and Synchrotron Radiation for Condensed Matter Studies, Vol. I: Theory, Instruments and Methods, Springer-Verlag, Berlin (1993).
18. Brückel T., Heger G., Richter D., Zorn R. (Eds.): *5th Laboratory Course Neutron Scattering*, Schriften des Forschungszentrums Jülich, Vol. 9 (2001).
19. Withers P.J.: Mapping residual and internal stress in materials by neutron diffraction. C.R. Physique **8** 806–820 (2007).
20. Von Der Hardt P., Röttger H.: Neutron Radiography Handbook. D. Reidel, Dordrecht (1981).
21. Young R. A.: The Rietveld Method. Oxford University Press, Oxford (1993)
22. Mc Intyre G.: Single Crystal diffractometry in Baruchel. J. Hodeau, J. L. Lehmann, M. S. Regnard, J. R. Schlenker, (eds.) Neutron and Synchrotron Radiation for Condensed Matter Studies, Vol. I: Theory, Instruments and Methods, Springer-Verlag, Berlin (1993).
23. Chacon C., Isnard O.: Neutron diffraction determination of the preferential substitution scheme of gallium and study of the magnetic features of the Nd₂Fe_{14-x}Ga_xB phases. J. Appl. Phys. **88** 3570–3577 (2000).
24. Chacon C., Isnard O.: Crystal and magnetic structures of the YCo_xFe_{4-x}B compounds investigated by powder neutron diffraction and magnetisation measurements. J. Appl. Phys **89** 71–75 (2001).
25. Marasinghe G. K., Pringle O. A., Long G. J., James W. J., Yelon W. B., Grandjean F.: A neutron diffraction and Mössbauer effect study of the magnetic structure of Y₂(Fe_{1-x}Mn_x)₁₄ B. J. Appl. Phys. **70** 6149–6151 (1991).
26. Isnard O., Miraglia S., Soubeyroux J. L., Fruchart D., Stergiou A.: Neutron diffraction study of the structural and magnetic properties of the R₂Fe₁₇H_x ternary compounds (R = Ce, Nd, Ho). J. Less-Common Met. **162** 273–284(1990).
27. Isnard O., Miraglia S., Soubeyroux J. L., Pannetier J., Fruchart D.: Neutron powder diffraction study of Pr₂Fe₁₇ and Pr₂Fe₁₇N₃. Phys. Rev. B **45** 2920–2926 (1992).
28. Sun H., Coey J. M. D., Otani Y., Hurley D. P. F.: Magnetic properties of a new series of rare-earth iron nitrides: R₂Fe₁₇N_y (y ~ 2.6). J. Phys. Condens. Matter. **2** 6465–6470 (1990).

29. Isnard O., Soubeyrou J. L., Miraglia S., Fruchart D., Garcia L. M., Bartolomé J.: Neutron powder diffraction study of the desorption of deuterium in $\text{Nd}_2\text{Fe}_{17}\text{D}_x = 5$. *Physica B* **180–181** 629–631 (1992).
30. Isnard O., Soubeyrou J. L., Fruchart D., Jacobs T. H., Buschow K. H. J.: Structural and magnetic behaviour of the series $\text{Th}_2\text{Fe}_{17}\text{C}_x$ ($x = 0$ to 1.25). *J. Alloys Comp.* **186** 135–145 (1992).
31. Mamontov E., Udovic T. J., Isnard O., Rush J. J.: Neutron scattering study of hydrogen dynamics in $\text{Pr}_2\text{Fe}_{17}\text{H}_5$. *Phys. Rev. B* **70** 214305 (2004).
32. Udovic T., Zhou W., Wu H., Brown C. M., Rush J. J., Yildirim T. Mamontov E., Isnard O.: Neutron vibrational spectroscopy of the $\text{Pr}_2\text{Fe}_{17}$ -based hydrides. *J. Alloys Comp.* **446–447** 504–507 (2007).
33. Mamontov E., Udovic T. J., Rush J. J., Isnard O.: Dynamics of hydrogen in $\text{Pr}_2\text{Fe}_{17}\text{H}_4$ and $\text{Pr}_2\text{Fe}_{17}\text{H}_5$. *J. Alloys Comp.* **422** 149–152 (2006).
34. Mc Intyre G. J., Lemée-Cailleau M. H., Wilkinson C.: High-speed neutron Laue diffraction comes of age. *Physica B* **385–386** 1055–1058 (2006).
35. Ouladdiaf B., Archer J., McIntyre G. J., Hewat A. W., Brau D., York S.: OrientExpress: A new system for Laue neutron diffraction. *Physica B* **385–386** 1052–1054 (2006).
36. Chung E. M. L., Lees M. R., McIntyre G. J., Balakrishnan G., Hague J. P., Visser D., Paul D. Mc K., Wilkinson C.: Magnetic properties of tapiolite (FeTa_2O_6); a quasi two-dimensional (2D) antiferromagnet. *J. Phys.: Cond. Matter* **16** 7837–7852 (2004).
37. Soubeyrou J. L., Claret N.: Magnetic properties and crystallization behaviour of $\text{Fe}_{28.75}\text{Co}_{28.75}\text{Ni}_{17.5}\text{X}_8\text{B}_{17}$ ($X = \text{Si}, \text{Ge}$) metallic glasses. *Physica B* **350** e59–e62 (2004).
38. Soubeyrou J. L., Claret N.: J. Magnetic properties and crystallization behavior of $\text{Fe}_{28.75}\text{Co}_{28.75}\text{Ni}_{17.5}\text{X}_8\text{B}_{17}$ ($X = \text{Si}, \text{Ge}$) metallic glasses. *Magn. Magn. Mater.* **1379**, 272–276 (2004)
39. Soubeyrou J. L., Claret N.: *Applied Phys. A* **74**, S1025–S1027 (2002).
40. Soubeyrou J. L., Pelletier J. M., Perrier de la Bâthie R.: In situ crystallization of Zirconium-based bulk metallic glasses. *Physica B* **276–278** 905–906 (2000).
41. Isnard O.: A review of in situ and/or time resolved neutron scattering *C.R. Physique* **8** 789–805 (2007)
42. Isnard O.: In situ and or time resolved neutron scattering for materials sciences. *J. Optoelec. Adv. Mat.* **8**, 411–417 (2006)
43. Lyubina J., Isnard O., Gutfleisch O., Müller K. H., Schultz L.: Ordering of nanocrystalline Fe-Pt alloys studied by in situ powder neutron diffraction. *J. Appl. Phys.* **100** 094308 (2006)
44. Lyubina J., Opahle I., Richter M., Gutfleisch O., Müller K. H., Schultz L., Isnard O.: Influence of composition and order on the magnetism of Fe-Pt alloys: Neutron powder diffraction and theory. *Appl. Phys. Letter* **89** 032506 (2006)
45. Prokhnenko O., Ritter C., Arnold Z., Isnard O., Kamarad J., Teplykh A., Kuchin A.: Neutron diffraction studies of the magnetic phase transitions in $\text{Ce}_2\text{Fe}_{17}$ compound under pressure. *J. Appl. Phys.* **91** 385–391(2002).
46. Prokhnenko O., Arnold Z., Kamarad J., Ritter C., Isnard O., Kuchin A.: Helimagnetic order in the re-entrant ferromagnet $\text{Ce}_2\text{Fe}_{15.3}\text{Mn}_{1.7}$. *J. Appl. Phys.* **97** 113909-1 to 8 (2005)
47. Kinast E. J., Antonetti V., Schmitt D., Isnard O., da Cunha J. B. M., Gusmao M. A., dos Santos C. A.: Bicriticality in $\text{Fe}_x\text{Co}_{1-x}\text{Ta}_2\text{O}_6$. *Phys. Rev. Letters* **91** 197208 (2003)
48. Zlotea C., Isnard O.: Neutron powder diffraction and magnetic study of RCo_4Ga intermetallic compounds ($R = \text{Y}$ and Pr). *J. Alloys Comp.* **346** 29–37 (2002).
49. Isnard O.: Diffusion, diffraction en temps réel et études réalisées in situ. *J. Phys. IV France* **103** 133–171(2003).
50. Gutfleisch O., Harris I. R.: Fundamental and practical aspects of the hydrogenation disproportionation, desorption and recombination process. *J. phys., D, Appl. phys.* **29** 2255–2265 (1996).

51. McGuinness P. J., Zhang X. J., Yin X. J., Harris I. R.: Hydrogenation, disproportionation and desorption (HDD): An effective processing route for Nd—Fe—B-type magnets. *J. Less-Common Met.* **158** 359–365 (1990).
52. Takeshita T. Nakayama, R.: 10th Int. Workshop on Rare-Earth and Their Applications. Kyoto, Japan 551–557 (1989).
53. Takeshita T.: Present status of the hydrogenation-decomposition-desorption-recombination process as applied to the production of magnets. *J. Alloys Comp.* **193** 231–234 (1993).
54. Gutfleisch O., Martinez N., Verdier M., Harris I. R.: Phase transformations during the disproportionation stage in the solid HDDR process in a Nd₁₆Fe₇₆B₈ alloy. *J. Alloys Comp.* **215** 227–233 (1994).
55. Liesert S., Fruchart D., de Rango P., Soubeyroux J. L.: The hydrogenation–disproportionation–desorption–recombination process of Nd₂Fe₁₄B studied by in-situ neutron diffraction and thermomagnetic measurements. *J. Alloys Comp.* **253–254** 140–143 (1997).
56. Soubeyroux J. L. Fruchart D., Liesert S., de Rango P., Rivoirard S.: In situ neutron diffraction study of the HDDR process of Nd—Fe—B magnets. *Physica B* **241–243** 341–343 (1998).
57. Isnard O., Yelon W. B., Miraglia S., Fruchart D.: Neutron diffraction study of the insertion scheme of hydrogen in Nd₂Fe₁₄B. *J. Appl. Phys.* **78** 1892–1898 (1995).
58. Goujon A., Gillon B., Debede A., Cousson A., Gukasov A., Jefic J., Mc Intyre G. J., Varret F.: Neutron Laue diffraction on the spin crossover crystal [Fe(1-*n*-propyltetrazole)₆](BF₄)₂ showing continuous photoinduced transformation. *Phys. Rev. B* **73** 104413 (2006).
59. Goujon A., Gillon B., Gukasov A., Jefic J., Nau Q., Codjovi E., Varret F.: Photoinduced molecular switching studied by polarized neutron diffraction. *Phys. Rev. B* **67** 220401(R) (2003).
60. de Gennes P. G.: Theory of neutron scattering by magnetic materials Chap. 3 in *Magnetism* Vol. III. G.T. Rado, H. Suhl (eds.) Academic Press New-York (1963).
61. Cox D. E.: Neutron-Diffraction determination of magnetic structures. *IEEE trans. Magn.* **8** 161–182 (1972).
62. Rossat-Mignot J.: Magnetic structures Chap. 19 in *Neutron Scattering*, part C. K. Sködl, L. D. Price (eds.) Academic Press New-York (1987).
63. Hicks T. J.: Experiments with neutron polarization analysis. *Adv. Phys.* **45** 243–298 (1996).
64. Tasset F.: Magnetic Structures and neutron polarimetry. *J. Magn. Mater.* **129** 47–52 (1994).
65. Tasset F.: Zero field neutron polarimetry, *Physica B* **156–157** 627–630 (1992).
66. Mirebeau I., Apetrei A., Rodriguez-Carvajal J., Bonville P., Forget A., Colson, D., Glaskov V., Sanchez J. P., Isnard O., Suard E.: Magnetic order induced by dipolar interactions in the spin liquid Tb₂Sn₂O₇. *Phys. Rev. Letters.* **94** 246402 (2005).
67. Givord D., Lemaire R.: Magnetic transition and amorphous thermal expansion in R₂Fe₁₇ compounds. *IEEE Trans. Magn.* **Mag-10**, 109–113 (1974).
68. Isnard O., Miraglia S., Fruchart D., Georgetti C., Pizzini S., Dartyge E., Kappler J. P., Krill G.: Magnetic circular X-ray dichroism study of the Ce₂Fe₁₇H_x compounds. *Phys. Rev. B* **49** 15692–15701 (1994).
69. Hautot D., Long G. J., Grandjean F., Isnard O. A. Mössbauer spectral study of the magnetic properties of Ce₂Fe₁₇ and its hydrides. *Phys. Rev. B* **62** 11731–11741 (2000).
70. Prokhnenko O., Ritter C., Arnold Z., Isnard O., Teplikh A., Kamarad J., Pirogov A., Kuchin A.: Effect of pressure and Mn substitution on the magnetic ordering of Ce₂Fe_{17-x}Mn_x. *Appl. Phys. A.* **74** S610–S612 (2002).
71. Teplykh A., Pirogov A., Kuchin A., Prokhnenko O., Ritter C., Arnold Z., Isnard O.: Magnetic field induced phase transition in Ce₂Fe_{17-x}Mn_x compounds. *Appl. Phys. A.* **74** S577–S579 (2002).
72. Moon R., Riste T., Koehler W.: Polarization Analysis of Thermal-Neutron Scattering. *Phys. Rev.* **181** 920–931 (1969).

73. Ziebeck K. R. A., Brown P. J. J.: Measurement of the paramagnetic response function in the weak itinerant magnetic compound MnSi using polarised neutron scattering. *Phys. F* **10** 2015–2024 (1980).
74. Nield V. M., Keen D. A.: *Diffuse neutron scattering from crystalline materials*. Clarendon Press, Oxford (2001).
75. Stewart J. R.: *Disordered materials studied using neutron polarization analysis*, collection SFN7 (2007) 173–197 EDP Sciences Publ. Paris doi: 10.1051/sfn:2007022
76. Tasset F.: Recent progress in polarised neutron diffraction at ILL and the emergence of a ^3He neutron polarisation filter. *Physica B* **174** 506–513 (1991).
77. Izyumov Yu. A., Naish V. E., Ozerov R. P.: *Neutron Diffraction of Magnetic Materials*, Consultant Bureau. Plenum Pub. New York (1991).
78. Cracknell A. P.: *Magnetism in crystalline materials*. Pergamon Press, New York (1975).
79. Ressouche E.: Investigating molecular magnetism with polarized neutrons. *Physica B* **267–268** 27–36 (1999).
80. Schweitzer J., Tasset F.: Polarised neutron study of the RCO_5 intermetallic compounds. I. The cobalt magnetisation in YCo_5 . *J. Phys. F* **10** 2799–2817 (1980).
81. Steinbeck L., Richter M., Eschrig H.: Itinerant-electron magnetocrystalline anisotropy energy of YCo_5 and related compounds. *Phys. Rev. B* **63**, 184431 (2001).
82. Givord D., Laforest J., Schweizer J.: Temperature dependence of the samarium magnetic form factor in SmCo_5 . *J. Appl. Phys.* **50** 2008–2010 (1979).
83. Givord D., Laforest J., Lemaire R.: Polarized neutron study of the itinerant electron metamagnetism in ThCo_5 . *J. Appl. Phys.* **50**, 7489–7491 (1979).
84. Givord D., Laforest J., Lemaire R.: Magnetic transition in ThCo_5 due to change of Comoment. *Physica B+C* **86–88**, 204–206 (1977).
85. Zheludev A., Bonnet M., Ressouche E., Schweizer J., Wan M., Wang H.: Experimental spin density in the first purely organic ferromagnet: the β para-nitrophenyl nitronyl nitroxide. *J. Magn. Mater.* **135** 147–160 (1994).
86. Givord D., Li H. S., Tasset F.: Polarized neutron on $\text{Y}_2\text{Fe}_{14}\text{B}$ and $\text{Nd}_2\text{Fe}_{14}\text{B}$. *J. Appl. Phys.* **57** 4100–4102 (1985)
87. Schweizer J., Golhen S., Lelièvre-Berna E., Ouahab L., Pontillon Y., Ressouche E.: Magnetic interactions and spin densities in molecular compounds. *Physica B* **297** 213–220 (2001).
88. Fermon C., Ott F. Menelle A.: *Neutron reflectometry*, in *X-Ray and Neutron Reflectivity: Principles and Applications*. J. Daillant, A. Gibaud (eds.) Springer, Berlin (1999).
89. Ott F.: Neutron scattering on magnetic surfaces. *C.R. Phys.* **8** 763–776 (2007).
90. Wills A. S., Lelièvre-Berna E., Tasset F., Schweizer J., Ballou R.: Magnetisation distribution measurements from powders using a ^3He spin filter. *Physica B* **356** 254–258 (2005).
91. Brown P. J.: Spherical neutron polarimetry Chap. 5 in *Neutron Scattering from magnetic materials*. T. Chatterji (eds.) Elsevier, Amsterdam (2006).
92. Guinier A., Fournet G.: *Small-Angle Scattering of x-rays*. John Wiley, New York (1955).
93. Kostorz G.: in *Neutron scattering*. G. Korstorz (ed.) Academic, New York 227 (1979).
94. Wiedenmann A.: *Small Angle Neutrons Scattering investigations of Magnetic Nanostructures* Chap. 10 in *Neutron Scattering from magnetic Materials*. T. Chatterji (ed.) Elsevier, Amsterdam 473 (2006).
95. Kostorz G.: Small-angle scattering studies of phase separation and defects in inorganic materials. *J. Appl. Cryst.* **24** 444–456 (1991).
96. Gerold V., Kostorz G.: Small-angle scattering applications to materials science. *J. Appl. Cryst.* **11** 376–404 (1978).
97. Fujii H., Saga M., Takeda T., Komura S., Okamoto T., Hiroshima S., Sagawa M.: Small angle neutron scattering from $\text{Nd}_{15}\text{Fe}_{77}\text{B}_8$ and $\text{Nd}_{15}\text{Fe}_{77}\text{AlB}_8$ permanent magnets. *IEEE trans. Magn.* **23** 3119–3121 (1987).
98. Vecchini C., Moze O., Suzuki K., Cadogan J. M., Pranzas K., Michels A., Weissmuller J.: Small angle neutron scattering investigations of spin disorder in nanocomposite soft magnets. *J. Alloys Compds.* **423** 31–36 (2006).

99. Ito N., Michels A., Kohlbrecher J., Garitaonandia J. S., Suzuki K., Cashion J. D.: Effect of magnetic field annealing on the soft magnetic properties of nanocrystalline materials. *J. Magn. Magn. Mater.* **316** 458–461 (2007).
100. Kohlbrecher J., Wiedenmann A., Wollenberger H.: SANS investigation of the nano-sized crystalline and magnetic microstructure of Fe-Si-B based alloys. *Physica B* **213–214** 579–581 (1995).
101. Hermann H., Wiedenmann A., Mattern N., Heinemann A.: SANS study of nanocrystalline Fe₃Si particles in amorphous FeSiBCuNb matrix. *Physica B* **276–277** 704–705 (2000).
102. Ohnuma M., Suzuki J., Funahashi S., Ishigaki T., Kuwano H., Hamaguchi Y.: Small-angle neutron scattering study on Fe-Cu-Nb-Si-B nanocrystalline alloys. *Physica B* **213–214**, 582–584 (1995).
103. Weissmüller J., Michels A., Barker J. C., Wiedenmann A., Erb U., Shull R. D.: Analysis of the small-angle neutron scattering of nanocrystalline ferromagnets using a micromagnetics model. *Phys. Rev. B* **63** 214414 (2001).
104. Wiedenmann A.: Magnetically controllable fluids and their applications, Lecture Notes in Physics Vol. 594. S. Odenbach (ed.) 33, Springer-Verlag, Berlin (2002).
105. Adveev M. V., Aksenov V. L., Balasoiu M., Garamus V. M., Schreyer A., Torok Gy., Rosta L., Bica D., Vekas L.: Comparative analysis of the structure of sterically stabilized ferrofluids on polar carriers by small-angle neutron scattering. *J. Coll. Interface Sci.* **295** 100–107 (2006).
106. Adveev M. V.: Contrast variation in small-angle scattering experiments on polydisperse and superparamagnetic systems: basic functions approach. *J. Appl. Cryst.* **40**, 56–70 (2007)
107. Farrell D. F., Ijiri Y., Kelly C. V., Borchers J. A., Rhyne J. J., Ding Y., Majetich S. A.: Small angle neutron scattering study of disordered and crystalline iron nanoparticle assemblies. *J. Magn. Magn. Mater.* **303** 318–322 (2006).
108. Forgan E. M., Paul D. M., Mook H. A., Timmins P. A., Keller H., Sutton S., Abell J. S.: Observation by neutron diffraction of the magnetic flux lattice in single crystal YBa₂Cu₃O_{7- δ} . *Nature* **343** 735–737 (1990).
109. Pannetier M., Ott F., Fermon C., Sanson Y.: Surface diffraction on magnetic nanostructures in thin films using grazing incidence SANS. *Physica B* **335** 54–58(2003).
110. Rhyne J. J., Salamon M. B., Flynn C. P., Erwin R. W., Borchers J. A.: Magnetic structures of superlattices. *J. Magn. Magn. Mater.* **129** 39–46 (1994).
111. Werner S. A., Rhyne J. J.: in *Recent Progress in Random Magnets*. E. D. Ryan (ed.) World Scientific, Singapore 237 (1992).
112. Rhyne J. J., Erwin R. W., Borchers J. A., Salamon M. B., Tsui F., Du R., Flynn C. P.: in *Science and Technology of nanostructured Magnetic Materials*. G. C. Hadjipanayis, G. A. Prinz (eds.) Plenum Press, New York 117 (1991).
113. Beach R. S., Borchers J. A., Matheny A., Erwin R. W., Salamon M. B., Everitt B., Pettit K., Rhyne J. J., Flynn C. P.: Enhanced Curie temperatures and magnetoelastic domains in Dy/Lu superlattices and film. *Phys. Rev. Lett.* **70** 3502–3505 (1993).
114. Baibich M. N., Broto J. M., Fert A., Nguyen Van Dau F., Petroff F., Eitenne P., Creuzet G., Friederich A., Chazelas J.: Giant magnetoresistance of (001)Fe/(001)Cr magnetic superlattices. *Phys. Rev. Lett.* **61** 2472–2475 (1988).
115. Majkrzak C. F., Cable J. W., Kwo J., Hong M., McWhan D. B., Yafet Y., Waszczak J. V., Vettier C.: Observation of a magnetic antiphase domain structure with long-range order in a synthetic Gd-Y superlattice. *Phys. Rev. Lett.* **56**, 2700–2702 (1986)
116. Ott F.: Neutron scattering on magnetic surfaces. *C.R. Physique* **8** 763–776 (2007).
117. Majkrzak C. F., O’Donovan K. V., Berk N. F.: Polarized neutron reflectometry Chap. 9 in *Neutron Scattering from magnetic materials*. T. Chatterji (ed). Elsevier, Amsterdam (2006).
118. Kentzinger E., Rucker U., Caliebe W., Goerigk G., Werges F., Nerger S., Voigt J., Schmidt W., Alefeld B., Fermon C., Brückel Th.: Structural and magnetic characterization of Fe/ δ -Mn thin films. *Physica B* **276–278** 586–587 (2000).
119. Nerger S., Kentzinger E., Rucker U., Voigt J., Ott F., Seeck O. H., Brückel Th.: Proximity effects in Fe_{1-x}Co_x/Mn/Fe_{1-x}Co_x trilayers. *Physica B* **297** 185–188 (2001).

120. Lauter H., Lauter-Pasyuk V., Toperverg B., Romashev L., Milyaev M., Krinitsina T., Kravtsov E., Ustinov V., Petrenko A., Aksenov V.: Domains and interface roughness in Fe/Cr multilayers: Influence on the GMR effect. *J. Magn. Magn. Mater.* **258–259**, 338–341 (2003).
121. Lauter-Pasyuk V., Lauter H. J., Toperverg B., Nikonov O., Kravtsov E., Romashev L., Ustinov V.: Magnetic neutron off-specular scattering for the direct determination of the coupling angle in exchange-coupled multilayers. *J. Magn. Magn. Mater.* **226–227**, 1694–1696 (2001).
122. Paul A., Kentzinger E., Rucker U., Burgler D. E., Grünberg P.: Measurement and simulation of polarized neutron reflectivity and off-specular scattering from evolving magnetic domain structure in Co/Cu multilayers. *Physica B* **356** 31–35 (2005).
123. Fermon C., Ott F., Gilles B., Marty, A. Menelle, A., Samson Y., Legoff G., Francinet G.: Towards a 3D magnetometry by neutron reflectometry. *Physica B* **267** 162–167 (1999).
124. Lauter-Pasyuk V.: Techniques de diffusion des neutrons en incidence rasante Collection SFN7 (2007) 221–240 EDP Sciences Publ. Paris DOI: 10.105/sfn:2007024
125. Chang-Peng Li, Roshchin I. V., Battle X., Viret M., Ott F., Schuller I. K.: Fabrication and structural characterization of highly ordered sub-100-nm planar magnetic nanodot arrays over 1 cm² coverage area. *J. Appl. Phys.* **100** 074318–25 (2006)
126. Szuskiewicz W., Fronc K., Hennion B., Ott F., Aleszkiewicz M.: Magnetic stripe domains in Fe/Fe–N multilayers. *J. Alloys Comp.* **423** 172–175 (2006).
127. Williams W. G., Boland B. C., Bowden Z. A., Taylor A. D., Culverhouse S., Rainford B. D.: Observation of intermultiplet transitions in rare-earth metal ions by inelastic neutron scattering. *J. Phys. F: Met. Phys.* **17** L151–L155 (1987).
128. Balcar E., Lovesey S.W.: Theory of magnetic neutron and photon scattering. Clarendon Press, Oxford (1989).
129. Balcar E., Lovesey S. W.: Neutron-electron spectroscopy of rare-earth ions. *J. Phys. C: Solid State Phys.* **19** 4605–4611 (1986).
130. Hippert F., Geissler E., Hodeau J. L., Lelièvre-Berna E., Regnard J. R.: Neutron and X-ray spectroscopy. Springer, Dordrecht (2006).
131. Fulde P., Loewenhaupt M.: Magnetic excitations in crystal-field split 4f systems. *Adv. phys.* **34** (1986) 589–661.
132. Loewenhaupt M., Fischer K. H.: Neutron Scattering n heavy fermion and valence fluctuation 4f-systems Chap. 6 in handbook of magnetic materials Vol. 7 **503** (1993).
133. Loewenhaupt M., Fischer K. H.: Valence fluctuation and heavy-fermion 4f systems Chap. 105 in Handbook on the physics and chemistry of rare-earths Vol. 16. K. A. Gschneidner and L. Eyring (eds.) North Holland Publisher 1 (1993).
134. Moze, O.: Crystal field effects in intermetallic compounds studied by inelastic neutron scattering, chapter 4 in Handbook of Magnetic Materials, Vol. 11. K. H. J. Buschow (ed.) Elsevier Science Amsterdam 493 (1998).
135. Stirling W. G., Mc Ewen K. A.: Magnetic excitations Chapter 20 in Methods of experimental physics, Vol. 23, Part. C 189 Academic Press Inc. (1987).
136. Fulde P., Loewenhaupt M.: Spin waves and magnetic excitations, I. A. S. Borovik-Romanov, S. K. Sinha (eds.) North-Holland, Amsterdam Ch. 6, 367. (1988)
137. Dönni A., Furrer A., Kitazawa H., Zolliker M.: Neutron Crystalline-Electric-Field Spectroscopy of RPd₂A₁₃ (R = Ce, Pr, Nd). *J. Phys. Condens. Matter.* **9** 5921–5933 (1997).
138. Gasser U., Allenspach P., Fauth F., Henggeler W., Mesot J., Furrer A., Rosenkrants S., Vored-erwisch P., Buchgesiter M.: Neutron crystal-field spectroscopy of RNi₂B₂C (Ho, Er, Tm). *Z. Phys. B* **101** 345–352 (1996).
139. Loewenhaupt M., Sosnovska I., Frick B.: Ground state multiplet of rare earth 3⁺ ions in R₂Fe₁₄B investigated by inelastic neutron scattering. *Phys. Rev.* **42** 3866–3876 (1990).
140. Isnard O., Sippel A., Loewenhaupt M., Bewley R.: A high energy inelastic neutron scattering investigation of the Gd-Fe exchange coupling in Gd₂Fe₁₇D_x (x = 0, 3 and 5). *J. Phys. Cond. Matter* **13** 1–11 (2001)
141. Isnard O., Loewenhaupt M., Bewley R.: A high energy inelastic neutron scattering investigation of the Gd-Fe exchange coupling in GdFe₁₁TiD_x (x = 0, 1). *Physica B* **350** suppl. 1 e31–e33 (2004).

142. Loewenhaupt M., Sosnovska I.: Exchange and Crystal fields in $R_2Fe_{14}B$ studied by inelastic neutron scattering. *J. Appl. Phys.* **70** 5967–5971 (1991).
143. Loewenhaupt M., Tils P., Buschow K. H. J., Eccleston R. S.: Exchange interactions in Gd-Fe compounds studied by inelastic neutron scattering. *J. Magn. Magn. Mater.* **152** 10–16 (1996).
144. Loewenhaupt M., Tils P., Buschow K. H. J., Eccleston R. S.: Intersublattice exchange coupling in Gd-Co compounds studied by INS. *J. Magn. Magn. Mater.* **138**, 52–56 (1994).
145. Tils P., Loewenhaupt M., Buschow K. H. J., Eccleston R. S.: Intersublattice exchange coupling in Gd–Mn compounds studied by INS. *J. Alloys Comp.* **279** 123–126 (1998).
146. Mirebeau I.: Magnetic neutron diffraction under high pressure. *C.R. Physique* **8** 737–744 (2007).
147. Lemée-Cailleau M-H, Kernavanois N., Fak B., Bellisent-Funel M-C.: Proceedings of the Medium pressure advances for neutron scattering. *J. Phys. Condens. Matter.* **17** (2003)
148. Mignot J. M.: Neutron scattering under extreme conditions. Collection SFN9 (2008) 159–179 EDP Sciences Publ. Paris doi: 10.1051/sfn: 2008012 (2008)
149. Somenkov V. A.: High-pressure neutron scattering over the ages. *J. Phys. Condens. Matter.* **17** S2991–S3003 (2003).
150. Goncharenko I. N.: Neutron diffraction experiments in diamond and sapphire anvil cells. *High Pressure Res.* **24** 193–204 (2003).
151. Goncharenko I. N.: New techniques for high-pressure neutron and x-ray studies. *High Press. Res.* **27** (1) 183–188 (2007).
152. PEARL ISIS <http://www.isis.rl.ac.uk/crystallography/hipr/index.htm> and <http://www.isis.rl.ac.uk/isis98/pearl.htm>
153. Mirebeau I., Goncharenko I. N., Golosovsky I. V.: Neutron diffraction in $Ho(Mn_{0.9}Al_{0.1})_2$ under pressure up to 7.8 GPa: Long-range magnetic order induced by pressure in a frustrated system. *Phys. Rev. B* **64** 140401R (2001).
154. Klotz S., Braden M., Besson M.: Inelastic neutron scattering to very high pressures. *J. Hyp. Int.* **128** 245–254 (2000).
155. Klotz S., Braden M.: Phys. Spin-phonon coupling in $CuGeO_3$. *Rev. Lett.* **80** 3634–3637 (1998).
156. Klotz S., Braden M.: Phonon dispersion of bcc Iron to 10 GPa. *Phys. Rev. Lett.* **85** 3209–3212 (2000).
157. Jyrkkiö T. A., Huiku M. T., Siemensmeyer K., Clausen K. N.: Neutron diffraction studies of nuclear magnetic ordering in copper. *J. Low Temp. Phys.* **74** 435–474 (1989).
158. Tuoriniemi J. T., Nummila K. K., Vuorinen R. T., Lounasmaa O. V., Metz A., Siemensmeyer K., Steiner M., Lefmann K., Clausen K. N., Rasmussen F. B.: Neutron experiments on anti-ferromagnetic nuclear order in silver at picokelvin temperatures. *Phys. Rev. Lett.* **75** 3744–3747 (1995).
159. Goncharenko I. N.: Evidence for a magnetic collapse in the epsilon phase of solid oxygen. *Phys. Rev. Lett.* **94** 205503 (2005)
160. Goncharenko I. N., Makarova O. A., Ulivi L.: Direct determination of the magnetic structure of the delta phase of oxygen. *Phys. Rev. Lett.* **93** 55502 (2004).
161. Grenier B., Ziman T.: Modern quantum magnetism by means of neutron scattering. *C.R. Physique* **8** 717–736 (2007).
162. Mezei F.: New perspectives from new generations of neutron sources. *C.R. Physique* **8** 909–920 (2007)

Chapter 6

Tunable Exchange Bias Effects

Ch. Binek

Abstract Extrinsic control mechanisms of the interface magnetization in exchange bias heterostructures are reviewed. Experimental progress in the realization of adjustable exchange bias is discussed with special emphasis on electrically tunable exchange bias fields in magnetic thin film heterostructures. Current experimental attempts and concepts of electrically controlled exchange bias exploit magnetic bilayer structures where a ferromagnetic top electrode is in close proximity of magnetoelectric antiferromagnets, multiferroic pinning layers, or piezoelectric thin films. Various experimental approaches are introduced and the potential use of electrically controlled exchange bias in spintronic applications is briefly outlined. In addition, isothermal magnetic field tuning of exchange bias fields and extrinsically tailored exchange bias training effects are reported. The latter have been studied in a variety of systems ranging from conventional antiferromagnetic/ferromagnetic bilayers and core-shell nanoparticles to all ferromagnetic heterostructures where soft and hard ferromagnetic thin films are exchange coupled across a non-magnetic spacer. Such ferromagnetic bilayers show remarkable analogies to conventional exchange bias systems. At the same time they have the experimental advantage to provide direct access to the magnetic state of the pinning layer by simple magnetometry. A large number of exchange-coupled magnetic systems with qualitative differences in materials composition and coupling share a common physical principle that gives rise to training or aging phenomena in a unifying framework. Deviations from the equilibrium spin configuration of the pinning layer generate a force that drives the system back toward equilibrium. The initial nonequilibrium states can be tuned by temperature and applied set fields providing control over various characteristics of the training effect ranging from enhancement to complete quenching.

Ch. Binek (✉)

Department of Physics and Astronomy and the Nebraska Center for Materials and Nanoscience,
University of Nebraska, Lincoln, NE 68588, USA
e-mail: cbinek2@unlnotes.unl.edu

6.1 Introduction

Proximity effects in general and those of magnetic materials in particular are cornerstones of modern condensed matter physics. The investigation of exchange-coupled magnetic thin films has enormous technological importance particularly for applications which utilize spin-dependent transport across magnetic interfaces [1–4]. Exchange bias (EB) is a prototypical magnetic proximity phenomenon widely used in modern magnetic field sensors and read heads exploiting giant magnetoresistance (GMR) and tunnel magnetoresistance (TMR) effects. Scalability of read head sizes toward smaller devices is a prerequisite for the ongoing exponential growth of the areal storage density in magnetic hard disk drives. Remarkably, this exponential growth known as Moore’s law [5] shows an even increased rate since 1997 when GMR-based read heads with exchange-biased electrodes were first introduced in hard drive technology.

The basic physics of the EB phenomenon is best studied at the interface of exchange-coupled ferromagnetic (FM) and antiferromagnetic (AF) heterostructures [6–12]. In the proximity of an AF pinning layer a FM film can experience an exchange-induced unidirectional anisotropy. The latter reflects its presence most prominently by a shift of the FM hysteresis along the magnetic field axis and is quantified by the amount $\mu_0 H_{\text{EB}}$ of the shift. The EB effect is initialized when field cooling an AF/FM heterosystem to below the blocking temperature, T_B , where AF order establishes at least on mesoscopic scales [13].

Microscopically the EB phenomenon depends on a large number of system-specific details like structural and magnetic interface roughness and anisotropy to name just a few. Therefore, a large number of theories have been proposed competing to explain the origin of the EB effect. This chapter will not attempt to give an overview of the microscopic theories or even favor a particular microscopic mechanism over another one. The interested reader is referred to a number of excellent review articles with emphasis on experimental and theoretical aspects, respectively [8–11, 14].

Despite the ongoing controversy about “the origin” of EB many of the macroscopic observations are satisfactorily summarized in the phenomenological description which goes back to Meiklejohn and Bean. It has often been stated that the Meiklejohn–Bean (MB) expression is an invalid oversimplification which overestimates the expected EB field typically by more than an order of magnitude. This overestimation arises when bulk properties and ideal interface conditions are naively assumed. However, when using the MB expression in its appropriate phenomenological sense and the non-trivial relation between macroscopic and microscopic parameters is carefully considered, the MB approach remains a useful description with even quantitative predictive power. State-of-the-art molecular beam epitaxial growth of EB heterostructures allows the fabrication of nearly ideal interfaces with no or negligible roughness on mesoscopic lateral length scales. In fact, such ideal interface regions follow precisely the MB prediction of vanishing EB for compensated AF interfaces [15]. Similar results are known already for nearly a decade now from experiments using artificial AF superlattices as virtually ideal pinning systems

confirming the MB approach [16]. Therefore, it is meanwhile widely accepted that EB requires a net irreversible AF interface magnetization S_{AF} coupling via exchange with the FM interface magnetization S_{FM} [17]. It turns out to be the major challenge for microscopic theories to explain why S_{AF} can be surprisingly large for antiferromagnets with compensated AF surfaces and can be surprisingly low in systems with uncompensated surfaces. The MB description does not address these questions. It is therefore not a flaw of the MB approach when unrealistic values for S_{AF} for instance are used which consequently overestimate the EB fields. It is one of the major experimental and theoretical insights in recent years that only a fraction of the AF interface magnetization remains stationary during the FM magnetization reversal. It is this stationary or irreversible fraction S_{AF} of the AF interface magnetization that should be used in the MB expression to estimate realistic EB field values.

Another potential flaw of the MB approach originating from the assumption of uniform rotation of the ferromagnet seems also significantly overrated. Intrinsic properties which determine for instance the absolute values of the coercive fields and the magnetization reversal process are not necessarily relevant for the EB field, only their asymmetry with respect to the magnetic zero field determines the EB field. The latter is therefore insensitive on microscopic and micromagnetic details as long as they do not affect the irreversible interface magnetization.

When considering the exchange coupling of strength J between S_{AF} and the FM interface magnetization, S_{FM} , as phenomenological parameters the original MB approach describes in fact major features of the EB effect in a correct manner. In particular, the EB field, $\mu_0 H_{EB}$, quantifying the shift of the FM hysteresis loop along the magnetic field axis is in its simplest form expressed as

$$\mu_0 H_{EB} = -\frac{J S_{AF} S_{FM}}{M_{FM} t_{FM}}, \quad (6.1)$$

where M_{FM} is the saturation magnetization of the FM film and t_{FM} is its thickness. The latter inverse thickness dependence on the FM film has been confirmed in countless investigations and reflects the true interface nature of the effect. Experimentally this interface sensitivity implies that control over interface properties is crucial for systematic studies of the phenomenon.

Meiklejohn and Bean derived Eq. (6.1) from the Stoner–Wohlfarth type model where uniform rotation of FM magnetization is induced by a magnetic field applied along the easy AF and FM axes. In addition to the free Stoner–Wohlfarth ferromagnet, exchange coupling at the interface between the ferromagnet and a stationary AF pinning system of infinite anisotropy is the major ingredient of the simple MB model. Equation (6.1) is analytically derived from the MB energy expression. The most convenient and original MB approach contracts the Zeeman and the AF/FM coupling energy into an effective Zeeman term where the renormalized field is interpreted as the sum of the applied field and $\mu_0 H_{EB}$.

MB-type approaches have been studied for a variety of generalizations including finite anisotropy of the antiferromagnet, finite AF film thickness, and arbitrary orientation of the applied field with respect to the easy axes to name just a few [18].

In contrast to the usual analytic MB approach discussed elsewhere, Fig. 6.1 provides a graphical illustration associated with the evolution of the MB energy on variation of the magnetic field. Here, as an example, the applied magnetic field makes an angle of $\alpha = \pi/6$ with respect to the easy axis of the Stoner–Wohlfarth-type ferromagnet with uniaxial anisotropy of energy density K . The displayed hysteresis loop, M/M_s vs. h , represents the projection, $M = M_s \cos(\alpha - \beta_{\min}(h))$, of the uniformly rotating magnetization vector \underline{M} of magnitude M_s onto the direction of the reduced magnetic field $h = \mu_0 M_s t_{\text{FM}} H$. Rotation of \underline{M} takes place in accordance with the evolution of the angle $\beta_{\min} = \beta_{\min}(h)$. The latter follows a crossover from a global energy minimum into a local minimum on approaching the coercive fields h_{c1} and h_{c2} , respectively. In addition to the hysteretic M/M_s vs. h curve the evolution of the corresponding energy density

$$E/A = -h \cos(\alpha - \beta) + K \sin^2 \beta - J S_{\text{AF}} S_{\text{FM}} \cos \beta \quad (6.2)$$

is plotted with $K=0.5$, $J S_{\text{AF}} S_{\text{FM}} = 0.2$ (solid line) for selected fields $h = \pm 2$ (upper right and lower left insets), and for the switching fields $h = h_{c1}$ (upper left inset) and $h = h_{c2}$ (lower right inset) where M changes sign, respectively. It is the asymmetry of the switching fields with respect to $h=0$ which determines the EB field $h_{\text{EB}} = (h_{c1} + h_{c2})/2$. Full lines in the insets of Fig. 6.1 show the respective energy densities when exchange coupling between the ferromagnet and the AF pinning layer is included. The dashed curves show the corresponding energy densities of the same Stoner–Wohlfarth ferromagnet in the absence of coupling ($J = 0$). The comparison of these energy curves in particular at h_{c1} and h_{c2} illustrates the mechanism giving rise to the EB shift h_{EB} .

In the presence of the strong positive field $h=2$ the magnetization vector aligns virtually parallel to the magnetic field. Here, in a state close to positive saturation, the Zeeman energy controls the pronounced minimum in E/A vs. β where β measures the orientation of the magnetization with respect to the easy axis of the ferromagnet. The dominance of the Zeeman energy over the AF/FM coupling energy is reflected in the fact that the energy densities with (solid line) and without coupling (dashed line) virtually coincide. On lowering the magnetic field toward $h = h_{c1}$, antiparallel orientation of M with respect to the applied field becomes unstable. The instability is reflected by a saddle point in E/A vs. β . The dashed curve in the upper left diagram of Fig. 6.1 indicates that in the absence of interface coupling the instability and, hence, magnetization reversal set in at $h_{c1}(J = 0) = h_{c1} - h_{\text{EB}}$. Finally, negative saturation at $h = -2$ is virtually achieved, corresponding to a pronounced minimum in E/A vs. β and parallel alignment of the magnetization vector with the applied field. With increasing magnetic field again antiparallel alignment of M with respect to h becomes unstable in accordance with a saddle point in E/A vs. β at $h_{c2} = h_{c2}(J = 0) + h_{\text{EB}}$. This switching field is lowered by the amount $|h_{\text{EB}}|$ in comparison to the switching field of the unpinned Stoner–Wohlfarth ferromagnet

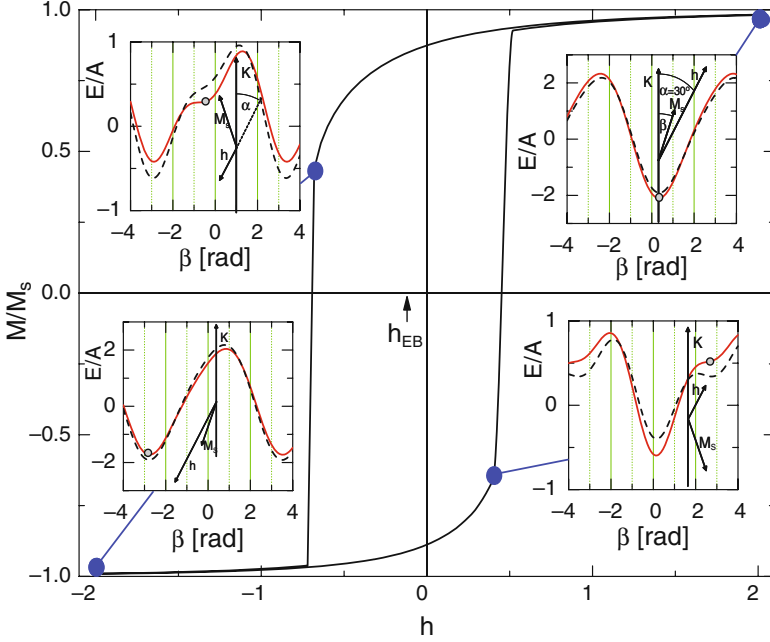


Fig. 6.1 Field dependence M/M_s vs. h of a uniaxial anisotropic Stoner–Wohlfarth ferromagnet exchange coupled to the stationary and field-independent interface magnetization of an adjacent pinning system. The coupling gives rise to the exchange bias effect shifting the loop along the field axis by the amount $|h_{EB}|$ indicated by an arrow. Insets show the energy densities E/A vs. β for $h = 2$ (upper right), $h = h_{c1}$ (upper left), $h = -2$ (lower left), and $h = h_{c2}$ (lower right) with (solid lines) and without (dashed lines) exchange coupling. Magnetization states of specific interest are marked by large dots on the M/M_s vs. h curve. The corresponding minima in E/A vs. β are indicated in the energy densities by small dots. Pictograms show the easy axis of the ferromagnet of anisotropy energy density K and the relative orientation of the magnetization and the magnetic field. The former rotates uniformly with constant magnitude M_s in contrast to h which is applied under a constant angle of $\alpha = \pi/6$ with respect to the easy axis

$[h_{c2}(J = 0)]$. The dashed E/A vs. β curve in the lower right inset of Fig. 6.1 shows still a clear local minimum when the actual system with coupling evolves already into the saddle point instability.

The shift of the FM hysteresis loop along the magnetic field axis is often accompanied by an EB-induced loop broadening [19, 20]. This effect is not included in the MB description. The understanding of the loop broadening makes it necessary to consider the role of the loosely coupled majority fraction of AF interface spins which do not affect the EB field. The magnetic moment of these loose spins is not irreversible but follows to some extent the magnetization reversal of the top ferromagnet giving rise to a drag effect which broadens the FM hysteresis. More quantitatively based on mean-field arguments it has been predicted that the FM coercivity is related to the AF interface susceptibility [21]. Loosely coupled spins

are in particular sensitive to either exchange or applied magnetic fields and, hence, increase the AF interface susceptibility and by that the FM coercivity. The coercivity enhancement accompanies the EB effect and is characteristically reduced when the blocking temperature T_B of vanishing EB is approached from $T < T_B$. While loosely coupled moments flip easier when their AF neighboring spins lost long-range order, nevertheless a drag effect on the adjacent FM film is still present above the blocking temperature and even above the Néel temperature, T_N , of the pinning layer allowing for persistence of loop broadening above T_N .

In addition to the EB loop shift and broadening, a gradual degradation of the EB field can take place when cycling the heterostructure through consecutive hysteresis loops [22–32]. This aging phenomenon is known as training effect. It is quantified by the $\mu_0 H_{EB}$ vs. n -dependence, where n labels the number of loops cycled after initializing the EB via field cooling. EB and its accompanying training effect have been observed in various magnetic systems [8, 33–39]. The MB expression does not directly address the phenomenon of EB training. However, Eq. (6.1) correlates the bias field with the AF interface magnetization S_{AF} . The latter can and typically does change during successively cycled hysteresis loops of the FM top layer such that $S_{AF} = S_{AF}(n)$ gives rise to an n -dependence in $\mu_0 H_{EB}$. This chapter dedicates a section on the recent progress in understanding aging phenomena in various exchange-coupled systems. Selected experiments evidence certain control over the aging effects through the initialization protocol that sets the magnetization state of the pinning system.

While many intrinsic details of the EB phenomenon are still a matter of scientific debate, extrinsic control of the EB has been added in recent years to the major research topics in this field. Among the various possible control mechanisms, electrically tuned EB appears most attractive for spintronic applications. Research on electrically controlled EB has been initiated by work on $\text{Cr}_2\text{O}_3/\text{CoPt}$ heterostructures stimulating at the same time a revived interest in magnetoelectric materials. The same motivation, namely control of magnetism via electric fields, created recently a tremendous renewed interest in multiferroic materials where multiple ferroic order parameters (magnetic, electric, and elastic) can be simultaneously present and sometimes significantly couple. Conjugate magnetic and electric fields can be used to manipulate the respective cross-coupled order parameter. Switching of FM order by an electric field for instance promises significant impact in the design of future spintronic devices. Note, however, that the magnetoelectric effect does not require multiferroics and multiferroics do not necessarily show appreciable magnetoelectric effects. Actually in most cases they do not [40]. Nevertheless, some of the multiferroic materials promise potential for spintronic applications in addition to their more general exciting physical properties. Most recently studied multiferroics can be classified into single-phase and two-phase systems. Single-phase multiferroics are predicted to be rare [41]; however, many perovskite-type oxides have been successfully exploited to control magnetic order to some extent by electrical means and vice versa.

Next, various attempts of electric and magnetic field control of EB-related phenomena are introduced. Some of them are based on multiferroics and most are not.

6.2 Electrically Tuned Exchange Bias

6.2.1 Electrically Tuned Exchange Bias with Magnetolectrics

Experiments on the perpendicular EB heterostructure $\text{Cr}_2\text{O}_3/\text{CoPt}$ pioneered the field of electrically tuned EB [42–46]. Here the magnetolectric Cr_2O_3 has a twofold role. It serves as an AF pinning layer allowing at the same time for electrical tuning of the AF interface magnetization. Exchange coupling of the latter with the FM interface magnetization of the perpendicular anisotropic CoPt gives rise to electrically tunable interface coupling energy and, hence, to electrically tunable EB fields. The AF Cr_2O_3 is a prototypical magnetolectric material. Its intrinsic magnetolectric effect sets in below the Néel temperature, $T_N = 307$ K, together with AF long-range order when spatial and time inversion symmetry are broken, respectively, but build a symmetry operation in combination. AF magnetolectrics do not depend on spontaneous ferroelectric polarization to achieve coupling between the magnetization and an electric field and are therefore complementary to the multiferroic materials discussed in Section 6.2.2.

In a magnetolectric material an applied electric field induces a net magnetic moment which can be used to electrically manipulate the magnetic states of adjacent exchange-coupled FM films. More specifically, the linear magnetolectric effect is characterized by a linear magnetic response M^i (electric response P^i) induced by the application of an electric field E_j (magnetic field H_j) such that $\mu_0 M^i = \alpha_{\text{me}}^{ij} E_j$ and $P^i = \alpha_{\text{em}}^{ij} H_j$, where $\alpha_{\text{em}}^{ij} = \alpha_{\text{me}}^{ji} = \alpha_{\text{em}}^{ji}$ are the tensors of magnetolectric susceptibility and its transpose counterpart while i, j label the vector and tensor components, respectively [47, 48]. The magnetolectric susceptibility tensor α_{me}^{ij} of Cr_2O_3 has diagonal structure with $\alpha_{\text{me}}^{11} = \alpha_{\text{me}}^{22} = \alpha_{\perp}$ and $\alpha_{\text{me}}^{33} = \alpha_{\parallel} \approx 4.13$ ps/m at its maximum value achieved close to $T = 263$ K. This magnetolectric susceptibility is small in comparison to some other magnetolectric materials [49]. However, the AF nature of Cr_2O_3 and its appreciably high T_N still make it a first choice candidate for an intrinsic magnetolectric material when applications at or close to room temperature are envisioned.

Figure 6.2 shows the schematics of a $\text{Cr}_2\text{O}_3/\text{CoPt}$ heterostructure for electrically tunable EB. Here the electric field orients along the (111) direction of Cr_2O_3 taking advantage of the parallel magnetolectric susceptibility. Note that EB requires a non-zero projection of S_{AF} on S_{FM} making a top ferromagnet with perpendicular anisotropy mandatory when α_{\parallel} is used.

The current status of the description of the microscopic origin of the magnetolectric effect in Cr_2O_3 has been summarized by Alexander and Shtrikman [50] and by Hornreich and Shtrikman [51]. Figure 6.2 shows a sketch of a section of the unit cell of Cr_2O_3 . It indicates the A (spin up) and B (spin down) sites of the Cr^{3+} ions along the threefold rotation axis. In the presence of a positive applied electric field, the Cr^{3+} ion on the A site moves toward the upper triangle of O^{2-} ions. The corresponding ion on the B site moves in the same direction along the symmetry axis toward the smaller triangle of O^{2-} ions. The latter triangle is shared among the two

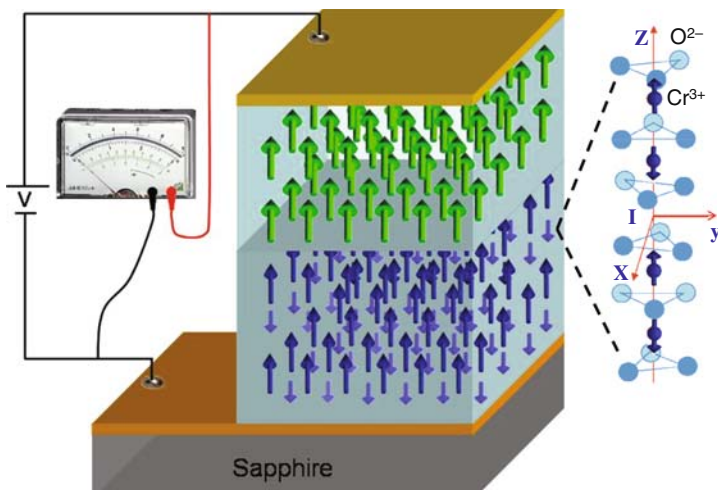


Fig. 6.2 Sketch of an electrically controlled EB heterosystem based on the magnetoelectric anti-ferromagnet Cr_2O_3 and a thin exchange-coupled CoPt multilayer. A voltage V applied across the *top* and *bottom* electrodes creates an electric field $E = V/d$ where d is the thickness of the insulating Cr_2O_3 film. The E field induced the magnetization $\Delta M \propto \alpha_{\parallel} E$ in Cr_2O_3 . It contributes to the interface magnetization S_{AF} and modifies the EB field. Arrows indicate the AF and FM spin structure in the Cr_2O_3 bottom and CoPt top layer, respectively. The right sketch depicts the crystal and spin structure of Cr_2O_3 . The spin orientations in the four sublattices are shown for one of the two 180° domains. The $S = 3/2$ spins of the Cr^{3+} ions are aligned along the threefold symmetry axis. O^{2-} ions form distorted octahedrons (distortion not shown) surrounding the Cr^{3+} ions. Electrically induced displacement of the latter into crystal fields of alternating higher and lower strength gives rise to the single ion contribution of the magnetoelectric effect (see text)

distorted octahedra of O^{2-} ions, which surround the Cr^{3+} ions on the A and B sites. The asymmetry in the change of the crystal fields experienced by A and B ions gives rise to the single-ion contributions of the magnetoelectric effect. In terms of a spin Hamiltonian, the single-ion contributions reflect the changes of the Landé g -tensor and the single-ion anisotropy, which differ for the spins at position A and B in the presence of an electric field. In addition, the asymmetric displacement of the ions gives rise to different modifications of the exchange interaction between Cr^{3+} ions. The resulting electric field-induced change of the exchange integrals is known as the two-ion contribution to the magnetoelectric effect.

Electric control of the EB field can be approached at least in two very distinct ways. An electric field can be applied simultaneously with a magnetic field in order to magnetoelectrically anneal the AF pinning layer. Magnetoelectric annealing is a well-known procedure to bring a magnetoelectric antiferromagnet into a single domain state by cooling the system from $T > T_N$ to below T_N in the presence of E and B fields. By energetically favoring one of the AF 180° domains over the other, the magnetic state of the AF interface magnetization is selected too and at least partially irreversibly frozen in. In an EB system using a magnetoelectric pinning layer the interface magnetic state can be magnetoelectrically selected. This type of

electric-controlled EB has been named magnetoelectric switching because it allows switching between positive and negative EB fields by controlling the sign of the product $E \cdot B$ [39]. This pronounced effect is highly interesting from a fundamental point of view. Spintronic applications, however, favor an electric control of the EB field at constant $T < T_N$ where ideally T_N is significantly above room temperature.

Recently, a reversible electrically induced shift of the magnetic hysteresis loops along the magnetic field axis has been achieved. The heterostructure follows the schema in Fig. 6.2 and is based for the first time on an all thin film $c\text{-Al}_2\text{O}_3/\text{Pt}5.7\text{nm}/\text{Cr}_2\text{O}_3$ 50 nm/ Pt 0.5 nm/ $[\text{Co}$ 0.3 nm/ Pt 1.5 nm] $_3/\text{Pt}$ 1.5 nm heterostructure.

Similar experiments have been performed earlier in $\text{Cr}_2\text{O}_3(111)/\text{CoPt}$ heterostructures using bulk Cr_2O_3 single crystals as AF pinning systems with magnetoelectric properties [40, 41]. Note, however, that millimeter thick single crystals require orders of magnitude higher voltages to achieve the electric fields that can be realized in nanometer thin films by a few millivolts. It is important to stress that the electrically controlled EB shown in Fig. 6.3 resembles a global effect. Here the tunable exchange anisotropy affects the entire FM top electrode and the EB field can be reversibly changed back and forth with the applied electric field. Competing EB systems based on multiferroic pinning layers show significantly larger isothermal EB tuning effect but are limited so far to local or irreversible control [52, 53]. A variety of spintronic applications based on electrically controlled exchange bias have been proposed. Those concepts of spintronic applications using electrically controlled EB have been pioneered by the authors in Refs. [42, 43]. Here spin-dependent transport

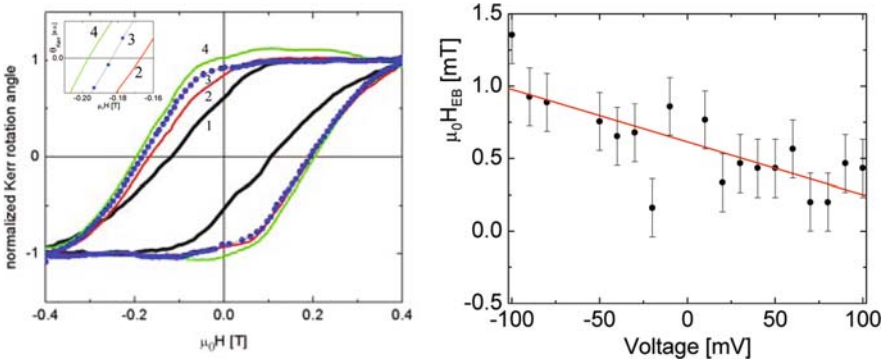


Fig. 6.3 The *left* frame shows normalized magnetic hysteresis loops of the all thin film $\text{Cr}_2\text{O}_3(111)/\text{CoPt}$ heterostructure measured by polar magneto-optical Kerr effect. Loop 1 is measured at $T=300$ K. Loops 2, 3, and 4 are measured after magnetoelectric annealing in $\mu_0 H = -0.4$ T and $V = -100$ mV from $T=300$ K to $T=250$ K $< T_N$. The isothermal loops have then been measured at $T=250$ K in the presence of applied axial voltages $V = -100$ mV (2), $+90$ mV (3), and $+100$ mV (4), respectively. The inset in the left frame provides a detailed look onto the electrically controlled change of the negative coercive fields of loops 2, 3, and 4. The right frame depicts the systematic results of the electric field control of the exchange bias field. The line is a linear best fit to the $\mu_0 H_{EB}$ vs. V data

devices with electrically controlled resistance states have been suggested. In general, magnetoelectrically induced interface magnetization provides control of the pinning in exchange-biased GMR- or TMR-type structures. In the GMR-type structures the active magnetoelectric material is used as a tunable pinning bottom layer offering new versatility for logic and memory devices based on a change of resistance due to a change of the magnetic configurations. In TMR-type structures the conventional passive tunneling barrier can be replaced by a magnetoelectrically active barrier material [42]. The electric field-induced magnetization of the latter allows switching magnetic states of exchange-coupled layers by pure electrical means. Following these suggestions numerous variations have been proposed [54]; often the magnetoelectric antiferromagnet has been replaced by a multiferroic component like BiFeO_3 [55–57].

6.2.2 Electrically Tuned Exchange Bias with Multiferroics

The above discussed attempts to achieve electrically tuned EB with the help of magnetoelectric antiferromagnets require further investigations and show clearly the need for an increase of the magnetoelectric response in order to accomplish appreciable electric tuning effects. In the case of magnetoelectric antiferromagnets significant efforts are made to further improve the structural and dielectric properties of Cr_2O_3 films allowing for higher applied electric fields and improved interface coupling [58].

Many research teams who currently focus on the use of multiferroic materials expect a qualitative progress from this class of materials. The latter show simultaneous presence of two or more ferroic order parameters like ferroelectric polarization and (anti)ferromagnetic order. This coexistence seems to make them obvious candidates for the quest of increased magnetoelectric response. The renewed excitement about multiferroics for spintronic applications is based on this hope. It is supported by a fundamental inequality which states that the square of the magnetoelectric susceptibility is limited by the product of the magnetic and the dielectric susceptibility [59]. Since multiferroics have spontaneous ferroelectric and ferromagnetic order the latter susceptibilities are high and their product limiting the magnetoelectric susceptibility α is high. However, to take advantage of this potential upper limit of α strong coupling between the ferroic order parameters is required. The coupling is, however, typically weak. Hence, the magnetoelectric susceptibility of most multiferroics is at room temperature or above disappointingly weak and it is not straightforward to exceed the magnetoelectric bulk susceptibility of, e.g., Cr_2O_3 which is of the order of 4 ps/m close to room temperature [60]. Nevertheless, in view of the potential applications there is an intense search for the ideal magnetoelectric single-phase multiferroic [61–69].

Currently there are at least two multiferroic single-phase materials under intense investigation for use in electrically controlled EB applications [44, 45]. Both YMnO_3 and BiFeO_3 order antiferromagnetically with Néel temperatures of 90 and

643 K, respectively. Despite their AF order the terminology multiferroics is still applied in the literature in a somewhat generalized sense.

Complete electrically induced suppression of EB has been achieved at $T=2$ K in an YMnO_3/Py heterostructure when applying a voltage of 1.2 V across the c-axis of the hexagonal YMnO_3 film of 90 nm thickness [44]. So far, the effect is, however, irreversible which means that a voltage of opposite sign does not recover any EB effect. Moreover, the limitation to low temperatures makes it an interesting system for proof of principle but little attractive for the envisioned applications.

This situation changes in part when BiFeO_3 is used as an electrically controllable pinning layer [45]. In heterostructures of the type $\text{BiFeO}_3/\text{CoFe}$ 10 times higher electric potential differences of ± 12 V were applied across the 100–150 nm thick BiFeO_3 films. The resulting electric fields achieved local magnetization reversal on a lateral length scale of about 2 μm . The limitation to local switching seems to originate from the characteristic domain pattern of the AF, ferroelectric, and ferroelastic order parameters. It remains to be shown if this limitation can be overcome. Subsequently, it is shown that magnetoelastic coupling alone is a very effective and simple way to achieve electrically controlled magnetization.

6.2.3 Piezomagnetically and Piezoelectrically Tuned Exchange Bias

As discussed above, one of the major challenges which microscopic theories of EB face is to explain the quantitative presence of net AF interface magnetization remaining stationary during the FM reversal. The details of the frozen interface magnetization in various systems are affected by a huge variety of crucial influences. Very likely this is one of the reasons why “the origin of EB” has not yet been found in terms of a universal mechanism despite countless attempts. It seems more likely that there is nothing like the universal microscopic mechanism. Many microscopic processes can lead to AF interface magnetization which couples with the adjacent ferromagnet giving rise to EB. For this reason even today a phenomenological description of the EB effect like the Meiklejohn–Bean approach is still valuable.

An exotic possible origin or at least contribution to EB is found for instance in the rutile structured antiferromagnet FeF_2 . The latter has been extensively studied as a prototypical EB pinning system. Compensated and uncompensated AF surfaces can be realized via (111) or (100) surfaces. The (111) surface has been studied at length in order to understand the origin of AF interface magnetization in the particularly puzzling case of compensated surfaces. In addition to the impact of surface roughness and defects which may create random field-type AF domains [70, 71] a more exotic mechanism of stress-induced piezomagnetism has been discussed as one of the possible contributions to the AF interface magnetization [72–75].

Piezomagnetism is known to create the vertical shift of the EB hysteresis loops in $\text{FeF}_2(110)/\text{Fe}$ [76]. Since correlation between the horizontal and vertical loop

shifts is well known [77] it is straightforward to correlate piezomagnetism also with EB fields. The concept of an activation of the symmetry-allowed piezomagnetism in FeF_2 via lattice mismatch-induced stress has been more systematically evidenced in an investigation of the EB heterostructure $\text{Fe}_{0.6}\text{Zn}_{0.4}\text{F}_2/\text{Fe}$. Here external shear stress along the [110] direction activates a piezomoment within the (110) plane that contributes to the AF interface magnetization S_{AF} and, hence, to the EB field [78].

More generally, stress-induced control of magnetic anisotropy which potentially includes also unidirectional anisotropy is a very promising tool to achieve electric control over magnetic states in very simple heterostructures. The use of magnetoelastic coupling for electrically controlled magnetism is well known from investigations of two-phase multiferroics which include artificially grown ferroelectric/ferromagnetic heterostructures such as $\text{BaTiO}_3/\text{La}_{0.66}\text{Sr}_{0.33}\text{MnO}_3$, $\text{BiFeO}_3/\text{SrTiO}_3$, nanopillar-embedded structures of $\text{BaTiO}_3-\text{CoFe}_2\text{O}_4$ or $\text{BiFeO}_3-\text{CoFe}_2\text{O}_4$, $\text{Pb}(\text{Zr}, \text{Ti})\text{O}_3/\text{CoPd}$, and $\text{Pb}(\text{Zr}, \text{Ti})\text{O}_3/\text{terfenol-D}$ [79–84]. The magnetoelastic behavior of these composite materials resembles the product properties of the magnetoelastic effect of the ferromagnetic component and the piezoelectric effect of the (relaxor) ferroelectric [85]. Complex oxides have been some of the most favored materials.

Recently, however, reversible control of magnetism has been reported for a remarkably simple ferroelectric/FM heterostructure. A polycrystalline Fe thin film deposited on the c-plane of a BaTiO_3 single crystal shows a large magnetization change in response to the ferroelectric switching and structural transitions of BaTiO_3 controlled by applied electric fields and temperature, respectively [86]. Interface strain coupling is the primary mechanism altering the induced magnetic anisotropy. As a result, coercivity changes up to 120% occur between the various structural states of BaTiO_3 . Up to 20% coercivity change has been achieved via electrical control at room temperature. This is remarkable considering the fact that the change of the BaTiO_3 lattice parameter within the c-plane is only a secondary effect of the far more pronounced piezoelectric deformation of the c-axis when the electric field is applied along the latter in the tetragonal phase of BaTiO_3 . Hence, much larger effects can still be expected. The concept of ferro- or piezoelectrically controlled magnetism can be straightforward generalized toward electrically controlled EB when taking advantage of the fact that the magnetoelastic coupling constant of some antiferromagnets like CoO is even higher than the corresponding values for the simple 3d metals [87].

6.3 Magnetic Field Control of Exchange Bias

The easiest way to tune the EB field in common EB heterostructures is achieved via the initializing field-cooling process. It takes place in the presence of a freezing field, h_f , applied on cooling the heterostructure to below the Néel temperature, T_N , of the AF pinning layer. Here, the orientation of the freezing field can select either negative or positive EB fields [69]. Note, however, that the positive EB fields established in

$h_f < 0$ have nothing in common with the effect known as positive EB. The latter is observed only when positive (negative) freezing fields give rise to positive (negative) EB fields. Positive EB is a rather unusual case but sometimes observed in systems where the interface exchange interaction is AF and, at the same time, the freezing field applied during the field-cooling procedure is strong enough to overcome the exchange interaction on cooling the system to below the blocking temperature [88–90].

Figure 6.4 illustrates this situation and clarifies a common misconception which confuses the presence of positive EB fields with a sufficient condition to identify the positive EB effect. The Zeeman energy of the interface magnetization in a freezing field favors parallel alignment of S_{AF} with respect to S_{FM} . AF interface coupling in turn favors antiparallel alignment of S_{AF} with respect to S_{FM} . The net effects of the competition between these two energies on the EB field has been experimentally and theoretically studied for instance in Ref. [91]. Inspection of Fig. 6.4 illustrates intuitively that the measurement of the EB field in a single freezing field is not an appropriate tool to determine the sign of the interface coupling, J . In fact, independent of the sign of J , field cooling allows setting the EB field at negative and positive values [92]. Next these details and the specific case of positive EB are discussed with the help of the spin structures displayed in Fig. 6.4.

The two upper frames of Fig. 6.4 show sketches of hysteresis loops after field cooling an EB heterostructure with FM interface coupling $J > 0$ in positive (left upper frame) and negative (right upper frame) freezing fields h_f . When applying h_f at $T > T_N$ no AF long-range order has established and pinning is absent. Hence, the FM top layer is free to align parallel to h_f giving rise to $S_{FM} > 0$ in $h_f > 0$ and $S_{FM} < 0$ in $h_f < 0$. This state of S_{FM} affects the orientation of the AF interface magnetization which establishes on cooling to below T_N . The coupling energy $J S_{AF} S_{FM}$ together with the Zeeman energy control the orientation of S_{AF} . In the case $J > 0$ both the exchange interaction and the Zeeman energy favor parallel alignment of S_{AF} and S_{FM} such that $J S_{AF} > 0$ for $h_f > 0$ and $J S_{AF} < 0$ for $h_f < 0$. Since S_{FM} follows the overall magnetization of the FM layer during a hysteresis loop it is the sign of the stationary product $J S_{AF}$ that determines the sign of the EB field in accordance with Eq. (6.1). Hence, in the case of $J > 0$ negative (positive) EB fields are achieved in positive (negative) freezing fields. Obviously, the positive EB field shown in the upper right frame has nothing in common with the phenomenon of positive EB.

The more complex scenario appears in the case of AF exchange coupling $J < 0$. Both of the two lower frames of Fig. 6.4 show sketches of hysteresis loops after field cooling an EB heterostructure with AF interface coupling in positive freezing fields. The lower left frame displays the situation of field cooling in a moderate magnetic field $0 < h_f < |J S_{FM}|$. Again, when applying h_f at $T > T_N$ there is no pinning effect and the FM top layer aligns parallel to $h_f > 0$ giving rise to $S_{FM} > 0$. The coupling energy $J S_{AF} S_{FM}$ favors now antiparallel alignment of S_{AF} relative to $S_{FM} > 0$. The product $J S_{AF} < 0$ can be interpreted as an exchange field acting on the AF interface magnetization S_{AF} on cooling. At the same time, S_{AF} has potential or Zeeman energy in the applied freezing field $h_f > 0$ which favors $S_{AF} > 0$.

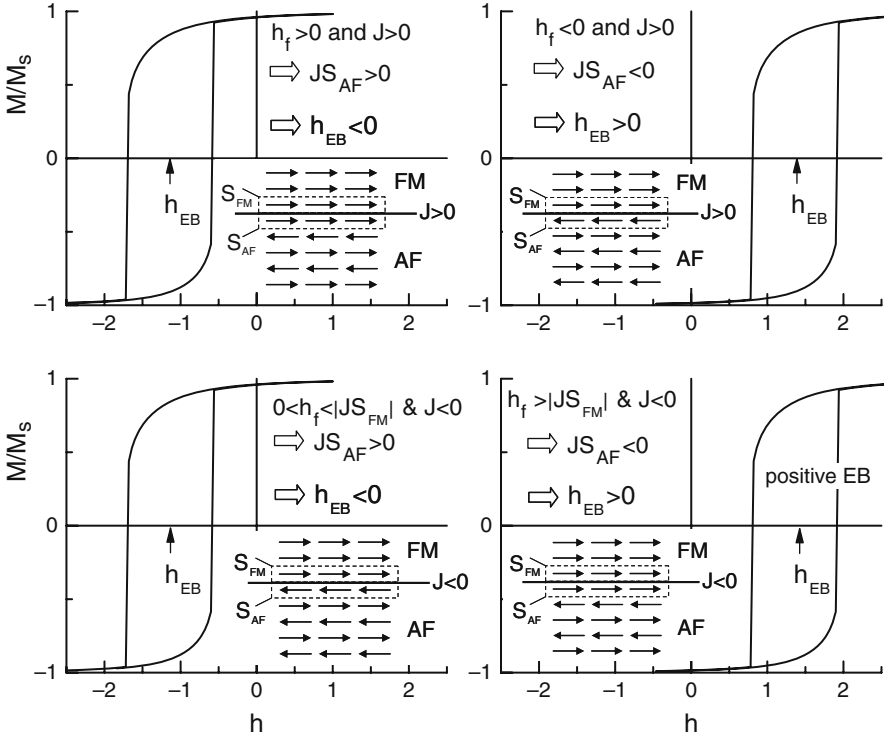


Fig. 6.4 Hysteresis loops of an ideal EB heterosystem with FM interface coupling $J > 0$ (upper left and right frames) and AF interface coupling $J < 0$ (lower left and right frames). For $J > 0$ (upper frames) negative (positive) EB fields h_{EB} are indicated by arrows and achieved by field cooling in a freezing field $h_f > 0$ ($h_f < 0$). For $J < 0$ (upper frames) field cooling in $0 < h_f < |J S_{FM}|$ creates a regular negative EB field while field cooling in $h_f > |J S_{FM}|$ gives rise to a positive EB field which is the fingerprint of the positive EB effect. The frozen AF spin structure and the FM spin structure during the field-cooling process are depicted by arrows. The ideal interface is indicated by a solid line, AF and FM interface spins are marked by boxes (dashed lines).

However, as long as $0 < h_f < |J S_{FM}|$ is fulfilled, the interface exchange energy overcomes the Zeeman energy resulting in $S_{AF} < 0$ and, hence, $J S_{AF} > 0$ giving rise to a regular negative EB field despite $J < 0$.

The situation changes, however, in the case of large positive freezing fields $h_f > |J S_{FM}|$. Now the Zeeman energy overcomes the AF interface coupling giving rise to a parallel alignment of S_{AF} and S_{FM} during the field-cooling process. Hence, $J S_{AF} < 0$ results in a positive EB field in accordance with Eq. (6.1). The latter scenario displayed in the lower right frame of Fig. 6.4 describes the positive EB effect. Out of all situations displayed in Fig. 6.4, only here a positive freezing field gives rise to a positive EB field due to AF interface coupling. Of course one can

repeat the arguments above for the analogous situation of negative EB fields when field cooling took place in negative freezing fields.

Tuning the EB field by cooling heterostructures in the presence of an applied magnetic field to below the blocking temperature is experimentally straightforward to do but not very attractive for most applications. Here, temperature is typically not a control parameter and the EB field needs to be tuned just with the applied magnetic field at about room temperature. For an AF system an applied homogeneous magnetic field affects the AF long-range order in many ways similarly as temperature does. Increased temperature and increased magnetic fields weaken or even completely suppress AF long-range order. It is therefore not surprising that even below T_B strong magnetic fields typically of the order of several 10 T can set the EB field to a new value which is observed when FM hysteresis loops are measured in moderate magnetic fields significantly smaller than the set field [93]. Again, for applications, it is far more attractive to achieve such a resetting of the EB with set fields of the order of 1 T or below such that no high-field technology is needed.

Recently, Cr_2O_3 has been used as an AF pinning system in a magnetic trilayer structure having two $\text{Cr}_2\text{O}_3/\text{Fe}$ EB interfaces [94]. Here, similar to the magneto-electrically switchable interface magnetization in $\text{Cr}_2\text{O}_3(111)/\text{CoPt}$ the AF surface magnetization in $\text{Cr}_2\text{O}_3(111)/\text{Fe}$ can be isothermally tuned by moderate applied magnetic fields.

Figure 6.5 shows two room temperature hysteresis loops of an Fe 10 nm/ Cr_2O_3 2.72 nm/Fe 10.8 nm trilayer structure after subjecting the system to negative (open circles) and positive (solid circles) DC fields of 1 T magnitude, respectively. The sign of the EB field is controlled exclusively by the applied set field. This is reminiscent of the scenario of changing the sign of the EB field depending on the strength of the cooling fields [86]. Note, however, that here EB tuning takes place isothermally. The pinning magnetization is reversed by a magnetic field only without breaking and reestablishing AF long-range order during a field-cooling process. Competition between AF exchange coupling of the pinning and the Fe magnetizations with the Zeeman interaction $\mu_0 H_{DC} \leq 0.2\text{T}$, AF coupling remains dominant

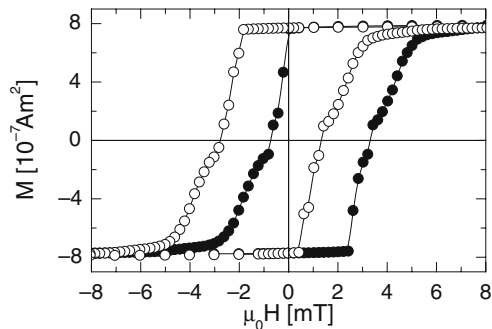


Fig. 6.5 Room temperature hysteresis loops of Fe10nm/ Cr_2O_3 2.72 nm Fe 10.8 nm trilayer after subjecting the system isothermally to $\mu_0 H_{DC} = -1\text{T}$ (open circles) and $\mu_0 H_{DC} = 1\text{T}$ (solid circles) DC magnetic fields. Lines are guide to the eye

over the Zeeman energy, resulting in regular (negative) EB. For larger $\mu_0 H_{DC}$, the Zeeman interaction overcomes the AF exchange coupling which aligns the pinning moments parallel to larger $\mu_0 H_{DC}$, leading to positive EB. The fact that very moderate magnetic fields are sufficient to isothermally tune the EB fields at room temperature promises applicability of this interesting effect in future spintronic devices.

So far we considered various possibilities in tuning the EB field by electric, thermal, and/or magnetic means. It has been mentioned earlier in this chapter that the EB fields can change with consecutively cycled hysteresis loops. Subsequently more light is shed on the physics of the training effect and means to tune strength and other characteristics of the training effect are presented.

6.4 Training Effect in Exchange-Coupled Bilayers

6.4.1 Physical Background of Training Effects in Various Systems

In a general sense training at finite temperature is observed as a consequence of changes in the spin structure taking place in most cases¹ away from a nonequilibrium toward an equilibrium configuration. This training effect deviates from the well-known aging phenomena in magnetic systems [95–100] by the fact that the spin configurational changes in the pinning system are triggered by the magnetic hysteresis loop of the pinned magnetic component which is magnetically coupled with the pinning system. The latter is AF in regular EB systems but can be a spin glass or a hard ferromagnet with a coercivity significantly larger than the coercivity of the pinned system.

Figure 6.6 shows a comparison of the physical mechanism of the training effect in regular AF/FM EB systems and hard/soft all FM bilayers. In both cases there is a pinning and a pinned layer. It is the pinning layer that experiences spin configurational changes on successively cycling the pinned layer through its magnetic hysteresis loop. The left column of sketches displays a regular AF/FM EB system where the pinning layer is an antiferromagnet. The right column displays an all FM hard/soft bilayer system. Here the pinning layer is a hard ferromagnet (HL). A soft ferromagnetic layer (SL) is pinned via AF RKKY interaction to the HL. In both cases the pinning layer can be initialized into a domain state which deviates from its perfect long-range order. In the case of an AF pinning layer an AF domain state is created during the field-cooling procedure which, in compensated EB systems, induces magnetization in the AF pinning layer and with that AF interface magnetization S_{AF} giving rise to EB in accordance with Eq. (6.1). Subsequently cycled hysteresis loops trigger spin configurational changes in the pinning layer which

¹ Hoffmann discussed the zero temperature training effect in EB systems with multiple AF easy anisotropy axes in terms of a triggered transition driving the pinning layer away from the equilibrium [31].

drive the antiferromagnet closer toward perfect long-range order characterized by the equilibrium AF order parameter η_e . The latter approach toward a new quasi-equilibrium spin configuration is accompanied by a decay of S_{AF} with increasing number of loops, n . The degrading AF interface magnetization reduces the magnitude of the EB field. This process resembles the training effect. It is again in accordance with Eq. (6.1) when a static interface magnetization is generalized into $S_{AF} = S_{AF}(n)$.

An analogous scenario takes place in the exchange-coupled HL/SL bilayers [3]. Here the initialization of the out-of-equilibrium domain state of the pinning layer is isothermally achieved by applying a negative (positive) set field after positive (negative) saturation of the HL. The sketches in the right column of Fig. 6.6 illustrate the HL domain state after its initializing in a negative set field (top). In this state the overall magnetization of the HL is reduced with respect to its saturation value and with it the HL interface magnetization. Therefore, the HL/SL coupling energy is reduced when the HL is in a FM domain state and the bias field characterizing the

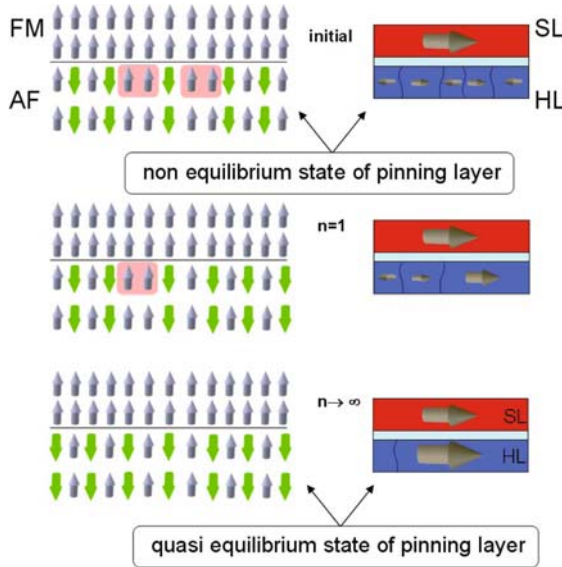


Fig. 6.6 Comparison of the training effect in an AF/FM and a HL/SL heterostructure. The left column depicts three sketches of an AF/FM EB heterostructure after initializing EB (top), after the first (middle), and after a very large number of hysteresis loops (bottom). The nonequilibrium AF domain state carries magnetization to the interface (horizontal line). Neighboring spin pairs with non-compensating moment contributing to S_{AF} are highlighted. The quasi-equilibrium state reflects the asymptotic approach of nearly perfect AF long-range order. S_{AF} is reduced and so is the EB field. The right column depicts sketches of a HL/SL heterostructure after initializing a FM domain state (top), after the first SL hysteresis loop (middle), and after a very large number of hysteresis loops (bottom). The nonequilibrium FM domain state reduces the HL interface magnetization. The latter recovers on subsequent cycling when the domain state asymptotically approaches nearly perfect FM long-range order

loop shift of the SL hysteresis is low. Subsequent SL hysteresis loops trigger spin configurational changes in the HL. The latter approaches asymptotically a quasi-equilibrium state of increased magnetization M_e . The increase in HL magnetization gives rise to an increase in its interface magnetization which increases the bias field.

Figure 6.7 displays the evolution of the free energy ΔF of the AF (upper left) and the FM HL (upper right) pinning layer when they change from their respective nonequilibrium states with order parameters η and M into the quasi-equilibrium states η_e and M_e . The pinning layer domain states associated with η and M and the final states associated with η_e and M_e are sketched, respectively. A harmonic approximation (dashed parabolas) of the Landau free energy landscape of the double well type catches already the essentials necessary to describe the triggered relaxation toward equilibrium quantitatively. The left bottom frame of Fig. 6.7 shows the evolution, $\mu_0 H_{EB}$ vs. n , of the EB field of the $\text{Cr}_2\text{O}_3/\text{Fe}$ heterostructure introduced previously. The solid squares are experimental data obtained from the hysteresis loop shifts measured at $T=300$ K by SQUID magnetometry. Open circles connected with eye-guiding lines are results of a single parameter fit of Eq. (6.5). The inset shows the 1st (solid diamonds), the 2nd (open diamonds), and the 10th (stars) hysteresis loop. The right bottom frame of Fig. 6.7 displays the evolution, $\mu_0 H_B$ vs. n , of the bias field of the all FM HL/SL system CoPtCrB 15 nm (HL)/ Ru 0.7 nm/ CoCr 3 nm (SL) [3]. The solid squares are experimental data obtained from the SL hysteresis loop shifts measured at $T=395$ K by SQUID magnetometry. The line represents a single parameter best fit of Eq. (6.4). Note that only integer values of n have physical meaning. The inset shows the 1st (solid diamonds), 2nd (open diamonds), and the 15th (stars) hysteresis loop of the SL. Despite the intuitive similarities between these two training phenomena the details of the EB and bias field evolution show significant differences in particular for the transition $n=1$ to $n=2$ but also for the asymptotic behavior.

Next we briefly sketch how these differences are reflected in the theoretical description. The latter has been introduced in Ref. [26] and is based on a discretized form of the Landau–Khalatnikov equation² which reads [26, 3]

$$\frac{S_{\text{AF/HL}}(n+1) - S_{\text{AF/HL}}(n)}{\tau} = -\frac{1}{\xi} \frac{\partial \Delta F}{\partial S_{\text{AF/HL}}} \quad (6.3)$$

for AF or ferromagnetic HL pinning systems, respectively. Figure 6.7 shows the harmonic approximation in the vicinity of the equilibrium used to obtain the simplest expressions for the free energy entering Eq. (6.2). In the case of all FM HL/SL systems the order parameter M is proportional to the interface magnetization S_{HL} which leads with the help of Eq. (6.3) straightforward to the explicit expression [3]

² While details of the dynamics between states n and $n+1$ are not relevant, the use of the discretized Landau Khalatnikov dynamic equation has to be justified. It is appropriate since the integral magnetization of the pinning layer is non-conserved.

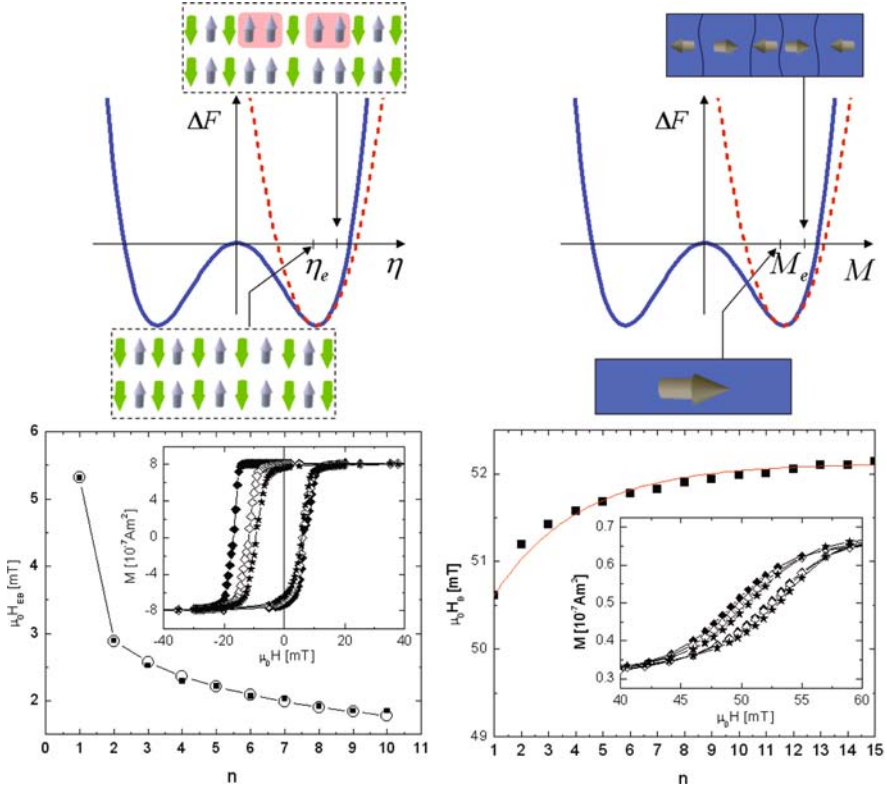


Fig. 6.7 Free energy ΔF vs. η (upper left graph) and M (upper right graph) for AF and FM pinning systems, respectively. Arrows assign sketches of the spin and domain structures of AF and FM (non)equilibrium states (η and M) η_e and M_e to the free energy graphs. Dashed lines show harmonic approximations of the Landau free energy landscape. The bottom left frame shows $\mu_0 H_{EB}$ vs. n for $\text{Cr}_2\text{O}_3/\text{Fe}$. The solid squares are experimental data measured at $T=300$ K. Open circles connected with eye-guiding lines are results of a single parameter fit of Eq. (6.4). The inset shows the 1st (solid diamonds), 2nd (open diamonds), and the 10th (stars) hysteresis loop. The bottom right frame displays $\mu_0 H_B$ vs. n of $\text{CoPtCrB } 15 \text{ nm/Ru } 0.7 \text{ nm/CoCr } 3 \text{ nm}$. Solid squares are experimental data measured at $T=395$ K. The line represents a single parameter best fit of Eq. (6.3). The inset shows the 1st (solid diamonds), 2nd (open diamonds), and 15th (stars) hysteresis loop of the SL.

$$\mu_0 H_B(n) = (K+1)^{n-1} \left\{ \mu_0 H_B(n=1) - K \mu_0 H_B^c \left[\frac{(K+1)^{n+1} - 1}{K(K+1)^{n-1}} - (K+2) \right] \right\}, \quad (6.4)$$

where $0 < K < 1$ is the fitting parameter that determines the rate of change of the bias field approaching the equilibrium value $\mu_0 H_B^c$ with exponential asymptotic.

The relation between the AF order parameter η and the interface magnetization S_{AF} is somewhat more involved [27]. With the help of the corresponding free energy expression one obtains the implicit sequence [26,27,29]

$$\mu_0(H_{\text{EB}}(n+1) - H_{\text{EB}}(n)) = -\gamma(\mu_0(H_{\text{EB}}(n) - H_{\text{EB}}^{\text{e}}))^3, \quad (6.5)$$

where the fitting parameter γ controls the rate of change of the EB field approaching the equilibrium EB field $\mu_0 H_{\text{EB}}^{\text{e}}$ with a $1/\sqrt{n}$ asymptotic behavior. The latter has been successfully applied very early as an empirical expression first suggested in Ref. [21]. Its consistency with the asymptotic behavior of Eq. (6.5) is a strong confirmation of the theoretical approach sketched here.

6.4.2 Tuning the Training Effect

From the previous discussion it can be concluded that any means affecting the initial spin structure of the pinning layer will have an impact on the training behavior. Therefore, one has to expect that training characteristics can be tuned with the help of magnetic fields strong enough to perturb the AF pinning layer. Recently it has been shown in NiO/Ni bilayers that a training behavior following Eq. (6.5) can be perturbed by a large out-of-plane magnetic field of about 1 T such that subsequent training data show a substantially accelerated training effect [101]. Brems et al. showed that it is possible in CoO/Co bilayers to partially reinduce the untrained state when measuring a hysteresis loop with an in-plane external field perpendicular to the cooling field [102]. A simultaneous isothermal quenching of training and EB has been achieved in the Fe/Cr₂O₃/Fe trilayer introduced above. After field cooling from $T=395$ K in $\mu_0 H = 50$ mT down to $T = 20$ K the system shows a large EB and EB training effect. However, when subjecting the system to large in-plane DC magnetic field of 7 T EB bias and with it EB training is completely quenched [103].

The AF order parameter of the pinning systems in regular AF/FM EB heterostructures does not directly couple to homogeneous applied magnetic fields. Therefore, all of the effects described above require either large fields or sources for significant imbalance in the sublattice magnetizations such as thermal excitation or imperfections giving rise to deviation from perfect AF long-range order. In all FM heterostructures the situation is different. Here, homogeneous applied magnetic fields are conjugate to the FM order parameter of the pinning system and can directly influence the magnetic state of the latter. A systematic field-induced variation of the training behavior has been demonstrated and the characteristics of the training effect have been directly related to the field-controlled magnetization of the pinning layer [3].

Equation (6.3) shows that training is a triggered relaxation phenomenon. Hence one has to expect that the magnetic sweep rate of the hysteresis loops also affects the relaxation dynamics of the pinning system. In accordance with this intuitive qualitative picture a dynamic enhancement of the exchange bias training effect has been observed in the same all FM bilayer discussed above [28]. A similar enhancement has been observed in regular AF/FM heterostructures as well [26].

6.5 Conclusion

This chapter reviewed selected modern attempts to tune the characteristics of a number of effects associated with the exchange bias phenomenon. The most prominent is certainly the emergence of an exchange bias field in field-cooled antiferromagnetic/ferromagnetic thin film heterostructures. Control of the exchange bias field has been reviewed with special emphasis on electrically controlled exchange bias. Its successful integration in novel device architectures promises tremendous impact on future spintronic applications. The exchange bias training effect is a less investigated field with many open questions on a microscopic level. A simple but powerful phenomenological description of the training effect has been introduced and its universality has been evidenced. In accordance with this intuitive understanding various attempts to control the exchange bias and its training effect have been reported.

Acknowledgments This chapter is supported in part by NSF through Career DMR-0547887, MRSEC DMR-0213808, NCMN, and NRI. The author gratefully acknowledges discussions with Sarbeswar Sahoo, Srinivas Polisetty, Xi He, Yi Wang, and Tathagata Mukherjee.

References

1. Th. Mühge, N. N. Garif'yanov, Yu. V. Goryunov, G. G. Khaliullin, L. R. Tagirov, K. Westerholt, I. A. Garifullin, and H. Zabel, "Possible Origin for Oscillatory Superconducting Transition Temperature in Superconductor/Ferromagnet Multilayers" *Phys. Rev. Lett.* **77**, 1857 (1996).
2. Chun-Gang Duan, S. S. Jaswal, and E. Y. Tsymbal, "Predicted Magnetoelectric Effect in Fe/BaTiO₃ Multilayers: Ferroelectric Control of Magnetism" *Phys. Rev. Lett.* **97**, 047201 (2006).
3. Ch. Binek, S. Polisetty, Xi He, and A. Berger, "Exchange Bias Training Effect in Coupled All Ferromagnetic Bilayer Structures" *Phys. Rev. Lett.* **96**, 067201 (2006).
4. I. Žutić, J. Fabian, and S. Das Sarma, "Spintronics: Fundamentals and applications" *Rev. Mod. Phys.* **76**, 323 (2004).
5. G. E. Moore, "Cramming more components onto integrated circuits" *Electronics* **38**, 114 (1965).
6. W. H. Meiklejohn and C. P. Bean, "New Magnetic Anisotropy" *Phys. Rev.* **102**, 1413 (1956).
7. W. H. Meiklejohn and C. P. Bean, "New Magnetic Anisotropy" *Phys. Rev.* **105**, 904 (1957).
8. J. Nogués and I.K. Schuller, "Exchange bias" *J. Magn. Magn. Mater.* **192**, 203 (1999).
9. A. Berkowitz and K. Takano, "Exchange anisotropy- a review" *J. Magn. Magn. Mater.* **200**, 552 (1999).
10. R. L. Stamps, "Mechanisms for exchange bias", *J. Phys. D* **33**, R247 (2000).
11. M. Kiwi, "Exchange bias theory", *J. Magn. Magn. Mater.* **234**, 584 (2001).
12. M. Ali, P. Adie, C. H. Marrows, D. Greig, B. J. Hickey, and R. L. Stamps, "Exchange bias using a spin glass" *Nat. Mater.* **6**, 70 (2007).
13. I. Roshchin, O. Petravic, R. Morales, Z.-P. Li, X. Battle, and I. K. Schuller, "Lateral length scales in exchange bias" *Europhys. Lett.* **71**, 297 (2005).
14. F. Radu and H. Zabel, "Exchange bias effect of ferro-/antiferromagnetic heterostructures" *Springer Tracts Modern Phys.*, **227** (2008).
15. W. Kuch, L. I. Chelaru, F. Offi, J. Wang, M. Kotsugi, and J. Kirschner, "Tuning the magnetic coupling across ultrathin antiferromagnetic films by controlling atomic-scale roughness" *Nat. Mater.* **5**, 128 (2006).
16. J. S. Jiang, G. P. Felcher, A. Inomata, R. Goyette, C. S. Nelson, and S. D. Bader, "Exchange bias in Fe/Cr double superlattices" *J. Vac. Sci Technol. A* **18**, 1264 (2000).

17. F. Nolting, A. Scholl, J. Stöhr, J. W. Seo, J. Fompeyrine, H. Siegwart, J.-P. Locquet, S. Anders, J. Lüüing, E. E. Fullerton, M. F. Toney, M. R. Scheinfein, and H. A. Padmore, “*Direct observation of the alignment of ferromagnetic spins by antiferromagnetic spins*” *Nature* **405**, 767 (2000).
18. Ch. Binek, A. Hochstrat, and W. Kleemann, “*Exchange Bias in a generalized Meiklejohn-Bean approach*” *J. Magn. Magn. Mater.* **234**, 353 (2001).
19. C. Leighton, J. Nogués, B. J. Jönsson-kerman, and I.K. Schuller, “*Coercivity Enhancement in Exchange Biased Systems Driven by Interfacial Magnetic Frustration*” *Phys. Rev. Lett* **84**, 3466 (2000).
20. S. Maat, K. Takano, S. S. P. Parkin, and E. E. Fullerton, “*Perpendicular Exchange Bias of Co/Pt Multilayers*” *Phys. Rev. Lett* **87**, 087202 (2001).
21. G. Scholten, K. D. Usadel, and U. Nowak, “*Coercivity and exchange bias of ferromagnetic/antiferromagnetic multilayers*” *Phys. Rev. B* **71**, 064413 (2005).
22. D. Paccard, C. Schlenker, O. Massenet, R. Montmory, and A. Yelon, “*A New Property of Ferromagnetic-Antiferromagnetic Coupling*” *Phys. Status Solidi* **16**, 301 (1966).
23. C. Schlenker, S. S. P. Parkin, J. C. Scott, and K. Howard, “*Magnetic disorder in the exchange bias bilayered FeNi-FeMn system*” *J. Magn. Magn. Mater.* **54**, 801 (1986).
24. K. Zhang, T. Zhao, and M. Fujiwara, “*Training effect of exchange biased iron-oxide/ferromagnet systems*”, *J. Appl. Phys.* **89**, 6910 (2001).
25. S. G. te Velthuis, A. Berger, G. P. Felcher, B. Hill, and E. Dahlberg, *J. Appl. Phys.* **87**, 5046 (2000).
26. Heiwan Xi, R. M. White, S. Mao, Z. Gao, Z. Yang, and E. Murdock, “*Low-frequency dynamic hysteresis in exchange-coupled Ni₈₁Fe₁₉/Ir₂₂Mn₇₈ bilayers*” *Phys. Rev. B* **64**, 184416 (2001).
27. Ch. Binek, “*Training of the exchange-bias effect: A simple analytic approach*” *Phys. Rev. B* **70**, 014421 (2004).
28. Ch. Binek, Xi He and S. Polisetty, “*Temperature dependence of the training effect in a Co/CoO exchange-bias layer*” *Phys. Rev. B* **72**, 054408 (2005).
29. S. Sahoo, S. Polisetty, Ch. Binek, and A. Berger, ” *Dynamic enhancement of the exchange bias training effect*” *J. Appl. Phys.* **101**, 053902 (2007).
30. S. Polisetty, S. Sahoo, and Ch. Binek, “*Scaling Behavior of the Exchange-Bias Training Effect*” *Phys. Rev. B.* **76**, 184423 (2007).
31. Haiwen Xi, S. Franzen, S. Mao, and R. M. White, “*Exchange bias relaxation in reverse magnetic fields*” *Phys. Rev. B* **75**, 014434 (2007).
32. A. Hoffmann, “*Symmetry Driven Irreversibilities at Ferromagnetic-Antiferromagnetic Interfaces*” *Phys. Rev. Lett.* **93**, 097203 (2004).
33. V. Skumryev, S. Stoyanov, Y. Zhang, G. Hadjipanayis, D. Givord, and J. Nogués, “*Beating the superparamagnetic limit with exchange bias*” *Nature (London)* **423**, 850 (2003).
34. A. Hochstrat, Ch. Binek, and W. Kleemann, “*Training of the exchange-bias effect in NiO-Fe heterostructures*” *Phys. Rev. B* **66**, 092409 (2002).
35. Yan-kun Tang, Young Sun, and Zhao-hua Cheng, “*Exchange bias associated with phase separation in the perovskite cobaltite La_{1-x}Sr_xCoO₃*” *Phys. Rev. B* **73**, 174419 (2006).
36. D. Niebieskikwiat, and M. B. Salamon, “*Intrinsic interface exchange coupling of ferromagnetic nanodomains in a charge ordered manganite*” *Phys. Rev. B* **72**, 174422 (2005).
37. R. Ang, Y. P. Sun, X. Luo, C. Y. Hao, X. B. Zhu, and W. H. Song, “*The evidence of the glassy behavior in the layered cobaltites*” *Appl. Phys. Lett.* **92**, 162508 (2008).
38. S. Karmakar, S. Taran, E. Bose, and B. K. Chaudhuri, C. P. Sun, C. L. Huang, and H. D. Yang, “*Evidence of intrinsic exchange bias and its origin in spin-glass-like disordered L_{0.5}Sr_{0.5}MnO₃ manganites (L=Y, Y_{0.5}Sm_{0.5}, and Y_{0.5}La_{0.5})*” *Phys. Rev. B* **77**, 144409 (2008).
39. J. Ventura, J. P. Araujo, J. B. Sousa, A. Veloso, and P. P. Freitas, “*Training effect in specular spin valves*” *Phys. Rev. B* **77**, 184404 (2008).
40. W. Eerenstein, N. D. Mathur, J. F. Scott, “*Multiferroic and magnetoelectric materials*” *Nature* **442** 759 (2006).

41. N.A. Hill, "Why are there so few magnetic ferroelectrics?" J. Phys. Chem. B **140**, 6694 (2000).
42. P. Borisov, A. Hochstrat, Xi Chen, W. Kleemann, and Ch. Binek, "Magnetoelectric Switching of Exchange Bias" Phys. Rev. Lett. **94**, 117203 (2005).
43. Ch. Binek, P. Borisov, X. Chen, A. Hochstrat, S. Sahoo, and W. Kleemann, "Perpendicular exchange bias and its control by magnetic, stress and electric fields" Eur. Phys. J. B **45**, 197 (2005).
44. A. Hochstrat, Ch. Binek, Xi Chen, W. Kleemann, "Extrinsic control of the exchange bias" J. Magn. Magn. Mater. **272**, 325 (2004).
45. Ch. Binek, B. Doudin, "Magneto-electronics with magnetoelectrics" J. Phys. Condens. Matter **17**, L39 (2005).
46. Ch. Binek, A. Hochstrat, X. Chen, P. Borisov, W. Kleemann, and B. Doudin, "Electrically controlled exchange bias for spintronic applications" J. Appl. Phys. **97**, 10C514 (2005).
47. P. Curie, J. de Physique, "Sur la symétrie dans les phénomènes physiques, symétrie d'un champ électrique et d'un champ magnétique" **3**, 393 (1894).
48. I. E. Dzyaloshinskii, "On the magneto-electric effect in antiferromagnets" Sov. Phys. JETP **10** 628 (1960).
49. W. Eerenstein, M. Wiora, J. L. Prieto, J. F. Scott and N. D. Mathur, "Giant sharp and persistent converse magnetoelectric effects in multiferroic epitaxial heterostructures" Nat. Mater. **6**, 348 (2007).
50. S. Alexander and S. Shtrikman, "On the origin of the axial magnetoelectric effect of Cr_2O_3 " Solid State Commun. **4**, 115 (1966).
51. R. Hornreich and S. Shtrikman, "Statistical Mechanics and Origin of the Magnetoelectric Effect in Cr_2O_3 " Phys. Rev. **161**, 506–512 (1967).
52. V. Laukhin, V. Skumryev, X. Martí, D. Hrabovský, F. Sánchez, M.V. García-Cuenca, C. Ferrater, M. Varela, U. Lüders, J. F. Bobo, and J. Fontcuberta, "Electric-Field Control of Exchange Bias in Multiferroic Epitaxial Heterostructures" Phys. Rev. Lett. **97** 227201 (2006).
53. Y.H. Chu, L. W. Martin, M. B. Holcomb, M. Gajek, S. J. Han, Q. HE, N. Balke, C. H. Yang, D. Lee, W. Hu, Q. Zhan, P. L. Yang, A. Fraile-Rodriguez, A. Scholl, S. X. Wang and R. Ramesh, "Electric-field control of local ferromagnetism using a magnetoelectric multiferroic" Nat. Mater. **7**, 478 (2008).
54. P. Borisov, Th. Eimüller, A. Fraile-Rodriguez, A. Hochstrat, X. Chen, W. Kleemann, "Application of the magnetoelectric effect to exchange bias" J. Magn. Magn. Mater. **310**, 2313 (2007).
55. H. Béa, M. Bibes, and S. Cherifi, "Tunnel magnetoresistance and robust room temperature exchange bias with multiferroic $BiFeO_3$ epitaxial thin films" Appl. Phys. Lett. **89**, 242114 (2006).
56. P. Borisov, A. Hochstrat, X. Chen, and W. Kleemann, "Multiferroically composed exchange bias systems" Phase Trans. **79**, 1123 (2006).
57. M. Bibes, and A. Barthélémy "Towards a magnetoelectric memory" Nat. mater. **7**, 425 (2008).
58. S. Sahoo and Ch. Binek, "Piezomagnetism in epitaxial Cr_2O_3 thin films and spintronic applications" Phil. Mag. Lett. **87**, 259 (2007).
59. M. Fiebig, "Revival of the magnetoelectric effect" J. Phys. D: Appl. Phys. **38**, R123 (2005).
60. P. Borisov, A. Hochstrat, V. V. Shvartsman, W. Kleemann, "Superconducting quantum interference device setup for magnetoelectric measurements" Rev. Sci. Instr. **78**, 106105 (2007).
61. T. Kimura, T. Goto, H. Shintani, K. Ishizaka, T. Arima, and Y. Tokura, "Magnetic control of ferroelectric polarization", Nature **426**, 55 (2003).
62. N. Hur, S. Park, P. A. Sharma, J. S. Ahn, S. Guha, and S-W. Cheong, "Electric polarization reversal and memory in a multiferroic material induced by magnetic fields" Nature **429**, 392 (2004).

63. M. Gajek, M. Bibes, S. Fusil, K. Bouzouane, J. Fontcubert, A. Barthélémy, and A. Fert, "Tunnel junctions with multiferroic barriers" *Nat. Mater.* **6**, 296 (2007).
64. T. Kimura, S. Kawamoto, I. Yamada, M. Azuma, M. Takano, and Y. Tokura, "Magnetocapacitance effect in multiferroic BiMnO_3 " *Phys. Rev. B* **67** 180401(R) (2003).
65. T. Lottermoser, T. Lonkai, U. Amann, D. Hohlwein, J. Ihringer, and M. Fiebig, "Magnetic phase control by an electric field" *Nature* **430**, 541 (2004).
66. J. Hemberger, P. Lunkenheimer, R. Fichtl, H.-A. Krug von Nidda, V. Tsurkan, and A. Loidl, "Relaxor ferroelectricity and colossal magnetocapacitive coupling in ferromagnetic CdCr_2S_4 " *Nature* **434**, 364 (2005).
67. Y. Yamasaki, S. Miyasaka, Y. Kaneko, J. P. He, T. Arima, and Y. Tokura, "Magnetic Reversal of the Ferroelectric Polarization in a Multiferroic Spinel Oxide" *Phys. Rev. Lett.* **96**, 207204 (2006).
68. C. Thiele, K. Dörr, O. Bilani, J. Rödel, and L. Schultz, "Influence of strain on the magnetization and magnetoelectric effect in $\text{La}_{0.7}\text{A}_{0.3}\text{MnO}_3/\text{PMN-PT}(001)$ ($\text{A}=\text{Sr,Ca}$)" *Phys. Rev. B* **75**, 054408 (2007).
69. T. Zhao, A. Scholl, F. Zavaliche, K. Lee, M. Barry, A. Doran, M. P. Cruz, Y. H. Chu, C. Ederer, N. A. Spaldin, R. R. Das, D. M. Kim, S. H. Baek, C. B. Eom, and R. Ramesh, "Electrical control of antiferromagnetic domains in multiferroic BiFeO_3 films at room temperature" *Nat. Mater.* **5**, 823 (2006).
70. A. P. Malozemoff, "Random-field model of exchange anisotropy at rough ferromagnetic-antiferromagnetic interfaces" *Phys. Rev. B* **35**, 3679 (1987).
71. P. Miltényi, M. Gierlings, J. Keller, B. Beschoten, G. Güntherodt, U. Nowak, K. D. Usadel, "Diluted Antiferromagnets in Exchange Bias: Proof of the Domain State Model" *Phys. Rev. Lett.* **84**, 4224 (2000).
72. A. S. Borovik-Romanov, "Piezomagnetism in the antiferromagnetic fluorides of cobalt and manganese" *Sov. Phys. JETP* **11**(1960) 786.
73. I. E. Dzialoshinskii, "The problem of piezomagnetism" *JETP* **33** 807 (1957).
74. J. Kushauer, C. Binek, and W. Kleemann, *J. Appl. Phys.* **75** 5856 (1994).
75. Ch. Binek, "Ising-type antiferromagnets: Model systems in statistical physics and the magnetism of exchange bias" *Springer Tracts Modern Phys.* **196**, (Springer, Berlin, 2003).
76. J. Nogués, T. J. Moran, D. Lederman, I. K. Schuller, and K. V. Rao, "Role of interfacial structure on exchange-biased $\text{FeF}_2\text{-Fe}$ " *Phys. Rev. B* **59**, 6984 (1999).
77. A. Hochstrat, Ch. Binek, and W. Kleemann, "Training of the exchange-bias effect in NiO-Fe heterostructures" *Phys. Rev. B* **66**, 092409 (2002).
78. Ch. Binek, Xi Chen, A. Hochstrat, and W. Kleemann, "Exchange bias in $\text{Fe}_{0.6}\text{Zn}_{0.4}\text{F}_2/\text{Fe}$ heterostructures" *J. Magn. Magn. Mater.* **240**, 257 (2002).
79. M. K. Lee, T. K. Nath, C. B. Eom, M. C. Smoak, and F. Tsui, "Strain modification of epitaxial perovskite oxide thin films using structural transitions of ferroelectric BaTiO_3 substrate" *Appl. Phys. Lett.* **77**, 3547 (2000).
80. X. Qi, H. Kim, and M. G. Blamire, "Exchange bias in bilayers based on the ferroelectric antiferromagnet BiFeO_3 " *Phil. Mag. Lett.* **87**, 175 (2007).
81. J. Wang, J. Neaton, H. Zheng, V. Nagarajan, S. B. Ogale, B. Liu, D. Viehland, V. Vaithyanathan, D. G. Schlom, U. Waghmare, N. A. Spaldin, K. M. Rabe, M. Wuttig, and R. Ramesh, "Epitaxial BiFeO_3 Multiferroic Thin Film Heterostructures" *Science* **299**, 1719 (2003).
82. H. Zheng, J. Wang, S. E. Lofland, Z. Ma, L. Mohaddes-Ardabili, T. Zhao, L. Salamanca-Riba, S. R. Sinde, S. B. Ogale, F. Bai, D. Viehland, Y. Jia, D. G. Schlom, M. Wuttig, A. Roytburd, and R. Ramesh, "Multiferroic $\text{BaTiO}_3\text{-CoFe}_2\text{O}_4$ " Nanostructures *Science* **303**, 661 (2004).
83. F. Zavaliche, H. Zheng, L. Mohaddes-Ardabili, S. Y. Yang, Q. Zhan, P. Shafer, E. Reilly, R. Chopdekar, Y. Jia, P. Wright, D. G. Schlom, Y. Suzuki, and R. Ramesh, "Electric field-induced magnetization switching in epitaxial columnar nanostructures" *Nano Lett.* **5**, 1793 (2005).

84. G. Srinivasan, E. T. Rasmussen, J. Gallegos, R. Srinivasan, Yu. I. Bokhan, and V. M. Laletin, “*Magnetolectric effects in bilayers and multilayers of magnetostrictive and piezoelectric perovskite oxides*” Phys. Rev. B **64**, 214408 (2001).
85. C.W. Nana, “*Magnetolectric effect in composites of piezoelectric and piezomagnetic phases*” Phys. Rev. B **50**, 6082 (1994).
86. S. Sahoo, S. Polisetty, C.-G. Duan, Sitaram S. Jaswal, E. Y. Tsymbal, and Ch. Binek, “*Ferroelectric control of magnetism in BaTiO₃/Fe heterostructures via interface strain coupling*”, Phys. Rev. B **76**, 092108 (2007).
87. B. D. Cullity, *Introduction to magnetic materials*. Reading, MA: Addison-Wesley (1972).
88. J. Nogués, D. Lederman, T. J. Moran, and Ivan K. Schuller, “*Positive Exchange Bias in FeF₂-Fe Bilayers*” Phys. Rev. Lett. **76**, 4624 (1996).
89. J. Nogués, C. Leighton and Ivan K. Schuller, “*Correlation between antiferromagnetic interface coupling and positive exchange bias*” Phys. Rev. B **61**, 1315 (2000).
90. T. L. Kirk, O. Hellwig, and Eric E. Fullerton, “*Coercivity mechanisms in positive exchange-biased Co films and CoPt multilayers*” Phys. Rev. B, **65**, 224426 (2002).
91. B. Kagerer, Ch. Binek, W. Kleemann, “*Freezing field dependence of the exchange bias in uniaxial FeF₂-CoPt heterosystems with perpendicular anisotropy*” J. Magn. Magn. Mater. **217**, 139 (2000).
92. Z. Y. Liu and S. Adenwalla, “*Oscillatory interlayer exchange coupling and its temperature dependence in [Pt/Co]₃/NiO/[Co/Pt]₃ multilayers with perpendicular anisotropy*” Phys. Rev. Lett. **91**, 037207-1 (2003).
93. J. Nogués, J. Sort, S. Suriñach, J. S. Muñoz, M. D. Baró, J. F. Bobo, U. Lüders, E. Haanappel, M. R. Fitzsimmons, A. Hoffmann, and J. W. Cai, “*Isothermal tuning of exchange bias using pulsed fields*” Appl. Phys. Lett. **82**, 3044 (2003).
94. S. Sahoo, T. Mukherjee, K. D. Belashchenko, and Ch. Binek, “*Isothermal low-field tuning of exchange bias in epitaxial Fe/Cr₂O₃/Fe*” Appl. Phys. Lett. **91**, 172506 (2007).
95. T. Jonsson, J. Mattsson, C. Djurberg, F. A. Khan, P. Nordblad, and P. Svedlindh, “*Aging in a Magnetic Particle System*” Phys. Rev. Lett. **75**, 4138 (1995).
96. S. Sahoo, O. Petracic, Ch. Binek, W. Kleemann, J. B. Sousa, S. Cardoso, and P. P. Freitas, “*Magnetic relaxation phenomena in the superspin-glass system [Co₈₀F₂₀/Al₂O₃]₁₀*” J. Phys. Condens. Matter **14**, 6729 (2002).
97. R. Skomski, J. Zhou, R. D. Kirby, and D. J. Sellmyer, “*Magnetic Aging*” Mater. Res. Soc. Symp. Proc. **887**, 133 (2006).
98. M. Pleimling “*Aging phenomena in critical semi-infinite systems*” Phys. Rev. B **70**, 104401 (2004).
99. K. H. Fischer and J. A. Hertz, *Spin Glasses*. Cambridge Univ. Press, Cambridge (1991).
100. J. A. Mydosh, *Spin Glasses: an Experimental Introduction*. Taylor and Francis, London (1993).
101. P. Y. Yang, C. Song, F. Zeng, and F. Pan, “*Tuning the training effect in exchange biased NiO/Ni bilayers*” Appl. Phys. Lett. **92**, 243113 (2008).
102. S. Brems, D. Buntinx, K. Temst, Ch. Van Haesendonck, F. Radu, and H. Zabel, “*Reversing the Training Effect in Exchange Biased CoO/Co Bilayers*” Phys. Rev. Lett. **95**, 157202 (2005).
103. S. Sahoo and Ch. Binek, “*Quenching of the Exchange Bias Training in Fe/Cr₂O₃/Fe Tri-layer*”, AIP. Conf. Proc. **1063**, 132 (2008).

Chapter 7

Dynamics of Domain Wall Motion in Wires with Perpendicular Anisotropy

Dafiné Ravelosona

Abstract Recently, much attention has been focused on new concepts of highly integrated spintronics devices based on magnetic domain walls driven by a spin-polarized current. However, several fundamental questions must be answered before the technology can be considered as feasible. This review covers the current understanding of DW propagation along sub-micronic size wires with ultra-thin films having perpendicular magnetic anisotropy. These films exhibit very narrow domain walls that interact strongly with pinning defects, making them model systems to study the dynamics of a 1D interface in a 2D weakly disorder medium. Three important issues are addressed: the peculiarities of domain wall motion driven by magnetic fields in nanoscale devices, the manipulation of the pinning potential for the control of efficient field induced domain wall motion, and the physics of current-driven domain wall motion.

7.1 Introduction

Domain walls (DWs) in thin ferromagnetic films may be considered as nano-objects (widths $\sim 5\text{--}200$ nm) separating regions of opposite magnetization. The field-driven motion of DWs has been studied extensively in thin films [1–5]. In the context of device applications, the first proposition for using domain walls was made almost 30 years ago for magnetic memories based on the motion of bubbles [2]. Within the last decade, a renewed interest in domain wall motion has led to many studies in nanoscale devices. The reason for this is twofold. First, vastly improved lithography and fabrication techniques have allowed for careful experimental studies of field-driven domain-wall motion along magnetic tracks on micrometer dimensions [6–10]. Second, the advent of current-driven domain wall motion, following a number of theoretical [11–17] and experimental work [17–35], has further fueled

D. Ravelosona (✉)

Institut d'Electronique Fondamentale UMR CNRS 8622, Université Paris Sud, 91405 Orsay, France

e-mail: dafine.ravelosona@u-psud.fr; dafine.ravelosona@ief.u-psud.fr

the intense activity on this subject. A general review describing the interaction of polarized currents and magnetic domain walls has been given recently by C.H Marrows [36]. Domain wall-mediated switching in spintronics devices promises very low power consumption, simple architectures, fast operation, and 3D stacking thus offering the potential to become a key technology for non-volatile memories, ultra-dense hard disk drives, sensors, and specific logic circuits [37–39]. The basic principle behind a device based on current-induced domain wall motion is quite simple: well-localized artificial pinning sites to control DW pinning while current pulses are used to depin and propagate one or several DWs. However, even if the proof of concepts has been demonstrated, several fundamental questions are to be addressed before any feasible applications can be considered. There are three main challenges: (1) to ensure thermal stability while reducing depinning current densities, (2) to control stochastic pinning/depinning effects on intrinsic defects, and then (3) to achieve high densities by moving dense sequence of DW in parallel.

For studying domain wall motion in patterned structures, the natural geometry to use is a wire. When the typical lateral dimensions become comparable with characteristic magnetic and structural length scale of the materials, magnetic wires may show drastic modifications in the processes involving magnetization reversal. For instance, the domain wall structure in soft nanowires such as those made from NiFe films is governed by magnetostatics and depends on the wire cross-section [40]. The stable structures are transverse walls and vortex walls for smaller and larger cross-sections, respectively, both of them having a different dynamical behavior. On the other hand, the propagation process of a DW driven by a small external force f results from the competition between an elastic energy that acts to straighten the DW and a random structural disorder which tends to roughen it by local pinning [41]. As a result, at zero temperature DWs are pinned until a critical force f_c is reached. At finite temperatures, DWs can move under applied forces below the critical depinning force f_c through thermal activation over energy barriers there are a result of a pinning potential. Since the possible paths for DW motion are reduced when reducing the lateral dimensions, the influence of the distribution of intrinsic defects in the virgin films becomes preponderant. Also, it is expected that fundamental domain wall physics in patterned structures is strongly influenced by the presence of lithography-induced defects and imperfections such as edge roughness, which give rise to additional pinning. Finally, one solution to precisely locate and trap DWs, as well as to ensure high enough thermal stability and resistance to external perturbation such as stray magnetic fields from nearby devices is to deliberately introduce artificial pinning sites.

This review will be devoted essentially to the study of DW motion along wires patterned from ultra-thin films ($0.5 \leq t \leq 2$ nm) with strong perpendicular anisotropy [5]. These films, which exhibits very high uniaxial anisotropy are a promising way of extending the scaling of spintronic devices down to the nanometer scale. In the limit, where the thickness t is smaller than the exchange length, the perpendicular magnetization is uniform across the film thickness which makes these films 2D Ising model system. Also, since the thickness of the magnetic layer t is smaller than the DW width

$$\Delta = \sqrt{A K_{eff}} \quad (7.1)$$

($\sim 1-10$ nm) where A is the exchange constant and

$$K_{eff} = K_u - 2\pi M_S^2 \quad (7.2)$$

is the effective anisotropy that includes dipolar energy (M_S is the saturation magnetization, K_u is the uniaxial anisotropy of the perpendicular material), DWs can be treated as perfect 1D Bloch walls (Fig. 7.1) [42]. Such narrow 1D DWs are very rigid interfaces in comparison with larger 3D Neel DWs in soft materials. On one hand, this makes such 1D nano-objects propagating in patterned ultra-thin magnetic films, a very good model system to study the physics of a 1D elastic interface moving in a confined 2D geometry. On the other hand, such narrow DWs interact very strongly with the presence of randomly distributed nanometric defects, which give rise to a high pinning force and important stochastic effects.

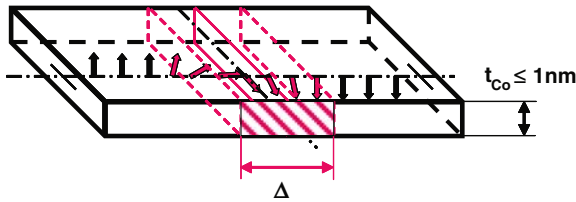


Fig. 7.1 1D Bloch domain wall profile in an ultra-thin films with strong perpendicular anisotropy. In Pt/Co($t_{Co} < 1$ nm)/Pt systems, the typical wall thickness is $\Delta \sim 1-10$ nm, which is higher than the film thickness t_{Co}

This chapter presents an overview of the results obtained in our group on the mechanism of DW motion in wires with perpendicular anisotropy [7, 10, 26, 32, 43, 34, 45]. I will first describe the basic properties of DW dynamics in continuous magnetic films with perpendicular anisotropy (Section 7.2). The method to inject, detect, and manipulate domain wall dynamics in magnetic tracks will be presented in Section 7.3. The effect of intrinsic structural defects on DW dynamics driven by a magnetic field along wires will be examined in Section 7.4. The manipulation of the pinning potential to control efficiently field-induced DW motion under magnetic field will be reviewed in Section 7.5 before finally the influence of polarized currents on DW motion will be given in Section 7.6.

7.2 Basics of Field-Induced DW Motion in Pt/Co/Pt Ultra-Thin Films

Extensive studies of reversal processes in continuous thin films with easy magnetization axis perpendicular to the film plane have been conducted by the group of J. Ferré. A general review was given a few years ago [5] and more recently the mechanisms of magnetic interactions in nanomagnet arrays with perpendicular anisotropy has also been reviewed [46]. Here, I will give a brief overview of the basics of

field-induced domain wall motion in continuous films by focusing on the magnetization reversal mechanisms in epitaxial Pt/Co($t \leq 1$ nm)/Pt systems where the out-of-plane magnetization results from strong anisotropies present at interfaces. These films can be considered as quasi-perfect 2D ultra-thin films.

7.2.1 Mechanisms of Magnetization Reversal in Pt/Co/Pt Trilayers

Let us consider high-quality Pt(35 Å)/Co($t \leq 1$ nm)/Pt(45 Å) trilayers epitaxially grown by sputtering on Al₂O₃(0001) substrates [47]. The interfaces are very smooth with a low roughness (0.2 nm rms) and substantial Co–Pt intermixing. In such Co/Pt multilayers with small Co thickness, interface anisotropy is strong enough to overcome the macroscopic shape anisotropy and to induce a high uniaxial perpendicular anisotropy ($K_u \sim 1 \times 10^7$ erg/cm³). The square shape of the hysteresis loop (Fig. 7.2a) reveals that magnetization reversal is dominated by easy domain wall motion following rare nucleation events down to low temperatures [44]. This is consistent

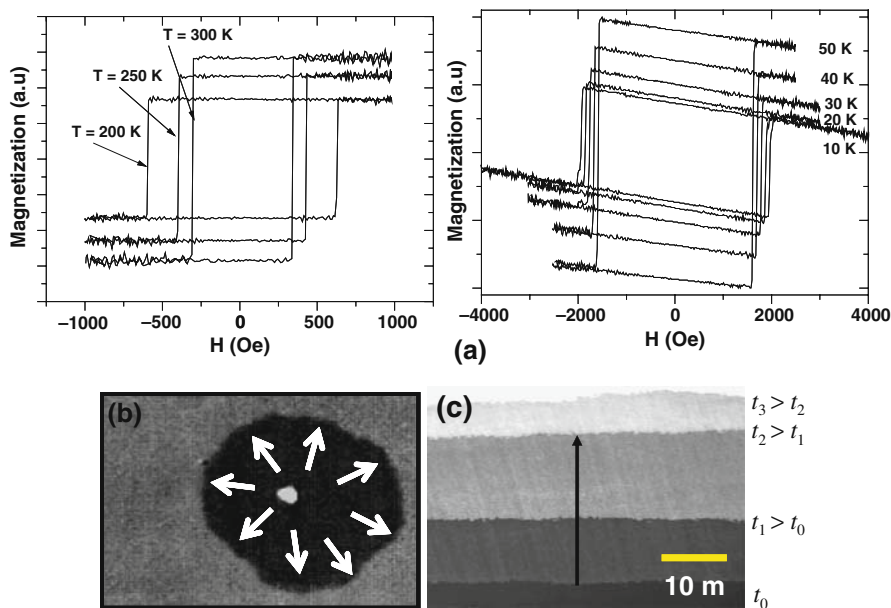


Fig. 7.2 (a) Hysteresis loops of a Pt/Co(0.5 nm)/Pt sandwich measured between $t=10$ and 300 K by extraordinary Hall effect. The squareness is consistent with magnetization reversal dominated by easy domain wall motion and $H_N > H_p$. (b–c) Polar MO Kerr images of domain nucleation and propagation within a Pt/Co(5 Å)/Pt sandwich at room temperature: (b) domain nucleation at an extrinsic defect: after nucleation, the domain expands quasi-circularly around the nucleation center, due to domain wall propagation driven by the applied magnetic field. (c) Homogenous domain wall propagation over several tens of micrometers in response to successive magnetic field pulses. The arrow corresponds to the direction of the DW motion and the different gray levels correspond to different stages of the domain wall propagation

with a nucleation field H_N larger than the propagation field H_p . As demonstrated by magneto-optical microscopy at low fields, nucleation of a reversed domain takes place at a restricted number of macroscopic extrinsic defects (Fig. 7.2b) and then rapid domain wall motion occurs in a very uniform way (Fig. 7.2c). At higher fields, nucleation is initiated at intrinsic defect sites, related to variation of the perpendicular anisotropy at nanometer scale. The nucleation process is a thermally activated phenomenon: the probability P of a nucleation event, assuming an Arrhénius law, can be written as [48]

$$P = P_0 \cdot \exp \left[-\frac{2M_S \cdot V_N \cdot (H_N - H)}{k_B T} \right] \quad (7.3)$$

where V_N corresponds to the nucleation volume. Equation (7.3) defines the nucleation field H_N as the field necessary to induce the nucleation without any thermal activation (at temperature $T=0$ K). At finite temperatures, nucleation occurs at fields $H < H_N$ by thermal activation.

7.2.2 Different Regimes of DW Motion: The Role of Defects

After nucleation, the magnetic domain expands by domain wall propagation. Far away from the nucleation centers, the DW interface appears quite straight on a length scale of a few tens of microns (Fig. 7.2b). The straightness of the DW and the rapid DW motion are consistent with a weak and very homogeneous pinning potential. However, if one looks carefully at a smaller spatial scale (Fig. 7.3a), DWs exhibit a certain degree of jaggedness. This originates from the domain wall pinning with the underlying random pinning disorder related to a large assembly of nano-defects (Fig. 7.3b). In Co/Pt ultra-thin films, the pinning potential is believed to originate from randomly distributed intrinsic inhomogeneities of the ultra-thin Co-film structure, such as atomic steps at Co/Pt interfaces that induce changes in

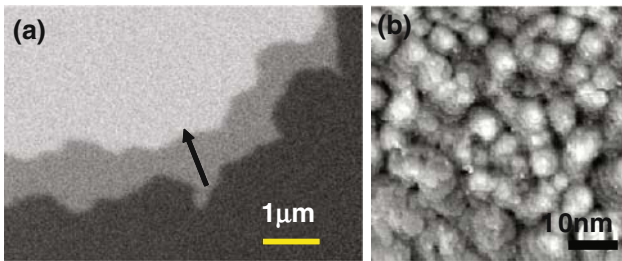


Fig. 7.3 (a) Polar MO Kerr image of domain propagation within a Pt/Co(5 Å)/Pt sandwich at room temperature. The high-resolution image reveals the jaggedness of the DW. The different gray levels correspond to two different stages of the domain wall propagation. (b) Scanning transmission microscopy image of a Pt/Co(5 Å)/Pt sandwich revealing the presence of grains and terraces of typical size ~ 10 nm

interface anisotropy energy [49]. In addition, at the boundaries of the crystallites, exchange interaction and anisotropy energy can be reduced.

In order to propagate, the domain wall has to overcome the corresponding local energy barriers, which gives rise to a threshold field H_p at $T=0$ K (so-called propagation field) as the field necessary to induce DW motion. Values of H_p for ultra-thin films with perpendicular anisotropy range from 0.1 to 1 kOe. An important feature of this dynamics is that at finite temperatures, a DW can move under an applied field even below the propagation field H_p by thermal activation. In this case, the propagation process of a DW driven by a magnetic field in presence of thermal fluctuations results from the competition between an elastic energy (the DW energy) that acts to straighten the DW and a quenched structural disorder which tends to roughen it by local pinning (Fig. 7.4). This competition can be described using a collective pinning approach of elastic interfaces pinned by a weak random pinning potential [41, 50–51]. The DW is described by a series of rigid segments of length L_c (the so-called collective pinning length) that can move independently by thermally activated jumps between metastable states separated by the activation length ξ . The collective pinning length defines the jaggedness of a DW, which increases with increasing disorder.

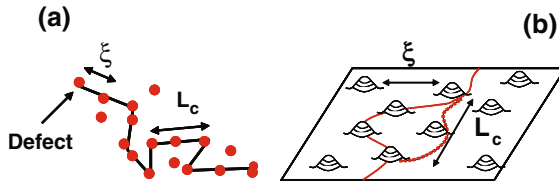


Fig. 7.4 (a) Collective pinning of a DW by an assembly of point defects. In a collective pinning approach, the DW is made of rigid segment of length L_c . The parameter L_c is the so-called collective pinning length which corresponds to the minimum length that cannot be deformed by the pinning potential. (b) Potential landscape experienced by the DW while propagating in a continuous film. Each segment L_c of DW proceeds by thermally activated jumps between metastable states separated by the activation length ξ . For $H > H_p$, ξ corresponds to the typical range of the pinning potential. In epitaxial Pt/Co($t \leq 1$ nm)/Pt sandwiches, $H_p \sim 300\text{--}900$ Oe, $\xi \sim 10$ nm, and $L_c \sim 30$ nm

Such a motion of a 1D DW in a 2D weakly disordered medium gives rise to a very rich dynamical behavior as seen in Fig. 7.5a. The average DW velocity $v(H)$ vs field at $T=300$ K was estimated over ten order of magnitude (from 1 nm/s to 1 m/s) by using Kerr microscopy measurements [44]. Two different regimes of DW motion are observed: a linear regime for which $H > H_p$ and a thermally activated regime for which $H < H_p$. The intersection between the linear regime and the $v=0$ allows the pinning field H_p to be determined. Moreover, the low-field regime $H < H_p$ is characterized by two distinct regions as described below.

For magnetic fields $0.8 H_p < H < H_p$, the DW velocity follows an Arrhenius law [48]

$$v = v_0 \cdot \exp \left[-\frac{2M_S \cdot V_B \cdot (H_p - H)}{k_B T} \right] \quad (7.4)$$

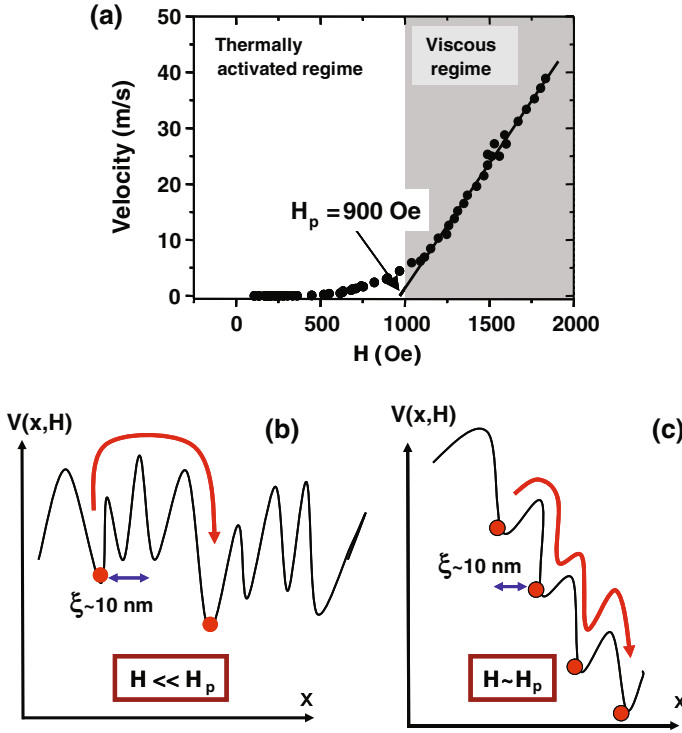


Fig. 7.5 (a) Domain wall velocity as a function of field in a Pt/Co(0.5 nm)/Pt sandwich. Two different behaviors are observed: at high fields $H > H_p$, the DW enters a viscous regime in which the velocity is linear in fields, whereas at low fields $H < H_p$, the DW motion is thermally activated as described in the text. The intersection between the linear regime and $v=0$ allows the pinning field H_p to be determined. (b–c) Schematic illustration of the pinning potential $V(x,H)$ experienced by a DW for $H \ll H_p$ and $H \sim H_p$. The red arrows correspond to the jump to the next metastable state

where the energy barrier $E(H) = 2M_S \cdot V_B \cdot (H_p - H)$ is linear in field, M_S is the saturation magnetization, V_B is the activation volume $V_B = L_B^2 t_{Co}$, which is expressed in terms of the Co thickness t_{Co} and the activation length ξ (close to H_p the parameter ξ corresponds to the range of the pinning potential as illustrated in Fig. 7.4b), and v_0 is the velocity for $H = H_p$. We find $\xi = 12$ nm, which corresponds typically to the size of crystallites and terraces in our films as seen in Fig. 7.3b.

For $H \ll H_p$, one finds that

$$v = v_0 \exp\left(-\frac{U_C}{k_B T} \left(\frac{H_p}{H}\right)^\mu\right) \quad (7.5)$$

where U_C is a scaling constant and $\mu=1/4$. This dynamical process corresponds to the response of a DW to a small external force H (well below the critical depinning force H_p) in the presence of thermal fluctuations. In that case, a weak pin-

ning potential can lead to diverging barriers when $H \rightarrow 0$ [50–51] and a so-called non-linear collective creep regime. The exponent μ is characteristic of the disorder and of the dimensionality of the system. Note that such creep processes are involved in a wide range of systems in which an elastic object moves in the presence of weak disorder such as superconducting vortices [50], ferroelectric systems [52], magnetic films [41, 53–54], growth phenomena [55], charge density waves [56], or fluid invasion [57].

The fundamental difference between the two thermally activated regimes is schematically illustrated in Figs. 7.5b and 7.5c. For $H \ll H_p$, the DW has to jump much further to find the next metastable state than for $H \sim H_p$ because the pinning potential is only slightly tilted under the action of the magnetic field. As a consequence, the activation length L_B in the creep regime is much larger than the range of the pinning potential ξ .

Finally, for high applied fields $H > H_p$, a viscous flow regime is attained in which, the domain wall velocity varies linearly with the applied field [2, 5]

$$v(H) = \mu(H - H_p) \quad (7.6)$$

where μ is the DW mobility ($\mu = \Delta\gamma/\alpha$, where γ is the gyromagnetic ratio and α the damping parameter). In this regime, the disorder only acts as a friction force that renormalizes the applied magnetic field. At higher applied fields $H > H_w > H_p$ (H_w is the Walker limit), the streaming wall motion characterized by a constant velocity is no longer a stable regime and a chaotic regime in which velocity anomalies occur is favored. Finally, for $H \gg H_w$, a precessional regime is expected [1–2, 58]. However, it was not possible to characterize these regimes in our samples since at high magnetic fields the nucleation process dominates over the propagation one. Here, we find a DW mobility $\mu = 0,045$ m/s. Oe which corresponds to a high value of the damping parameter $\alpha \sim 1.5$. However, one has to be very careful in determining the damping parameter of a DW from the flow regime. The group of J. Ferré has showed that the Walker breakdown field H_w can lie in the depinning regime below the propagation field H_p [58]. In that case, the observed linear flow regime is precessional and one can deduce reasonable value of $\alpha \sim 0.4$.

7.3 Control and Detection of Single DW Motion in Magnetic Wires

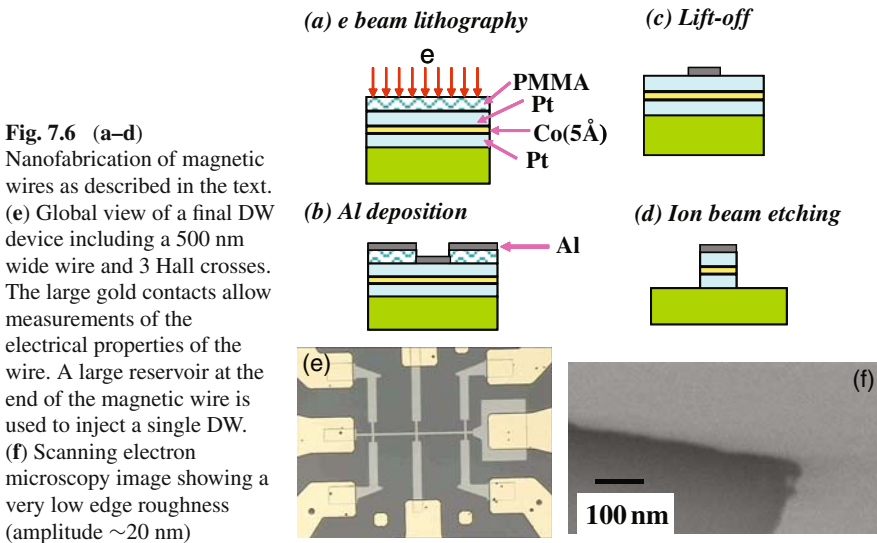
In order to observe geometrical-induced effects on DW motion, the typical lateral dimensions of the nanowire have to be comparable with characteristic magnetic and structural lengths of the materials. This corresponds to wire sizes of a few hundreds of nanometers. Here, give a brief overview of the patterning process needed to obtain high-quality nanowires down to 100 nm. A particular care has to be taken in order not to introduce major extrinsic defects from the patterning process. The method to inject a single DW into the wire will be described. Then I will show that extraordi-

nary Hall effect (EHE) in single ferromagnetic films and the giant magnetoresistance (GMR) effect in spin valves are a very useful way to detect with a high spatial sensitivity DW motion in perpendicularly magnetized wires.

7.3.1 Wires Nanofabrication and Injection of a Single Domain Wall

Domain wall devices down to 100 nm in size are usually patterned using electron beam lithography and ion beam etching. They generally consist in a 10–100 μm long and 0.1–1 μm wide wires that can also include Hall crosses for EHE measurements. Macroscopic electrical contacts have to be included in order to detect DW motion via electrical measurements. An example of a complete process is detailed below (Figs. 7.6a–7.6d):

- (i) Optical lithography and “lift off” are used to fabricate macroscopic electrical gold contacts on top of a Pt/Co/Pt sandwich. A 10 nm chromium layer, deposited before the gold layer, promotes a good adhesion on the Pt/Co/Pt film.
- (ii) The wire pattern is then defined by e-beam lithography in 0.4 μm thick PMMA resist (Fig. 7.6a).
- (iii) Fabrication of a 60 nm thick Al etch mask by a “lift-off” process (Fig. 7.6b)
- (iv) Ion beam milling of the magnetic film (Fig. 7.6c).
- (v) Wet chemical removal of the Al mask (Fig. 7.6d).



A final DW device including 3 Hall crosses is shown in Fig. 7.6e. We have checked the quality of the patterning processes by using ultra-high resolution scanning electron microscopy. Although no patterning-induced major defects are visible, we have observed for all wires a slight roughness of the edges (amplitude ~ 20 nm, period 200 nm) which is symmetric on both sides as a consequence of the e-beam writing process (Fig. 7.6f). In order to inject a single DW into the device, we have controlled the nucleation of a single reversed domain outside the wire by adjoining a large nucleation area to one of the current probe of the wire (Fig. 7.7a). The magnetic sequence to inject a single DW is the following. First, a strong negative field is applied in order to saturate the magnetization in one direction. Next, a positive field pulse is applied in order to control the nucleation of a single reversed domain in the large nucleation area and its injection into the wire (Fig. 7.7b). MO microscopy has confirmed that a single and coherent DW is propagating in the wire (Fig. 7.7c).

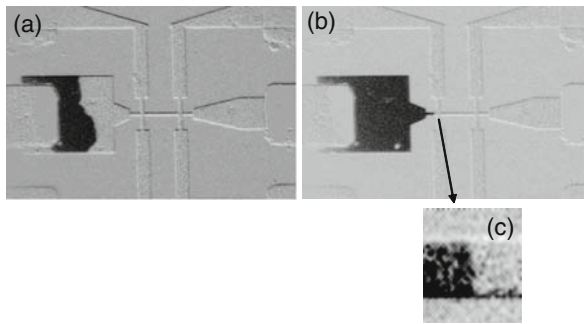


Fig. 7.7 Magneto-optic images taken in a $w=1$ μm wide wire made from an epitaxial Pt/Co(1 nm)/Pt film indicating (a) a single domain nucleation in the large magnetic area, (b) the injection of a single domain wall into the magnetic wire, and (c) the propagation of a straight DW in the wire

7.3.2 Electrical Methods to Detect DW Motion Along Tracks

In films with perpendicular anisotropy, single DW motion can be detected via both the GMR by measuring the longitudinal resistance between two contacts and the extraordinary Hall effect (EHE) by measuring the transverse voltage at Hall crosses.

The extraordinary Hall effect (EHE) is a very well-known magnetotransport phenomenon [59]. The Hall resistivity ρ_{xy} in homogeneous thin films of ferromagnetic metals can be written as the sum of the ordinary Hall effect and the extraordinary Hall effect

$$\rho_{xy} = R_0 H + R_S 4\pi M_{\perp} \quad (7.7)$$

where H is the applied field, M_{\perp} the perpendicular magnetization, R_0 the ordinary Hall coefficient, and R_S the extraordinary Hall coefficient. The origin of the EHE is

still very controversial in thin ferromagnetic multilayers. It arises from asymmetrical scattering of the conduction electrons due to the spin orbit interaction [43, 44]. Two mechanisms are identified as origins of the asymmetrical scattering, the skew scattering and the side-jump scattering. In Pt/Co/Pt systems, we found that diffusion at Co/Pt interfaces and at the surface are the main contributions to EHE [43, 44]. Due to the high spin-orbit coupling of Pt, the EHE component $|4\pi M_{\perp} R_S| \gg |R_0 H|$ up to $H=1\text{T}$ and thus ρ_{xy} is directly proportional to the perpendicular magnetization. This makes EHE a very useful technique to detect DW motion through a Hall cross. Using lock-in detection together with low noise pre-amplifiers, DW motion can be detected in a Hall cross with a spatial resolution down to 10 nm. This is illustrated in Fig. 7.8a that gives the Hall voltage V_{xy} as a function of field for an

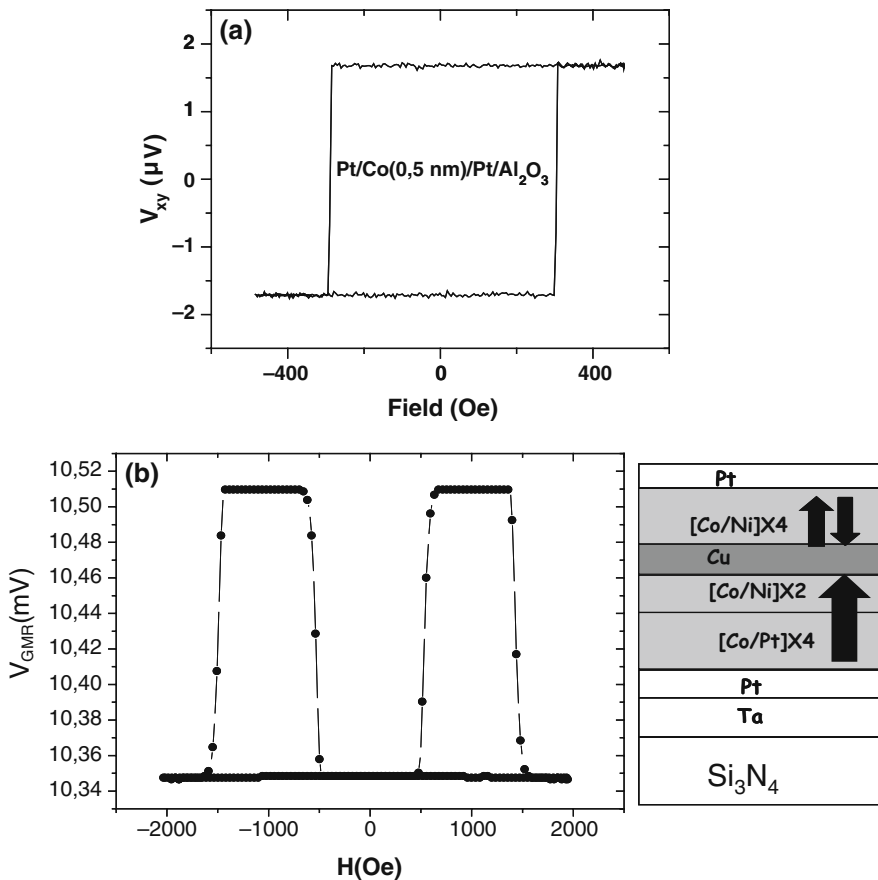


Fig. 7.8 (a) Typical measurement of EHE as a function of field in a $200 \times 200 \text{ nm}^2$ Hall cross made in a Pt/Co(0.5 nm)/Pt sandwich. (b) Typical measurement of GMR as a function of field in a 500 nm wide wire made in a textured CoNi-based spin valve showing the reversal of the free and hard layer by domain wall motion between two electrodes separated by $40 \mu\text{m}$

epitaxial Pt(35 Å)/Co(5 Å)/Pt(45 Å) trilayers systems. The strong voltage variation of V_{xy} corresponds to the propagation of a 10 nm wide and 0.5 nm thick DW through a 200 nm wide Hall cross. If the geometrical shape of the DW is known as it propagates through the Hall cross, it is then possible to determine the DW position very accurately from the value of the electrical signal [7].

A major drawback of using the EHE is that it is only sensitive to DW motion through a Hall cross, which limits the investigation of DW motion to small distances. Furthermore, the domain wall structure itself can undergo some deformation as it propagates through the Hall cross, as we will see in Section 7.5.2. Exploiting the giant magnetoresistance (GMR) effect in this respect, proves to be advantageous since the domain wall position can be tracked along the whole wire. Up to now, the use of the GMR effect to track domain wall motion in wires has only been made in spin valves with in-plane magnetization [6]. Figure 7.8b shows that high GMR ratio of 1.5% can be obtained in perpendicular spin valves made of Co/Ni multilayers (see Section 7.4.2), which allows us to detect DW motion on large distances (few tens of microns) with a spatial sensitivity down to 500 nm. Note that the major drawback of GMR effect is that it can be used only in spin valves where the additional layers may play a role in the mechanism of DW motion.

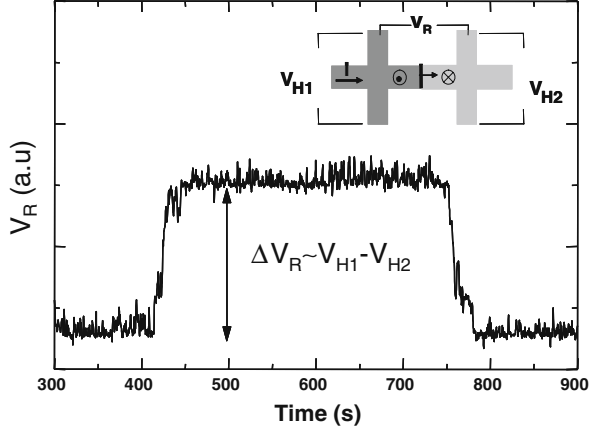
7.4 Field-Induced DW Motion Along Wires: Role of Structural Defects

As discussed in Section 7.2, the field driven propagation of a DW is dominated by a competition between an elastic energy and a structural disorder. In the following, I will address the mechanisms of DW motion in a 2D-confined geometry in which both intrinsic defects from the continuous films and defects introduced by the patterning technique play a crucial role. For that, I will first describe the dynamics of a 1D DW in magnetic wires with different width w_0 patterned in epitaxial Co/Pt magnetic films. In this case, the intrinsic pinning potential is very homogeneous and the dynamics of DW motion is strongly influenced by the edge roughness. This behavior is then contrasted with DW motion in wires patterned from Co/Ni spin valves in which in this case a large distribution of intrinsic defects from the virgin films governs the dynamics.

7.4.1 *The Role of Edge Roughness on the Creep Regime in Co/Pt Films*

We have used extraordinary Hall effect to detect domain wall propagation in sub-micron size wires that include double symmetric Hall crosses made from epitaxial Pt/Co(1 nm)/Pt trilayers as described in Section 7.2. In order to evidence edge-induced effects, the influence of the wire width on the creep regime has been investigated [10, 44]. By measuring the time dependence of the extraordinary Hall voltage

Fig. 7.9 Time dependence of the longitudinal voltage V_R between 2 Hall crosses H1 and H2 during magnetization reversal. The voltage V_R is proportional to the Hall voltage difference $V_{H1} - V_{H2}$: the first (second) step corresponds to the DW moving inside the first (second) cross. This allows the determination of DW velocity between the 2 Hall crosses separated by $10 \mu\text{m}$



difference $V_{H1} - V_{H2}$, between 2 Hall crosses, one can precisely deduce the average DW velocity $v(H)$ inside the connecting wire as can be seen in Fig. 7.9. Results are shown in Fig. 7.10a where $\log v(H)$ vs $H^{-1/4}$ is plotted for four different wire w_0 widths ranging from 0.5 to $1.5 \mu\text{m}$. Surprisingly, we observe a huge reduction of the velocity $v(H)$ when the wire width is reduced, which indicates an increase of the energy barrier for DW motion in a confined geometry. For all widths, the straight lines of Fig. 7.10a indicate that the data are compatible with a creep formula (Eq. 7.5) given by

$$v(H) = v_0 \exp(-\beta U_{cw} (H_{cw} / H)^{1/4}) \quad (7.8)$$

where H_{cw} and U_{cw} are the critical field and the scaling energy constant in the wire, respectively. The value $\mu=1/4$, which was already found in similar but unpatterned continuous films (Eq. 7.5), is expected for the case of a 1D interface moving in one transverse direction. The width $w_0=1.5 \mu\text{m}$ corresponds to the highest velocity and a curvature at high fields is observed which suggests that the system leaves the creep regime. Figure 7.10b shows that the effective critical field $H_c^{eff} = (\beta U_{cw})^4 H_{cw}$ deduced from the slope of the curves in Fig. 7.10a scales as $(1/w_0)$. This dependence is an indication that the reduction of $v(H)$ is induced by a mechanism linked to the edges of the magnetic wires where only a slight sinusoidal-like edge roughness symmetric on both sides (period $p \sim 200 \text{ nm}$, amplitude $a \sim 20 \text{ nm}$) is present.

In order to demonstrate that edge roughness play a role in the reduction of DW velocity, we have fabricated wires with artificially induced strong edge roughness of the simple form $w(x) = w_0 + 2a|\sin(kx)|$ symmetric on both sides as presented in Fig. 7.11a (x is the position along the wire, $w(x)$ is the wire width, w_0 is a constant width, a the amplitude of the roughness, and $k = \pi/p$ its wave vector). Figure 7.11b shows $\log v(H)$ vs $H^{-1/4}$ for a wire of width $w_0=1 \mu\text{m}$ exhibiting either natural roughness ($a=20 \text{ nm}$ and $p=200 \text{ nm}$) or strong artificial roughness ($a=200 \text{ nm}$ and $p=1 \mu\text{m}$), compared to the dependence inside the large reservoir in which we

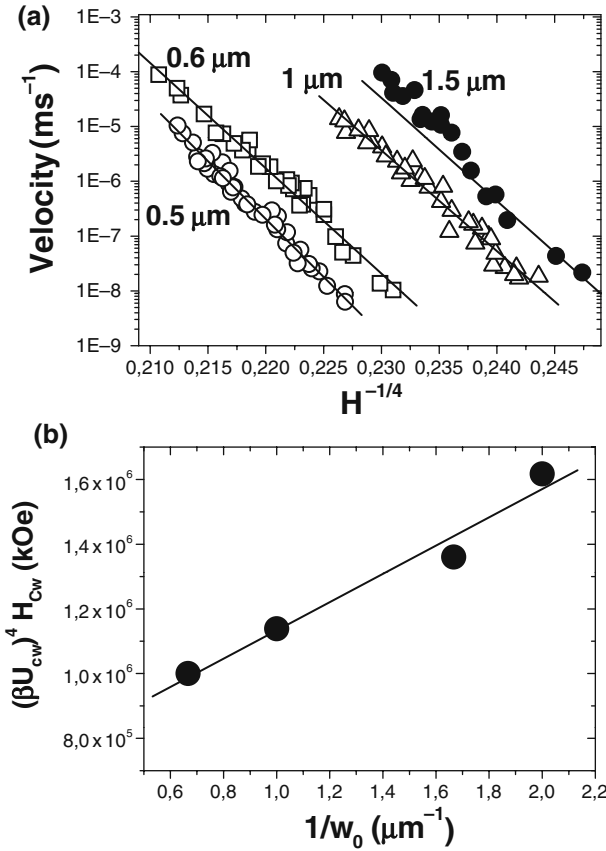


Fig. 7.10 (a) Average DW velocity as a function of $H^{-1/4}$ for 1.5, 1, 0.6, and 0.5 μm wide wires patterned in a 1 nm thick Co layer. (b) Effective critical field H_c^{eff} as a function of $(1/w_0)$

assume the intrinsic properties of the non-patterned film are preserved (as determined by a MO microscopy study). The velocity measurements have been done in the same sample. We observe a reduction in the DW velocity inside the “natural” wire by about one order of magnitude with respect to the velocity measured inside the reservoir. This clearly indicates that additional pinning effects drive the DW dynamics in magnetic wires. But the most important feature is that the velocity is further reduced by the presence of the strong artificial edge roughness. This result is consistent with an influence of edge modulation on DW dynamics.

In the following, I will show that the variation of the DW length due to the modulation of the wire width induced by the edge roughness leads to a reduction of DW velocity. Consider a straight DW of constant length L reaching the input of a magnetic wire of width $w(x)$. To propagate further under an applied field H , the DW has to change its length. First, let us neglect the presence of intrinsic structural defects. Its static properties can be energetically described by the balance between wall energy (which favors a reduction of the wall length) and the Zeeman energy

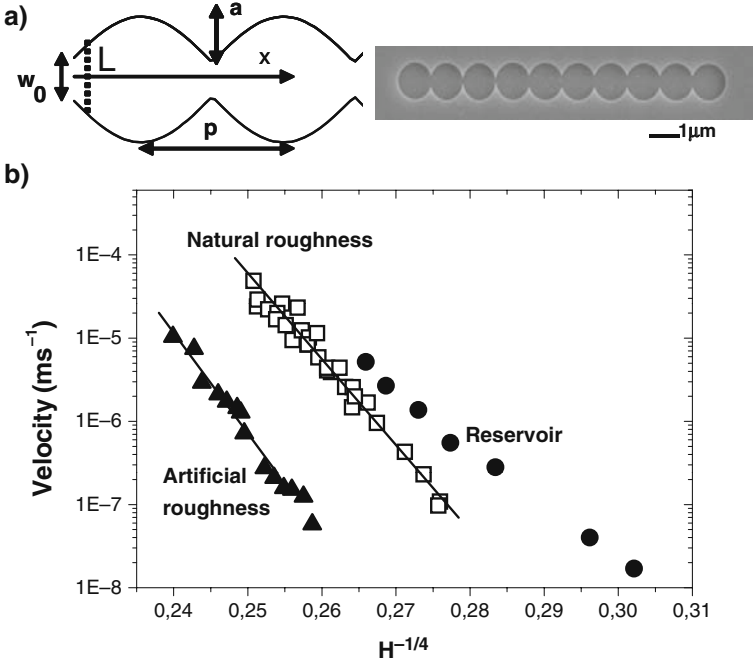


Fig. 7.11 (a) DW propagating in a wire where the lateral width is varying as $w(x)=w_0+2a|\sin(kx)|$ and SEM image after the PMMA writing process of a wire with artificial ER of form $w(x)$ ($a=200$ nm, $p=1$ μm). (b) Average DW velocity inside a wire of $1\mu\text{m}$ with natural ER ($a=20$ nm, $p=200$ nm) and with artificially induced ER (Fig. 7.11a) patterned in a same 0.5 nm thick Co layer, compared to the DW velocity inside the large reservoir

(which favors an increased reversed area). If the DW center propagates by dx and the corresponding reversed surface is dS , the wall energy and Zeeman energy variations are

$$dE_\sigma = \sigma t_{\text{Co}}(\partial L/\partial x)dx \text{ and } \sigma = 4(AK_{\text{eff}})^{1/2} \quad (7.9)$$

is the wall energy per unit surface (A is the exchange stiffness), and

$$dE_Z = -2M_S H t_{\text{Co}}(\partial S/\partial x) dx \quad (7.10)$$

The change of total energy is

$$dE_{\text{tot}}/dx = \sigma t_{\text{Co}}(dL/dx) - 2M_S H t_{\text{Co}}(dS/dx) \quad (7.11)$$

This energy is minimized at a given position x of the wire for a field

$$H_{\text{top}}(x) = \frac{\sigma}{2M_S} \left(\frac{dL}{dx} \right) \frac{1}{w(x)} \quad (7.12)$$

This field corresponds to the minimum field which needs to be applied at position x in order for the DW to propagate further. This geometrical induced pinning field is either positive when the DW has to increase its length $dL > 0$ ($dw/dx > 0$) or negative when it has to reduce its length $dL < 0$ ($dw/dx < 0$). If $dw/dx \gg 1$, the DW is bent as we will see for DW propagation through a Hall cross (Section 7.5.2). Here, however, as $w(x)$ varies smoothly (the aspect ratio $a/p \ll 1$ is small), it is a good approximation to consider that the DW remains straight, i.e., $L(x) = w(x)$. Let's now consider a wire of width $w(x)$ exhibiting sinusoidal edge roughness of the form $w(x) = w_0 + 2a|\sin(kx)|$. At each constriction where $w(x) = w_0$, the DW has to overcome an energy barrier which is maximum because $H_{top}(x)$ reaches its highest value

$$H_{top}^{\max} = (\sigma / M_s)(ka/w_0) \quad (7.13)$$

One finds that $H_{top}^{\max} \sim 20$ Oe for the natural edge roughness ($a = 20$ nm and $p = 200$ nm) and ~ 70 Oe for the artificial one ($a = 200$ nm and $p = 1 \mu\text{m}$). By using an approach deduced from collective pinning theory developed for vortices in superconductors [50], one can demonstrate [10] that the critical field H_w of the wire is simply

$$H_w(x) = H_p + H_{top}(x) \quad (7.14)$$

where H_p is the intrinsic pinning field due to the random pinning potential of the film. Thus the creep law can be renormalized by introducing the effective critical field $H_w(x)$

$$v(H) = v_0 \exp[-\beta U_w ((H_p + H_{top}(x))/H)^{1/4}] \quad (7.15)$$

In the creep regime DW propagation is characterized by jumps over energy barrier from one metastable state to another (Fig. 7.5c). Assuming the validity of the Arrhenius–Neel law

$$\tau(E) = \tau_0 \exp[E(H)/kT] \quad (7.16)$$

where τ_0 is the inverse of the attempt frequency (values of τ_0 for ultra-thin films are in the range of 1–100 ns), one can consider that at position x a thermally activated jump takes an average time given by

$$\tau(H, x) = \tau_0 \exp(\beta U_w (H_w(x)/H)^{1/4}) \quad (7.17)$$

As such, the total average time measured in our experiment (Fig. 7.10) is dominated by the pinning times at constrictions where $H_w(x)$ is maximum (strong pinning positions). A good approximation is therefore to consider that the critical field in the wire is simply

$$H_w(x) = H_p + H_{top}^{\max} = H_p + (\sigma / M_s)(ka/w_0) \quad (7.18)$$

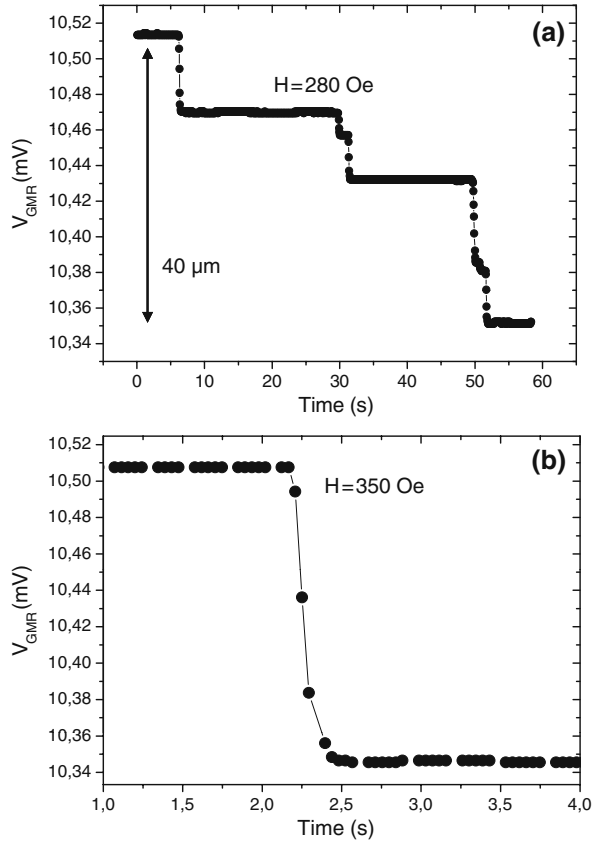
In this case, H_w is found to be proportional to l/w_0 which is qualitatively consistent with the experimental results of Fig. 7.10. These results indicate that even a slight edge roughness corresponding to an additional pinning field of $H_{\text{top}} \sim 20$ Oe can strongly influence the DW propagation in a magnetic wire.

7.4.2 The Role of Intrinsic Defects in Co/Ni Films

In the previous Section, I have shown that domain wall propagation mechanisms are qualitatively consistent with additional DW pinning due to wire width modulation introduced by edge roughness. However, the main drawback of a technique based on EHE is that it is only sensitive to the DW motion in the Hall cross. As such, this technique is not useful if one wants to track the DW motion along the wire in order to confirm the hypothesis of DW pinning due to edge modulation. Exploiting the giant magnetoresistance (GMR) effect in spin valves is more powerful since it can deliver an electrical signal which is directly proportional to the position of a DW along a wire in one of the layers. However, in spin valves based on Co/Pt multilayers, the GMR effect is very small (about 0.1%) due to the high spin-orbit coupling of Pt. Instead, the use of Co/Ni magnetic multilayers provides perpendicular anisotropy with much higher GMR ratio compared to Co/Pt multilayers.

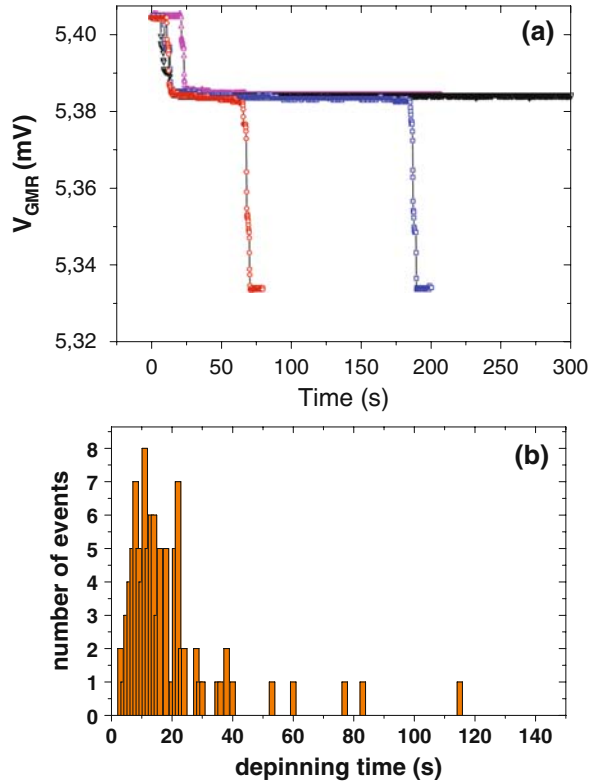
We have developed specific spin valve structures based on Co/Ni multilayers with PMA [60–61] to detect DW motion over large distances in wires. The structure consists of a Pt/reference layer/Cu/free layer/Pt multilayer film. The reference layer is a composite [(Co/Pt)₄/(Co/Ni)₂] to enhance perpendicular anisotropy (5×10^6 erg/cm³), while the free layer is a single (Co/Ni)₄ film exhibiting a lower PMA. We have fabricated high quality 100- μm long and 0.2–1 μm wide wires with lower edge roughness (<10 nm) than in our previous Pt/Co/Pt systems. As described in Section 7.3.2, GMR ratio up to 1.5% (Fig. 7.8b) allows the detection of DW motion in the free layer with a spatial resolution down to 500 nm. Measurements of the GMR as a function of time in constant fields allow the DW motion to be tracked along the magnetic wire. This is illustrated in Fig. 7.12a for a 200-nm wide nanowire in a perpendicular applied field $H=280$ Oe. This field is below the field required to reverse the free layer in Fig. 7.8. The variation of the GMR vs time corresponds to a DW motion between two contacts that are 40 μm apart. The DW motion occurs in a series of abrupt jumps separated by long plateaus. These features are consistent with the presence of strong random pinning sites that interact with the DW during its propagation in the wire. The abrupt jumps correspond to thermal activation of the DW from a pinning site and easy DW motion to the next pinning event. The distribution of jumps reflects the distribution of pinning sites along the wires. The average velocity estimated for the DW to travel the 40 μm wire is ~ 0.9 $\mu\text{m/s}$. Note that the pinning events seen in Fig. 7.12a have been observed for more than 10 different wires ranging from 200 nm to 1 μm in size. In all cases, the typical field to get steady DW motion is about 320 Oe. Figure 7.12b shows the corresponding GMR vs time for an applied field of $H=350$ Oe. The variation of the GMR corresponds to a steady DW motion, which gives rise to an average DW velocity of

Fig. 7.12 Measurement of GMR as a function of time in a 200 nm wide wire made from CoNi spin valves (Fig. 7.8b) for a magnetic field of (a) $H=280$ Oe and (b) $H=350$ Oe. The plateaus correspond to a few DW pinning events on local defects along a 40- μm long wire



$\sim 200 \mu\text{m/s}$. Shown in Fig. 7.13a are multiple measurements of DW motion at fixed fields ($H=300$ Oe) for a 500-nm wide wire. The presence of pinning centers combined with thermal activation leads to a dynamical behavior that is not reproducible. Particularly, the distribution of pinning time from the same pinning position is very large (Fig. 7.13b), which induces a stochastic behavior along the wire. Let us discuss the origin of such pinning centers here. Contrary to the Pt/Co/Pt systems described previously, we have not observed any dependence of DW motion on the wire width. As stated before, the typical field to get steady DW motion is always about 320 Oe independently of the wire width. This rules out the edge roughness as the culprit, which is consistent with its low amplitude here as measured by SEM (<10 nm). A possible explanation as evidenced by MO Kerr microscopy in the virgin films is the presence of a large distribution of pinning defects with some hard pinning centers contrary to the very homogeneous Pt/Co/Pt ultra-thin films used before. These pinning centers can be related to surface roughness, boundaries between crystallites, atomic steps at interfaces, or dislocations. Dws can avoid the hard pinning centers by circumventing them to propagate further in the virgin films, but the possible paths

Fig. 7.13 (a) Four different measurements of DW motion in a 500-nm wide wire at fixed field $H=300$ Oe exhibiting a stochastic behavior. (b) Distribution of pinning time for a single pinning event obtained after 200 measurements at the same magnetic field



for DW motion are reduced in wires because of the reduction of the lateral dimension. Thus, while propagating in the wire, the DW is probing the distribution of pinning fields H_p during the course of propagation and it is the highest part of the distribution that determines the field necessary to reverse the entire wire by steady DW motion.

7.5 Control of the Pinning Potential

As illustrated in Section 7.4, the control of both the distribution of intrinsic defects in continuous films and the defects introduced by the patterning technique is a key challenge to obtain reproducible and easy DW motion over large scale in magnetic wires. Here we will show that it is possible to reduce the influence of intrinsic defects in Co/Pt films by using irradiation with light He^+ ions. We will also describe a method to precisely locate and hold DWs by deliberately fabricating artificial pinning centers.

7.5.1 Ion Irradiation of Co/Pt Films: A Way to Reduce Intrinsic Structural Defects

Ion irradiation of 3rd metallic magnetic systems has been extensively investigated [62], since Chappert et al. [63] reported that He⁺ irradiation at 30 keV reduces the anisotropy and coercivity in perpendicular magnetized Pt/Co/Pt sandwiches and Pt/Co multilayers. The basic motivation of ion irradiation of Pt/Co systems arises from the possibility to modify the PMA through irradiation-induced intermixing at the interfaces. In Co/Pt multilayers with small Co thickness, interface anisotropy is strong enough to overcome the macroscopic shape anisotropy and to induce a perpendicular easy axis of magnetization. Therefore, in order to modify and to control the magnitude of the anisotropy, one only has to change the properties at the interfaces. Mixing induced by light ion irradiation, since it preserves the crystal structure while gradually mixing the interfaces [62], is a perfect tool for that purpose.

We have studied the influence of irradiation on DW velocity in magnetic wires [45]. For that purpose, the structures used are epitaxial Pt(35 Å)/Co(5 Å)/Pt(45 Å) trilayers grown by sputtering on Al₂O₃(0001) substrates as described in Section 7.2.1. The continuous films were patterned to obtain high-quality 1 μm wide and 15 μm long wires connected by double Hall crosses. Macroscopic 250 μm wide Hall structures were also fabricated using the same patterning process. The dynamical properties of these large structures were probed by means of polar magneto-optical Kerr microscopy and compare to the narrow wires. Large and narrow wires were then irradiated with 10 keV He ions up to a fluence of 10¹⁵ He cm⁻², which leads to a marked reduction in¹⁰ the perpendicular anisotropy. The fluence was limited in order to keep the anisotropy perpendicular and to preserve magnetization switching via domain wall propagation. One micron and 250 μm wide irradiated and non-irradiated wires were designed on the same sample in order to maintain the same intrinsic film properties. Then as described in Section 7.4.1, we have used Extraordinary Hall effect to measure domain wall velocity for temperatures ranging from 10 to 300 K.

In Figure 7.14 we present a comparison of the velocity curves $v(H)$ for irradiated and non-irradiated 250 μm wide wires measured on a very wide dynamical range by Kerr microscopy. We observe a large increase of the DW velocity $v(H)$ on the whole velocity range for irradiated wires, which is consistent with a reduction of the DW pinning energy barriers. For $0.8H_p < H < 1.2H_p$, we find (see inset 1)

$$E(H, H_p) = -2M_S V(H - H_p) \quad (7.19)$$

where H_p is found from extrapolation to the high field curves to $v=0$. We deduced that H_p is reduced from 850 to 450 Oe and the disorder correlation length x deduced from the activation volume V increases from 20 to 30 nm under irradiation. The fact that H_p is reduced under irradiation shows that the efficiency of the pinning potential has been lowered. The increase of ξ is a clear evidence of the reduction of the density of pinning defects. We believe that these features mainly originate

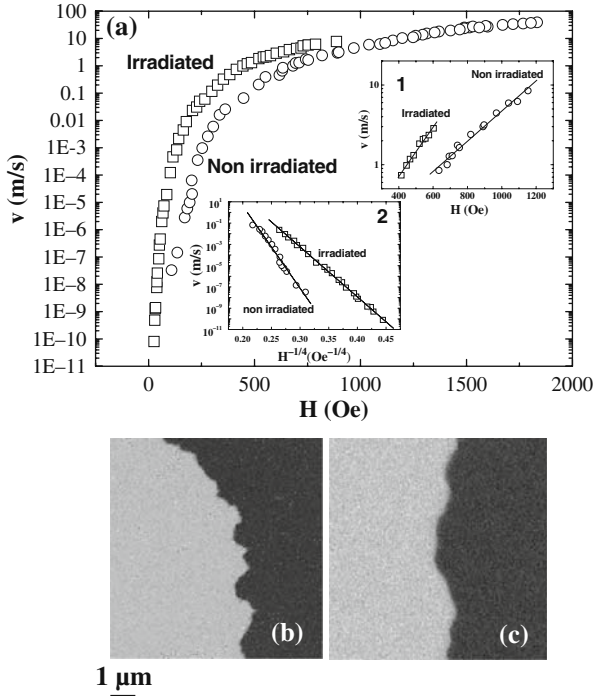


Fig. 7.14 (a) Variation of the domain wall velocity as a function of the applied field for the irradiated (*squares*) and non-irradiated (*dots*) 250 μm wide wires. The insets represent (1) the thermally activated regime close to H_p and (2) the creep regime for $H \ll H_p$. (b–c) Kerr images of the domain wall for values of $H \ll H_p$ for (b) a virgin wire and (c) an irradiated wire

from the reduction of the perpendicular anisotropy leading to lower pinning barriers and making the weakest pinning defects inefficient through thermal fluctuations. In addition, although we do not know the correlation length of K_u , we hypothesize that the weak ion-induced intermixing may average out the role of defects at interfaces such as atomic steps, leading to easier DW motion. Finally, since the DW width increases through the reduction of anisotropy, the interaction of the DW with defects becomes screened.

As shown in the second inset 2 of Fig. 7.14, for $H \ll H_p$ one obtains a linear dependence of $\ln v(H)$ vs $H^{-1/4}$ for irradiated and non-irradiated wires. This result is consistent with a creep process given by Eq. 7.5. The universal exponent $1/4$ is not modified under irradiation which is consistent with the remaining 2D dimensionality of the system and the presence of a weak disorder. The effective energy barrier $U_{eff} = (\beta U_c) H_p^{1/4}$ deduced from the slope of the curves in Fig. 7.14a is reduced from $80 \text{ Oe}^{1/4}$ to $40 \text{ Oe}^{1/4}$ under irradiation. This reduction of H_c^{eff} in the creep regime is driven by both the decrease in threshold field H_p (from 850 to 450 Oe) and the U_c (by a factor of 1.5). The parameter U_c relates to elastic and pinning energies stored by the DW on a segment of length L_c . Its reduction indicates that the DW adjusts elastically in the potential landscape to reach much optimal local

configuration. This is well illustrated in Fig. 7.14b–c in which snapshots of the DW in the creep regime are shown for 250 μm wide non-irradiated and irradiated wires. The short wavelength wall roughness is highly reduced under irradiation as a result of a lower density of efficient pinning sites.

Finally, let us consider the domain wall propagation process in the narrow 1 μm wide wires where edge effect can become more important. Figure 7.15a compares the temperature dependence of the V – H curves in the thermally activated regime between non-irradiated and irradiated wires. We observe an increase of the DW velocity under irradiation at all temperatures. For both wires, the data are also consistent with a creep formula with $\mu=1/4$ which suggests that the propagation is still dominated by weak random disorder. For the irradiated wire, the curvature present at high fields indicates that the system departs from the creep regime since H begins to be closer to H_p , which is reduced as compared to its value in the non-irradiated film. The transition occurs at higher fields when the temperature is reduced (200, 300, and 450 Oe at 250, 200, and 150 K, respectively) because H_p is enhanced due to a higher anisotropy and lower thermal fluctuations. The easier DW motion is confirmed in Fig. 7.15b in which the temperature variation of the effective energy barrier U_{eff} is shown for both wires. The energy barrier decreases under irradiation by a factor of about 2 as in the case of 200 μm wide wires. However, one observes that the energy barrier for the narrower wires is higher than for the wider wires. This is consistent with the discussion in Section 7.4.1 where we show that in submicron

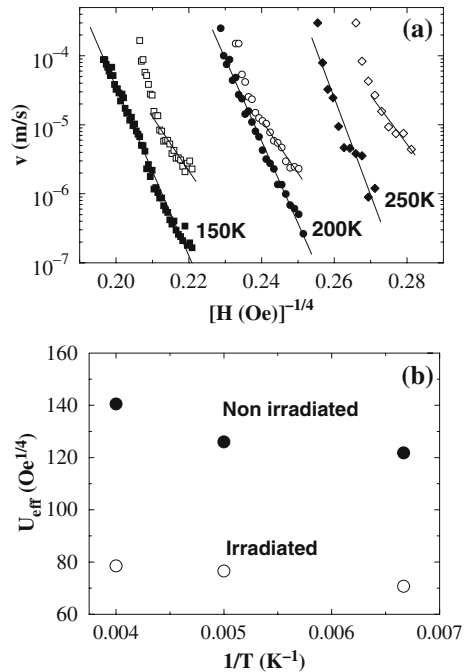


Fig. 7.15 (a) Variation of the domain wall velocity as a function of the applied field for irradiated (*open symbols*) and non-irradiated (*full symbols*) 1 μm wide wires at 150 K (*squares*), 200 K (*circles*), and 250 K (*diamonds*). (b) Temperature dependence of the effective energy barrier for irradiated and non-irradiated 1 μm wide wires

wires the edge roughness introduced by patterning can increase the critical field. The temperature variation of U_{eff} indicates that the thermal stability of a single DW is reduced by irradiation as a consequence of a lower pinning energy.

7.5.2 A DW Propagating in a Hall Cross: An Artificial Pinning Potential

One prerequisite to develop applications based on DW motion is to use well-localized artificial pinning sites. This allows a DW to be trapped at a given position in a device and ensure high enough thermal stability as well as allowing a better reproducibility of the depinning process. Such pinning sites also give the DWs the stability to resist external perturbations such as stray magnetic fields from nearby devices. There are several means of creating such pinning sites; for instance by patterning notches along the edges of the wire, modifying locally the magnetic properties of the material, or modulating the thickness of the magnetic film. Here, I will present the use of a very well-controlled artificial pinning potential. Particularly, I will describe the mechanism of geometrically induced DW pinning resulting from the motion of a DW in a Hall cross [7, 43].

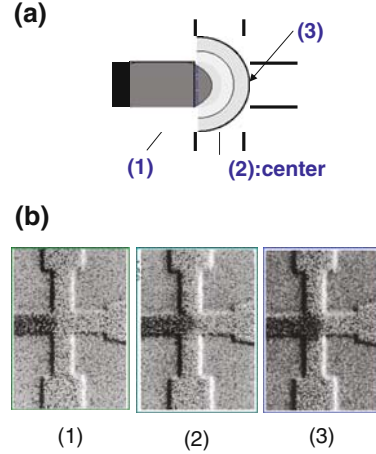
As indicated in Eqs. (7.12) and (7.14), the propagation field $H_w(x)$ at position x of a DW of length $L(x)$ in a wire of non-constant width $w(x)$ can be written

$$H_w(x) = H_p + H_{top}(x) \text{ and } H_{top}(x) = \frac{\sigma}{2M_s} \left(\frac{dL}{dx} \right) \frac{1}{w(x)} \quad (7.20)$$

where $H_{top}(x)$ is the geometrical-induced propagation field. Thus by designing specific local geometry, it is expected to control artificially the local pinning of a DW. Particularly, let's consider a single flat DW propagating in a wire of constant width and reaching the input of a symmetric Hall cross (Fig. 7.16a). In order to propagate further, the DW has to increase its length L . Since $dw/dx \gg 1$ in a Hall cross, the DW configuration inside the cross (Fig. 7.16a) is an expanding arc of circle ($L(x) \neq w(x)$), which corresponds to a maximal reversed surface S bordered by the smallest possible wall length L [7]. More precisely, at the input of the cross, the flat DW stays pinned to the corners and bends like a 2D bubble until it coincides with a half circle at the cross center with a radius of $w/2$. Then, above this semi-circle position it becomes energetically favorable for the DW to be depinned from the input corners and to expand as a bubble half circle until reaching the output corners. As seen in Fig. 7.16b for a $1 \mu\text{m}$ wide Hall cross made from an epitaxial Pt(35 Å)/Co(10 Å)/Pt(45 Å) film, such a bubble-like behavior is confirmed by MO Kerr images. The maximum propagation field $H_{top}(x)$ is obtained when the DW reaches the cross center (semi-circle at position (2)). With a perfect 1D Bloch DW, this maximum corresponds to a topologically induced pinning field

$$H_{top}^{center} = (\sigma/w M_s) \quad (7.21)$$

Fig. 7.16 (a) Bubble-like behavior of an ideal 1D Bloch DW in a magnetic Hall cross. (b) This process is shown by Kerr microscopy measurements



In addition, due to the homogeneously distributed intrinsic structural defects, the total pinning field corresponding to position (2) for the bent DW is

$$H_{cross}(center) = H_p + H_{top}^{center} \quad (7.22)$$

Thus by varying the width w of a Hall cross, one can control accurately the strength of the pinning potential (Fig. 7.17a). This is also clearly indicated in Fig. 7.17b where we show the pinning time $\tau(H)$ as a function of field H for two different widths as measured by EHE. The results can be described by a classical thermally activated depinning behavior (Eq. 7.16) given by

$$\tau(H) = \tau_0 \exp \left[2M_S V (H_{cross} - H) / k_B T \right] \quad (7.23)$$

As an example for a 500 nm and 1 μm wide Hall cross made from the same Pt(35 Å)/Co(10 Å)/Pt(45 Å) film, this leads to $H_{cross}=480$ Oe and 370 Oe, respectively. Assuming $H_{top}^{center} = (\sigma/w M_S)$ (~ 150 Oe for $w=500$ nm and ~ 75 Oe for $w=1$ μm), we deduce an intrinsic pinning field $H_p \sim 300$ Oe which is consistent with the value found in our virgin films with $t_{Co}=0.1$ nm. Note that the edge defects may not play any role provided the two input corners of the Hall cross are the same.

7.6 Current Induced DW Depinning

Manipulating DW in nanodevices has the potential to become a key underlying technology for non-volatile memories, HDs, sensors, and logic circuits. However, the generation of magnetic field in nanodevices is a very challenging technological issue. One means of circumventing this problem, is to use spin-transfer torques,

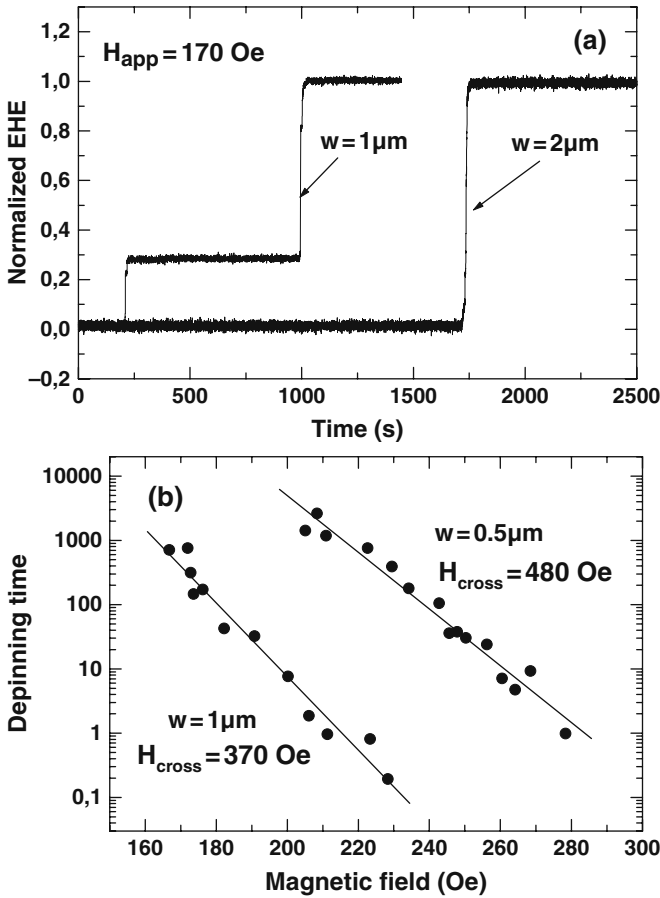


Fig. 7.17 (a) Measurement of EHE as a function of time for 2 and 1 μm wide wires patterned in a 1 nm thick Co layer. The plateau for the 2 μm wide wire corresponds to DW pinning at the center of the Hall cross (position (2) in Fig. 7.16). (b) Depinning time at the cross center as a function of the applied magnetic field for 1 and 0.5 μm wide wires patterned in a 1 nm thick Co layer

which lead to considerable design simplifications because the currents involved are passed directly through the DW. This is a very appealing concept, but maybe the more exploratory one compared to other MRAM propositions. Building on Berger’s pioneering work [63–65], the understanding of the mechanisms behind current induced domain wall motion remains a challenging problem. Particularly, the origin of the threshold current J_{th} ($\sim 10^7 \text{ A/cm}^2$) to move DW is still unclear. Previous measurements of current-driven DW motion in wires have mainly used in-plane magnetized wires having a 3D Neel-type DW configuration [18–23, 25, 27–31, 33–35]. Since the DW width is large ($\sim 100 \text{ nm}$), these experiments are expected to have investigated only the “adiabatic” limit where the spins of electrons follow the local magnetization [17]. Using narrow DWs created in thin films with perpendicular magnetic

anisotropy (PMA) is expected to increase the ST efficiency due to the contribution of the non-adiabatic term (the so-called β term) [14]. For strong pinning and/or narrow DWs, theories also predict that the threshold current is determined by the pinning potential [17]. In this Section, I will describe our recent work on the mechanisms of DW motion driven by a polarized current in wires with PMA. Particularly, I will discuss the underlying origin of the threshold current J_{th} that is of crucial interest for low current applications to memory devices.

For this study, our films are textured F1/Cu/F2 spin valves with F1 and F2 both exhibiting PMA. F1/Cu/F2 consist of a [Co(0.5)/ Pt(1)]₄/ Co(0.5)/ Cu(6)/ Co(0.5)/ Pt(3) multilayer grown on a high quality Si/ Si₃N₄/ Pt(1)/ Au(20)/ Pt(5) (thicknesses given in nm) buffer layer. F1 acts as the reference layer due to the higher PMA of the [Co/Pt] multilayers ($\sim 2 \cdot 10^7$ erg/cm³), while the free layer F2 having a single Co/Pt interface exhibits a lower PMA ($\sim 6 \cdot 10^6$ erg/cm³). Our sample geometry is depicted in Fig. 7.18a. We have used the extraordinary Hall effect (EHE) to detect DW motion inside a magnetic Hall cross (contacts E–F). The small GMR (0.1%) was only used here to monitor the motion of the DW from the reservoir to the Hall cross (contacts C–G). The GMR and EHE have been measured using a high sensitivity ac ($\sim 10 \mu\text{A}$) Wheatstone bridge with the magnetic field H applied perpendicular to the film. Because of the dipolar field H_d generated by the hard layer whose magnetization is pointing down here, the net perpendicular field in the free layer is $H_{fre} = H + H_d$ with $H_d = -140$ Oe.

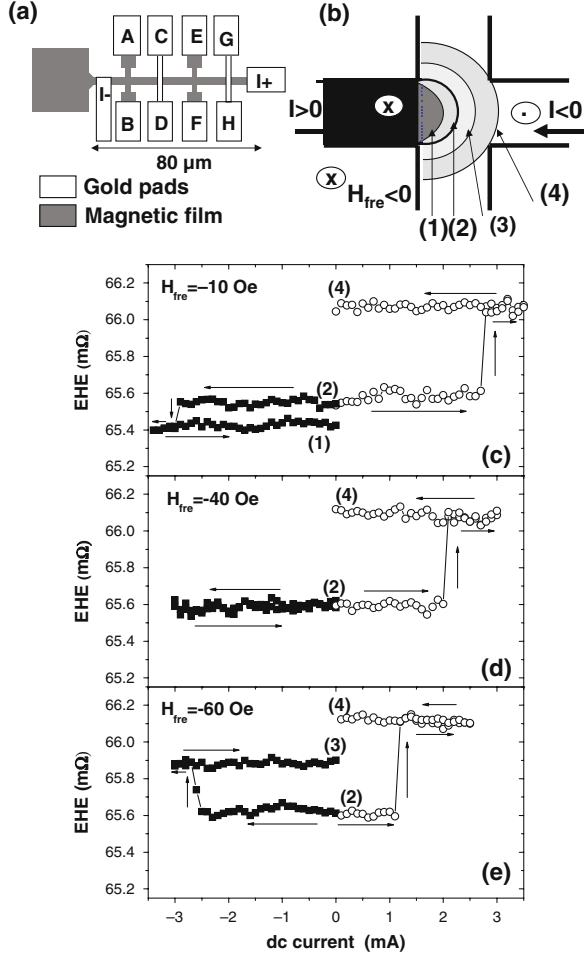
In order to study the effect of a dc current on pinning, we used the artificial pinning potential obtained at the center of a 200×200 nm² Hall cross due to the bending of the DW as described in Section 7.5.2. The total pinning field corresponding to position (2) in Fig. 7.18b is found to be (Eq. 7.22) $H_{cross}(\text{center}) = 400$ Oe with $H_p = 100$ Oe and $H_{top}^{center} = 300$ Oe as measured by the field dependence of the pinning time $\tau(H)$. Note that H_p is quite low as a result of using textured samples grown on Si/SiO₂ substrates at room temperature instead of epitaxial ones. The device is first prepared with a DW frozen at position (2) in the Hall cross, and then the current I is increased by steps of 0.1 mA over time intervals of $\Delta t \leq 1$ s. The depinning of the DW in the Hall cross is monitored from the value of the EHE resistance. Figure 7.18c–e shows the EHE resistance as a function of the dc current for net fields $H_{fre} = -10, -40, \text{ and } -60$ Oe in the free layer. For a positive current above a critical value $I_{th+}(H_{fre})$, the DW abruptly moves from position (2) to position (4) (exit of the Hall cross), which corresponds to a distance of ~ 90 nm. When the field is increased, I_{th+} is reduced and the dependence of I_{th+} on $H_{fre} \leq 0$ is given by a monoatomic variation

$$I_{th}(H_{fre}) = I_{th}(0)[1 - H_{fre}/H_0] \quad (7.24)$$

where $I_{th+}(0) = 3.6$ mA and $H_0 = -95$ Oe. This corresponds to a low critical current density at zero field of $J_{th}(0) \sim 1 \cdot 10^7$ A/cm². For a negative current exceeding $I_{th-}(-10 \text{ Oe}) = -2.9$ mA, the DW moves in the opposite direction, from position (2) to (1), over a smaller distance of ~ 20 nm, against the pressure exerted by the net field. This behavior has been observed for net fields $-20 \text{ Oe} < H_{fre} < 0$ Oe. By

Fig. 7.18 (a) Schematic of a top view of the device. (b) Bubble-like behavior of an ideal 1D Bloch DW in a magnetic Hall cross. (c–e) EHE as a function of the applied dc current for fields (c) $H_{fre} = -10$ Oe (d) $H_{fre} = -40$ Oe, and (e) $H_{fre} = -60$ Oe.

Measurements have been done by increasing the current from $I=0$ to $I=\pm 3$ mA and then reducing it to $I=0$, with a DW initially pinned at position (2). The negative (closed symbols) and positive (open symbols) current measurements have been realized independently. The states (1) to (4) refer to the positions in Fig. 7.18b. The small Joule heating contribution has been subtracted



increasing the field up to $H_{fre} = -40$ Oe, a negative current up to a limit of -3 mA has no effect, whereas at $H_{fre} = -60$ Oe, the DW once depinned by a negative current moves over a distance of ~ 45 nm (position (3)) in the direction of the field pressure, as one might expect due to the larger net field opposing negative current-driven motion. The depinning time as a function of the net field H_{free} and current density J is found [25] to follow an Arrhenius law

$$\tau(H_{free}, J) = \tau_0 \exp [E(H_{free}, J)/k_B T] \tag{7.25}$$

where $E(H_{free}, J)$ is the energy barrier given by

$$E(H_{free}, J) = 2M_S V [H_p - (A/2M_S V)J - H_{free}] \tag{7.26}$$

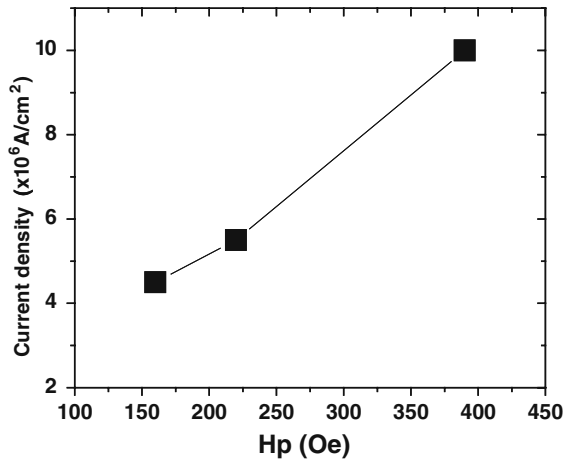
and A is a parameter related to the spin transfer mechanism and V is the activation volume. This expression simply shows that in this thermally activated regime, the depinning threshold is simply governed by $H_p - H_J$ where

$$H_J = (A/2M_S V)J \quad (7.27)$$

is an effective perpendicular field due to the polarized current opposing H_p (here $A/2 M_S V \sim 20 \text{ Oe}/10^6 \text{ A}/\text{cm}^2$).

In order to study the influence of the pinning field H_p on the threshold current J_{th} , we have artificially controlled the strength of the pinning field H_p by varying the width w of a Hall cross (0.2, 0.5 and $1 \mu\text{m}$) in the same Co/Pt sample [32]. Under the influence of the critical current density J_{th} , the DW is always depinned from the center to the output of the cross in the same direction as the electron flow. Figure 7.19 shows that the threshold current J_{th} decreases when reducing H_p , leading to a value of $J_{th} \sim 5 \times 10^6 \text{ A}/\text{cm}^2$ for the lowest H_p . This shows that the threshold current density strongly depends on the strength of the pinning. Interestingly, it should be noted that by extrapolating the linear behavior to $H_p=0$, we find $J_{th} \sim 0$.

Fig. 7.19 Critical current density J_{th} to depin the DW from the center of the Hall cross as a function of the pinning field H_p



Despite a much stronger pinning in our devices with PMA, we measure a critical current density $J_{th} \sim 10^7 \text{ A}/\text{cm}^2$ similar to the lowest value found for in-plane magnetized metallic wires [18, 33]. This indicates in our case a much higher efficiency of the current-induced force on the DW. We want to emphasize two different possible reasons to explain this feature. On one hand, the dependence of J_{th} on H_p is consistent with the theoretical prediction of the presence of a non-adiabatic contribution (β term) [17]. Due to the presence of very narrow DWs, it is expected that this contribution is much higher in our films with perpendicular anisotropy. On the other hand, in previous experiments, the critical current density has been determined from observation of 3D Neel walls motion on a micron scale and in the m/s velocity range, leading to critical current values above the real threshold

depinning current J_{th} . Conversely, in our measurements, the current does not drive the wall over a long distance, but rather depins a static 1D DW in presence of thermal fluctuations below J_{th} and displaces the wall between two metastable states. One striking feature is that these two regimes involve quite distinct dynamical magnetization processes. Recent theories have confirmed [14, 17] that spin momentum transfer can drive for $J > J_{td}$, a steady motion of the DW by continuous precession of the DW magnetization. In this precessional regime, the complicated spin structure of a 3D-Neel wall can be transformed by a current, inducing a reduction of the spin transfer efficiency [27]. In addition, as for the viscous regime under a magnetic field, the spin momentum transfer might be strongly reduced by damping through, for example, excitations of spin waves as invoked in Ref. [22]. Conversely, in our simple 1D DW case, for current induced forces below J_{th} , the DW motion proceeds by thermally activated jumps over energy barriers. In this quasi-static regime for which the pinning potential landscape plays the major role, the 1D DW structure is very rigid and unlike a precessional motion regime damping processes are not relevant. As a consequence, the spin transfer efficiency is expected to be higher.

Finally, note that here a current density of 10^6 A/cm² is qualitatively equivalent to a magnetic field H_I of ~ 20 Oe. This is quite a huge effect but the efficiency is still not sufficient if one wants to depin a high thermally stable DW from an artificial pinning position where $H_p \gg 100$ Oe. Also, preliminary results in our group in Co/Ni spin valves indicate that it is not possible to move a DW on a large scale (> 10 μm) using a current only as a consequence of the presence of strong pinning sites as those shown in Fig. 7.12 where $H_p \sim 320$ Oe.

7.7 Conclusion

This chapter has covered the current understanding of DW propagation along patterned wires with ultra-thin films with perpendicular magnetic anisotropy. These films exhibit very narrow domain walls that interact strongly with pinning defects, such as intrinsic defects from the virgin films or defects introduced by the patterning process. This interaction leads to uncontrollable and stochastic behavior. The realization of nanodevices with a very low distribution of pinning centers together with well-controlled artificial pinning potential is the prerequisite to control very accurately DW motion for future applications. DWs in wires with PMA can be moved on short distances with a high efficiency using a polarized current. This ability to manipulate DW in high-anisotropy magnetic elements is a promising way of extending the scaling of spintronic devices down to the nanometer scale. However, there remain important challenges to overcome. Among these are the demonstration of low current density while maintaining a high enough thermal stability and high DW velocity. The next steps involve a further understanding of the origin of the β term contribution as well as the way to improve efficiency by exploring new materials and heterostructures.

Acknowledgments I wish especially to thank the collaborators of my group at Institut d'Electronique Fondamentale who have been involved in this work: F.Cayssol, J. Wunderlich, C. Burrowes, Y. Lemaho, J.L. Menendez, C. Chappert, V. Mathet, N. Vernier, J.V Kim and T. Devolder. This review is also based on many contributions of the Paris-Sud teams working on magnetization reversal in magnetic nanostructures: J. Ferré, J.P. Jamet, P. Meyer, S. Lemerle, H. Bernas, A. Thiaville, and J. Miltat. I would also like to give a special thank to S. Mangin, B. Terris, E.E. Fullerton, J. Katine, and J.P. Attane, Y. Samson for being involved in this work. A special thank to J.V Kim for the careful reading of the manuscript.

References

1. J.C Slonczewski: Dynamics of magnetic domain walls, *Intern. J. Magnetism* 2, 85 (1972)
2. A.P Malozemoff and J.C Slonczewski: *Magnetic domain Walls in Bubble materials*. Academic, New York (1979)
3. G. Bar'yakkhtar et al.: *Dynamics of Topological Magnetic Solitons*. Springer-Verlag, Berlin (1994)
4. A. Hubert and R. Schafer: *Magnetic Domains: The Analysis of Magnetic Microstructures*. Springer, New York (2001)
5. J. Ferré: *Dynamics of Magnetization Reversal: From Continuous to Patterned Ferromagnetic Films*. Springer-Verlag, Berlin (2002)
6. T. Ono, H. Miyajima, K. Shigeto, K. Mibu, N. Hosoito, and T. Shinjo: propagation of a Magnetic Domain Wall in a Submicrometer Magnetic Wire, *Science* 284, 468 (1999)
7. J. Wunderlich, D. Ravelosona, C. Chappert, F. Cayssol, V. Mathet, J. Ferre, J.P. Jamet, and A. Thiaville: Influence of geometry on domain wall propagation in a mesoscopic wire, *IEEE. Trans. Mag.* 37, 2104 (2001)
8. D. Atkinson, Dan A. Allwood, G. Xiong, M.D. Cooke, C.C. Faulkner, and R.P. Cowburn: Magnetic domain-wall dynamics in a submicrometre ferromagnetic structure, *Nat Mater* 2, 85 (2003)
9. Geoffrey S. D. Beach, Corneliu Nistor, Carl Knutson, Maxim Tsoi and James L. Erskine: Dynamics of field-driven domain-wall propagation in ferromagnetic nanowires, *Nat. Mater.* 4, 741 (2005)
10. F. Cayssol, D. Ravelosona, C. Chappert, J. Ferreacete, and J.P. Jamet, *Phys. Rev. Lett.* 92, Domain wall creep in magnetic wires, 107202 (2004)
11. J. Slonczewski: Current driven excitations of magnetic multilayers, *J. Magn. Magn. Mater.* 159, L1 (1996)
12. L. Berger: Emission of spin waves by a magnetic multilayer traversed by a current, *Phys. Rev. B* 54, 9353 (1996)
13. Z. Li and S. Zhang: Domain-wall dynamics driven by adiabatic spin-transfer torques, *Phys. Rev. B* 70, 024417 (2004)
14. G. Tatara and H. Kohno: Theory of Current-Driven Domain Wall Motion: Spin Transfer versus Momentum Transfer, *Phys. Rev. Lett* 92, 086601 (2004)
15. S.E. Barnes and S. Maekawa: Current-spin coupling for ferromagnetic domain walls in fine wires, *Phys. Rev Lett.* 95, 107204 (2005)
16. S. Zhang and Z. Li: Roles of Nonequilibrium Conduction Electrons on the Magnetization Dynamics of Ferromagnets, *Phys. Rev. Lett.* 93, 127204 (2004)
17. A. Thiaville, Y. Nakatani, J. Miltat, and Y. Susuki: Micromagnetic understanding of current-driven domain wall motion in patterned nanowires, *Europhys. Lett* 69, 990 (2005)
18. J.Grollier, P. Boulenc, V. Cros, A. Hamzic, A. Vaurs, A. Fert, and G. Faini: Switching a spin valve back and forth by current-induced domain wall motion, *Appl. Phys. Lett.* 83, 509 (2003)

19. M. Kläui, C.A.F. Vaz, J.A.C. Bland, G.Faini, E. Cambril, and L.J. Heyderman: Domain wall motion induced by spin polarized currents in ferromagnetic ring structures, *Appl. Phys. Lett.* 83, 105 (2003)
20. M. Tsoi, R.E. Fontana, and S.S. Parkin: Magnetic domain wall motion triggered by an electric current, *Appl. Phys. Lett.* 83, 2617 (2003)
21. N. Vernier, D.A. Allwood, D. Atkinson, M.D. Cooke, and R.P. Cowburn: Domain wall propagation in magnetic nanowires by spin-polarized current injection, *Europhys. Lett.* 65, 526 (2004)
22. A. Yamaguchi, T. Ono, S. Nasu, K. Miyake, K. Mibu, and T. Shinjo: Real-Space Observation of Current-Driven Domain Wall Motion in Submicron Magnetic wires, *Phys. Rev. Lett* 92, 077205 (2004).
23. E. Saitoh, H. Miyajima, T. Yamaoka, and G. Tatara: Current-induced resonance and mass determination of a single magnetic domain wall, *Nature* 432, 203 (2004)
24. M. Yamanouchi, D. Chiba, F. Matsukura, and H. Ohno: Current-induced domain-wall switching in a ferromagnetic semiconductor structure, *Nature* 428, 539 (2004)
25. A. Yamaguchi, S. Nasu, H. Tanigawa, T. Ono, K. Miyake, K. Mibu, and T. Shinjo: Effect of Joule heating in current-driven domain wall motion, *Appl. Phys. Lett.* 86, 12511 (2005)
26. D. Ravelosona, D. Lacour, J.A. Katine, B.D. Terris, and C. Chappert: Nanometer scale observation of high efficiency thermally assisted current-driven domain wall depinning, *Phys. Rev. Lett.* 95, 117203 (2005)
27. M. Kläui, P.-O. Jubert, R. Allenspach, A. Bischof, J.A.C. Bland, G. Faini, U. Rüdiger, C.A.F. Vaz, L. Vila, and C. Vouille, *Phys. Rev. Lett.* 95: Direct Observation of Domain-Wall Configurations Transformed by Spin Currents, *Phys. Rev. Lett.* 95, 026601 (2005)
28. M. Kläui, M. Laufenberg, L. Heyne, D. Backes, U. Rudiger, C.A.F. Vaz, J.A.C. Bland, L.J. Heyderman, S. Cherifi, A. Locatelli, T. O. Montes and L. Aballe: Current-induced vortex nucleation and annihilation in vortex domain walls, *Appl. Phys. Lett.* 88, 232507 (2006)
29. M. Hayashi, L. Thomas, Ya. B Bazaliy, C. Rettner, R. Moriya, X. Jiang, and S.S.P. Parkin: Influence of current on field-driven domain wall motion in permalloy nanowires from time resolved measurements of anisotropic magnetoresistance, *Phys. Rev. Lett.* 96, 197207 (2006)
30. A. Yamaguchi, K. Yano, H. Tanigawa, S. Kasai, and T. Ono: Reduction of threshold current density for current-driven domain wall motion using shape control, *Jap. Jour. Appl. Phys.* 45, 3850 (2006)
31. L. Thomas, M. Hayashi, X. Jiang, R. Moriya, C. Rettner, and S. S. P. Parkin: Oscillatory dependence of current-driven magnetic domain wall motion on current pulse length, *Nature* 443, 197 (2006)
32. D. Ravelosona, S. Mangin, J.A. Katine, E.E. Fullerton, B.D. Terris: Threshold currents to move domain walls in films with perpendicular anisotropy, *Appl. Phys. Lett.* 90, 072508 (2007)
33. S. Laribi, V. Cros, M. Muñoz, J. Grollier, A. Hamzi, C. Deranlot, and A. Fert, E. Martinez: Reversible and irreversible current induced domain wall motion in CoFeB based spin valves stripes, *Appl. Phys. Lett* 90, 232505 (2007)
34. S.P. Parkin, M. Hayashi, L. Thomas: Magnetic Domain-Wall Racetrack Memory, *Science* 320, 190 (2008)
35. M. Hayashi, L. Thomas, R. Moriya, C. Rettner, and S.P. Parkin: Current-Controlled Magnetic Domain-Wall Nanowire Shift Register, *Science* 320, 209 (2008)
36. C.H. Marrows: Spin-Polarised currents and magnetic domain walls, *Adv. Phys.* 54(8) (2005)
37. C. Chappert, A. Fert, F.N. Van Dau: The emergence of spin electronics in data storage, *Nat. Mater.* 6, 813–823 (2007)
38. S.S.P. Parkin: U.S. Patent No. 6834005 (2004)

39. D.A. Allwood, G. Xiong, M.D. Cooke, C.C. Faulkner, D. Atkinson, N. Vernier, and R. P. Cowburn: Submicrometer Ferromagnetic NOT Gate and Shift Register, *Science* 296, 5575 (2002)
40. Y. Nakatani and A. Thiaville: Head-to-head domain walls in soft nano-strips: a refined phase diagram, *J. Magn. Magn. Mater.* 290–291, 750 (2005)
41. S. Lemerle, J. Ferré, C. Chappert, V. Mathet, T. Giamarchi, and P. Le Doussal: Domain Wall Creep in an Ising Ultrathin Magnetic Film, *Phys. Rev. Lett.* 80, 849 (1998)
42. Y. Yafet and E.M. Gyorgi: Ferromagnetic strip domains in an atomic monolayer, *Phys. Rev. B* 38, 9145 (1988)
43. J. Wunderlich: Extraordinary Hall effect in multilayered magnetic films. Application to the study of magnetization reversal mechanism, thesis of Université Paris Sud, France (2001)
44. F. Cayssol: Etude de la dynamique de paroi de domaine magnétique dans des pistes sub-microniques, thesis of Université Paris Sud, France (2003)
45. F. Cayssol, J.L. Menendez, D. Ravelosona, C. Chappert, J. Ferre, J.P. Jamet: Enhancing domain wall motion in magnetic wires by ion irradiation, *App. Phys. Lett.* 86, 22503, (2005)
46. J. Ferré and J.P. Jamet: Alternative patterning techniques: magnetic interactions in nanomagnets arrays. *Handbook of Magnetism and Advanced Magnetic Materials*, Wiley & Sons (2008)
47. V. Mathet, T. Devolder, C. Chappert, J. Ferré, S. Lermele, L. Belliard, and G. Guentherodt: Morphology and magnetic properties of Pt/Co/Pt sandwiches grown by argon sputter deposition, *J. Mag. Mag. Mat.*, 260, 295 (2003)
48. M. Labrune, S. Andrieu, F. Rio, and P. Bernstein: Time dependence of the magnetization process of RE-TM alloys, *J. Magn. Magn. Mater.* 80, 211 (1989)
49. P. Bruno, G. Bayreuther, P. Beauvillain, C. Chappert, G. Lugert, D. Renard, J.P. Renard, and J. Seiden: Hysteresis properties of ultrathin ferromagnetic films, *J. Appl. Phys.* 68, 5759 (1990)
50. G. Blatter, M.V. Feigel'man, V.B. Geshkenbein, A.I. Larkin, and V.M. Vinokur: Vortices in high-temperature superconductors, *Rev. Mod. Phys.* 66, 1125 (1994)
51. M. V. Feigel'man, V. B. Geshkenbein, A. I. Larkin, and V. M. Vinokur: Theory of collective flux creep, *Phys. Rev. Lett.* 63, 2303 (1989)
52. T. Tybell, P. Paruch, T. Giamarchi, and J.-M. Triscone: Domain Wall Creep in Epitaxial Ferroelectric Pb(Zr_{0.2}Ti_{0.8})O₃. *Thin Films*, *Phys. Rev. Lett.* 89, 097601 (2002)
53. L. Krusin-Elbaum, T. Shibauchi, B. Argyle, L. Gignac and D. Weller: Stable ultrahigh-density magneto-optical recordings using introduced linear defects, *Nature* 410, 444 (2001)
54. T. Shibauchi, L. Krusin-Elbaum, V.M. Vinokur, B. Argyle, D. Weller, and B.D. Terris: Deroughening of a 1D Domain Wall in an Ultrathin Magnetic Film by a Correlated Defect, *Phys. Rev. Lett* 87, 267201 (2001)
55. M. Kardar: *Dynamic Scaling Phenomena in Growth Processes*, *Physica B* 221, 60 (1996)
56. G. Gruner: *The Dynamics of Charge Density Waves*, *Rev. Mod. Phys.* 60, 1129 (1988)
57. D. Wilkinson and J.F. Willemsen: Invasion percolation: a new form of percolation theory, *J. Phys. A* 16, 3365 (1983)
58. P.J. Metaxas, J.P. Jamet, A. Mougin, M. Cormier, J. Ferré, V. Baltz, B. Rodmacq, B. Dieny, and R. L. Stamps: Creep and flow regimes of magnetic domain-wall motion in ultrathin Pt/Co/Pt films with perpendicular anisotropy, *Phys. Rev. Lett.* 99, 217208 (2007)
59. C.M. Hurd: *The Hall effect in metals and alloys*. New York, NY: Plenum press (1972)
60. S. Mangin, D. Ravelosona, J.A. Katine, M.J. Carey, B.D. Terris, and E.E. Fullerton: Current-induced magnetization reversal in nanopillars with perpendicular anisotropy, *Nat. Mater.* 5, 210 (2006)
61. D. Ravelosona, S. Mangin, Y. Lemaho, J.A. Katine, B.D. Terris, and Eric. E. Fullerton: Domain wall creation in nanostructures driven by a spin-polarized current, *Phys. Rev. Lett.* 96, 186604 (2006)
62. J. Fassbender, D. Ravelosona, and Y. Samson: Tailoring magnetism by light-ion irradiation, *J. Phys. D: Appl. Phys.* 37, R179 (2004)

63. C. Chappert, H. Bernas, J. Ferré, V. Kottler, J.-P. Jamet, Y. Chen, E. Cambril, T. Devolder, F. Rousseaux, V. Mathet, and H. Launois: Planar patterned magnetic media obtained by ion irradiation, *Science* 280, 1919 (1998)
64. L. Berger: Low-field magnetoresistance and domain drag in ferromagnets, *J. Appl. Phys.* 49, 2156 (1978)
65. P.P Freitas and L. Berger: Observation of s-d exchange force between domain walls and electric current in very thin Permalloy films, *J. Appl. Phys.* 57, 1266 (1985)
66. C. Hung and L. Berger: Exchange forces between domain wall and electric current in permalloy films of variable thickness, *J. Appl. Phys.* 63, 4276 (1988)

Chapter 8

Magnetic Nanowires for Domain Wall Logic and Ultrahigh Density Data Storage

R.P. Cowburn

Abstract Spintronics describes the concept of attempting to use both the charge and the spin on the electron in microelectronic devices [1, 2]. One of the most highly sought after functionalities in microelectronics is non-volatility, i.e. the ability to retain memory even when power is removed. This is particularly true as the popularity of mobile electronic communication and computing devices grows. In principle, ferromagnetic materials could provide this functionality, due to the hysteresis, and hence memory, that accompanies most ferromagnets. Unfortunately, no suitable room temperature ferromagnetic semiconductor material has yet been identified [3]; the most common ferromagnetic materials are metals. The aim of this research has been to see how far we can push the properties of basic ferromagnetic metallic alloys, which are usually considered to have relatively simple magnetic and electrical properties, towards highly functional devices which mimic and complement the digital logic functions and non-volatile data storage functions of semiconductor microelectronics. Using the concept of the domain wall conduit, we show how information can be represented, moved, processed and stored in networks of ferromagnetic nanowires.

8.1 Domain Wall Propagation and Nucleation

All of the devices described in this chapter are based upon magnetic nanowires made from the common ferromagnetic alloy Permalloy ($\text{Ni}_{80}\text{Fe}_{20}$). Magnetic nanowires are nanometer-sized magnetic structures which are artificially fabricated using laboratory-scale versions of the lithographic techniques commonly used in microchip manufacture. In particular, the work in this chapter uses either electron beam lithography (EBL) or focused ion beam (FIB) milling [4]. A typical

R.P. Cowburn (✉)
Blackett Physics Laboratory, Imperial College London, Prince Consort Road, London
SW7 2BW, UK
e-mail: r.cowburn@imperial.ac.uk

process will involve the deposition of a thin magnetic film, either using thermal evaporation or sputter deposition and the exposure of a computer-generated pattern by rastering either a focused electron beam (EBL) or a focused gallium ion beam (FIB). A development and pattern transfer step then transfers the exposed image into the deposited magnetic metal. The ability to create high-definition shapes of precisely the designer's choice is extremely important, since the underlying principle at work throughout this research is that magnetic properties may be artificially modified by changing the shape and size of the nanostructure. This principle is not commonly seen on the macroscopic scale: the coercivity and the anisotropy of a bulk material are usually intrinsic properties which do not depend strongly on the shape of the sample. On the nanometer scale, however, the local demagnetizing fields are of comparable strength to the exchange fields (the quantum mechanical interaction responsible for ferromagnetism). A rich interplay results which leads to magnetic properties being strongly dependent on shape and size.

Magnetic properties throughout this chapter are measured using a high-sensitivity laser probe [5] based on the Magneto Optical Kerr Effect (MOKE) [6]. The Kerr effect causes the polarization state of light to be slightly modified when it is reflected from a magnetic surface by an amount that is proportional to the component of magnetization in a given direction. Although the polarization rotations are small (typically 0.1° if all of the light is focused onto magnetic material, and proportionately less if the nanostructure is smaller than the focused beam size), MOKE is an excellent highly localized magnetometry.

Figure 8.1 shows an example of a magnetic nanowire that behaves as a so-called domain wall conduit. The nanowire is made from 8 nm thick Permalloy and is fabricated by electron beam lithography. One sees two hysteresis loops measured from the nanowire using the MOKE magnetometer described above. We apply a magnetic field which is oriented along the wire axis for most of its sweep, but which rotates to 45° towards the extrema of the loop. This guarantees the starting magnetization state in both arms of the L-shaped nanowire as the applied field sweeps back towards zero. We generate such an applied field sequence by controlling the current in two pairs of coils which apply fields in the X- (nanowire axis) and Y-(transverse) directions. If, as in the upper hysteresis loop, we choose the relative signs of the X- and Y-fields such that the 45° pulse is tangential to the corner of the L-shaped nanowire, then no domain wall exists in the wire and so the coercivity corresponds to a nucleation-limited reversal. In this case, we measure a coercivity of 205 Oe, which we define to be the *nucleation field*, H_n . If we now reverse the sign of the y-field, the 45° pulse becomes perpendicular to the corner, resulting in a single domain wall being created there. The coercivity is now defined as the *propagation field*, H_p , since reversal in the main length of the wire is achieved simply by pushing that already-created domain wall around the corner and along the wire. Remarkably, we find in the lower hysteresis loop a value of just 3 Oe for H_p . The coercivity of the nanowire has been modified by a factor of 65 simply by the presence of absence of a single domain wall.

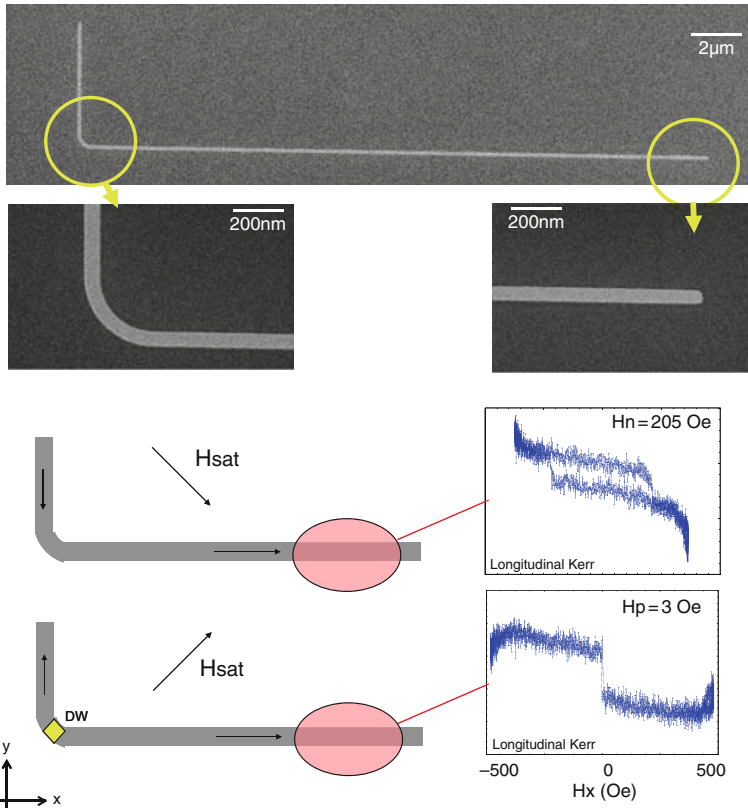


Fig. 8.1 Domain nucleation and domain wall propagation in a 120 nm wide, 8 nm thick Permalloy nanowire

8.2 Domain Wall Conduits

When the ratio between H_p and H_n is substantial, we describe the magnetic nanowires as *domain wall conduits*. This is because if one applies a magnetic field H in the range $H_p < H < H_n$, then the nanowire will accept any domain wall introduced to it and propagate it along the wire, but will not reverse if no domain wall is given. For the nanowires shown here, this range is very large (any field between 3 Oe and 205 Oe in the case of Fig. 8.1 will result in domain wall conduit behaviour). There is thus a parallel between electrical conductors and domain wall conduits: an electrical conductor transports the electrical potential applied at one end to the other by a flow of electrons; a domain wall conduit transports the magnetization direction applied at one end to the other by the flow of a single domain wall. Interestingly, electrical conduction results in losses due to the resistance of the conductor; the potential at the far end will always be slightly different to the potential at the near end. Although

there are also losses in the transport of a domain wall through spin wave emission by the wall as it moves, these energy losses are exactly compensated by the energy absorbed from the externally applied magnetic field, H . The externally applied magnetic field therefore has a parallel to a power supply, and the domain wall conduit should be considered as being an active component that can draw on that power supply, rather than the simpler passive 2-terminal component that is an electrical conductor. The propagation field is loosely analogous to a contact potential: it is the offset field which must be overcome before domain wall conduction will occur. The nucleation field is loosely analogous to breakdown: it is the strength of field at which the magnetization state of the domain wall conduit no longer relates to the input, but it is overridden by the externally applied magnetic field or power supply.

Domain wall conduits allow us to propagate magnetization states from one place to another, and so for spintronic applications it is natural to assign those magnetization states to Boolean states, allowing us to move information. We define a Boolean ‘1’ as being when the magnetization direction is parallel to the direction in which information flows, and a Boolean ‘0’ as being when the magnetization direction is anti-parallel to the direction in which information flows.

There is an additional complexity in propagating information through nanowire domain wall conduits, caused by the vector nature of magnetization. Figure 8.2 demonstrates the problem. Suppose we wish to propagate a data sequence made up of 1s and 0s. Domain walls in nanowires carry a magnetic charge, due to the divergence of magnetization which occurs at the wall. Walls that lie between the two heads of the magnetization arrows are called ‘head-to-head’ domain walls and carry a positive charge (since the magnetization has a positive divergence in the vicinity of the wall). Conversely, walls that lie between the two tails of the magnetization arrows are called ‘tail-to-tail’ domain walls and carry a negative charge. When a magnetic field is applied to the domain wall, positive walls move in the direction of the field, but negative walls move against the direction of the field. Consequently, any data pattern that is more complex than simply all 1s will not propagate correctly; rather, the 1s will expand and annihilate the 0s.

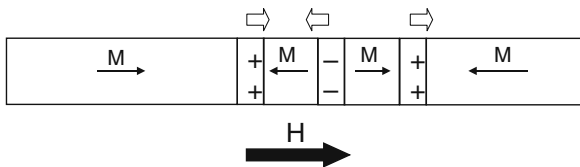


Fig. 8.2 The problem of propagating a data pattern in a nanowire under an externally applied magnetic field, H . The *white arrows* show the direction of motion of the different domain walls

What is required is some form of shift register which can be used to pump both head-to-head and tail-to-tail domain walls in the same direction. One possible approach to solving this problem is the use of spin-momentum transfer, in which a spin-polarized electrical current is used to drive the domain walls through the nanowire [7–10]. Spin-momentum transfer through a domain wall does not depend

upon the sign of the charge carried by the wall, and so all walls move in the same direction. However, this phenomenon is relatively weak and is not yet well understood. While it may provide an interesting solution in the future, at this stage we wish to find a way of using externally applied magnetic fields to pump the data. In particular, we choose to use devices that are constructed to operate within a globally applied rotating magnetic field. This rotating field acts as power supply and clock for all of the signals within a network of magnetic nanowires. Providing that the magnitude of the field is between the propagation and nucleation fields of the wires, the field serves to propagate domain walls around the network. This provides the basic interconnect architecture. To realize a proper shift register (and indeed other more complex logic functions), additional functionality must be created by careful shaping of the nanowires themselves.

8.3 The NOT Gate and Shift Register Element

Figure 8.3 shows a nanowire domain wall conduit which has been shaped into a cusp. See [11] for experimental detail. As the nanowire turns through the first quarter cycle of the cusp, the magnetization attempts to remain parallel to the nearest edge, in order to minimize its potential energy (the principle of shape anisotropy). The magnetization therefore rotates with the cusp. During the second quarter cycle of the cusp, the magnetization continues rotating, with the result that the magnetization on the input side of the cusp is 180° rotated with respect to that on the output side. There are two consequences of this rotation. The first is that data

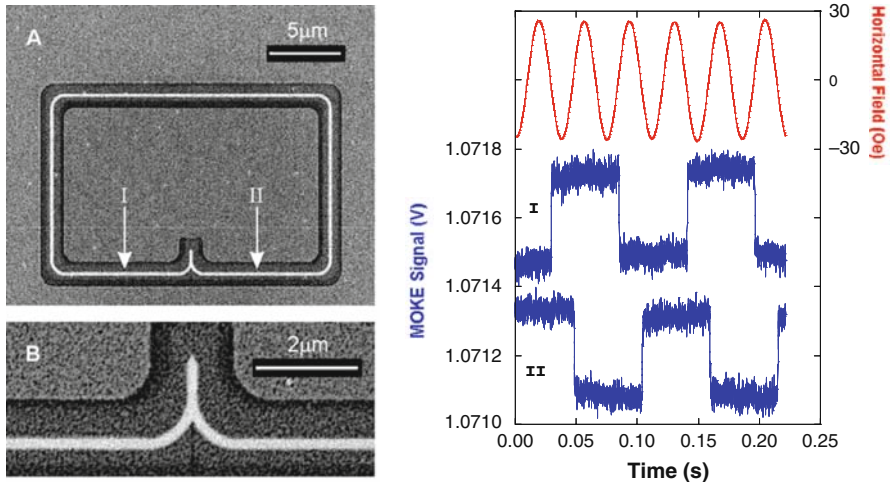


Fig. 8.3 A NOT gate in a closed loop to form a synchronous *ring* oscillator. The bright white shade is 5 nm thick Permalloy. Signal measurements are made by MOKE at the two positions I and II. The device is bathed in an in-plane rotating magnetic field, one component of which is plotted

values (as represented by the magnetization direction) have been inverted, i.e. we have performed the Boolean NOT function. The second is that we have introduced a synchronous delay of one half-cycle of the externally applied rotating field. Wherever there is a synchronous delay in digital electronics, there is an associated memory function and the possibility of shift register action.

The simplest way to test a NOT gate is by connecting its output to its input and thus forming a ring oscillator, as shown experimentally in Fig. 8.3. While in microelectronics this would result in a high-frequency oscillation, the frequency of which would be determined by the propagation delay on the gate, the synchronous nature of domain wall logic leads to a slightly different result. Figure 8.4 shows the equivalent electronic circuit. The half-cycle synchronous delay associated with propagating the domain wall through the cusp (or, put another way, because 1s and 0s propagate half a clock cycle apart in this architecture, the output of the NOT function must change half a cycle after its input) is shown as a $T/2$ delay, where T is the period of the rotating field. Additionally, there is a further delay of T due to the synchronous way in which the domain walls will move through the loop connecting the output to the input. The total loop time is therefore $3T/2$, which simple analysis shows will lead to a self-sustained oscillation with a periodicity of $3T$.

Fig. 8.4 The equivalent electronic circuit for the synchronous *ring* oscillator shown in Fig. 8.3. The *square blocks* are delay elements; T is the periodic time of the rotating magnetic field

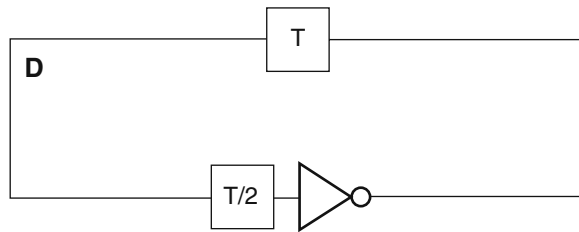


Figure 8.3 shows the result of measuring the magnetization on firstly the input arm I and then the output arm II of the NOT gate using the MOKE laser spot while the entire chip is bathed in a rotating magnetic field. All of the expected features are visible. There is a half clock cycle delay between the rising edge on the input of the gate and the corresponding falling edge on the output of the gate. The periodicity of the result is also seen to be three times the rotating field frequency, as expected. Although in this experiment we do not see the domain wall directly, the response periodicity of $3T$ is the signature that everything is functioning correctly. See [12] for direct magnetic force microscopy images of the domain wall moving around the loop and through the gate.

Figure 8.5 demonstrates the ability to concatenate 11 NOT gates to form a serial shift register [11]. The measured circuit response shows a periodicity of $13T$ (T is the periodicity of the rotating field). This is exactly what would be expected: there is a loop delay time of $11/2 T$ due to the $T/2$ delay introduced by each of the 11 NOT gates, and then there is an extra T delay for the closed loop, making a total loop delay of $13/2 T$, and hence an oscillating periodicity of $13T$. Note in particular

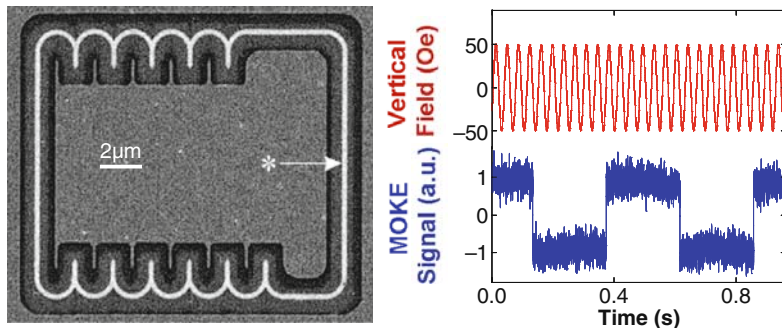


Fig. 8.5 Eleven NOT gates connected to form a serial shift register. A MOKE measurement at the asterixed point shows a synchronous oscillation at 1/13th of the rotating field frequency (one component of which is plotted)

that both positively charged head-to-head and negatively charged tail-to-tail domain walls are circulating in the same direction around the loops of Figs. 8.3 and 8.5 Unlike the simple case of Fig. 8.2, the propagation direction is determined by the NOT gate/shift register elements (and the relationship of the sense of their cusp to the sense of the externally applied rotating field) and not by the magnetostatic charge on the domain wall.

By extending the central stub of the NOT gate, an interim copy of the data held in the gate can be accessed. This allows a variation on the shift register theme to be formed, namely a serial-in-parallel-out (SIPO) shift register. Figure 8.6 shows an example of a ring oscillator connected to a SIPO shift register formed from a chain of NOT gates with accessible stubs. The ring oscillator in this case is simply providing a convenient signal to trace through the shift register. The shift in the MOKE signal as we move the laser probe from one nanowire to the next shows the correct operation.

The twists on the end of the nanowires perform an important role by preventing domain walls from reflecting and re-entering the system. Depending upon the precise shape of the end of a nanowire, a domain wall may or may not annihilate. If it does not annihilate, it will be back-propagate half a clock cycle later and may interfere with the correct operation of the logic gates. If annihilation at the end of the conduit cannot be guaranteed, the conduit can be correctly terminated by ensuring that there are two 90° corners between its end and the final logic element. The 180° turn forms what we refer to as a ‘domain wall black hole’: should a domain wall enter into it and not annihilate at the end, the rotating field will be unable to back-propagate it through the double corner, since these corners are of the wrong chirality. In the rotating field scheme, whatever goes into a black hole never re-emerges.

We have concentrated here on describing how nanowires can be shaped to perform shift register action. We have found that other logic functions are also possible. In particular, an AND gate has been demonstrated, as well as a fan-out structure and a cross-over structure. These are described more fully in reference [13].

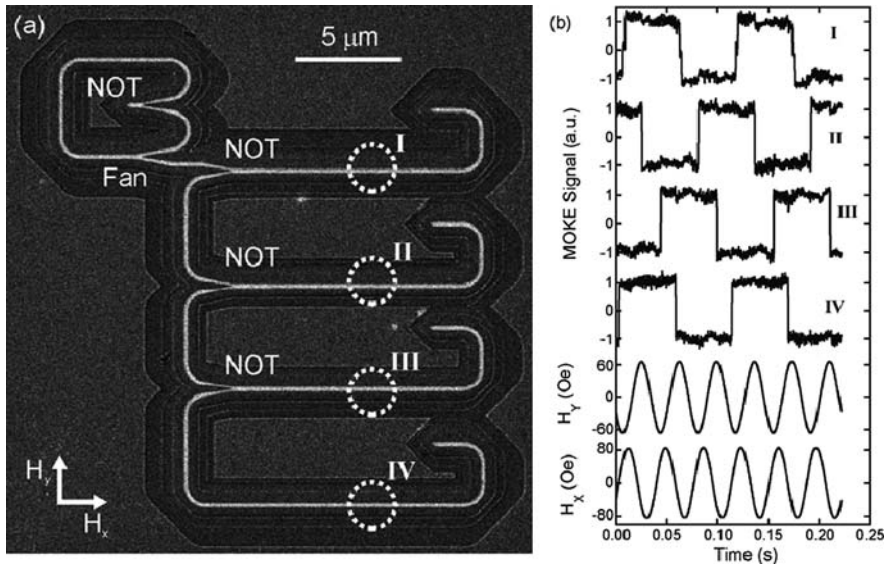


Fig. 8.6 A four-stage serial-in-parallel-out shift register nanocircuit which uses the central stub of the NOT gate to replicate the input signal

8.4 Data Input–Output

The recently developed technology of magnetic random access memory (MRAM) [14] has already solved most of the engineering issues involved in interfacing between a soft ferromagnetic layer and an underlying CMOS system. Specifically, in MRAM, data writing is achieved by passing an electrical current through a conductor placed close to the magnetic element, allowing the magnetic field generated around the current to nucleate a reverse domain in the magnetic nanostructure. Data reading is achieved by the use of a magnetic tunnel junction (MTJ) [15] in which the electrical resistance of two magnetic layers separated by a thin film of insulator is found to depend strongly on the relative magnetization directions. By fixing the magnetization direction of one layer, it becomes a reference against which the magnetization direction of the other layer may be measured. Signal levels large enough to interface directly to CMOS transistors are achieved by this method. We intend to piggyback off these developments for interfacing signals between the magnetic system and the conventional electronics. Domain wall logic can be considered as an extension to MRAM. In MRAM, the data storing magnetic layer is very simple and is only used to store a single bit of information. The concepts developed in magnetic logic can be used to extend the functionality of that storage layer, allowing data to be processed as well as stored.

We have developed an alternative data input method which may be important if 3D structures are implemented in domain wall logic. One of the major limitations to creating ultrahigh density 3D microelectronic circuits is the cost of making

connections to the multiple layers. A useful strategy for realizing the ultrahigh data density of 3D structures without increasing the cost is to attempt to find a way in which the input and output to the 3D structure is maintained in two dimensions. Figure 8.7 shows a device we have developed which allows this to be done with domain wall logic. See reference [13] for further experimental details. The figure shows a chain of eight NOT gates, where one gate has had its central stub enlarged. This reduces the shape anisotropy in that stub and hence reduces its nucleation field a little. Consequently, if the *globally applied* rotating magnetic field is modulated in amplitude slightly, it is possible to cause nucleation in the NOT gate with the elongated pad, thus forcing its data state to the direction of the global field. Importantly, the strength of modulation needed to achieve this is not so strong as to lie outside of the operating margin of all of the other gates in the chain, and so they continue to work normally. Thus, by modulating the global field, we can write data directly into the serial shift register and then shift that same data throughout the rest of the shift register. In this case, the globally applied rotating magnetic field is not only serving as a power supply and clock, as it does in all other domain wall circuits, but also acting as a serial input data channel. Figure 8.7 shows a working demonstration of this experiment, where we have written the data sequence 11010 into the shift register by modulating the rotating field. This writing sequence is applied only once. An hour later, we then begin cycling the rotating field without modulation and use the MOKE laser probe to read the serial data circulating around the shift register. We see the sequence 11010 repeatedly, as it goes around the circular shift register. We have thus succeeded in injecting data into the nanoscale storage ring, even though the source of field modulation was 1 cm away from the chip itself. As a

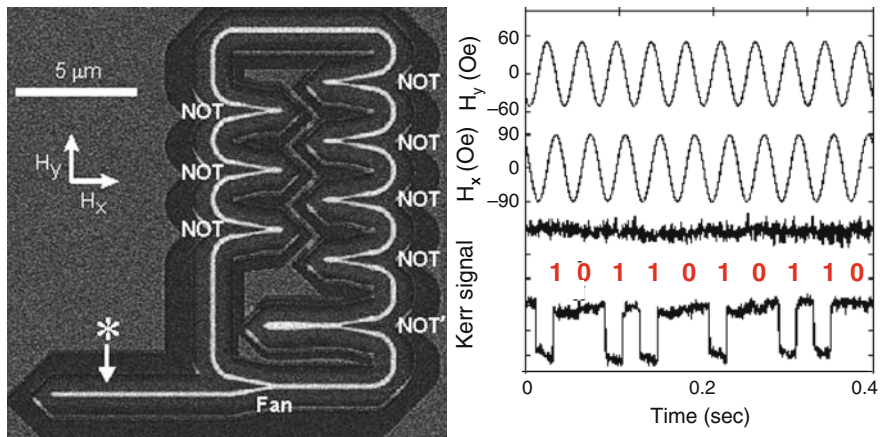


Fig. 8.7 A serial shift register formed from eight NOT gates, with the central stub of one NOT gate enlarged to form a data input element. The data sequence 11010 is written into the shift register by modulating the rotating magnetic field. The signal traces show the recovered data sequence circulating around the shift register, as well as a flat trace showing the result when the writing sequence is not performed

control experiment, we show also in Fig. 8.7 a straight trace, obtained during reading when the 11010 sequence had not been previously written. The reasons that we do not see a $10T$ periodic signal as might be expected based on earlier results is that there is an even number of NOT gates in this loop, which prevents it from acting as a ring oscillator.

This result is significant because it demonstrates the ability to write data into nanoscale storage rings from a distance. This immediately opens up the possibility of a 3D data storage cube, in which all magnetic field generation and sensing is performed on the bottom CMOS layer, but where data can be remotely targeted to specific parts of the 3D volume simply according to where one places the NOT gate with the enlarged stub [16]. Such a device would have the storage density of a 3D device but the fabrication cost structure of a 2D device. This idea will be explored further later in this chapter.

8.5 Using the Chirality of the Transverse Domain Wall

So far in this chapter, it has been the magnetization direction of the *domains* separated by the domain walls that have been used to represent data. There is, however, a further degree of freedom accessible in these domain wall conduit structures, namely the chirality of the domain wall itself. Figure 8.8 shows a schematic of the transverse domain walls that are expected to exist in such nanowires [17]. The magnetization in the centre of the domain wall points is seen to point at 90° to the nanowire axis. However, there are two possible states: it may turn clockwise or anti-clockwise, leading to two different chiralities of transverse domain wall. In a simple nanowire, these two states are energetically degenerate and could possibly be used to code data. The V-shape that is seen in the centre of the domain wall is coupled to the transverse magnetization direction and is not an independent degree of freedom.

Using the chirality of the transverse domain wall to code data is interesting because it separates the data value from the direction of the force that an external

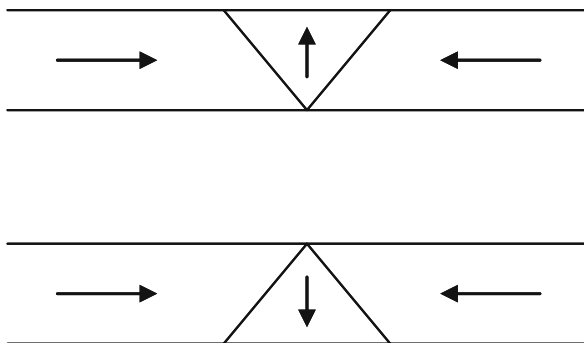


Fig. 8.8 The two chiralities of transverse domain walls in magnetic nanowires

field applies to a domain wall. We have already discussed how head-to-head and tail-to-tail domain walls respond oppositely to an applied magnetic field, leading to the need for shift register structures if data are to be propagated unidirectionally. In contrast, there is no dependence of the way that the domain wall responds to an external field on the domain wall’s chirality. Shift register structures will still be needed using chirality coding since both head-to-head and tail-to-tail domain walls will still be present, but they may become simpler since the charge on the wall (i.e. head-to-head or tail-to-tail) can become predictable and independent of the data value being carried.

In order to use the domain wall chirality, two key questions need to be addressed. The first is how stable is the chirality. It is known that in general when a domain wall moves quickly, the direction of magnetization in the centre precesses [18]. In the ribbon geometry of our nanowires, this precession takes the form of occasional nucleation of an anti-vortex at one end of the wall, followed by the propagation of the anti-vortex along the length of the wall, resulting in a 180° reversal of the transverse part of the magnetization [19]. We have performed a number of experiments to determine the distance that a domain can move on average before such reversal occurs. Figure 8.9 shows an example of the one of the experimental structures. The domain wall is nucleated (with known chirality, depending on whether the ‘P’ structure or the ‘AP’ structure is fabricated) at the corner of the wire in the same fashion as in Fig. 8.1. The wall then runs a certain distance before it meets a cross arm. The cross arm acts as a chirality filter. We find that if the transverse component of

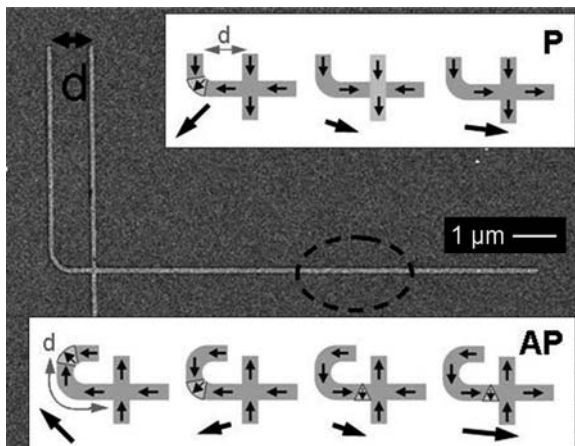


Fig. 8.9 SEM image of an L-shaped nanostructure with a cross at a distance d from the corner (the lower part of the transverse arm extends $5\ \mu\text{m}$ below the cross); the position of the MOKE measurement is indicated by the dashed ellipse. Insets: (P) left to right: first half of field sequence (black arrows) for L-shaped nanostructure, and schematics indicating magnetization configurations in the absence of chirality reversal. (AP) First half of field sequence for C-shaped structure. The labels P and AP indicate that the DW is created with core magnetization initially parallel or anti-parallel to the magnetization in the transverse arm

the domain wall magnetization lies parallel to the magnetization in the cross arm, then the domain wall is able to pass across the arm relatively easily. If, conversely, the transverse component of the domain wall magnetization is anti-parallel to the magnetization in the cross arm, the domain wall is heavily repelled and is unable to pass. The cross arm thus acts like an analyzer for domain wall chirality. By putting the MOKE probe on the right-hand side of the cross, we can probe the chirality of the domain wall at the instant it arrived at the cross: one chirality leads to switching of the nanowire to the right of the cross, the other chirality does not. This is a very powerful experimental technique as it effectively amplifies the number of spins that need to be detected: the magnetization in the entire nanowire to the right of the cross arm is much larger than the magnetization in the core of the domain wall itself.

Figure 8.10 shows a summary of the results. For structures that have a distance of $1\ \mu\text{m}$ or less between the starting point and the analyzer, the domain wall is found to be transmitted through the cross 100% of the time, i.e. the chirality of the domain wall was preserved. For distances greater than this, there is a finite probability of the chirality reversing. We can thus define a coherence length for the chirality, i.e. a distance over which the chirality is predictable. Figure 8.10c shows measurements of this coherence length as a function of applied field strength. An interesting feature of these experiments is that we find that the coherence length is reset every time the domain wall passes through a cross. Figure 8.11 shows a nanowire that has been periodically patterned by crosses to form a comb structure. We find that the domain wall is able to propagate all the way to the end of the wire (and indeed backwards

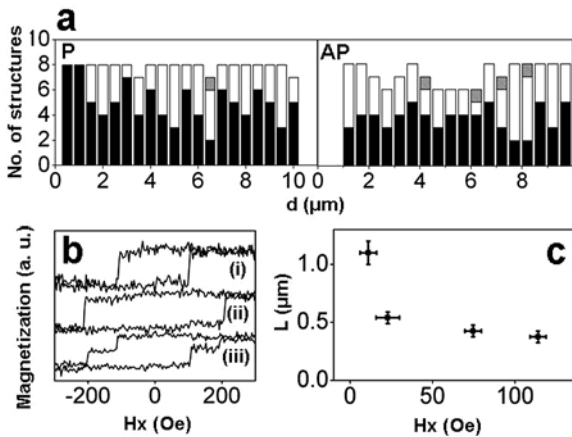
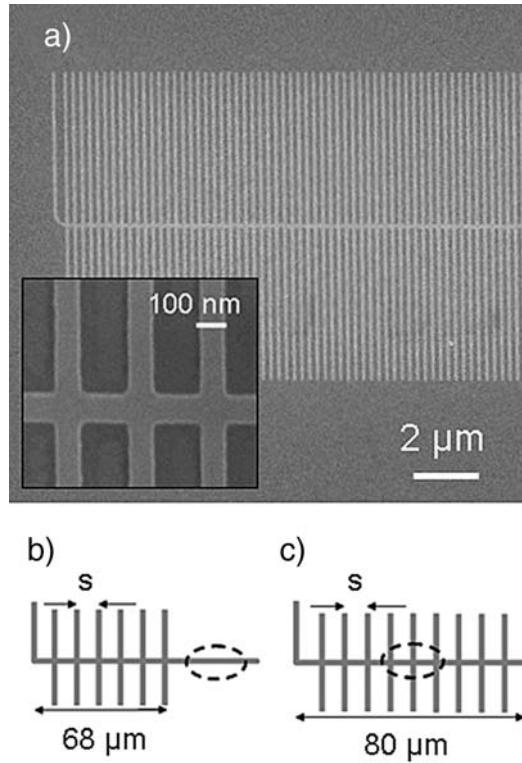


Fig. 8.10 (a) Number of structures showing each type of switching pattern as a function of distance, d , for both P and AP cases as shown in Fig. 8.1. *Black*: switching corresponding to the DW reaching the cross with the chirality set by the initial field pulse; *gray*: switching corresponding to DW reaching the cross with the opposite chirality; *white*: double transition. Chirality reversal is not observed for $d \leq 1\ \mu\text{m}$. (b) Typical MOKE loops, vertically offset for clarity. (i, ii) MOKE loops showing single transitions at H_T and H_N . (iii) MOKE loop showing double transition. (c) Measured coherence length, L , as a function of field

Fig. 8.11 Comb structures. (a) SEM image of left-hand part of comb structure with cross spacing $s = 250$ nm. (b) Schematic of L-shaped comb. (c) Schematic of U-shaped comb. The position of the MOKE measurement is indicated by the dashed ellipse



and forwards many times) without any chirality flipping, because each cross acts as an error corrector, suppressing any chirality reversal that was about to occur. Thus, although chirality is not perfectly stable, careful design of the nanowire structures does allow it to be used as a predictable vector for data.

The second key question has already been touched on in the previous paragraphs and concerns how easy it is to manipulate and control the chirality of a domain wall. The cross structures used in the previous experiment give one example of chiral control and filtering. Figures 8.12 and 8.13 give a related example in which a high-efficiency domain wall switch is presented. We find that a T-stub interacts even more efficiently with the chirality of the domain wall, largely because both the direction of the transverse magnetization within the wall and also the shape of the V-structure contribute to the discrimination between chiral states. We find that when the chirality of the domain wall is such that the transverse magnetization is parallel to the T-stub magnetization, the domain wall is able to pass through the gate with virtually no increase in propagation field; when anti-parallel, the field to transmit through the gate becomes greater than or equal to the nucleation field of the wire, i.e. there is perfect discrimination between the two chiral states. Such a highly discriminating structure could form the basis of a number of new spin-dependent devices that work with the domain wall chirality.

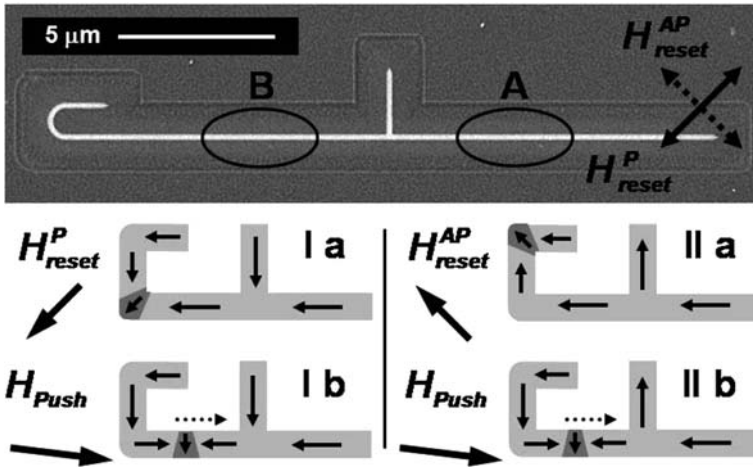
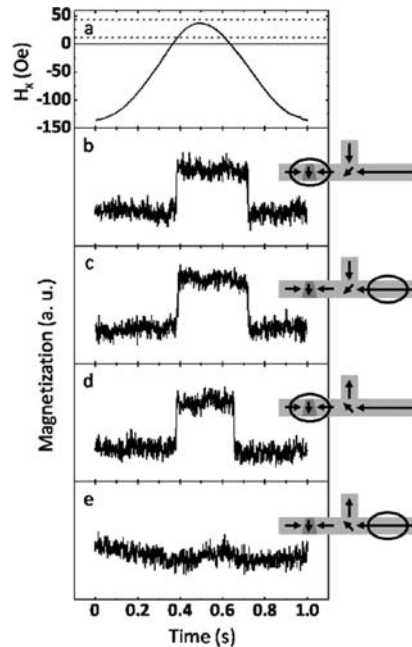


Fig. 8.12 Secondary electron image by FIB irradiation of a 200 nm wide Permalloy structure with a DW gate at its *middle*. Ellipses A and B show the two positions of the laser beam during MOKE measurements; the *double arrows* show the directions H_P reset and H_{reset}^{AP} . *Bottom*: schematics illustrating the field sequences used to measure the switching properties of the structures. I a, b, illustrate the creation and displacement of a head-to-head domain walls in the parallel configuration; II a, b, show the anti-parallel configuration. The large *arrows* indicate the direction of the external magnetic field, the narrow *arrows* show the direction of the magnetization in the nanostructure, and the *dotted arrows* show the direction of displacement of DWs

Fig. 8.13 Horizontal field H_x (a) and MOKE traces (b, c) measured after the gate when the magnetization in the core of the incoming DW is (b) parallel to the magnetization in the gate and (c) anti-parallel. The DW is created during the negative part of H_x and pushed towards the trap during the positive part. The *upper dotted line* indicates the transmission field for parallel configuration, the *lower dotted line* for anti-parallel configuration



8.6 Potential Applications of Domain Wall Logic

Domain wall logic is not a contender for a wholesale replacement of CMOS microelectronics. CMOS is a highly mature technology with many advantages, and still has many years of scaling available to it. However, a strong trend in microelectronics which is expected to apply to the relationship between CMOS and many other areas of nanotechnology in the future is to combine multiple technologies on a single platform: the System on Chip (SoC). Mature economies usually break into a large number of specialists each doing what he or she does best. The same principle applies to complex microelectronic devices. In this context, domain wall logic brings another item to the menu of available technologies. So what does domain wall logic do well?

- It gives high level of functionality to relatively simple structures. To implement shift register in CMOS would take several transistors; domain wall logic achieves it simply by bending a nanowire into a cusp.
- The power dissipation per logic gate is extremely low. Microelectronic engineers usually measure dissipation from a gate by the power-delay product, that is to say the product of how much power is dissipated multiplied by how long the gate takes to process a single function. The units of this quantity are energy, corresponding to the energy dissipated during the evaluation of the function performed by the gate. CMOS' power-delay product depends upon the size of the devices. In order to compare like with like, we therefore take the 200 nm minimum feature size CMOS value of 10^{-2} pJ [20]. On very general magnetic grounds, we can say that an upper bound for the power-delay product for domain wall logic is $2M_s V H$, where M_s is the saturation magnetization of the magnetic material, V is the volume of magnetic material in a gate and H is the amplitude of the applied field. Applying the parameters for a typical 200 nm domain wall logic gate gives 10^{-5} pJ, i.e. 1000 times lower than the equivalent CMOS device. Because of the inefficiencies inherent in the generation of high-speed magnetic fields (see above), this does not necessarily mean that domain wall logic chips will not consume much power. What it does mean, however, is that the waste heat will be generated from the global field generator and not from the logic devices themselves. This is of particular relevance if one comes to stack the devices into 3D neural-like circuits. The two key technical difficulties to doing this in CMOS are (i) distributing the power and clock to everywhere inside the volume of network; (ii) extracting the waste heat from the centre of the network so that the device does not melt. We believe that domain wall logic is an excellent choice of primitive for 3D architectures.
- Non-volatility comes as standard. In a world of mobile computing and portable (or even wearable) devices, the concept of 'instant-on' is becoming increasingly important. Users accept that devices cannot be expected to operate when there is no power. However, as soon as power becomes available, users want the device to be ready, and not have to undergo a long boot process, or to have forgotten what it was doing when the power last failed. Since there are currently very few non-volatile memory technologies available which can be embedded directly

into CMOS, a data transfer process is usually required between a high-speed, volatile memory register in the heart of the CMOS logic and an off-chip low speed, non-volatile store where the state variables of the system are stored. With domain wall logic, all of this becomes redundant. Providing that the rotating field is properly controlled so that it stops gracefully as power fails and does not apply intermediate levels of field leading to data corruption, the domain wall logic circuit should simply stop and retain all of its state variables. As soon as the power returns, the logic continues from where it left off.

- Domain wall logic can make use of redundant space on top of CMOS. Because no complex heterostructures are required, the logic elements can sit in a single layer fabricated as a Back End Of Line process after the CMOS has been laid down. This can improve the efficiency of the underlying CMOS by farming out some space-consuming task to the domain wall logic on top. Since this space was never accessible to CMOS itself anyway, it all counts as a gain.
- Being metals, the basic computational elements of domain wall logic are automatically radiation hard and so are suitable for use in space or in military applications.
- We have already demonstrated that domain wall logic is very good at forming high-density shift registers. These could be used as non-volatile serial memory. Serial memory is used for storing entire files, and so does not require high-speed random access. The hard disk drive and NAND Flash devices (e.g. as used to store the photographs in a digital camera) are examples of non-volatile serial memory. Both of these devices are currently 2D in form. Shift registers made from domain wall logic elements have the potential to be stacked into three dimensions without incurring extra wiring complexity, since data and power can be transmitted remotely through magnetic fields, as demonstrated earlier in this chapter. In a hard disk drive, the data are stored as rows of magnetic domains, and this would remain the same in a domain wall logic serial memory. What would differ is that in a hard disk, the domains are mechanically rotated on their disk underneath a static sensor, while in domain wall logic the domains themselves would move under the action of an externally applied magnetic field along static domain wall conduits, potentially stacked into an ultrahigh density 3D array.

The weaknesses of domain wall logic are (i) limited operational speed and (ii) unconventional synchronous interconnect. Whether the latter should be regarded as an advantage or a disadvantage is open to debate, since it is the same property which makes domain wall logic so suitable for high-density serial memory. Nevertheless, interfacing with conventional design tools remains a challenge.

8.7 Conclusion

While bulk magnetic alloys usually exhibit very simple linear properties, structuring on the nanoscale introduces more complex, non-linear behaviour which can be used for a new generation of spintronic devices. In particular, the coercivity of the

magnetic material, which is usually an intrinsic property in the bulk, becomes very dependent on whether the magnetization reversal mechanism is limited by domain nucleation or by domain wall propagation. We have demonstrated modifications to the coercivity of as much as a factor of 65 simply by whether a domain wall is artificially injected or not. The huge ratio between the domain wall propagation field and domain nucleation field that exists in magnetic nanowires has allowed us to introduce the concept of the domain wall conduit, in which the nanowire can be considered to be a highly efficient conductor for domain walls. If information is encoded by the domains, then domain wall conduits allow that information to be moved around an arbitrary network, and the possibility of building computational devices emerges. Furthermore, we have shown that by precisely modifying the shape of the nanowire, we can exert control over the information and hence implement Boolean gates. An alternative approach to information coding has also been demonstrated, in which the chirality of the domain wall itself rather than its magnetostatic charge is used to code data. In this case, propagation of data along nanowires is possible providing the coherence length of the chirality is respected. Very high-efficiency gates, switches and filters can be implemented by intersecting nanowires in the shapes of crosses or T-stubs.

We have discussed the strengths and weaknesses of domain wall logic when compared against other mainstream digital technologies and concluded that like most nanoscale devices, domain wall logic is not a one-stop replacement for all areas of digital logic, but rather should be used selectively to perform the functions that it does best. We have highlighted in particular the benefits of forming 3D shift registers from domain wall logic elements for the purpose of ultrahigh density data storage.

Acknowledgments This chapter draws heavily on work performed by current and past researchers in my research team: Dan Allwood, Dorothee Petit, Dan Read, Emma Lewis, Del Atkinson, Gang Xiong, Colm Faulker and Vanessa Jausovec. I express my thanks to all of them.

References

1. G.A. Prinz, *Science* 282, 1660 (1998)
2. S.A. Wolf et al., *Science* 294, 1488 (2001)
3. T. Dietl, H. Ohno, F. Matsukura, J. Cibert, D. Ferrand, *Science* 287, 1019 (2000)
4. G. Xiong, D.A. Allwood, M.D. Cooke, R.P. Cowburn, *Appl. Phys. Lett.* 79, 3461–3463 (2001)
5. R.P. Cowburn, D.K. Koltsov, A.O. Adeyeye, M.E. Welland, *Appl. Phys. Lett.* 73, 3947–3949 (1998)
6. A. Hubert, R. Schaeffer, *Magnetic Domains: The Analysis of Magnetic Microstructures*. Springer Verlag New York (1998) ISBN 3-540-64108-4
7. L. Berger, *J. Appl. Phys.* 55, 1954–1956 (1984)
8. N. Vernier, D.A. Allwood, D. Atkinson, M.D. Cooke, R.P. Cowburn, *Europhys. Lett.* 65, 526 (2004)
9. C.K. Lim, T. Devolder, C. Chappert, J. Grollier, V. Cros, A. Vaurès, A. Fert, G. Faini, *Appl. Phys. Lett.* 84, 2820 (2004)
10. A. Yamaguchi, T. Ono, S. Nasu, K. Miyake, K. Mibu, T. Shinjo, *Phys. Rev. Lett.* 92, 077205 (2004)

11. D.A. Allwood, G. Xiong, M.D. Cooke, C.C. Faulkner, D. Atkinson, N. Vernier, R.P. Cowburn, *Science* 296, 2003–2006 (2002)
12. X. Zhu, D.A. Allwood, G. Xiong, R.P. Cowburn, P. Grutter, *Appl. Phys. Lett.* 87, 062503 (2005)
13. D.A. Allwood et al., *Science* 309, 1688 (2005)
14. B.N. Engel, J. Akerman, B. Butcher, R.W. Dave, M. DeHerrera, M. Durlam, G. Grynkewich, J. Janesky, S.V. Pietambaram, N.D. Rizzo, J.M. Slaughter, K. Smith, J.J. Sun, S. Tehrani, *Magn. IEEE Trans.* 41, 132–136 (2005)
15. J.S. Moodera, L.R. Kinder, T.M. Wong, R. Meservey, *Phys. Rev. Lett.* 74, 3273–3276 (1995)
16. R.P. Cowburn, UK Patent GB2430318.
17. R.D. McMichael, M.J. Donahue, *IEEE Trans. Mag.* 33, 4167 (1997)
18. N.L. Schryer, L.R. Walker, *J. Appl. Phys.* 45, 5406 (1974)
19. Y. Nakatani, A. Thiaville, J. Miltat, *Nat. Mater.* 2, 521 (2003)
20. R. Waser, Ed., *Nanoelectronics and Information Technology*. Wiley VCH, Weinheim p. 330 (2003)

Chapter 9

Bit-Patterned Magnetic Recording: Nanoscale Magnetic Islands for Data Storage

Thomas R. Albrecht, Olav Hellwing, Ricardo Ruiz, Manfred E. Schabes, Bruce D. Terris, and Xiao Z. Wu

Abstract Bit-patterned recording shows potential as a route to thermally stable data recording at densities greater than 1 Tbit/in², provided that a number of challenging requirements can be met. Micromagnetic modeling of the write process shows that high write-field gradient (>350 Oe/nm) and tight tolerances on island fabrication and write synchronization (both in the range of ~ 1 nm sigma) are required for addressability (the ability to write a given island without detrimentally affecting neighboring islands). Magnetically uniform islands are also required, with tight island switching-field distribution (5–10% of H_k). We show that magnetic multilayer films with perpendicular anisotropy (e.g., Co/Pd multilayers and laminated films of Co/Pd with other materials) are promising candidates for magnetic layer deposition onto pre-patterned substrates. A suitable strategy for patterned media fabrication begins with master pattern generation using electron beam lithography to create chemical contrast guiding patterns for self-assembly; this approach produces higher quality and higher density patterns than e-beam alone. Patterns are replicated over large volumes of disks by UV-cure nanoimprint lithography, followed by etching of the substrate or magnetic layer. Integration of bit-patterned media into a functional recording system requires write synchronization, in which the timing of current switching in the write head is synchronized with the passage of individual islands under the write head. Write synchronization may be implemented using a sector synchronization system, in which the write clock is frequency- and phase-locked to timing bursts read from the disk during periodic interruptions in the writing process.

T.R. Albrecht (✉)
Hitachi Global Storage Technologies, San Jose Research Center, San Jose, CA 95123, USA
e-mail: Thomas.Albrecht@hitachigst.com

9.1 Introduction

Magnetic recording, invented over 100 years ago, has played a key role in the development of information storage technologies, including analog audio, video, and digital data recording. Since the sale of the first magnetic hard disk drive by IBM in 1956, the capacity and storage density, i.e., the number of bits per square inch (bits/in^2), have increased dramatically. The increase in density has required continuous scaling of the components of the disk drive to ever smaller dimensions. As a result of scaling, the head flies closer to the disk, write and read resolution are increased, write fields and field gradients from the head increase, the recording medium becomes thinner, the grains in the medium become both thinner and smaller in diameter, and the medium coercivity is increased, all allowing for a growth in areal density and a corresponding increase in data rate [1, 2].

Recording demonstrations at densities of 412 Gb/in^2 [3] and 519 Gb/in^2 [4] have been reported on conventional perpendicular continuous granular media (CGM), and system designs have been discussed for Tb/in^2 densities [5–8]. This increase in density has been achieved by scaling the grain size in the media with the bit size, thus keeping the number of grains/bit approximately constant (not strictly true in recent years) and maintaining a sufficient signal-to-noise ratio. In order to prevent long-term signal decay caused by thermally activated magnetization reversal, the magnetic anisotropy must increase with decreasing grain size. Ultimately, the recording density will be limited by the inability of the head to reverse grains having the required anisotropy for thermal stability.

Growth in areal density beyond the original predicted onset of superparamagnetism has been made possible in part by new media incorporating exchange spring structures [8]. These media have a lower anisotropy “capping” grain exchange coupled to a higher anisotropy “storage” grain. The cap grain enables the reversal process to proceed by in-coherent rotation and allows the writing of higher anisotropy materials than otherwise possible. However, at some density, even this strategy is likely to reach a limit, and a new recording paradigm may be required.

There are two approaches to enabling recording at densities beyond the reach of conventional continuous granular recording (CGR). The first approach, known as “energy-assisted recording,” involves assisting the head to write higher anisotropy media, either by means of locally heating the bit [9] or by adding a radio frequency magnetic field [10]. The high anisotropy enables small grains to be thermally stable, and adding a new energy source to the head enables writing the bits. The second class of approaches, the use of lithographically patterned media, uses heads similar to those today but with radically different media, lithographically patterned media. Two forms of such media have been proposed, discrete (or patterned) track media and bit-patterned media (BPM) [11–13].

Discrete track media is a modified form of CGM, in which the magnetic film has been lithographically patterned into tracks separated by nonmagnetic material or empty gaps. In discrete track recording, the bit transitions along the track are

still defined by the field gradient from the write head as in conventional CGR. This chapter, however, will focus on the challenges for bit-patterned recording (BPR), which will offer a larger density gain than discrete track recording. For BPM, each bit is lithographically patterned to be one grain, or more precisely, one magnetic switching volume (which may consist of a few strongly coupled grains), referred to as an “island.” The magnetic energy $K_u V$ is thus no longer governed by the grain volume but rather by the entire island volume. The anisotropy can thus be reduced due to the increased magnetic switching volume to achieve both thermal stability and writability at high density.

While BPR may be a route to thermally stable recording, such a recording system differs substantially from a CGR system. For example, while signal-to-noise ratio and data error rate in a CGR system depend on transition jitter which is strongly affected by media grain (or cluster) size and distribution (as well as switching-field distribution and write-field gradient), for BPR a major source of media noise is patterning tolerances in the island fabrication process. Another striking difference between CGR and BPR is the need for synchronized writing – synchronization of the write clock to the passage of individual islands under the write head – in BPR, which is not necessary for CGR.

General requirements for BPR and fabrication approaches for BPM have been previously reviewed [13], and thus we will focus primarily on the foremost unresolved issues for developing a robust BPR system that may be applicable to future disk drives.

In Section 9.2, the writing process for BPR is analyzed via micromagnetic modeling, highlighting some of the key parameters and tolerances that need to be met for addressability and thermal stability at 1 Tbit/in² and beyond. In particular, a tight island switching-field distribution is required, as well as high write-field gradient, fabrication tolerances on the order of $\sigma = 1$ nm, and synchronization of the write clock to within a small fraction of the island period.

Section 9.3 explores the challenges of creating magnetic films with properties needed for BPR, including discussions of the feasibility of achieving the necessarily tight island switching-field distribution, the measurement of switching-field distribution, the effects of noise from trench material, and a method to eliminate trench noise.

Sections 9.4 and 9.5 address the issues of BPM fabrication, showing how a combination of top-down e-beam lithography and bottom-up self-assembly may provide a method of producing suitable master patterns. Self-assembly plays a vital role in producing high-quality patterns at island densities beyond the reach of e-beam alone. Nanoimprint lithography and etching can be used for high volume pattern replication on millions of disks.

Section 9.6 analyzes BPR system requirements for write synchronization and proposes a practical implementation of a “sector sync” system. Also included are experimental measurements of timing errors in working disk drives and how they relate to the feasibility of the proposed implementation.

9.2 Theoretical Perspective of Bit-Patterned Recording

This section gives a brief theoretical introduction to the physics of BPR. We want to convey here some of the important differences between BPR and the more traditional continuous-granular recording (CGR). In this way, we not only show that BPR is a candidate for recording at Tb/in² densities but also identify some of the novel challenges associated with BPR. As will become apparent in Sections 9.2.1 and 9.2.2, profound differences between CGR and BPR arise from the fact that the write process of BPR needs to be synchronized with the fixed island geometry of the media in order to give adequate addressability error rate. We will revisit the topic of write synchronization in Section 9.6, where we discuss recent experimental spin-stand data. A detailed analysis of the addressability error rate from micromagnetic and analytical models has recently been given in reference [14], which will be heavily used in the following pages. The areal density potential of BPR has been discussed for various head/media combinations in reference [15].

9.2.1 Island Addressability in Bit-Patterned Recording

One of the fundamental differences between BPR and CGR stems from the fact that BPR generally employs a write process that is synchronized with the fixed island geometry, while CGR uses a write process that is asynchronous with respect to the media grains [14]. Asynchronous writing on BPR has been considered via specialized signal processing techniques with insertion/deletion channels [16]; however, it appears to be fraught with too high a penalty for the channel capacity to be a viable option. In the following, we therefore will not further consider asynchronous BPR.

To appreciate the required fabrication tolerances for BPM, it is useful to view writing on BPM as a two-stage process: (1) spatial patterning and (2) magnetic addressing [14]. The first step creates the spatial components of each bit cell by placing carefully controlled features (“islands”) on the surface of a substrate. The second step magnetizes each island in one of its magnetic configurations. Most current versions of BPM aim to provide two possible states per island, e.g., by using perpendicular magnetic data layers on top of each island. In the two-state approach to BPR, each island forms a single magnetic domain. More than two states per island would be desirable to multiply bit densities similar to density enhancements in FLASH memories [17]. Multilevel BPM are discussed, e.g., in reference [18, 19]. However, the following sections will discuss the recording physics mainly for BPM with two-level islands.

Before discussing models of BPR, we would like to make a few comments regarding the extendibility challenges of CGR technology. In CGR, the write process does not keep track of the morphological grain structure during writing of magnetic bit cells. As a consequence, the bits are placed asynchronously relative to the magnetic grains, leading to stochastic variations of the shape, phase, and magnetic uniformity of magnetic bit cells during writing and reading. These fluctuations

are referred to as granular media noise and may significantly contribute to the total noise power of the recording system [20]. If the recording density needs to be increased at constant media signal-to-noise ratio, a number of steps can be taken in CGR: (1) a reduction of the magnetic cluster size (which often means also smaller physical grains), (2) a tightening of the distributions of the granular materials properties, and (3) use of laminated media (including antiferromagnetically coupled, or AFC media). There are however significant difficulties to improving granular properties at grain sizes below about 4 nm with sufficiently reduced magnetic correlations, while at the same time maintaining sufficient thermal stability [21, 22]. Furthermore, thickness considerations limit the use of lamination approaches for improving media noise statistics. Currently efforts exist to utilize exchange-spring effects [23] to master some of the difficulties associated with unpatterned granular media. However, the obstacles of grain-size reduction become sufficiently severe at bit densities in excess of about 1 Tb/in² to motivate exploration of synchronous approaches, like BPR. Furthermore, as we will argue at the end of this section, BPR appears advantageous even when energy-assisted write methods are considered [14].

An example of a set of bit-patterned islands is shown in Fig. 9.1a. The islands have the shape of orthogonal parallelepipeds and are arranged along orthogonal axes with down-track period λ_1 and cross-track period λ_2 . The widths of the trenches in the down-track and cross-track directions are γ_1 and γ_2 , respectively. Of course, on a rotating disk medium, the orthogonality of the down-track and cross-track direction is satisfied only locally, since the islands are arranged along circular tracks. However, the curvature of the tracks can be neglected for the purpose of the following discussion.

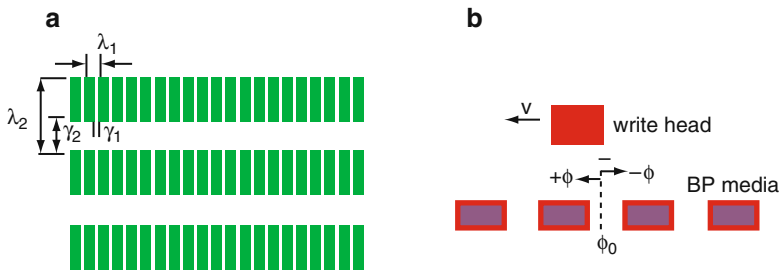
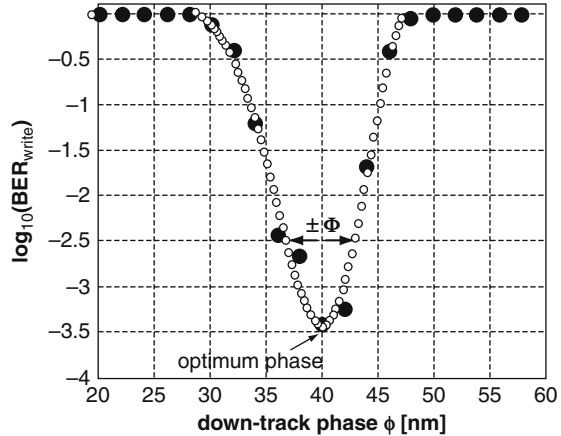


Fig. 9.1 (a) Example of BPM topology. (b) Write head moving above stationary BPM. ϕ is the down-track measured relative to optimum phase ϕ_0 (reproduced from Ref. [14])

Next, consider a magnetic recording head moving above the islands of Fig. 9.1a from right to left with velocity v as depicted in Fig. 9.1b. It has been shown experimentally [24] and theoretically [14, 15] that the ability to address islands is a strong function of the write phase ϕ relative to an optimum phase ϕ_0 . The ability to magnetically write precisely the targeted island has been termed “addressability” [14, 25] and is at the center of calculating geometrical and magnetic fabrication tolerances

of BPM. Figure 9.2 shows that the addressability error rate BER_w rapidly increases from about $10^{-3.5}$ at the optimum phase ϕ_0 to $10^{-2.5}$ at a phase misalignment of about 3.1 nm. Another way of stating this result is to say the phase margin Φ at $BER_w = 10^{-2.5}$ is about ± 3.1 nm. The phase margin Φ is a useful metric for quantifying the robustness of a BPR system design. As discussed in references [14, 15, 25], Φ depends also strongly on the magnetic materials parameters of the islands, in particular, their switching-field distribution.

Fig. 9.2 Probability of an addressability error as a function of down-track phase ϕ for $\sigma_{kl} = 4\%$ (reproduced from Ref. [14])



9.2.2 Fabrication Tolerances of BPM

In the design of BPR systems, a number of variables need to be carefully balanced to achieve a given target for the areal density. Leading terms are, in particular, the fabrication tolerances of the islands σ_{print} , the write-synchronization jitter σ_{synch} , the gradient of the effective write-field ∂H_{eff} , the switching-field distribution (SFD), and magnetostatic interaction fields which fluctuate depending on the magnetic bit configuration of the islands. Furthermore, good island addressability requires tight distributions of the magnetic material properties of the islands. It is therefore clear that the design space of a BPR system is large and that we need to focus on the most dominant variables to obtain a reasonable survey of the opportunities and requirements of BPR designs. For this objective, we will estimate fabrication tolerances of BPM by pooling geometrical and magnetic fluctuations assuming uncorrelated Gaussian distributions [14, 15, 25].

As shown in Ref. [14] and in a similar approach in [15], an upper bound of the addressability error rate BER_w can be computed for arrays of islands where the down-track period λ_I satisfies the constraint

$$\lambda_I \geq 2u, \quad (9.1)$$

with u given by

$$u = \beta_w \sqrt{\left(\frac{\sigma_{H_s}}{\frac{\partial H_{\text{eff}}}{\partial x}}\right)^2 + \sigma_{\text{print}}^2 + \sigma_{\text{synch}}^2}, \quad (9.2)$$

where σ_{H_s} is the standard deviation of the switching-field distribution (including contributions from pattern-dependent interactions between islands), and β_w is defined by the upper bound of the targeted addressability error rate defined by

$$BER_w = \frac{1}{2} \operatorname{erfc}\left(\frac{\beta_w}{\sqrt{2}}\right). \quad (9.3)$$

The quantity u has been called the ‘‘uncertainty zone’’ in references [14, 25] because the upper bound for BER_w is not known, if islands are placed inside the region of size $2u$, i.e., if $\lambda_I < 2u$. The above equations require that the effective write-field profile H_{eff} is approximately linear within the required operating range (due to SFD and interaction fields, see also Fig. 9.21). Additional fluctuations will also be present not only for recording on BPM but also on CGM, e.g., tracking errors from nonrepeatable spindle run-out and other sources as well as the possibility that the write-field profile of the head has a temporal distribution [26]. However, these additional effects are neglected here.

Choosing λ_1 as the upper bound of the Eq. (9.1), the achievable areal density can be calculated for given fabrication and magnetic tolerances from

$$A = \frac{A_0}{\lambda_1^2 \chi_{\text{cell}}}, \quad (9.4)$$

where A is the areal density in Tb/in^2 , A_0 is 645.16, $\chi_{\text{cell}} = \lambda_2/\lambda_I$ is the bit-aspect ratio (BAR) of the bit cell. The areal density in Eq. (9.4) scales inversely proportional to the aspect ratio of the bit cell, since the constraint of Eq. (9.1) is imposed.

9.2.3 Thermal Constraints

At the relatively modest bit densities of current magnetic recording systems (CGR based) of a few hundred Gb/in^2 , the size of the BPM bit cells would allow for islands that have very large thermal energy barriers. Thermal decay of islands would be of no concern in this case. However, when we consider BPR at multiple Tb/in^2 , we need to be more cautious because both the island size and the size of the write pole are reduced. The reduction in island size leads to a reduction of the island volume V and hence to a reduction in thermal barrier $\beta_I = K_I V/k_B T$, where $k_B = 1.38 \times 10^{-23}$ J/K is the Boltzmann constant. The reduction in the size of the write pole depends on the bit-aspect ratio BAR and generally leads to a reduction of the available write field. At constant vertical spacing between head and media, the smaller write field

needs to be accompanied by a commensurate reduction of the switching field of the islands. Unless exchange-spring materials [23] are used, the diminished switching field would necessitate a reduction in K_I , hence a reduction of energy barrier β_I . At a BAR of 1, the footprint of an island at 1 Tb/in² might be of the order 20×20 nm², with write-pole width on the order of 25 nm.

At 10 Tb/in², the island size is reduced to about 6×6 nm², and the size of the write pole is on the order of a mere 8 nm. The reduction of maximum perpendicular flux (thickness-averaged for 8 nm thick islands) from scaled write poles is shown in Fig. 9.3. It is seen that a reduction in pole width from about 30 nm to 15 nm (at constant pole aspect ratio) leads to a loss in perpendicular write field of about 30–50% depending on magnetic spacing.

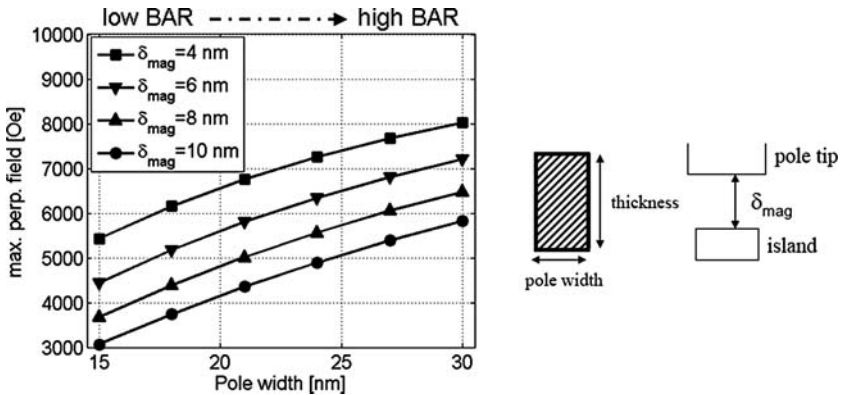


Fig. 9.3 Maximum perpendicular field as a function of pole width and magnetic spacing. The pole tip is assumed saturated with magnetic polarization $J_s = 2.4$ T; thickness/width = 2.5 = const

Magnetostatic interaction fields need to be included in the stability estimates. A rough measure for thermal stability is obtained in a mean-field treatment of the magnetostatic interaction field by defining a thermal stability ratio β_2 as

$$\beta_2 = (K_I - 2\pi < M >^2)V/(k_B T), \tag{9.5}$$

where K_I is the magnetic anisotropy (crystalline or interfacial) of the island material, V is the volume of the island, and $< M >$ is the magnetic moment density averaged over the islands and trenches. Generally, we have to cope with a distribution of β_2 since K_I has a dispersion. We require that the weakest island has a $\beta_2 > \beta_{min}$, where β_{min} depends on the attempt frequency of island reversal. The center of the K_I distribution depends on its width and on β_{min} . Using β_w from Eq. (9.2) and denoting the standard deviation of β_2 with σ_{β_2} , we obtain

$$< \beta_2 > = \beta_{min} + \beta_w \sigma_{\beta_2}. \tag{9.6}$$

A rigorous theory of the required β_{min} that is acceptable without having to refresh the BPM is still lacking. However, at bit densities of about 1 Tb/in², it is relatively

easy to obtain $\langle \beta_2 \rangle$ which is conservatively large. For example, the islands of Ref. [14] have $\langle \beta_2 \rangle \sim 100$ for BPM at 1 Tb/in². Reference [15] calculates the minimum required energy barrier from estimates of adjacent track interference (ATI).

9.2.4 Magnetostatic Interaction Fields Between Islands

The interaction field between islands depends on the magnetic configuration of the neighboring islands and will be stronger if more of the adjacent islands are magnetized in the same direction. Figure 9.4 shows the interaction fields as a function of the length of a block DC magnetized islands and the bit density. The interaction field is calculated at the center of the island at the middle of the track segment. The self-term is excluded from the plotted field values. Figure 9.4 shows that the interaction field increases with block size. The interaction field is about 305 Oe for blocks of length 9. This is an increase of about 15–20% relative to a block size of three (i.e., only the nearest neighbor islands). However, the probability of large blocks (in particular, on multiple tracks) decreases with block size. Fluctuations of the interaction fields can be reduced by avoiding large DC blocks. Note that increasing the density from 0.77 Tb/in² to 2.2 Tb/in² leads to an increase of the interaction fields by about 20%. A Monte Carlo simulation of fluctuations due to random choices of magnetic patterns of islands was carried out in Ref. [15] and showed a distribution of interaction fields that was approximately Gaussian with standard deviations of 15–30% of the maximum demagnetization field for a 1 Tb/in² design. In the following, we assume the Gaussian-distributed interaction fields and pool them with the distribution of anisotropy fields into a single Gaussian switching-field distribution with standard deviation σ_{H_s} for use in Eq. (9.2).

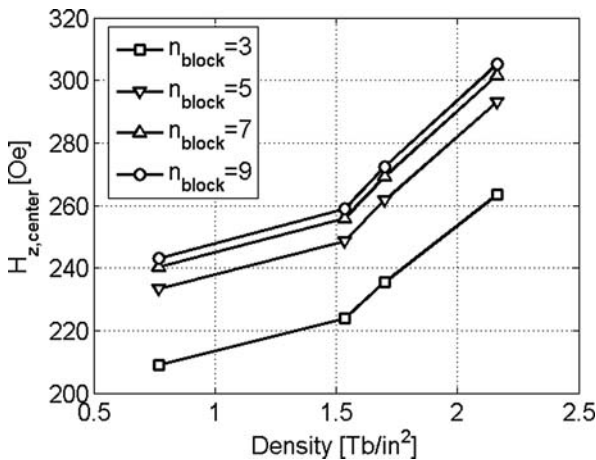


Fig. 9.4 Magnetostatic interaction fields for different sizes of blocks of DC-magnetized islands along a single track; no self-term; $M_s = 425 \text{ emu/cm}^3$

9.2.5 BPM Designs for Tb/in^2 Densities

We are now in the position to discuss various design options for Tb/in^2 BPM designs. Reference [15] gives tables of designs in the range of 1–5 Tb/in^2 based on similar methods as described above. It also includes specific head-field profiles and their off-track capabilities. Here we apply the somewhat more generic treatment of the previous section to BPM designs, first at 1–2 Tb/in^2 , then at extensions toward 10 Tb/in^2 , as discussed in reference [14]. The only assumptions about the write head are the gradient of the effective field and a sufficiently linear range of writeability. In this way, we brush aside the many as-of-now unsolved challenges for the design of write heads at the required levels of miniaturization. Similarly we do not attempt to impose constraints originating from the read head. This media centric view is motivated by the fact that technology for BPR is still early in its development, and we are optimistic that innovation will fill in the many gaps not only for the media but also for the transducers at low BAR. For example, recent work on novel write heads with planar designs [27] showed many interesting properties of the write-field profile at narrow write-width as will be important for us, even though these heads are not available with present head manufacturing technologies.

In Fig. 9.5 we apply Eqs. (9.1) through (9.4) to survey the design space of about 0.7–2.0 Tb/in^2 . The gray scale encodes the areal density in Tb/in^2 with overlaid density contours (large font). The contours with the smaller font give the thermal

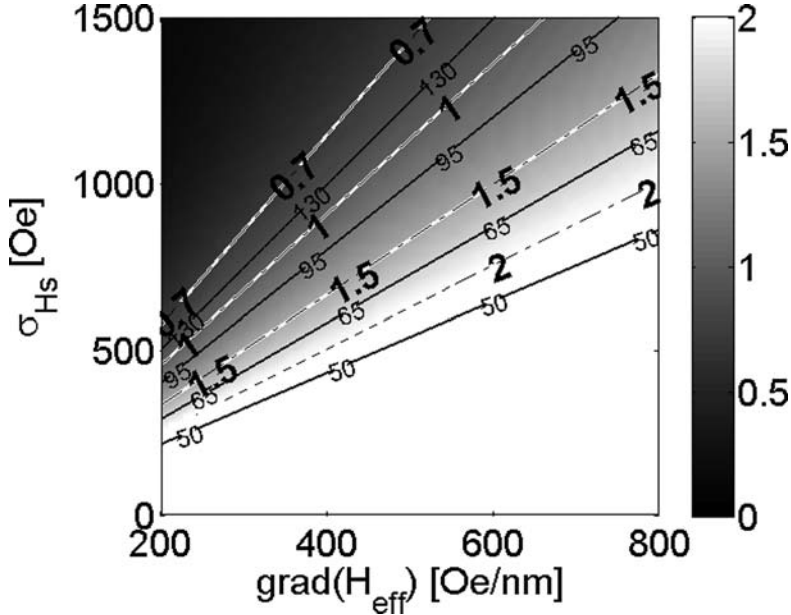


Fig. 9.5 Design chart for $\sigma_{print} = \sigma_{synch} = 1$ nm, $\chi_{cell} = 1$, $M_s = 430$ emu/cm³, $K_I = 2.7 \times 10^6$ erg/cm³, and $BER_w = 10^{-6}$ (after Ref. [14])

stability ratio $\beta_2 = (K_J - 2\pi \langle M \rangle^2) V / (k_B T)$, as defined previously. The design chart of Fig. 9.5 shows that 1 Tb/in² can be achieved with an addressability error rate $BER_w = 10^{-6}$, if the switching-field distribution is on the order of 1000 Oe, head-field gradient is about 430 Oe/nm, fabrication tolerance $\sigma_{print} = 1$ nm, and write-synchronization tolerance $\sigma_{synch} = 1$ nm. The BP periods are $\lambda_1 = \lambda_2 = 25.4$ nm, with island size of $17.9 \times 17.9 \times 8$ nm³, and trench widths $\gamma_1 = \gamma_2 = 7.5$ nm; mean energy barrier $\langle \beta_2 \rangle$ is ~ 113 at $T = 350$ K. The chart makes visible the inherent tradeoff between larger switching-field distributions and increased head-field gradients.

Choosing a bit-aspect ratio of one has the advantage of equally distributing lithography requirements in the down-track and cross-track directions. While a larger bit-aspect ratio χ_{cell} would be preferred for larger pole size with more write field (see Fig. 9.3) and less stringent servo tolerances, it requires also tighter fabrication and synchronization tolerances. Some relaxation of these tolerances is possible by further narrowing switching-field distributions or sharpening the head-field gradients. For example, increasing the BAR from 1 to 2 in Fig. 9.5 and keeping $\sigma_{print} = \sigma_{synch} = 1$ nm requires a reduction of the switching-field distribution σ_{Hs} to less than about 500 Oe (unless the write-field gradient is increased).

Figure 9.6 examines the extendibility of BPR by providing a design chart for areal densities of about 2–10 Tb/in² at fabrication and synchronization tolerances $\sigma_{print} = \sigma_{synch} = 0.4$ nm, and $\chi_{cell} = 1$. As in Fig. 9.5, an addressability error rate $BER_w = 10^{-6}$ is targeted, although different BER_w targets may be possible, if different write strategies (including multi-write, refresh, etc.) can be implemented in

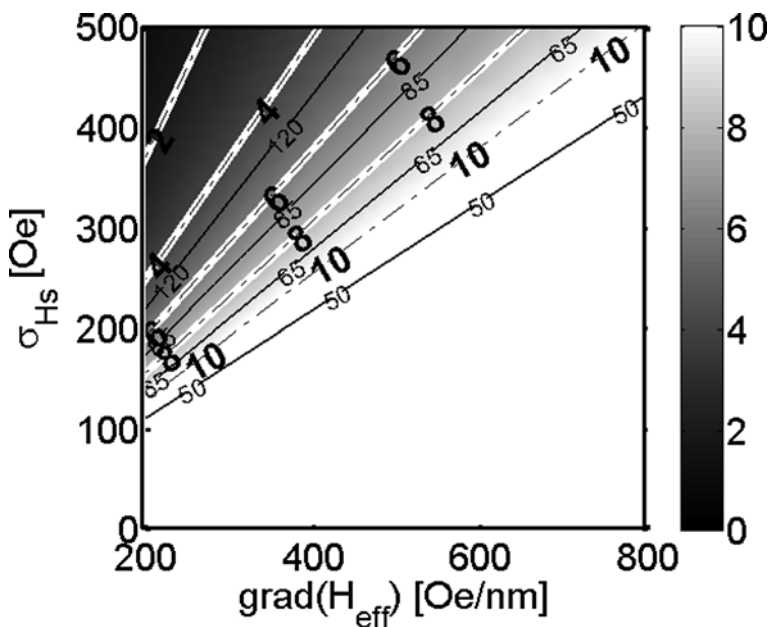


Fig. 9.6 Design chart for $\sigma_{print} = \sigma_{synch} = 0.4$ nm, $\chi_{cell} = 1$, and $BER_w = 10^{-6}$ (after Ref. [14])

advanced microcode architectures. Novel write-strategies may become more acceptable at ultrahigh areal densities considering that at 10 Tb/in² with $\gamma_1/\lambda_1 = \gamma_2/\lambda_2 = 0.25$ (as in Fig. 9.6), the island size is about 6 nm for trench widths of 2 nm. In this case, the bit-patterned island has similar size as an average grain in current CGM. A write-field gradient of about 700–800 Oe/nm is required to allow for a switching-field distribution σ_{HS} of about 450 Oe. However, since σ_{HS} includes the fluctuation of the interaction fields, the island–island interactions will need to be small to have any margin for the K_I distribution. In Fig. 9.6, $M_s = 430$ emu/cm³, $K_I = 1.8 \times 10^7$ erg/cm³, and island thickness is 4.5 nm. To maintain adequate energy barriers of the islands, exchange-spring effects [23] or other techniques, e.g., energy-assisted methods [14, 28, 29], are needed. The nominal anisotropy field of the islands in Fig. 9.6 is $H_k = 2K_I/M_s = 8.4$ T, which means that the islands are writeable only if the switching fields are sufficiently lowered by exchange-spring effects, thermal assist [28], microwave assist [29], or a combination of these methods. Currently neither the required exchange-spring materials nor the write heads (with or without energy assist) are available at write-widths of about 8 nm. Clearly, many open technological challenges exist for extending magnetic data storage toward 10 Tb/in².

9.3 Optimization of the Magnetic Materials

In general, there are two fabrication approaches for BPM. In one approach, substrates are patterned prior to any magnetic media deposition, and then subsequently the magnetic thin film is deposited on these pre-patterned substrates. The major advantage of this technique is that the pattern fabrication process and the magnetic recording media can be optimized independently from each other, and etching of magnetic material is avoided. In the other approach, the magnetic media is deposited as a continuous thin film and then patterned subsequently into discrete islands. Here the major advantage is that there is no magnetic material between the islands or in the etched trenches (which can cause increased readback noise). An additional advantage is that the magnetic film is grown on a flat substrate, and thus overgrowth and curvature effects that may disturb the magnetic film growth on pre-patterned substrates are avoided [2, 13, 30, 31].

Choosing one of these two fabrication methods also has an impact on the range of possible magnetic material systems. In general, perpendicular anisotropy systems are most suitable. In the case of pre-patterned substrates, thin underlayers are required, and thus magnetic multilayer (ML) systems, dominated by interface anisotropy, are preferred. However, when post-etching magnetic films thicker seed layers are possible. Thus it may be preferable to use high anisotropy ordered alloys or more traditional CoPtCr-based alloys, where the c-axis crystal orientation determines the anisotropy direction. In addition, these systems are less susceptible to edge damage in the etching process as compared to the multilayer systems [32].

In the following, we will discuss the optimization and fabrication issues for the pre-patterned substrate approach. However, where necessary, we will comment on

corresponding issues with respect to post-patterning an initially continuous magnetic system. In Fig. 9.7 we show plan-view scanning electron micrographs (SEM) and cross-sectional-view transmission electron micrographs (TEM) of BPM fabricated by deposition onto pre-patterned substrates. While for the 100 nm period a square island shape is still visible, the higher density pattern appears as circular islands due to the resolution limits of the electron beam lithography process. The cross-sectional images reveal some degree of undesired sidewall deposition. However by depositing Co/Pd multilayer media from targets at different angles with respect to the substrate surface, one can avoid the formation of a magnetic phase on the sidewalls and thus ensure magnetically isolated islands. Overgrowth and curvature effects are also visible at the island edges, especially for the higher density pattern, where the flat area in the center of the island is quite small.

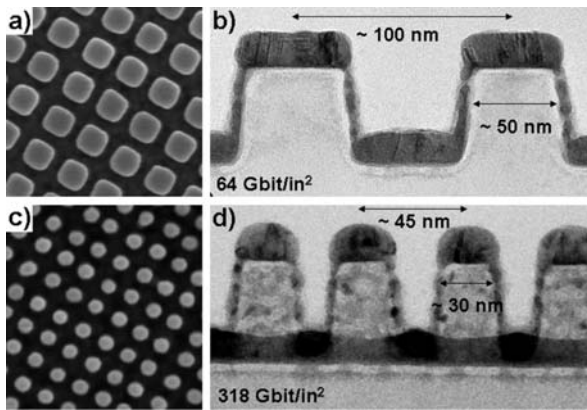


Fig. 9.7 Plan-view SEM (a, c) and cross-sectional-view (b, d) TEM images of pre-patterned substrates after magnetic media deposition for 50 nm islands on 100 nm pitch (64 Gbit/in²) (a, b) and 30 nm islands on 45 nm pitch (318 Gbit/in²) (c, d)

For both fabrication approaches, it is quite expensive and time consuming to produce large patterned areas by electron beam lithography. Therefore, as discussed in Section 9.4, it is likely that a master pattern will be created by electron beam lithography and self-assembly, and then this pattern will be copied to disks using nanoimprint lithography. However, for initial media optimization studies, small patterned test areas of typically (100 μm)² in size can be fabricated by electron beam lithography.

9.3.1 Magnetic Characterization

Remanent reversal curves can be measured from small patterned areas fabricated by e-beam lithography using the polar magneto-optical Kerr effect (PMOKE) with a laser focused down to a 20 μm spot size. An example is presented in Fig. 9.8, where we show a remanent reversal curve of a typical Co/Pd multilayer media deposited

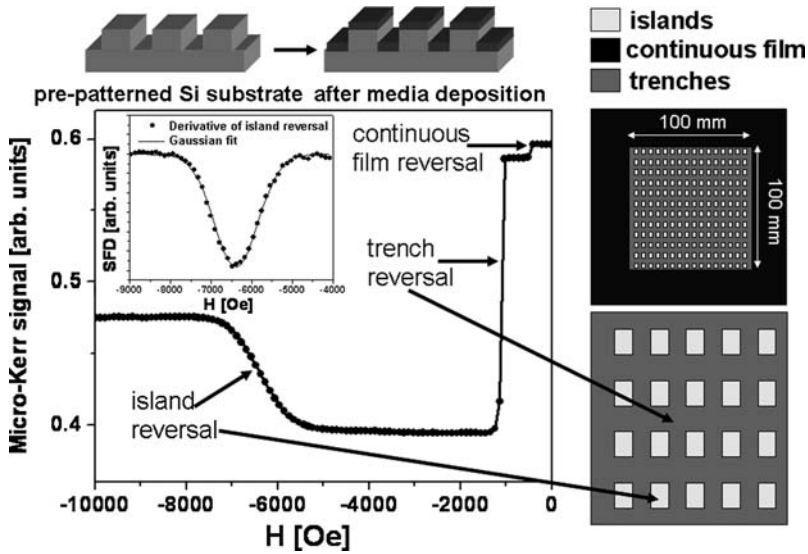
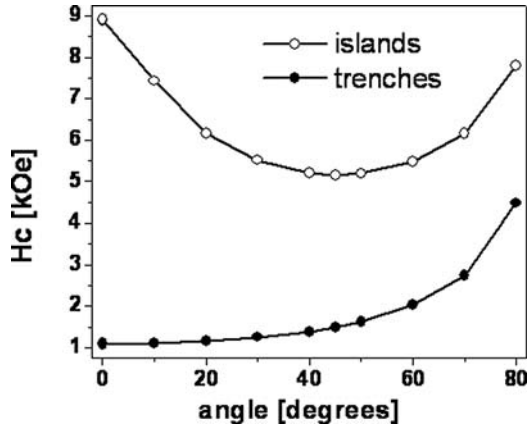


Fig. 9.8 Remanent reversal curve of a typical Co/Pd multilayer media deposited onto a pre-patterned substrate area of $(100 \mu\text{m})^2$ as illustrated on the right. The inset shows the derivative of the island reversal fitted with a Gaussian distribution in order to determine the SFD

onto a pre-patterned substrate [33]. In order to obtain a remanent reversal curve, we initially apply a large positive field of about 20 kOe. Each point of the reversal curve is then measured in remanence after applying a negative reverse field of increasing strength as plotted on the horizontal axis. Since the magnetic material was deposited into the trenches as well as onto the islands, we obtain two separate reversal regions. At low fields, we observe abrupt switching of the continuous film (500 Oe) around the patterned area (which is still illuminated by the tails of the focused laser beam) and the inter-connected trench material (1 kOe). Both continuous film and trench material reverse via nucleation and rapid domain wall motion [34]. However, the switching field of the trench material is slightly higher since the missing magnetic material at the island positions acts as defects and pinning centers. At significantly higher fields of about 6.5 kOe, we observe the more gradual switching of the islands, which individually reverse via uniform rotation. The height difference of about 30–40 nm ensures exchange decoupling of island and trench material, allowing islands to switch independently. The sign of the Kerr rotation is different for the signal from the trenches and the islands, an effect that is frequently found in PMOKE measurements and purely optical in nature [35]. This Micro-Kerr technique may be used to achieve quick results in initial reversal studies of BPM. However, such optical methods provide only relative information and no absolute magnetic moments, such as vibrating sample magnetometry (VSM) or superconducting quantum interference devices (SQUIDS).

In Fig. 9.9, we confirm the above described reversal mechanisms on the islands and in the trenches by varying the angle of the externally applied magnetic field

Fig. 9.9 External field angle dependence of the switching field for trenches and islands in BPM



between out-of-plane (0°) and in-plane (90°) direction. For the islands, we obtain the well-known Stoner–Wohlfarth-like reversal behavior with a minimum switching field at 45° . This angular dependence is typical of a single particle uniform reversal. In contrast the trenches show a very different angular dependence, which follows a $1/\cos(\theta)$ behavior typical of domain wall motion. Overall these findings confirm the presence of small isolated magnetic islands switching by uniform rotation and an interconnected network of magnetic trench material reversing via domain wall motion.

In Fig. 9.10 we show remanent island reversal curves for a variety of island sizes and spacings. In general we observe an increase in coercivity with decreasing island diameter, while the switching-field distribution (SFD) increases quite dramatically

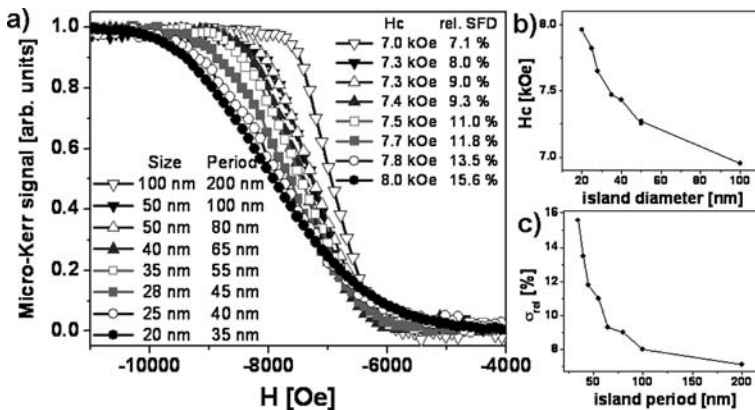


Fig. 9.10 (a) Remanent island reversal curves for different pattern sizes ranging from 100 nm islands on 200 nm pitch (16 Gbit/in²) to 20 nm islands on 35 nm pitch (530 Gbit/in²). (b) Average coercivity vs. island diameter. (c) Relative SFD vs. island period

below 60 nm island spacing. This behavior is typical of islands fabricated using pre-patterned substrates and can be understood by assuming a natural intrinsic anisotropy distribution in the corresponding ML media alone [33]. Other effects due to patterning, such as edge damage of the islands due to lithography or etching in post-patterning an originally continuous film, can lead to decreases in coercivity and increases in the SFD. The physical origin of this natural intrinsic anisotropy distribution is still under discussion. Post-patterning of epitaxially grown Co/Pd MLs has not proved to be an advantage for reducing the SFD [36, 37]. However, this result may be partly due to the fact that the anisotropy of ML media originates from the interface anisotropy of the chemical layering in the ML rather than from the crystal structure.

9.3.2 *Magnetic Switching-Field Distribution*

In general SFDs with a standard deviation larger than 10%, if normalized to the average island reversal field, have shown to be insufficient to guarantee proper addressability of single islands without overwriting any neighbor islands (see Section 9.2). Thus the reduction of the SFD in BPM is a central issue. Due to averaging of the bit signal over multiple grains in continuous perpendicular recording, the SFD of these grains does not have to meet such high standards as for BPM. A miswritten grain in continuous perpendicular recording lowers the bit signal a little. However, if no more than 10–20% of the 20–30 grains per bit are wrongly written, the read head will still identify the write polarity of this bit correctly. In contrast every island written in the wrong polarity in BPM is a single-bit write error (a so-called hard error).

In general the SFD has two components: an intrinsic part and a dipolar contribution. The intrinsic SFD is due to local variations of the island properties. It is the SFD the islands would exhibit, if there were no interactions, e.g., dipolar fields between the islands. This local variation of individual island properties depends on the amount of intrinsic material variation in the magnetic thin film and is also influenced by lithographic irregularities of the pre-patterned substrate, such as island size and shape. The dipolar contribution to the SFD arises from the magnetostatic interaction of an island with its neighbors, which for perpendicular anisotropy tends to broaden the distribution [36].

In Fig. 9.11 we demonstrate an experimental approach to quantitatively determine the dipolar contribution to the SFD, thus allowing an exact assessment of the intrinsic part of the SFD for a density of 318 Gbit/in². In Fig. 9.11a we show the Micro-Kerr reversal curve together with an MFM image after demagnetization. Figure 9.11c shows partial reversal curves obtained by setting initially 64%, 38%, and 22% of the islands into the positive magnetized state. In this magnetization plot, we compare at any fixed horizontal level the reversal of different portions of islands in the same average dipolar environment, i.e., the same average magnetization. The observed horizontal field displacements of the partial reversal curves with respect

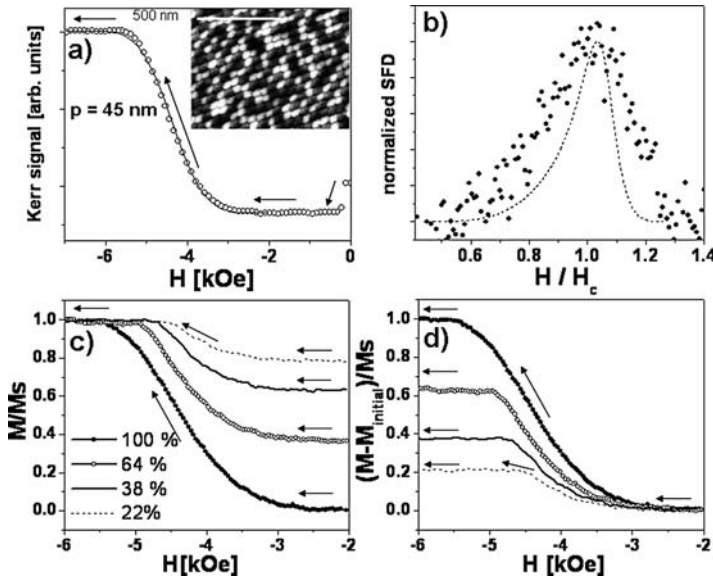


Fig. 9.11 (a) Remanent island reversal curve for 30 nm islands on 45 nm pitch (318 Gbit/in²). The inset shows an MFM image of the corresponding pattern after demagnetization. (b) Total SFD as obtained from the reversal curve in (a) (*solid dots*) and corresponding intrinsic SFD as determined from the minor remanent reversal curves in (c) and (d) using the $\Delta H(M, \Delta M)$ method [38,39,40] (*dashed line*). (c) and (d) show a set of partial remanent reversal curves for switching 64%, 38% and 22% of the islands and matching curves at the saturation level (c) and onset of the reversal (d) respectively

to the full reversal curve reflect the intrinsic SFD of the islands. If the intrinsic SFD were a delta function and the reversal were only broadened by dipolar interactions, then the partial reversal curves in Fig. 9.11c would show no horizontal displacement from the full reversal curve. In Fig. 9.11d we plot the same partial reversal curves after subtracting the initial magnetization values, such that the initial Kerr amplitudes match. Here we compare the reversal of the same islands in different dipolar environments. In the absence of dipolar interactions, the partial reversal curves should follow the major reversal curve until saturation is reached. The observed horizontal displacements in reversal field for the different curves thus provide a direct measure of the dipolar interaction strength.

While the plots in Figs. 9.11c and 9.11d provide a straightforward visualization of the intrinsic SFD and the dipolar interactions, a more quantitative determination is obtained by using the $\Delta H(M, \Delta M)$ method [38–40]. Corresponding results are presented in Fig. 9.11b, where we compare the total SFD as obtained from Fig. 9.11a with the intrinsic SFD as [41] extracted via the $\Delta H(M, \Delta M)$ method [38, 39, 40] from the partial reversal curves in Fig. 9.11c,d. For an observed SFD of $\sigma = 645$ Oe, dipolar broadening contributes $\sigma_{\text{dip}} = 202$ Oe (31%), which yields an intrinsic SFD width of $\sigma_{\text{int}} = 443$ Oe. In addition, we find a pronounced asymmetry in the

intrinsic SFD with a low field tail that is somewhat masked by the dipolar interactions [36]. In order to tighten the SFD in BPM, it is necessary to address both the intrinsic SFD as well as the dipolar contribution. The intrinsic SFD can be tightened by optimizing pattern and media uniformity, but may also be influenced by tuning the reversal mechanism of the islands via more advanced media structures. The dipolar broadening can be reduced by decreasing the magnetic moment of the islands. However, this approach is limited, as it is the field from an island that generates the response in the read sensor and thus more sensitive read heads would be required [36].

9.3.3 Laminated Magnetic Media

One approach for tuning the coercivity and for reducing the intrinsic SFD in BPM is using laminated magnetic layers with different anisotropy values and different sources of anisotropy as demonstrated in Fig. 9.12. Here we combine a hard magnetic Co/Pd and a soft magnetic Co/Ni perpendicular ML system (Fig. 9.12a). While the Co/Pd ML obtains its strong perpendicular anisotropy from the direction of the chemical layering, i.e., from the Co/Pd interfaces, the much weaker Co/Ni perpendicular anisotropy is strain induced, thus the two anisotropies are uncorrelated. For the laminated system, we obtain a thickness and moment-averaged switching field. Therefore it is easily possible to tune the island reversal field via variation of the relative thickness of the hard and the soft layer portions as demonstrated experimentally in Fig. 9.12b for reversal fields from 2 kOe up to 13 kOe. Moreover, for equal standard deviations of the SFDs $\sigma_{K1} = \sigma_{K2}$ and no cross-correlation, we obtain a reduction in intrinsic SFD by a factor of $\sqrt{2}$. Corresponding experimental results are displayed in Fig. 9.12c. Here we compare a regular Co/Pd ML with intermediate anisotropy ([Co(5)Pd(9)] \times 8), with two different Co/Pd–Co/Ni-laminated sys-

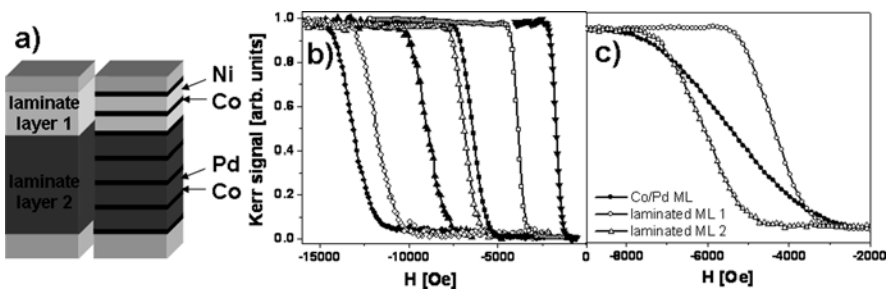


Fig. 9.12 (a) Illustration of an advanced laminated recording media consisting of a hard magnetic Co/Pd and soft magnetic Co/Ni ML structure for tuning the reversal field and reducing the SFD. (b) Remanent reversal curves for a variety of laminated patterned media structures with different island reversal fields for 50 nm islands on 100 nm pitch. (c) Comparison of conventional Co/Pd ML patterned media and laminated Co/Pd–Co/Ni ML patterned media with similar reversal field for 50 nm islands on 100 nm pitch

tems of similar total anisotropy. Clearly the SFD of the laminated system is reduced significantly. In our case we observe a reduction by nearly a factor of 2, which indicates that in addition to the expected anisotropy benefit, one may gain a further advantage due to an exchange-spring effect in such hard/soft laminated structures, which may alter the reversal mechanism to our advantage [42, 43].

9.3.4 Magnetic Trench Noise Reduction

Another issue that needs attention when fabricating BPM via pre-patterned substrates is the magnetic trench material (see Fig. 9.7) that may cause an increased background noise level as illustrated in the static read/write test images in Fig. 9.13 [44, 45]. Here we show the readback signal after writing an alternating bit pattern into the center island row. From the images, it is apparent that all islands are written correctly. However there is a large amount of readback noise originating from the magnetic material in the trenches, which has much lower switching field and thus is easily affected by the write process. Since the reversal in the trenches occurs via domain wall motion, trench domains start spreading out perpendicular to the track direction. In order to reduce this undesired trench noise, one can use a substrate trench material different from the island material and specifically designed to inter-diffuse with the deposited magnetic material during a modest post-annealing step [45]. We demonstrate this selective “trench poisoning” technology in Fig. 9.14, where we show Co/Pd ML media deposited onto pre-patterned substrates consisting of SiN islands fabricated on a Si substrate. In the as-deposited state, we obtain large trench domains after out-of-plane demagnetization as shown in Fig. 9.14b.

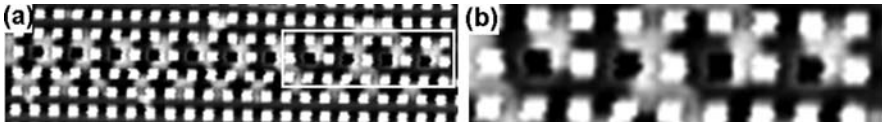


Fig. 9.13 Static read/write test images of an alternating bit pattern written into a BPM of 200 nm islands on 400 nm pitch **(b)** is the expanded view of the boxed region in **(a)**. The magnetic image contains both the patterned bits (*black and white squares*) and the larger scale domains arising from the trench material [44, 45]

The corresponding TEM image shows the same amount of magnetic material in trenches and on islands. After an additional annealing step at about 250°C, the trench domains in the MFM image have vanished as shown in Fig. 9.14c and TEM reveals massive inter-diffusion that has occurred in the trenches and below the islands. However, the island material itself (SiN) is not affected by the inter-diffusion process, and the magnetic material on top of the islands remains magnetically functional as visible in the MFM image and as confirmed by Micro-Kerr measurements. The Si–Pd inter-diffusion process has a low-energy barrier. Thus moderate annealing at 250°C already initiates a rapid inter-diffusion process at the Pd/Si interfaces in the trenches. The Pd moves into the Si, partially dragging the Co

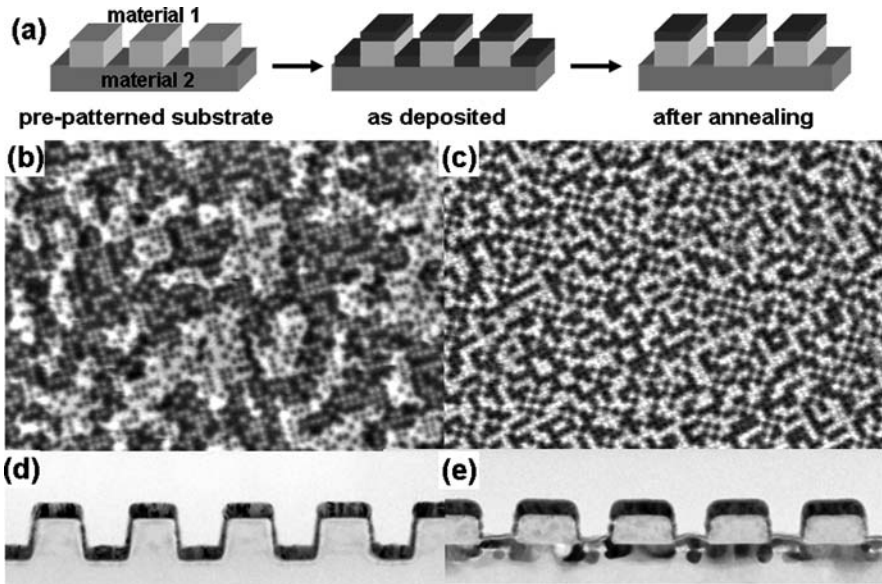


Fig. 9.14 (a) Illustration of the trench poisoning concept: The pre-patterned substrate consists of islands of a material 1 and trenches of a material 2. After media deposition, we end up with magnetic material on the islands as well as in the trenches. An additional annealing step triggers inter-diffusion of the magnetic trench material with the underlying trench substrate material, while the magnetic material on top of the islands remains unaltered. (b) and (c) show MFM images of the demagnetized state for 50 nm islands on 100 nm pitch in the as deposited state (b) and after trench poisoning (c). (d) and (e) show cross-sectional TEM images of the same two structures

along, thus completely destroying the ML structure that provides the perpendicular anisotropy. In addition, the Si moves toward the trench surface, thus destroying the magnetic moment in the trenches completely. In general Fig. 9.14 demonstrates the successful implementation of trench poisoning into BPM. However, with the Si surface diffusion length becoming comparable to the island spacing, undesired partial poisoning of the islands sets in and makes the implementation of the trench poisoning technique a challenge for densities above 200 Gbit/in². Different materials though may reveal better scalability with respect to higher areal density.

9.4 Fabrication of Bit-Patterned Media

Fabricating BPM in a manner which is both cost effective and capable of meeting the requirements specified in Sections 9.2 and 9.3 requires significant innovation. Although manufacturers of semiconductor devices and the equipment suppliers that provide their fabrication solutions are generally at the forefront of conventional micro- and nanofabrication technology, the semiconductor industry roadmap [46] does not provide for solutions at the feature sizes for BPM in the time frame needed.

BPM, at 1 Tbit/in², has features with a half-pitch of <13 nm, which does not appear on the semiconductor roadmap until around 2019, a number of years later than the disk drive industry would need a solution like BPR.

Currently envisioned fabrication processes for BPM would abandon optical lithography – the perennial preference of the semiconductor industry – in favor of a combination of e-beam lithography, self-assembly (see Section 9.5), and nanoimprint lithography for the creation and replication of patterns. As shown in Fig. 9.15, a single topographic *master pattern*, generated at considerable expense, is replicated by a two-generation nanoimprint lithography process, first to create a number of imprinting templates that are copies of the master pattern, and then to replicate the patterns from the imprinting templates onto millions of disks.

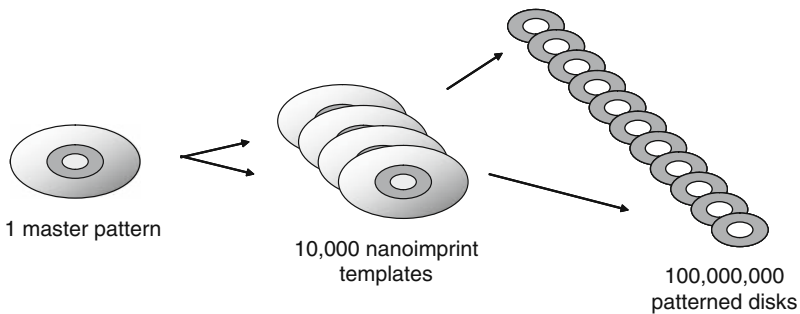


Fig. 9.15 Using a two-generation nanoimprinting process, a single master pattern is first replicated to create a large number of intermediate nanoimprinting templates, which in turn are each used to create a large number of patterned disks. With a sufficiently large multiplier at each generation (e.g., 10,000 X), many millions of disks can be inexpensively patterned from a single master pattern

This process is shown in a simplified single-generation version in Fig. 9.16. The master pattern is generated using e-beam lithography. A rotary-stage e-beam writer is necessary to avoid problematic “stitching” errors which are generally unavoidable in conventional Cartesian (X–Y) e-beam writers. X–Y writers create large patterns (such as needed for a full disk pattern) by stitching together many small rectangular fields, and the alignment of features at field boundaries generally cannot meet the tolerance requirements as given in Section 9.2. Rotary-stage writers produce large circular patterns with a continuously rotating stage, which eliminates stitching boundaries. Resolving the feature sizes needed for BPM (e.g., 15 nm diameter islands with 25 nm period for 1 Tbit/in² media) pushes the limits of e-beam lithography. Although chemically amplified resists would allow reduced dose and faster overall pattern writing time, their resolution is generally not sufficient for BPM needs; non-chemically amplified resists such as poly-methyl-methacrylate (PMMA), ZEP [47], or hydrogen silsesquioxane (HSQ) provide the best resolution but can require extraordinarily long write times (from around 100 h to as much as >1000 h, depending on pattern size, beam current, and resist). Approaches such as cold ultrasonic developing [48] for improving resolution, blankerless writing [49]

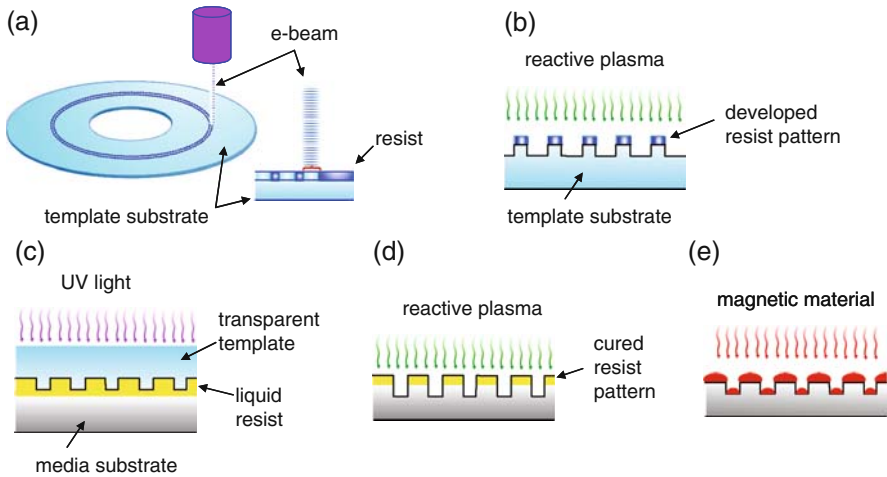


Fig. 9.16 (a) A master pattern is formed by rotary-stage e-beam lithography and converted into a topographic pattern (b) by reactive ion etching into the substrate of the master. In the single-generation simplified process shown here, a transparent master is used, which serves directly as a nanoimprinting template. This template is inverted (c) and brought into contact with a liquid film of imprint resist on the surface of a disk substrate. After exposure to UV light, the resist solidifies, creating a solid inverse topographic replica of the master pattern. The resist pattern is subsequently transferred to the disk substrate (d) by reactive ion etching to form pillars on the substrate. Magnetic material is blanket deposited (e) on the substrate, forming islands on the tops of the pillars

for maximizing writing speed, and multiple pass exposure [49] to optimize feature placement tolerances are all useful for extending the capability of e-beam lithography for BPM pattern generation. Pattern densities as high as 4.5 Tbit/in² have been shown [50], although requirements for island uniformity and placement tolerance will likely limit e-beam lithography to ~ 1 Tbit/in².

The e-beam-generated pattern is converted to a topographic pattern by reactive ion etching (RIE). This topographic pattern can be inexpensively replicated using UV-cure nanoimprint lithography [51, 52], in which ultraviolet light is used to cure a liquid imprint resist, rapidly converting it to a solid. The resist is dispensed on the disk substrate using an ink jet process. As the topographic master pattern is brought into contact with the resist, the resist flows and conforms to the pattern. After a brief (~ 1 s) exposure to UV light, the resist solidifies into a permanent negative copy of the topographic master pattern. With appropriately engineered resist and template surface properties, the template can be cleanly separated from the resist, leaving the patterned resist on the disk substrate. With careful control of the dispensed resist amount, the residual layer thickness (resist thickness in the thin resist regions) can be controlled to within a specific tolerance. Reactive ion etching can then be used to clear the residual layer and etch a specified depth into the disk substrate, leaving an array of pillars protruding from a recessed background on the substrate.

Magnetic material, such as Co–Pd multilayers or other materials as discussed in Section 9.3, can then be blanket deposited on the pillars. Material deposited on the pillar tops forms isolated magnetic islands, and the remaining material falls into the trenches and is dealt with as discussed in Section 9.3. An alternative approach (also discussed in Section 9.3) to creating isolated magnetic islands is to deposit a continuous film of magnetic material on an unpatterned disk substrate, followed by nanoimprint lithography and etching of the magnetic film into islands.

The remaining steps in media fabrication (not shown in Fig. 9.16) include *planarization*, in which the trenches between islands are filled with nonmagnetic material, and application of a suitable overcoat and surface lubricant. Planarization, while not mandatory in an absolute sense, is highly beneficial for creating a disk surface well suited to flying an air-bearing slider over at low flying height (<5 nm), high stiffness, and tight flying height tolerance.

Fabrication cost is a major factor in whether hard disk drives, using BPM, will retain their competitive advantage over solid-state data storage from a cost point of view. Conventional nonpatterned disks require no lithographic steps, while BPM disks, like solid-state data storage devices, require lithographic patterning at the single bit level. However, unlike solid-state devices, which require multiple lithographic steps, with nm-scale overlay alignment tolerances, BPM fabrication requires a single lithographic step, with no overlay requirement (other than μm -scale centering of the patterning on the disk center hole). Equipment and process costs for BPM fabrication are therefore significantly less expensive than what is needed for solid state storage devices, allowing future hard disk drives using BPM to compete favorably on a cost basis. Equipment cost on a per-bit basis for nanoimprinting BPM will likely be an order of magnitude less expensive than the advanced optical lithography tools used for solid-state device manufacturing.

9.5 Generation of Master Patterns Beyond $1\text{Tbit}/\text{in}^2$ via Guided Self-Assembly of Block Copolymer Domain Arrays

Patterned media for magnetic storage at densities over $1\text{ Tb}/\text{in}^2$ involves fabrication of uniform periodic features with a full pitch under 27 nm depending on the lattice and bit-aspect ratio chosen. These dimensions are beyond current optical lithography resolution and beyond current e-beam limitations such as resist resolution, writing time, feature placement, proximity effects, and stitching errors.

Block copolymer self-assembly provides a route to achieve sub-lithographic resolution in the range of 10–100 nm [53–55], i.e., with potential to achieve $\sim 5\text{ Tb}/\text{in}^2$. Linear diblock copolymer molecules consist of two immiscible chains joined by a covalent bond. Driven by the Flory–Huggins interaction parameter χ , the immiscible, but bonded materials microphase separate to minimize the number of contacts between the incompatible blocks [56] forming periodic arrays with a well-defined periodic structure. The resulting morphology (most commonly spherical, cylindrical, or lamellar) is dictated by the volume fraction of the individual blocks in the

copolymer chain while the degree of polymerization N determines the characteristic periodic distance between features L_o .

In block copolymer lithography, a self-assembled thin-film acts as a sacrificial layer to transfer the pattern into a substrate or to an active material. Most commonly, the pattern transfer process involves selective removal of one of the two blocks. The remaining template is then used as a sacrificial mask in a variety of creative ways that range from reactive ion etching (RIE) [54, 55, 57, 58] to lift-off [59] or ion-milling [60, 61]. Pattern transfer is more faithfully achieved when the cross-sectional profile is uniform from the top of the film down to the substrate as is the case for conventional resists [62, 63]. For this reason, we will only consider here the perpendicular cylinder [Fig. 9.17a] and the perpendicular lamellae morphologies as templates to produce arrays of dots and lines respectively. We will also limit our discussion to the generation of a high-quality block copolymer template. For details on pattern transfer techniques, the reader is referred to previous reviews and references therein [63–67].

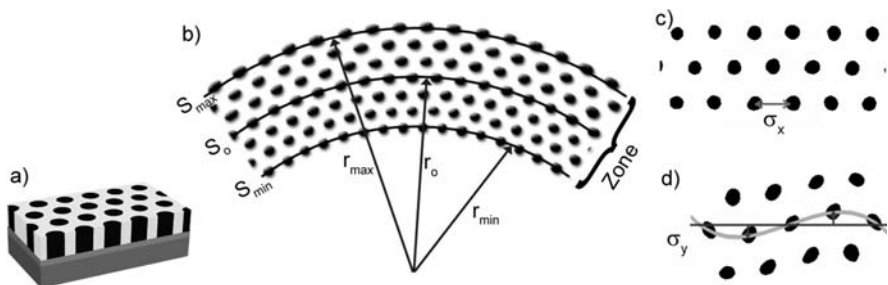


Fig. 9.17 (a) Schematic of a cylindrical phase block copolymer thin film with cylinders perpendicular to the substrate. (b) Schematic of a distorted hexagonal lattice over circular tracks. (c) Representation of down-track and (d) cross-track jitter

9.5.1 Ordering, Size Distribution, and Scalability: Patterned Media Requirements vs. Block Copolymer Fundamental Limitations

A *guided* self-assembly method is more likely to succeed than a pure *bottom-up* approach in addressing challenges such as long-range ordering, placement jitter, feature size distribution, and pattern registration needed to meet the specifications set in Section 9.2 for patterned media applications.

The final quality of the template is determined by both the guiding method and the block copolymer limitations. In this section, we discuss some of the polymer properties such as the interaction parameter χ , degree of polymerization N , glass transition temperature T_g , and surface energies that determine the fundamental limits to pattern quality.

In HDDs, data are stored along circumferential tracks. Tracks are grouped into zones depending on their distance to the center of the disk. Tracks are also divided into angular arcs called sectors. The number of bits per sector is constant (usually

512 bytes plus overhead). Within each zone, the angular span of each sector is kept constant. A block copolymer template would need to be stretched in the outer tracks of the zone and compressed in the inner ones. The amount of circular distortion that can be induced to the block copolymer lattice without introducing other defects determines the maximum zone width achievable. The extent of this achievable distortion is determined by the free energy of the system and the competition between the penalty paid by distorting the lattice or introducing a defect. To estimate the maximum sector width that a block copolymer pattern could support without introducing defects, we consider a zone with track sectors like the ones depicted in Fig. 9.17b. The arc defined by the central track sector is $S_o = r_o\theta = nL_o$ where r_o is the radius at the central track, θ is the angle spanned by the arc, L_o is the block copolymer pitch, and n is the number of features (or bits) in the sector. We assume the block copolymer pattern at this track to be relaxed. As we move to outer tracks, the pattern stretches to preserve the number of bits n . Assuming we could stretch or compress 10% of the lattice [68, 69], then the maximum and minimum arcs S_{max} and S_{min} spanned by the outermost and innermost tracks with a maximum and minimum radius r_{max} and r_{min} are $S_{max} = r_{max}\theta = 1.1 nL_o$ and $S_{min} = r_{min}\theta = 0.9 nL_o$ respectively. Therefore a first estimate for the maximum zone width would be $r_{max} - r_{min} = r_o(1.1-0.9) = 0.2r_o$.

For a 65 mm disk with an inner radius of 10 mm, the maximum zone width at the inner part of the disk could be 2 mm. In reality, this maximum zone width could be further limited by additional “jitter” or loss of translational order caused by the lattice distortions. For the above zone size estimate, we have only included the distortion due to compression or elongation along the track direction. Cross-track deformation due to the circular bending is negligible from one lattice point to the next at radius >10 mm.

Even within a pattern that has no defects disrupting the orientational order, there are small placement variations (jitter) that disrupt translational order. Jitter definition and tolerances will vary for different applications. In the scope of HDD geometries, we address jitter in the down-track and cross-track directions. Down-track jitter σ_x is the standard deviation of the lattice pitch in the track direction. Cross-track jitter refers to the standard deviation of the distance between the bit center and the track line [See Fig. 9.17c–d].

Translational order is limited by the ratio F_c/F_o of the free energy per polymer chain in the confined or *directed* state, F_c , to the free energy per chain in the non-confined state F_o [70–72]. The translational order is also affected by the amount of thermal energy available to the system. This thermal energy at finite temperatures above the glass transition temperature may introduce thermal fluctuations that distort the pattern. As a reference, from the theoretical considerations set forth in Section 9.2, the target for the total jitter tolerance is $\sigma_{print} = (\sigma_x^2 + \sigma_y^2)^{1/2} = 1$ nm at 1 Tb/in² ($L_o = 27$ nm for a hexagonal lattice).

In block copolymer patterns, the characteristic distance between features scales with the degree of polymerization as $L_o \sim N^\delta$, where δ is a scaling exponent ($\delta = 2/3$ in the strong segregation regime [56, 73, 74], but more generally $0.5 < \delta < 1$ [66]). This is an attractive property to sustain the technology for future product

generations. The viability of scaling self-assembly lattice dimensions below 27 nm (beyond 1 Tb/in²) is limited by the strength of the segregation between the immiscible blocks, dominated by the product χN . For a given volume fraction, there is a $(\chi N)_{ODT}$ that signals the onset of the order–disorder transition temperature. For $\chi N \ll (\chi N)_{ODT}$, the block copolymer melt is disordered, and the only correlations are of the order of the radius of gyration of the copolymer [56, 75]. For $\chi N \gg (\chi N)_{ODT}$, the copolymer pattern contains sharp interfaces separating the nearly pure block microdomains. In the vicinity around $\chi N \approx (\chi N)_{ODT}$, the polymer is only weakly segregated resulting in a broader interface width with a sinusoidal compositional profile [56].

The interface width Δ between the two blocks at the domain boundary limits the minimum definable feature size and the feature size distribution. As a first approximation, in the strong segregation limit, the interface width scales with the interaction parameter as $\Delta \sim \chi^{-1/2}$. (Ignoring higher order corrections, the interface width is independent of the molecular weight. As we scale feature sizes down, the leading term for Δ remains constant making the interface/bulk ratio larger).

High bit-aspect ratios (BAR) can be achieved using a striped pattern from a lamellar phase block copolymer rather than a dot (cylindrical) pattern. Rectangular shaped bits with $\text{BAR} > 1$ are better suited for the reading/writing processes as discussed in Section 9.2. However, using a rectangular lattice with high BAR demands even smaller lithographic features to keep the same density. For example, a 1 Tb/in² rectangular lattice with $\text{BAR} = 2$ needs a full pitch of $L_o \approx 18$ nm in the down-track direction.

Finding the right materials for high-density patterning is challenging. Block copolymers with the right set of intrinsic properties that comply with the set of tolerances set in Section 9.2 at densities beyond 1 Tb/in² have to be found within the list of materials suitable for the fabrication process. New synthetic materials may be required to meet these goals.

9.5.2 Approaches to Long-Range Orientational and Translational Order in Block Copolymer Templates

Orientalional order in block copolymer patterns can be achieved by various techniques such as graphoepitaxy [76, 77], chemical pre-patterning [78, 79], electric fields [80], thermal gradients, and shear [81]. However, a suitable combination of both orientational and translational ordering plus feature registration can only be achieved, at present, by graphoepitaxy or by chemical pre-patterning.

For a patterned media application, a chemical pre-patterning technique [41] may prove a better candidate to a more efficient use of available area while providing a stronger influence to minimize defect formation in the assembled pattern. Chemical pre-patterning does not come at expense of storage area (as opposed to graphoepitaxy) and can provide uniform guiding for the self-assembled pattern. To justify the additional effort required for self-assembly compared to direct lithographic pattern-

ing (e.g., e-beam alone), the self-assembled pattern must have a higher resolution or better image quality. This implies that the block copolymer film must exercise some pattern rectification action or a feature density multiplication or both.

E-beam lithography is a good candidate as a *guiding* method due to its high resolution and flexibility to design arbitrary patterns (i.e., a circularly distorted lattice). However, as discussed in Section 9.4, e-beam lithography is limited by resist resolution, proximity effects, stitching errors, placement tolerances, and speed. The current outlook for e-beam lithography seems questionable for generating high-quality patterns beyond 1 Tb/in² for patterned media applications.

A combination of e-beam lithography and block copolymer self-assembly has potential to deliver high-quality patterns beyond 1 Tb/in². E-beam lithography can be used to pre-pattern a substrate creating chemical contrast to guide the assembly of a block copolymer film as shown in Fig. 9.18. A powerful advantage of block copolymer patterns is their ability to keep a uniform size distribution regardless of the feature sizes on the pre-patterned substrate. The bit-size distribution is then limited by the block copolymer properties and not by the e-beam pattern allowing some relaxation of tolerances for the e-beam lithographic step. Placement jitter is also commonly introduced by the e-beam writing process. The ability of the self-assembly to keep a uniform lattice also helps to reduce down-track and cross-track jitter.

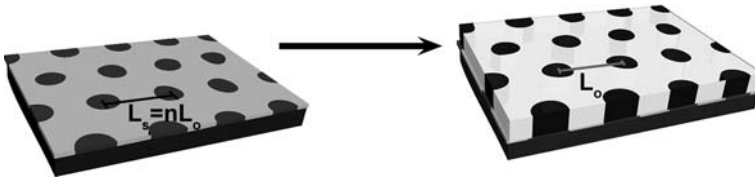


Fig. 9.18 Schematic representation of a chemical pre-patterned substrate (*left*) and a *guided* block copolymer film on *top* (*right*)

A more attractive approach to go beyond current e-beam lithography resolution consists of a substrate with a suitable surface energy chemically pre-patterned at a lower bit density than the self-assembled pattern (i.e., with a lattice constant $L_s = nL_o$, where n is an integer greater than 1). The block copolymer film can then use the pre-pattern lattice as a guiding template (analogous to heteroepitaxial film growth), effectively multiplying the feature density. One could think of using e-beam to write a pattern right at the limit of its resolution and then use self-assembly as a density multiplier beyond e-beam lithographic resolution.

Recent results on pattern rectification and density multiplication demonstrate the feasibility of this approach [41]. Figure 9.19 shows scanning electron micrographs of e-beam resist patterns written at various densities; next to them are images of block copolymer patterns assembled on the pre-patterned substrates defined by the e-beam patterns. In Fig. 9.19a,c the e-beam pattern was written at the same density as the block copolymer pattern (490 Gb/in² or $L_o = 39$ nm and 1 Tb/in² or

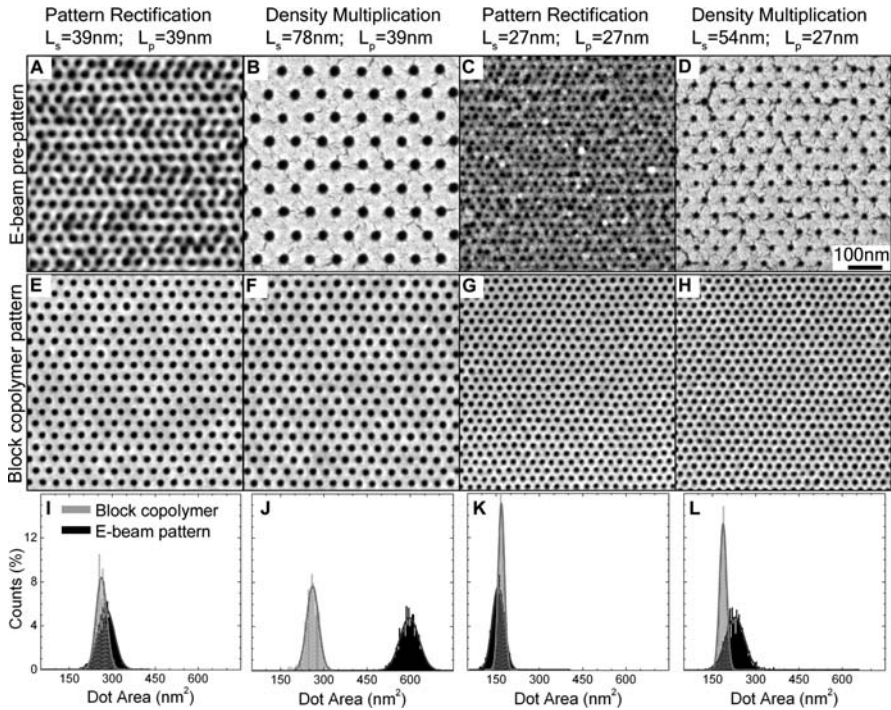


Fig. 9.19 (a–h) SEM micrographs of e-beam resist pre-patterns at densities of 490 Gb/in², 122.5 Gb/in², 1 Tb/in², and 250 Gb/in². (e–h) Block copolymer pattern on top of a pre-patterned substrate defined by the mask above. (a) and (e) show the effects of pattern rectification while (f) and (h) show density multiplication by a factor of four. (i–l) are plots of the dot-size distribution for e-beam resist patterns (*black*) and block copolymer patterns (*gray*). (Figure reproduced from reference [41])

$L_o = 27$ nm respectively); the block copolymer in Fig. 9.19 e,g effectively rectifies dot-size distribution and placement jitter. In Fig. 9.19b,d e-beam patterns were written at a quarter of the density 122.5 Gb/in² and 250 Gb/in², respectively, and then a suitable block copolymer was used to fill a feature every other dot to multiply the density by a factor of four to 490 Gb/in² in (f) and 1 Tb/in² in (h). Dot-size uniformity is preserved all across the block copolymer patterns, regardless of the large size variations in the e-beam pattern [see for example the large-size disparity between Fig. 9.19b,f as illustrated in plot (j)]. Directed-assembly patterns are possible with a quality that is difficult to achieve with e-beam lithography alone.

These results show that combining a high-resolution *top-down* technique (such as e-beam lithography) with a denser *bottom-up* self-assembled process may open a path to deliver densities in excess of 1 Tb/in² in compliance with requirements for bit-patterned media.

9.6 Write Synchronization

In conventional magnetic recording where the data bits are written on continuous granular media (CGM), there is no requirement to write to predetermined locations on the media since the entire surface contains magnetic material. Circular data tracks are defined by servowriting – a factory process during which spatial “servo” markers are written periodically around each track. Since these spatial markers need to survive for the life of the drive, writing of data is synchronized to the rotation of the disk and confined to certain timing windows which avoid overwriting the servo marks. Synchronization on a very fine scale, however, is not needed, and due to spindle speed fluctuations and other factors, the actual location of individual magnetic transitions can have uncertainties in the range of 1 μm .

In contrast, writing bit-patterned media (BPM), as discussed in Section 9.2, requires nm-scale synchronization of the write head current waveform to the passage of individual islands under the head. This requires tight tolerance control in the fabrication of the media, the tight control of spindle speed and vibrations, and a synchronization system that can follow and correct for disturbances. This section will discuss synchronization requirements, options for implementation, and some experimental results.

9.6.1 Requirements for Write Synchronization

In Section 9.2.2, the effects of various tolerances on the write error rate are quantitatively analyzed. The results of this analysis are summarized in Eqs. (9.1) through (9.4), and specific design spaces are explored in Figs. 9.5 and 9.6. While there are opportunities to trade higher error rate $\text{BER}_{\text{write}}$, higher write-field gradient $\partial H_{\text{eff}}/\partial x$, or tighter sigmas in one area (e.g., fabrication tolerance σ_{print} or magnetic switching-field distribution σ_{H_s}) for a relaxation in write-synchronization tolerance σ_{sync} , a typical value of $\sigma_{\text{sync}} = 1 \text{ nm}$ can serve as a reference point in setting the design requirement for a write-synchronization system for a BPR system with bit-aspect ratio (BAR) $\chi_{\text{cell}} = 1$ at a density of 1 Tbit/in².

Head-media velocities of 40 m/s for a high-performance server-class drive and 10 m/s for a mobile drive translate $\sigma_{\text{sync}} = 1 \text{ nm}$ (4% of 25 nm island period) into temporal synchronization tolerances of 25 ps and 100 ps for server and mobile drives respectively. A guideline of $\sigma_{\text{sync}} = (\text{island period})/25$ can also be used with higher bit-aspect ratios, provided that σ_{print} , like σ_{sync} , scales with the island period.

9.6.2 Options to Achieve Write Synchronization

In the readback process for both CGM and BPM, it is important that the sampling points on the signal waveform are well synchronized to the stream of pulses generated by the head as it passes over magnetic transitions on the media. Synchronization

during readback is accomplished by a digital phase-locked loop in the timing recovery circuitry of the channel, which continuously compares the sampled readback signals with the target values and adjusts the sampling positions accordingly. However, during the write process, no synchronization is required on continuous media, other than to insure that there is no overwriting of factory-written servo or other sector header information. For successful writing in a BPR system, a write-synchronization system needs to be implemented which can meet the requirements discussed in Section 9.6.1.

One option would be to use the read sensor on a continuous basis to update the frequency and phase of the write clock, based on the readback signal. Although the read and write heads flying over the media generally have a physical separation of a few μm on the slider, the readback signal can be used to synchronize the write clock, provided there is a known frequency and phase relationship between the islands on the tracks where the read vs. write heads are located, and a known offset between the heads. A major shortcoming of this approach, however, is interference in the readback signal caused by large currents being applied to the write element and stray field generated by the write element, which can be highly detrimental to the signal-to-noise ratio (SNR) of the readback signal during writing. In drives with multiple heads, one might consider the option of using a read sensor on a head other than the active write head to achieve satisfactory SNR. Unfortunately, mechanical drift and vibration would likely prevent such a system from achieving the necessary synchronization tolerance. Another possible solution would be the use of an independent sensor (perhaps sensing by means other than magnetic field) on the slider to provide a synchronization reference with good SNR while writing [82]. However, the increased complexity and cost of adding a sensor can make this solution unattractive.

The preferred approach, which makes use of the existing read sensor, but does not require reading while writing, is the *sector synchronization* system. A sector sync system locks the write clock in frequency and phase to periodic bursts or markers in the sector headers which precede the data regions in each sector of a track. Data tracks are typically divided into hundreds of sectors, so there are many opportunities per revolution for updating the frequency and phase of the write clock. The operation of a sector sync system is analogous to the way sector servo systems are used to control the arm actuator in conventional drives to maintain proper centering of the head over a track while reading and writing.

9.6.3 Timing Variations Observed in a Conventional Drive

In order for a sector sync system to successfully meet the synchronization requirements, it is essential that the variations in phase of the passage of islands under the write head during a sector (i.e., between updates of the write clock) be either small enough or sufficiently predictable so that the system can “coast” through a sector with no further synchronization information until the arrival of the next sector header. There are several sources of phase fluctuations, including spindle motor

speed variation, write clock frequency error, data track eccentricity, media fabrication tolerances, and mechanical vibrations in the head or disk. Some of these sources are repeatable or predictable and can therefore be compensated for.

Figure 9.20 shows experimental measurements in a 15 KRPM server-class drive of sector-to-sector timing accomplished by precise timing of the intervals between sector identification (SID) marks over ten revolutions. In this drive, the revolution period is 4 ms, and there are 280 equal sectors per revolution, for an average SID–SID time of 14.28 μ s. The measured sigma is 0.14 ns. However, as can be seen in the figure, some of the variation is repeatable or predictable and can therefore be compensated using appropriate feed-forward methods.

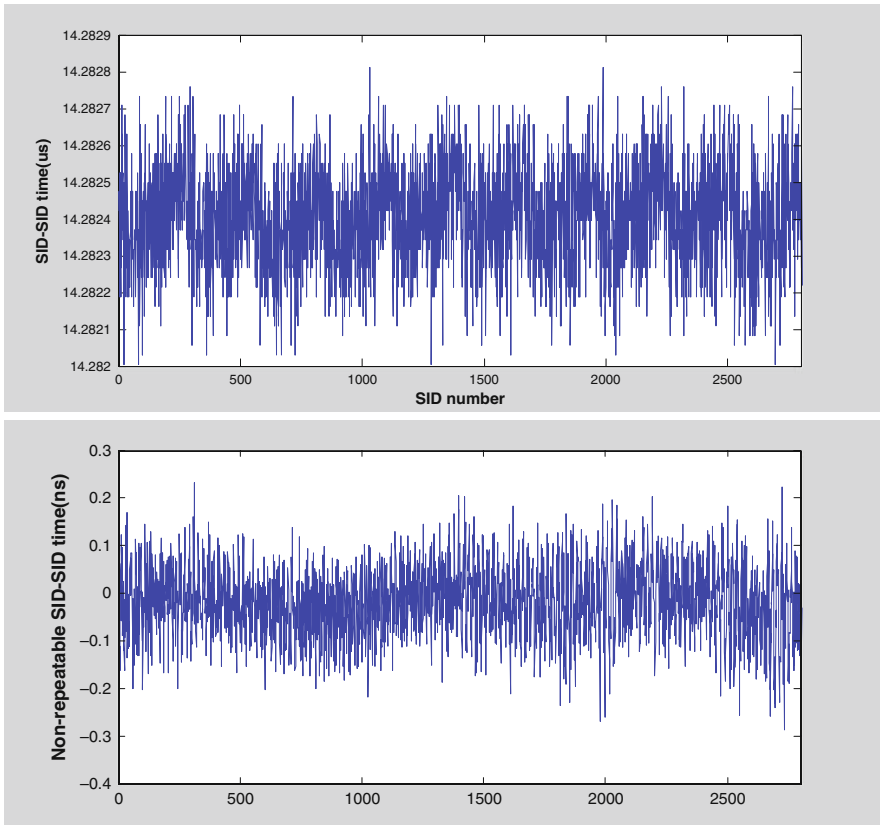


Fig. 9.20 Measurements of sector-to-sector time intervals over ten revolutions of a 15 KRPM server-class drive (*top*). Removal of repeatable- and low-frequency variations (*bottom*) reveals that the residual nonrepeatable and noncorrectable component of the variation has a sigma of 71 ps

If the repeatable and low frequency variation is removed (to simulate the effects of feed-forward correction), the remaining nonrepeatable component of the timing variation has a much tighter distribution, with a sigma of 71 ps.

In this drive, the observed sigma of 71 ps exceeds the 25 ps target mentioned in Section 9.6.1 by nearly a factor of three. Unless it is possible to tighten this sigma, other system improvements would be needed, such as higher write-field gradient or tighter media switching-field distribution. Another alternative would be to design the recording system with error correction capability capable of handling a relaxed write error rate. Improving the timing sigma may be possible by reducing mechanical disturbances or inserting more frequent updates via an increased number of synchronization marks per revolution.

Measurements of sector timing variations were also performed on a mobile drive. Because of lower overall speed, lower spindle inertia, and a less sophisticated spindle controller, this drive had a sigma of 310 ps for the nonrepeatable and nonpredictable components of the sector-timing variation. This sigma is also about a factor of 3 higher than what is needed for the design guidelines discussed in Section 9.6.1.

9.6.4 Implementation of a Sector Synchronization System

A sector synchronization system adjusts not only the phase of the write clock but also the frequency on a sector-by-sector basis. A frequency error in the write clock results in an integrated phase error over the length of a sector. For a sector of N islands, the timing error will be equal to $N(T-T_0)$, where T is the period of the write clock, and T_0 is the correct target period. If frequency error were the only contributor to timing error in the sector sync system, the constraint on frequency accuracy would be given by $(T-T_0)/T_0 < \varepsilon/N$, where ε is the maximum allowed phase error expressed as a fraction of the island period. For the example discussed in Section 9.6.1, in which $\varepsilon = 4\%$ and assuming $N = 4500$ islands (typical for a 512 byte data sector plus overhead), this would translate to a frequency accuracy requirement of 8.9×10^{-6} . In reality, the frequency accuracy should be significantly better than this, since errors in setting the absolute phase of the write clock (due to jitter in detecting the absolute position of a sync mark) subtract from the allowance for frequency error.

Write synchronization has been demonstrated experimentally using a spin stand outfitted with a read/write channel having specialized write clock synchronization functions. The channel used in these experiments has the ability to trigger on a unique trigger pattern read from the media and to adjust the phase of the write clock and the timing of the write gate by a programmable shift relative to the trigger, with a resolution of 1/64 cycle.

Experiments were performed on bit-patterned media with a bit period of 80 nm and a media velocity of 16 m/s. The frequency of the write clock in these experiments was manually adjusted to match the observed island frequency to better than one part in 100,000, and the length of the written sector was about 3000 islands.

The effects of shifting the phase of the write clock relative to a trigger pattern on the media can be observed in Fig. 9.21. The write clock phase was shifted by a total of 160 nm (two island periods) in 25 steps. The pattern being written was a simple square wave, with a period equal to two island periods, such that a sequence of alternating polarity islands is written if the write clock is properly synchronized

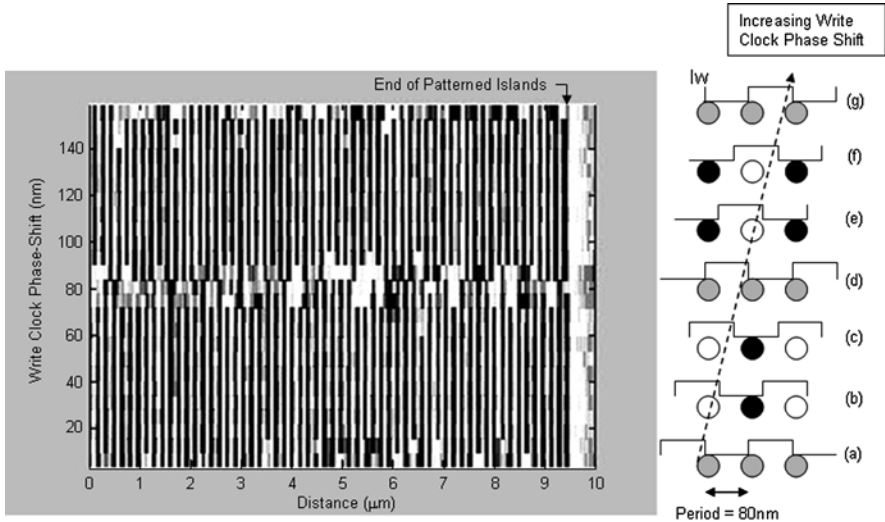


Fig. 9.21 Plot of readback signal (white/positive = maximum + amplitude; black = negative -) along a row of 118 patterned islands (9.44 μm long) with 80 nm island period. The 160 nm period square wave pattern was written and read 25 times, with the first readback trace shown at the bottom of the figure. Write clock phase is advanced slightly for each subsequent write, such that the phase advances by 160 nm over 25 writes. Diagrams to the right illustrate the effects of shifting the phase. (a) The first track is written with current switching occurring nearly at the moment the edge of the write bubble passes through the centers of the islands, resulting in uncertain outcome for each island. As phase advances, writing is sufficiently well synchronized over a broad phase window for (b) and (c) such that there are few or no errors, as is evident from the properly alternating polarity seen in the readback signal. Once the phase has advanced 80 nm (d), synchronization is again unfavorable, and the pattern is not properly written. In (e) and (f), phase has advanced by a full island period, resulting in well-defined writing, but with opposite polarity (note black areas in lower half of plot line up with white areas in upper half). Finally, after the phase advances 160 nm (g), synchronization is again unfavorable

to the passage of islands under the head. In the figure, the starting phase has poor synchronization, with the result that a number of islands have incorrect polarity. As the phase is progressively shifted, it can be observed that there is a wide phase window in which no writing errors occur. After a total shift of ~ 80 nm, synchronization is again poor, reproducing the effects seen for the initial phase. Over the next 80 nm of phase shift, the writing behaves in a manner similar to what was observed in the first 80 nm of shift, with one important distinction – the islands are written with opposite polarity, as would be expected for shifting the write waveform by a single island period.

In the above experiment, the frequency of the write clock was fixed, and only the phase was automatically adjusted to register with the synchronization mark as read by the read element of the head. In a drive, where full tracks (many sequential sectors) are written, both frequency and phase need to be adjusted on a

sector-by-sector basis. Frequency can be updated by means of computations based on precise time interval measurement between SIDs.

Proper operation of a sector sync system requires that sync marks (trigger patterns for setting the phase of the write clock) exist within sector headers. Sync marks may consist of specially patterned islands (with a sequence of sizes and shapes that are different than regular data islands), or they may consist of a unique magnetic pattern recorded on regular data islands. The simplest case is to lithographically form special island shapes during the fabrication of the disk, and use them in a DC magnetized (single polarity of magnetization) state. In this case, signal is derived from the contrast seen by the read head between magnetized islands and the spaces between them.

An alternative [83] is to use a sync pattern with bipolar magnetization (either with or without unique island shapes). This approach results in higher readback signal amplitude, since the contrast is derived from islands of opposite magnetization. Amplitude for bipolar patterns can be more than two times larger than for unipolar patterns, resulting in better signal-to-noise ratio, which allows the use of shorter patterns that consume less media real estate. A disadvantage of bipolar patterns is that a magnetic formatting operation (similar to servowriting) is necessary to polarize, or “format,” the sync patterns.

Since the read and write elements on the head in a drive are physically separated by a few μm , and this offset varies from head to head within the manufacturing tolerances, a calibration procedure is needed to establish the correct phase offsets needed between the phase of the sync mark as observed by the read element and the phase of the write clock to be used by the write head. One way of determining such offsets is to perform a series of writes as shown in Fig. 9.2 to find the optimal phase offset.

A complete sector sync system combines all of the above – phase locking of the write clock to sync marks, adjustment of the frequency of the write clock based on SID–SID time interval measurement, and compensation for read–write offset and skew angle – to keep the write clock well synchronized to the passage of islands under the write pole of the head. Stringent control of fabrication tolerances, precise calibration and measurements of applicable parameters, minimization of velocity disturbances, and providing sufficiently frequent sync marks are all necessary to keep the synchronization tolerance σ_{sync} within the range needed to achieve the target write error rate for the recording system.

Although there are many other factors that affect the error rate of a bit-patterned media recording system, write synchronization stands out as a new challenge facing the system designer – a challenge not seen in conventional granular media recording.

9.7 Conclusion

Bit-patterned magnetic recording shows promise as a route to recording densities beyond 1 Tbit/in² with adequate thermal stability and writability. Theoretical analysis and micromagnetic modeling of the behavior of BPM during the write process

reveal a number of stringent requirements to achieve sufficient addressability – the ability to reliably write a specific island without affecting the state of its neighbors. In addition to the need for sufficient write head field strength and write-field gradient, a number of media fabrication challenges become apparent. These challenges include cost-effective fabrication of trillions of nm-scale magnetic islands on a disk, with nm-scale physical uniformity, and tight control of magnetic properties. Media fabrication will likely draw on some of the most advanced and recently developed techniques available, including guided self-assembly for master pattern generation, and low cost replication of patterns – with nm-scale fidelity – using nanoimprint lithography. Magnetic materials need to be deposited and formed into islands with stringent control over film quality and magnetic uniformity. Innovative approaches such as the use of exchange-spring layers for writability, laminated media for tight SFD, and trench poisoning for trench noise control may be required.

Integration of bit-patterned media into a functional recording system also presents unique requirements and drives innovation. Synchronized writing, which is required for achieving acceptable error rates, requires that the write clock be phase- and frequency-locked to the passage of individual islands under the write head. A sector synchronization approach appears to be a likely candidate for successful implementation of such a system.

The rate of progress in providing solutions to these challenges will dictate whether BPR succeeds as the next major step in magnetic recording technology, or whether competing technologies such as thermally assisted recording succeed instead. Further into the future, some combination of features from these and other new technologies may be needed in the regime around 10 Tbit/in² and beyond.

References

1. Richter, H.J., *Recent advances in the recording physics of thin-film media*. Journal of Physics D-Applied Physics, 1999. **32**(21): R147–R168.
2. Moser, A., et al., *Magnetic recording: advancing into the future*. Journal of Physics D-Applied Physics, 2002. **35**(19): R157–R167.
3. Seagate. in *presented at Idema Discon, Sept 2006*.
4. Mao, S. *from Westen Digital presented at PMRC 2007, Tokyo Japan*.
5. Shen, X., et al., *Issues in recording exchange coupled composite media*. IEEE Transactions on Magnetics, 2007. **43**(2): 676–681.
6. Miles, J.J., et al., *Parametric optimization for terabit perpendicular recording*. IEEE Transactions on Magnetics, 2003. **39**(4) (IEEE Transactions on Magnetics): 1876–1890.
7. Gao, K.Z. and H.N. Bertraum, *Magnetic recording configuration for densities beyond 1 Tb/in(2) and data rates beyond 1 Gb/s*. IEEE Transactions on Magnetics, 2002. **38**(6): 3675–3683.
8. Richter, H.J., *The transition from longitudinal to perpendicular recording*. Journal of Physics D-Applied Physics, 2007. **40**(9): R149–R177.
9. McDaniel, T.W., *Ultimate limits to thermally assisted magnetic recording*. Journal of Physics-Condensed Matter, 2005. **17**(7): R315–R332.
10. Zhu, J.G., X.C. Zhu, and Y.H. Tang, *Microwave assisted magnetic recording*. IEEE Transactions on Magnetics, 2008. **44**(1): 125–131.

11. Chou, S.Y., P.R. Krauss, and L.S. Kong, *Nanolithographically defined magnetic structures and quantum magnetic disk*. Journal of Applied Physics, 1996. **79**(8): 6101–6106.
12. New, R.M.H., R.F.W. Pease, and R.L. White, *Lithographically patterned single-domain cobalt islands for high-density magnetic recording*. Journal of Magnetism and Magnetic Materials, 1996. **155**(1–3): 140–145.
13. Terris, B.D. and T. Thomson, *Nanofabricated and Self-Assembled Magnetic Structures as Data Storage Media*. Journal of physics D: Applied physics, 2005. **38**: R199–222.
14. Schabes, M.E., *Micromagnetic Simulations for Tb/in2 recording systems*. Journal of Magnetism and Magnetic Materials, 2008. **320**(22): 2880–2884.
15. Richter, H.J., et al., *Recording on bit-patterned media at densities of 1 Tb/in(2) and beyond*. IEEE Transactions on Magnetics, 2006. **42**(10): 2255–2260.
16. Hu, J., et al., *Bit-patterned media with written-in errors: Modeling, detection, and theoretical limits*. IEEE Transactions on Magnetics, 2007. **43**(8): 3517–3524.
17. Kish, L.B. and P.M. Ajayan, *TerraByte flash memory with carbon nanotubes*. Applied Physics Letters, 2005. **86**: 093106.
18. Albrecht, M., et al., *Magnetic dot arrays with multiple storage layers*. Journal of Applied Physics, 2005. **97**(10): 103910.
19. Baltz, V., et al., *Multilevel magnetic media in continuous and patterned films with out-of-plane magnetization*. Journal of Magnetism and Magnetic Materials, 2005. **290**: 1286–1289.
20. Bertram, H.N. and M. Williams, *SNR and density limit estimates: A comparison of longitudinal and perpendicular recording*. IEEE Transactions on Magnetics, 2000. **36**(1): 4–9.
21. Weller, D., et al., *High K-u materials approach to 100 Gbits/in(2)*. IEEE Transactions on Magnetics, 2000. **36**(1): 10–15.
22. Klemmer, T.J., et al., *Structural studies of LI(0) FePt nanoparticles*. Applied Physics Letters, 2002. **81**(12): 2220–2222.
23. Suess, D., *Multilayer exchange spring media for magnetic recording*. Applied Physics Letters, 2006. **89**(18): 113105; 189901.
24. Albrecht, M., et al., *Writing of high-density patterned perpendicular media with a conventional longitudinal recording head*. Applied Physics Letters, 2002. **80**(18): 3409–3411.
25. Schabes, M.E. *The write process and thermal stability in bit patterned recording media*. in *10th Joint MMM/Intermag Conference*. 2007. Baltimore, MD.
26. Schrefl, T. 2007, Private communication.
27. Ise, K., et al., *New shielded single-pole head with planar structure*. IEEE Transactions on Magnetics, 2006. **42**(10): 2422–2424.
28. McDaniel, T.W., W.A. Challener, and K. Sendur, *Issues in heat-assisted perpendicular recording*. IEEE Transactions on Magnetics, 2003. **39**(4): 1972–1979.
29. Nembach, H.T., et al., *Microwave assisted switching in a Ni81Fe19 ellipsoid*. Applied Physics Letters, 2007. **90**(6): 062503.
30. Richter, H.J., et al., *Recording potential of bit-patterned media*. Applied Physics Letters, 2006. **88**: 222512.
31. Moritz, J., et al., *Magnetization dynamics and thermal stability in patterned media*. Applied Physics Letters, 2005. **86**(6): 063512.
32. Rettner, C.T., et al., *Magnetic characterization and recording properties of patterned Co₇₀Cr₁₈Pt₁₂ perpendicular media*. IEEE Transactions on Magnetics, 2002. **38**(4): 1725–1730.
33. Thomson, T., G. Hu, and B.D. Terris, *Intrinsic Distribution of Magnetic Anisotropy in Thin Films Probed by Patterned Nanostructures*. Physical Review Letters, 2006. **96**: 257204.
34. Hu, G., et al., *Magnetization Reversal in Co/Pd Nanostructures and Films*. Journal of Applied Physics, 2005. **97**: 10J702.
35. Bardou, N., et al., *Light-Diffraction Effects in the Magneto-optical Properties of 2d Arrays of Magnetic Dots of Au/Co/Au(111) Films with Perpendicular Magnetic-Anisotropy*. Journal of Magnetism and Magnetic Materials, 1995. **148**(1–2): 293–294.
36. Hellwig, O., et al., *Separating dipolar broadening from the intrinsic switching field distribution in perpendicular patterned media*. Applied Physics Letters, 2007. **90**: 162516.

37. Shaw, J.M., et al., *Origins of switching field distributions in perpendicular magnetic nanodot arrays*. Journal of Applied Physics., 2007. **101**: 023909.
38. Tagawa, I. and Y. Nakamura, *Relationship between High-Density Recording Performance and Particle Coercivity Distribution*. IEEE Transactions on Magnetics, 1991. **27**(6): 4975–4977.
39. Berger, A., B. Lengsfeld, and Y. Ikeda, *Determination of intrinsic switching field distributions in perpendicular recording media (invited)*. Journal of Applied Physics, 2006. **99**(8): 08E705.
40. Berger, A., et al., *Delta H(M, Delta M) method for the determination of intrinsic switching field distributions in perpendicular media*. IEEE Transactions on Magnetics, 2005. **41**(10): 3178–3180.
41. Ruiz, R., et al., *Density multiplication and improved lithography by directed black copolymer assembly*, Science, 2008. **321**(5891): p. 936–939.
42. Suess, D., *Micromagnetics of exchange spring media: Optimization and limits*. Journal of Magnetism and Magnetic Materials, 2007. **308**(2): 183–197.
43. Suess, D., et al., *Optimization of exchange spring perpendicular recording media*. IEEE Transactions on Magnetics, 2005. **41**(10): 3166–3168.
44. Moser, A., et al., *Off-track margin in bit patterned media*. Applied Physics Letters, 2007. **91**: 162502.
45. Hellwig, O., et al., *Suppression of magnetic trench material in bit patterned media fabricated by blanket deposition onto pre-patterned substrates*, Applied Physics Letters, 2008. **93**: 192501.
46. *International Technology Roadmap for Semiconductors (ITRS)*, <http://www.itrs.net/home.html>. 2007.
47. *ZEP520A electron beam resist*, Zeon Chemicals, L.P.
48. Yasin, S., D.G. Hasko, and H. Ahmed, *Fabrication of < 5 nm width lines in poly (methyl-methacrylate) resist using a water : isopropyl alcohol developer and ultrasonically-assisted development*. Applied Physics Letters, 2001. **78**(18): 2760–2762.
49. Tiberio, R., *private communication*.
50. Yang, X., et al., *Challenges in 1 Teradot/ in.2 dot patterning using electron beam lithography for bit-patterned media*. The Journal of Vacuum Science and Technology, 2007. **25**(6): 2202–2209.
51. Colburn, M., et al., *Step and flash imprint lithography: a new approach to high resolution patterning*. Proceedings of SPIE, 1999. **3676**: 379.
52. Lentz, D., et al., *Whole wafer imprint patterning using step and flash imprint lithography: a manufacturing solution for sub-100-nm patterning*. Proceedings of SPIE, 2007. **6517**: 65172F.
53. Morkved, T.L., et al., *Mesoscopic self-assembly of gold islands on diblock-copolymer films*. Applied Physics Letters, 1994. **64**(4): 422–424.
54. Mansky, P., P. Chaikin, and E.L. Thomas, *Monolayer films of diblock copolymer microdomains for nanolithographic applications*. Journal of Materials Science, 1995. **30**(8): 1987–1992.
55. Park, M., et al., *Block Copolymer Lithography: Periodic Arrays of ~1011 Holes in 1?Square Centimeter*. Science, 1997. **276**(5317): 1401–1404.
56. Bates, F.S. and G.H. Fredrickson, *Block Copolymer Thermodynamics: Theory and Experiment*. Annual Review of Physical Chemistry, 1990. **41**(1): 525–557.
57. Thurn-Albrecht, T., et al., *Nanoscale templates from oriented block copolymer films*. Advanced Materials, 2000. **12**(11): 787–791.
58. Asakawa, K. and T. Hiraoka, *Nanopatterning with microdomains of block copolymers using reactive-ion etching selectivity*. Japanese Journal of Applied Physics Part 1-Regular Papers Short Notes & Review Papers, 2002. **41**(10): 6112–6118.
59. Guarini, K.W., et al., *Nanoscale patterning using self-assembled polymers for semiconductor applications*. Journal of Vacuum Science & Technology B, 2001. **19**(6): 2784–2788.
60. Cheng, J.Y., et al., *Magnetic properties of large-area particle arrays fabricated using block copolymer lithography*. IEEE Transactions on Magnetics, 2002. **38**(5): 2541–2543.
61. Naito, K., et al., *2.5-inch disk patterned media prepared by an artificially assisted self-assembling method*. IEEE Transactions on Magnetics, 2002. **38**(5): 1949–1951.

62. Park, S.-M., et al., *Directed Assembly of Lamellae-Forming Block Copolymers by Using Chemically and Topographically Patterned Substrates*. *Advanced Materials*, 2007. **19**(4): 607–611.
63. Black, C.T., et al., *Polymer self assembly in semiconductor microelectronics*. *IBM Journal of Research and Development*, 2007. **51**(5): 605–633.
64. Segalman, R.A., *Patterning with block copolymer thin films*. *Materials Science & Engineering R-Reports*, 2005. **48**(6): 191–226.
65. Lazzari, M. and M.A. Lopez-Quintela, *Block copolymers as a tool for nanomaterial fabrication*. *Advanced Materials*, 2003. **15**(19): 1583–1594.
66. Hamley, I.W., *The physics of block copolymers*. 1998, Oxford, New York, Oxford University Press. viii, 424 pp.
67. Hamley, I.W., *Nanostructure fabrication using block copolymers*. *Nanotechnology*, 2003. **14**(10): R39–R54.
68. Edwards, E.W., et al., *Precise control over molecular dimensions of block-copolymer domains using the interfacial energy of chemically nanopatterned substrates*. *Advanced Materials*, 2004. **16**(15): 1315.
69. Edwards, E.W., et al., *Dimensions and shapes of block copolymer domains assembled on lithographically defined chemically patterned substrates*. *Macromolecules*, 2007. **40**(1): 90–96.
70. Cheng, J.Y., A.M. Mayes, and C.A. Ross, *Nanostructure engineering by templated self-assembly of block copolymers*. *Nature Materials*, 2004. **3**(11): 823–828.
71. Turner, M.S., *Equilibrium Properties Of A Diblock Copolymer Lamellar Phase Confined Between Flat Plates*. *Physical Review Letters*, 1992. **69**(12): 1788–1791.
72. Walton, D.G., et al., *A Free-Energy Model For Confined Diblock Copolymers*. *Macromolecules*, 1994. **27**(21): 6225–6228.
73. Helfand, E. and Y. Tagami, *Theory of the Interface Between Immiscible Polymers*. *The Journal of Chemical Physics*, 1972. **57**(4): 1812–1813.
74. Semenov, A.N., *Contribution to the theory of microphase layering in block-copolymer melts*. *Soviet Physics – JETP*, 1985. **61**(4): 733.
75. Leibler, L., *Theory of Microphase Separation in Block Copolymers*. *Macromolecules*, 1980. **13**(6): 1602–1617.
76. Black, C.T. and O. Bezenenet, *Nanometer-scale pattern registration and alignment by directed diblock copolymer self-assembly*. *IEEE Transactions On Nanotechnology*, 2004. **3**(3): 412–415.
77. Segalman, R.A., A. Hexemer, and E.J. Kramer, *Edge Effects on the Order and Freezing of a 2D Array of Block Copolymer Spheres*. *Physical Review Letters*, 2003. **91**(19): 196101.
78. Rockford, L., et al., *Polymers on Nanoperiodic, Heterogeneous Surfaces*. *Physical Review Letters*, 1999. **82**(12): 2602.
79. Kim, S.O., et al., *Epitaxial self-assembly of block copolymers on lithographically defined nanopatterned substrates*. *Nature*, 2003. **424**(6947): 411–414.
80. Morkved, T.L., et al., *Local Control of Microdomain Orientation in Diblock Copolymer Thin Films with Electric Fields*. *Science*, 1996. **273**(5277): 931–933.
81. Angelescu, D.E., et al., *Macroscopic orientation of block copolymer cylinders in single-layer films by shearing*. *Advanced Materials*, 2004. **16**(19): 1736.
82. Rettner, C.T. and B.D. Terris US Patent 6,754,017 *Patterned media magnetic recording disk drive with timing of write pulses by sensing the patterned media*
83. Albrecht, T.R. and Z.Z. Bandic US Patent 7,236,325 *Method for formatting a magnetic recording disk with patterned nondata islands of alternating polarity*

Chapter 10

The Magnetic Microstructure of Nanostructured Materials

Rudolf Schäfer

Abstract The magnetic microstructure and magnetization processes of nanostructured materials are reviewed in a phenomenological way, mainly based on domain observation by magneto-optical Kerr microscopy. This covers nanocrystalline soft magnetic ribbons and films as well as nanostructured hard magnetic materials. For comparison also the domain structure in coarse-grained material and amorphous ribbons are briefly touched to provide the frame for the nanostructured materials.

In nanocrystalline ribbons or films, the random magnetocrystalline anisotropy of the ultrafine grain structure is largely averaged out by exchange coupling. The soft magnetic properties are rather controlled by uniaxial, induced anisotropies that are uniform on a scale much larger than the exchange length. The interplay between these uniform and the random anisotropy results in a different degree of microscopic magnetization disorder which is reflected in the magnetization processes.

In high-anisotropy materials with exchange-coupled grains in the 10 nm regime (exchange-enhanced nanocrystalline permanent magnets), a highly irregular domain structure is found, consisting of immobile and high-coercive patch domains. If exchange coupling between the grains is interrupted, the so-called interaction domains are observed due to the predominance of magnetostatic interactions between the (single domain) grains.

10.1 Overview

The hysteresis loop of a ferromagnetic material is determined by the underlying magnetic microstructure, i.e., the domains and domain walls present in the material and their reaction in magnetic fields. A number of parameters determine the domain structure [1]. Magnetic anisotropy defines the so-called easy axes for the magnetization. If the surface of a specimen does not contain an easy axis (misoriented

R. Schäfer (✉)

Leibniz Institute for Solid State and Materials Research (IFW Dresden), Institute for Metallic Materials, Helmholtzstr. 20, 01069 Dresden, Germany
e-mail: r.schaefer@ifw-dresden.de

surface), more-or-less complicated domains are formed in order to decrease or avoid stray field energy. The domain character then depends on the degree of misorientation, the relative size of the anisotropy, and the thickness of the specimen. Also the microstructure of the material, noticeably the grain size D , is essential for the domain character and thus the hysteresis loop. As an example, Fig. 10.1 summarizes the grain size dependence of coercivity together with typical domain images along the curve. The whole range of structural correlation lengths is covered, starting from atomic distances in amorphous ribbons over grain sizes in the nanometer regime in so-called nanocrystalline materials up to macroscopic grain sizes in the 100- μm regime that are typical for conventional soft magnets.

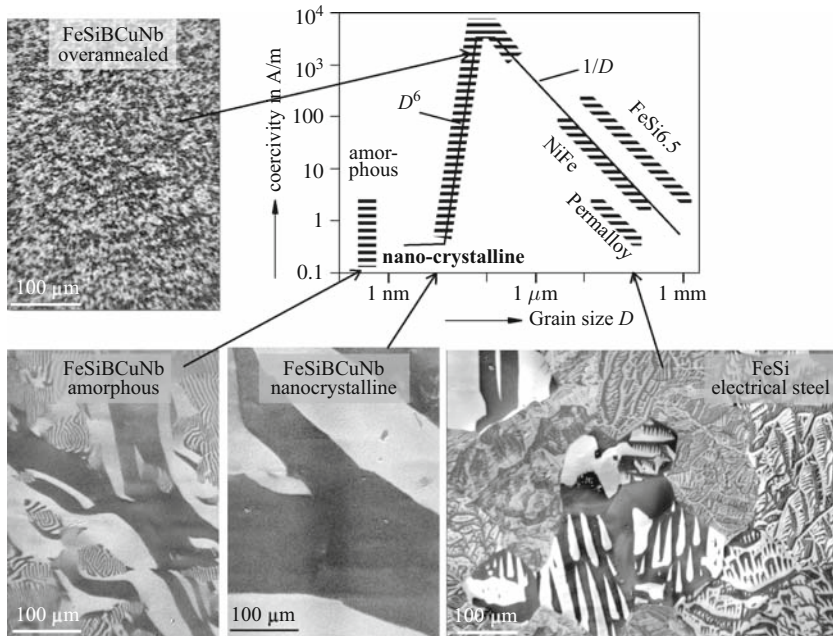


Fig. 10.1 Coercivity versus grain size (schematically, after [2]) for a number of materials, together with typical domain images observed by Kerr microscopy in the indicated materials

In coarse-grained material, the domain character is (mainly) determined by the surface orientation of the individual grains. The rising influence of grain boundary domains with decreasing grain size contributes to the characteristic $1/D$ dependence of coercivity. Maximum coercivity along this line is found when the particle size is reduced to the 100-nm regime which corresponds to the domain wall width depending on the size of anisotropy present. The coercivity maximum can be applied for hard magnets. Immobile, patchy domains are characteristic for this regime. With further decreasing grain size, coercivity drastically falls of with D^6 , leading to extremely soft magnetic nanocrystalline and finally amorphous materials. In nanocrystalline magnets, the random magnetocrystalline anisotropy of the grains

is fluctuating on a scale much smaller than the domain wall width and is therefore averaged out by the smoothing action of exchange interaction. Amorphous materials can be discussed along the same line. The very low-effective anisotropy in the two material classes is the prerequisite for their good soft magnetic properties. Nevertheless, there are residual anisotropies in both, nanocrystalline and amorphous materials, that are responsible for the domain character. By annealing in a magnetic field these anisotropies can be controlled to tailor hysteresis curves or power losses.

In this chapter, the magnetic microstructure of nanostructured materials is reviewed in a phenomenological way, mainly based on domain observation by magneto-optical Kerr microscopy. This covers nanocrystalline soft magnetic ribbons and films as well as nanostructured hard magnetic materials. “Nanostructures” in the sense of patterned films are not discussed. At the beginning, the domain structure in coarse-grained material and amorphous ribbons are briefly touched. These two classes form the border lines to the nanostructured materials in the sense of Fig. 10.1 and the comparison with these material is helpful to understand the peculiarities of domains in the nanocrystalline cases.

10.2 Coarse-Grained Material and Amorphous Ribbons

The grain orientation determines the domain character in coarse-grained material. As an example, Fig. 10.2a gives an impression of the huge variety of domains on the surface of non-oriented silicon iron material (Fe 3 wt% Si) commonly used in rotating electrical machines. Like in pure iron, the (1 0 0) directions are easy axes also for this alloy. Domain complexity depends on crystal orientation. Domains in an ideal Goss-grain [i.e. 1 1 0 surface, grain A] or slightly misoriented Goss-grain (grain B) are well known [1] and can be readily identified. In the (1 0 0)-oriented grain (C), a simple four-phase surface pattern is found according to the two surface-parallel easy axes. A slightly misoriented (1 0 0) surface (grain D) shows fir-tree domains – a supplementary pattern that distributes the perpendicular flux between neighboring basic domains by shallow surface domains as sketched in Fig. 10.2b. With stronger misorientation, the supplementary domain system becomes increasingly complicated (grain E), and above a critical misorientation branched domain patterns take over (grain F) which culminates in the most complex pattern of an extremely misoriented grain with (1 1 1) surface (grain G). The beauty and complexity of domains in strongly misoriented grains are emphasized in the high-resolution Kerr images of Fig. 10.2c.

Figure 10.3, which was obtained by metallographic domain analysis [3], gives an impression of the variation of domains toward the volume of a crystallite with extremely misoriented surface. On a crystal with (1 1 1) surface, the two requirements of using only easy directions and avoiding stray fields are incompatible [1]. A compromise is found by domain branching: toward the surface, the pattern is refined in several generations of easy-axis domains, so that the hard-axis closure

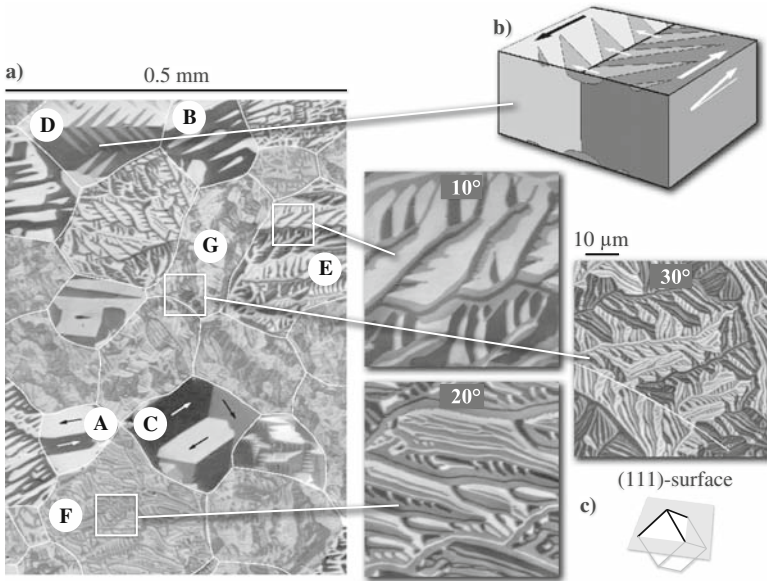


Fig. 10.2 (a) The domains on the surface of non-oriented silicon iron electrical steel (thickness 0.5 mm) depend on the orientation of the crystallites. The sketch of the fir-tree pattern (b – taken from [1]) illustrates the mechanism of supplementary domains observed on slightly misoriented surfaces. Patterns of selected grains with increasing misorientation are enlarged in (c)

domains (necessary to completely avoid stray fields) are getting as small as possible, being restricted to the outermost surface. Far away from the surface the domains stay wide to save wall energy. The branching process connects the wide and narrow domains. The wide volume domains are responsible for the permeability in such material, whereas the surface domains and their complex reorganization during a magnetization cycle are contributing to unavoidable energy loss.

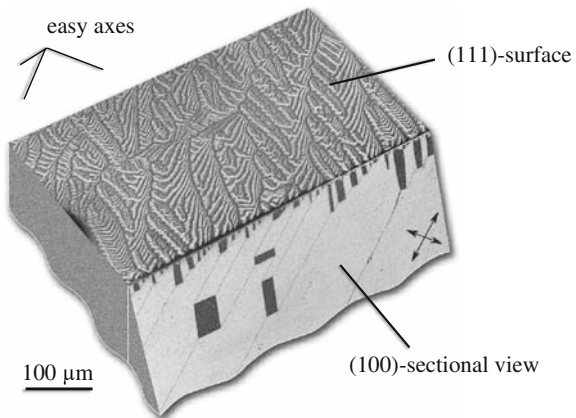


Fig. 10.3 (1 1 1)-surface and (1 0 0) cross section of a 1-mm thick high-silicon iron crystal of composition Fe 6.5 wt% Si. The domains were “frozen-in” as precipitation pattern during annealing at 580 °C, allowing to cut the sample without generating new domains (Reprinted with permission from Schäfer and Schinnerling [3])

In polycrystalline material the orientation of the free surface is important. Even if there might be grains for which this surface is well oriented, there can be inner grain boundaries that are strongly misoriented, consequently dominating the domain pattern in the whole grain. Of importance for the grain size dependence of coercivity are the domains around grain boundaries, which are created to avoid, or at least reduce, magnetic poles that might arise at a grain boundary due to the different crystallographic orientation of neighboring grains. Examples of such domains are shown in Fig. 10.4. They typically extend by 50 – 100 μm around a boundary. The requirement of stray field reduction causes a “stiffening” of the grain boundary domains in small external magnetic fields. Above a field threshold, however, these domains are destroyed and new domains are formed (Fig. 10.4d–f) during the magnetization process in order to allow flux guidance across the grain boundary while at the same time keeping the pole density and stray field energy low again. The rearrangement of domains costs energy and therefore contributes to coercivity. With decreasing grain size, the relative volume of the grain boundary domains increases, consequently leading to a rise in coercivity as seen in Fig. 10.1. Of course also the pinning of domain walls at grain boundaries contributes to this effect.

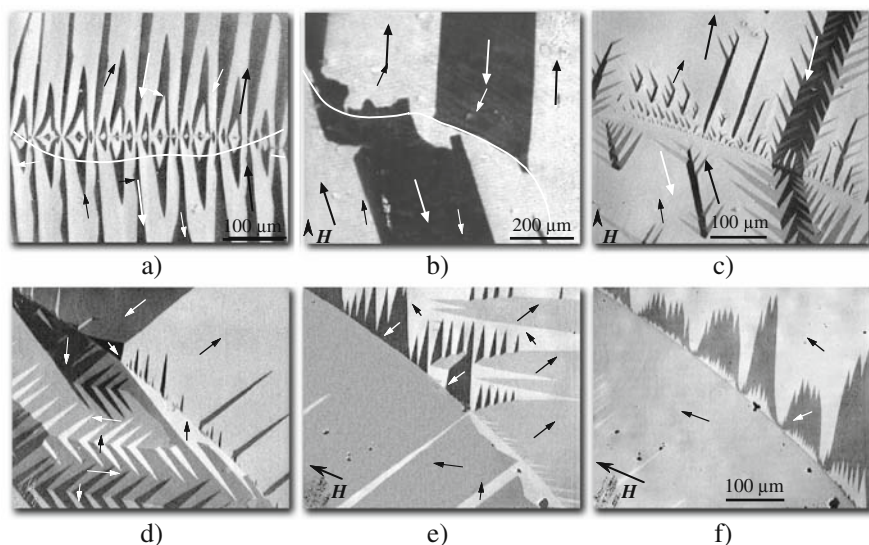


Fig. 10.4 Grain boundary domains in (a) NiFe material (55% Ni), (b) FeSi Goss-textured sheet, and (c) FeSi cube-textured material. The magnetization process with increasing magnetic field, observed in cube-textured FeSi material (d–f), demonstrates the disappearance and creation of new domains at a grain boundary (after [1])

The other extreme in Fig. 10.1 in terms of coercivity are amorphous ribbons. Here the structural correlation length is of the order of atomic distances. Amorphous alloys typically consist of 80% iron, cobalt, or nickel and 20% metalloids like silicon or boron. They are quenched from the melt with a thickness around 20 μm . Magnetocrystalline anisotropy is absent in metallic glasses by definition. Nevertheless,

regular domains do exist in such ribbons, caused by residual anisotropies. The main source of anisotropy is internal stress, frozen in by the rapid quenching process. The magnetization is coupled to the stress by the magnetostriction constant, so that the domain complexity in as-quenched ribbons depends on magnetostriction as shown in Fig. 10.5. Two types of domains are typical: wide-curved domains that follow a varying in-plane easy axis (caused by dominating tensile stress for positive magnetostriction constant) and narrow fingerprint-domains. The fingerprints are closure domains of underlying perpendicular domains, caused by planar compressive stress which induces an easy axis perpendicular to the surface. Even magnetostriction-free metallic glasses show regular (but wide) domains in the as-quenched state (Fig. 10.5d). They are often aligned along the ribbon axis, caused by magnetization-induced anisotropy. Magnetization-induced anisotropy is based on minute deviations from random pair orientations of the atomic components of the material and is induced by the magnetization pattern present during cooling through the Curie point. The easy axis thus follows the magnetization direction present during quenching, which is along the ribbon axis for magnetostatic reasons. Such induced anisotropies are also present in magnetostrictive materials where it is difficult to separate them from stress-induced contributions. Residual anisotropies may also be caused by the flow pattern during quenching, by the surface structure of the ribbons (due to, for example, air bubbles on the wheel side) and by mechanical creep due to different quenching speed at different ribbon locations. For the large variety of domains possible we refer to reviews in [1] and [4].

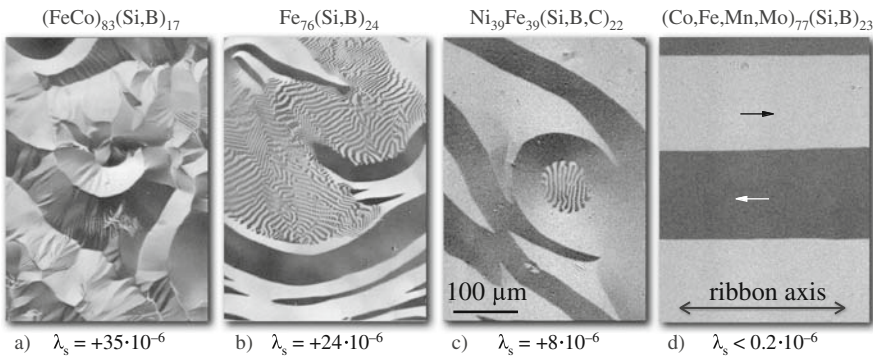


Fig. 10.5 Typical zero-field domain patterns in 20- μm thick amorphous ribbons of different compositions and thus magnetostriction constants λ_s as indicated (Reprinted with permission from Schäfer [4])

Controlling anisotropy in metallic glasses is possible. Frozen-in stress can be relaxed by more than 95% by carefully annealing below the crystallization temperature. In addition, annealing can be performed in uniform magnetic fields below the Curie temperature which leads to a well-defined uniaxial, magnetization-induced (often called field-induced) anisotropy by the same mechanism as discussed before. Annealing under external mechanical load creates creep-induced anisotropy, a basi-

cally planar anisotropy with an easy plane perpendicular to the creep direction. By demagnetizing effects, the in-plane direction transverse to the applied stress axis is favored, so that effectively a transverse uniaxial anisotropy is created in creep-annealed ribbons. A variety of ordered domain states are possible by such annealing treatments [1], allowing to tailor magnetization curves for specific applications. For instance, the transverse domains shown in Fig. 10.6 are essentially magnetized by rotation in fields along the ribbon axis, causing a linear hysteresis curve with only minor domain rearrangement processes. Losses are correspondingly low.

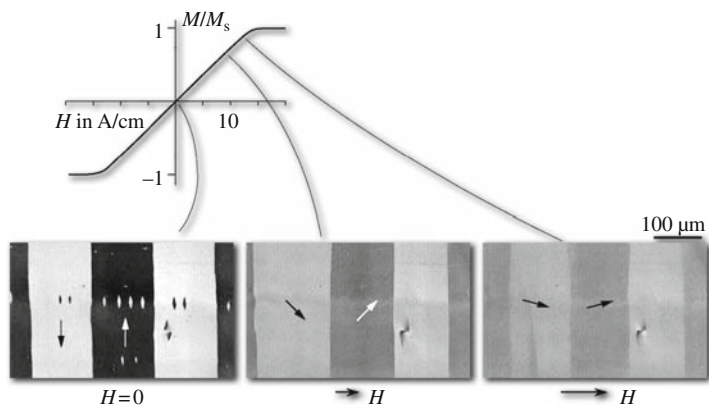


Fig. 10.6 Rotational magnetization process in magnetostriction-free CoFeSiB amorphous ribbon with an induced anisotropy axis that was created by annealing in a magnetic field transverse to the ribbon axis, together with its f -shaped magnetization curve (after [1])

In summary, the domain character in polycrystalline materials with “macroscopic” grain size is determined by magnetocrystalline anisotropy, which is often orders of magnitude larger than any induced anisotropy. Each individual grain has its own domain structure, the character of which is determined by the orientation of grain surface and grain boundaries relative to the orientation of the easy anisotropy axes. The increasing influence of grain boundary pinning and grain boundary domains with decreasing grain size D leads to an increase in coercivity and thus decrease of permeability. The conventional rule that good soft magnetic properties require very large grains is reflected in the $1/D$ dependence of coercivity (Fig. 10.1). The extremely good soft magnetic properties of amorphous material, on the other hand, are due to the relatively small anisotropies and the absence of grain boundaries in this material class. The magnetic domains in amorphous ribbons are determined by these residual anisotropies that can be controlled by magnetic field annealing thus allowing a convenient tailoring of hysteresis loops. In the following chapter, it is discussed what happens if the structural correlation length approaches the nanometer regime, still being on the low-coercivity side of Fig. 10.1 before the onset of the D^6 law.

10.3 Domains in Nanocrystalline Ribbons

The most prominent nanocrystalline soft magnet is the FeCuNbSiB ribbon, introduced by Yoshizawa et al. [5] in 1988. Alloys around the composition $\text{Fe}_{bal}\text{Si}_{12-16}\text{B}_{6-9}\text{Cu}_{0.5-1}\text{Nb}_{2-3}$ are produced as amorphous ribbons by rapid quenching, being then transformed in the nanocrystalline state by subsequent annealing between 500 and 600°C. These nanocrystalline ribbons reveal a homogeneous ultrafine grain structure of bcc Fe_{~80}Si_{~20} grains with typical sizes of 10–15 nm and random orientation, embedded in a residual amorphous minority matrix that separates the crystallites by 1–2 nm (Fig. 10.7). In this microstructure, the anisotropy axes randomly vary their orientation on a scale much smaller than the domain wall width. Exchange interaction therefore impedes the magnetization to follow the local easy axes of the individual grains – the nanocrystalline anisotropy is largely washed out and the total effective anisotropy is strongly reduced compared to the crystal anisotropy. The degree to which the crystal anisotropy of the nano-grains is averaged out is described by the *random anisotropy model*, which was originally developed for the description of amorphous ferromagnets by Alben et al. [6] and then transferred to nanocrystalline material by Herzer [7–10]. The very low-effective anisotropy, together with a vanishing magnetostriction (achieved by the balance of magnetostriction among the structural phases in the nanocrystalline state), makes nanocrystalline material (almost) ideal soft magnetic with coercivities of less than 1 A/m and high initial permeabilities of up to 10^5 . Such values are otherwise only achieved in permalloys (NiFe alloys) or Co-based amorphous alloys. Compared to these materials, the nanocrystalline ribbons have a much higher saturation magnetization of up to 1.3 T. For a recent and comprehensive review on this novel and important class of soft magnetic material we refer to Herzer [11].

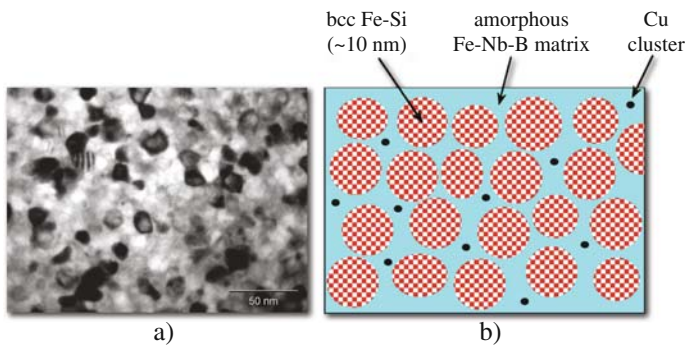


Fig. 10.7 (a) Microstructure of a $\text{Fe}_{73}\text{Si}_{16}\text{B}_7\text{Cu}_1\text{Nb}_3$ nanocrystalline ribbon observed by transmission electron microscopy (courtesy *S. Flohrer* and *C. Mickel*), and (b) schematics of the microstructure

Despite their very low anisotropy, *regular* magnetic domains are observed in nanocrystalline ribbons as shown in the corresponding image of Fig. 10.1. Observed

at low resolution, the domains resemble those in amorphous ribbons [12] and – like in amorphous ribbons – they are determined by residual anisotropies (like field- or creep-induced anisotropy) that are uniform on a macroscopic scale. Imaged at higher resolution, however, there are significant differences to amorphous material (Fig. 10.8). Depending on the relative size of random and induced anisotropies, the domain magnetization can more or less fluctuate on a microscopic scale, which has significant impact on the magnetization process, domain dynamics, and consequently loss. Before returning to these specific features, the basics of the random anisotropy model are reviewed in the following section.

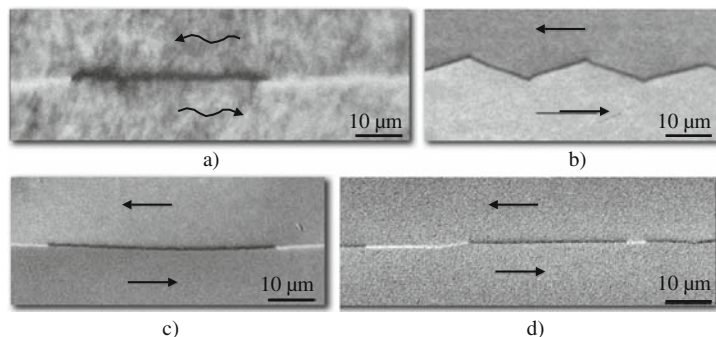


Fig. 10.8 High-resolution observations on (a) $\text{Fe}_{73}\text{Cu}_1\text{Nb}_3\text{Si}_{16}\text{B}_7$ nanocrystalline ribbon with low induced anisotropy of 3 J/m^3 and (b) the same material with a strong creep-induced anisotropy of about 30 J/m^3 (see reference [1] for an explanation of the zigzag walls). For comparison, an FeSiB amorphous ribbon (c) and a Fe 3 wt% Si sheet in Goss orientation (d) are shown. A strong patchy modulation of magnetization is observed in the low-anisotropy nanocrystalline material that is absent in the other materials

10.3.1 Random Anisotropy Model

The basic concept of the random anisotropy model is illustrated in Fig. 10.9. Consider a microstructure in which (for simplicity) a uniaxial magnetocrystalline anisotropy axis is assumed that randomly varies its orientation over the scale of the grain size (Fig. 10.9a). The anisotropy of the grains is given by the first-order anisotropy constant K_{c1} . From grain to grain, the magnetization cannot immediately adapt to the local anisotropy axes due to the stiffness effect of exchange interaction that basically favors a homogeneous magnetization. The expense of exchange energy rather requires a certain transition width for the magnetization till it can follow the anisotropy axes of a neighboring grain. A well-known example for this effect is the continuous transition between two antiparallel domains, the 180° Bloch wall. In a material with uniaxial anisotropy the width of a Bloch wall is given by $\pi\sqrt{A/K_u}$, where A is the exchange stiffness constant (dimension J/m) and K_u is the anisotropy constant (dimension J/m^3).

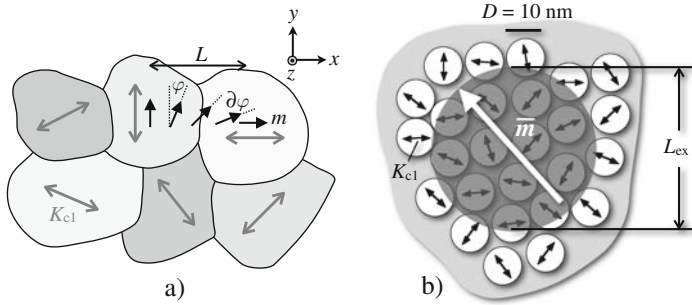


Fig. 10.9. (a) Assembly of grains, each of them having a randomly fluctuating anisotropy axis as indicated by the *double arrows*. (b) Visualization of the correlation volume of size L_{ex} in nanocrystalline material consisting of grains that are imbedded in an ideally soft magnetic matrix. Within the correlation volume, the orientation m of the magnetization is constant

The exchange stiffness energy is given by [1]

$$E_{ex} = A \int (\mathbf{grad} \mathbf{m})^2 dV. \quad (10.1)$$

For a quantitative estimate, consider two grains with a relative orientation of their anisotropy axes of 90° as depicted in Fig. 10.9a. The magnetization shall adapt to the local anisotropy axes over a distance L . For this one-dimensional case with $\varphi = kx$, $m_1 = \sin \varphi$, $m_2 = \cos \varphi$, $m_3 = 0$, the integrand of equation (10.1) writes as $(\mathbf{grad} \mathbf{m})^2 = (\partial m_1 / \partial x)^2 + (\partial m_1 / \partial y)^2 + (\partial m_1 / \partial z)^2 + \dots + (\partial m_3 / \partial z)^2 = k^2$. With $\partial \varphi / \partial x = k$, the stiffness energy (volume) density is expressed as

$$e_{ex} = A(\mathbf{grad} \mathbf{m})^2 = A(\partial \varphi / \partial x)^2. \quad (10.2)$$

If L is 1 mm, the stiffness energy density amounts to $e_{ex} = A(\partial \varphi / \partial x)^2 = A[(\pi/2)/0.001 \text{ m}]^2 \approx 2.5 \cdot 10^{-5} \text{ J/m}^3$. Clearly, on this macroscopic scale the exchange energy is negligible. Microscopically, however, the situation is different. If L is 10 nm, the stiffness energy density rises by ten orders of magnitude to $e_{ex} \approx 2.5 \cdot 10^{+5} \text{ J/m}^3$. The exchange energy thus exceeds the maximum anisotropy energy that can be estimated by $e_{Ku} \approx K_{c1} \sin^2 90^\circ = 4.7 \cdot 10^4 \text{ J/m}^3$ and that arises when the magnetization deviates from the easy axis by 90° (here a uniaxial anisotropy was assumed with $K_{c1} = 4.7 \cdot 10^4 \text{ J/m}^3$ which is the value of the first-order anisotropy constant of iron that in reality exhibits a cubic anisotropy rather than a uniaxial one). Nature therefore tends to diminish the exchange energy by aligning the magnetization vectors along a common direction even though this will locally cause anisotropy energy.

The critical scale for this effect to occur can be easily derived [11]. From Eq. 10.2, it is obvious that the exchange energy density scales as A/L^2 if the magnetization changes its orientation on the length scale L . For $A/L^2 > K_{c1}$ the

exchange energy would exceed the local anisotropy energy, which is the case on a scale smaller than

$$L_0 = \sqrt{A/K_{c1}}. \quad (10.3)$$

The quantity L_0 is a basic ferromagnetic correlation length, also known as *exchange length*. Micromagnetic objects that manage to avoid stray fields (like the classical, infinitely extended Bloch wall mentioned previously) scale with L_0 . Note that K can be any anisotropy constant, not just magnetocrystalline anisotropy. It should also be noted that micromagnetic configurations that cannot avoid magnetic poles, such as magnetic vortices, scale with another characteristic length that is also called exchange length and which is given by $\sqrt{A/K_d}$, where $K_d = 2\pi M_s^2$ is the stray field energy constant in the Gaussian unit system [1]. In any case, the correlation length L_0 represents the characteristic minimum scale below which the direction of magnetization cannot vary appreciably by the smoothing action of the exchange interaction.

If the structural length (grain size D in case of the polycrystalline microstructure of Fig. 10.9a) is smaller than the magnetic correlation length L_0 , a continuous magnetization transition at the grain boundaries is not possible. Exchange coupling then rather tends to align the magnetization of a certain grain neighborhood along a common direction thus averaging out the random anisotropies of the individual grains. The preferred direction of the averaged magnetization can be determined by statistical fluctuations or by a superimposed induced anisotropy as discussed below. The typical grain size of about 10 nm in FeCuNbSiB ribbons is clearly smaller than the exchange length of 35 nm, which is calculated with $K_{c1} = 8 \text{ kJ/m}^3$ and $A = 10 \cdot 10^{-11} \text{ J/m}$ that are the typical values for FeSi (20 at%), the alloy of the nano-grains in these ribbons. Also amorphous alloys fall into the regime $L_0 > D$. Here the structural length D is on the atomic scale.

The derivation of the effective anisotropy in nanocrystalline ribbons can be found in articles by *G. Herzer* (see [2, 11] for reviews). Here just the most important results are summarized that are necessary to interpret the domain observations in this material. Let us assume a microstructure as sketched in Fig. 10.9b, consisting of exchange-coupled grains of size $D < L_0$ and volume fraction v_x with a uniaxial magnetocrystalline anisotropy K_{c1} oriented at random. When the local anisotropy K_{c1} is averaged out by exchange interaction, the scale on which the exchange-interaction dominates expands at the same time and hence the local anisotropies are averaged out even more efficiently. This results in a renormalized exchange length L_{ex} , which follows from the basic exchange length L_0 as defined by Eq. 10.3 by self-consistently substituting the average anisotropy constant $\langle K_{c1} \rangle$ for the local anisotropy constant K_{c1} :

$$L_{ex} = \sqrt{A/\langle K_{c1} \rangle}. \quad (10.4)$$

The renormalized exchange length defines the (renormalized) ferromagnetic correlation volume $V_{ex} = L_{ex}^3$ that is represented by the hatched area in Fig. 10.9b. Within

the correlation volume, the magnetization direction is kept constant by exchange interaction. Due to statistical fluctuations there will be some easiest direction for the $N = (L_{\text{ex}}/D)^3$ grains in the correlation volume. Hence, the average anisotropy, determined by the mean fluctuation amplitude of the anisotropy energy of the N grains, scales down as

$$\langle K_{\text{c1}} \rangle = v_x K_{\text{c1}} / \sqrt{N} = \sqrt{v_x} K_{\text{c1}} (D/L_{\text{ex}})^{3/2}. \quad (10.5)$$

Combining Eqs. (10.4) and (10.5) finally yields for the average anisotropy

$$\langle K_{\text{c1}} \rangle = v_x^2 K_{\text{c1}} (D/L_0)^6. \quad (10.6)$$

The variation of $\langle K_{\text{c1}} \rangle$ with the sixth power of the grain size explains the corresponding increase of coercivity shown in Fig. 10.1, as the coercivity is proportional to anisotropy. The result of Eq. (10.6), which is based on scaling arguments, is not restricted to the hitherto considered uniaxial anisotropies, but also applies to other symmetries like the cubic anisotropy of the FeSi grains in the FeCuNbSiB nanocrystalline ribbons. In this material with $D \approx L_0/3$ the local magnetocrystalline anisotropy is thus reduced from 8 kJ/m^3 by three orders of magnitude to a few Joules per cubic meter. According to Eq. (10.4), this substantial reduction of effective anisotropy results in a renormalized exchange length that expands into the micrometer regime and which is almost two orders of magnitude larger than the basic exchange length L_0 . This circumstance becomes immediately visible in the high-resolution image of Fig. 10.8a where a wall width of about $2 \mu\text{m}$ is observed, indicative of the very low-effective anisotropy of the material. For comparison, in a single crystalline FeSi transformer sheet (Fig. 10.8d) much narrower domain walls with a surface width of just 150 nm [4] are found due to the relatively high magnetocrystalline anisotropy of $\approx 4.6 \cdot 10^4 \text{ kJ/m}^3$. The patchy domain modulation visible in Fig. 10.8a is the subject of the following section.

Two further material classes, which are not nanocrystalline but where the random anisotropy effect nevertheless applies, are noteworthy. The first class is bulk nickel – iron alloys around 80%Ni. These high-permeability alloys, known as Permalloy or Mumetal, reach zeros of the first-order anisotropy constant K_{c1} (and of the magnetostriction constant) by proper adjustment of composition. The individual grains of this material thus have much smaller anisotropy levels compared to the silicon iron grains in conventional nanocrystalline materials. Therefore the exchange length is much larger than in FeSi, and the threshold for nanocrystalline behavior is shifted from the 10-nanometer to the micrometer range. The images in Fig. 10.10 prove this fact: In the coarse-grained material (a) the domains scale with the grain size, while in the fine-grained material (b) macroscopic domains extend over many grains. They are more or less homogeneously magnetized along a macroscopically preferred axis, being only modulated somehow by the local anisotropies in the grains.

The other class is bulk soft magnetic MnZn ferrites. Van der Zaag et al. [13, 14] explored the domain size as a function of grain size by neutron depolarization

analysis and found a sharp transition from uniformly magnetized grains below $4\ \mu\text{m}$ thickness to multidomain states in larger grains. Although the authors in reference [13] offered exchange decoupling between the grains as an explanation for the single-domain behavior, it seems more likely that the neutron experiments could also indicate the transition from strongly disturbed domains extending over the grains to domain patterns that are closed partially inside the grains in the same sense as discussed for the NiFe material.

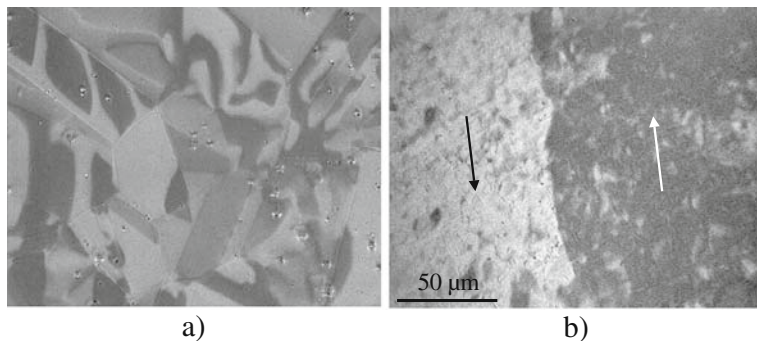


Fig. 10.10 (a) Demagnetized state of (a) coarse- and (b) fine-grained $\text{Ni}_{81}\text{Fe}_{13}\text{Mo}_6$ sheets of $20\ \mu\text{m}$ thickness; the average grain size is around $40\ \mu\text{m}$ and $13\ \mu\text{m}$, respectively. For the fine-grained material, the domains extend over the grains (together with M. Müller, see [15])

10.3.2 Interplay of Random and Uniaxial Anisotropies

The arguments in the previous section are based on single-phase materials. In typical nanocrystalline ribbons, however, the randomly oriented crystallites are embedded in an amorphous matrix which can also be described by the random anisotropy model with randomly oriented easy axes fluctuating on the scale of atomic distances. Moreover, additional anisotropies are present in nanocrystalline material, such as magnetoelastic, field-, or creep-induced anisotropies. Also shape anisotropy may be caused by surface roughness and the sample geometry. As the average random anisotropy is very small in optimized material (typically of the order of some Joules per cubic meter), these *uniaxial* anisotropies, which are uniform on a macroscopic scale, in fact dominate the soft magnetic properties. The situation is thus very similar to amorphous ribbons. Examples of domain states that are created by field- and creep-induced anisotropies in nanocrystalline ribbons are presented in Fig. 10.11. However, there are nevertheless situations, where the random magnetocrystalline anisotropy becomes significant as will be elaborated in this section.

Both the multiphase microstructure and the macroscopic anisotropies have been considered by Herzer [10, 16, 11] in extended random anisotropy models. Accordingly, the average anisotropy $\langle K \rangle$ of a coupled multiphase system with anisotropies

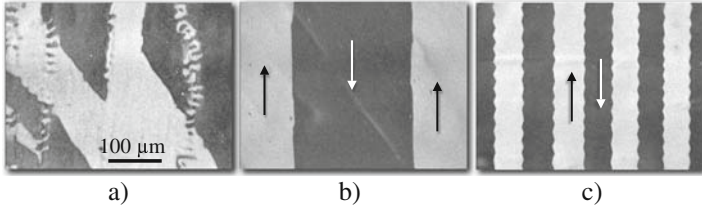


Fig. 10.11 Low-resolution domain images on $\text{Fe}_{73}\text{Cu}_1\text{Nb}_3\text{Si}_{16}\text{B}_7$ nanocrystalline ribbons with (a) low induced anisotropy of some J/m^3 , annealed in the absence of magnetic field, (b) with a field-induced anisotropy of about $30 \text{ J}/\text{m}^3$, and (c) with a creep-induced anisotropy of about the same size (see Fig. 10.8b for a high-resolution image of the same material)

randomly oriented on a scale smaller than the correlation length L_{ex} can be described by

$$\langle K \rangle = \sqrt{K_{\text{u}}^2 + \sum_{\nu} x_{\nu} \beta_{\nu}^2 K_{1,\nu}^2 (D_{\nu}/L_{\text{ex}})^3}. \quad (10.7)$$

The constant K_{u} represents a uniaxial, induced anisotropy of any origin that is uniform on a macroscopic scale. The size of such uniaxial anisotropy can be controlled by field or creep annealing, properly choosing the annealing time and temperature (see [11] for a review). Also annealing without magnetic field will cause induced anisotropy which follows the direction of the local spontaneous magnetization of the domains present during annealing. Field-free annealing thus generates a distribution of uniaxial anisotropies that fluctuate on the scale of the domain pattern present during annealing. The second term in Eq. (10.7) considers the random anisotropies of the different structural phases labeled by the index ν , where $K_{1,\nu}$ represents the local anisotropy constants, D_{ν} the grain sizes, and x_{ν} the volume fractions of the phases. The parameter β_{ν} depends on the symmetry of anisotropy and includes some statistical corrections. According to Eq. (10.7), the average anisotropy is determined by the competition between random and uniaxial anisotropies. For the theoretical treatment of this interplay, we refer to Herzer's articles. In this chapter, we restrict ourselves to a qualitative description by reference to domain observation (see [17] for details).

As discussed in connection with Fig. 10.9 b, some easiest direction will dominate in each renormalized correlation volume L_{ex} due to statistical fluctuations. Theoretical estimates within the random anisotropy model typically yield $\langle K_{\text{cl}} \rangle \approx 4 \text{ J}/\text{m}^3$ for the average random magnetocrystalline anisotropy in optimized nanocrystalline Fe-base alloys. Only in ribbons for which the induced anisotropies are in the order of or lower than the random anisotropy, the random contribution [the second term in Eq. 10.7] can become significant for the effective anisotropy. The easiest axes then reveal a large angular dispersion from one correlation volume to the other, leading to an enhanced patchy modulation of magnetization on the scale of typically a few micrometers – the scale of the renormalized exchange length [17].

This effect, which is illustrated in Fig. 10.12c, was already visible in Fig. 10.8a. More prominent examples, observed on two different material classes, are shown in Fig. 10.12a,b. The patchy magnetization fluctuates within otherwise regular and wide domains with a net magnetization direction that is given by residual macroscopic (induced) anisotropies. Observed at low resolution like in Fig. 10.11a, it is just these regular, macroscopic domains that are seen. If the induced anisotropies are getting stronger, the patchy modulation tends to disappear the more the long-range anisotropies dominate, leading to more and more homogeneously magnetized domains also on the microscopic scale. Figure 10.13 demonstrates this effect for two ribbons with low and strong macroscopic anisotropies, respectively, that have

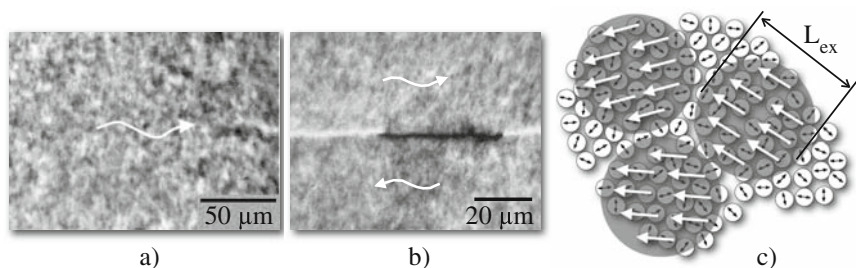


Fig. 10.12 Patchy modulation of magnetization in low-anisotropy nanocrystalline ribbons of composition $\text{Fe}_{73}\text{Cu}_1\text{Nb}_3\text{Si}_{16}\text{B}_7$ (a) and $\text{Fe}_{84}\text{Zr}_{3.5}\text{Nb}_{3.5}\text{B}_8\text{Cu}_1$ (b). The total anisotropy of the ribbon in (a) was reduced to a few Joules per cubic meter by applying a rotating magnetic field during crystallization annealing to reduce the formation of induced anisotropy (see [19]). For the sample in (b) the anisotropy is unknown. (c) Schematic illustration of the patchy modulation. The easiest axes of each (homogeneously magnetized) exchange volume strongly fluctuate

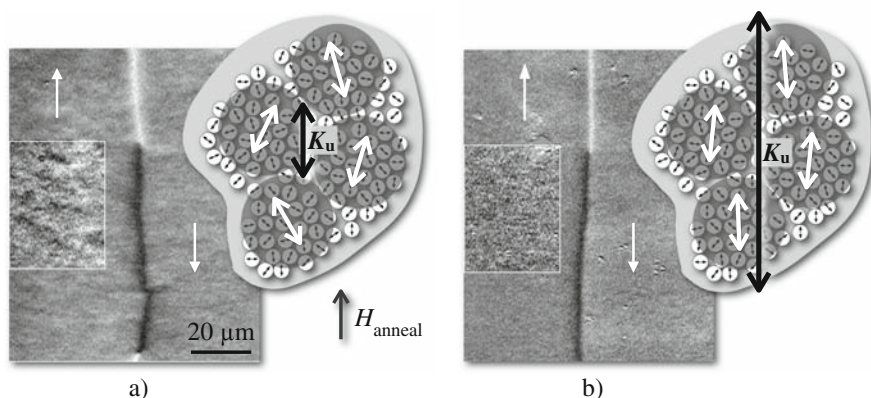


Fig. 10.13 The interplay of effective random and induced anisotropies determines the degree of magnetization modulation on a microscopic scale. Shown are high-resolution observations on $\text{Fe}_{73}\text{Cu}_1\text{Nb}_3\text{Si}_{16}\text{B}_7$ nanocrystalline ribbons with different strengths of induced anisotropy, about 3 J/m^3 in (a) and about 30 J/m^3 in (b). In the highlighted areas, the contrast was digitally enhanced to show more details. The sketches indicate the degree of fluctuation of the correlation volumes

been carefully adjusted by choosing proper annealing conditions. In soft magnetic *amorphous* alloys comparable patches are usually invisible due to the extremely small contribution of the averaged random anisotropy of $\langle K_1 \rangle \leq 10^{-3} \text{ J/m}^3$, i.e., a ratio of $K_u/\langle K_1 \rangle \geq 10^3$ [10]. More detailed experimental informations on correlated magnetization fluctuations in random anisotropy ferromagnets were obtained by small-angle neutron scattering (SANS) [18].

Additional experimental evidence for the interplay of random and induced anisotropies in nanocrystalline ribbons can be obtained by domain observation of FeCuNbSiB material at elevated temperatures (Fig. 10.14). At room temperature, the exchange coupling between the randomly oriented bcc FeSi grains mainly occurs via the intergranular amorphous matrix. The latter has a much lower Curie temperature than the crystalline phase. Above the Curie temperature of the amorphous phase, which is $T_c^{am} \approx 250^\circ\text{C}$ for the alloy shown in the figure, the exchange interaction between the nanocrystalline grains is largely reduced. Exchange coupling, however, is the prerequisite for the suppression of magnetocrystalline anisotropy of the grains. In case of reduced exchange interaction, the local random anisotropy will consequently be less effectively averaged out. Its average magnitude increases with increasing temperature and the soft magnetic properties will degrade, i.e., coercivity rises by two orders of magnitude and permeability drops accordingly [11]. Simultaneously, the domain structure changes [12, 17] from wide domains at room temperature (see Fig. 10.14a) to a pattern of small and irregular patch domains (Fig. 10.14b), thus approaching the domain state of high-coercivity material in Fig. 10.1. This feature is reversible and not connected to microstructural changes during the measurement. The drastic change in domain structure is only true, however, for material with low induced anisotropy. Nanocrystalline ribbons with relatively strong induced anisotropy (Fig. 10.14c, $K_u \approx 30 \text{ J/m}^3$) reveal wide domains oriented along the direction of the induced easy axis even far above T_c^{am} . The regular domain structure proves that the field-induced anisotropy of this sample still plays a significant role even at elevated temperatures. This becomes evident also from the hysteresis loops shown in Fig. 10.15. They were measured on nanocrystalline ring cores with a transverse field-induced anisotropy of about 30 J/m^3 . The linear shape of the hysteresis loops clearly indicates that the field-induced anisotropy of this core still plays a significant role in the magnetization process even at elevated temperatures. At the same time, however, the increase in coercivity and remanence above 300°C reflects an increasing contribution from the random magnetocrystalline anisotropy. The latter becomes evident in the irregular domain picture of Fig. 10.14d that was obtained after demagnetizing a high- K_u nanocrystalline ribbon transverse to its induced anisotropy axis at high temperature. A relatively strong induced anisotropy obviously shifts the temperature at which the random anisotropy starts to dominate to higher values.

The presence of regular domains in high- K_u material far above the Curie point of the amorphous phase, together with the increase in coercivity and remanence shown in Fig. 10.15 indicates that the grain coupling is largely, but not completely interrupted above T_c^{am} . The coupling mechanism above T_c^{am} is still under discussion, as pointed out by Herzer [11]. Two possible explanations are offered: exchange

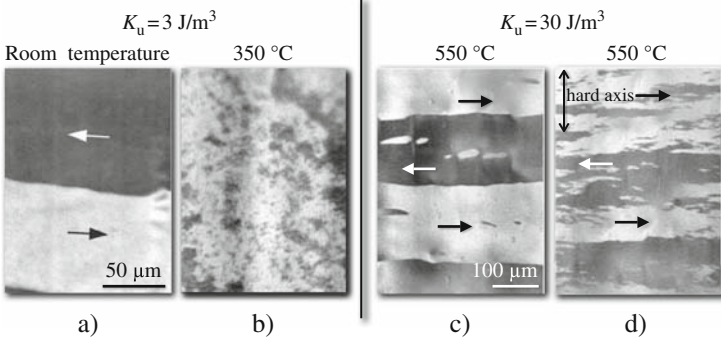


Fig. 10.14 Domain observation on $\text{Fe}_{73}\text{Cu}_1\text{Nb}_3\text{Si}_{16}\text{B}_7$ ribbons with different induced anisotropy at elevated temperature. In low-anisotropy material (a, b) the domains drastically and reversibly change above the Curie point T_c^{am} of the amorphous matrix phase. In high-anisotropy material the regular, wide domains are preserved even well above T_c^{am} (c), whereas changes are only visible after hard-axis demagnetization (d). Reprinted with permission from Flohrer et al. [17]

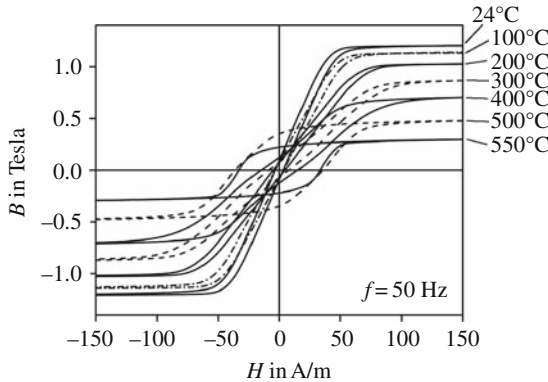


Fig. 10.15 Hysteresis loops at various temperatures and a frequency of 50 Hz of a nanocrystalline $\text{Fe}_{73}\text{Cu}_1\text{Nb}_3\text{Si}_{16}\text{B}_7$ tape wound core with a transverse field-induced anisotropy of about 30 J/m^3 , Reprinted with permission from Flohrer et al. [17]

penetration through the paramagnetic intergranular phase [20] and dipolar interaction [9, 18]. Both decrease with increasing temperature (the latter due to the decrease of the magnetization of the bcc grains), so that the soft magnetic properties are degrading anyway above T_c^{am} .

According to the random anisotropy model, the effective anisotropy constant $\langle K_{cl} \rangle$ is about equal to $|K_{c1}|/\sqrt{N}$ [see Eq. 10.5], where K_{c1} is the magnetocrystalline anisotropy and N is the number of exchange-coupled grains within the renormalized correlation volume. Consequently, the magnetic microstructure of nanocrystalline ribbons can be modified by either changing K_1 or N . The influence of N on the domains was shown in the heating experiments of the previous paragraphs (Fig. 10.14). The influence of K_1 is presented in Fig. 10.16. Adding cobalt to the standard FeCuNdFeB alloy significantly increases the magnetocrystalline

anisotropy, leading to a stronger effective anisotropy and immobile patch domains (Fig. 10.16a). Patchy domains are also observed in (b), where a regular FeCuNdFeB ribbon was “overannealed” beyond the optimum crystallization temperature. Here Fe₂B precipitates with a typical dimension of 50–100 nm have been formed [2] that have a high magnetocrystalline anisotropy, thus increasing the effective anisotropy while at the same time the grain size of the bcc FeSi grains remains unchanged. The presence of these precipitates thus effectively hardens the ultrafine bcc matrix.

These observations demonstrate the appearance of a patchy and immobile domain structure if the random anisotropy is less effectively averaged out. The magnetization process is then governed by nucleation rather than by wall motion. If the annealing temperature of FeCuNdFeB material is further increased, grain coarsening sets in, which leads (together with the FeB precipitations) to a complete degradation of the soft magnetic properties. A fine, highly coercive patch domain pattern is then formed as shown in Fig. 10.16c. Such domains are typical for materials in the coercivity maximum of Fig. 10.1. Small angle neutron scattering experiments [21] indicate that the magnetization process in this state proceeds by an avalanche-like reversal of the patch domains. We will return to such domains in Section 10.5.

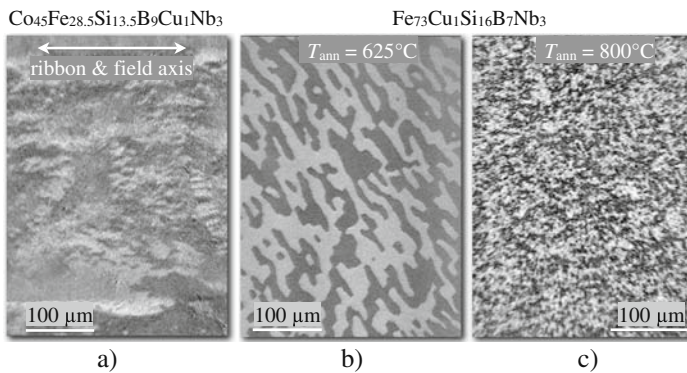


Fig. 10.16 (a) Patch domains in a $\text{Co}_{45}\text{Fe}_{28.5}\text{Si}_{13.5}\text{B}_9\text{Cu}_1\text{Nb}_3$ ribbon (provided by *Pilar Marin, Madrid*). Patchy domains are also observed in (b), where a regular FeCuNbSiB ribbon was “overannealed” at 625° C. In both cases, the magnetocrystalline anisotropy is increased as compared to optimized material, so that the random anisotropy is not averaged out efficiently. In strongly overannealed ribbons (c, annealed at 800° C), the patch size decreases by two orders of magnitude

10.3.3 Magnetization Process

In amorphous ribbons with well-defined uniaxial anisotropy, the magnetization process at low frequency or in the quasistatic limit is based either on rotational processes in hard-axis fields (see Fig. 10.6) or on domain wall motion in easy axis fields; both processes occur rather homogeneous and smooth, respectively. In nanocrystalline ribbons, the processes can differ, depending on the relative strength of the random anisotropy as discussed in the previous section. This is true for both, easy- and hard-axis processes. Typical domain states during the quasistatic *easy*-

axis process of nanocrystalline FeCuNdFeB ring cores with different strengths of the field-induced anisotropy K_u are presented in Fig. 10.17. For strong K_u regular domain walls separating homogeneous domains are shifted during magnetization (Fig. 10.17c). This situation is comparable to that of amorphous ribbons of similar anisotropy. For weak K_u , however, the random anisotropy becomes significant. The enhanced microscopic modulation of magnetization (as shown already in Fig. 10.12), which also leads to strongly deformed domain walls (Fig. 10.17a), causes locally strong inclinations to the exciting field direction and is thus responsible for enhanced nucleation. The magnetization process is therefore characterized by a superposition of wall motion and domain nucleation. The energy penalty due to the high wall density is limited as the specific wall energy is low at weak K_u .

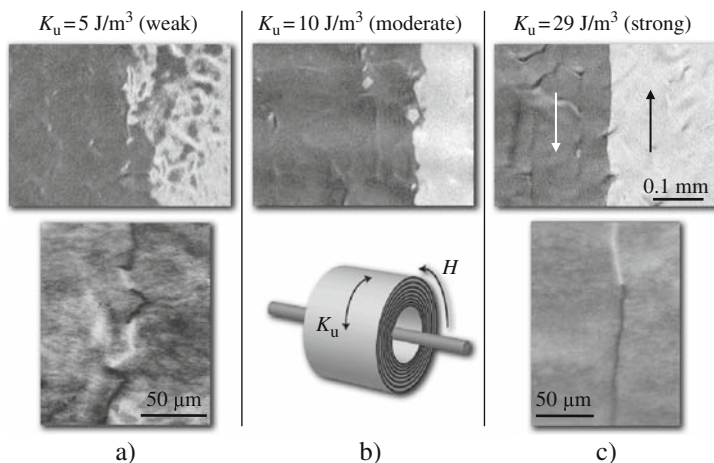


Fig. 10.17 Characteristic domain states during the easy-axis magnetization process around the coercive field, observed at low (*upper row*) and high resolution (*lower row*). Compared are three Fe₇₃Cu₁Nd₃Si₁₆B₇ nanocrystalline ring cores with circumferentially induced anisotropy of different strengths as indicated

The difference in microscopic disorder for weak and strong K_u is also resembled in the hard-axis process as shown in Fig. 10.18. Homogeneous rotation, as in amorphous ribbons, is observed in high- K_u material, whereas inhomogeneous rotational processes and domain splitting are typical for low- K_u ribbons. Surprisingly, these are the ribbons with the highest rotational permeability. The degree of inhomogeneity depends on the relative size of the induced anisotropy. The domain splitting found at elevated temperature in hard-axis field (see Fig. 10.14d) is another example of this phenomenon. Due to the decoupling the influence of the random anisotropy becomes significant despite the strong induced anisotropy.

The degree of microscopic modulation has also a strong impact on the dynamic magnetization processes at elevated frequencies. In Fig. 10.19 the increase in magnetic loss with rising frequency due to eddy currents is shown for a ring core excited along the circumferential easy axis [22]. As typical for soft magnetic materials, the

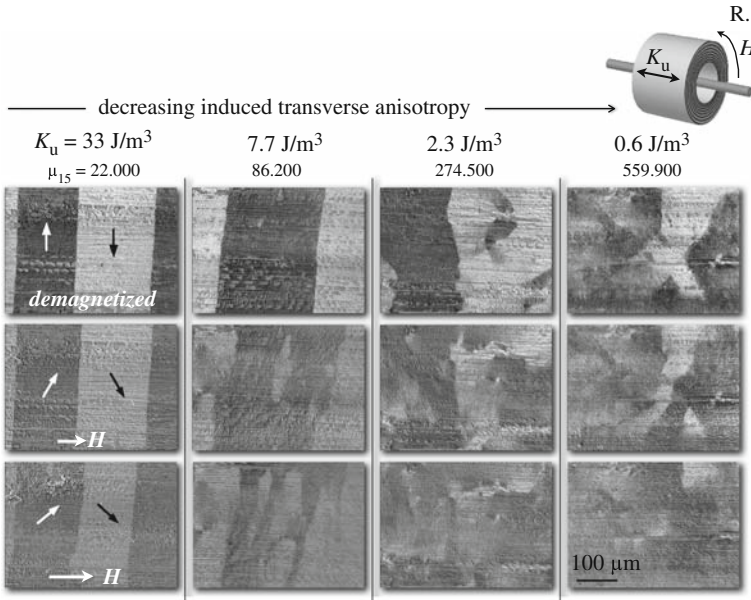


Fig. 10.18 Characteristic domain states during the hard-axis magnetization process of $\text{Fe}_{73}\text{Cu}_1\text{Nd}_3\text{Si}_{16}\text{B}_7$ ring cores with transversely induced anisotropy of different strengths and thus permeability as indicated. Three images at increasing field strengths are shown in each case

excess eddy current losses (beyond the classical eddy current loss and hysteresis loss) are increasing with rising frequency, but with a slower speed as compared to low frequencies. This indicates that the number and activity of domain walls increase with frequency (see [1]). The larger the density of domain walls, the smaller the velocity of every wall to achieve a given induction change, the lower the eddy current losses. The domain images in Fig. 10.19, obtained by stroboscopic Kerr microscopy, prove this expectation, but the character of domain refinement strongly depends on the mentioned interplay of random and induced anisotropies. In the core with high induced anisotropy regular easy-axis domains are refined with increasing frequency (as also found in amorphous ribbons or in transformer steel). In the case of low induced anisotropy, however, the regular domains of the ground state are replaced by fine patch domains with rising frequency. The magnetization process thus changes from wall motion to a nucleation type process. A full dynamic hysteresis cycle, displaying details of domain nucleation and growth at 1 kHz, is presented in Fig. 10.20.

Stroboscopic imaging relies on reproducible magnetization processes [23]. Each of the time-resolved images shown in Figs. 10.19, 10.20 are obtained by accumulating thousands of single images after driving the core into saturation for each image [24]. The sharp domain contrast, especially in case of patch domains, indicates that the nucleation-dominated process is indeed reproducible, i.e., the domains and their walls are periodically located always at the same position. This is not true for amorphous ribbons where usually blurred stroboscopic images are obtained [23, 25, 26], indicating non-reproducible wall displacement processes. Obviously the

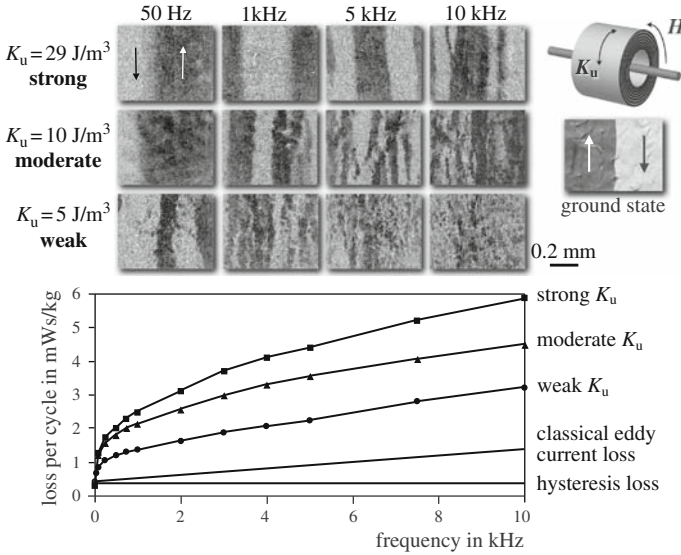


Fig. 10.19 Specific power loss per cycle versus frequency and corresponding domain images of nanocrystalline FeCuNbSiB cores with different strengths of the induced anisotropy K_u . The domain images are taken by stroboscopic Kerr imaging around the point of zero magnetic induction. Domain refinement is distinctive with increasing frequency (Reprinted with permission from Flohrer et al. [24])

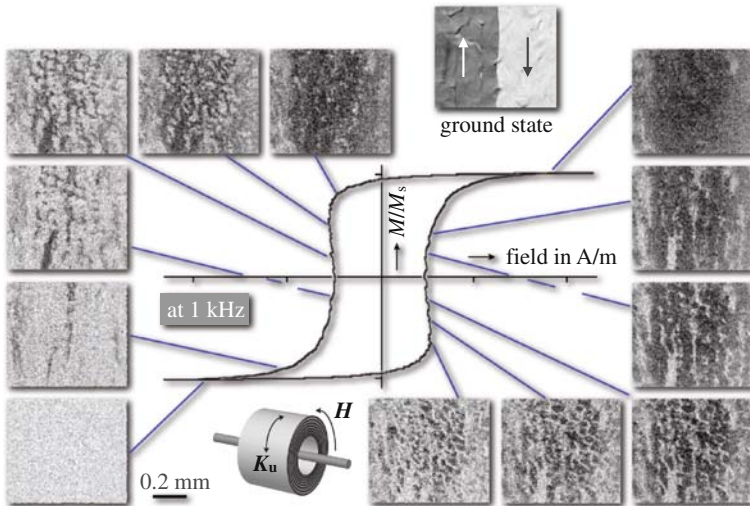


Fig. 10.20 Stroboscopic observation of the dynamic easy-axis process at 1 kHz on a low-anisotropy nanocrystalline ring core. The regular 180° domains of the ground state are replaced by patch domains at high frequency (Reprinted with permission from Flohrer et al. [24])

patchy fluctuation of magnetization in low- K_u material provides energetically favorable locations for reproducible domain nucleation. The preference for the nucleation process can therefore again be clearly related to the strong microscopic modulation of magnetization in the low- K_u material as already discussed in connection with Fig. 10.17. Interestingly, the material with the smallest induced anisotropy (i.e., strongest modulation) reveals the lowest power loss due to the highest density of domain walls at higher frequencies.

The influence of the random anisotropy on energy loss was also found in nanocrystalline FeCuNbSiB cores with *transverse* field-induced anisotropy [22]. A significant excess loss component was found, in particular for high induction levels, which cannot be explained by homogeneous magnetization rotation. In fact, dynamic domain observation revealed inhomogeneous rotation of magnetization, wall displacement processes, and domain nucleation besides homogeneous rotation. Like in the longitudinal case, domain refinement was observed with increasing frequency with the smallest domain width for cores with weak induced anisotropy, where excess loss is the lowest.

10.4 Domains in Nanocrystalline Magnetic Films

Ferromagnetic films, e.g., made of Permalloy or cobalt and deposited by sputtering, evaporation, or electrochemical methods, have a nanocrystalline microstructure already in the as-deposited state with typical grain sizes in the some 10-nm regime. Like in nanocrystalline ribbons the exchange interaction therefore averages over the magnetocrystalline anisotropy of the (more or less) randomly oriented nano-grains. Also uniaxial anisotropies are usually present, induced either by field annealing or during film deposition in the presence of a magnetic field. The considerations of Section 10.3 therefore also apply to (non-epitaxial) magnetic films. In contrast to ribbons, however, where the influence of the random anisotropy may lead to a patchy magnetization modulation, a “ripple” modulation of magnetization is observed in films [1]. Ripple has been discovered by Lorentz microscopy [27] and is characterized by fine, wave-like fluctuations in the micrometer range (thus being much wider than the grain size) that run perpendicular to the average magnetization direction.

Early theoretical explanations for the ripple phenomenon were given in [28, 29]. In these theories, it is assumed that the film consists of grains with a randomly oriented easy axis in the plane of the film. The arguments are then similar to the random anisotropy model. The grain size is so small that the magnetization cannot follow the preferential direction in each single grain, because the exchange energy and the magnetostatic energy at the grain boundaries would become too large. The magnetostatic effect thus adds to the exchange interaction in the ripple theory. The direction of the magnetization adapts itself to the sum of the anisotropy energies of a finite number of randomly oriented grains and not to the anisotropy of a single grain. The magnetization can only rotate uniformly in a region which is much larger than a single grain. It will do so if the sum of the anisotropy energies of the grains in the

region considered is lowered by this rotation. It then turns out most advantageous if the magnetization rotates uniformly in an oblong region with the long axis perpendicular to the average magnetization. The reason for this characteristic texture is the stray field energy that is smaller for a longitudinal modulation than for a transverse modulation as illustrated in Fig. 10.21a. An induced easy axis, oriented vertically and in the film plane, is assumed in the figure. Consider two neighborhoods of grains (correlation volumes), in which by statistical fluctuations two local anisotropy axes dominate that are superimposed onto the average (induced) anisotropy axis. The fixed magnetization directions of the two correlation volumes are given by ϑ_1 and ϑ_2 relative to the average magnetization direction. In case of transverse neighborhood, a “transverse” charge $\lambda_{\text{trans}} = \sin \vartheta_1 - \sin \vartheta_2$ is generated at the volume boundary. For small ϑ this is much larger than the longitudinal charge $\lambda_{\text{lon}} = \cos \vartheta_1 - \cos \vartheta_2$ appearing at the boundary of longitudinally neighbored correlation volumes. The stray field energy therefore suppresses lateral variations of the magnetization, but allows small longitudinal variations, particularly for the case $\vartheta_1 = -\vartheta_2$ for which λ_{lon} stays zero even for large deviations [1]. The resulting ripple texture, orthogonal to the average anisotropy axis, is illustrated in Fig. 10.21b.

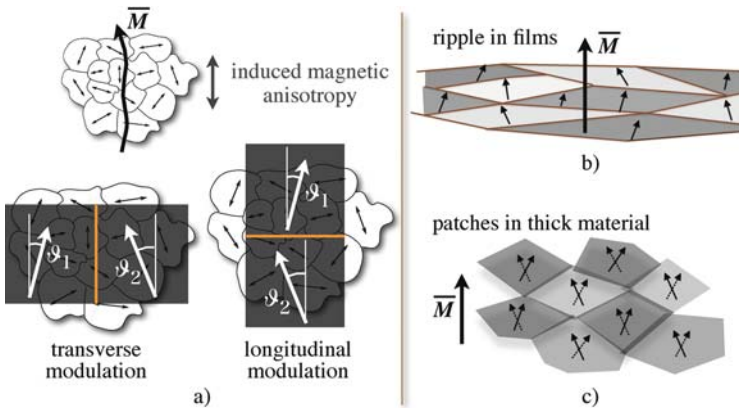


Fig. 10.21 (a) Stray field argument in favor of longitudinal magnetization ripple in magnetic films. The ripple modulation around an average magnetization direction is schematically indicated in (b). In case of bulk nanocrystalline material like ribbons the cancellation of transverse magnetization allows a patchy modulation (c). A macroscopic induced anisotropy, here aligned vertically, was assumed for all sketches

Numerical micromagnetic simulation on the ripple effect in thin polycrystalline films with random anisotropy and the parameters of hexagonal cobalt were presented in [30], considering exchange and long-range dipolar interaction. The influence of exchange coupling at the grain boundaries and the film thickness on the ripple was systematically investigated. Larger exchange coupling leads to a coarser ripple pattern. In films with just 1 nm thickness no ripple pattern was found at all. Obviously the magnetic moment of the individual grains is so small that intergrain

interactions play no role. The film rather behaves like an assembly of non-interaction single-domain particles with randomly distributed anisotropy axes.

Here we do not want to go deeper in the ripple theory, but rather stress the mentioned connection of ripple in films and the patches in ribbons. This connection becomes immediately evident in the experiment of Fig. 10.22. Here a nanocrystalline ribbon was thinned from 20 μm down to the micrometer regime and below. The patchy modulation then gradually changes to a classical ripple pattern with the typical textured modulation. This observation proves that both ripple and patches are in fact due to the statistical perturbation by the crystal anisotropy. Ripple in nanocrystalline ribbons that were thinned for transmission electron microscopy was also observed by electron holography in [31].

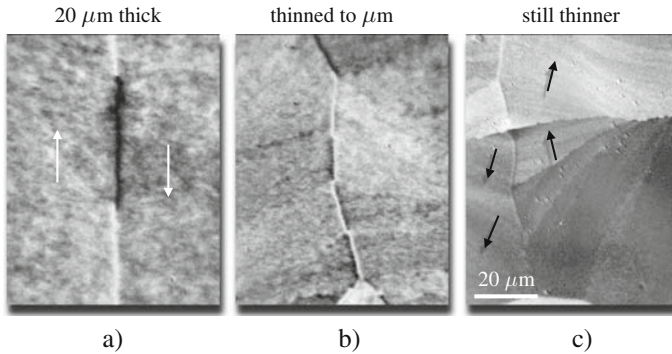


Fig. 10.22 (a) Patch-like modulated domains in nanocrystalline $\text{Fe}_{84}\text{Zr}_{3.5}\text{Nb}_{3.5}\text{B}_8\text{Cu}_1$ ribbon (thickness 20 μm), which transform into ripple (b, c) by thinning the ribbon (Reprinted with permission from Schäfer [4])

Similar stray field arguments as for the ripple also apply to the patch phenomenon. The ripple discussion is based on the fact that in thin films the magnetization vector is forced parallel to the film plane by the demagnetizing field, leaving the textured modulation as only possibility to avoid magnetic charges. In bulk material, however, there is the additional freedom of magnetization modulation also in the third dimension as sketched in (Fig. 10.21c). If one correlation volume is magnetized to the left, there can be another one underneath that is magnetized to the right. This leads to a cancellation of transverse magnetization components so that stray fields, which would enforce certain wall orientations, are irrelevant. Arbitrarily oriented walls, i.e., patch domains, are the consequence. A theory based on this argument seems not to be available.

The interplay of random and induced anisotropies, discussed for nanocrystalline ribbons in Section 10.3, also applies to films. A stronger magnetocrystalline anisotropy leads to less-effective averaging effects, i.e., a stronger microscopic dispersion of magnetization. Consequently, Permalloy films with their inherently very small crystal anisotropy show a much weaker ripple effect than cobalt films (Fig. 10.23a) or films made of CoFe alloys. A strong ripple modulation favors a

nucleation-dominated magnetization process as demonstrated for a very thin cobalt film in Fig. 10.23b, whereas in Permalloy films the magnetization process is governed by wall motion. This difference is also manifested in the characteristic domain patterns after ac-demagnetizing the films (Fig. 10.24). A Permalloy film contains wide domains with walls that more or less follow the induced anisotropy axis after easy-axis demagnetization. After hard-axis demagnetization, a finer pattern is obtained due the so-called blocking mechanism during demagnetization (see [1] for details). In cobalt films much more complex patterns are found with both field

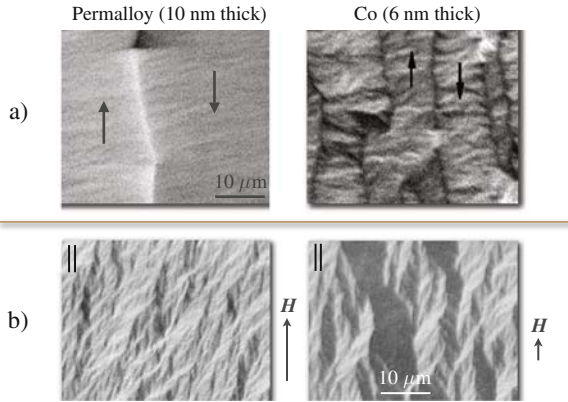


Fig. 10.23 (a) Polycrystalline Co films with strong magnetocrystalline anisotropy show a stronger ripple effect than Permalloy. (b) The large microscopic dispersion in Co films leads to a nucleation-dominated magnetization process. Shown are two domain states in decreasing magnetic field, observed on a 6-nm thick Co film. All films were prepared by sputtering, thus having a nanocrystalline microstructure

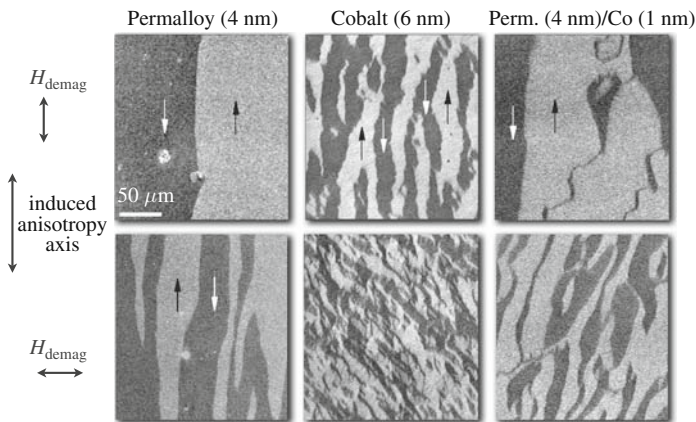


Fig. 10.24 Low-resolution observations on very thin Permalloy and cobalt films as well as a Permalloy/Co double layer as indicated. The films were demagnetized at 50 Hz in an external field aligned along (*upper row*) and transverse to the easy axis (*lower row*) (Reprinted with permission from Schäfer et al. [32])

histories. If Permalloy and cobalt films are combined in a bilayer, the degree of complexity is somewhere in between that of the pure films. Further observations of such effects, including patterned cobalt and Permalloy thin films as well as spin-valve-type multilayers are presented in [32].

By employing multilayers, the angular magnetization dispersion effect can be altered. This is especially true for films with higher saturation magnetization than Permalloy. The Permalloy–cobalt bilayer, presented before, points already in this direction. Often iron is used to obtain high-moment films. Single iron films, however, show a high degree of dispersion due to the high magnetocrystalline anisotropy of iron and typical grain sizes in the 100-nm regime (if the films are *not* grown epitaxially – see [33]). To reduce dispersion, a significant reduction in grain size is required to diminish the random anisotropy. This is possible in multilayers consisting of alternating iron films (for the high moment) and ferromagnetic interlayers (like amorphous FeCrB films) which serve mostly to avoid the harmful properties of the main layer material such as the high magnetocrystalline anisotropy. At the same time grain growth is renucleated each time a new layer is grown, so that small grains result also in the high-anisotropy layers. Alloying certain elements that inhibit grain growth can support this effect. In this way thick, high-moment ferromagnetic films can be grown with a nanocrystalline microstructure. In fact, the ripple dispersion is strongly suppressed in such films as shown in ref. [34] for Fe–NiFe multilayers. Also the magnetostriction constant can be tuned by selecting materials with proper magnetostriction in the same sense as already mentioned for the two-phase FeCuNbSiB nanocrystalline ribbons. A review of such multilayer films is given in [35].

Also the interspacing of ferromagnetic films with non-magnetic layers has effects on the angular magnetization dispersion. If the films are ferromagnetically coupled, regular ripple modulation is observed, while patches are found for antiferromagnetic coupling [36, 33]. The patchy modulation can be explained with the argument of Fig. 10.21c, with the full and hatched arrows corresponding to the magnetization vectors of neighboring layers. If exchange coupling between the ferromagnetic films is suppressed, magnetostatic coupling can nevertheless cause film interaction, again based on the argument of Fig. 10.21c. An example for such an observation is shown in Fig. 10.25. The modulation within the domains is of mixed patch and ripple nature.

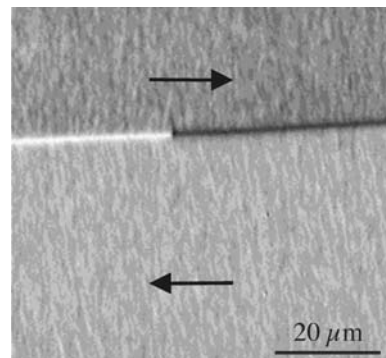


Fig. 10.25 Ordered patch pattern in FeN (150 nm)/Al₂O₃ (2.5 nm)/FeN (150 nm) trilayer film with horizontal-induced anisotropy (Courtesy J. McCord [37])

10.5 Domains in Fine- and Nanostructured Permanent Magnets

The microstructure of common permanent magnets like hexaferrites, NdFeB- or CoSm-type magnets consists of highly anisotropic grains in the size range of 10 μm in a polycrystalline, textured compound that are prepared in such a way that the switching of one grain has little influence on its neighbors [1]. After demagnetization or during switching, regular domains are observed in such material, the character of which depends on the orientation of the observed surface. But permanent magnets can also be prepared from *single-domain particles*. Domain patterns in such particles are impossible or at least unstable. Classical examples are the Alnico alloys, consisting of fine filaments of a high-saturation FeCo alloy that are embedded into a non-magnetic NiAl matrix. As FeCo is a low-anisotropy material, the individual particles must have an elongated shape to achieve high switching fields based on shape anisotropy.

Modern small particle magnets, as reviewed in [38, 39], are based on high-anisotropy materials that consist of single-domain *grains* which are usually strongly correlated. They can therefore not be treated as an aggregate of independent particles as shown below. A number of techniques can be used to prepare fine-crystalline magnets out of precursors such as $\text{Nd}_2\text{Fe}_{14}\text{B}$ [40]: rapid quenching and subsequent crystallization, mechanical alloying, and the hydrogenation disproportionation desorption recombination (HDDR) process. All these methods generate a fine powder with a particle size around 100 μm and a grain size between some 10 nm and some 100 nm, which then has to be compacted into solid magnets by resin bonding or hot pressing. Oriented magnets can be produced by “die-upsetting”, an anisotropic hot squeezing process. Also by the HDDR process an anisotropic powder can be produced which can be oriented in a magnetic field. If the grains or particles are decoupled, an oriented microstructure (texture) is necessary to achieve sufficient remanence.

But even non-oriented nanocrystalline materials remain interesting as a relatively weak exchange interaction between very small grains can lead to an enhanced remanence without a significant loss in coercivity (*exchange-enhanced magnets*). The coupling enhances the remanence above the average $M_r = 0.5M_s$ of independently oriented uniaxial grains (see Fig. 10.26). For significant remanence enhancement at sufficient coercivity the grains have to be small enough (Fig. 10.26c), but still large enough to avoid the averaging effect of magnetocrystalline anisotropy that leads to soft magnets as described in Section 10.3. A further possibility of achieving high remanence in non-oriented nanocrystalline materials consists in adding a high-saturation soft magnetic phase, which is strongly exchange coupled to the basic hard magnetic phase if the extension of the soft phase is sufficiently small [42]. The coercivity in these two-phase nanocrystalline magnets is dominated by the hard phase, whereas the high remanence is primarily a consequence of the soft phase. A highly irregular magnetic microstructure that is modulated on the scale of the grain size (i.e., of the order of some ten nanometers) is found in such material by numerical micromagnetic simulation [43] (Fig. 10.27 a). Lorentz microscopy reveals submicron domains which decrease in scale with decreasing

grain size [44] (Fig. 10.27 b). The complex character of the domains somehow resembles the irregular patch domains of the overannealed FeCuNbSiB ribbons (see Fig. 10.16c), although on a much finer scale due to the higher anisotropy and smaller grain size.

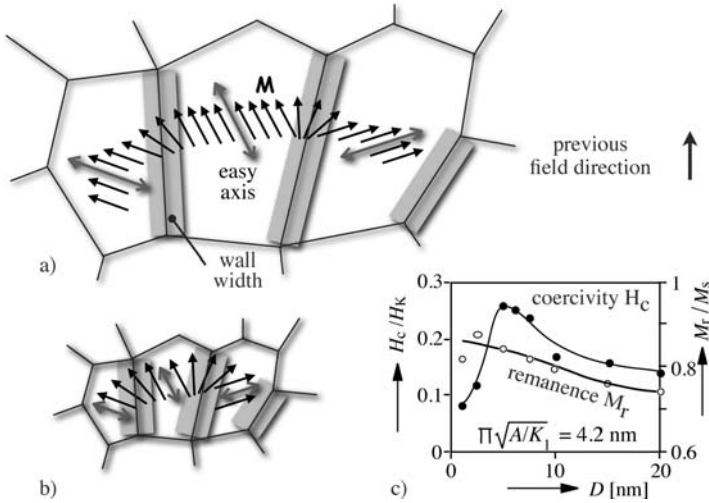


Fig. 10.26 Mechanism of remanence enhancement in non-oriented, nanocrystalline NdFeB magnets. The rotational zones around the grain boundaries in the order of the domain wall width contribute to the remanence. Their relative volume increases with decreasing grain size [compare (a) and (b)]. Simulated coercivity and remanence curves are shown in (c) (Reprinted with permission from Rave and Ramstöck [41])

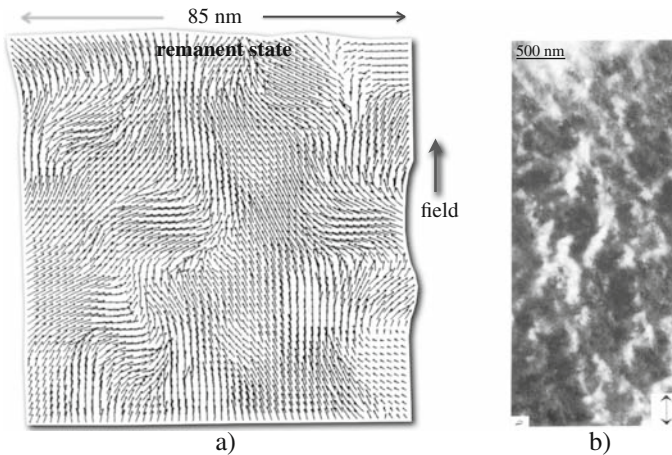


Fig. 10.27 (a) Finite element simulation of remanence-enhanced $\text{Nd}_2\text{Fe}_{14}\text{B} / \text{Fe}_3\text{B}$ magnet (taken from [43]). (b) Domain image of $\text{Nd}_2\text{Fe}_{14}\text{B} / \text{Fe}$ material, obtained by transmission electron microscopy in the Foucault mode (Reprinted with permission from Chapman et al. [44])

If the exchange coupling between single-domain grains is weak or interrupted, the predominant dipolar interaction between the grains causes *magnetostatic interaction domains* [1] (Figs. 10.28, 10.29). They are characterized by grain neighborhoods, in which all grains are correlatively saturated along their individual easy axis along a certain net direction. This kind of irregular domains was first observed in Alnico material [45] and later also in fine-grained rare-earth magnets [46]. Obviously also in these materials dipolar interactions between the grains dominate over the (certainly present) exchange interaction. The characteristic feature of interaction domains is their elongated shape extending along the preferred axis of the material as visible in the right image of Fig. 10.28. Consequently, the more pronounced the interaction domains the better the texture of the material [47]. Interaction domains are not in equilibrium as can be seen by comparing the thermally demagnetized state with a field-demagnetized state as elaborated in [1]. Interestingly, such domains have recently also been found in the classical $\text{Sm}_2\text{Co}_{17}$ -pinning magnets, which indicates predominant magnetostatic interaction between the $\text{Sm}_2(\text{CoFe})_{17}$ -cells that are interrupted by precipitation phases [48].

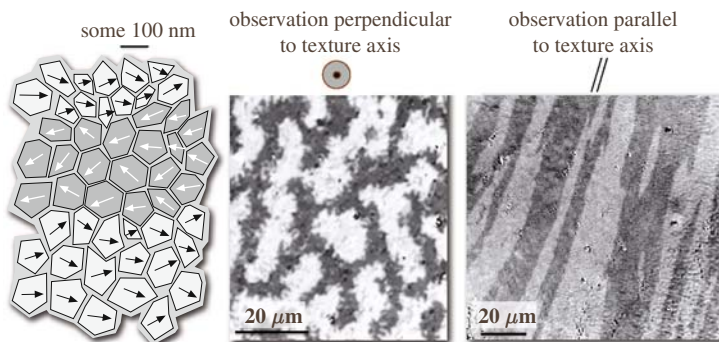


Fig. 10.28 Magnetostatic interaction domains in fine-crystalline NdFeB material, where the $\text{Nd}_2\text{Fe}_{14}\text{B}$ grains are exchange decoupled by a paramagnetic grain boundary phase. The sketch indicates the cooperatively magnetized grain neighborhoods due to predominant dipolar interaction

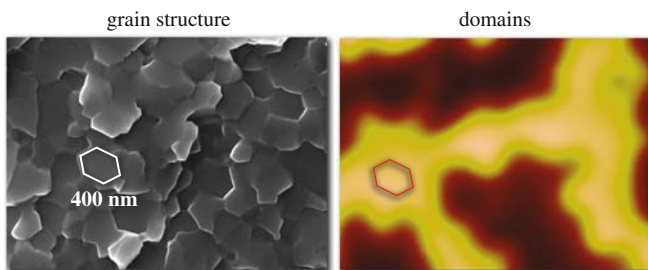


Fig. 10.29 The comparison between grain structure and interaction domains (here imaged by magnetic force microscopy) directly proves that the domains extend over several correlated grains (courtesy O. Gutfleisch, taken from [49])

Note that the “softening-effect” due to random anisotropy as described in Section 10.1 is irrelevant for nanostructured permanent magnets, even in the case of exchange-coupled grains. The exchange length L_{ex} is 1.3 nm in NdFeB (with $K_u = 4.3 \cdot 10^6$ kJ/m³ and $A = 8 \cdot 10^{-12}$ J/m), being far below the typical grain size of 20 nm in exchange coupled and some 100 nm in magnetostatically coupled magnets.

10.6 Summary

If in a magnetic material the structural correlation length (grain size) is smaller than the ferromagnetic correlation length (exchange length), magnetocrystalline anisotropy is significantly reduced by the smoothing effect of the exchange interaction. This provides the basis for extremely good soft magnets with a saturation magnetization higher than in conventional NiFe or amorphous material. The magnetic microstructure in such nanocrystalline materials is determined by the interplay of random and induced macroscopic anisotropies. This is true for both bulk material (ribbons) and magnetic films. A strong patchy, respectively ripple modulation of magnetization is found if the random anisotropy is sufficiently large. The microscopic disorder gives rise to a nucleation-dominated magnetization process, which (in case of the ribbons) is favorable at higher frequencies due to reduced anomalous losses. In any case the (average) domain magnetization follows the axis of any induced anisotropy.

In high-anisotropy materials the transition to such soft magnetic behavior is shifted toward very small grain sizes due to the small ferromagnetic correlation length. By making use of the coercivity maximum at larger grain sizes (still below the single-domain limit) nanostructured permanent magnets are obtained. Exchange coupling between the grains can be exploited in exchange-spring material where it enhances the remanence. Highly immobile and fine patch domains are characteristic for such material. If exchange coupling between the grains is interrupted, so-called interaction domains are observed due to the predominance of magnetostatic interactions between the (single domain) grains.

Acknowledgments Many domain pictures in the chapter on nanocrystalline ribbons have been obtained by *Sybille Flohrer* (IFW Dresden, now at Vacuumschmelze, Hanau). For their interpretation *Giselher Herzer* (Vacuumschmelze) made decisive contributions. He also provided us with most of the NdCuFeBSi ribbons for domain imaging. Many thanks to both of them. Thanks also to *Jeffrey McCord* (IFW Dresden) for fruitful discussion on thin film magnetism and to *Ludwig Schultz* (IFW Dresden) for his continuous support and interest in domain research.

References

1. A. Hubert and R. Schäfer: *Magnetic Domains. The Analysis of Magnetic Microstructures*. Springer, Berlin (1998)
2. G. Herzer: Nanocrystalline soft magnetic alloys. In: K.H.J. Buschow, editor. *Handbook of magnetic materials*, vol. 10., Elsevier Science, pp. 415 – 462 (1997)

3. R. Schäfer and S. Schinnerling: Bulk domain analysis in FeSi crystals. *J. Magn. Magn. Mat.* **215–216**, 140–146 (2000)
4. R. Schäfer: Domains in extremely soft magnetic materials. *J. Magn. Magn. Mat.* **215–216**, 652–663 (2000)
5. Y. Yoshizawa, S. Oguma, K. Yamauchi: New Fe-based soft magnetic alloys composed of ultrafine grain structure. *J. Appl. Phys.* **64**, 6044 (1988)
6. R. Alben, J. Becker, M.C. Chi: Random anisotropy in amorphous ferromagnets. *J. Appl. Phys.* **49**, 1653–1658 (1978)
7. G. Herzer: Grain structure and magnetism of nanocrystalline ferromagnets. *IEEE Trans. Magn.* **25**, 3327–3329 (1989)
8. G. Herzer: Grain size dependence of coercivity and permeability in nanocrystalline ferromagnets. *IEEE Trans. Magn.* **26**, 1397–1402 (1990)
9. G. Herzer: Soft magnetic nanocrystalline materials, *Scripta Metallurgica* **33**, 1741–1756 (1995)
10. G. Herzer: The random anisotropy model – a critical review and update. In *Properties and Applications of Nanocrystalline alloys from amorphous precursors*, In: B. Idzikowski, P. Svec and M. Miglierini editors. Kluwer Academic Publishers, pp. 15–34 (2005)
11. G. Herzer: Soft magnetic materials – nanocrystalline alloys. In: H. Kronmüller and S. Parkin editors. *Handbook of magnetism and advanced magnetic materials*, vol. 4., John Wiley & Sons Ltd, p. 1882 (2007)
12. R. Schäfer, A. Hubert, G. Herzer: Domain observation on nanocrystalline material. *J. Appl. Phys.* **69**, 5325 (1991)
13. P.J. van der Zaag, J.J.M. Ruigrok, A. Noordermeer, M.H.W.M. van Delden, et al.: The initial permeability of polycrystalline MnZn ferrites: The influence of domain and microstructure. *J. Appl. Phys.* **74**, 4085–4095 (1993)
14. P.J. van der Zaag, P.J. van der Valk, M.T. Rekveldt: A domain size effect in the magnetic hysteresis of NiZn-ferrite. *Appl. Phys. Lett.* **69**, 2927–2929 (1996)
15. M. Müller, T. Lederer, K.H. Fornaçon, R. Schäfer: Grain structure, coercivity and high frequency noise in soft magnetic Fe-81Ni-6Mo alloys. *J. Magn. Magn. Mat.* **177**, 231–232 (1998)
16. G. Herzer: Anisotropies in soft magnetic nanocrystalline alloys. *J. Magn. Magn. Mat.* **294**, 99–106 (2005)
17. S. Flohrer, R. Schäfer, Ch. Polak, G. Herzer: Interplay of uniform and random anisotropy in nanocrystalline soft magnetic alloys. *Acta Mat.* **53**, 2937–2942 (2005)
18. A. Michels and J. Weissmüller: Magnetic-field-dependent small-angle neutron scattering on random anisotropy ferromagnets. *Rep. Prog. Phys.* **71**, 066501 (2008)
19. R. Schäfer and G. Herzer: Continuous Magnetization Patterns in Amorphous Ribbons. *IEEE Trans. Magn.* **37**(4), 2245–2247 (2001)
20. A. Hernando and T. Kulik: Exchange interactions through amorphous paramagnetic layers in ferromagnetic nanocrystals. *Phys. Rev. B* **49**, 7064–7067 (1994)
21. J. Löffler, H.B. Braun, W. Wagner, K. Kostorz, A. Wiedenmann: Magnetization processes in nanostructured metals and small-angle neutron scattering. *Phys. Rev. B* **71**, 134410 (2005)
22. S. Flohrer, R. Schäfer, J. McCord, S. Roth, L. Schultz, F. Fiorillo, W. Günther, G. Herzer: Dynamic magnetization process of nanocrystalline tape wound cores with transverse field-induced anisotropy. *Acta Mat.* **54**, 4693–4698 (2006)
23. R. Schäfer: Investigation of Domains and Dynamics of domain walls by the magneto-optical Kerr effect. In: H. Kronmüller and S. Parkin editors. *Handbook of magnetism and advanced magnetic materials*, vol. 3., John Wiley & Sons Ltd, p. 1513 (2007)
24. S. Flohrer, R. Schäfer, J. McCord, S. Roth, G. Herzer, L. Schultz: Magnetization loss and domain refinement in nanocrystalline tape wound cores. *Acta. Mat.* **54**, 3253–3259 (2006)
25. S. Flohrer, R. Schäfer, G. Herzer: Magnetic microstructure of nanocrystalline FeCuNbSiB soft magnets. *J. Magn. Magn. Mat.* (1998), *J. Non-Cryst. Sol.* **354**, 47–51 (2008)

26. A.J. Moses, P.I. Williams, O.A. Hoshtanar: A novel instrument for real-time dynamic observation in bulk and micromagnetic materials. *IEEE Trans. Magn.* **41**, 3736–3738 (2005)
27. H.W. Fuller and M.E. Hale: Determination of magnetization distribution in thin films using electron microscopy. *J. Appl. Phys.* **31**, 238–248 (1960)
28. K.J. Harte: Theory of magnetization ripple in ferromagnetic films. *J. Appl. Phys.* **39**, 1503–1524 (1968)
29. H. Hoffmann: Theory of magnetization ripple. *IEEE Trans. Magn.* **4**, 32–38 (1968)
30. D.V. Berkov and N.L. Gorn: Quasistatic remagnetization processes in two-dimensional systems with random on-site anisotropy and dipolar interaction: Numerical simulations. *Phys. Rev. B* **57**, 14332–14343 (1998)
31. Y. Gao, D. Shindo, T. Bitoh, A. Makino: Magnetic microstructure of Fe₈₄Nd₇B₉ alloys observed by electron holography. *J. Appl. Phys.* **93**, 7462–7464 (2003)
32. R. Schäfer, D. Chumakov, O. de Haas, L. Schultz, W. Maaß, K.U. Barholz, R. Mattheis: Magnetization Processes in Spin-Valve Meanders for Sensor Applications. *IEEE Trans. Magn.* **39**, 2089–2097 (2003)
33. M. Rührig, R. Schäfer, A. Hubert, R. Mosler, J.A. Wolf, S. Demokritov, P. GruumInberg: Domain Observations on Fe-Cr-Fe Layered Structures. *Phys. Stat. Sol. (a)* **125**, 635–656 (1991)
34. M. Rührig, W. Bartsch, M. Vieth, A. Hubert: Elementary magnetization processes in a low-anisotropy circular thin film disk. *IEEE Trans. Magn.* **26**, 2807–2809 (1990)
35. H.J. de Wit: Soft magnetic multilayers. *Rep. Prog. Phys.* **55**, 113–155 (1992)
36. D. Elefant, R. Schäfer, J. Thomas, H. Vinzelberg, C.M. Schneider: Competition of spin-flip and spin-flop dominated processes in magnetic multilayers: magnetization reversal, magnetotransport and domain structure in the NiFe/Cu system, *Phys. Rev. B.* **77**, 014426 (2008)
37. J. McCord, J. Westwood: Domain formation in Fe-N multilayers. *J. Appl. Phys.* **87**, 6502–6504 (2000)
38. J. Fidler, D. Suess, T. Schrefl: Rare-earth intermetallics for permanent magnet applications. In: H. Kronmüller and S. Parkin editors. *Handbook of magnetism and advanced magnetic materials*, vol. 4., John Wiley & Sons Ltd, p. 1945 (2007)
39. M. Marinescu, A. Gabay, G. Hadjipanayis: Rare-earth nanocrystalline and nanostructured magnets. In: H. Kronmüller and S. Parkin editors. *Handbook of magnetism and advanced magnetic materials*, vol. 4., John Wiley & Sons Ltd, p. 2005 (2007)
40. O. Gutfleisch, A. Bollero, A. Handstein, D. Hinz, A. Kirchner, A. Yan, K.-H. Müller, L. Schultz: Nanocrystalline high performance magnets, *J. Magn. Magn. Mat.* **242–245**, 1277–1283 (2002)
41. W. Rave and K. Ramstöck: Micromagnetic calculation of the grain size dependence of remanence and coercivity in nanocrystalline permanent magnets, *J. Magn. Magn. Mat.* **171**, 69–82 (1997)
42. R. Coehoorn, D.B. de Mooij, J.P.W.B. Duchateau, K.H.J. Buschow: Novel permanent magnetic materials made by rapid quenching. *J. de Phys. (Colloque)* **49**, C8-669–670 (1989)
43. T. Schrefl and J. Fidler: Finite element modeling of nano-composite magnets. *IEEE Trans. Magn.* **35**, 3223 (1999)
44. J.N. Chapman, S. Young, H.A. Davies, P. Zhang, A. Manaf, R.A. Buckley: A TEM investigation of the magnetic domain structure in nanocrystalline NdFeB samples. *Proc. 13th Int. Workshop on RE Magnets and their applications*, p. 95, Birmingham (1994)
45. E.A. Nesbitt, H.J. Williams: Mechanism of magnetization in Alnico V. *Phys. Rev.* **80**, 112–113 (1950)
46. L. Folks, R. Street, R.C. Woodward: Domain structures of die-upset melt-spun NdFeB. *Appl. Phys. Lett.* **65**, 910–912 (1994)
47. K. Khlopkov, O. Gutfleisch, R. Schäfer, D. Hinz, K.-H. Müller, L. Schultz: Interaction domains in die-upset NdFeB magnets in dependence on the degree of deformation. *J. Magn. Magn. Mat.* **272–276**, E1937–E1939 (2004)

48. O. Gutfleisch, K.-H. Müller, K. Khlopkov, M. Wolf, A. Yan, R. Schäfer, T. Gemming, L. Schultz: Evolution of magnetic domain structures and coercivity in high-performance SmCo 2:17 type permanent magnets, *Acta Mat.* **54**, 997–1008 (2006)
49. K. Khlopkov, O. Gutfleisch, D. Hinz, K.-H. Müller, L. Schultz: Evolution of interaction domains in textured fine-grained Nd₂Fe₁₄B magnets. *J. Appl. Phys.* **102**, 023912, (2007)

Chapter 11

Exchange-Coupled Nanocomposite Permanent Magnets

J.P. Liu

Abstract Exchange-coupled nanocomposite magnets are a new type of permanent magnetic materials. Large amounts of theoretical and experimental research have been carried out in the past two decades in understanding the inter-phase exchange interactions and in processing bulk nanocomposite magnets with enhanced energy products. This chapter reviews recent advancements in both the fundamental research and the materials processing technologies. Details in the new findings about the effects of soft phase properties and interface conditions on the hard/soft phase exchange interactions are presented. Various methods for characterizing the inter-phase exchange coupling are reviewed. In materials processing aspects, the development of the bottom-up approaches is discussed. Novel methodology for nanoparticle synthesis including the salt-matrix annealing and surfactant-assisted ball milling is described. Unconventional compaction techniques including warm compaction and dynamic compaction are recommended because they can be used to retain the desired nanoscale morphology for effective exchange coupling in the nanocomposites. At the end of this chapter, perspectives on fabrication of anisotropic nanocomposite magnets are given.

11.1 Introduction

When Coehoorn and his coworkers discovered in 1989 [1] the inter-phase exchange coupling that enhanced the remanent magnetization and the energy product in the rapidly quenched $\text{Nd}_2\text{Fe}_{14}\text{B}-\text{Fe}_3\text{B}$ two-phase ribbons with very fine grain size, their report did not draw immediate attention. Addition of soft magnetic phases was normally considered harmful to performance of conventional permanent magnets

J.P. Liu (✉)

Department of Physics, University of Texas at Arlington, Arlington, TX 76019, USA
e-mail: pliu@uta.edu

because it dramatically deteriorates magnetic coercivity of sintered or cast single-phase permanent magnets and therefore reduces the energy product.

Two years later, Kneller and Hawig [2] published their simulation model of an exchange-coupled hard/soft nanocomposite magnet (also called an exchange-spring magnet) based on the experimental finding by Coehoorn et al. The model shows that the nanocomposite magnets with desired nanoscale morphology would be a new approach to obtain high energy products in permanent magnetic materials. This paper triggered off a strong reaction in the community. Since 1992 a great deal of experimental and theoretical work has been devoted to investigation of exchange-coupled nanocomposite systems. Various hard–soft composite systems were studied using different processing techniques including rapid quench, mechanical alloying, and thin film deposition. Remarkable results in remanent magnetization enhancement and energy product enhancement have been reported in nanocomposite ribbons, powders, and thin films [3–11].

Since 2001, a research team in the United States led by the author of this chapter started a bottom-up approach – a processing approach starting from nanoparticles, to produce nanocomposite permanent magnets with well-controlled nanoscale morphology. Zeng et al. [12] demonstrated in 2002 FePt/Fe₃Pt nanocomposite magnets with ~40% enhanced energy products compared to the single-phase FePt counterpart. This kind of thin-layer nanocomposite magnets was made from the FePt/Fe₃O₄ nanoparticle self-assemblies with particle size of several nanometers.

Great efforts to produce bulk nanocomposite magnets have also been made by the team since 2001. Chen et al. [13] reported shock compaction of Nd₂Fe₁₄B-based nanocomposite ribbons and nearly fully dense bulk samples with retained nanoscale grain size and magnetic properties. Rong et al. [14] fabricated bulk FePt/Fe₃Pt nanocomposite magnets with density higher than 95% of the theoretical density by directly compressing FePt/Fe₃O₄ nanoparticles using a warm compaction technique. Recently, Rong et al. [15] showed the results of SmCo₅/α-Fe fully dense bulk nanocomposite magnets produced by warm compaction with ~90% energy product enhancement in comparison to the single-phase counterpart.

Permanent magnetic materials, since their first application as compasses thousands of years ago in ancient China, have been indispensable in human civilization. Today, conventional and advanced applications of permanent magnets are still growing in a large scale, like in computer devices, MEMS, biomedical facilities, and in the energy-related applications such as in hybrid vehicles and wind power generators. Discovery of nanocomposite magnets has opened a new chapter in the history of permanent magnet development. A timely marriage with nanotechnology has revived the research in both the fundamentals and the materials processing of advanced permanent magnetic materials. Exchange-coupled nanocomposite permanent magnets are at the center of the research stage. In this chapter we will review the major development and milestones in the fundamental study and experimental research in exchange-coupled nanocomposite magnets. Emphasis will be given to recent advancements in understanding the exchange coupling and in processing of bulk nanocomposite magnets.

11.2 Fundamental Aspects

11.2.1 The Early Models

Energy product $(BH)_{\max}$, the figure of merit of permanent magnets, of a ferromagnetic material is based on magnetization and coercivity (originating from magnetocrystalline anisotropy) of the material. Energy product of permanent magnets has been increased from less than 1 MGOe to more than 50 MGOe in the last century. This impressive many-fold leap was based on successive discoveries of novel magnetic compounds, especially the rare earth–transition metal compounds discovered in the 1970s and 1980s. Since the discovery in early 1980s of $\text{Nd}_2\text{Fe}_{14}\text{B}$ compound, which is the major phase of the strongest permanent magnets thus far, people have continued to search for even better hard magnetic materials to beat the neodymium magnets. For a quarter century, the search has not achieved anticipated results. It should not be a surprise if one says that there is very low probability for nature to construct a magnetic structure with significantly higher magnetization and magnetocrystalline anisotropy as well as Curie temperature than $\text{Nd}_2\text{Fe}_{14}\text{B}$. It is even obvious for many that to realize further increase of energy product (hopefully as what we had in last century), we have to look for other approaches instead of just searching for new compounds because the highest magnetization and anisotropy possibly coexisting in one magnetic phase will not increase with time.

If nature does not provide a desired magnetic structure for new permanent magnets, artificially constructed magnetic structures (referred also as *metamaterials*) can then be a solution. Based on the experimental observation by Coehoorn et al. [1], Kneller and Hawig [2] proposed a new micromagnetic principle for producing

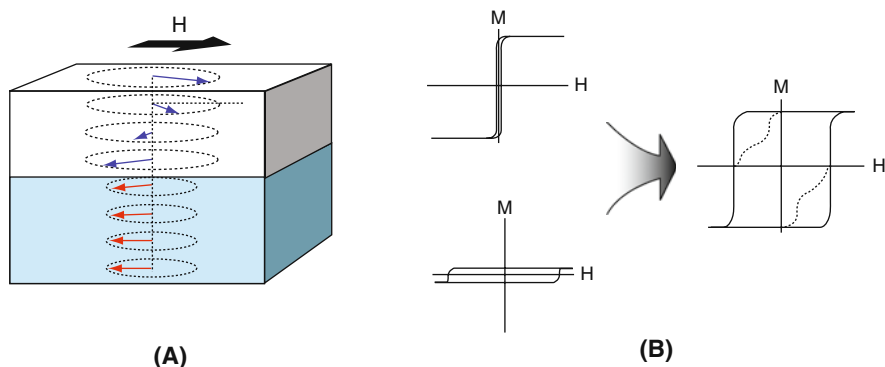


Fig. 11.1 (A) A bilayer structure with a hard phase *bottom* layer and a soft phase *top* layer. (B) Exchange coupling between a magnetically soft ferromagnet with a tall hysteresis loop and a magnetically hard ferromagnet with a wide hysteresis loop leads to a beneficial combination of the two loops – formation of a composite with a wide and tall hysteresis loop. The *dashed* loop with kinks refers to a decoupled composite with the wide and the tall loops superposed

strong permanent magnets by fabricating nanostructured hard/soft phase composite materials. The principle was derived from a one-dimensional model with alternating hard and soft phase regions. Figure 11.1 shows the schematic of a hard/soft bilayer structure with inter-phase exchange coupling. When the soft phase layer (upper layer) is thin enough, magnetic moments in both layers will be switched coherently. The magnetization loops of the bilayer will then be like the loop indicated by the arrow. With the geometry of the composite suggested by Kneller and Hawig, the hard phase volume fraction may be as low as 10% without losing coercivity necessary for a high energy-product value.

Schrefl et al. [16] used a finite element method to analyze a hard–soft composite structure with soft phase grains embedded in the hard phase matrix and concluded that in order to introduce magnetic hardness from the hard phase into the soft magnetic regions, a size of the soft phase region smaller than twice the domain wall width of the hard phase is required.

Skomski and Coey [17] investigated more geometrical configurations of hard/soft phase composites by considering the following energy items in a ferromagnetic composite:

$$E = \int \left[A \left(\nabla \frac{\mathbf{M}}{M_s} \right)^2 - K_1 \frac{(\mathbf{n} \cdot \mathbf{M})^2}{M_s^2} - \mu_0 \mathbf{M} \cdot \mathbf{H} \right] dV \quad (11.1)$$

In the bracket the first term is the energy of magnetic exchange interaction, A is the exchange stiffness. The second term is the anisotropy energy. K_1 is the anisotropy constant. \mathbf{n} is the unit vector in the easy-axis direction. The third term is the magnetostatic energy. Magnetic moment configuration is determined by competition between these terms. Exchange interaction favors parallel spin alignment, whereas the random anisotropy, supported by random magnetostatic fields, tends to disalign the spins.

By minimizing the energy, equilibrium conditions can be obtained and the equilibrium parameters can be calculated by solving the equations with approximation. One of the assumptions and approximations in solving the equations is that K_1 of a soft phase is zero. Based on the approximation, a similar conclusion about soft phase critical dimension was drawn as what Schrefl et al. obtained [16]. Skomski and Coey have been frequently cited for their calculated result about the energy product of 120 MGOe possibly achieved in an ideal $\text{Sm}_2\text{Fe}_{17}\text{N}/\text{FeCo}$ multilayer nanocomposite structure.

Sabiryanov and Jaswal [18, 19] calculated by first principles the theoretical values of energy products of the FePt–Fe and the SmCo–Co layered systems. They found that the energy products for these two systems can reach 90 and 65 MGOe, respectively.

Kronmüller et al. have done a systematic study in micromagnetic simulation of the exchange-coupled nanocomposite systems; the details can be found in Ref. [20] and references therein.

11.2.2 The Soft Phase Effects

The above-mentioned micromagnetic models did not take anisotropy of soft magnetic phases into account, as an approximation that helps for solving the equations, which leads to a conclusion that no matter what kind of soft phases are used, the critical dimension of the soft phases for effective exchange coupling remains unchanged for a given hard magnetic phase. This conclusion, however, sounds unrealistic since soft magnetic phases may have very different properties and as one of the two components in a nanocomposite magnet, the properties of the soft phases should have important effect on the inter-phase exchange coupling. Our simulations and experimental investigations [21, 22] have shown that the early models need to be amended. The critical soft phase length is also related to the soft phase properties if we do not ignore the anisotropy of the soft phase component in the composite. Magnetization values of the soft phases also have a strong effect on the critical dimension. Equation (11.2) is an analytical solution for the critical soft phase dimension derived from a simple exchange-coupled bilayer system:

$$t_{S-Critical} = \frac{J/M_S}{\frac{2K_H t_H - J}{M_H t_H} - \frac{2K_S}{M_S}} \quad (11.2)$$

where J is the exchange strength, K 's are anisotropy constants, and M 's are saturation magnetizations (subscripts S and H denote the soft phase and the hard phase, respectively).

This equation reveals that the soft phase magnetization and anisotropy have a direct effect on the critical soft phase dimension. A "less soft" phase will lead to a larger critical soft phase dimension.

In a more sophisticated modeling analysis in which we consider a twist structure of magnetic moments in soft magnetic phases (see Fig. 11.1A) under a magnetic field which is close to practical situation, the exchange field, H_{ex} , between the hard and soft phase can be expressed as the following [22]:

$$H_{ex} = -(2\sqrt{K_S A_S})/(M_S t_S) \quad (11.3)$$

where A_S is the exchange interaction strength in the soft phase and other parameters have the same meanings as in Eq. (11.2).

We can see from these two equations that the exchange strength between the hard phase and the soft phase is strongly dependent on the soft phase parameters. The soft phase critical dimensions in various hard phases have been calculated according to this equation, and a good agreement with experimental results has been achieved. Table 11.1 shows the values of critical soft phase dimensions determined with the old model and our new model as well as the experimental data for Fe and Co soft phase layers on SmCo layers obtained. Related data for several other soft phases are also listed in the table. It is interesting to see the big difference between the critical dimensions for Fe and Co. It is also seen that according to our

Table 11.1 Critical dimensions (t_C) of soft phase in hard/soft exchange-coupled nanocomposite magnets

	M_s (10^6 A/m)	A (10^{-11} J/m)	K (10^5 J/m ³)	t_{C^*} (nm)	$t_C^{\textcircled{R}}$ (nm)	$t_C^{\textcircled{R}}$ (SmCo) (nm)	$t_C^{\textcircled{R}}$ (NdFeB) (nm)
Fe	1.70	2.8	0.47	2.7–9.0	2.5–10	4.4–6.0	9.2
Fe ₉₇ Si ₃	1.58	2.6	0.47	2.8–9.3	–	4.4–6.0	9.2
Fe ₃ B	1.29	1.25	0.32	6.2–20.7	–	4.4–6.0	9.2
Fe ₆₅ Co ₃₅	1.93	3.6	3.11	6.9–23.1	–	4.4–6.0	9.2
Co	1.40	4.0	8.00	16.2–53.9	>20	4.4–6.0	9.2
NdCo	0.68	1.05	6.20	15.0–50.0	>7.8	4.4–6.0	9.2

t_{C^*} is calculated from $H_{\text{ex}} = 4(AK)/M_s t$, $t_C = 2t$ for the single-phase-like reversal between 0.3 and 1.0 T. $t_C^{\textcircled{R}}$ is the experimental results for SmCo/(Fe,Co) bilayers, $t_C^{\textcircled{R}}$ is from the model of Kneller and Hawig. A values for Fe₉₇Si₃ and Fe₆₅Co₃₅ are estimated from their Curie temperatures, 963 and 1253 K, respectively.

new model, FeCo alloy with proper composition is the best soft phase for exchange-coupled nanocomposite magnets due to its high magnetization and relatively high anisotropy.

A more detailed micromagnetic analysis by Asti et al. [23] has reached a similar conclusion to the above statement about the correlation between the soft phase “hardness” and the critical dimension.

Recently, we have investigated experimentally the effect of soft phases on the exchange coupling using combinatorial synthesis technique to produce hard/soft phase bilayer “libraries” with continuously varying soft phase composition and thickness. Zambano et al. [24] found that within the range of relatively low anisotropy of soft magnetic phases, magnetization of the soft phases plays the major role in determining critical dimension.

Clearly, the above discussed modeling and experimental investigations have provided a deeper insight into the soft phase effect on inter-phase exchange coupling and have opened a general approach to “materials design” of exchange-coupled nanocomposite magnets by engineering the soft phase components.

11.2.3 The Interface Effects

Effect of interface on the inter-phase exchange coupling was another unclear issue when exchange-coupled nanocomposite magnets came to the landscape. An intuition may tell that interface plays little role in magnetic interactions since the interactions are mainly a function of distance. Inter-phase magnetic interactions, especially the exchange interactions, are still new to the community.

Our early experiments in heat treatments of SmCo/Fe nanocomposite magnetic thin films revealed that a multi-step heat treatment processing could improve the magnetic performance significantly, even though the late step of the treatments did

not alter the composite compositions and microstructures [25]. An inference was that the interface condition was changed upon the late step treatment. However, to explore the interface in solid metallic materials is a centennial challenge and it is even more difficult to study the interface in a nanocomposite material.

A pioneering work by Jiang et al. [26] showed that inter-diffused interface resulted in a greatly enhanced energy product in a SmCo/Fe nanocomposite. A careful investigation with nanoscale composition profile determination suggested that the intermixing led to the formation of a region with intermediate anisotropy values, thus making the demagnetization process more single-step-like reversal. In comparison with a sharp interface, the graded interface created a region in the soft phase side that is “less soft” (or “semi-hard”) so that the “used-to-be soft phase region” became more resistant to magnetization reversal and thus increased the apparent coupling effectiveness between the soft and the hard phases. This result is also consistent with the conclusion we just discussed in the last section about the soft phase effect. An intermixed boundary means a direct contact of a hard phase with a semi-hard phase at the interface.

Figure 11.2 is the simulation result by Jiang et al. [26] showing correlation between the intermixed interface thickness and the demagnetization curves of the SmCo/Fe nanocomposite. It is found that increased inter-diffusion enhances the energy product by up to 30%. A recent detailed investigation based on element-specific magnetization measurements using synchrotron X-ray performed by Choi et al. [27] has given more quantitative information about the interface effects. A first-principles calculation on SmCo₅/Co(Fe) interface reached a similar result [28]. A conclusion can be therefore drawn that a graded interface structure that forms a wave-like composition profile in a nanocomposite will give rise to a further enhanced energy product in exchange-coupled spring magnets.

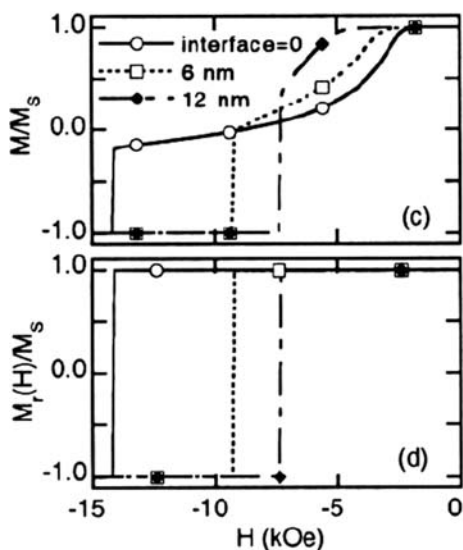


Fig. 11.2 Calculated demagnetization and remanence curves of SmCo(20 nm)/Fe(10 nm) bilayers with interfacial regions of various thickness (from Jiang et al. [26])

11.2.4 Coercivity Mechanisms

Understanding of the soft phase effect and the interface effect is not the end of understanding of all the fundamental aspects on exchange-coupled nanocomposite magnets. There are still issues to be understood. One of the unclear problems is the coercivity mechanisms in nanocomposite magnets.

Although early theoretical models showed that more than 50% soft phase can be added to the nanocomposite magnets to achieve high-energy products, practically, however, any addition of soft phase is accompanied with sacrifice in coercivity. A trade-off between the magnetization and coercivity is a major barrier for experimentalists to reach high-energy products in nanocomposite magnets. Therefore, coercivity is a restricting factor for obtaining high-energy products in soft/hard nanocomposite magnets.

People have tried to explain coercivity mechanisms in exchange-coupled nanocomposite magnets with the conventional reversal domain nucleation or domain wall pinning models. In exchange-coupled soft/hard nanocomposite magnets, however, the situation seems more complicated. Coercivity dependence on soft phase dimension has been observed by researchers from different groups. We reported in 1998 [29] that the coercivity mechanism changes from pinning-like to nucleation-like in PrCo–Co nanocomposite with increasing Co layer thickness, as observed from the initial magnetization curves. In contradiction to this observation, Zhao et al. [30, 31] reported that in the nanocomposite systems under their investigation, relatively thinner soft phase layers lead to a nucleation mechanism whereas in the composite with thicker soft phase layers, pinning is dominant.

The complication in coercivity mechanisms may be related to the nature of *interaction domains* with which a single domain contains multiple nanoscale grains with different crystalline orientation [32]. Further investigation is highly needed to understand the domain structure and coercivity mechanism in the hard/soft phase nanocomposite magnets.

11.2.5 Characterization of Inter-phase Exchange Coupling

To exchange, or not to exchange? This is a good question, especially for the new case of *inter-phase* exchange interactions. People have gained considerable knowledge and experience in studies of magnetic exchange interactions of inter-spin, inter-atom, inter-molecule, inter-sublattice, inter-layer and so on. Inter-phase magnetic exchange coupling (sometimes referred as “inter-grain” exchange interactions because granular materials are the most common situation in composite magnetic materials) seems to be more difficult to understand than the above-mentioned cases because the inter-phase interactions are often influenced by many factors that are difficult to quantify, like the grain size and shape, and interface conditions. In addition, the inter-phase exchange interactions in composite magnets always coexist with magnetic dipolar interactions. Characterizing and distinguishing these interactions become nontrivial and even very challenging. In this section we briefly review the major characterization methods to identify inter-phase exchange coupling in nanocomposite magnets.

11.2.5.1 The “Kink” Method

The simplest way to check the inter-phase exchange coupling is to measure a hysteresis loop of a nanocomposite magnet. In case of “decoupling” between the two phases, there will be a kink (or shoulder) on the curve. The kink originates from superposed loops of a composite sample from its hard and soft component loops, as we can see from Fig. 11.1B. This method, however, does not distinguish single-phase loops and loops of effectively exchange-coupled nanocomposite magnets.

11.2.5.2 Low-Temperature Measurements

To distinguish a single-phase loop and a loop of well-exchange-coupled nanocomposite magnet, low-temperature measurements are often helpful. If magnetocrystalline anisotropy of the hard phase component in the composite is enhanced at low temperatures (this is the normal situation), the exchange length will be decreased at a low temperature which will lead to a decoupling between the hard and soft phase components [33, 34]. Figure 11.3 shows magnetic hysteresis loops at different temperatures of a PrCo–Co nanocomposite magnet. One sees that at 300 K, the magnetization reversal behavior is almost one-step mode (effectively exchange coupled). At lower temperatures, however, two-step magnetization reversal becomes more pronounced because of decoupling. This temperature-induced two-step mode cannot be observed in single-phase ferromagnetic materials at any temperature.

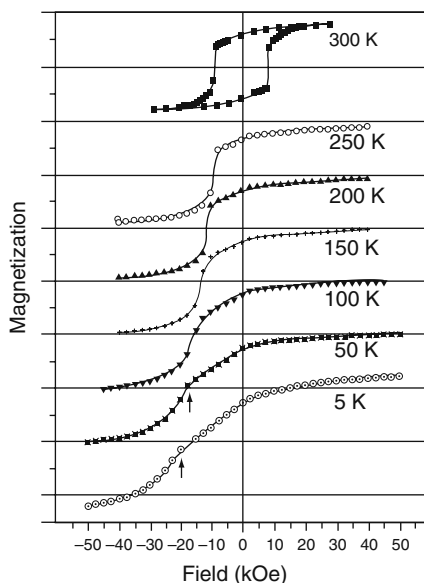


Fig. 11.3 Hysteresis loops of PrCo–Co nanocomposite at different temperatures (from Liu et al. [34])

11.2.5.3 Recoil Loop Measurements

Recoil loops are measured by removing and reapplying a demagnetizing field to a ferromagnetic material, as the demagnetizing field is increased successively. Open recoil loops refer to the situation where the magnetizing and demagnetizing branches do not overlap, thereby enclosing an area [33, 35, 36]. Recoil measurements are often used to characterize exchange-coupled nanocomposite permanent magnets because the recoil characteristics are sensitive to inter-phase interactions. Open recoil loops are observed in hard/soft nanocomposite magnets, and thus the presence of open recoil loops is seen as a manifestation of breakdown in the exchange coupling and the enclosed area is attributed to the decoupled volume in the soft phase. Figure 11.4 shows recoil loops measured on three SmCo/Fe bilayers with different Fe layer thicknesses. Recent studies show that additional factors like magnetocrystalline inhomogeneity in the hard phases and thermal fluctuation also have influence on the openness of recoil loops [37, 38].

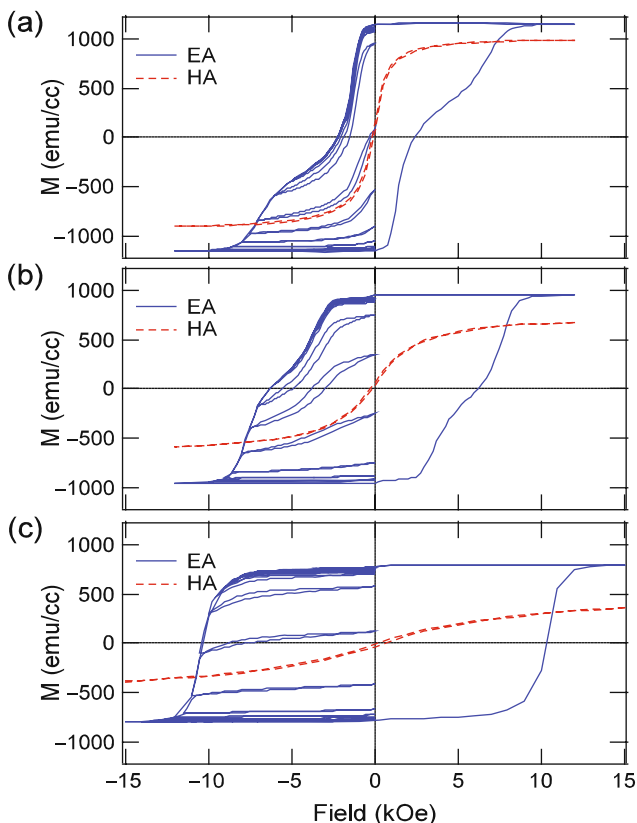


Fig. 11.4 Recoil hysteresis loops measured on SmCo(20 nm)/Fe(x nm) bilayers with different Fe thicknesses. (a) $x = 20$; (b) $x = 10$; (c) $x = 5$. The recoil loop measurements were done along the easy axis (EA). Hard axis (HA) measurements are also shown

11.2.5.4 δM Method (Henkel Plot)

δM measurement (Henkel plot) method is based on a comparison between remanent magnetization of a ferromagnetic sample to an ideal Stoner–Wohlfarth (S–W) system so that any magnetic interactions in the sample can be characterized. To make the comparison, two different remanent magnetizations must be measured. One is the magnetization remanence $M_r(H)$ which is acquired after the application and subsequent removal of a directly applied field H . The other is demagnetization remanence $M_d(H)$ which is obtained after saturation in one direction and the subsequent application and removal of a direct field H in the reverse direction. A linear relation between these remanences exists in a noninteracting S–W ferromagnetic system [39]:

$$M_d(H) = 1 - 2M_r(H) \tag{11.4}$$

It should be noted that this relation is only valid with an initial zero-magnetization sample. Henkel first proposed that the deviation from zero magnetization in real systems is caused by magnetic interactions in the system [40]. The expression of a Henkel plot is as follows:

$$\delta m(H) = [M_d(H) - M_r(\infty) + 2M_r(H)] / M_r(\infty) \tag{11.5}$$

where $M_r(\infty)$ is the saturation remanence introduced to normalize the $\delta m(H)$ value.

Normally, positive values of $\delta m(H)$ are due to exchange interactions promoting the magnetized state, while negative values of $\delta m(H)$ are caused by interactions tending to assist magnetization reversal (e.g., dipolar interaction). Figure 11.5 shows the Henkel plots for FePt–Fe₃Pt nanocomposite magnets with different soft phase fraction. The positive values are interpreted as a result of magnetic exchange coupling while the negative values are interpreted as a result of magnetic dipolar interaction. It is interesting to see that the dipolar interaction is enhanced with increasing soft phase.

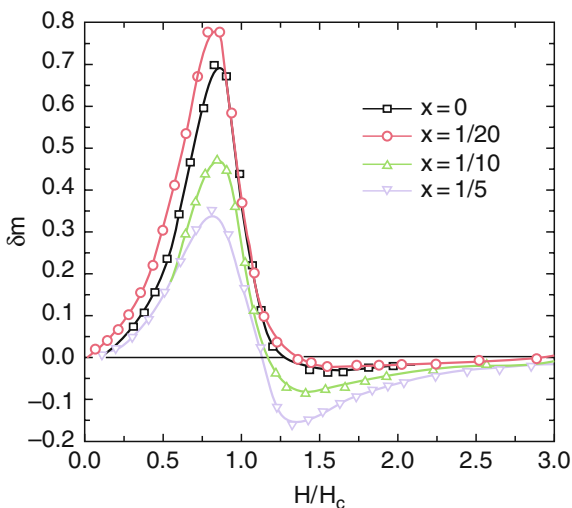


Fig. 11.5 δm plots of FePt–Fe₃Pt nanocomposites displaying the magnetic interactions between compacted nanoparticles. The x values represent the weight portion of Fe₃O₄ nanoparticles that are the precursor of the soft phase added into FePt nanoparticles before a heat treatment

11.2.5.5 Element-Specific Measurements (Synchrotron Measurements)

Synchrotron-based X-ray magnetic measurements are used to characterize exchange-coupled composite magnets because the X-ray measurements enable characterizing different elements separately, by taking advantage of enhanced magnetic sensitivity to a resonant element when the incoming X-ray energy is tuned to an atomic absorption edge of the element of interest [41]. In comparison with conventional magnetometry techniques that measure the overall magnetic behavior, the X-ray measurements can distinguish magnetic contributions from individual components in composite magnets. Using this technique, element-specific magnetic hysteresis loops can be obtained from a composite magnet, and the effect of exchange coupling between constituting layers or phases can be inferred by correlating the result with the overall hysteresis loops from a conventional magnetometer. Figure 11.6 shows element-specific hysteresis loops from SmCo/Fe bilayers

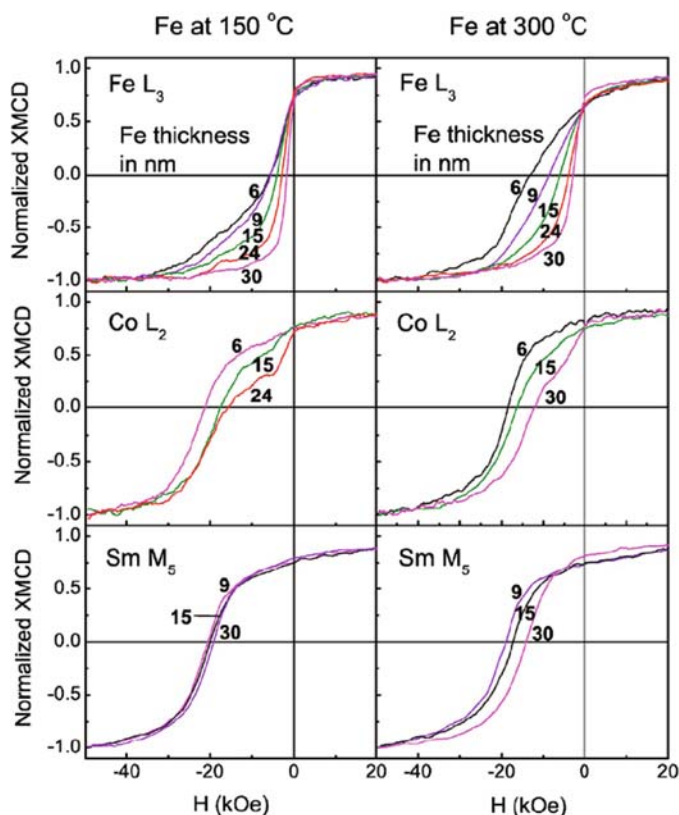


Fig. 11.6 Element-specific hysteresis loops from SmCo/Fe bilayer films with gradient Fe thickness [42]. The hysteresis loops were measured by collecting fluorescence yields at the Fe L_3 , Co L_2 , and Sm M_5 absorption edges

that were grown via a combinatorial approach [42]. Here, X-ray magnetic circular dichroism measurements were performed as a function of external field while collecting magnetic dichroic signals. Separate measurements with the incident X-ray energy near the Sm, Co, and Fe resonant energies provide magnetic behavior of each element so that magnetic exchange coupling can be observed between the hard phase elements and the soft phase elements.

Besides the above discussed methods, there are also a few other techniques that can be used to detect and characterize inter-phase exchange coupling. In the early paper by Kneller and Hawig [2], the authors suggested a method to judge the inter-phase exchange coupling by observing shapes of the hysteresis loops and by measuring “half-way” demagnetization curves. We also used a simple method to detect the exchange-spring behavior by measuring the $M_r(H)$ curve [29]. Davies et al. [43] discussed a first-order reversal curve (FORC) method based on analysis of FORC distribution that provides information about irreversible switching processes and switching fields. In exchange-coupled magnets, collective switching behavior of soft and hard phases can be detected by monitoring the onset of irreversibility in FORC curves.

The complex nature of inter-phase exchange interactions gives rise to difficulties in identifying and characterizing the interactions. To determine and characterize the inter-phase magnetic exchange interactions with enhanced reliability and accuracy, using more than one of the methods for a “double check” is suggested.

11.3 Experimental Approaches

As discussed above, remarkable progress has been made recently in understanding inter-phase magnetic interactions in nanocomposite magnets. The study in inter-phase magnetic interactions deals with “large objects” compared with the research on magnetic interactions between “small objects” like atoms and molecules and morphological parameters such as grain size and interface conditions have to be considered in the study. This study is significant for materials design and has resulted in an “exchange coupling” between the fundamental magnetism research and the materials processing research. Next we will review recent progress in materials processing of nanocomposite magnets.

11.3.1 The Early Approaches

After Coehoorn et al. [1] first observed the experimental evidence of inter-phase (inter-grain) exchange coupling in their melt-spun $\text{Nd}_2\text{Fe}_{14}\text{B}/\text{Fe}_3\text{B}$ permanent magnet, many groups have studied rapidly quenched hard/soft nanocomposite magnets [3, 4, 43–45]. Remarkable remanent magnetization enhancement and energy product enhancement have been observed in isotropic or partially anisotropic ribbons. The processing includes rapid quench and subsequent heat treatments. The quench

process is for producing amorphous materials and the heat treatments are for crystallization with controlled nanoscale grain size. Rapid quench technique has the advantage of accurate overall composition control and is also good for mass production. The disadvantages include inhomogeneity in microstructure in the ribbons. Grain size distribution can be very large (usually larger than 100%).

Mechanical alloying technique has also been adopted in producing nanocomposite magnets [5, 6, 46, 47]. This method is suitable for systems that cannot be easily quenched to form amorphous materials. High-energy mechanical deformation during the mechanical movement deposits large amounts of energy into the raw materials and amorphous powders are therefore formed. Similar to that in the rapid quench technique, subsequent heat treatments can produce nanocrystalline composite materials. Disadvantage of this method includes contamination of the raw materials from the containers and vibration materials (like metallic balls).

As for modeling system investigations, many groups studied hard/soft bilayers and multilayer nanocomposite magnets [7, 10, 48–52]. Most of the bilayer and multilayer thin films were prepared by sputtering followed by heat treatments to obtain required microstructures. It was found that rapid thermal annealing (RTA) is more effective in tailoring nanoscale morphology than the conventional furnace annealing.

11.3.2 Nanoparticle Approaches

Since 2001, our research team has started to build up nanocomposite magnets with magnetically hard and soft nanoparticles. By self-assembly of chemically synthesized 4 nm FePt and Fe₃O₄ nanoparticles, homogenous FePt/Fe₃Pt hard/soft phase nanocomposites were formed after annealing the assemblies in a reducing atmosphere. Up to 40% energy product enhancement has been achieved compared to the single-phase counterpart [12]. This work signified a novel approach from the bottom to control nanoscale morphology of nanocomposite magnets. The advantage of this approach is clear: the composite morphology can be well controlled since the building blocks of the composites have their size starting from a few nanometers. Even after grain growth during subsequent heat treatments, the grain size can be well controlled below the critical length for effective exchange coupling. On the other hand, success of this bottom-up approach also relies on synthesis of hard and soft phase magnetic nanoparticles with controllable size and size distribution which is a significant challenge itself. Next we will review the major methods used to produce hard and soft magnetic nanoparticles for building up nanocomposite magnets.

11.3.2.1 Chemical Synthesis of Nanoparticles

Compared with other methods for preparing nanoparticles, the chemical solution method has its unique advantages in producing particles with small particle size (down to 2 nm) and narrow size distribution (deviation can be as small as 5%), as

well as good crystallinity and stability. Sun et al. [53] reported in 2000 synthesis of FePt nanoparticles with well-controlled size and size distribution which were the first available nanoparticles of a hard magnetic phase. We have worked since then in size and shape control of FePt nanoparticles.

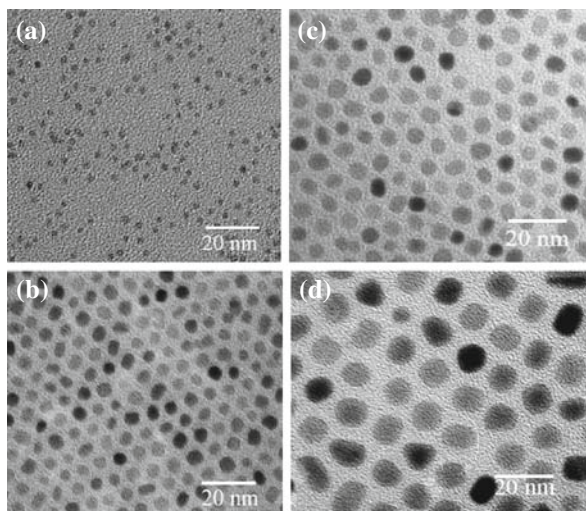


Fig. 11.7 TEM images of the as-synthesized FePt nanoparticles with size of (a) 2 nm, (b) 5 nm, (c) 6 nm, and (d) 9 nm

Figure 11.7 shows the TEM images of as-synthesized FePt nanoparticles with different sizes. By adjusting synthesis parameters we have been able to obtain FePt nanoparticles with size from 2 to 9 nm with 1 nm accuracy [54]. We also worked in shape control of FePt nanoparticles. Nanorods and nanowires with controlled length have been synthesized. Figure 11.8 shows some examples [55]. Shape control of

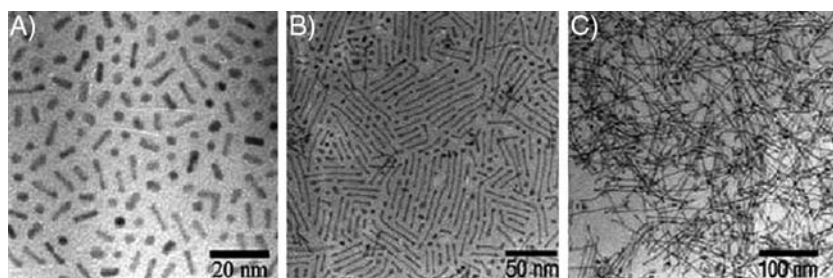


Fig. 11.8 TEM images of FePt nanorods/nanowires with average length of (A) 15 nm, (B) 50 nm, and (C) 150 nm

the nanoparticles gives the possibility to align the building blocks by using shape anisotropy to form anisotropic nanocomposite magnets.

11.3.2.2 Salt-Matrix Annealing

FePt nanoparticles are the first ever available nanoparticles of hard magnetic phases, thanks to the pioneering work by Sun et al. [53]. However, as-synthesized FePt nanoparticles always take a disordered fcc structure that has vanishing magnetic anisotropy and therefore the particles display superparamagnetism at room temperature. The real FePt hard magnetic phase is the $L1_0$ phase with a tetragonal structure. The fcc structure can be transformed to the $L1_0$ structure only after heat treatments at temperatures above 600°C . At these high temperatures, unfortunately, monodisperse nanoparticles agglomerate and sinter together that spoils monodisperse nanoscale morphology. To solve this problem, a great deal of effort was made by doping elements to reduce the transformation temperature and by coating high-melting-point oxide layers on the fcc particle surfaces. In 2005, we first adopted the salt-matrix annealing technique and successfully solved the problem in a facile way [56–58]. Figure 11.9 shows the TEM images of the FePt nanoparticles before and after the high-temperature salt-matrix annealing. Application of this technique has led to scalable production of ferromagnetic FePt nanoparticles of few nanometers with giant room-temperature coercivity (up to 30 kOe). The recovered nanoparticles after annealing contain no non-magnetic impurity and are therefore very suitable for permanent magnet fabrication. Availability of single-domain ferromagnetic

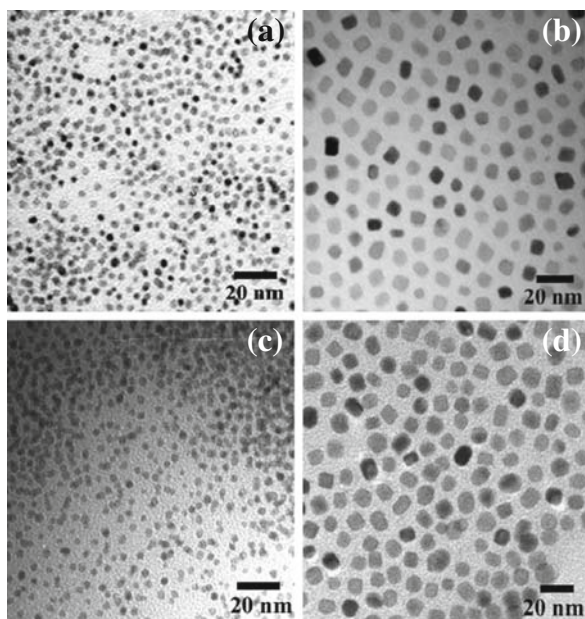


Fig. 11.9 TEM images of the as-synthesized (a) 4 nm and (b) 8 nm particles. (c) and (d) are the images of the 4 and 8 nm particles after salt-matrix annealing at 700°C for 4 h, respectively

nanoparticles also opens a new window for further exploration of low- and high-dimensional magnetic materials and devices with controlled magnetic structures (including high-density data storage media). This technique is also economic and can be used for preparing any other nanostructures that need to be heat treated without sintering.

Chemical synthesis has worked very well in producing hard magnetic FePt nanoparticles (in combination with the special heat treatment techniques). It is natural for people to attempt to produce other hard magnetic nanoparticles including the rare earth-containing SmCo and NdFeB nanoparticles. Great efforts have been made to synthesize SmCo nanoparticles with various chemical methods, but no room-temperature coercivity of the produced nanoparticles was reported [59–61]. The reason is not difficult to understand: rare earth metallic materials are very sensitive to oxygen and their nanoparticles are even more prone to oxidation because of the huge surface area of nanoparticles. Hou et al. [62] developed a method to synthesize SmCo₅/Fe nanocomposite particles with micrometer size by reducing SmCoO nanoparticles with Ca. To prevent excessive grain growth, KCl was added, similar as in the salt-matrix annealing. It turned out that KCl also played a good role in preventing the Sm loss during the reduction.

11.3.2.3 Surfactant-Assisted Ball Milling

Given the importance for applications of single-domain hard magnetic nanoparticles with size of few nanometers, and the difficulties in preparing the rare earth-containing nanoparticles by chemical methods, an alternative ball milling method has been developed to obtain nanoparticles directly from ingots of SmCo and NdFeB hard magnetic materials. By using suitable surfactants, nanoparticles of the ingot materials can be obtained. Those nanoparticles, however, have large-size distributions. A size selection process was then necessary to obtain nanoparticles with desired size ranges. This process has led to first available SmCo and NdFeB nanoparticles with room-temperature coercivity [63, 64]. Figure 11.10 shows the TEM images of the Sm₂Co₁₇ nanoparticles. Room-temperature coercivity up to 3 kOe has been obtained from the nanoparticles with size larger than 10 nm, which were the first ferromagnetic rare earth intermetallic nanoparticles with significant room-temperature coercivity.

11.3.2.4 Gas-Phase Condensed Nanoparticles

Besides the methods discussed above, gas-phase condensation has also been used to produce FePt nanoparticles and FePt-based nanocomposite particles. The particles are formed in a plasma sputter chamber with controlled pressure and temperature. Rui et al. [65] reported energy product of 25 MGOe of isotropic FePt–Fe₃Pt nanocomposite particle assemblies prepared by gas-phase condensation. Chen et al. [66] and Qiu and Wang [67] have worked to obtain direct ordering of FePt

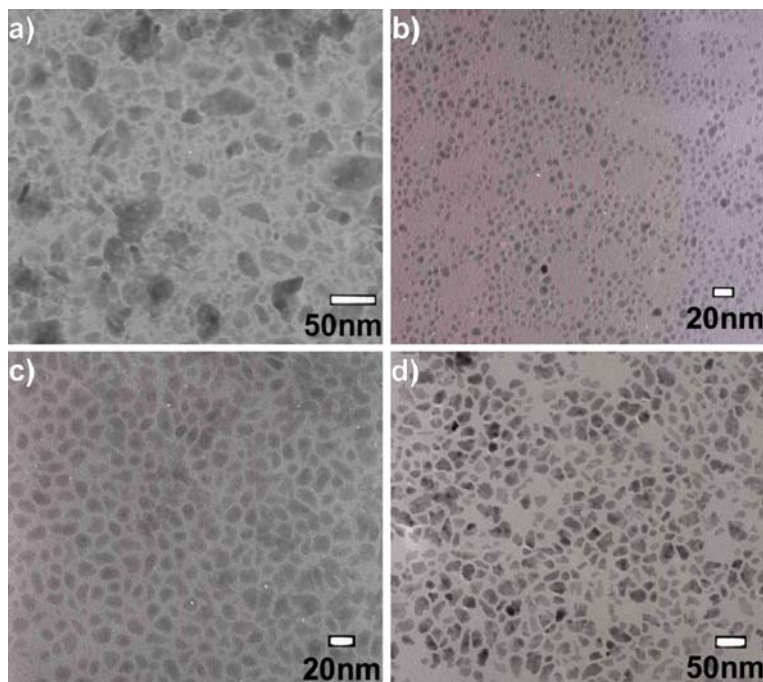


Fig. 11.10 Nanoparticles of $\text{Sm}_2\text{Co}_{17}$ produced by surfactant-assisted ball milling: (a) without size selection; (b) selected particles with average size <10 nm; (c) with size in $10\text{--}20$ nm; (d) with size in $20\text{--}30$ nm

nanoparticles using the plasma sputtering technique. Ferromagnetic FePt nanoparticles with L1_0 structure were obtained upon deposition.

11.3.2.5 Core/Shell Structured Nanoparticles

Self-assembly of hard and soft phase nanoparticles is a good way to obtain well-mixed nanocomposite magnets because it leads to an intimate contact between two phases and a highly homogenous distribution of the two phases which are essential for effective inter-phase exchange coupling. However, self-assembly does not always take place in nanoparticles. Conditions for self-assembly include a suitable size difference between the components and an extremely narrow size distribution of each component. These conditions are not easy to be met experimentally. In addition, these conditions may also bring restrictions in nanocomposite composition adjustment.

An excellent way to solve this dilemma is to prepare core/shell nanoparticles. Figure 11.11 shows an example of FePt/Fe₃O₄ core/shell nanoparticles with tunable shell thickness. After reductive heat treatments, the oxide shells transform to soft magnetic Fe or Fe₃Pt phases. Then each nanoparticle is an exchange-coupled

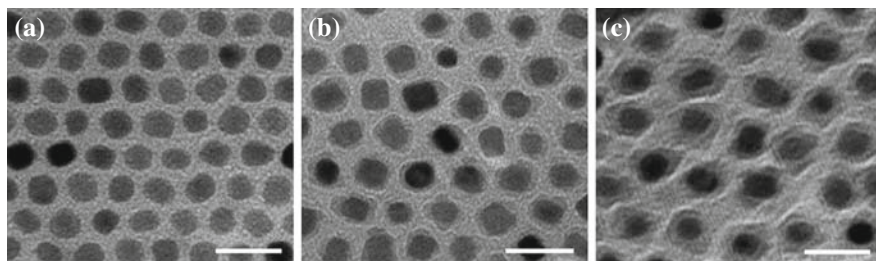


Fig. 11.11 TEM images of the as-synthesized (a) 7 nm FePt nanoparticles; (b) 7 nm FePt nanoparticles coated with 1 nm Fe_3O_4 shell; and (c) 7 nm FePt nanoparticles coated with 3 nm Fe_3O_4 shell. (Scale bar is 20 nm)

nanocomposite magnet so that homogenous nanocomposite magnets can be guaranteed. An additional advantage of the core/shell approach is that the core size and shell thickness can be adjusted in a continuous way so that the soft phase fraction and the overall composite composition can be finely tuned. Our experiments showed that 8 nm FePt nanoparticles coated with 2 nm Fe_3O_4 shells have the highest performance. About 36% energy product enhancement has been achieved compared to the single-phase FePt core particles.

Other bimagnetic nanoparticles include the brick-like nanoparticles and heterobimer that can also be used as building blocks of nanocomposite magnets [68, 69].

11.3.3 Fabrication of Nanocomposite Bulk Magnets

Fabrication of bulk nanocomposite magnets remains a grand challenge. Traditional compaction and sintering techniques do not work because the traditional techniques are based on extensive heat treatments which lead to excessive grain growth. To date, there have been very limited data reported on direct compaction of intermetallic nanoparticles, especially for nanoparticles with size down to several nanometers, though reports on micro-sized powder particles with nanoscale grain size can be found. We have attempted to fabricate bulk nanostructured magnets by using unconventional compaction techniques including warm compaction, spark plasma sintering, and dynamic compaction. Next we will review the methodology and the bulk magnet properties fabricated by using these techniques.

11.3.3.1 Warm Compaction

High-pressure warm compaction is one of the advanced compaction techniques in powder metallurgy and has been widely used in automobile parts manufacturing in the past decade [70–72]. This technique is established on the knowledge that metallic powders have better plasticity and compressibility at elevated temperatures and therefore are easier to be deformed to form high-density bulk materials

under a certain pressure, compared with cold pressing. Unlike hot pressing, warm compaction is performed at modest temperatures at which the metallic powders are chemically stable and no excessive grain growth occurs. To reach high density, one needs not only high pressure but also optimized compaction parameters including temperature and time. For metallic nanoparticles, lack of dislocations makes their deformation behavior different from their large-size materials and therefore grain boundary (and/or particle surface) creep is very important for reaching high density. Figure 11.12 shows the density dependence on compaction temperature of a FePt-based nanocomposite bulk magnet system compacted from 4 nm FePt and 4 nm Fe₃O₄ nanoparticles. It was found that satisfactory density (>95% theoretical density) can be achieved at below 600°C under pressure equal or larger than 2.5 GPa. To understand the effect of surface condition on the compaction, we compared the density dependence of FePt nanoparticles with surface-treated nanoparticles (coated with carbon, the triangle-symbol curve). The substantially lower density of the surface-treated samples suggests the importance of surface diffusion and deformation in the consolidation process.

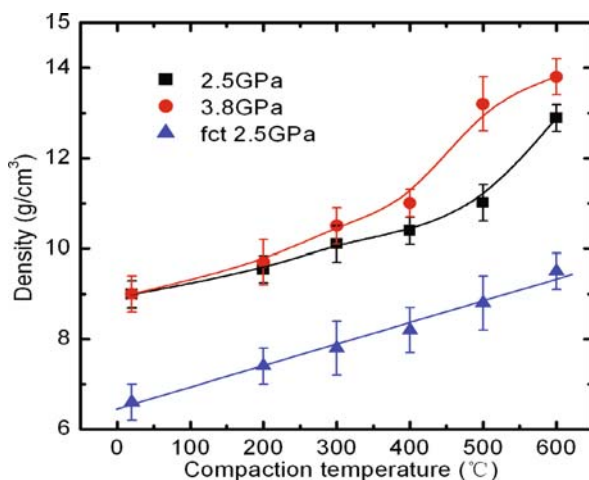
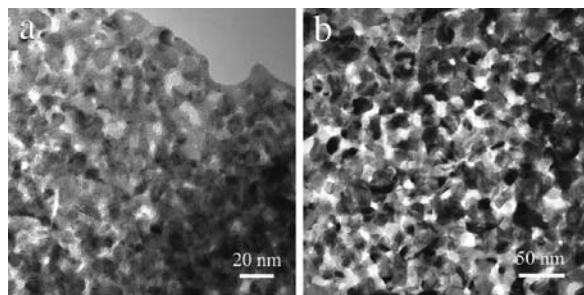


Fig. 11.12 The dependence of density of the bulk FePt/Fe₃O₄ samples on compaction temperature

TEM observation (Fig. 11.13) shows that the grain size was not excessively increased after the warm compaction. More importantly, the size distribution is quite small compared to bulk materials fabricated by traditional techniques. Magnetic characterization confirmed the effective exchange coupling in the bulk samples and it was revealed that increased density leads to enhanced exchange coupling. Similar results have been obtained recently in SmCo₅/Fe bulk nanocomposite magnets processed by warm compaction. Energy product enhancement of 90% has been achieved [15].

Fig. 11.13 TEM micrographs of bulk FePt-based samples compacted at (a) 20°C and (b) 400°C



11.3.3.2 Spark Plasma Sintering Compaction

Spark plasma sintering (SPS) is a technique based on pulsed DC current Joule heating in powder particles. The heat generates plasma between particles and the plasma conducts electric current also that enhances the Joule heating, leading to sintering between the heated particles. Since the heating can be controlled within a very short time while reaching very high temperatures on the particle surfaces, this technique has been adopted in recent years to produce nanostructured bulk materials including nanocomposite magnets [73–75]. It has been observed that this technique is very effective in compacting nanostructured melt-spun ribbons of nanocomposite magnetic materials. We tested the SPS compaction of the 4 nm FePt/Fe₃Pt nanoparticles and obtained 70% density at 600°C under pressure of 100 MPa [76]. Grain size of the sintered samples remains at the nanoscale even after a post-annealing at 700°C. It was also found that pressure rather than temperature was more effective in enhancing inter-grain exchange coupling.

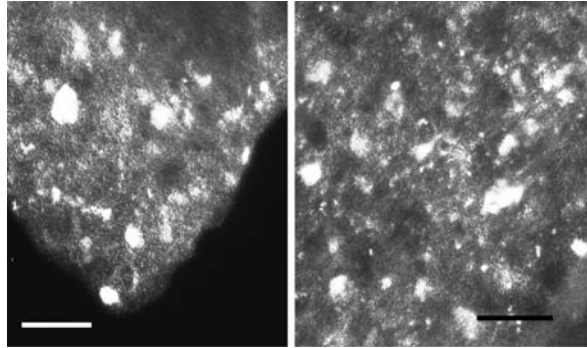
11.3.3.3 Dynamic Compaction

Dynamic compaction (including shock compaction and explosive compaction) is another method to produce nanostructured bulk materials without long-term thermal exposure. Raw powder materials can be compressed and condensed under extremely fast and strong shock waves within a period of microseconds and so grain growth is suspended while high density is achieved.

We prepared successfully the NdFeB-based bulk nanocomposite magnets with nearly full density (up to 99%) by shock compaction of the melt-spun ribbons using a gas-gun compaction system [77]. No grain growth was found; instead a decrease in the grain size of both the hard and soft phases was observed [78]. Further observation has revealed that the reduction of the grain size can be attributed to shear bands during the deformation with high strain rate. The decrease of grain size has been proved by X-ray diffraction and TEM observations. Figure 11.14 shows TEM images of the samples before and after the shock compaction.

Direct compaction of nanoparticles by shock compressing has been tested with 25 nm Fe nanoparticles [79]. It is found that the density–pressure correlation

Fig. 11.14 TEM dark-field micrographs of grain morphology of starting PrFeB materials (*left*) and center part of recovered shock-compacted specimens (*right*). The scale bars represent 50 nm



(Hugoniot) for the Fe nanoparticle powders cannot be fully described using analytical models that are otherwise capable of predicting the correlation of micron-sized powders or highly porous materials. This is an experimental evidence that deformation behavior of nanoparticles is profoundly different from micro-sized powders, as we mentioned earlier. The reason may be related to lack of dislocations in nanoparticles.

We have extended our research to explosive compaction to produce large-size bulk magnets [80]. Figure 11.15 shows the recovered bulk samples by explosive compaction with size $\Phi 2'' \times 6''$. The dynamic and heterogeneous nature of rapid plastic deformation during shock compaction can often lead to local melting and resolidification, as well as formation of macrocracks due to longitudinal tension generated by the interaction of released waves in the compacted samples. Controlling overheating and preventing macrocracks are the key to success for explosive compaction. Shock speed adjustment with suitable addition of ceramic particles in the



Fig. 11.15 A cylinder-shaped bulk nanocomposite magnet fabricated by explosive compaction. The diameter of the cylinder is 2 in.

explosive materials is one of the major methods to achieve the optimized results. We have obtained 98% density in our explosively compacted samples and found similar phenomenon of grain size reduction as found in the gas-gun compacted samples. Magnetic properties of the nanocomposite powders have been retained and even improved owing to the reduced grain size. Further work in dynamic compaction of nanoparticles including the chemically synthesized particles is still underway.

Besides shock compaction and explosive compaction, combustion-driven compaction technique [81] has also been adopted in consolidation of bulk nanocomposite magnets.

11.4 Work Toward Anisotropic Nanocomposite Magnets

Though great progress in understanding inter-phase exchange coupling and in processing nanocomposite magnets has been made, there are still many challenges en route to achieving super high energy products. One of the major challenges is how to produce anisotropic bulk nanocomposite magnets. Although energy product enhancement up to 90% has been achieved in isotropic nanocomposite magnets, the goal to achieve energy products that beat the current highest single-phase magnet energy products can only be reached when well-aligned nanocomposite magnets are fabricated.

To align nano-sized crystals to special crystalline directions has been proved to be a challenge, either in the case of isolated single-crystal nanoparticles or in the case of nanostructured polycrystalline powder or bulk materials.

Isolated nanoparticles (single crystals) tend to orient their crystalline directions randomly even when they are patterned or self-assembled. However, it has been observed that faceted nanoparticle assemblies with narrow size distribution may have their preferred crystalline directions [82].

To align single-domain ferromagnetic nanoparticles in a magnetic field is possible theoretically. Practically, however, ferromagnetic single-domain nanoparticles will become agglomerated by magnetic attraction as soon as they are synthesized. Therefore, to align single-domain ferromagnetic nanoparticles can be even more difficult than for non-magnetic nanoparticles.

It has been hoped that anisotropic nanostructured magnets can be made by utilizing both magnetocrystalline anisotropy and shape anisotropy. For this purpose, high aspect ratio nanoparticles like nanorods and nanowires of FePt and FeCo materials have been prepared [55, 83]. However, most of the nanorods and nanowires are not ferromagnetic at room temperature. Further work is underway to produce ferromagnetic nanorods and nanowires to realize magnetic field-induced alignment. For example, salt-matrix annealing is applied to produce $L1_0$ -structured FePt and FeCo nanowires.

Traditional methods used in producing anisotropic sintered magnets, namely the field alignment of powder particles before pressing, cannot be used to produce nanostructured bulk magnets unless the nanostructured powder particles contain nano-sized grains that all have the same magnetocrystalline orientation. Our

experiments showed that this kind of *aligned nanostructured powder particles* may be prepared by *magnetic field ball milling* [84]. Small nano-sized grains inside a micro-sized particle can be formed either from the plastic deformation of the particles during milling or from joining (welding) of small nanoparticles. In the latter situation, external magnetic fields applied to the milling vial will lead to formation of aligned nanostructured powder particles.

Another way to fabricate anisotropic bulk nanocomposite magnets is by *severe plastic deformation*. This method is based on formation of texture after plastic deformation which has been routinely adopted for producing anisotropic NdFeB bulk magnets. An attempt to produce two-phase FePt/Fe exchange-coupled magnets by cyclic co-rolling of Fe and Pt foils was made by N.H. Hai et al. [85] and Cui et al. [86]. Saha et al. [87] worked on FePd-based nanocomposite systems with a similar technique. Effect of *magnetic field annealing* on magnetic anisotropy of the plastically deformed ribbons has also been investigated [86, 88]. The primary challenge in synthesizing nanocomposites via cyclic co-rolling is how to maintain sufficient ductility to continue mechanical deformation without exposing the samples to high-temperature treatments which lead to recrystallization, grain growth, or undesired phase transformation and inter-diffusion. As indicated early, deformation of nanocrystals can be very different from large-size crystalline materials. Many fundamental problems and processing technical issues remain to be solved.

Acknowledgments First I would like to thank my former promoter and colleague Prof. D.J. Sellmyer (one of the editors of this book) who guided me to enter this research area in 1995. I would also like to thank my students, postdoctoral researchers, and collaborators who have contributed directly to the work reviewed in this chapter: H. Zeng, T. S. Vedantam, B. Altuncevahir, N. Poudyal, V. Chakka, K.E. Elkins, V. Nandwana, K.H. Chen, Z.Q. Jin, C.-b Rong, G. Chaubey, Y. Li, K. Yano, D. Li, Y. Wang, M. Yue, T. Black, Q. Zhang, D. Wu, Z.J. Guo, Y. Choi, J.S. Jiang, S.D. Bader, S. Saha, J.A. Barnard, W. Sofa, S.G. Sankar, G. Zangari, C. O'Connor, M.-h Yu, A.J. Zambano, I. Takeuchi, S.S. Yan, B.Z. Cui, K. Han, H. Garmestani, H. Schneider-Muntau, J. Crow, M. Chen, Y. Hou, S. Sun, K. Gallagher, S.-F. Cheng, J. Li, Y. Ding, Y. Liu, Y. Zhang, M.J. Kramer, C.D. Dai, N.N. Thadhani, and Z.L. Wang. This work has been supported in part by US DoD/DARPA through ARO under grant DAAD 19-03-1-0038 and DoD/MURI grant N00014-05-1-0497. Dr. V. Browning and Dr. J. Prater are highly appreciated for their long-term support to this effort.

References

1. R. Coehoorn, D.B. de Mooij and C. de Waard, *J. Magn. Magn. Mat.* 80 (1989) 101.
2. E. F. Kneller and R. Hawig, *IEEE Trans. Magn.* 27 (1991) 3588.
3. A. Manaf, R.A. Buckley and H.A. Davis, *J. Magn. Magn. Mat.* 128 (1993) 302.
4. L. Withanawasam, G.C. Hadjipanayis and R.F. Krause, *J. Appl. Phys.* 76 (1994) 6646.
5. J. Ding, P.G. McCormick and R. Street, *JMMM*, 124 (1993) LI.
6. O'Donnell, C. Kuhrt and J.M.D. Coey, *JAP*, 76 (1994) 7068.
7. I.A. Al-Omari and D.J. Sellmyer, *Phys. Rev. B* 52 (1995) 3441.
8. L.H. Lewis, D.O. Welch and V. Panchanathan, *J. Magn. Magn. Mat.*, 175 (1997) 275.
9. M. Ddahlgren, R. Grossinger, E. de Morais, S. Gama, G. Mendoza, J.F. Liu and H.A. Davis, *IEEE Trans. Magn.*, 33 (1997) 3895.
10. J.P. Liu, C.P. Luo, Y. Liu and D.J. Sellmyer, *Appl. Phys. Lett.* 72 (1998) 483–485.

11. X. Rui, J. E. Shield, Z. Sun, Y. Xu and D. J. Sellmyer, *Appl. Phys. Lett.* 89 (2006) 122509.
12. H. Zeng, J. Li, J. P. Liu, Z. L. Wang and S.H. Sun, *Nature*, 420 (2002) 395–398.
13. K.H. Chen, Z.Q. Jin, J. Li, G. Kennedy, H. Zeng, S.-F. Cheng, Z.L. Wang, N. N. Thadhani and J.P. Liu, *J. Appl. Phys.* 96 (2004), 1276–1278.
14. C.B. Rong, V. Nandwana, N. Poudyal, J.P. Liu, M.E. Kozlov, R.H. Baughman, Y. Ding and Z. L. Wang, *J. Appl. Phys.*, 101 (2007) 023908.
15. C. Rong, Y.Z. Liu, M. Kramer and J.P. Liu, in preparation
16. T. Schrefl, H. Kronmüller and J. Fidler, *J. Magn. Magn. Mater.* 127 (1993) L273.
17. R. Skomski and J.M.D. Coey, *Phys. Rev. B* 48 (1993) 15812.
18. R.F. Sabiryanov and S.S. Jaswal, *J. Magn. Magn. Mater.*, 177–181(1998a) 989.
19. R.F. Sabiryanov and S.S. Jaswal, *Phys. Rev. B* 58(1998b) 12071.
20. H. Kronmüller, R. Fisher, M. Bachmann and T. Leinewber, *J. Magn. Magn. Mater.* 203 (1999) 12.
21. Z.S. Shan, J.P. Liu, V.M. Chkka, H. Zeng and J.S. Jiang, *IEEE Trans on Magn*, 38 (2002) 2907.
22. Z.J. Guo, J.S. Jiang, J.E. Pearson, S.D. Bader and J.P. Liu, *Appl. Phys. Lett.*, 81 (2002) 2029.
23. G. Asti, M. Solzi, M. Ghidini and F.M. Neri, *Phys. Rev. B* 69 (2004) 174401.
24. A.J. Zambano, H. Oguchi, I. Takeuchi, Y. Choi, J.S. Jiang, J.P. Liu, S.E. Lofland, D. Josell and L.A. Bendersky, *Phys. Rev. B* 75 (2007) 144429-1-7.
25. J.P. Liu, Y. Liu, R. Skomski and D.J. Sellmyer, *IEEE Trans on Magn.* 35 (1999) 3241.
26. J.S. Jiang, J.E. Pearson, Z.Y. Liu, B. Kabius, S. Trasobares, D.J. Miller, S.D. Bader, D.R. Lee, D. Haskel, G. Srajer and J.P. Liu, *Appl. Phys. Lett.* 85(2004) 5293.
27. Y. Choi, J.S. Jiang, Y. Ding, R.A. Rosenberg, J.E. Pearson, S.D. Bader, A. Zambano, M. Murakami, I. Takeuchi, Z.L. Wang and J.P. Liu, *Phys. Rev. B* 75 (2007) 104432-1-6.
28. D.X. Wu, Q.M. Zhang, J.P. Liu, D.W. Yuan and R.Q. Wu, *Appl. Phys. Lett.* 92 (2008) 052503.
29. J.P. Liu, Y. Liu and D.J. Sellmyer, *J. Appl. Phys.* 83 (1998) 6608.
30. G.P. Zhao and X.L. Wang, *Phys. Rev. B* 74 (2006) 012409.
31. G.P. Zhao, M.G. Zhao, H.S. Lim, Y.P. Feng, and C.K. Ong, *Appl. Phys. Lett.* 87 (2005) 162513.
32. D.J. Craik and E.D. Isaac, *Proc. Phys. Soc.* 76 (1960) 160.
33. D. Goll, M. Seeger and H. Kronmüller, *J. Magn. Magn. Mater.* 185 (1998) 49.
34. J.P. Liu, R. Skomski, Y. Liu and D.J. Sellmyer, *J. Appl. Phys.* 87 (2000) 6740.
35. K. Kang, L.H. Lewis, J.S. Jiang, and S.D. Bader, *J. Appl. Phys.* 98 (2005)113906.
36. D.C. Crew, J. Kim, L.H. Lewis, and K. Barmak, *J. Magn. Magn. Mater.* 233 (2001) 257.
37. Y. Choi, J.S. Jiang, J.E. Pearson, S.D. Bader and J. P. Liu, *Appl. Phys. Lett.* 91(2007) 022502.
38. C.B. Rong, Y. Liu and J.P. Liu, *Appl. Phys. Lett.* 93 (2008) 042508.
39. E.P. Wohlfarth, *J. Appl. Phys.* 29 (1958) 595.
40. P.E. Kelly, K. O'Grady, P.I. Mayo and R.W. Chantrell, *IEEE Trans. Magn.* 25 (1989) 3881.
41. G. Srajer, L.H. Lewis, S.D. Bader, A.J. Epstein, C.S. Fadley, E.E. Fullerton, A. Hoffmann, J.B. Kortright, K.M. Krishnan, S.A. Majetich, T.S. Rahman, C.A. Ross, M.B. Salamon, I.K. Schuller, T.C. Schulthess and J.Z. Sun, *J. Magn. Magn. Mater.* 307 (2006) 1.
42. M.-h. Yu, J. Hattrick-Simpers, I. Takeuchi, J. Li, Z.L. Wang, S.E. Lofland, S. Tyagi, J.W. Freeland, D. Giubertoni, M. Bersani and M. Anderle, *J. Appl. Phys.* 98 (2005) 063908.
43. J.E. Davies, O. Hellwig, E.E. Fullerton, J.S. Jiang, S.D. Bader, G.T. Zimanyi and K. Liu, *Appl. Phys. Lett.* 86 (2005) 262503.
44. G.C. Hadjipanayis, *J. Magn. Magn. Mater.* 200 (1999) 373.
45. D.H. Ping, K. Hono and S. Hirose, *J. Appl. Phys.* 83 (1998) 7769.
46. Y. Gao, J.H. Zhu, Y.Q. Weng, E.B. Park, C.J. Yang, *J. Magn. Magn. Mater.* 191 (1999) 146.
47. P.G. McCormick, W.F. Miao, P.A.I. Smith, J. Ding and R. Street, *J. Appl. Phys.* 83 (1998) 6256.
48. Z.D. Zhang, W. Liu, X.K. Sun, X.G. Zhao, Q.F. Xiao, Y.C. Sui and T. Zhao, *J. Magn. Magn. Mater.* 184 (1998) 101.

49. E.E. Fullerton, J.S. Jiang, C.H. Sowers, J.E. Pearson, and S.D. Bader, *Appl. Phys. Lett.*, 72 (1998) 380.
50. J.P. Liu, Y. Liu, Z.S. Shan and D.J. Sellmyer, *IEEE Trans. Magn.* 33 (1997) 3709.
51. J.P. Liu, Y.Liu and D.J. Sellmyer, *J. Appl. Phys.* 83 (1998) 6608.
52. J.P. Liu, Y. Liu, R. Skomski and D.J. Sellmyer, *J. Appl. Phys.* 85 (1999) 4812.
53. S. Sun, C.B. Murray, D. Weller, L. Folks and A. Moser, *Science* 287 (2000) 1989.
54. V. Nandwana, K.E. Elkins, N. Poudyal, G.S. Chaubey, K. Yano and J.P. Liu, *J. Phys. Chem. C* 111(2007) 4185.
55. N. Poudyal, G.S. Chaubey, V. Nandwana, C.B. Rong, K. Yano and J.P. Liu, *Nanotechnology* 19 (2008) 355601.
56. K. Elkins, D.R. Li, N. Poudyal, V. Nandwana, Z.Q. Jin, K.H. Chen and J. P. Liu, *J. Phys. D: Appl. Phys.* 38 (2005) 2306.
57. C.B. Rong, D.R. Li, V. Nandwana, N. Poudyal, Y. Ding, Z.L. Wang, H. Zeng and J.P. Liu, *Adv. Mater.* 18 (2006) 2984.
58. J.P. Liu, K. Elkins, D. Li, V. Nandwana and N. Poudyal, *IEEE Trans on Magn.* 42 (2006) 3036.
59. K. Ono, Y. Kakefuda, R. Okuda, Y. Ishii, S. Kamimura, A. Kitamura and M. Oshima *J. Appl. Phys.* 91 (2002) 8480.
60. H. Gu, B. Xu, J. Rao, R.K. Zheng, X.X. Zhang, K.K. Fung and C.Y. Wong, *J. Appl. Phys.* 93 (2003) 7589.
61. X. Teng, H. Yang, *J. Nanosci. Nanotechnol.* 7 (2007) 356.
62. Y.L. Hou, Z.C. Xu, S. Peng, C.B. Rong, J. P. Liu and S.H. Sun, *Adv. Mater.*, 19 (2007) 3349.
63. V.M. Chakka, B. Altuncevahir, Z.Q. Jin, Y. Li and J. P. Liu, *J. Appl. Phys.* 99 (2006) 08E912.
64. Y.P. Wang, Y. Li, C.B. Rong and J.P. Liu, *Nanotechnology* 18 (2007) 465701.
65. X. Rui, J.E. Shield, Z.Sun, R. Skomski, Y.Xu, D.J. Sellmyer, M.J. Kramer and Y.Q. Wu, *J. Magn. Mater.* 320 (2008) 2576.
66. J.S. Chen, C.Y. Tan and G.M. Chow, *Nanotechnology* 18 (2007) 435604.
67. J.M. Qiu and J.P. Wang, *Adv. Mater.* 19 (2007) 1703.
68. G.S. Chaubey, V. Nandwana, N. Poudyal, C.B. Rong, and J.P. Liu, *Chem. Mater.* 20 (2008) 475.
69. V. Nandwana, G.S. Chaubey, K. Yano, C.B. Rong and J.P. Liu, *J. Appl. Phys.* 105 (2009) 014303.
70. H.G. Rutz, F.G. Hanejko and S.H. Luk, *Met. Powder Rep.* 49 (1994) 40.
71. G.E. Fougere, J.R. Weertman and R.W. Siegel, *Nanostructured Mater.* 5 (1995) 127.
72. K. Kondoh, T. Takikawa and R. Watanabe, *JJSPM*, 47 (2000) 94.
73. N. Tamari, T. Tanaka, K. Tanaka, I. Kondoh, M. Kawahara and M. Tokita, *J. Ceramic Soc. Jpn.* 103 (1995) 740.
74. H. Ono, *IEEE Trans. Magn.* 37 (2001) 2552.
75. M. Yue, M. Tian, et al., *Mater. Sci. Eng. B* 131 (2006), 1–3, 18–21.
76. C.B. Rong, V. Nandwana, N. Poudyal, J.P. Liu, T. Saito, Y.Q. Wu and M. J. Kramer, *J. Appl. Phys.* 101 (2007) 09K505.
77. K.H. Chen, Z.Q. Jin, J. Li, G. Kennedy, H. Zeng, S.F. Cheng, Z.L. Wang, N.N. Thadhani, and J.P. Liu, *J. Appl. Phys.* 96 (2004) 1276.
78. J. Li, Z.Q. Jin, J. P. Liu, Z. L. Wang, and N.N. Thadhani, *Appl. phys. Lett.* 85 (2004) 2223.
79. C.D. Dai, D. Eakins, N. Thadhani and J.P. Liu, *Appl. Phys. Lett.* 90 (2007) 071911.
80. Z.Q. Jin, N.N. Thadhani, M. McGill, Y. Ding, Z.L. Wang, M. Chen, H. Zeng, V.M. Chakka and J.P. Liu, *J. Mater. Res.* 20 (2005) 599.
81. M. Sachan and S.A. Majjetich, *IEEE Trans. On Magn.* 41 (2005), 3874.
82. M. Chen, J. Kim, J.P. Liu, H.Y. Fan and S.H. Sun, Synthesis of FePt Nanocubes and Their Oriented Self-Assembly, *J. Am. Chem. Soc.* 128 (2006) 7132.
83. C.Wang, Y.H. Hou, J. Kim and S.H. Sun, *Angew. Chem. Int. Ed.* 46 (2007).
84. N. Poudyal, B. Altuncevahir, V. Chakkal, K.H. Chen, T.D. Black, J.P. Liu, Y. Ding and Z.L. Wang, *J. Phys. D: Appl. Phys.* 37 (2004) L45.
85. N.H. Hai, N.M. Dempsey and D. Givord, *J. Magn. Mater.* 262 (2003) 353.

86. B.Z. Cui, K. Han, D.S. Li, H. Garmestani, J.P. Liu, N.M. Dempsey and H.J. Schneider-Muntau, *J. Appl. Phys.* 100 (2006) 013902.
87. S. Saha, A. Kulovits, W.A. Soffa, and J. A. Barnard, *J. Appl. Phys.* 97 (2005) 10F301.
88. D. S. Li, H. Garmestani, Shi-shen Yan, M. Elkawni, M.B. Bacaltchuk, H.J. Schneider-Muntau, J.P. Liu, S. Saha and J.A. Barnard, *J. Magn. Magn. Mater.* 281 (2004) 272.

Chapter 12

High-Temperature Samarium Cobalt Permanent Magnets

Oliver Gutfleisch

Abstract This chapter reviews the development of SmCo-type magnets over the last 40 years. First, the physical metallurgy and crystal structures are considered; then the focus is on the recent developments in high-temperature $\text{Sm}(\text{Co}_{\text{bal}}\text{Fe}_w\text{Cu}_x\text{Zr}_y)_z$ magnets suitable for operation temperatures up to 500°C. It is elucidated that the evolution of coercivity and microchemistry in the respective phases of the heterogeneous nanostructure as well as magnetic domain structure is very sensitive to details of the processing procedure, especially to the slow cooling ramp as the last step where the hard magnetic properties evolve. These changes give rise to rather complex pinning mechanisms in a three-phase precipitation structure, which again depend in a subtle manner on the microchemistry of the 1:5-type cell boundary phase in the 2:17-type magnets. It is the amount and distribution of Cu in and at the cell boundary phase which is the prevalent factor determining the pinning strength and which can yield a non-monotonic temperature dependence of coercivity. The chapter concludes with an overview of novel non-equilibrium processing routes used to obtain SmCo-type nanocomposites.

12.1 Introduction

The last century has been the golden age of permanent magnetism, and the progress in the field of permanent magnets has been dramatic over the last 40 years. Permanent magnets are widely used in our daily life and feature in a large variety of domestic products such as quartz analogue watches, earphones, microwaves, cordless tools, mobile phones, and voice coil motors. A modern car, for example, contains at least 50 permanent magnets. In this case, most of the magnets are so-called hard ferrites ($\text{BaFe}_{12}\text{O}_{19}$ and $\text{SrFe}_{12}\text{O}_{19}$), a low cost–low performance type of

O. Gutfleisch (✉)

Leibniz Institute for Solid State and Materials Research (IFW Dresden), Institute for Metallic Materials, Helmholtzstr. 20, 01069 Dresden, Germany
e-mail: o.gutfleisch@ifw-dresden.de

magnet. In more sophisticated applications, where, e.g., miniaturization is an issue or completely new designs are needed, high-performance permanent magnets based on rare earth–transition metal compounds are used. $\text{Nd}_2\text{Fe}_{14}\text{B}$, generating a field of the order of 1 T, is mostly used in computer or portable electronic devices, but also in medicine for (intraoperative) diagnostics using a magnetic resonance imaging apparatus. Other examples for new applications are hybrid electric vehicles (HEV), electronic cyclotron resonance ion source, magnetic refrigeration, and wind generators. Modern high-performance magnets are based on compounds of a magnetic light rare earth (Pr, Nd, Sm) for strong magnetic anisotropy and a 3d element (Fe, Co) for large magnetization and high Curie temperature. A favorable combination of these values is only a prerequisite for a good hard magnetic material; the ultimate suitability can only be gauged when coercive field H_c , remanent magnetization B_r , and maximum energy density $(BH)_{\text{max}}$, as the most relevant extrinsic properties, fulfill certain criteria. This is done by the preparation of appropriate microstructures with typical length scales of 1 nm to 100 μm (for more detailed descriptions the reader is referred to overviews by Cullity [14], Gavigan and Givord [29], Coey [12], Chikazumi [11], Strnat [95, 96], Buschow [5, 6], Skomski and Coey [88], Gutfleisch [39, 41], and Khlopkov et al. [53]).

The intrinsic magnetic properties are determined by magnetic moments and interactions on an atomic scale and are independent of the microstructure of the specific material. In rare earth–transition metal (R–T) compounds three types of exchange interactions occur: T–T, R–T, and R–R. In the case of SmCo_5 , for example, where the transition metal carries a well-established magnetic moment, the T–T interactions dominate. The strong ferromagnetic coupling is responsible for the magnetic order up to very high Curie temperature. The R–R exchange coupling proceeds indirectly via 4f–5d–5d–4f and is generally very small compared to the R–T interaction. The latter proceeds also via an indirect mechanism (4f–5d–3d) in which the strong interatomic direct 5d–3d exchange is transmitted to the 4f electrons via the intra-atomic 4f–5d ferromagnetic interaction. The 5d–3d exchange is antiferromagnetic when the 5d band is less than half full and the 3d band is more than half full as it is the case for compounds of rare earths with ferromagnetic 3d metals. Qualitatively it can be summarized that as the transition metal spin S_T couples antiparallel to the rare earth spin S_R , the magnetizations of R and T sublattices couple parallel for the light rare earth elements ($J = L - S$) and antiparallel for the heavy rare earth elements ($J = L + S$) according to Hund's rule. The orbital magnetic moments in rare earth metals remain unquenched by crystalline fields because the magnetic moments are produced by 4f electrons well inside the atoms and protected from the surrounding atoms. However, the electrostatic crystalline electric field acting on the non-spherical 4f charge distribution favors a certain orientation of its preferred axis and thus also directions of the magnetization. The result of this interaction is an enormous magnetocrystalline anisotropy. The rare earth series presents an incomplete filling of the 4f shell. The number of electrons in the inner 4f shell vary from 0 to 14 through the series La (atomic number in the periodic table: $Z = 57$) to Lu ($Z = 71$). The total magnetic moment of an R atom has both orbital and spin components. However, the 4f shell is not the outermost shell of the atom. The R–R

exchange coupling between two R atoms in a solid is indirect because the direct overlap between the 4f shells of adjacent rare earth atoms is negligible. The resulting weak magnetic interaction with the 4f electrons of neighboring atoms causes the low Curie temperatures of the rare earth metals; in fact only Gd ($T_C = 16^\circ\text{C}$) is ferromagnetic close to room temperature.

Microwave tubes, gyroscopes and accelerometers, reaction and momentum wheels to control and stabilize satellites, magnetic bearings, sensors, and actuators are examples of applications where high-energy density magnets with magnetic fields stable over a variety of environmental conditions and wide temperature ranges are required. SmCo_5 - and $\text{Sm}_2\text{Co}_{17}$ -type magnets [3, 57, 83, 84, 94, 95] are ideal for these applications because of their high magnetocrystalline anisotropy and Curie temperature. Standard commercial magnets of these types satisfy these requirements over the temperature range from 50 to 250°C . In addition, they exhibit a high corrosion resistance; their disadvantages are the costly raw materials and the difficult magnetization. A slight increase in temperature stability can be achieved when substituting heavy rare earth elements for Sm [111]. Even better temperature coefficients of remanence ($\alpha = dM_r/dT$) and coercivity ($\beta = dH_c/dT$) are required for higher operating temperatures above 450°C [43, 100], which are needed for rare earth permanent magnets (RPMs) for electric vehicles, hybrid magnetic bearings for turbine engines and advanced power systems. The availability of these newly developed magnets could also open completely new applications such as magnetic brakes with performance close to normal friction brakes.

12.2 Physical Metallurgy and Crystal Structures

SmCo phases show a variety of crystal structures and these alloys have been studied for more than 40 years now. Here, the focus is on the SmCo binaries with Curie temperatures surpassing 400°C and which are stable at room temperature, or which can be easily retained at room temperature in a metastable state by quenching from higher temperatures. Their crystal structure data are shown in Table 12.1. Note that the 1:7- and the 1:5-type structures are closely related to each other and have the same space group $P6/mmm$ [4]. The rhombohedral $\text{Th}_2\text{Zn}_{17}$ structure can be derived from the SmCo_5 structure by an ordered substitution of a dumbbell of Co atoms for one-third of the Sm atoms. When a random substitution by Co pairs occurs, a

Table 12.1 Crystal structure data of SmCo binaries [3]

Compound	Lattice constant (nm)	Structure type	Space group
SmCo_5	$a=0.5002$ $c=0.3964$	CaCu_5	$P6/mmm$
$\text{Sm}_2\text{Co}_{17}$	$a=0.4856$ $c=0.4081$	TbCu_7	$P6/mmm$
$\text{Sm}_2\text{Co}_{17}$	$a=0.8360$ $c=0.8515$	$\text{Th}_2\text{Ni}_{17}$	Pb_3/mmc
$\text{Sm}_2\text{Co}_{17}$	$a=0.8395$ $c=1.2216$	$\text{Th}_2\text{Zn}_{17}$	$R3m$

disordered Co-rich phase of TbCu_7 is formed [52]. This phase becomes unstable when 22% of Sm atoms have been replaced by Co pairs resulting in a phase separation into the two neighboring phases, SmCo_5 and $\text{Sm}_2\text{Co}_{17}$.

Figure 12.1 shows the structures of the RCO_5 and R_2Co_{17} compounds. Depending on the stacking sequence of the mixed SmCo planes one distinguishes the rhombohedral $\text{Th}_2\text{Zn}_{17}$ (ABCABCABC...) and the hexagonal $\text{Th}_2\text{Ni}_{17}$ (ABABAB...) modifications. The Co-rich part of the SmCo equilibrium phase diagram shown in Fig. 12.2 illustrates the congruent melting of $\text{Sm}_2\text{Co}_{17}$ at 1,338°C and the peritectic reaction at 1,292°C to form SmCo_5 .

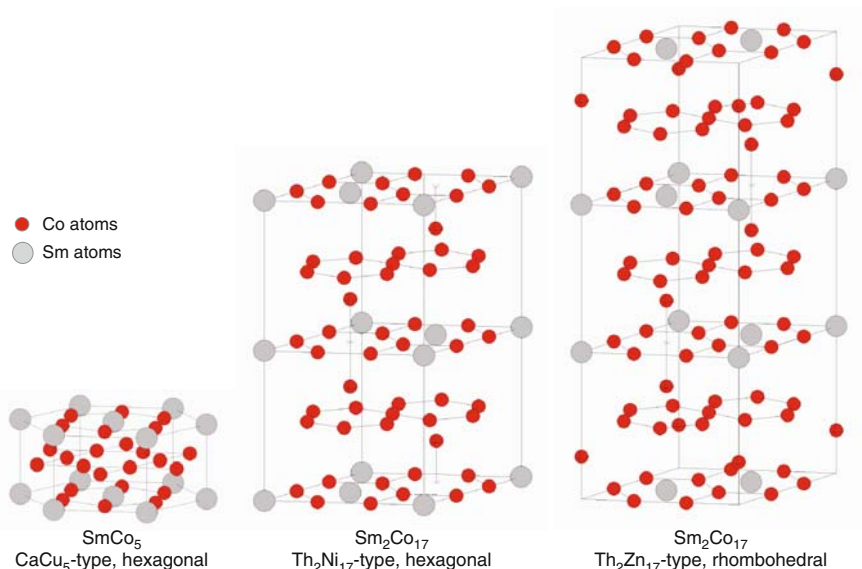
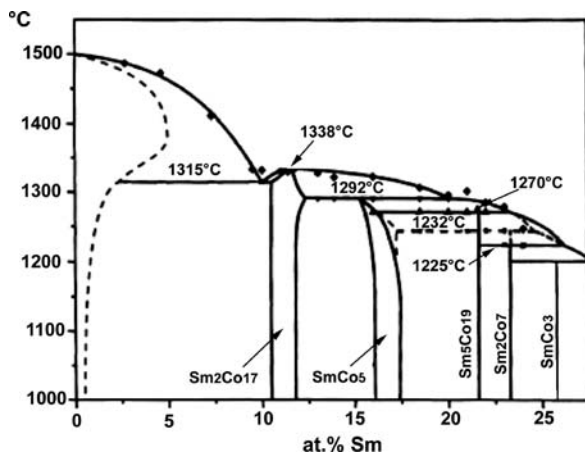


Fig. 12.1 Structures of the RCO_5 and R_2Co_{17} compounds (after [26])

The used terminology of “1:5”- and “2:17”-type magnets is rather simplistic; in fact the real magnets are multiphase magnets with a complex sequence of annealing steps and, especially in the case of 2:17, a heterogeneous nanostructure.

Both the 1:5 and the 2:17 types are usually produced via the powder metallurgical sintering route. Unlike the $\text{Nd}_2\text{Fe}_{14}\text{B}$ phase, the hexagonal SmCo_5 compound [94] with the CaCu_5 structure shows a relatively large homogeneity region in the SmCo phase diagram [7, 90, 91] as shown in Fig. 12.2. This region, however, becomes asymmetric when approaching the peritectic melting temperature of 1,292°C. The 2:17 type shows currently the best temperature coefficients α and β of all RPMs, and its hard magnetic properties are achieved by an elaborate series of heat treatments resulting in a complex microstructure. Commercially produced SmCo -type sintered magnets based on the 2:17R-type phase (with the rhombohedral (R) $\text{Th}_2\text{Zn}_{17}$ -type structure) have usually a composition close to $\text{Sm}(\text{Co,Fe,Cu,Zr})_{7.5}$. The homogeneity region of the 2:17R phase narrows with decreasing temperature [7, 79], and a fine cellular precipitation structure develops from the single-phase metastable

Fig. 12.2 SmCo phase diagram. Reproduced with permission of Elsevier from [7]

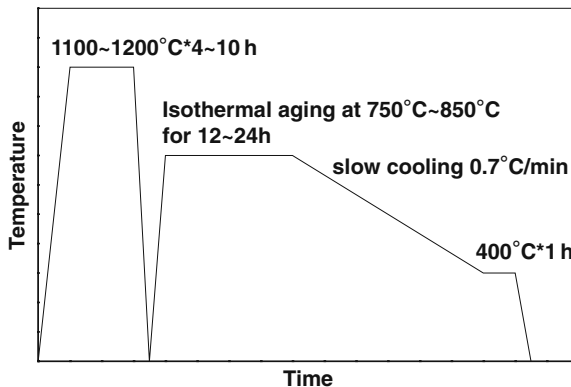


precursor, obtained by solid solution treatment at $\sim 1,200^{\circ}\text{C}$, quenching and subsequent annealing at $\sim 800^{\circ}\text{C}$, and slow cooling to 400°C (Fig. 12.3). The structure of the homogenized high-temperature phase has been described differently. Whereas Rabenberg et al. [81, 82] assumed the hexagonal (H) $\text{Th}_2\text{Ni}_{17}$ -type structure (2:17H), it has been reported later that the hexagonal TbCu_7 -type structure (1:7H) is more realistic and, after quenching from $\sim 1,200^{\circ}\text{C}$, the material consists of the supersaturated 1:7H phase with partial 2:17R-type order [68]. According to these authors the 2:17R cells originate from nucleation and growth out of the 1:7 structure. This induces a related increase of Cu (according to Perry [79] the solubility of Cu in 2:17R at 850°C is only 4 at.%) and Sm contents in the surrounding 1:7 matrix, which tends to 1:5 stoichiometry and forms the cell boundaries that have a thickness of 5–10 nm (note that the 1:7- and the 1:5-type structures have the same space group $P6/mmm$ [4]). A similar scenario had been already proposed by Livingston and Martin [66] who, however, speak of a disordered 1:5 structure instead of the 1:7 structure as the homogenized high-temperature phase. The development of the specific form of the cellular precipitation structure is governed by the elastic energy due to lattice misfit of the 1:5 and the 2:17R phases. The cell interior (cell diameter of typically 100 nm) has the 2:17R-type structure and shows boundaries of coherent twins in the basal plane [27, 28]. The 2:17R phase is the majority phase of the material. The 1:5 cell boundary phase is coherent (or at least semi-coherent) with the cell interior [66].

A so-called platelet phase (also referred to as lamellar or Z-phase) rich in Zr is observed additionally parallel to the 2:17R basal plane. In Fig. 12.4, this Z-phase manifests itself as thin lines extending over many 2:17R cells. The reported thickness of the lamellae is very small ranging from 1 nm [68] to 3 nm [42]. The lattice structure of the Z-phase is still somewhat controversially discussed. Rabenberg et al. [81, 82] reported the rhombohedral Be_3Nb -type structure, which has been confirmed by Maury et al. [68], Xiong et al. [102], and Stadelmaier et al. [92]. On the

other hand, Fidler and Skalicky [27, 28] found the 2:17H-type structure for the Z-phase, which is accepted by various authors (e.g., [35]). The Z-phase is considered to stabilize the cellular microstructure and to provide diffusion paths for Cu, Fe, and Co, thereby modifying phase-ordering kinetics [81, 82].

Fig. 12.3 Schematic heat treatment regime for precipitation-hardened $\text{Sm}_2\text{Co}_{17}$ -type magnets



In order to optimize $\text{Sm}_2\text{Co}_{17}$ -type magnets for a particular high-temperature application, the profound knowledge of the effects of alloying elements is necessary (the quinary Sm-Co-Fe-Cu-Zr phase diagram has been studied by Lefèvre et al. [59]). It has been shown that Cu and Zr stabilize the SmCo_7 -type phase and Fe favors the $\text{Sm}_2\text{Co}_{17}$ -type phase with $\text{Th}_2\text{Zn}_{17}$ structure [70]. The substitution of Co by Fe results in the precipitation of a Co-Fe phase and in a reduction of coercivity but improved saturation magnetization [76–78]. This undesired precipitation can be reduced by the addition of small amounts of Zr [74]. Cu induces the precipitation of the SmCo_5 cell boundary phase surrounding the $\text{Sm}_2\text{Co}_{17}$ -R cells [66, 71]. Cu is considered to have complete solubility in SmCo_5 and to stabilize this structure, in

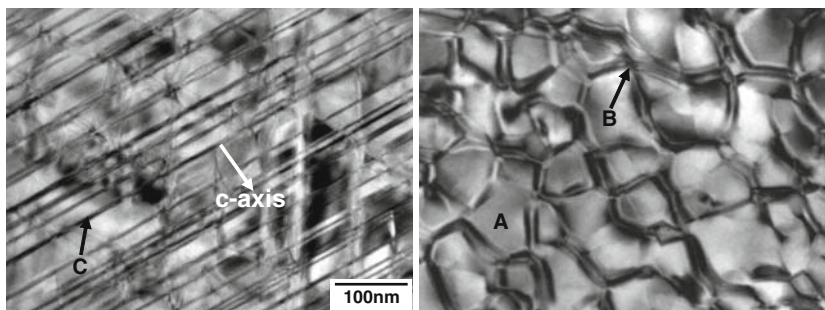


Fig. 12.4 TEM bright field images of a $\text{Sm}(\text{Co}_{0.784}\text{Fe}_{0.100}\text{Cu}_{0.088}\text{Zr}_{0.028})_{7.19}$ -sintered magnet with the nominal c-axis of the 2:17R main phase parallel (*left*) and perpendicular (*right*) to the imaging plane (A indicates the 2:17R type, B the 1:5-type cell boundary, and C the Z-phases). Reproduced with permission of Elsevier from [41]

fact changing the peritectic reaction of SmCo_5 to an eutectic one [79]. The influence of Cu has been thoroughly investigated [61, 62]. The effect of Zr has been studied at fixed Cu and Sm contents [98]. A strong interaction between Sm and Zr is expected [91], although it is somehow accepted that Zr is substituting Co.

12.3 Coercivity Mechanism and the Development of High-Temperature 2:17-Type Magnets

12.3.1 The $\text{Sm}(\text{CoCu})_5$ Cell Boundary Phase

The complex preparation process leads to the aforementioned heterogeneous nanostructure in the $\text{Sm}(\text{Co}_{\text{bal}}\text{Fe}_w\text{Cu}_x\text{Zr}_y)_z$ magnets. Subtle changes in microchemistry result in a system in which the domain wall energy ($\gamma = 4(K_1A)^{1/2}$) depends sensitively on the wall position and in which the walls remain pinned in regions where their energy is reduced. The gradient in Cu across the cell boundaries is facilitated by the presence of the Zr-rich lamellae and coincides with the gradient in the domain wall energy. This pinning-type coercivity mechanism is responsible for the high coercivities in these solid-state precipitation-hardened magnets.

Due to the large variety in heat treatment and compositional parameters an optimization of the $\text{Sm}(\text{Co}_{\text{bal}}\text{Fe}_w\text{Cu}_x\text{Zr}_y)_z$ magnets in terms of high-temperature magnetic properties is a complex task. Studies by J.F. Liu et al. [61–63] as well as C. Chen et al. [8] show that lower z values and higher amounts of Cu lead to a finer microstructure, which in turn results in a smaller temperature dependence of coercivity provided the appropriate Cu content is chosen. More specifically it was shown that for $z \sim 8.5$ and $x = 0.088$ a room temperature coercivity of $\mu_{0i}H_c = 4\text{ T}$ was achieved, whereas for $z \sim 7$ and $x = 0.128$ a very high coercivity of 1.08 T at 500°C was obtained. Further work showed that increased Co content (lower Fe content) leads to maximum operation temperatures from 400 to 550°C. These magnets show a straight demagnetization curve (BH loop) in this temperature range, which is a requirement for dynamic applications [9]. Analytical electron microscopy across the $\text{Sm}(\text{CoCu})_5$ cell boundary phase showed that the Cu content differs significantly from that of the matrix phase. It is also reported [58] that the anisotropy constant K_1 as well as the Curie temperature of this phase decreases dramatically with increasing Cu content as shown for K_1 in Fig. 12.5 and is finally lower than that of the 2:17-type matrix phase. Consequently, a transition from repulsive to attractive pinning could be expected with increasing Cu content. The pinning of domain walls has been related to the changes of K_1 during the complex annealing regime [43, 55, 102, 108, 109]. Another point of view is the consideration of the crystal structure of the cell boundary phase. Reports on the changes in phase equilibria and microstructure [15–20, 69] indicate that the cell boundary phase is actually composed of a mixture of 2:7 and 5:19-type phases, which are superlattices of the 1:5 phase, after annealing at 850°C, i.e., before the slow cooling ramp [15, 16]. The latter point has been reiterated by Goll et al. [35]. The intrinsic magnetic properties of the 2:7- and

5:19-type phases are not known and might differ somewhat from those of the 1:5 phase. However, most likely, they are in the range of those of the $\text{Sm}(\text{Co}_{1-x}\text{Cu}_x)_5$ system and thus one can expect finally very similar effects on the domain wall pinning behavior regardless of whether the changes are attributed to microchemical changes within or crystallographic variations of the cell boundary phase.

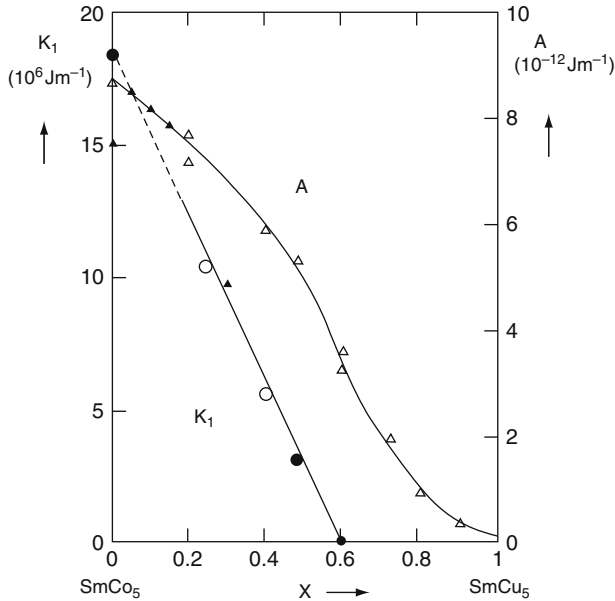


Fig. 12.5 Anisotropy constant K_1 at 300 K and exchange stiffness A of $\text{Sm}(\text{Co}_{1-x}\text{Cu}_x)_5$. K_1 shows a linear decrease with increasing Cu content. Reproduced with permission of American Institute of Physics from [58]

12.3.2 Alloy Optimization

Figure 12.6 shows the coercivity of $\text{Sm}(\text{Co}_{\text{bal}}\text{Fe}_w\text{Cu}_x\text{Zr}_y)_z$ samples as a function of z at room temperature, which were prepared by powder metallurgy production route [85], including jet milling, powder blending and compaction of oriented powder, and heat treatment (homogenization at 1,180–1,210°C, precipitation hardening at 800–860°C, and finally slow cooling to 400°C).

The coercivities of samples with the composition $\text{Sm}(\text{Co}_{\text{bal}}\text{Fe}_{0.144}\text{Cu}_{0.076}\text{Zr}_{0.022})_z$ show a narrow z -range with high coercivities, with a peak value above 3.87 T. With increased Zr, the maximum of coercivity is shifted to higher z values; a maximum coercivity of 4.4 T is found for $z = 8.35$. Even for $z > 8.5$ coercivities above 3.1 T were achieved. Zr is generally assumed to promote the desired microstructure for high coercivities. The compositions with higher Zr content were not single phase after homogenization. Some magnets contained considerable amounts of a Zr-rich

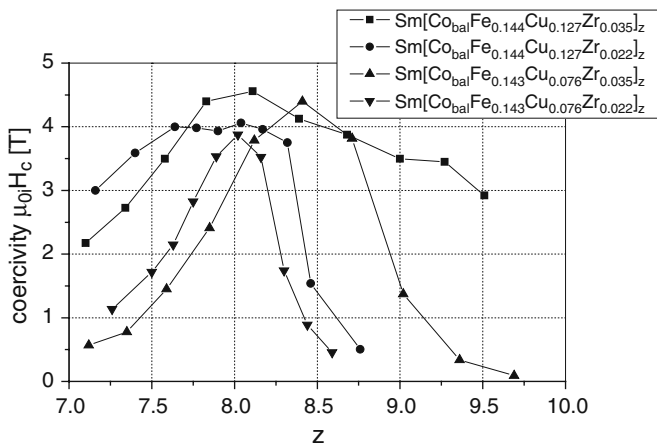


Fig. 12.6 Coercivity μ_0H_c vs. z at room temperature. Reproduced with permission of Elsevier from [85]

phase, which was identified as $Zr_6(Co,Fe,Cu)_{23}$ with the Th_6Mn_{23} structure [67]. Nevertheless, these magnets had excellent coercivities and demagnetization curves with good squareness. The combination of higher Cu and higher Zr content leads to a very broad range of useful z values, with good coercivity (>2.7 T) up to $z = 9.5$. A higher Cu content considerably extends the useful range of z to lower z values, consistent with the results of Liu et al. [61, 62].

Figure 12.7 (left) shows the coercivity as a function of z for a selection of these compositions at 450°C . The highest coercivity is achieved with the compositions high in Cu. The influence of Cu is fairly well understood: the high coercivity in the Sm_2Co_{17} -type magnets is commonly attributed to the difference in magnetic properties between the $Sm_2(Co,Fe)_{17}$ matrix and the $Sm(Co,Cu)_5$ cell boundary phase [24, 25, 84, 93]. This difference is enhanced by an increasing Cu content in the

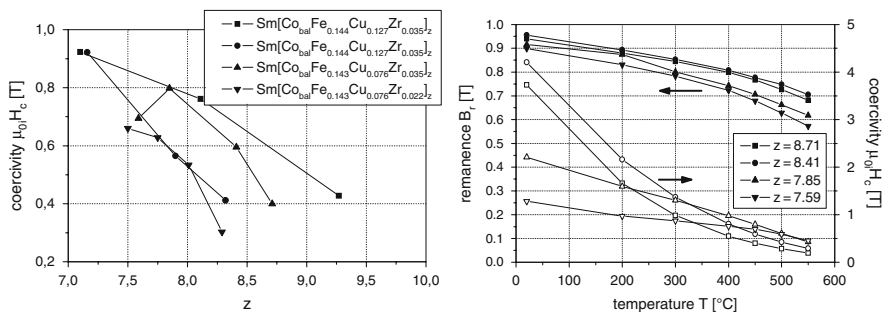
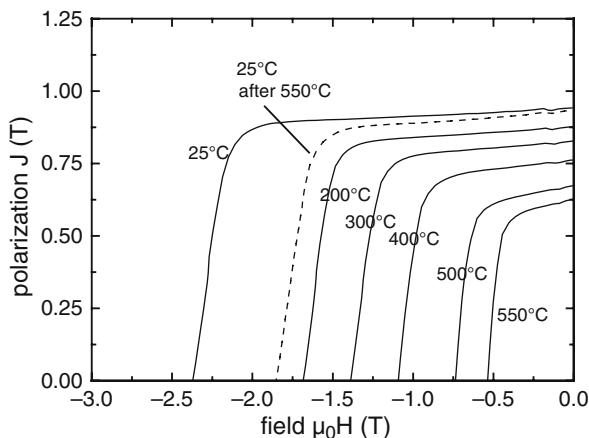


Fig. 12.7 Coercivity μ_0H_c vs. z at 450°C (left); remanence B_r (full symbols \rightarrow left axis) and coercivity μ_0H_c (empty symbols \rightarrow right axis) vs. temperature of $Sm(Co_{bal}Fe_{0.144}Cu_{0.076}Zr_{0.035})_z$ (right)

$\text{Sm}(\text{Co},\text{Cu})_5$ phase leading to a dramatic decrease of the anisotropy constant K_1 of this phase [58]. The maximum of the coercivity is shifted to lower z values, which are thus seen to lead to a better temperature coefficient of the intrinsic coercivity [63]. As an example, remanence and coercivity of $\text{Sm}(\text{Co}_{\text{bal}}\text{Fe}_{0.144}\text{Cu}_{0.076}\text{Zr}_{0.035})_z$ are shown in Fig. 12.7 (right) for the temperature range from room temperature to 550°C .

Fig. 12.8 Second quadrant demagnetization loops of $\text{Sm}(\text{Co}_{0.784}\text{Fe}_{0.1}\text{Cu}_{0.088}\text{Zr}_{0.028})_{7.19}$ for various temperatures. Reproduced with permission of Elsevier from [41]



The effect of compositional changes in $\text{Sm}(\text{Co}_{\text{bal}}\text{Fe}_v\text{Cu}_y\text{Zr}_x)_z$ alloys on the high-temperature magnetic properties has been studied systematically. A high level of both Cu and Zr is found to be effective for improving the high-temperature properties. The real benefit in compositions with high Cu content lays in the possibility to increase the Sm level and still achieve a high Cu concentration in the $\text{Sm}(\text{Co},\text{Cu})_5$ cell boundary phase. An increased Zr level shifts the optimum Sm content to lower levels, and magnets with excellent high-temperature coercivities were prepared with a samarium content well below the “2:17” stoichiometry. Figure 12.8 shows second quadrant demagnetization loops of $\text{Sm}(\text{Co}_{0.784}\text{Fe}_{0.100}\text{Cu}_{0.088}\text{Zr}_{0.028})_{7.19}$ for temperatures up to 550°C illustrating the excellent high-temperature properties ($(BH)_{\text{max}} = 82 \text{ kJ/m}^3$, $B_r = 0.67 \text{ T}$, and $\mu_{0i}H_c = 0.74 \text{ T}$) at 500°C [41].

SEM micrographs of the $\text{Sm}(\text{Co}_{0.784}\text{Fe}_{0.1}\text{Cu}_{0.088}\text{Zr}_{0.028})_{7.19}$ -sintered magnet (Fig. 12.9) show a uniform cellular structure (the corresponding TEM bright field images are shown in Fig. 12.4). Figure 12.10 shows the STEM and HRTEM images of typical $\text{Sm}(\text{Co}_{0.784}\text{Fe}_{0.1}\text{Cu}_{0.088}\text{Zr}_{0.028})_{7.19}$ magnets (imaging plane perpendicular to the c -axis). The HRTEM image shows the 1:5 cell boundary phase with a width of about 5–10 nm. In the composition maps of Cu, Co, Fe, and Sm (Fig. 12.11), the bright regions represent a high concentration of the respective element and the dark regions are depleted in the element: the 2:17 matrix phase is rich in Co and Fe, while the cell boundary phase is rich in Cu and Sm.

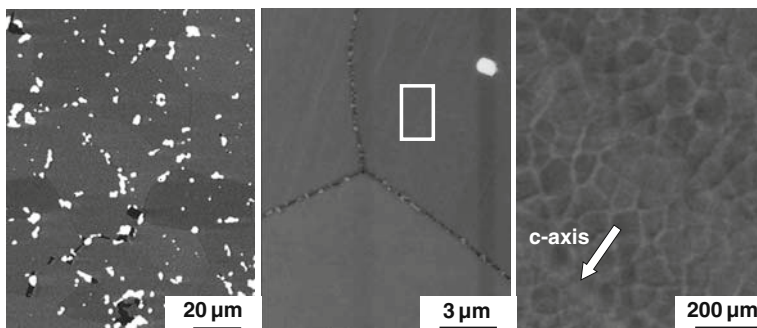


Fig. 12.9 Backscattered electron mode SEM images of a $\text{Sm}(\text{Co}_{0.784}\text{Fe}_{0.100}\text{Cu}_{0.088}\text{Zr}_{0.028})_{7.19}$ -sintered magnet showing the coarse grain structure with some Sm-rich precipitates (*left*), a grain boundary with Zr-rich regions (*middle*) and (*right* – image taken within the area indicated by the frame in the *middle image*) the cellular network of 1:5-type phase and indications of the lamellar phase (c-axis approximately parallel to the imaging plane and perpendicular to the lamellar phase). Reproduced with permission of Elsevier from [41]

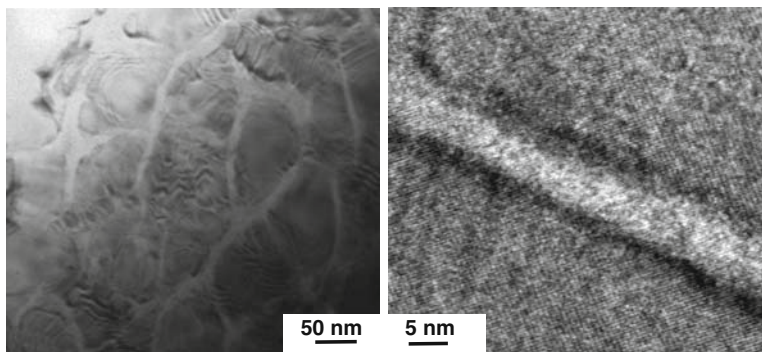


Fig. 12.10 STEM (*left*) image of a $\text{Sm}(\text{Co}_{0.784}\text{Fe}_{0.100}\text{Cu}_{0.088}\text{Zr}_{0.028})_{7.19}$ magnet (c-axis perpendicular to the imaging plane) and HRTEM (*right*) image showing the cellular phase in detail. Reproduced with permission of Elsevier from [41]

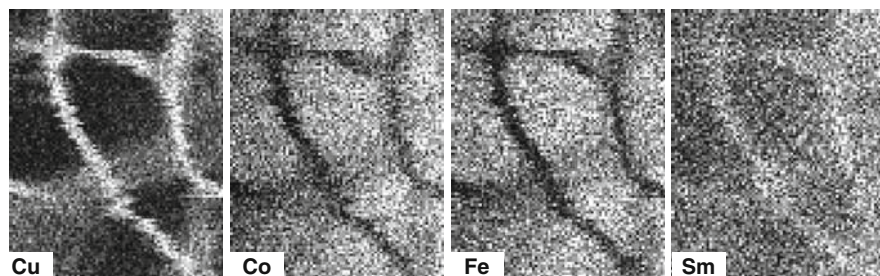


Fig. 12.11 Element mapping for Cu, Co, Fe, and Sm in a $\text{Sm}(\text{Co}_{0.784}\text{Fe}_{0.100}\text{Cu}_{0.088}\text{Zr}_{0.028})_{7.19}$ magnet (width of each image is 200 nm) confirming that the cell boundary phase is rich in Cu and Sm. Reproduced with permission of Elsevier from [41]

12.3.3 Stability at Operating Temperature

An important question is the stability of magnetic properties at operating temperatures exceeding 400°C. An analysis of the evolution of coercivity at room temperature after measurements at different temperatures shows that the coercivity of the magnets is decreased with increasing measurement temperature. A coercivity of up to 0.5 T was obtained at 550°C. No obvious change in the coercivity at room temperature is detected after high-temperature measurements below or at 400°C. However, the coercivity measured at RT starts to reduce after HT measurements above 400°C and the higher the measurement temperature, the larger the loss of coercivity at RT. After the measurement at 550°C, the coercivity at room temperature is reduced from 2.8 to 2.3 T [45]. The observed decrease in coercivity above 400°C was found to be due to microstructural changes in the bulk and not due to surface degradation. The losses in coercivity can be fully recovered when the last segment of the original heat treatment of the magnet (550–400°C with 0.7 K/min and 3 h at 400°C) is repeated (as shown in Fig. 12.12 (left)).

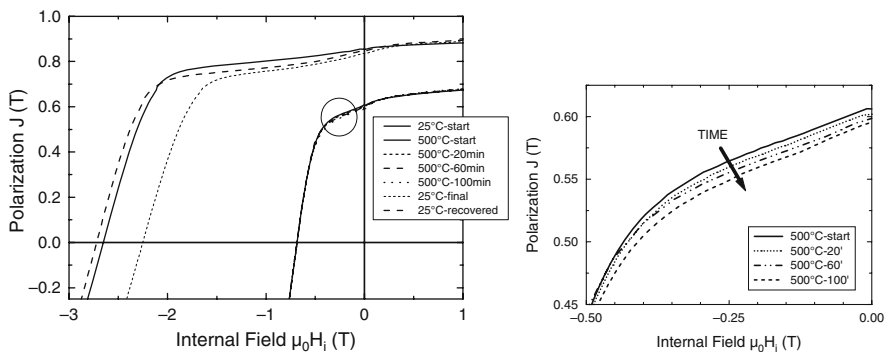


Fig. 12.12 Demagnetization curves of a $\text{Sm}(\text{Co}_{0.784}\text{Fe}_{0.100}\text{Cu}_{0.088}\text{Zr}_{0.028})_{7.19}$ -sintered magnet at RT (25°C – start), at 500°C after various time intervals, and again at RT after the high-temperature measurements (25°C – final) (left); enlargement of the circled area in the top figure showing the degradation of remanence during in situ high-temperature VSM measurements with increasing time (right). Reproduced with permission of IEEE Trans. Magn. from [45]

The exposure to temperatures as high as 550°C presents new challenges because of the reactions between the magnet and the environment. It has been demonstrated that exposure to air leads to a severe loss in the magnetic properties of the 2:17 SmCo magnets. Samples annealed in air form a surface region of about 20 μm thickness with enhanced oxygen content and a decreasing Sm content [45]. It was reported that the major cause for the magnetic loss is Sm depletion [10]. Sm is lost by vaporization from the surface, leaving an oxide of Fe–Co, and preventing the vaporization of Sm seems to be more challenging than preventing the surface oxidation. The Sm loss at the surface causes an increasing dip in the second quadrant

demagnetization curve with increasing annealing time. Thus, surface protection by coating can minimize Sm depletion and is crucial for the application of the magnets at high temperature in air. The oxidation mechanism of high-temperature magnet grades has been examined in detail by Kardelky et al. [48].

12.4 Microchemistry and Pinning Behavior in $\text{Sm}_2\text{Co}_{17}$ -Type Magnets

12.4.1 Redistribution of Cu and Slow Cooling

The temperature dependence of coercivity of the $\text{Sm}_2\text{Co}_{17}$ -type magnets is determined by microstructure and microchemistry of the various phases. The cellular and lamellar phases are formed during isothermal aging but the coercivity after this stage is still low. Cu diffusion into the 1:5 cell boundary phase is assumed to take place during slow cooling and the higher the quenching temperature, the lower the Cu content in 1:5 phase [84]. The diffusion of Cu into the 1:5-type cell boundary phase leads to a modification of the magnetic properties of the 1:5-type phase and thus a significant domain wall energy difference between 2:17- and 1:5-type phases. Slow cooling is necessary to develop high coercivity at room temperature and the concomitant evolution of microchemistry of the phases in the $\text{Sm}_2\text{Co}_{17}$ -type magnets needs to be understood in detail.

Figure 12.13 shows typical hysteresis loops of the $\text{Sm}(\text{Co}_{0.74}\text{Fe}_{0.1}\text{Cu}_{0.12}\text{Zr}_{0.04})_{7.5}$ ribbons subjected to aging at 850°C for 3 h without slow cooling or followed by slow cooling to different temperatures (600°C and 400°C). A coercivity of 3.0 T as well as strong domain wall pinning is observed at room temperature for the ribbons after aging at 850°C for 3 h and subsequent slow cooling to 400°C (type I), which is much higher than that of the ribbons without slow cooling (0.32 T); the latter sample is in the following referred to as type II. The coercivity of ribbons develops

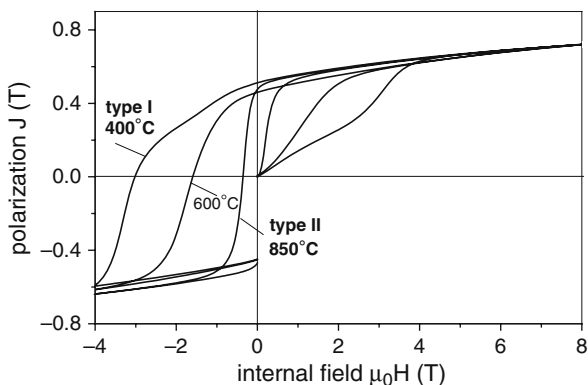


Fig. 12.13 Typical hysteresis loops of $\text{Sm}(\text{Co}_{0.74}\text{Fe}_{0.1}\text{Cu}_{0.12}\text{Zr}_{0.04})_{7.5}$ ribbons subjected to aging at 850°C for 3 h without slow cooling (type II) or followed by slow cooling to different temperature (600°C and 400°C (type I)). Reproduced with permission of American Institute of Physics from [108, 109]

mainly during slow cooling, very similar to the behavior observed in bulk and melt-spun $\text{Sm}(\text{Co},\text{Fe},\text{Cu},\text{Zr})_z$ materials subjected to a conventional precipitation-hardening regime.

Uniform cellular and lamellar structures are formed upon isothermal aging the as-spun ribbons at 850°C for 3 h, without subsequent slow cooling. The cell size is about 40 nm, which is smaller than that observed in the conventional sintered $\text{Sm}(\text{Co},\text{Fe},\text{Cu},\text{Zr})_z$ magnets [27, 28]. After slow cooling no obvious changes in cell size and density of lamellar phase are observed [105, 107].

Thus, the evaluation of coercivity should be attributed to chemical modifications of the cell boundary phase, especially of the Cu distribution. Nanoprobe energy dispersive X-ray analysis (EDX) profiles of Cu in the vicinity of a matrix/cell boundary phase in the type I and type II samples (Fig. 12.14) show that the 1:5 cell boundary phases are enriched in Cu, in contrast to the 2:17 matrix phase, but the Cu distribution in the cell boundary phase varies significantly in the type I and type II samples: a large gradient of the Cu content is observed in the cell boundary phase of the type I sample. The Cu content in the middle of the cell boundary phase (24 at.%) is three times as high as that of the region near the 2:17 phase, similar to that observed in bulk and melt-spun $\text{Sm}(\text{Co},\text{Fe},\text{Cu},\text{Zr})_z$ materials subjected to conventional magnetic hardening [33, 43]. However, the Cu content in the cell boundary phase of the type II sample is more uniform, revealing the redistribution of Cu within the cell boundary

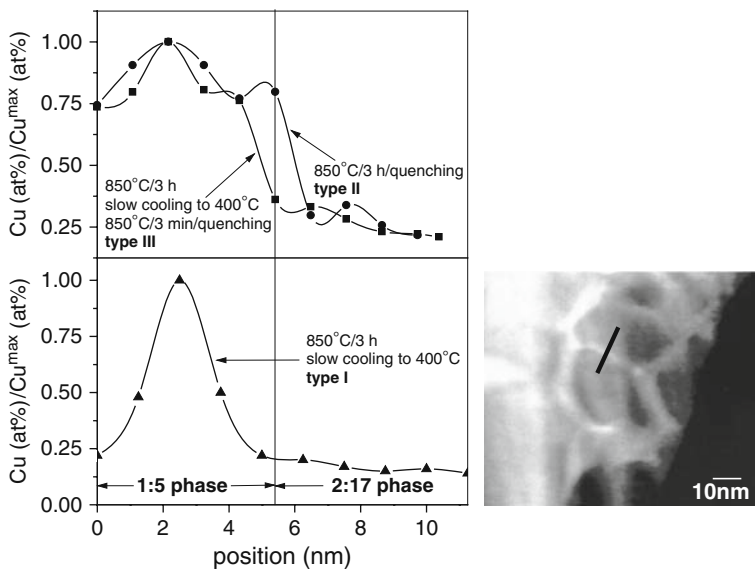


Fig. 12.14 EDX line scans (marked as a *black line* in the STEM image) for Cu across a matrix/cell boundary interface in $\text{Sm}(\text{Co}_{0.74}\text{Fe}_{0.1}\text{Cu}_{0.12}\text{Zr}_{0.04})_{7.5}$ ribbons, which have been aged at 850°C for 3 h and (1) slow cooled to 400°C and quenched (*bottom* – type I), (2) quenched from 850°C without slow cooling (*top* – type II), and (3) slow cooled to 400°C and quenched, then rapidly reheated to 850°C and quenched after a 5 min dwell (*top* – type III). Reproduced with permission of American Institute of Physics from [108, 109]

phase during slow cooling. An obvious difference of the chemical composition is not observed in the 2:17 matrix phase of the type I and type II samples (these results are consistent with three-dimensional atom probe (3DAP) analysis [36]). The solubility of Cu in 2:17 SmCo phase is 16 at.% at 1,200°C, which is significantly reduced to 4 at.% at 800°C [79]. Thus, most of the Cu atoms in the ribbons should already segregate in the 1:5 cell boundary phase during isothermal aging due to the very low solubility of Cu in the 2:17 matrix phase at that temperature, and the amount of Cu diffusing into the cell boundary phase during slow cooling should be quite limited.

The coercive force of Sm(Co,Cu)₅ alloys can be significantly increased by aging at low temperature due to the occurrence of a spinodal decomposition [72]. Hofer [46] reported an ideal mixing of Co and Cu in the 1:5 composition at high temperature (>800°C) and a separation into a SmCo₅ phase containing some Cu in solution and a Co-modified SmCu₅ phase due to a spinodal-type decomposition at low temperature. The annealing temperature, time, and cooling rate are of great importance because the resulting properties of Sm(Co,Cu)₅ alloy are very structure dependent. It could be argued that it is a kind of decomposition-type reaction taking place in the Cu-rich Sm(Co,Cu)₅ cell boundary phase of 2:17 SmCo magnets during slow cooling, leading to a large gradient of the Cu content within this phase. On the other hand, the formation of the gradient could also help to reduce lattice strain between the cell and the boundary phases.

Magnetic viscosity $S = -dM/d\ln t$ (with M the magnetization of the samples and t the time) measurements in the two types of Sm₂(Co,Fe,Cu,Zr)₁₇ ribbons have been used to deduce the activation volume v_a and its temperature dependence, in relation to that of the coercive field [40]. A clear difference in the $v_a(T)$ between the two types of ribbons, consistent with differences in $H_c(T)$, has been found. At room temperature the type I ribbon has a high coercivity, iH_c , in contrast to the relatively low coercivity of type II. In type II iH_c and H_c almost coincide in the whole range of T and their T dependence is related linearly to that of $v_a^{-2/3}$. According to the “Global model” of coercivity and magnetic viscosity [2, 31, 32] such a behavior is expected for materials in which (i) the critical elementary magnetization reversal processes (CEMRPs) are mainly governed by the intrinsic properties of the magnetic main phase of the material and (ii) second-order anisotropy is dominant. These CEMRPs are assumed to be concentrated in small critical volumes of typical size v_a , as derived from viscosity data. In Sm₂Co₁₇-type magnets, the CEMRPs are domain wall unpinning events. The difference in iH_c and H_c and the stronger T dependence of $v_a^{-2/3}$ in the type I material can naturally be related to the more complicated chemical microstructure of this sample, in particular, the large Cu concentration gradient in the 1:5 cell boundary phase. Here the CEMRPs are not simply related to the intrinsic properties of the main phase (thus v_a depends not only on main phase properties). iH_c of type I decreases monotonically with increasing T whereas that of type II becomes almost constant when approaching RT. This is attributed to the different Cu concentration gradients in the 1:5 cell boundary phase in the two types of ribbon. In the same manner, the positive T coefficient of coercivity between 473 and 773 K (compare Fig. 12.18) for type II can be explained. The large differences in the $v_a(T)$ of the two types of ribbons are consistent with their $H_c(T)$ behavior. The

activation length $l_a = v_a^{1/3}$ of type I decreases from 7.8 nm at room temperature to 2.4 nm at 20 K, whereas that of type II decreases from 12.1 nm at room temperature to 3.7 nm at 4 K. The typical width of the 1:5 cell boundary phase in the ribbons is ~ 7 nm, which roughly agrees with the room temperature domain wall width δ_w of the main phase.

The coercive field of a 180° domain wall can be approximated by [55] $H_c = 1/(2 J_s \cos\psi_0) \times (d\gamma(z)/dz)_{\max} - N_{\text{eff}}M_s$ (J_s : spontaneous polarization; ψ_0 : angle between applied field and the easy direction; $(d\gamma(z)/dz)_{\max}$: maximum slope of the wall energy in the phase boundary; the term $N_{\text{eff}}M_s$ describes the force of a locally acting effective demagnetizing field). A homogeneous Cu content thus leads to a low gradient of the domain wall energy $(d\gamma(z)/dz)_{\max}$ in the sample without slow cooling and thus weak domain wall pinning and low coercivity. In contrast, the larger gradient of the Cu content in the cell boundary phase after slow cooling yields stronger domain wall pinning within the cell boundary phase, resulting in high coercivities. The main contribution of slow cooling to the coercivity of 2:17 SmCo magnets is the development of a large Cu gradient within the Cu-rich $\text{Sm}(\text{Co},\text{Cu})_5$ cell boundary phase. The significant improvement in the coercivity of 2:17 SmCo magnets could result from the large gradient of domain wall energy within the Cu-rich $\text{Sm}(\text{Co},\text{Cu})_5$ cell boundary phase and not from the Cu diffusion from the 2:17 phase to the 1:5 phase, as proposed by the well-known two-phase domain wall pinning model, the latter being based on a uniform Cu content and domain wall energy in the cell boundary phase [22, 24, 25, 27, 28, 34, 43, 66].

12.4.2 Stability of Microchemistry

The stability of microchemistry in $\text{Sm}(\text{Co},\text{Fe},\text{Cu},\text{Zr})_z$ magnets at high temperature and its effect on the magnetic properties need to be addressed. Figure 12.15 shows that an additional aging at 850°C for only 5 min, after having completed the slow cooling regime, has a dramatic effect on the magnetic properties. Figure 12.16(a) shows the dependence of the coercivity of the ribbons upon aging temperature for an additional 5 min annealing in more detail. A higher aging temperature leads to higher losses in the coercivity, and the ribbons subjected to only 5 min aging at 850°C (type III) show a very low coercivity of 0.16 T, which is only 5% of the value of the original ribbon (type I). Further changes in coercivity are not observed with further increasing aging time at 850°C , i.e., all the changes took place within the initial 5 min (Fig. 12.16(b)).

Figure 12.14 shows also the nanoprobe EDX profile of Cu obtained by a line scan across the interface between the 2:17 matrix and the 1:5 cell boundary phase in the type III sample. After an additional 5 min aging at 850°C (type III), no obvious change of chemical composition is observed in the 2:17 matrix phase, but the Cu distribution within the cell boundary phase becomes again more homogeneous and the large gradient of the Cu content is no longer detectable. A rapid redistribution of Cu within the cell boundary phase has taken place and is very similar to that

Fig. 12.15 Hysteresis loops of ribbons before (type I) and after (type III) additional aging at 850°C for 5 min. Reproduced with permission of American Institute of Physics from [108, 109]

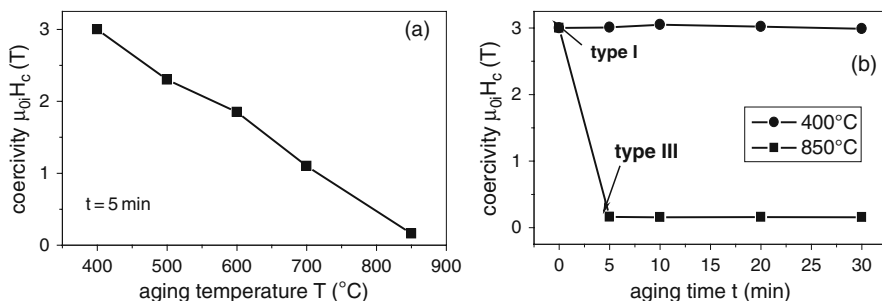
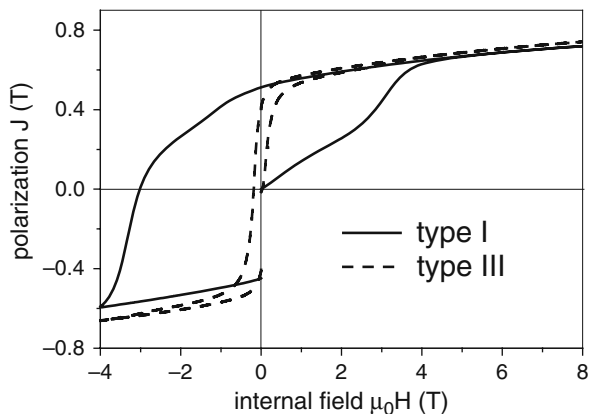


Fig. 12.16 Dependence of the coercivity of $\text{Sm}(\text{Co}_{0.74}\text{Fe}_{0.1}\text{Cu}_{0.12}\text{Zr}_{0.04})_{7.5}$ ribbons on (a) aging temperature T (additional isothermal aging for 5 min after having completed the slow cooling regime) and (b) aging time t (for isothermal aging at 850 and 400°C). Reproduced with permission of American Institute of Physics from [108, 109]

observed in the ribbons subjected to isothermal aging at 850°C for 3 h without slow cooling (type II).

It is generally accepted that a high Cu content in the cell boundary is beneficial for the development of high coercivity in $\text{Sm}(\text{Co},\text{Fe},\text{Cu},\text{Zr})_z$ magnets both at room temperature and at high temperatures since more Cu in the 1:5 boundary phase leads to a lower domain wall energy of the 1:5 cell boundary phase and a larger domain wall energy difference, assuming that the anisotropy of the 2:17 matrix phase does not change. According to this well-known two-phase domain wall pinning model, the dramatic loss of the coercivity in the type II sample can be attributed to the significant reduction of the Cu content in the 1:5 cell boundary phase, and Cu should diffuse into the 2:17 matrix phase during the subsequent short-time aging. However, the above EDX shows that the Cu content in the 2:17 matrix phase remains more or less constant after the short aging. In fact, the solubility of Cu in the 1:5 phase is much higher than that in the 2:17 matrix phase and a complete solubility is expected between SmCo_5 and SmCu_5 only above 800°C [79]. Thus, most of the Cu should already segregate in the 1:5 cell boundary phase during isothermal aging due to

the very low solubility of Cu in the 2:17 matrix phase at this temperature, and the amount of Cu diffusing into the cell boundary phase during slow cooling should be quite limited. Moreover, a short time such as 5 min seems not to be sufficient for a significant diffusion of Cu from the 1:5 phase into the 2:17 phase to take place. Thus, Cu appears to be present in the 1:5 cell boundary phase after the additional aging at 850°C for only 5 min, and a redistribution of atoms (Sm,Co,Cu,Fe,Zr) within the very thin cell boundary phase (width around 5–10 nm) appears to be more likely.

Based on the Cu content dependence of the anisotropy constant K_1 as well as the domain wall energy γ for Cu-substituted $\text{Sm}(\text{Co,Cu})_5$ alloys [58], simplistic γ profiles across the 1:5 cell boundary phase for samples of type I and II can be derived. In the case of a high-coercivity state (type I), a strong pinning occurs within the cell boundary phase due to the very large slope of the domain wall energy. For a thickness of the cell boundary phase larger than that of the domain wall, the domain wall may be attractively pinned at the center of the cell boundary phase, due to the lower domain wall energy of these Cu-rich regions. In addition, the redistribution of Cu within the 1:5 cell boundary phase during slow cooling leads to a significant reduction in Cu content in the 1:5 phase close to the interface to the 2:17 matrix phase. Thus, due to the irregularity of the domain wall energy at this interface the pinning mechanism might be even more complex after slow cooling. The 2:17 domain walls may be repelled at this interface by a Cu-deficient 1:5 phase with higher domain wall energy (repulsive pinning). However, when the size of the inhomogeneities, i.e., the thickness of the 1:5 cell boundary phase, is comparable to or smaller than the domain wall thickness, $\delta_w \approx 5$ nm, the characterization of the pinning is more complicated.

Further, temperature-dependent changes of the domain wall energy γ profile across the 1:5 cell boundary phase need to be considered. For the ribbons without slow cooling, the EDX analysis shows that the Cu distribution within the 1:5 cell boundary phase is roughly uniform. The coercivity at low or room temperature is caused by a repulsive pinning at the cell boundaries and the complicated temperature dependence of the coercivity can still be explained by the conventional repulsive/attractive model, i.e., a crossover between repulsive and attractive pinning at a certain temperature T . When the sample is slowly cooled to lower temperatures, the Cu distribution within 1:5 phase becomes inhomogeneous and a large gradient of Cu content and domain wall energy is formed, leading to a significant improvement of the coercivity at room temperature. It can be assumed that the Cu-rich 1:5 layer in the middle of the cell boundary becomes paramagnetic at a certain temperature, depending on the amount of Cu. The higher the measuring temperature, the more the fraction of paramagnetic 1:5 phase. In this case, coercivity may be controlled by a competition between domain wall pinning at the magnetic Cu-poor 1:5 layer near the 2:17 cell and nucleation of reversed domains in the ferromagnetic 1:5 layers or 2:17 cells. When the measuring temperature is further increased, all of the 1:5 phase becomes paramagnetic and the coercivity could be related to nucleation of reversed domains in the ferromagnetic 2:17 cells.

Another point to be considered, apart from microchemical modifications, is the possibility that the cell boundary phase is actually composed of a mixture of 2:7- and

5:19-type phases after annealing at 850°C, i.e., before slow cooling [15, 16]. This scenario cannot be excluded and this might well affect the above-mentioned differences in domain wall energy between matrix and cell boundary phases [35]; however, it is difficult to imagine that these crystal structure changes are also reversible as demonstrated for the microchemical changes. In any case, these considerations illuminate that the magnetic and microchemical properties of the Sm(Co,Cu)₅-type cell boundary phase, corresponding in fact to the oldest rare earth–transition metal magnet (compare, for example, “Giant intrinsic magnetic hardness in SmCo_{5-x}Cu_x” as reported by Oesterreicher et al. [73] or Kerschel et al. [51]), deserve more attention and a full understanding of the magnetic, structural, and microchemical properties of the cell boundary phase during slow cooling is indispensable for clarifying the very complex coercivity mechanism of 2:17 SmCo magnets.

12.4.3 “Anomalous” Coercivity Behavior

The quenching temperature dependence of coercivity at room temperature and the temperature stability of Sm(Co_{0.74}Fe_{0.1}Cu_{0.12}Zr_{0.04})_{7.5} ribbons are shown in Fig. 12.17. The coercivity at room temperature continues to decrease with increasing quenching temperature and is reduced to only 0.32 T for the ribbons after aging at 850°C for 3 h without slow cooling, revealing that the coercivity at room temperature develops mainly during slow cooling. The temperature coefficient of the coercivity is negative over the entire temperature range (RT–500°C) for the ribbons quenched at 750°C and below. In contrast, a higher quenching temperature leads to a lower coercivity at room temperature but a smaller temperature coefficient and even a positive one (200–500°C), the last phenomenon also called an “anomalous” coercivity behavior. Coercivities of 0.22 T at 200°C and 0.32 T at 500°C are obtained in the ribbons aged at 850°C for 3 h without slow cooling, similar to those observed in bulk and melt-spun Sm(Co,Fe,Cu,Zr)_z magnets with very low Cu content subjected to the conventional aging program [33, 61, 62, 80, 113].

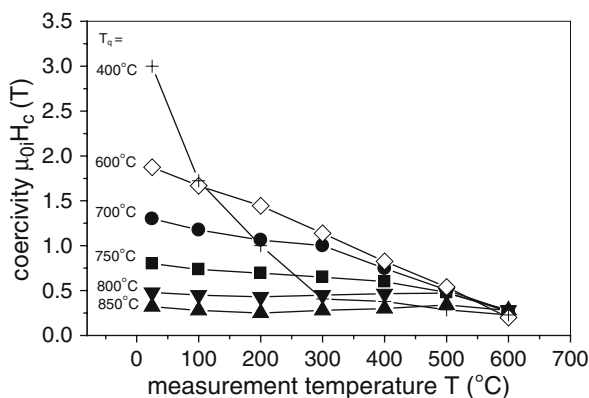


Fig. 12.17 Coercivity vs. measurement temperature of Sm(Co_{0.74}Fe_{0.1}Cu_{0.12}Zr_{0.04})_{7.5} ribbons (3 h at 850°C, then slow cooling to temperature T_q (as indicated on the left), followed by quenching). Reproduced with permission of IEEE Trans. Magn. from [104–107]

Figure 12.18 (left) shows the coercivity vs. measurement temperature of the ribbons quenched from 850 and 800°C indicating a complex coercivity behavior upon changing temperature with three distinguished regions for the domain wall energy γ : the transition from I – repulsive pinning with $\gamma_{2:17} < \gamma_{1:5}$ to II – attractive pinning with $\gamma_{2:17} > \gamma_{1:5}$. Furthermore, one can assume a nucleation-type mechanism (III) to be active in a comparatively narrow temperature window (III) between the Curie temperature of the 1:5 cell boundary phase and that of the 2:17 matrix phase. These findings are consistent with results by Tang et al. [99]. At the crossover from region II to III, one can assume that the 2:17 cells become magnetically isolated, provided the thickness of the cell boundary phase is sufficient to assure magnetic decoupling (compare Skomski et al. [89] for an evaluation of exchange through non-magnetic insulating matrix), and the CEMRPs are governed by nucleation in the cell interior. At this point, i.e., above $T_C(1:5)$, one should also expect a drastic deviation from the phenomenological relationship $\nu_a \sim \delta_w^3$ [30], and this has actually been shown by Panagiotopoulos et al. [75]. The temperature coefficient of coercivity (Fig. 12.19 (right)) becomes negative when the ribbons are cooled below 750°C and the lower the quenching temperature, the more negative the temperature coefficient of coercivity. A coercivity of 0.53 T at 500°C was obtained in the sample quenched at 600°C.

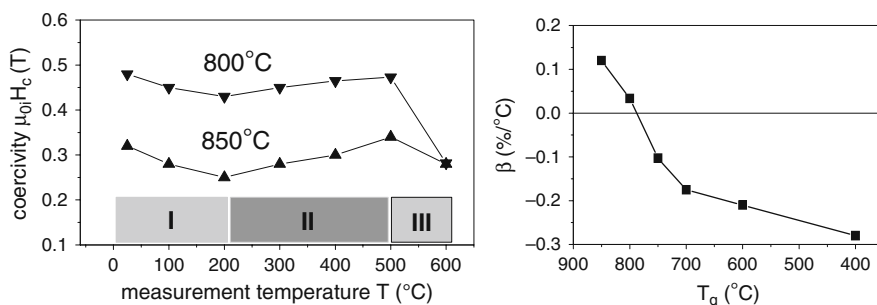


Fig. 12.18 Coercivity vs. measurement temperature of $\text{Sm}(\text{Co}_{0.74}\text{Fe}_{0.1}\text{Cu}_{0.12}\text{Zr}_{0.04})_{7.5}$ ribbons quenched from 850 and 800°C indicating an unconventional coercivity behavior with temperature: the transition from I – repulsive pinning with $\gamma_{2:17} < \gamma_{1:5}$ to II – attractive pinning with $\gamma_{2:17} > \gamma_{1:5}$ and III – nucleation type with $T > T_C(1:5)$ (left). Temperature coefficient of intrinsic coercivity β (200–500°C) vs. quenching temperature T_q (right). Reproduced with permission of IEEE Trans. Magn. from [104–107]

The Cu content in the 1:5 cell boundary phase can be controlled by the quenching temperature and thus the coercivity and its temperature coefficient are affected strongly not only by the alloy composition but also by the aging program. A low Cu content in the 1:5 cell boundary phase is helpful to develop positive temperature coefficients [33, 61, 62, 113]. A positive temperature coefficient of coercivity as well as a negative one can be obtained even in $\text{Sm}(\text{Co,Fe,Cu,Zr})_z$ ribbons with a quite high Cu content by quenching from high temperature. On the other hand, a lower quenching temperature leads to a more negative temperature coefficient of the coercivity.

12.5 Magnetic Domains and Coercivity

12.5.1 Analysis of Magnetic Microstructure

The analysis of the magnetic microstructure in these complex multiphase nanostructures can further the understanding of the evolution of coercivity during the slow cooling ramp (usually around 0.7 K/min). Lorentz microscopy on thinned specimen reveals a zigzag-shaped domain pattern, which follows the cell boundaries [27, 28, 43, 112]. This observation is consistent with the domain walls being pinned at the cell boundaries of the prismatic cellular microstructure and based on the intrinsic magnetic properties of the various phases present (the anisotropy constant K_1 of the cell matrix is about 2.6 times larger than that of the cell boundary phase whereas the exchange constant A can be assumed to be comparable [93]). It can be assumed that this interaction is of attractive type at room temperature. It should be noted, however, that domain observation by TEM has only limited relevance concerning the domain structures of bulk materials and the change of those structures in a magnetization process because domain structures are very sensitive to the sample thickness [47], and therefore, the domains in samples thinned for TEM investigation can be very different from those in the bulk. Some early work using magneto-optic Kerr microscopy reports an irregular laminar domain structure [54, 23, 24, 25, 65] and that reverse domains originate at grain boundaries [60].

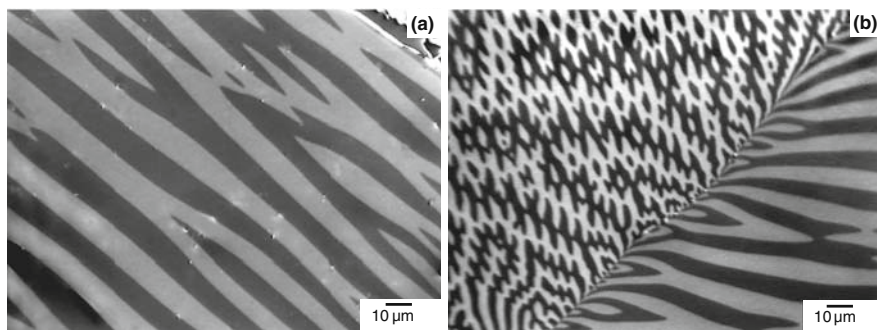


Fig. 12.19 Kerr microscopy images taken in a coarse-grained and homogeneous region of the $\text{Sm}_2\text{Co}_{17}$ as-cast alloy. (a) Wide domains separated by 180° domain walls on the surface of a grain with its magnetically easy axis (c -axis) almost parallel to the imaging plane – “well-oriented grain”; (b) domain structures of a misoriented grain (*left*) and a well-oriented grain (*right*). At the grain boundary, the latter shows the effect of two-phase domain branching on its boundary perpendicular to the easy axis. Reproduced with permission of Elsevier from [41]

Figure 12.19 shows Kerr microscopy images of as-cast $\text{Sm}_2\text{Co}_{17}$; a domain structure typical for single-phase bulk high-anisotropy easy-axis-type ferromagnets is observed [47, 64]. The domain structure on the surface of such polycrystalline samples depends on the intrinsic magnetic properties of the material, in particular the spontaneous polarization J_s , the exchange stiffness A , and the anisotropy constants, most importantly K_1 . But it also depends on the size (thickness) of the grains as

well as the orientation of the grain surface with respect to the magnetically easy axis. Domains separated by 180° domain walls on a weakly misoriented surface of a grain (i.e., the easy axis is almost parallel to the imaging plane) can be seen in Fig. 12.19(a). Domain patterns on a strongly misoriented surface are shown in Fig. 12.19(b – top part), and so-called two-phase domain branching at the boundary of a well-oriented grain is shown in Fig. 12.19(b – bottom part).

12.5.2 Domains and Processing Parameters

The aforementioned high-temperature grades of sintered SmCo 2:17-type magnets have been cooled slowly from the aging temperature of 850°C to different temperatures T_q and then quenched. The $\text{Sm}(\text{Co}_{0.784}\text{Fe}_{0.1}\text{Cu}_{0.088}\text{Zr}_{0.028})_{7.19}$ magnet slowly cooled to 400°C develops the coercivity fully, whereas magnets quenched from $T_q = 750^\circ\text{C}$ or higher show very small or almost no coercivity. A relatively sharp increase in coercivity can be observed around $T_q = 725^\circ\text{C}$ (Fig. 12.20).

Fig. 12.20 Evolution of coercivity at room temperature in dependence on quenching temperature T_q from the slow cooling ramp of $\text{Sm}(\text{Co}_{0.784}\text{Fe}_{0.100}\text{Cu}_{0.088}\text{Zr}_{0.028})_{7.19}$ -sintered magnets

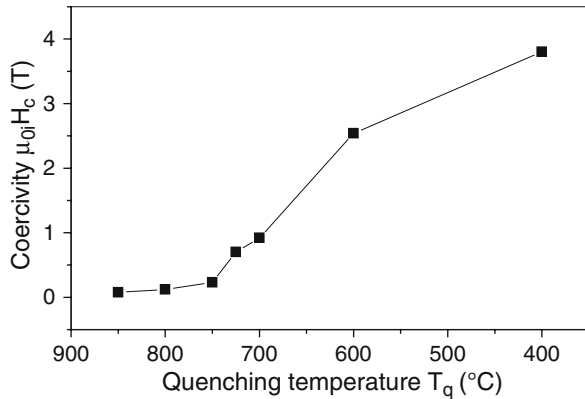


Figure 12.21 shows the magnetic domain structure observed by Kerr microscopy and magnetic force microscopy (MFM) of thermally demagnetized magnets, which have been annealed at 850°C and quenched, or slowly cooled from 850°C to $T_q = 800 - 750 - 700 - 600 - 400^\circ\text{C}$ and then quenched. The nominal c-axis is in all cases perpendicular to the imaging plane. The magnets quenched from $T_q \geq 750^\circ\text{C}$ show very coarse domain structures. According to Fig. 12.20 the coercivity of these three magnets is very small. A comparison of these coarse structures in the upper two rows of Fig. 12.21 with those in the lower row shows that MFM and Kerr microscopy yield the same results if the characteristic lengths of the investigated magnetic structure are larger than the optical resolution limit of about 300 nm.

The magnet slowly cooled to 400°C , thus exhibiting maximum coercivity, and shows a very fine magnetic domain contrast, hardly resolved by Kerr microscopy. As MFM senses here only the vertical components of the force gradient of the magnetic stray field, all regions (here cells) that have the same magnetization direction

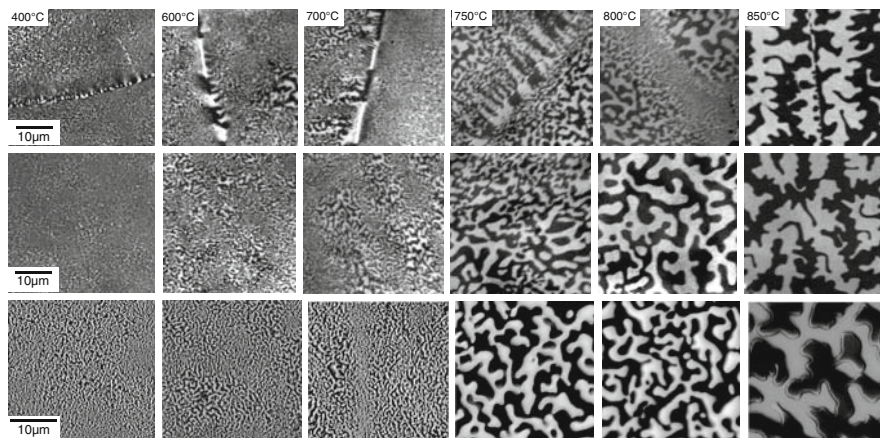


Fig. 12.21 Domain structure observed by Kerr microscopy (*two top rows*) and MFM (*bottom row*) of thermally demagnetized high-temperature grade $\text{Sm}(\text{Co}_{0.784}\text{Fe}_{0.100}\text{Cu}_{0.088}\text{Zr}_{0.028})_{7.19}$ magnets (nominal *c*-axis is perpendicular to the imaging plane) quenched from different temperatures (as indicated in the *bottom row images*) on the slow cooling ramp. The Kerr images of the *first row* show clearly that the grain boundary also has a very specific magnetic contrast. Reproduced with permission of Elsevier from [41]

will constitute a single feature in the magnetic contrast. The high-resolution MFM images in Fig. 12.22 (left: scan size of $10\ \mu\text{m} \times 10\ \mu\text{m}$) with the nominal *c*-axis perpendicular (a) and parallel (b) to the imaging plane clarify that the areas of uniform magnetic contrast extend over several dozens of individual cells. The overall morphology of the cellular structure with cell sizes of about 100 nm and the overlying Zr-rich lamellar phase within grains of several tens of microns are comparable for all of these magnets, regardless of the quenching temperature T_q .

In the whole range of considered quenching temperatures T_q and, consequently, in the whole range of $i H_c$, the magnetic domain structure is considerably coarser than the cellular structure. Nevertheless, the physical nature of the domains in the left and in the right parts in Fig. 12.21 is obviously different. For the samples cooled from $T_q \geq 750^\circ\text{C}$ the differences in the intrinsic magnetic properties (in particular in the anisotropy constant K_1) of the 2:17R-type cells and the 1:5-type cell boundary phase are relatively small. Thus, because the cells as well as the cell boundaries are coherent to each other within the large grains, the latter can be considered as single crystals with weakly fluctuating intrinsic magnetic properties. As a first approximation, the coarse domain structure is associated with effectively homogeneous intrinsic magnetic properties close to those of the 2:17R phase. Therefore, as expected, the domain structure of Fig. 12.23 is similar to that of coarse-grained 2:17R material, shown in Fig. 12.19(a), which does not have a cellular microstructure and Z-phase lamellae. In the case of Fig. 12.23, however, the cellular microstructure and the Z-phase are present, but no influence of them on the magnetic microstructure can be recognized.

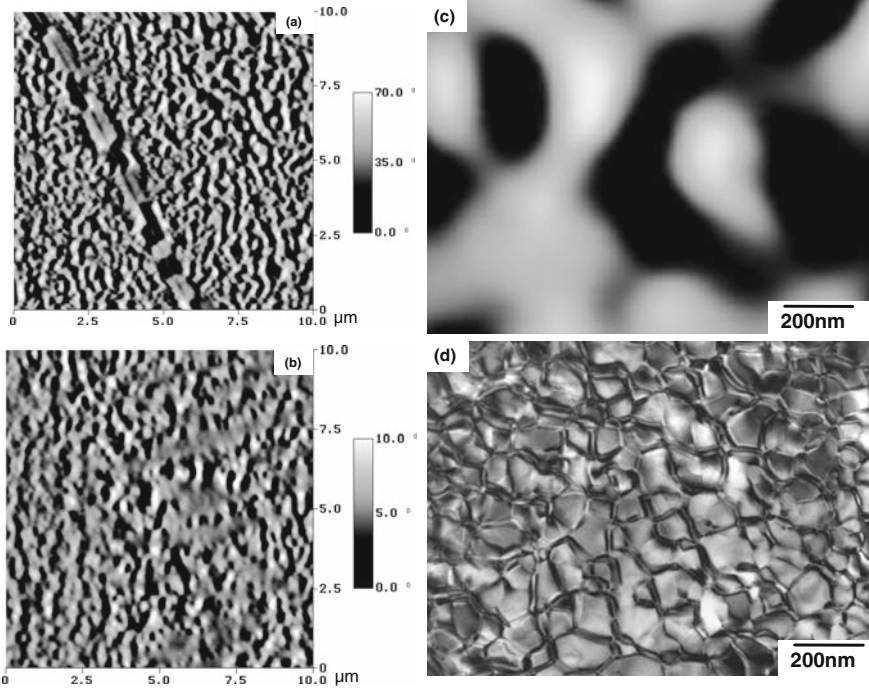
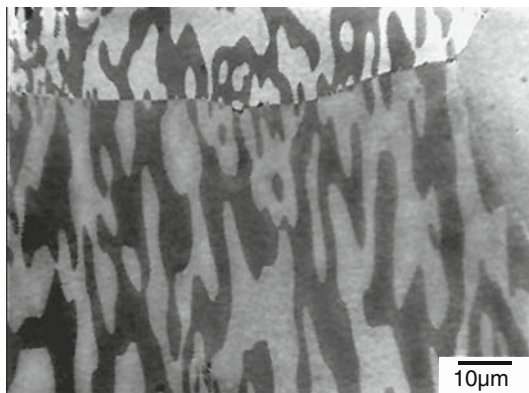


Fig. 12.22 Domain structure observed by MFM of thermally demagnetized $\text{Sm}(\text{Co}_{0.784}\text{Fe}_{0.100}\text{Cu}_{0.088}\text{Zr}_{0.028})_{7.19}$ magnets (slow cooled to 400°C , i.e., in the high-coercivity state): (a) nominal c-axis perpendicular to the imaging plane showing also a distinct magnetic contrast in the grain boundary phase and (b) nominal c-axis parallel to the imaging plane showing some strip-like features, which could be attributed to the lamellar phase. The large difference in the phase shift could be consistent with the difference in the stray field along the easy and hard directions of magnetization (*left*). Magnetic domain structure observed by MFM (c) and microstructure observed by TEM (d). The MFM image has been digitally enlarged to match the magnification of the TEM image (*right*) (nominal c-axis is in both cases perpendicular to the imaging plane; not the same area)

On the other hand, in optimized, i.e., slowly cooled to 400°C , magnets the high gradient in the Cu concentration in the 1:5 cell boundary phase will give rise to large fluctuations in the intrinsic properties of this phase. In particular, K_1 and the spontaneous magnetization M_s will be considerably smaller in the cell boundary regions than in the 2:17R-type cells. Therefore, the domain structures in Fig. 12.22 and in the left part of Fig. 12.21 may be considered as cooperative phenomena similar and akin to interaction domains [13] well known for fine-grained ferromagnetic materials where the interaction between the small grains is predominantly of magnetostatic nature [47, 53]. In the highly coercive materials considered here, the magnetic interaction between the 2:17R cells is not purely magnetostatic but the exchange interaction between the cells is expected to be much smaller compared to the exchange interaction within the cells and to the exchange coupling between the cells of the low-coercivity samples of the right part of Fig. 12.21.

Fig. 12.23 Kerr microscopy image of $\text{Sm}(\text{Co}_{0.784}\text{Fe}_{0.100}\text{Cu}_{0.088}\text{Zr}_{0.028})_{7.19}$ quenched from 850°C (corresponding to the *right column* of Fig. 12.21) with the nominal *c*-axis parallel to the imaging plane



Subtle microchemical changes [108, 109], mainly the change of the concentration and distribution of Cu in the cell boundary phase, occurring in the slow cooling ramp, can explain the hysteresis phenomena observed. The cell boundaries are usually considered as pinning centers for domain walls. To a lesser extent, interface deformation strains due to the lattice misfit between the different phases that increases during the slow cooling may also enhance the strength of pinning [66]. Xiong et al. [102] reported that the composition of the Z-phase is also affected by the slow cooling treatment, more specifically they observed that zirconium replaces samarium to form $\text{Zr}(\text{Co},\text{Fe})_3$ at this processing stage. This in turn might have implications with regard to the domain wall energy of the Z-phase and thus also might be of relevance when considering local wall energy minima acting as pinning sites for the domain wall movement [49, 50, 87].

However, the concept of domain walls (to be pinned) is to some degree questionable in the case of the high-coercivity magnets. Classic domain walls are thin transition regions between homogeneously magnetized domains that can be well determined by methods of micromagnetism [47]. In the magnetic microstructure of Fig. 12.22, the walls are expected to be quite different from classic domain walls and the exact pinning mechanism still has to be elucidated. In ideal interaction domains, the elementary magnetic units are single-domain particles, which would correspond here to the uniformly magnetized 2:17R cells. Consequently, the boundaries of the interaction-domain-like structures in Fig. 12.22 could coincide with boundaries of 2:17R cells, similar as the zigzag-shaped patterns observed in thinned samples, by using Lorentz-mode TEM.

The nature of the magnetic domain structure (in particular the domain width) is very sensitive to details of the processing procedure, which is needed to attain high coercivity. In high-temperature $\text{Sm}(\text{Co}_{0.784}\text{Fe}_{0.1}\text{Cu}_{0.088}\text{Zr}_{0.028})_{7.19}$ magnets, the typical domain width is less than $1\ \mu\text{m}$, but significantly larger than the typical size of 2:17R phase cells of about 100 nm, the latter surrounded by the 1:5 cell boundary phase. On the other hand, if such a magnet is quenched straight from the aging temperature, i.e., the slow cooling ramp is omitted, the resulting domain structure is much coarser (domain width $\sim 10\ \mu\text{m}$) and the coercivity is small ($< 0.1\ \text{T}$), although

no significant changes in the microstructure occur during slow cooling (only subtle microchemical changes take place within and near the 1:5 cell boundary phase).

12.6 Non-equilibrium Processing Routes

Due to their large magnetocrystalline anisotropy SmCo_5 and $\text{Sm}_2\text{Co}_{17}$ compounds are prototypical candidates for developing coercivity through a decrease of grain sizes. Non-equilibrium processing routes such as melt spinning [33], mechanical alloying [1, 21, 86, 97, 101, 114], or reactive milling [38, 56] as a variation of the hydrogenation, disproportionation, desorption, and recombination (HDDR) process [37] typically yield the required nanostructures, in which several phases, often of metastable type, can efficiently exchange couple.

12.6.1 Rapidly Quenched $\text{SmCo}_5/\text{Sm}_2\text{Co}_{17}$ Magnets

The aforementioned complex aging regime can be simplified when using the melt-spinning method. $\text{Sm}(\text{Co}_{0.74}\text{Fe}_{0.1}\text{Cu}_{0.12}\text{Zr}_{0.04})_{7.5}$ and $\text{Sm}(\text{Co}_{0.75}\text{Fe}_{0.15}\text{Cu}_{0.08}\text{Zr}_{0.02})_{7.6}$ ribbons show high coercivities without the lengthy solid solution treatment [105, 107]. Ribbons were produced by melt spinning using a low surface speed of the Cu wheel of 5 m/s and then aged isothermally at 850°C for up to 12 h, followed by slow cooling at 0.7 K/min to different temperatures and then quenched to room temperature. Figure 12.24 (left) shows the room temperature coercivity as a function of isothermal aging time, and it can be seen that the coercivity is sensitive to the alloy composition. A coercivity of above 2.8 T is developed immediately after slow cooling the as-spun $\text{Sm}(\text{Co}_{0.74}\text{Fe}_{0.1}\text{Cu}_{0.12}\text{Zr}_{0.04})_{7.5}$ sample even without isothermal aging. The coercivity increases with increasing isothermal aging time and a peak

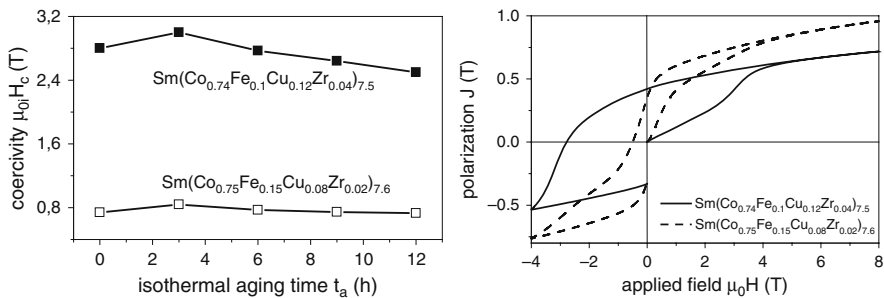


Fig. 12.24 Coercivity $\mu_0 i H_c$ as a function of isothermal aging time at 850°C for $\text{Sm}(\text{Co}_{0.74}\text{Fe}_{0.1}\text{Cu}_{0.12}\text{Zr}_{0.04})_{7.5}$ and $\text{Sm}(\text{Co}_{0.75}\text{Fe}_{0.15}\text{Cu}_{0.08}\text{Zr}_{0.02})_{7.6}$ ribbons (left). Typical hysteresis loops of the $\text{Sm}(\text{Co}_{0.74}\text{Fe}_{0.1}\text{Cu}_{0.12}\text{Zr}_{0.04})_{7.5}$ and $\text{Sm}(\text{Co}_{0.75}\text{Fe}_{0.15}\text{Cu}_{0.08}\text{Zr}_{0.02})_{7.6}$ ribbons subjected to aging at 850°C for 3 h followed by slow cooling to 400°C (right). Reproduced with permission of Elsevier from Yan et al. [110]

coercivity of up to 3.0 T can be obtained after aging at 850°C for 3 h, followed by slow cooling to 400°C. For $\text{Sm}(\text{Co}_{0.75}\text{Fe}_{0.15}\text{Cu}_{0.08}\text{Zr}_{0.02})_{7.6}$ ribbons, however, the coercivity remains almost unchanged around 0.8 T even after a long aging at 850°C followed by a slow cooling to 400°C. A higher Cu and Zr contents promote stronger domain wall pinning and higher coercivity (Fig. 12.24 (right)).

Cu/Zr-poor samples show an incomplete cellular microstructure along with the lamellar phase (Fig. 12.25), underlining that Cu and Zr play very important roles in the formation of the cellular/lamellar microstructure as they modify the phase-ordering kinetics.

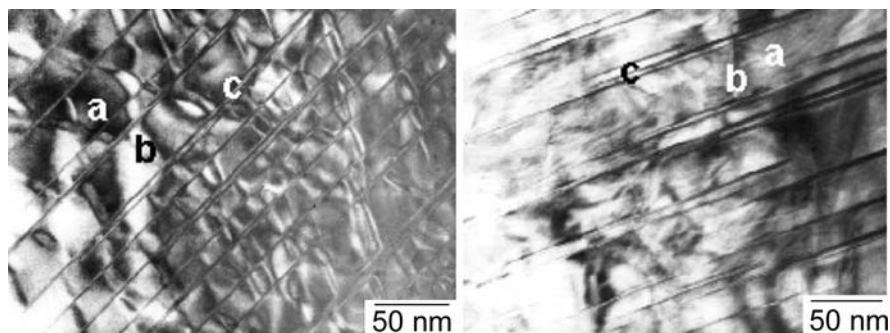


Fig. 12.25 TEM microstructures of annealed ribbons with different Cu and Zr content: *left* – $\text{Sm}(\text{Co}_{0.74}\text{Fe}_{0.1}\text{Cu}_{0.12}\text{Zr}_{0.04})_{7.5}$; *right* – $\text{Sm}(\text{Co}_{0.75}\text{Fe}_{0.15}\text{Cu}_{0.08}\text{Zr}_{0.02})_{7.6}$ (a – 2:17-type matrix phase, b – 1:5-type cell boundary phase, and c – lamellar phase). Reproduced with permission of Elsevier from Yan et al. [110]

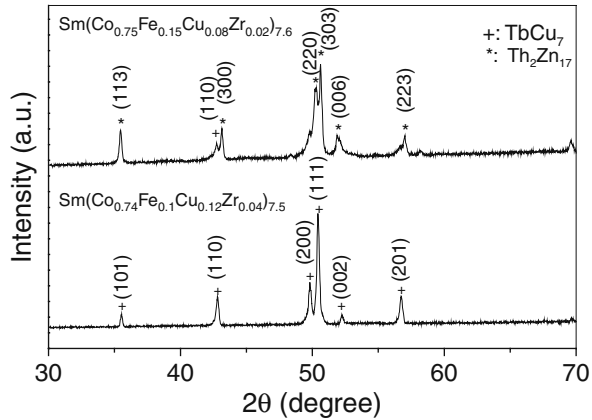
The formation of a highly twinned, single-phase TbCu_7 crystal structure and the supersaturation of Cu and Zr in the matrix phase prior to aging are required to develop the cellular/lamellar microstructure and high coercivity [84]. The structures of as-spun ribbons vary significantly with Cu and Zr contents (Fig. 12.26). The ribbon with high Cu and Zr contents exhibits a single phase with TbCu_7 structure. On the other hand, reflections of $\text{Th}_2\text{Zn}_{17}$ are observed in the Cu/Zr-poor as-spun samples, indicating a mixture of $\text{Th}_2\text{Zn}_{17}$ and TbCu_7 structures.

Magnetically textured SmCo_5 - [103] and $\text{Sm}_2\text{Co}_{17}$ -type ribbons can be prepared by single-roller melt spinning at low wheel velocities. The magnetic texture is found to be due to a crystallographic texture formed during the melt-spinning process, with the c-axis parallel to the longitudinal direction of the ribbons. Cu and Zr suppress the formation of a crystallographic texture of 2:17 ribbons prepared at low wheel speed although they are key elements for obtaining the uniform cellular and lamellar microstructures [104–107].

12.6.2 Mechanically Alloyed $\text{SmCo}_5/\text{Sm}_2\text{Co}_{17}$ Magnets

Remanence-enhanced magnet powders consisting of two magnetically hard phases, i.e., SmCo_5 and $\text{Sm}_2\text{Co}_{17}$ nanocomposites, can be prepared by high-energy ball

Fig. 12.26 XRD patterns of as-spun $\text{Sm}(\text{Co},\text{Fe},\text{Cu},\text{Zr})_2$ ribbons. Reproduced with permission of Elsevier from Yan et al. [110]

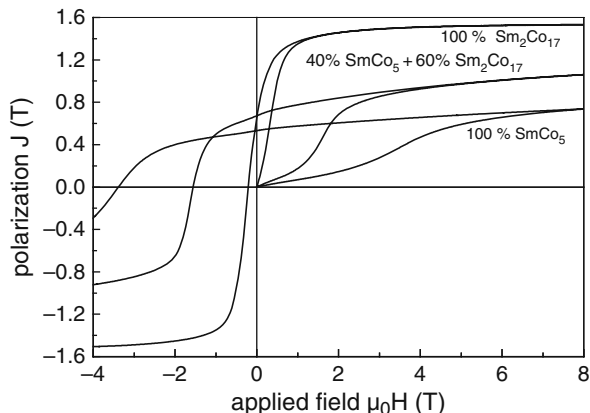


milling and subsequent annealing [104–107]. As-milled powders were found to be amorphous. After annealing, the mean grain sizes of SmCo_5 , $\text{Sm}_2\text{Co}_{17}$, and fcc-Co in the powders determined by the Scherrer method from XRD patterns are about 30, 30, and 35 nm, respectively. The saturation polarization J_s (at 8 T) increases monotonically and the coercivity decreases with increasing volume fraction of $\text{Sm}_2\text{Co}_{17}$ due to its higher saturation polarization and lower anisotropy field. Consequently, the remanent polarization J_r and the maximum energy density $(BH)_{\max}$ first increase and then decrease with the $\text{Sm}_2\text{Co}_{17}$ volume fraction. The highest remanence of 0.72 T is obtained in the 80% $\text{Sm}_2\text{Co}_{17}$ powders. Optimum magnetic properties of $J_s = 1.07$ T, $J_r = 0.67$ T, $J_r/J_s = 0.63$, $\mu_{0i} H_c = 1.56$ T, and $(BH)_{\max} = 78$ kJ/m³ are obtained in the mixture consisting of 40% SmCo_5 and 60% $\text{Sm}_2\text{Co}_{17}$. The relatively low remanence of the nominally 100% $\text{Sm}_2\text{Co}_{17}$ powder is attributed to its poor coercivity (0.29 T), although the saturation polarization (1.5 T) is much higher than that of rhombohedral $\text{Sm}_2\text{Co}_{17}$ (which is 1.25 T [95]), due to the presence of elemental fcc-Co. The initial magnetization and demagnetization curves of $\text{SmCo}_5/\text{Sm}_2\text{Co}_{17}$ powders with 0, 60, and 100% $\text{Sm}_2\text{Co}_{17}$ are shown in Fig. 12.27. All the hysteresis loops show a magnetically single-phase behavior. The smooth demagnetization curves and the enhanced remanence in the two-phase composite can be attributed to the exchange coupling between grains of different phases.

12.6.3 Hydrogen Disproportionated SmCo_5 and $\text{Sm}_2\text{Co}_{17}$ Alloys

For many materials, the conventional HDDR process [37] is not applicable. However, mechanical-induced gas–solid reactions [38] or increased hydrogen pressure [44] can be used to hydrogen disproportionate thermodynamically very stable intermetallic compounds such as those of SmCo type. This reactive milling procedure in enhanced hydrogen pressure and temperature and subsequent vacuum annealing can be employed to first hydrogen disproportionate and second to desorb and recombine the material with the aim to obtain a nanocomposite.

Fig. 12.27 Hysteresis loops of $\text{SmCo}_5/\text{Sm}_2\text{Co}_{17}$ powders with $\text{Sm}_2\text{Co}_{17}$ volume fraction of 0, 60, and 100%. Reproduced with permission of American Institute of Physics from [104–107]



The effect of reactive milling on $\text{Sm}_2\text{Co}_{17}$ and as a comparison $\text{Nd}_{12}\text{Fe}_{82}\text{B}_6$ and $\text{Nd}_{12}\text{Co}_{82}\text{B}_6$ is illustrated in Fig. 12.28 (left). The extremely broad reflections of $\text{RH}_{2+\delta}$, bcc-Fe, and fcc-Co (note that SmCo_5 behaves very similar to $\text{Sm}_2\text{Co}_{17}$) indicate a nanocrystalline structure. Lattice strain induced by the milling procedure and stoichiometric inhomogeneities of the hydride phase lead to an additional peak broadening. The average grain size of the $\text{RH}_{2+\delta}$ phases is estimated to be around 10 nm. This is a much finer structure than that of disproportionated $\text{Nd}_2\text{Fe}_{14}\text{B}$ -type materials [38] prepared by the conventional HDDR method. The desorption curves of the reactively milled powders are shown in Fig. 12.29 (right). Peak (A) in the curves between 100 and 400°C is attributed to the desorption of the δ hydrogen from $\text{RH}_{2+\delta}$, whereas peak (B) between 450 and 675°C

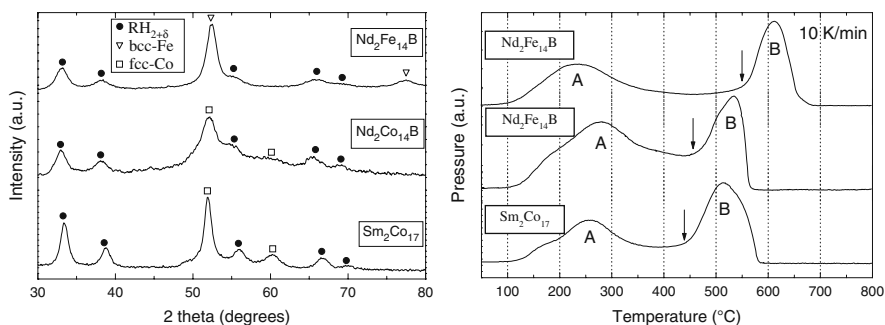


Fig. 12.28 (left) XRD patterns of $\text{Nd}_{12}\text{Fe}_{82}\text{B}_6$, $\text{Nd}_{12}\text{Co}_{82}\text{B}_6$, and $\text{Sm}_2\text{Co}_{17}$ after 20 h (the former) and 40 h (the Co-based alloys) of milling in hydrogen at 350°C. The corresponding disproportionation products are indicated in each case: $\text{RH}_{2+\delta}$ with R: Nd, Sm, bcc-Fe, and fcc-Co. (right) Desorption behavior of these powders upon heating in vacuum (10 K/min). Peak (A) corresponds to the desorption of the over-stoichiometric hydrogen and peak (B) to the recombination to $\text{Nd}_2\text{Fe}_{14}\text{B}$, $\text{Nd}_2\text{Co}_{14}\text{B}$, and $\text{Sm}_2\text{Co}_{17}$, respectively; the arrows indicate the onset recombination temperatures

corresponds to the recombination to $\text{Nd}_2\text{Fe}_{14}\text{B}$, $\text{Nd}_2\text{Co}_{14}\text{B}$, and $\text{Sm}_2\text{Co}_{17}$. Grain sizes of 20 nm (600°C), 30 nm (700°C), and 100 nm (800°C) are estimated from the XRD patterns for the recombined samples. Thus, reactively milled and subsequently recombined powders show grain sizes much smaller than the average grain size of standard HDDR-treated (around 300 nm) $\text{Sm}_2\text{Fe}_{17}$ -type and NdFeB -type materials. In fact, grain sizes are rather comparable to those of mechanically alloyed SmCo [101].

Despite the presence of two different phases, the demagnetization curves of the $\text{Sm}_2\text{Co}_{17}$ -type powders have a magnetically single-phase-like appearance for low recombination temperatures (Fig. 12.29 (left)). The presence of a second phase with a high-anisotropy field is indicated by the gradual approach toward saturation magnetization when recombined at higher temperatures. The remanence $J_r = 0.71$ T for the sample recombined at 600°C is higher than the theoretical maximum value $J_s/2 = 0.65$ T [12] of isotropically distributed single-domain $\text{Sm}_2\text{Co}_{17}$ particles, which is attributed to the effect of exchange coupling between the nanoscaled grains. It has also to be taken into account that the amount of SmCo_5 phase within the sample should decrease the J_r value even further due to the lower value of the saturation magnetization compared to that of $\text{Sm}_2\text{Co}_{17}$. An energy product $(BH)_{\text{max}} = 82$ kJ/m³ was achieved for the sample recombined at 600°C . Figure 12.29 (right) shows that for temperatures below 700°C , a magnetic behavior typical for exchanged coupled magnets can be observed. With decreasing temperature and decreasing grain size, the remanence is enhanced corresponding to a decrease in coercivity. Above 800°C the coercivity decreases for recombination temperatures due to grain growth.

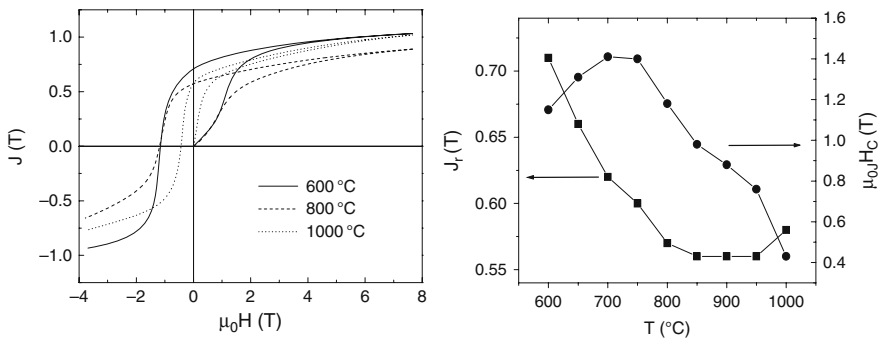


Fig. 12.29 Initial magnetization curves and demagnetization curves of reactively milled $\text{Sm}_2\text{Co}_{17}$ recombined at different temperatures (left). Dependence of remanence J_r and coercivity $\mu_0 H_c$ of reactively milled $\text{Sm}_2\text{Co}_{17}$ powders on the recombination temperature T (right). Reproduced with permission of American Institute of Physics from [38]

The preparation of highly coercive magnet powders by reactive milling is a novel processing route for the magnetic hardening of compounds, which are highly stabilized toward the reaction with hydrogen and, therefore, disproportionate very sluggishly or, as in the case of NdCoB - and SmCo -type materials, do not react at all

under standard HDDR conditions. Nanocrystalline, multiphase but magnetically isotropic SmCo-type powders can be obtained after reactive milling and subsequent recombination at low temperatures. They show a magnetically single phase behavior and enhanced remanences [38].

Acknowledgments Many thanks to *Aru Yan* (then IFW Dresden) for a productive cooperation, to *K.-H. Müller* (IFW Dresden) for fruitful discussion on samarium cobalt magnets and to *L. Schultz* (IFW Dresden) for his continuous support and interest in permanent magnet research.

Acronyms

CEMRP	critical elementary magnetization reversal process
Nano-EDS	nano-beam energy-dispersed spectrometry
HEV	hybrid electric vehicles
HDDR	hydrogenation, disproportionation, desorption, and recombination
HRTEM	high-resolution transmission electron microscopy
MFM	magnetic force microscopy
RPM	rare earth permanent magnets
R–T	rare earth–transition metal compound
SEM	scanning electron microscopy
TEM	transmission electron microscopy
VSM	vibrating sample magnetometer
XRD	X-ray diffraction

References

1. Al-Omari, I.A., J. Shobaki, R. Skomski, D. Leslie-Pelecky, J. Zhou and D.J. Sellmyer. (2002). High-temperature magnetic properties of SmCo_{6,7-x}Cu_{0,6}Ti_x magnets. *Physica B: Cond. Matter* 321: 107–111.
2. Barthem, V.M.T.S., D. Givord, M.F. Rossignol and P. Tenaud. (2002). An approach to coercivity relating coercive field and activation volume. *Physica B* 319: 127–132.
3. Buschow, K.H.J. and A.S. van der Goot. (1968). Intermetallic compounds in the system samarium-cobalt. *J. Less-Common Met.* 14: 323–328.
4. Buschow, K.H.J. and A.S. van der Goot. (1971). Composition and crystal structure of hexagonal Cu-rich rare earth-copper compounds. *Acta Cryst. B* 27: 1085–1088.
5. Buschow, K.H.J., (1989). Chapter 1, Permanent magnet materials based on 3d-rich ternary compounds. In: *Ferromagnetic Materials*, vol. 4, E. P. Wohlfarth and K.H.J. Buschow (eds.), North-Holland Elsevier, Amsterdam, Netherlands.
6. Buschow, K.H.J. (1997). Chapter 4, Magnetism and processing of permanent magnet materials. In: *Handbook of Magnetic Materials*, vol. 10, K.H.J. Buschow (ed.), North Holland Elsevier, Amsterdam, Netherlands.
7. Cataldo, L., A. Lefevre, F. Ducret, M.Th. Cohen-Adat, C.H. Allibert and N. Valignat. (1996). Binary system Sm-Co: revision of the phase diagram in the Co rich field. *J. Alloys Comp.* 241: 216–223.

8. Chen, C., M.S. Walmer, M.H. Walmer, S. Liu, G.E. Kuhl and G. Simon. (1998). $\text{Sm}_2(\text{Co}, \text{Fe}, \text{Cu}, \text{Zr})_{17}$ magnets for use at temperature $\geq 400^\circ\text{C}$. *J. Appl. Phys.* 83: 6706–6708.
9. Chen, C., M.S. Walmer, M.H. Walmer, S. Liu, G.E. Kuhl and G.K. Simon. (1999). New series of $\text{Sm}_2\text{TM}_{17}$ magnet materials for application at temperatures up to 550°C . In: *MRS Symp. Proc. Advanced Hard and Soft Magnets*, vol. 577, J. Fidler, M. Coey et al. (eds.), Materials Research Society, Pittsburgh, USA, pp. 277–287.
10. Chen, C., M.H. Walmer, E.H. Kottcamp and W. Gong. (2001). Surface reaction and Sm depletion at 550°C for high temperature Sm-TM magnets. *IEEE Trans. Mag.* 37: 2531–2533.
11. Chikazumi, S. (1997). *Physics of Ferromagnetism*, 2nd ed. Oxford Science Publications, Oxford, p. 276.
12. Coey, J.M.D. (ed.). (1996) *Rare Earth Iron Permanent Magnets*. Clarendon Press, Oxford, UK.
13. Craik, D.J. and E.D. Isaac. (1960). Magnetic interaction domains. *Proc. Phys. Soc. (Research Notes)* 76.
14. Cullity, B.D. (1972). *Introduction to Magnetic Materials*. Addison-Wesley Publishing Company, Reading, MA.
15. Delannay, F., S. Derkaoui and C.H. Allibert. (1987a). The influence of zirconium on $\text{Sm}(\text{CoFeCuZr})_{7,2}$ alloys for permanent magnets I: identification of the phases by transmission electron microscopy. *J. Less-Common Met.* 134: 249–262.
16. Delannay, F., S. Derkaoui and C.H. Allibert. (1987b). Transmission electron microscopy of $\text{Sm}(\text{CoFeCuZr})_{7,2}$ alloys for permanent magnet. *Micron Microscopica Acta* 18: 243.
17. Derkaoui, S., C.H. Allibert, F. Delannay and J. Laforest. (1987). The influence of zirconium on $\text{Sm}(\text{Co}, \text{Fe}, \text{Cu}, \text{Zr})_{7,2}$ alloys for permanent magnets II: composition and lattice constants of the phases in heat-treated materials. *J. Less-Common Met.* 136: 75–86.
18. Derkaoui, S. and C.H. Allibert. (1989). Redetermination of the phase equilibria in the system Sm-Co-Cu for Sm content 0–20 at.% at 850°C . *J. Less-Common Met.* 154: 309–315.
19. Derkaoui, S., N. Valignat and C.H. Allibert. (1996a). Co corner of the system Sm-Co-Zr: decomposition of the phase 1:7 and equilibria at 850°C . *J. Alloys Comp.* 235: 112–119.
20. Derkaoui, S., N. Valignat and C.H. Allibert. (1996b). Phase equilibria at 1150°C in the Co-rich alloys Sm-Co-Zr and structure of the 1:7 phase. *J. Alloys Comp.* 232: 296–301.
21. Ding, J., P.G. McCormick and R. Street. (1994). A study of $\text{Sm}_{13}(\text{Co}_{1-x}\text{Fe}_x)_{87}$ prepared by mechanical alloying. *J. Magn. Magn. Mat.* 135: 200–204.
22. Durst, K.D. and H. Kronmüller. (1985). Magnetic hardening mechanisms in sintered Nd-Fe-B and $\text{Sm}(\text{Co}, \text{Fe}, \text{Cu}, \text{Zr})_{7,6}$ permanent magnets. *Proc. 4th Int. Symp. Magn. Anisotropy and Coercivity in RETM Alloys*, Dayton, USA, pp. 725–735.
23. Durst, K.D., H. Kronmüller, F.T. Parker and H. Oesterreicher. (1986). Temperature dependence of coercivity of cellular $\text{Sm}_2\text{Co}_{17}$ - SmCo_5 permanent magnets. *Phys. Stat. Sol. (a)* 95: 213–219.
24. Durst, K.D., H. Kronmüller and W. Ervens. (1988a). Investigations of the magnetic properties and demagnetisation processes of an extremely high coercive $\text{Sm}(\text{Co}, \text{Cu}, \text{Fe}, \text{Zr})_{7,6}$ permanent magnet – I Determination of intrinsic magnetic material parameters. *Phys. Stat. Sol. (a)* 108: 403–416.
25. Durst, K.D., H. Kronmüller and W. Ervens. (1988b). Investigations of the magnetic properties and demagnetisation processes of an extremely high coercive $\text{Sm}(\text{Co}, \text{Cu}, \text{Fe}, \text{Zr})_{7,6}$ permanent magnet – II The coercivity mechanism. *Phys. Stat. Sol. (a)* 108: 705–719.
26. Ervens, W. (1979). Rare earth-transition metal 2:17 permanent magnet alloys, state and trends. *Goldschmidt Informiert* 48: 3–9.
27. Fidler, J. and P. Skalicky. (1982a). Coercivity of precipitation hardened cobalt rare earth 17:2 permanent magnets. *J. Magn. Magn. Mat.* 30: 58–70.
28. Fidler, J. and P. Skalicky (1982b, September). Domain wall pinning in REPM. In: *Proc. 3rd Int. Symp. Magnetic Anisotropy and Coercivity in Rare Earth-Transition Metal Alloys*, J. Fidler(ed.), Baden, Austria, pp. 585–597.

29. Gavigan, J.P. and D. Givord. (1990). Intrinsic and extrinsic properties of rare earth-transition metal compounds and permanent magnets. *J. Magn. Magn. Mat.* 84: 288–298.
30. Givord, D., A. Lienard, P. Tenaud and T. Viadieu. (1987). Magnetic viscosity in Nd-Fe-B sintered magnets. *J. Magn. Magn. Mat.* 67: L281–L285.
31. Givord, D., P. Tenaud and T. Viadieu. (1988). Coercivity mechanisms in ferrites and rare earth transition metal sintered magnets(SmCo₅,Nd-Fe-B). *IEEE Trans. Magn.* 24: 1921–1923.
32. Givord, D., M. Rossignol and V.M.T.S. Barthem. (2003). The physics of coercivity. *J. Magn. Magn. Mat.* 258–259: 1–5.
33. Goll, D., I. Kleinschroth, W. Sigle and H. Kronmüller. (2000). Melt-spun precipitation-hardened Sm₂(Co,Cu,Fe,Zr)₁₇ magnets with abnormal temperature dependence of coercivity. *Appl. Phys. Lett.* 76: 1054–1056.
34. Goll, D. and H. Kronmüller. (2002). Micromagnetic analysis of pinning-hardened nanostructured, nanocrystalline Sm₂Co₁₇ based alloys. *Scripta Mat.* 47: 545–550.
35. Goll, D., H. Kronmüller and H.H. Stadelmaier. (2004). Micromagnetism and the microstructure of high-temperature permanent magnets. *J. Appl. Phys.* 96: 6534–6545.
36. Gopalan, R., K. Hono, A. Yan and O. Gutfleisch. (2009). Direct evidence on Cu-concentration variation and its correlation to coercivity in Sm(Co_{0.74}Fe_{0.1}Cu_{0.12}Zr_{0.4})_{7.4} ribbons, *Scripta. Mat.* 60: 764–767.
37. Gutfleisch, O. and I.R. Harris. (1996). Fundamental and practical aspects of the hydrogenation, disproportionation, desorption and recombination process. *J. Phys. D: Appl. Phys.* 29: 2255–2265.
38. Gutfleisch, O., M. Kubis, A. Handstein, K.H. Müller and L. Schultz. (1998). Hydrogenation disproportionation desorption recombination in Sm–Co alloys by means of reactive milling. *Appl. Phys. Lett.* 73: 3001–3003.
39. Gutfleisch, O. (2000). Controlling the properties of high energy density permanent magnetic materials by different processing routes. *J. Phys. D: Appl. Phys.* 33: R157–R172.
40. Gutfleisch, O., N.M. Dempsey, A. Yan, K.-H. Müller and D. Givord. (2004). Coercivity analysis of melt-spun Sm₂(Co,Fe,Cu,Zr)₁₇. *J. Magn. Magn. Mat.* 272–276: 647–649.
41. Gutfleisch, O., K.-H. Müller, K. Khlopkov, M. Wolf, A. Yan, R. Schäfer, T. Gemming and L. Schultz. (2006). Evolution of magnetic domain structures and coercivity in high-performance SmCo 2:17 type permanent magnets. *Acta Mat.* 54: 997–1008.
42. Hadjipanayis, G.C. (1996). Microstructure and magnetic domains. In: *Rare-Earth Iron Permanent Magnets*, J.M.D. Coey (ed.), Oxford University Press, Oxford, UK, pp. 286–335.
43. Hadjipanayis, G.C., W. Tang, Y. Zhang, S.T. Chui, J.F. Liu, C. Chen and H. Kronmüller. (2000). High temperature 2:17 magnets: relationship of magnetic properties to microstructure and processing. *IEEE Trans. Magn.* 36: 3382–3387.
44. Handstein, A., M. Kubis, O. Gutfleisch, B. Gebel and K.H. Müller. (1999). HDDR of Sm–Co alloys using high hydrogen pressures. *J. Magn. Magn. Mat.* 192: 73–76.
45. Handstein, A., A. Yan, G. Martinek, O. Gutfleisch, K.H. Müller and L. Schultz. (2003). Stability of magnetic properties of Sm₂Co₁₇-type magnets at operating temperatures larger than 400°C. *IEEE Trans. Magn.* 39: 2923–2925.
46. Hofer, F. (1970). Physical metallurgy and magnetic measurements of SmCo₅-SmCu₅ alloys. *IEEE Trans. Magn.* 6: 221–224.
47. Hubert, A. and R. Schäfer (1998). *Magnetic Domains – The Analysis of Magnetic Microstructures*. Springer Verlag, Berlin, Germany.
48. Kardelky, S., A. Gebert, O. Gutfleisch, A. Handstein, G. Martinek and L. Schultz. (2004). Corrosion behavior of Sm-Co based permanent magnets in oxidizing environments. *IEEE Trans. Magn.* 40: 2931–2933.
49. Katter, M., J. Weber, W. Assmus, P. Schrey and W. Rodewald. (1996). A new model for the coercivity mechanism of Sm₂(Co,Fe,Cu,Zr)₁₇ magnets. *IEEE Trans. Magn.* 32: 4815–4817.
50. Katter, M. (1998). Coercivity calculation of Sm₂(Co,Fe,Cu,Zr)₁₇ magnets. *J. Appl. Phys.* 83: 6721–6723.

51. Kersch, P., A. Handstein, K. Khlopkov, O. Gutfleisch, D. Eckert, K. Nenkov, J.-C. T  llez-Blanco, R. Gr  ssinger, K.-H. M  ller and L. Schultz. (2005). High-field magnetisation of $\text{SmCo}_{5-x}\text{Cu}_x$ ($x \approx 2.5$) determined in pulse fields up to 48 T. *J. Magn. Magn. Mat.* 290–291(part 1): 420–423.
52. Khan, Y. (1973). The crystal structures of R_2Co_{17} intermetallic compounds. *Acta Crystall. Section B* 29: 2502–2507.
53. Khlopkov, K., O. Gutfleisch, D. Eckert, D. Hinz, B. Wall, W. Rodewald, K.-H. M  ller, and L. Schultz. (2004). Local texture in Nd-Fe-B sintered magnets with maximised energy density. *J. Alloys Comp.* 365: 259–265.
54. Kronm  ller, H., K.-D. Durst, W. Ervens and W. Fernengel. (1984). Micromagnetic analysis of precipitation hardened permanent magnets. *IEEE Trans. Magn.* 20: 1569–1571.
55. Kronm  ller, H. and D. Goll. (2002). Micromagnetic theory of the pinning of domain walls at phase boundaries. *Physica B* 319: 122–126.
56. Kubis, M., A. Handstein, B. Gebel, O. Gutfleisch, K.H. M  ller and L. Schultz. (1999). Highly coercive SmCo_5 magnets prepared by a modified hydrogenation-disproportionation-desorption-recombination process. *J. Appl. Phys.* 85: 5666–5668.
57. Kumar, K. (1988). RETM_5 and $\text{RE}_2\text{TM}_{17}$ permanent magnets development. *J. Appl. Phys.* 63: R13–R57.
58. Lectard, E., C.H. Allibert and R. Ballou. (1994). Saturation magnetization and anisotropy fields in the $\text{Sm}(\text{Co}_{1-x}\text{Cu}_x)_5$ phases. *J. Appl. Phys.* 75: 6277–6279.
59. Lef  vre, A., L. Cataldo, M.Th. Cohen-Adad, and B.F. Mentzen. (1997). A representation of the Sm-Co-Zr-Cu-Fe quinary system: a tool for optimisation of 2/17 permanent magnets. *J. Alloys Comp.* 262–263: 129–133.
60. Li, D. and K.J. Strnat. (1984). Domain structures of two Sm-Co-Cu-Fe-Zr “2–17” magnets during magnetization reversal. *J. Appl. Phys.* 55: 2103–2105.
61. Liu, J.F., T. Chui, D. Dimitrov and G.C. Hadjipanayis. (1998a). Abnormal temperature dependence of intrinsic coercivity in $\text{Sm}(\text{Co}, \text{Fe}, \text{Cu}, \text{Zr})_z$ powder materials. *Appl. Phys. Lett.* 73: 3007–3009.
62. Liu, J.F., Y. Zhang, Y. Ding, D. Dimitrov, and G.C. Hadjipanayis (1998b). Rare earth permanent magnets for high temperature applications. In: *Proc. of 15th Int. Workshop on Rare Earth Magnets and their Appl.*, Dresden, Germany, vol. 2, pp. 607–622.
63. Liu, J.F., Y. Zhang, D. Dimitrov and G.C. Hadjipanayis. (1999). Microstructure and high temperature magnetic properties of $\text{Sm}(\text{Co}, \text{Cu}, \text{Fe}, \text{Zr})_z$ ($z = 6.7–9.1$) permanent magnets. *J. Appl. Phys.* 85: 2800–2804.
64. Livingston, J.D. and M.D. McConnell. (1972). Domain-wall energy in cobalt-rare-earth compounds. *J. Appl. Phys.* 43: 4756–4762.
65. Livingston, J.D. (1975). Domains in sintered Co-Cu-Fe-Sm magnets. *J. Appl. Phys.* 46: 5259–5262.
66. Livingston, J.D. and D.L. Martin. (1977). Microstructure of aged $(\text{Co}, \text{Cu}, \text{Fe})_7\text{Sm}$ magnets. *J. Appl. Phys.* 48: 1350–1354.
67. Matthias, T., G. Zehetner, J. Fidler, W. Scholz, T. Schrefl, D. Schobinger and G. Martinek. (2002). TEM-analysis of $\text{Sm}(\text{Co}, \text{Fe}, \text{Cu}, \text{Zr})_z$ magnets for high-temperature applications. *J. Magn. Magn. Mat.* 242–245: 1353–1355.
68. Maury, C., L. Rabenberg and C.H. Allibert. (1993). Genesis of the cell microstructure in the $\text{Sm}(\text{Co}, \text{Fe}, \text{Cu}, \text{Zr})$ permanent magnets with 2:17 type. *Phys. Stat. Sol. (a)* 140: 57–72.
69. Meyer-Liautaud, F., S. Derkaoui, C.H. Allibert and R. Castanet. (1987). Structural and thermodynamic data on the pseudobinary phases $\text{R}(\text{Co}_{1-x}\text{Cu}_x)_5$ with $\text{R} \equiv \text{Sm}, \text{Y}, \text{Ce}$. *J. Less-Common Met.* 127: 231–242.
70. Morita, Y., T. Umeda and Y. Kimura. (1987). Phase transformation at high temperature and coercivity of $\text{Sm}(\text{Co}, \text{Cu}, \text{Fe}, \text{Zr})_{7-9}$ magnet alloys. *IEEE Trans. Magn.* 23: 2702–2704.
71. Nagel, H. (1979). Coercivity and microstructure of $\text{Sm}(\text{Co}_{0.87}\text{Cu}_{0.13})_{7.8}$. *J. Appl. Phys.* 50: 1026–1030.

72. Nesbitt, E.A., R.H. Willens, R.C. Sherwood and E. Bühler. (1968). New permanent magnet materials. *Appl. Phys. Lett.* 12: 361–362.
73. Oesterreicher, H., F.T. Parker and M. Misroch. (1979). Giant intrinsic magnetic hardness in $\text{SmCo}_{5-x}\text{Cu}_x$. *J. Appl. Phys.* 50: 4273–4278.
74. Ojima, T., S. Tomizawa, T. Yoneyama and T. Hori. (1977). Magnetic properties of new type of rare-earth cobalt magnets. *IEEE Trans. Magn.* 13: 1317–1319.
75. Panagiotopoulos, I., M. Gjoka and D. Niarchos. (2002). Temperature dependence of the activation volume in high-temperature $\text{Sm}(\text{Co,Fe,Cu,Zr})_Z$ magnets. *J. Appl. Phys.* 92: 7693–7695.
76. Perkins, R.S., S. Gaiffi and A. Menth. (1975). Permanent magnet properties of $\text{Sm}_2(\text{Co,Fe})_{17}$. *IEEE Trans. Magn.* 11: 1431–1433
77. Perkins, R.S. and S. Strässler. (1977). Interpretation of the magnetic properties of pseudobinary $\text{Sm}_2(\text{Co,M})_{17}$ compounds. I. Magnetocrystalline anisotropy. *Phys. Rev. B* 15: 477–489; Interpretation of the magnetic properties of pseudobinary $\text{Sm}_2(\text{Co,M})_{17}$ compounds. II. Magnetization. *Phys. Rev. B* 15: 490–495.
78. Perry, A.J. and A. Menth. (1975). Permanent magnets based on $\text{Sm}(\text{Co,Cu,Fe})_Z$. *IEEE Trans. Magn.* 11: 1423–1425.
79. Perry, A.J. (1977). The constitution of copper-hardened samarium-cobalt permanent magnets. *J. Less-Common Met.* 51: 153–162.
80. Popov, A.G., A.V. Korolev and N.N. Shchegoleva. (1990). Temperature dependence of the coercive force of $\text{Sm}(\text{Co,Fe,Cu,Zr})_{7.3}$ alloys. *Phys. Met. Metall.* 69: 100–106.
81. Rabenberg, L., R.K. Mishra, and G. Thomas. (1982a). Microstructure of precipitation hardened SmCo permanent magnets. *J. Appl. Phys.* 53: 2389–2391.
82. Rabenberg, L., R.K. Mishra, and G. Thomas. (1982b, September). Development of the cellular microstructure in the $\text{SmCo}_{7.4}$ -type magnets. In: *Proc. 3rd Int. Symp. Magnetic Anisotropy and Coercivity in Rare Earth-Transition Metal Alloys*, J. Fidler (ed.), Baden, Austria, pp. 599–608.
83. Ray, A.E. (1984). Metallurgical behavior of $\text{Sm}(\text{Co,Fe,Cu,Zr})_Z$ alloys. *J. Appl. Phys.* 55: 2094–2096.
84. Ray, A.E. and S. Liu. (1992). Recent progress in 2:17 type permanent magnets. *Proc. 12th Int. Workshop on RE Magnets and their Appl.*, Canberra, Australia, pp. 552–573.
85. Schobinger, D., O. Gutfleisch, D. Hinz, K.H. Müller, L. Schultz and G. Martinek. (2002). High temperature magnetic properties of 2:17 Sm–Co magnets. *J. Magn. Magn. Mat.* 242–245: 1347–1349.
86. Schultz, L., K. Schnitzke, J. Wecker, M. Katter and C. Kuhrt. (1991). Permanent magnets by mechanical alloying. *J. Appl. Phys.* 70: 6339–6344.
87. Skomski, R. (1997). Domain-wall curvature and coercivity in pinning type Sm-Co magnets. *J. Appl. Phys.* 81: 6527–6529.
88. Skomski, R. and J.M.D. Coey. (1999). *Permanent Magnetism*. Institute of Physics, Bristol.
89. Skomski, R., A. Kashyap, Y. Qiang, and D.J. Sellmyer. (2003). Exchange through nonmagnetic insulating matrix. *J. Appl. Phys.* 93: 6477–6479.
90. Stadelmaier, H.H., E.-Th. Henig, G. Schneider and G. Petzow. (1988). The metallurgy of permanent magnets based on $\text{Co}_{17}\text{Sm}_2$. *Z. Metallkd.* 79: 313–316.
91. Stadelmaier, H.H., B. Reinsch, and G. Petzow. (1998). Samarium-cobalt phase equilibria revisited; relevance to permanent magnets. *Z. Metallkd.* 89: 114–118.
92. Stadelmaier, H.H., D. Goll, H. Kronmüller. (2005). Permanent magnet alloys based on $\text{Sm}_2\text{Co}_{17}$; phase evolution in the quinary system Sm-Zr-Fe-Co-Cu. *Z. Metallkd.* 96: 17–23.
93. Streibl, B., J. Fidler and T. Schrefl. (2000). Domain wall pinning in high temperature $\text{Sm}(\text{Co,Fe,Cu,Zr})_{7-8}$ magnets. *J. Appl. Phys.* 87: 4765–4767.
94. Strnat, K.J., G. Hoffer, J. Olson, W. Ostertag and J.J. Becker. (1967). A family of new cobalt-base permanent magnetic materials. *J. Appl. Phys.* 38: 1001–1002.

95. Strnat, K.J. (1988). Chapter 2, Rare earth–cobalt permanent magnets. In: *Ferromagnetic Materials*, vol. 4, E.P. Wohlfarth, K.H.J. Buschow (eds.), North-Holland, Amsterdam, Netherlands.
96. Strnat, K.J. and R.M.W. Strnat. (1991). Rare earth–cobalt permanent magnets. *J. Magn. Magn. Mat.* 100: 38–56.
97. Tang, H., Y. Liu and D.J. Sellmyer. (2002). Nanocrystalline $\text{Sm}_{12.5}(\text{Co,Zr})_{87.5}$ magnets: synthesis and magnetic properties. *J. Magn. Magn. Mat.* 241: 345–356.
98. Tang, W., Y. Zhang and G.C. Hadjipanayis. (2000). Effect of Zr on the microstructure and magnetic properties of $\text{Sm}(\text{Co}_{\text{bal}}\text{Fe}_{0.1}\text{Cu}_{0.088}\text{Zr}_x)_{8.5}$ magnets. *J. Appl. Phys.* 87: 399–403.
99. Tang, W., A.M. Gabbay, Y. Zhang, G.C. Hadjipanayis and H. Kronmüller. (2001). Temperature dependence of coercivity and magnetisation reversal in $\text{Sm}(\text{Co}_{\text{bal}}\text{Fe}_{0.1}\text{Cu}_y\text{Zr}_{0.4})_{7.0}$ magnets. *IEEE Trans. Magn.* 37: 2515–2517.
100. Walmer, M.S., C.H. Chen and M.H. Walmer. (2000). A new class of Sm-TM magnets for operating temperatures up to 550°C . *IEEE Trans. Magn.* 36: 3376–3381.
101. Wecker, J., M. Katter and L. Schultz. (1991). Mechanically alloyed Sm-Co materials. *J. Appl. Phys.* 69: 6058–6060.
102. Xiong, X.Y., T. Ohkubo, T. Koyama, K. Ohashi, T. Tawara and K. Hono. (2004). The microstructure of sintered $\text{Sm}(\text{Co}_{0.72}\text{Fe}_{0.20}\text{Cu}_{0.055}\text{Zr}_{0.025})_{7.5}$ permanent magnet studied by atom probe. *Acta Mat.* 52: 737–748.
103. Yan, A., W.-Y. Zhang, H.-W. Zhang and B. Shen. (2000). Melt-spun magnetically anisotropic SmCo_5 ribbons with high permanent performance. *J. Magn. Magn. Mat.* 210: 10–14.
104. Yan, A., A. Bollero, O. Gutfleisch and K.H. Müller. (2002a). Microstructure and magnetization reversal in nanocomposite $\text{SmCo}_5/\text{Sm}_2\text{Co}_{17}$ magnets. *J. Appl. Phys.* 91: 2192–2196.
105. Yan, A., A. Bollero, K.-H. Müller and O. Gutfleisch. (2002b). Fast development of high coercivity in melt-spun $\text{Sm}(\text{Co,Fe,Cu,Zr})_z$ magnets. *Appl. Phys. Lett.* 80: 1243–1245.
106. Yan, A., A. Bollero, K.H. Müller and O. Gutfleisch. (2002c). Influence of Fe, Zr and Cu on microstructure and crystallographic texture of melt-spun 2:17 SmCo ribbons. *J. Appl. Phys.* 91: 8825–8827.
107. Yan, A., K.H. Müller and O. Gutfleisch. (2002d). Highly coercive melt-spun $\text{Sm}(\text{Co, Fe, Cu, Zr})_z$ magnets prepared by simple processing. *IEEE Trans. Magn.* 38: 2937–2939.
108. Yan, A., O. Gutfleisch, T. Gemming and K.-H. Müller. (2003a). Microchemistry and reversal mechanism in 2:17-type Sm-Co magnets. *Appl. Phys. Lett.* 83: 2208–2210.
109. Yan, A., O. Gutfleisch, A. Handstein, T. Gemming and K.-H. Müller. (2003b). Microstructure, microchemistry, and magnetic properties of melt-spun $\text{Sm}(\text{Co,Fe,Cu,Zr})_y$ magnets. *J. Appl. Phys.* 93: 7975–7977.
110. Yan, A., A. Bollero, O. Gutfleisch, K.-H. Müller, L. Schultz, (2004). Melt-spun precipitation hardened $\text{Sm}(\text{Co,Fe,Cu,Zr})_z$ magnets. *Mat. Sci. Eng.* A375–377: 1169–1172.
111. Yang, W., W. Ping, S. Zhenhua and Z. Shouzeng. (1992). 2:17 type temperature compensated magnets with high coercivity. In: *Proc. of the 12th Int. Workshop on RE Magnets and their Appl.*, Canberra, Australia, pp. 249–257.
112. Zhang, Y., W. Tang, G.C. Hadjipanayis, C. Chen, C. Nelson and K. Krishnan. (2000). Evolution of microstructure, microchemistry and coercivity in 2:17 type Sm–Co magnets with heat treatment. *IEEE Trans. Magn.* 37: 2525–2527.
113. Zhou, J., I.A. Al-Omari, J.P. Liu and D.J. Sellmyer. (2000). Structure and magnetic properties of $\text{SmCo}_{7-x}\text{Ti}_x$ with TbCu_7 -type structure. *J. Appl. Phys.* 87: 5299–5301.
114. Zhou, J., R. Skomski, and D.J. Sellmyer. (2003). Magnetic hysteresis of mechanically alloyed Sm–Co nanocrystalline powders. *J. Appl. Phys.* 93: 6495–6497.

Chapter 13

Nanostructured Soft Magnetic Materials

Matthew A. Willard and Maria Daniil

Abstract Reduction of the grain size to less than 20 nm has provided major advances in soft magnetic materials performance, including reduced core losses and coercivities. These promising results have stimulated research efforts, worldwide, in the areas of nanocrystalline alloy design, alloy processing, materials performance evaluation, and transition to various applications. This chapter presents recent advances in nanocrystalline soft magnetic alloy processing methods, phase transformations, microstructure evaluation, magnetic property measurement and analysis, and applications.

13.1 Introduction

The synthesis and characterization of soft magnetic materials with nanocrystalline microstructures has been an intense field of research in recent years. In an effort to improve their soft magnetic performance by controlling the microstructure, novel techniques and alloying element combinations have been used. The resulting materials show unique combinations of magnetic properties that are possible only when the magnetic correlation and structural correlation lengths are similar. The morphology of the material, whether it is particles, rods, platelets, wires, thin films, or bulk polycrystalline alloys, can have a profound influence on their resulting properties and potential applications [1–4]. Other chapters in this volume discuss the recent contributions in the fields of magnetic nanoparticles and thin films, for this reason this chapter will focus primarily on polycrystalline soft magnetic alloys primarily formed by rapid solidification, which are important materials for power generation, filtering, conversion, and sensing applications.

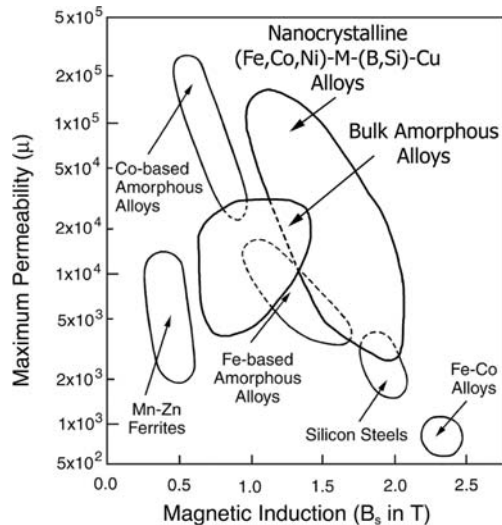
The figures of merit for soft magnetic materials include small coercivity, large magnetic permeability, and large magnetization. Additionally for applications where

M.A. Willard (✉)
US Naval Research Laboratory, Washington, DC, USA
e-mail: willard@anvil.nrl.navy.mil

a magnetic material is switched frequently, it is desirable to have a small area swept by the hysteresis loop experiment during the regular cycling of the magnetic field. This area, called the core loss, should be minimized at the switching frequency. A fast-switching frequency results in induced currents in the magnetic material adding to the overall losses of the core, making a large resistivity desirable for applications above 1 kHz. In recent years, developments in amorphous and nanocrystalline alloys have received increasing examination due to their favorable combination of these electric and magnetic properties.

Figure 13.1 plots the values of permeability against saturation magnetization for a variety of premiere soft magnetic materials. As previously mentioned, the most successful material will have large values for both of these properties. It can clearly be seen that while conventional alloys (e.g., Si-steel, Fe-Co) possess large magnetization but low permeability and Co-based amorphous alloys possess large permeability but low magnetization, the nanocrystalline soft magnetic alloys have the best combination of both permeability and magnetization. These factors in addition to materials processing, microstructure development, high-frequency losses, and applications will be discussed in this chapter.

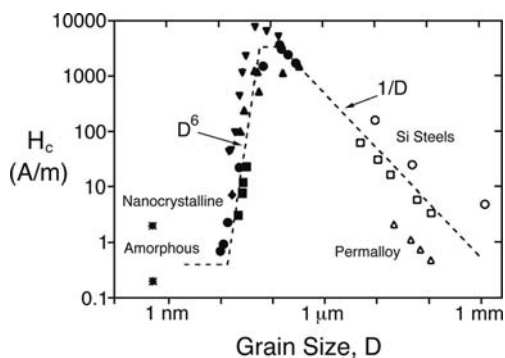
Fig. 13.1 The magnetic permeability at 1 kHz plotted against the saturation induction ($\mu_0 M_s$) for many premiere soft magnetic materials (adapted from Refs. [1, 5]). The symbol M in the composition of nanocrystalline alloys represents early transition metals (e.g., Nb, Zr, Hf, Ta)



Nanocrystalline soft magnetic alloys were first developed in 1988 when Yoshizawa et al. added small amounts of Nb and Cu simultaneously to a typical Fe-Si-B amorphous alloy [6, 7]. Excellent magnetic softness was reportedly due to the fine-grained microstructure and near-zero magnetostriction coefficients. The combination of low coercivity (<2 A/m) necessary for efficient operation, large saturation flux density (>1.3 T) allowing miniaturization of cores, and Fe-rich composition resulting in inexpensive costs made this alloy a desirable alternative to the Co-based metallic glasses previously possessing the best magnetic softness. The

improved magnetic properties of nanocrystalline alloys, including large permeability and saturation magnetization, stem from their combination of refined grain size, the intergranular amorphous matrix phase, and the composition of each phase. Other alloy compositions of nanocrystalline soft magnetic alloys were formulated through the 1990s. These alloys were rich in magnetic transition metals with dominant crystalline phases (in nanocrystalline form), which mimic the best soft magnetic alloy phases in conventional alloys. These include Fe- or (Fe,Si)-based alloys having the body centered cubic (BCC) structure, (Ni,Fe)- or Co-rich alloys with face centered cubic (FCC) structure, and intermetallic phases, including FeCo-based alloys with the B2 (CsCl) crystal structure or Fe₃Si-based alloys with the D0₃ structure.

Fig. 13.2 Coercivity plotted against the grain size of various soft magnetic alloys (modified from [8])



The excellent magnetic softness was attributed to the small size and random orientation of nanocrystalline grains embedded in an exchange-coupled amorphous matrix phase. A plot of the magnetic softness (represented by coercivity) as a function of grain size is shown in Fig. 13.2 [8, 9]. Two switching mechanisms – exchange-averaged anisotropy and domain wall pinning – are represented in the diagram by lines with slope D^6 and D^{-1} , respectively. The point of intersection of these two switching mechanisms is the exchange correlation length (roughly the width of the magnetic domain wall) and results in the worst soft magnet performance. Conventional crystalline alloys (e.g., permalloy and Si-steels) were improved by increasing the grain size, which resulted in lesser amounts of domain wall pinning at grain boundaries. The amorphous alloys, with no grains and therefore no grain boundaries, resulted in lower losses than the conventional large-grained alloys. Alloys with grain sizes less than 100 nm were largely unexplored until the first ultra-fine grained microstructures were presented in 1988 [10]. The effects of microstructure on the magnetic performance of the material will be discussed in this chapter.

A key advancement that enabled this technology was the novel alloy design allowing a combination of widespread nucleation of crystallites with little grain growth. This was accomplished in the Finemet-type alloys by the simultaneous addition of Nb and Cu to a Fe–Si–B amorphous alloy. A two-stage processing route was used: first, processing of an amorphous alloy (by rapid solidification

or deposition techniques) and then annealing to promote partial crystallization. Microstructure control as the crystallites were devitrified from the amorphous precursor alloy was a primary concern as it was found to have an exceptional influence on the coercivity and permeability (extrinsic magnetic properties). Since these early investigations, the design of novel alloy compositions to improve the saturation magnetization, magnetocrystalline anisotropy, Curie temperature, and magnetostriction has expanded the study of nanocrystalline soft magnetic alloys into an active field of research. Resulting from these efforts, three classes of alloys with nanocrystalline microstructures have emerged for use under differing operation conditions. Alloys based on the α -(Fe,Si) phase with composition Fe–Si–Nb–B–Cu (e.g., FinemetTM, VitropermTM) have extremely low losses with moderate saturation magnetization and operation temperatures [9, 10]. The α -Fe-based Nanoperm-type alloy (e.g., Fe–Zr–B–(Cu)) has slightly larger losses and lower operation temperature, but the advantage of 20% larger magnetization [11]. The final class of Fe–Co–Zr–B–(Cu) alloys with α - and α' -(Fe,Co) crystallites has much higher Curie temperature, allowing them to operate at higher operation temperatures (referred to as Hitperm-type alloys) [12, 13]. The differences between these different classes of alloys will be discussed in this chapter.

Based on the improved performance of these materials relative to amorphous alloys and ferrites, nanocrystalline soft magnetic materials are being used for core materials in power conditioning and power conversion applications, including choke cores for switched-mode power supplies. Recently, they have been also considered for electromagnetic interference, sensor, and automotive applications. Optimizing the magnetic properties of the nanocrystalline alloys to meet the wide variety of demands is a significant and ongoing challenge. This chapter will provide information about the state of the art in alloy development and applications.

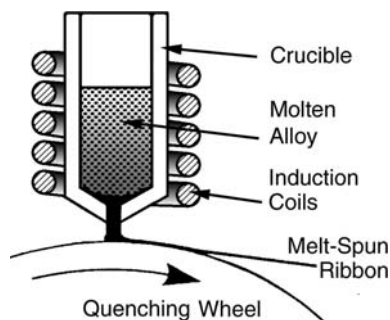
13.2 Materials Development

Few processes naturally result in magnetic materials with features on the nanometer size scale (exceptions include magnetotactic bacteria and magnetite particles found in Martian meteorites) [14]. This is largely thermodynamically driven since small grains have higher surface energies than large grains giving a strong driving force for microstructure coarsening. Achieving nanocrystalline features therefore requires special processing by chemical (e.g., spin spray [15] or various nanoparticle syntheses [3]), vapor/plasma (e.g., sputtering [16, 17], physical laser deposition [18]), or non-equilibrium methods (e.g., melt spinning [1, 5], plasma torch [19], mechanical milling [20]). The resulting materials may be particulate, films, or bulk depending on the composition and technique employed. Rapid solidification processing has been the primary route to bulk material fabrication for the applications discussed in this chapter. For this reason, the following sections will all pertain to melt spun materials and their properties (unless otherwise indicated).

13.2.1 Alloy Processing and Design

The conventional melt spinning technique uses an induction coil to melt ingots of a desired composition and then expels the melt through an orifice in the crucible onto a rapidly rotating wheel, giving effective quench rates of up to 10^6 °C/s (see Fig. 13.3). Using this technique, alloys with compositions near deep eutectics are routinely formed into ribbons 20–50 μm in thickness, a few millimeters to many centimeters in width, and meters in length. Typical parameters that influence processing include the alloy composition, melt temperature, wheel speed, and orifice size. During the melt spinning process, a partial pressure of either inert gas or air is used to eject the melt onto the wheel, overcoming the surface tension of the melt that holds it inside the crucible. Post-quench annealing procedures are then employed to optimize the alloy performance as necessary.

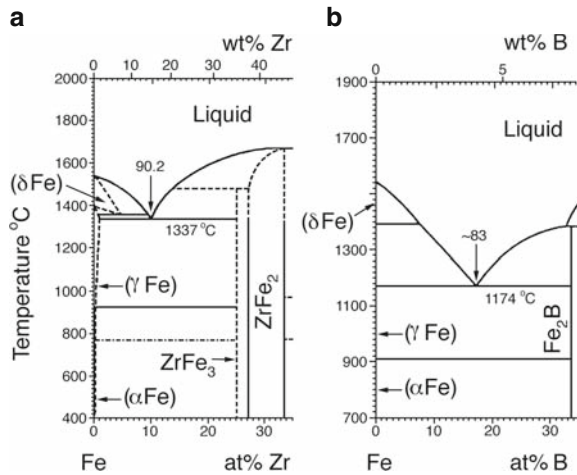
Fig. 13.3 Schematic diagram of a single-wheel melt spinner used for rapid solidification of the precursors to nanocrystalline soft magnetic ribbon materials (after Refs. [21, 22])



As previously mentioned, the majority alloy components are the ferromagnetic transition metals – Fe, Co, and Ni. These elements are required to provide large magnetization and Curie temperature for the alloy. However, the nanocrystalline microstructure can only be achieved by partial devitrification of an amorphous alloy precursor. For this reason, additional alloying elements that stabilize the liquid to low temperatures must be added (i.e., deep eutectic compositions). Selection of elements from two groups tends to provide the necessary increase in stability of the liquid, while maximizing the amount of magnetic transition metal in the alloy. These groups are the early transition metals (e.g., $M = \text{Zr, Nb, Hf, Ta}$) and metalloids (e.g., B, Si, P, C). The Fe-rich section of the Fe–Zr and Fe–B phase diagrams of Fig. 13.4 shows the reduction in melting point at the eutectics from 1,538°C for pure Fe to 1,337°C and 1,174°C for the eutectic compositions of Fe with Zr and B, respectively. The eutectic compositions for Fe–Zr and Fe–B are also shown with values of 90.2 and 83 at.% Fe, respectively. Small amounts of noble metals (e.g., Cu, Au, Ag) are essential to developing the optimal magnetic properties in some nanocrystalline alloys by creating heterogeneous nucleation sites throughout the alloy during the early stages of annealing [23, 24].

The classes of nanocrystalline alloys are defined by their compositions and resulting magnetic properties. Finemet-type alloys have composition Fe–Si–M–B–Cu and

Fig. 13.4 Fe-rich portions of the (a) Fe–Zr and (b) Fe–B phase diagrams, displaying the deep eutectics and limited solubility of Zr and B in the Fe-rich primary crystalline phases (modified from [1, 25])



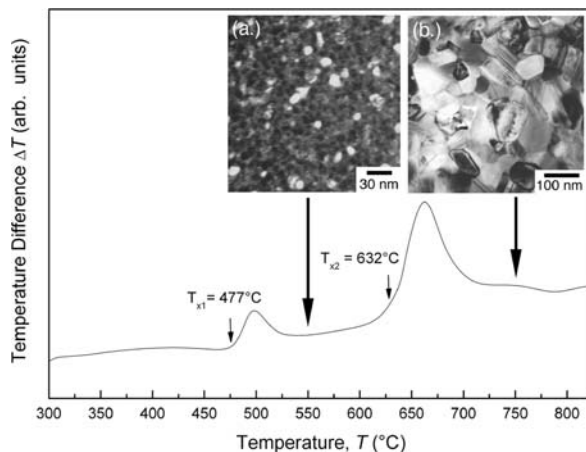
form α' -(Fe–Si) crystallites during primary crystallization. The optimal magnetic properties are achieved by annealing to control the Si-content of the crystalline phase [26]. The resulting alloy has ultra-fine grain size which reduces the magnetocrystalline anisotropy and near-zero magnetostrictive coefficient. The combination of small amounts of both early transition and noble metals was found to be necessary for the development of exceptional magnetic softness [27]. Nanoperm-type alloys have the composition Fe–M–B–(Cu) with α -Fe (BCC) primary crystallites [11]. These alloys benefit from reduced solubility of the early transition and metalloids in the primary crystalline phase. The limited solubility, shown in Fig. 13.4, is a desirable feature of the phase diagram from an alloy design perspective. Although it has been found that the primary crystallites contain a larger amount of these elements than expected [28], limiting their solubility helps to avoid their deleterious effects on the magnetization. Hitperm-type alloys with composition Fe–Co–M–B–(Cu) and α' -FeCo (CsCl-type) phase have shown similar solubility of M and B elements in the primary crystallites [29] and similarly benefit from limiting solubility [13].

13.2.2 Phase Transformations

Annealing the as-spun amorphous precursor at temperatures exceeding the primary crystallization temperature results in crystallite formation by a nucleation and growth process. When the nuclei density (or nucleation rate) is large and the growth rate is small, the nanocrystalline microstructure is developed. Optimally, this microstructure consists of nanocrystallites less than 15 nm in diameter surrounded by a residual amorphous matrix phase. If the annealing temperature is too high, no residual amorphous phase is retained, instead magnetic and early transition metals

form intermetallic phases, which deteriorate the magnetic performance of the alloy. For this reason, a large temperature difference between the two crystallization temperatures is important (at least 100°C).

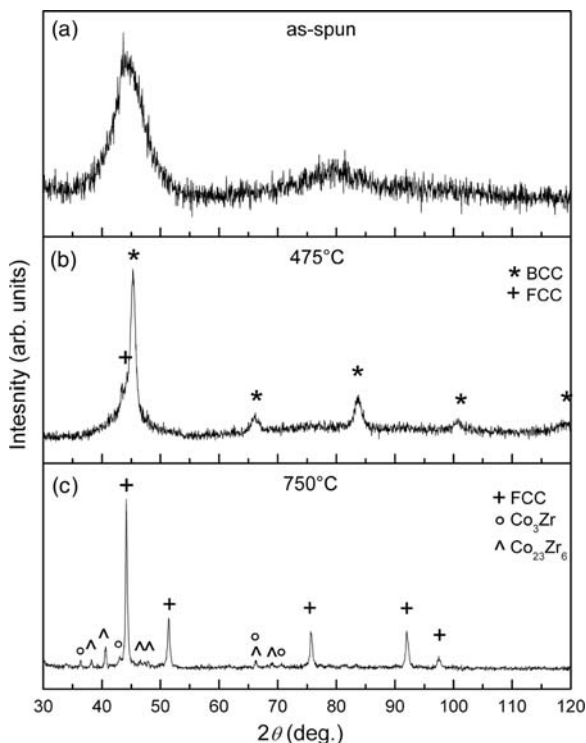
Fig. 13.5 Differential thermal analysis data for a high Co-type Hitperm $((\text{Co}_{0.95}\text{Fe}_{0.05})_{88}\text{Zr}_7\text{B}_4\text{Cu}_1)$ alloy when heated at 20°C/min. Insets show the resulting microstructure when the as-spun alloy was annealed at (a) near primary crystallization (at 550°C) and (b) above secondary crystallization (at 750°C) each for 3.6 ks (modified from [30, 31])



Differential thermal analysis is commonly used to determine the crystallization temperatures and the temperature interval between primary and secondary crystalline (see Fig. 13.5). As an example, a Hitperm-type, Co-based nanocrystalline alloy is presented in Figs. 13.5 and 13.6 to illustrate the phase transformations for nanocrystalline alloys. Similar crystallization behavior is observed for other types of nanocrystalline alloys (e.g., Finemet/Nanoperm-type). Regardless of the alloy type, the early transition metal acts to reduce the diffusivity of the magnetic transition metal resulting in limited growth rate during primary crystallization. This is evident from the insets in Fig. 13.5, where the refined grain size of ~ 8 nm is found for a sample annealed at 550°C (above $T_{x1} = 477^\circ\text{C}$) in contrast to the coarsened microstructure for a sample annealed above T_{x2} (grains ~ 45 nm).

The phases formed at the primary and secondary crystallization temperatures are typically determined by X-ray or electron diffraction techniques. Figure 13.6(b) shows representative X-ray diffraction data for a Co-rich Hitperm-type alloy annealed near primary crystallization. The BCC(Co,Fe) phase was identified as the primary crystalline phase. The breadth of the diffraction peaks is increased due to the limited size of the grains, and the full width at half maximum can be used for grain size estimation; in this case, the grains were about 10 nm in diameter. While there are no planes of atoms to diffract in the as-spun alloy, a broad scattering peak typical of an amorphous alloy is observed (Fig. 13.6(a)), and the residual amorphous phase in Fig. 13.6(b) shows a peak at a similar 2Θ position. More diffraction peaks with higher intensity are found for alloys annealed above the secondary crystallization temperature. The extra peaks indicate the presence of $(\text{Co,Fe})_3\text{Zr}$ and $(\text{Co,Fe})_{23}\text{Zr}_6$ phases (see Fig. 13.6(c)); the increased intensity and reduced peak width are evidence of the increased grain size, and the scattering peak from the

Fig. 13.6 X-ray diffraction data for a high Co-type Hitperm $((\text{Co}_{0.95}\text{Fe}_{0.05})_{88}\text{Zr}_7\text{B}_4\text{Cu}_1)$ alloy annealed (a) near primary crystallization (at 475°C) and (b) above secondary crystallization (at 750°C) each for 3.6 ks



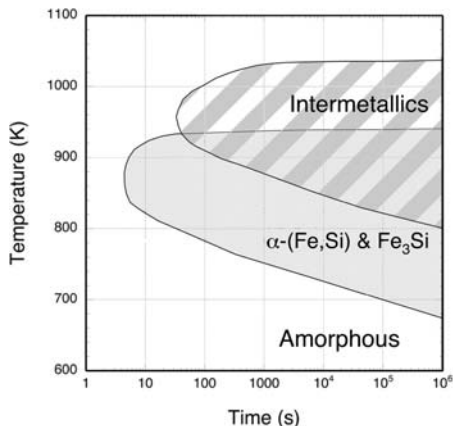
amorphous phase is absent in this sample. Typical values for the crystallization temperatures and resulting phases formed at primary and secondary crystallization are shown in Table 13.1.

The coarsened microstructure and formation of intermetallic phases deteriorates the magnetic performance of the alloy, so it is important to know the range of

Table 13.1 Soft magnetic nanocrystalline alloys and some relevant thermodynamic and kinetic properties. All values of E_A are for primary crystallization and are accurate to ± 20 kJ/mol. Nanoperm- and Hitperm-type alloys were limited to Zr-containing compositions

Alloy	T_{x1} (K)	T_{x2} (K)	ΔT_x (K)	E_A (kJ/mol)	Primary phase	Secondary phases
Finemet	775–830	920–1,010	130–205	375	α -(Fe,Si)/ Fe ₃ Si	Fe ₂ B, Fe ₂₃ B ₆ , Fe ₃ B
Nanoperm	785–835	980–1,030	145–240	350	α -Fe	Fe ₃ Zr, Fe ₂₃ Zr ₆ , Fe ₂ Zr, ZrB ₂
HiTperm	780	970	210	340	α -(Fe,Co)	(Fe,Co) ₃ Zr, (Fe,Co) ₂₃ Zr ₆
Co-rich Hitperm	745–770	905–925	135–180	320	α -(Co,Fe) (γ -(Co,Fe))	(Co,Fe) ₃ Zr, (Co,Fe) ₂₃ Zr ₆

Fig. 13.7 Schematic diagram of the time–temperature–transformation curves for primary and secondary crystallization in a Finemet-type alloy



annealing conditions, which are sufficient for primary crystallization but not for secondary crystallization. Both primary and secondary crystallization processes are thermally activated. For this reason, the rate at which the sample is heated will change the temperature at which crystallization occurs. This information can be used to determine the time–temperature–transformation (TTT) curve for the alloy system, which is a helpful tool for determining the optimal annealing conditions. A schematic of the TTT curve for a Finemet-type ($\text{Fe}_{73.5}\text{Si}_{13.5}\text{B}_9\text{Nb}_3\text{Cu}_1$) alloy is shown in Fig. 13.7. Quenching by rapid solidification processing must occur at a rate fast enough to pass by the “nose” of the primary crystalline phase to create an amorphous phase. The diagram can then be used to determine where crystallization begins (thin lines in the diagram) for primary phases (e.g., α -(Fe,Si) or Fe_3Si) at low temperatures and short times and secondary phases (e.g., Fe_2B , Fe_{23}B_6 , Fe_3B) for higher temperatures and longer times.

Experimentally, the lower edge of the TTT curve can be approximated using activation energies measured by thermal analysis techniques (summarized in Table 13.1). Measuring the crystallization temperature as a function of heating rate can provide essential information for determining the activation energy for each crystallization process. Typical annealing procedures are performed at temperatures between 750 and 825 K and times between 900 and 3,600 s.

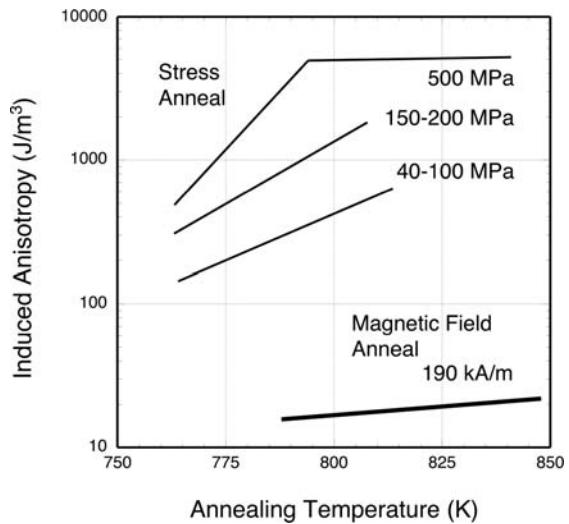
13.2.3 Annealing Techniques

The as-spun alloys, consisting of primarily or entirely amorphous phase, require annealing to provide partial crystallization and thereby achieve the best soft magnetic performance. Conventional, magnetic field, stress field, or rapid thermal annealing processes are used to achieve primary crystallization of the amorphous precursor alloy. While conventional annealing is carried out at sufficient tem-

peratures to crystallize the alloy, it does not control the magnetic domain structure. Stress fields or magnetic fields can be used to control the domains in the alloys by providing a uniaxial magnetic anisotropy to shear the hysteresis loop in a controlled manner without introducing an air gap in the core. This is important for many applications where a controlled reduced permeability is necessary during use.

A significant induced anisotropy has been found for all types of nanocrystalline soft magnetic alloys from the introduction of an applied magnetic field (in transverse, longitudinal, or rotating with respect to the sample length) or an applied tensile stress (along the length of the ribbon). The results shown in Fig. 13.8 for Finemet-type alloys show the much stronger influence of moderate stress annealing than annealing in a magnetic field [32]. In Finemet-type alloys, magnetic field annealing in a longitudinal orientation reduces the permeability by producing an induced anisotropy [7]. Similar field annealing procedures using a transverse magnetic field make the loop squarer.

Fig. 13.8 Induced anisotropy values for primary crystallization with applied stress field (*thin lines* [33–36]) or longitudinal magnetic field (*thick line* [7, 32, 37]) for Finemet-type ($\text{Fe}_{73.5}\text{Si}_{13.5}\text{B}_9\text{Nb}_3\text{Cu}_1$) alloys annealed for 3.6 ks



13.3 Magnetic Performance

Processing considerations aside, the effects of both microstructure and composition have direct consequences on the magnetic performance of the alloy. The significant challenges in maintaining a refined microstructure, increasing the magnetization, and reducing the core losses remain important fields of investigation. Optimizing alloys for elevated or cryogenic temperatures presents additional challenges. The following sections will address some of the design principles used to optimize an alloy for applications in some of these environments.

13.3.1 Exchange-Averaged Anisotropy

The remarkable reduction in coercivity when grain sizes are reduced to the nanocrystalline regime was first described in the well-known work of G. Herzer [8, 9]. Noting the fact that randomly oriented grains were exchange coupled through the residual amorphous matrix, a random anisotropy model was applied to show that the coercivity was proportional to the grain size to the sixth power. This is possible when the exchange correlation length (L_{ex}) is larger than the structural correlation length (grain size), an effect referred to as exchange softening which results from exchange-averaged anisotropy (see Fig. 13.9). Materials with grains much larger than L_{ex} show strong angular dependence of the magnetization with respect to the crystalline lattice through the magnetocrystalline anisotropy (K_1). However, in nanocrystalline materials, the local easy axes of the nanocrystalline grains influence the magnetization direction (represented by dashed lines in Fig. 13.9(a)), but do not dominate it. This is illustrated in the schematic diagram shown in Fig. 13.9(b), where the integrated anisotropy energy is unchanged by the averaging but the fluctuations (which are more important to soft magnetic properties) are significantly reduced.

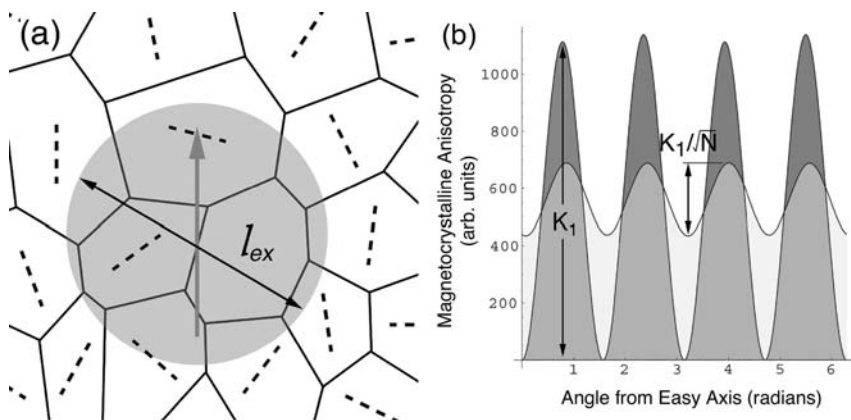


Fig. 13.9 (a) Schematic representation of the magnetic exchange correlation length compared to the grain size in the alloy. (b) Schematic diagram showing the effect of grain orientation averaging on the magnetocrystalline anisotropy of a nanocrystalline soft magnetic alloy

The magnetic exchange correlation length (L_{ex}) indicates the minimum size scale over which the atomic moments must remain aligned due to exchange forces. The magnitude of this fundamental magnetic material parameter can be found by $L_{ex} = (A/K_1)^{1/2}$, where A is the exchange stiffness and K_1 is the first magnetocrystalline anisotropy constant. The resulting value of 35 nm was calculated for Fe–Si-based nanocrystalline alloys. Since the structural correlation length of the material (i.e., grain size, $D \sim 10$ nm) is much smaller than the exchange correlation length, the magnetic moments in each individual grain cannot relax into the local easy direction dictated by the grain orientation. This results in an averaging

of the local magnetocrystalline anisotropy over the exchange correlation volume. Using a random walk type, random anisotropy model, an effective magnetocrystalline anisotropy, $\langle K \rangle$, representing the material response can be determined as $\langle K \rangle = K_1/N^{1/2}$, with N being the number of grains within the exchange correlation length. The value of N in a cubic volume with sides L_{ex} can be estimated by the relation $N = (L_{ex}/D)^3$. Using these three equations, the effective anisotropy can be determined in terms of the crystalline materials parameters, K_1 , A , and D : $\langle K \rangle = K_1^4 D^6 / A^3$. The exchange softening described by this model breaks down as the grains become decoupled, especially as the Curie temperature of the amorphous intergranular phase is exceeded, as discussed in Section 13.3.3. More sophisticated models that take induced anisotropy or two-phase microstructures have been investigated, but are beyond the scope of this chapter (see Refs. [38, 39]).

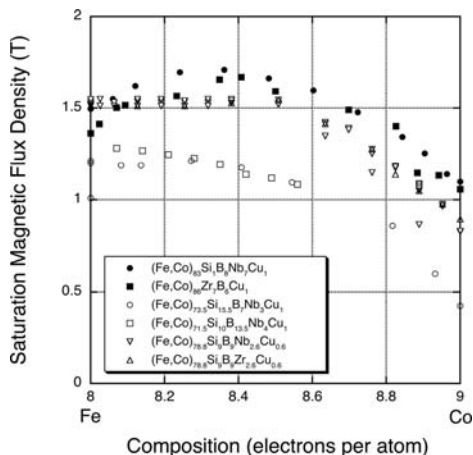
13.3.2 Intrinsic Magnetic Properties

The magnetic transition metal composition has a major influence on the magnetization, magnetostriction, magnetocrystalline anisotropy, and Curie temperature. Adjusting the ratios of Co, Ni, and Fe has been shown to influence the crystallization behavior and resulting magnetic performance. While Fe-based alloys have the strong advantage of low cost and strong performance in terms of magnetization and low losses, improvements can be made by adjusting the composition to increase the operation temperature and saturation magnetization. Figure 13.10 shows the saturation flux density (B_s) for nanocrystalline alloys as a function of the number of valence electrons per magnetic transition metal atom (as a way of representing composition). The Finemet-type alloys (open symbols) show only slight increases in saturation flux density as Co is substituted for Fe up to about 50% replacement. However, a marked increase in magnetization is found for similar substitution in Nanoperm-type alloys (i.e., formation of Hitperm-type). The maximum occurs at about 30% Co substituted for Fe, a similar result to that of crystalline alloys (the peak of the Slater–Pauling curve). The reduced effect of Co substitution in the Finemet-type alloy is likely linked to the redistribution of Si in the crystalline phase. Enrichment in Co above 50% substitution results in a strong reduction in saturation flux density for all compositions, consistent with crystalline alloys made by conventional methods (i.e., not nanocrystalline).

The Curie temperature of the amorphous phase (T_c^{am}) determines the upper bound of the operation temperature for nanocrystalline soft magnetic alloys. When a nanocrystalline soft magnetic alloy is used at temperatures approaching T_c^{am} , the grains begin to decouple and the magnetic correlation length shortens significantly. This results in a strong increase in coercivity as exchange averaging is reduced, and the grains begin to couple magnetostatically [40]. The Curie temperature of the amorphous phase is near 600 K for Finemet-type alloys allowing operation up to about 120°C without degradation of performance (see Fig. 13.11 (open symbols)). Nanoperm-type alloys have a much lower T_c^{am} limiting their use to room

temperature applications. Significant improvements in T_c^{am} are found for Hitperm-type alloys, with values exceeding 600°C as the substitution of Co for Fe approaches 50% (closed symbols – Fig. 13.11). The name Hitperm originates from the combination of high permeability and high-potential operation temperature.

Fig. 13.10 Saturation flux density as a function of magnetic transition metal composition for various nanocrystalline soft magnetic alloys. *Open symbols* are Finemet-type compositions and *solid symbols* are Nanoperm/Hitperm-type compositions [41–47]



The exchange averaging effect helps to reduce the effective magnetocrystalline anisotropy, leaving the magnetostriction as the major influence on the core losses. Residual stress in the alloy magnetoelastically couples with the magnetization resulting in the increased loss. This can be avoided by choosing compositions where the magnetostrictive coefficient is near zero. Finemet-type alloys have been optimized for near-zero magnetostrictive coefficients by controlling the Si:B ratio and annealing temperature. Figure 13.12 shows the magnetostrictive coefficient for Finemet-type alloys with composition $\text{Fe}_{73.5}(\text{Si}_x\text{B}_{1-x})_{22.5}\text{Nb}_3\text{Cu}_1$ and annealed at 813 K for 3.6 ks. When x is near 0.7 (e.g., Si = 15.5), the magnetostrictive coefficient is near zero and the coercivity has a low value of 1.6 A/m [45].

13.3.3 Domain Structure

The magnetic domain structure of a soft magnet has a strong influence on the material's switching behavior. In the case of nanocrystalline alloys, induced anisotropy produced by stress or magnetic field annealing has been shown to result in controlled magnetic domain structures. The magnetic domain structure of a Finemet-type alloy, as measured by stroboscopic Kerr microscopy, shows significant differences depending on the degree of induced anisotropy (see insets to Fig. 13.13). The domain wall velocity was observed to also have a strong dependence on the induced anisotropy especially at high frequencies [56].

Fig. 13.11 Curie temperature of the amorphous phase as a function of magnetic transition metal composition for various nanocrystalline soft magnetic alloys. *Open symbols* are Finemet-type compositions and *solid symbols* are Nanoperm/Hitperm-type compositions [44, 47–53]

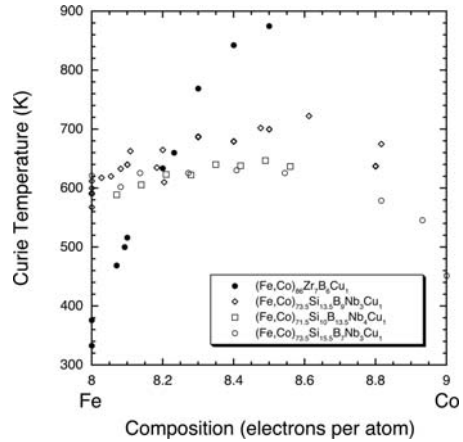
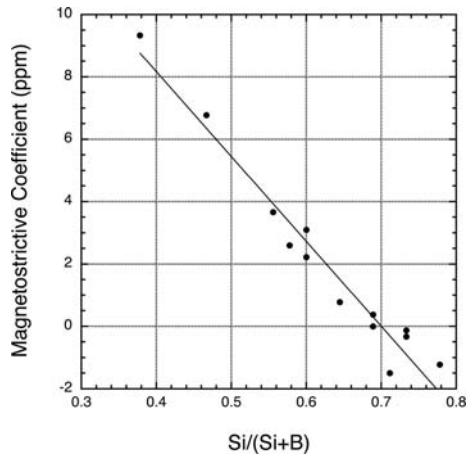


Fig. 13.12 Saturation magnetostriction coefficient for $Fe_{73.5}(Si_xB_{1-x})_{22.5}Nb_3B_9Cu_1$ alloys (annealed at 813 K) as a function of $x = Si/(Si+B)$ [8, 35, 54, 55]

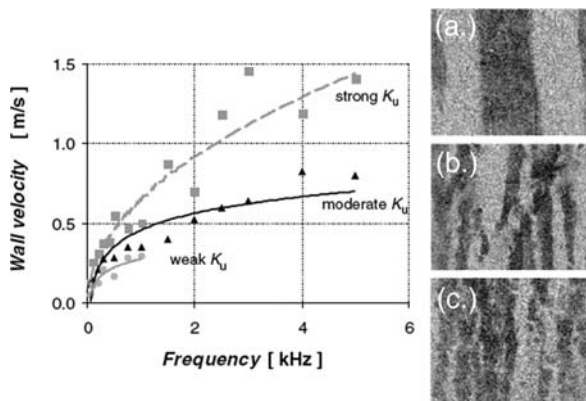


13.3.4 Hysteretic Losses

Much of the interest in the nanocrystalline class of alloys has been in the excellent soft magnetic performance of these alloys including the extremely large permeability and low-core losses for an alloy with such large saturation magnetization. The properties for nanocrystalline soft magnetic alloys and potential applications are presented in Table 13.2.

The frequency-independent losses are typically measured by slowly varying magnetic measurement techniques, including vibrating sample and superconducting quantum interference device magnetometries. Desirable features of the hysteresis loop produced by these techniques include small coercivity and large magnetization, resulting in a tall narrow loop with little enclosed area. The softest magnetic materials, with coercivities less than 2 A/m, have compositions with small values of magnetocrystalline anisotropy that are further reduced by exchange averaging and

Fig. 13.13 Domain wall velocity as a function of switching frequency for a Fe₇₃Si₁₆B₇Nb₃Cu₁ alloy annealed under varying field annealing conditions. The insets are Kerr microscopy images of (a) a high-induced anisotropy alloy at 5 kHz; (b) a medium-induced anisotropy alloy at 5 kHz; and (c) a low-induced anisotropy alloy at 1 kHz [56]



near-zero values of magnetostriction. Exchange averaging refers to the reduction in effective magnetocrystalline anisotropy due to the magnetic correlation length being much larger than the grain size. This behavior was previously described in the context of the random anisotropy model (Section 13.3.1).

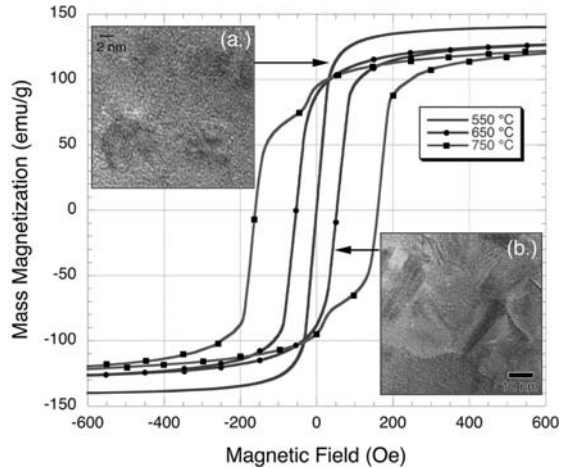
Table 13.2 Soft magnetic nanocrystalline alloys and some relevant properties. The application of these materials varies as listed in the “Use” column, where the following listing corresponds to the designated activity. A: distribution/power transformers; B: EMI filters; C: choke coils; D: electromagnetic sensors; E: switched-mode power supplies; F: magnetomechanical sensors; G: magnetic shielding; H: pulse-power cores; I: saturable reactors; J: high-frequency transformers; K: magnetic switches; L: flux gate magnetometers [11, 22, 57–61]

Alloy	B _s (T)	μ _r (max.)	H _c (A/m)	λ _s (ppm)	ρ (mWcm)	T _c (°C)	Use
Finemet	1.23–1.35	5,000–100,000	0.5–3	0–2	115	570–600	A,B,C,D,E,G,I,K
Nanoperm	1.52–1.60	4,000–48,000	3–8	–1–1	56	100	A,B,C,H,L
HiTperm	1.80	1,000–3,000	~60	>30	175	980	A,B,C,F (High T)
Co-rich Hitperm	1.49	1,000–10,000	9–21	12	~50	>800	D,F,J

Hysteresis loops for a Co-based nanocrystalline alloy are shown in Fig. 13.14, contrasting the effect of primary and secondary crystallization. The line without symbols shows an optimally annealed alloy, with coercivity of ~10 A/m and specific magnetization of 140 emu/g. The inset (a) shows a high-resolution transmission electron microscopy image of the sample showing 8–10 nm grains surrounded by a residual amorphous matrix phase. At higher annealing temperatures, the magnetization is reduced and the coercivity substantially increased (line with square/circle symbols). The corresponding coarsened microstructure made up of α-Co, Co₃Zr,

and $\text{Co}_{23}\text{Zr}_6$ phases is shown in inset (b). At 750°C , the grains coarsen to greater than 45 nm and the different phases decouple from each other as evidenced by the separate switching fields in the hysteresis loop.

Fig. 13.14 Hysteresis loops from a Co-based nanocrystalline alloy $((\text{Co}_{0.95}\text{Fe}_{0.05})_{88}\text{Zr}_7\text{B}_4\text{Cu}_1)$. Each sample was isothermally annealed with examples of optimal annealing (550°C anneal) and over-annealing (650 and 750°C). HRTEM micrographs show (a) the optimal microstructure when annealed above the first peak (at 550°C) and (b) undesirable large-grained microstructure when annealed at the second peak (650°C) (modified from [62])



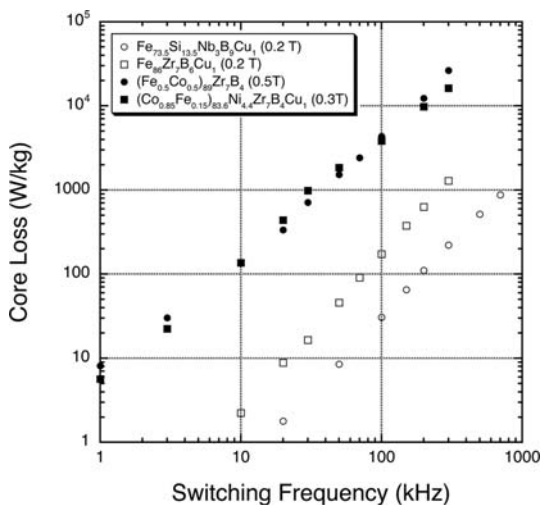
13.3.5 AC Properties

The main advantage of nanocrystalline soft magnetic alloys over conventional large-grained materials is their better performance at switching frequencies above 1 kHz . This is due in part to (a) the smaller interaction of domain walls with the nanocrystalline grains and (b) the higher resistivity of these alloys. The hysteretic loss is present at all frequencies but does not have strong frequency dependence. Controlling the microstructure and composition of the alloy can lead to reduction of hysteretic losses. As the switching frequency is increased, eddy currents are formed in the alloy resulting in increased core losses. Reducing lamination thickness and increasing the resistivity of the alloy help to limit the eddy current loss contribution. At high frequencies (especially above 10 kHz), the dynamic eddy current losses dominate. These eddy currents are localized at the domain walls and can be minimized by refinement of the domain structure in the alloy.

Examples of the core losses for different classes of nanocrystalline soft magnetic alloys are presented in Fig. 13.15. The Finemet-type alloy (open circles) shows the best loss performance, with the lowest losses across the entire frequency range. Comparatively, the Nanoperm-type alloy (open squares) has higher losses by a factor of 5, but has 20% higher magnetization than the Finemet alloy, which is useful for applications where size and weight are a strong consideration. The Hitperm-type alloys (closed symbols) show higher losses, however some of this increase

is due to the higher switching induction amplitude (e.g., 0.3–0.5 T versus 0.2 T for the Fe-based alloys). The remainder of the increased losses is likely due to the combined effects of lower resistivity and higher magnetostriction for these Co-rich alloys.

Fig. 13.15 Core loss as a function of switching frequency for nanocrystalline soft magnetic alloys. Note: Hitperm-type compositions (closed symbols) are presented at a higher magnetic flux density than Nanoperm/Finemet-type (open symbols) [7, 63–65]



13.3.6 Thermomagnetics

At elevated temperatures, the coercivity increases and the losses become larger as the Curie temperature of the intergranular amorphous phase is exceeded. This is a limiting condition for use of Finemet-type alloys above 200°C and Nanoperm-type alloys above room temperature. The Hitperm-type alloys have been specifically designed to operate at temperatures above 100°C. The coercivity of a Finemet-type alloy and a Co-rich Hitperm-type alloy are plotted against the measurement temperature in Fig. 13.16. The Curie temperature of the amorphous phase is about 225°C for Finemet, the temperature at which the coercivity begins to increase rapidly (dark symbols) [66]. The Hitperm alloy possesses much larger coercivity than the Finemet alloy, only becoming comparable at temperatures above 300°C. However, the magnetization of the Finemet alloy is substantially reduced above 200°C whereas the Hitperm alloy's magnetization remains high well above 450°C (see Fig. 13.17). The combined relatively low coercivity and the large magnetization at elevated temperatures make the Hitperm alloys suitable for high-temperature operation.

Fig. 13.16 Coercivity as a function of measurement temperature for a Finemet-type (*squares*) and Co-rich nanocrystalline soft magnetic alloy (*circles*) [31, 66]

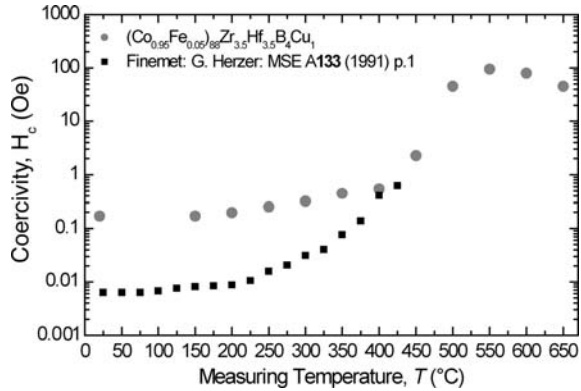
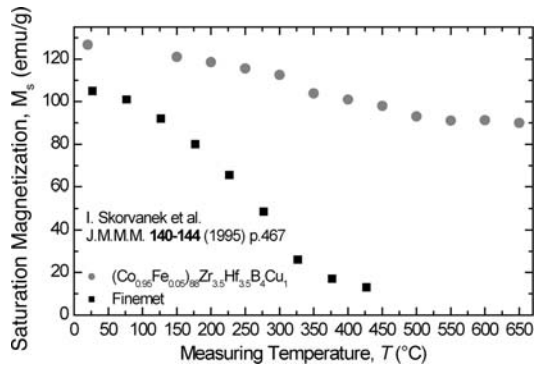


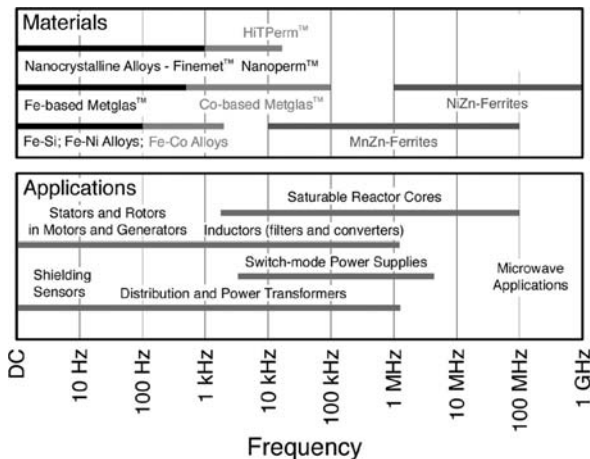
Fig. 13.17 Saturation magnetization as a function of measurement temperature for a Finemet-type (*squares*) and Co-rich nanocrystalline soft magnetic alloy (*circles*) [31, 67]



13.4 Applications

Soft magnetic materials are desirable for a wide range of applications and can be classified by the frequency of operation, as shown in Fig. 13.18. Satisfactory materials for sub-MHz applications include crystalline, nanocrystalline, and amorphous alloys. However, the detrimental effects of eddy currents cause large losses in these materials in the higher part of this frequency range. For this reason, the highly resistive spinel ferrites are used for applications above 1 MHz out of simple necessity to reduce eddy current losses. Their undesirable small values of magnetic induction (<0.4 T) provide an opportunity for advanced nanocrystalline alloys to make an impact if the eddy currents can be curtailed. This would allow a smaller magnet size to produce the same output as their ferrite counterparts. The following section will illustrate some of the applications which nanocrystalline soft magnetic alloys may have a strong impact. In many cases, some classes of nanocrystalline alloys are already in service for the described application.

Fig. 13.18 Diagram showing common applications and potential materials for each as a function of operation frequency



13.4.1 Power Applications

In recent years, substantial federal and private investments have targeted improvements in the packaging and performance of power electronic components. Specifically, these efforts address the standardization, modularization, and miniaturization of active components in power electronic devices. These active components are typically semiconductor-based devices that have been designed to operate at higher loads and frequencies. In contrast, the passive components (i.e., inductors and capacitors) have not experienced commensurate support and show more modest improvements over this same time interval. As a result, the advances realized in the packaging, performance, and functionality of the active components have been marginalized by the state of passive components. This situation has limited the miniaturization and modularization of integrated power electronic components. This is a leading motivation for the development of advanced soft magnetic materials with high magnetization and low losses at frequencies above 1 kHz.

Power electronics devices are used to supply a specific voltage with a limited noise threshold. This typically requires conversion of AC line frequencies to DC, followed by DC/DC power conversion to match the different components the power electronics support. In the voltage regulation circuit, the soft magnetic alloy acts as a magnetic switch (sometimes referred to as a magnetic amplifier) that requires low and high remanent states of the magnetization with small applied switching fields between the two [68]. Ideally, the soft magnetic material switches very sharply at the coercivity and the hysteresis loop has good squareness (i.e., $B_r/B_s > 0.9$). Conventionally annealed nanocrystalline alloys possess suitable magnetic properties for these applications.

Power converters also use choke coils to reduce high-frequency harmonics in the current source. In this case, the inductor coil will have a large amount of current, and the inductor should not be allowed to saturate under this condition. A soft magnetic

alloy with induced anisotropy, low remanence (i.e., $B_r/B_s < 0.3$) and high saturation magnetization is desired for this application. The recent use of Finemet-type alloys for a 1 MV DC power supply illustrates the importance of nanocrystalline materials to power-conditioning applications [69]. Power conditioning refers to reducing the harmonic distortion in the output signal, from a switched-mode power supply, for instance, caused by the fast switching during DC/DC conversion. A common mode choke is used in this case and requires a broadband high permeability.

Many modern power applications require magnets to switch at frequencies above 1 kHz, which limits the choices of materials to those with high resistivity. The materials used for 60 Hz applications (e.g., Si-steels) are not suitable for higher frequency use due to the increased losses caused by eddy currents. While MnZn-ferrites have been used as cores for applications, their small saturation magnetization values require a much larger amount of material for a given power load.

13.4.2 Electromagnetic Interference Applications

The ubiquitous use of portable electronic devices (including cell phones, laptops, and personal digital assistants) that operate at high frequencies (above 1 MHz) has resulted in new regulations to prevent their disruption of other common electrical devices (including medical devices and personal computers), which are susceptible to an increased high-frequency noise from portable devices. Common mode choke coils provide protection of these devices by acting as a low impedance wire for differential mode currents (i.e., the signal) and high impedance inductor for common mode currents (i.e., the high-frequency noise). Chokes of this type are used in switched-mode power supplies, uninterruptible power supplies, inverters, and frequency converters.

Both Finemet-type and Nanoperm-type nanocrystalline materials possess favorable properties for common mode choke coil applications [6, 70]. These properties include high saturation magnetization (M_s) and low remanence ratio (M_r/M_s), which provide a large pulse voltage attenuation that is broadband (100 kHz to 10 MHz). Reduction of the permeability in nanocrystalline soft magnetic alloys allows them to store magnetic energy. This is especially important for choke coils that are used to prevent signal distortion in reactor elements of phase-modifying devices by smoothing out the higher harmonic ripples in the rectified voltage waveform. Lowering of the permeability can be accomplished by field annealing, putting an air gap in the core, or powdering samples of the ribbon materials.

Reduced size of the core material is a desired improvement for these applications as the core is one of the bulkiest components. Miniaturization of the core requires materials with higher saturation magnetization and lower core losses. The saturation magnetization must be increased when the core is made smaller to maintain a constant stored magnetic energy. At the same time, the core loss must be reduced because an increased saturation magnetization tends to increase the hysteresis loop size. Smaller cores increase the importance of thermal management due

to the reduced surface area to shed the generated heat. The rise in temperature is directly proportional to the core losses in the alloy, illustrating the importance of using materials with low core losses [71]. Nanocrystalline soft magnetic alloys with induced magnetic anisotropy provide excellent soft magnetic properties for choke coil applications using the core principles described here.

The effects of powdering and gapping the cores have both shown increased losses when compared to ribbon wound cores [72, 73]. Therefore induced anisotropy from field or stress annealing provides improved magnetic performance if these techniques can achieve the desired permeability. The higher permeability (above 10,000 μ_0 at 10kHz) and impedance over a wide frequency range are significant advantages for nanocrystalline cores compared to Mn–Zn-ferrites for noise suppression applications. Finemet-type alloys show little change in permeability ($<\pm 10\%$) during sustained use at temperatures as high as 100°C and over the broad temperature range -40°C to 150°C. Due to their low values of magnetostriction, the acoustic noise emission is also small. These features make the nanocrystalline material favorable over amorphous and ferrite cores for use in switched-mode power supplies, frequency inverters, uninterruptible power supplies, adjustable speed drives, and other applications requiring robust noise suppression from rapid current changes.

13.4.3 Sensor Applications

Ultra-sensitive flux gate sensors used for the detection of small magnetic fields (~ 0.1 nT) have been shown to work well using nanocrystalline alloys [35]. The sensor is made of two identical saturable cores with high permeability and opposite winding sense. A small AC field is applied to each coil, and a differential voltage drop is measured when an unvarying external field is applied. The difference is proportional to the magnitude of the external magnetic field. These sensors are used for magnetic direction sensing applications. The near-zero value of magnetostriction, high permeability, and low Barkhausen noise makes nanocrystalline soft magnetic alloys competitive for these applications. Finemet-type ribbons processed in a transverse magnetic field during the crystallization process have shown 0.04 nT noise level for a 16 nT peak-to-peak square applied waveform [35].

Recently Ong et al. have shown that the higher harmonics created in a soft magnetic amorphous ribbon can be used for accurate, remote temperature measurement [74]. The high permeability and the low coercivity found to be important for this sensor are similar to those in nanocrystalline materials, which might also be used in this capacity.

13.5 Summary

As the first 20 years of research on nanocrystalline soft magnetic alloys come to a close, the impact of these materials in a variety of applications is just beginning to be

exploited. Our understanding of fundamental magnetic properties at the nano-scale has opened many possibilities for improvement of the properties of soft magnets due to the diligent work of researchers in this field. While much progress has been made due to the concerted effort of basic and applied researchers, the significant need for further improvements to the state of the art will drive continued research in this field.

References

1. McHenry ME, Willard MA, Laughlin DE. Amorphous and nanocrystalline materials for applications as soft magnets. *Progress in Materials Science*. 1999;44(4):291–433.
2. McHenry ME, Laughlin DE. Nano-scale materials development for future magnetic applications. *Acta Materialia*. 2000 Jan 1;48(1):223–38.
3. Willard MA, Kurihara LK, Carpernter EE, Calvin S, Harris VG. Chemically prepared magnetic nanoparticles. *International Materials Reviews*. 2004;49(3–4):125–70.
4. Skomski R. Nanomagnetism. *Journal of Physics: Condensed Matter*. 2003;15:R841–96.
5. Makino A, Inoue A, Masumoto T. Nanocrystalline Soft-Magnetic Fe-M-B (M=Zr, Hf, Nb) Alloys Produced by Crystallization of Amorphous Phase (Overview). *Materials Transactions JIM*. 1995 Jul;36(7):924–38.
6. Yoshizawa Y, Yamauchi K, Yamane T, Sugihara H. Common-mode choke cores using the new Fe-based alloys composed of ultrafine grain-structure. *Journal of Applied Physics*. 1988 Nov 15;64(10):6047–9.
7. Yoshizawa Y, Yamauchi K. Effects of magnetic-field annealing on magnetic properties in ultrafine crystalline Fe-Cu-Nb-Si-B alloys. *IEEE Transactions on Magnetics*. 1989 Sep;25(5):3324–6.
8. Herzer G. Nanocrystalline soft magnetic materials. *Journal of Magnetism and Magnetic Materials*. 1992 Jul;112(1–3):258–62.
9. Herzer G. Grain-size dependence of coercivity and permeability in nanocrystalline ferromagnets. *IEEE Transactions on Magnetics*. 1990 Sep;26(5):1397–402.
10. Yoshizawa Y, Oguma S, Yamauchi K. New Fe-based soft magnetic-alloys composed of ultrafine grain-structure. *Journal of Applied Physics*. 1988 Nov 15;64(10):6044–6.
11. Suzuki K, Kikuchi M, Makino A, Inoue A, Masumoto T. Changes in microstructure and soft magnetic-properties of an Fe₈₆Zr₇B₆Cu₁ amorphous alloy upon crystallization. *Materials Transactions JIM*. 1991 Oct;32(10):961–8.
12. Iwanabe H, Lu B, McHenry ME, Laughlin DE. Thermal stability of the nanocrystalline Fe-Co-Hf-B-Cu alloy. *Journal of Applied Physics*. 1999 Apr 15;85(8):4424–6.
13. Willard MA, Laughlin DE, McHenry ME, Thoma D, Sickafus K, Cross JO, et al. Structure and magnetic properties of (Fe_{0.5}Co_{0.5})₈₈Zr₇B₄Cu₁ nanocrystalline alloys. *Journal of Applied Physics*. 1998 Dec 15;84(12):6773–7.
14. Swaminathan R, Willard MA, McHenry ME. Experimental observations and nucleation and growth theory of polyhedral magnetic ferrite nanoparticles synthesized using an RF plasma torch. *Acta Materialia*. 2006;54:807–16.
15. Matsushita N, Chong CP, Mizutani T, Abe M. Ni-Zn ferrite with high permeability ($\mu' \sim 30$, $\mu'' \sim 30$) at 1 GHz prepared at 90°C. *Journal of Applied Physics*. 2002;91(10):7376–8.
16. Kataoka N, Shima T, Fujimori H. High-frequency permeability of nanocrystalline Fe-Cu-Nb-Si-B single and multilayer films. *Journal of Applied Physics*. 1991;70(10):6238–40.
17. Osaka T, Takai M, Hayashi K, Ohashi K, Saito M, Yamada K. A soft magnetic CoNiFe film with high saturation magnetic flux density and low coercivity. *Nature*. 1998;392:796–8.
18. Joshi SD, Yoon SD, Yang A, Vittoria C, Harris VG, Goswami R, et al. Structure and magnetism of pulsed laser deposited (Ni₅₉Co₂₂Fe₇)₈₈Zr₇B₄Cu_x (x=0,1) thin films. *Journal of Applied Physics*. 2006;99(8):08F115.

19. Turgut Z, Scott JH, Huang MQ, Majetich SA, McHenry ME. Magnetic properties and ordering in C-coated $\text{Fe}_x\text{Co}_{1-x}$ alloy nanocrystals. *Journal of Applied Physics*. 1998;83(11):6468–70.
20. Kuhrt C, Schultz L. Formation and magnetic properties of nanocrystalline mechanically alloyed Fe-Co. *Journal of Applied Physics*. 1992;71(4):1896–900.
21. McCaig M, Clegg AG. *Permanent Magnets in Theory and Practice*, 2nd ed. New York: John Wiley & Sons, 1987.
22. Willard MA. *Structural and magnetic characterization of HITPERM soft magnetic materials for high temperature applications*. Pittsburgh: Carnegie Mellon University, 2000.
23. Ayers JD, Harris VG, Sprague JA, Elam WT, Jones HN. On the formation of nanocrystals in the soft magnetic alloy $\text{Fe}_{73.5}\text{Nb}_3\text{Cu}_1\text{Si}_{13.5}\text{B}_9$. *Acta Materialia*. 1998 Mar 23;46(6):1861–74.
24. Hono K, Ping DH, Ohnuma M, Onodera H. Cu clustering and Si partitioning in the early crystallization stage of an $\text{Fe}_{73.5}\text{Si}_{13.5}\text{Nb}_3\text{Cu}_1$ amorphous alloy. *Acta Materialia*. 1999 Feb;47(3):997–1006.
25. Massalski TB, ed. *Binary Alloy Phase Diagrams*, 2nd ed. Materials Park, OH: ASM International, 1990.
26. Herzer G. Soft-magnetic nanocrystalline materials. *Scripta Metallurgica Et Materialia*. 1995 Dec 1;33(10–11):1741–56.
27. Yoshizawa Y, Yamauchi K. Fe-based soft magnetic-alloys composed of ultrafine grain-structure. *Materials Transactions JIM*. 1990 Apr;31(4):307–14.
28. Hono K, Zhang Y, Inoue A, Sakurai T. APFIM studies on nanocrystallization of amorphous alloys. *Materials Science and Engineering a-Structural Materials Properties Microstructure and Processing*. 1997 Jun 15;226:498–502.
29. Ping DH, Wu YQ, Hono K, Willard MA, McHenry ME, Laughlin DE. Microstructural characterization of $(\text{Fe}_{0.5}\text{Co}_{0.5})_{88}\text{Zr}_7\text{B}_4\text{Cu}_1$ nanocrystalline alloys. *Scripta Materialia*. 2001 Oct 10;45(7):781–6.
30. Willard MA, Claassen JC, Stroud RM, Francavilla TL, Harris VG. (Ni,Fe,Co)-based nanocrystalline soft magnets with near-zero magnetostriction. *IEEE Transactions on Magnetics*. 2002 Sep;38(5):3045–50.
31. Daniil M, Willard MA. Structure and magnetic properties of CoFeZrMBCu soft nanocrystalline alloys. *Journal of Applied Physics*. 2008;103:07E727.
32. Herzer G. Magnetic-field-induced anisotropy in nanocrystalline Fe-Cu-Nb-Si-B alloys. *Materials Science and Engineering a-Structural Materials Properties Microstructure and Processing*. 1994 May 15;182:876–9.
33. Alves F, Desmoulins JB, Herisson D, Rialland JF, Costa F. Stress-induced anisotropy in Finemet- and Nanoperm-type nanocrystalline alloys using flash annealing. *Journal of Magnetism and Magnetic Materials*. 2000 Jun;215:387–90.
34. Lachowicz HK, Neuweiler A, Poplawski F, Dynowska E. On the origin of stress-anneal-induced anisotropy in FINEMET-type nanocrystalline magnets. *Journal of Magnetism and Magnetic Materials*. 1997 Sep;173(3):287–94.
35. Nielsen OV, Petersen JR, Herzer G. Temperature-dependence of the magnetostriction and the induced anisotropy in nanocrystalline FeCuNbSiB alloys, and their fluxgate properties. *IEEE Transactions on Magnetics*. 1994 Mar;30(2):1042–4.
36. Hofmann B, Kronmuller H. Stress-induced magnetic anisotropy in nanocrystalline FeCuNb-SiB alloy. *Journal of Magnetism and Magnetic Materials*. 1996 Jan;152(1–2):91–8.
37. Ferrara E, De Luigi C, Beatrice C, Appino C, Fiorillo F. Energy loss vs. magnetizing frequency in field-annealed nanocrystalline alloys. *Journal of Magnetism and Magnetic Materials*. 2000 Jun;215:466–8.
38. Suzuki K, Cadogan JM. Random magnetocrystalline anisotropy in two-phase nanocrystalline systems. *Physical Review B*. 1998 Aug 1;58(5):2730–9.
39. Hernando A, Marin P, Vazquez M, Barandiaran JM, Herzer G. Thermal dependence of coercivity in soft magnetic nanocrystals. *Physical Review B*. 1998 Jul 1;58(1):366–70.
40. Herzer G. Grain-structure and magnetism of nanocrystalline ferromagnets. *IEEE Transactions on Magnetics*. 1989 Sep;25(5):3327–9.

41. Yoshizawa Y, Ogawa Y. Magnetic properties of high B-s nanocrystalline FeCoCuNbSiB alloys. *IEEE Transactions on Magnetics*. 2005 Oct;41(10):3271–3.
42. Yoshizawa Y, Fujii S, Ping DH, Ohnuma M, Hono K. Magnetic properties of nanocrystalline Fe-Co-Cu-M-Si-B alloys (M: Nb, Zr). *Materials Science and Engineering a-Structural Materials Properties Microstructure and Processing*. 2004 Jul 15;375–77:207–12.
43. Ohnuma M, Ping DH, Abe T, Onodera H, Hono K, Yoshizawa Y. Optimization of the microstructure and properties of Co-substituted Fe-Si-B-Nb-Cu nanocrystalline soft magnetic alloys. *Journal of Applied Physics*. 2003 Jun 1;93(11):9186–94.
44. Inoue A, Shen BL. Soft magnetic properties of nanocrystalline Fe-Co-B-Si-Nb-Cu alloys in ribbon and bulk forms. *Journal of Materials Research*. 2003 Dec;18(12):2799–806.
45. Chau N, Luong NH, Chien NX, Thanh PQ, Vu LV. Influence of P substitution for B on the structure and properties of nanocrystalline Fe_{73.5}Si_{15.5}Nb₃Cu₁B_{7-x}P_x alloys. *Physica B-Condensed Matter*. 2003 Apr;327(2–4):241–3.
46. Mattern N, Muller M, Stiller C, Danzig A. Short-range structure of amorphous and nanocrystalline Fe-Si-B-Cu-Nb alloys. *Materials Science and Engineering a-Structural Materials Properties Microstructure and Processing*. 1994 May 1;179:473–8.
47. Muller M, Grahl H, Mattern N, Kuhn U, Schnell B. The influence of Co on the structure and magnetic properties of nanocrystalline FeSiB-CuNb and FeZrBCu-based alloys. *Journal of Magnetism and Magnetic Materials*. 1996 Jul;160:284–6.
48. Gercsi Z, Mazaleyrat F, Varga LK. High-temperature soft magnetic properties of Co-doped nanocrystalline alloys. *Journal of Magnetism and Magnetic Materials*. 2006 Jul;302(2):454–8.
49. Barandiaran JM, Barquin LF, Sal JCG, Gorria P, Hernando A. Resistivity changes of some amorphous-alloys undergoing nanocrystallization. *Solid State Communications*. 1993 Oct;88(1):75–80.
50. Chau N, Chien N, Hoa NQ, Niem PQ, Luong NH, Tho ND, et al. Investigation of nanocomposite materials with ultrasound and high performance hard magnetic properties. *Journal of Magnetism and Magnetic Materials*. 2004 Nov;282:174–9.
51. Gomez-Polo C, Perez-Landazabal JI, Recarte V. Temperature dependence of magnetic properties in Fe-Co and Fe-Cr base nanocrystalline alloys. *IEEE Transactions on Magnetics*. 2003 Sep;39(5):3019–24.
52. Blazquez JS, Borrego JM, Conde CF, Conde A, Greneche JM. On the effects of partial substitution of Co for Fe in FINEMET and Nb-containing HITPERM alloys. *Journal of Physics-Condensed Matter*. 2003 Jun 18;15(23):3957–68.
53. Mazaleyrat F, Gercsi Z, Ferenc J, Kulik T, Varga LK. Magnetic properties at elevated temperatures of Co substituted Finemet alloys. *Materials Science and Engineering a-Structural Materials Properties Microstructure and Processing*. 2004 Jul 15;375–77:1110–5.
54. Butvinova B, Butvin P, Schafer R. Influence of heterogeneity on magnetic response of nanocrystalline ribbons. *Sensors and Actuators a-Physical*. 2003 Sep;106(1–3):52–5.
55. Todd I, Tate BJ, Davies HA, Gibbs MRJ, Kendall D, Major RV. Magnetic properties of ultrasoft-nanocomposite FeAlSiBNbCu alloys. *Journal of Magnetism and Magnetic Materials*. 2000 Jun;215:272–5.
56. Flohrer S, Schafer R, McCord J, Roth S, Schultz L, Herzer G. Magnetization loss and domain refinement in nanocrystalline tape wound cores. *Acta Materialia*. 2006 Jul;54(12):3253–9.
57. Available from: www.metglas.com
58. Yoshizawa Y, Yamauchi K. Magnetic properties of ultrafine crystalline (Fe-Cu1-Nb3)-Si-B quasi-ternary alloys and improvement of their magnetic properties by magnetic field annealing. *Journal of the Magnetics Society of Japan*. 1989;13:231–6.
59. Hasiak M, Ciurzynska WH, Yamshiro Y, Fukunaga H, Yamamoto KI. Microstructure and magnetic properties of Fe_{86-x}Co_xZr₆B₈ alloys. *IEEE Transactions on Magnetics*. 2001 Jul;37(4):2271–4.
60. Shen BL, Kimura H, Inoue A. Structure and magnetic properties of Fe_{42.5}Co_{42.5}Nb₇B₈ nanocrystalline alloy. *Materials Transactions*. 2002 Mar;43(3):589–92.

61. Suzuki D, Yokosawa K, Miyashita T, Kandori A, Tsukada K, Tsukamoto A, et al. Simplified magnetically shielded cylinder using flexible magnetic sheets for high-T_c superconducting quantum interference device cardiogram systems. *Japanese Journal of Applied Physics Part 2-Letters*. 2001 1 Oct;40(10A):L1026–8.
62. Willard MA, Harris VG. Nanocrystalline inductor materials for power electronics applications. *Passive Component Industry*. July/August 2005;6–12.
63. Ohodnicki PR, Park SY, Laughlin DE, McHenry ME, Keylin V, Willard MA. Crystallization and thermomagnetic treatment of a Co-rich Co-Fe-Ni-Zr-B-Cu based nanocomposite alloy. *Journal of Applied Physics*. 2008;(in press).
64. Suzuki K, Makino A, Inoue A, Masumoto T. Soft magnetic-properties of nanocrystalline Bcc Fe-Zr-B and Fe-M-B-Cu (M = Transition-Metal) alloys with high saturation magnetization (invited). *Journal of Applied Physics*. 1991 Nov 15;70(10):6232–7.
65. Johnson F, Garmestani H, Chu SY, McHenry ME, Laughlin DE. Induced anisotropy in FeCo-based nanocrystalline ferromagnetic alloys (HITPERM) by very high field annealing. *IEEE Transactions on Magnetics*. 2004 Jul;40(4):2697–9.
66. Herzer G. Magnetization process in nanocrystalline ferromagnets. *Materials Science and Engineering a-Structural Materials Properties Microstructure and Processing*. 1991 Mar 15;133:1–5.
67. Skorvanek I, OHandley RC. Fine-particle magnetism in nanocrystalline Fe-Cu-Nb-Si-B at elevated-temperatures. *Journal of Magnetism and Magnetic Materials*. 1995 Feb;140:467–8.
68. Hasegawa R. Applications of amorphous magnetic alloys. *Materials Science & Engineering A*. 2004;375–377:90–7.
69. Watanabe K, Kashiwagi M, Kawashima S, Ono Y, Yamashita Y, Yamazaki C, et al. Development of a dc 1 MV power supply technology for NB injectors. *Nuclear Fusion*. 2006 Jun;46(6):S332–9.
70. Naitoh Y, Bitoh T, Hatanai T, Makino A, Inoue A, Masumoto T. Development of common mode choke coil made of new nanocrystalline soft magnetic alloy "NANOPERM(R)". *Science Reports of the Research Institutes Tohoku University Series A-Physics Chemistry and Metallurgy*. 1997 Mar;43(2):161–5.
71. Naitoh Y, Bitoh T, Hatanai T, Makino A, Inoue A. Application of nanocrystalline soft magnetic Fe-M-B (M=Zr, Nb) alloys to choke coils. *Journal of Applied Physics*. 1998 Jun 1;83(11):6332–4.
72. Naitoh Y, Bitoh T, Hatanai T, Makino A, Inoue A, Masumoto T. Applications of nanocrystalline soft magnetic Fe-M-B (M = Zr, Nb) alloys. *Nanostructured Materials*. 1997 Dec;8(8):987–95.
73. Kim GH, Noh TH, Choi GB, Kim KY. Magnetic properties of FeCuNbSiB nanocrystalline alloy powder cores using ball-milled powder. *Journal of Applied Physics*. 2003 May;93(10):7211–3.
74. Ong KG, Grinmes DM, Grimes CA. Higher-order harmonics of a magnetically soft sensor: Application to remote query temperature measurement. *Applied Physics Letters*. 2002;80(20):3856–8.

Chapter 14

Magnetic Shape Memory Phenomena

Oleg Heczko, Nils Scheerbaum, and Oliver Gutfleisch

Abstract Giant magnetically induced strain up to 50 times larger compared to the strain of giant magnetostriction was observed in some Heusler alloys, particularly in Ni–Mn–Ga. In analogy with the shape memory phenomenon this effect was called magnetic shape memory effect. The effect includes two different phenomena: a magnetically induced structural phase transformation (usually a martensitic transformation) and a magnetically induced structural reorientation occurring in the martensitic phase. Transformation behavior, structure of the martensite, and phenomenology of the magnetically induced reorientation are described. The description is based mainly on the well-studied compound Ni–Mn–Ga.

14.1 Introduction

Smart materials combine sensors, intelligence, and actuators to allow a material to respond to its environment [1]. Magnetic shape memory (MSM) materials can be used as both sensors and actuators in such materials. The observed large magnitude of up to 11% magnetically induced strain in MSM materials has generated an intensive interest in the material research community [2].

The history of the effect starts with a publication by K. Ullakko et al. in 1996 describing 0.2% deformation of a Ni₂MnGa single crystal in a field of 1 T [3]. The underlying mechanism of the field-induced deformation was described there and was also patented. However, after initial optimism it appeared difficult to explore the effect in applications. The main obstacle was the availability of well-defined single crystalline materials. The key MSM properties of a single crystal depend very strongly on composition, structure, defects, and therefore on the preparation conditions. Many properties seemed to be sample dependent, thus the basic under-

O. Heczko (✉)
Institute of Physics, Academy of Sciences, Czech Republic Na Slovance 2,
CZ-182 21 Praha 8, Czech Rep.
e-mail: heczko@fzu.cz

standing of the material properties has been progressing slowly and there are conflicting reports.

We will concentrate on the basic phenomenology of the MSM effect and use a simple model based on total energy. Despite the relatively simple approach, the model allows to describe and to predict basic properties of MSM materials correctly. The model is based and tested on the Ni–Mn–Ga compounds. The testing of the model for other compounds, however, has yet to be done. But it is assumed that the specific knowledge obtained from the Ni–Mn–Ga system can be applied to other compounds too. We will skip any atomic and thermodynamical models of martensitic transformation, which can be found in other reviews.

Perhaps due to the novelty of the phenomena and the different points of view of researchers involved, the terminology of the effect is far from being settled. The effect is often called magnetic shape memory (MSM) effect [3–5], magnetic field-induced strain (MFIS) [6], magnetoplasticity [7], giant magnetostriction [8], or effect in ferromagnetic shape memory alloys [9–11].

All these names are somehow inaccurate and ambiguous. MFIS can be considered as a general term describing any deformation in a magnetic field. Magnetostriction by definition refers to a different effect although one of the first surveys on the magnetic shape memory effect is presented under the label “giant magnetostrictive materials” [8]. The term magnetoplasticity suggests some irreversible changes of the structure (as slip), which is not exactly true for this effect. Some ferromagnetic shape memory alloys (FSMA) show the MSM effect; however, the effect is not limited to ferromagnets, as it was observed also in antiferromagnetic [12] and paramagnetic [13] materials.

We will use the term magnetically induced reorientation (MIR) to describe the microstructure reorientation (without structural changes) taking place via magnetically induced twin boundary motion. The magnetic field-induced structural transformation will be referred to as magnetically induced martensite (MIM) and magnetically induced austenite (MIA) depending on which phase is stabilized in the field. Magnetic shape memory (MSM) effect then includes these two effects, MIR and MIM/MIA, which both macroscopically can show large strain in magnetic fields. Our focus will be on the Ni–Mn–Ga system as a prototypical MSM material.

The potential of MIR was recognized straight from the first publications [2, 14]. It is expected that the material can be used in

- Actuating (large field-induced deformation)
- Vibration damping (energy absorption, variable stiffness)
- Sensing (magnetization changes during mechanical deformation)
- Energy harvesting (converting mechanical vibration to electrical energy)

Compared with other active materials as piezoelectric and magnetostrictive materials, MSM materials have similar work output per mass. The piezoelectric and magnetostrictive effects can work in high frequencies but show only low strains (order of 0.1%). MIR on the other hand can work in medium frequencies with relatively

low loads but results in large strains (order of 1–10%). The thermal shape memory materials can deliver very high work output compared to all active materials due to the high stress and strain but at very low frequencies as they are thermally driven.

14.2 Martensitic Transformation and Twinning

Fundamental to the MSM phenomena is the occurrence of a thermoelastic martensitic transformation. A martensitic transformation is a structural phase transformation of the diffusionless and cooperative type, where the rearrangement of atoms occurs with relatively small displacements compared to interatomic distances. There is a rigorous crystallographic connection between the lattices of the initial and final phases. The transformation is of the first order. The martensitic transformation is called thermoelastic, when it is thermally reversible.

During martensitic transformation, the high-temperature phase (usually with high symmetry, e.g., cubic), called austenite, transforms to the low-temperature phase (usually with lower symmetry, e.g., tetragonal), called martensite. As it is a first-order structural phase transformation, the high-temperature austenite and the low-temperature martensitic phases coexist in a specific temperature range. This is due to the elastic strains that accompany the nucleation and growth of the martensitic or austenitic phase. The austenite–martensite phase boundaries are fully or partially coherent. The elastic strains due to the martensitic transformation increase with increasing martensite fraction. To compensate the transformation strains, different crystallographic domains (twin variants) are formed within the martensite [15–18]. Macroscopically, they are often visible as parallel bands on the sample surface.

The simplest martensitic transformation is from the cubic austenite to the tetragonal martensitic phase. It results in three martensitic twin variants with different *c*-axis orientation. The volume of the Bravais cell is (nearly) conserved. The transformation strain is described by transformation matrices which depend on lattice constants [17]. They have only diagonal components proportional to a/a_0 and c/a_0 . Here *a* and *c* are the lattice constants of the tetragonal martensite and a_0 is the lattice constant of the cubic austenite, respectively.

A martensitic transformation in two dimensions is schematically depicted in Fig. 14.1. The tetragonal distortions of the cubic lattice occur with the same probability along each of the crystallographic equivalent axes $\langle 100 \rangle$, if there are no additional constraints favoring a single orientation. Therefore, equal amounts of these three differently oriented twin variants appear in the sample and are connected by twin boundaries.

Several alloy systems undergo such a martensitic transformation, like BaTiO₃, Fe–Ni–C, Fe–Pd, In–Tl, Ni–Al, Ni–Mn, or Ni–Mn–Ga. The most important cubic-to-tetragonal martensitic transformation occurs in steels (Fe–C) and the terms austenite and martensite originate from here. This transformation, however, is not thermoelastic [19].

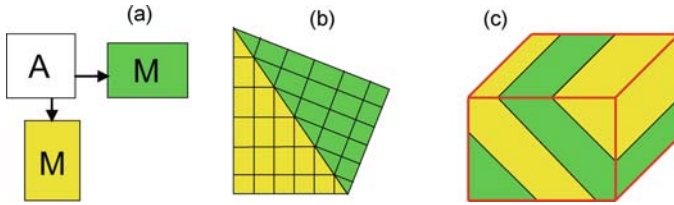


Fig. 14.1 Schematics in 2D of the cubic-to-tetragonal martensitic transformation. (a) Two different tetragonal twin variants (martensite-M) originate from cubic austenite (A), (b) twinned microstructure formed from two twin variants connected by one twin boundary, and (c) 3D sample containing two martensitic twin variants

At an atomic level, two twin variants connected with a twin boundary are depicted in Fig. 14.2. The twin structure is created by a simple shear of one part of the crystal along the shear plane. For a coherent twin boundary, the twin boundary plane is a mirror plane between the adjacent variants.

The martensitic transformations can be detected by many different methods, e.g., by calorimetry (DSC), by the resistivity changes, or in the case of magnetic materials by the change of magnetic properties (Fig. 14.3). The increase of resistivity during the transformation from austenite to martensite is ascribed to the existence of twin boundaries in the martensite or/and to the Jahn–Teller effect [20]. Thanks to different magnetocrystalline anisotropies of martensite and austenite, magnetic susceptibility can be used to detect the martensitic transformation temperatures [15]. Differential scanning calorimetry (DSC) is a usual detection method for phase transformations. As the transformation is of first order it is revealed by peaks in the heating and cooling curves.

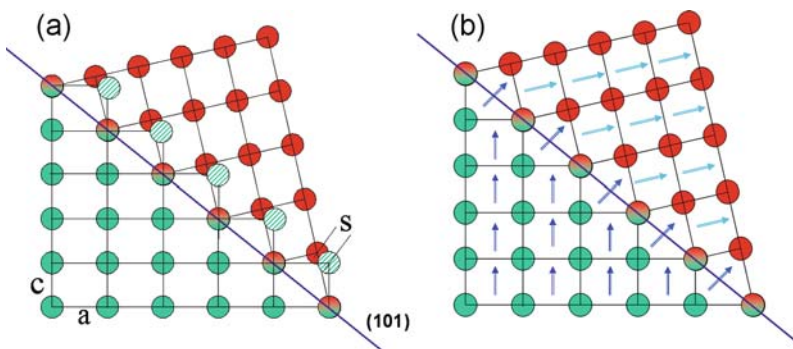


Fig. 14.2 Schematics of twinning in 2D. (a) The magnitude of twin shear is denoted s and the direction of twin shear is parallel to the twin plane (101). Here, $c/a = 0.8$ is used for the sake of visibility. (b) Direction of magnetic moments in adjacent twin variants. The easy axis of magnetization corresponds to the short crystallographic axis. In reality, the rotation of magnetic moments is gradual across the twin boundary creating a 90° magnetic domain wall

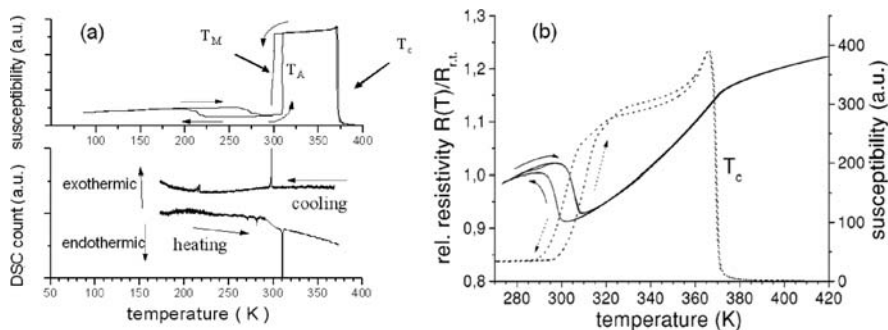


Fig. 14.3 Transformation behavior of a Ni–Mn–Ga compound. (a) Magnetic susceptibility and DSC indicate the transformations in a single crystal (T_M : austenite to martensite; T_A : martensite to austenite; T_c : Curie temperature) [21]. (b) Magnetic susceptibility (*dotted*) and resistivity (*solid*) for polycrystalline ribbons [22]. (Reprinted with permission of IEEE Transactions on Magnetics)

14.3 Modes of Magnetic Field-Induced Strain

Any shape changes of a material in a magnetic field can be called magnetic field-induced strain (MFIS). The term, however, is often used in a narrow sense to describe the strain in magnetic shape memory alloys. Here, we will use it as a general term for any field-induced strain, whatever the physical origin. In an applied magnetic field, the material either shrinks or expands and can therefore produce external work. In the following we shortly discuss magnetostriction and the effect of magnetic field-induced structural phase transformation. The rest of the chapter will then be devoted to magnetic field-induced reorientation (MIR) of microstructure.

14.3.1 Magnetostriction

The broad definition of magnetostriction is the change in any dimension of a magnetic material caused by a change in its magnetic state. In that sense, this definition includes all MFIS-generating effects. However, magnetostriction is not accompanied by either structural or microstructural changes, only the material's magnetic state is changed. Any observed hysteresis is due to magnetic hysteresis. The change in linear dimension parallel to an applied magnetic field with volume conservation is called Joule magnetostriction [23, 24].

The magnetostrictive strain originates from the rotation of atomic magnetic moment in a magnetic field without changing crystallographic orientation or structure. When the sample is magnetically saturated, all magnetic moments lie in field direction and magnetostriction reaches the maximum value (saturation magnetostriction). In contrast to MIR, a small magnetic anisotropy is desirable for magnetostriction as it allows magnetization rotation in low fields. Magnetostriction is

well known and strains in order of 100 ppm are observed in usual ferromagnetic materials and up to 0.2% in giant magnetostrictive materials at room temperature.

14.3.2 Magnetic Field-Induced Phase Transformation

MFIS can also be caused by a structural phase transformation, which is initiated by an applied magnetic field. The transformation is driven by the difference in magnetic energy of both phases (in saturation equal to the Zeeman energy difference $-MH$) [15, 16]. The phase with the higher saturation magnetization is stabilized in the magnetic field H , resulting in a shift of the phase transformation temperature, T_M . The shift is described by the Clausius–Clapeyron equation as

$$dH/dT = -Q/(T_M \Delta M), \quad (14.1)$$

where Q is the latent heat of enthalpy of transformation and ΔM is the change in saturation magnetization during transformation. If Q is small compared to ΔM , the shift in transformation temperature can be rather pronounced [15, 16, 27].

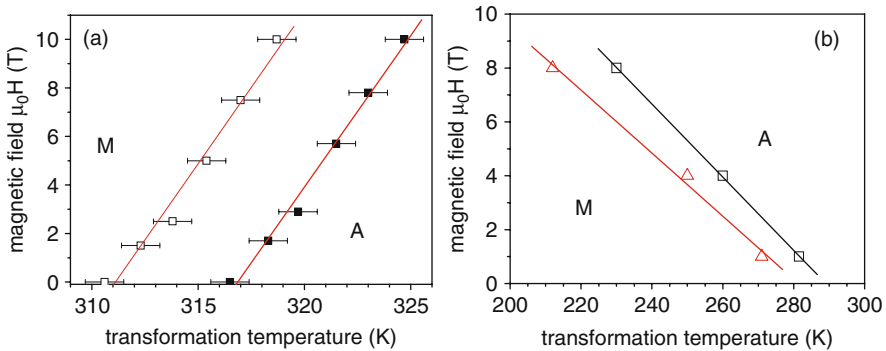


Fig. 14.4 Phase diagram of magnetically induced transformation. Letters A and M mark austenite and martensite, respectively. (a) In the case with a high magnetization of the low-temperature phase ($\text{Ni}_{53.8}\text{Mn}_{20.2}\text{Fe}_1\text{Ga}_{25}$), T_M is shifted to higher temperatures with increasing field [26]. (Reprinted with permission of Physics Letters A.) (b) In the case with high magnetization of the high-temperature parent phase ($\text{Ni}_{45}\text{Mn}_{36.6}\text{Co}_5\text{In}_{13.4}$), T_M is shifted to lower temperatures with increasing fields

From the experimentally obtained phase diagrams in Fig. 14.4, it is apparent that the application of a field at a constant temperature close to the transformation temperature can lead to transformation from the phase with low magnetic moment to the phase with high magnetic moment. The structural transformation results in strain, due to the different lattice constants of the phases.

In Ni–Mn–Ga–Fe [16, 26], the magnetization of the tetragonal martensite is higher than that of the cubic austenite, the martensite can be induced by an applied magnetic field (magnetically induced martensite: MIM). The maximum theoretical strain ε_0 is given by the difference in lattice constants of austenite (A) and martensite (M) as $\varepsilon_0 = (a_A - c_M)/a_A$.

Recently, a magnetically induced transformation was reported in Ni–Mn–In. Here, the cubic austenite is ferromagnetic and has high magnetization [25, 27]. The martensite on the other hand has a very low magnetization. The application of a magnetic field stabilizes the austenite, and the martensitic transformation is shifted to lower temperature. This is formally close to the thermal shape memory behavior. Twinned martensite can be easily deformed by external stress via twin redistribution. Due to the application of a magnetic field the material undergoes a magnetically induced austenitic transformation and shape recovery occurs. As the previous deformation by twin boundary motion is deleted, the material assumes the original shape. In contrast to thermal shape memory materials this occurs at a constant temperature.

In general, the transformation can be induced in any temperature, as long as the magnetic field is high enough. Practically, as the field is limited, the necessary conditions for the effect are a reversible martensitic transformation with a small hysteresis, and a large difference of magnetization between both phases.

14.4 Magnetically Induced Structure Reorientation

In contrast to the magnetically induced structural phase transformation, the magnetic field-induced structure reorientation or shortly magnetically induced reorientation (MIR) occurs in one phase, without any structural phase transformation. Thus, there is no latent or transformation heat or change of order parameters. MIR usually takes place via twin boundary motion. On the microscopic scale, twin boundary motion results in change of the crystal orientation. As the structural unit cell is of low symmetry, structure reorientation may lead to change of dimensions, to strain. MIR is accompanied by a change in the magnetic behavior, which is reflected in the magnetization curve.

The magnetization loop during microstructure reorientation and the accompanied strain of a single crystal exhibiting MIR are shown in Fig. 14.5. Initially, the single crystal magnetization vector \mathbf{M} is perpendicular to the magnetic field \mathbf{H} . The applied field gradually rotates the magnetization from the easy magnetization axis to the field direction. When the energy needed for the rotation exceeds the energy needed for MIR, the microstructure changes by nucleation and growth of those twin variants, having the smallest angle between their magnetic easy axis and the applied field direction. The growth occurs due to twin boundary motion. This results in a macroscopic strain. The onset of reorientation is indicated by a steep increase in the magnetization. This sharp increase of magnetization is superficially similar to a metamagnetic transition. However, in metamagnetic transition no microstructural changes are observed.

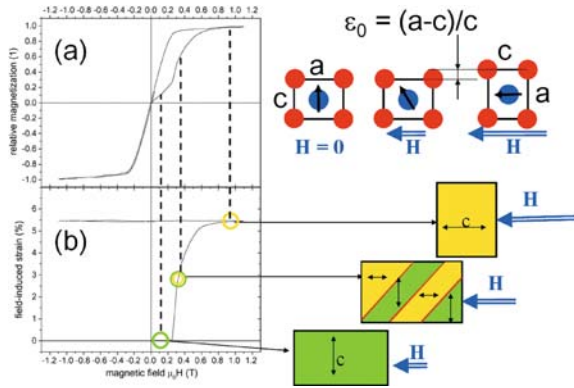


Fig. 14.5 Magnetically induced reorientation (MIR) in a Ni_2MnGa single crystal. (a) Magnetization loop. Initially, the c -axis of the unit cell is oriented perpendicular to the magnetic field $\mu_0 H$. Magnetic moment is marked by *arrows* inside unit cells. Magnetization rotation occurs in low fields only. Due to twin boundary motion, reorientation of the unit cell takes place and the c -axis changes to the field direction. The difference between the lattice constants gives the maximum strain ε_0 . (b) Simultaneously measured magnetically induced strain. The redistribution of twin variants with increasing magnetic field and the resulting shape changes are sketched

The increasing field leads to further reorientation of other parts of the crystal and to magnetization rotation, where MIR is not occurring. When the applied field exceeds the anisotropy field, the magnetization is completely aligned with the field direction and magnetic saturation is reached. When saturation is reached, increasing the field further will not result in an increase of driving force for MIR. Thus, increasing the field will not increase the strain. This is similar to magnetostriction, which is constant above the saturation field. Due to structure reorientation the maximum theoretical strain during MIR, ε_0 , is determined by the difference of lattice constants of the non-cubic martensite as $\varepsilon_0 = a/c - 1$.

If no restoring force acts on the crystal it stays in the reoriented state. Measuring the magnetization loop a second time in the same direction produces a square-like loop, as the easy axis lies already in field direction. MIR results in a hysteresis in the first loop and first quadrant only. The area between initial and return curves denotes the energy consumed during the reorientation. This hysteresis is an important but not sufficient indication for MIR. This kind of loop can also originate from exchange anisotropy, anisotropic elastic coupling, or particular domain structures. Therefore, an independent confirmation of microstructure changes is needed.

The main focus in studying MIR is on the actuation properties, i.e., magnetically induced strain as a function of field H at a constant external stress σ_{ext} . [3–7]. But there is also the complementary effect, which can be called magnetic field-induced (pseudo)superelasticity [28–30]. Here, reorientation and therefore magnetization and strain are changed as a function of the external stress σ_{ext} , at constant magnetic field H . The experimental observations of magnetization and strain changes are shown in Fig. 14.6.

Full macroscopic description of MIR can be given by strain

$$\varepsilon = \varepsilon(H, \sigma_{\text{ext}}, T) \quad (14.2)$$

and magnetization

$$M = M(H, \sigma_{\text{ext}}, T) \quad (14.3)$$

as a function of the compressive stress σ_{ext} , the applied magnetic field H , and the temperature T . The simultaneous measurements of strain and magnetization give a complete characterization of the effect [28, 29].

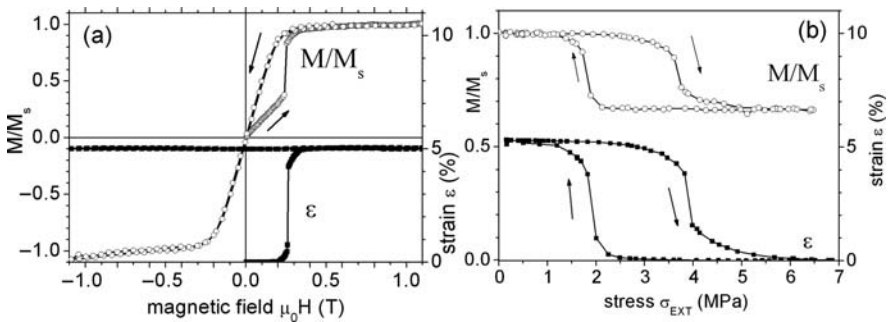


Fig. 14.6 MIR in Ni–Mn–Ga. (a) Magnetically induced strain and (b) magnetically induced superelasticity in $\mu_0 H = 1\text{T}$. Simultaneous measurement of strain and magnetization is shown [28]. (Reprinted with permission of Journal of Magnetism and Magnetic Materials)

There are two basic requirements for the existence of MIR. The magnetization vector should be strongly bound to one preferential crystallographic direction or plane, i.e., the magnetic anisotropy should be large. However, the most demanding requirement is the existence of highly mobile twin boundaries. The magnetic anisotropy can be determined from the magnetization curve and the twin boundary mobility can be measured as the twinning (detwinning) stress in mechanical stress–strain curves. Additionally, in order to have MIR in reasonable low fields, the saturation magnetization should be high. A more quantitative estimation will be given later in the frame of a simple energy model.

MIR was observed in many ferromagnetic materials. An analog structure reorientation by twin boundary motion, but driven by an electric field, was observed in ferroelectric martensites [31]. The effect is called electro-shape memory effect. There is an attempt to build a unified theory of these two effects [32].

Concerning MIR in ferromagnetic materials, probably the first observation of MIR was published in the 1960s when large field-induced strain was observed in Dy and Tb [33, 35]. A strain of several percent was observed in temperatures close to absolute zero in very high fields up to 30 T. The observed change in the

magnetization loop and the existence of a twin structure are in agreement with today's knowledge of MIR. The reorientation occurs in such high fields thanks to a very high magnetic anisotropy of the rare earths. From optical observation it was concluded that the observed strain is due to twin variant redistribution but was not studied further [33]. In that time the effect was not recognized as such and it served as an interesting but exotic case of magnetic behavior. The effect was somehow also confused with magnetostriction.

In 1996, Ullakko et al. [3] published the first account on the field-induced strain of about 0.2% in a Ni–Mn–Ga single crystal and described the mechanism of martensitic structure reorientation by twin boundary motion. Later, MIR strains of 6% in 5 M [4, 9] and of 10% in 7 M [5, 34] martensite were observed in Ni–Mn–Ga single crystals. Shortly after the discovery in Ni–Mn–Ga, MIR was also observed in Fe–Pd and Fe–Pt at low temperatures [11, 36, 37] as well as in anti-ferromagnetic materials [12]. Also some previous observations on metamagnetic transitions in CuCo_2 , which were called Ising axis changes, were relabeled to MIR [13].

Many other materials are labeled as promising to show large MFIS and are derived from the generic Ni–Mn–Ga system, like the Heusler alloys Co–Fe–Ga and Ni–Fe–Ga [38–45]. However, the large strain observed in many of these alloy systems is due to MIM or MIA, and not MIR. Often, large MIR strains are demonstrated in stress-assisted experiments, which correspond to only a fraction of percent MIR strain without the stress assistance (only the free strain is interesting for application). To date the most intensively studied alloy system is Ni–Mn–Ga to which we will devote the rest of the chapter.

14.5 The Ni–Mn–Ga System

14.5.1 Compositional Dependence of Structure and Transformation

The Ni–Mn–Ga alloys belong to the class of Heusler alloys [46] which are ternary, intermetallic compounds of the type X_2YZ with a L_{21} atomic order [47]. Ni–Mn–Ga solidifies from the melt into the $\text{B}2'$ structure at about 1100°C . Below the ordering temperature of about $750\text{--}800^\circ\text{C}$, the Heusler phase with L_{21} long range order is formed [48]. Therefore, the atomic order of the compound is affected by the heat treatment and quenching rate [47–49]. In non-stoichiometric alloys (deviation from Ni_2MnGa), the excess atoms do not occupy arbitrary empty positions but a complex redistribution of atoms takes place [50, 51]. The Ni–Mn–Ga compounds are rich in different martensites and the transformation path is strongly dependent on chemical composition, atomic order, and possibly also on the thermo-mechanical history of the specimens [52, 53]. The martensitic transformation behavior has been described by a thermodynamical theory, which is based on the Landau theory of phase transformation [15, 16].

There is a very strong and complex dependence of the transformation temperatures on the composition [16, 54]. As a general tendency, the martensitic transformation temperature increases with increasing the Ni content from about 200 K for 50 at.% Ni to 330 K for 55 at.% Ni. In the high-temperature region, it merges with the ferromagnetic–paramagnetic transition, the Curie temperature T_c . Further increase of the Ni content increases the martensitic transformation above T_c and the structural transformation occurs in the paramagnetic state. T_c is only weakly dependent on the Ni content and decreases with increasing the Ni content.

The dependence on other elements is complex and not well understood. The martensitic transformation temperature increases by replacing Ga with Mn and decreases by replacing Ni with Ga. The substitution of Ni with Mn results in a monotonic increase of T_c accompanied first with a decrease and then with an increase of martensitic transformation temperature up to NiMn₂Ga [55]. The observed strong compositional dependence of transformation temperatures results in a quite complex phase diagram for a relatively narrow compositional range.

Additionally, at low temperatures transformations between different kinds of martensite can occur, the so-called intermartensitic transformation (Fig. 14.3a) [21, 56, 57]. This shows that it is very important to know the precise chemical composition and chemical order in the studied compounds, which is not often satisfied. The complex dependence on composition is often approximated by the electron concentration *ela* [15, 58, 59]. However, the universality of this approach is not clear [60]. For that approach Ni is considered to contribute ten, Mn seven, and Ga three electrons.

Also a premartensitic phenomenon was observed in many compounds, particularly for low *ela* concentrations. Whether this affects the MIR-related properties is still under discussion [18, 61]. This precursor phenomenon in shape memory alloys is associated with unstable acoustic modes [62]. It is found that the softening of the transversal acoustic branch occurs in the austenite in a wide compositional range of Ni–Mn–Ga, with martensitic transformation from far below room temperature to near the Curie temperature [63].

The martensitic phase transformation in Ni–Mn–Ga is thermoelastic. Thus, Ni–Mn–Ga also displays the thermal shape memory effect and superelasticity. The transformation temperature can be affected by stress as in other shape memory alloys and by magnetic field. Therefore, the martensitic phase can be induced by a magnetic field (MIM) [26] and by stress (stress-induced martensite or superelasticity) [64, 65].

In order to increase the Curie and the martensitic transformation temperatures of Ni–Mn–Ga, various fourth elements were added with mixed success. Design and preparation of a quaternary alloy is a complex task, where both structural and magnetic transformation temperatures have to be raised [66]. Doping with Fe seems to increase T_c ; however, it also seems to suppress the martensitic transformation [67]. So far, there is no guide for the alloying from theoretical calculations, apart from a consideration of the *ela* concentration [57].

14.5.2 Martensitic Phases in Ni–Mn–Ga

It is generally accepted that three different martensitic phases can be distinguished in Ni–Mn–Ga [50, 54, 56–58, 68]. There are also reports about some additional phases, which may differ by the modulation period. But it is not clear yet whether these might be only an averaging of known phases. The three basic Ni–Mn–Ga martensitic phases are listed together with a number of possible martensitic variants:

- Five-layered modulated martensite (named 5 M or 10 M): original cubic austenitic unit cell is distorted being pseudotetragonal with $a \approx b$ and $c/a \sim 0.94$, modulation over 10 (220) atomic planes along $[-110]$ direction, three twin variants.
- Seven-layered modulated martensite (named 7 M or 14 M): original cubic austenitic unit cell is distorted being orthorhombic with $a > b > c$ and $c/a \sim 0.89$, modulation over 14 (220) atomic planes along $[-110]$ direction, six twin variants.
- Non-modulated martensite (named NM or 2 M): original cubic austenitic unit cell is distorted being tetragonal with $a = b$ and $c/a \sim 1.2$; no modulation three twin variants.

The maximum MIR strains reported are about 6% for 5 M and 11% for 7 M martensite. These strains are very close to theoretical maximum given by the lattice constants. No MIR strain was observed in the non-modulated martensite.

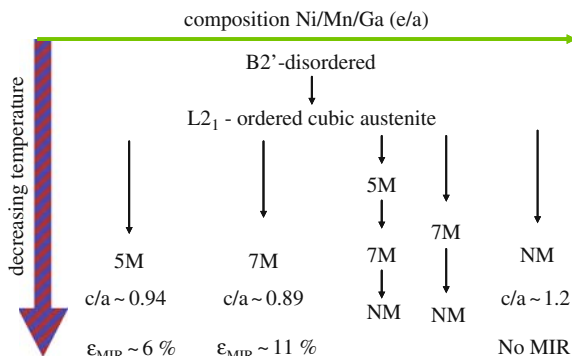
Here we use 5 M and 7 M labelings, referring to the number of the basic crystallographic unit cells within the modulation containing supercell. The martensites can also be labeled as 10 M and 14 M, respectively [50, 68–70]. This refers to the amount of crystallographic planes within the supercell.

The basic unit cells are usually described in two different coordinate systems. One is the coordinate system originating from the cubic $L2_1$ austenitic unit cell [68]. This unit cell simplifies the magnetic and twinning descriptions, as the tetragonal or orthorhombic distortions, the resulting easy magnetization axis, the twin boundary plane, and the maximum strain are directly apparent. This coordinate system is used here.

The other coordinate system is derived from the $\langle 110 \rangle$ direction of the cubic $L2_1$ coordinate system. The unit cell in the first case is twice as large as in the second one. The second approach is more favorable from the crystallographic viewpoint (because of its small volume) and the modulation describing supercell is easily constructed by combining 5 (for 5 M) or 7 (for 7 M) of these basic unit cells.

There is still a discussion about the character of the modulated phases, whether the modulation can be considered as a harmonic wave or as a stepwise shuffling of lattice planes [64, 68–74]. Additionally, the question whether the modulated 5 M crystal structures can be considered as commensurate or incommensurate is not solved [75]. Since the structure strongly depends on composition and on thermal and mechanical history, any slight differences in composition and preparation

Fig. 14.7 Phase schema of the different phases in Ni–Mn–Ga as a function of temperature and e/a ratio (increasing to the left)



methods may result in conflicting reports about different structures. These dependencies make the precise structure determination difficult.

An approximate guide to which martensitic phases are stable for different temperatures and e/a ratios is given in Fig. 14.7. Above $e/a = 7.7\text{--}7.8$ (martensitic transformation temperature $> T_c$), only the NM martensite is observed [15, 50, 56]. The calculations also show that in general the NM martensite has the lowest total energy [71–73]. However, the 5M martensite was found to persist down to 4 K in many alloys with low e/a ratio. Experiment and ab initio calculations suggest further that 7M also is an unstable phase which tends to transform to NM if it is not stabilized by some external means, e.g., stress [76–78].

The sequence of the martensitic transformations can be detected by DSC and susceptibility measurements (see Fig. 14.3). When the martensitic transformation temperature is below T_c , the high-temperature paramagnetic austenite transforms to a ferromagnetic austenite on cooling, resulting in a large increase of the susceptibility. Due to low anisotropy in the vicinity of T_c , a small but typical Hopkinson peak develops upon transformation. On further cooling, ferromagnetic austenite transforms to ferromagnetic 5M martensite, which is marked by a significant decrease of the susceptibility. The decrease is due to the high magnetic anisotropy of the martensitic variants. Despite the large decrease of susceptibility, the saturation magnetization increases about 10% upon transformation to the martensite (Fig. 14.8). At the martensitic transformation, the DSC curve exhibits a peak due to the released or consumed latent heat.

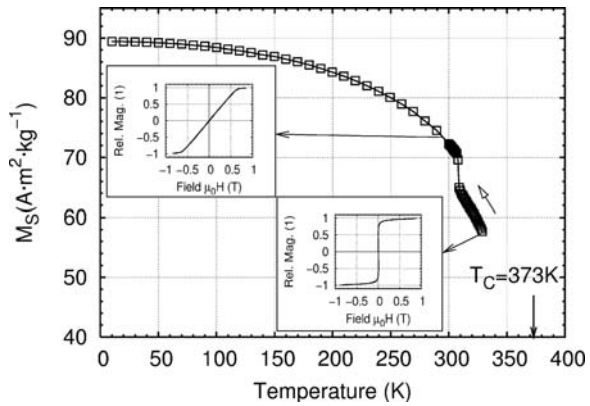
On cooling within martensite phase, the susceptibility is nearly constant and slightly increases upon intermartensitic transformation to another martensitic phase. The DSC curve shows small peaks indicating that the latent heat of the intermartensitic transformation is small. On heating, the sequence of the transformations is reversed, i.e., the transformations go from NM to 7M to 5M and then finally to the cubic austenite, showing a hysteresis upon the (inter)martensitic transformations, which are therefore thermoelastic.

In polycrystalline materials the sharp changes might be smeared by gradual transformation in individual grains. Grain boundaries and grain size can influence the

martensitic transformation. In quenched polycrystals, the Hopkinson peak is more pronounced possibly due to the presence of stress-induced anisotropy (Fig. 14.3b), which is caused by the residual stress after quenching [22].

The transformation from austenite to martensite results for the 5M martensite in an equivalent and random distribution of all three variants. To prepare a single crystal in a specific variant distribution, the transformation to the martensite has to take place under mechanical stress or magnetic field. A transformation to the 5M martensite under compressive stress results in a single-variant martensite with the short c-axis in the direction of the stress. Cooling in saturation field can have the same effect, but the variant selection potential is limited by the anisotropy energy [79].

Fig. 14.8 Saturation magnetization as a function of temperature and magnetization loops corresponding to austenite and martensite (measured in hard direction). Loops are corrected for demagnetization



14.5.3 Magnetic Properties of Ni–Mn–Ga

In Heusler alloys, generally the magnetic order is associated with the Mn–Mn distance [47, 48, 80]. The cubic parent phase of stoichiometric compounds is ferromagnetic below $T_c = 376$ K, which depends only weakly on composition. The magnetic moment is about $4.17 \mu_B$ per formula unit mostly confined to the Mn atoms and with a small moment ($<0.3 \mu_B$) associated with the Ni atoms [48, 50]. The saturation magnetization of martensite is about 10% larger than that of the austenite (Fig. 14.8). The redistribution of electronic charges, due to the structure changes, increases the absolute magnitude of atomic moments. This increase is, however, small, which was confirmed by calculations and experiments. The main reason for the higher saturation magnetization of the martensitic phase is considered to be the higher Curie temperature of the martensitic phase. The saturation magnetization at low temperatures has a maximum at stoichiometry and decreases with increasing the Mn content. This is ascribed to an antiferromagnetic ordering of the excess Mn

atoms [81]. Naturally, the magnetization also decreases with decreasing Mn content from stoichiometry, as Mn atoms carry most of the magnetic moment.

One crucial parameter for MIR is the magnetic anisotropy. By measuring the field-dependent magnetization in different crystallographic directions, the anisotropy constant K_u can be determined as the area between these curves. The anisotropy of the cubic phase compared to the martensite is very low, which is reflected in the square-like magnetization curve shown in Fig. 14.8 [82–84]. After transformation to the martensite the magnetic anisotropy sharply increases. The magnetization curves of the 5M, 7M, and NM martensites are shown in Fig. 14.9. The curves indicate the strong anisotropy with easy axis along the c-axis for 5M and 7M and with easy a–b plane for NM martensite [84–86].

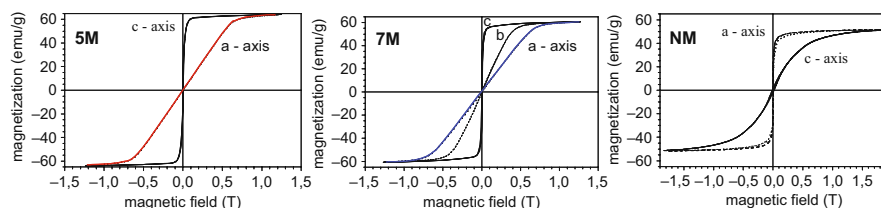


Fig. 14.9 Magnetization loops for 5M, 7M, and NM martensites of Ni–Mn–Ga single crystals. The samples were prepared to contain only one single variant as close as possible [82]. (Reprinted with permission of Journal de Physique IV)

The temperature dependence of the anisotropy constant and the scaling with the saturation magnetization suggest a one-ion origin of the anisotropy [84]. Especially, a non-symmetrical surrounding of the Ni atoms was suggested as the origin of the anisotropy [87]. Other calculations also indicate that the anisotropy of the non-modulated phase should be much higher than for the modulated phases, which was, however, not observed. The magnitude indeed increases with the lattice distortion but it is not proportional and it saturates [88]. The anisotropy constant of 5M martensite is about $1.6 \times 10^5 \text{ J/m}^3$ at room temperature and increases to about $3.3 \times 10^5 \text{ J/m}^3$ at 10 K. It depends weakly on the Mn and Ga contents [86, 89]. The sum of the anisotropy constants of the NM martensite is $K_a + K_b = 3.5 \times 10^5 \text{ J/m}^3$ at 100 K [84].

The magnitude of magnetostriction of the cubic phase increases in the vicinity of martensitic transformation to about $\lambda = -150$ ppm [83]. The magnetostriction of the martensite is difficult to measure as the small deformation due to magnetostriction is masked by much stronger MFIS due to MIR. According to Tickle and James [83], the magnetostriction of the martensitic phase is about -275 ppm at 265 K. This large value was not confirmed later on and it has been suggested that the magnetostriction is below 100 ppm in 5M martensite [90]. The large value observed by Tickle and James might be due to MIR not considered in their experiment.

14.5.3.1 Magnetization Process in Twinned Martensitic Single Crystals

Magnetization curves of a single crystal containing a single tetragonal variant measured in easy and hard directions are shown in Fig. 14.9. The single-variant state was prepared by compression in one direction, i.e., the compression axis corresponds to the easy magnetization axis [001] (c-axis). Magnetizing along the [001] direction (c-axis) results in a square-like curve $M_{\text{easy}}(H)$ with steep increase of the magnetization in low fields. Contrary to the high magnetic anisotropy of martensite, the magnetization curves exhibit low coercivities. In easy direction, this indicates easy nucleation of magnetic domains and a high mobility of magnetic domain walls.

Magnetizing the single variant along the [100] (a-axis) or [010] (b-axis) directions (both perpendicular to c-axis) results in linear curves $M_{\text{hard}}(H)$ with low and constant permeability up to saturation. Above the anisotropy field H_A the magnetization reaches the saturation value M_{sat} . The magnetic hysteresis of the hard axis is low as the magnetizing process is a reversible magnetization rotation.

If the sample contains multiple variants, the magnetization curve is a linear combination of the magnetization curves of all these variants. An example for the 5 M martensite containing all three variants is shown in Fig. 14.10. The total magnetization, M_{tot} , in that case can be written as

$$M_{\text{tot}}(H) = \nu M_{\text{easy}}(H) + (1 - \nu)M_{\text{hard}}(H), \quad (14.4)$$

where ν is the volume fraction of the variant with easy axis parallel to the applied field direction [91, 92]. For the 5 M tetragonal martensite, there is one variant (with volume fraction ν) having easy axis in field direction and two variants (with volume fraction $1 - \nu$) having hard axis in field direction. The variants with a-axis and b-axis in field direction are in this approximation considered to be equivalent and perpendicular to each other. This is not exactly true, as due to the tetragonal distortion the misorientation across a twin boundary is equal to $2 \arctan(c/a)$.

In the 7 M orthorhombic martensite all three crystallographic directions (a, b, c) have different magnetic anisotropy (Fig. 14.9b), which, for a multiple variant state, results in three different slopes for the magnetization curve [78, 85]. Above H_A the magnetization reaches saturation.

When MIR occurs, the magnetization curves change (Figs. 14.5 and 14.6). On magnetizing a variant perpendicular to its easy axis of magnetization, due to MIR, variants with easy axis in the field direction nucleate and grow, i.e. their volume fraction ν increases. This causes a fast increase of magnetization, which results in a jump on the linear part of the magnetization curve. If the entire volume has transformed to one variant with easy axis in field direction, the magnetization curve reaches saturation in fields lower than H_A . If μ is the volume fraction, which transforms due to MIR, the total magnetization can be written as

$$M(H) = (\nu + \mu)M_{\text{easy}}(H) + (1 - \nu - \mu)M_{\text{hard}}(H). \quad (14.5)$$

The magnetization loops for an arbitrary magnetic field orientation can be approximated using the Stoner–Wohlfarth model for uniaxial particles [23]. This method can be expanded for polycrystalline samples considering each grain with different orientation and volume fraction.

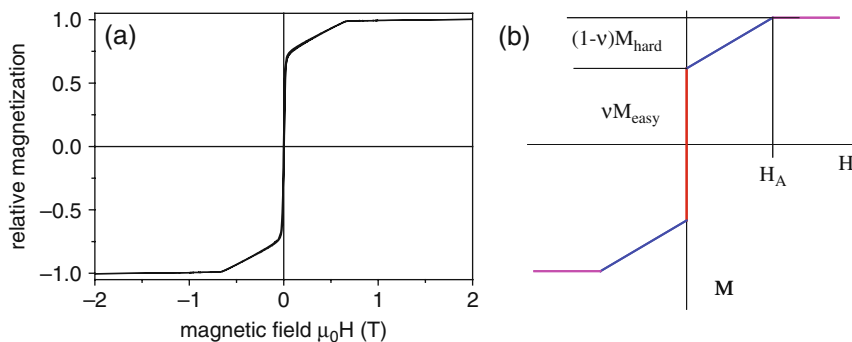


Fig. 14.10 Magnetization curve of a 5M single crystal sample containing multiple variants and field nearly parallel/perpendicular to easy/hard axes. (a) Experiment and (b) model. Slight tilt in experimental curve is caused by demagnetization

14.5.3.2 Magnetic Domain Structure

Thanks to the relatively high anisotropy the magnetization vector follows the easy axis, independently of the surrounding. The magnetization within a twin variant is not strongly affected by the adjacent twin variants. The domain structures in twinned 5M martensite single crystals were studied in detail using SEM [93, 94] and optical methods [95, 96]. Typical magnetic domain patterns are sketched in Fig. 14.11. On a surface with two variants both having c-axes in plane, the domain and twin structures create a staircase-type pattern (Fig. 14.11b–e). Due to magnetostatic energy, each twin variant usually consists of several magnetic domains separated by 180° walls. As the direction of the easy axis changes at the twin boundary by $\sim 90^\circ$, the twin boundary itself also corresponds to a $\sim 90^\circ$ domain wall. For the perpendicular crystal surfaces, the easy magnetization axis of one variant points out from the crystal surface, whereas that of the second variant lies in plane (Fig. 14.11f,g). This results in a different magnetic domain pattern with a maze domain structure for the variants with c-axis out of plane. The domain structure becomes more complex for arbitrary surface orientations [97]. The domain structure of the 7M and NM martensites were not studied in detail.

The domain structure of the cubic austenite is similar to other cubic materials. The domain structure is not easily visualized, due to low Kerr effect of Ni–Mn–Ga and the very low magnetic anisotropy resulting in very small stray fields. Therefore, the domain patterns are easily disturbed by external fields when using AFM or SEM.

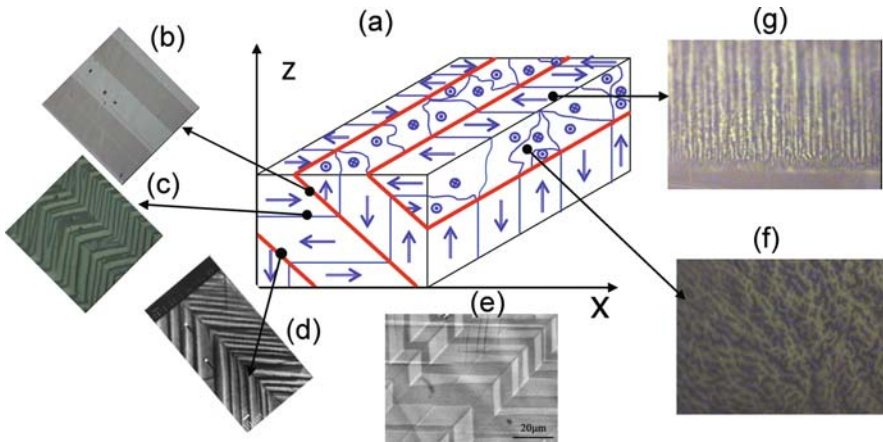


Fig. 14.11 Magnetic domain structure of a 5M martensite single crystal containing two variants. (a) Schematic of the domain structure. *Thick lines* – twin boundaries, *thin lines* – magnetic domain boundaries. (b) Twin variants. (c) Overlaid magnetic domain structure in these variants. (d) SEM image of magnetic domains across one twin boundary. (e) Staircase-type twin and domain structures corresponding to the front face. (f) Maze domain structure in variants with c-axis perpendicular to surface. (g) Parallel domain structure with branching on the edge to reduce stray field. If not stated otherwise, images were taken by polarized optical microscopy. For the magnetic domains visualization an additional magneto-optical indicator film was used

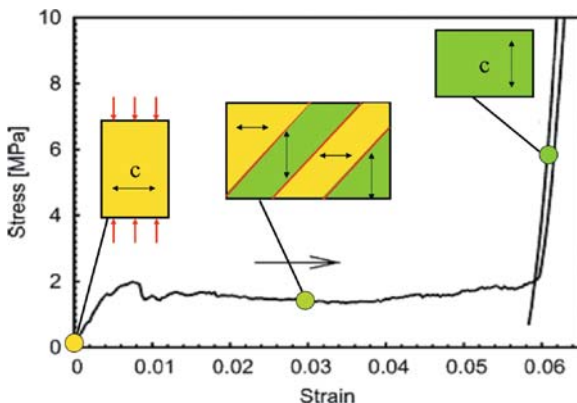
14.6 Twin Boundary Mobility

After transformation from austenite the resulting martensitic structure consists of several twin variants. For the 5M martensite, all three tetragonal variants occur in the sample randomly distributed, when the transformation is without constraints. Considering the tetragonal unit cell of 5M and NM martensite $a = b \neq c$ (coordinate system of cubic $L2_1$ unit cell of austenite), there are four different twin planes $\{101\}$ in each variant. As there are three variants, this results in twelve non-equivalent twin planes (boundaries) for 5M and NM. For the orthorhombic 7M martensite, there are six different variants, which increase the amount of non-equivalent twinning systems.

For the existence of MIR the twin boundary mobility has to be high. Experimentally, the twin boundary mobility can be evaluated from stress–strain curves measured during stress-induced reorientation and quantified by the twinning stress. In general, the nucleation of new variants may need higher energies compared to growth of existing variants by twin boundary motion. The stress-induced movement of twin boundaries leads to reorientation and causes a plateau on the stress–strain curve (Fig. 14.12). The twinning stress is then defined as the stress which causes the nucleation or the movement of twin boundaries (stress plateau). The twinning stress is an experimentally obtained parameter and up to now there is no reasonable way to derive it theoretically [98]. The stress-induced reorientation of the martensitic microstructure is analog to the magnetic field-induced reorientation.

The twinning stress depends on pinning sites (e.g., defects, precipitates, voids, and imperfections) within the microstructure and can differ significantly in various samples, due to thermo-mechanical history, production route, and so on. Additionally, there is also a large difference in the twinning stress for different martensites [88, 99].

Fig. 14.12 Stress–strain curve of 5 M martensite. Initially the material is in one variant state and the compressive stress is applied perpendicular to the c -axis (as marked). The strain is measured in stress direction. For this sample, a stress of less than 2 MPa induces a reorientation by twin boundary motion. Inset shows the variant configuration in different stages of deformation



One example of a stress–strain curve of a Ni–Mn–Ga single crystal (5 M martensite) is shown in Fig. 14.12. Initially the deformation is elastic and a linear behavior is observed. At about 2 MPa new twins with a favorable orientation (c -axis) to the applied compressive stress direction nucleate and grow by twin boundary motion. The external uniaxial stress can be resolved to shear stress along the twin boundary (Fig. 14.2). The instability against shear leads to twinning, which results in a plateau in the stress–strain curve. The slope of the plateau can be positive, zero, or even partly negative, like in Fig. 14.13. This indicates that twin nucleation is more difficult than moving twin boundaries. At high stress, the specimen has transformed fully to the variant with short c -axis in stress direction. This process is called detwinning. When the reorientation is completed, the sample is deformed elastically again. The elastic modulus in $[001]$ direction can be determined from the slope and it was found to vary from 2 to 20 GPa [56, 100–102].

Although the macroscopic twin reorientation, as observed by optical microscopy and magnetic measurements, seems to be finished in rather low stresses of a few MPa, a full reorientation of the entire specimen can demand much higher stresses. The acoustic signal ascribed to reorientation was detected up to 60 MPa [103]. Also neutron diffraction indicates that the reorientation of martensite is not completed at a stress of 30 MPa [104, 105].

Twin boundaries interact with pinning points (defects) in the crystal structure resulting in the non-zero twinning stress [98, 106]. Two extreme stress–strain curves exhibiting stress-induced twin boundary motion are shown in Fig. 14.13. In the first case (Fig. 14.13a) there is a maximum at the initial part followed by a stress decrease with increasing strain. The second curve shows a continuous stress increase with increasing strain (Fig. 14.13b). When the twinning stress is reached during the initial

elastic loading of a single variant, the accumulated elastic energy suffices to nucleate new, favorable oriented variants and their subsequent growth by twin boundary motion. Small nuclei of other favorable oriented variants can also be already present but pinned in the material. At the twinning stress the twin boundaries are released from their pinning sites [107]. If there are no other pinning sites with a higher “pinning strength”, the twin boundary proceeds through the whole specimen leading to large reorientation without increasing the stress (Fig. 14.13a). In Fig. 14.13b, the twin boundary motion becomes gradually more difficult with proceeding deformation, due to pinning sites or the twin boundaries mutual hindrance. These two cases are reflected not only in the strain but also in the magnetization dependence of MIR. In the first case MIR is initiated by one large jump in strain and magnetization, whereas in the second case the reorientation proceeds continuously with field.

Although the role of pinning sites for twin boundary motion seems to be understood on the level mentioned above, it is not clear which kind of pinning sites hinder twin boundary motion. They can be precipitation or incoherent impurities with $\sim 20\text{--}100$ nm in size, chemical disorder, antiphase boundaries, and low-angle grain boundaries [108, 109]. There might be different phases, voids, and micro-cracks from production. Also pinning of twin boundary on the surface has to be considered [110]. The mobility of twin boundaries also depends on microstructure and twin variant configuration, as one twin boundary can block the motion of others [111]. In polycrystalline materials there are additional constraints due to the surrounding grains.

Therefore, the movement of twin boundaries and their pinning is a complex process and only few theoretical predictions were made [98, 112]. Usually, the value of twinning stress is taken from experimentally obtained stress–strain curves.

The twinning stress can be decreased by a repeated reorientation induced either by a mechanical stress or by a magnetic field application in different directions; this is usually called mechanical or magnetic training, respectively, or as a combination magneto-mechanical training. By this, a preferable twin structure is created, which ideally consists of one type of twin boundary only [107, 111]. Therefore, the twin boundaries cannot block each other.

14.7 Energy Model for MIR

From the point of thermodynamics, there are several phenomenology models which describe the field-induced motion of twin boundaries [113–122]. These models in general include the Zeeman energy, the magnetic anisotropy energy, and the external stress for each variant. They may also include magnetostatic and, magnetoelastic contributions twin formation, and pinning of twin boundaries. These models are compared by O’Handley et al. [122]. However, a fully developed microscopic model of twin boundary motion due to a magnetic field has not yet been put forward [98, 112].

Here we will examine the model case of a specimen containing only two variants and one twin boundary. The easy axes (c-axes) of the variants are perpendicular and

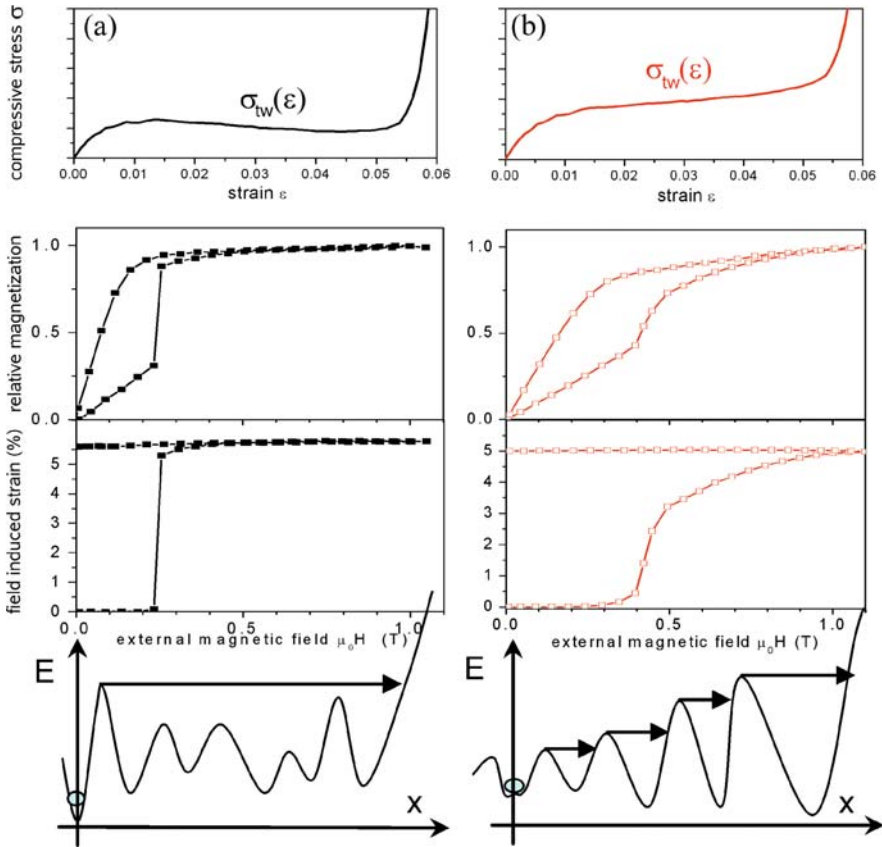
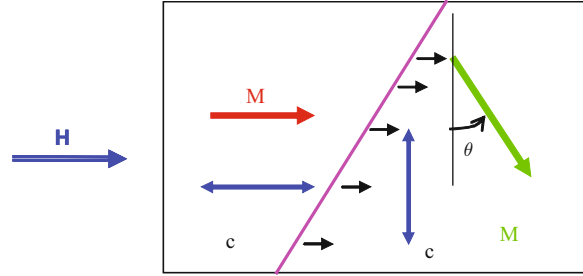


Fig. 14.13 (a, b) Two extreme stress–strain curves (*first row*), the corresponding magnetization (*second row*), and MIR strain curves (*third row*). Sketched potential energy landscapes for the observed behavior (*last row*)

parallel to the field direction (Fig. 14.14). In zero magnetic fields both variants have the same energy and no movement occurs. If a magnetic field H is applied, a difference in the magnetic energy between both variants develops. In the variant with easy axis parallel to the field direction, the magnetic energy corresponds to the Zeeman energy $-M_{sat}H$, where M_{sat} is the saturation magnetization. In the variant with easy axis perpendicular to the field, the magnetic energy is given by $-MH + K_u \sin^2\theta$, which includes the rotation of the magnetization M in the field H , i.e., the anisotropy. Therefore, the magnetic field induces an energy difference $\Delta E_{mag}(H)$ across the twin boundary. This creates a driving force on the twin boundary to increase the volume fraction of the favored variant with easy axis in field direction.

A simple energy model describing the twin boundary motion in a magnetic field was first presented by Likhachev and Ullakko [115, 116] and later applied to different experimental cases by Straka and Heczko [28, 29] and Sozinov et al. [123, 124].

Fig. 14.14 Schematic of a two-variant sample with one twin boundary. H - external magnetic field, c - easy axis of magnetization, M - magnetization, θ - angular deviation between c and M due to H



The model is based on the equivalence of the magnetic and elastic energies in the variants. The model assumes that MIR occurs when the magnetic energy difference between the variants exceeds the elastic energy needed for twin boundary motion:

$$\Delta E_{\text{mag}} > \sigma_{\text{tw}} \varepsilon_0, \quad (14.6)$$

where σ_{tw} is the twinning stress and ε_0 the tetragonal distortion [$\varepsilon_0 = (1 - c/a)$]. This is equivalent to stress-induced twin boundary motion and the condition can be rewritten in the form of the equivalent magnetic stress σ_{mag} :

$$\sigma_{\text{mag}} = \frac{\Delta E_{\text{mag}}}{\varepsilon_0} > \sigma_{\text{tw}} (+\sigma_{\text{ext}}), \quad (14.7)$$

where σ_{ext} is an additional external compressive stress applied perpendicularly to the magnetic field. This equation describes the usual setup of an actuator. In saturation, the magnetic energy difference of two 5 M martensitic variants is equal to the magnetic anisotropy constant:

$$\Delta E_{\text{mag}}^{\text{max}} = K_u \text{ and thus } \sigma_{\text{mag}}^{\text{max}} = K_u / \varepsilon_0. \quad (14.8)$$

The magnetic energy difference between differently oriented variants in field H is given by

$$\Delta E_{\text{mag}}(H) = \int_0^H M_{001}(H') dH' - \int_0^H M_{100}(H') dH'. \quad (14.9)$$

$\Delta E_{\text{mag}}(H)$, and therefore σ_{mag} , can be directly determined from the magnetization curves of one variant measured in easy and hard directions (Fig. 14.15).

The determination of σ_{mag} assumes that the demagnetization factors in both variants are the same. For a simple uniaxial material, like the tetragonal 5 M martensite, ΔE_{mag} can be easily calculated for the easy axis parallel or perpendicular to H [29]. When the anisotropy field H_A , the demagnetization field H_D , and the saturation magnetization M_s are known, the energy difference is

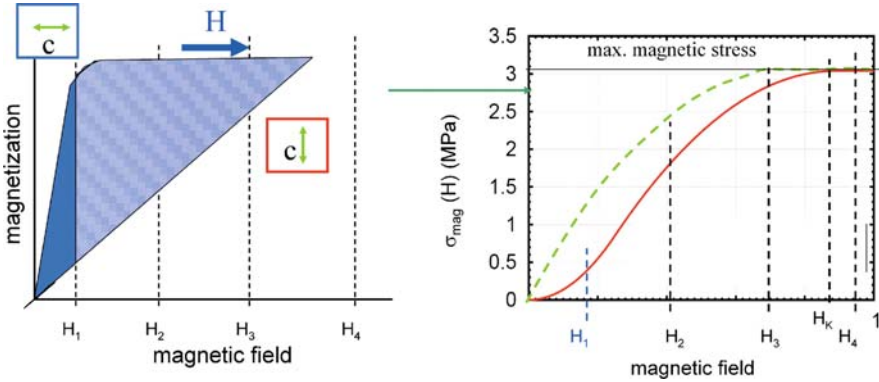


Fig. 14.15 The magnetic stress as a function of the external field is derived from the magnetization curves measured in easy and hard directions. The *broken line* gives the magnetic stress without considering the demagnetization

$$\begin{aligned}
 \Delta E_{mag} &= \frac{1}{2} M_S H^2 \left(\frac{1}{H_D} - \frac{1}{H_A} \right) \text{ for } 0 < H < H_D \\
 \Delta E_{mag} &= -\frac{1}{2} M_S H_D + M_S H - \frac{M_S H^2}{2H_A} \text{ for } H_D < H < H_A \\
 \Delta E_{mag} &= \frac{1}{2} M_S (H_A - H_D) \text{ for } H > H_A
 \end{aligned} \tag{14.10}$$

which in the last case is equal to K_u . In this calculation, the measured magnetization curves in easy and hard directions are approximated by linear dependencies. No magnetic interaction between variants is assumed for this model. The variants behave independently in the field and the magnetic energy density depends on the volume fraction of different variants, but not on their distribution and size.

14.8 Angular Dependence

MIR and the model predictions were mostly studied in single crystals with austenitic $\{100\}$ planes parallel to the crystal surfaces. The angular dependence of MIR is important for applications, e.g., when considering polycrystalline bulk or composites with small, differently oriented crystallites. There are no experimental studies on the angular dependence.

Applying the field along the twin boundary, i.e., in a 45° inclination to the easy axes of both the variants the magnetic energies of both variants are the same for any field strength. Therefore, there is no driving force for twin boundary motion. The maximum driving force is reached for the model case considered above, with the field parallel to one easy axis (Fig. 14.14). The situation is more complex for any other crystal orientation in relation to the applied field.

The magnetization curves of variants can be calculated for arbitrary field angles by the Stoner–Wohlfarth model, assuming a uniaxial anisotropy [23]. The calculated

magnetization curves for a 30° and 60° angle between easy axis and field are shown in Fig. 14.16. The difference in magnetic energies between two variants is again equal to the area between the calculated magnetization curves. In the calculation, the easy axes of the variants are assumed to be perpendicular to each other.

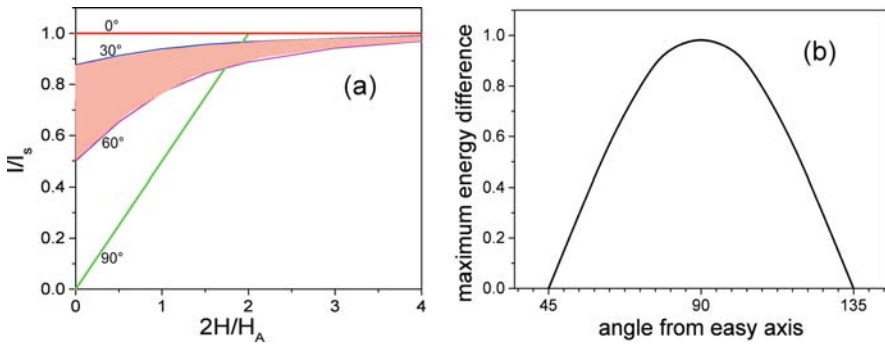


Fig. 14.16 Schematic magnetization curves for a 30° and 60° deviation between field and easy axis. The difference (*hatched area*) gives the magnetic driving force for MIR. *Straight lines* are magnetization curves for a 0° and 90° deviation. Angular dependence of the maximum energy difference calculated from the magnetization loops for different field to easy axis orientation (up to saturation)

The magnetic energy difference decreases with increasing deviation between magnetic field and hard axes of the magnetically unfavoured variant and becomes zero for 45°. Additionally, for any non-zero deviation the difference in magnetic energy is not saturated at the anisotropy field. Thus, the driving force for MIR keeps increasing above the anisotropy field, in contrast to a field orientation parallel to the hard axis.

14.9 Reversible and Irreversible MIR Strain

The twin boundary motion due to field or external stress is irreversible, if no stress or magnetic field is applied in a perpendicular direction (Fig. 14.6) [4, 28, 125]. But the constant stress cannot be too large as this would block MIR. Thus, there is only a narrow window of reversibility. From the basic stress consideration one can write the condition for a MIR deformation to be, due to an external stress, reversible in the form

$$K_u/\varepsilon_0 - \sigma_{tw} > \sigma_{ext} > \sigma_{tw}, \tag{14.11}$$

which is valid for a magnetically saturated sample. The equation also shows that the requirements for reversibility further decrease the usable actuation stress obtained from the material. To obtain a reversible strain twinning stress has to fulfill [125]

$$2\sigma_{tw} < K_u/\epsilon_0. \tag{14.12}$$

This indicates that a twinning stress as low as possible is desirable for the application in a reversible actuator. Simultaneous measurement of MFIS and magnetization curves in different stresses σ_{ext} are shown in Fig. 14.17. At a low external stress the effect is (nearly) irreversible. With increasing stress a partly reversible structure reorientation takes place, resulting in reversible strain ϵ_r and increased magnetic hysteresis. The hysteresis in the first and third quadrants denotes consumed energy needed for the structure reorientation.

With increasing stress the onset of the reorientation is shifted to higher magnetic fields and the maximum strain slightly decreases, whereas the reversible strain increases. At 1 MPa the strain and magnetization curves are symmetrical due to

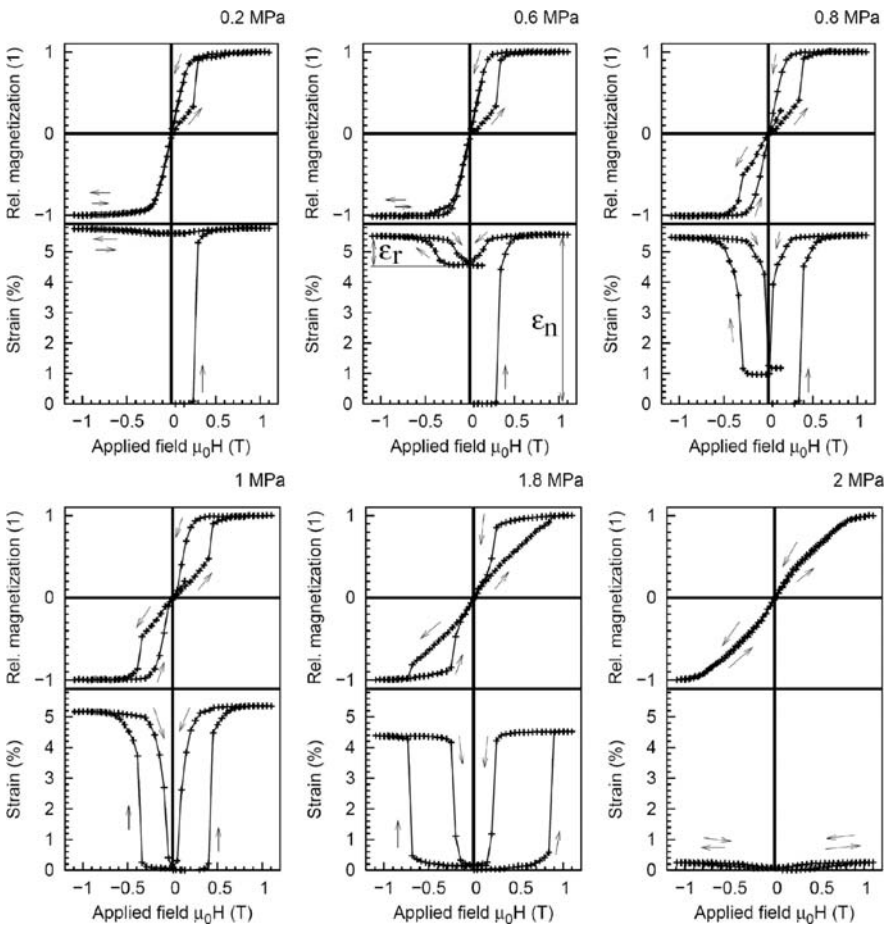


Fig. 14.17 Magnetically induced strain and magnetization curves for different external stresses [126]

a full reversible reorientation. At 1.8 MPa the initial magnetization curve is linear nearly up to saturation. As the onset of reorientation occurs nearly at the anisotropy field, the sample is magnetized until H_A in the hard direction. Further increase of the external stress (2 MPa) suppresses the reorientation and no hysteresis and strain occur.

The reciprocal effect to reversible MIR strain, due to stress-induced reorientation, is the magnetically induced superelasticity [125, 127, 128]. In this case the magnetic field is constant and the external stress changes. Initially the easy axis is in the field direction and perpendicular to the stress. The external stress causes the deformation by twin boundary motion, whereas the magnetic field provides restoring force by MIR. The effect in different fields is shown in Fig. 14.18. In low fields, MIR does not occur. Therefore, the stress-induced reorientation is irreversible and could be rather called superplasticity. With increasing field MIR occurs and restores in the decreasing stress path the initial variant. The stress needed for reorientation increases as it must work not only against the twinning stress but also against the magnetic stress provided by the field.

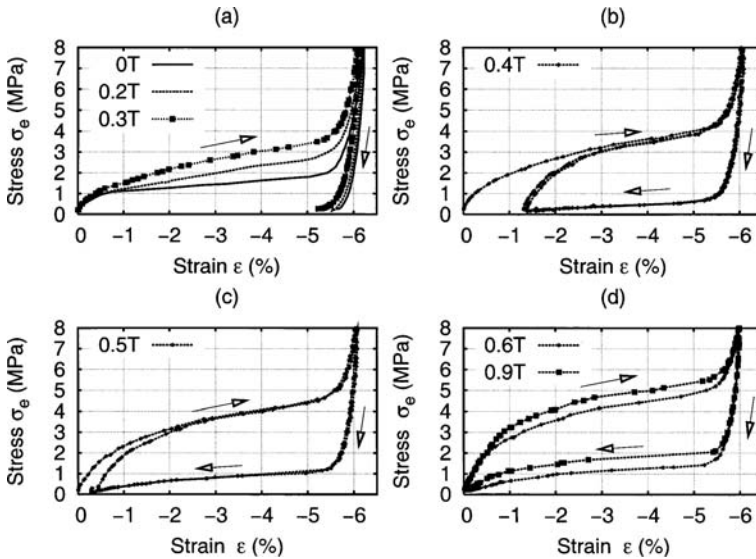


Fig. 14.18 Stress–strain curves for different values of the applied magnetic field. (a) For zero or small fields, the sample is superplastic. (b) For a few cycles in the field of 0.4 T, the process is partly reversible (superelastic). (c) Further increasing the field to 0.5 T brings more reversibility. (d) Strain is fully reversible for a field of 0.6 T and above [29]. (Reprinted with permission of IEEE Transactions on Magnetics)

The simple inequality from Eq. (14.6) gives a straightforward criterion to evaluate the possibility of MIR in any potentially active material, regardless of the microscopic mechanism of MIR. To estimate the possibility of MIR and its magnitude [28, 29, 91, 92], only a few material parameters are needed: twinning stress, magnetic

anisotropy, and the tetragonal distortion. The magnitude of the twinning stress can be obtained from the mechanical testing, the magnetic anisotropy from evaluating the magnetization curves, and the tetragonal distortion of the lattice is given by X-ray measurements. Validity of the model for Ni–Mn–Ga was confirmed by comparison with many basic experiments [28, 29, 91, 92, 115, 116, 123, 124]. However, the universality of the model for other materials has not been widely tested [129].

From the model the stress limit for irreversible or reversible MIR can be predicted. For that the twinning stress was taken as the stress value needed for a 3% deformation. The agreement between experiment and calculation is shown in Fig. 14.19. The model was also used to predict the magnitude of MIR in 7 M martensite using twinning stress obtained from experimental stress–strain curves [111].

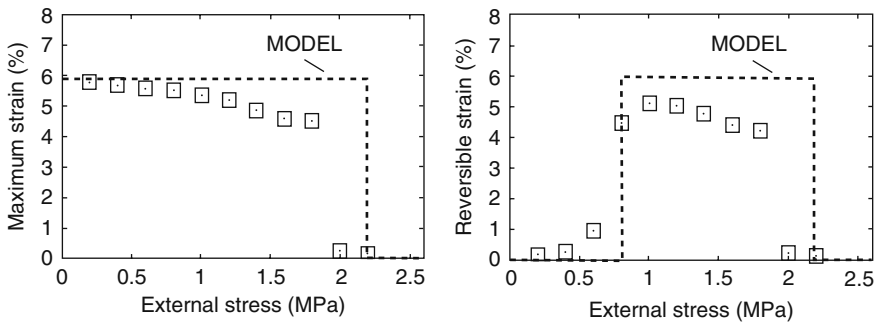


Fig. 14.19 Experiment and prediction for the magnitude of irreversible (left) and reversible (right) MIR strains in 5 M martensite [126]. (Reprinted with permission of Journal of Magnetism and Magnetic Materials)

Superelasticity and the increase of mechanical stress, due to the opposing magnetic field, were shown in Fig. 14.18. The prediction from the model agrees well with the experiment and is shown in Fig. 14.20 for 5 M martensite [29]. The increase of the mechanical stress due to a magnetic field was also confirmed for the 7 M and NM martensites [123, 124].

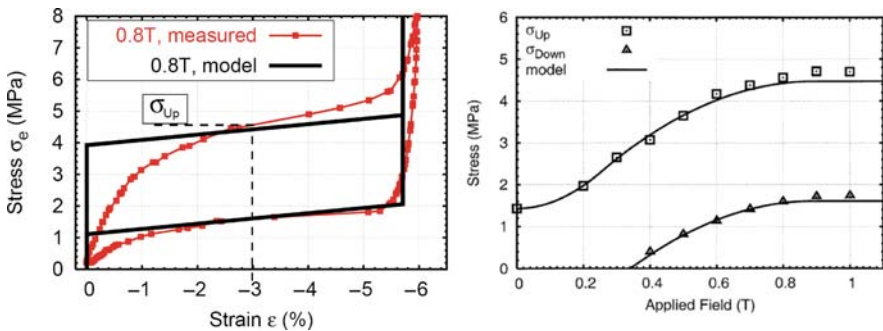


Fig. 14.20 Magnetically induced superelasticity in 5 M martensite (left). The model prediction and measured values of stress needed for reorientation as a function of magnetic field (right) [29]. (Reprinted with permission of IEEE Transactions on Magnetics)

14.10 Temperature Dependence of MIR

The twin boundary moves due to a resolved mechanical or magnetic shear stress. In magnetic fields, this shear stress might originate from the torque [113, 122] or the magnetoelastic interaction [128, 129]. However, the maximum magnetic energy difference across a twin boundary $\sim 10^5 \text{ J/m}^3 \approx 10 \text{ } \mu\text{eV/atom}$ is much less than the thermal energy of $\sim k_B T \approx 20 \text{ meV/atom}$ at room temperature. Thus, due to thermal activation the atoms randomly change their positions. The magnetic energy difference, due to an applied field, just increases the probability for a position change in a certain direction [122, 130].

The experiments show that MIR is strongly temperature dependent and is limited to a certain temperature range. The switching field, i.e., onset of MIR ($\sigma_{\text{mag}} = \sigma_{\text{tw}}$), increases with decreasing temperature [131]. An example of the simultaneous measurements of strain and magnetization at different temperatures is shown in Fig. 14.21. As the twin boundary mobility decreases with decreasing temperature, the reversibility of MIR also decreases [132].

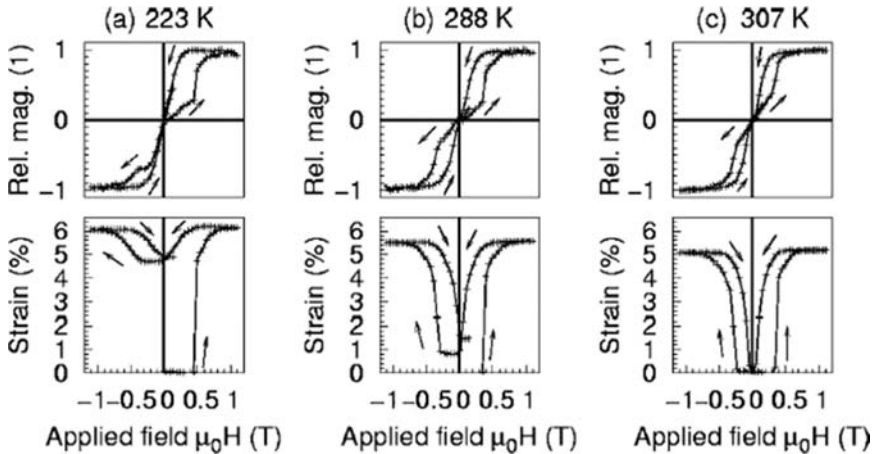


Fig. 14.21 Temperature dependence of MIR in a 5 M Ni–Mn–Ga single crystal. An external stress of 1 MPa was applied to obtain reversible MIR [132]. (Reprinted with permission of Scripta Materialia)

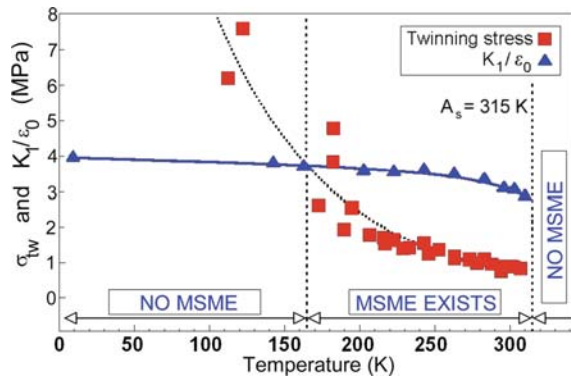
Not only is σ_{tw} temperature dependent, but also K_u and ε_0 . All parameters increase with decreasing temperature. The tetragonal distortion increases with decreasing temperature about 20% and saturates at low temperatures [133]. The magnetic anisotropy increases about twice from room temperature to 10 K [84]. The most important is the temperature dependence of the twinning stress, which strongly increases with decreasing temperature, e.g., about ten times by cooling to 150 K [134, 135]. An example of the temperature dependence of twinning stress is shown in Fig. 14.22.

The magnetic anisotropy K_u denotes the maximum magnetic energy difference between variants. MIR ceases to exist when the magnetic driving force is lower than

the elastic energy barrier necessary to drive the twin boundary [134]. The effect can also be limited by intermartensitic transformation to another kind of martensite (Figs. 14.3 and 14.7), especially to the NM martensite with a dramatically increased twinning stress and changes in magnetic anisotropy and tetragonal distortion [82]. As the tetragonal distortion increases with decreasing temperature, the maximum obtained strain can also increase with decreasing temperature (Fig. 14.21).

The upper limit of MIR is determined by the transformation to austenite and/or transformation to paramagnetic martensite. As K_u decreases much faster than M_s on heating to the vicinity of T_c [23], MIR can cease to exist well before T_c is reached.

Fig. 14.22 Temperature limit of MIR (here MSME = MSM effect). The calculated maximum magnetic stress is compared with the experimentally obtained twinning stress [134]. (Reprinted with permission of Journal of Applied Physics)



14.11 MIR in Polycrystals, Composites, and Films

Reports of MIR are rare for non-single crystalline materials. As a large deformation is involved during MIR, random polycrystalline materials can be expected to fail due to a different deformation in each grain. Additionally, random polycrystals are not expected to show large deformation due to blocking by adjacent grains. However, textured polycrystals might exhibit significant MIR as all grains deform in unison, which results in less strained grain boundaries. This decreases the constraints for twin boundary motion and provides a better structural stability [136, 137]. Recently, 1% MFIS due to MIR have been shown at room temperature in Ni-Mn-Ga polycrystals [137, 143].

Another way to have bulk MSM material and to avoid mechanical failure is to embed active MSM particles in a soft polymer matrix. The matrix has to be stiff enough to maintain a coupling of the MSM particles with each other and the matrix, so that a deformation of the composite can lead to stress-induced twin boundary motion in the MSM particles (e.g., for use in mechanical dampers). Such a composite may also be used as an actuator. In this case, the polymer matrix has to be soft enough to allow MIR in the MSM particles, which may lead to a deformation of the composite. The MSM properties of a composite are naturally diluted as compared

to an ideal MSM bulk material. However, there are several advantages to be considered. Firstly, textured MSM–polymer composites are relatively simple to prepare in near-net-shape form by mixing MSM particles with the polymer and curing the polymer matrix within a desired mold with an applied magnetic field. Secondly, a problem of both single and polycrystalline bulk MSM materials (for magnetic field-controlled dampers and actuators) is the loss generated in high-frequency applications due to formation of eddy currents. This would be reduced by a non-conducting polymer matrix in MSM–polymer composites. Thirdly, the individual MSM particles are relatively free to deform by MIR, due to the thin and soft polymer layer between them. Fourthly, one can expect an improved fatigue behavior. Unlike the bulk material, the fracture of some MSM particles does not destroy the MSM properties of the entire MSM–polymer composite.

There have been several approaches to prepare small, ideally single crystalline particles for those composites. Direct milling of Ni–Mn–Ga bulk material, which shows MIR, usually results in powder, which does not show MIR anymore. This is caused by the stress-induced intermartensitic transformation and/or the high dislocation and crack density. Thus, preparation of small MSM particles without strong mechanical milling is desirable. Therefore, melt-spun ribbons were studied [22, 138]. The ribbons were annealed and milled. Only a short milling time is needed, also due to the inherent brittleness of Ni–Mn–Ga. Although the structure of martensite was shown to be similar to bulk, no MIR was observed. Nearly single crystalline particles were also prepared by spark erosion (no MIR observed). The composites prepared from these particles using a polyurethane matrix show stress-induced twin boundary motion and therefore an enhanced degree of mechanical vibration damping [140, 141].

Polycrystalline fibers were prepared by crucible melt extraction. The fibers have a bamboo-type grain structure, show MIR, easily break along their grain

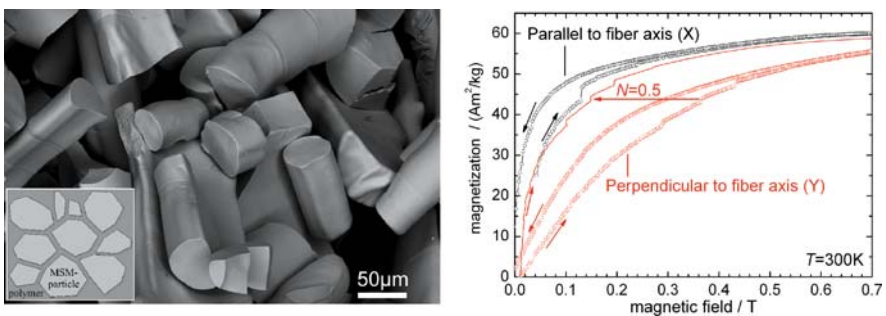


Fig. 14.23 Single- and oligo-crystalline Ni_{50.9}Mn_{27.1}Ga_{22.0} MSM particles (fractured pieces of long fibers) for use in composites. Inset shows sketch of a MSM–polymer composite, where the MSM particles are separated from each other by a thin polymer layer. The VSM measurement of a free Ni_{50.9}Mn_{27.1}Ga_{22.0} fiber shows the typical MIR jumps in the $M(H)$ dependence parallel and perpendicular to the fiber axis [142, 143]. (Reprinted with permission of Acta Materialia and New Journal of Physics)

boundaries, and are therefore promising MSM particles for composite actuators (Fig. 14.23) [142, 143]. MSM-polymer-composites using these particles also show stress-induced reorientation [144].

For use in micro-devices the active materials have to be prepared in the shape of films. The most promising approach is to prepare epitaxial films, as a significant strain is only obtained in single crystals. However, it is apparently very difficult to prepare epitaxial Ni–Mn–Ga films and previous research was mostly restricted to polycrystalline films [145, 146]. Until recently, epitaxial growth of Ni–Mn–Ga has been reported on GaAs (001) substrates using a $\text{Sc}_{0.3}\text{Er}_{0.7}$ [147] buffer and on Al_2O_3 (110) substrates [148].

Recently, epitaxial Ni–Mn–Ga films on SrTiO_3 , MgO , and Al_2O_3 single crystal substrates have been prepared, which possess a ferromagnetic martensitic structure at room temperature. Despite constraints from the substrate, MIR was indicated by magnetic measurements and confirmed by X-ray diffraction (Fig. 14.24) [74, 149]. Due to constraints from the substrate, the film does not exhibit a macroscopic deformation. MIR is still possible due to the finely twinned orthorhombic film structure, which generates an additional degree of freedom for MIR. As a corollary, the developed model suggests that no macroscopic deformation may occur during MIR in orthorhombic martensite if the material is constrained by external stresses.

Also free standing Ni–Mn–Ga epitaxial films were prepared by deposition on NaCl substrates [150]. These films have the ferromagnetic 5M martensitic structure at room temperature and exhibit shape memory properties [139]. In these films, field-induced martensitic transformation, but not yet MIR, has been demonstrated.

Another way to overcome the constraints of a polycrystalline bulk material is to prepare foams. The porosity limits the constraints between misaligned grains and makes the material light. The polycrystalline martensitic foams display a fully reversible magnetic field-induced strain of up to 0.1% [151].

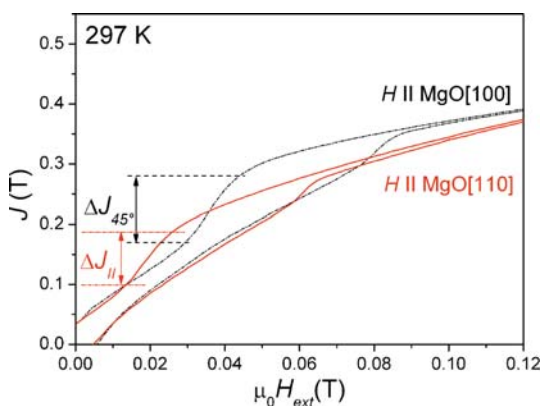


Fig. 14.24 Magnetization curves of an epitaxial Ni–Mn–Ga film deposited on MgO [74]. (Reprinted with permission of New Journal of Physics)

14.12 Other Applications Based on MSM Alloys

The MSM phenomena can be used for active and passive vibration damping [152, 153]. In shape memory alloys, the energy dissipative motion of boundaries between different phases or martensitic twin variants damps the external mechanical vibrations. In ferromagnetic alloys the magneto-mechanical damping is based on the hysteretic motion of magnetic domain walls. In MSM materials both kinds of damping can be expected and can be controlled by external magnetic fields. The MSM materials are relatively soft, provide large deformation, and exhibit large losses of energy during cycling [141].

The large changes of magnetization during stress-induced reorientation can be used as a sensor. Additionally, these changes can also provide the means for energy harvesting from mechanical vibration. Although the suggestions for energy harvesting have been around from the discovery of MIR, only a few reports show direct measurements of the power generation [154, 155].

Magnetocaloric effect in Ni–Mn–Ga was examined by direct measurement of the magnetically induced temperature changes in the material [156]. For materials where the ferromagnetic and the structural (martensitic) transformations coincide, the effect is particularly large. The changes of magnetic entropy can be quite significant; however, the large magnetic and thermal hysteresis losses might disable the preparation of real magnetic refrigerants [157, 158].

14.13 Conclusion

MSM alloys like Ni–Mn–Ga are promising materials with multiple potentials [159]. There has been a large research effort in understanding the principles, although the use in applications is still some time off. The main research effort was concentrated on the magnetically induced reorientation (MIR).

Over a long time, observation of MIR was limited to bulk single crystals. But, the demonstration of MIR on different forms of material recently offers new ways for applications. As magnetic driving force for MIR is limited, a low twinning stress is crucial for its existence. The ability to control the mobility of twin boundaries may decide the usefulness of MIR for applications.

Important for MIR are also a high magnetic anisotropy and saturation magnetization. The upper temperature limit for MIR is determined by the Curie temperature and/or austenitic transformation temperature. The lower limit is determined either by a too high twinning stress or by an intermartensitic transformation.

In applications, the strong thermal dependence and high nonlinearity of MIR strain have to be faced. There are also other problems not mentioned previously and scarcely investigated, such as the existence of magneto-mechanical creep [160], the low resistance to mechanical failure [31, 161], and magneto-mechanical fatigue [162, 163].

Further Reading

- Martensite*, Eds. G. B. Olson and W. S. Owen, ASM International (1992). ISBN-13: 978-0871704344
- Shape Memory Materials*, Eds. K Otsuka and C. M. Wayman, Cambridge University Press (1998).
- Bhattacharya K. *Microstructure of Martensite*, Oxford University Press Inc., New York (2003).
- O’Handley. R. C. *Modern Magnetic Materials*, John Wiley & Sons, Inc, New York (2000)
- Hubert, A. and Schäfer, S. *Magnetic Domains*, Springer, Berlin (1998)
- Cullity, B. D. *Introduction to Magnetic Materials*, Addison-Wesley, Reading, MA, London (1972)

References

1. K. Bhattacharya, R. D. James. *Science* 307, 53 (2005);. Carolyn Yeates, “Are Smart Materials Intelligent?” *INSPEC Matters* 77 (1994).
2. Publications about MSM or MIR effect increases nearly exponentially, the quoted literature can be only small incomplete selection. There are specialized conferences as, e.g., ESOMAT and ICOMAT, which in part (particularly after year 2000) concentrate on MSM effect.
3. K. Ullakko, J. K. Huang, C. Kanter, V. V. Kokorin and R. C. O’Handley. Large magnetic-field-induced strains in Ni₂MnGa single crystal. *Appl. Phys. Lett.* 69, 1966–1968 (1996).
4. O. Heczko, A. Sozinov and K. Ullakko. Giant field-induced reversible strain in magnetic shape memory NiMnGa alloy. *IEEE Trans. Magn.* 36, 3266–3268 (2000).
5. A. Sozinov, A. A. Likhachev, N. Lanska and K. Ullakko. Giant magnetic-field induced strain in NiMnGa seven-layered martensitic phase. *Appl. Phys. Lett.* 80, 1746–1748 (2002).
6. N. Glavatska, G. Mogilniy, I. Glavatsky, S. Danilkin, D. Hohlwein, A. Beskrovnij, O. Söderberg and V. K. Lindroos. Temperature dependence of martensite structure and its effect on magnetic-field-induced strain in Ni₂MnGa magnetic shape memory alloys. *J. de Physique IV* 112, 963–967 (2003).
7. P. Mullner, V. A. Chernenko and G. Kosterz, A microscopic approach to the magnetic-field-induced deformation of martensite (magnetoplasticity). *J. Magn. Magn. Mater.* 267, 325–334 (2003).
8. O. Söderberg, A. Sozinov, Y. Ge, S.-P. Hannula and V. K. Lindroos. Giant magnetostrictive materials. In: Buschow J (ed.) *Handbook of Magnetic Materials*, Elsevier Science, Amsterdam, Vol. 16, pp. 1–39 (2006).
9. S. J. Murray, M. A. Marioni, A. M. Kukla, J. Robinson, R. C. O’Handley and S. M. Allen. Large field-induced strain in single crystalline Ni–Mn–Ga ferromagnetic shape memory alloy. *J. Appl. Phys.* 87, 5774–5776 (2000).
10. I. Takeuchi, O. O. Famodu, J. C. Read, M. A. Aronova, K. S. Chang, C. Craciunescu, S. E. Lofland, M. Wuttig, F. C. Wellstood, L. Knauss and A. Orozco. Identification of novel compositions of ferromagnetic shape-memory alloys using composition spreads. *Nat. Mater.* 2, 180–184 (2003).
11. M. Wuttig, J. Li and C. Craciunescu. A new ferromagnetic shape memory alloy system. *Scr. Mater.* 44, 2393–2397 (2001).
12. A. N. Lavrov, S. Komiya, Y. Ando. Antiferromagnets: Magnetic shape-memory effects in a crystal. *Nature* 418, 385(2002).
13. S. Raasch, M. Doerr, A. Kreyssig, M. Loewenhaupt, M. Rotter, J. Hoffmann. Magnetic shape memory effect in the paramagnetic state in RCu₂ (R = rare earth) antiferromagnets. *Phys. Rev. B* 73, 064402 (2006).

14. K. Ullakko. Magnetically controlled shape memory alloys: A new class of actuator materials. *J. Mater. Eng. Perform.* 5, 405–409, (1996).
15. A. N. Vasil'ev, A. D. Bozhko, V. V. Khovailo, I. E. Dikshtein, V. G. Shavrov, V. D. Buchelnikov, M. Matsumoto, S. Suzuki, T. Takagi and J. Tani. Structural and magnetic phase transitions in shape-memory alloys $\text{Ni}_{2+x}\text{Mn}_{1-x}\text{Ga}$. *Phys. Rev. B* 59, 1113 (1999).
16. A. N. Vasil'ev, V. D. Buchel'nikov, T. Takagi, V. V. Khovailo, E. I. Estrin. *Physics Uspekhi* 46(6), 559–588 (2003).
17. K. F. Hane and T. W. Shield. Symmetry and microstructure in martensites. *Philos. Mag. A: Phys. Condens. Matter* 78, 1215–1252 (1998).
18. L. Mañosa and A. Planes. Structural and magnetic phase transitions in Ni–Mn–Ga shape-memory alloys. *Adv. Solid State Phys.* 40, 361–374 (2000).
19. M. S. Wechsler, D. S. Lieberman and T. A. Read. On the Theory of the formation of martensite. *Trans. AIME* 197, 1503–1515, (1953).
20. P. J. Brown, A. Y. Bargawi, J. Crangle, K.-U. Neumann and K. R. A. Ziebeck. Direct observation of a band Jahn-Teller effect in the martensitic phase transition of Ni_2MnGa . *J. Phys. – Cond. Mat.* 11, 4715–4722 (1999).
21. O. Heczko, A. Sozinov, N. Lanska, O. Söderberg and K. Ullakko. Temperature variation of structure and magnetic properties of Ni–Mn–Ga magnetic shape memory alloys. *J. Magn. Magn. Mater.* 242–245, 1446 (2002).
22. O. Heczko, P. Svec, N. Lanska and K. Ullakko. Magnetic properties of Ni–Mn–Ga ribbon prepared by rapid solidification. *IEEE Trans. Mag.* 38, 2841 (2002).
23. Sôshin Chikazumi. *Physics of Ferromagnetism*, 2nd edition, Clarendon Press, Oxford (1997) ISBN 0198517769.
24. E. Du T. De Lacherisserie. *Magnetostriction: Theory and Applications of Magnetoelasticity*, CRC Press (1993).
25. R. Kainuma, Y. Imano, W. Ito, Y. Sutou, H. Morito, S. Okamoto, O. Kitakami, K. Oikawa, A. Fujita, T. Kanomata and K. Ishida. Magnetic-field-induced shape recovery by reverse phase transformation. *Nature* 439, 957 (2006).
26. Cherechukin, A. A. et al. Shape memory effect due to magnetic field-induced thermoelastic martensitic transformation in polycrystalline Ni–Mn–Fe–Ga alloy. *Phys. Lett. A* 291, 175 (2001).
27. J. Liu, N. Scheerbaum, D. Hinz and O. Gutfleisch. Magnetostructural transformation in Ni–Mn–In–Co ribbons. *Appl. Phys. Lett.* 92, 162509 (2008).
28. O. Heczko. Magnetic shape memory effect and magnetization reversal. *J. Magn. Magn. Mater.* 290–291, 787–794 (2005).
29. L. Straka and O. Heczko. Superelastic response of Ni–Mn–Ga martensite in magnetic fields and a simple model. *IEEE Trans. Magn.* 39, 3402 (2003).
30. P. Müllner, V. A. Chernenko and G. Kostorz. Stress-induced twin rearrangement resulting in change of magnetization in a Ni–Mn–Ga ferromagnetic martensite. *Scripta Mater* 49, 129 (2003).
31. X. Ren, Large electric-field-induced strain in ferroelectric crystals by point-defect mediated reversible domain switching. *Nat. Mater.* 3, 91 (2004).
32. A. L. Roytburd, T. S. Kim, Quanmin Su, J. Slutsker and M. Wuttig. Martensitic transformation in constrained films. *Acta Mater.* 46(14), 5095–5107 (1998).
33. H. H. Liebermann and C. D. Graham Jr. Plastic and magnetoplastic deformation of Dy single crystals. *Acta Metallurgica* 25, 715 (1977).
34. P. Müllner, V. A. Chernenko and G. Kostorz. Large cyclic magnetic-field-induced deformation in orthorhombic (14 M) Ni–Mn–Ga martensite. *J. Appl. Phys.* 95, 1531 (2004).
35. J. J. Rhyne, S. Foner, E. J. McNiff, Jr. and R. Doclo. Rare earth metal single crystals. I. High-field properties of Dy, Er, Ho, Tb, and Gd. *J. Appl. Phys.* 39, 892 (1968).
36. R. D. James and M. Wuttig. Magnetostriction of martensite. *Phi. Mag. A* 77, 1273 (1998).
37. T. Kakeshita, et al. Giant magnetostriction in an ordered Fe_3Pt single crystal exhibiting a martensitic transformation. *Appl. Phys. Lett.* 77, 1502–1504 (2000).

38. J. Pons, et al. Ferromagnetic SMA's: Alternatives to Ni-Mn-Ga. *Mat. Sci. Eng. A* 481, 57 (2008).
39. T. Sakamoto, T. Fukuda, T. Kakeshita, T. Takeuchi and K. Kishio. Magnetic field-induced strain in iron-based ferromagnetic shape memory alloys. *J. Appl. Phys.* 93, 8647–8649 (2003).
40. Y. Sutou, et al. Magnetic and martensitic transformations of NiMnX (X = In, Sn, Sb) ferromagnetic shape memory alloys. *Appl. Phys. Lett.* 85, 4358–4360 (2004).
41. J. Liu, N. Scheerbaum, D. Hinz and O. Gutfleisch. Martensitic transformation and magnetic properties in NiFeGaCo magnetic shape memory alloys. *Acta Materialia* 56, Nr. 13, S. 3177–3186 (2008).
42. K. Oikawa, et al. Promising ferromagnetic Ni–Co–Al shape memory alloy system. *Appl. Phys. Lett.* 79, 3290–3292 (2001).
43. K. Oikawa, et al. Magnetic and martensitic phase transitions in ferromagnetic Ni–Ga–Fe shape memory alloys. *Appl. Phys. Lett.* 81, 5201–5203 (2002).
44. H. Morito, A. Fujita, K. Fukamichi, R. Kainuma, K. Ishida and K. Oikawa. Magnetic-field-induced strain of Fe–Ni–Ga in single-variant state. *Appl. Phys. Lett.* 83, 4993 (2003).
45. H. Morito, A. Fujita, K. Oikawa, K. Ishida, K. Fukamichi and R. Kainuma. Stress-assisted magnetic-field-induced strain in Ni–Fe–Ga–Co ferromagnetic shape memory alloys. *Appl. Phys. Lett.* 90, 062505 (2007).
46. J. G. Booth. Ch. 3, Heusler alloys in *Ferromagnetic Materials* Vol. 4, edited by E. P. Wohlfarth and K. H. J. Buschow. Elsevier, Amsterdam, (1988).
47. P. J. Webster. Heusler alloys. *Contemporary Physics* 10, 559–577 (1969).
48. P. J. Webster, K. R. A. Ziebeck, S. L. Town and M. S. Peak. Magnetic order and phase transformation in Ni₂MnGa alloy. *Philos. Mag. B: Phys. Condens. Matter: Statistical Mechanics, Electronic, Optical and Magnetic Properties* 49, 295–310 (1984).
49. V. V. Khovailo, T. Takagi, A. N. Vasilev, H. Miki, M. Matsumoto and R. Kainuma. On order-disorder (L2₁-B2') phase transition in Ni_{2+x}Mn_{1-x}Ga Heusler alloys. *Physica Status Solidi (a)* 183, R1 (2001).
50. P. J. Brown, J. Crangle, T. Kanomata, M. Matsumoto, K.-U. Neumann, B. Ouladdiaf and K. R. A. Ziebeck. The crystal structure and phase transitions of the magnetic shape memory compound Ni₂MnGa. *J. Phys.: Condens. Mat.* 14, 10159 (2002).
51. M. Richard, J. Feuchtwanger, D. Schlagel, T. Lograsso, S. M. Allen and R. C. O'Handley. Crystal structure and transformation behavior of Ni–Mn–Ga martensites. *Scripta Materialia* 54, 1797 (2006).
52. M. Kreissl, K. U. Neumann, T. Stephens and K. R. A. Ziebeck. The influence of atomic order on the magnetic and structural properties of the ferromagnetic shape memory compound Ni₂MnGa. *J. Phys.* 15, 3831 (2003).
53. U. Gaitzsch, M. Potschke, S. Roth, N. Mattern, B. Rellinghaus, L. Schultz. Structure formation in martensitic Ni₅₀Mn₃₀Ga₂₀ MSM alloy. *J. Alloys Comp.* 443, 99 (2007).
54. V. V. Khovaylo, V. D. Buchelnikov, R. Kainuma, V. V. Koledov, M. Ohtsuka, V. G. Shavrov, T. Takagi, S. V. Taskaev and A. N. Vasilev. Phase transitions in Ni_{2+x}Mn_{1-x}Ga with a high Ni excess. *Phys. Rev. B* 72, 224408 (2005).
55. G. D. Liu, J. L. Chen, Z. H. Liu, X. F. Dai, G. H. Wu, B. Zhang and X. X. Zhang. Martensitic transformation and shape memory effect in a ferromagnetic shape memory alloy: Mn₂NiGa. *Appl. Phys. Lett.* 87, 262504 (2005).
56. Chernenko V. A., Segui C., Cesari E., Pons J. and Kokorin V. V. Sequence of martensitic transformations in Ni–Mn–Ga alloys. *Phys. Rev. B* 57, 2659–2662 (1998).
57. V. A. Chernenko, E. Cesari, V. V. Khovailo, J. Pons, C. Segui and T. Tagaki. Intermartensitic phase transformations in Ni–Mn–Ga studied under magnetic field. *J. Magn. Magn. Mater.* 290, 871 (2005).
58. N. Lanska, O. Söderberg, A. Sozinov, Y. Ge, K. Ullakko and V. K. Lindroos. Composition and temperature dependence of the crystal structure of Ni–Mn–Ga alloys. *J. Appl. Phys.* 95, 8074 (2004).

59. X. Jin, M. Marioni, D. Bono, S. M. Allen, R. C. O'Handley and T. Y. Hsu. Empirical mapping of Ni–Mn–Ga properties with composition and valence electron concentration. *J. Appl. Phys.* 91, 8222 (2002).
60. P. Entel, V. D. Buchelnikov, V. V. Khovailo, et al. Modelling the phase diagram of magnetic shape memory Heusler alloys. *J. Phys. D-Appl. Phys.* 39(5), 865 (2006).
61. L. Manosa, A. G. Comas, E. Obradó and A. Planes. Premartensitic phase transformation in the Ni₂MnGa shape memory alloy. *Mat. Sci. Eng. A* 273–276, 329–332 (1999).
62. L. Manosa, A. Gonzalez-Comas, E. Obradó, A. Planes, V. A. Chernenko, V. V. Kokorin and E. Cesari. Anomalies related to the TA₂-phonon-mode condensation in the Heusler Ni₂MnGa alloy. *Phys. Rev. B*, 55(17), 11068, (1997).
63. L. Manosa, A. Planes, J. Zarestky, T. A. Lograsso, D. L. Schlagel and C. Stassis. Phonon softening in Ni–Mn–Ga alloys. *Phys. Rev. B*, 64, 024305 (2001).
64. V. V. Martynov and V. V. Kokorin. The crystal structure of thermally- and stress-induced Martensites in Ni₂MnGa single crystals. *J. Phys. III France* 2, 739 (1992).
65. V. A. Chernenko, V. L'Vov, J. Pons and E. Césari. Superelasticity in high-temperature Ni–Mn–Ga alloys. *J. Appl. Phys.* 93, 2394–2399 (2003).
66. O. Söderberg, K. Koho, T. Sammi, X. W. Liu, A. Sozinov, N. Lanska and V. K. Lindroos. Effect of the selected alloying on Ni–Mn–Ga alloys. *Mat. Sci. Eng. A* 378/1–2, 386–393 (2004).
67. G. H. Wu, W. H. Wang, J. L. Chen, L. Ao, Z. H. Liu, W. S. Zhan, T. Liang and H. B. Xu. Magnetic properties and shape memory of Fe-doped Ni₅₂Mn₂₄Ga₂₄ single crystals. *Appl. Phys. Lett.* 80, 634 (2002).
68. Y. Ge, O. Söderberg, N. Lanska, A. Sozinov, K. Ullakko and V. K. Lindroos. Crystal structure of three NiMnGa alloys in powder and bulk materials. *J. de Physique IV* 112, 921 (2003).
69. J. Pons, V. A. Chernenko, R. Santamarta and E. Césari. Crystal structure of martensitic phases in Ni–Mn–Ga shape memory alloys. *Acta Materialia* 48, 3027–3038 (2000).
70. B. Wedel, M. Suzuki, Y. Murakami, C. Wedel, T. Suzuki, D. Shindo and K. Itagaki. Low temperature crystal structure of Ni–Mn–Ga alloys. *J. Alloys Comp.* 290, 137–143 (1999).
71. A. T. Zayak, P. Entel, J. Enkovaara, A. Ayuela and R. M. Nieminen. First principles investigations of homogeneous lattice-distortive strain and shuffles in Ni₂MnGa. *J. Phys.: Condens. Mat.* 15, 159–164 (2003).
72. K. Zasimchuk, V. V. Kokorin, V. V. Martynov, A. V. Tkachenko and V. A. Chernenko. Crystal structure of martensite in Heusler alloy Ni₂MnGa. *Phys. Met. Metall.* 69, 104 (1990)
73. J. Pons, R. Santamarta, V. A. Chernenko and E. Césari. HREM study of different martensitic phases in Ni–Mn–Ga alloys. *Mater. Chem. Phys.* 81, 457 (2003).
74. J. Pons, R. Santamarta, E. Césari and V. A. Chernenko. Martensitic structures in Ni–Mn–Ga. *Appl. Cryst.* 18, 186–199 (2001).
75. A. Zheludev, S. M. Shapiro P. Wochner and L. E. Tanner. Precursor effects and premartensitic transformation in Ni₂MnGa. *Phys. Rev. B* 54, 15045–15050 (1996).
76. A. Ayuela, J. Enkovaara and R. M. Nieminen. Ab initio study of tetragonal variants in Ni₂MnGa alloy. *J. Phys. – Cond. Matt.* 14, 5325 (2002).
77. J. Enkovaara, A. Ayuela, A. T. Zayak, P. Entel, L. Nordstrom, M. Dube, J. Jalkanen, J. Impola and R. M. Nieminen. Magnetically driven shape memory alloys. *Mater. Sci. Eng. A* 378, 52 (2004).
78. M. Thomas, O. Heczko, J. Buschbeck, U. K. Röbber, J. McCord, N. Scheerbaum, L. Schultz and S. Fähler. Magnetically induced reorientation of martensite variants in constrained epitaxial Ni–Mn–Ga films grown on MgO (100). *New J. Phys.* 10, 023040 (2008).
79. L. Straka, O. Heczko, V. Novak and N. Lanska. Study of austenite-martensite transformation in Ni–Mn–Ga magnetic shape memory alloy. *J. de Physique IV – Proceedings* 112, 911 (2003).

80. T. Kanomata, K. Shirakawa and T. Kaneko. Effect of hydrostatic pressure on the Curie temperature of the Heusler alloys nickel-manganese-Z (Ni₂MnZ) (Z = aluminum, gallium, indium, tin and antimony). *J. Magn. Magn. Mater.* 65, 76–82 (1987).
81. J. Enkovaara, O. Heczko, A. Ayuela and R. M. Nieminen. Coexistence of ferromagnetic and antiferromagnetic order in Mn-doped Ni₂MnGa. *Phys. Rev. B* 67, 212405 (2003).
82. O. Heczko, L. Straka and K. Ullakko. Relation between structure, magnetization process and magnetic shape memory effect of various martensites occurring in Ni–Mn–Ga alloys. *J. de Physique IV*, 112, 959 (2003).
83. R. Tickle and R. D. James. Magnetic and magnetomechanical properties of Ni₂MnGa. *J. Magn. Magn. Mat.* 195, 627 (1999).
84. L. Straka and O. Heczko. Magnetic anisotropy in Ni–Mn–Ga martensites. *J. Appl. Phys.* 92, 8636 (2003).
85. L. Straka, O. Heczko and N. Lanska. Magnetic properties of various martensitic phases in Ni–Mn–Ga alloy. *IEEE Trans. Magn.* 38, 2835–2837 (2002).
86. F. Albertini, L. Pareti, A. Paoluzi, L. Morellon, P. A. Algarabel, M. R. Ibarra and Righi L. Composition and temperature dependence of the magnetocrystalline anisotropy in Ni_{2+x}Mn_{1+y}Ga_{1+z} (x+y+z=0) Heusler alloys. *Appl. Phys. Lett.* 81, 4032 (2002).
87. J. Enkovaara, A. Ayuela, L. Nordstrom and R. M. Nieminen. Structural, thermal, and magnetic properties of Ni₂MnGa. *J. Appl. Phys.* 91, 7798 (2002).
88. A. Sozinov, A. A. Likhachev and K. Ullakko. Magnetic and magnetomechanical properties of Ni–Mn–Ga alloys with easy axis and easy plane of magnetization. In: C.S. Lynch (Ed.) *Proceedings of SPIE*, 4333, 189–196 (2001).
89. O. Heczko and L. Straka. Compositional dependence of structure, magnetization and magnetic anisotropy in Ni–Mn–Ga magnetic shape memory alloys, *J. Magn. Magn. Mat.* 272–276, 2045 (2004).
90. O. Heczko and L. Straka. Determination of ordinary magnetostriction in Ni–Mn–Ga magnetic shape memory alloy, *J. Magn. Magn. Mat.* 290–291, 846 (2005).
91. O. Heczko, L. Straka, I. Aaltio and S.-P. Hannula. Strain and concurrent magnetization changes in magnetic shape memory Ni–Mn–Ga single crystals – experiment and model. *Mat. Sci. Eng. A* 481–482, 283 (2008).
92. O. Heczko, L. Straka and S.-P. Hannula. Stress dependence of magnetic shape memory effect and its model. *Mat. Sci. Eng. A* 438–440, 1003–1006 (2006).
93. O. Heczko, K. Jurek and K. Ullakko. Magnetic properties and magnetic domain structure of magnetic shape memory Ni–Mn–Ga alloy. *J. Magn. Magn. Mat.* 226–230, 996–998 (2001).
94. Y. Ge, O. Heczko, O. Söderberg and V. K. Lindroos. Various magnetic domain structures in a Ni–Mn–Ga martensite exhibiting magnetic shape memory effect. *J. Appl. Phys.* 96, 2159 (2004).
95. Y. Ge, O. Heczko, O. Söderberg and S.-P. Hannula. Direct optical observation of magnetic domains in Ni–Mn–Ga martensite. *Appl. Phys. Lett.* 89, 082502 (2006).
96. Y. W. Lai, N. Scheerbaum, D. Hinz, O. Gutfleisch, R. Schäfer, L. Schultz and J. McCord. Absence of magnetic domain wall motion during magnetic field induced twin boundary motion in bulk magnetic shape memory alloys. *Appl. Phys. Lett.* 90, 192504 (2007)
97. H. D. Chopra, C. Ji and V. V. Kokorin. Magnetic-field-induced twin boundary motion in magnetic shape-memory alloys. *Phys. Rev. B* 61, R14913 (2000).
98. D. I. Paul, W. McGehee, R. C. O’Handley and M. Richard. Ferromagnetic shape memory alloys: A theoretical approach. *J. Appl. Phys.* 101, 123917 (2007).
99. V. Soolshenko, N. Lanska and K. Ullakko. Structure and twinning stress of martensites in non-stoichiometric Ni₂MnGa single crystal. *J. de Physique IV France* 112, 947 (2003).
100. L. Dai, J. Cullen and M. Wuttig. Intermartensitic transformation in a NiMnGa alloy. *J. Appl. Phys.* 95, 6957–6959 (2004).
101. I. Aaltio, O. Heczko, O. Söderberg and S.-P. Hannula, ch. 20. Shape Memory alloys and Effects: Types, Functions, Modeling and Applications (Magnetically Controlled Shape

- Memory Alloys). In M. Schwartz (Ed.), *Smart Materials*, CRC Press, Taylor and Francis Group, LLC (2009).
102. M. Stipcich, L. Manosa, A. Planes, M. Morin, J. Zarestky, T. A. Lograsso and C. Stassis. Elastic constants of Ni–Mn–Ga magnetic shape memory alloys. *Phys. Rev B*, 70, 054115 (2004).
 103. L. Straka, V. Novak, M. Landa and O. Heczko. Acoustic emission of Ni–Mn–Ga magnetic shape memory alloy in different straining modes. *Mat. Sci. Eng. A* 374, 263–269 (2004).
 104. P. Molnar, P. Sittner, P. Lukas, S-P. Hannula and O. Heczko. Stress-induced martensite variant reorientation in magnetic shape memory Ni–Mn–Ga single crystal studied by neutron diffraction. *Smart Mater. Struct.* 17, 035014 (5 pp) (2008).
 105. P. Molnar, P. Sittner, V. Novak and O. Heczko. Magnetic field induced reorientation and mechanical training process in NiMnGa single crystal, Proc. ICOMAT 2008, Santa Fe, to be published in TMR.
 106. O. Heczko, A. Soroka and S.-P. Hannula. Magnetic shape memory effect in thin foils. *Appl. Phys. Lett.* 93, 022503, (2008).
 107. P. Molnar, P. Sittner, V. Novak, J. Prokleska, V. Sechovsky, B. Ouladdiaf, S. P. Hanulla and O. Heczko. In situ neutron diffraction study of magnetic field induced martensite reorientation in Ni–Mn–Ga under constant stress. *J. Phys.: Condens. Mat.* 20, 104224 (2008).
 108. O. Heczko, K. Prokes and S-P. Hannula. Neutron diffraction studies of magnetic shape memory Ni–Mn–Ga single crystal. *J. Magn. Magn. Mater.* 316, 386 (2007).
 109. M. L. Richard. Systematic analysis of the crystal structure, chemical ordering and microstructure of Ni–Mn–Ga ferromagnetic shape memory alloys. Ph.D. thesis, MIT (2005).
 110. L. Dai, M. Wuttig and E. Pagounis. Twin stabilization in a ferromagnetic shape memory alloy. *Scripta Materialia* 55, 807–810 (2006).
 111. L. Straka, O. Heczko, H. Hänninen. Activation of magnetic shape memory effect in Ni–Mn–Ga alloys by mechanical and magnetic treatment. *Acta Materialia* 56, 5492–5499 (2008).
 112. D. I. Paul, J. Marquiss and D. Quattrochi. Theory of magnetization: Twin boundary interaction in ferromagnetic shape memory alloys. *J. Appl. Phys.* 93, 4561 (2003).
 113. R. C. O’Handley, D. I. Paul, M. Marioni, C. P. Henry, M. Richard, P. G. Tello and S. M. Allen. Micromagnetic and micromechanics of Ni–Mn–Ga actuation. *J. Phys. IV France*, 112, 973 (2003).
 114. E. V. Gomonaj and V. A. Lvov. Martensitic phase transition with two-component order parameter in a stressed cubic crystal. *Phase Transitions* 41, 9 (1994).
 115. A. A. Likhachev and K. Ullakko. Magnetic-field-controlled twin boundaries motion and giant magneto-mechanical effects in Ni–Mn–Ga shape memory alloy. *Phys. Lett. A* 275, 142 (2000).
 116. A. A. Likhachev, A. Sozinov and K. Ullakko. Different modeling concepts of magnetic shape memory and their comparison with some experimental results obtained in Ni–Mn–Ga. *Mater. Sci. Eng. A* 378, 513–518 (2004),.
 117. R. C. O’Handley. Model for strain and magnetization in magnetic shape memory alloys. *J. Appl. Phys.* 83, 3263–3270 (1998).
 118. B. Kiefer and D. C. Lagoudas. Magnetic field-induced martensitic variant reorientation in magnetic shape memory alloys, *Philos. Mag.* 85, 4289 (2005).
 119. N. Okamoto, T. Fukuda and T. Kakeshita. Magnetocrystalline anisotropy constant and twinning stress in martensite phase of Ni–Mn–Ga. *Mat. Sci. Eng. A* 438, 948 (2006).
 120. J. Kiang and L. Tong. Modelling of magneto-mechanical behaviour of Ni–Mn–Ga single crystals. *J. Magn. Magn. Mater.* 292, 394 (2005).
 121. R. C. O’Handley, S. J. Murray, M. Marioni, H. Nembach and S. M. Allen. Phenomenology of giant magnetic-field-induced strain in ferromagnetic shape-memory materials, *J. Appl. Phys.* 87, 4712 (2000).

122. R. C. O'Handley and S. M. Allen. Ferromagnetic shape memory materials. *Encyclopedia of Smart Materials*, John Wiley and Sons, New York 936–951 (2001). And R. C. O'Handley, D. I. Paul, S. M. Allen, M. Richard, J. Feuchtwanger, B. Peterson, R. Techapiesancharoenkij, M. Barandiaran, P. Lazpita. Model for temperature dependence of field-induced strain in ferromagnetic shape memory alloys, *Mat. Sci. Eng. A* 438–440, 445–449 (2006).
123. A. Sozinov, A. A. Likhachev, N. Lanska, O. Söderberg, K. Koho, K. Ullakko and V. K. Lindroos. Stress-induced variant rearrangement in Ni–Mn–Ga single crystals with nonlayered tetragonal martensitic structure. *J. Physique IV*, 115, 127 (2004).
124. A. Sozinov, A. A. Likhachev, N. Lanska, O. Söderberg, K. Ullakko and V. K. Lindroos. Stress- and magnetic-field-induced variant rearrangement in Ni–Mn–Ga single crystals with seven-layered martensitic structure. *Mat. Sci. Eng. A* 378, 401 (2006).
125. L. Straka and O. Heczko. Reversible 6% strain of Ni–Mn–Ga martensite using opposing external stress in static and variable magnetic field. *J. Magn. Magn. Mat.* 290–291, 829 (2005).
126. L. Straka. Magnetic and magneto-mechanical properties of Ni–Mn–Ga magnetic shape memory alloys. PhD thesis, TKK Helsinki (2007).
127. L. Straka and O. Heczko. Magnetization changes in Ni–Mn–Ga magnetic shape memory single crystal during compressive stress reorientation. *Scripta Materialia* 54, 1549–1552 (2006).
128. V. A. Chernenko, V. A. L'vov, P. Mullner and G. Kostorz, T. Takagi. Magnetic-field-induced superelasticity of ferromagnetic thermoelastic martensites: Experiment and modeling. *Phys. Rev. B* 69, 134410 (2004).
129. T. Kakeshita, T. Fukuda and T. Takeuchi. Magneto-mechanical evaluation for twinning plane movement driven by magnetic field in ferromagnetic shape memory alloys. *Mat. Sci. Eng. A* 438–440, 12 (2006).
130. R. C. O'Handley, D. I. Paul, S. M. Allen, M. Richard, J. Feuchtwanger, B. Peterson, R. Techapiesancharoenkij, M. Barandiaran and P. Lazpita. Model for temperature dependence of field-induced strain in ferromagnetic shape memory alloys. *Mat. Sci. Eng. A* 438–440, 445–449 (2006).
131. O. Heczko and K. Ullakko. Effect of temperature on magnetic properties of Ni–Mn–Ga Magnetic Shape Memory (MSM) alloys. *IEEE Trans. Magn.* 37, 2672 (2001).
132. L. Straka, O. Heczko and S.-P. Hannula. Temperature dependence of reversible field-induced strain in Ni–Mn–Ga single crystal. *Scripta Mat.* 54, 1497 (2006).
133. N. Glavatska, G. Mogylny and S. Danilkin. Temperature dependence of lattice parameters in martensite and effect of the external magnetic field on martensite structure in Ni₂MnGa studied in-situ with neutron diffraction. *Mater. Sci. Forum* 443–444, 397–400 (2004).
134. O. Heczko and L. Straka. Temperature dependence and temperature limits of magnetic shape memory effect. *J. Appl. Phys.* 94(12), 7139–7143 (2003).
135. O. Soderberg, L. Straka, O. Heczko, V. Novak and V. K. Lindroos. Tensile/compressive behavior of non-layered tetragonal NiMnGa alloy. *Mat. Sci. Eng. A* 386, 27 (2004).
136. K. Ullakko, Y. Ezer, A. Sozinov, G. Kimmel, P. Yakovenko, V. K. Lindroos. Magnetic-field-induced strains in polycrystalline Ni–Mn–Ga at room temperature. *Scripta Mat.* 44, 475 (2001).
137. U. Gaitzsch, M. Potschke, S. Roth, B. Rellinghaus, L. Schultz. A 1% magnetostrain in polycrystalline 5M Ni–Mn–Ga. *Acta Materialia* 57, 365–370 (2009).
138. J. Pons, C. Seguí, V. A. Chernenko, E. Cesari, P. Ochin and R. Portier. Transformation and ageing behaviour of melt-spun Ni–Mn–Ga shape memory alloys. *Mat. Sci. Eng. A*, 273–275, 315 (1999).
139. O. Heczko, M. Thomas, R. Niemann, L. Schultz and S. Fähler. Magnetically induced martensite transition in freestanding epitaxial Ni–Mn–Ga films, *Appl. Phys. Lett.* 94, 152513 (2009).
140. J. Feuchtwanger, N. Vidal, J. M. Barandiaran, J. Gutierrez, T. Hansen, M. Peel, C. Mondelli, R. C. O'Handley and S. M. Allen. Rearrangement of twin variants in ferromagnetic shape

- memory alloy-polyurethane composites studied by stroboscopic neutron diffraction. *J. Phys. Condens. Matt.* 20, 4247 (2008). A. Berkowitz, UCSD, personal communication, 2005.
141. J. Feuchtwanger, M. L. Richard, Y. J. Tang, A. E. Berkowitz, R. C. O'Handley and S. M. Allen. Large energy absorption in Ni–Mn–Ga/polymer composites. *J. Appl. Phys.* 97, 10M319 (2005).
 142. N. Scheerbaum, D. Hinz, O. Gutfleisch, K.-H. Muller and L. Schultz. Textured polymer bonded composites with Ni–Mn–Ga magnetic shape memory particles. *Acta Mat.* 55, 2707 (2007).
 143. N. Scheerbaum, O. Heczko, J. Liu, D. Hinz, L. Schultz and O. Gutfleisch. Magnetic field-induced twin boundary motion in polycrystalline Ni–Mn–Ga fibres. *New J. Phys.* 10, 073002 (2008).
 144. N. Scheerbaum, D. Hinz, O. Gutfleisch, W. Skrotzki and L. Schultz. Compression-induced texture change in NiMnGa–polymer composites observed by synchrotron radiation. *J. Appl. Phys.*, 101 09C501 (2007).
 145. F. J. Castaño, B. Nelson-Cheeseman, R. C. O'Handley, C. A. Ross, C. Redondo and F. Castaño. Structure and thermomagnetic properties of polycrystalline Ni–Mn–Ga thin films. *J. Appl. Phys.*, 93(10), 8492(2003).
 146. V. A. Chernenko, M. Hagler, P. Müllner, V. M. Kniazkyi, V. A. L'vov, M. Ohtsuka and S. Besseghini. Magnetic susceptibility of martensitic Ni–Mn–Ga film. *J. Appl. Phys.* 101, 053909 (2007).
 147. J. W. Dong, et al. Molecular beam epitaxy growth of ferromagnetic single crystal (001) Ni₂MnGa on (001) GaAs. *Appl. Phys. Lett.* 75, 1443 (1999).
 148. G. Jakob and H. J. Elmers. Epitaxial films of the magnetic shape memory material Ni₂MnGa. *J. Magn. Magn. Mater.* 310, 2779 (2007).
 149. O. Heczko, M. Thomas, J. Buschbeck, L. Schultz and S. Fähler. Epitaxial Ni–Mn–Ga films deposited on SrTiO₃ and evidence of magnetically induced reorientation of martensitic variants at room temperature. *Appl. Phys. Lett.* 92, 1 (2008).
 150. M. Thomas, O. Heczko, J. Buschbeck, Y.W. Lai, J. McCord, L. Schultz and S. Fähler. Stray field induced actuation mode of freestanding magnetic shape memory films, *Adv. Mat.* (2009), DOI: 10.1002/adma.200900469.
 151. Y. Boonyongmaneerat, M. Chmielus, D. C. Dunand and P. Mullner. Increasing magneto-plasticity in polycrystalline Ni–Mn–Ga by reducing internal constraints through porosity. *Phys. Rev. Lett.* 99, 247201 (2007).
 152. I. Aaltio, M. Lahelin, O. Soderberg, O. Heczko, B. Lofgren, Y. Ge, J. Seppala and S.-P. Hannula. Temperature dependence of the damping properties of Ni–Mn–Ga alloys. *Mat. Sci. Eng. A* 481–482, 314–317 (2008).
 153. I. Aaltio, K. P. Mohanchandra, O. Heczko, M. Lahelin, Y. Ge, G.P. Carman, O. Soderberg, B. Lofgren J. Seppala and S.-P. Hannula. Temperature dependence of mechanical damping in Ni–Mn–Ga austenite and non-modulated martensite. *Scripta Mat.* 59, 550 (2008).
 154. I. Suorsa, J. Tellinen, K. Ullakko and E. Pagounis. Voltage generation induced by mechanical straining in magnetic shape memory materials. *J. Appl. Phys.* 95, 8054 (2004).
 155. I. Karaman, B. Basaran, H. E. Karaca, A. I. Karsilayan and Y. Chumlyakov. Energy harvesting using martensite variant reorientation mechanism in a NiMnGa magnetic shape memory alloy. *Appl. Phys. Lett.* 90, 172505 (2007).
 156. V. V. Kokorin, V. A. Chernenko, V. I. Val'kov, S. M. Konoplyuk and E. A. Khapalyuk. Magnetic transformation in Ni₂MnGa compounds. *Phys. Solid State* 37, 2049–2051 (1995).
 157. M. Pasquale, C. P. Sasso, L. H. Lewis, L. Giudici, T. Lograsso, and D. Schlagel. Magnetostructural transition and magnetocaloric effect in Ni₅₅Mn₂₀Ga₂₅ single crystals. *Phys. Rev B*, 72, 094435 (2005).
 158. J. Marcos, A. Planes, L. Manosa, F. Casanova, X. Batlle, A. Labarta and B. Martinez. Magnetic field induced entropy change and magnetoelasticity in Ni–Mn–Ga alloys. *Phys. Rev B*, 66, 224413 (2002).

159. O. Soderberg, I. Aaltio, Y. Ge, O. Heczko and S.-P. Hannula. Ni–Mn–Ga multifunctional compounds. *Mat. Sci. Eng. A* 481–482, 80–85 (2008).
160. N. Glavatska. Origin of the time-dependent magnetoplasticity in the Ni–Mn–Ga magnetic shape memory martensites. *Mat. Sci. Eng. A* 481–482, 73–79F (2008).
161. F. Xiong, Y. Liu and E. Pagounis. Thermally induced fracture of single crystal Ni–Mn–Ga ferromagnetic shape memory alloy. *J. Alloys Comp.* 415, 188 (2006).
162. J. Tellinen, I. Suorsa, A. Jääskeläinen, I. Aaltio, K. Ullakko and H. Borgmann (Ed.). *Proc. ACTUATOR 2002*, Bremen, Germany (2002), pp. 566–569.
163. O. Heczko, L. Straka, O. Söderberg and S.-P. Hannula. Magnetic shape memory fatigue, *Smart Structures and Materials 2005: Active Materials: Behavior and Mechanics*, edited by William D. Armstrong, *Proceedings of SPIE Vol. 5761* (2005) p. 513.

Chapter 15

Magnetocaloric Effect and Materials

J.R. Sun, B.G. Shen, and F.X. Hu

Abstract A brief review for magnetocaloric effect (MCE), including its potential application to magnetic refrigeration and the corresponding magnetic materials, has been given. Focuses are recent progresses in the exploration of magnetocaloric materials which exhibit a first-order phase transition, thus a giant MCE. Special issues such as proper approaches to determine the MCE associated with the first-order transition and the effects of lattice and electronic entropies are discussed. The applicability of the giant MCE materials to the magnetic refrigeration near ambient temperature is evaluated.

15.1 Introduction

Magnetic materials can absorb or expel heat in magnetizing or demagnetizing process. This phenomenon is called magnetocaloric effect (MCE). When magnetized, magnetic moments of the materials tend to aligning in parallel. This causes a decrease of magnetic entropy (ΔS), thus a heat release (amounted to $T|\Delta S|$) to environment, where T is temperature. On the contrary, the arrangement of magnetic moments becomes disordered after removing magnetic field. Corresponding to the increase of magnetic entropy, heat from the surroundings has to be absorbed to keep the materials at a constant temperature. The former causes an increase, whereas the latter a decrease of environment temperature. This is the principle based on which magnetic refrigerator works. The MCE of the materials is characterized by two important quantities. The first one is the field-induced isothermal entropy change ΔS and the second one the adiabatic temperature change ΔT_{ad} . There is an approximate relation between ΔS and ΔT_{ad} : $\Delta T_{\text{ad}} \approx T\Delta S/C$, where C is the heat capacity of the materials.

J.R. Sun (✉)

State Key Laboratory for Magnetism, Institute of Physics, Chinese Academy of Sciences,
Beijing 100080, Peoples' Republic of China
e-mail: jrsun@g203.iphy.ac.cn

In addition to the potential application to magnetic refrigeration, the MCE is also fundamentally important for the study of magnetism. It can provide valuable information, which may be unavailable for other techniques, about magnetic transition. It also has a strong impact on physical arguments such as entropy, specific heat, and thermal conduction, etc.

The MCE was first discovered by Warburg in 1881 when studying the magnetic behaviors of Iron [1]. Langevin gave the first theoretical explanation [2]. He found that reversible temperature change generally occurred when the magnetization (M) of a paramagnetic (PM) system altered under applied field. The ones who first foresaw the technological potential of this effect is Debye and Giauque [3, 4]. They pointed out, independently, that ultra-low temperatures could be reached through the reversible temperature change of PM salts with the alternation of magnetic field. The first experiment of magnetic refrigeration was performed in 1933, by Giauque and MacDougall [5]. With the use of this technology, the temperatures below 1 K were successfully gained, which won Giauque the Nobel Prize of 1949. Subsequent work proved that, via adiabatic demagnetizing of nuclear magnetism, ultra-low temperatures in nanokelvin range can be reached [6]. Nowadays, magnetic refrigeration has become one of the basic technologies getting ultra-low temperatures.

In contrast to the success in the ultra-low temperature range, the application of this technique in lifted temperature ranges such as 1.5–20 K, the range for liquid helium, and 20–80 K, the range for liquid hydrogen and liquid nitrogen, is relatively limited. The mature refrigerants for the range from 1.5 to 20 K are the garnets of the formula $R_3M_5O_{12}$ ($R = \text{Nd, Gd, and Dy}$; $M = \text{Ga and Al}$), $\text{Gd}_2(\text{SO}_4)_3 \cdot 8\text{H}_2\text{O}$ [7], $\text{Dy}_3\text{Al}_5\text{O}_{12}$ (DAG) [8]. The most typical material is $\text{Gd}_3\text{Ga}_5\text{O}_{12}$ (GGG), which has been successfully used to the precooling for the preparation of liquid helium. As for the temperature range 20–80 K, the modest refrigerants are Nd, Er, Tm, and RAl_2 ($R = \text{Er, Ho, Dy, Dy}_{0.5}\text{Ho}_{0.5}, \text{Dy}_x\text{Er}_{1-x}, \text{ and GdPd}$), RNi_2 ($R = \text{Gd, Dy, and Ho}$). The RAl_2 -type compounds have obvious advantages over others because of its broad phase transition. For example, $(\text{ErAl}_{2.15})_{0.312}(\text{HoAl}_{2.15})_{0.198}(\text{Ho}_{0.5}\text{Dy}_{0.5}\text{Al}_{2.15})_{0.49}$ has the curie temperature between 10 and 40 K [9] and $(\text{ErAl}_{2.2})_{0.3055}:(\text{HoAl}_{2.2})_{0.1533}(\text{Ho}_{0.5}\text{Dy}_{0.5}\text{Al}_{2.2})_{0.252}$ between 15 and 77 K [10]. A detailed review of the magnetic refrigeration technology and corresponding materials in these temperature ranges has been given by Tishin and Spichkin [11] and will not be repeated here.

Magnetic refrigeration near room temperature is of special interest because of its great social effect and economical benefit. Compared with the technology based on the gas compression/expansion, which is widely used today, magnetic refrigeration is environment friendship and energy saving. It is also a silent cooling technique because of the absence of compressor. The great challenge to room-temperature magnetic refrigeration, in addition to the improvement of refrigerator apparatus, is the lacking of effective refrigerants. Due to the significant increase of heat capacity near the ambient temperature, the heat transferred by each magnetizing–demagnetizing cycling of the refrigerator should be considerably large to guarantee refrigeration efficiency. As a result, most of the materials working at low temperatures cannot be directly utilized, and new materials with great entropy change around the ambient temperature must be explored.

The first milestone in the long march to room-temperature refrigeration is the work of Brown in 1976 [12], which showed that Gd is a reasonable working material near room temperature. Based on this result, Zimm and his colleagues designed the first proof-of-principle magnetic refrigerator in 1998 [13]. This machine worked for 18 months with a coefficient of performance (COP) of 15 and a maximal cooling power of 600 W over a temperature span of 10 K for the field change of 0–5 T. This is the first demonstration that magnetic refrigeration is a competitive cooling technology near room-temperature region. Another important breakthrough is the discovery of giant MCE by Gschneidner and his colleagues in 1997 [14, 15]. It was found that the entropy change of $\text{Gd}_5\text{Si}_2\text{Ge}_2$, for a field variation of 0–5 T, is ~ 18 J/kgK around 280 K, significantly larger than that of Gd (~ 10 J/kgK) under similar conditions. New materials such as $\text{LaFe}_{13-x}\text{Si}_x$ [16, 17], $\text{MnAs}_{1-x}\text{Sb}_x$ ($0 < x < 0.3$) [18], and $\text{MnFeP}_{0.45}\text{As}_{0.55}$ [19] were subsequently reported showing the entropy changes from 18 to 30 J/kgK near the ambient temperature. These achievements stimulated a new wave of MCE research.

A common feature of the giant MCE is that it usually occurs accompanying a first-order magnetic transition. The sharp phase transition and its shift under applied field confine ΔS to a narrow temperature range, which is the apparent reason for the enhancement of MCE. However, several basic problems involved in the MCE arising from the first-order phase transition must be solved. For example, the determination of MCE, the contributions other than magnetic entropy to MCE, and the effects of magnetic/thermal hysteresis as far as practical application being concerned. In this article, we will give first a brief discussion about these problems, then a review for the typical magnetic materials with giant MCE. Special attention has been paid to recent progresses in the MCE researches.

15.2 Theoretical Description of Magnetocaloric Effect

In this section, the general description of the MCE will be discussed. Based on the standard thermodynamics, the differential free energy of a system under magnetic field H , pressure P , and at temperature T will be $dG = VdP - SdT - MdH$. The entropy of the system has the form

$$S(T, H, P) = - \left(\frac{\partial G}{\partial T} \right)_{H, P}, \quad (15.1)$$

and the magnetization the form

$$M(T, H, P) = - \left(\frac{\partial G}{\partial H} \right)_{T, P}. \quad (15.2)$$

Based on Eqs. (15.1) and (15.2), the well-known Maxwell relations can be obtained,

$$\left(\frac{\partial S}{\partial H} \right)_{T, P} = \left(\frac{\partial M}{\partial T} \right)_{H, P} \quad (15.3)$$

In the case of fixed pressure and temperature, we have the following equation:

$$dS = \left(\frac{\partial M}{\partial T} \right)_{H,P} dH. \quad (15.4)$$

The isothermal entropy change can be obtained by integrating Eq. (15.4),

$$\Delta S(T, H, P) = S(T, H, P) - S(T, H = 0, P) = \int_0^H \left(\frac{\partial M}{\partial T} \right)_{H,P} dH \quad (15.5)$$

In general, the entropy change induced by external field is calculated by Eq. (15.5) based on magnetic data $M(T, H)$. In practice, the following formula is also used

$$\Delta S(T, H, P) = \int_0^T \frac{(C_{H,P} - C_{0,P})}{T} dT \quad (15.6)$$

where $C_{H,P}$ and $C_{0,P}$ are the heat capacities in the fields of H and 0, respectively, under a constant pressure of P .

For a simple PM system or a ferromagnetic (FM) system above Curie temperature, $M = C_J H/T$ or $CH/(T-T_C)$, where $C_J = N\mu_B^2 g_J^2 J(J+1)$ is the Curie–Weiss constant. The corresponding magnetic entropy change is $\Delta S = -C_J \Delta H^2/2T^2$ or $-C_J \Delta H^2/2(T-T_C)^2$.

In fact, the entropy of a magnetic material is composed of magnetic entropy S_M , electronic entropy S_E , and lattice entropy S_L . The magnetic entropy of the spin system is determined by the free energy of the magnetic sublattice, and it has the form

$$S_M(T, H) = Nk_B \left[\ln \frac{\sinh(\frac{2J+1}{2J}x)}{\sinh(\frac{1}{2J}x)} - xB_J(x) \right] \quad (15.7)$$

within the mean-field approximation, where $x=gJ\mu_B H/k_B T$, with J being the quantum number of angular momentum, k_B the Boltzmann constant, g the Landé factor, and B_J the Brillouin function. In the high temperature and low-field limit ($x \ll 1$), we have

$$S_M = Nk_B \left[\ln(2J+1) - \frac{1}{2} \frac{C_J H^2}{(T-T_C)^2} \right] \quad (15.8)$$

For a complete order–disorder transition, the magnetic entropy will get its maximal value of $S_M = Nk_B \ln(2J+1)$.

The electronic entropy has the form of $S_E = \gamma T$, where γ is the coefficient of electronic heat capacity. Contribution from electronic entropy can be ignored at high temperatures. Based on the Debye approximation, entropy associated with phonon can be expressed as

$$S_L = R \left[-3 \ln(1 - e^{\theta_D/T}) + 12 \left(\frac{T}{\theta_D} \right)^3 \int_0^{\theta_D/T} \frac{x^3 dx}{e^x - 1} \right] \quad (15.9)$$

where R is the gas constant, and θ_D the Debye temperature. In the case of $T > \theta_D$, a direct estimation indicates that the higher the θ_D is, the smaller the lattice entropy will be. For a first-order transition, contributions of electronic and lattice entropy, which is negligible for a second-order one, cannot be simply ignored due to the discontinuous change of order parameter at T_C .

After a simple derivation, the adiabatic temperature change ΔT_{ad} , upon the variation of external field, can also be obtained. According to the standard thermodynamics, the differential entropy has the form,

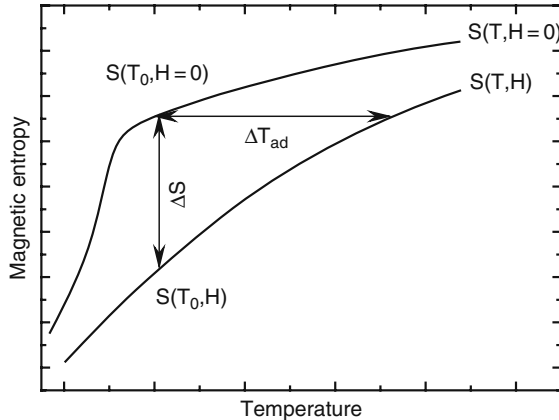
$$dS = \left(\frac{\partial S}{\partial T} \right)_{H,P} dT + \left(\frac{\partial S}{\partial H} \right)_{T,P} dH + \left(\frac{\partial S}{\partial P} \right)_{T,H} dP \quad (15.10)$$

$dS = 0$ under the adiabatic condition, then the adiabatic temperature change will be,

$$dT = - \frac{T}{C_{H,P}} \left(\frac{\partial M}{\partial T} \right)_{H,P} dH, \quad (15.11)$$

where $C_{H,P} = T(\partial S/\partial T)_{H,P}$ denotes heat capacity. Integrating Eq. (15.11) over $H = 0-H$, we get the adiabatic temperature change. Therefore, to obtain ΔT_{ad} , both the magnetic data $M(H,T)$ and the heat capacity are required. As will be discussed later, this is an indirect technique for the determination of ΔT_{ad} .

Fig. 15.1 A schematic for the entropies under the fields of 0 and H, respectively. The horizontal arrow marks adiabatic temperature change, and the vertical one marks the entropy change as magnetic field increases



There is a simple relation between ΔS and ΔT_{ad} as shown by the schematic in Fig. 15.1, which illustrates the entropies under the field of 0 and H, respectively. In the case of increasing magnetic field while keeping temperature constant, the entropy change will be the perpendicular distance of the two curves at T_0 . However, if there is no heat exchange between magnetic material and its surroundings, that is,

$\Delta S = 0$, the application of a magnetic field will cause an increase in temperature (ΔT_{ad}) of the magnetic materials.

15.3 Experimental Determination of Magnetocaloric Effect

The two quantities ΔT_{ad} and ΔS that characterize the MCE of magnetic materials can be determined either directly or indirectly [20].

15.3.1 Direct Measurement of Adiabatic Temperature Change

Without heat exchange with surroundings, temperature of the magnetic materials will suffer from a detectable change while an external field is applied as schematically shown in Fig. 15.1. If the initial temperature of the sample is T_i and the final temperature T_f corresponding to the field increase from 0 to H , the adiabatic temperature change will be $\Delta T_{\text{ad}} = T_f(H) - T_i(0)$.

The adiabatic property of the measuring unit where the sample is settled, the thermal contact between the sample and the temperature sensors, the sensitivity of temperature sensors, influence of external field on temperature sensor, and thermal or magnetic hysteresis of the materials are crucial factors affecting the accuracy of the measurement. The detected ΔT_{ad} is generally smaller than the real value, with an error about 10%.

To minimize the effect of thermal leakage, a field change as rapid as possible is desired for the direct measurement of ΔT_{ad} . It is not easy to realize a rapid field change, especially for the superconducting magnet. As an alternative, the sample is usually moved rapidly into or out of the magnetic field. In the past 80 years, much effort has been devoted to the improvement of experiment accuracy, and various technologies have been developed. A detailed description can be found in the monograph of Tishin and Spichkin [11].

15.3.2 Indirect Measurement of Entropy and Adiabatic Temperature Changes

Direct measurement gives only the information about adiabatic temperature change. To determine isothermal magnetic entropy change, two important indirect methods have to be invoked. The first one is the estimation of ΔS by Eq. (15.5) using the magnetization isotherms collected under different temperatures in the interested region. In reality, an alternative formula, equivalent to Eq. (15.5), is usually used for numerical calculation,

$$\Delta S = \sum_i \frac{M_{i+1} - M_i}{T_{i+1} - T_i} \Delta H_i, \quad (15.12)$$

where M_i and M_{i+1} are the magnetizations at the temperatures T_i and T_{i+1} , respectively. This is the most frequently used approach for the determination of ΔS because of its effectiveness, efficiency, and convenience. The accuracy of the ΔS values thus obtained is influenced by the uncertainty of magnetic moment, temperature, and magnetic field, and the errors are estimated to be 3–10%.

Alternatively, ΔS can also be estimated from the heat capacity data. According to the thermodynamics, there is a relation between entropy and heat capacity

$$S(T, H) = \int_0^T \frac{C(T, H)}{T} dT, \quad (15.13)$$

where the constant pressure P has been omitted. Two S – T relations $S(T, H=0)$ and $S(T, H)$ can be obtained based on Eq. (15.13) using the data collected under corresponding fields, which lead to the isothermal entropy change of the form: $\Delta S(T, H) = S(T, H) - S(T, H=0)$. Noting the one-to-one correspondence between S and T , a $T(S, H)$ relation can be derived from $S(T, H)$. This in turn gives the adiabatic temperature change: $\Delta T_{\text{ad}}(T, H) = T(S, H) - T(S, 0)$.

The accuracy of the ΔS and ΔT_{ad} values thus obtained depends on the precision of heat capacity, and the errors are generally the order of 10%, varying with temperature. Pecharsky and Gschneidner have given a systematic analysis about the uncertainty of the entropy and adiabatic temperature changes experimentally determined [20].

15.4 Magnetocaloric Effect Associated with First-Order Phase Transition

It should be noted that Eq. (15.5) is derived for the second-order phase transition. Because of the discontinuous change of M at T_C for the first-order magnetic transition, it is a problem whether the Maxwell relation can be utilized to determine entropy changes. Two different cases, an idealized and a non-idealized first-order phase transitions, should be considered.

15.4.1 MCE Due to an Idealized First-Order Phase Transition

In this case, Eq. (15.12) can still be used to calculate ΔS . For an idealized first-order transition, that is, the magnetization is a step function of temperature, Sun et al. [21] showed that the Maxwell relation and the Clausius–Clapeyron equation gave similar results. Based on the integrated Maxwell relation, entropy change can be expressed as

$$\Delta S(T) = \int_0^H \left(\frac{\partial M}{\partial T} \right)_{H,P} dH = \int_{T_C(0)}^{T_C(H)} \Delta M \delta(T - T_C) \left(\frac{dT_C}{dH} \right)_{H,P}^{-1} dT_C = \frac{\Delta H \Delta M}{\Delta T_C}, \quad (15.14)$$

where the equalities $(\partial M/\partial T)_{H,P} = -\Delta M\delta(T-T_C)$ and $dT_C/dH = \Delta T_C/\Delta H$ have been used. The right side of Eq. (15.14) is exactly the entropy change predicted by the Clausius–Clapeyron equation. It reveals a constant entropy change in the temperature range between $T_C(0)$ and $T_C(H)$ whereas null otherwise, without the effects from the variation of magnetic order parameter. This work proves the applicability of the Maxwell relation to first-order phase transition.

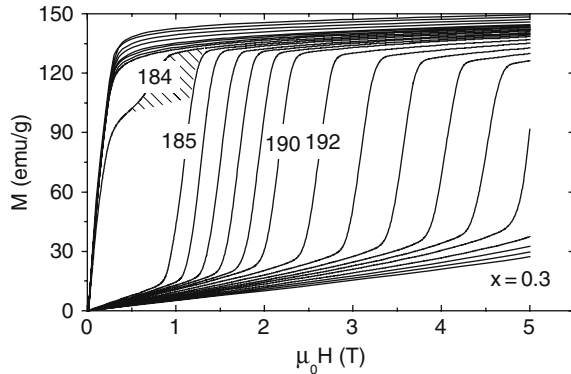
15.4.2 MCE Due to a Non-Idealized First-Order Phase Transition

15.4.2.1 In the Vicinity of Curie Temperature

In reality, a first-order phase transition occurs in a finite temperature range, and two phases coexist in the transition process. Liu et al. [22] found that in this case the Maxwell relation can yield a spurious ΔS peak in the vicinity of the Curie temperature $T_C(H = 0)$.

A typical example is the cubic NaZn₁₃-type intermetallic La_{0.7}Pr_{0.3}Fe_{11.5}Si_{1.5}. Figure 15.2 shows the magnetization isotherms of La_{0.7}Pr_{0.3}Fe_{11.5}Si_{1.5} measured in the field ascending process. The compound is completely FM below 183 K and PM above 185 K without external field. A stepwise magnetic behavior appears at the temperature of 184 K, signifying the coexistence of FM and PM phases. The first steep increase of magnetization marks the contribution of the FM phase, while the subsequent stair-like variation signifies the field-induced FM transition of the PM phase.

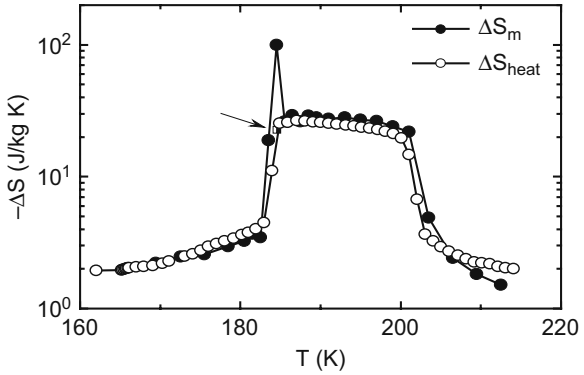
Fig. 15.2 Magnetization isotherms of La_{0.7}Pr_{0.3}Fe_{11.5}Si_{1.5} measured by ascending magnetic field. Hatched area marks the area that contributes to entropy change. Numbers in the figure denote the temperature in the units of Kelvin (Ref. [22])



The corresponding entropy change calculated by the Maxwell relation is shown in Fig. 15.3 ($\Delta H = 5$ T). In addition to the flat ΔS plateau of the height of ~ 28 J/kg K, an extra spike-shaped peak of the height of ~ 99.6 J/kgK appears at exactly the same temperature where stepwise magnetic behaviors appear. The heat capacity of this compound was also measured under the fields of 0 and 5 T, and the entropy change calculated by Eq. (15.13) indicates the absence of the spike ΔS

peak. These results show the failure of the Maxwell relation, which cannot give a correct result for the entropy change near T_C .

Fig. 15.3
Temperature-dependent entropy changes of $\text{La}_{0.7}\text{Pr}_{0.3}\text{Fe}_{11.5}\text{Si}_{1.5}$ calculated from magnetic data (solid circles) and heat capacity (open circles), respectively (Ref. [22])



Considering the fact that magnetic field affects only the magnetic state of PM phase, which coexists with the FM phase near T_C , only the PM phase contributes to thermal effect. With this in mind, a modified equation for the calculation of ΔS can be established. Figure 15.4 is a schematic showing the determination of ΔS for the system with an idealized stepwise behavior. Denoting the area surrounded by the two $M-H$ curves at T_1 and T_2 as $\Sigma_1 + \Sigma_2$, the Maxwell relation gives $\Delta S = (\Sigma_1 + \Sigma_2) / (T_1 - T_2)$. Considering the fact that the field-induced meta-magnetic transition takes place in the PM phase, only Σ_1 contributes to ΔS . This implies $\Delta S = \Sigma_1 / (T_1 - T_2)$.

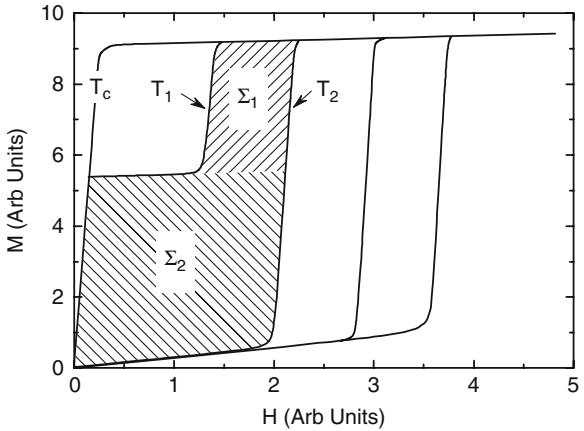


Fig. 15.4 A schematic showing the calculation of entropy change when stepwise magnetic behaviors occur (Ref. [22])

Stepwise magnetic behaviors widely exist in magnetic materials such as $\text{MnAs}_{1-x}\text{Fe}_x$ [23] and $\text{Gd}_5\text{Si}_{4-x}\text{Ge}_x$ [24]. It was also observed in MnAs [25] and $\text{Mn}_{1-x}\text{Cu}_x\text{As}$ [26] under high pressures. It could be a general feature of the first-order phase transition because the finite temperature width of the phase transition. In this case, ΔS should be handled carefully.

15.4.2.2 MCE Associated with Complex Magnetic Phase Transitions

When more than two phases coexist in a wide temperature range, applicability of the Maxwell relation should also be checked carefully considering the fact that this relation is derived for a homogeneous system in the equilibrium state. Liu et al. [27] found that if the proportions of the coexisted phases change with either magnetic field or temperature, the Maxwell relation may predict incorrect results.

A typical example is manganite $\text{Eu}_{0.55}\text{Sr}_{0.45}\text{MnO}_3$. It exhibits a complex magnetic behavior. As shown in Figure 15.5, two magnetic processes take place sequentially on cooling under a field between 0.5 and 2 T. The first one is a PM to FM transition, while the second one is a FM to antiferromagnetic (AFM) transition. In the intermediate, temperature and magnetic field range FM and AFM/PM phases coexist. The fully FM polarized state is obtained above ~ 2.3 T.

Fig. 15.5 Thermal magnetization of $\text{Eu}_{0.55}\text{Sr}_{0.45}\text{MnO}_3$ measured under different magnetic fields

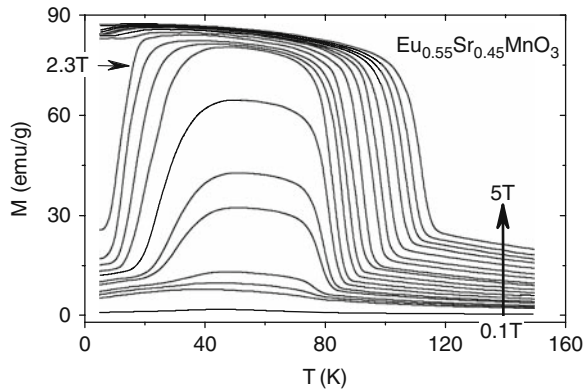


Fig. 15.6 Entropy changes in $\text{Eu}_{0.55}\text{Sr}_{0.45}\text{MnO}_3$ determined by Maxwell relation (symbols) and specific heat (solid line)

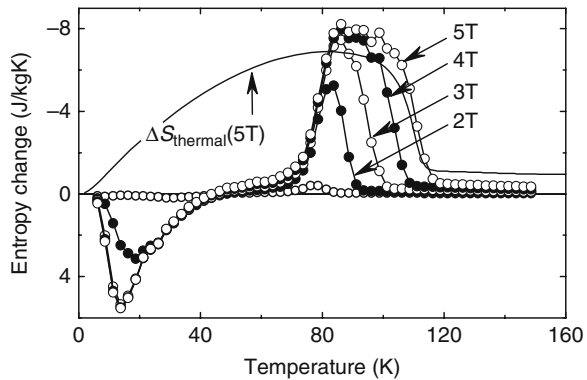


Figure 15.6 exemplifies the entropy changes calculated by Eqs. (15.12) and (15.6), based on magnetization isotherms and heat capacity data, respectively. The most striking observation is the significant discrepancy between the two results.

Different from the entropy increase below ~ 40 K predicted by the Maxwell relation, the calorimetric measurement declares an entropy decrease in the whole temperature range below ~ 110 K. Similar results are also observed in other compounds such as $\text{La}_{0.27}\text{Nd}_{0.40}\text{Ca}_{0.33}\text{MnO}_3$, etc. [27].

According to the standard thermodynamics theory, when two phases coexist the entropy change will be

$$\Delta S = X_0 \Delta S_2 + \int_0^T (\Delta X_1 C_{p1} - \Delta X_1 C_{p2}) dT/T \quad (15.15)$$

where X_0 is the total volume, and X_1 the volume occupied by FM phase, C_{p1} and C_{p2} are the heat capacities (per volume) of the FM and non-FM phases, respectively. $\Delta S_2 = S_2(T, H) - S_2(T, 0)$ and $\Delta X_1 C_p = X_1(T, H) C_p(T, H) - X_1(T, 0) C_p(T, 0)$ (S_2 the entropy of non-FM phase). In contrast, the Maxwell relation gives

$$\begin{aligned} \Delta S = X_0 \Delta S_2 + \int_0^T (\Delta X_1 C_{p1} - \Delta X_1 C_{p2}) dT/T \\ + \int_0^H (M_1 - M_2) (\partial X_1 / \partial T)_H dH \\ - \int_0^T dT/T \int_0^H (C_{p1} - C_{p2}) (\partial x_1 / \partial H)_T dH \end{aligned} \quad (15.16)$$

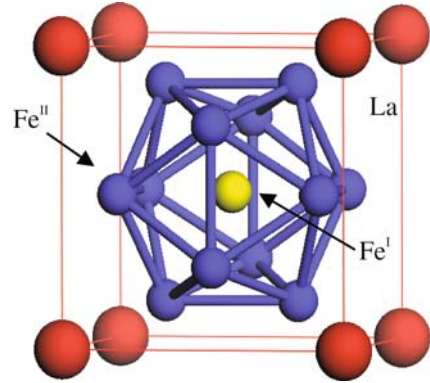
where the relation $M = X_0 M_2 + X_1 (M_1 - M_2)$ has been used. It is obvious that the same results are obtained only when X_1 is independent of T and H . In most of the phase-separated compounds, the field-induced FM transition does not occur until a threshold field is reached. Below this field, the Maxwell relation can still be used based on the above arguments. However, when the applied field is so large as to affect the proportion of the FM or non-FM phase in the compound, calorimetric data have to be used.

15.5 Typical Materials with Giant Magnetocaloric Effect

Since the success of the magnetic refrigeration at ultra-low temperatures, the attempt to apply this technology to higher temperatures has never stopped. Because of the increase of heat capacity, the materials working in the low-temperature region cannot be directly used at high temperatures. To get effective MCE materials becomes one of the key problems to be solved. The discovery of new magnetic materials with giant MCE in the last decade, together with the successful demonstration of the proof-of-principle refrigerators working near the ambient temperature, displays a bright prospect of magnetic cooling.

There are three categories of magnetocaloric materials as classified by the temperature where the maximal MCE occurs: the low-temperature materials (below 20 K), the materials for intermediate temperatures (20–80 K), and the materials

Fig. 15.7 A schematic of the atomic structure of LaFe_{13}

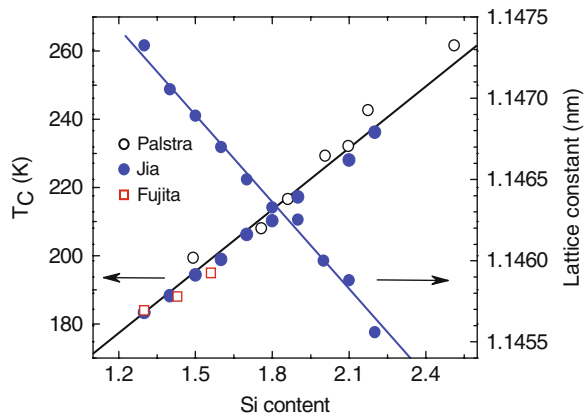


for the temperatures above 80 K. A detailed description for the first two kinds of materials can be found elsewhere [11, 28]. In the following, we will focus our attention on the recently discovered high-temperature MCE materials.

15.5.1 $\text{LaFe}_{3-x}\text{M}_x$ ($M = \text{Al}, \text{Si}$) Intermetallics

The cubic NaZn_{13} -type intermetallics $\text{LaFe}_{13-x}\text{M}_x$ ($M = \text{Si}$ and Al) have attracted great attention due to their giant MCE, small hysteresis loss, and high thermal conductivity and have been regarded as one of the most promising candidates for magnetic refrigerants.

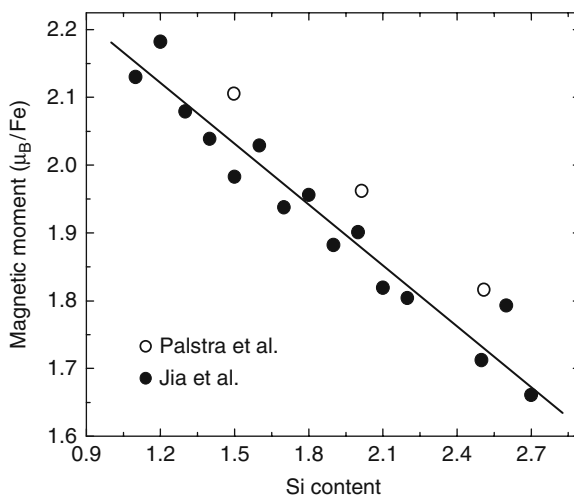
Fig. 15.8 Curie temperature and lattice constant as functions of Si content for $\text{LaFe}_{13-x}\text{Si}_x$. Data were obtained from Refs. [32] (Palstra), [38] (Jia), and [39] (Fujita)



15.5.1.1 Generic Magnetic Properties

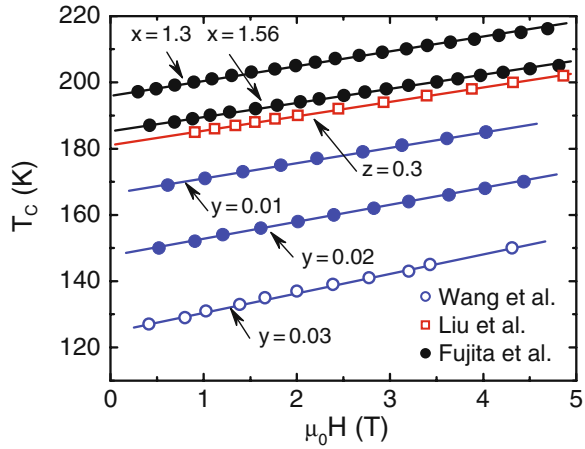
LaCo_{13} is the only stable NaZn_{13} -type La-transition-metal intermetallic showing a Curie temperature of $\sim 1,318$ K [29]. Different from LaCo_{13} , LaFe_{13} is unstable due to its positive formation enthalpy, and minor additions such as Si and/or Al are required to stabilize the structure [30]. Figure 15.7 is the fictitious structure of LaFe_{13} . The crystal structure is cubic, and the space group is $\text{Fm}\bar{3}\text{c}$. Fe atoms occupy two different crystallographic sites of 8b (Fe^{I}) and 96i (Fe^{II}) at a ratio of 1:12. Eight LaFe_{13} clusters are contained in each unit cell. La and Fe^{I} form the CsCl structure, and each La is surrounded by 24 Fe^{II} atoms. Fe^{I} situates at the center of the icosahedron formed by 12 Fe^{II} atoms.

Fig. 15.9 Magnetic moment of Fe atoms in $\text{LaFe}_{13-x}\text{Si}_x$. Data were obtained from Refs. [32] (Palstra) and [38] (Jia)



The $\text{LaFe}_{13-x}\text{M}_x$ compounds were first successfully synthesized by Kripyakevich et al. in 1968 [30]. With the incorporation of Al or Si, the lattice parameter increases or decreases linearly. The magnetic properties of $\text{LaFe}_{13-x}\text{M}_x$ were investigated by Palstra et al. [31, 32], Heimhold et al. [33], Tang et al. [34], Fujita and Fukamichi [35], Fujita et al. [36], and Hu et al. [37]. These studies showed that $\text{LaFe}_{13-x}\text{Si}_x$ is PM near the ambient temperature and undergoes a FM transition upon cooling at a temperature between 200 and 250 K (depending on Si content). Palstra et al. found that T_C increased linearly from ~ 199 K for $x=1.5$ to ~ 261 K for $x=2.5$. These results were confirmed by the subsequent work by Jia et al. [38] and Fujita et al. [39] (Fig. 15.8). Palstra et al. [32] and Jia et al. [38] also observed a monotonic decrease of saturation magnetization, at a rate of $-0.286 \mu_B$ for each Si, with the increase of Si content (Fig. 15.9). This means that the decrease of saturation magnetization is not a simple dilution effect of Fe by Si. A first-principle calculation conducted by Wang et al. [40] indicated the occurrence of hybridization between the Fe-3d and the Si-2p electrons and the change of the density of state below Fermi surface after the introduction of Si, which could be the reason for the change of Fe magnetic moment.

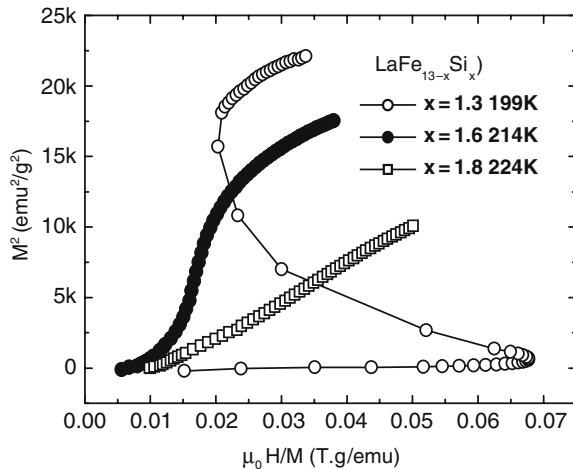
Fig. 15.10 Curie temperature as a function of magnetic field for the compounds $\text{LaFe}_{13-x}\text{Si}_x$ (Ref. [39]), $\text{La}(\text{Fe}_{1-y}\text{Mn}_y)\text{Si}_{1.3}$ (Ref. [41]), and $\text{La}_{1-z}\text{Pr}_z\text{Fe}_{11.5}\text{Si}_{1.5}$ (Ref. [21])



The magnetic transition was found to be first order when x is small for $M=\text{Fe}$, manifested by the steep drop of magnetization across T_C and the occurrence of considerable thermal or magnetic hysteresis. An evolution of the phase transition from first order to second order takes place as x increases, and a typical second-order transition appears when $x > 1.8$.

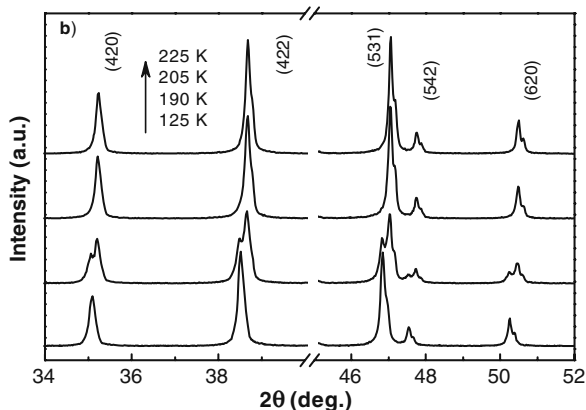
Magnetic field can drive T_C of the first-order transition to high temperatures at a rate of ~ 4.3 K/T. This is an effect essentially independent of the composition of the compounds. Figure 15.10 displays the field-dependent Curie temperature for the compounds of $\text{LaFe}_{13-x}\text{Si}_x$, $\text{La}_{1-z}\text{Pr}_z\text{Fe}_{11.5}\text{Si}_{1.5}$, and $\text{LaFe}_{11.7-y}\text{Mn}_y\text{Si}_{1.3}$, based on data obtained by Wang et al. [41], Liu et al. [22] and Fujita et al. [39] respectively. These results indicate that magnetic field affects the LaFe_{13} -based compounds in essentially the same way, regardless of composition.

Fig. 15.11 Arrott plots of $\text{LaFe}_{13-x}\text{Si}_x$ at the temperature just above T_C



The high-temperature shift of T_C under applied field implies the occurrence of field-induced meta-magnetic transition of the PM phase, an itinerant-electron meta-magnetic (IEM) transition as claimed by Fujita et al. [36]. The FM state becomes more stable than the PM state under applied field due to the field-induced change in the band structure of 3d electrons. The IEM transition is usually marked by the appearance of “S”-shaped M^2 - H/M isotherms (Arrott plot). For the LaFe_{13} -based compounds, the lower the Si content is, the stronger the first-order nature of the magnetic transition will be (Fig. 15.11).

Fig. 15.12 X-ray diffraction spectra of $\text{LaFe}_{13-x}\text{Si}_x$ for $x = 1.2$ collected under different temperatures. The peak splitting at the temperature of 190 K is a result of two-phase coexistence (Ref. [37])

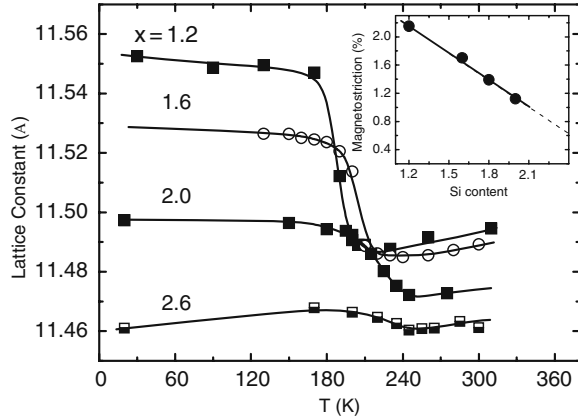


The lowest Si content in the previously studied compound is $x=1.5$. Hu et al. [37] successfully extended x to lower values by vacuum annealing the as-prepared samples at a temperature as high as $\sim 1,150^\circ\text{C}$ for more than 30 days and found that the lowest Si content required for the stabilization of the compound is $x \sim 1.2$. Figure 15.12 shows the powder X-ray diffraction spectra of $\text{LaFe}_{13-x}\text{Si}_x$ with $x=1.2$ collected under different temperatures. No secondary phase is detected. Insufficient annealing will lead to the presence of α -Fe.

When the content of Si is high, the structure of $\text{LaFe}_{13-x}\text{Si}_x$ becomes tetragonal of the $\text{Ce}_2\text{Ni}_{17}\text{Si}_9$ -type as reported by Tang et al. [34]. Ferromagnetism remains for $2.6 < x < 3$, while vanishes when $3 < x < 5$.

The introduction of Al, instead of Si, can also stabilize LaFe_{13} -type intermetallics [32]. Different from Si doping, however, the incorporation of Al leads to complex magnetic behaviors. The compound is paramagnetic at high temperatures, regardless of Al content. In the low-temperature range, in contrast, it is micromagnetic for $0.4 < x < 0.6$, FM for $0.7 < x < 1.04$, and antiferromagnetic for $1.04 < x < 1.82$. It is interesting that partial replacement of Fe by Co can completely depress the AFM state. Hu et al. [42] found that $\text{La}(\text{Fe}_{1-y}\text{Co}_y)_{13-x}\text{Al}_x$ ($x=1.3$) becomes FM when minor Co atoms ($y=0.02$) are introduced. This result reveals the small difference between the free energies of the AFM and the FM states.

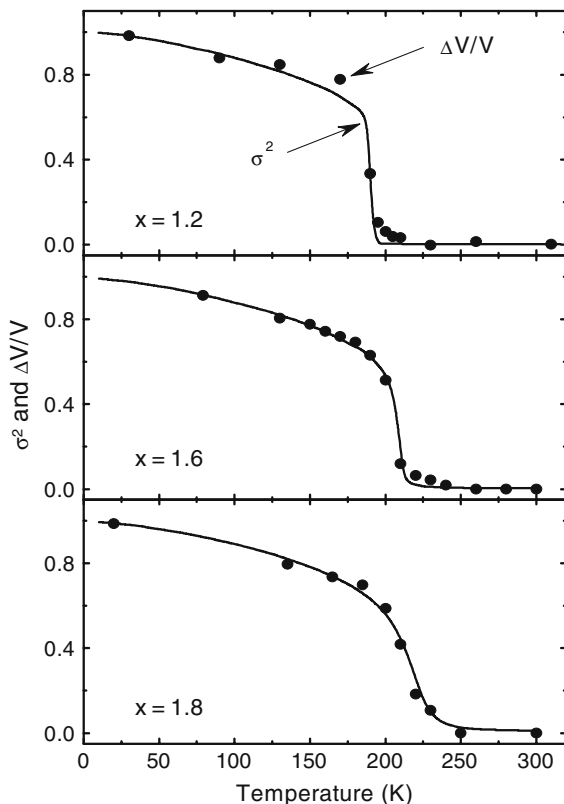
Fig. 15.13 Lattice constant as a function of temperature of $\text{LaFe}_{13-x}\text{Si}_x$ (Ref. [44])



15.5.1.2 Spontaneous Magnetostriction of $\text{LaFe}_{13-x}\text{Si}_x$

The lattice constant of $\text{LaFe}_{13-x}\text{Si}_x$ with a Si content below $x=1.8$ is weakly temperature dependent, decreasing slightly as temperature increases. Accompanying the PM to FM transition, a significant, yet sharp, change in phase volume takes place, especially when the Si content is low. The relative volume change at T_C is $\sim 1.2\%$ for $x=2$ and $\sim 2.1\%$ for $x=1.2$, as shown in Fig. 15.13. Wang et al. [43] proved that the peculiar temperature dependence of the lattice constant is a combined effect of spontaneous magnetostriction and thermal expansion. For the $\text{LaFe}_{13-x}\text{Si}_x$ compounds, the spontaneous magnetostriction is particularly obvious. Based on the analysis of neutron diffraction data, Wang et al. [43] established a quantitative relation $(\Delta V/V - 3\gamma T) = 0.018\sigma^2$ for the sample $\text{LaFe}_{13-x}\text{Si}_x$ ($x=1.6$), where $\Delta V/V$ is the relative volume change, σ the normalized magnetization, and γ the linear thermal expansivity. It means a maximum magnetostriction of $\sim 1.8\%$, quite similar to that of FeNi-invar alloy (1.9%). The result of Wang et al. was obtained in the temperature range below T_C . By comparing the $\Delta V/V - T$ (obtained from the X-ray diffraction analyses) and the $\sigma - T$ dependences in a wide temperature range below 300 K, alternatively, Jia et al. [44] obtained a similar relation $(\Delta V/V - 3\gamma T) = k\sigma^2$ with the k values of 0.0215 for $x=1.2$, 0.017 for $x=1.6$, and 0.0139 for $x=1.8$, where $\gamma \approx 8.2 \times 10^{-6} \text{ K}^{-1}$. Figure 15.14 presents a comparison of the $\Delta V/V - T$ and $\sigma^2 - T$ relations, after a thermal expansion correction and an appropriate amplification. A satisfactory agreement between the two sets of data is observed in the whole temperature range from 20 to 300 K, especially near the Curie temperature, where rapid changes in V and σ take place. The decrease of k with x indicates the weakening of spontaneous magnetostriction, that is, the weakening of the first-order nature of the phase transition. It should be noted that although the second-order nature of the transition prevails for $x > 1.8$, the magnetostriction remains significant. Based on the results shown in the inset in Fig. 15.13, magnetostriction could exist up to a x value as high as ~ 2.4 .

Fig. 15.14
Temperature-dependent normalized thermal magnetization and the lattice constant after thermal expansion correction and proper amplification (Ref. [44])



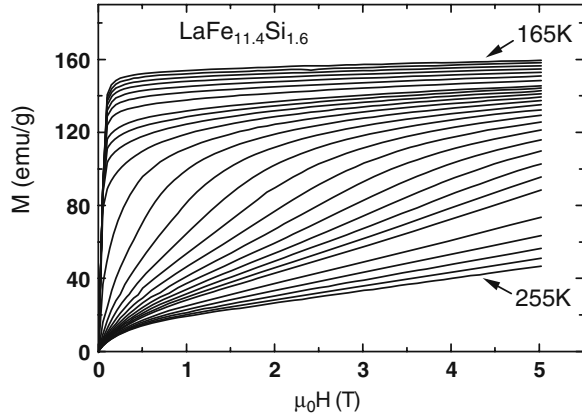
15.5.1.3 Magnetocaloric effect in $\text{LaFe}_{13-x}\text{M}_x$ ($M = \text{Si, Al, and Co}$)

Magnetocaloric effect in $\text{LaFe}_{13-x}\text{Si}_x$

The most attractive property of $\text{LaFe}_{13-x}\text{M}_x$ is its giant magnetocaloric effect, which did not come into the vision of the people until the work of Hu et al. [16, 17], who observed an entropy change as high as $\sim 20 \text{ J/kgK}$, for a field change of 0–5 T, in $\text{LaFe}_{13-x}\text{Si}_x$ ($x=1.6$). This discovery excited a new wave of materials exploration. Figure 15.15 displays the magnetization isotherms of $\text{LaFe}_{11.4}\text{Si}_{1.6}$ measured in the temperature range from 200 to 255 K. The temperature step is 2 K from 200 to 230 K, 5 K from 165 to 200 K, and from 230 to 255 K. The magnetization is smoothly saturated and its magnitude gradually decreases with increasing temperature below T_C . Above T_C , the M – H curve exhibits a weak “S”-like behavior, which is a signature of IEM transition as explained above.

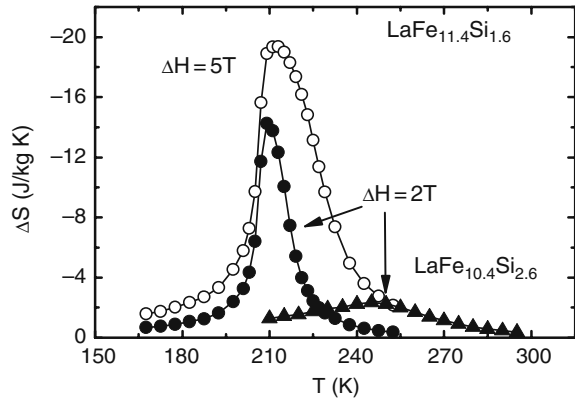
Magnetic entropy change ΔS can be calculated by Eq. (15.12) based on the data in Fig. 15.15, and the corresponding results are shown in Fig. 15.16 as functions of temperature. The peak values of ΔS for the field changes of 2 T and 5 T are ~ 10.5

Fig. 15.15 Magnetization isotherms of $\text{LaFe}_{11.6}\text{Si}_{1.6}$ measured around T_C (Ref. [17])



and ~ 19.4 J/kg K, respectively, appearing at ~ 210 K. Such a large $|\Delta S|$ is rare for transition metal alloys in this temperature range.

Fig. 15.16 Entropy change of $\text{LaFe}_{11.6}\text{Si}_{1.6}$ (Ref. [17])



A remarkable phenomenon is the asymmetric broadening of the ΔS peak with applied field. This is a typical feature of first-order phase transition which has a field-dependent critical temperature. It is the increase of T_C with H that yields the expansion of ΔS .

As shown in Section 15.5.1.2, the lattice constant experiences a sudden contraction when the FM to PM transition occurs. The lower the Curie temperature is, the greater the magnetostriction, thus the magnetization change will be. This actually implies that the large entropy change occurs always accompanying a great lattice expansion upon the magnetic transition, as claimed by Hu et al. [17].

Fujieda et al. [45, 46] performed the first measurement of adiabatic temperature change for $\text{LaFe}_{13-x}\text{Si}_x$ ($x=1.3, 1.43, \text{ and } 1.56$) and concluded that the MCE is enhanced as the content of Si decreases. ΔS and ΔT_{ad} for the compound of $x=1.56$

Fig. 15.17 Adiabatic temperature change of $\text{LaFe}_{11.44}\text{Si}_{1.56}$ for different field changes (Ref. [46])

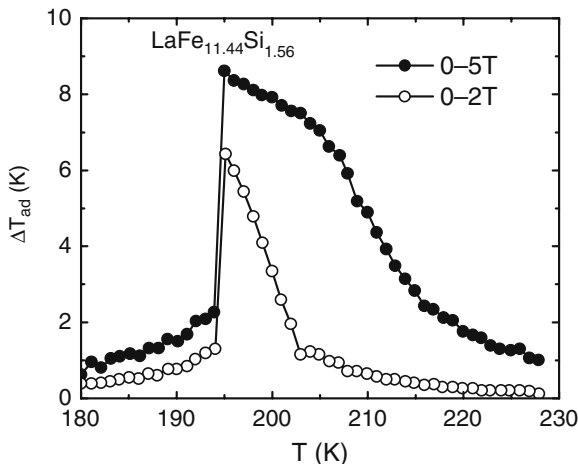
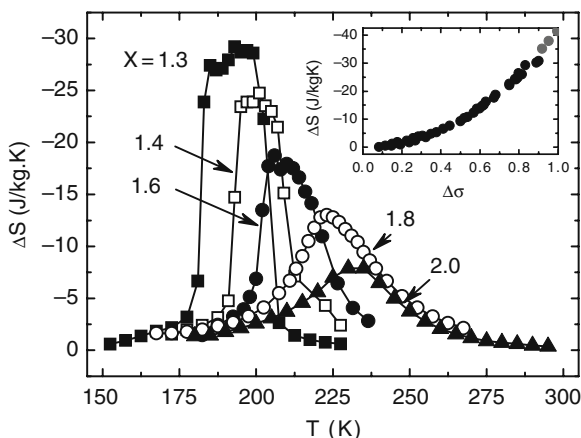


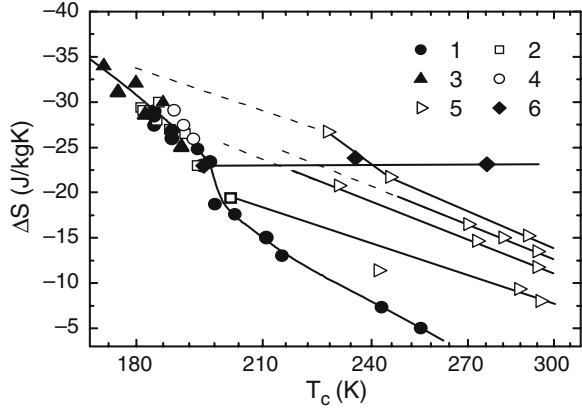
Fig. 15.18 Entropy of $\text{LaFe}_{13-x}\text{Si}_x$ for a field change of 5 T. Inset plot shows ΔS as a function of σ (Ref. [37])



were found to be ~ 22.8 J/kgK and ~ 8.1 K, respectively, by changing the magnetic field from 0 to 2 T, where ΔS has been calculated by Eq. (15.12), and ΔT_{ad} by comparing the $S(T)$ curves (calculated from the heat capacity data) under different magnetic fields as described in Section 15.3.2 (Fig. 15.17).

As mentioned above, MCE enhances as the content of Si decreases. Figure 15.18 displays the typical $\Delta S-T$ ($\Delta H=5$ T) relations of $\text{LaFe}_{13-x}\text{Si}_x$ for $x=1.3, 1.4, 1.6,$ and 2.0 [37]. It is clear that the reduction in x causes a significant decrease in T_C , whereas a rapid increase in ΔS . The maximal ΔS is ~ 29 J/kgK, appearing at ~ 190 K when $x=1.3$. It is unfortunate that the compounds with the Si content lower than 1.2 cannot be obtained. However, by a simple analysis, it can be concluded that the maximal ΔS for $\text{LaFe}_{13-x}\text{Si}_x$ will be ~ 40 J/kgK. It is easy to see that there should be a one-to-one correspondence between the field-induced magnetization change ($\Delta\sigma$) and ΔS . By comparing the data of different compounds, a

Fig. 15.19 $\Delta S-T_C$ relations for LaFe₁₃-based compounds. 1 – LaFe_{13-x}Si_x (Refs. [37, 39]), 2 – La_{1-z}Pr_zFe_{13-x}Si_x (Refs. [58,59,60,61]), 3 – La_{1-z}Ce_zFe_{13-x}Si_x (Refs. [52–56]), 4 – La_{1-z}Nd_zFe_{13-x}Si_x (Ref. [57]), 5 – La_{1-z}Pr_zFe_{13-x-y}Co_ySi_x (Ref. [57]), and 6 – LaFe_{13-x}Si_xH_δ (Ref. [39])



$\Delta S-\Delta\sigma$ relation can be obtained, and the utmost entropy change will be the result corresponding to $\Delta\sigma=1$ (inset in Fig. 15.18). To get a comprehensive picture of ΔS , in Fig. 15.19, we gave a summary for the $T_C\sim\Delta S$ relations of different compounds. It shows the presence of a general correspondence between ΔS and T_C : the former decreases as the latter grows irrespective of whether T_C is modified by the Si or the R content (R = magnetic rare earth, its effects will be discussed below). A remarkable feature is the steep drop of ΔS near ~ 194 K. It is a signature of the crossover of the magnetic transition from first order to second order. This result reveals a fact that large entropy changes occur always accompanying the first-order phase transition.

Magnetocaloric Effect in Transition-Metal-Doped LaFe_{13-x}(Si,Al)_x

Although the LaFe_{13-x}Si_x compounds exhibit a giant MCE, the ΔS peak usually appears at low temperatures (< 210 K). For the purpose of practical application, it is highly desired that the maximal entropy change can take place near the ambient temperature. According to Fig. 15.19, unfortunately, the MCE weakens rapidly as T_C increases. It is therefore an important issue how to shift T_C to high temperatures without significantly affecting ΔS . Hu et al. [47] found that the best effect can be obtained by replacing Fe with appropriate amount of Co. Figures 15.20 and 15.21 display the magnetization isotherms and the corresponding entropy change of La(Fe_{1-x}Co_x)_{11.9}Si_{1.1} ($x=0.04, 0.06$ and 0.08), respectively. The Curie temperature increases from 240 to 293 K as x increases from 0.02 to 0.08, while only a slow decrease of ΔS from ~ 23 to ~ 15.6 J/kgK ($\Delta H=5$ T). It is noteworthy that the sample with $x=0.6$ shows nearly the same ΔS (~ 20 J/kgK at ~ 274 K) as that of Gd₅Si₂Ge₂ and MnFeP_{0.45}As_{0.55} whereas there is no obvious magnetic hysteresis, which is highly desired by practical application. Similar results were obtained by other groups [48]. Substituting Fe with Co in LaFe_{11.2}Si_{1.8} and La_{0.6}Pr_{0.4}Fe_{11.2}Si_{1.8}, the former exhibits a second-order transition, results in similar effects as those described above. It is interesting to note that the $\Delta S-T_C$ curves obtained by varying

Co content while fixing the Si content are nearly parallel with each other (marked by the open triangles in Fig. 15.19).

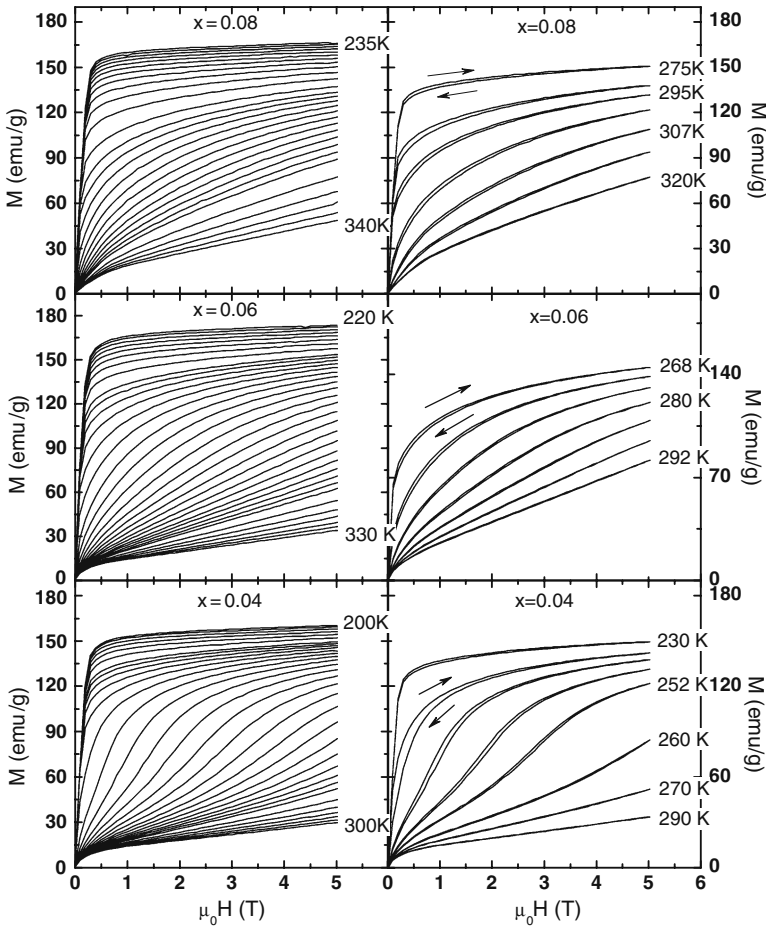


Fig. 15.20 Magnetization isotherms of $\text{La}(\text{Fe}_{1-x}\text{Co}_x)_{11.9}\text{Si}_{1.1}$ (Ref. [47])

Although both the Si-doping and the Co-doping drive T_C to high temperatures, the reduction of ΔS is much slower in the latter case. According to Fig. 15.19, ΔS is ~ 22 J/kgK for $\text{La}_{0.8}\text{Ce}_{0.2}\text{Fe}_{11.7-y}\text{Co}_y\text{Si}_{1.3}$ and ~ 7 J/kgK for $\text{LaFe}_{13-x}\text{Si}_x$ ($x=2.4$), while T_C takes nearly the same value of ~ 242 K. Therefore, reducing the Si content in $\text{LaFe}_{13-x}\text{Si}_x$ as low as possible and partial replacing Fe by Co is a promising way to get room temperature giant MCE.

Hu et al. [42] found that partial replacement of Fe with Co droved the samples from the AFM to the FM state and, similar to $\text{LaFe}_{13-x}\text{Si}_x$, T_C shifts to high temperatures when the Co content increases. A distinctive feature is that the entropy

Fig. 15.21 Entropy changes of $\text{La}(\text{Fe}_{1-x}\text{Co}_x)_{11.9}\text{Si}_{1.1}$ (Ref. [47])

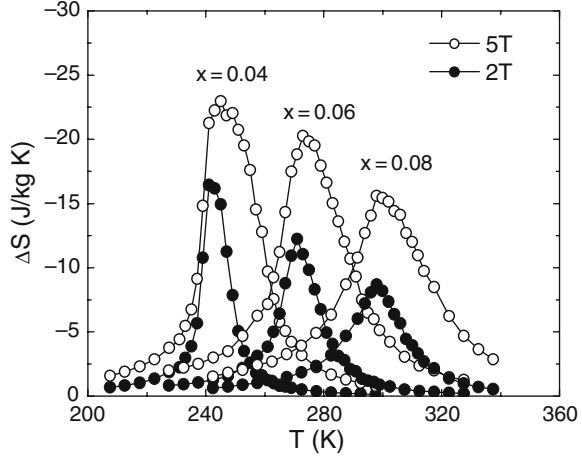
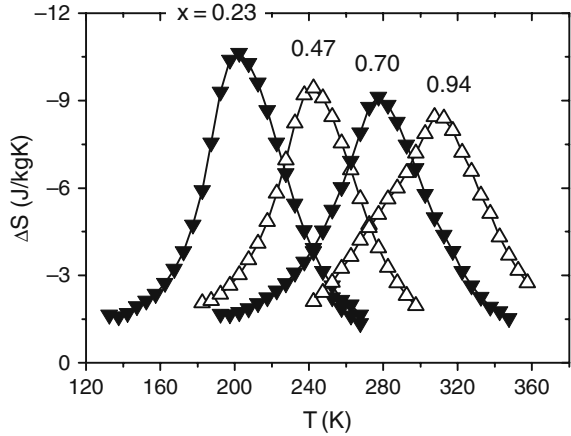


Fig. 15.22 Entropy change of $\text{LaFe}_{13-x}\text{Co}_x\text{Al}_{1.3}$ (Ref. [37])



change keeps nearly constant as Curie temperature grows, though the value of ΔS is not very large. Figure 15.22 shows the entropy change of $\text{LaFe}_{11.7-y}\text{Co}_y\text{Al}_{1.3}$ with different Co contents.

In an attempt to find out a way to depress T_C while effectively retaining the large ΔS , Wang et al. [49] studied the effect of substituting Fe by Mn, which may have a AFM coupling with adjacent Fe. The Mn content in $\text{LaFe}_{11.7-y}\text{Mn}_y\text{Si}_{1.3}$ is $y=0, 0.117, 0.234,$ and 0.351 . The cubic NaZn_{13} -type structure keeps unchanged except for the appearance of minor α -Fe phase (< 5 wt%) for $x \geq 0.234$. A decrease in saturation magnetization much larger than that expected by a simple dilution effect is observed, which is consistent with the anticipated antiparallel arrangements of Fe and Mn (Fig. 15.23). The Curie temperature is found to decrease linearly at a rate of ~ 174 K for 1% Mn. A large ΔS is gained in a wide temperature range,

Fig. 15.23 Saturation magnetization of $\text{LaFe}_{13-x}\text{Mn}_x\text{Si}_{1.3}$ (Ref. [75])

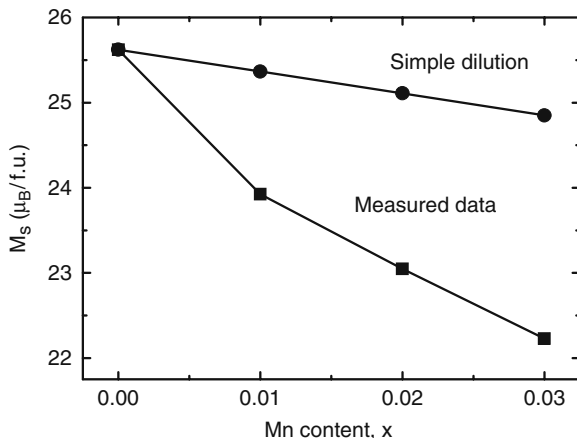
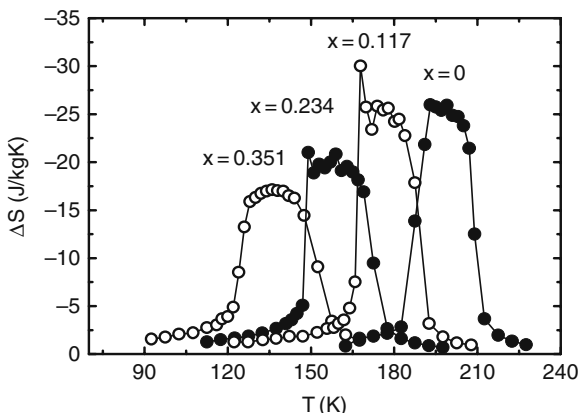


Fig. 15.24 Entropy change of $\text{LaFe}_{13-x}\text{Mn}_x\text{Si}_{1.3}$ ($\Delta H=5$ T) (Ref. [75])



though a tendency toward degeneration appears as y increases (Fig. 15.24). It is ~ 17 J/kgK for $T_C=130$ K and ~ 25 J/kgK for $T_C=188$ K, for a field change of 0–5 T. Increase of the temperature span of ΔS is obvious. It is ~ 21.5 K for $y=0$ and ~ 31.5 K for $y=0.351$ ($\Delta H=5$ T). Fujieda et al. [50] observed similar phenomena in $\text{La}_{1-z}\text{Ce}_z\text{Fe}_{13-x-y}\text{Mn}_y\text{Si}_x$. When the content of Mn is high enough ($y > 0.9$), long-range FM order will be destroyed, and typical spin glass behavior appears [49].

Magnetocaloric Effect in Magnetic Rare-Earth-Doped $\text{LaFe}_{13-x}\text{Si}_x$

Effects of magnetic rare-earth (R) doping were first studied by Anh et al. in 2003 [51]. The authors declared an increase of T_C and a decrease of MCE in $\text{La}_{1-z}\text{Nd}_z\text{Fe}_{11.44}\text{Si}_{1.56}$ ($z=0-0.4$) with the incorporation of Nd. However, these results are inconsistent with those subsequently obtained by other groups. Fujieda

Fig. 15.25 Temperature dependence of the entropy changes of $\text{LaFe}_{11.44}\text{Si}_{1.56}$ and $\text{La}_{0.7}\text{Ce}_{0.3}\text{Fe}_{11.44}\text{Si}_{1.56}$ (Ref. [54])

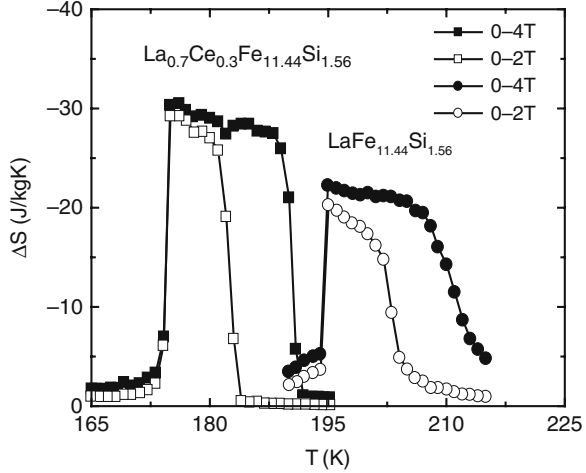
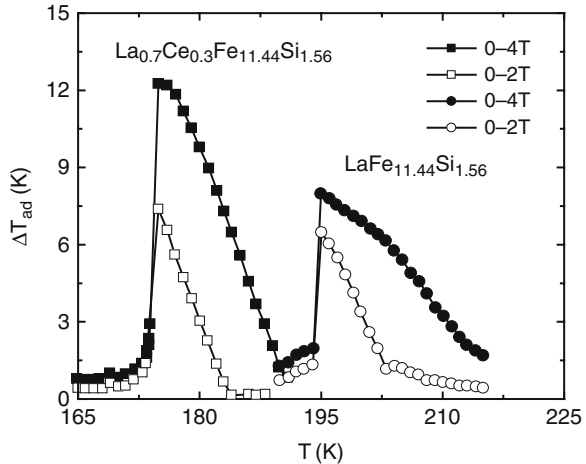
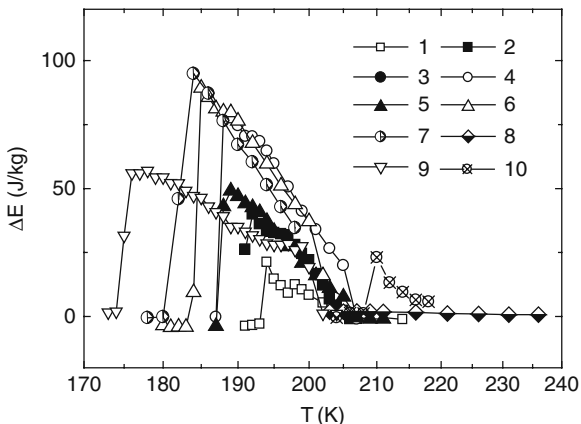


Fig. 15.26 Adiabatic temperature change of $\text{LaFe}_{11.44}\text{Si}_{1.56}$ and $\text{La}_{0.7}\text{Ce}_{0.3}\text{Fe}_{11.44}\text{Si}_{1.56}$ (Ref. [54])



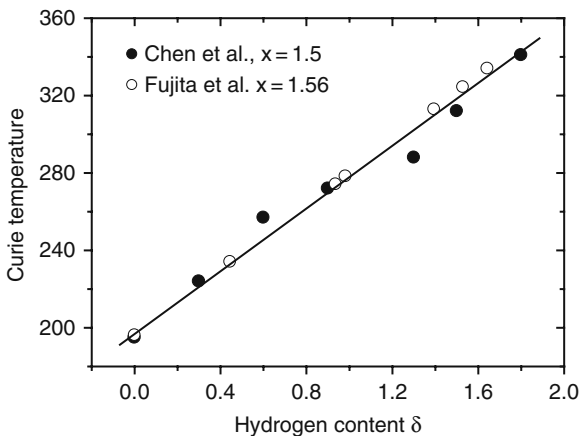
et al. [52–56] performed a systematic study on the effect of Ce-doping for the compounds $\text{LaFe}_{13-x}\text{Si}_x$ with $x=1.3, 1.56, \text{ and } 1.82$. There is a limitation to the content of R in the compound, beyond which impurity phases will appear. The maximal Ce content studied is 0.3. There are two remarkable observations. The first one is the low temperature shift of T_C and the second one is the enhancement of MCE with the incorporation of Ce. The entropy and adiabatic temperature changes of $\text{La}_{0.7}\text{Ce}_{0.3}\text{Fe}_{11.44}\text{Si}_{1.56}$ are, respectively, shown in Figs. 15.25 and 15.26. Results without Ce are also presented for comparison. It indicates that the presence of 30% Ce reduces T_C by ~ 24 K whereas increases ΔS by ~ 8 J/kgK ($\Delta H=4$ T). The maximal entropy change is ~ 34 J/kgK, appearing in $\text{La}_{0.9}\text{Ce}_{0.2}\text{Fe}_{11.7}\text{Si}_{1.3}$. Effects of other magnetic rare earths were also studied, such as Nd, by Shen et al. [58], and Pr, by

Fig. 15.27 Magnetic hysteresis loss in LaFe₁₃-based compounds (unpublished data of the authors). 1 – LaFe_{11.5}Si_{1.5}, 2 – La_{0.9}Nd_{0.1}Fe_{11.5}Si_{1.5}, 3 – La_{0.8}Nd_{0.2}Fe_{11.5}Si_{1.5}, 4 – La_{0.7}Nd_{0.3}Fe_{11.5}Si_{1.5}, 5 – La_{0.8}Pr_{0.2}Fe_{11.5}Si_{1.5}, 6 – La_{0.7}Pr_{0.3}Fe_{11.5}Si_{1.5}, 7 – La_{0.5}Pr_{0.5}Fe_{11.5}Si_{1.5}, 8 – La_{0.7}Pr_{0.3}Fe_{11.5}Si_{1.5}, 9 – LaFe_{11.83}Si_{1.17}, and 10 – La_{0.5}Pr_{0.5}Fe_{11.5}Si_{1.5}C_{0.3}



Shen et al. [58] and Fujieda et al. [59, 60]. Fujieda et al. [59] successfully extended the content of Pr up to 0.7 when Si content is 1.82. Analyses of these results lead to the following conclusions: (i) the incorporation of magnetic rare earth causes a low temperature shift of T_C , thus a strengthening the first-order nature of the phase transition. Sometimes a second-order phase transition becomes first order after the introduction of R. (ii) The MCE enhances with the increase of the R content.

Fig. 15.28 Curie temperature as a function of hydrogen concentration. Data were obtained from Refs. [66] and [39] for $x=1.5$ and 1.56, respectively



It is obvious that the enhancement of MCE occurs accompanying the decrease of T_C , which can be realized by tuning the content of R or Si. It would be instructive to analyze the $\Delta S-T_C$ relations resulted by changing Si content without introducing R or changing R content while keeping the Si concentration constant, which will allow a comparison of the ΔS values at the same temperature. A remarkable observation is the equivalence of increasing z to reducing x , as demonstrated by the coincidence of the two sets of data in Fig. 15.19.

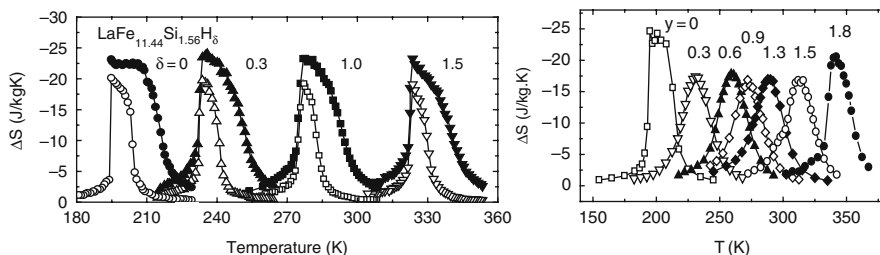
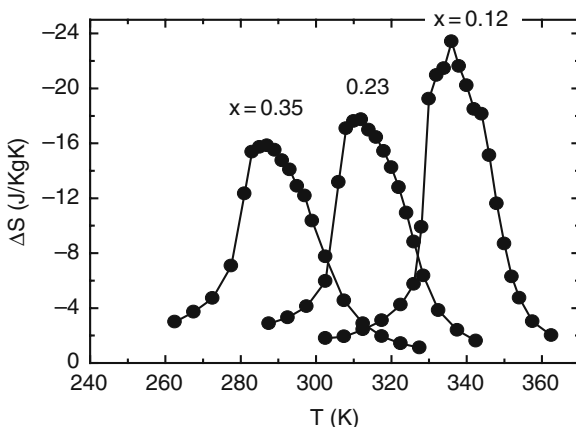


Fig. 15.29 Entropy change of the hydrides $\text{LaFe}_{11.44}\text{Si}_{1.56}\text{H}_\delta$ (left, Ref. [39]) and $\text{LaFe}_{11.5}\text{Si}_{1.5}\text{H}_\delta$ (right, Ref. [66]) ($\Delta H=5$ T)

Although R and Si have similar effects on ΔS , their influence on magnetic hysteresis is different. Defining the energy loss (ΔE) due to magnetic hysteresis as the area encircled by the two magnetization isotherms, we obtained the $\Delta E-T$ relation shown in Fig. 15.27, based on the data of different compounds $\text{La}_{1-z}\text{R}_z\text{Fe}_{13-x}\text{Si}_x$. It is clear that ΔE is negligible for $T > 220$ K and increases rapidly as T decreases. Comparing the hysteresis loss at the same temperature, it can be seen that ΔE increases when R is introduced. This conclusion is different from that of Fujieda et al. [53], who claimed a depression of ΔE in $\text{La}_{0.7}\text{Ce}_{0.3}\text{Fe}_{11.18}\text{Si}_{1.82}$ compared with $\text{LaFe}_{11.44}\text{Si}_{1.56}$. The disappearance of ΔE demonstrates again the prevalence of the second-order transition above 210 K.

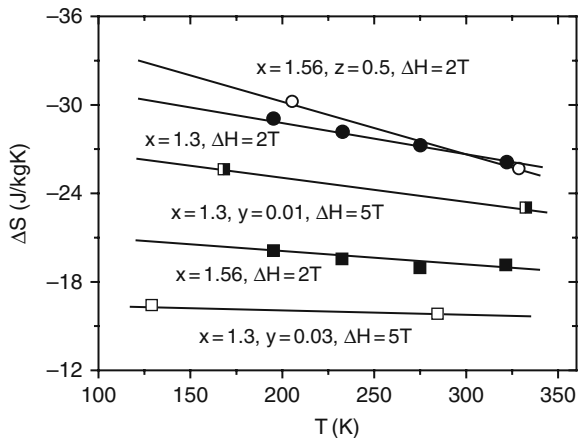
Fig. 15.30 Entropy change of the $\text{LaFe}_{11.7-x}\text{Mn}_x\text{Si}_{1.3}\text{H}_\delta$ hydrides ($\Delta H=5$ T)



Interstitial Effect in $\text{La}(\text{Fe}_{1-x}\text{Si}_x)_{13}$

For the purpose of practical application, as mentioned in the previous sections, it is required that the giant MCE can occur near the ambient temperature. However, as shown in Fig. 15.19, ΔS decreases rapidly as T_C increases for the $\text{LaFe}_{13-x}\text{Si}_x$ compounds. It is therefore highly desired to find out an effective approach to push

Fig. 15.31 Entropy changes of $\text{La}_{1-z}\text{Pr}_z\text{Fe}_{11.44}\text{Si}_{1.56}\text{H}_\delta$ for $z=0$ (Ref. [39]) and 0.5 (Ref. [76]) and $\text{LaFe}_{11.7-y}\text{Mn}_y\text{Si}_{1.3}\text{H}_\delta$ for $y=0$ (Ref. [75]) and $y=0.117$ and 0.234 (Ref. [77]).



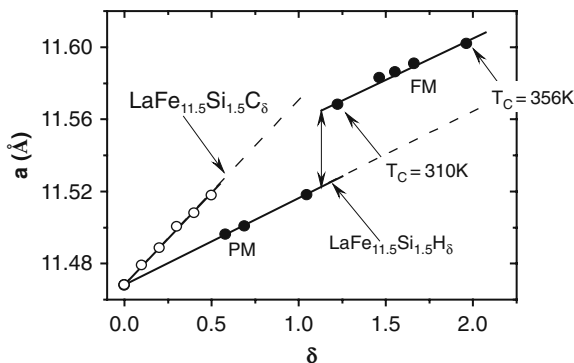
ΔS to high temperatures without reducing its height. Fujieda et al. [62,63,64] and Chen et al. [65, 66] independently found that the incorporation of interstitial hydrogen shifted T_C to high temperatures, while the MCE essentially remains. The effects are completely different from those of replacing Fe with Co, Ni, Si, or Al and were inattentive before, though magnetic properties of the relevant nitrides [67,68,69,70] and hydrides [71, 72] have been studied since 1993.

By changing either the pressure of hydrogen atmosphere or annealing temperature, the concentration of interstitial hydrogen in $\text{LaFe}_{13-x}\text{Si}_x\text{H}_\delta$ was controlled by Fujieda et al. [39]. The hydrogen concentration was determined by both gas chromatograph and gas fusion analyses. In contrast, Chen et al. [65, 66] tuned the content of hydrogen by carefully regulating the desorption of absorbed hydrogen. The Curie temperature was found to increase linearly with the content of hydrogen, while the magnetic transition remains first order. This is completely different from the effect of Si- and/or Co doping, which causes an evolution of magnetic transition from first order to second order. In this way, the giant MCE that usually appears at low temperatures can be pushed toward high temperatures. Figure 15.28 shows the variation of T_C with δ . The effect of interstitial atom on T_C is similar for the $\text{La}(\text{Fe}, \text{Si})_{13}\text{H}_\delta$ hydrides and other R-Fe-based interstitial compounds, for which lattice expansion caused by interstitial atoms depresses the overlap between Fe-3d electrons, thus leads to a reduction of T_C [65–70].

The typical entropy changes of $\text{LaFe}_{13-x}\text{Si}_x$ for $x=1.5$ [66] and 1.56 [39] are shown in Fig. 15.29. The peak height of ΔS keeps at ~ 23 J/kgK ($\Delta H = 5$ T) for $x=1.56$ as T_C increases from ~ 195 to ~ 330 K. Due to the broadening of magnetic transition caused by hydrogen desorption, the ΔS value in $\text{LaFe}_{11.5}\text{Si}_{1.5}$ is somewhat lower in the intermediated hydrogen concentration range.

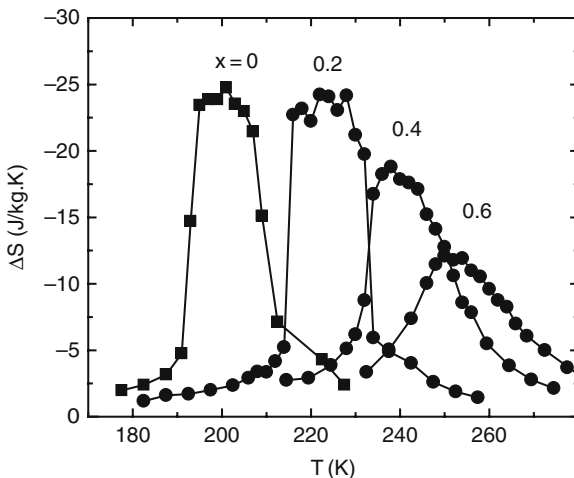
Fukamichi et al. [73] further studied the effect of interstitial hydrogen for $\text{LaFe}_{13-x}\text{Si}_x$ with $x=1.3$, which exhibits a much larger ΔS . It was found that ΔS , for a field change of 0–2 T, varied from ~ 29 J/kgK for $T \approx 195$ K to ~ 26 J/kgK

Fig. 15.32 Lattice constant as a function of the content of interstitial atoms for $\text{LaFe}_{11.5}\text{Si}_{1.5}(\text{H/C})_{\delta}$ (Ref. [77])



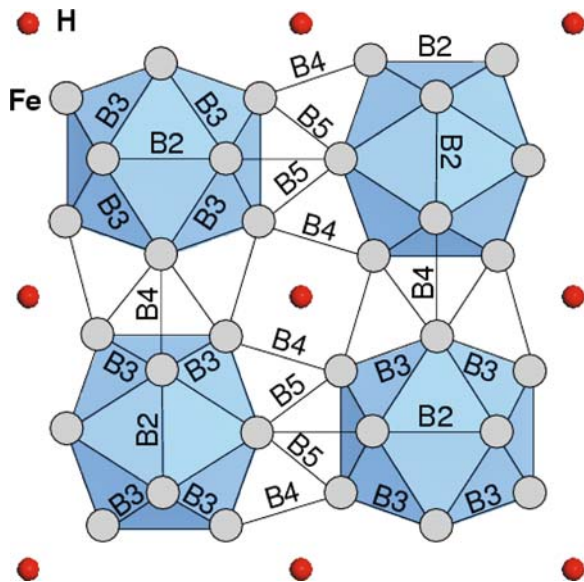
for $T \approx 320$ K, again a slow decay of ΔS with T_C . Influence of interstitial atoms on MCE was also investigated for $\text{La}_{1-x}\text{Pr}_x\text{Fe}_{11.44}\text{Si}_{1.56}$ [74]. The decrease of ΔS with the increase of T_C is more rapid compared with other compounds without R, as shown in Fig. 15.31, which could be a consequence of the broadening of magnetic transition due to the bad crystal quality of the samples. Wang et al. [75] studied the MCE of the $\text{LaFe}_{11.7-y}\text{Mn}_y\text{Si}_{1.3}\text{H}_{\delta}$ hydride (Fig. 15.30), which exhibits a much lower T_C , and obtained the same conclusion that the incorporation of interstitial hydrogen drives ΔS to higher temperatures at the least expense of ΔS value (Fig. 15.31). According to Fig. 15.31, the Curie temperature of $\text{LaFe}_{13-x}\text{Si}_x\text{H}_{\delta}$ can be tuned between ~ 130 and ~ 340 K by the content of hydrogen while large ΔS retains.

Fig. 15.33 Entropy change of $\text{LaFe}_{11.5}\text{Si}_{1.5}\text{C}_{\delta}$ ($\Delta H = 5$ T) (Ref. [78])



It is unfortunate that the hydrides are usually chemically unstable above 150°C , which could be a fatal problem for practical applications. It is therefore necessary to develop chemically stable interstitials with high T_C s and great ΔS values. Chen

Fig. 15.34 A schematic for the atomic structure of $\text{LaFe}_{13}\text{H}_3$ (La is omitted for clarity) (Ref. [77])

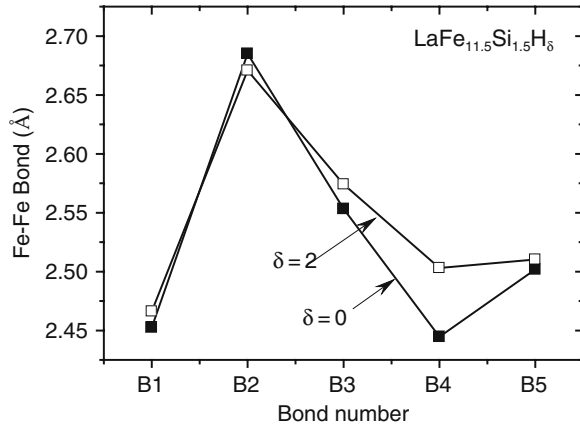


et al. [76] studied the effects of interstitial carbon for the $\text{LaFe}_{13-x}\text{Si}_x\text{C}_\delta$ carbides, which are stable up to the melting point. The $\text{LaFe}_{11.4}\text{Si}_{1.4}\text{C}_\delta$ ($\delta=0, 0.2, 0.4,$ and 0.6) carbides were prepared by the solid–solid phase reaction technique, that is, arc melting Fe–C intermediate alloy together with La, Fe and Si. X-ray diffraction analyses indicate the volume expansions of $\sim 0.29, \sim 0.75,$ and $\sim 0.93\%$ corresponding to $\delta=0.2, 0.4,$ and $0.6,$ respectively, though the cubic NaZn_{13} -type structure remains unchanged. Compared with hydrides, the lattice expansion of carbides is much stronger [77], as shown in Fig. 15.32. Minor α -Fe phase appears (6%) when the carbon concentration is $\delta=0.6$. The Curie temperatures of $\text{LaFe}_{11.6}\text{Si}_{1.4}\text{C}_x$ are 195, 218, 238, and 250 K for $\delta=0, 0.2, 0.4,$ and $0.6,$ respectively, increasing with carbon content.

Figure 15.33 shows the entropy change of $\text{LaFe}_{11.6}\text{Si}_{1.4}\text{C}_\delta$ [76]. The maximal ΔS is ~ 24.2 J/kgK for $\delta=0.2,$ ~ 18.8 J/kgK for $\delta=0.4,$ and ~ 12.1 J/kgK for $x=0.6$. The entropy change remains constant when x is below 0.2, while decreases rapidly for $x > 0.4$. The latter could be a consequence of the appearance of impurity phase, which affects crystal quality of the sample, thus broadens the phase transition. A little different carbides $\text{LaFe}_{11.5}\text{Si}_{1.5}\text{C}_\delta$ were also studied and similar effects were observed.

Structure changes due to the introduction of hydrogen were studied by Jia et al. [77] for the $\text{LaFe}_{11.5}\text{Si}_{1.5}\text{H}_\delta$ hydrides ($\delta=0, 1.2,$ and 2), based on the Rietveld analyses of powder X-ray diffraction spectra. It was found that the incorporation of interstitial atoms causes a lattice expansion of the compounds while leaves the structural symmetry unchanged. Accompanying the lattice expansion, as shown in Figs. 15.34 and 15.35, Fe–Fe bond exhibits a concomitant variation. Four of the

Fig. 15.35 Change of Fe–Fe bond length upon hydrogenating for the compound $\text{LaFe}_{11.5}\text{Si}_{1.5}\text{H}_\delta$ (Ref. [77])



five Fe–Fe bonds show a tendency to expansion. The largest elongation occurs for the shortest inter-cluster bond (B_4), and the relative change is as large as $\sim 2.37\%$ as δ increases from 0 to 2. In contrast, the longest Fe–Fe bond (B_2) shrinks considerably (-0.53%). Effect of Ce doping was also studied by the same authors for comparison. It is fascinating that the increase in Ce content produces essentially the same effect on Fe–Fe bonds as the decrease of hydrogen content, though interstitial atoms occupy different crystallographic sites from rare earths. A linear increase of Curie temperature with lattice constant, at a rate of $\sim 1,779 \text{ K}/\text{\AA}$ for $\text{LaFe}_{11.5}\text{Si}_{1.5}\text{H}_\delta/\text{La}_{1-x}\text{Ce}_x\text{Fe}_{11.5}\text{Si}_{1.5}$ and $\sim 1,089 \text{ K}/\text{\AA}$ for $\text{LaFe}_{11.5}\text{Si}_{1.5}\text{C}_\delta$, is observed. This is a signature of the strengthening of magnetic coupling as lattice expands. It is found that the change of the shortest Fe–Fe bond dominates the magnetic coupling in the $\text{LaFe}_{13-x}\text{Si}_x$ -based intermetallics. A relation between exchange integral and Fe–Fe distance has been proposed to explain the volume effects observed.

In Table 15.1, we give a summary of the magnetic/crystallographic transition temperature T_C , isothermal entropy change ΔS , adiabatic temperature change ΔT_{ad} for $\text{LaFe}_{13-x}\text{Si}_x$, and related compounds.

Thermal and Magnetic Hystereses of $\text{La}(\text{Fe}_{1-x}\text{Si}_x)_{13}$

A typical feature of the first-order transition is the appearance of thermal and magnetic hystereses. This will affect the efficiency of magnetic refrigeration. As mentioned in previous sections, although MCE enhances in the materials that show first-order transitions, thermal and magnetic hystereses intensify simultaneously. This phenomenon is especially obvious in R-doped $\text{LaFe}_{13-x}\text{Si}_x$, $\text{Gd}_5(\text{Si}_{1-x}\text{Ge}_x)_4$ and MnAs-based compounds. It is therefore necessary to find a method to depress magnetic hysteresis without spoiling the giant MCE, which is actually equivalent to depressing the driving force of the phase transition. Recently Shen et al. [78] found that the hysteresis can be significantly depressed by introducing

Table 15.1 Magnetic/crystallographic transition temperature T_C , isothermal entropy change ΔS , adiabatic temperature change ΔT_{ad} for $\text{LaFe}_{13-x}\text{Si}_x$, and related compounds for the field changes from 0 to 2 T and from 0 to 5 T

Material	T_C (K)	$\Delta S(\text{J/kgK})$ (0–2 T)	$\Delta S (\text{J/kgK})$ (0–5 T)	ΔT_{ad} (K) (0–2 T)	ΔT_{ad} (K) (0–5 T)	References
$\text{LaFe}_{13-x}\text{Si}_x$						
$x = 1.3$	184	-28	-30		12.1	[39]
$x = 1.43$	188	-24	-26		10.7	[39]
$x = 1.56$	195	-20	-23	6.5	8.6	[39, 56]
$x = 1.6$	208	-14				[37]
$x = 1.8$	220	-7.48	-13			[37]
$x = 2.0$	234	-4	-7.2			[37]
$x = 2.4$	250	-3	-4.8			[37, 79]
$\text{La}_{1-x}\text{Ce}_x\text{Fe}_{11.44}\text{Si}_{1.56}$						
$x = 0.1$		-22.9				[53, 54]
$x = 0.2$		-26.4				[53, 54]
$x = 0.3$		-28.9		7.3		[53, 54]
$\text{La}_{1-z}\text{Pr}_z\text{Fe}_{11.5}\text{Si}_{1.5}$						
$Z = 0.1$	191.0		-16.5			[57]
$Z = 0.2$	187.5		-27.0			[57]
$Z = 0.3$	184.5		-28.0			[57]
$Z = 0.4$	181.5		-29.1			[57]
$Z = 0.5$	181.0		-29.4			[57]
$\text{La}_{1-x}\text{Pr}_x\text{Fe}_{11.44}\text{Si}_{1.56}$						
$Z = 0$	195.9		-23.0		8.6	[74]
$Z = 0.1$	193.8		-25.7		10.5	[74]
$Z = 0.2$	192.2		-25.4		10.4	[74]
$Z = 0.3$	191.1		-26.0		11	[74]
$Z = 0.4$	188.0		-27.5		11.3	[74]
$Z = 0.5$	186.1		-29.9		11.9	[74]
$\text{LaFe}_{11.7}\text{Si}_{1.3}\text{H}_\delta$						
$\delta = 1.1$	287	-28	-31	7.1	15.4	[39]

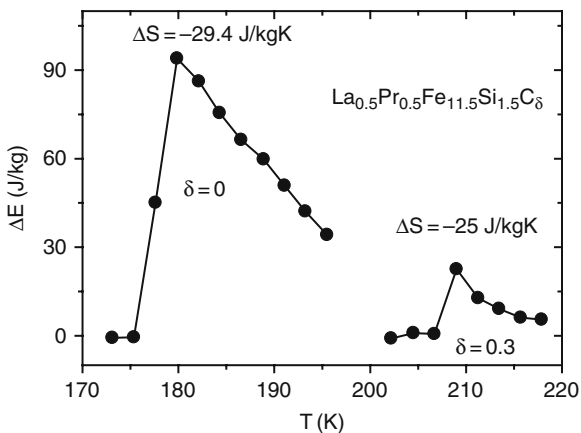


Fig. 15.36 Temperature-dependent hysteresis loss of $\text{La}_{0.5}\text{Pr}_{0.5}\text{Fe}_{11.5}\text{Si}_{1.5}\text{C}_\delta$ ($\delta=0$ and 0.3) (Ref. [78])

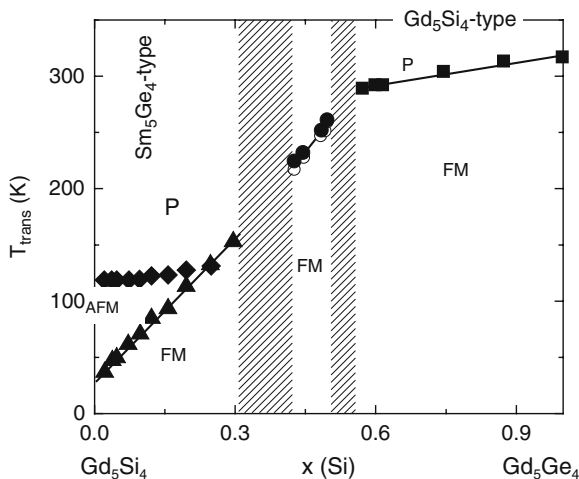
interstitial atoms into the compound. Figure 15.36 displays the hysteresis loss of $\text{La}_{0.5}\text{Pr}_{0.5}\text{Fe}_{11.5}\text{Si}_{1.5}\text{C}_{\delta}$. ΔE decreases from ~ 91 to ~ 22 J/kgK when δ increases from 0 to 0.3. The high-temperature shift of the phase transition, where the maximal ΔS occurs, could be the main reason for the reduction of ΔE : Strong thermal fluctuation at high temperatures reduces the driving force required. This result indicates that introducing interstitial atoms could be also be a promising method to get giant MCE while without significant ΔE .

15.5.2 $\text{Gd}_5(\text{Ge},\text{Si})_4$ and Related Compounds

The large entropy change observed in $\text{Gd}_5\text{Si}_2\text{Ge}_2$ [14, 15] triggered the exploration of the MCE effect in $\text{Gd}_5(\text{Ge},\text{Si})_4$ and related compounds [80,82,83,84,85]. In the following, we will give a brief introduction to this kind of materials. A detailed review can be found elsewhere [86]. In fact, the crystal structures of Gd_5Si_4 , Gd_5Ge_4 and $\text{Gd}_5(\text{Ge},\text{Si})_4$ were studied 40 years ago [87], and three categories of structures were identified, which are, respectively, the Gd_5Si_4 - and Gd_5Ge_4 -based structures, and an unknown phase when the Ge or Si content is in the intermediate range. It was originally believed that the Gd_5Si_4 and Gd_5Ge_4 -based solutions have the Sm_5Ge_4 -type structure. A completed phase diagram of the $\text{Gd}_5(\text{Si}_x\text{Ge}_{1-x})_4$ system was recently established by Pecharsky and Gschneidner [80]. Three extended solid solution regions and two two-phase coexisted regions were confirmed, see Fig. 15.37. The first one is Si-rich region when $0.575 \leq x \leq 1$. The compounds in this region crystallize in the Gd_5Si_4 structure and they undergo a second-order magnetic transition on warming, without structural changes. All of the compounds exhibit a moderate MCE. The second region is for $0.4 < x \leq 0.503$, where the $\text{Gd}_5\text{Si}_2\text{Ge}_2$ -type solid solutions with monoclinic structure appear. The alloys in this region experience a first-order magnetic transition that is coupled with a Gd_5Si_4 to $\text{Gd}_5\text{Si}_2\text{Ge}_2$ structure change and display a giant MCE. The last region is for $0 < x \leq 0.3$, where the Sm_5Ge_4 -type structure is supported. Two regions with coexisted phases were also identified. The first one is the coexistence of the Sm_5Ge_4 -type and the $\text{Gd}_5\text{Si}_2\text{Ge}_2$ -type phases when $0.3 < x \leq 0.4$, and second one is the coexistent $\text{Gd}_5\text{Si}_2\text{Ge}_2$ -type and Gd_5Si_4 -type structure when $0.503 < x < 0.575$. Both the monoclinic $\text{Gd}_5\text{Si}_2\text{Ge}_2$ -type and the orthorhombic Sm_5Ge_4 -type alloys exhibit giant MCE around respective transition temperatures because of the first-order phase transformations.

The major difference between the three crystallographic modifications in the $\text{Gd}_5(\text{Si}_x\text{Ge}_{1-x})_4$ system is due to different bonding arrangements between the well-defined sub-nanometer thick slabs [80]. The orthorhombic Sm_5Ge_4 type, where none of the slabs are interconnected via covalent-like Ge—Ge bonds, belongs to space group $Pnma$. The $\text{Gd}_5\text{Si}_2\text{Ge}_2$ type is the monoclinic phase, which belongs to space group $P112/a$, and the covalent-like (Si,Ge)—(Si,Ge) bonds connect the slabs into pairs, but no (Si,Ge)—(Si,Ge) bonds are found between the pairs of the slabs. The Gd_5Si_4 type is also an orthorhombic structure and it has the same space group as

Fig. 15.37 Magnetic phase diagram of the $\text{Gd}_5\text{Si}_4\text{--Gd}_5\text{Ge}_4$ pseudobinary system. The *thin solid lines* indicate magnetic phase boundaries, and the *vertical dotted lines* delineate the regions where the alloys are single-phase materials (the compositions within *shaded areas* are two-phase alloys). This figure is reprinted from Ref. [80]



the Sm_5Ge_4 -type structure, but all the slabs are interconnected via covalent-like Si–Si bonds. During the Gd_5Si_4 -type to Sm_5Ge_4 -type phase change, the a lattice parameter expansion exceeds that of the other two lattice parameters by nearly a factor of 5. On the atomic resolution scale, the distances between the Si(Ge) atoms increase from 2.5 to 2.6 Å (Gd_5Si_4) to 3.4–3.5 Å (Gd_5Ge_4), indicating much stronger interactions between the slabs in the former when compared with the latter.

The structural change at the phase transition in the $\text{Gd}_5(\text{Si}_x\text{Ge}_{1-x})_4$ system also brings about a strong magneto-elastic effect, and an anomalous electrical resistivity, indicating a strong coupling between electronic structure and lattice.

Because of the coupled magnetic and structural transitions, $\text{Gd}_5(\text{Si}_x\text{Ge}_{1-x})_4$ exhibits great magnetic entropy change ΔS covering the temperatures from ~ 50 to ~ 300 K [15]. The ΔS value first reported in a polycrystalline sample $\text{Gd}_5\text{Si}_2\text{Ge}_2$ [14] in 1997 reached 18.8 J/kgK for a field change of 5 T, and the corresponding adiabatic temperature change is 15 K. It is nearly doubled of the known materials at that time. By improving the crystal quality of $\text{Gd}_5\text{Si}_2\text{Ge}_2$, the ΔS value was further enhanced by 80% and ΔT_{ad} by 55% [87]. A minor addition of other elements such as Fe, Co, Ni, Cu, Ga, Al, and C can shift the temperature of the phase transition but did not enhance the MCE effect [88]. By altering the Si to Ge ratio in $\text{Gd}_5(\text{Si}_x\text{Ge}_{1-x})_4$, the transition temperature shifts from ~ 50 to ~ 300 K, and a great MCE was resulted (Fig. 15.38).

Although the $\text{Gd}_5(\text{Si}_x\text{Ge}_{1-x})_4$ system shows a great MCE, it exhibits considerable magnetic and thermal hystereses, which will impede its practical application as refrigerants. It is therefore necessary to reduce hysteresis loss while retaining the MCE. Unfortunately, a satisfy solution cannot be found in literature. Although changing the Si to Ge ratio can push T_C to high temperatures, no significant improvement in hysteresis loss was observed. It was recently reported that the addition

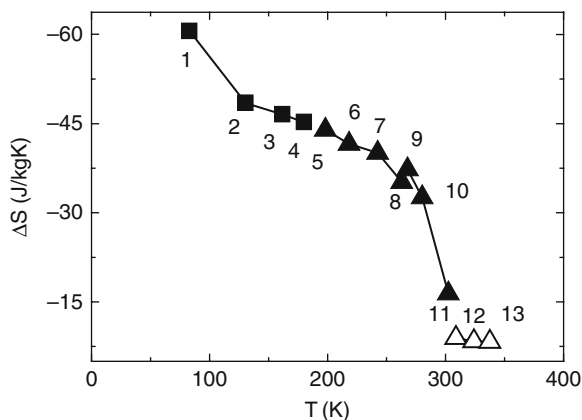


Fig. 15.38 Magnetic entropy change of the $\text{Gd}_5(\text{Si}_x\text{Ge}_{1-x})_4$ for a field change of 5 T. *Solid squares* are for the compounds which exhibit a coupled magnetic and structural transition; *solid triangles* represent those for the first-order magnetic transition coupled with Gd_5Si_4 -type to $\text{Gd}_5\text{Si}_2\text{Ge}_2$ -type structural transformation, while the open triangles are for the second-order ferromagnetic–paramagnetic transition with Gd_5Si_4 -type structure unchanged. The data of this figure were obtained from Ref. [86]. 1 – $\text{Gd}_5\text{Si}_{0.5}\text{Ge}_{3.5}$, 2 – Gd_5SiGe_3 , 3 – $\text{Gd}_5\text{Si}_{1.2}\text{Ge}_{2.8}$, 4 – $\text{Gd}_5\text{Si}_{1.3}\text{Ge}_{2.7}$, 5 – $\text{Gd}_5\text{Si}_{1.5}\text{Ge}_{2.5}$, 6 – $\text{Gd}_5\text{Si}_{1.6}\text{Ge}_{2.4}$, 7 – $\text{Gd}_5\text{Si}_{1.8}\text{Ge}_{2.2}$, 8 – $\text{Gd}_5\text{Si}_{1.95}\text{Ge}_{2.05}$, 9 – $\text{Gd}_5\text{Si}_{1.98}\text{Ge}_{2.02}$, 10 – $\text{Gd}_5\text{Si}_{2.02}\text{Ge}_{1.98}$, 11 – $\text{Gd}_5\text{Si}_{2.1}\text{Ge}_{1.9}$, 12 – $\text{Gd}_5\text{Si}_{2.3}\text{Ge}_{1.7}$, 13 – $\text{Gd}_5\text{Si}_3\text{Ge}$, and 14 – Gd_5Si_4

Fig. 15.39 Magnetic hysteresis loss (*top panel*) and magnetic entropy change (*bottom panel*) as functions of temperature for the $\text{Gd}_5(\text{Si}_{1-x}\text{Ge}_x)_4$ compounds (unpublished data of the authors)

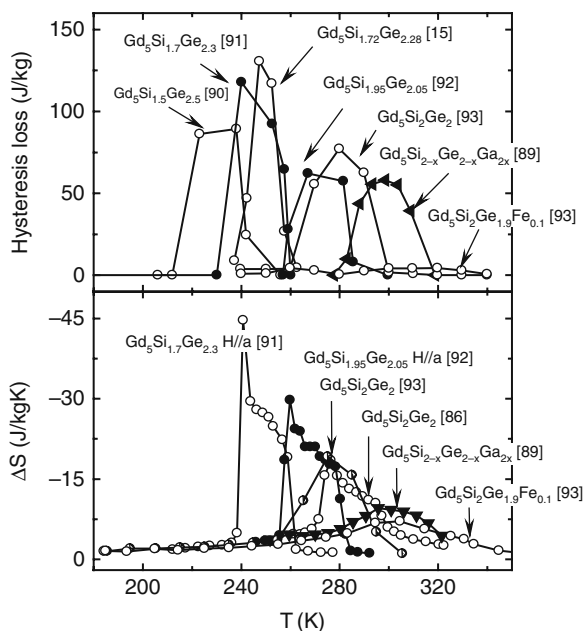


Fig. 15.40 A schematic structure of Heusler alloy X_2YZ

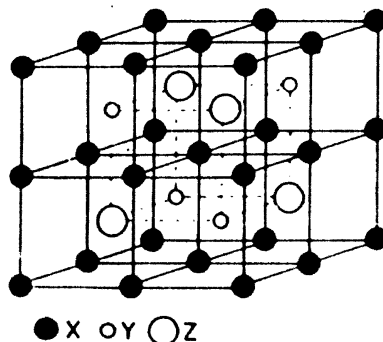
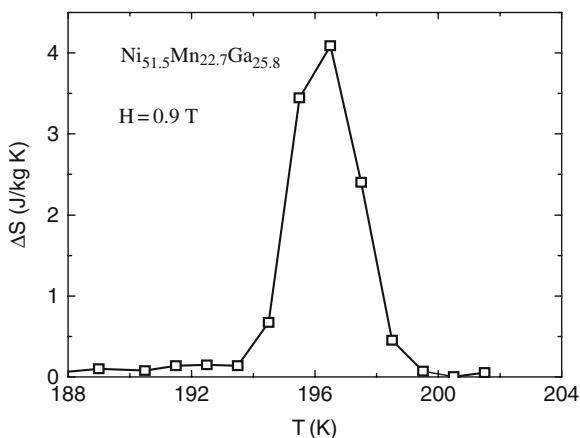


Fig. 15.41 Magnetic entropy change of a polycrystalline alloy $Ni_{51.5}Mn_{22.7}Ga_{25.8}$ under a field change from 0 to 0.9 T (Ref. [96])



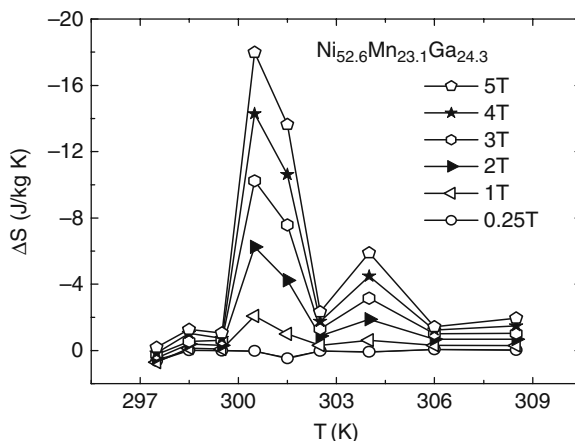
of Fe can remarkably reduce the hysteresis loss, however, ΔS was simultaneously depressed by 63% [93]. Figures 15.39(a) and (b) show the magnetic hysteresis loss and the entropy change as functions of temperature for the $Gd_5(Si_xGe_{1-x})_4$ compounds.

For practical applications, the production cost of the refrigerant is also an important factor to be considered. It has been reported that the MCE of $Gd_5(Si_xGe_{1-x})_4$ depends strongly on the purity of starting materials [88]. Impurity atoms such as carbon and oxygen in the starting materials can hamper the formation of the monoclinic structure, and the $Gd_5(Si_xGe_{1-x})_4$ alloys thus obtained only show a second-order phase transition with a much weaker MCE [80, 90, 91, 93]. However, high purity starting materials increase the production cost, which will limit the broad application of this kind of materials.

Replacing Gd with Tb, it was found that the $Gd_5Si_2Ge_2$ -type structure can also be obtained, and a large MCE shows up when the structural transition coincides with the magnetic one, which can be realized by applying a pressure of 8.6 kbar as

shown by Morellon et al. [94]. The maximal entropy change reaches ~ 22 J/kgK for a field change of 5 T ($P=10.2$ kbar).

Fig. 15.42 Magnetic entropy change of a single crystal alloy $\text{Ni}_{52.6}\text{Mn}_{23.1}\text{Ga}_{24.3}$ under different magnetic fields (Ref. [97])



15.5.3 Mn-Based Heusler Alloys

The Heusler alloys with the nominal formula of X_2YZ crystallize in the $L2_1$ structure [95]. As shown in Fig. 15.40, the structure is composed of four interpenetrating fcc sublattices, with two of them being occupied by X atoms. In general, the X is a noble or a transition metal, and Z is the atoms with s and p valence electrons. In Mn-based Heusler alloys, Mn occupies the Y sites, and it exhibits a magnetic moment of $4 \mu_B$ if the X sites are not occupied by Co or Fe. As shown by Fig. 15.40, the Mn atom has eight nearest neighboring X and six second neighboring Z. The neighboring Mn atoms appear in the third shell. The typical distance between first, second, and third neighbors are 2.6, 3, and 4.2 Å, respectively. Because of the large distance between Mn atoms, a direct exchange interaction is negligible and the magnetic coupling is mediated by the itinerant electrons of X and Y atoms. Therefore, the magnetic interaction is sensitive to the electronic structure of X and Z. The structural and magnetic properties of the alloys are sensitive to chemical order, compositions, and the lattice parameter. Most of the Mn-based Heusler alloys are FM, such as the typical compound Ni_2MnGa , which is well known for its shape-memory effect, superelasticity, and magnetic-field-induced strain. AFM state appears when the Z sites are occupied by Al or In. Mn carries a magnetic moment of $4 \mu_B$, while Ni a rather small moment.

Ni–Mn–Ga undergoes a martensitic–austenitic structure transition on heating. Both the martensite and the austenite phases are FM. However, the magnetic behaviors of the two phases are significantly different. The former is hard to be magnetically saturated because of its large magnetocrystalline anisotropy. The

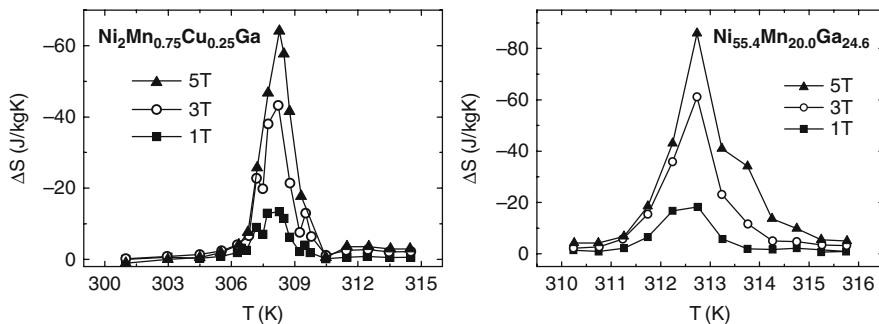
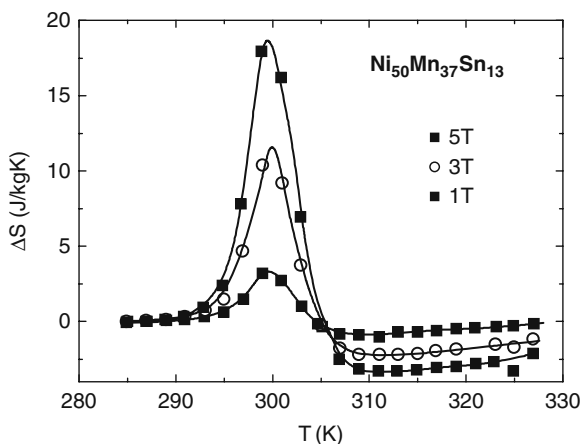


Fig. 15.43 Magnetic entropy change as a function of temperature for a polycrystalline alloys $\text{Ni}_2\text{Mn}_{0.75}\text{Cu}_{0.25}\text{Ga}$ (left, Ref. [102]) and $\text{Ni}_{55.4}\text{Mn}_{20.0}\text{Ga}_{24.6}$ (right, Ref. [103])

simultaneous change of structure and magnetic properties at the phase transition yields significant entropy changes. Since the first report of large ΔS associated with the structure transition in $\text{Ni}_{51.5}\text{Mn}_{22.7}\text{Ga}_{25.8}$ in 2000 (Fig. 15.41) [96], an intensive study on the magnetic and magnetocaloric properties of various Heusler alloys has been stimulated [96,97,98,99,100,101,102,103,104]. It was found that ΔS is positive under low magnetic fields. It becomes negative and increases with applied field when magnetic field is high [98]. As shown in Fig. 15.42, the entropy change of the single crystal $\text{Ni}_{52.6}\text{Mn}_{23.1}\text{Ga}_{24.3}$ is $\sim 18 \text{ J/kgK}$ ($\Delta H=5 \text{ T}$) [97], nearly the same as that of $\text{Gd}_5\text{Si}_2\text{Ge}_2$. The martensitic transition temperature, thus the ΔS peak, can be tuned by the chemical compositions between 150 and 300 K as required. It was recently found an extremely high ΔS can be gained when the structural and magnetic transition coincides with each other. The reported ΔS of -64 J/kgK ($\Delta H=5 \text{ T}$ and $T_C=308 \text{ K}$) and -86 J/kgK ($\Delta H=5 \text{ T}$ and $T_C=313 \text{ K}$) occurred in polycrystalline $\text{Ni}_2\text{Mn}_{0.75}\text{Cu}_{0.25}\text{Ga}$ [102] and single crystal $\text{Ni}_{55.4}\text{Mn}_{20.0}\text{Ga}_{24.6}$ [103], respectively (Fig. 15.43). However, there is still no evidence from the thermal data for the giant entropy change at present. The adiabatic temperature change ΔT_{ad} of the Heusler alloys is rarely reported, and the only result is 1.2 K ($\Delta H=2.6 \text{ T}$), for a polycrystalline alloy $\text{Ni}_{54.8}\text{Mn}_{20.2}\text{Ga}_{25.0}$.

A new kind of Heusler alloys, named meta-magnetic shape-memory alloys (MSMAs), has recently attracted intensive attention [105]. In these materials, the magnetization of martensite phase is very low. Magnetic fields can induce a martensitic-austenitic transformation, thus a huge shape-memory effect. Meanwhile, the structure transition is accompanied by a significant MCE, and a ΔS spanned in a relatively wide temperature range has been observed [104, 106,107,108]. ΔS is positive, and amounts to $\sim 18 \text{ J/kgK}$ ($\Delta H=5 \text{ T}$ and $T_C=307 \text{ K}$) for $\text{Ni}_{50}\text{Mn}_{37}\text{Sn}_{13}$ [104] and $\sim 6.8 \text{ J/kgK}$ ($\Delta H=1 \text{ T}$ and $T_C=307 \text{ K}$) for $\text{Ni}_{50}\text{Mn}_{39}\text{Sn}_{11}$ [106] (Fig. 15.44). The wide temperature span (about 5–30 K) of ΔS may be the main advantages of MSMAs over the traditional Heusler alloys. The adiabatic temperature change ΔT_{ad} of $\text{Ni}_{50}\text{Mn}_{34}\text{In}_{16}$ is -0.6 K for a field change of 1.3 T [108, 109].

Fig. 15.44 Magnetic entropy change as a function of temperature for a polycrystalline alloy $\text{Ni}_{50}\text{Mn}_{37}\text{Sn}_{13}$ for various changes in applied magnetic field. This figure is reprinted from Ref. [104]



Significant thermal and magnetic hysteresis exists in both the FSMAs and the MSMA alloys because of the first-order transition. In general, the thermal hysteresis varies between 5 and 20 K, and the magnetic one between 0 and 60 J/kg, crucially depending on compositions. The preparation of Heusler alloys is fairly simple. Polycrystalline samples can be obtained by the arc melting technique. The resulting ingots were homogenized at 1,100 K within 10 days, then quenched into ice water.

15.5.4 Mn–As-Based Compounds

MnAs is a ferromagnet with saturation magnetization of $3.4 \mu_{\text{B}}/\text{Mn}$ [110]. A first-order FM–PM transition takes place at $T_{\text{C}} \approx 318$ K. Accompanying this transition, a hexagonal (NiAs-type) to orthorhombic (MnP-type) structure transformation occurs. The resulting MCE is pretty large, and ΔS reaches ~ 40 J/kgK and $\Delta T_{\text{ad}} \sim 13$ K for a field change of 5 T [18, 110]. The MnAs alloy shows large thermal and magnetic hystereses. A substitution of Sb for As can reduce thermal hysteresis and lower T_{C} to ~ 280 K while the MCE effect is not remarkably affected. ΔS still has a value of -30 J/kgK even 10% As was replaced by Sb [18, 110].

$\text{MnFeP}_{0.45}\text{As}_{0.55}$ is another kind of compounds showing significant MCE [111]. It crystallizes in the hexagonal Fe_2P -type structure, with a Curie temperature of ~ 307 K. The magnetic transition is first order with a thermal hysteresis less than 1 K. The maximal ΔS is ~ -18 J/kgK for a field change of 5 T. A variation of the P to As ratio between 3:2 and 1:2 tunes T_{C} between 200 and 350 K without obviously affecting MCE [112].

The preparation of the $\text{MnAs}_{1-x}\text{Sb}_x$ and $\text{MnFeP}_{1-x}\text{As}$ alloys is simple [18, 110, 111, 112]. However, the high vapor pressure of As and P and the toxicity of As may limit their applications in commercial devices.

15.6 Concluding Remarks

The discovery of giant MCE in $\text{Gd}_5\text{Si}_2\text{Ge}_2$, $\text{LaFe}_{13-x}\text{Si}_x$, and $\text{MnFeP}_{1-x}\text{As}_x$, etc. leads the interest of researchers to the material that experience a first-order phase transition, which causes an entropy change concentrated in a narrow temperature range, thus a giant MCE. In addition to the materials discussed here, considerable MCE is also observed in perovskite manganese oxides [113], antiperovskite Mn_3GaC [114], and many other compounds.

In this case, lattice or electronic entropy can also undergo a significant change on the application of magnetic field, therefore is usable for magnetic cooling. These results display a bright prospect of the magnetic refrigeration near ambient temperature.

Compared with other materials, the $\text{LaFe}_{13-x}\text{Si}_x$ intermetallics show considerable advantages as far as magnetic hysteresis loss, thermal conductive property, and production cost of the materials being concerned. There are also attempts to verify the efficiency of this kind of materials as magnetic refrigerants by putting sphere-shaped $\text{LaFe}_{11.18}\text{Si}_{1.82}\text{H}_8$ into an active magnetic regenerator (AMR) test module, and satisfactory result is obtained [115]. However, the existing materials are still far from practical applications. New materials with much stronger MCE are desired to guarantee the high efficiency of the magnetic refrigeration, especially when permanent magnet is used in refrigerators. As far as the practical application being concerned, furthermore, several basic issues involved in the MCE arising from the first-order phase transition must be considered. For example, the effects of magnetic/thermal hysteresis and magnetostriction, the latter may cause a degeneration of the performance of materials because of the mechanical fatigue.

Acknowledgments The authors wish to thank Mrs. Jia Lin for her assistant in preparing part of the figures.

References

1. E. Warburg, *Ann. Phys.* **13**, 141 (1881).
2. P. Langevin, *Ann. Chim. Phys.* **5**, 70 (1905).
3. P. Debye, *Ann. Phys.* **81**, 1154 (1926).
4. W. F. Giauque, *J. Amer. Chem. Soc.* **49**, 1864 (1927).
5. W. F. Giauque, I. D. P. MacDougall, *Phys. Rev.* **43**, 768 (1933).
6. P. J. Hakonen, S. Yin, and O. V. Lounasmaa, *Phys. Rev. Lett.* **64**, 2707 (1990).
7. W. F. Giauque, *J. Amer. Chem. Soc.* **49**, 1864 (1927); W. F. Giauque and D. P. McDougall, *Phys. Rev.* **43**, 768 (1933).
8. R. D. McMichael, J. J. Ritter, and R. D. Shull, *J. Appl. Phys.* **73**, 6946 (1993); R. D. Shull and R. D. McMichael, *Nanostructure Mater.* **2**, 205 (1993); R. D. Shull, *IEEE Trans. Magn.* **29**, 2614 (1993).
9. T. Hashimoto, T. Kuzuhara, M. Sahashi, K. Inomata, A. Tomokiyo and H. Yayama, *J Appl. Phys.* **62**, 3873 (1987).
10. T. Hashimoto, T. Kuzuhara, K. Matsumoto, M. Sahashi, K. Imonata, A. Tomokiyo, and H. Yayama, *IEEE Trans. Mag.* **MAG-23**, 2847 (1987).
11. Tishin A. M. and Y. I. Spichkin, *The magnetocaloric effect and its application*, IOP Publishing Ltd, 2003.

12. G. V. Brown, *J. Appl. Phys.* **47**, 3673 (1976).
13. C. Zimm, A. Jastrab, A. Sternberg, V. K. Pecharsky, K. Gschneidner Jr, M. Osborne, and I. Anderson, *Adv. Cryog. Eng.* **43**, 1759 (1998).
14. V. K. Pecharsky and K. A. Gschneidner Jr., *Phys. Rev. Lett.* **78**, 4494 (1997).
15. V. K. Pecharsky and K. A. Gschneidner Jr., *Appl. Phys. Lett.* **70**, 3299 (1997).
16. F. X. Hu, B. G. Shen, J. R. Sun, and X. X. Zhang, *Chinese Phys.* **9**, 550 (2000).
17. F. X. Hu, B. G. Shen, J. R. Sun, and Z. H. Cheng, *Appl. Phys. Lett.* **78**, 3675 (2001).
18. H. Wada and Y. Tanabe, *Appl. Phys. Lett.* **79**, 3302 (2001).
19. O. Tegus, E. Brück, K. H. J. Buschow, and F. R. de Boer, *Nature* **415**, 150 (2002).
20. V. K. Pecharsky and K. A. Gschneidner Jr., *J. Appl. Phys.* **86**, 565 (1999).
21. J. R. Sun, F. X. Hu, and B. G. Shen, *Phys. Rev. Lett.* **85**, 4191 (2000).
22. G. J. Liu, J. R. Sun, J. Shen, B. Gao, H. W. Zhang, F. X. Hu, and B. G. Shen, *Appl. Phys. Lett.* **90**, 032507 (2007).
23. A. de Campos, D. L. Rocco, A. M. G. Carvalho, L. Caron, A. A. Coelho, S. Gama, L. M. da Silva, F. C. G. Gandra, A. D. dos Santos, L. P. Cardoso, P. J. von Rank, and N. A. de Oliveira, *Nat. Mater.* **5**, 802 (2006).
24. A. Giguère, M. Foldeaki, B. Ravi Gopal, R. Chahine, T. K. Bose, A. Frydman, and J. A. Barclay, *Phys. Rev. Lett.* **83**, 2262 (1999).
25. S. Gama, A. A. Coelho, A. de Campos, A. Magnus G. Carvalho, and F. C.G. Gandra, *Phys. Rev. Lett.* **93**, 237202 (2004).
26. A. A. Coelho, S. Gama, F. C. G. Gandra, A. O. dos Santos, L. P. Cardoso, P. J. von Ranke, and N. A. de Oliveira, *Appl. Phys. Lett.* **90**, 242507 (2007).
27. G. J. Liu, J. R. Sun, J. Z. Wang, and B. G. Shen, *Appl. Phys. Lett.* **89**, 22503 (2006).
28. V. K. Pecharsky, K. A. Gschneidner Jr., *J. Magn. Magn. Mater.* **200**, 44 (1999).
29. K. H. J. Buschow, *Rep. Progr. Phys.* **40**, 1179 (1977).
30. P. I. Kripyakevich, O. S. Zarechnyuk, E. I. Gladushevsky, and O. I. Bodak, *Z. Anorg. Chem.* **358**, 90 (1968).
31. T. T. M. Palstra, J. A. Mydosh, G. J. Nieuwenhuys, A. M. van der Kraan, and K. H. J. Buschow, *J. Magn. Magn. Mater.* **36**, 290 (1983).
32. T. T. M. Palstra, G. J. Nieuwenhuys, J. A. Mydosh and K. H. J. Buschow, *Phys. Rev. B* **31**, 4622 (1985).
33. R. B. Helmholdt, T. T. M. Palstra, G. J. Nieuwenhuys, J. A. Mydosh, A. M. van der Kraan, and K. H. J. Buschow, *Phys. Rev. B* **34**, 169 (1986).
34. W. H. Tang, J. K. Liang, G. H. Rao, and X. Yan, *Phys. Stat. Sol.* **141**, 217 (1994).
35. A. Fujita and K. Fukamichi, *IEEE. Magb.* **35**, 3796 (1999).
36. A. Fujita, Y. Akamatsu, and K. Fukamichi, *J. Appl. Phys.* **85**, 4756 (1999).
37. F. X. Hu, *Magnetic properties and magnetic entropy change of Fe-based La(Fe,M)₁₃ compounds and Ni-Mn-Ga alloys*, Ph. D thesis, Institute of Physics of Chinese academy of Sciences, 2002.
38. L. Jia, J. R. Sun, J. Shen, B. Gao, and B. G. Shen (unpublished).
39. A. Fujita, S. Fujieda, Y. Hasegawa, and K. Fukamichi, *Phys. Rev. B* **67**, 104416 (2003).
40. G. J. Wang, F. Wang, N. L. Di, B. G. Shen, and Z. H. Cheng, *J. Magn. Magn. Mater.* **303**, 84 (2006).
41. F. Wang, J. Zhang, Y. F. Chen, G. J. Wang, J. R. Sun, S. Y. Zhang, and B. G. Shen, *Phys. Rev. B* **69**, 094424 (2004).
42. F. X. Hu, B. G. Shen, J. R. Sun, Z. H. Cheng, and X. X. Zhang, *J. Phys.: Condens. Matter* **12**, L691 (2000).
43. F. W. Wang, G. J. Wang, F. X. Hu, A. Kurbakov, B. G. Shen, and Z. H. Cheng, *J. Phys.: Condens. Matter* **15**, 5269(2003).
44. L. Jia, J. R. Sun, H. W. Zhang, F. X. Hu, C. Dong, and B. G. Shen, *J. Phys.: Condens. Matter* **18**, 9999 (2006).
45. A. Fujita, S. Fujieda, K. Fukamichi, Y. Yamazaki, Y. Iijima, *Mater. Trans.* **43**, 1202 (2002).
46. S. Fujieda, A. Fujita, and K. Fukamichi, *Appl. Phys. Lett.* **81**, 1276 (2002).

47. F. X. Hu, J. Gao, X. L. Qian, M. Ilyn, A. M. Tishin, J. R. Sun, and B. G. Shen, *J. Appl. Phys.* **97**, 10M303 (2005).
48. M. Balli, D. Fruchart, and D. Gignoux, *J. Phys.: Condens. Matter* **19**, 236230 (2007).
49. F. Wang, J. Zhang, Y. F. Chen, G. J. Wang, J. R. Sun, S. Y. Zhang, and B. G. Shen, *Phys. Rev. B* **69**, 094424 (2004).
50. S. Fujieda, A. Fujita, N. Kawamoto, and K. Fukamichi, *Appl. Phys. Lett.* **89**, 062504 (2006).
51. D. T. Kim Anh, N. P. Thuy a,b, N. H. Duca, T. T. Nhiena, and N. V. Nong, *J. Magn. Magn. Mater.* **262**, 427 (2003).
52. S. Fujieda, A. Fujita, and K. Fukamichi, *Mater. Trans.* **45**, 3228 (2004).
53. S. Fujieda, A. Fujita, and K. Fukamichi, *IEEE Trans. Magn.* **41**, 2787 (2005).
54. S. Fujieda, A. Fujita, K. Fukamichi, N. Hirano, and S. Nagaya, *J. Alloys. Comp.* **408–412**, 1165 (2006).
55. S. Fujieda, A. Fujita, N. Kawamoto, and K. Fukamichi, *J. Appl. Phys.* **99**, 08K910 (2006).
56. A. Fujita, S. Fujieda, and K. Fukamichi, *J. Magn. Magn. Mater.* **310**, E1006–E1007 (2007).
57. J. Shen, Y. X. Li, B. Gao, F. X. Hu, J. R. Sun, and B. G. Shen (unpublished).
58. J. Shen, B. Gao, L. Q. Yan, Y. X. Li, H. W. Zhang, F. X. Hu, and J. R. Sun, *Chinese Phys.* **16**, 3848 (2007).
59. S. Fujieda, A. Fujita, and K. Fukamichi, *J. Magn. Magn. Mater.* **310**, e1004 (2007).
60. S. Fujieda, A. Fujita, and K. Fukamichi, *J. Appl. Phys.* **102**, 023907 (2007).
61. Sun et al. unpublished.
62. S. Fujieda, A. Fujita, K. Fukamichi, Y. Yamazaki, and Y. Iijima, *Appl. Phys. Lett.* **79**, 653 (2001).
63. A. Fujita, S. Fujieda, K. Fukamichi, Y. Yamazaki, and Y. Iijima, *Mater. Trans.* **43**, 1202–1204 (2002).
64. A. Fujita, S. Fujieda, Y. Hasegawa, and K. Fukamichi, *Phys. Rev. B* **67**, 104416 (2003).
65. Y. F. Chen, F. Wang, B. G. Shen, F. X. Hu, Z. H. Cheng, G. J. Wang, and J. R. Sun, *Chin. Phys.* **11**, 741 (2002).
66. Y. F. Chen, F. Wang, B. G. Shen, F. X. Hu, J. R. Sun, G. J. Wang, and Z. H. Cheng, *J. Phys.: Condens. Matter* **15**, L161–L167 (2003).
67. Z. X. Tang, X. H. Deng, G. C. Hadjipanayis, V. Papaefthymiou and D. J. Sellmyer, *IEEE Trans. Magn.* **29**, 2839 (1993).
68. J. P. Liu, N. Tang, F. R. de Boer, P. F. de Chatel, and K. H. J. Buschow, *J. Magn. Magn. Mater.* **140–144**, 1035 (1995).
69. O. Moze, W. Kockelmann, J. P. Liu, F. R. de Boer, and K. H. J. Buschow, *J. Magn. Magn. Mater.* **195**, 391 (1999).
70. O. Moze, W. Kockelmann, J. P. Liu, F. R. de Boer, and K. H. J. Buschow, *J. Appl. Phys.* **87**, 5284 (2000).
71. K. Irisawa, A. Fujita, K. Fukamichi, Y. Yamazaki, Y. Iijima, and E. Matsubara, *J. Alloys Comp.* **316**, 70 (2001).
72. S. Fujieda, A. Fujita, K. Fukamichi, Y. Yamazaki, and Y. Iijima, *Appl. Phys. Lett.* **79**, 653 (2001).
73. K. Fukamichi, A. Fujita, and S. Fujieda, *J. Alloys Comp.* **408–412**, 307 (2006).
74. S. Fujieda, A. Fujita, and K. Fukamichi, *J. Appl. Phys.* **102**, 023907 (2007).
75. F. Wang, *Magnetic and magnetocaloric properties of NaZn₁₃-type La(Fe,M)₁₃ intermetallics*, *Ph.D. thesis, Institute of Physics of Chinese Academy of Sciences*, 2004.
76. Y. F. Chen, F. Wang, B. G. Shen, F. X. Hu, J. R. Sun, G. J. Wang, and Z. H. Cheng, *J. Appl. Phys.* **93**, 1323 (2003).
77. L. Jia, J. R. Sun, J. Shen, B. Gao, T. Y. Zhao, H. W. Zhang, F. X. Hu, and B. G. Shen (unpublished).
78. J. Shen, B. Gao, H. W. Zhang, F. X. Hu, Y. X. Li, J. R. Sun, and B. G. Shen, *Appl. Phys. Lett.* **91**, 142504 (2007).
79. X. X. Zhang, G. H. Wen, F. W. Wang, W. H. Wang, C. H. Yu, and G. H. Wu, *Appl. Phys. Lett.* **77**, 3072 (2000).

80. A. O. Pecharsky, K. A. Gschneidner Jr., V. K. Pecharsky, and C. E. Schindler, *J. Alloys Comp.* **338**, 126 (2002).
81. V. K. Pecharsky, A. O. Pecharsky, and K. A. Gschneidner Jr., *J. Alloys Comp.* **344**, 362 (2002).
82. A. O. Pecharsky, K. A. Gschneidner Jr., and V. K. Pecharsky, *J. Magn. Magn. Mater.* **267**, 60 (2003).
83. Y. Zhuo, R. Chahine, and T. K. Bose, *IEEE Trans. Magn.* **39**, 3358 (2003).
84. A. Giguere, M. Foldeaki, B. R. Gopal, R. Chahine, T. K. Bose, A. Frydman, and J. A. Barclay, *Phys. Rev. Lett.* **83**, 2262 (1999).
85. K. A. Gschneidner Jr., V. K. Pecharsky, E. Brück, H. G. M. Duijn, and E. M. Levin, *Phys. Rev. Lett.* **85**, 4190 (2000).
86. K. A. Gschneidner Jr., V. K. Pecharsky, and A. O. Tsokoll, *Rep. Prog. Phys.* **68**, 1479 (2005).
87. F. Holtzberg, R. J. Gambino, T. R. McGuire, *J. Phys. Chem. Solids*, **28**, 2283 (1967).
88. A. O. Pecharsky, K. A. Gschneidner Jr., and V. K. Pecharsky, *J. Appl. Phys.* **93**, 4722 (2003).
89. V. K. Pecharsky and K. A. Gschneidner Jr., *J. Magn. Magn. Mater.* **167**, L179 (1997).
90. E. M. Levina, K. A. Gschneidner Jr., and V. K. Pecharsky, *J. Magn. Magn. Mater.* **231** (2001) 135.
91. O. Tegus, E. Bruck, L. Zhang, Dagula, K. H. J. Buschow, and F. R. de Boer, *Physica B* **319** (2002) 174.
92. H. Tang, A. O. Pecharsky, D. L. Schlagel, T. A. Lograsso, V. K. Pecharsky, and K. A. Gschneidner Jr., *J. Appl. Phys.* **93**, 8298 (2003).
93. V. Provenzano, A. J. Shapiro, and R. D. Shull, *Nature* **429**, 853 (2004).
94. L. Morellon, Z. Arnold, C. Magen, C. Ritter, O. Prokhnenko, Y. Skorokhod, P. A. Algarabel, M. R. Ibarra, and J. Kamarad, *Phys. Rev. Lett.* **93**, 137201 (2004).
95. P. J. Webster, *Contemp. Phys.* **10**, 559 (1969).
96. F. X. Hu, B. G. Shen, and J. R. Sun, *Appl. Phys. Lett.* **76**, 3460 (2000).
97. F. X. Hu, B. G. Shen, J. R. Sun, and G. H. Wu, *Phys. Rev. B* **64**, 132412 (2001).
98. F. X. Hu, J. R. Sun, G. H. Wu, and B. G. Shen, *J. Appl. Phys.* **90**, 5216 (2001).
99. J. Marcos, L. Mañosa, A. Planes, F. Casanova, X. Batlle, and A. Labarta, *Phys. Rev. B* **68**, 094401 (2003).
100. F. Albertini, F. Canepa, S. Cirafici, E. A. Franceschi, M. Napoletano, A. Paoluzi, L. Pareti, and M. Solzi, *J. Magn. Magn. Mater.* **272–276**, 2111 (2004).
101. X. Zhou, W. Li, H. P. Kunkel, and G. Williams, *J. Phys.: Condens. Matter* **16**, L39 (2004).
102. S. Stadler, M. Khan, J. Mitchell, N. Ali, A. M. Gomes, I. Dubenko, A. Y. Takeuchi, and A. P. Guimarães, *Appl. Phys. Lett.* **88**, 192511 (2006).
103. M. Pasquale, C. P. Sasso, L. H. Lewis, L. Giudici, T. Lograsso, and D. Schlagel, *Phys. Rev. B* **72**, 094435 (2005).
104. T. Krenke, E. Duman, M. Acet, E. F. Wassermann, X. Moya, L. Mañosa, and A. Planes, *Nat. Mater.* **4**, 450 (2005).
105. R. Kainuma, Y. Imano, W. Ito, Y. Sutou, H. Morito, S. Okamoto, O. Kitakami, K. Oikawa, A. Fujita, T. Kanomata, and K. Ishida, *Nature* **439**, 957 (2006).
106. Z. D. Han, D. H. Wang, C. L. Zhang, H. C. Xuan, B. X. Gu, and Y. W. Du, *Appl. Phys. Lett.* **90**, 042507 (2007).
107. T. Krenke, E. Duman, M. Acet, and E. F. Wassermann, X. Moya, L. Mañosa, A. Planes, E. Suard, and Bachir Ouladdiaf, *Phys. Rev. B* **75**, 104414 (2007).
108. X. Moya, L. Mañosa, A. Planes, S. Aksoy, M. Acet, E. F. Wassermann, and T. Krenke, *Phys. Rev. B* **75**, 184412 (2007).
109. C. Guillaud, *J. Phys. Radium* **12**, 223 (1951).
110. H. Wada, T. Morikawaa, K. Taniguchia, T. Shibatab, Y. Yamadab, and Y. Akishige, *Physica B* **328**, 114 (2003).
111. O. Tegus, E. Brück, K. H. J. Buschow, and F. R. de Boer, *Nature* **415**, 150 (2002).
112. O. Tegus, E. Brück, L. Zhang, Dagula, K. H. J. Buschow, and F. R. de Boer, *Physica B* **319**, 174 (2002).

113. M.-H. Phana and S.-C. Yub, *J. Magn. Magn. Mater.* **308**, 325 (2007).
114. T. Tohei, H. Wada, and T. Kanomata, *J. Appl. Phys.* **94**, 1800 (2003).
115. A. Fujita, S. Koiwai, S. Fujieda, K. Fukamichi, T. Kobayashi, H. Tsuji, S. Kaji, and A. T. Saito, *Jpn. J. Appl. Phys. Pt. 2*, **46**, L154 (2007).

Chapter 16

Spintronics and Novel Magnetic Materials for Advanced Spintronics

Jiwei Lu, Kevin G. West, Jiani Yu, Wenjing Yin, David M. Kirkwood, Li He, Robert Hull, Stuart A. Wolf, and Daryl M. Treger

Abstract This chapter contains both the description of advanced spintronic devices for logic and memory applications and the synthesis and characterization of some new magnetic materials that would lead to new paradigms in spintronics. The first part gives a brief introduction to spintronics and its history. First-generation spintronics has entered the mainstream of information technology through its utilization of the magnetic tunnel junction in applicable devices such as read head sensors for hard disk drives and magnetic random access memory. We also discuss the conceptual spintronic devices, including spin torque transfer random access memory, spin-polarized field-effect transistor, and spin-based qubit quantum processor, and their potential impacts on information technology. The future of spintronic devices requires next-generation spintronic materials. The second part of the chapter is dedicated to the synthesis and characterization of some novel magnetic materials, including ferromagnetic oxides and diluted magnetic Group IV semiconductors.

16.1 Introduction to Spintronics

The term “spintronics” usually refers to the branch of physics concerned with the manipulation, storage, and transfer of information by means of electron spins in addition to or in place of the electron charge as in conventional electronics. Introduced in 1996, spintronics was originally the name for a Defense Advanced Research Projects Agency (DARPA) program managed by one of the authors (S. A. Wolf).

In conventional electronics, only the charge of the electrons is of consequence for device operation. Using the electron’s other fundamental property, its spin, has opened up this new field. Major advances in electron spin transport started in the

S.A. Wolf (✉)
Department of Materials Science and Engineering, University of Virginia, Charlottesville,
VA, 22904, USA
e-mail: saw6b@virginia.edu

late 1970s and 1980 with the discovery of large, low-temperature magnetoresistance in metallic superlattices [1, 2]. Later demonstrations of the “Giant” effect at room temperature evolved toward applications to practical devices [3].

Spintronics promises the possibility of integrating memory and logic into a single device. In certain cases, switching times approaching a picosecond are possible, which can greatly increase the efficiency of optical devices such as light-emitting diodes (LEDs) and lasers. The control of spin is central as well to the efforts to create entirely new ways of computing, such as quantum computing or analog computing that uses the phases of signals for computations.

Spin is a fundamental quantum–mechanical property. It is the intrinsic angular momentum of an elementary particle, such as the electron. Of course, any charged object possessing spin also possesses an intrinsic magnetic moment. It has been known for decades that in ferromagnetism the spins of electrons are preferentially aligned in one direction. Then, in 1988, it was demonstrated that currents flowing from a ferromagnet into an ordinary metal retain their spin alignment for distances longer than interatomic spaces, so that spin and its associated magnetic moment can be transported just as charge [2]. This means that magnetization as well can be transferred from one place to another.

The first practical application of this phenomenon is in the giant magnetoresistive (GMR) effect. The GMR is observed in thin-film materials composed of alternate ferromagnetic and nonmagnetic layers (Fig. 16.1a) [4]. The resistance of the material is lowest when the magnetic moments in ferromagnetic layers are aligned in the same direction and highest when they are anti-aligned. This is because the spin-aligned currents from one layer are scattered strongly when they encounter a layer that is magnetically aligned in the opposite direction, creating additional resistance. But when the magnetic fields are oriented in the same direction, the spin-aligned currents pass through easily. The discovery of the GMR effect won Drs. Albert Fert and Peter Grünberg the Nobel prizes in physics in 2007.

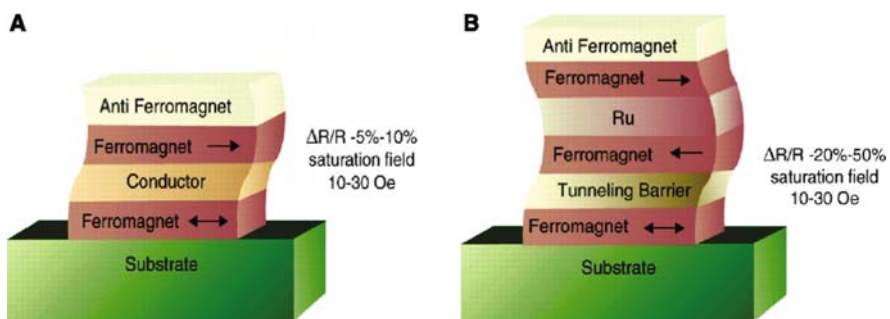


Fig. 16.1 Spin-dependent transport structures. (A) Spin valve. (B) Magnetic tunnel junction [4]

Current GMR materials operate at room temperature and exhibit significant changes in resistivity when subjected to relatively small external magnetic fields. Thus they can be used as magnetic field sensors. The imposed magnetic field

changes the magnetic orientation of one of the two layers, disrupting their relative orientation and thus changing the resistivity. The first GMR-based magnetic field sensor was created in 1994, and high-performance disk drives utilizing GMR-based read heads to detect magnetic fields were realized in 1997 and now are ubiquitous. These read heads are responsible for the very rapid growth in magnetic storage densities that has occurred in the last decade.

A spin-dependent tunneling (STD) device is similar to a GMR cell but replaces the metal between the two ferromagnetic layers with a very thin insulator through which a current can tunnel preferentially when the two magnetic orientations are aligned (Fig. 16.1b). The difference in resistance between the spin-aligned and the nonaligned cases is much greater than for GMR devices and large enough that the low-resistance state can encode, say, a “1” and the high-resistance state a “0” [5]. Recently, an SDT device was used in the first commercial magnetoresistive random access memory (MRAM), a fast RAM that is nonvolatile, meaning it does not require power to retain information [6, 7].

Significant developments assure that MRAM will be able to scale down to 60 nm and below. The most notable of these was the discovery of the spin torque transfer (STT) effect, predicted theoretically in 1996 [8, 9], in which the angular momentum carried by a spin-polarized current can exert a torque on the magnetization of a magnetic film that is magnetized in any nonparallel direction. This effect was experimentally observed in 2000 [10].

Conventional MRAM utilizes current-generated magnetic fields to rotate the magnetization in the free layer whereas STT-RAM uses the spin torque to rotate the magnetization in the free layer. In spite of advances in the switching methodology to make the switching robust to disturbances, increase the yield, and lower the switching current by magnetic cladding of the word and bit lines, STT-RAM potentially uses much lower energy per bit write compared to conventional MRAM and other memory technologies. Apparently STT switching can significantly improve the performance of MRAM and make it a truly universal memory. Key areas of research to be addressed in the near future include using MRAM in embedded memory and for multibit memory (stacked memory).

A summary of the projected performance of MRAM and STT-MRAM is presented in Table 16.1, in which the performance of the more conventional semiconductor memories is included. STT-MRAM has the potential to dominate this aspect of memory technology particularly because of its nonvolatility and very low power. Even at the 90-nm node, STT-MRAM competes favorably with FLASH memory in density and has advantages over FLASH in speed, energy, and endurance.

While fast nonvolatile memories could be very important to increasing computer capabilities, a key bottleneck is moving information between memories and logic circuits. Ideally, if individual devices could both process and store information, transfer delays could be eliminated, at least for data in immediate use. A spin-based device that could accomplish this dual task is a spin-polarized field-effect transistor. In a conventional FET, when a bias voltage is applied, a conducting channel is created between the source and the drain regions, allowing the transistor to act as a switch. If source and drain contacts are made from ferromagnetic materials, the

Table 16.1 Projected performance of MRAM, STT-RAM, and more conventional semiconductor memories

	MRAM (180 nm)	DRAM (45 nm)+	SRAM (45 nm)+	FLASH (45 nm)+	STT-RAM (45 nm)
Cell size (μm^2)	1.25	0.03	0.18	0.03	0.03
Read time	35 ns	1 ns	0.5 ns	10–50 ns	5 ns
Write time	5 ns	1 ns	0.5 ns	0.1–100 ms	5 ns
Write energy/bit	150 pJ	0.02 pJ	5 pJ	10 nJ	0.04 pJ
Endurance	$>10^{15}$	Needs refresh $>10^{15}$	$>10^{15}$	$>10^{15}$ read, $>10^6$ write	$>10^{15}$
Nonvolatile	Yes	No	No	Yes	Yes

+ compared to the Industry (ITRS) Roadmap [11]

electrons emitted from each contact have a preferential spin. Thus the current can be controlled either by applying a bias voltage as in a conventional FET or by changing the orientation of the spins as they move from the source to the drain either by rotation or by electric-field-controlled scattering [12].

There is, however, a serious difficulty which has so far prevented the development of practical spin FETs. The conductivity of ferromagnetic materials, generally metals, is much higher than that of the semiconductors that make up the rest of the FET. This means that there are far more mobile electrons in the ferromagnet than in the semiconductors, so only a few of the spin-aligned electrons are able to enter the semiconductor. For a large transfer of spin-aligned electrons, the conductivity of the ferromagnets and the semiconductors must be closely matched, or there must be a tunneling contact between the ferromagnet and the semiconductor to match the conductivities. One way to achieve this match is to utilize ferromagnetic semiconductors as the source and the drain.

The first ferromagnetic semiconductors with Curie temperatures (T_C) above 50K (-223°C or -370°F), developed in 1996, were diluted magnetic semiconductors—alloys in which some atoms are randomly replaced by magnetic atoms, such as manganese. However, these early materials still had to be cooled to cryogenic temperatures to exhibit ferromagnetism. Subsequent research has shown that other types of semiconductors can exhibit ferromagnetism at much higher temperatures. In 1998 ferromagnetic behavior in GaMnAs was reported with a Curie temperature of about 110K (-163°C or -262°F), which was subsequently raised to nearly 200 K (-73°C or -100°F). In 2000 room-temperature ferromagnetism in TiCoO_2 was discovered in Japan [13, 14]. There have also been reports, not widely reproduced and confirmed, of ferromagnetism in many other semiconductors near or above room temperature. One of the key features that is highly desired and has been demonstrated in a very limited number of these materials is that they exhibit carrier-mediated ferromagnetism, in which the ferromagnetism is caused by the interaction of the magnetic ions with the carriers—electrons or holes. The Curie temperature and other magnetic properties can be modified by changing the carrier concentration with

electric fields (gates) or with optical excitation. This ability to gate the magnetism by changing carrier concentration presents a new paradigm for novel devices in which carrier concentration and spin polarization are controlled concurrently. These discoveries appear to bring practical spin FETs within reach.

Another avenue for using the spins of elementary particles comes from the rapidly developing field of quantum computing. The states of spin of electrons or other spin- $\frac{1}{2}$ particles can be used as an implementation of a qubit (quantum bit, the unit of quantum information). Information can be encoded using the polarization of the spin, manipulation (computation) can be done using external magnetic fields or laser pulses, and readout can be done by measuring spin-dependent transport. Quantum computers execute a series of simple unitary operations (gates) on one or two qubits at a time. The computation on a quantum computer is a sequence of unitary transformations of an initial state of a set of qubits. After the computation is performed, the qubits can be measured and the outcome of the measurement is the result of the quantum computation. Quantum effects like interference and entanglement are used as computational resources and make fast solutions to hard problems possible. For some very special problems, such as factorization of large prime numbers or exhaustive database searches, quantum computing algorithms have been developed that show a very significant speed-up in computation time and a reduction in complexity [15, 16]. For certain calculations that find global properties of functions like factoring and discrete logarithms, the speed-up for a quantum processor is dramatic. For these operations, a 30-logical-qubit quantum processor can perform the same calculation in the same time as a 10^9 -bit classical computer.

Scientists are searching for quantum-mechanical two-state systems with long decoherence times, which would provide the ability to carry out computations before stored information is lost. It must be possible to readily fabricate and scale these quantum systems if they are to perform quantum algorithms. One very viable candidate for quantum information is electron spins in coupled quantum dots. However, other two-level systems have been proposed for implementing qubits and include nuclear magnetic resonance (NMR), which involves nuclear spins in special molecules; excited states of ions in traps; cavity quantum electrodynamic systems; Josephson junctions; and SQUIDs (superconducting quantum interference devices). The potential uses of quantum qubit systems range from quantum key distribution, quantum encryption, and quantum dense coding to quantum teleportation and ultra-precise clock synchronization.

16.2 Novel Magnetic Oxide Thin Films by Reactive Bias Target Ion Beam Deposition

First-generation spintronics has already entered mainstream information technology with the widespread use of hard drive read head sensors for magnetic disk storage, as well as the recent commercialization of a magnetic random access memory (MRAM) technology by Freescale Semiconductor. The revolution in electronics

that this will create and advance the next-generation spintronic devices into mainstream memory and logic requires the exploration and development of novel magnetic materials that will scale to nano-dimensions. In the following text, we will discuss some of our results on developing and characterizing novel magnetic oxides and semiconductors which could potentially be used in the next-generation memory and logic devices.

16.2.1 Reactive Bias Target Ion Beam Deposition (RBTIBD)

RBTIBD is a novel sputter deposition process utilizing low-energy ion beam source and bias target sputtering technique [17], which can be used to prepare oxide thin films. It was recently demonstrated that this deposition technique provided very smooth interfaces in a GMR multilayer structure [18, 19]. Figure 16.2 illustrates the schematic of RBTIBD system and explains the operation of this deposition system. This process utilizes a low-energy broad beam ion source that reliably produces a very high density of low energy (5–50 eV) inert gas ions. A large negative potential bias is applied to the metal sputtering target. The high density of low-energy inert gas ions in front of the sputtering target, seeing a very large potential difference, are accelerated to the target surface at a near normal incidence angle at high-enough

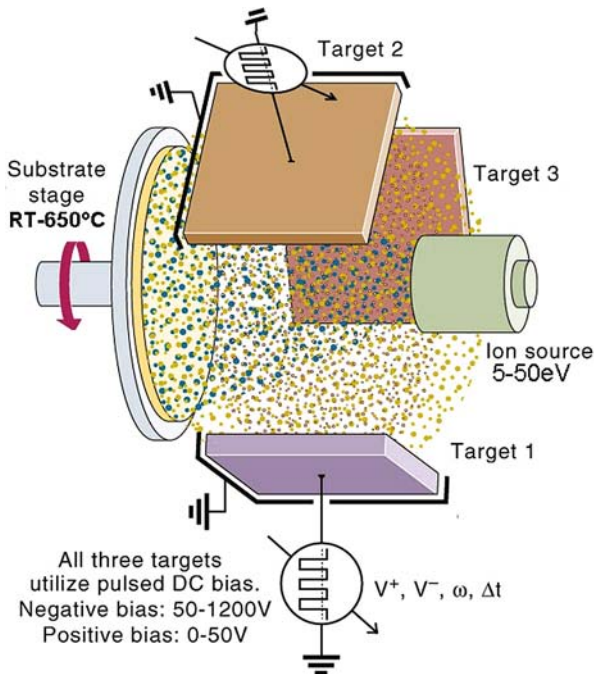


Fig. 16.2 Reactive bias target ion beam deposition system

energies to induce sputtering. Reactive gases (e.g., oxygen, nitrogen) can be mixed in with the inert gas in a precise and controlled manner to react with the sputtered metal atoms and form the desired compound. A pulsed DC bias is used to avoid target poisoning during reactive processing. The main advantage of this novel sputter technique is the ability to precisely control adatom energies, the composition, and phase formation and to operate in a rather wide processing window. This system has the capability of sputtering from three targets simultaneously, giving us the opportunity of rapidly exploring a wide range of dopants. It is also capable of developing multilayer structures and providing a very smooth interface. This system is also equipped with a substrate heater which can heat substrates to 650°C.

16.2.2 $Cr_x V_{1-x} O_2$ Thin Films

Chromium dioxide (CrO_2) is a ferromagnetic half-metal with a high degree of spin polarization [20, 21]. It is an ideal candidate for practical spintronic devices because it has a T_c above room temperature [22, 23]. Recent theoretical and experimental analysis indicates CrO_2 is nearly 100% spin polarized [24, 25]. However, preparation of single-phase CrO_2 thin films is difficult, and present growth methods, such as chemical vapor deposition (CVD) [26, 27, 28], are not well suited for multilayer devices such as spin valve and magnetic tunnel junctions. Furthermore, chromium has many oxidation states, including CrO_3 , Cr_2O_5 , CrO_2 , and Cr_2O_3 , and as such the CrO_2 phase is unstable and is known to readily irreversibly decompose to the Cr_2O_3 phase at elevated temperatures [29, 30]. CrO_2 has a rutile structure, similar to that of the high-temperature phase of vanadium dioxide (VO_2). Vanadium dioxide (VO_2) undergoes a first-order metal-insulator transition (MIT) at 341 K. The first-order phase change is dominated by a structural transformation from a high-temperature tetragonal structure to a low-temperature monoclinic structure. The abruptness of the phase transition is characterized by an abrupt change in electrical conductivity and infrared transmission characteristics, making it an excellent candidate for sensor and switching applications. It has previously been demonstrated that high-quality single-phase VO_2 thin films have been prepared using RBTIBD technique over a rather wide range of phase composition [31]. In our experiments, the approach was to deposit CrO_2 and VO_2 concurrently and stabilize CrO_2 by combining with a VO_2 matrix. The newly discovered $CrVO_2$ thin films exhibited a unique combination of magnetic and electrical properties.

The stoichiometry of the films was determined using inductively coupled plasma-mass spectrometry (ICP-MS) after chemically dissolving the films and confirmed by X-ray fluorescence (XRF) using peak ratios. We have chosen to focus on two thin films doped with 10 and 20 at.% Cr. The X-ray diffraction (XRD) patterns of the 10 and 20% $Cr_x V_{1-x} O_2$ films correspond to the rutile VO_2 structure with lattice constants of 2.270 and 2.273 Å respectively as shown in Fig. 16.3a. The observed rutile (020) VO_2 peaks had FWHM values of 0.19 and 0.20 respectively, indicating the highly crystalline nature of the material. The metal insulator transition from

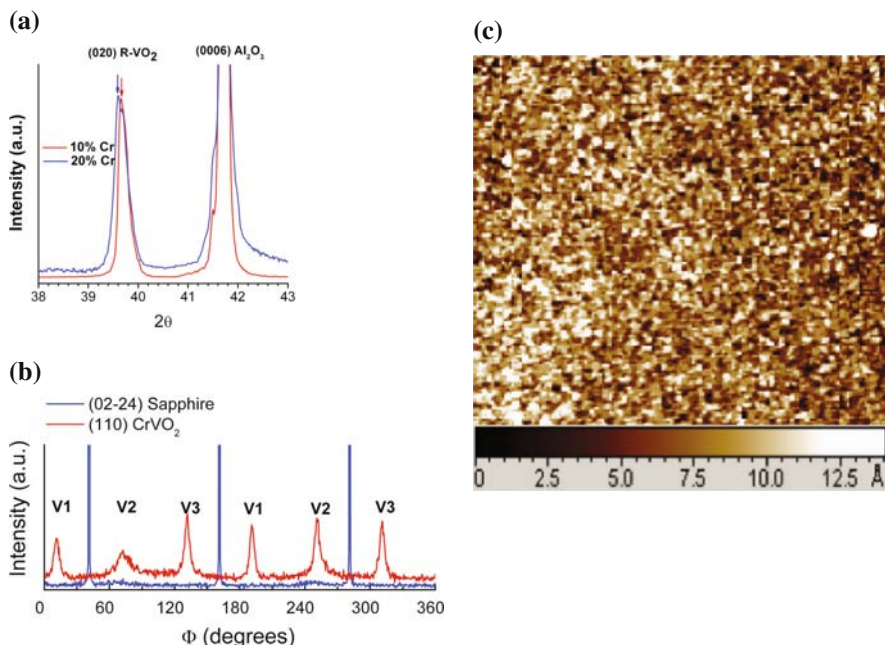


Fig. 16.3 (a) XRD $2\theta/\theta$ scan for 10% Cr and 20% Cr-doped VO_2 thin films deposited on (0001) Al_2O_3 single crystalline substrates. The rutile (020) VO_2 peak is observed; (b) Φ scans of (110) CrVO_2 and (02 $\bar{2}$ 4) sapphire; (c) atomic force microscopy (AFM) image of $2 \times 2 \mu\text{m}^2$ area of a 20% Cr-doped VO_2 thin film surface. The root mean squared (RMS) surface roughness was calculated to be 0.3 nm over a $5 \times 5 \mu\text{m}^2$ area

the tetragonal to monoclinic structure is apparently suppressed at room temperature with the addition of Cr ions into the VO_2 matrix. A clear shift in the peaks to lower angles is observed with increasing Cr concentration indicating an increase in lattice constant. This behavior is not completely understood; the addition of substitutional Cr^{4+} to the VO_2 matrix should cause a decrease in the lattice constant, since they are smaller than the V^{4+} ion. It is believed that the 20% Cr-doped VO_2 sample is more oxygen deficient than that of the 10% Cr-doped VO_2 sample and could account for this observation. No secondary chromium oxide phases were detected in the X-ray diffraction analysis. X-ray diffraction (XRD) Φ -scans (Fig. 16.3b) show six off-axis reflections at $\Psi = 45^\circ$ corresponding to a (110) orientation of $\text{Cr}_x\text{V}_{1-x}\text{O}_2$. The presence of six peaks in the phi scans is due to the presence of three orientation variants of $\text{Cr}_x\text{V}_{1-x}\text{O}_2$ that are rotated in-plane by 60° about the $\text{Cr}_x\text{V}_{1-x}\text{O}_2$ [020] axis. The (110) $\text{Cr}_x\text{V}_{1-x}\text{O}_2$ reflections of each orientation variant are rotated by 30° with respect to the (02 $\bar{2}$ 4) sapphire reflections. This indicates that orientation relationship can be described as follows:

$$(010)_{\text{Cr}_x\text{V}_{1-x}\text{O}_2} \parallel (0001)_{\text{Al}_2\text{O}_3} \text{ and } [100]_{\text{Cr}_x\text{V}_{1-x}\text{O}_2} \parallel [10\bar{1}0]_{\text{Al}_2\text{O}_3}$$

The surface morphology was characterized on a typical sample by atomic force microscopy (AFM). AFM measurements indicated remarkably smooth films with a root-mean-square (RMS) roughness of 3.0 Å over a $5 \times 5 \mu\text{m}^2$ scan area in Fig. 16.3c. One plausible explanation for the smoothness of our films is growth chamber configuration, and its use of low-energy ion beam-assisted growth, which has already been demonstrated to smooth metal and oxide thin films during processing.

Cross-sectional transmission electron spectroscopy characterization was made on the 20% Cr-doped VO_2 thin film to ascertain information on the microstructure, and Cr distribution throughout the crystal lattice. Figure 16.4a shows a bright field image taken at 293 K, parallel to the Al_2O_3 $\langle 110 \rangle$ zone. From the cross-sectional bright field image, an oriented columnar crystal structure is observed, with no clear presence of Cr clustering or secondary phases. Electron diffraction patterns, parallel to the Al_2O_3 $\langle 110 \rangle$ and $\langle 100 \rangle$ zones, are taken at 100 and 293 K as indicated in Fig. 16.4b. The electron diffraction patterns show the classic presence of stacking faults, but they support the identification of the tetragonal VO_2 structure at room temperature, and coincide with observations made with XRD experiments. There is no change in the electron diffraction pattern between room temperature and 100 K, suggesting that the structure transition in VO_2 is suppressed at least to temperatures of 100 K. Electron energy loss spectroscopy (EELS) elemental mappings near the film surface and substrate–film interface indicate no significant Cr concentration variation throughout the film. Figure 16.4c shows the corresponding Cr L edge (575 eV) image for both the film surface and substrate–film interface.

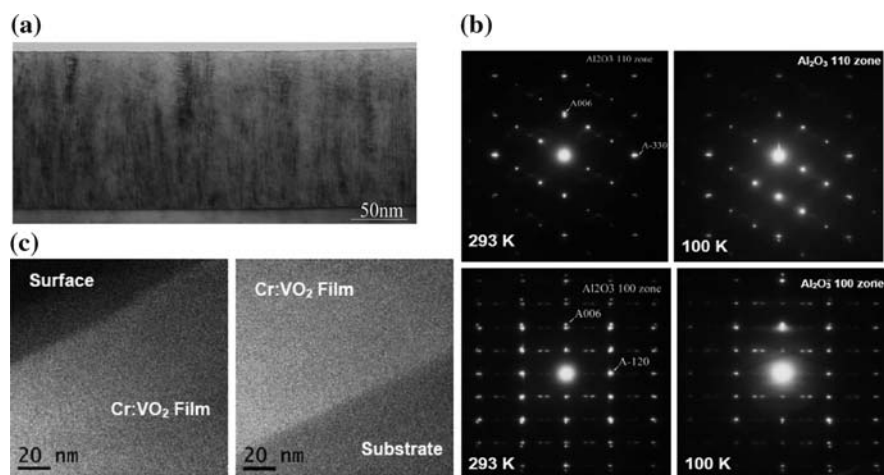


Fig. 16.4 (a) Bright field cross-section TEM image of 20% Cr-doped VO_2 thin film parallel to Al_2O_3 substrate $\langle 110 \rangle$ zone; (b) Electron diffraction patterns for 20% Cr-doped VO_2 at 293 and 100 K for both the $\langle 110 \rangle$ and the $\langle 100 \rangle$ zones. The “A” denotes the Al_2O_3 substrate; (c) Elemental mapping for 20% Cr-doped VO_2 near the film surface and substrate/film interface using Cr L edge (575 eV). The brightness represents the concentration of Cr ions

Figure 16.5 shows resistivity as a function of temperature for an undoped VO_2 and a $\text{Cr}_{0.2}\text{V}_{0.8}\text{O}_2$ thin film. The undoped VO_2 thin film has a resistivity of $3.4 \times 10^{-4} \Omega\text{-cm}$ at 380 K and then undergoes an abrupt change of 10^3 in resistivity at its MIT temperature of 341 K, and then increases several orders of magnitude as temperature decreases to $1.7 \times 10^3 \Omega\text{-cm}$ at 100 K, following a variable-range-hopping conduction mechanism. The $\text{Cr}_{0.2}\text{V}_{0.8}\text{O}_2$ thin film has a resistivity of $1.4 \times 10^{-3} \Omega\text{-cm}$ at 380 K and then increases several orders of magnitude as temperature decreases to 27.5 $\Omega\text{-cm}$ at 100 K, again following a variable-range-hopping conduction mechanism. It is important to note the absence of an abrupt transition in the $\text{Cr}_{0.2}\text{V}_{0.8}\text{O}_2$ thin film as is seen in the undoped VO_2 thin film. This observation supports the electron diffraction analysis which shows no apparent change in the tetragonal structure from 293 K down to 100 K. Below 285 K the experimental data were fitted to a variable-range-hopping conduction mechanism described by the following equation:

$$\sigma = \sigma_0 \exp\left(\frac{-B}{T^{1/4}}\right)$$

where $B = 4E / (k_B T^{3/4})$, E is the activation energy, and k_B is the Stephan-Boltzmann constant. The resistivity vs. temperature plot for the $\text{Cr}_{0.2}\text{V}_{0.8}\text{O}_2$ sample is typical of all Cr-doped VO_2 samples studied.

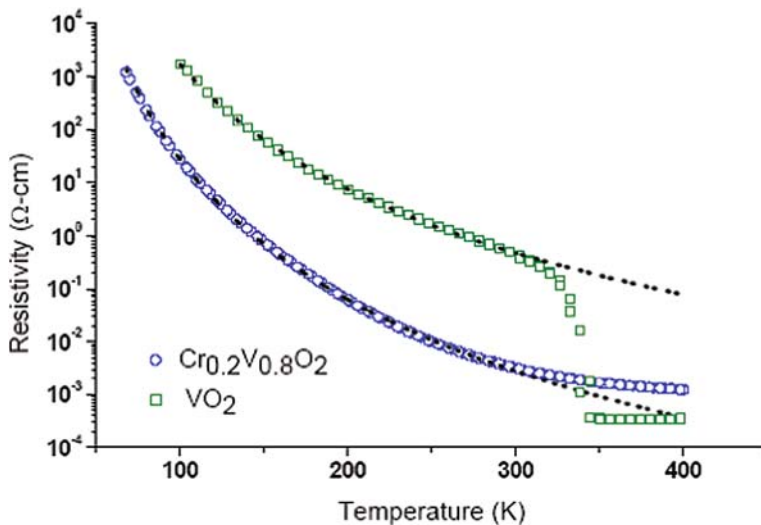


Fig. 16.5 Resistivity as a function of temperature of undoped VO_2 and 20% Cr-doped VO_2 thin films deposited on (0001) sapphire substrates. Below 285 K the experimental data follow a variable-range-hopping conduction mechanism

The magnetic properties were investigated using a vibrating sample magnetometer (VSM) attached to the PPMS tool from quantum design and verified using a

superconducting quantum interference device (SQUID) magnetometer. The magnetic behavior of the 10% Cr and 20% Cr-doped VO₂ thin films was investigated over a range of temperatures. Figure 16.6a shows the magnetization as a function of applied magnetic field (M–H) as measured at 5 and 300 K for 10% Cr and 20% Cr-doped VO₂ thin films. The magnetic field was applied parallel to the plane of the film, and the diamagnetic contribution from the sapphire substrate is subtracted. An algorithm was used to smooth the presented data. Hysteresis measurements were made in the range of $-1.5 \text{ T} \leq H \leq 1.5 \text{ T}$. The coercivity of 20% Cr-doped VO₂ thin film was 400 and 150 Oe at 5 and 300 K respectively, while the 10% Cr-doped VO₂ thin film had coercivity of 600 and 500 Oe at 5 and 300 K respectively. The saturation magnetization was determined to be $0.95 \mu_B/\text{Cr}$ and $0.40 \mu_B/\text{Cr}$ for the 20% Cr-doped VO₂ thin film at 5 and 300 K respectively, whereas the 10% Cr-doped VO₂ thin film saturation moments were $0.90 \mu_B/\text{Cr}$ and $0.20 \mu_B/\text{Cr}$ at 5 and 300 K respectively. Figure 16.6b shows the saturation magnetization vs. temperature for the 10% Cr and 20% Cr-doped VO₂ thin films using an applied field of 1.5 T. From the magnetization vs. temperature data, it appears that the magnetic interactions are significantly enhanced below 50 K which could be due to some inherent compositional or strain inhomogeneity. The magnetization at higher temperatures appears to increase significantly with Cr concentration, which is promising for future device applications, where one can tune the magnetic properties by varying the dopant concentration.

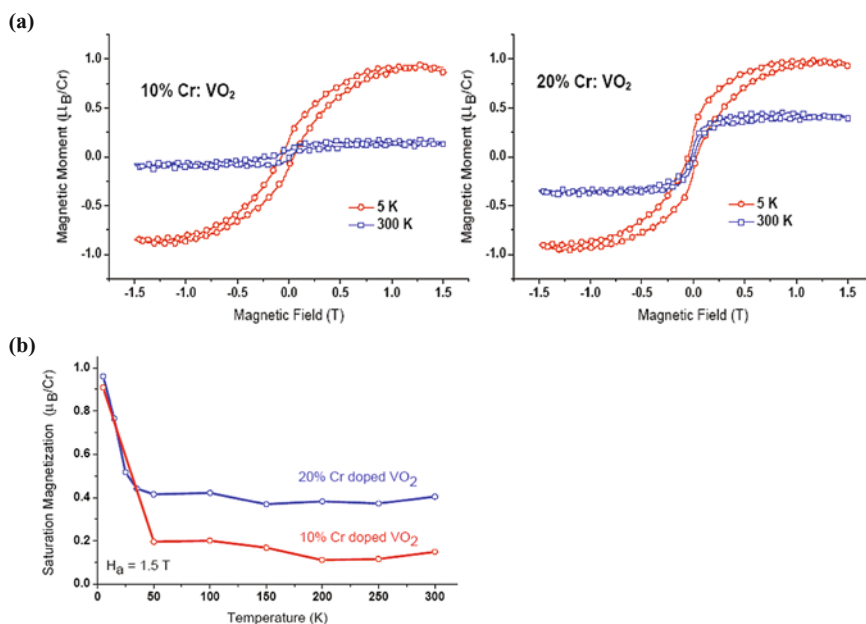


Fig. 16.6 (a) Magnetization vs. applied magnetic field (M–H) plots for 10% Cr and 20% Cr-doped VO₂ at 5 and 300 K, respectively; (b) Saturation magnetization vs. temperature plot with 1.5 T applied field for 10% Cr and 20% Cr-doped VO₂ thin films

In summary, we prepared rutile $\text{Cr}_x\text{V}_{1-x}\text{O}_2$ ($0.1 \leq x \leq 0.2$) thin films on sapphire substrates. These films have a rutile structure, have a high crystalline quality, and are remarkably smooth, which may prove important in future devices where interface engineering is a concern. TEM studies conclude that the films have the rutile VO_2 structure and a uniform distribution of Cr throughout the host matrix. The films display “poor metal” like conduction at temperatures above room temperature and variable-range-hopping conduction below that. Ferromagnetism was observed at room temperature, and the moment is dependent on the Cr-dopant concentration. Further characterization on the spin polarization of $\text{Cr}_x\text{V}_{1-x}\text{O}_2$ is underway, and the unique combination of magnetic and ferromagnetic properties could be useful in spin injection or sensor application if a very high spin polarization is obtained in $\text{Cr}_x\text{V}_{1-x}\text{O}_2$. It is also important to understand the ferromagnetic exchange mechanism in this new material and study the impact of defects on the transport and magnetic properties.

16.2.3 $\text{Co}_x\text{Ti}_{1-x}\text{O}_2$ Thin Films

The ferromagnetism in Co-doped TiO_2 has attracted considerable attention since Matsumoto et al. first reported the room temperature ferromagnetism in Co-doped anatase TiO_2 [13]. The room temperature in Co-doped rutile TiO_2 thin films has also been reported [32] and the Anomalous Hall Effect (AHE) was observed which indicated that the nature of ferromagnetism was carrier mediated [33]. However, a consensus on whether the origin of the ferromagnetism is intrinsic or extrinsic has not yet been reached. Reports [34, 35] on the observation of Cobalt nano-clusters in both rutile and anatase Co-doped TiO_2 indicated that the metallic Co clusters caused the room temperature ferromagnetism in $\text{Co}:\text{TiO}_2$. The AHE was also observed in rutile $\text{Co}:\text{TiO}_2$ with the presence of Co nano-clusters, which brought doubts on determining the nature of the diluted magnetism of the $\text{Co}:\text{TiO}_2$ system using AHE [34]. On the other hand, Chambers’ group has done extensive studies on TiO_2 thin films doped with Co and Cr, and he presented strong evidence that the structural defects such as oxygen vacancies may cause the ferromagnetism in Cr-doped TiO_2 [36].

It is important to identify the origin of ferromagnetism in TiO_2 films as well as to investigate the AHE in this system in order to utilize the room temperature ferromagnetic TiO_2 in any practical spintronic applications. Having this as the objective, we start to investigate the influence of the phase, the microstructure, the crystal quality, and the impurity phases on the ferromagnetism and transport properties of Co-doped TiO_2 thin films prepared by the new RBTIBD processing. In the following section, we present some preliminary results we obtained.

We were able to synthesize both rutile and anatase TiO_2 thin films doped with Co on (100) LaAlO_3 substrates by controlling the growth parameters; the two parameters mainly controlled were the total growth pressure and oxygen content. Figure 16.7 shows XRD spectra of TiO_2 thin films deposited on LaAlO_3 substrates using different growth conditions. In both cases, TiO_2 thin films were highly textured.

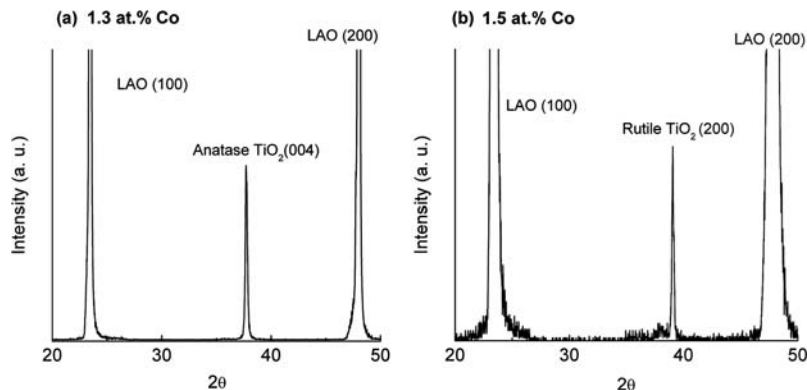


Fig. 16.7 XRD spectra of (a) an anatase Co-doped TiO₂ thin film on LaAlO₃; (b) a rutile Co-doped TiO₂ thin film on LaAlO₃

Figure 16.8 shows the magnetic moments of Co:TiO₂ thin films as a function of magnetic field (H) at 10 and 300 K respectively. The Co concentration has been determined using X-ray fluorescence (XRF). It is clear that the Curie temperature (T_c) of the anatase thin film is much higher than room temperature based on the fact that there is no significant change in the hysteresis loop between 10 and 300 K. We have been very careful with the sample handling and VSM operation to make sure that no ferromagnetic contamination was introduced during the measurements. The saturation magnetic moment for this anatase TiO₂ doped with 2.3 at.% Co is ~ 2 Bohr magneton (μ_B) per Co. On the other hand, the rutile thin film exhibits much higher saturation magnetic moment ($\sim 4 \mu_B$ per Co) with a smaller Co concentration (~ 1.5 at.%). In addition, the hysteresis loop in the rutile phase thin film disappears at 300 K, which indicates that the film becomes superparamagnetic at room temperature.

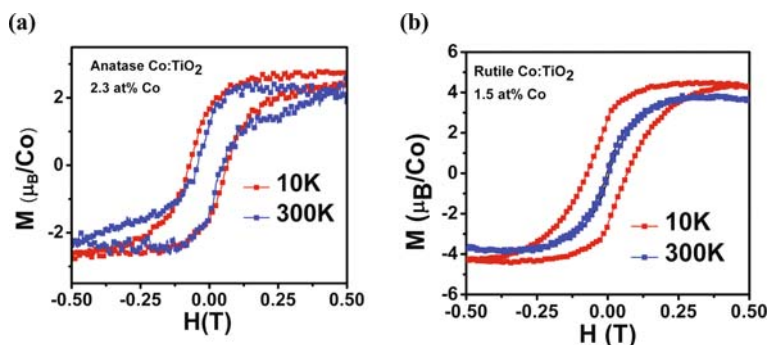
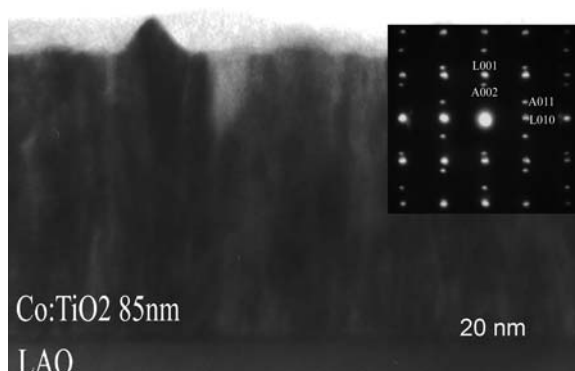


Fig. 16.8 Hysteresis loops of (a) 2.3 at.% Co-doped anatase TiO₂ film; (b) 1.5 at.% Co-doped rutile TiO₂ film

Transmission electron microscopy (TEM) was used to reveal the microstructure of TiO_2 thin films with different phase compositions. Figure 16.9 shows a cross-section bright field image of the same sample whose magnetic properties are shown in Fig. 16.3(a). The strong surface faceting indicates that the film is strongly textured with a very high crystal quality. There is no observation of any secondary phase, which implies that the ferromagnetism comes from a uniform single phase of diluted magnetic anatase TiO_2 . The inset in the micrograph is an electron diffraction pattern taken on the film as well as the LAO substrate. It further confirms the epitaxial relationship obtained from XRD.

Fig. 16.9 Cross-section bright field TEM image of anatase TiO_2 doped with 2.3 at.% Co



In contrast, nano-sized clusters (~ 2 nm) have been observed all through the rutile TiO_2 thin film as shown in Fig. 16.10. Energy dispersive spectroscopy (EDS) technique was used to identify the chemical composition of the nano-clusters. The inset shows EDS spectra taken on the nano-clusters and on the background matrix. It is found that these clusters are much richer in Co compared to the background. In the literature, the observation of Co clusters has been reported and the presence of Co clusters brings either ferromagnetism or supermagnetism to TiO_2 thin films depending on the size and temperature. It is likely that the high saturation moment of this rutile TiO_2 thin film is due to these Co-rich clusters, which is undesired for a diluted magnetic semiconductor.

We performed transport measurements on the anatase sample using the Van de Pauw method. The preliminary temperature dependence of resistivity shows a semi-conducting behavior as shown in Fig. 16.11. We also observed the nonlinear Hall effect on the same sample at 100 K (not shown here), and this implies the presence of the AHE. However, the data are very noisy due to the high resistance of this sample. Further characterization on micro-fabricated devices is underway.

In summary, we deposited both anatase and rutile TiO_2 films doped with Co. The saturation magnetic moment for the anatase TiO_2 doped with 2.3 at.% Co was $\sim 2 \mu_B/\text{Co}$ at 10 and 300 K, which implies that T_c is much higher than room temperature. Meanwhile, the rutile TiO_2 film exhibits much higher saturation magnetic moment ($\sim 4 \mu_B/\text{Co}$) with a smaller Co concentration (~ 1.5 at.%) at 10 K but the

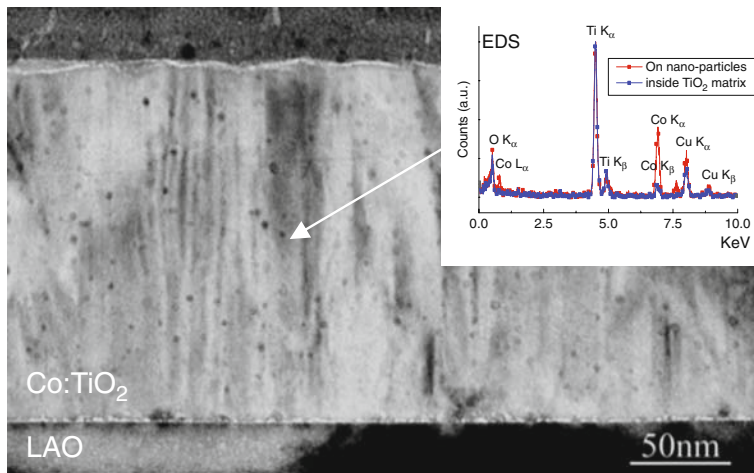
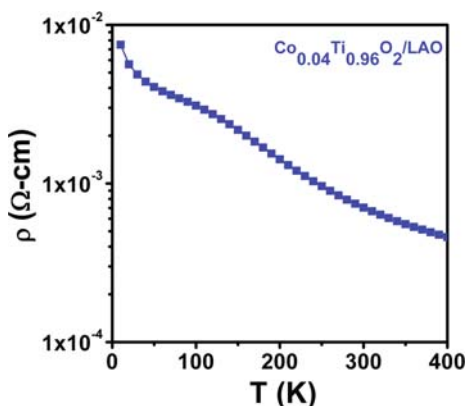


Fig. 16.10 Cross-section bright field TEM image of rutile TiO_2 doped with 1.5 at.% Co

Fig. 16.11 Temperature vs. resistivity of an anatase TiO_2 thin film doped with 4 at.% Co



hysteresis loop disappears at room temperature. TEM revealed that both films were highly textured. In the rutile film, nano-size Co-rich clusters (~ 2 nm) have been identified using EDS. We concluded that the ferromagnetism in the rutile films was caused by these nano-clusters. While in the anatase film, we did not observe Co-rich clusters and therefore the ferromagnetism in the anatase film may arise from intrinsic diluted magnetism. The preliminary result on the transport properties showed that the anatase film was semiconducting at room temperature. More detailed AHE experiments are necessary to understand the influence of Co doping on the carrier concentration and the correlation between the carriers and ferromagnetism.

16.3 Diluted Ferromagnetic $\text{Ge}_{1-x}\text{Mn}_x$ by Ion Implantation

The search for semiconductors with room temperature ferromagnetism has been a longstanding goal because of their potential as spin-polarized carrier sources and possible new spintronic devices [4]. The discovery of diluted ferromagnetism in transition metal-doped III–V semiconductors [37–39] has helped bring practical semiconductor spintronic devices within reach. One of the key features of some of these materials is that they exhibit carrier-mediated ferromagnetism, in which the ferromagnetism is caused by the interaction of the magnetic ions with the carriers—electrons or holes. The Curie temperature and other magnetic properties can be modified by changing the carrier concentration with electric fields (gates) or with optical excitation. This ability to gate the magnetism by changing carrier concentration presents a new paradigm for memory/logic integrated devices [4] which has the potential for much lower power dissipation compared to conventional CMOS [40]. Recently there has been some active research on the ferromagnetism in Group IV semiconductors in both theory [41, 42] and experiments [43–53] due to the interests stated above. Most efforts have been on the growth of the GeMn system using molecular beam epitaxy (MBE) [44, 47, 54, 55], and a few groups employed the ion implantation technique [45, 51, 53]. In $\text{Ge}_{1-x}\text{Mn}_x$ prepared by either technique, the formation of intermetallic secondary phases especially the ferromagnetic Mn_5Ge_3 phase has been reported, and it is highly undesirable to have such phases in $\text{Ge}_{1-x}\text{Mn}_x$ for any anticipated device applications. In this study, ion implantation, a standard technique in the semiconductor industry, was used to introduce Mn ions into n-type Ge thin films. We will focus on the magnetic and electric properties of precipitate-free $\text{Ge}_{1-x}\text{Mn}_x$ samples produced by Mn ion implantation.

Germanium-on-insulator (GOI) substrates were used for this study. The sample is composed of 200 nm thick Ge/400 nm thick SiO_2 on the top of a boron-doped Si handle wafer. Thus the electrical transport properties of Mn-doped Ge thin films could be studied without the influence of the underlying substrate. Mn ions were introduced into Ge by ion implantation performed by Core Systems, Inc. Both single implantation and multi-implantation methods were used. The implantation energies and doses were calculated by SRIM (stopping and range of ions in matter) software [7] based on the desired Mn concentration which ranged from 0.5 to 4 at.%. Single implantation was performed at a temperature of 300°C and an implantation energy of 200 keV. Dual ion implantations were also performed at a lower implantation temperature 75°C. The first implant used a lower dose with a higher implantation energy of 170 keV, and the average depth of Mn ions was around 100 nm from the surface. The second implantation used a higher dose and a lower implantation energy of 60 keV and resulted in an average ion depth ~ 30 nm from the surface. The combination of the two Mn ion implantations yields a more uniform distribution of Mn ions across the Ge thin films compared to that by the single implantation.

Figure 16.12a shows a cross-section TEM bright field image of an as-implanted 2 at.% Mn-doped Ge thin film prepared by a single implantation. A secondary crystalline phase was embedded in the Ge matrix that has been also observed in the post-annealed 2 at.% Mn-doped Ge sample. The diffraction pattern acquired by a

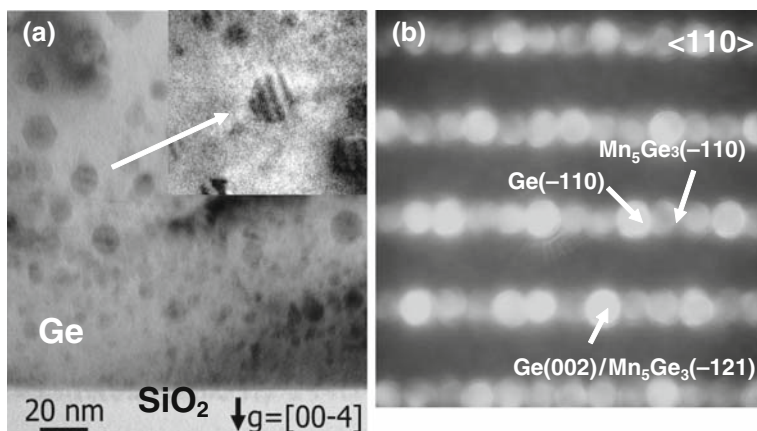


Fig. 16.12 (a) Cross-section bright field TEM images for 2 at.% Mn-doped Ge by the single implantation and annealed at 650°C for 5 min. (b) Nano-beam electron diffraction pattern of the impurity phase and Ge matrix. Both images were taken along the Ge $\langle 110 \rangle$ zone axis

nano-beam diffraction showed that the impurity phase can be indexed as a Mn-rich alloy Mn_5Ge_3 with the hexagonal structure as shown in Fig. 16.12b. Figure 16.13a shows a cross-section TEM bright field image of an annealed 4 at.% Mn-doped Ge sample by the dual implantation method. It can be seen that the most of Ge thin films remained amorphous after annealing. There is some crystalline Ge close to the Ge/ SiO_2 interface. But the secondary phase was not observed in the entire film. In addition, XRD spectra (not shown here) also shows that there are no diffraction peaks from the Mn_5Ge_3 phase in both as-implanted and annealed dual-implanted $\text{Ge}_{1-x}\text{Mn}_x$. Thus, we are confident that we can rule out the existence of an Mn-rich secondary phase in these dual-implanted 4% Mn-doped Ge samples.

The implantation temperature is a very critical parameter in controlling the formation of the secondary phase. For the single implantation, the temperature was kept at 300°C, and the Mn_5Ge_3 phase was formed during the implantation when the Mn dose was 2.73×10^{15} ions/cm³ corresponding to 2 at.% Mn. However, during the dual implantation, the implantation temperature was 75°C, and the intermetallic secondary phase did not form in the as-implanted sample even with a much higher Mn dose (8×10^{15} ions/cm³). In comparison, it has been established that the ferromagnetic Mn_5Ge_3 phase appears in GeMn at the growth temperature higher than 85°C prepared by MBE [47, 49]. A recent report on MBE grown $\text{Ge}_{1-x}\text{Mn}_x$ indicated that the annealing temperature above 250°C caused the nucleation of Mn_5Ge_3 [56]. However, we did not observe the formation of ferromagnetic Mn_5Ge_3 in the dual-implanted samples following the rapid thermal annealing at 300°C.

Figure 16.13b and c is the zero loss and Mn M-edge (49 eV) elemental mapping images near the sample surface of the 4% Mn dual-implanted Ge sample, respectively. In Fig. 16.13b, some dark regions with the size of ~ 3 nm occurred near the sample surface. The features corresponding to these dark spots have the brighter

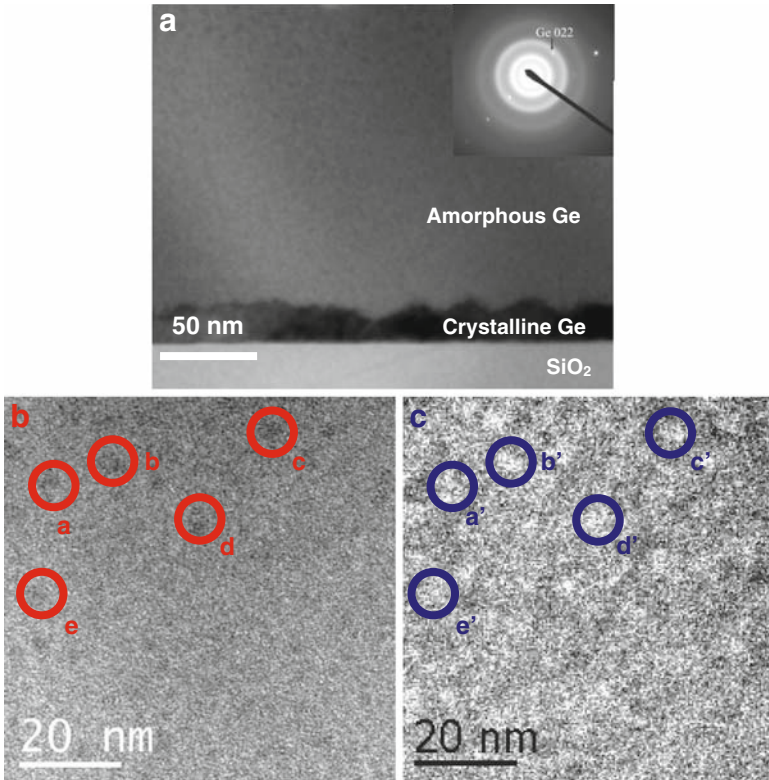


Fig. 16.13 (a) Cross-sectional bright field image of the 4% Mn dual-implanted Ge sample, annealed at 300°C for 1 min. The inset is the electron diffraction pattern. Energy-filtered images taken near the sample surface: (b) electron energy zero-loss image and (c) Mn M-edge (49 eV) map of the same area. The brightness in (c) represents the concentration of Mn ions. We circled and marked the interested areas to show the correlation of these spots in both images

contrast compared to the background in Fig. 16.13c. The brightness in Fig. 16.13c represents the richness of Mn ions. Therefore, these spots are likely the Mn-rich clusters.

Mn-doped samples of 0.5 and 1% showed very small magnetization after the Mn implantation at 375°C, but the 2% sample showed strong ferromagnetism close to room temperature due to the intermetallic Mn₅Ge₃ secondary phase as shown in Fig. 16.14. Figure 16.14a shows that the hysteresis loop of this sample disappeared between 200 and 300 K, and the Curie temperature is close to 300 K as indicated by M vs. T (Fig. 16.14b). Mn₅Ge₃ has a Curie temperature of 296 K [57, 58]. The magnetic properties of the single-implanted 2% Mn-doped sample were dominated by the Mn-rich secondary phase which excludes it from any spintronics applications that we are interested in. Therefore, we will focus on the characterization of dual-implanted samples only which are free of the Mn₅Ge₃ phase.

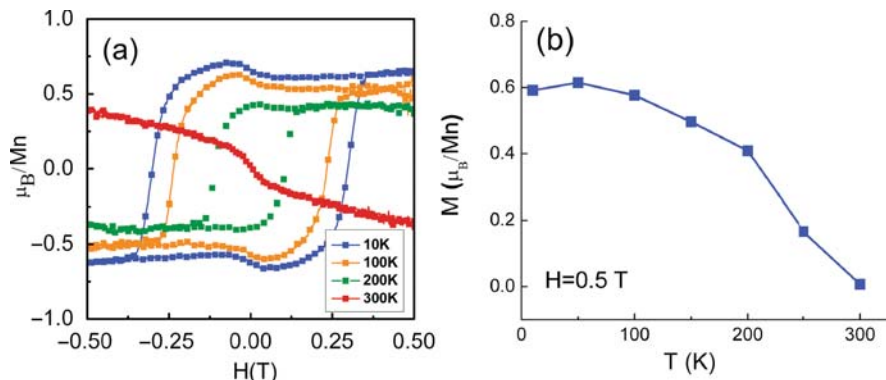


Fig. 16.14 Magnetic properties of 2 at.% Mn-doped Ge thin film by single implantation and annealing at 600°C for 5 min. (a) Hysteresis loops as a function of temperature. A diamagnetic background caused by Si substrate was subtracted. (b) Magnetization as a function of temperature under the magnetic field of 0.5 T

Figure 16.15 shows the hysteresis loops of the 4% Mn-doped Ge by dual implantation at 5 K after the post-annealing at different conditions. The optimal magnetic property, namely the saturation moment, was achieved at 300°C. The annealing temperature above 300°C resulted in the decrease in the saturation moments at 5 K. The magnetization curves as a function of temperature measured on the dual-implanted 4% Mn-doped Ge sample before and after the annealing at 300°C are shown in Fig. 16.16. The as-implanted sample shows a hysteresis loop and a very small saturation moment ($\sim 0.04 \mu_B/\text{Mn}$) below 10 K. It became superparamagnetic between 10 and 25 K and eventually showed only weakly paramagnetism at 50 K.

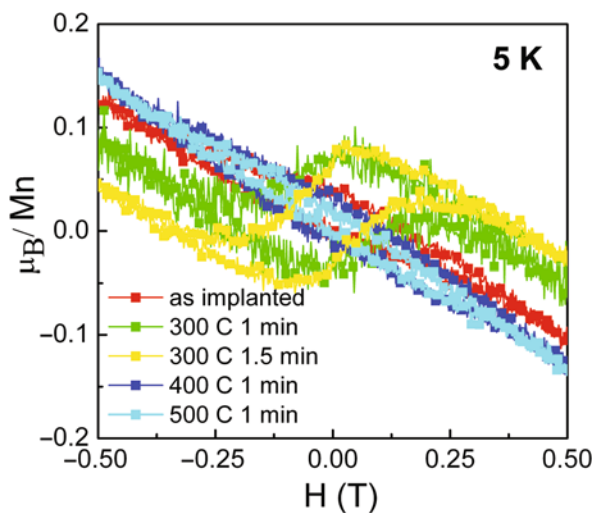


Fig. 16.15 Hysteresis loops of 4 at.% Mn-doped Ge samples at 5 K following dual implantation and annealing under different conditions. The diamagnetic background is caused by the underlying Si wafer

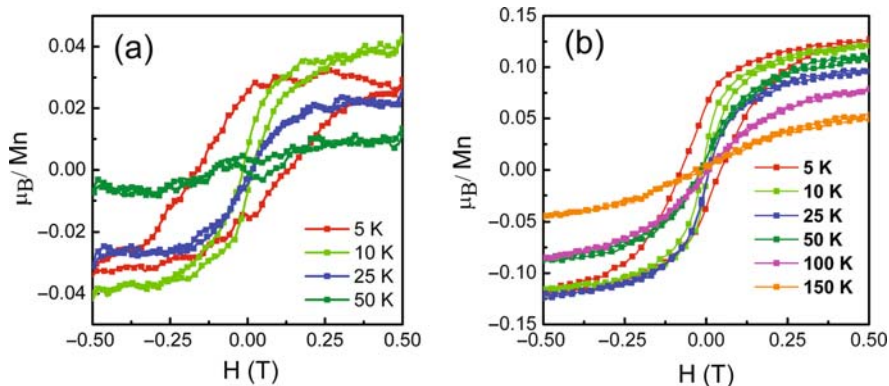


Fig. 16.16 Hysteresis loops as function of temperature of 4 at.% Mn-doped Ge thin films following dual implantation (a) as implanted and (b) annealed at 300°C for 1 min. A diamagnetic background caused by the Si substrate was subtracted

The hysteresis loop was observed up to 25 K then the magnetization curve was paramagnetic at higher temperatures (above 50 K). The saturation moment at 5 K was $\sim 0.12 \mu_B/\text{Mn}$. We estimated that only $\sim 4\%$ of the Mn ions were magnetically active based on the expected $3 \mu_B/\text{Mn}$ of theoretical predictions [41, 44]. The annealing temperature of 300°C was relatively moderate, and it can be seen in Fig. 16.13a that the amorphous Ge caused by the ion implantation did not fully re-crystallize at this temperature. However, the magnetic properties were degraded following the annealing at higher temperatures. The magnetic properties in dual-implanted samples are likely determined by the distribution of Mn ions rather than the crystallinity of $\text{Ge}_{1-x}\text{Mn}_x$.

Figure 16.17 shows both the zero-field magnetization and the magnetization at 1 T as a function of temperature for 4% Mn sample. The spontaneous magnetization

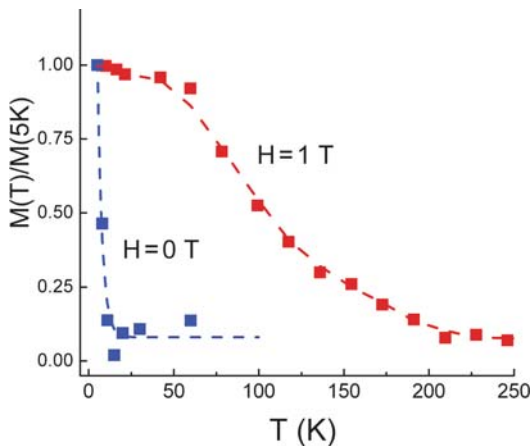
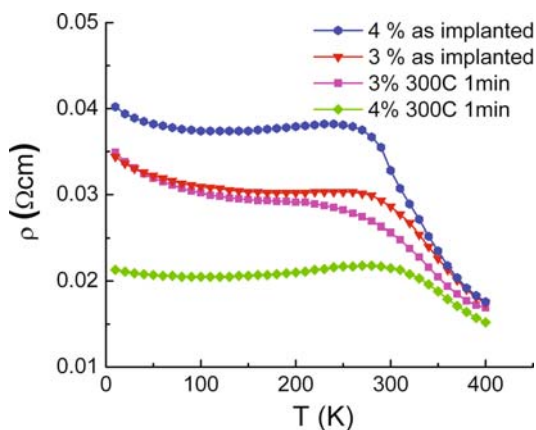


Fig. 16.17 Temperature dependence of the magnetization at the zero fields and 1 T. The dashed lines were added to guide the eye

disappeared between 15 and 20 K, and we estimated that T_C is ~ 20 K. The external field induced magnetization can be observed to much higher temperature (~ 200 K), which we denote as T_C^* . The shape of the magnetization curve was different with or without the external magnetic field. At zero magnetic field, the magnetization has a very steep decrease from 5 to 20 K, and the shape can be approximately fit to a first-order exponential decay function. A similar magnetic behavior has been predicted using the percolation theory of magnetic polarons [59]. Meanwhile, the magnetization curve at 1 T showed two distinguishable regions. It showed a small change below 60 K and a much more rapid decrease in the magnetization from 60 to 200 K. The discrepancy in the two ordering temperatures has been reported previously on GeMn thin films grown by MBE, and it has been attributed to interacting “spin clusters” [47, 54]. These Mn-rich regions in Ge as seen in Fig. 16.13c probably have local magnetic ordering from 20 to 200 K, therefore T_C^* represents the Curie temperature of Mn rich clusters in the system.

Figure 16.18 shows the resistivity as a function of temperature for the as-implanted samples and samples annealed at various conditions. The as-implanted samples have the highest resistivity probably due to implantation damage. After annealing, the resistivity decreased and a higher dose of Mn resulted in a lower resistivity at the same annealing condition. The thermal annealing promoted Mn ion substitution into the Ge lattice, and as a result, Mn ions released carriers (two holes) into the Ge film which we believe caused the improvement in electrical conduction. The carriers created in this process, especially localized carriers, play an important role in the exchange interaction between Mn ions, and it will be the topic of a forthcoming paper.

Fig. 16.18 Resistivity as a function of temperature of Mn-doped Ge thin films following dual implantation and annealing under different conditions



Now we focus on the electric properties of the dual-implanted 4% Mn sample annealed at 300°C, which showed the optimal magnetic properties. Figure 16.19a shows the magnetoresistance ratio (MR) of the 4% sample after annealing as a function of external field and temperatures. The MR is defined as

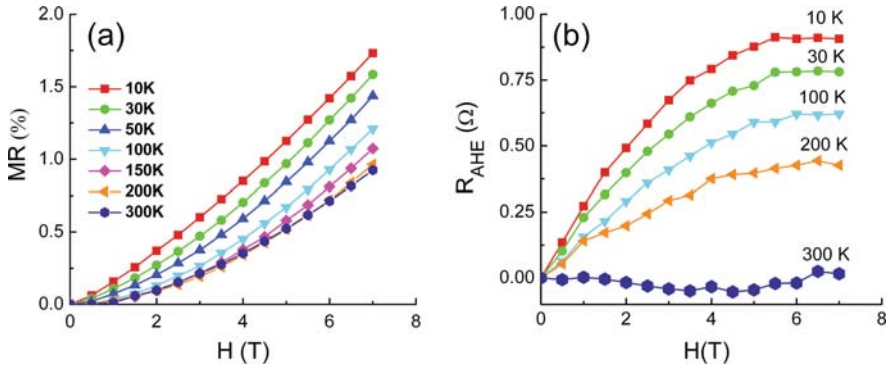


Fig. 16.19 (a) Magnetoresistance ratios as a function of magnetic field and temperature; (b) Anomalous Hall resistances as a function of field and temperature of 4 at.% Mn-doped Ge annealed at 300°C for 1 min

$$MR = \frac{\rho_H - \rho_0}{\rho_0}$$

where ρ_0 and ρ_H are the zero-field resistivity and the resistivity at an external magnetic field of H . A small positive MR ratio of $\sim 1.5\%$ is obtained at 10 K and 7 T. The MR decreases monotonically with an increase in temperature however it is still 0.8% at 300 K and 7 T. It has been suggested that the MR in this system appears to be closely tied to the Mn distribution rather than the magnetic properties [56]. Further studies are necessary to clarify the origin of the MR in dual-implanted $\text{Ge}_{1-x}\text{Mn}_x$ samples at room temperature.

There are two components that contribute to the Hall resistance: the Ordinary Hall Effect (OHE) and the AHE which comes from spin-orbit coupling. The Hall resistance R_{Hall} can be expressed as:

$$R_{\text{Hall}} = R_0 B + R_s \mu_0 M$$

where R_0 is the normal Hall coefficient, R_s is the anomalous Hall coefficient, B is the external magnetic field, M is the magnetic moment, and μ_0 is the magnetic permeability of vacuum. The second term in the above equation $R_s \mu_0 M$ is the anomalous Hall resistance and is directly determined by the magnetization of a ferromagnet. Hall measurements of Mn-doped Ge samples were dominated by R_{OHE} , and we had to subtract the linear component from R_{Hall} to extract R_{AHE} as shown in Fig. 16.19b. R_{AHE} persists to 200 K, which coincides with T_C^* . R_{AHE} disappeared above 200 K which was well above the spontaneous magnetization temperature (~ 20 K). This implies that the external field induced magnetization is carrier mediated.

In summary, $\text{Ge}_{1-x}\text{Mn}_x$ thin films (n-type Ge on SiO_2) were prepared by Mn implantation using different parameters. The dual implantation at a lower temperature (75°C) prevented the formation of the intermetallic MnGe compounds and allowed higher Mn-doping concentrations (up to ~ 4 at.%). TEM showed a rather

uniform Mn ion distribution in dual-implanted 4% Mn-doped Ge following a post-annealing at 300°C however Mn-rich clusters were observed close to the sample surface. The optimal ferromagnetic properties were achieved following post-annealing at 300°C. This relatively low annealing temperature did not fully recover the implantation damages as suggested by the TEM results. Two different ordering temperatures were observed on dual-implanted 4% Mn samples following post-annealing at 300°C for 1.5 min. The spontaneous magnetization disappeared around 20 K, and this temperature represented the Curie temperature for the entire $\text{Ge}_{1-x}\text{Mn}_x$ thin film. The external field induced magnetization was observed up to 200 K, and it was likely caused by the magnetization of Mn-rich clusters. The electrical characterization showed that the external field induced magnetization was carrier mediated, and the anomalous effect was observed up to 200 K. We are currently investigating the influence of the initial carrier type and concentration on the diluted magnetism in the GeMn system in order to understand the coupling of carriers and ferromagnetic ordering. Further studies on Mn ions redistribution and the crystallization of amorphous Ge are also needed to explain that the optimal ferromagnetic properties of GeMn were obtained at a relatively moderate annealing temperature.

Acknowledgment The authors thank for the financial support from the Defense Advanced Research Projects Agency (DARPA), the Office of Naval Research (ONR), the Defense Microelectronics Activity (DMEA), and the joint program of National Science Foundation and Nano-electronics Research Initiative (NRI).

Additional Reading on Spintronics

- S. Wolf and D. Treger, Spintronics: A new paradigm for electronics for the new millennium, IEEE Trans. Magnet. **36**, 2748 (2000).
Proceedings of the IEEE special issue on Spintronics Technology, May 2003, vol. 91, no. 5.
S. Wolf et al., Spintronics: A spin-based electronics vision for the future, Science **294**, 1488–1495 (2001).

References

1. I.K. Schuller. *Transport properties of the compositionally modulated alloy Cu/Ni*. in *AIP Conf. Proc.* 1979.
2. M.N. Baibich, J.M. Broto, A. Fert, F.N. Vandau, F. Petroff, P. Eitenne, G. Creuzet, A. Friederich, and J. Chazelas, *Giant magnetoresistance of (001)Fe/(001) Cr magnetic superlattices*. Physical Review Letters, 1988. **61**(21): 2472–2475.
3. G.A. Prinz, *Device physics – Magnetoelectronics*. Science, 1998. **282**(5394): 1660–1663.
4. S.A. Wolf, D.D. Awschalom, R.A. Buhrman, J.M. Daughton, S. von Molnar, M.L. Roukes, A.Y. Chtchelkanova, and D.M. Treger, *Spintronics: A spin-based electronics vision for the future*. Science, 2001. **294**(5546): 1488–1495.
5. S.S.P. Parkin, K.P. Roche, M.G. Samant, P.M. Rice, R.B. Beyers, R.E. Scheuerlein, E.J. O’Sullivan, S.L. Brown, J. Bucchigano, D.W. Abraham, Y. Lu, M. Rooks, P.L. Trouilloud, R.A. Wanner, and W.J. Gallagher, *Exchange-biased magnetic tunnel junctions and application to nonvolatile magnetic random access memory (invited)*. Journal of Applied Physics, 1999. **85**(8): 5828–5833.

6. M. Durlam, D. Addie, J. Akerman, B. Butcher, P. Brown, J. Chan, M. DeHerrera, B.N. Engel, B. Feil, G. Grynkewich, J. Janesky, M. Johnson, K. Kyler, J. Molla, J. Martin, K. Nagel, J. Ren, N.D. Rizzo, T. Rodriguez, L. Savtchenko, J. Salter, J.M. Slaughter, K. Smith, J.J. Sun, M. Lien, K. Papworth, P. Shah, W. Qin, R. Williams, L. Wise, and S. Tehrani, *A 0.18 μm 4MB Toggling MRAM*. IEDM Technical Digest, 2003, pp. 34.6.1–34.6.3.
7. D. Lammers, *Freescale begins selling 4-Mbit MRAM*. 2006. EE Times.
8. L. Berger, *Emission of spin waves by a magnetic multilayer traversed by a current*. Physical Review B, 1996. **54**(13): 9353–9358.
9. J.C. Slonczewski, *Current-driven excitation of magnetic multilayers*. Journal of Magnetism and Magnetic Materials, 1996. **159**(1–2): L1–L7.
10. J.A. Katine, F.J. Albert, R.A. Buhrman, E.B. Myers, and D.C. Ralph, *Current-driven magnetization reversal and spin-wave excitations in Co/Cu/Co pillars*. Physical Review Letters, 2000. **84**(14): 3149–3152.
11. *International Technology Roadmap for Semiconductors*, (2006).
12. K.C. Hall, W.H. Lau, K. Gundogdu, M.E. Flatte, and T.F. Boggess, *Nonmagnetic semiconductor spin transistor*. Applied Physics Letters, 2003. **83**(14): 2937–2939.
13. Y. Matsumoto, M. Murakami, T. Shono, T. Hasegawa, T. Fukumura, M. Kawasaki, P. Ahmet, T. Chikyow, S. Koshihara, and H. Koinuma, *Room-temperature ferromagnetism in transparent transition metal-doped titanium dioxide*. Science, 2001. **291**(5505): 854–856.
14. H. Ohno, *Making nonmagnetic semiconductors ferromagnetic*. Science, 1998. **281**(5379): 951–956.
15. D.P. Divincenzo, *Quantum computation*. Science, 1995. **270**(5234): 255–261.
16. A. Steane, *Quantum computing*. Reports on Progress in Physics, 1998. **61**(2): 117–173.
17. V.V. Zhurin, H.R. Kaufman, J.R. Kahn, and T.L. Hylton, *Biased target deposition*. Journal of Vacuum Science & Technology a-Vacuum Surfaces and Films, 2000. **18**(1): 37–41.
18. J.J. Quan, S.A. Wolf, and H.N.G. Wadley, *Low energy ion beam assisted deposition of a spin valve*. Journal of Applied Physics, 2007. **101**(7): 074302.
19. J.J. Quan, X.W. Zhou, and H.N.G. Wadley, *Low energy ion assisted atomic assembly of metallic superlattices*. Surface Science, 2006. **600**(11): 2275–2287.
20. S. von Molnar, *Spin electronics: From concentrated to diluted magnetic semiconductors and beyond*. Journal of Superconductivity, 2003. **16**(1): 1–5.
21. J.M.D. Coey and C.L. Chien, *Half-metallic ferromagnetic oxides*. Mrs Bulletin, 2003. **28**(10): 720–724.
22. K. Suzuki and P.M. Tedrow, *Resistivity and magnetotransport in CrO₂ films*. Physical Review B, 1998. **58**(17): 11597–11602.
23. X.W. Li, A. Gupta, T.R. McGuire, P.R. Duncombe, and G. Xiao, *Magneto-resistance and hall effect of chromium dioxide epitaxial thin films*. Journal of Applied Physics, 1999. **85**(8): 5585–5587.
24. R.J. Soulen, J.M. Byers, M.S. Osofsky, B. Nadgorny, T. Ambrose, S.F. Cheng, P.R. Broussard, C.T. Tanaka, J. Nowak, J.S. Moodera, A. Barry, and J.M.D. Coey, *Measuring the spin polarization of a metal with a superconducting point contact*. Science, 1998. **282**(5386): 85–88.
25. K. Schwarz, *CrO₂ Predicted as a half-metallic ferromagnet*. Journal of Physics F-Metal Physics, 1986. **16**(9): L211–L215.
26. H.A. Bullen and S.J. Garrett, *Epitaxial growth of CrO₂ thin films on TiO₂(110) surfaces*. Chemistry of Materials, 2002. **14**(1): 243–248.
27. W.J. DeSisto, P.R. Broussard, T.F. Ambrose, B.E. Nadgorny, and M.S. Osofsky, *Highly spin-polarized chromium dioxide thin films prepared by chemical vapor deposition from chromyl chloride*. Applied Physics Letters, 2000. **76**(25): 3789–3791.
28. S.J. Liu, J.Y. Juang, K.H. Wu, T.M. Uen, Y.S. Gou, and J.Y. Lin, *Transport properties of CrO₂ (110) films grown on TiO₂ buffered Si substrates by chemical vapor deposition*. Applied Physics Letters, 2002. **80**(22): 4202–4204.

29. L. Ranno, A. Barry, and J.M.D. Coey, *Production and magnetotransport properties of CrO₂ films*. Journal of Applied Physics, 1997. **81**(8): 5774–5776.
30. K. Kohler, M. Maciejewski, H. Schneider, and A. Baiker, *Chromia supported on titania .5. Preparation and characterization of supported CrO₂, CrOOH, and Cr₂O₃*. Journal of Catalysis, 1995. **157**(2): 301–311.
31. K.G. West, J.W. Lu, J. Yu, D.M. Kirkwood, W. Chen, Y. Pei, J. Claassen, and S.A. Wolf, *Growth and characterization of vanadium dioxide thin films prepared by reactive-biased target ion beam deposition*. Journal of Vacuum Science & Technology A, 2008. **26**(1): 133–139.
32. Y. Matsumoto, R. Takahashi, M. Murakami, T. Koida, X.J. Fan, T. Hasegawa, T. Fukumura, M. Kawasaki, S.Y. Koshihara, and H. Koinuma, *Ferromagnetism in co-doped TiO₂ rutile thin films grown by laser molecular beam epitaxy*. Japanese Journal of Applied Physics Part 2-Letters, 2001. **40**(11B): L1204–L1206.
33. H. Toyosaki, T. Fukumura, Y. Yamada, K. Nakajima, T. Chikyow, T. Hasegawa, H. Koinuma, and M. Kawasaki, *Anomalous Hall effect governed by electron doping in a room-temperature transparent ferromagnetic semiconductor*. Nature Materials, 2004. **3**(4): 221–224.
34. S.R. Shinde, S.B. Ogale, J.S. Higgins, H. Zheng, A.J. Millis, V.N. Kulkarni, R. Ramesh, R.L. Greene, and T. Venkatesan, *Co-occurrence of superparamagnetism and anomalous Hall effect in highly reduced cobalt-doped rutile TiO₂-delta films*. Physical Review Letters, 2004. **92**(16): 166601.
35. D.H. Kim, J.S. Yang, K.W. Lee, S.D. Bu, T.W. Noh, S.J. Oh, Y.W. Kim, J.S. Chung, H. Tanaka, H.Y. Lee, and T. Kawai, *Formation of Co nanoclusters in epitaxial Ti_{0.96}Co_{0.04}O₂ thin films and their ferromagnetism*. Applied Physics Letters, 2002. **81**(13): 2421–2423.
36. S.A. Chambers, *Ferromagnetism in doped thin-film oxide and nitride semiconductors and dielectrics*. Surface Science Reports, 2006. **61**(8): 345–381.
37. H. Munekata, H. Ohno, S. Vonmolnar, A. Segmuller, L.L. Chang, and L. Esaki, *Diluted magnetic III-V semiconductors*. Physical Review Letters, 1989. **63**(17): 1849–1852.
38. J. De Boeck, R. Oesterholt, A. Van Esch, H. Bender, C. Bruynseraede, C. Van Hoof, and G. Borghs, *Nanometer-scale magnetic MnAs particles in GaAs grown by molecular beam epitaxy*. Applied Physics Letters, 1996. **68**(19): 2744–2746.
39. H. Ohno, A. Shen, F. Matsukura, A. Oiwa, A. Endo, S. Katsumoto, and Y. Iye, *(Ga,Mn)As: A new diluted magnetic semiconductor based on GaAs*. Applied Physics Letters, 1996. **69**(3): 363–365.
40. D.D. Awschalom and M.E. Flatté, *Challenges for semiconductor spintronics*. Nature Physics, 2007. **3**(3): 153–159.
41. A. Stroppa, S. Picozzi, A. Continenza, and A.J. Freeman, *Electronic structure and ferromagnetism of Mn-doped group-IV semiconductors*. Physical Review B, 2003. **68**(15): 155203.
42. H.M. Weng and J.M. Dong, *First-principles investigation of transition-metal-doped group-IV semiconductors: R(x)Y1(-x) (R=Cr,Mn,Fe; Y=Si,Ge)*. Physical Review B, 2005. **71**(3): 035201.
43. Y.D. Park, A. Wilson, A.T. Hanbicki, J.E. Mattson, T. Ambrose, G. Spanos, and B.T. Jonker, *Magnetoresistance of Mn: Ge ferromagnetic nanoclusters in a diluted magnetic semiconductor matrix*. Applied Physics Letters, 2001. **78**(18): 2739–2741.
44. Y.D. Park, A.T. Hanbicki, S.C. Erwin, C.S. Hellberg, J.M. Sullivan, J.E. Mattson, T.F. Ambrose, A. Wilson, G. Spanos, and B.T. Jonker, *A group-IV ferromagnetic semiconductor: Mn_xGe_{1-x}*. Science, 2002. **295**(5555): 651–654.
45. L.F. Liu, N.F. Chen, C.L. Chen, Y.L. Li, Z.G. Yin, and F. Yang, *Magnetic properties of Mn-implanted n-type Ge*. Journal of Crystal Growth, 2004. **273**(1–2): 106–110.
46. J.S. Kang, G. Kim, S.C. Wi, S.S. Lee, S. Choi, S. Cho, S.W. Han, K.H. Kim, H.J. Song, H.J. Shin, A. Sekiyama, S. Kasai, S. Suga, and B.I. Min, *Spatial chemical inhomogeneity and*

- local electronic structure of Mn-doped Ge ferromagnetic semiconductors*. Physical Review Letters, 2005. **94**(14): 147202.
47. A.P. Li, J.F. Wendelken, J. Shen, L.C. Feldman, J.R. Thompson, and H.H. Weitering, *Magnetism in $MnxGe1-x$ semiconductors mediated by impurity band carriers*. Physical Review B, 2005. **72**(19): 195205.
 48. N. Pinto, L. Morresi, M. Ficcadenti, R. Murri, F. D’Orazio, F. Lucari, L. Boarino, and G. Amato, *Magnetic and electronic transport percolation in epitaxial $Ge1-xMnx$ films*. Physical Review B, 2005. **72**(16): 165203.
 49. S. Ahlers, D. Bougeard, N. Sircar, G. Abstreiter, A. Trampert, M. Opel, and R. Gross, *Magnetic and structural properties of $GexMn1-x$ films: Precipitation of intermetallic nanomagnets*. Physical Review B, 2006. **74**(21): 214411.
 50. M. Jamet, A. Barski, T. Devillers, V. Poydenot, R. Dujardin, P. Bayle-Guillemaud, J. Rothman, E. Bellet-Amalric, A. Marty, J. Cibert, R. Mattana, and S. Tatarenko, *High-Curie-temperature ferromagnetism in self-organized $Ge1-xMnx$ nanocolumns*. Nature Materials, 2006. **5**(8): 653–659.
 51. L. Ottaviano, P. Parisse, M. Passacantando, S. Picozzi, A. Verna, G. Impellizzeri, and F. Priolo, *Nanometer-scale spatial inhomogeneities of the chemical and electronic properties of an ion implanted Mn-Ge alloy*. Surface Science, 2006. **600**(20): 4723–4727.
 52. M. Passacantando, L. Ottaviano, F. D’Orazio, F. Lucari, M. De Biase, G. Impellizzeri, and F. Priolo, *Growth of ferromagnetic nanoparticles in a diluted magnetic semiconductor obtained by $Mn+$ implantation on Ge single crystals*. Physical Review B, 2006. **73**(19): 195207.
 53. J.J. Chen, K.L. Wang, and K. Galatsis, *Electrical field control magnetic phase transition in nanostructured $MnxGe1-x$* . Applied Physics Letters, 2007. **90**(1): 012501.
 54. D. Bougeard, S. Ahlers, A. Trampert, N. Sircar, and G. Abstreiter, *Clustering in a precipitate-free $GeMn$ magnetic semiconductor*. Physical Review Letters, 2006. **97**(23): 237202.
 55. H.L. Li, Y.H. Wu, Z.B. Guo, P. Luo, and S.J. Wang, *Magnetic and electrical transport properties of $Ge1-xMnx$ thin films*. Journal of Applied Physics, 2006. **100**(10): 103908.
 56. A.P. Li, C. Zeng, K. van Benthem, M.F. Chisholm, J. Shen, S.V.S.N. Rao, S.K. Dixit, L.C. Feldman, A.G. Petukhov, M. Foygel, and H.H. Weitering, *Dopant segregation and giant magnetoresistance in manganese-doped germanium*. Physical Review B, 2007. **75**(20).
 57. N. Yamada, *Atomic magnetic-moment and exchange interaction between Mn atoms in intermetallic compounds in Mn-Ge system*. Journal of the Physical Society of Japan, 1990. **59**(1): 273–288.
 58. C.G. Zeng, S.C. Erwin, L.C. Feldman, A.P. Li, R. Jin, Y. Song, J.R. Thompson, and H.H. Weitering, *Epitaxial ferromagnetic $Mn5Ge3$ on $Ge(111)$* . Applied Physics Letters, 2003. **83**(24): 5002–5004.
 59. A. Kaminski and S. Das Sarma, *Polaron percolation in diluted magnetic semiconductors*. Physical Review Letters, 2002. **88**(24): 247202.

Chapter 17

Growth and Properties of Epitaxial Chromium Dioxide (CrO_2) Thin Films and Heterostructures

Guo-Xing Miao and Arunava Gupta

Abstract CrO_2 is a remarkable ferromagnetic material that is simultaneously an excellent metal for majority spin electrons and an insulator for minority spin electrons [1–3]. For this reason, CrO_2 is called a half-metal, and in fact, it is the only one experimentally demonstrated [4–6]. Because of this, CrO_2 has received considerable interest for spintronic applications in recent years. Band structure calculations have shown that the conduction bands in the spin minority channel of this system are completely shifted away from the Fermi level, resulting in 100% spin polarization. This makes it an attractive choice as a ferromagnetic material for spin-dependent devices such as spin injectors and spin detectors. In this chapter, we briefly describe the bonding characteristics in CrO_2 , based on first principles band structure calculations, as well as discuss some of its intrinsic structural, electrical, and magnetic properties. The strain-induced magnetic anisotropy resulting from lattice mismatch with the substrates is also discussed. Finally, we provide some details regarding the fabrication of epitaxial rutile-based heterostructures and their transport properties in micron-sized tunnel junction and GMR devices.

17.1 Density of States (DOS) of Half-Metallic CrO_2 and the Double Exchange Mechanism

We use the DOS of half-metallic oxide (CrO_2), a non-magnetic metallic oxide (RuO_2), and an insulating oxide (TiO_2), all belonging to the rutile family, to illustrate the differences between a half-metal and other materials. Figure 17.1 illustrates the unit cell of a rutile structure. We choose TiO_2 (with the rutile structural polymorph) for comparison because $\text{Ti}(Z = 22)$ is very close to $\text{Cr}(Z = 24)$ in the periodic table, and it is also the most common member within the rutile family.

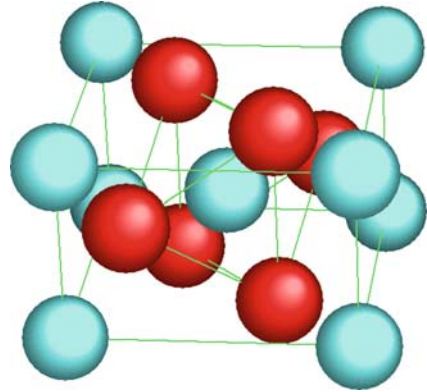
A. Gupta (✉)

Center for Materials for Information Technology (MINT), The University of Alabama, Tuscaloosa, AL 35487, USA

e-mail: agupta@mint.ua.edu

Further, very high-quality single crystal substrates of TiO_2 with cuts of different orientations ((100), (110), and (001)) are available commercially. We choose RuO_2 as an example of a non-magnetic metallic rutile oxide. We can epitaxially grow thin films of these rutile oxides using the technique of chemical vapor deposition (CVD) and also form heteroepitaxial structures with each other.

Fig. 17.1 The rutile crystal structure. The *dark spheres* indicate the O ions, and the *light spheres* indicate the cations (Ti, Cr, Sn, Ru, etc.) in the unit cell. The octahedral coordination of the central cation is depicted in the drawing



In the following examples of DOS results for various rutile oxides, we have carried out the calculations using the generalized gradient approximation (GGA) method in the VASP code allowing the atoms to relax to their equilibrium positions by minimizing the stress tensors acting on them. Figure 17.2 illustrates the total DOS for CrO_2 , TiO_2 , and RuO_2 . The half-metallic nature of CrO_2 is apparent from comparing the three plots. The spin-up DOS of CrO_2 closely resembles the DOS of RuO_2 , while the spin-down DOS of CrO_2 is similar to the DOS of TiO_2 . Therefore, CrO_2 is metallic in its spin-up channel, and insulating in its spin-down channel, hence the name “half-metal.” The *s*, *p*, and *d* electron sub-DOS of CrO_2 are also illustrated in Fig. 17.2. Below the Fermi energy in the energy range $-8\text{eV} < E < -2\text{eV}$, the *p* and *d* electron DOS have similar shapes, although with differing intensities. As a consequence, there is covalent bonding between the $\text{Cr}(3d)$ and the $\text{O}(2p)$ electrons. The crystalline field due to the octahedral coordination of the Cr ions splits the $\text{Cr}3d$ orbitals into t_{2g} and e_g sub-bands, occupying the energy range $-2\text{eV} < E < -2\text{eV}$ and $2\text{eV} < E < -2\text{eV}$, respectively. The spin-down DOS is rigidly shifted because of exchange interaction by approximately $2rmeV$, resulting in a band gap of about 2eV in the spin minority channel. The local distortion of the CrO_6 octahedra further splits the t_{2g} bands into xy , $yz + zx$, and $yz - zx$ orbitals. Cr^{4+} (d^2) has two valence electrons. One of them, with xy character, is buried below the Fermi level (the DOS peak between $-eV$ and $0eV$) and strongly localized at each site. The other, with mainly $yz + zx$ character, lies across the Fermi level and is strongly hybridized with $\text{O}2p$ electrons. It has been proposed that such an electronic configuration makes CrO_2 “a self-doped double exchange ferromagnet” [3]. The valence electrons themselves provide the localized and mobile

electrons, and according to Hund's rule the free-moving electrons travel between sites and have the effect of ferromagnetically aligning the neighboring spins.

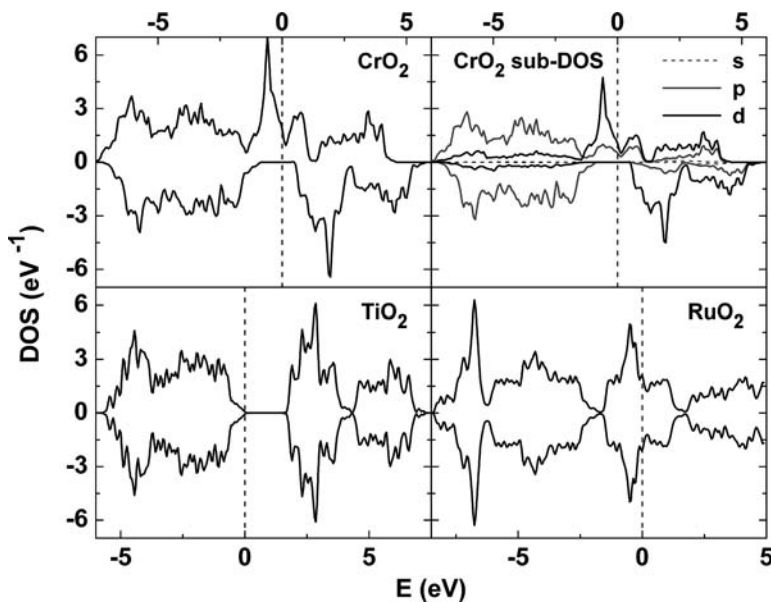


Fig. 17.2 The DOS for half-metallic CrO₂, metallic RuO₂, and insulating TiO₂. The angular momentum dependent sub-DOS of CrO₂ is also shown in the *upper right panel*. The Fermi level is defined as energy zero

17.2 Intrinsic Properties of Epitaxial CrO₂ Films

As mentioned earlier, CrO₂ has a tetragonal rutile structure with bulk lattice parameters of $a = b = 0.4421$ nm and $c = 0.2916$ nm. The short c axis is a consequence of the distortion of the oxygen octahedral. Being a metastable phase, the nucleation of CrO₂ is critically dependent on the substrate lattice structure and the formation temperature. For aiding the nucleation and epitaxial growth of CrO₂, we choose an isostructural and well-lattice-matched substrate, namely (100)-TiO₂ with lattice parameters of $a = b = 0.4594$ nm, and $c = 0.2958$ nm. We have deposited high-quality epitaxial CrO₂ thin films using a simple CVD reactor consisting of a quartz tube placed inside a two-zone furnace with independent temperature control of the two zones [7, 8]. Before film growth, the single crystal (100)-TiO₂ substrates are cleaned with organic solvents and dilute hydrofluoric (HF) acid solution and loaded into the CVD chamber. The films are grown at a substrate temperature of 400°C in the primary reaction zone, with the solid CrO₃ precursor being placed in the secondary zone of the furnace that is heated to about 260°C for sublimation. Oxygen is used as a carrier gas with a flow rate of 100 sccm.

Due to the difficulty in the formation of CrO_2 under ambient conditions, deposition during the CVD growth process occurs selectively on the lattice-matched TiO_2 substrate in a very narrow temperature window of $\pm 20^\circ\text{C}$, with the quartz tube and the susceptor remaining clean after the deposition. The selective deposition of CrO_2 [9, 10] can be exploited for the patterned growth of the material using TiO_2 substrates that are pre-patterned using SiO_2 [10]. The lattice match between the film and the substrate results in epitaxial strain in the film that can lead to significant modifications in the film properties. We will detail the influence of strain on the magnetic properties in the next section. Because the lattice parameters of rutile TiO_2 are larger than those for CrO_2 by 3.91 and 1.44% along the b - and the c -directions, respectively, the epitaxial films experience tensile stress in both in-plane directions and consequently shrink in the out-of-plane a direction. The strain increase shows up as a shift in the normal θ - 2θ XRD peak to higher angles with decreasing film thickness (Fig. 17.3). In addition, we have performed off-axis XRD scans to determine the in-plane CrO_2 film lattice parameters for various thicknesses, and the strain relaxation roughly follows a $t^{1/3}$ dependence along all three lattice directions [11]. A slower relaxation rate than predicted by the equilibrium Matthews–Blakeslee (M-B) model [12] is commonly observed for epitaxial oxide films and has been attributed to kinetic barriers in the propagation and multiplication of the misfit dislocations needed for relaxation due to the ionic nature of the oxides [13, 14]. The strain relaxation mechanism in CrO_2 results in changes in the film quality with thickness. The inset to Fig. 17.3 illustrates the variation of the CrO_2 rocking curve FWHM of the (200) peak with film thickness. The peak width is a measure of the dispersion of the films out-of-plane alignment and is a direct indication of the film quality. A peak in the FWHM is observed for a film thickness of around 100 nm. For thinner films,

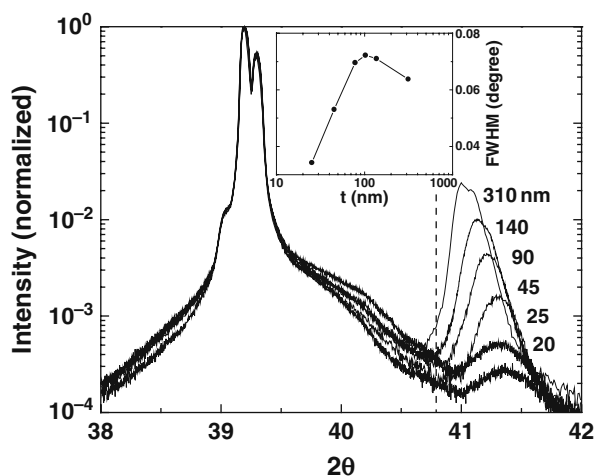


Fig. 17.3 XRD data around the (200) TiO_2 substrate and different thickness CrO_2 film peaks. Dashed line indicates the bulk CrO_2 (200) peak position. Inset shows the rocking curve FWHM

dislocations are not energetically favored, and the films grow coherently on the substrate. On the other hand, for thicker films, most of the strain is relaxed by dislocations, and the films grow relatively strain free. For films of intermediate thickness, the strain is only partially relaxed and is distributed relatively inhomogeneously across the thickness of the film. The effect of inhomogeneous strain distribution on the magnetic properties will be discussed in the next section.

The epitaxial CrO₂ films exhibit a strong anisotropy in the electrical conductivity between the long axes (a , b) and the short axis (c) directions, (Fig. 17.4). The resistivity for an 84 nm thick film along the a - and c -directions is 150 $\mu\Omega\text{-cm}$ and 200 $\mu\Omega\text{-cm}$ at room temperature, and 10.9 $\mu\Omega\text{-cm}$ and 5.6 $\mu\Omega\text{-cm}$ at 5 K, respectively. Apparently, transport along the a -direction is more favorable at RT, but it is overtaken by the c -direction at lower temperatures. The cross-over temperature between the two resistivity curves decreases with film thickness, and it ranges from 220 K for a 17 nm film to 130 K for a 400 nm film (Fig. 17.4 inset). The residual resistivity ratio (rrr) is much larger along the c - than in the a -direction. The larger rrr in the c -direction is not primarily a result of the increased phonon scattering, as normally interpreted for larger rrr . Instead it is a result of enhanced magnon scattering in this direction [15]. For comparison, similarly structured nonmagnetic RuO₂ films deposited by CVD on (100) TiO₂ substrates do not exhibit any significant transport anisotropy.

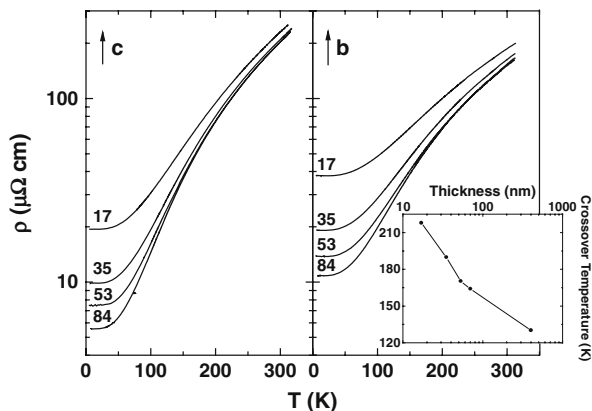


Fig. 17.4 Thickness dependence of the CrO₂ resistivity along the c - and b -axis directions. Thicknesses are marked in nanometers. Inset shows the cross-over temperature as a function of film thickness

The magnetic measurements presented here have been carried out on films of dimension $5 \times 5 \text{ mm}^2$, with the film thickness being no more than 2×10^{-4} of the lateral dimension. We thus expect the magnetization to be confined to the plane of the substrate with negligible in-plane demagnetizing field ($H_D < 0.50\text{e}$) and shape anisotropy. The thinnest film we have studied is about 9 nm thick (corresponding to about 40 atomic layers) and the surface anisotropy contribution, as is usually

observed in ultrathin (1–10 atomic layers) transition metal films, is not expected to be significant. For very thick films, the strain anisotropy can also be neglected. Figure 17.5 summarizes the magnetic properties of a bulk-like CrO₂ epitaxial film of 1 μm thickness. Irrespective of film thickness, the epitaxial (100) CrO₂ films that we have grown display a Curie temperature (T_C) of ~390 K. The room temperature and 7 K saturation magnetization M_S have been determined to be 475 emu/cm³ and 640 emu/cm³, respectively. The corresponding anisotropy energy constant K_1 values are 2.2×10^5 and 4.5×10^5 erg/cm³ (Fig. 17.5), and for K_2 are 4×10^4 and 3×10^4 erg/cm³, respectively [16]. The anisotropy field values H_K are determined from the in-plane hard axis (b -axis) hysteresis loops, and the crystalline anisotropy energy constant K_1 is calculated from the relation $K_1 = H_K M_S / 2$. Generally speaking, bulk CrO₂ is a relatively soft material as compared to most traditional ferromagnets. Its crystalline anisotropy energy along the c -axis decreases monotonically with temperature, rendering the bulk CrO₂ film's easy axis to be more closely aligned along the c -axis at lower temperatures due to the increased energy barrier in the hard b -axis direction. In competition, the strain arising from the misfit between the CrO₂ thin film and the TiO₂ substrate creates an additional uniaxial

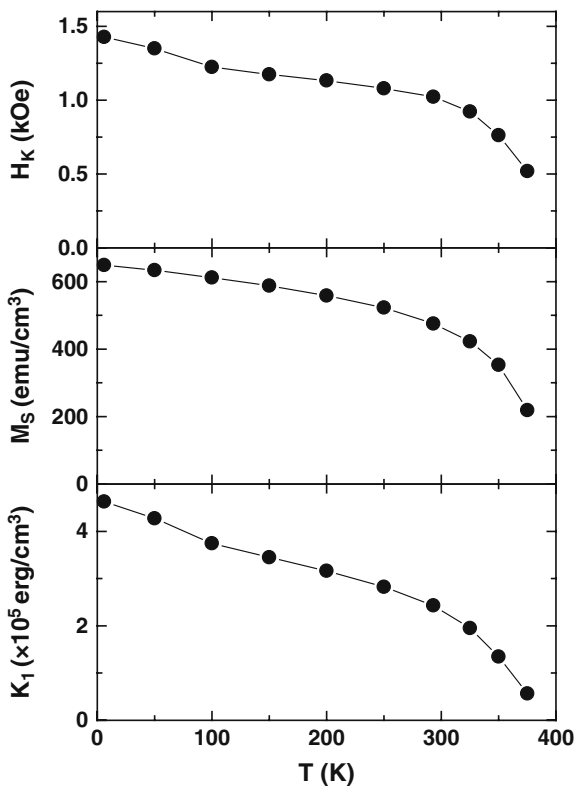


Fig. 17.5 Temperature dependence of the CrO₂ anisotropy field (H_K), saturation moment (M_S), and anisotropy energy constant (K_1), measured for a 1 μm thick CrO₂ film

anisotropy which favors the b -axis direction. With decreasing film thickness, this strain-induced anisotropy can become large enough to compete with and eventually surpass the intrinsic crystalline anisotropy. We will discuss the details of this effect in the next section.

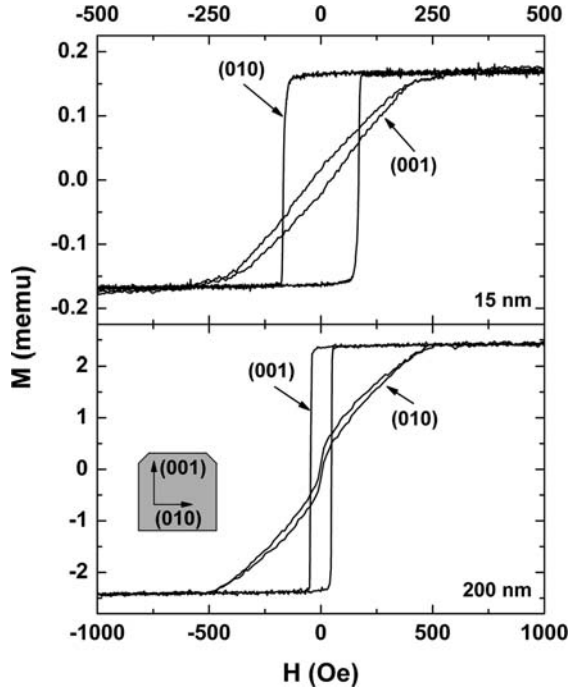
17.3 Influence of Strain on the Magnetic Properties of CrO₂ Thin Films

For the practical implementation of CrO₂-based spintronic devices, it is important to gain a better understanding of its switching characteristics and magnetic anisotropy and to explore possible approaches to control these properties. With such knowledge, one can potentially realize independent switching of two separate CrO₂ layers, and thus manipulate the relative spin orientations of the layers. The latter is important for the operation of GMR and TMR-based devices. This section attempts to provide a comprehensive investigation of the magnetic properties of epitaxial CrO₂ thin films, with emphasis on the strong sensitivity of its magnetic anisotropy to strain and temperature.

17.3.1 Film Growth on Atomically Smooth TiO₂ Substrates

In this section, we discuss the magnetic properties of CrO₂ films deposited on atomically smooth (100)-TiO₂ substrates. A dilute HF treatment of the substrates is essential to achieve such smoothness. There are two competing anisotropies present in the as-deposited CrO₂ films – the magnetocrystalline and the strain anisotropy – that are considered significant. The former, a volume effect, is an intrinsic property of the material that favors the magnetic easy axis to orient along the in-plane c -direction. The latter is an interface effect, and highly strained thin films grown on (100)-TiO₂ substrates exhibit magnetic easy-axis alignment along the b -direction, since the lattice mismatch is larger along the b than in the c -axis direction (3.91% vs. 1.44%). We have found that the relative magnitude of these two anisotropies is dependent on the film thickness [17]. As illustrated in Fig. 17.6, the magnetic easy axis is aligned along the c -direction for thick CrO₂ films, but it becomes the hard axis for thin films due to the dominance of the strain anisotropy. The cross-over thickness is approximately 50 nm. Figure 17.7 clearly demonstrates the rotation of easy axis with film thickness, as evidenced from the 90° out of phase between the thick and thin films' magnetic switching properties. Based on simple estimates, one expects the ratio of the magnetocrystalline energy to the strain anisotropy energy to be approximately proportional to the film thickness t , which is related to the volume-to-surface ratio. We will show, based on a simplified model of residual strain in the film, that a more complex thickness dependence is appropriate in the heavily strained CrO₂ thin films.

Fig. 17.6 Hysteresis loops for a thin (15 nm) and a thick (200 nm) CrO₂ film along the *c*- and *b*-axis directions



We here attempt to explain the thickness dependence of the magnetic anisotropy and easy axis rotation. We describe the free energy of the system as follows:

$$\begin{aligned}
 E &= K_0 + K_1 \sin^2 \theta + K_2 \sin^4 \theta + (K_{\sigma c} \sin^2 \theta + K_{\sigma b} \cos^2 \theta) \\
 &= \text{const} + K_1 \sin^2 \theta + K_{\sigma} \sin^2 \theta + K_2 \sin^4 \theta
 \end{aligned}
 \tag{17.1}$$

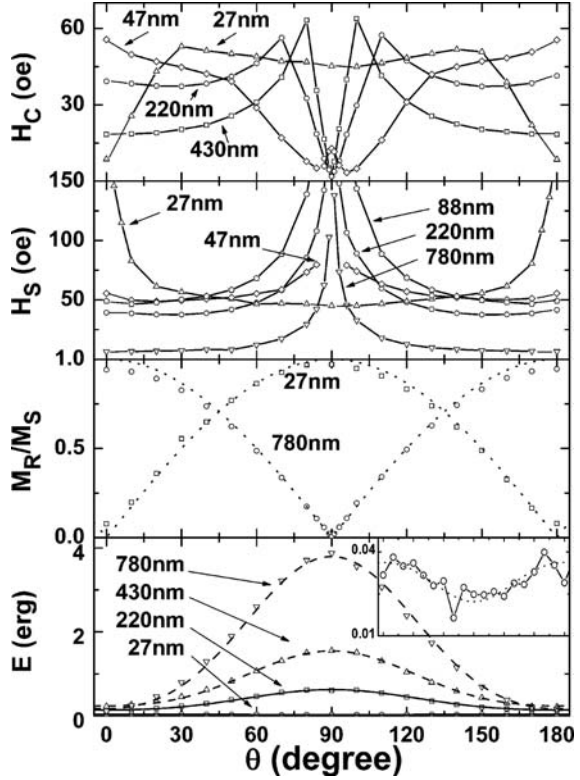
where K_1 and K_2 are the magnetocrystalline anisotropy energy constants; $K_{\sigma b}$ and $K_{\sigma c}$ are the strain anisotropy energy constants associated with the *b*- and *c*-axis directions, respectively.

$$K_{\sigma} = K_{\sigma c} - K_{\sigma b} = \frac{3}{2} \lambda (\sigma_c - \sigma_b) = \frac{3}{2} \lambda Y (\varepsilon_c - \varepsilon_b)$$

where θ is the angle between the magnetization and the *c*-axis; σ_c and σ_b are the stress components [18]. We have represented K_{σ} in terms of the strain components in the two directions by using the relationship $K_{\sigma} = \frac{3}{2} \lambda Y \varepsilon$, where λ is the magnetostriction coefficient, Y is the Young's modulus, and ε is the strain [18].

It is well known that for epitaxial growth on lattice-mismatched substrates the film usually grows coherently strained to match the substrate for thin layers. However, above a critical thickness, dislocations are generated to relieve the misfit strain. By minimizing the sum of the energy of the misfit dislocations and the elastic misfit strain, Matthews and Blakeslee (M-B) [12, 19] have derived the thickness dependence for the residual equilibrium strain,

Fig. 17.7 Thickness dependence of the CrO₂ anisotropies. Inset shows the enlarged curve for the 27 nm film



$$\varepsilon = \frac{1 - \nu \cos^2 \varphi}{8\pi(1 + \nu) \cos \phi} \frac{b}{t} \ln \left(\frac{4t}{b} \right) \tag{17.2}$$

where b is the magnitude of the Burgers vector of the dislocation, and $\alpha = \frac{1 - \nu \cos^2 \varphi}{8\pi(1 + \nu) \cos \phi}$ is a constant that depends on the Poisson ratio ($\nu \cong 0.3$), the angles of the Burgers vector with respect to the dislocation line (φ), and the angles between the interface and the normal to the slip plane (ϕ). By neglecting the K_2 term in Eq. (17.1), we can relate the effective magnetic anisotropy energy constant $K_{1eff} = K_1 + K_\sigma$ to the film thickness t ,

$$K_{1eff} = K_1 + \frac{3}{2} \lambda Y \alpha \left[\frac{c}{t} \ln \left(\frac{4t}{c} \right) - \frac{b}{t} \ln \left(\frac{4t}{b} \right) \right] \tag{17.3}$$

In the above equation, we have approximated the magnitudes of the Burgers vectors in the b - and c -directions with the corresponding lattice parameters. From Eq. (17.3), it is seen that the ratio between K_1 and K_σ is proportional to $\frac{t}{\ln t + const}$ for films thicker than a few tens of nanometers (i.e., when $t \gg b, c$). By analyzing the

anisotropy fields based on the hysteresis loop measured along the hard-axis direction at room temperature (e.g., Fig. 17.6), we have determined the values of K_{1eff} for CrO_2 films over a large range of thicknesses, and a fairly good match has been observed between the model and the experiment [17]. We have carried out X-ray measurements of the off-axis CrO_2 (220) and (202) peaks to determine the in-plane b and c lattice parameters, and the value of α is determined to be 0.39 from the experimentally measured strain in a 50 nm CrO_2 film. If we assume the Young's modulus to be 2.5×10^{12} dyne/cm², as in the case of bulk TiO_2 , the magnetostriction coefficient of CrO_2 at room temperature is estimated to be 9.4×10^{-6} . Because of differences in the thermal expansion coefficient between the film and the substrate, the temperature can also induce easy axis reorientation in CrO_2 films, especially for films with thickness around 50 nm.

From the above discussion, it is clear that the nature of the strain relaxation as a function of thickness has a strong influence on the magnetic anisotropy of CrO_2 films. The crystalline and strain anisotropy directions for growth on (100) TiO_2 substrate are orthogonal to each other. If coherent rotation can be achieved for all thicknesses, the easy axis should be along the c -direction for films thicker than 50 nm, and along the b -direction for films below 50 nm, as suggested by the change in the sign of K_{1eff} [17]. However, our results show that the anisotropy of CrO_2 films is more complicated than a simple switching of easy axis for an intermediate range of thicknesses. In the thickness range of about 50–250 nm, we find that the CrO_2 films do not exhibit a simple uniaxial switching behavior. Figure 17.9(a) shows the hysteresis loops for a 65 nm film with fields applied along various angles relative to the c -axis. Clearly, there exist two different switching fields, and they are 90° out of phase, corresponding to the easy axis being along the b - or c -direction. A similar behavior is observed for thicker films up to about 250 nm, with the c -axis switching component increasing in magnitude while the b -axis component decaying with increasing film thickness.

The original M–B model was developed for relatively thin films in which the thickness is not much larger than the spacing between neighboring edge dislocation lines, and therefore the strain distribution is assumed to be homogeneous throughout the film. In reality, especially for thick oxide films, the strain is more concentrated near the interface and is gradually relaxed by forming dislocations. This is evidenced from the non-uniform distribution of dislocations at various depths in the films [20, 21]. Using a simple model for the strain distribution throughout the film thickness, we have demonstrated that it is energetically more favorable to form a 90° -domain wall in the middle of the film, and it thus results in the observed double-switching phenomena [17]. The key factors that favor such a phenomena are that the material must have low exchange stiffness constant (A), higher strain anisotropy ($K_b \sim 3/2 \lambda Y \epsilon$) of the bottom layers, and sufficient thickness to form the domain wall. For films not too thin, and the strain distributed linearly near the substrate–film interface up to thickness t_0 , the criterion is $\frac{1}{2} K_b t_0 \geq \frac{\beta}{2} \pi [A(K_b + K_t)]^{1/2}$. Here K_t is the top layer crystalline anisotropy energy constant, β is a dimensionless factor depending on the distribution of strains, and in the above-mentioned case, it is 0.22. CrO_2 satisfies the

criterion because it has a low Curie temperature (low A), a relatively large lattice mismatch with the substrate, and yet can maintain epitaxial growth.

17.3.2 Films Grown on As-Polished TiO₂ Substrates

The growth morphology of the CrO₂ films is critically dependent on the TiO₂ substrate-cleaning procedure utilized prior to deposition. Films grown on as-polished (100)-TiO₂ substrates that are cleaned with organic solvents (acetone and isopropanol) and then rinsed in distilled water are relatively rougher and have a columnar morphology with only a small residual strain [11]. The strain effect is much more pronounced in films grown on substrates that are briefly treated with dilute HF prior to deposition. AFM images confirm that the HF-treated substrates have an atomically smooth surface (Fig. 17.8), and this is the origin of the large strain established in the films described above. Furthermore, the CrO₂ films deposited on top of HF-treated substrates show elongated grains, while those on as-polished substrates show square-shaped grains. This is yet another consequence

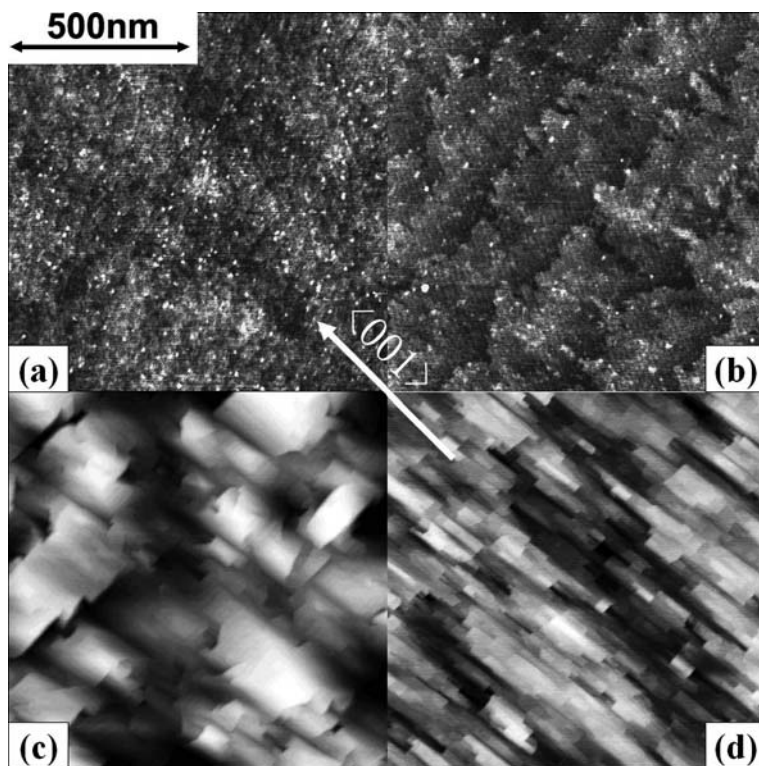


Fig. 17.8 AFM images of (100)-TiO₂ substrates before (a) and after (b) HF treatment, and CrO₂ films grown on top of them, 65 nm (c) and 37 nm (d)

of the effect of residual strain. Hereafter, we refer to the CrO_2 films grown on TiO_2 substrates that do not or do undergo the additional HF treatment as strain-free and strained films, respectively. Note that the “strain-free” films are not completely strain free, but exhibit a much lower level of strain as compared to the other type of films. Further improvements in the CrO_2 film morphology is expected with use of TiO_2 substrates that are annealed at high temperatures (700–1,000°C) after the HF chemical treatment [22]. Depending on the miscut angle, the annealing step can lead to formation of large flat terraces with well-defined unit cell steps on the substrate surface.

We next focus on the magnetic properties of the strained and strain-free films. As previously noted, the strained films that grow on atomically ordered substrates are much more heavily strained than the strain-free films.

The effective anisotropy energy constant $K_{1\text{eff}}$ can thus be negative, resulting in an easy axis reorientation toward the b -axis. In the case of strain-free films, the nucleation and growth of the film occurs more randomly since the surface is rough on an atomic scale. Correspondingly, the strain anisotropy in these films is significantly lower than the crystalline anisotropy. Because of the presence of a large number of defects, the RMS roughness of these films is typically about twice as large as those of the strained films. Despite an inferior crystalline quality, these films exhibit magnetic switching behavior close to that observed in bulk single crystals of CrO_2 . Figure 17.9 shows the hysteresis loops of a strained and a strain-free

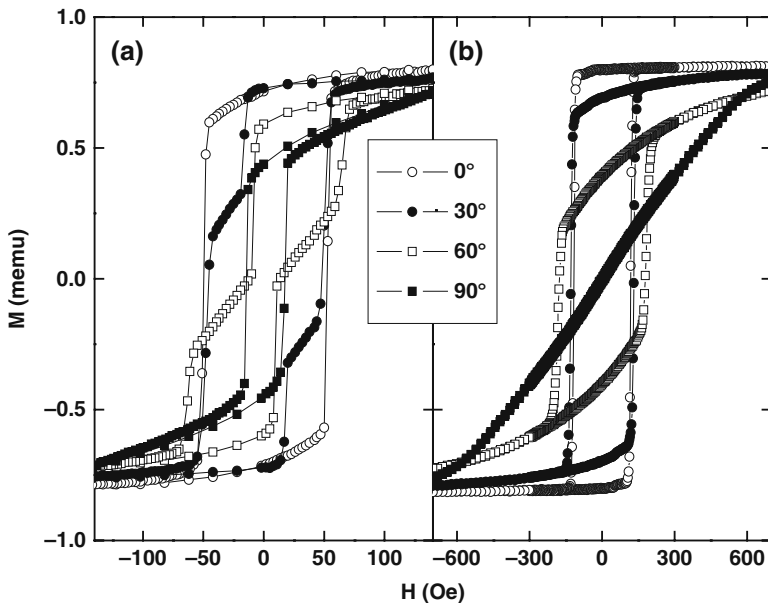


Fig. 17.9 Comparison of the hysteresis loops for a heavily strained (a) and a relatively strain-free (b) CrO_2 film. Both films are 65 nm. The indicated angles are the field direction with respect to the film c -axis

film, both of which are nominally 65 nm thick. The double-switching phenomena, resulting from non-uniform distribution of strain, that normally appear in the heavily strained films of intermediate thickness, are not observed in the strain-free films. Furthermore, because of the lack of any significant influence of strain in the latter, the magnetic anisotropy is close to being uniaxial with a much more uniform magnetization, resulting in a higher nucleation field.

The CrO₂ films grown on TiO₂ substrates can be readily etched by chemical treatment using a commercial chromium etchant solution. The cleaned substrates can then be reused (after HF pre-treatment) for growth of CrO₂ films. We have found that TiO₂ substrates that have been repeatedly re-cleaned also lead to the growth of strained CrO₂ films, but progressively less so with increasing usage as compared to virgin HF-treated substrates [11]. This is not surprising considering that the surface becomes increasingly rougher with each deposition and surface cleaning cycle. In addition, we have found that ion milled substrates also lead to the growth of less-strained films. This suggests that it is important to start with an atomically smooth surface in order to obtain coherently strained epitaxial films.

17.4 CrO₂-Based Heterostructures

We have taken advantage of the fact that the switching field of CrO₂ thin films is strain dependent to achieve differential magnetic switching in CrO₂/epitaxial spacer layer/CrO₂ heteroepitaxial structures without resort to exchange biasing of one of the magnetic layers. Exchange biasing would in general require an additional anti-ferromagnetic layer that can potentially degrade the epitaxy. The spacer layers we have explored include SnO₂, RuO₂, and Cr₂O₃. In all cases, the bottom CrO₂ layer is grown on an atomically smooth TiO₂ surface as described above, while the top layer is deposited on top of a somewhat rougher spacer layer that is either formed naturally (Cr₂O₃) or deposited by CVD (SnO₂, RuO₂), and is less strained than the bottom layer. With spacer layer thicknesses of ≥ 2 nm, the top and bottom CrO₂ layers can be magnetically decoupled (Fig. 17.10). Indeed, the XRD results in Fig. 17.11 show that the two layers are strained differently, as reflected by the presence of two separate peaks in the $\theta-2\theta$ scans. However, when using Cr₂O₃ as a spacer layer, the two peaks are indistinguishable, suggesting that the very thin Cr₂O₃ reverts back to CrO₂ during the deposition step for the top CrO₂ layer. The extremely low resistance of MTJs fabricated using CrO₂-CrO₂ layers separated by a natural barrier provides further evidence of the absence of interface Cr₂O₃ after the second deposition step. Interestingly, high-resolution TEM images show that the formation of either RuO₂ or SnO₂ on top of the CrO₂ surface also results in the removal of the native Cr₂O₃ surface layer [15, 23], but at the expense of increased interface roughness. The increased interface roughness, or what we term intermixing, has a significant influence on the spin polarized transport as described later. We have observed substantial magnetoresistance (MR) in these heterostructures with using Co as a counter-electrode. But the observed MR values are far lower than what would be expected based on the simple Julliere model. Surprisingly, negligible MR has been

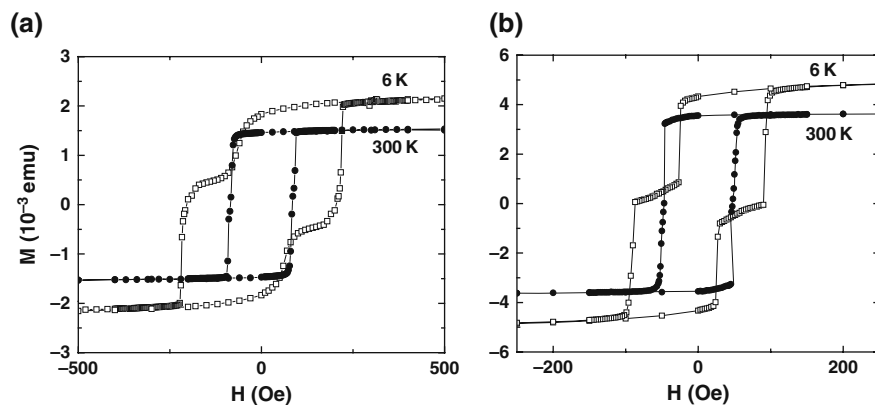


Fig. 17.10 Hysteresis loops for (a) 80 nm CrO_2 /3 nm SnO_2 /60 nm CrO_2 trilayer; (b) 160 nm CrO_2 /3 nm RuO_2 /140 nm CrO_2 trilayer measured at 6 and 300 K

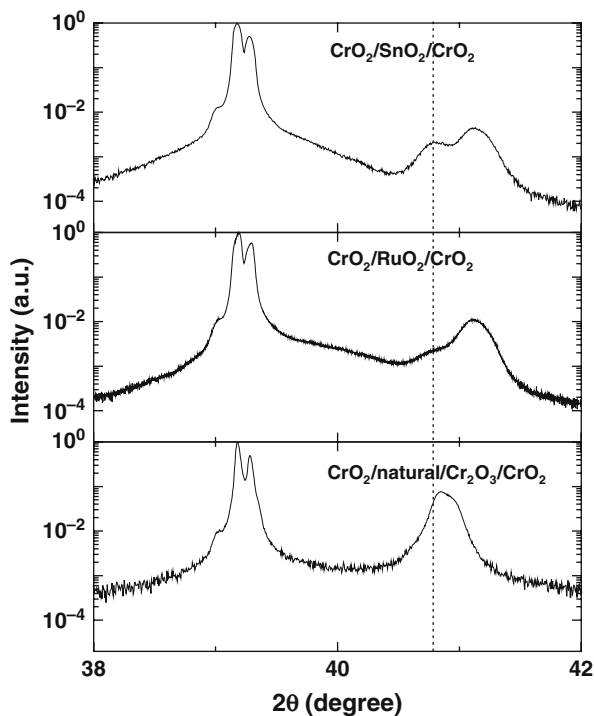


Fig. 17.11 XRD of epitaxial trilayers with thin SnO_2 , RuO_2 , and Cr_2O_3 spacer layers sandwiched between two magnetic CrO_2 layers. All the barrier layers are in the thickness range of 2–3 nm. Dashed line indicates the bulk CrO_2 (200) peak position

observed in the more interesting fully epitaxial CrO₂ heterostructures using SnO₂ and RuO₂ spacer layers.

17.4.1 Epitaxial SnO₂ Barrier Layer

Despite a large difference in the lattice parameters, epitaxial SnO₂ ($a = b = 0.4737$ nm, $c = 0.3185$ nm; lattice mismatch with CrO₂ being 7.2 and 9.2%, respectively) layers can be deposited on top of CrO₂ in a separate CVD step. The epitaxy has been confirmed using both TEM and off-axis XRD measurements [23]. We have used tin (IV) iodide as a precursor for the growth of thin SnO₂ layers. Figure 17.12 shows a cross-sectional Z-contrast image of the interface region for a 50 nm CrO₂/20 nm SnO₂ heterostructure. The two layers are well aligned and form an abrupt interface, with no evidence of an interfacial layer of Cr₂O₃, overall indicating that the SnO₂ layer is indeed highly crystalline and uniform.

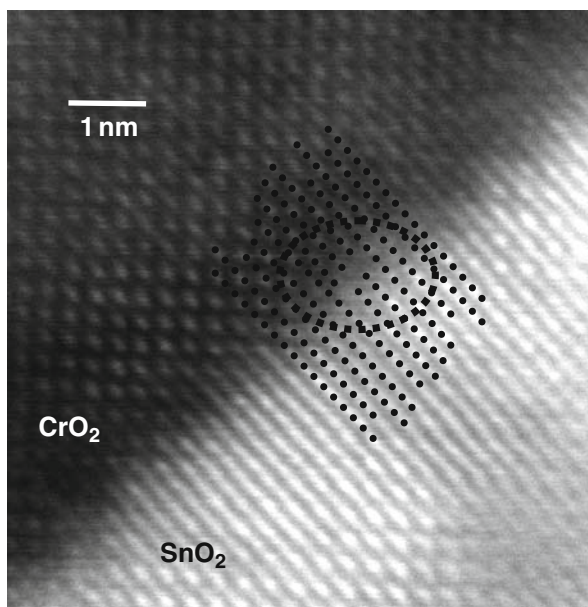


Fig. 17.12 High-resolution STEM image at the CrO₂/SnO₂ interface of a film deposited on a (100) TiO₂ substrate. One of the edge dislocation cores resulting from the lattice mismatch is highlighted. (Courtesy of M. Varela and S. J. Pennycook, Oak Ridge National Laboratory)

Amongst the three layers investigated, SnO₂ is the barrier material that has yielded the highest MR in the CrO₂-based systems. Using Co as counter-electrode, the MR is about 14% at 10 K for an optimized barrier layer thickness of about 1.7 nm. Figure 17.13b shows one example of such a MTJ. Since SnO₂ is a semiconductor, MTJs based on it exhibit some unusual behavior. Firstly, the

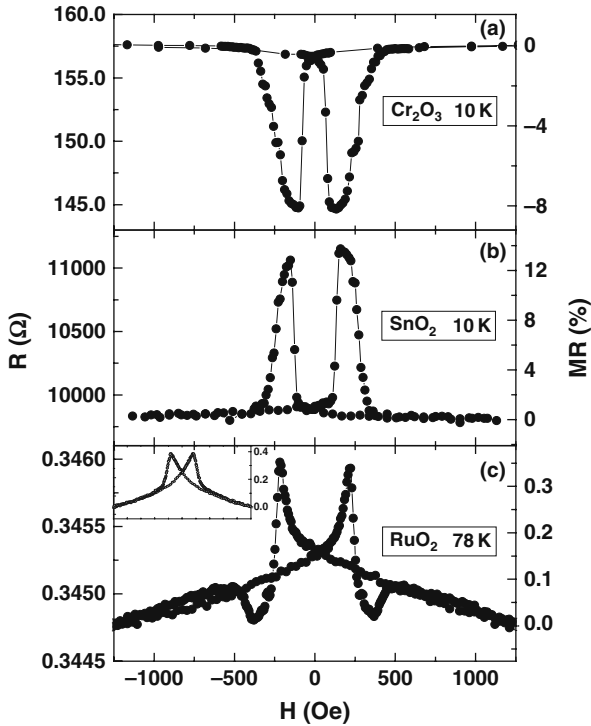


Fig. 17.13 Comparison of the MR loops in CrO_2 -Co-based junctions with natural Cr_2O_3 , epitaxial SnO_2 and RuO_2 as spacer layers, respectively. Junction areas are $35 \times 7 \mu\text{m}^2$. Inset in (c) shows the AMR signal measured from the CrO_2 bottom electrode

tunneling magnetoresistance (TMR) is negative for very small SnO_2 thicknesses, reverses sign at around 0.8 nm, and then peaks for a barrier thickness of 1.7 nm. This behavior is shown in Fig. 17.14. As the SnO_2 thickness is reduced, the chemical bonding at the top interface shifts from being predominantly Co- SnO_2 to being mostly Co- Cr_2O_3 . For small SnO_2 thicknesses, the tunneling is dominated by the negatively polarized d -like electrons due to $sd\sigma$ bonding, whereas for larger thicknesses positively polarized s -like electrons dominate because of $ss\sigma$ bonding. The increase of the TMR is correlated with the exponential increase of the junction RA product, consistent with an elastic tunneling process. As the barrier thickness is increased further, a cross-over into the diffusive regime is evidenced.

In this case, the hopping mechanism dominates, and the TMR decreases with increasing SnO_2 thickness. Interestingly, the RA value also decreases as the barrier thickness increases. A rapid drop in the SnO_2 resistivity with film thickness has been reported for as-grown epitaxial SnO_2 films using CVD [24]. This is dependent on the deposition method used for the growth of SnO_2 . In an oxygen environment at elevated temperatures, thinner CVD-grown SnO_2 films are closer to being stoichiometric, while thicker films tend to develop more oxygen vacancies.

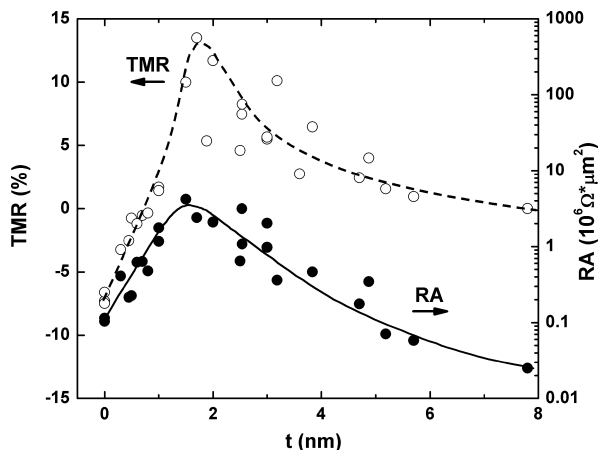


Fig. 17.14 Thickness dependence of TMR and junction RA at 10 K and 1 mV bias voltage; the dashed and solid lines are for visual guidance

From the results, we can estimate the concentration of oxygen vacancies in the barrier layer. For this, we assume the existence of two parallel conduction channels – a ballistic tunneling channel and a diffusive channel. When the direct conduction becomes equal to the tunneling conductance, a cross-over in the RA value is observed. Assuming that at the cross-over point the conductances of the two channels are equal, we can estimate the barrier resistivity at 10 K to be about $6 \times 10^5 \Omega\text{-cm}$. For the 8 nm barrier, which is sufficiently thick that direct conduction dominates, the barrier resistivity is estimated to be only $3 \times 10^2 \Omega\text{-cm}$. The large decrease of the SnO₂ resistivity is a signature of the dramatic increase in the concentration of oxygen vacancies in the thicker SnO₂ films, as well as the associated decrease in the carrier mobility [25]. Even so, using an approximate mobility value of $7 \text{ cm}^2/\text{V}\cdot\text{s}$ [26], we estimate a carrier concentration of only $3 \times 10^{15} \text{ cm}^{-3}$ for the 8 nm barrier at 10 K, and the estimated oxygen vacancy (assuming each O vacancy contributes two charge carriers) is below 0.03 ppm. If the spin coherence can be maintained in the direct conduction pathway, the MR should not change significantly with the emergence of this conduction channel. However, because of large spin-orbit coupling, the Sn atoms ($Z = 50$) are strong spin scattering centers, and the spin diffusion length in SnO₂ is only about 4 nm as estimated from the decay rate of the MR.

Figure 17.15 shows the bias-dependence results for one of the SnO₂-based MTJ. A clear signature of defect mediated tunneling is inferred from the data. Firstly, the samples exhibit a rapid drop in TMR with applied bias voltage, which points to the existence of spin-flip scattering resulting from impurities in the barrier [27]. Two sources of impurities are possible – Cr ions and oxygen vacancies. The former is a consequence of the intermixing at the SnO₂/CrO₂ interfaces, and the latter has been theoretically predicted and experimentally observed in SnO₂, resulting in its semiconducting properties [28]. Secondly, a clear TMR reversal with applied bias voltage is observed [29,30,31]. Unlike previous findings [32,33,34], the TMR

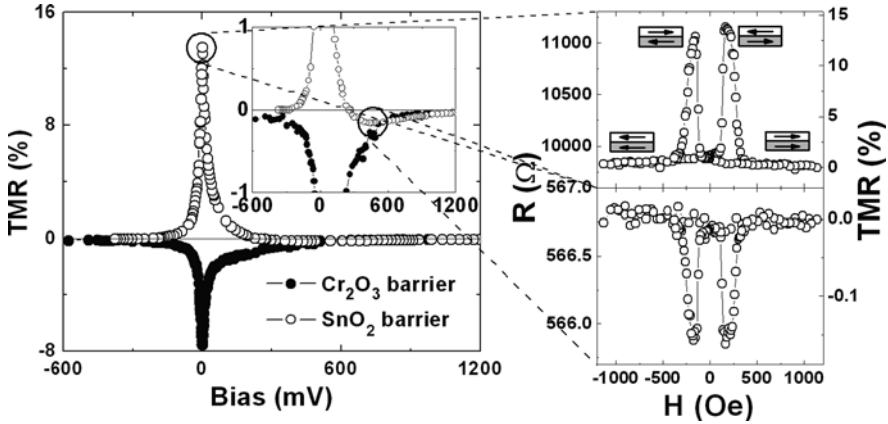


Fig. 17.15 Comparison of bias dependence for $\text{Cr}_2\text{O}_2/\text{Co}$ junctions with 2 nm SnO_2 barriers (white) and natural Cr_2O_3 barriers (black), inset shows the zoomed-in region. The magnetoresistance of the SnO_2 sample at 1 and 450 mV bias values are shown on the right. $T = 10$ K

reversal with bias cannot be attributed to the DOS peak in the Co 3d minority bands at about 400 mV bias [33, 34], since that would imply a negative TMR at zero bias and a positive TMR at high-bias values. Based on the model proposed by Tsymbal et al. [29,30,31], we attribute the observed TMR reversal at higher bias voltages (250–400 mV depending on the barrier thickness, Fig. 17.15) to the existence of impurity levels within the barrier.

Figure 17.16 illustrates the tunneling spectra for an MTJ with a 2.5 nm SnO_2 barrier sandwiched between two epitaxial CrO_2 layers. The nonlinear I – V characteristics provide evidence of tunneling transport. However, the large temperature dependence of the conductance indicates that the tunneling is dominated by multistep hopping instead of direct tunneling. Surprisingly, no MR has been observed in these MTJs. On the other hand, a sample prepared in the same run, but with Co as the top electrode, showed finite TMR at 10 K (Fig. 17.13b). The results are puzzling, and we believe part of the problem is in the rough/intermixed interfaces in the all-heteroepitaxial structures. The deposition of the second CrO_2 layer is performed at an elevated temperature, which may introduce additional spin scattering centers at the interfaces and also inside the barrier layer itself. High-resolution microscopy images of the top interface in these epitaxial heterostructures are needed in order to identify the influence of deposition of the top layer.

17.4.2 Epitaxial RuO_2 Barrier Layer

Epitaxial RuO_2 thin films can also be deposited on TiO_2 and CrO_2 using CVD methods [15, 35]. The lattice parameters of RuO_2 ($a = b = 0.4499$ nm and $c = 0.3107$ nm) provide a better lattice match with CrO_2 in the two in-plane directions (1.8 and 5.0%, respectively) than with SnO_2 . For the growth of RuO_2 , we have

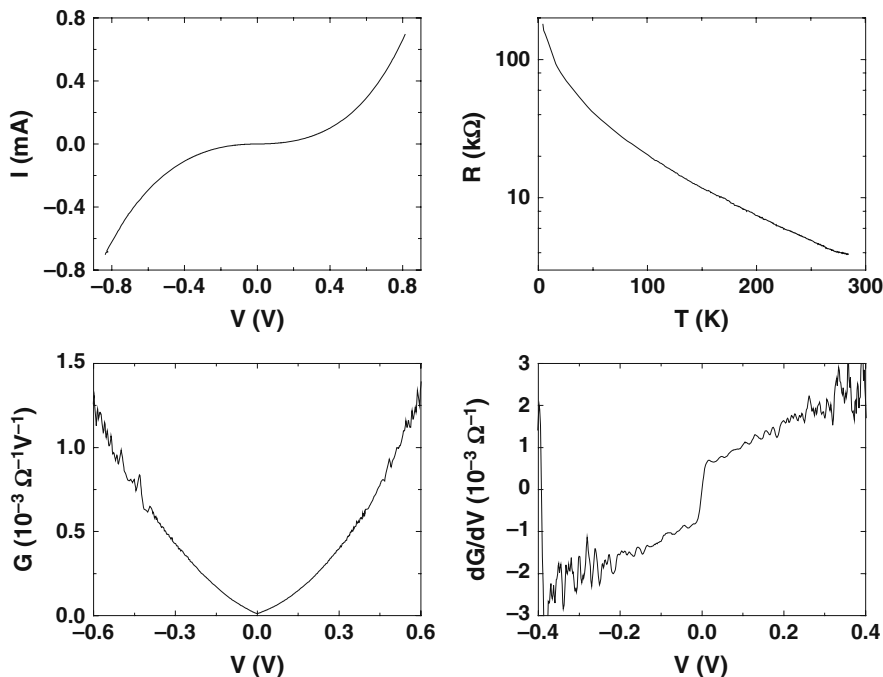


Fig. 17.16 Tunneling spectroscopy measurements for a 100 nm CrO₂/2.5 nm SnO₂/200 nm CrO₂ MTJ. The junction area is $35 \times 7 \mu\text{m}^2$, and the measurement temperature $T = 10 \text{ K}$

used tris(2,2,6,6-tetramethyl-3,5-heptanedionato) ruthenium(III) (Ru(TMHD)₃) as a precursor. RuO₂ exhibits good metallic behavior, with room temperature resistivity of $\sim 40 \mu\Omega\text{-cm}$, and can thus be used as a spacer layer in GMR structures. CrO₂ – RuO₂ – CrO₂ should be an “ideal” spintronic system based on electronic structure. For parallel alignment of the magnetizations of the two CrO₂ layers, the resistance should be extremely small because of the close majority band matching between CrO₂ and RuO₂. For anti-parallel alignment, however, the resistance should be extremely high, giving $\sim 100\%$ magnetoresistance for the ideal case.

The detailed structural and electrical properties of CVD-deposited RuO₂ thin films are provided in [15]. Using CrO₃ as a precursor for the CrO₂ growth, and Ru(TMHD)₃ for depositing RuO₂, we have the advantage that the entire structure can be grown under process conditions compatible with the growth and stability of CrO₂. However, although both films can be grown under similar conditions, it is still necessary to stop the growth after each layer and exchange the precursors to grow the next layer. This is because both of the precursors are solids at room temperature, and there is no convenient scheme for switching from one to the other in situ using our setup.

As the TEM micrograph in Fig. 17.17 shows, the RuO₂ spacer forms a continuous spacer layer in the heterostructure, but the RuO₂/CrO₂ interfaces are quite rough and intermixed. Surprisingly, we find that that despite stopping the growth

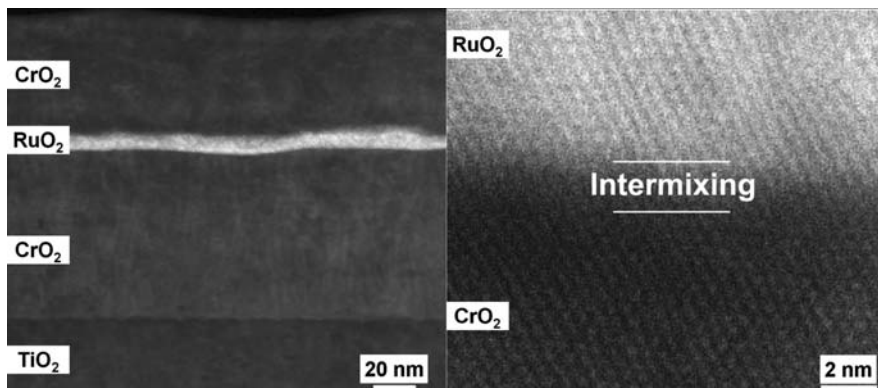


Fig. 17.17 HRTEM of a $\text{CrO}_2/\text{RuO}_2/\text{CrO}_2$ heteroepitaxial structure. The *right side figure* shows a high-magnification image of the interface intermixed region (adapted from Ref. [35])

and exchanging precursors after the CrO_2 deposition, the typical Cr_2O_3 natural barrier on the CrO_2 surfaces is absent after the RuO_2 deposition (similar to that of $\text{CrO}_2 - \text{SnO}_2$ discussed previously). This yields a highly conductive interface that has a resistance at least four orders of magnitude lower than if the Cr_2O_3 were present. The high-resolution TEM (shown as an inset in Fig. 17.17) and electron diffraction pattern at and around the $\text{CrO}_2/\text{RuO}_2$ interface reveals a highly intermixed region ~ 2 nm wide, with a lattice parameter between those of CrO_2 and RuO_2 . In our interpretation, this intermixed region results from the transformation of a Cr_2O_3 surface layer formed after CrO_2 deposition (but before RuO_2 deposition) into the rutile structure upon RuO_2 deposition, giving a $\text{CrO}_2/\text{RuO}_2$ mixture.

So far, we have observed very limited MR in these heteroepitaxial structures (Fig. 17.13c). At least part of the reason for the low MR might be from poor magnetic ordering and spin alignment at the mixed $\text{CrO}_2/\text{RuO}_2$ (001) interface. Preliminary first principles calculations suggest that non-collinear spins resulting from interface mixing may play a role. In these calculations, we find that the moments of the Cr atoms prefer to align at an angle of $\sim 150^\circ$, while the Ru atoms develop a small moment that aligns opposite to that of the sum of two Cr atoms [36]. Such non-collinear spin arrangements, which will depend on the details of the Cr and Ru occupation of the disordered rutile structure, are expected to cause mixing of the spin channels, drastically reducing the GMR effect.

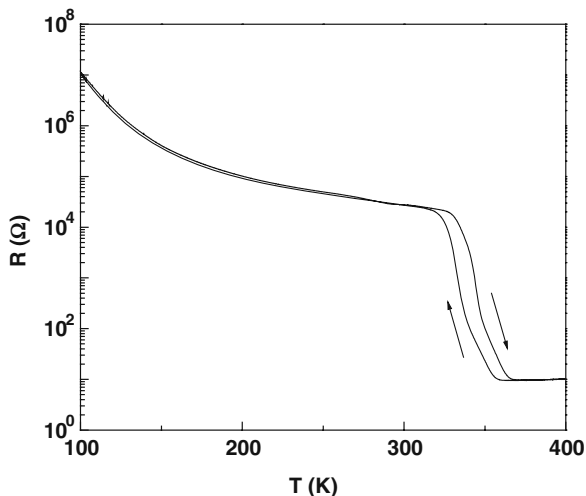
17.4.3 VO_2 Barrier Layer

VO_2 is yet another rutile oxide that has been investigated extensively, primarily for its unique metal–insulator transition occurring at around 340 K resulting in dramatic change in electrical resistivity. Because of the large change in the resistance of the spacer layer at the transition temperature, a change in the magneto-transport

characteristics from TMR to CPP-GMR would be expected in CrO₂ – VO₂ – CrO₂ heterostructures. This may involve both changes in the MR magnitude as well as its bias dependence, and could lead to novel effects to be exploited for new applications for storage and memory devices.

Chemical vapor deposition can be used to grow VO₂ thin films at relatively low temperatures [37]. We have used vanadium (III) acetylacetonate as a precursor for the growth of VO₂ films. Above the transition temperature, VO₂ has a rutile structure ($a = b = 0.4556$ nm, $c = 0.2859$ nm), which matches fairly well with CrO₂ (3.1 and –2.0%). Below the transition temperature, VO₂ has a monoclinic structure ($a = 0.5743$, $b = 0.4517$, $c = 0.5375$, and $\beta = 122.6^\circ$). Figure 17.18 shows the M–I transition in an as-deposited epitaxial VO₂ film (~100 nm thick) on (100) TiO₂ substrate. The high quality of the film is confirmed by the sharpness of the transition and the associated hysteretic behavior. Vanadium has a number of stable oxidization states, and different phase(s) of vanadium oxide (VO, V₂O₃, VO₂, V₂O₅) can be stabilized in thin film form, particularly when they are very thin. XPS result shows that a 2–3 nm thick VO_x film deposited on top of a CrO₂ film is primarily V₂O₅ (Fig. 17.19), instead of the desired VO₂ phase. Indeed, preliminary measurements on MTJs fabricated using such a VO_x barrier with Co counter-electrode did not show any evidence of an M–I transition above room temperature. The TMR in these junctions is negative, similar to that observed with a natural Cr₂O₃ barrier.

Fig. 17.18 Metal–insulator transition in an epitaxial VO₂ film (~100 nm)



17.4.4 TiO₂ Barrier Layer

TiO₂ is the most common rutile structure oxide. The name rutile comes from the mineral composed mainly of TiO₂. The lattice parameter of rutile TiO₂ are $a = b = 0.4594$ nm, $c = 0.2958$ nm, providing a good match with CrO₂ (3.9 and 1.4%).

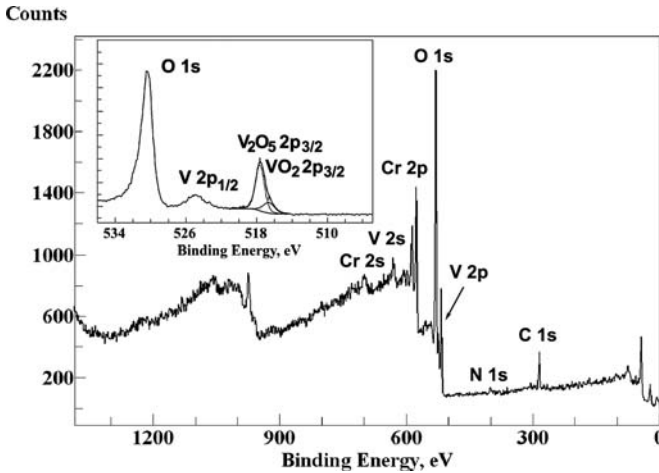


Fig. 17.19 XPS result for a thin VO_x film deposited on top of a CrO_2 film. Inset shows the O 1s and V 2p spectra. Peakfit of the V 2p_{3/2} line suggest the presence of VO_2 (23%) and V_2O_5 (77%) states

Indeed, as a substrate material, rutile TiO_2 provides an excellent template for the epitaxial growth of CrO_2 films as discussed earlier. We have used titanium(IV) isopropoxide as a precursor for the growth of TiO_2 films. Although rutile TiO_2 is the most stable and abundant phase of TiO_2 , the primary challenge is to stabilize TiO_2 in its rutile structure at low enough temperatures on top of CrO_2 since the latter readily decomposes at temperatures much higher than 400°C (see next section). At lower temperatures, the anatase and brookite phases of TiO_2 are formed, and they can be converted to the rutile phase only at temperatures above 750°C . Direct deposition of rutile TiO_2 films using CVD at temperatures as low as 490°C has been reported [38]. With plasma enhancement, it is possible to reduce the temperatures even lower [39]. However, using standard CVD, we have thus far succeeded in only growing the anatase phase of TiO_2 at temperatures compatible with the stability of CrO_2 . To the best of our knowledge, there have been no other reports in the literature on the growth and transport measurements of heteroepitaxial $\text{CrO}_2/\text{TiO}_2$ -based MTJs.

17.4.5 Cr_2O_3 Barrier Layer

Cr_2O_3 , an antiferromagnetic insulator ($T_N = 307\text{ K}$), is the most stable phase in the Cr oxide family. The formation of the different phases of Cr oxide by CVD is dependent on the deposition temperature, background pressure, and lattice mismatch with the substrate [40]. The air-exposed surface of an as-grown CrO_2 film tends to be reduced to Cr_2O_3 forming a native insulating layer. This insulating layer can be utilized as a tunneling barrier. From the STEM and EELS data shown in Fig. 17.20, the thickness of the barrier is estimated to be $\sim 2\text{ nm}$. An example of the TMR measured in a $\text{CrO}_2/\text{natural barrier}/\text{Co}$ tunnel junction is shown in Fig. 17.12a, and the first results on such junctions were reported in [41]. One striking feature of the natural

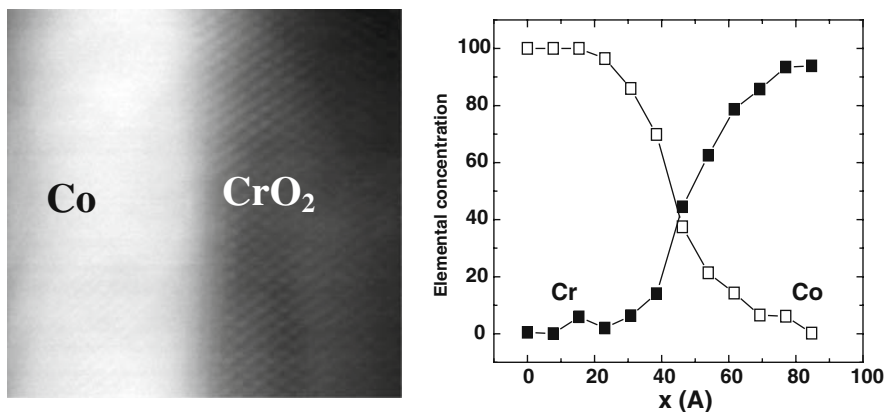


Fig. 17.20 STEM image and EELS line scan data for a Co/natural barrier/CrO₂ stack. The interface chemical width, which includes the natural barrier, is about 2 nm. (Courtesy of M. Varela and S. J. Pennycook, Oak Ridge National Laboratory)

barrier-based MTJs is the inverse sign of the TMR, which has been attributed to the dominance of *d*-like tunneling electrons [23]. The thickness of the Cr₂O₃ can be controllably increased by thermally annealing the CrO₂ films. The transverse susceptibility results on CrO₂ films that have been partially converted to Cr₂O₃, by annealing in an oxygen environment at 450°C for different lengths of time, have been reported in [42]. Figure 17.21a shows the XRD pattern for a 200 nm CrO₂ film after thermal annealing. Clearly the CrO₂ peak intensity decreases with increasing anneal time, with the emergence of the Cr₂O₃ (110) and (006) product peaks. The corresponding magnetic hysteresis loops of the samples are shown in Fig. 17.21b, confirming the decrease in magnetization with increasing anneal time.

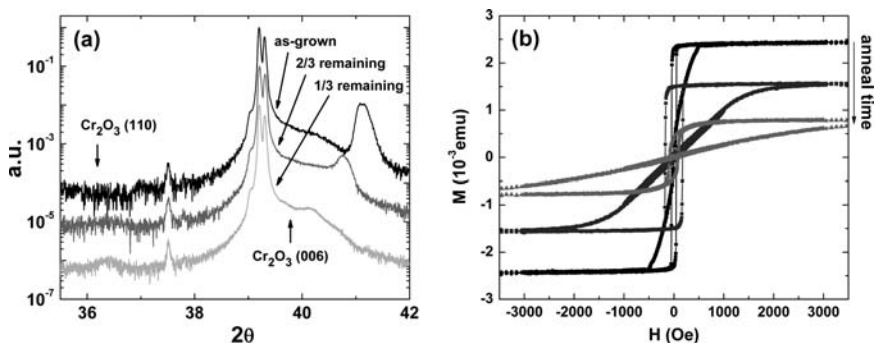


Fig. 17.21 (a) XRD for CrO₂ films partially decomposed into Cr₂O₃. The starting CrO₂ film thickness is around 200 nm, and the curves are systematically shifted upwards by a decade for clarity. (b) Hysteresis loops for the samples with increasing anneal time

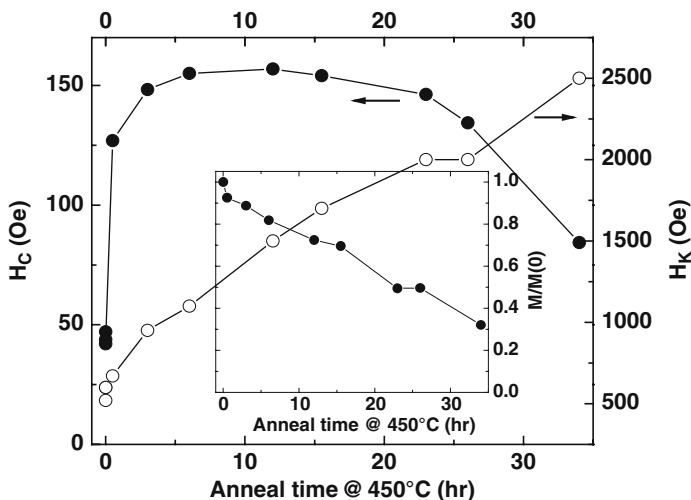


Fig. 17.22 Variations in the coercive and anisotropy fields for thermally decomposed $\text{CrO}_2 - \text{Cr}_2\text{O}_3$ bilayer structures. Inset shows the decrease of the saturation moment with increasing anneal

Large changes in the coercive and anisotropy fields are observed in these $\text{CrO}_2 - \text{Cr}_2\text{O}_3$ bilayer structures. The anisotropy field, H_K , increases monotonically with increasing thickness of Cr_2O_3 , while the coercivity, H_C , exhibits an initial sharp increase and then decreases slowly with further annealing (Fig. 17.22). The dramatic changes in the film magnetic properties indicate the presence of exchange interactions between the AFM Cr_2O_3 and FM CrO_2 . However, the exchange bias in such an FM-AFM system is quite small. From the exchange bias measured for a 100 nm CrO_2 film that is 3/4th decomposed into Cr_2O_3 , the exchange energy is estimated to be only ~ 0.028 erg/cm² at 6 K, and the exchange field further drops to about 1/3rd its initial value after cycling through saturation ten times (the training effect). From the decrease in the magnetic moment with anneal time (Fig. 17.22 inset), the formation rate of Cr_2O_3 from CrO_2 decomposition is estimated to be about 4 nm/h. The TMR measured in junctions with thicker Cr_2O_3 barriers formed by annealing still remains negative, and the junction resistance increases slowly. For example, for a Cr_2O_3 layer thickness of 10 nm, the junction resistance is measured to be only 10 times higher than that for a natural barrier of 2 nm thickness. Furthermore, the junction resistance is strongly temperature dependent. These results suggest that the Cr_2O_3 layer has a high concentration of defects, and the conduction through such a barrier most likely involves multistep hopping instead of direct tunneling.

Acknowledgments Most of the work reviewed in this chapter has been carried out by the authors over a period of several years in collaboration with a number of other colleagues. We express our gratitude to all the collaborators for their contributions, support, and help. In particular, we would like to acknowledge Alexander Anguelouch, William Butler, Chia-Ling Chien, Supratik Guha, Srikanth Hariharan, Patrick LeClair, Xin-Wei Li, Stephen Pennycook, Maria Varela, and Gang Xiao.

References

1. K. Schwarz, *J. Phys. F: Met. Phys.* **16**, L211 (1986).
2. S. P. Lewis, P. B. Allen, and T. Sasaki, *Phys. Rev. B* **55**, 10 253 (1996).
3. M. A. Korotin, V. I. Anisimov, D. I. Khomskii, and G. A. Sawatzky, *Phys. Rev. Lett.* **80**, 4305 (1998).
4. R. J. Soulen, J. M. Byers, M. S. Osofsky, B. Nadgorny, T. Ambrose, S. F. Cheng, P. R. Broussard, C. T. Tanaka, J. Nowak, J. S. Moodera, A. Barry, and J. M. D. Coey, *Science* **282**, 85 (1998).
5. Y. Ji, G. J. Strijkers, F. Y. Yang, C. L. Chien, J. M. Byers, A. Anguelouch, G. Xiao, and A. Gupta, *Phys. Rev. Lett.* **86**, 5585 (2001).
6. A. Anguelouch, A. Gupta, G. Xiao, D. W. Abraham, Y. Ji, S. Ingvarsson, and C. L. Chien, *Phys. Rev. B* **64**, 180408R (2001).
7. S. Ishibashi, T. Namikawa, and M. Satou, *Mater. Res. Bull.* **14**, 51 (1979).
8. X. W. Li, A. Gupta, and G. Xiao, *Appl. Phys. Lett.* **75**, 713 (1999).
9. K. Suzuki and P. M. Tedrow, *Solid State Comm.* **107**, 583 (1998).
10. A. Gupta, X. W. Li, S. Guha, and G. Xiao, *Appl. Phys. Lett.* **75**, 2996 (1999).
11. G. X. Miao, G. Xiao, and A. Gupta, *Phys. Stat. Sol. A* **203**, 1513 (2006).
12. J. W. Matthews and A. E. Blakeslee, *J. Cryst. Growth* **27**, 118 (1974).
13. T. Suzuki, Y. Nishi, and M. Fujimoto, *Philos. Mag. A* **79**, 2461 (1999).
14. S. H. Oh, C. G. Park, *J. Appl. Phys.* **95**, 4691 (2004).
15. G. X. Miao, A. Gupta, G. Xiao, and A. Anguelouch, *Thin Solid Films* **478**, 159 (2004).
16. D. S. Rodbell, *J. Phys. Soc. Jpn.* **21**, 1224 (1966).
17. G. X. Miao, G. Xiao, and A. Gupta, *Phys. Rev. B* **71**, 094418 (2005).
18. B. D. Cullity, *Introduction to Magnetic Materials* (Addison-Wesley, London, 1972).
19. J. W. Matthews, *J. Vac. Sci. Technol.* **12**, 126 (1975).
20. S. H. Oh and C. G. Park, *J. Appl. Phys.* **95**, 4691 (2004).
21. Y. Konishi, M. Kasai, M. Izuma, M. Kawasaki, and Y. Tokura, *Mater. Sci. Eng. B* **56**, 158 (1998).
22. Y. Yamamoto, K. Nakajima, T. Ohsawa, Y. Matsumoto, and H. Koinuma, *Jpn. J. Appl. Phys.* **44**, L511 (2005).
23. G. X. Miao, P. LeClair, A. Gupta, G. Xiao, M. Varela, and S. Pennycook, *Appl. Phys. Lett.* **89**, 022511 (2007).
24. A. Rosental, A. Tarre, A. Gerst, J. Sundqvist, A. Harsta, A. Aidla, J. Aarik, V. Sammelselg, and T. Uustare, *Sens. Actu. B* **93**, 552 (2003).
25. C. G. Fonstad and R. H. Rediker, *J. Appl. Phys.* **42**, 2911 (1971).
26. J. E. Dominguez, L. Fu, and X. Q. Pan, *Appl. Phys. Lett.* **81**, 5168 (2002).
27. J. S. Moodera, J. Nassar, and G. Mathon, *Annu. Rev. Mater. Sci.* **29**, 381 (1999).
28. A. Kilic, A. Zunger, *Phys. Rev. Lett.* **88**, 095501-1 (2002), and references therein.
29. E. Y. Tsymlal, D. G. Pettifor, *Phys. Rev. B* **64**, 212401-1 (2001).
30. E. Y. Tsymlal, A. Sokolov, I. F. Sabirianov, and B. Doudin, *Phys. Rev. Lett.* **90**, 186602-1 (2003).
31. L. Sheng, D. Y. Xing, and D. N. Sheng, *Phys. Rev. B* **69**, 132414 (2004).
32. M. Sharma, S. X. Wang, and J. H. Nickel, *Phys. Rev. Lett.* **82**, 616 (1999).
33. J. M. Teresa, A. Barthelemy, A. Fert, J. P. Contour, R. Lyonnet, F. Montaigne, P. Seneor, and A. Vaures, *Phys. Rev. Lett.* **82**, 4288 (1999).
34. J. M. Teresa, A. Barthelemy, A. Fert, J. P. Contour, F. Montaigne, and P. Seneor, *Science* **286**, 507 (1999).
35. G. X. Miao, A. Gupta, H. Sims, W. H. Butler, S. Ghosh, and G. Xiao, *J. Appl. Phys.* **97**, 10C924 (2005).
36. G. X. Miao, Ph. D. thesis (Brown University, Providence, RI, 2006).
37. M. B. Sahana, G. N. Subbanna, and S. A. Shivashankar, *J. Appl. Phys.* **92**, 6495 (2002).
38. M. Schuisky and A. Harsta, *J. Phys. IV* **9**, 381 (1999).

39. Y. Kumashiro, A. Kinoshita, Y. Takaoka, and S. Murasawa, *J. Ceramic Soc. Jpn.* **101**, 514 (1993).
40. P. G. Ivanov, S. M. Watts, and D. M. Lind, *J. Appl. Phys.* **89**, 1035 (2001).
41. A. Gupta, X. W. Li, and G. Xiao, *Appl. Phys. Lett.* **78**, 1894 (2001).
42. N. A. Frey, S. Srinath, H. Srikanth, M. Varela, S. Pennycook, G. X. Miao, and A. Gupta, *Phys. Rev. B* **74**, 024420 (2006).

Chapter 18

FePt and Related Nanoparticles

J.W. Harrell, Shishou Kang, David E. Nikles, Gregory B. Thompson, Shifan Shi, and Chandan Srivastava

Abstract This chapter reviews recent studies of chemically synthesized FePt and related nanoparticles. Various methods for synthesizing the nanoparticles and controlling their shape are described. Thermal effects in nanoparticles near the superparamagnetic limit are discussed. Some of the methods for reducing sintered grain growth during annealing to obtain the $L1_0$ phase are described, including the use of a hard shell, annealing in a salt matrix, and flash annealing. The effect of metal additives on the ordering temperature and on sintered grain growth is discussed. Additive Ag and Au significantly not only reduce the ordering temperature but also the grain growth temperature in close-packed 3-D arrays. Preliminary experiments that show additive Ag also reduces the ordering temperature when sintering is prevented. Easy-axis alignment of $L1_0$ FePt nanoparticles can be achieved by drying a nanoparticle dispersion in a magnetic field, and the effect of thermal fluctuations on orientation is discussed. Large particle-to-particle compositional distributions in chemically synthesized FePt nanoparticles have been measured. A method of determining the anisotropy distribution is described. Theoretical and experimental works showing the size effect on chemical ordering of FePt nanoparticles are discussed.

Acronyms

Nano-EDS	nano-beam energy dispersed spectrometry
HRTEM	high-resolution transmission electron microscopy
SCA	strong coupling approximation
TEM	transmission electron microscopy
TEOS	tetraethoxysilane
THF	tetrahydrofuran
TMA	tetramethylammonium
VSM	vibrating sample magnetometer

J.W. Harrell (✉)

Department of Physics & Center for Materials for Information Technology, The University of Alabama, Tuscaloosa, AL 35487-0209, USA
e-mail: iharrell@bama.ua.edu

XRD	X-ray diffraction
ZFC	zero-field-cooled

18.1 Introduction

There has been a dramatic increase in the interest in magnetic nanoparticles in recent years. Much of this interest has been a result of the development of new chemical and physical processes for synthesizing nanoparticles. Magnetic nanoparticles are finding applications in areas such as information storage, biomedicine, and catalysis. The properties of magnetic particles change significantly from the bulk as their size approaches the nanometer scale. Surface effects play a major role as the surface to volume ratio increases, and thermal effects become important at small volumes. The development of the chemistry for synthesizing highly monodisperse FePt nanoparticles by Sun et al. [53] and the potential for these nanoparticles for ultra-high density data storage has been a major factor in the surge in interest in chemically synthesized nanoparticles for a variety of applications. The interest in FePt is primarily because of its high magnetocrystalline anisotropy, K_u , in the ordered $L1_0$ phase. The equilibrium order–disorder temperature for bulk FePt is $\sim 1,300^\circ\text{C}$. Above this temperature, the equilibrium phase is A1 (disordered fcc), while below this temperature, the equilibrium phase is $L1_0$ (ordered fct). Typical low temperature syntheses yield nanoparticles in the A1 phase, and high-temperature annealing is required to obtain the $L1_0$ phase. Annealing close-packed arrays of nanoparticles leads to sintered grain growth, which is usually undesirable. In addition to grain growth, there are other materials issues involved in obtaining high-anisotropy $L1_0$ FePt nanoparticles with uniform properties, such as compositional distributions, easy-axis orientation, and size effects on chemical ordering.

This chapter is mostly a review of some of research done in addressing these issues. It draws heavily from the research of the authors and their associates. Sections 18.2 and 18.3 discuss thermal effects. Chemical methods for synthesizing FePt and related nanoparticles are reviewed in Section 18.4. Section 18.5 discusses some techniques for reducing sintered grain growth during annealing. Easy-axis orientation of arrays of nanoparticles is discussed in Section 18.7. Sections 18.8 and 18.9 discuss particle-to-particle compositional distributions and the resulting anisotropy distribution. Finally, the effect of particle size on chemical ordering is discussed in Section 18.10.

18.2 Thermal Effects in Magnetic Nanoparticles

The magnetization of all materials is temperature dependent, even well below the Curie temperature where the saturation magnetization and anisotropy become zero. In bulk materials, this temperature dependence may be negligible; however, it can be significant in nanoparticles. For particles with first-order uniaxial anisotropy, the energy in an applied field is given by

$$E = KV \sin^2 \theta - M_s H \cos(\theta - \alpha), \quad (18.1)$$

where θ and α are the directions of the magnetization and applied field with respect to the easy axis. In zero field, the magnetization fluctuates between the energy minima at $\theta = 0^\circ$ and 180° , which are separated by an energy barrier $\Delta E_0 = K_u V$. Thus, if the magnetization is initially in one direction, its average value will decay in time as

$$M(t) = M_0 \exp(-t/\tau), \quad (18.2)$$

where

$$\frac{1}{\tau} = 2f_0 \exp\left(-\frac{K_u V}{k_B T}\right). \quad (18.3)$$

and where f_0 is the attempt frequency, k_B Boltzmann's constant, and T the temperature. f_0 depends on the anisotropy constant and ranges from about 10^9 to 10^{11} Hz. In bulk materials, $K_u V \gg k_B T$ and the magnetization is stable for long times. When $K_u V$ is sufficiently small, then τ becomes comparable to the measuring time, and the decay of M becomes significant. The particle is then said to be superparamagnetic. The temperature above which particles are superparamagnetic is the blocking temperature.

For example, if $t = 100$ s (typical for VSM), then $K_u V \sim 27 k_B T$, assuming $f_0 = 10^{10}$ Hz. For a spherical hcp Co particle with $K_u = 4 \times 10^6$ erg/cc, the superparamagnetic diameter at room temperature is $d = 8$ nm. On the other hand, for $L1_0$ FePt with $K_u = 6 \times 10^7$ erg/cc, $d = 3.3$ nm. Surface effects can impact the actual superparamagnetic size. This would be especially true for FePt since about 1/3 of the atoms of a 3.3 nm FePt particle are on the surface.

For superparamagnetic particles for which $K_u V \ll M_s H$, the magnetization curve will have zero coercivity and can be described by the Langevin function, $M = M_s L(\mu H/k_B T)$, where $\mu = M_s V$ is the moment of the particle. The magnetization curve can be fit to give μ , from which the particle size can be determined if M_s is known (or vice versa).

Thermally activated reversal can also be important for particles above the superparamagnetic limit and can give rise to time-dependent coercivity. The remanent coercivity, H_{cr} , is the reverse field required, after applying a saturation field, to give zero remanent magnetization. For a reverse field applied along the easy axis, the energy barrier is

$$\Delta E = K_u V \left(1 - \frac{H}{H_k}\right)^2, \quad (18.4)$$

where $H_k = 2 K_u/M_s$. The magnetization will decay in time as

$$M = M_s(2e^{-t/\tau} - 1), \tag{18.5}$$

where now

$$\frac{1}{\tau} = f_0 \exp\left(-\frac{\Delta E}{k_B T}\right) \tag{18.6}$$

The remanent coercivity is obtained from the above equations by setting $M = 0$ and solving for H to give the ‘‘Sharrock equation’’ [44],

$$H_{cr} = H_0 \left\{ 1 - \left[\frac{k_B T}{K_u V} \ln(f_0 t) \right]^n \right\}, \tag{18.7}$$

where $H_0 = H_k$ and $n = 1/2$. In Eq. (18.7) a factor of $\ln(2)$ is absorbed in the definition of f_0 ($f_0/\ln(2) \rightarrow f_0$). When the applied field is at an angle α with respect to the easy axis, then the field dependence of the energy barrier can be approximated by a power relationship similar to Eq. (18.4), but with exponent q varying from 2 at $\alpha = 0^\circ$ to 1.43 at $\alpha = 45^\circ$ [16]. This leads to a Sharrock relationship similar to that above but with $n = 1/q$ and with H_0 varying from H_k at $\alpha = 0^\circ$ to $0.5H_k$ at $\alpha = 45^\circ$. For a random distribution of easy axes, a Sharrock type relationship still applies with $H_0 \approx 0.5H_k$ and $n \approx 2/3$.

Thermally activated reversal also leads to a dependence of the coercivity, H_c , on the sweep rate used in measuring the hysteresis loop. The coercivity is given by a Sharrock-type equation with an effective wait time that depends on the sweep rate [38]. Time-dependent coercivity measurements (H_{cr} or H_c) can be fit to determine the zero-field energy barrier, $K_u V$, and the short-time coercivity, H_0 .

The graph below (Fig. 18.1) shows the remanent coercivity calculated from Sharrock’s equation for randomly oriented high anisotropy spherical nanoparticles as a

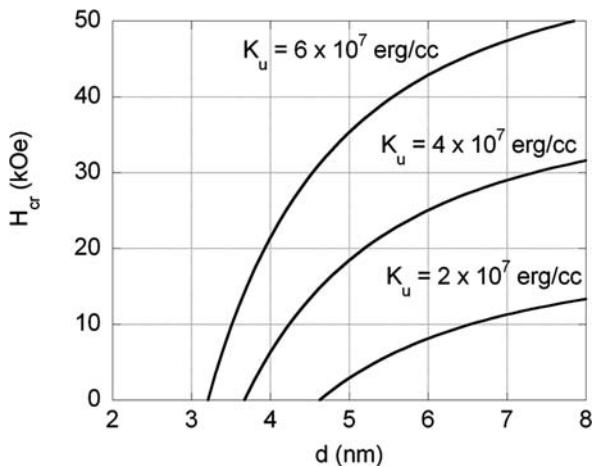


Fig. 18.1 Calculated remanent coercivity as a function of particle size and anisotropy for $t = 100$ s and $T = 300$ K

function of size and anisotropy, assuming a measuring time of 100 s, a temperature of 300 K, and $f_0 = 10^{10}$ Hz. For nanoparticles near the superparamagnetic limit, the coercivity will be strongly time dependent. As a consequence, distributions in size and anisotropy will have a strong effect on the coercivity.

18.3 Magnetic Recording and the Superparamagnetic Limit

Current hard disk media consists of granular hcp Co-based thin film alloys. In conventional perpendicular recording, each bit consists of tens of grains magnetized perpendicular or nearly perpendicular to the film. Areal storage densities for hard disk media have increased by about 8 orders of magnitude since the first commercial drive was introduced in 1956. This increase in density has required a corresponding decrease in grain size in order to maintain adequate signal to noise. Grain diameters are now below 10 nm and further significant reductions in grain size of Co-based media are limited by thermal fluctuations. For 10-year stability, the zero-field energy barrier of the grains must be of the order $K_u V \sim 50 k_B T$ or larger, depending on the coercivity distribution. The smallest allowable grain size of Co-based media is limited by the achievable anisotropy. Because of its very high anisotropy, $L1_0$ FePt is a choice material for the next-generation media. The bulk value of K_u is about $6.6\text{--}10 \times 10^7$ erg/cc [63]. This would allow stable cylindrical grains with diameters as small as ~ 3 nm.

FePt media, however, cannot be written with the fields achievable with conventional heads, since $H_k \sim 116$ kOe in the fully ordered phase. Heat-assisted magnetic recording, in which the grains are heated during writing to reduce H_k , is a possible write scheme that is under investigation [34]. Another possibility is to reduce the write field by using anisotropy-graded grains with one end consisting of a low anisotropy material and the other end consisting of $L1_0$ FePt [49].

Much attention has been given to potential media consisting of chemically synthesized FePt nanoparticles [51]. The size distribution of chemically synthesized nanoparticles can be much narrower than the grains in sputtered films. Self-assembly allows the further possibility of producing patterned media in which each particle would represent a single bit. There are considerable problems, however, associated with fabricating suitable nanoparticle media, as was previously mentioned.

18.4 Chemical Synthesis and Shape Control of FePt and Related Nanoparticles

18.4.1 Synthesis

Chemical reduction techniques have been extensively investigated in the preparation of nanoparticles because these methods can be implemented under simple and mild

conditions and can be used to prepare nanoparticles on a large scale. The chemical reduction of transition metal salts in the presence of stabilizing agents to generate zero-valent metal colloids in aqueous or organic media was first published in 1857 by M. Faraday [13]. This approach has become one of the most common and powerful synthetic methods in this field. Turkevich et al. proposed a mechanism for the stepwise formation of nanoparticles based on nucleation, growth, and agglomeration, which in essence is still valid [56]. In the embryonic stage of the nucleation, the metal salt is reduced to give zero-valent metal atoms. These can collide in solution with other metal ions, metal atoms, or clusters to form a stable metal particle. Within mainly the past decade, a series of chemical reductants has been utilized for the preparation of noble metal nanoparticles, which include H_2 [1], $NaBH_4$ [5], N_2H_4 [6], NH_2OH [4], $(CH_3)_2NHBH_3$ [55], ethanol [37], ethylene glycol [62], citrate [35], formamide [15], formaldehyde [33], Tollen's reagents [67], ascorbic acid [21], and polyaniline [59]. The reducing ability of a reductant plays an important role in the preparation of the metal nanoparticles by the reduction reaction. A strong reductant will result in fast nucleation of particles, and a weak reductant will result in slow reaction for the formation of metal atoms, which may be favorable for the size and morphology control of the metal nanoparticles obtained.

To make magnetic FePt nanoparticles, initially, S. Sun et al. combine two specially selected iron pentacarbonyl and platinum acetylacetonate chemicals in a heated solution with reducing reagent and surfactants [53]. As the platinum acetylacetonate ($Pt(acac)_2$) molecule reacts with the reducing reagent, the platinum separates from its organic segment. At high temperature, the iron pentacarbonyl decomposes into iron and carbon monoxide. Thus, the zero-valent iron and platinum coalesce into spherical nanoparticles of an iron–platinum alloy each containing several thousand atoms in about equal elemental proportions. Surrounding the growing nanoparticles is a flexible layer of surfactant molecules (oleic acid and oleyl amine) that keep the particles physically and magnetically independent as they self-assemble into a regular array as the solvent is allowed to evaporate. Experiments show that oleic acid bonds to the FePt nanoparticles in both monodentate and bidentate forms, while the oleylamine bonds to the FePt nanoparticles through electron donation from the nitrogen atom of the NH_2 group [46]. The typical synthetic procedure is as follows: Under the nitrogen atmosphere, platinum acetylacetonate (0.5 mmol), 1,2-hexadecanediol (1.5 mmol), and dioctyl ether or phenyl ether (20 ml) are mixed in a three-neck flask and heated to $100^\circ C$. After the chemical powders are completely dissolved, oleic acid (0.5 mmol), oleylamine (0.5 mmol), and $Fe(CO)_5$ (1 mmol) are injected into this solution via syringes. Then the mixture is heated to reflux and held for 30 min. The heat source is then removed, and the reaction mixture is allowed to cool to room temperature. The inert gas protected system can be opened to ambient environment at this point. The black product is precipitated by adding ethanol (~ 40 ml) and separated by centrifugation. The yellow-brown supernatant is discarded. The black precipitate is dispersed in hexane (~ 25 ml) in the presence of oleic acid (~ 0.05 ml) and oleylamine (~ 0.05 ml) and precipitated out by adding ethanol (~ 20 ml) and centrifuging. The product is dispersed in hexane (~ 20 ml), centrifuged to remove any unsolved precipitation,

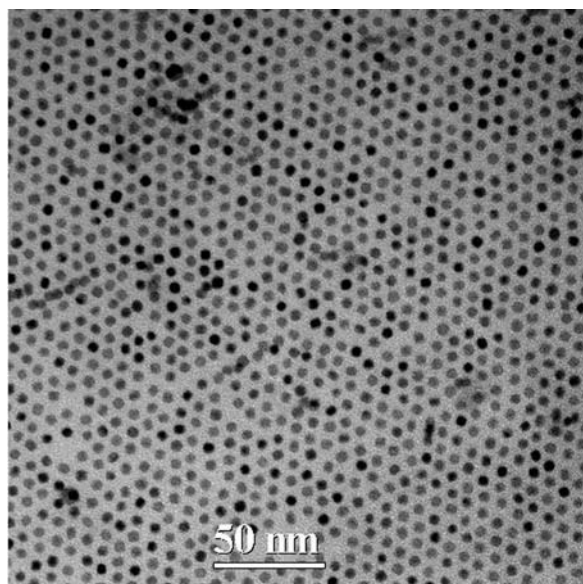
and again precipitated out by adding ethanol (~15 ml) and centrifuging. The final black materials, FePt nanoparticles, are redispersed in hexane and stored under N_2 .

However, for future practical applications, several issues regarding this decomposition/reduction process need to be addressed. $Fe(CO)_5$ is a well-known toxic chemical and thermally unstable, gradually releasing CO and Fe at ambient temperature. In order to make FePt nanoparticles with stoichiometric structures, an excess of $Fe(CO)_5$ is needed during the high-temperature condition of the synthesis and the chemical composition of the final particles is hard to control. A correlation between the molar ratio of $Fe(CO)_5/Pt(acac)_2$ and FePt composition always needs to be established in order to determine the final composition of the particles [51]. Metal borohydrides are a class of well-known reducing agents for the reduction of various metal salts to metal nanoparticles [14]. Specifically, a borohydride derivative, such as superhydride ($LiBEt_3H$), is easily dissolved in organic ether solvent, facilitating homogeneous reduction of metal salt and formation of metal nanoparticles [52]. For controlled synthesis of FePt nanoparticles, S. Sun et al. combined iron chloride and platinum acetylacetonate chemicals in a heated solution through the superhydride co-reduction process [50]. The main advantage of using $LiBEt_3H$ over other metal borohydrides is that the final material, FePt nanoparticles, is easy to wash, clean, and separate from the by-product. Since the Li^+ cation from the superhydride will combine with the Cl^- or $acac^-$ anion from $FeCl_2$ and $Pt(acac)_2$ to form Li salt, it can be easily washed off from the product with alcohol. After reduction, BEt_3 is usually released from the mixture. The BEt_3 may be removed from the system under nitrogen, or it can combine with other organic ether/amine/alcohol species in the mixture to form organic adducts, leading to pure FePt nanoparticles. The typical co-reduction procedure for making $Fe_{50}Pt_{50}$ nanoparticles is as follows: $Pt(acac)_2$ (0.5 mmol), $FeCl_2 \cdot 4H_2O$ (0.50 mmol), 1,2-hexadecanediol (2 mmol), and phenyl ether (25 mL) are added under nitrogen atmosphere into a flask equipped with a N_2 in/outlet, septa rubber, and a thermometer. The mixture is heated to $100^\circ C$ for 10 min to dissolve the precursors. Then, oleic acid (0.5 mmol) and oleyl amine (0.5 mmol) are added, and the mixture is continuously heated to $200^\circ C$ for 20 min to remove water and other low boiling point impurities. $LiBEt_3H$ (1 M tetrahydrofuran (THF) solution, 2.5 mL) is slowly dropped into the mixture over a duration of ~2 min. The black dispersion is stirred at $200^\circ C$ for 5 min under N_2 to remove low boiling solvent (THF). Then the mixture is heated to reflux at $263^\circ C$ for 20 min. Finally, the heating source is removed, and the black reaction mixture is cooled to room temperature. The FePt nanoparticles are cleaned and separated from the by-product with ethanol. The final FePt nanoparticles are re-dispersed in hexane solvent for further use. The initial molar ratio of two metal precursors is carried over to the final product, and the composition of the final FePt is easily tuned. By analogy, a number of additives, such as Cu [54], Ag [23], Au [28], Pd [24], Cr [48], Sb [66], Mn [57], and Co [8], have been successfully introduced into FePt nanoparticles by modifications of these original techniques with proper metal additive reagents.

In order to make thin films for characterization, the FePt nanoparticles are well dispersed in a 50/50 mixture of hexane and octane with small amounts of oleic acid

and oleyl amine and dropped on a solid substrate, such as glass or Si wafer. The typical size of the substrate is about 1 by 2 cm. The solvent is allowed to evaporate slowly (~ 5 min) at room temperature. During the drying process, the FePt nanoparticles self-assemble into regular arrays. The thickness of the films can be roughly controlled by the amount of drops. For transmission electron microscopy (TEM) observation, a drop ($0.5 \mu\text{L}$) of a dilute FePt nanoparticles dispersion (1 mg/mL) is deposited on a carbon-coated copper grid or SiN membrane. Figure 18.2 shows some typical TEM images of self-assembled monodispersed FePt nanoparticles.

Fig. 18.2 TEM of self-assembled chemically synthesized FePt nanoparticles



18.4.2 Shape Control

Controlled synthesis of FePt nanoparticles with tunable size and different morphology was reported by Sun's group with a one-pot reaction method [7]. They changed the molar ratio of stabilizers to $\text{Pt}(\text{acac})_2$ and heating conditions to control the size of particles in the range of 3–9 nm. More importantly, this one-pot reaction could also lead to particles with either spherical or cubic shape. Slow evaporation of the particle dispersion yielded nanoparticle superlattices on solid substrates. The nanoparticles within the superlattice exhibited preferred alignment of crystal orientations correlated with their shape (See Fig. 18.3). With this texture control, the shaped nanoparticles could become useful building blocks for the construction of functional nanostructures. Generally, the spherical FePt particles exhibit a 3D random distribution of the crystalline orientation, while the cubic FePt nanoparticles prefer a (200) texture. By controlling the stabilizers ratio and replacing oleic acid

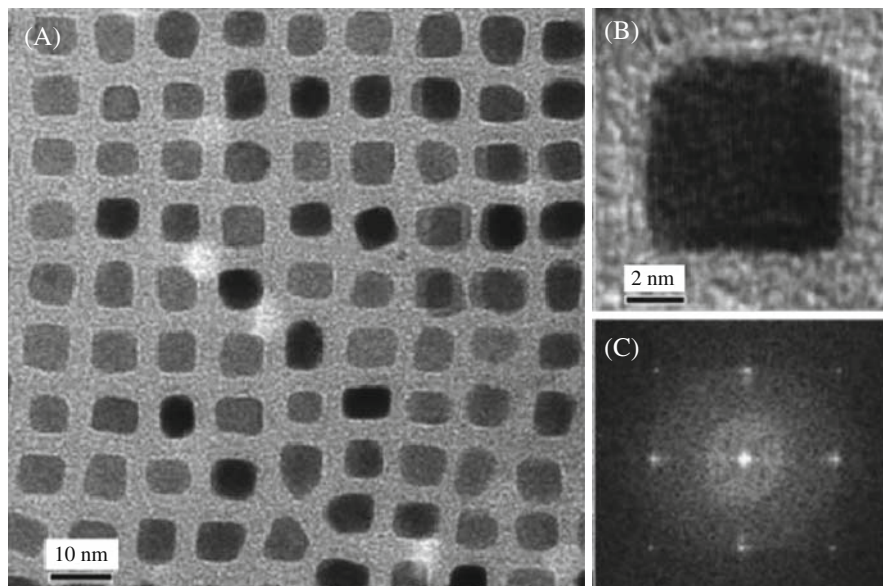


Fig. 18.3 Chemically synthesized FePt nanoparticles with cubic shape. (Reprinted with permission from *Journal of American Chemical Society*. © 2006 American Chemical Society)

with octadecene, FePt nanowires and nanorods can be formed [58]. Length control of the FePt nanowires/nanorods was realized by tuning the volume ratio of oleyl amine/octadecene, with lengths ranging from over 200 nm for nanowires down to 20 nm for nanorods. For example, FePt nanowires with a length of over 200 nm were made when only oleyl amine was used as both surfactant and solvent, while an oleyl amine/octadecene ratio of 3:1 gave FePt nanowires of length 100 nm, and a 1:1 volume ratio of oleyl amine/octadecene led to FePt nanorods of length 20 nm (See Fig. 18.4).

18.5 Prevention of Sintered Grain Growth During Annealing

As previously discussed, the procedures for synthesizing monodispersed FePt nanoparticles yield particles with the fcc phase. Partially ordered FePt nanoparticles can be synthesized using high-temperature solvents; however, the synthesized nanoparticles have a distribution of sizes and degree of chemical order, and the average anisotropy is not high. In order to achieve high-anisotropy monodisperse nanoparticles, sintered grain growth must be inhibited during high-temperature annealing. In this section, three methods for inhibiting sintered grain growth are discussed – use of a hard shell, annealing in an inert matrix, and short-time annealing.

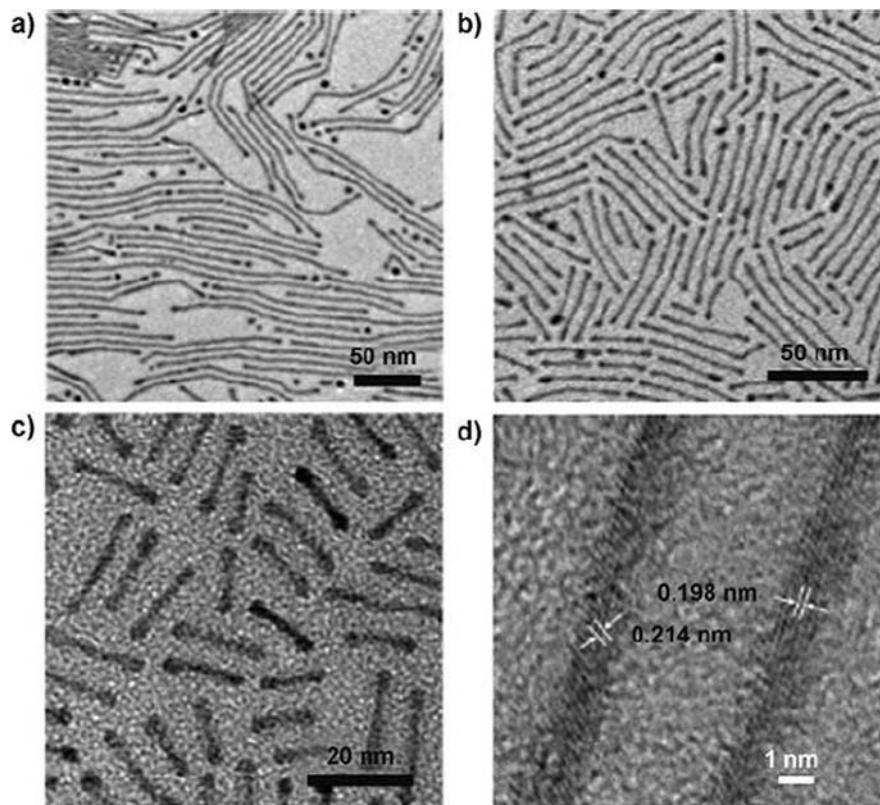


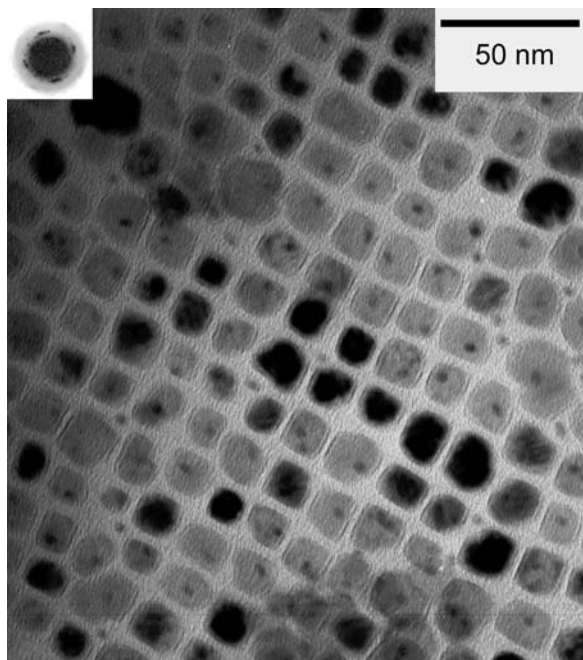
Fig. 18.4 Chemically synthesized FePt nanorods and nanowires. (Reprinted with permission from *Angewandte Chemie International Edition*. © 2007 Wiley-VCH Verlag GmbH & Co. KGaA)

18.5.1 FePt/MnO Core/Shell Nanoparticles

MnO has been used as a hard shell on FePt nanoparticles to prevent sintering during annealing [26]. The MnO shell was formed by adding 3–4 nm FePt nanoparticles to a solution containing an Mn source (manganese acetylacetonate ($\text{Mn}(\text{acac})_2$), a reducing agent (1,2-hexadecanediol), and surfactants (oleic acid, oleylamine), with benzyl ether as a solvent, and heating to reflux. The thickness and shape of the MnO shell (spherical or cubic) could be controlled by varying the ratio of the $\text{Mn}(\text{acac})_2$ and surfactants. Figure 18.5 shows a TEM image of FePt/MnO core/shell nanoparticles with a cubic shell. Most of the nanoparticles consist of a single 3–4 nm FePt nanoparticle inside a cubic MnO shell.

Annealing the core/shell nanoparticles at 600°C for 30 min resulted in the $L1_0$ phase with very little evidence of sintered grain growth of the core FePt nanoparticles, based on TEM, XRD, and magnetic measurements. One of the consequences of preventing grain growth is a distribution of anisotropies and coercivities. This is

Fig. 18.5 TEM of FePt/MnO core/shell nanoparticles with cubic shell. (Reprinted with permission from *Journal of American Chemical Society*. © 2006 American Chemical Society)



evident from the shape of the hysteresis loop and from a large ratio of the remanent to hysteresis coercivity. This distribution is thought to be a result of a particle-to-particle composition distribution. Anisotropy and composition distributions will be discussed in more detail in later sections.

Bulk MnO is antiferromagnetic below 122 K. Exchange bias was observed in the unannealed FePt/MnO nanoparticles by a shift in the hysteresis loop at 10 K after cooling in an applied magnetic field. The core-shell interaction also had the effect of enhancing the thermal stability at 10 K. Evidence for this was enhanced coercivity, saturation field, and blocking temperature determined from zero-field-cooled (ZFC) measurements. The core-shell interaction also appears to restore some of the particle moment that is lost in unannealed FePt nanoparticles with a surfactant coating.

18.5.2 FePt/SiO₂ Core/Shell Nanoparticles

There have been several reports of the synthesis of FePt/SiO₂ core/shell nanoparticles [2, 20, 30, 40, 42, 64, 65, 69]. Generally, the procedure is a sol-gel process involving the hydrolysis and condensation of tetra-ethoxysilane (TEOS) in a solution of NH₄OH to form a SiO₂ shell on the surface of pre-synthesized FePt nanoparticles. Figure 18.6 shows a TEM image of FePt/SiO₂ core/shell nanoparticles with

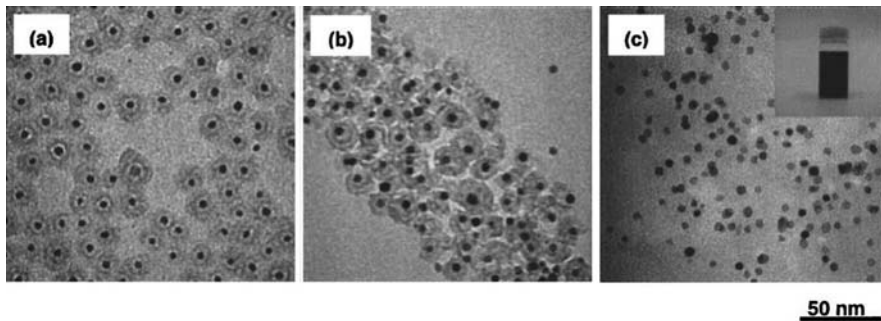


Fig. 18.6 FePt/SiO₂ nanoparticles (a) before and (b) after annealing at 900°C. (c) Annealed FePt nanoparticles after removal of SiO₂ shell. (Reprinted with permission from *Applied Physics Letters*. © 2005 American Institute of Physics)

an FePt core size of 6.5 nm synthesized by Yamamoto et al. [64]. Figure 18.6(a) shows the core/shell nanoparticles before annealing, and Fig. 18.6(b) shows the core/shell nanoparticles after annealing at 900°C, with no evidence of sintered grain growth of the FePt core nanoparticles. The SiO₂ could be removed by dissolving the core/shell nanoparticles in tetramethylammonium (TMA) hydroxide. The resulting FePt nanoparticles were dispersible in water (Fig. 18.6(c)), reportedly because of a charged surface. Yamamoto et al. also were able to get apparent easy-axis orientation of the nanoparticles by freezing a water dispersion of the SiO₂-free FePt nanoparticles in a magnetic field.

18.5.3 Salt Matrix Annealing

Liu and co-workers [12] have developed a simple procedure for annealing FePt nanoparticles in a NaCl matrix to prevent sintered grain growth. Finely ground NaCl is mixed with FePt in a solvent such as hexane. After evaporating the solvent, the mixture is furnace annealed in an inert atmosphere. The salt is then removed by dissolving in water. A key to minimizing sintered grain growth is to use small salt crystals ($\sim 20 \mu\text{m}$) and a large salt to FePt ratio (>100). Figure 18.7 shows TEM images of FePt nanoparticles with sizes from 2 to 15 nm before and after annealing in salt at 600°C. The images show no evidence of sintered grain growth.

Salt annealed FePt nanoparticles exhibit high coercivities indicating a high degree of chemical order. Liu et al. [31] measured the temperature dependence of the coercivity of salt-annealed 4-nm, 8-nm, and 15-nm nanoparticles. At room temperature, the 8-nm particles had the highest coercivity ($\sim 25 \text{ kOe}$), whereas at 4 K the 4-nm particles had the highest coercivity. This behavior is apparently related to the fact that the 4-nm particles were single crystalline, whereas the 8-nm and 15-nm particles were multicrystalline. Particles with multivariant c-axes are expected to have reduced average magnetocrystalline anisotropy relative to particles with a single c-axis [43].

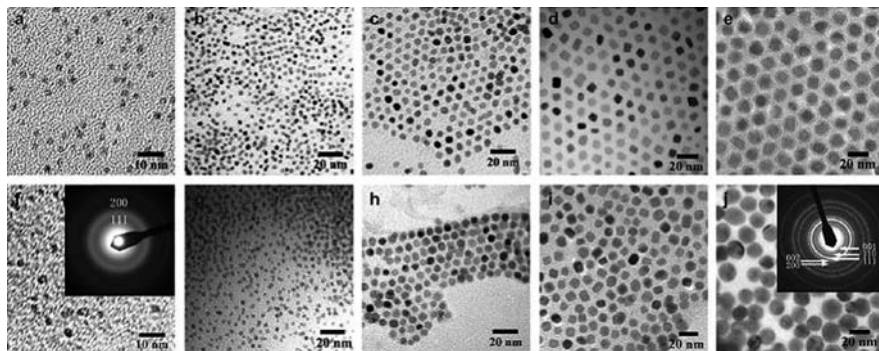


Fig. 18.7 TEM of as-made (*top*) and salt-annealed (*bottom*) FePt nanoparticles. Particle sizes for (a)–(e) are 2, 4, 6, 8, and 15 nm. (Reprinted with permission from *Advanced Materials*. © 2006 Wiley-VCH Verlag GmbH & Co. KGaA)

18.5.4 Flash Annealing

One possible method for reducing sintered grain growth is to anneal with millisecond temperature pulses. Chemical ordering involves diffusion of atoms over atomic dimensions, whereas sintered grain growth involves the breakdown of the surfactant coating, nanoparticle displacement, and atomic diffusion over nanometer distances. Although chemical ordering and sintered grain growth are correlated, these processes are expected to occur over different time and temperature regimes. Shi et al. [45] have carried out a series of annealing experiments in the millisecond regime using a high-density plasma arc lamp at Oak Ridge National Laboratory. The lamp could produce infrared pulses with pulse widths down to 20 ms.

Figure 18.8 shows the XRD spectrum of 3-nm FePt nanoparticles that were annealed with a series of five 250 ms pulses. The sample was spin-coated onto a

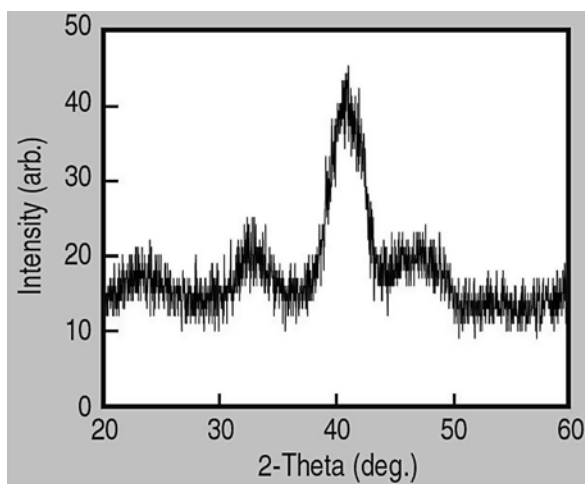


Fig. 18.8 XRD spectrum of spin-coated film of FePt nanoparticles annealed with 250 ms infrared pulse. (Reprinted with permission from *JOM*. © 2006 The Minerals, Metals & Materials Society)

silicon wafer and had a thickness of about 80 nm. The XRD spectrum shows well-defined (001) and (110) peaks corresponding to the $L1_0$ phase, and the width of the XRD peaks suggests very little sintered grain growth during annealing. The coercivity at 10 K was 5.6 kOe, which was much less than expected for the highly ordered phase. This relatively low H_c was attributed in part to a large distribution in anisotropies, which is expected for small nanoparticles that are annealed without sintered grain growth. Evidence for this distribution was a large ratio of remanent to hysteresis loop coercivity, which will be discussed in Section 18.9.

Large coercivities could be obtained by flash annealing thick nanoparticle films made by drop drying a particle dispersion on a substrate. However, grain growth was evident for these thick films. Also, flash annealing thick films caused sample damage due to rapid decomposition of the surfactant. Flash annealing is a potential method for obtaining phase transformation while minimizing sintered grain growth; however, finding optimum annealing conditions is challenging.

18.6 Effect of Metal Additives on Chemical Ordering and Sintered Grain Growth

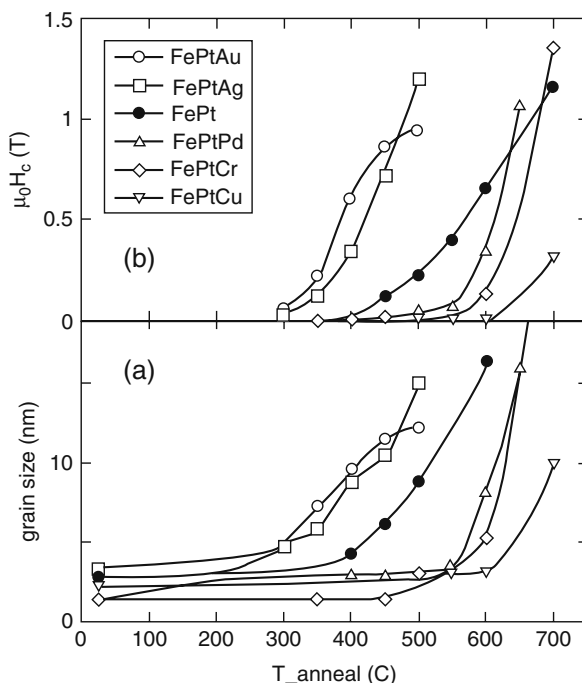
There have been a number of studies showing that metal additives such as Au, Ag, and Cu lower the ordering temperature in sputtered thin films of FePt [3, 9, 32, 36, 39]. This has motivated studies of the effect of various metal additives on chemical ordering in chemically synthesized FePt nanoparticles. Lowering the ordering temperature was seen as a possible way of reducing sintered grain growth.

Harrell and co-workers [18, 19, 22–24, 28, 29, 48, 54] synthesized a series of FePtX nanoparticles, where $X = \text{Au, Ag, Cu, Pd, and Cr}$. Furnace annealing experiments were done on samples that were drop dried on a silicon or glass substrate. Generally, the effect of the additives on the ordering temperature was found to depend on the type and amount of additive. Additive Au and Ag lowered the ordering temperature, leading to a maximum reduction of about 100–150°C. Evidence of weak ordering could be seen in the XRD spectra at an annealing temperature of 300°C. The largest reduction in ordering temperature was obtained for about 24 at.% Au and for about 15 at.% Ag. The reduction in the ordering temperature as seen by XRD was confirmed by a corresponding reduction in the temperature at which coercivity appeared in the annealed nanoparticles. The Au and Ag appear to be fully incorporated into the lattice in the as-made particles and expand the lattice relative to FePt. XRD spectra show that during annealing the additive Au and Ag segregate from the FePt nanoparticles and form aggregates. Although the exact reason why the additives reduce the ordering temperature is not known, it is reasonable to assume that lattice strain and diffusion of the additives from the nanoparticles facilitate ordering by enhancing the atomic mobility of the Fe and Pt atoms. In contrast to additive Au and Ag, additive Pd, Cr, and Cu were found to increase the ordering temperature [24, 48, 50, 54, 61]. In addition, these additives did not segregate during annealing. The effect of additive Cu in the nanoparticles is opposite to that

reported for sputtered films, where additive Cu significantly reduced the ordering temperature [32].

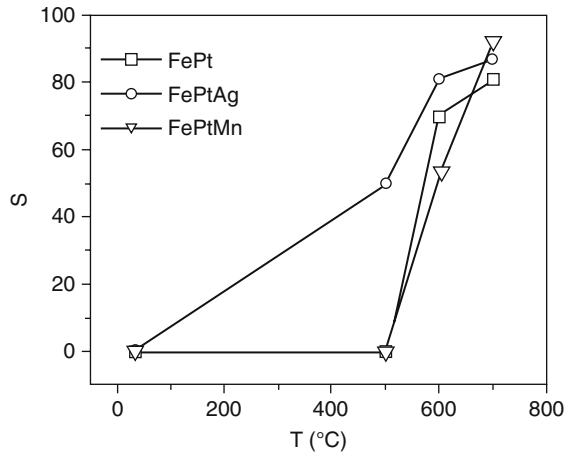
Although additive Au and Ag lower the ordering temperature in FePt nanoparticles, they also promote sintered grain growth [19]. Figure 18.9(a) shows the grain size as a function of annealing temperature for additive Au, Ag, Pd, Cr, Cu, and for no additive. The grain size was obtained from a Scherrer analysis of the (111) XRD diffraction peak. Figure 18.9(b) shows the coercivity as a function of annealing temperature for these same samples. A comparison of the two figures shows that there is a one-to-one correspondence between the effect of additives on the thresholds for chemical ordering (as inferred from coercivity) and grain growth. One can infer from these results that either chemical ordering promotes grain growth or grain growth promotes chemical ordering. The latter is more likely because of the possible effect of particle size and grain boundary diffusion on ordering.

Fig. 18.9 Grain size and coercivity as a function of annealing temperature for FePtX nanoparticles. (Reprinted with permission from *Scripta Materialia*. © 2005 Elsevier)



Because of grain growth, these experiments do not show the intrinsic effect of additives on chemical ordering. In order to study the intrinsic effect of additives, 4-nm $\text{Fe}_{55}\text{Pt}_{45}$, $\text{Fe}_{44}\text{Pt}_{41}\text{Ag}_{15}$, and $\text{Fe}_{45}\text{Pt}_{42}\text{Mn}_{13}$ nanoparticles have been annealed in a salt matrix, and the order parameter has been measured as a function of annealing temperature. The order parameter was determined from the relative integrated intensity of the (110) and (111) XRD diffraction peaks. The results, shown in Fig. 18.10, show that the order parameter for all particles is about the same (0.8–0.9) when annealed at 700°C; however, order develops at a lower annealing temperature for

Fig. 18.10 Order parameter versus salt-matrix annealing temperature for 4-nm FePt, FePtMn, and FePtAg nanoparticles



additive Ag than for Mn or no additive. Further studies are necessary to elucidate the intrinsic effect of additives since small differences in particle size can be important in the 4-nm size range.

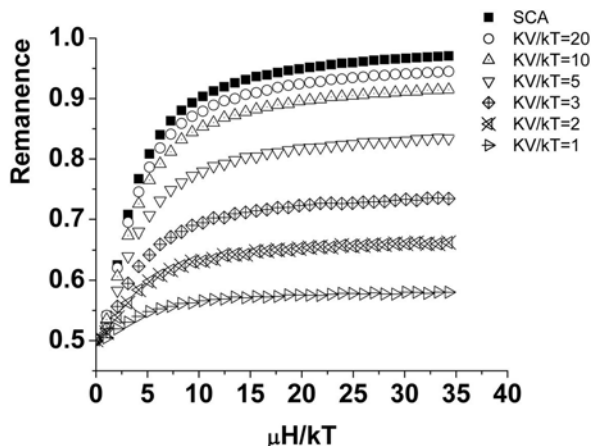
18.7 Easy-Axis Orientation

The magnetic response of a nanoparticle with uniaxial anisotropy, such as $L1_0$ FePt, depends strongly on the orientation of its easy axis with respect to an applied field. For magnetic media applications, it is important to have the easy axes of the nanoparticles aligned in the same direction. Self-assembled arrays of spherical $L1_0$ FePt nanoparticles formed by drying a dispersion of the nanoparticles will have nearly random orientations. One approach to achieve orientation is to dry a particle dispersion in a magnetic field, similar to what is done with magnetic tapes. Tape particles, however, are typically acicular in shape, and orientation is facilitated by shear forces during the coating. Also, tape particles are sufficiently large that thermal fluctuations are not important during the orientation process. Thermal fluctuations, however, can limit the field orientation of small nanoparticles.

18.7.1 Model of Easy-Axis Orientation

Harrell et al. [17] have modeled the thermal effect on the orientation of an array of non-interacting nanoparticles obtained by drying a dispersion of particles in a magnetic field. The orientation depends on the coupling of the moment to the applied field, which depends on $\mu H/k_B T$, and the coupling of the easy axis to the moment, which depends on $K_u V/k_B T$. Figure 18.11 shows the results of a Monte Carlo calculation of the normalized remanent magnetization as a function of $\mu H/k_B T$ for

Fig. 18.11 Monte Carlo calculation of the normalized remanent magnetization. (Reprinted with permission from *Applied Physics Letters*. © 2005 American Institute of Physics)

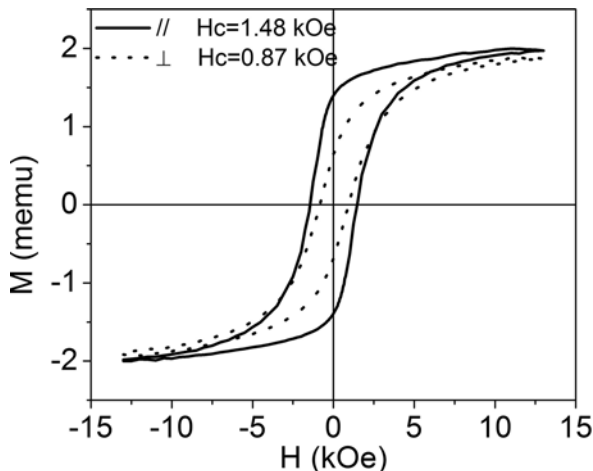


different values of $K_u V/k_B T$. Orientation increases with increasing both $\mu H/k_B T$ and $K_u V/k_B T$. It is interesting to note that significant orientation can be achieved even for superparamagnetic particles. The orientation for $K_u V/k_B T = 20$ is nearly the same as for infinite $K_u V/k_B T$ (strong coupling approximation, SCA). It should be pointed out, however, that the calculated remanence is what one would measure at $T = 0$ K. So even though “superparamagnetic” particles can in principle be well oriented, the remanence measured with a VSM at room temperature would be zero. The results show that high fields are required to achieve significant orientation in small particles. For example, for 5-nm FePt particles with very high thermal stability ratios (SCA case), a 1 kOe field would yield a remanence of 0.59, whereas a 10 kOe field would yield a remanence of 0.94. The orientation increases rapidly with particle diameter since $\mu \sim d^3$.

18.7.2 Easy-Axis Orientation Measurements

Kang et al. [25] measured the orientation of partially chemically ordered FePt nanoparticles that were dried in a magnetic field. FePt nanoparticles with diameter 6–7 nm and coercivity 1.3 kOe were synthesized using a high-temperature solvent. The particle dispersion was dropped onto a substrate and dried in a longitudinal field, and the remanence was measured as a function of the aligning field. The dependence of the remanence on aligning field was qualitatively similar to that shown in Fig. 18.11, although the value of the remanence was less than predicted. Figure 18.12 shows the hysteresis loops measured parallel and perpendicular to the aligning field for a field value of 20 kOe. The normalized remanence values are 0.72 and 0.33, and the coercivities are 1.48 kOe and 0.87 kOe in the easy and hard directions, indicating significant orientation. The easy direction remanence, however, is less than predicted. The discrepancy is believed to be due to interparticle interactions and to a distribution in particle size and anisotropy.

Fig. 18.12 Hysteresis curves measured for oriented FePt nanoparticles measured parallel and perpendicular to the aligning field. (Reprinted with permission from *Applied Physics Letters*. © 2005 American Institute of Physics)



Kang et al. [27] also studied the orientation of salt-annealed FePt nanoparticles which had a diameter of 8 nm and coercivity of about 30 kOe. The degree of orientation that could be achieved in thick films was much less than that obtained for the 6–7 nm particles with low coercivity. The reason is believed to be due to larger magnetic dipolar interactions, which increase roughly as d^3 . In-plane orientation of monolayer films was obtained based on the angular dependence of TEM diffraction rings; however, the extent of the orientation was not quantified. Monolayer films should be easier to orient than thick films since the dipolar interactions should be smaller in the monolayer films. Particles with nonspherical shape (e.g., cubic or cylindrical) could be easier to orient in a field if the c-axis is appropriately aligned with respect to the particle.

18.8 Composition Distribution

Although FePt nanoparticles can be synthesized with a narrow size distribution, there can be a substantial variation in the composition from particle to particle. Yu et al. [28] used field emission electron nano-beam energy dispersive spectrometry (nano-EDS) to measure the compositions of about 500 individual FePt nanoparticles. The nanoparticles were synthesized using the iron pentacarbonyl method of Sun et al. [53] and had an average particle size of 3 nm and average composition $\text{Fe}_{51}\text{Pt}_{49}$. They found that only about 29% of the $\text{Fe}_x\text{Pt}_{100-x}$ nanoparticles were within the composition range $40 < x < 60$. In the absence of sintered grain growth, such a compositional distribution can obviously give rise to a very large anisotropy distribution since most of the particles would have compositions outside the range for formation of the $L1_0$ phase. When sintered grain growth occurs during annealing, the compositional distribution is largely averaged out and significant chemical ordering can then occur.

Kang et al. [27] studied salt-annealed 8-nm FePt nanoparticles using high-resolution TEM (HRTEM) and nano-EDS, and a correlation was found between individual particle ordering and composition. Those particles with nearly equiatomic compositions were highly ordered while those that were strongly Fe or Pt rich were partially ordered. Figure 18.13 shows an HRTEM image of nanoparticles with composition $\text{Fe}_{51}\text{Pt}_{49}$ and $\text{Fe}_{65}\text{Pt}_{35}$. The nearly equiatomic particle on the left is a single crystal with lattice fringes consistent with the $\{001\}$ interplanar spacing of the $L1_0$ phase. The iron-rich particle on the right has two crystalline phases: one with lattice fringes consistent with the $L1_0$ $\{001\}$ spacing and the other with lattice fringes consistent with the A1 $\{002\}$ spacing.

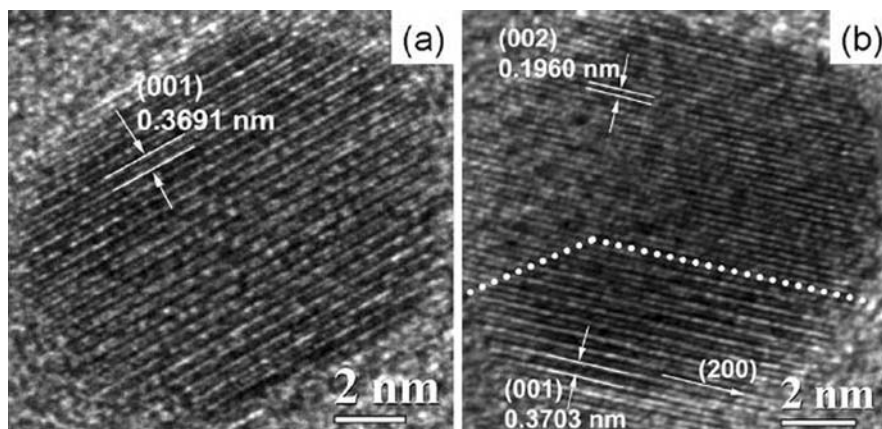


Fig. 18.13 HRTEM image of (a) equiatomic and (b) iron-rich FePt nanoparticles. (Reprinted with permission from *Journal of Applied Physics*. © 2007 American Institute of Physics)

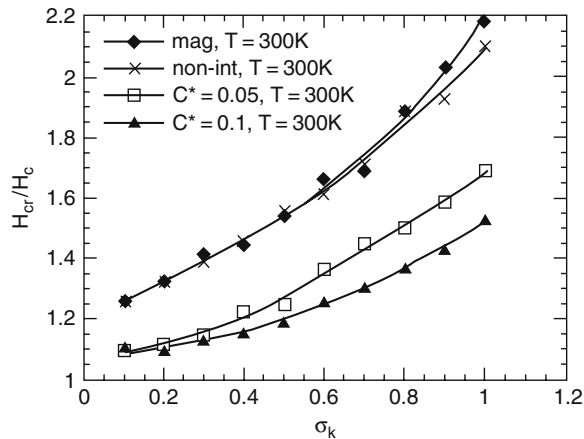
The reasons for the large composition distribution of chemically synthesized FePt nanoparticles are not fully understood. However, it is reasonable to ask if the distribution depends on the type of nanoparticle synthesis. Srivastava et al. [47] have compared the compositional distribution of 3-nm FePt nanoparticles synthesized by the decomposition of iron pentacarbonyl and the reduction of platinum acetylacetonate with 3-nm nanoparticles synthesized using the superhydride reduction of iron chloride and platinum acetylacetonate. Because of the volatility of iron pentacarbonyl, the latter method is known to be better for controlling the average composition of FePt. It was found that the nanoparticles synthesized by the superhydride reduction process had a more narrow composition distribution. Whether this difference is inherent in the two different methods and how the distribution depends on variabilities in the syntheses need further study. It was found, for example, that the composition distribution could be narrowed in the superhydride method by increasing the reflux time.

18.9 Anisotropy Distribution

The maximum achievable atomic order of FePt nanoparticles depends on composition. Thus, a compositional distribution will give a distribution in the magnetocrystalline anisotropy energy, K_u . A particle size distribution can also affect the anisotropy distribution since smaller particles are inherently more difficult to order. Wang et al. [60] developed a method for determining the anisotropy distribution from the ratio of the remanent coercivity, H_{cr} , to the hysteresis loop coercivity, H_c . For aligned, non-interacting Stoner–Wolffarth particles $H_{cr} = H_c$ in the absence of thermal effects. For randomly oriented easy axes, $H_{cr} = 1.1 H_c$ if there is no anisotropy distribution. However, the coercivity ratio H_{cr}/H_c will increase with increasing anisotropy distribution.

Wang et al. calculated the coercivity ratio as a function of anisotropy distribution. Figure 18.14 shows Monte Carlo calculations of the coercivity ratio at $T = 300$ K for an assembly of FePt nanoparticles with mean diameter 5.2 nm and mean anisotropy energy 4×10^7 erg/cc. If interparticle interactions and thermal effects are excluded, then the coercivity ratio increases linearly with the log-normal distribution width σ_K . Exchange interactions between nanoparticles (e.g., when sintered) will reduce the ratio, while dipolar interactions will increase the ratio. The effect of dipolar interactions in high-anisotropy particles such as $L1_0$ FePt is negligible but can be significant in lower anisotropy particles such as hcp Co. Thermal effects on the coercivity ratio can be eliminated by making low-temperature measurements or by comparing intrinsic, short-time coercivities obtained from time-dependent remanent and sweep-rate coercivity measurements.

Fig. 18.14 Calculated coercivity ratio at $T = 300$ K for FePt nanoparticles with mean diameter 5.2 nm and mean anisotropy constant 4×10^7 erg/cc. (Reprinted with permission from *Physical Review B*. © 2003 American Institute of Physics)

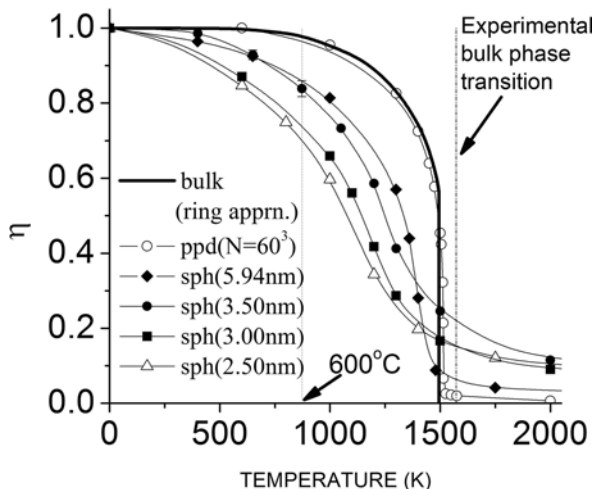


18.10 Size Effect on Chemical Ordering

There have been several experimental and theoretical studies which have suggested a size effect on chemical ordering of FePt nanoparticles. Chepulskii and co-workers [10, 11] have used first-principles methods to calculate the dependence of the

equilibrium $L1_0$ order parameter on temperature and particle size. The results are shown in Fig. 18.15. For bulk materials, the equilibrium order parameter changes discontinuously with increasing temperature, whereas in particles of finite size, the order parameter continuously decreases with increasing temperature. At any given temperature, the order parameter decreases with decreasing particle size. For example, at 700° , a typical annealing temperature for getting the $L1_0$ phase, the equilibrium order parameter for a 3.5-nm particle is 0.78.

Fig. 18.15 Calculated equilibrium order parameter for FePt nanoparticles as a function of temperature and particle size. (Reprinted with permission from *Physical Review B*. © 2005 American Institute of Physics)

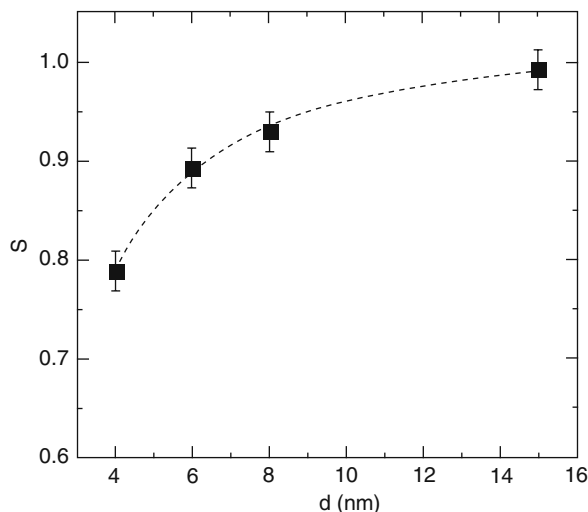


Rong et al. [41] have measured the order parameter of FePt nanoparticles that were annealed in a salt matrix at 700°C as a function of particle size. The results, shown in Fig. 18.16, are qualitatively similar to the calculations of Chepulskii et al. The order parameter decreases from about 0.99 for the 15-nm particles down to about 0.79 for the 4-nm particles. More recently, Liu et al. [31] have reported an order parameter of 0.62 for 3-nm particles.

18.11 Summary and Conclusions

Some recent studies of chemically synthesized FePt and related nanoparticles have been reviewed. Because of its high magnetocrystalline anisotropy in the ordered phase, chemically synthesized FePt nanoparticles have attracted great interest. Various chemical methods for making FePt and related nanoparticles have been described. The high anisotropy of $L1_0$ FePt allows thermally stable nanoparticles as small as ~ 4 nm. Some of the issues regarding thermal stability of nanoparticles both above and below the “superparamagnetic” limit have been discussed. Although FePt nanoparticles with a narrow size distribution can be made by chemical synthesis, transforming the nanoparticles to the $L1_0$ phase without sintered grain growth is a major challenge. Some of the methods for reducing or eliminating grain growth

Fig. 18.16 Measured order parameter for FePt nanoparticles annealed in a salt matrix at 700°C for 3 h. (Reprinted with permission from *Advanced Materials*. © 2006 Wiley-VCH Verlag GmbH & Co. KGaA)



include the use of a hard shell, annealing in a salt matrix, and flash annealing. Additive Au and Ag have been shown to significantly lower the ordering temperature in close-packed arrays of nanoparticles. It was shown, however, that the reduction in ordering temperature comes at the expense of increased grain growth. Preliminary experiments on salt-annealed FePtAg show that additive Ag may nevertheless intrinsically lower the ordering temperature in the absence of grain growth. Easy-axis alignment of $L1_0$ FePt nanoparticles can be achieved by drying a nanoparticle dispersion in a magnetic field, and the limiting effect of thermal fluctuations on orientation has been discussed. Significant field orientation has been achieved experimentally for 6 nm FePt particles; however, the orientation is less than predicted due in part to interparticle interactions. Large particle-to-particle variations in the composition of chemically synthesized nanoparticles have been measured, and the compositional distribution has been shown to depend on the type of synthesis. Compositional distributions lead to anisotropy distributions in the chemically ordered nanoparticles. The anisotropy distribution can be determined by measuring the ratio of the remanent to hysteresis loop coercivity. Finally, theoretical and experimental work has been described showing that the maximum achievable chemical order, and by inference the maximum anisotropy, is limited by particle size.

Acknowledgments This work has been supported by the NSF Materials Research Science and Engineering Center Award No. DMR-0213985.

References

1. Ahmadi, T.S., Wang, Z.L., Green, T.C., Henglein, A., ElSayed, M.A.: Shape-controlled synthesis of colloidal platinum nanoparticles. *Science* **272**, 1924–1926 (1996)
2. Aslam, M., Fu, L., Li, S., Dravid, V.P.: Silica encapsulation and magnetic properties of FePt nanoparticles. *J. Colloid. Interface Sci.* **290**, 444–449 (2005)

3. Barmak, K., Kim, J., Berry, D.C., Wierman, K.W., Svedberg, E.B., Howard, J.K.: Calorimetric studies of the A1 to L1₀ transformation in FePt and related ternary alloy thin films. *J. Appl. Phys.* **95**, 7486–7488 (2004)
4. Brown, K.R., Walter, D.G., Natan, M.J.: Seeding of colloidal Au nanoparticle solutions. 2. Improved control of particle size and shape. *Chem. Mater.* **12**, 306–313 (2000)
5. Brust, M., Bethell, D., Schiffrin, D.J., Kiely C.J.: Novel gold-dithiol nano-networks with non-metallic electronic properties. *Adv. Mater.* **7**, 795–798 (1995)
6. Burshtain, D., Zeiri, L., Efrima, S.: Control of colloid growth and size distribution by adsorption-silver nanoparticles and adsorbed anisate. *Langmuir* **15**, 3050–3055 (1999)
7. Chen, M., Kim, J., Liu, J.P., Fan, H.Y., Sun, S.H.: Synthesis of FePt nanocubes and their oriented self-assembly. *J. Am. Chem. Soc.* **128**, 7132–7133 (2006)
8. Chen, M., Nikles, D.E.: Synthesis, self-assembly, and magnetic properties of Fe_xCo_yPt_{100-x-y} nanoparticles. *Nano Lett.* **2**, 211–214 (2002)
9. Chen, S.K., Yuan, F.T., Shiao, S.N.: Magnetic property modification of L1₀ FePt thin films by interfacial diffusion of Cu and Au overlayers. *IEEE Trans. Magn.* **41**, 921–923 (2005)
10. Chepulskii, R.V., Butler, W.H.: Temperature and particle-size dependence of the equilibrium order parameter order parameter of FePt alloys. *Phys. Rev. B* **72**, 134205-1–134205-18 (2005)
11. Chepulskii, R.V., Velez, J., Butler, W.H.: Monte Carlo Monte Carlo simulation of equilibrium L1₀ ordering in FePt nanoparticles. *J. Appl. Phys.* **97**, 10J311-1–10J311-3 (2005)
12. Elkins, K., Li D., Poudyal, N., Nandwana, V., Jin, Z., Chen, K., Liu, J.P.: Monodisperse face-centred tetragonal FePt nanoparticles with giant coercivity. *J. Phys. D: Appl. Phys.* **38**, 2306–2309 (2006)
13. Faraday, M.: Experimental relations of gold (and other metals) to light. *Philos. Trans. R. Soc. Lond.* **B 147**, 145–181 (1857)
14. Glavee, G.N., Klabunde, K.J., Sorensen, C.M., Hadjipanayis, G.C.: Borohydride reduction of nickel and copper ions in aqueous and nonaqueous media – controllable chemistry leading to nanoscale metal and metal boride particles. *Langmuir* **10**, 4726–4730 (1994)
15. Han, M.Y., Quek, C.H., Huang, W., Chew, C.H., Gan, L.M.: A simple and effective chemical route for the preparation of uniform nonaqueous gold colloids. *Chem. Mater.* **11**, 1144–1147 (1999)
16. Harrell, J.W.: Orientation dependence of the dynamic coercivity of Stoner-Wohlfarth particles. *IEEE Trans. Magn.* **37**, 533–537 (2001)
17. Harrell, J.W., Kang, S., Jia, Z., Nikles, D.E., Chantrell, R., Satoh, A.: Model for the easy-axis alignment of chemically synthesized L1₀ FePt nanoparticles. *Appl. Phys. Lett.* **87**, 202508-1–202508-3 (2005a)
18. Harrell, J.W., Nikles, D.E., Kang, S.S., Sun, X.C., Jia, Z.: Effect of additive Cu, Ag, and Au on L1₀ ordering of chemically synthesized FePt nanoparticles. *J. Mag. Soc. Japan* **28**, 847–852 (2004)
19. Harrell, J.W., Nikles, D.E., Kang, S.S., Sun, X.C., Jia, Z., Shi, S., Lawson, J., Thompson, G.B., Srivastava, C., Seetala, N.V.: Effect of metal additives on L1₀ ordering of chemically synthesized FePt nanoparticles. *Scripta Mater.* **53**, 411–416 (2005b)
20. Hyun, C., Lee, D.C., Korgel, B.A., de Lozanne, A.: Micromagnetic study of single-domain FePt nanocrystals overcoated with silica. *Nanotech.* **18**, 055704-1–055704-7 (2007)
21. Jana, N.R., Gearheart, L., Murphy, C.J.: Evidence for seed-mediated nucleation in the chemical reduction of gold salts to gold nanoparticles. *Chem. Mater.* **13**, 2313–2322 (2001)
22. Kang, S. et al.: Sintering behavior of spin-coated spin-coated FePt and FePtAu nanoparticles. *J. Appl. Phys.* **99**, 08N704-1-08N704-3 (2006a)
23. Kang, S., Harrell, J.W., Nikles, D.E.: Reduction of ordering temperature of self-assembled FePt nanoparticles by the addition of Ag. *Nano Lett* **2**, 1033–1036 (2002)
24. Kang, S., Jia, Z., Nikles, D.E., Harrell J.W.: Synthesis and phase transition of self-assembled FePd and FePdPt nanoparticles. *J. Appl. Phys.* **95**, 6744–6746 (2004)
25. Kang, S., Jia, Z., Shi, S., Nikles, D.E., Harrell, J.W.: Easy axis alignment of chemically partially ordered FePt nanoparticles. *Appl. Phys. Lett.* **86**, 062503-1–1062503-3 (2005)

26. Kang, S., Miao, G.X., Shi, S., Jia, Z., Nikles, D.E., Harrell, J.W.: Enhanced magnetic properties of self-Assembled FePt nanoparticles with MnO shell. *J. Am. Chem. Soc.* **128**, 1042–1043 (2006b)
27. Kang, S., Shi, S., Jia, Z., Thompson, G.B., Nikles, D.E., Harrell, J.W.: Microstructures and magnetic alignment of L1₀ FePt nanoparticles. *J. Appl. Phys.* **101**, 09J113-1–09J113-1 (2007)
28. Kang, S.S., Jia, Z., Nikles, D.E., Harrell, J.W.: Synthesis, chemical ordering and magnetic properties of [FePt]_{1-x}Au_x nanoparticles. *IEEE Trans. Magn.* **39**, 2753–2757 (2003a)
29. Kang, S.S., Nikles, D.E., Harrell, J.W.: Synthesis, chemical ordering and magnetic properties of FePt-Ag nanoparticles. *J. Appl. Phys.* **93**, 7178–7180 (2003b)
30. Lee, D.C., Mikulec, F.V., Pelaez, K., Koo, B., Korgel, B.A.: Synthesis and magnetic properties of silica-coated FePt nanocrystals. *J. Phys. Chem.* **110**, 11160–11166 (2006)
31. Liu, J.P., Elkins, K., Li, D., Nandwana, V., Poudyal, N.: Phase transformation of FePt nanoparticles. *IEEE Trans. Magn.* **42**, 3036–3031 (2006)
32. Maeda, T., Kai, T., Kikitsu, A., Nagase, T., Akiyama, J.: Reduction of ordering temperature of an FePt-ordered alloy by addition of Cu. *Appl. Phys. Lett.* **80**, 2147–2149 (2002)
33. Mayer, A.B.R., Grebner, W., Wannemacher, R.: Preparation of silver-latex composites. *J. Phys. Chem. B* **104**, 7278–7285 (2000)
34. McDaniel, T.W., Challener, W.A., Sendur, K.: Issues in heat-assisted perpendicular recording. *IEEE Trans. Magn.* **39**, 1972–1979 (2003)
35. Munro, C.H., Smith, W.E., Garner, M., Clarkson, J., White, P.C.: Characterization of the surface of a citrate reduced colloid optimized for use as a substrate for surface enhanced resonance Raman scattering. *Langmuir* **11**, 3712–3720 (1995)
36. Nishimura, K., Takahashi, K., Uchida, H., Inoue, M.: Effects of third elements (Ag, B, Cu, Ir) addition and high Ar gas pressure on L1₀ FePt films. *J. Magn. Magn. Mater.* **272**, 2189–2190 (2004)
37. Pathak, S., Greci, M.T., Kwong, R.C., Mercado, K., Prakash, G.K.S., Olah, G.A., Thompson, M.E.: Synthesis and applications of palladium-coated poly(vinylpyridine) nanospheres. *Chem. Mater.* **12**, 1985–1989 (2000)
38. Peng, Q.Z., Richter, H.J.: Field sweep rate dependence of media dynamic coercivity. *IEEE Trans. Magn.* **40**, 2446–2448 (2004)
39. Platt, C.L., Wierman, K.W., Svedberg, E.B., van de Veerdonk, R., Howard, J.K., Roy, A.G., Laughlin, D.E.: L1₀ ordering and microstructure of FePt thin films with Cu, Ag, and Au additive. *J. Appl. Phys.* **92**, 6104–6109 (2002)
40. Reed, D.: Use of silicate shells to prevent sintering during thermally induced chemical ordering of FePt nanoparticles. Ph.D. dissertation, University of Alabama (2007)
41. Rong, C. et al.: Size-dependent chemical and magnetic ordering in L1₀-FePt nanoparticles. *Adv. Mater.* **18**, 2984–2988 (2006)
42. Salgueirino-Maceira, V., Correa-Duarte, M.A., Farle, M.: Manipulation of chemically synthesized FePt nanoparticles in water, core-shell silica/FePt nanocomposites. *Small* **1**, 1073–1076 (2005)
43. Scholz, W., Fidler, J., Schrefl, T., Suess, D., Forster, H., Dittrich, R., Tsiantos, V.: Numerical micromagnetic simulation of Fe-Pt nanoparticles with multiple easy axes. *J. Magn. Magn. Mater.* **272**, 1524–1525 (2004)
44. Sharrock, M.P., McKinney, J.T.: Kinetic effects in coercivity measurements. *IEEE Trans. Magn.* **17**, 3020–3022 (1981)
45. Shi, S., Kang, S., Lawson, J., Jia, Z., Nikles, D., Harrell, J.W., Ott, R., Kadolkar, P.: Pulsed-thermal processing of chemically synthesized FePt nanoparticles. *JOM* **58**, 43–45 (2006)
46. Shukla, N., Liu, C., Jones, P.M., Weller, D.: FTIR study of surfactant bonding to FePt nanoparticles. *J. Magn. Magn. Mater.* **36**, 178–184 (2003)

47. Srivastava, C., Balasubramanian, J., Turner, C.H., Wiest, J.M., Bagaria, H.G., Thompson, G.B.: Formation mechanism and composition distribution of FePt nanoparticles. *J. Appl. Phys.* **102**, 104310 (2007)
48. Srivastava, C., Thompson, G.B., Harrell, J.W., Nikles, D.E.: Size effect ordering in FePt_{100-x}Cr_x nanoparticles. *J. Appl. Phys.* **99**, 054304-1–054304-6 (2006)
49. Suess, D.: Multilayer exchange spring media for magnetic recording. *Appl. Phys. Lett.* **89**, 113105-1–113105-3 (2006)
50. Sun, S.H., Anders, S., Thomson, T., Baglin, J.E.E., Toney, M.F., Hamann, H.F., Murray, C.B., Terris, B.D.: Controlled synthesis and assembly of FePt nanoparticles. *J. Phys. Chem. B* **107**, 5419–5425 (2003a)
51. Sun, S.H., Fullerton, E.E., Weller, D., Murray, C.B.: Compositionally controlled FePt nanoparticle materials. *IEEE Trans. Magn.* **37**, 1239–1243 (2001)
52. Sun, S.H., Murray, C.B.: Synthesis of monodisperse cobalt nanocrystals and their assembly into magnetic superlattices. *J. Appl. Phys.* **85**, 4325–4330 (1999)
53. Sun, S.H., Murray, C.B., Weller, D., Folks, L., Moser, A.: Monodisperse FePt nanoparticles and ferromagnetic FePt nanocrystal superlattices. *Science* **287**, 1989–1992 (2000)
54. Sun, X.C., Kang, S.S., Harrell, J.W., Nikles, D.E., Dai, Z.R., Li, J., Wang, Z.L.: Synthesis, chemical ordering, and magnetic properties of FePtCu nanoparticle films. *J. Appl. Phys.* **93**, 7337–7339 (2003b)
55. Torigoe, K., Suzuki, A., Esumi, K.: Au(III)-PAMAM interaction and formation of Au-PAMAM nanocomposites in ethyl acetate. *J. Colloid. Interface Sci.* **241**, 346–356 (2001)
56. Turkevich, J., Kim, G.: Palladium: preparation and catalytic properties of particles of uniform size. *Science* **169**, 873–879 (1970)
57. Tzitzios, V., Basina, G., Gjoka, M., Boukos, N., Niarchos, D., Devlin, E., Petridis, D.: The effect of Mn doping in FePt nanoparticles on the magnetic properties of the L1(0) phase. *Nanotechnology* **17**, 4270–4273 (2006)
58. Wang, C., Hou, Y.L., Kim, J.M., Sun, S.H.: A general strategy for synthesizing FePt nanowires and nanorods. *Angew. Chem. Int. Ed.* **46**, 6333–6335 (2007)
59. Wang, J.G., Neoh, K.G., Kang, E.T.: Preparation of nanosized metallic particles in polyaniline. *J. Colloid Interface Sci.* **239**, 78–86 (2001)
60. Wang, S., Kang, S.S., Harrell, J.W., Wu, X.W., Chantrell, R.W.: Coercivity ratio and anisotropy distribution anisotropy distribution in chemically-synthesized L1₀ FePt nanoparticle systems. *Phys. Rev. B* **68**, 104413-1–104413-7 (2003a)
61. Wang, S., Kang, S.S., Nikles, D.E., Harrell, J.W., Wu, X.W.: Magnetic properties of self-organized L1₀ FePtAg nanoparticle arrays. *J. Magn. Magn. Mater.* **266**, 49–56 (2003b)
62. Wang, Y., Ren, J.W., Deng, K., Gui, L.L., Tang, Y.Q.: Preparation of tractable platinum, rhodium, and ruthenium nanoclusters with small particle size in organic media. *Chem. Mater.* **12**, 1622–1627 (2000)
63. Weller, D. et al.: High Ku materials approach to 100 Gbits/in². *IEEE Trans. Magn.* **36**, 10–15 (2000)
64. Yamamoto, S., Morimoto, Y., Ono, T., Takano, M.: Magnetically superior and easy to handle L1₀-FePt nanocrystals. *Appl. Phys. Lett.* **87**, 032503-1–032503-3 M (2005)
65. Yan, Q., Purkayastha, A., Kim, T., Kröger R., Bose, A., Ramanath, G.: Synthesis and assembly of monodisperse high-coercivity silica-capped FePt nanomagnets of tunable size, composition, and thermal stability thermal stability from microemulsions. *Adv. Mater.* **18**, 2569–2573 (2006a)
66. Yan, Q.Y., Kim, T., Purkayastha, A., Xu, Y., Shima, M., Gambino, R.J., Ramanath, G.: Magnetic properties of Sb-doped FePt nanoparticles. *J. Appl. Phys.* **99**, 08N709-1–08N709-3 (2006b)
67. Yin, Y.D., Li, Z.Y., Zhong, Z.Y., Gates, B., Xia, Y.N., Venkateswaran, S.: Synthesis and characterization of stable aqueous dispersions of silver nanoparticles through the Tollens process. *J. Mater. Chem.* **12**, 522–527 (2002)

68. Yu, A.C.C., Mizuno, M., Sasaki, Y., Kondo, H.: Atomic composition effect on the ordering of solution-phase synthesized FePt nanoparticle films. *Appl. Phys. Lett.* **85**, 6242–6244 (2004)
69. Yu, C.H., Caiulo, N., Lo, C.C.H., Tam, K., Tsang, S.C.: Synthesis and fabrication of a thin film containing silica-encapsulated face-centered tetragonal FePt nanoparticles. *Adv. Mater.* **18**, 2312–2314 (2006)

Chapter 19

Magnetic Manipulation of Colloidal Particles

Randall M. Erb and Benjamin B. Yellen

Abstract We review some recent advances in the field of magnetic manipulation techniques, with particular emphasis on the manipulation of mixed suspensions of magnetic and nonmagnetic colloidal particles. We will first discuss the theoretical framework for describing magnetic forces exerted on particles within fluid suspensions. We will then make a distinction between particle systems that are highly dependent upon Brownian influence and those that are deterministic. In both cases, we will discuss the type of structures which are observed in colloidal suspensions as a function of the size and type of particles in the fluid. We will discuss the theoretical issues that apply to modeling the behavior of these systems, and we will show that the recently developed theoretical models correlate strongly with the presented experimental work. This chapter will conclude with an overview of the potential applications of these magnetic manipulation techniques.

19.1 Introduction

The manipulation of particle suspensions is an essential capability for various engineering applications ranging from self-assembled nano-manufacturing to life science analysis tools. Methods for manipulating the particles in parallel have mainly relied on the use of optical [1, 2], electrical [3, 4], or magnetic field traps [5–10], which have the advantage of being shaped remotely through the use of lasers, electrodes, or external coils. Magnetic manipulation techniques, in particular, have the practical advantage of being biologically and chemically invisible [11], as compared to electrical and optical systems which are prone to overheating or chemically altering the specimen [12, 13]. There are several comprehensive reviews in the literature

Benjamin B. Yellen (✉)

Department of Mechanical Engineering and Materials Science, Center for Biologically Inspired Materials and Material Systems, Hudson Hall, Box 90300, Duke University, Durham, NC 27708, USA

e-mail: yellen@duke.edu

describing developments in the field of magnetic manipulation systems over the last four decades [14–17]. This chapter will instead focus on the interesting capabilities that have recently been demonstrated in mixed magnetic and nonmagnetic particle suspensions, and we will emphasize our own recent advances in controlling particles of various sizes, shapes, and degrees of magnetization. Due to the inherent complexity in modeling systems composed of strongly interacting particles, this topic poses considerable theoretical and experimental challenges; however, we will show that continuum models can be effective at describing the equilibrium behavior of colloidal suspensions exposed to external magnetic fields.

The most common use of magnetic particles is in the field of separation, where magnetic manipulation schemes are applied to capture and separate various biological materials of interest (e.g., cells [18, 19], viruses [20, 21], and proteins [22, 23]). For magnetic separation applications, magnetic particle surfaces are typically functionalized with proteins and antibody receptors that can recognize and associate with various biological materials by affinity binding. Once attached, the biological materials are separated from solution by applying force to the magnetic particle. Consequently, there has been much effort in the synthesis and characterization of these colloidal magnetic particles, reviewed elsewhere [24].

Recently, we have demonstrated an alternative method for separating and manipulating biological and other nonmagnetic materials using a suspension of magnetic nanoparticles to provide “magnetic contrast” to the surrounding fluid. Nonmagnetic materials immersed within the suspension of magnetic nanoparticles are shown to become effectively magnetized with respect to the surrounding fluid, allowing them to be manipulated by magnetic fields and field gradients [6,7, 25–28]. This manipulation strategy has been given the name negative magnetophoresis in order to draw parallels with the corollary “negative dielectrophoresis” commonly referred to in the literature [29, 30].

The theoretical analysis of magnetic nanoparticle suspensions poses considerable challenges with respect to accurately calculating the magnetic force on submerged nonmagnetic materials. Compared with negative dielectrophoresis where continuum equations are generally applicable due to the solvent being much smaller than most colloidal materials, the analysis of magnetic nanoparticle suspensions is complicated by the larger size of the magnetic nanoparticles (~ 10 nm) which is commensurate with the size of many proteins and macromolecules. Furthermore, the strong interactions between 10 nm sized magnetic nanoparticles lead to a phenomenon (e.g., chaining), which is not observed in corollary dielectric systems where the solvent is of molecular length scale [31–33]. Larger particle size brings into question the applicability of continuum equations for fluid magnetization when considering nonmagnetic particles that are only slightly larger than the magnetic nanoparticles in the fluid. By investigating the agreement between theory and experiment, we show continuum models are applicable when the nonmagnetic particles are at least 2–3 times larger than the magnetic nanoparticles [10, 28].

The rest of this work will be organized as follows. In Section 19.2, we will introduce the theoretical basis of controlling magnetic and nonmagnetic particles and establish the role that is played by Brownian motion. In Section 19.3, we will

review some non-Brownian particle manipulation systems including surface-based assemblies and substrate-based transport. In Section 19.4, we will present magnetic and nonmagnetic particle systems where the manipulation of individual particles is influenced, but not dominated, by Brownian motion, such as chain growth, self-organizing structures, and the alignment of anisotropic particles. In Section 19.5, we will expand these models to account for the behavior within populations of nanoparticles which are dominated by Brownian fluctuations and must be modeled using Boltzmann distributions. We will demonstrate the validity of our theoretical predictions by comparing theoretical models with experimental results. In Section 19.6, we will conclude this discussion by outlining open questions and future directions for this field.

19.2 Magnetic Manipulation of Particles

19.2.1 *Deterministic and Brownian-Dominated Particle Systems*

Throughout this chapter, we will be discussing either particles which follow deterministic trajectories or ones dominated by random Brownian motion. The general principle of Brownian motion suggests that the positions of particles will fluctuate due to random collisions with the solvent molecules [34]. Owing to its smaller mass, the fluctuations of nanoparticles (i.e., <100 nm) tends to be much larger than microparticles; however, the Brownian interactions can be overlooked in some cases where the magnetic forces are particularly strong. In either case, it is worthwhile to establish a general guideline for when a particle's motion can be modeled deterministically and when random motions must be taken into account. Under an applied force, \vec{F}_p , a particle will experience a change of potential energy of $\Delta U(\vec{r}) = \vec{F}_p(\vec{r}) dr$. In this work, the particle's trajectory is considered to be deterministic when the change in potential energy during its movement over a distance commensurate with its own radius, a , is larger than thermal fluctuation energy (i.e., $2aF \geq k_B T$). If the change in potential energy is smaller than thermal fluctuation energy, then random Brownian motion cannot be ignored. To make this distinction for each type of motion, it is first necessary to discuss how to calculate magnetic forces on colloidal particles.

19.2.2 *Material Properties*

Before embarking on a discussion concerning the calculation of different forces, we first review the type of magnetic materials used in magnetic manipulation technology and their field-dependent behavior. Magnetic particles are typically composed of iron, nickel, or cobalt, and their various oxidized forms. A division in nomenclature is used to distinguish between the different types of magnetic ordering of spins within these materials. Iron, nickel, and cobalt in pure metal form are referred to

as ferromagnets, whereas their oxidized forms are referred to as ferrimagnets. For more discussion, see Ref. [35] or other chapters in this handbook. Regardless of these differences, both types of material classes display common magnetic properties, including the ability to store magnetization in the absence of external field (i.e., remanence), and a history-dependent magnetization (i.e., hysteresis). The hysteretic magnetization behavior of typical ferro/ferrimagnetic material below the Curie temperature is presented in Fig. 19.1A [35, 36].

When ferro/ferrimagnetic materials are heated above the Curie temperature, the spin–spin coupling within the material is no longer sufficient to overcome thermal fluctuation energy, and as a result these materials begin to display different behavior referred to as *paramagnetism*, which is characterized by a lack of remanence and hysteresis. In other words, paramagnetic materials can magnetize in an external field, but they promptly lose their magnetization when the field is removed. The classic paramagnetic hysteresis graph is shown in Fig. 19.1B, and the linear region is called the magnetic susceptibility, χ , which describes how easily the material can magnetize in an external field.

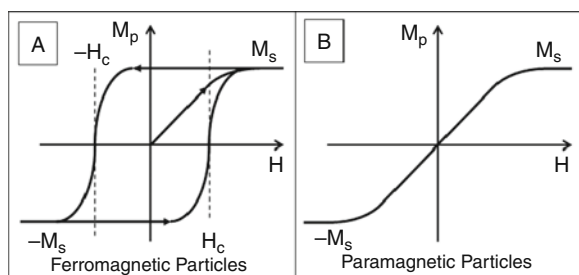


Fig. 19.1 Hysteresis curves for (A) ferromagnetic and (B) paramagnetic material. The magnetization, \bar{M}_p , of the particles increases with an applied field, \bar{H} , until the saturation magnetization, M_s , of the particle is reached. Ferromagnetic particles retain a magnetization in zero field that can only be switched in a reversal field exceeding the coercive field, H_c .

Recently, the term “superparamagnetism” has been given to a class of very small metal or metal-oxide nanoparticles (usually smaller than 10 nm) that display extraordinarily large paramagnetic response to an external field even at temperatures below the Curie point, where the bulk material would have magnetic remanence. This behavior originates from the competition between the nanoparticle’s magnetic crystalline anisotropy energy and the thermal fluctuation energy of the surrounding bath. Since the crystalline anisotropy energy is proportional to the volume of the nanoparticle, there exists a critical size below which the particles cannot retain its preferred magnetization orientation inside the material’s crystalline structure. This “superparamagnetic limit” is of particular interest to magnetic data storage technology, since it dictates the smallest nanoparticle that can store binary data. These materials are also of interest as magnetic nanoparticle fluids, since they remain stable in the absence of magnetic field but respond strongly when external field is applied.

In the last few decades, there have been significant advances in synthesizing fluidic suspensions of magnetic particles for various applications in drug delivery, cell, and molecular separation, and a variety of other applications [14]. One type of suspension, referred to as *magnetorheological fluid*, consists of 100 nm to 10 μm sized *magnetic beads* suspended in nonmagnetic carrier fluid. These magnetic beads are typically composed of a spherical polymer matrix which encapsulates a dispersion of magnetic nanoparticle grains. If the magnetic grains are small enough and spaced sufficiently far apart inside the polymer matrix, then the composite particle will behave superparamagnetically yet it will have a large dipole moment due to the collective response of the large number of magnetic grains inside the bead. The magnetic susceptibility of these commercially available beads is typically in the range of 0.1–1.0.

Another type of suspension, referred to as *ferrofluid*, consists of 5–20 nm sized magnetic nanoparticles that are freely suspended inside a nonmagnetic carrier fluid. The magnetic properties of the fluid can be modeled as a continuum when the fluid volume element under consideration is much larger than the individual nanoparticles. In our work, for example, we have found that ferrofluids having at least 0.1% volume fraction of magnetic nanoparticle material will behave as a magnetic continuum on the 100 nm length scale [64]. These fluids can also be characterized by a magnetic susceptibility which can be tuned by changing the concentration of nanoparticles within the fluid.

It is interesting to note that in some ferrofluids the overall fluid magnetization can display superparamagnetic properties despite its being composed of nanoparticles that are larger than the superparamagnetic limit. The mechanism for achieving superparamagnetic behavior is due to the Brownian rotational diffusion of the nanoparticles, as opposed to through the classic Neel mechanism (i.e., rotation of the magnetic moment inside the crystalline structure) [35]. For these fluids to remain stable, the nanoparticle cannot be too large, since force interactions between the ferro/ferrimagnetic nanoparticles can lead to irreversible aggregation. In most cases, ferro/ferromagnetic nanoparticles smaller than about 20 nm will remain colloidally stable, since thermal fluctuations will dominate not only the particle–particle magnetic force interactions but also other surface forces of relevance to this size scale. Thus, the criteria for modeling a medium as superparamagnetic must consider not only the properties of the material itself but also the mobility of particles inside their host matrix.

Finally, it is important to mention the role of shape in the particle magnetization process, which is commonly referred to as the “shape anisotropy” of the material. The magnetization of various particle shapes can be modeled using discrete dipole approximation techniques [36]. When the particle shapes conform to certain symmetrical geometries (e.g., spherical and ellipsoidal), these calculations can often be simplified with analytical functions at negligible cost to accuracy. Simplified models are especially beneficial for treating spherical particles, which are the most abundant particle geometry [35–37], and are unique in that the particle’s field is identical to a point dipole when it is uniformly magnetized. However, some corrections may be needed when the particle shape is slightly irregular or if the particle’s magnetization

is not uniform due to the presence of nearby magnetic sources [36, 38] (e.g., a permanent magnet or another particle). Numerical techniques can achieve better accuracy; however, the gains in improved accuracy are relatively minor and frequently not worth the computational investment [27] when applied to applications in magnetic separation and manipulation.

19.2.3 Magnetic Force

The stability of any colloidal suspension is highly dependent upon short-range forces (e.g., steric, Van der Waals, and depletion); however, particle trajectories are dominated by long-range forces (e.g., electrical, gravitational, and magnetic) [39, 40]. Electrical forces often exist in suspensions in the form of electric surface charges, which assist in stabilizing the suspension by repelling neighboring particles. These charges, however, will negligibly affect particle motion in dilute suspensions which are not exposed to electric fields. Gravitational forces can also be ignored for small magnetic particle suspensions over short-time scales [44]. Hence for the magnetic particle systems discussed in the following sections, we have neglected other forces entirely and have focused on the formation of colloidal structures solely due to magnetic forces.

The magnetic force on particles can be computed by considering the equivalent magnetic poles distributed inside the particle volume and on the particle surface. In the case of uniform magnetization, the magnetic poles are strictly on the particle's surface, and the equivalent magnetic pole density can be determined from the divergence in the normal component of magnetization at the particle surface, $\sigma = \mu_o (\vec{M}_p - \vec{M}_f) \cdot \hat{n}$, where \vec{M}_p and \vec{M}_f are the respective magnetizations of the particle and the surrounding fluid, and \hat{n} is the normal surface vector of the particle, S_p . The constant μ_o represents the magnetic permeability of free space, $\mu_o = 4\pi \cdot 10^{-7}$ [H/m]. The magnetic force, \vec{F}_p , that acts upon these magnetic poles is defined by

$$\vec{F}_p \equiv \oint_{S_p} \sigma \vec{H} dS = \mu_o \oint_{S_p} (\vec{M}_p - \vec{M}_f) \cdot \hat{n} \vec{H} dS \quad (19.1)$$

\vec{H} is the local magnetic field using SI notation where the magnetic flux density, \vec{B} , is related to the magnetization and local field by $\vec{B} = \mu_o (\vec{H} + \vec{M})$. Applying Gauss divergence theorem [14, 41], Eq. (19.1) can be reduced for a spherical particle of volume V_p to

$$\vec{F}_p \equiv \mu_o V_p \left[(\vec{M}_p - \vec{M}_f) \cdot \nabla \right] \vec{H} \quad (19.2)$$

Equation (19.2) indicates that in order to achieve significant magnetic force, the particles should have large volumes, there should be a large contrast between the magnetization of the particle and the fluid, and the manipulation system should

be capable of applying large magnetic field gradients. Equation (19.2) also indicates that both magnetic and nonmagnetic particles can be magnetically manipulated depending on the fluid magnetization. For example, magnetic microparticles surrounded by water, for which $\vec{M}_f = 0$, can experience large magnetic forces as evidenced by the numerous applications in magnetic manipulation [14], detection [42], and separation [8]. In weak magnetic fields where $M_p \ll M_s$, the particle magnetization follows a linear constitutive relationship $\vec{M}_p = \chi \vec{H}$, where χ is the bulk material susceptibility, as shown in Fig. 19.1B. This relationship allows the force to be expressed as

$$\vec{F}_p = \mu_o V_p (\vec{M}_p \cdot \nabla) \vec{H} = \frac{1}{2} \mu_o V_p \bar{\chi} \nabla \vec{H}^2 \quad (19.3)$$

where $\bar{\chi}$ is the susceptibility of the particle. The geometry of the particle also affects its ability to magnetize in an external magnetic field [43]; for example, spherical particles have a shape corrected susceptibility of $\bar{\chi} = 3\chi/(\chi + 3)$.

Magnetic force can also be applied to nonmagnetic particles provided the surrounding fluid has nonzero magnetization, such as ferrofluid. It is convenient to represent the fluid magnetization using continuum models, and this assumption tends to be reasonably accurate in cases when the fluid volume of consideration is much larger than the individual ferrofluid particles. An alternative method for modeling these suspensions would consist of considering each particle as a discrete dipole and using Monte Carlo techniques [44, 45] to track the average position and density of particles over time. Due to its computational complexity, these techniques are only applied by a limited number of groups, while most advances have employed continuum approximations. The force on a relatively large nonmagnetic particle (i.e., >50 nm) immersed in ferrofluid can be rewritten as

$$\vec{F}_p = -\mu_o V_p \left(\left\langle \vec{M}_f \right\rangle \cdot \nabla \right) \vec{H} \quad (19.4)$$

The effective fluid magnetization is a function of the magnetization of the individual magnetic particles, $\vec{M}_{p,m}$, and their volume fraction, C_m , as $\left\langle \vec{M}_f \right\rangle = \vec{M}_{p,m} C_m$. For very low magnetic fields where $M_{p,m} \ll M_s$, a linear constitutive relationship can be employed to describe the magnetization of the individual magnetic particles as $\vec{M}_{p,m} = \chi \vec{F}$. However, in strong magnetic field, the particle magnetization is more accurately characterized by Langevin's function, $L(x) = \coth(x) - x^{-1}$, which provides a mechanism to describe magnetization saturation [46], given by

$$\left\langle \vec{M}_f \right\rangle = \vec{M}_{p,m} C_m = M_s C_m L(\xi) \hat{H} \quad (19.5)$$

where ξ is a dimensionless ratio between the magnetic and thermal energy as $\xi = \mu_o M_{s,m} V_m |\vec{H}| / k_B T$, where V_m is the volume of the individual magnetic particles that comprise the ferrofluid. Combining Eq. (19.5) with Eq. (19.4) yields the force on nonmagnetic particles submerged in ferrofluid and subjected to magnetic field gradients as:

$$\vec{F}_p = -V_p M_s C_m L(\xi) (\hat{H} \cdot \nabla) \vec{H} = -k_B T C_m L(\xi) \nabla \xi \quad (19.6)$$

Thus, Eqs. (19.3) and (19.6) represent the forces experienced by magnetic particles surrounded by nonmagnetic carrier fluid, such as water, and by nonmagnetic particles surrounded by ferrofluid, respectively. These expressions will be applied to describe magnetic manipulation techniques in various colloidal particle systems and elucidate the role of magnetic force played in forming colloidal particle chains and other self-organizing structures, controlling alignment of anisotropically shaped colloidal particle, as well as the transport and assembly of colloidal particles onto magnetically patterned surfaces.

19.3 Deterministic Particle Manipulation

19.3.1 Substrate-Based Self-Assembly of Particles

In this section, we begin by discussing microfluidic systems in which the motion of colloidal particles is dominated everywhere by magnetic force. Brownian diffusion is assumed to play a negligible role, and thus the trajectory of particles will be calculated solely from the magnetic force and the viscous response of the environment. One example type of system is a magnetically patterned surface, containing an array of closely spaced magnets which produce both strong local field and field gradients, leading to magnetic forces exceeding piconewton strength on nearby colloidal particles. These types of magnetic separation systems can be fabricated by various lithographic techniques and have been studied by a number of researchers for applications in biochip technologies, manufacturing, and purification [8, 16, 46].

In some instances, the magnetic templates or islands are fabricated from ferromagnetic material that allow for magnetic information to be stored in the substrate and used to program the particle assembly instructions [47]. This programmability allows for the controlled placement of magnetic or nonmagnetic particles into desired regions of the substrate. For a particle near an island, the classical dipole field pattern for an island is shown in Fig. 19.2 superimposed on the uniform field. Without external fields, the field of the island, \vec{H}_{island} , will remain symmetric, having maxima of equal magnitudes near both magnetic poles and minima far away from the island; however, when an external field bias is applied to the system it is possible to change the locations of magnetic field maxima and minima.

As seen in Fig. 19.2, the magnitude of the local field can be altered by applying an external field, \vec{H}_o , such that the external field adds to the island's field in some locations and subtracts in other locations. In this particular example, \vec{H}_o adds to the magnitude \vec{H} on the right side of the island and reduces \vec{H} on the left, creating a field maximum and minimum, respectively. Thus, magnetic particles will be forced toward the right side of the island while nonmagnetic particles in ferrofluid will be forced to the left side. Because photolithographic patterning techniques are well developed, a magnetic template with a controllable field distribution is a very

straightforward method to create self-assembled arrays of particles onto specific locations of a surface.

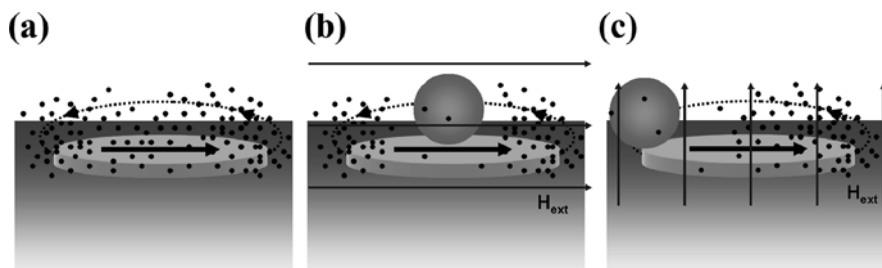


Fig. 19.2 Schematic illustration of nonmagnetic particle immersed in ferrofluid assembling on top of a micromagnet (grey disc with arrow denoting the island's magnetization). (A) Under no external field, the ferrofluid accumulates near the island, whereas the particle is forced away from the island toward the region of lower magnetic field. (B) The external magnetic field is applied parallel to the island's magnetization, causing the ferrofluid to accumulate around the edges of the island where the external field adds to the island's field (denoted by dotted line with arrow), meanwhile the nonmagnetic particle is pulled directly on top of the island where the external field subtracts from the island's field. (C) The external field is applied in the vertical direction that causes the nonmagnetic particle to move to the left edge of the island and the magnetic nanoparticles are pulled toward the right edge

19.3.2 Substrate-Based Transport and Separation

Time-varying magnetic fields applied to substrates of magnetic islands provide a new class of interesting physical behavior with potential ramifications in the transport and separation of colloidal particles. For example, a rotating external field applied to the system will move the locations of magnetic minima and maxima across the surface of the substrate. The transverse motion of these maxima and minima can be modeled as a traveling wave, as shown in Fig. 19.3, which transports individual particles horizontally across the substrate [8].

A simplified analytical model can be developed to model the particle's motion in response to a traveling wave. In this system, a rectangular array of circular magnetic islands patterned from thin ferromagnetic film will have an effective magnetic pole density on the array surface which is well approximated by a 1-D Fourier expansion. For the purpose of this analysis, we will still assume that the substrate's field can still be accurately modeled if only the first harmonic in the Fourier expansion is retained [48]. The sinusoidal pole distribution has an amplitude equal to the island's average pole density, σ_o , with the minimum and maximum of the sinusoid corresponding with the left and right side, respectively, of the island. In addition to the static field produced by the substrate, a spatially uniform rotating field is assumed to be applied to the substrate with frequency, ω . The total magnetic field will be the superposition of the island's field and the external field, and it will depend upon the particle radius, a , the periodicity of the island array, d , and time t , as

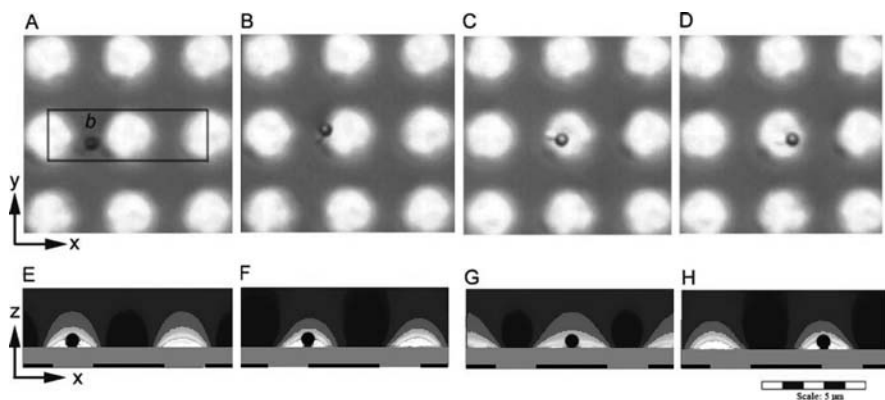


Fig. 19.3 (A–D) A magnetic label attached to a large virus transverse a magnetic array (magnetized in the + x direction) in the presence of a rotating field (also directed in the + x direction in (A) and rotating counterclockwise). (E–G) A finite element analysis of the magnetic array shows the magnetic field maxima (white) moving across the array with the rotating field. *Reproduced by permission of The Royal Society of Chemistry* [8]

$$\vec{H}_x = \vec{H}_{island,x} + \vec{H}_{o,x} = \frac{\sigma_o}{2} e^{-2\pi a/d} \sin\left(\frac{2\pi}{d}x\right) + H_o \sin(\omega t) \quad (19.7)$$

Thus, the force on a particle will be dependent upon the current position and time as $F_x = F_{p,x} \sin(2\pi x/d - \omega t)$, where $F_{p,x}$ can be input from either Eq. (19.3) or Eq. (19.6) depending on the type of system considered. The particle trajectory can be modeled from the equations of motion:

$$F_{net} = m \frac{d^2x}{dt^2} = F_x - D \frac{dx}{dt} \quad (19.8)$$

where m is the mass of the particle, and D is the viscous drag coefficient. In low Reynold's number flow, the inertial term can be ignored, thus the magnetic force is found to exactly balance the drag force on the particle, assumed in this case to be Stokes' drag on a sphere. It is convenient to write Eq. (19.8) in dimensionless form as

$$\frac{d\phi}{d\tau} = \sin(\phi) - \frac{\omega}{\omega_c} \quad (19.9)$$

where $\phi = 2\pi x/d - \omega t$, $\omega_c = 2\pi F_p/(dD)$ is a particle's critical frequency, and $\tau = \omega_c t$ is the dimensionless time variable. This equation of motion is similar to a nonlinear harmonic oscillator observed in many physical systems [49–51]. The behavior of a nonlinear harmonic oscillator suggests that two regimes of motion may be observed depending on the velocity of the traveling wave. If the traveling wave is moving too rapidly, then the substrate cannot supply enough magnetic force to maintain the particle's relative position within the traveling wave. On the

other hand, when the traveling wave is moving less rapidly, the particle becomes locked into the traveling wave and can move linearly across the substrate at a constant rate. Mathematically, this behavior is described as follows. When the system is below the critical frequency, Eq. (19.9) has a stable solution, and the velocity of the particle is found to be independent of drag forces as $dx/dt = \omega d / (2\pi)$. However, when the frequency exceeds ω_c , the viscous drag forces cause the particle to slip from the moving field maxima and reduce the particles linear velocity by $dx/dt = \left(\omega - \sqrt{\omega^2 - \omega_c^2} \right) d / (2\pi)$.

For simple transport systems, maintaining the rotating field below the critical frequency (i.e., $\omega < \omega_c$) can produce very reliable particle trajectories; however, the ability to separate magnetic particles of different sizes can be accomplished by adjusting the frequency close to or exceeding the critical frequency of the system (i.e., $\omega > \omega_c$). For most colloidal transport systems, the damping of the particle velocity is due solely from a Stokes' drag force of $F_{d,x} = 6\pi\eta a (dx/dt)$, where η is the viscosity of the fluid. The critical frequency can then be solved for as a function of a particle's susceptibility and radius:

$$\omega_c = \frac{\bar{\chi}\mu_o\sigma_o H_o}{18\eta} \left(\frac{2\pi a}{d} \right)^2 e^{-2\pi a/d} \quad (19.10)$$

From the dependencies of this equation, the transport velocity of particles with different size and susceptibility has a different frequency response. Exploiting this nonlinearity, the frequency of the rotating field can be adjusted to allow particles of certain size or magnetization to move freely while the motion of others is greatly impeded. For example, 3 μm magnetic particles have higher critical frequencies than similar 1 μm magnetic particles, shown in Fig. 19.4, which allows for their separation. Another separation system involves attaching bio-particles to magnetic particles, effectively reducing the magnetization of any reacted magnetic particle [8]. Then free magnetic particles could be separated quickly from the suspension, and any left over magnetic particles, those attached to the bio-particles, could be subsequently transported elsewhere on the chip (possibly for detection, extraction, or further analysis) by reducing the frequency of the rotating field.

19.4 Brownian-Influenced Particle Manipulation

19.4.1 Magnetic and Nonmagnetic Particle Chains

The motion of large magnetic beads is not always dominated by magnetic force. There may be regions in the fluid where relatively weak magnetic force is experienced by the particle, in which case its trajectory is dominated completely by random Brownian motion. However, when other particles are present in the fluid, the Brownian diffusion does not play a lasting role as particle-particle interactions begin to dominate. Here, we review some of the interesting particle-particle

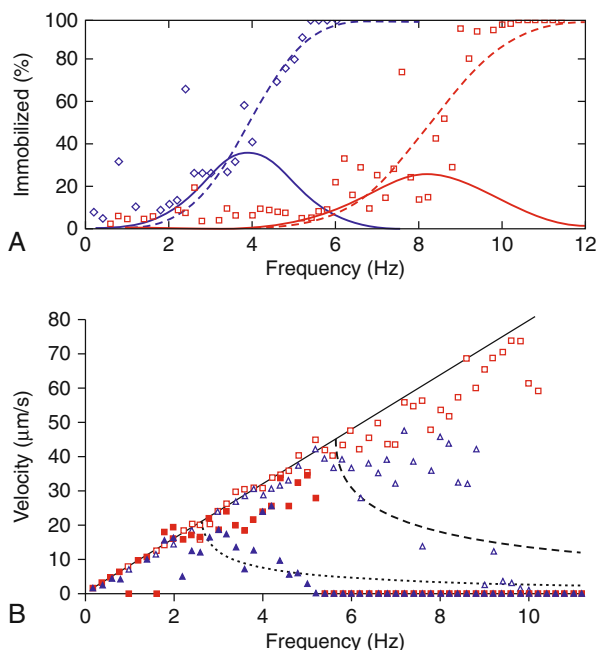


Fig. 19.4 (A) Percentage of immobile 1.0 μm (\diamond) and 2.7 μm particles (\square) is plotted as a function of the frequency of rotation of the external magnetic field. The cumulative distribution function (CDF) and probability distribution function (PDF) are presented as *dashed* and *solid* lines, respectively. In (B), the velocity of the 1.0 μm ($\blacktriangle, \blacktriangle$) and 2.7 μm particles (\triangle, \square) is presented as a function of the rotation frequency. The *squares* represent the mean velocity of the mobile particles, while the *triangles* represent the mean velocity of the entire population of particles. The *dashed* or *dotted* lines are the simulated velocity for the 2.7 μm and 1 μm particles, respectively, based on an appropriate choice for the critical frequency for each particle size. *Reproduced by permission of The Royal Society of Chemistry* [8]

structures which can be formed inside fluids. In general, the forces can be either attractive or repulsive depending upon the relative position and orientation of the particles [29]. As seen in Fig. 19.5, attractive forces exist between two identical particles when the position vector connecting the particle centers is parallel to the local field (i.e., opposite poles are in close proximity). Repulsive forces are present when this position vector is perpendicular to the local field (i.e., magnetic equators are in close proximity). This anisotropic behavior leads to the pole-to-pole chaining of similar particles that has been well characterized [52–54].

In computing forces between particles in the suspension, it is important to account for both the field and the field gradient of one particle on another. Assuming that these particles behave approximately as dipoles, the field of a particle, \vec{H}_p , can be determined from the classical dipole field equation [35]:

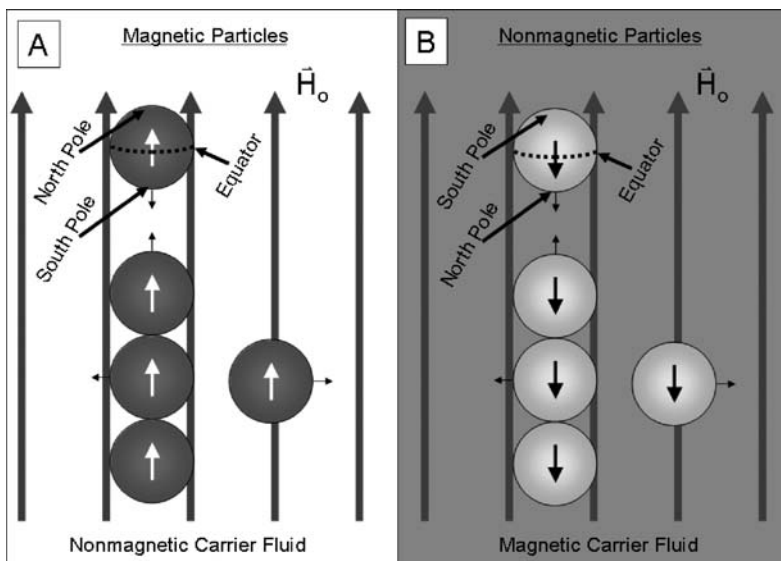


Fig. 19.5 (A) Magnetic particles suspended in a nonmagnetic carrier fluid form chains in local field, \vec{H}_0 . The particles' moments align parallel with the field. (B) Nonmagnetic particles suspended in a magnetic carrier fluid also form chains; however, the particle moments are aligned antiparallel with the field. In both cases, particles are attracted toward the magnetic poles of other particles and repelled from the magnetic equators, exemplified by the small force arrows

$$\vec{H}_p = \frac{3[V_p(\vec{M}_p - \vec{M}_f) \cdot \vec{r}] \cdot \vec{r}}{r^5} - \frac{V_p(\vec{M}_p - \vec{M}_f)}{r^3} \quad (19.11)$$

where \vec{r} is the distance between the point of observation and the particle location. It is important to note that the magnetization of the particle is a function of the local field, which includes the fields produced by neighboring particles. In a system with more than one particle, the field needs to be solved self-consistently [55].

In general, the formation of particle chains is a time-dependent process dominated by translational diffusion on the long length scale. For two particles or chains of particles to link, the groups need to diffuse through the suspension until their proximity substantially increases the magnetic attraction energy between them, at which point the particle trajectory becomes dominated by magnetic force. This type of chain growth is a random-walk, Smulochowski-type growth that has been investigated in the past [60, 61, 62]. Two particles will only be significantly attracted or repelled from one another if the change in potential energy experienced by the particle as it moves a distance of one particle diameter becomes significant relative to $k_B T$. At this point, the particles undergo a transition from Brownian-dominated motion to trajectory-dominated motion, and the chain formation process quickly occurs.

19.4.2 Magnetic and Nonmagnetic Mixed Assemblies in Ferrofluid

An interesting branch of these physical systems occurs when several different types of particles are mixed together, such as the mixture of magnetic particles, nonmagnetic particles, and ferrofluid. The magnetic particles will behave as positive dipoles if their magnetization is stronger than that of the ferrofluid, while the nonmagnetic particles still behave as negative dipoles. The net effect is that the magnetic and nonmagnetic particles will still attract one another; however, the magnetic and nonmagnetic particles will not align head to tail, but instead will align in an anti-ferromagnetic fashion.

In these systems, interesting structures have been observed to self-organize depending on the applied field strength, the bulk ferrofluid concentrations, and the sizes of the particles. For example, if commensurately sized magnetic and nonmagnetic particles are suspended within ferrofluid, they can form simple cubic rectangular arrays in an applied external field as seen in Fig. 19.6A,C.

In addition to these particle arrays, other self-assembled structures can be observed in mixed suspensions when the magnetic and nonmagnetic particles are of two different sizes. For example, if one of the particles is much larger than the other (e.g., tripling the size of the highly magnetic particles as seen in Fig. 19.6B), Saturn-like structures take form as the smaller particles are attracted only to the magnetic equator of the large particle, shown also in Fig. 19.6D,E [56].

19.4.3 Anisotropic Particle Alignment

In addition to translational forces, torques also can be applied to particles that have shape anisotropy. This effect can occur for either magnetic or nonmagnetic particles depending on the surrounding fluid magnetization. The energetics of particle alignment is schematically illustrated in Fig. 19.7, in which a magnetized particle develops magnetic poles on its surface which act to oppose the field \vec{H} within the particle. This field, known as the demagnetizing field, \vec{H}_D , contributes to the total magnetic field within the interior of the particle, \vec{H}_{int} , according to the following equation:

$$\vec{H}_{int} = \vec{H} - \vec{H}_D = \vec{H} - G(\vec{M}_p - \vec{M}_f) \quad (19.12)$$

Here the tensor G represents the demagnetizing factor and is based solely on the particle's aspect ratio and the direction of the external field. In general, demagnetizing factors are smaller when the longest particle axis (i.e., the easy axis) is aligned with the field.

Though many particles can be approximated as spherical, there exist many particle geometries that are better modeled as ellipsoids [57, 58], such as rod-like colloidal particles which can be represented very accurately as prolate spheroids when

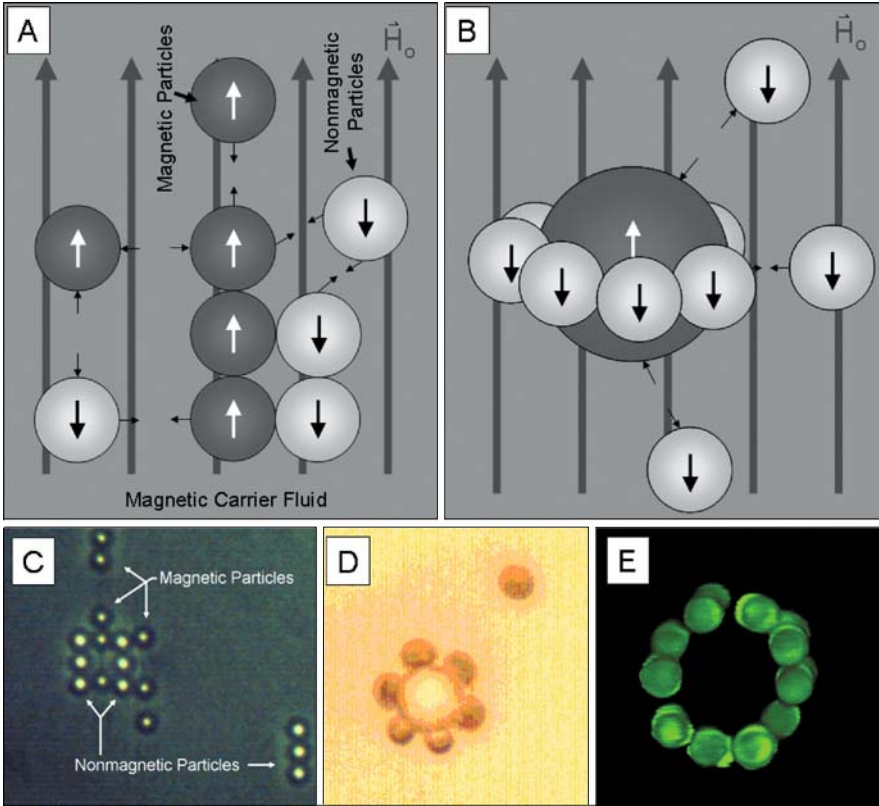


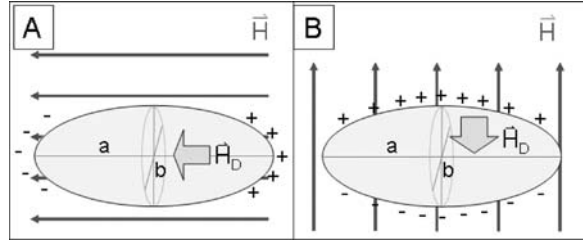
Fig. 19.6 (A) Equal-sized nonmagnetic and magnetic microparticles suspended in ferrofluid form array-like structures. (B) Enlarging one particle size leads to ring-like structures. Simplified directional forces are shown with small *arrows*. (C) Micrograph showing 3 μm magnetic and 3 μm nonmagnetic particles forming a simple cubic lattice in ferrofluid. (D) Micrograph of 1 μm magnetic particles forming a *ring* around a 3 μm nonmagnetic particle in ferrofluid. (E) Fluorescent micrograph of 1 μm nonmagnetic particles forming around a 3 μm magnetic particle (non-fluorescent) into a *ring* structure in ferrofluid

the aspect ratio is larger than 10. When the long axis of the prolate spheroid, labeled a in Fig. 19.7, is aligned parallel or perpendicular to \vec{H} , the respective demagnetizing factors of G_a and G_b are well established [67]:

$$G_a = \frac{(a/b)^2}{2} \int_0^\infty \frac{ds}{(s+a^2)^{3/2}(s+b^2)}, G_b = \frac{(a/b)^2}{2} \int_0^\infty \frac{ds}{(s+a^2)^{1/2}(s+b^2)^2} \tag{19.13}$$

As seen in Eq. (19.13), alignment away from the easy axis requires more energy to achieve due to substantial increase in demagnetizing fields. Because particles are more likely to be in lower energy states, the particle experiences a torque driving

Fig. 19.7 A magnetic ellipsoidal particle shown in a local field directed (A) parallel and (B) perpendicular to the easy axis, a . Magnetic poles on the particle surfaces create a demagnetizing field, \vec{H}_D , within the particle



its easy axis to point along the external field direction. The rotational energy of an ellipse aligned at an angle of θ from the magnetic field is well characterized and found to be [59, 60]:

$$U(\theta) = \frac{2\pi ab^2}{3} \frac{\mu_f (\mu_p - \mu_f)^2 (G_b - G_a) H^2 \sin^2(\theta)}{(\mu_f - (\mu_p - \mu_f) G_a) (\mu_f - (\mu_p - \mu_f) G_b)} \quad (19.14)$$

where μ_p and μ_f are the respective magnetic permeabilities of the particle and the fluid derived from the material susceptibility (e.g., $\mu_p = \mu_o (1 + \chi_p)$).

This rotational energy can be used to determine the alignment distribution within a population of prolate spheroids using a Boltzmann distribution function. For larger particles with strong fluid magnetization mismatches, the rod's alignment is completely determined by the direction of the external field; however, smaller particles can experience larger orientational variation when the average alignment energy, $\langle U(\theta) \rangle$, is close to thermal fluctuation energy. The average energy of particle alignment energy is given by

$$\langle U(\theta) \rangle = \frac{\int_0^{2\pi} U(\theta) e^{-U(\theta)/k_B T} d\theta}{\int_0^{2\pi} e^{-U(\theta)/k_B T} d\theta} \quad (19.15)$$

In order to describe the orientation variation, nematic order parameters [62] can be used such as $S = \langle (3 \cos^2 \theta - 1) / 2 \rangle$ where S ranges from 0, for completely disordered suspensions of particles, to 1, for completely ordered suspensions of particles. For a suspension of magnetic or nonmagnetic elliptical particles within nonmagnetic or magnetic carrier fluid, respectively, typical order parameters, like those shown in Fig. 19.8, depend upon particle geometry, surrounding fields, and relative magnetizations. Such studies have been carried out for both nonmagnetic rods in ferrofluid [63], seen in Fig. 19.8, and magnetic particles in water [64].

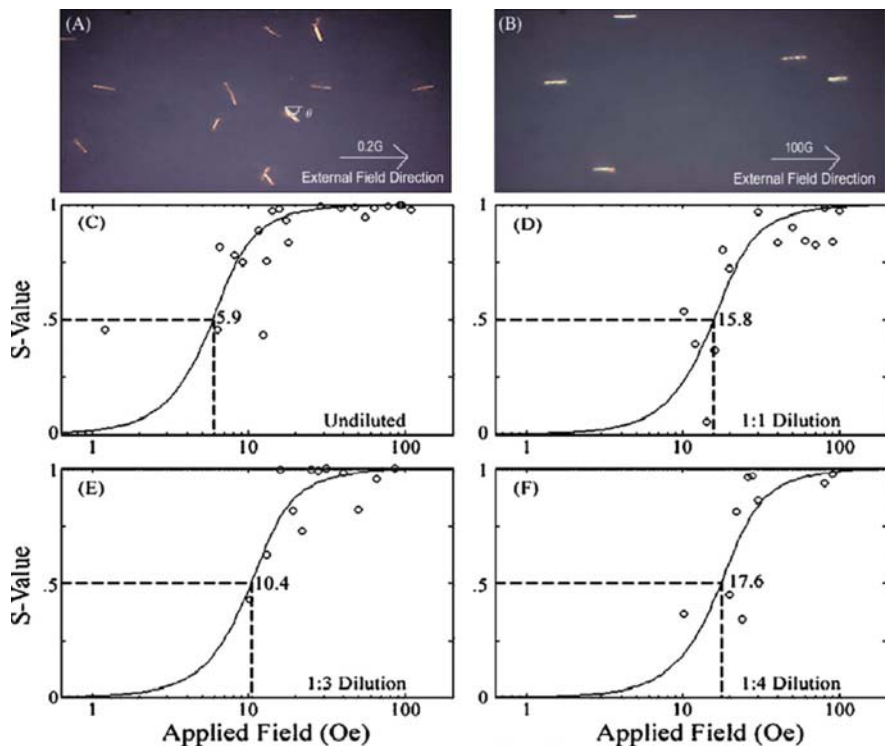


Fig. 19.8 Optical micrographs (A) and (B) demonstrate the orientation distribution of nonmagnetic nanorods in ferrofluid for external fields of (A) 0.2 G and (B) 100 G. Data in (C–F) show the effective orientation of nanorods at ferrofluid volume fractions of (C) 3.6%, (D) 1.8%, (E) 1.2%, and (F) 0.9%. The theoretical fitting curves from the nematic order parameter S are shown by the solid lines and demonstrate a nice fit of the experimental data points. Reused with permission from Chinchun Ooi, *Journal of Applied Physics*, 103, 07E910 (2008). Copyright 2008, American Institute of Physics [61]

19.5 Brownian-Dominated Manipulation of Particle Populations

19.5.1 Modeling Thermal Diffusion

When the nanoparticle is reduced to a critical size, its motion becomes dominated by Brownian diffusion regardless of the applied field, and the role of thermal fluctuations in modeling the distribution within nanoparticle suspensions can become very important. Moreover, at these length scales, the thermal energy of the particles, $k_B T$, may no longer be diminutive relative to the particle's magnetization energy, $M_s V H$, even in strong magnetic fields. Thus, the role of thermal fluctuations in several aspects will need to be incorporated in order to attain representative models. The models will no longer follow the individual trajectories of nanoparticles but instead will be concerned with the average particle flux in the statistical sense. The overall

flux of the local particle concentrations, \vec{J}_{net} , can be modeled through the sum of the thermally driven diffusion flux, $\vec{J}_{diffusion}$, and the deterministically forced drift flux, \vec{J}_{drift} . The diffusion flux is proportional to the local diffusion coefficient, D , and the local variation of the particle concentration, C , as $\vec{J}_{diffusion} = -D\nabla C$. The drift flux is also based on the velocity of the particle, \vec{v}_p , due to migration forces as $\vec{J}_{drift} = \vec{v}_p C$. The local net particle flux is time dependent and can be written in terms of the continuity equation: $-\nabla \cdot \vec{J}_{net} = \partial C / \partial t$. The encompassing characterizing equation for the local net particle flux, known as Fick's Law [65], can be written as follows:

$$\partial C / \partial t = -\nabla \cdot \vec{J}_{net} = -\nabla \cdot (\vec{J}_{drift} - \vec{J}_{diffusion}) = -\nabla \cdot (\vec{v}_p C - D\nabla C) \quad (19.16)$$

There arises a special case for this equation where the drift and the diffusion fluxes exactly balance. This can be viewed as a quasi-equilibrium state where, although the individual particles have a nonzero velocity, the average particle population densities are static. In this case, where $\partial C / \partial t = 0$, concentration distributions can be obtained by solving the equation $\vec{v}_p C = D\nabla C$ if the local particle velocity and the diffusion coefficient are known or can be calculated.

In a viscous medium where inertial effects are unimportant, there is a direct relationship between the magnetic force \vec{F}_p and the particle's velocity according to $\vec{v}_p = \eta \vec{F}_p$, where η is the hydrodynamic mobility of the particle. Inserting this relationship into Eq. (19.16) under steady-state conditions yields

$$\frac{\nabla C}{C} = \frac{\eta}{D} \vec{F}_p \quad (19.17)$$

The Einstein relation, $D = \eta k_B T$, presents a convenient simplification at this point. This relation assumes that the diffusion coefficient and particle mobility are independent of local particle concentration which is a good assumption in dilute suspensions [41]. However, in the case of very high local particle concentrations, this relation may not be accurate and a concentration-dependent diffusion coefficient is needed.

Assuming the force is given by Eqs. (19.2), (19.17) can be rewritten as

$$\frac{\nabla C}{C} = \frac{\mu_o}{k_B T} V \left[\left(\vec{M}_p - \langle \vec{M}_f \rangle \right) \cdot \nabla \right] \vec{H} \quad (19.18)$$

Here, V represents the volume of the effective ferrofluid particle size, and $k_B T$ is taken as a constant assuming isothermal equilibrium conditions. This equation is general as it allows for the local concentration to be obtained for both magnetic and nonmagnetic particles based upon the local magnetic field and the particle and fluid magnetizations. When the Langevin saturation model is combined with Eq. (19.18), the following differential equation is obtained:

$$\frac{\nabla C}{C} = \frac{\mu_o}{k_B T} V \left[\left(\vec{M}_p - M_s C_m L(\xi) \hat{H} \right) \cdot \nabla \right] \vec{H} \quad (19.19)$$

This equation can be used either to model the local concentration of the ferrofluid particles, in which case the parameters become $C = C_m$ and $\vec{M}_{p,m} = M_s L(\xi) \hat{H}$, or to model the local concentration of nonmagnetic particles within the ferrofluid, in which case the parameters become $C = C_n$ and $\vec{M}_{p,n} = 0$.

19.5.2 Magnetic Particle Concentration

Initially, we restrict our discussion of Eq. (19.19) to model the local concentration of the magnetic particles that comprise the ferrofluid. This is the logical starting point as the system becomes even more complicated when nonmagnetic particles are introduced. For a suspension of magnetic particles, Eq. (19.19) becomes

$$\frac{\nabla C_m}{C_m (1 - C_m)} = L(\xi) \nabla \xi \quad (19.20)$$

This represents a first-order differential equation that can only be analytically integrated when ξ is independent of C_m . However, some caution must be taken when using this model. In the present representation of Eq. (19.20), the magnetic energy is assumed to be independent of the local particle concentration. When the volume fraction of magnetic particles is large ($>5\%$ V.F.), particles can be shielded by their neighbors, effectively lowering the local magnetic field that determines $\xi(\vec{H})$. In order to incorporate this shielding phenomenon, the local magnetic field must be solved at the same time as solving for the local particle concentration (i.e., $\vec{H}(C_m)$). By solving this continuum model self-consistently, the fluid magnetization is more accurate in both the high-field and the high-concentration regimes. However, this self-consistent solution prevents the derivation of analytic models that are useful for first-order approximations or for systems with relatively low particle concentration. In relatively low concentrations, minor errors may be acceptable, in which case an analytical expression can be obtained for particle concentration. Equation (19.20) can be directly integrated to yield

$$\frac{C_m}{(1 - C_m)} = A \frac{\sinh(\xi)}{\xi} \quad (19.21)$$

where $A = C_m \xi / [(1 - C_m) \sinh(\xi)]$ is an integration constant that can be solved through forcing the resultant equation to satisfy bulk conditions in a gradient-free regions. Away from field gradients, the local particle concentrations must equal bulk particle concentrations, Φ_m , and the local field will be equal to the magnetic field external to any local magnetic sources that has an energy ratio of ξ_o . Substitution of the boundary conditions leads to the integration constant,

$A = \Phi_m \xi_o / [(1 - \Phi_m) \sinh(\xi_o)]$. By inserting the integration constant back into Eq. (19.21), the local concentration of the magnetic particles within ferrofluid can be attained:

$$C_m = \left(1 + \frac{(1 - \Phi_m) \sinh(\xi_o) \xi}{\Phi_m \sinh(\xi) \xi_o} \right)^{-1} \quad (19.22)$$

Equation (19.22) is very useful as it can predict the local particle concentration as a function solely of the local energy ratio, ξ . In addition, Eq. (19.22) exhibits the appropriate asymptotic behavior; at very large local fields, ($\xi \gg \xi_o$), $C_m \rightarrow 1$, and at very small local fields, ($\xi \ll \xi_o$), $C_m \rightarrow 0$. An experimental image of a typical ferrofluid concentrating near high-gradient magnetic sources is presented in Fig. 19.9A. Here, the ferrofluid particles concentrate very densely between rectangular islands, where the fields created by the islands add to a transverse external field.

Experimental work has verified the accuracy of this expression in regions of strong field and relatively low particle concentrations through the use of optical absorption measurements [10]. Attenuation of the intensity of light through a distance r of ferrofluid follows a well-defined Beer–Lambert relationship of $I = I_o e^{-\alpha r}$. Here α is a material-dependent absorption coefficient that needs to be experimentally determined independently for a ferrofluid. For example, the well-characterized ferrofluid EMG 705 from Ferrotec (Nashua, NH) shown in Fig. 19.9A is found to exhibit an adsorption coefficient of $\alpha = K (C_m)^\beta / (2L)$, where K and β are proportionality constants and $2L$ is the total path length the light travels (twice the fluid height for a reflected light microscopy setup). For a fluid height of 3 μm , a calibration curve was created, shown in Fig. 19.9B, that relates the bulk particle concentration to collected light intensity. For proper characterization of this calibration data, the proportionality constants were found to be $K = 9.24$ and $\beta = 0.79$.

With this calibration relationship established, a theoretical light intensity can be calculated for suspensions of ferrofluid near micromagnets. To determine these intensities, the Beer–Lambert relationship can be integrated across the fluid height to account for variation in particle concentration with height above the micromagnets as

$$I(x, y) = 2 \int_0^L e^{-KzC_m^\beta/L} dz \quad (19.23)$$

Equation (19.23) allows for a theoretical relationship between local field energies and light intensities to be established and correlated to the local concentration profile of ferrofluid. For different bulk particle concentrations, this relationship produces different plots as shown in Fig. 19.9C. Using photo analysis software, the relative light intensities of experimentally collected micrographs, such as the one in Fig. 19.9A, can be directly compared to the theoretical plots as presented with dotted lines in Fig. 19.9C. For these experiments, the areas directly between two islands were sampled for intensity data for two reasons. First, the particle concentrations in

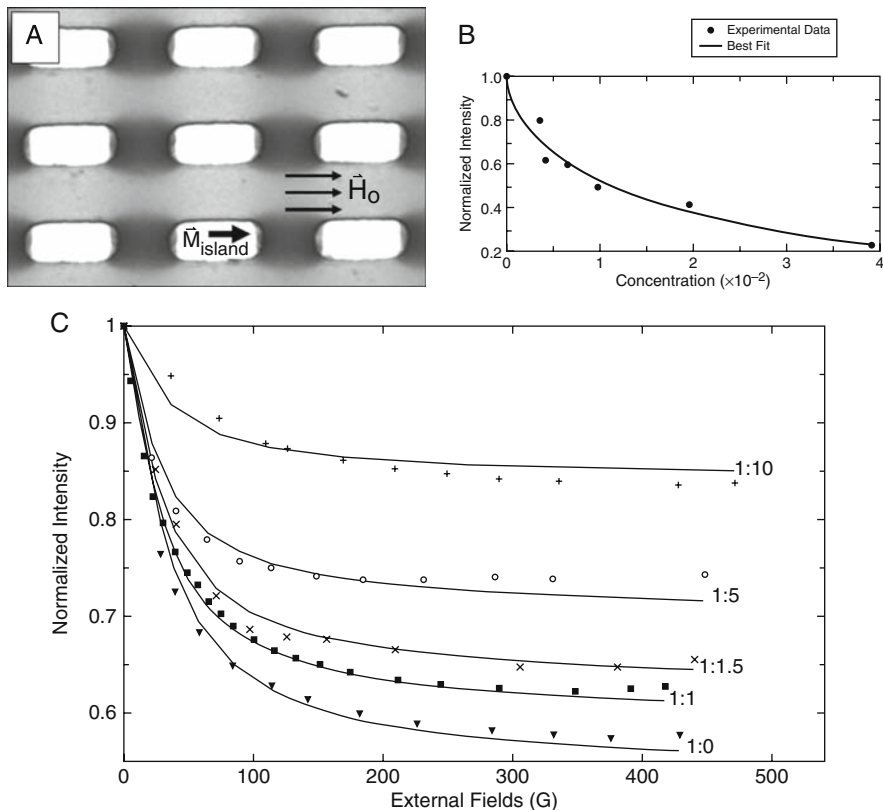


Fig. 19.9 (A) Experimental micrograph shows rectangular cobalt islands that are 8 μm by 4 μm . Magnetic ferrofluid particles concentrate between the islands in the field maxima. (B) A calibration curve is shown comparing bulk concentration versus bulk light intensity. (C) Plots of local concentration of magnetic particles versus local field for different dilutions of ferrofluid. The local concentration can be described fairly accurately using Eq. (19.22) with an effective nanoparticle diameter of ~ 24 nm. Reused with permission from Randall M. Erb, *Journal of Applied Physics*, 103, 063916 (2008). Copyright 2008, American Institute of Physics [10]

these areas are within the low-concentration regime ($< 10\%$ V.F.), which is necessary for the validity of Eq. (19.22). Second, the fields produced by cobalt thin-film islands can be well predicted at large distances away from the islands poles (i.e., distances on the order of the width of an island).

Our experimental results indicated that the ferrofluid is best characterized by an average aggregate size, which is much larger than the individual ferrofluid particles observed within the suspension. The underlying reason for this effect can be explained from aggregation phenomenon occurring in colloidal physics. For example, other forces in colloidal suspensions exist including steric, electrostatic, Van der Waals, and depletion forces, some of which are attractive and others repulsive. In general, all colloidal suspensions are thermodynamically unstable due to the deep

attractive potential energy minimum when two particles are touching; however due to the presence of a repulsive energy barrier, the time scales over which particles aggregate can be sufficiently long to consider them stable. For certain sized colloids, the attractive Van der Waals forces, which scale with the particle radius, may be stronger than the repulsive electrostatic forces, which scale with the total charge on the particle. The net result is that aggregation will be present; however, the aggregation has been shown to be self-limiting based on generic scaling relationships between these attractive and repulsive interactions [66]. Specifically, it has been shown that when the repulsive energy barrier between neighboring particles exceeds $15k_B T$, the suspension is conventionally considered stable. If the energy barrier is smaller, then the particles within the suspension will aggregate until this constraint is met. This self-limiting aggregation is common in particle suspensions, and the average particle size is often well larger than an individual particle at conception [67–70]. These large average aggregate sizes must be included to form a realistic model for the particle suspension since the larger magnetic volumes of the aggregates play a major role in the force upon a particle and, ultimately, its velocity. For this reason, it was not surprising that the ferrofluid particles in our experiments were behaving as small aggregates.

19.5.3 Nonmagnetic Particle Concentrations

Once the magnetic nanoparticle concentration can be determined, it is possible to describe the local particle concentration of nonmagnetic particles, C_n , submerged within a ferrofluid. In this situation, the nonmagnetic particles have negligible magnetization ($\vec{M}_{p,n} = 0$), and Eq. (19.19) becomes

$$\frac{\nabla C_n}{C_n} = -\gamma C_m L(\xi) \nabla \xi \quad (19.24)$$

where $\gamma = V_n/V_m$ represents a nondimensional size ratio between the ferrofluid and nonmagnetic particles. Equation (19.24) indicates that the concentration of nonmagnetic particles depends upon the local ferrofluid concentration, which considerably complicates the general analysis. For scenarios where the ferrofluid is in the high-concentration regime, C_m , a self-consistent approach should be used to solve Eq. (19.20). If the ferrofluid concentration is reasonably low, then Eq. (19.22) can be inserted into Eq. (19.24) and an analytic expression can be obtained. Considering the low-concentration regime, Eq. (19.24) can be integrated as

$$C_n = A^{-1} \left[2 \frac{\sinh(\xi)}{\xi} + 2 \left(\frac{1 - \Phi_m \sinh(\xi_o)}{\Phi_m \xi_o} \right) \right]^{-\gamma} \quad (19.25)$$

where the integration constant, A , can again be arrived at by satisfying bulk conditions within gradient-free regions. In these regions, the local nonmagnetic particle concentration must equal the nonmagnetic bulk concentration, Φ_n , and the local

magnetic energy will be equal to the bulk energy ratio of ξ_o . Satisfying these requirements determines the value of the integration constant which can be incorporated into Eq. (19.25) to yield

$$C_n = \Phi_n \left[1 + \Phi_m \left(\frac{\sinh(\xi)}{\sinh(\xi_o)} \frac{\xi_o}{\xi} - 1 \right) \right]^{-\gamma} \tag{19.26}$$

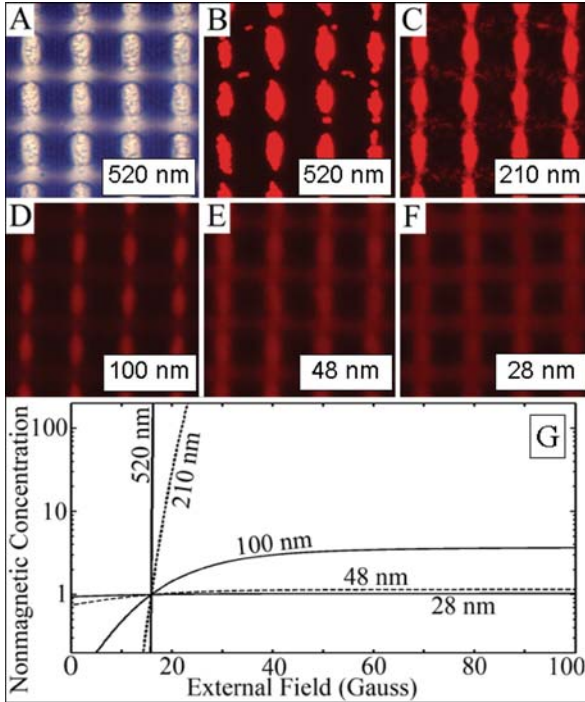


Fig. 19.10 (A) Bright field and (B–F) fluorescent images of 5 μm circular cobalt ferromagnetic islands magnetized in an external field directed rightward. On top of the islands, nonmagnetic particles in ferrofluid concentrate to different extents depending on particle size. (G) Plots of local concentration of nonmagnetic particles versus external field for different sizes of nanoparticles with bulk volume fractions of particles and ferrofluids as 1% and 3.6%, respectively. Below ~ 15 Gauss, the external field is too weak to create field minima on top of the islands, and the nonmagnetic particles are forced away. *Reused with permission from Randall M. Erb, Journal of Applied Physics, 103, 07A312 (2008). Copyright 2008, American Institute of Physics [28]*

In regions of very high local field, where the ferrofluid particles will densely concentrate, Eq. (19.26) shows the nonmagnetic particle concentration to approach 0. This expression, unlike Eq. (19.22), has no inherent saturation since the nonmagnetic concentration will breach the non-physical close-packing threshold with large enough local fields. To resolve this, an artificial restriction on the geometric packing factor can be placed upon Eq. (19.26) that limits the possible values

of the concentration strictly to those that are physical (e.g., $C_n \leq 1$). The main benefit of Eq. (19.26) is that it conveniently predicts the local concentration of nonmagnetic particles based only upon local energy ratios, size ratios, and bulk concentrations.

To test the validity of Eq. (19.26), nonmagnetic fluorescent polystyrene particles of various sizes were mixed with 705 EMG ferrofluid and concentrated on top of cobalt islands, shown in Fig. 19.10A–F [28]. For these experiments, the fluid height was held at 3 μm , and the bulk volume fraction of ferrofluid and nonmagnetic particles were 3.6% and 1.0%, respectively. Nonmagnetic particle sizes of 210 and 520 nm are seen to close-pack on top of the magnetic islands. Conversely, the 24 and 48 nm particles do not seem to concentrate substantially on the islands, while the 100 nm particles somewhat concentrate. In comparison with these experimental studies, the behavior of Eq. (19.26) for these experimental bulk conditions is plotted in Fig. 19.10G across different field strengths and particle sizes. Comparison between these plots and the experimental fluorescent micrographs confirms a qualitative agreement between theoretical predictions and experimental results, and moreover it indicates that continuum equations are still reasonably accurate even when the nonmagnetic nanoparticles are only 2–3 times larger than the magnetic nanoparticles in the fluid.

19.5.4 Applications of Concentration Gradients

The concentration gradients that arise in various ferrofluid mixtures are complex phenomena that lend themselves to certain unique applications. The particles within a magnetic particle suspension can be strongly concentrated within certain regions of HGMS systems, and in some cases can reach close-packing, which implies a localized phase transformation has occurred in the fluid. Regions of the substrate where the particles become close-packed will experience substantial changes in the local viscosity and rheological properties. Furthermore, these regions become effectively inaccessible (i.e., masked) from the surrounding suspension. For example, these close-packed regions can be used as a UV photomask to block light from interacting with the underlying surface [71–72].

In addition to blocking electromagnetic waves, these close-packed particles can possibly block certain chemical hybridization reactions from taking place. Such applications are enhanced since in the regions of high magnetic concentration there are very low concentrations of nonmagnetic particles as per Eq. (19.26). For this reason, magnetically programming the chemisorption or physisorption of nonmagnetic particles onto surfaces becomes physically plausible as demonstrated in Fig. 19.11. This technique can be used for applications including cell manipulation, concentration of fluorescent labels onto biosensors, and even production of protein arrays. However, due to the recent development of this niche of colloidal physics, there remain many applications yet to be conceived.

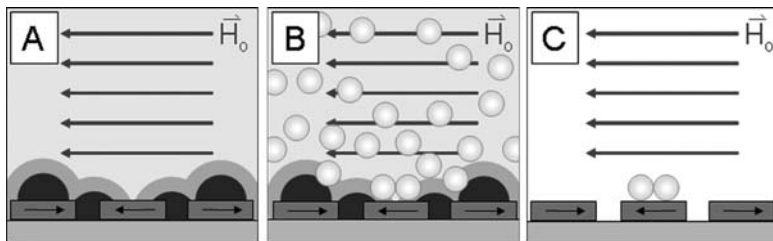


Fig. 19.11 Example setup of magnetically controlled adsorption of nonmagnetic particles to the surface. In **(A)**, ferrofluid is concentrated in regions to be blocked. In **(B)**, nonmagnetic particles are introduced into solution and allowed to diffuse throughout suspension, avoiding areas of high magnetic particle concentration. In **(C)**, suspension is rinsed or diluted and adsorbed particles remain

19.6 Conclusions and Outlook

Here we reviewed the magnetic manipulation of particles within suspensions. Compared with other reviews that focused on high-gradient magnetic separation systems, including by one of the authors, this chapter has instead focused on the magnetic manipulation of mixed suspensions of magnetic and nonmagnetic particles. In this chapter, we developed a theoretical basis for determining the effect of Brownian motion within a system, through determining the magnitude of the magnetic forces present. We first detailed several deterministic systems that are minimally influenced by Brownian motion, in which we described recent theoretical and experimental work on surface-based assembly and substrate-based transport of colloidal particles. Due to the programmability of these systems, they have potential in self-assembled fabrication techniques and lab-on-a-chip platforms. We then turned our attention to particle systems that can be influenced, but are not dominated, by Brownian motion. Several types of self-organizing structures we presented included particle arrays, particle rings, and chain growth. The use of multiple different colloidal components may lead to more complex assemblies than those presented here; thus, this field appears to be very promising for future discoveries. This discussion was followed by the analysis of Brownian-dominated systems, which despite the inherent randomness, can still allow for controllable manipulation of groups of colloidal particles. The theoretical predictions developed in this section based on ensemble modeling techniques for determining local particle concentrations were shown to agree reasonably well with experimental results. However, these models are limited to the low particle concentration regime, and future numerical work is needed to determine the degree of inaccuracy when these models are applied to regions of high particle concentrations.

References

1. Grier, D.G.: A revolution in optical manipulation. *Nature* **424** (6950), 810–816 (2003)
2. Ashkin, A., Dziedzic, J. M., Yamane, T.: Optical trapping and manipulation of single cells using infrared-laserbeams. *Nature* **330** (6150), 769–771 (1987)
3. Huang, Y., Ewalt, K. L., Tirado, M., Haigis, T. R., Forster, A., Ackley, D., Heller, M. J., O'Connell, J. P., Krihak, M.: Electric manipulation of bioparticles and macromolecules on microfabricated electrodes. *Analytical Chemistry* **73** (7), 1549–1559 (2001)
4. Pethig, R.: Dielectrophoresis: Using inhomogeneous AC electrical fields to separate and manipulate cells. *Critical Reviews in Biotechnology* **16** (4), 331–348 (1996)
5. Helseth, L. E., Fischer, T. M., Johansen, T. H.: Domain wall tip for manipulation of magnetic particles. *Physical Review Letters* **91** (20), 208302 (2003)
6. Yellen, B. B., Hovorka, O., Friedman, G.: Arranging matter by magnetic nanoparticle assemblers. *Proceedings of the National Academy of Sciences* **102** (25), 8860–8864 (2005)
7. Yellen, B. B., Erb, R. M., Halverson, D. S., Hovorka, O., Friedman, G.: Arraying nonmagnetic colloids by magnetic nanoparticle assemblers. *IEEE Transactions on Magnetics* **42** (10), 3548–3553 (2006)
8. Yellen, B. B., Erb, R. M., Son, H. S., Hewlin Jr., R., Shang, H., Lee, G. U.: Traveling wave magnetophoresis for high resolution chip based separations. *Lab on a Chip* **7**, 1681–1688 (2007)
9. Gerber, R., Takayasu, M., Friedlaender, F. J.: Generalization of HGMS theory – the capture of ultrafine particles. *IEEE Transactions on Magnetics* **19** (5), 2115–2117 (1983)
10. Erb, R. M., Sebba, D. S., Lazarides, A. A., Yellen, B. B.: Magnetic field induced concentration gradients in magnetic nanoparticle suspensions: Theory and Experiment. *Journal of Applied Physics*. **103** (6), 063916–5 (2008)
11. Adair, R. K.: Constraints on Biological Effects of Weak Extremely-Low-Frequency Electromagnetic Fields. *Physical Review A* **43** (2), 1039–1048 (1991)
12. Grahl, T., Markl, H.: Killing of microorganisms by pulsed electric fields. *Applied Microbiology and Biotechnology* **45** (1–2), 148–157 (1996)
13. Peterman, E. J. G., Gittes, F., Schmidt, C. F.: “Laser-induced heating in optical traps” *Biophysical Journal* **84** (2), 1308–1316 (2003)
14. Friedman, G., Yellen, B.: Magnetic separation, manipulation and assembly of solid phase in fluids. *Current Opinion in Colloid and Interface Science* **10** (3–4), 158–166 (2005)
15. Ito, A., Shinkai, M., Honda, H., Kobayashi, T.: Medical application of functionalized magnetic nanoparticles. *Journal of Bioscience and Bioengineering* **100** (1), 1–11 (2005)
16. Gijs, M. A. M.: Magnetic bead handling on-chip: new opportunities for analytical applications. *Microfluidics and Nanofluidics* **1** (1), 22–40 (2004)
17. Gillies, G. T., Ritter, R. C., Broaddus, W. C., Grady, M. S., Howard, M. A., McNeil, R. G.: Magnetic manipulation instrumentation for medical physics research. *Review of Scientific Instruments* **65** (3), 533–562 (1994)
18. Xia, N., Hunt, T. P., Mayers, B. T., Alsborg, E., Whitesides, G. M., Westervelt, R. M., Ingber, D. E.: Combined microfluidic-micromagnetic separation of living cells in continuous flow. *Biomedical Microdevices* **8** (4), 299–308 (2006)
19. Hancock, J. P., Kemshead, J. T.: A rapid and highly selective approach to cell separations using an immunomagnetic colloid. *Journal of Immunological Methods* **164** (1), 51–60 (1993)
20. Heermann, K. H., Hagos, Y., Thomssen, R.: Liquid-phase hybridization and capture of Hepatitis-B virus-DNA with magnetic beads and fluorescence detection of PCR product. *Journal of Virological Methods* **50** (1–3), 43–57 (1994)
21. Pipper, J., Inoue, M., Ng, L. F. P., Neuzil, P., Zhang, Y., Novak, L.: Catching bird flu in a droplet. *Nature Medicine* **13** (10), 1259–1263 (2007)
22. Kim, S. K., Devine, L., Angevine, M., DeMars, R., Kavathas, P. B.: Direct detection and magnetic isolation of Chlamydia trachomatis major outer membrane protein-specific CD8(+) CTLs with HLA class I tetramers. *Journal of Immunology* **165** (12), 7285–7292 (2000)

23. De Palma, R., Reekmans, G., Liu, C. X., Wirix-Speetjens, R., Laureyn, W., Nilsson, O., Lagae, L.: Magnetic bead sensing platform for the detection of proteins. *Analytical Chemistry* **79** (22), 8669–8677 (2007)
24. Vatta, L. L., Sanderson, R. D., Koch, K. R.: Magnetic nanoparticles: Properties and potential applications. *Pure and Applied Chemistry* **78** (9), 1793–1801 (2006)
25. Okuno, M., Hamaguchi, H. O., Hayashi, S.: Magnetic manipulation of materials in a magnetic ionic liquid. *Applied Physics Letters* **89** (13), 132506 (2006)
26. Halverson, D., Kalghatgi, S., Yellen, B., Friedman, G.: Manipulation of nonmagnetic nanobeads in dilute ferrofluid. *Journal of Applied Physics* **99** (8), 08P504 (2006)
27. Erb, R. M., Yellen, B. B.: Model of detecting nonmagnetic cavities in ferrofluid for biological sensing applications. *IEEE Transactions on Magnetics* **42** (10), 3554–3556 (2006)
28. Erb, R. M., Yellen, B. B.: Concentration gradients in mixed magnetic and nonmagnetic colloidal suspensions. *Journal of Applied Physics* **103** : 07A312–3 (2008)
29. Jones, T. B., *Electromechanics of Particles*. Cambridge University Press, New York (1995)
30. Huang, Y., Pethig, R.: Electrode design for negative dielectrophoresis. *Measurement Science and Technology* **2** (12), 1142–1146 (1991)
31. Shkel, Y. M., Klingenberg, D. J.: Magnetorheology and magnetostriction of isolated chains of nonlinear magnetizable spheres. *Journal of Rheology* **45** (2), 351–368 (2001)
32. Ivanov, A. O., Wang, Z. W., Holm, C.: Applying the chain formation model to magnetic properties of aggregated ferrofluids. *Physical Review E* **69** (3), 031206 (2004)
33. Philipse, A. P., Maas, D.: Magnetic colloids from magnetotactic bacteria: Chain formation and colloidal stability. *Langmuir* **18** (25), 9977–9984 (2002)
34. Einstein, A.: The theory of the Brownian Motion. *Annalen Der Physik* **19** (2), 371–381 (1906)
35. Boal, A. K., Frankamp, B. L., Uzun, O., Tuominen, M. T., Rotello, V. M.: Modulation of spacing and magnetic properties of iron oxide nanoparticles through polymer-mediated ‘bricks and mortar’ self-assembly. *Chemistry of Materials* **16** (7), 3252–3256 (2004)
36. Lim, J. K., Tilton, R. D., Eggeman, A., Majetich, S. A.: Design and synthesis of plasmonic magnetic nanoparticles. *Journal of Magnetism and Magnetic Materials* **311** (1), 78–83 (2007)
37. Sun, S., Murray, C. B., Weller, D., Folks, L., Moser, A.: Monodisperse FePt Nanoparticles and Ferromagnetic FePt Nanocrystal Superlattices. *Science* **287** (5460), 1989 (2000)
38. Odenbach, S., Liu, M.: Invalidation of the Kelvin force in ferrofluids. *Physical Review Letters* **86** (2), 328–331 (2001)
39. Bowen, W. R., Liang, Y., Williams, P. M.: Gradient diffusion coefficients – theory and experiment. *Chemical Engineering Science* **55** , 2359–2377 (2000)
40. Israelachvili, J. N., *Intermolecular and Surface Forces*. Academic Press, New York (1985)
41. Kelland, D. R., Hiresaki, Y., Friedlaender, F. J., Takayasu, M.: Diamagnetic particle capture and mineral separation. *IEEE Transactions Magnetics* **17** , 2813–2815 (1981)
42. Ferreira, H. A., Graham, D. L., Freitas, P. P., Cabral, J. M. S.: Biotdetection using magnetically labeled biomolecules and arrays of spin valve sensors (invited). *Journal of Applied Physics* **93** (10), 7281–7286 (2003)
43. Baselt, D. R., Lee, G. U., Natesan, M., Metzger, S. W., Sheehan, P. E., Colton, R. J.: A biosensor based on magnetoresistance technology. *Biosens Bioelectron* **13** , 731–739 (1998)
44. Ivanov, A. O., Kantorovich, S. S., Reznikov, E. N., Holm, C., Pshenichnikov, A. F., Lebedev, A. V., Chremos, A., Camp, P. J.: Magnetic properties of polydisperse ferrofluids: A critical comparison between experiment, theory, and computer simulation. *Physical Review E* **75** (6), 061405 (2007)
45. Bradbury, A., Menear, S., Chantrell, R. W.: A Monte-Carlo calculation of the magnetic-properties of a ferrofluid containing interacting polydispersed particles. *Journal of Magnetism and Magnetic Materials* **54** (7), 745–746 (1986)
46. Brown, W. F.: Thermal fluctuations of a single-domain particle. *Physical Review* **130** (5), 1677–1686 (1963)
47. Madou, M. J., *Fundamentals of Microfabrication*. CRC Press, New York (2002)
48. Morse, P. M., Feshbach, H., *Methods of theoretical physics*. McGraw-Hill, New York (1953)

49. McNaughton, B. H., Kehbein, K. A., Anker, J. N., Kopelman, R.: Sudden breakdown in linear response of a rotationally driven magnetic microparticle and application to physical and chemical microsensing. *The Journal of Physical Chemistry*. **110** , 18958–18964 (2006)
50. Bonin, K., Kourmanov, B., Walker, T. G.: Light torque nanocontrol, nanomotors and nanorockers. *Optics Express*. **10** , 984–989 (2002)
51. Reichhardt, C., Nori, F.: Phase locking, devil's staircases, Farey trees, and Arnold tongues in driven vortex lattices with periodic pinning. *Physical Review Letters*. **82** , 414 (1999)
52. Fermigier, M., Gast, A.: Structure evolution in a paramagnetic latex suspension. *Journal of Colloid and Interface Science*. **154** , 522–539 (1992)
53. Promislow, J. H. E., Gast, A. P., Fermigier, M.: Aggregation kinetics of paramagnetic colloidal particles. *The Journal of Physical Chemistry*. **102** , 5492–5498 (1995)
54. Hagenbuchle, M., Liu, J.: Chain formation and chain dynamics in a dilute magnetorheological fluid. *Applied Optics* **36** (30), 7664–7671 (1997)
55. Yellen, B., Friedman, G., Feinerman, A.: Analysis of interactions for magnetic particles assembling on magnetic templates. *Journal of Applied Physics* **91** (10), 8552–8554 (2002)
56. Son, H.S., R.M. Erb, B. Samanta, V.M. Rotello, and B.B. Yellen, *Magnetically actuated assembly of anisotropic micro- and nano-structures*. Nature, 2008 (in submission): 1–4.
57. Camp, P. J., Allen, M. P., Hard ellipsoid rod-plate mixtures: Onsager theory and computer simulations. *Physica A* **229** (3–4), 410–427 (1996)
58. San Martin, S. M., Sebastian, J. L., Sancho, M., Miranda, J. M.: A study of the electric field distribution in erythrocyte and rod shape cells from direct RF exposure. *Physics in Medicine and Biology*. **48** (11), 1649–1659 (2003)
59. Kao, K.C.: Some electromechanical effects on dielectrics. *British Journal of Applied Physics*. **12** , 629–632 (1961)
60. Stratton, J.A., *Electromagnetic Theory*. McGraw-Hill, New York (1941)
61. Ooi, C., R.M. Erb, and B.B. Yellen, On the controllability of nanorod alignment in magnetic fluids. *Journal of Applied Physics*. 2008. **103** (7): 07E910-3.
62. Crawford, G. P., OndrisCrawford, R. J., Doane, J. W.: Systematic study of orientational wetting and anchoring at a liquid-crystal-surfactant interface. *Physical Review E*. **53** (4), 3647–3661 (1996)
63. Ooi, C., R.M. Erb, and B.B. Yellen, On the controllability of nanorod alignment in magnetic fluids. *Journal of Applied Physics*. 2008. **103** (7): 07E910-3.
64. Tanase, M., Felton, E. J., Gray, D. S., Hultgren, A., Chen, C. S., Reich, D. H., Assembly of multicellular constructs and microarrays of cells using magnetic nanowires. *Lab on a Chip*. **5** (6), 598–605 (2005)
65. Truskey, G. A., Yuan, F., Katz, D. F., *Transport Phenomena in Biological Systems*. Pearson Education, Inc., Upper Saddle River (2004)
66. Meyer, M., Le Ru, E. C., Etchegoin, P. G.: Self-limiting aggregation leads to long-lived metastable clusters in colloidal solutions. *The Journal of Physical Chemistry B*. **110** (12), 6040–6047 (2006)
67. Ivanov, A. O., Kuznetsova, O. B.: Magnetic properties of dense ferrofluids: An influence of interparticle correlations. *Physical Review E*. **64** (4), 041405–12 (2001)
68. da Silva, M. F., Neto, A. M. F.: Optical- and x-ray-scattering studies of ionic ferrofluids of MnFe_2O_4 , $\gamma\text{-Fe}_2\text{O}_3$, and CoFe_2O_4 . *Physical Review E*. **48** (6), 4483–4491 (1993)
69. Weber, J. E., Goni, A. R., Pusiol, D. J., Thomsen, C.: Raman spectroscopy on surfactated ferrofluids in a magnetic field. *Physical Review E*. **66** (2), 021407-06 (2002)
70. Kruse, T., Krauthäuser, H. G., Spanoudaki, A., Pelster, R.: Agglomeration and chain formation in ferrofluids: Two-dimensional x-ray scattering. *Physical Review B*. **67** (9), 094206-10 (2003)
71. Yellen, B. B., Fridman, G., Friedman, G.: Ferrofluid lithography. *Nanotechnology* **15** (10), S562–S565 (2004)
72. Yellen, B. B., Friedman, G., Barbee, K. A.: Programmable self-aligning ferrofluid masks for lithographic applications. *IEEE Transactions on Magnetics*, **40** (4), 2994–2996 (2004)

Chapter 20

Applications of Magnetic Nanoparticles in Biomedicine

Carlos Bárcena, Amandeep K. Sra, and Jinming Gao

Abstract In recent years, magnetic nanoparticles have played an increasing role in biomedical applications and have been the subject of extensive research investigations. Physical properties, including nanoparticle size, composition, and surface chemistry, vary widely and influence their biological and pharmacological properties and, ultimately, their clinical applications. Among different magnetic nanoparticles, superparamagnetic iron oxide nanoparticles (SPIOs) were found nontoxic and used as magnetic resonance imaging (MRI) contrast agents, in molecular and cellular imaging applications. SPIOs are used in detection of liver metastases, metastatic lymph nodes, and inflammatory and/or neural degenerative diseases. In addition, drug delivery via magnetic targeting, hyperthermia, and labeling/tracking of stem cells have also been explored as potential therapeutic options.

20.1 Introduction

The use of magnetic particles in medicine has long been recorded since ancient times [69]. Often regarded as the first philosopher in the Greek tradition, Thales of Miletus (ca. 624–547 BC) believed man and magnet were somehow connected and each possessed a soul. Hippocrates of Kos (ca. 460–370 BC), father of medicine, made medical references to magnetism. He used the styptic iron oxides magnetite and hematite to stop bleeding and control hemorrhage. In the first century, Roman scholar Pliny the Elder (23–79 AD) described the treatment of burns with pulverized magnets.

In more modern times, medical uses for magnets and magnetic particles have spread to numerous fields including dentistry, cardiology, neurology, oncology, and

J. Gao (✉)

Harold C. Simmons Comprehensive Cancer Center, University of Texas Southwestern Medical Center at Dallas, Dallas TX 75390; Department of Chemistry, University of Texas at Dallas, Richardson, TX 75080, USA

e-mail: jinming.gao@utsouthwestern.edu

radiology. In dentistry, magnets are commonly applied to aid in the retention of oral prostheses [50]. Magnetic intrauterine devices for use in contraception have recently been developed [121]. Purification of healthy bone marrow cells from tumor cell with magnetic microspheres was established *ex vivo* [184, 185]. Moving from the macroscale to the nanoscale, magnetic nanoparticles have found increasing use in biomedical applications. Working in unison, strong local magnets can be used to target specific organs where magnetic nanoparticles can accumulate in targeted sites for imaging and/or therapy. In magnetic resonance imaging (MRI), superparamagnetic iron oxide (SPIO) nanoparticles are used as negative contrast agents to enhance imaging contrast. Furthermore, these SPIO nanoparticles have been used as imaging probes for cell labeling and tracking throughout the human body.

Unlike bulk ferromagnetic materials, SPIO nanoparticles have no net magnetic moment until they are placed in an external magnetic field [30]. Quantum size effects and the large surface area of magnetic nanoparticles dramatically affect their magnetic properties such as exhibition of superparamagnetic phenomena and quantum tunneling effect of magnetization [61]. Therefore, based on their unique physical, chemical, thermal, and mechanical properties, SPIOs demonstrate great potential for various biomedical applications.

20.2 Nanoparticle Classification

Magnetic nanoparticles can be classified in a variety of categories based on composition and physical or biological properties. Typically, most magnetic nanoparticles for biomedical applications are comprised of iron oxide-based nano-crystalline structures of magnetite (Fe_3O_4) and/or maghemite ($\gamma\text{-Fe}_2\text{O}_3$) encased or coated with polysaccharide, organic or polymeric stabilizers, or inorganic coatings. Recently, however, novel nanoparticles with advanced magnetic properties are being actively pursued for potential biomedical applications. One such class of materials is transition metal ferrites (MFe_2O_4) nanoparticles, where M is a divalent metal ion, while others are metal alloys such as iron cobalt (FeCo) [164] or iron platinum (FePt) [42] nanoparticles.

In addition to composition, size also plays a critical role in determining the magnetic and biological properties of these nanoparticles. Focusing on clinically relevant nanoparticles, SPIO hydrodynamic diameters can vary widely depending on the type of surface modification, but the nanoparticles themselves can range from 3 to 1,000 nm in diameter. In general, SPIOs are categorized based on their overall diameter (iron oxide core and hydrated coating) including [179, 195] “large” oral SPIO agents (300 nm–3.5 μm), standard SPIO (SSPIO, 60–150 nm), ultra-small SPIO (USPIO, 10–40 nm) [198], a subset of USPIO named monocrystalline iron oxide nanoparticles (MION, 10–30 nm) to emphasize the single crystal nature of the core [165], and very small SPIO (VSOP, 7 nm) [178]. Other acronyms include cross-linked iron oxide (CLIO) [207], monodisperse iron oxide nanoparticle (variation of MION), and magnetism-engineered iron oxide (MEIO) [114]; all fall in the initial categories above.

20.3 Syntheses of SPIO Nanoparticles

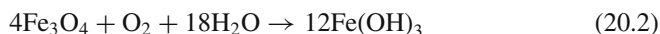
Several methods are generally used to produce iron oxide nanoparticles. Historically, physical grinding of bulk magnetite with a stabilizing surfactant produced the first documented ferrofluids [136]. However, for biomedical applications, several chemical methods were established to synthesize SPIOs. Some of the more commonly used methods are co-precipitation, microemulsion, and thermal decomposition, although numerous other methods exist. The main challenge is to produce and reproduce monodisperse SPIO without any complex purification steps. Ideally, the synthetic scheme should also yield highly crystalline nanoparticles with a high saturation magnetization (M_s).

20.3.1 Co-precipitation

The most common method for producing SPIO nanoparticles is a one-step co-precipitation reaction of Fe^{2+} and Fe^{3+} salts in an alkaline solution [22, 26, 40, 63, 67, 78, 97, 101, 115, 132, 177, 205]. The precipitate is recovered through magnetic isolation or centrifugation. The overall reaction may be written as shown in Eq. (20.1) [67, 101].



According to the thermodynamics for this reaction, a complete precipitation of Fe_3O_4 should be expected between pH 7.5 and 14, while maintaining a molar ratio of $\text{Fe}^{2+}:\text{Fe}^{3+}$ at 1:2 under a nonoxidizing, oxygen-free environment. Otherwise, Fe_3O_4 may also be oxidized to $\text{Fe}(\text{OH})_3$ (Eq. 20.2).



This dramatically affects the physical and chemical properties of the nanoparticles. In order to prevent possible oxidation and aggregation, Fe_3O_4 nanoparticles are usually coated with organic or inorganic molecules during the precipitation process. The resulting precipitate is reddish brown (maghemite) to brownish black (magnetite) in color, depending on the oxidation state of iron. Maghemite is the ferrimagnetic cubic form of $\text{Fe}(\text{III})$ oxide and differs from the inverse spinel structure of magnetite through vacancies on the cation sublattice. However, both possess very similar lattice parameters at 8.346 and 8.396 Å for maghemite and magnetite [27, 179], respectively, making chemical identification very difficult with techniques such as x-ray diffraction. To prevent possible oxidation, the synthesis is carried out in an inert environment by bubbling inert gas through the reaction solution.

Although co-precipitation methods are widely used due to its simplicity and ability to be scaled up for large reaction, the nanoparticles produced are fairly polydisperse. Another disadvantage of these bulk solution syntheses is that the pH value of the reaction mixture needs to be adjusted during both the synthesis and the

purification steps. Advancement in the use of magnetic particles for biomedical applications depends on new synthetic methods with better control over size distribution, magnetic properties, and particle surface characteristics. As a result, other methods have been developed to synthesize nanoparticles with more uniform dimensions.

20.3.2 Microemulsion

A microemulsion is a thermodynamically stable isotropic mixture of two immiscible liquids and surfactant [141]. Microemulsions may be classified as water-in-oil (w/o) or oil-in-water (o/w) emulsion, depending on the dispersed and continuous phases. In both cases, the dispersed phase consists of monodispersed droplets ranging from 10 to 100 nm in diameter. The main advantage is that microemulsions provide compartmentalized liquid structures with high surface area. These structures then serve as versatile media for chemical reactions, where the resulting nanoparticles of desired size reflect the shape and the environment of the aqueous/organic droplets [141]. For biomedical applications, the water-in-oil approach is a more common technique for preparing highly monodisperse iron oxide nanoparticles.

The general strategy involves enclosing “nanodroplets” of aqueous metal salts in a surfactant coat that separates them from the surrounding organic solution to form reverse micelles [49, 83, 116, 117, 120, 141, 162, 193]. An alkaline solution precipitates and oxidizes the SPIO within the micelle. For example, ferric and ferrous salts are mixed with dioctyl sulfosuccinate sodium salt (AOT) and lecithin (phosphatidylcholine) in an organic hydrocarbon phase. After centrifugation to remove impurities, ammonium hydroxide/AOT solution is added to the metal/AOT mixture with stirring. The metal hydroxides are precipitated and are oxidized to ferrite within the nanosized micelle. After stirring to achieve complete conversion, the solvent is removed and the nanoparticles are re-dispersed in water (Fig. 20.1). The size of the synthesized nanoparticles is relatively uniform and can be varied from 3 to 20 nm by varying the iron salt or the surfactant concentrations.

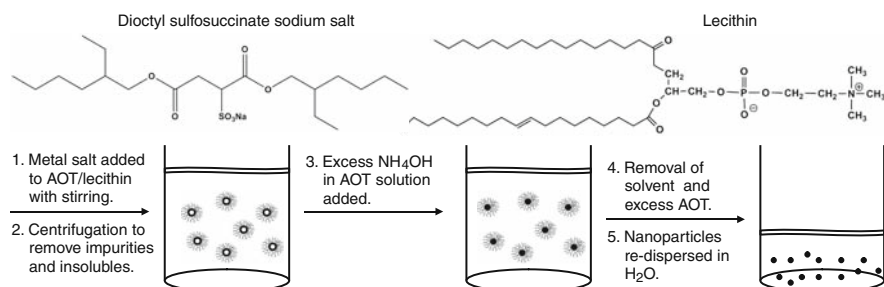


Fig. 20.1 Scheme for preparing monodisperse SPIO inside w/o microemulsion droplets

20.3.3 Thermal Decomposition

More recently, organic solution-phase decomposition of iron precursors at high temperature has been used in iron oxide nanoparticle synthesis. Advances in the synthesis process has demonstrated that direct decomposition of iron cupferron complex (FeCup_3 , Cup: *N*-nitrosophenylhydroxylamine) [154] or decomposition of iron pentacarbonyl ($\text{Fe}(\text{CO})_5$) [80, 139] followed by oxidation can lead to high-quality monodisperse $\gamma\text{-Fe}_2\text{O}_3$ nanoparticles. The preparation of metal cupferron complexes is based on the precipitation of a metal salt from aqueous solution at a specific pH with cupferron. The synthesis of highly crystalline and monodisperse $\gamma\text{-Fe}_2\text{O}_3$ nanoparticles also result from high temperature aging of the iron–oleic acid metal complex. This complex was prepared by thermal decomposition of $\text{Fe}(\text{CO})_5$ in the presence of oleic acid. The resulting iron nanoparticles were transformed into monodisperse $\gamma\text{-Fe}_2\text{O}_3$ by controlled mild oxidation using trimethylamine oxide. By controlling experimental parameters, the particle size can be varied from 4 to 16 nm. However, these synthetic procedures only form $\gamma\text{-Fe}_2\text{O}_3$, not the more desired Fe_3O_4 .

Sun et al. [172, 173] for the first time demonstrated that high-temperature solution phase reaction of iron(III) acetylacetonate, $\text{Fe}(\text{acac})_3$, with 1,2-hexadecanediol in the presence of oleic acid and oleylamine can be used to make monodisperse magnetite (Fe_3O_4) nanoparticles under 20 nm. This procedure creates highly crystalline nanoparticles with high M_s (16 nm particles, ~ 83 emu/g) approaching 84.5 emu/g for commercial magnetite fine powder. In addition, this process can be readily extended to the synthesis of other types of ferrite (MFe_2O_4) nanoparticles, where M is a divalent metal ion (e.g., Mn^{2+} , Fe^{2+} , Co^{2+} , Ni^{2+} , Cu^{2+} , Mg^{2+} , Zn^{2+} , Cd^{2+}) [81, 95, 114, 173, 210]. The benefit of these mixed ferrite structures would be an increase in M_s due to the increased moment of the M^{2+} ion. These results were shown by Cheon et al. [114] who synthesized NiFe_2O_4 , CoFe_2O_4 , FeFe_2O_4 , and MnFe_2O_4 and observed an increase in the transverse relaxivity coefficient, a measure of MR contrast effect, due to the increase in M_s . However, one of the major challenges for the Sun method is that the resulting nanoparticles from the initial reaction are subsequently used as seed crystals to grow larger magnetite nanoparticles, which makes scale-up for mass production tedious and possibly problematic. In addition, the cost of the starting materials for this reaction is relatively high at today's prices.

To address this issue, Hyeon et al. [138] developed an economical mass-production method to produce magnetic nanoparticles using inexpensive and non-toxic metal salts as reactants. This relatively simple procedure is shown in Fig. 20.2 (sodium-oleate = $\text{CH}_3(\text{CH}_2)_7\text{CH}=\text{CH}(\text{CH}_2)_7\text{COONa}$).

In this reaction, an iron–oleate complex is first made by reacting iron chloride and sodium oleate. The iron–oleate complex along with oleic acid in a high boiling point solvent is then heated to 320°C . The nanoparticles are then washed and separated by centrifugation to provide monodispersed SPIO nanoparticles.

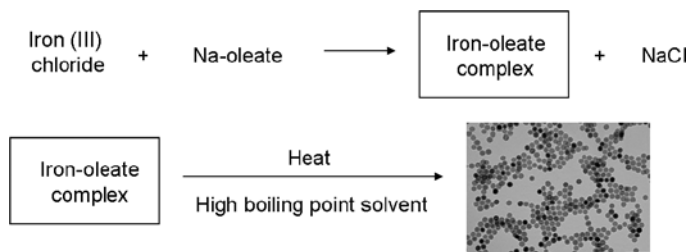


Fig. 20.2 Scheme for the mass production of SPIO (scale bar = 100 nm)

20.3.4 Alternative Methods

Other methods that exist for the controlled syntheses of SPIO particles include ultrasound sonication and spray and laser pyrolysis. During ultrasound sonication, stable ferromagnetic colloids of iron are formed using high-intensity ultrasound to sonchemically decompose volatile organometallic compounds. Volatile organometallic precursors, such as $\text{Fe}(\text{CO})_5$, inside the cavitating bubble are decomposed in the presence of a stabilizer to create a nanosized iron colloid. The collapse of bubbles generates localized hot spots with transient temperatures of approximately 5000 K which induce particle formation [174]. In spray pyrolysis, a solution is sprayed into a series of reactors where the solute condenses as the solvent evaporates. Here in an organic compound, the Fe ions are reduced to a mixture of Fe^{2+} and Fe^{3+} ions, leading to SPIO formation [38, 122]. Pure $\gamma\text{-Fe}_2\text{O}_3$ particles are prepared by a continuous wave CO_2 laser-induced pyrolysis of $\text{Fe}(\text{CO})_5$ vapor in an oxidizing atmosphere [188]. This synthesis method initiates and sustains a chemical reaction. Above a certain pressure and laser power, a critical concentration of product nuclei is formed in the reaction zone. Finally, another synthetic route is a layer-by-layer deposition method [48]. Chemisorption of ions allows shells or nanoparticle cores around existing particles to form by repeated submersion of a substrate or colloidal template in solution of oppositely charged polyelectrolytes.

20.4 Surface Modifications of Magnetic Nanoparticles

Pristine magnetic SPIOs are not very useful in practical applications due to their tendency to form aggregates. Also, aggregation may result in alteration of magnetic properties. Therefore, a suitable stabilizer coating is required to overcome this limitation. Stabilizers such as organic molecules, surfactants, or polymers are often added during or after synthesis to prevent aggregation of the SPIOs. However, one of the major issues that need to be addressed is the stability of these nanoparticles in a physiological aqueous environment, and the surface kinetics play a major role in this respect.

Typically, SPIOs are synthesized by two basic methodologies. In the first method, bare SPIOs are synthesized by addition of concentrated base to di- and trivalent

Fe salt solution. These bare SPIOs can then be coated in monomer and polymers through nonspecific adsorption following their purification to make them more biocompatible. Alternatively, the stabilizers can be introduced during the co-precipitation steps to prevent aggregation of the nanoscale particulate. High-temperature decomposition polyol synthesis of SPIO in the presence of fatty acids as the stabilizers yields highly crystalline and monodispersed nanoparticles. However, these as-synthesized nanoparticles are water insoluble due to the hydrophobic ligands. For biomedical applications, it is necessary to render these nanoparticles hydrophilic as the body recognizes hydrophobic particles as foreign and are rapidly taken up by the mononuclear phagocytic system (MPS) [35, 111]. Thus the goal of surface modification is to make the nanoparticles unrecognizable by the MPS and to guide them to the desired site.

20.4.1 Organic and Polymeric Stabilizers

20.4.1.1 Organic Stabilizers

Several studies have dealt with a variety of methodologies including ligand exchange, phosphine oxide polymers, and dendrons to improve the stability of SPIOs in aqueous solutions. The ligand exchange method involves adding an excess of ligand to the nanoparticle solution to displace the original ligand on the nanoparticles surface. Cheon et al. [91] have demonstrated the use of a ligand exchange method using *meso*-2,3-dimercaptosuccinic acid (DMSA). The DMSA first forms a stable coating through its carboxylic chelate bonding, and further stabilization is attained through the formation of disulfide cross-linkages between the ligands. The remaining free thiol groups are used for the attachment of target-specific antibodies. They have reported conjugation of water soluble SPIOs with a cancer-targeting antibody such as Herceptin[®] which specifically binds to the HER2/neu marker over-expressed in breast and ovarian cancer. Caruso et al. [58] demonstrated the transfer of various metallic nanoparticles from toluene to water using 4-(dimethyl-amino) pyridine (DMAP).

Wang reported the design and synthesis of hydrophilic organic dendron ligands for stabilizing high-quality nanocrystals in aqueous solutions. Oleic acid-stabilized monodispersed nanoparticles of Fe oxides were surface modified through the formation of an inclusion complex between surface-bound surfactant molecules and α -cyclodextrin (α -CD). After the modification, the nanoparticles can be transferred from hydrophobic solvents, such as hexane, to α -CD aqueous phase. Their efficiency depends on the initial α -CD concentration [196].

20.4.1.2 Polymeric Stabilizers

Several synthetic and natural polymers such as dextran, polyethylene glycols (PEGs), and polyvinylpyrrolidone are known to be biocompatible and promote monodispersity of SPIOs in aqueous medium (Table 20.1). Hasegawa and Hokkoku

proposed a typical manufacturing method for magnetic iron oxide particles coated with alkali-treated dextran [73]. Their method has been improved and technically modified. Many coating materials have been proposed, such as dextran, starch, arabinogalactan, glycosaminoglycan, and carboxydextran. Dextran-coated commercial products include Feridex[®]/Endorem[®], Combidex[®]/Sinerem[®], MION, and CLIO [35, 43, 111]. The presence of aminated dextran on the surface provides a platform for further chemical manipulations.

Surface stabilization with PEG derivatives significantly increases blood circulation time by preventing opsonization and thus avoids MPS uptake [35, 43, 111]. Additional advantages include easy excretion by the kidney; nonimmunogenic and nonantigenic properties. Nonionic block copolymer composed of PEO–PPO–PEO, such as poloxamers, has received attention due to low toxicity, non-irritation, and good performance in emulsification [143]. When the nanoparticles are stabilized with poloxamer in the aqueous phase, the PEO segment forms a “hairy” structure that cloaks the modified nanoparticles from the immune systems.

Muhammed et al. [143] reported the use of Pluronic F127 (PF127) – an ABA – type triblock copolymer consisting of poly(propylene oxide) (PPO) and poly(ethylene oxide) (PEO) to transfer the hydrophobic SPIOs coated with oleic acid to water. The PPO block associates with the alkyl tail of the oleic acid through hydrophobic interactions, while the two appending PEO chains solubilize the particles in aqueous medium. Recently, Lee et al. [112] reported the fabrication of thermal cross-linked SPION (TCL-SPION), using Si-OH containing copolymer. The carboxyl TCL-SPION was converted to an amine-modified SPION and finally to Cy5.5 TCL-SPION which even in the absence of any targeting ligand could be used efficiently in dual in vivo cancer imaging. Pellegrino et al. [140] developed a general methodology by decorating hydrophobic nanocrystals with a hydrophilic polymer shell by exploiting the nonspecific hydrophobic interactions between the alkyl chains of poly(maleic anhydride alt-1-tetradecene) and the nanocrystal surfactant molecules. Addition of bis(6-aminoethyl)amine results in the cross-linking of the polymer chains around each nanoparticles.

Our group has recently reported the use of lipid and polymeric micelles to solubilize SPIOs in water. The lipid micelles from 1,2-distearoyl-*sn*-glycero-3-phosphoethanolamine-*N*-[methoxy(polyethylene glycol)] (DSPE-PEG) lipids formed single SPIO-loaded micelles. The polymeric poly(ϵ -caprolactone)-*b*-poly(ethylene glycol) (PCL-*b*-PEG) copolymers resulted in clustered SPIO nanoparticles [1].

20.4.2 Inorganic Molecules

Metal core shell type SPIOs with inner iron oxide core and outer metallic shell of inorganic materials have been investigated by a growing number of researchers. Typical shell materials include silica, gold, and graphite. Silica-based core-shell nanoarchitectures composed of magnetic iron oxide cores and amorphous silica

shells are typically synthesized through a sol–gel approach. A good control of the silica shell thickness (10–100 nm) can be achieved by adjusting the silane concentration. A significant advantage of the silica shell is related to the use of well-known conjugation chemistry that allows covalent bonding of various chemical or biological species onto the silica surface. Arruebo et al. [19] proved this concept by covalent coupling of the anti-human chorionic gonadotropin (anti-hCG) antibody to the silica shell of the superparamagnetic nanoparticles, yielding potential targeted contrast agents for MRI. Zhang et al. [211] synthesized USPIO particles with silica and alkoxy silane coatings that showed high T_2 relaxivities, and were intensely internalized in immortalized progenitor cells, making them suitable for MR cell-labeling and cell-tracking experiments.

Cheon et al. [113] reported the development of the next-generation nanoprobe by fusing multiple fluorescent dyes and multiple magnetic nanoparticles into a single nanoprobe that provides superior fluorescence and MR imaging capabilities through the synergistic enhancement of its respective components. “Core-satellite” structured dual functional nanoparticles comprised of a dye-doped silica “core” (rhodamine-dye-doped silica) and multiple “satellites” of magnetic nanoparticles (Fe_3O_4) were synthesized and their utilization demonstrated as simultaneous optical and MR imaging of neuroblastoma cells expressing polysialic acids (PSAs).

One of the major challenges of use of magnetic nanoparticles in biomedical applications is the lack of surface tunability. Coating the magnetic particles with an Au shell provides an intriguing class of biomaterials to overcome such an obstacle. Because of the well-established Au–S surface chemistry and biological reactivity, Au can impart the magnetic particles with the desired chemical and/or biomedical properties. The coating also renders the magnetic nanoparticles with plasmonic properties. This makes the core/shell composite nanoparticles extremely interesting for magnetic, optical, and biomedical applications. Sun et al. [209] have synthesized core/shell structured $\text{Fe}_3\text{O}_4/\text{Au}$ and $\text{Fe}_3\text{O}_4/\text{Au}/\text{Ag}$ nanoparticles in aqueous solution and room temperature reaction conditions. The control on shell thickness allows the tuning of plasmonic properties of the core/shell nanoparticles to be either red-shifted (to 560 nm) or blue-shifted (to 501 nm). Zhong also demonstrated that the magnetically active iron oxide core and thiolate-active Au shell is a viable candidate for exploiting the Au surface protein-binding reactivity for bioassay and the iron oxide core magnetism for magnetic bioseparation [137]. Choa reported the synthesis of $\text{Au}/\text{Fe}_3\text{O}_4$ nanocomposite and the immobilization of glutathione (GSH) onto the $\text{Au}/\text{Fe}_3\text{O}_4$ nanocomposite thus demonstrating the possibility of using these nanoparticles in applications involving the separation and purification of biomolecules [102].

Dai and coworkers reported a novel use of a single graphitic shell coating of FeCo magnetic nanoparticles synthesized using chemical vapor deposition method nanocrystals [164]. The nanocrystals exhibit ultra-high saturation magnetization, r_1 and r_2 relaxivities, and high optical absorbance from the graphitic shell in the near-infrared region. Mesenchymal stem cells are able to internalize these nanoparticles, showing high negative-contrast enhancement in MRI.

20.5 Pharmacokinetics and Toxicology

Pharmacokinetics (absorption, distribution, metabolism, excretion) and toxicity (acute and chronic, mutagenicity) of SPIO are dependent on a number of factors including concentration (dose), hydrodynamic diameter, coating agent, charge, and method of delivery. Size differences are reflected not only in MR relaxivity differences (ratio of r_2/r_1) but also by significant differences in blood half life and distribution. As described earlier, SPIO can be coated with a myriad of surface coatings, all affecting their characteristics and distribution.

Ideal SPIO contrast agents have diameters no larger than 200 nm (SPIO plus biodegradable coating) because this prolongs blood half life and extends the particle circulation times from minutes to hours allowing SPIO to accumulate or target a site before being cleared by the body [64, 170, 202, 212]. The blood half life of all iron oxide nanoparticles is dependent on dose as well as on their hydrodynamic volume. Blood half life of SPIO nanoparticles administered to patients can vary from minutes to greater than 24 h, depending on particle size (Table 20.1) [43]. The spleen (sinusoidal lining cells) filters particles greater than 200 nm in diameter including SPIOs. Below 5–6 nm, particles are rapidly removed by extravasation and renal clearance [41]. When comparing the SPIO with the same coating material, USPIO is less prone to liver uptake as opposed to SPIO due to their small size (e.g., ferumoxtran-10 vs. ferumoxides and SHU 555 C vs. SHU 555 A).

To date, studies have shown that iron oxide nanoparticles are nontoxic and have minimal impact on cell viability and function [7, 14, 16, 17, 43, 66, 70, 125, 135, 145, 171]. SPIOs share their specific uptake by macrophages through phagocytosis. In a study by Metz et al. [127], the capacity of human monocytes to phagocytose SPIO (Ferucarbotran) and USPIO (SHU 555 C) at different concentrations and incubation times was evaluated. The results showed no loss in cell viability and confirm spontaneous uptake of particulate contrast agent by a macrophage cell line. Monocytes are capable of ingesting large quantities of particulate SPIO by phagocytosis, with subsequent compartmentalization in secondary lysosomes within the cytoplasm. As opposed to other, non-phagocytic cells such as lymphocytes, monocytes do not need the aid of transfection agents for iron oxide internalization. A maximum iron oxide uptake up to 50 pg Fe/cell was measured without impairment of cell viability. In a different study [161], SPIO distribution and elimination were evaluated by double-labeling using ^{14}C and ^{59}Fe ferumoxtran-10 nanoparticles. In the end, it was shown ferumoxtran-10 is completely degraded in the macrophage lysosomal compartment within 7 days. After uptake by the macrophages, the dextran coating undergoes progressive degradation by intracellular dextranases and is almost exclusively eliminated in the urine (89% in 56 days). The iron contained in ferumoxtran-10 is incorporated into the body's iron stores and is progressively found in the red blood cells. Like endogenous iron, the radiolabeled ^{59}Fe is very slowly eliminated from the body. Similar rates of erythrocyte incorporation have been reported for radiolabeled ferritin, the physiological storage form of iron. In addition, similar behavior has also been described for ferumoxides [198]. Dextran-coated CLIO nanoparticles showed that iron incorporation did not affect cell viability,

differentiation, or proliferation of human hematopoietic cells [119]. Similarly, the influence of PEG-modified SPIO nanoparticles on human fibroblasts was studied [65]. The PEG-coated nanoparticles did not affect the cell adhesion behavior or morphology. In general, iron oxide nanoparticles coated in biodegradable coating appear to have no long-term toxicity and are safe for use.

In animal trials, pharmacokinetics and toxicology of AMI-25 (Endorem[®]/Feridex[®]) were evaluated by ⁵⁹Fe radiotracer in Sprague-Dawley rats and beagle dogs [197]. One hour after administration of AMI-25 to rats (18 μ mol Fe/kg; 1 mg Fe/kg), 82.6% of the administered dose was sequestered in the liver and 6.2% in the spleen. Peak concentrations of the ⁵⁹Fe radiotracer were found in the liver after 2 h and in the spleen after 4 h. ⁵⁹Fe slowly cleared from the liver (half life, 3 days) and the spleen (half life, 4 days). The iron was incorporated into hemoglobin of erythrocytes in a time-dependent fashion. Only minimal amounts of ⁵⁹Fe were detected in other tissue, such as the kidney, lung, and brain. The whole body clearance of ⁵⁹Fe was 20% after 14 days and 35% after 28 days with an extrapolated half life of whole body clearance of 45 days. Studies on acute toxicity revealed that AMI-25 had no lethal effect on the animals at the highest dose injected (3,000 μ mol Fe/kg), 150 times the dose proposed for MR imaging of the liver. Subacute toxicity studies revealed no effect on mortality, morbidity, body weight, or food consumption. The final conclusion was that AMI-25 is a fully biocompatible contrast agent.

Human clinical trials with AMI-25 were performed by Berlex Laboratories [25]. In this study, AMI-25 was administered to three, healthy adult male volunteers (dose = 0.56 mg/kg diluted in 100 mL of 5% dextrose and intravenously infused over 30 min). Bolus injections are usually not administered because of cardiovascular side effects and lumbar pain. For example, the amount of iron in a single dose is calculated to be 39.2 mg of iron for a 70 kg individual. This equates to less than 1/5 the amount of iron contained in one whole unit of blood. Normal liver contains approximately 0.2 mg of iron per gram, and total human iron stores amount to 3,500 mg. The total amount of iron oxide necessary for diagnostic imaging is small compared to the body's normal iron store. Chronic iron toxicity develops only after the liver iron concentration exceeds 4 mg of iron per gram [30]. Hypoglycemia may accompany liver dysfunction. Peak serum iron concentration was 5.5 μ g/mL and AMI-25 was completely cleared from the blood by 25 h after administration (half life 2.4 ± 0.2 h). At 24 h, serum iron increased, and the percent saturation of iron-binding capacity decreased in a dose-dependent fashion. By 7 days, serum iron returned to pre-administration levels, and serum ferritin increased. These results are consistent with the iron in AMI-25 entering the usual iron metabolism cycle. MR imaging results showed no difference in loss of signal intensity on images obtained between 0 and 3.5 h after infusion indicating a wide scan window for imaging. Unfortunately, acute severe back, leg, or groin pain occurred in some patients. In clinical trials, 2.5% (55/2240) of the patients experienced pain severe enough to cause interruption or discontinuation of the infusion. In most patients, the symptoms developed within 1–15 min (and lasted up to 45 min). Most other adverse reactions were mild to moderate, of short duration, and resolved spontaneously without treatment. However, in a few cases, anaphylactic-like reactions and

Table 20.1 Physical properties of iron oxides commercially available or under clinical investigation

Names	Coating	Hydrodynamic diameter ^a (nm)	Human blood half life (h)	r_2 , relaxivity ($\text{mM}^{-1}\text{s}^{-1}$)	r_2/r_1	References
Ferumoxsil AMI-121 Lumirem [®] Gastromark [®]	Silicon	300	Oral	72 (0.47 T) ^b	22.5	[70, 92]
Ferumoxide AMI-25 Feridex [®] Endorem [®]	Dextran T10	80–150	Biexponential: 0.1–0.33, 2–3	107 (0.47 T) ^b 152 (0.47 T) ^c 41 (1.5 T) ^c	4.5 5.6 8.7	[92, 156, 169, 197]
Ferucarbotran SHU-555A Resovist [®]	Carboxydextran	62	Biexponential: 0.065–0.1, 2.4–3.6	151 185.8	5.9 9.6	[150, 195]
Ferumoxytol AMI-7228	Carboxydextran	28–32	10–14	83 (0.47 T) ^b	2.2	[167]
Ferumoxtran AMI-227 BMS 180549 Sinerem [®] Combidex [®]	Dextran T10, T1	15–30	>24	44.1 (0.47 T) 53.1 (0.47 T) ^b	2.0 2.3	[92, 126, 198]
SHU-555C Supravist [®]	Carboxydextran	20	6	60 (0.47 T) ^d	2.5	[167]
NC100150 Feruglose Clariscan [®]	Pegylated starch	11–15	4	36 (1.4 T) ^c	2.3	[29, 44]

^a dynamic light scattering^b 0.5% agar, 39°C^c water, 37°C^d plasma, 40°C

hypotension have been noted in some patients receiving AMI-25 or other iron and dextran-containing formulations [8, 25, 54, 216]. In clinical trials, anaphylactic and allergic adverse events occurred in 0.5% (11/2240) of the patients who received Feridex®. These events include dyspnea, other respiratory symptoms, angioedema, generalized urticaria, and hypotension all requiring treatment.

20.6 Biomedical Applications of Magnetic Nanoparticles

20.6.1 Magnetic Resonance Imaging

Since the advent of MRI, there has been rapid development and study of magnetic nanoparticles for use in the biomedical field. MRI is based on a physics phenomenon called nuclear magnetic resonance discovered in the 1930s by Bloch and Purcell (Nobel Prize in Physics 1952), where the magnetic properties of atomic nuclei are investigated. In 1971, Damadian discovered the basis for using magnetic resonance imaging as a tool for medical diagnosis. He found that different kinds of animal tissue emit response signals with varying length, and that cancerous tissue emits response signals that last much longer than non-cancerous tissue [45]. The world's first patent issued in the field of MRI was granted to Damadian in 1974 [46]. In 2003, the Nobel Prize in Medicine was awarded to Lauterbur and Mansfield for their discoveries concerning MRI.

MRI provides excellent *in vivo* imaging capability with high spatial (<1 mm) and temporal resolution, excellent soft tissue contrast, and sensitivity to blood flow. However, the primary limitation of MRI has been its low sensitivity. In order to overcome this disadvantage, signal amplification strategies, such as the use of contrast agents, are employed to provide greater signal intensity that generates higher contrast from the surrounding tissue. Of particular interest are magnetic particles, specifically, SPIO nanoparticles, consisting of maghemite ($\gamma\text{-Fe}_2\text{O}_3$), magnetite (Fe_3O_4), and other metal ferrites. These contrast agents are extremely strong enhancers of transverse proton relaxation.

20.6.1.1 Anatomical Imaging

Gastrointestinal Tract Imaging

One of the first applications for SPIO nanoparticles was as an oral contrast agent used to image the gastrointestinal (GI) tract [43, 70, 195]. In MRI as well as computed tomography (CT), it is necessary to increase the contrast between the GI tract and the surrounding organs with negative contrast agents being better suited for these types of applications. Oral SPIO contrast formulations are usually composed of larger SPIO particles coated with a non-biodegradable, insoluble matrix and suspended in viscosity-increasing agents (usually based on ordinary food additives, such as starch and cellulose) [23, 70]. These formulations prevent the ingested iron from being absorbed and metabolized by the body and to improve homogenous

contrast distribution throughout the bowel. If SPIO do aggregate, magnetic susceptibility artifacts may result, especially at high field and when gradient echo pulse sequences are used [32].

A first agent, ferumoxsils are composed of approximately 10 nm nanoparticles coated by a layer of inert silicon with a hydrodynamic diameter of 300 nm. Ferumoxsils are also known as AMI-121 or have trade names “Gastromark®” and “Lumirem®,” manufactured by Advanced Magnetics (US) and Guerbet (EU), respectively. The reported T_2 and T_1 relaxivity for AMI-121 are 72 and $3.2 \text{ mM}^{-1}\text{s}^{-1}$, respectively [70, 92]. A second agent, oral magnetic particles (OMP), trade name “Abdoscan®” manufactured by Nycomed (EU), are composed of polystyrene-coated (ferristene) particles below 50 nm with a total particle size of $3.5 \mu\text{m}$ [23, 24, 85, 124, 189]. The OMP concentration typically used is 0.5 g/L with the particles containing 25% (w/w) SPIO. Oral SPIO are normally administered over a 30–60 min period, with a volume of 400 mL for upper abdomen imaging, and 900 mL for contrast enhancement of the whole abdomen. Figure 20.3 illustrates the proton density images of the rat abdomen before and after the oral administration of OMP agents. Significant image darkening was observed after OMP ingestion, leading to clear demarcation of the stomach in the axial images. Generally, GI contrast agents are well tolerated, with mild side effects, such as nausea and vomiting occurring in 1–5% of patients [110].

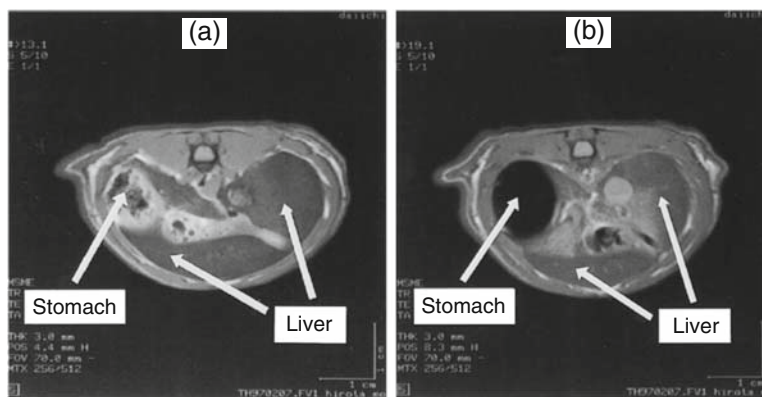


Fig. 20.3 Proton density-weighted MR imaging of rat abdomen: (a) no administration and (b) administration of the suspension of fast dispersible OMP granules, 4 mL/rat. Copyright © (1998) Elsevier. All rights reserved

Liver and Spleen Imaging

In addition to GI tract imaging, SPIOs are frequently used in hepatic imaging. After intravenous injection, SPIOs are nonspecifically taken up by the reticuloendothelial system (RES) of the liver and spleen. With T_2 -weighted (T_{2-w}) sequences, the presence of SPIO nanoparticles decreases signal intensity of normal parenchyma of liver

and spleen. For example, Kupffer cells are located exclusively in healthy liver tissue. The absence of these cells in malignancies can be exploited to discriminate between healthy and diseased tissues through SPIO-enhanced contrast [43]. Tumors have a lesser decrease in signal intensity after SPIO administration because they lack these macrophages. Liver tumors or metastases as small as 2–3 mm can be detected [43]. In addition to detection and characterization of liver lesions, SPIOs have also been shown capable of detecting focal splenic tumors. The use of SPIO increases both lesion conspicuousness and lesion detection compared to non-enhanced imaging [163].

The first contrast agents to be developed and marketed for this purpose were ferumoxides. Ferumoxides are also known as AMI-25, trade names “Feridex[®]” and “Endorem[®]” manufactured by Advanced Magnetics (US) and Guerbet (EU), respectively. They consist of a T10-dextran-coated particle with a hydrodynamic diameter of 120–180 nm (particle and crystal size approximately 15 and 5 nm, respectively) [43]. The reported T_2 and T_1 relaxivity range from 107 to 152 and 23.7–27.0 $\text{mM}^{-1}\text{s}^{-1}$, respectively [92, 156]. The recommended mode of administration is a biphasic infusion (2 mL/min over 10 min and 4 mL/min over 20 min) of a dose of 15 $\mu\text{mol Fe/kg}$ in 100 mL of 5% glucose [197]. AMI-25 allows a wide window for T_2 and T_{2-w}^* imaging of 0.5 to 6 h after administration [149]. AMI-25 effectively accumulates in the liver (approximately 80% of the injected dose) and spleen (5–10% of the injected dose) within minutes of administration; blood half life is 6 min (see Table 20.1) [197]. Similarly, ferucarbotran is a SSPIO characterized by a carboxydextran coating. Ferucarbotran is also known as SHU 555A or trade name “Resovist[®]” manufactured by Schering AG (EU). The crystal of SHU 555A is 4.2 nm, and the hydrodynamic diameter is 62 nm. The reported T_2 and T_1 relaxivities range from 151.0 to 185.8 and 19.4–25.4 $\text{mM}^{-1}\text{s}^{-1}$, respectively [150, 195]. A dose of 8 $\mu\text{mol Fe/kg}$ is the recommended quantity for T_{2-w} imaging. Due to its smaller size and thus stronger T_1 effect, SHU 555A has also been used for T_{1-w} imaging and MR angiography.

Numerous preclinical and clinical trials have been carried out to demonstrate SPIO efficacy in detection of focal lesions in both the liver and the spleen [60, 71, 94, 98, 99, 106]. Arbab et al. [13] investigated whether ferumoxide-enhanced T_{2-w} MR images alone can allow for differentiation of metastases from benign lesions in the non-cirrhotic liver. In this study, 60 lesions (22 metastases, 20 hemangiomas, and 18 cysts) were identified in 42 patients, and fast spin-echo T_{2-w} MR images were obtained before and after administration of ferumoxides. Ferumoxides-enhanced images showed significantly higher diagnostic accuracy than that of unenhanced images and concluded ferumoxides-enhanced T_{2-w} MR images appear useful in differentiating metastases from benign, nonsolid lesions in the liver. Namkung et al. [131] evaluated the efficacy of ferucarbotran for characterizing focal liver lesions. In this study, 68 patients with 46 malignant and 22 benign focal liver lesions were evaluated. The group concluded that the percentage of signal intensity loss due to the nonspecific uptake of SPIO can be an accurate tool for characterizing benign and malignant lesions. Finally, Kim et al. [103] compared the diagnostic performance of gadobenate dimeglumine (Gd-BOPTA)-enhanced MR imaging vs. SPIO-enhanced

imaging for detection of liver metastases. Twenty-three patients with 59 liver metastases underwent Gd-BOPTA- and SPIO-enhanced MR imaging on a 1.5 T unit. Figure 20.4 shows the dramatic difference in detecting these types of liver metastases. With Gd-BOPTA-enhanced imaging, only two low intensity liver masses were visible. In the opposite image, SPIO-enhanced imaging clearly shows the branched structure of the liver. Within the same image, the two larger masses as well as a smaller mass are easily identified.

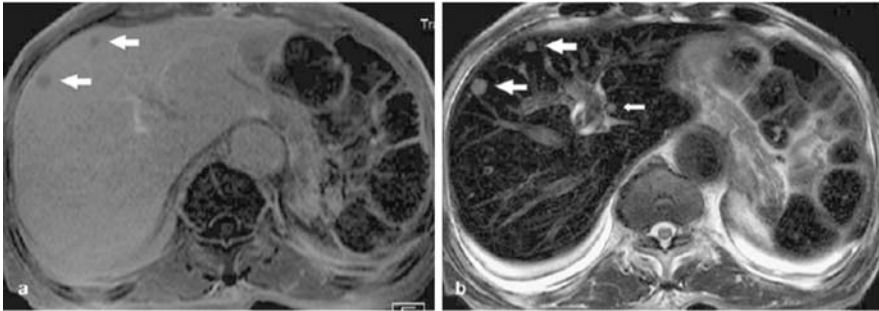


Fig. 20.4 Multiple liver metastases in a 48-year-old man with gastric carcinoma: (a) gadobenate dimeglumine-enhanced 1-h delayed phase MR image shows two low signal intensity liver masses (*arrows*), (b) superparamagnetic iron oxide-enhanced respiratory-triggered T₂-weighted turbo spin echo image shows another tiny high signal intensity mass (*small arrow*) as well as two masses (*large arrows*) in the right lobe of the liver. Copyright © (2005) Springer-Verlag. All rights reserved

Lymph Node Imaging

Nodal disease is an independent, adverse prognostic factor in many types of cancers. However, diagnostic imaging of lymph node metastases is difficult because signal intensities of metastatic nodes differ from those of normal nodes only in size. This poor preoperative staging can then influence the oncologist's decision to use neoadjuvant therapy or the surgeon's decision to perform nodal dissection [105]. SPIOs which can be taken up by normal nodes following intravenous or subcutaneous injection have made differentiation possible. Specifically, the SPIO extravasate from the vasculature to the interstitial space, where they are transported to the lymph nodes via the lymphatic vessels. Hence, metastatic nodes can be differentiated from normal nodes based on the absence of signal intensity change between pre- and post-contrast scans [11, 12, 72, 195].

In contrast to SSPIO, smaller iron oxide nanoparticles are found to accumulate in the lymph nodes. The first agent and most widely studied is ferumoxtran-10. Ferumoxtran-10 is characterized as an USPIO and is also known as AMI-227, trade names "Combidex[®]" and "Sinerem[®]" manufactured by Advanced Magnetics (US) and Guerbet (EU), respectively. The iron oxide core is approximately 5 nm surrounded by an 8–12 nm layer of T10 dextran coating resulting in a final size of

less than 30 nm. The reported T_2 and T_1 relaxivity for the USPIO are 44.1–53.1 and 21.6–22.7 $\text{mM}^{-1}\text{s}^{-1}$, respectively [92, 198]. After administration, the USPIO is taken up by macrophages within the lymph nodes, appearing dark on the MR images. In contrast, metastatic nodes that are partially or completely replaced by tumor cells do not possess the same levels of phagocytotic activity as normal nodes and maintain the same signal intensity on post-contrast MR images as shown in Figure 20.5. In this study by Harisinghani et al. [72], MRI was performed on 80 patients with pre-surgical clinical stage T1, T2, and T3 prostate cancer who underwent lymph node resection or biopsy. MRI was performed pre- and 24 h post-intravenous injection of 2.6 mg/kg of ferumoxtran-10. Sixty-three lymph nodes from 33 patients had histopathological detected metastases. Of these, 45 (71.4%) did not fulfill the imaging criteria for malignancy. However, ferumoxtran-1-enhanced MRI was able to correctly identify all patients with nodal metastases. Nodal metastatic infiltration measuring 5–10 nm was identified. Anzai et al. [10] investigated the efficiency of MR imaging with dextran-coated USPIO to distinguish metastatic and benign nodes in patients with head and neck cancer. In this study involving 12 patients, 40 out of 42 histologically proven metastatic nodes and 41 out of 49 benign nodes were detected, yielding a 95% sensitivity and 84% specificity for diagnosis of tumor-bearing lymph nodes. In a comparative study, 16 patients with esophageal cancer underwent MRI scanning before and 24 h after intravenous administration

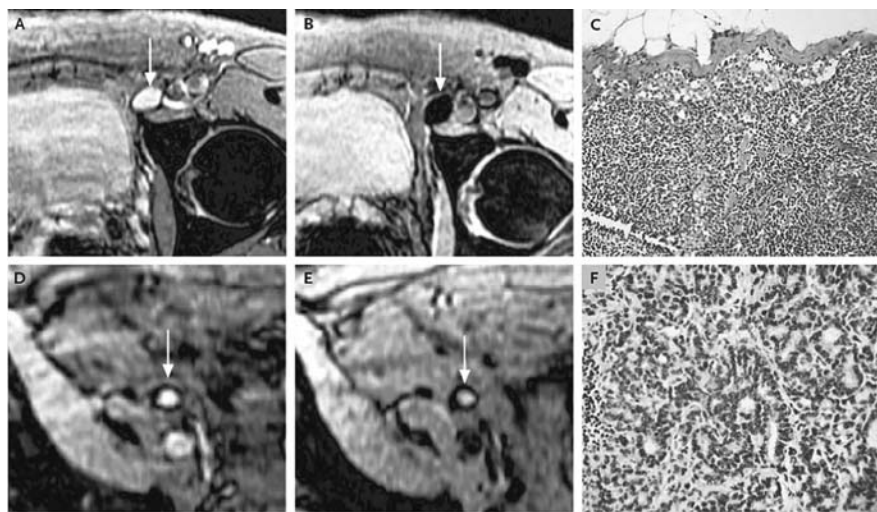


Fig. 20.5 MRI nodal abnormalities in patients with prostate cancer: (A) conventional MRI of normal lymph node, (B) MRI of a normal lymph node obtained 24 h after IV administration shows accumulation of lymphotropic SPIO, (C) corresponding histology (hematoxylin and eosin, 125X), (D) conventional MRI shows a high signal intensity in an enlarged iliac node completely replaced by tumor, (E) nodal signal intensity remains high after SPIO administration, and (F) corresponding histology (hematoxylin and eosin, 200X). Copyright © (2003) Massachusetts Medical Society. All rights reserved

of ferumoxtran-10 [134]. Of the 408 resected lymph nodes, imaging results of 133 nodes could be compared with histopathologic findings. Twenty-four lymph nodes had histopathologic metastases. Using their enhancement criteria, sensitivity was 100%, specificity was 95.4%, and accuracy was 96.2% for the diagnosis of metastatic nodes. Therefore, without SPIO-enhanced MRI, metastatic lymph nodes in these studies would have been missed had size criteria alone been used.

20.6.1.2 Molecular Imaging and Targeting

Molecular imaging can be broadly defined as the “non-invasive and repetitive imaging of targeted macromolecules and biological processes in living organisms” [35]. Molecular imaging using MRI requires the use of ligands (e.g., antibodies, proteins, peptides) for selective binding to targeted disease markers. These ligands, in turn, need to be conjugated to MR contrast agents in order to induce a contrast difference from non-targeted tissue. In this way, anatomical information on MR images can be discerned or marked in order to detect diseases, such as cancer, at its earliest stage. Numerous examples demonstrate the potential application of SPIO for molecular imaging.

As a typical example, targeting agents such as proteins are coupled to insoluble polysaccharides using simple conjugation methods. Periodate oxidation/borohydride reduction is used to produce reactive aldehyde groups on the nanoparticle's surface, which will react with amino groups on the proteins (e.g., HSA or transferrin attachment to carboxydextran nanoparticle or a monoclonal antibody (mAb) or wheat germ agglutinin lectin on a dextran nanoparticle) [51, 108, 151, 158, 201]. Using this method, antimyosin Fab (R₁₁D₁₀) was attached to MIONs for immunospecific MR imaging of myocardial infarction [201], to intact mAbs for immunospecific detection of intracranial small cell lung carcinoma [151], as well as to human polyclonal immunoglobulin (IgG) for the detection of induced inflammation [200], and to synaptotagmin I for detection of apoptotic tumor cells [214]. However, in the case of the transferrin receptor, a substantial loss of the protein biological activity was observed [159]. To minimize this type of detrimental effect, new non-oxidative chemistry was developed. For example, a dextran-coated nanoparticle is cross-linked by epichlorohydrin and ammonia resulting in an amine-terminated CLIO nanoparticle capable of conjugating biovectors with a vast range of heterobifunctional linkers [207]. Weissleder's group has used this strategy to graft transferrin, annexin, V, anti-VCAM, or anti-E-Selectin antibodies, oligonucleotides, and TAT peptides to CLIO nanoparticles [77, 89, 96, 142, 215]. This technology platform was subsequently used to develop a wide nanoparticle library consisting of 146 nanoparticles decorated with different synthetic small ligands that recognizes apoptotic cells [160, 204].

Alternate methods to attach mAbs to magnetic nanoparticles include glutaraldehyde cross-linking chemistry [152], biotin streptavidin system [20, 21, 36], amine-sulfhydryl group linkage [180, 181], and disulfide chemistry [53, 155]. Specific examples of some proteins/peptides used for MR visualization include cholecystokinin- [148] and secretin-linked [166] nanoparticles used for their

respective pancreatic receptor and may aid in the diagnosis of pancreatic cancer. Transferrin-SPIO nanoparticles have been used for specific labeling and detection of gliosarcoma [82, 128, 203] and breast carcinoma [108], with and without transfection of the transferrin receptor encoding gene, respectfully. Finally, targeting of beta-amyloid plaques in a transgenic mouse model of Alzheimer's disease has resulted in specific enhancement of lesions on the ex vivo images. Specific plaque enhancement was obtained in vivo using MIONs labeled with Abeltal-40 peptide [190]. Table 20.2 shows current examples of targeted MR contrast agents in molecular imaging applications.

20.6.1.3 Cellular Imaging and Tracking

Similar to molecular imaging, a promising new direction for SPIO is their use in tracking the distribution of cells in vivo [35, 43, 179]. MR cell tracking, with its excellent spatial resolution, can be used as a noninvasive tool to provide unique information on the dynamics of cell movements. These studies usually involve implanting SPIO-loaded cells into living subjects, tracking their movement in the body, and/or localization in specific tissues. Alternately, cellular imaging in the future could be applied to monitor cell therapy in patients. Currently, SPIOs are the MR contrast agent of choice for cell labeling due to their biocompatibility and strong T_2 effect. Various strategies have been developed to efficiently load cultured cells with sufficient quantities of SPIO to ensure enough contrast for in vivo imaging.

Within the MR cellular imaging field, a major focus of study is stem cells, given their remarkable potential to develop into many different cell types within the body. But before their therapeutic possibilities can be exploited, the dynamics of cell migration and differentiation after implantation into the host organ must be studied. MR tracking may serve in experimental animal models to study how lesions and stimuli target cell migration, at what speed cells migrate, and for how long they persist at the target site. For example, visualizing transplanted cells in experimental central nervous system (CNS) diseases has yielded good examples for such use of this tool. Oligodendrocyte progenitors were magnetically labeled using anti-Tfr mAbs and transplanted into the spinal cord of 7-day old myelin-deficient rats [34]. Ten to fourteen days later, the spinal cords were removed and imaged at 4.7 T at 78 μm resolution. Migration of labeled cells was easily identified on MR images as streaks of hypointensity, primarily along the dorsal column, over a distance of up to 10 mm away from the injection site. This study showed that magnetically labeled oligodendrocyte progenitor cells responded adequately to the normal development signals in the post-natal myelinating CNS and retained their capacity to myelinate axons in vivo. Neural stem cell transplantation has been shown to attenuate the severity of experimental autoimmune encephalomyelitis (EAE), an animal model of multiple sclerosis. Using magnetically labeled mouse neurospheres and human embryonic stem cell (hESC)-derived neurospheres, serial MRI was used to assess the biodynamics of transplanted cell migration in a chronic mouse EAE model [28]. Magnetic labeling did not affect the in vitro and in vivo characteristics of cells as

Table 20.2 Targeted superparamagnetic iron oxide nanoparticles for molecular imaging

Targeted contrast media	Experimental conditions	Ligand	Biological target	Result	References
MION-IgG	In vivo	Ab	Inflammation	Accumulation at inflammation site and confirmed with histology.	[200]
USPIO-AG	In vitro, in vivo	Arabinogalactan	Asialoglycoprotein receptors on hepatocytes	Due to lack of ASG receptors in primary tumors, high tumor-liver contrast possible.	[146, 147, 199]
USPIO-RGD	In vitro, in vivo, ex vivo	c-RGD peptide	Thrombus imaging	USPIO-RGD resulted in better thrombus visualization than control ex vivo and maximum enhancement post ~ 1 h.	[88]
CLJO-Cy5.5-annexin V	In vitro	Dye-annexin	Jurkat T cells	Bimodal approach to recognize normal and apoptotic cells.	[160]
SPIO-PEG-folate	In vitro	Folic acid	Breast cancer cells	SPIO-PEG-FA internalized into BT-20 cancer cells and show higher cellular uptake compared to PEG or folate alone.	[213]
CLJO-transferrin	In vitro	Glycoprotein	Gliosarcoma	Successful development of high throughput screening and detection of cellular uptake.	[77]
USPIO-transferrin	In vivo	Glycoprotein	Mammary carcinoma	Showed a signal reduction (25–55%) 150 min post-injection.	[108]
USPIO-transferrin	In vitro, in vivo	Glycoprotein	Tf receptors	Imaging of gene expression.	[82, 108, 128, 203]
CLJO-F(ab') ₂ (anti-human E-selectin)	In vitro	mAb	E-selectin	Showed a highly specific T ₂ weighted signal darkening associated with treated endothelial cells.	[96]
MION-antiHer-2/ <i>neu</i>	In vitro	mAb	Melanoma and mammary cell lines	Receptor-specific T ₂ contrast change on Her-2/ <i>neu</i> positive tumor cells.	[56]
MION-L6 antibody	In vivo	mAb	Surface antigen on human carcinoma	Specific pattern enhancement in LX-1 intracranial tumors 6 h post-injection.	[151]
SPIO-528	In vitro, in vivo	mAb	EGFR	Immunoreactivity is preserved with specific binding to squamous cell carcinoma of the oesophagus.	[175]
SPIO-A7	In vitro, in vivo	mAb	Colorectal carcinoma	Significant in vivo tumor accumulation of targeted SPIO as compared to the control group.	[182]

Table 20.2 (continued)

Targeted contrast media	Experimental conditions	Ligand	Biological target	Result	References
SPIO-antibody	In vitro, in vivo	mAb	Surface antigen on neuroblastoma T cells	Specific binding of these particles is demonstrated.	[152]
SPIO-antiCD4+, -antiCD8+	In vivo	mAb		Monitored the infiltration of T cells in the CNS over time in infected animals.	[142]
SPIO-antiCEA	In vitro, in vivo	mAb	Carcinoembryonic antigen (CEA)	Peptide carrier for magnetite showed very good in vitro characteristics but caused severe in vivo problems.	[180, 181]
SPIO-antiHer-2/ <i>neu</i>	In vitro, in vivo	mAb	Breast cancer cells	Enhanced T ₂ and T ₂ * images at 9.4 T for pre-labeled mAb-biotin tumor cells followed by incubation with labeled-SPIO demonstrated with positive controls.	[20, 21]
SPIO-antilymphocyte	In vitro	mAb	Lymphocyte	Biotinylated-SPIO + labeled biotinylated anti-lymphocyte-mAb + streptavidin gave strong and selective negative contrast enhancement of suspensions at 2.0 T.	[36]
USPIO-610	In vitro, in vivo	mAb	Surface antigen on colon carcinoma	Immunoreactivity is preserved with specific tumor binding.	[39]
USPIO-antimyosin	Ex vivo	mAb	Myocardial infarction	Marked decrease in signal intensity of infarcted myocardium 1 h post IV.	[201]
CLJO-EPPT	In vitro, in vivo	Peptide	uMUC-1	Specific accumulation of the probe in uMUC-1-positive tumors and virtually no signal in control tumors.	[129]
CLJO-TAT	In vitro	Peptide	Hematopoietic C344 cells	Internalization into hematopoietic cells without toxicity.	[119]
CLJO-TAT peptide	In vitro	Peptide	Cellular uptake	Significant uptake of TAT-labeled CLJO.	[89, 215]
MION- $\text{A}\beta$ 1-40	In vivo	Peptide	$\text{A}\beta$ -amyloid plaque	Intraarterial injection of magnetically labeled $\text{A}\beta$ 1-40, with mannitol to transiently open the BBB, enabled the detection of many amyloid- β plaques.	[190]
USPIO-pep(VCAM-1)	In vitro, in vivo	Peptide	VCAM-1	Binding of targeted USPIO in atherosclerotic lesions of ApoEko mice and in TNFa-inflammatory mice.	[100]
MION-20-CCK	In vitro, in vivo	Peptide hormone	Pancreas	Studies show a decrease in T ₂ times in pancreatic tissue but not in tumor.	[148]
MION-46-strept-secretin	In vitro, in vivo	Peptide hormone	Pancreas	Distribution studies in rats showed a higher pancreatic accumulation as compared to the control group.	[166]
SPIO-C2	In vitro, in vivo	Synaptotagmin I	Phosphatidylserine of apoptotic cells	Feasible to detect of apoptotic cells treated by chemotherapy.	[214]

multipotential precursors. It was also shown that cell migration occurred along white matter tracts, especially the corpus callosum, fimbria, and internal capsule predominantly early in the acute phase of disease and in an asymmetric manner. The distance of cell migration also correlated well with clinical severity of disease and the number of microglia in the white matter tracts, supporting the idea that inflammatory signals promote transplanted cell migration.

MR tracking outside the CNS has also been performed for other cell types and disease models including mesenchymal stem cells (MSCs), found in bone marrow, for cellular repair of cardiovascular and myocardial injury. The concept is that these cells can contribute to stromal support, angiogenesis, or the formation of new cardiomyocytes [35]. The goal is to non-invasively identify transplanted MSCs months post-injection and be able to correlate myocardial function and infarct size with MRI. In a swine myocardial infarction (MI) model, injected iron fluorophore-labeled MSC into normal and infarcted myocardium enabled ready detection in the beating heart on a conventional 1.5 T cardiac MR scanner after transplantation [75]. At 3 weeks, hypointense artifacts were still present and appeared to persist up to 12 weeks post-injection. In a similar swine MI model with x-ray fluoroscopic intramyocardial injection of Feridex[®]-PLL labeled MSCs, successful contrast-enhanced MRI and serial MSC tracking was demonstrated in two animals (5 total including control) [107]. Additional examples of MR tracking, distribution, and migration of stem cells and progenitor cells in different animal models are shown in Table 20.3.

20.6.2 Therapeutic Applications

20.6.2.1 Hyperthermia

Magnetic fluid hyperthermia is a treatment modality for the eradication of cancer tissues using an alternating magnetic field. The magnetic waves are not absorbed by living tissue and can permeate throughout the body. When subjected to a variable magnetic field, magnetic nanoparticles generate heat due to magnetic hysteresis loss. The amount of heat generated depends on the physical properties of the magnetic material and the magnetic field parameters [59, 74]. Cancer cells are destroyed at elevated temperatures (42–46°C), whereas normal cells can survive at these temperatures [33, 67, 194]. The architecture of the vasculature inside solid tumors is chaotic, resulting in regions with hypoxia and low pH, which is not found in normal tissues [187]. These environmental factors make cells more sensitive to hyperthermia. At temperatures above 42°C, the exposure time can be halved with each 1°C rise in temperature, which will result in equivalent cell death [144]. Most normal tissues, with the exception of central nervous tissue, remain undamaged by treatment for 1 h at a temperature up to 44°C [52]. For the CNS, irreversible damage was found after treatment at 42–43°C for longer than 40 to 60 min [168]. Treatment of peripheral nerve tissue for times greater than 30 min at 44°C, or equivalent

Table 20.3 Examples of magnetically labeled cells for MR cell tracking

Animal model	Stem cells	Labeled nanoparticle	Result	References
E.G7-OVA tumor bearing mice	Activated T-cells	Citrated SPIO	Tumor regression correlated with T-cell uptake.	[79]
Thrombotic stroke in rats	Bone marrow and ESC	Endorem®	Hypointense signal persisted for more than 50 days.	[86]
C57B I/6 mice injected with melanoma cell lines	CD8 + cytotoxic T lymphocytes	CLIO-HD	In vivo detection of CLIO-HD-CD8 + T cells with threshold of ~3 cell/voxel.	[104]
C-6 rat glioma tumor-bearing nude mice	hAC133 ⁺ cells	Feridex® + protamine sulfate	Demonstrated incorporation of labeled cells into the neovasculature of implanted flank tumors at 7 T.	[18]
Neonatal NOD- SCID mice	hCNS-SCns	Feridex® + protamine sulfate	Transplanted hCNS-SC respond to cues characteristic for the ambient microenvironment resulting in distinct migration patterns.	[68]
Nude rats	hMSCs	Ferumoxides + poly-L-lysine	Site-specific delivery of hMSCs (liver) via magnetic targeting.	[15]
Mdx mice (muscular dystrophy)	mc13 cells	Ferumoxides + poly-L-lysine	Endosomal accumulation of SPIO resulted in 3-D, noninvasive detection of labeled cells.	[37]
Mice with muscle disorder	MD-100	SPIO	May be useful for noninvasive monitoring of stem cell transfer, replacing sequential muscle biopsies and tissue harvesting.	[191]
Myocardial infarction in mice	Mouse ESC	Ferumoxides + lipofectamin	Stem cells were observable for at least 5 weeks after injection.	[76]
CCl ₄ -induced hepatocyte necrosis and inflammation in rats	Rat MSCs	Endorem® + Superfect®	Signal intensity loss in renal cortex; cells were detected for up to 7 days in kidney and 12 days in liver.	[31]
Rats with acute kidney injury	Rat MSCs	Resovist®	Qualitative and quantitative in vivo cell tracking and monitoring of organ distribution feasible in MRI at 3T.	[84]
CCl ₄ -induced liver damage in rats	Rat bone MSCs	Fe ₂ O ₃ + poly-L-lysine	Intrasplenic transplantation of the labeled cells could be depicted in vivo.	[90]
Sprague-Dawley rats	Rat neural stem cells	Au-MION	Grafted cells do not migrate efficiently when implanted in the intact rat spinal cord; also very few cells appeared to have survived to the 1 month time point.	[192]
Glioma-bearing SCID mice	Scal ¹⁺ bone marrow cells	Feridex® + poly-L-lysine	MRI can detect incorporated labeled Scal ¹⁺ cells in tumor vasculature as part of ongoing angiogenesis and neovascularization.	[9]

dose, resulted in temporary functional loss, which can be recovered within 4 weeks [206]. To this end, much work has been done *in vitro* and with animal experiments to manifest hyperthermia as a therapeutic modality for cancer. Significant improvement in clinical outcome has been demonstrated for tumors of the head and neck, breast, brain, bladder, cervix, rectum, lung, oesophagus, vulva and vagina, and also for melanoma [187].

In a pilot study by Johannsen et al. [87], magnetic fluid hyperthermia was evaluated as a minimally invasive technique for treatment of prostate cancer. This was the first clinical application of interstitial hyperthermia using magnetic nanoparticles in locally recurrent prostate tumors. Nanoparticle suspensions were injected transperineally into the prostate under transrectal ultrasound and fluoroscopy guidance. The nanoparticles used in this study were coated with an aminosilane-type shell in water (MagForce[®] MFL AS, MagForce[®] Nanotechnologies GmbH, Berlin, Germany) and had an average particle core size of 15 nm. Concentration of ferrites in aqueous solutions was 120 mg/mL. Using an alternating magnetic field with a frequency of 100 kHz and variable field strength (0–18 kAm⁻¹), invasive thermometry of the prostate was carried out with CT scans following treatment to monitor nanoparticle distribution and probe position. In the first patient treated, maximum and minimum intraprostatic temperatures measured at a field strength of 4.0–5.0 kAm⁻¹ were 48.5°C and 40.0°C during the first treatment and 42.5 and 39.4°C during the sixth treatment, respectively. In this first clinical application of hyperthermia using magnetic nanoparticles in prostate cancer, the aims to prove feasibility as a minimally invasive technique and to obtain thermoablative temperatures in the prostate were achieved. These first clinical successes prompted phase I studies in order to further evaluate feasibility, toxicity, and quality of life during hyperthermia using magnetic nanoparticles in patients with biopsy-proven local recurrence of prostate cancer following radiotherapy with curative intent.

In many cases, hyperthermia is used in conjunction with other therapies such as radiotherapy or chemotherapy for improved efficacy. In phase I and II studies, Secord et al. [6] conducted studies combining Doxil[®], PEG-coated non-thermosensitive liposomal doxorubicin, with whole abdomen hyperthermia on patients with refractory ovarian cancer. Liposomal doxorubicin combined with hyperthermia has been shown to increase both liposomal delivery and drug extravasation into tumor xenografts resulting in enhanced cytotoxic effects. Xia et al. [208] investigated the feasibility of hyperthermia combined with weekly chemoradiotherapy for patients with malignant pleural mesothelioma (MPM), a disease that affects the lining of the lungs, and estimated the efficacy of this regimen. Although complete response was not achieved in any of the 11 patients, partial response was achieved in 3 patients and the disease did not worsen in 6 patients. Prognosis for patients with MPM remains poor and, as such, patients require intensive treatment. Finally, Albrechts et al. [2] have investigated the feasibility and toxicology of external deep locoregional hyperthermia combined with concurrent chemotherapy in localized primarily operable carcinoma of the thoracic oesophagus and gastro-oesophageal junction. The thermal data indicated that it was technically feasible to heat the oesophagus to a median temperature of 40.0°C with maximum

tumor temperatures considered adequate but suboptimal. One tried to evaluate tumor responses and found a complete remission rate of 9%, however, partial remission and progression are difficult to assess. In many such cases, the use of hyperthermia either alone or in conjunction with other modalities has significantly improved patient's quality of life.

20.6.2.2 Drug Delivery via Magnetic Targeting

Another possible and promising therapeutic application of SPIO nanoparticles is the site-specific delivery of drugs via a magnetic field (magnetic drug targeting, MDT) [55, 67, 183]. Because of the nonspecificity of chemotherapy and radiotherapy, there is considerable toxicity to normal tissue even under optimized conditions. MDT enjoys some advantages in that the drug-loaded SPIO can be guided to the target area through external magnetic fields to the desired site. The ability to deliver high effective dosages to specific sites in the human body is the ultimate goal of drug delivery research.

For drug delivery applications, these magnetic nanocarriers need to be water soluble, biocompatible, and nontoxic. Diameter, which affects the magnetic properties, charge, and surface chemistry, are very important and strongly affect both the blood circulation time and the bioavailability of the particles within the body. If one recalls, larger particles with a diameter greater than 200 nm are sequestered by the liver and spleen. Below 10 nm, USPIO will be quickly removed through extravasation and renal clearance. More over, particles over 5 μm will induce capillary blockade. Particles need be of optimal size ($\sim 10\text{--}100$ nm) to prolong blood circulation times to enhance their magnetic targeting efficiency.

Magnetic fields are well suited for such biological applications as they do not interfere with most biological processes. However, there are still several problems associated with MDT in humans [153]. One such limitation is the influence of blood flow at the target site of SPIO accumulation. Stronger magnetic fields would be required to retain magnetic particles in large arteries. The linear velocity of blood in large arteries is 50–100 times faster than blood flow in capillaries (~ 0.5 cm/s). Yet another problem associated with MDT in humans is the depth of penetration by the magnetic field at the target site. Sites that are more than 2 cm deep in the body are difficult to target because the magnetic field strength decreases with distance [157]. In fact, through mathematical modeling, Grief and Richardson claim that it is impossible to specifically target internal organs using an externally applied field [62]. However, recent work by Takeda et al. [133, 176] describes the development of a novel drug delivery system using externally applied magnetic fields (using superconducting magnets) for targeting magnetic particles in blood vessels located deep inside the body.

Despite the challenges, progress has translated into clinical trials from in vitro [5, 47, 65, 109, 186] and in vivo [3, 4, 57, 93, 130] studies. The first clinical evaluations in human patients with MDT worldwide were reported by Lübke et al. [123]. Following successful tolerance and efficacy results in animal experiments, studies were performed on 14 patients with advanced solid tumors (adenocarcinoma of the colon

or hypernephroma). Intravenous injection of epirubicin-loaded ferrofluids (particle size of 100 nm) were administered with bedside magnetic fields of approximately 0.8 T. The distance between the tumor surface and the magnets were also assured to be less than 0.5 cm. As a result, the magnetic particles were successfully directed into half of the patients after a 60–120 min application period confirmed by MRI, and histology. In a different clinical study [118], 11 patients with unsuccessful conventionally treated malignant tumors were treated by MDT and examined by MRI. The tumors of all 11 patients varied in location but were intentionally chosen for their superficial site. Diseases in these patients varied from thoracic wall carcinomata, metastasis of breast carcinomata, metastatic chondrosarcomata, histiocytoma, sarcoma, etc. Once again, Farmorubicin (epirubicin-loaded ferrofluid) was administered at field strength of ~ 0.8 T. Overall, the tolerance of the magnetic drug targeting was very good. Within the surveillance period, three patients showed partial tumor response, five patients showed stable disease, and three patients showed progressive disease. It is evident that MDT does have great potential therapeutic benefit despite several limitations.

20.7 Conclusion

Magnetic nanoparticles have become an increasingly important tool in disease diagnosis and therapy. To date, most of the clinical use of magnetic nanoparticles has focused on SPIO due to their chemical stability, biocompatibility, and relative ease of production. However, the search for more efficient contrast agents with increased sensitivity has led to the development of novel SPIO and other magnetic nanoparticles with improved magnetic properties. These nanoparticles can now be extended to study biology at the cellular and even the molecular level in different endeavors including cell tracking, gene expression, and biomolecular recognition. In the case of MRI, many challenges still remain in pursuit of the ideal MR imaging probe with imaging ultrasensitivity and disease specificity. A major limitation is the loss of signal that occurs using SPIOs, creating ‘black holes’ that prevent direct anatomical MR evaluation of the tissue in question and make it difficult to discriminate between targeted molecules and cells and image artifacts. Development of novel imaging methods (e.g. SWIFT imaging, white marker method) can overcome these limitations by turning the SPIO probes to positive contrast agents. Although current clinically used contrast agents do not have active targeting characteristics, a lot of work is in progress on the functionalization of these particles in order to widen their diagnostic ability. Magnetic nanoparticle-aided drug delivery is still very much in its infancy. However, with continuing advancement in the field, nanomagnetism will continue to play a significant role in biomedical research and nanomedicine.

Abbreviations

Ab	antibody
AG	arabinogalactan

AOT	dioctyl sulfosuccinate sodium salt
CCK	cholecystokinin
α -CD	α -cyclodextrin
CEA	carcinoembryonic antigen
CLIO	cross-linked iron oxide
CNS	central nervous system
CT	computed tomography
DMAP	4-(dimethyl-amino) pyridine
DMSA	<i>meso</i> -2,3-dimercaptosuccinic acid
DSPE-PEG	1,2-distearoyl- <i>sn</i> -glycero-3-phosphoethanolamine- <i>N</i> -[methoxy(polyethylene glycol)]
EAE	experimental autoimmune encephalomyelitis
Gd-BOPTA	gadobenate dimeglumine
GI	gastrointestinal tract
GSH	glutathione
hCG	human chorionic gonadotropin
HSA	human serum albumin
IgG	Immunoglobulin G
mAb	monoclonal antibody
MDT	magnetic drug targeting
MRI	magnetic resonance imaging
MION	monocrystalline iron oxide nanoparticles
MEIO	magnetism-engineered iron oxide
MI	myocardial infarction
M_s	saturation magnetization
MSC	mesenchymal stem cells
MPM	malignant pleural mesothelioma
MPS	mononuclear phagocytic system
MPM	malignant pleural mesothelioma
OMP	oral magnetic particles
PCL-b-PEG	poly(ϵ -caprolactone)-b-poly(ethylene glycol)
PEG	polyethylene glycols
PEO	poly(ethylene oxide)
PLL	poly(L-lysine)
PPO	poly(propylene oxide)
PSA	polysialic acids
RES	reticuloendothelial system
RGD	arginine-glycine-aspartic acid containing synthetic peptide
SC	stem cells
SPIO	superparamagnetic iron oxide
SSPIO	standard superparamagnetic iron oxide
TAT	transactivator of transcription peptide
TCL-SPION	thermal cross-linked superparamagnetic iron oxide
USPIO	ultra-small superparamagnetic iron oxide
VCAM-1	vascular cell adhesion molecule-1

References

1. Ai, H., et al.: Magnetite-loaded polymeric micelles as ultrasensitive magnetic-resonance probes. *Adv. Mater.* **17**, 1949–1952 (2005)
2. Albrechts, M., et al.: A feasibility study in oesophageal carcinoma using deep loco-regional hyperthermia combined with concurrent chemotherapy followed by surgery. *Int. J. Hyperthermia* **20**, 647–659 (2004)
3. Alexiou, C., et al.: Locoregional cancer treatment with magnetic drug targeting. *Cancer Res.* **60**, 6641–6648 (2000)
4. Alexiou, C., et al.: Magnetic drug targeting: biodistribution and dependency on magnetic field strength. *J. Magn. Magn. Mater.* **252**, 363–366 (2002)
5. Alexiou, C., et al.: In vitro and in vivo investigations of targeted chemotherapy with magnetic nanoparticles. *J. Magn. Magn. Mater.* **293**, 389–393 (2005)
6. Alvarez Secord, A., et al.: Phase III trial of intravenous Doxil[®] and whole abdomen hyperthermia in patients with refractory ovarian cancer. *Int. J. Hyperthermia* **21**, 333–347 (2005)
7. Amsalem, Y., et al.: Iron-oxide labeling and outcome of transplanted mesenchymal stem cells in the infarcted myocardium. *Circulation* **116(suppl. 1)**, I-38–I-45 (2007)
8. Anastase, S., et al.: Affinity chromatography of human anti-dextran antibodies: isolation of two distinct populations. *J. Chromatogr. B, Biomed. Sci. Appl.* **686**, 141–150 (1996)
9. Anderson, S.A., et al.: Noninvasive MR imaging of magnetically labeled stem cells to directly identify neovasculature in a glioma model. *Blood* **105**, 420–425 (2005)
10. Anzai, Y., et al.: Initial clinical experience with dextran-coated superparamagnetic iron oxide for detection of lymph node metastases in patients with head and neck cancer. *Radiology* **192**, 709–715 (1994)
11. Anzai, Y., et al.: Initial clinical experience with dextran-coated superparamagnetic iron oxide for detection of lymph node metastases in patients with head and neck cancer. *J. Magn. Reson. Imaging* **7**, 75–81 (1997)
12. Anzai, Y., et al.: Evaluation of neck and body metastases to nodes with ferumoxtran 10-enhanced MR imaging: phase III safety and efficacy study. *Radiology* **228**, 777–788 (2003)
13. Arbab, A.S., et al.: Ferumoxides-enhanced double-echo T2-weighted MR imaging in differentiating metastases from nonsolid benign lesions of the liver. *Radiology* **225**, 151–158 (2002)
14. Arbab, A.S., et al.: Characterization of biophysical and metabolic properties of cells labeled with superparamagnetic iron oxide nanoparticles and transfection agent for cellular MR imaging. *Radiology* **229**, 838–846 (2003)
15. Arbab, A.S., et al.: In vivo trafficking and targeted delivery of magnetically labelled stem cells. *Hum. Gene Ther.* **15**, 351–360 (2004)
16. Arbab, A.S., et al.: Comparison of transfection agents in forming complexes with ferumoxides, cell labeling efficiency, and cellular viability. *Mol. Imag.* **3**, 24–32 (2004)
17. Arbab, A.S., et al.: Labeling of cells with ferumoxides-protamine sulfate complexes does not inhibit function or differentiation capacity of hematopoietic or mesenchymal stem cells. *NMR Biomed.* **18**, 553–559 (2005)
18. Arbab, A.S., et al.: Labeled endothelial progenitor cells trafficking to sites of tumor angiogenesis magnetic resonance imaging and confocal microscopy studies of magnetically. *Stem Cells* **24**, 671–678 (2006)
19. Arruebo, M., et al.: Antibody-functionalized hybrid superparamagnetic nanoparticles. *Adv. Funct. Mater.* **17**, 1473–1479 (2007)
20. Artemov, D., et al.: MR molecular imaging of the Her-2/neu receptor in breast cancer cells using targeted iron oxide nanoparticles. *Magn. Reson. Med.* **49**, 403–408 (2003)
21. Artemov, D., et al.: Magnetic resonance molecular imaging of the HER-2/neu receptor. *Cancer Res.* **63**, 2723–2727 (2003)
22. Babes, L., et al.: Synthesis of iron oxide nanoparticles used as MRI contrast agents: a parametric study. *J. Colloid Interface Sci.* **212**, 474–482 (1999)

23. Bach-Gansmo, T.: Ferrimagnetic susceptibility contrast agents. *Acta Radiol. Suppl.* **387**, 1–30 (1993)
24. Bach-Gansmo, T., et al.: Abdominal MRI using a negative contrast agent. *Br. J. Radiol.* **66**, 420–425 (1993)
25. Bayer HealthCare Pharmaceuticals: Feridex®. <http://imaging.bayerhealthcare.com/html/feridex/index.html> (2007). Accessed 5 November 2007
26. Bee, A., et al.: Synthesis of very fine maghemite particles. *J. Magn. Magn. Mater.* **149**, 6–9 (1995)
27. Belin, T., et al.: Influence of grain size, oxygen stoichiometry, and synthesis conditions on the γ -Fe₂O₃ vacancies ordering and lattice parameters. *J. Solid State Chem.* **163**, 459–465 (2002)
28. Ben-Hur, T., et al.: Serial in vivo MR tracking of magnetically labeled neural spheres transplanted in chronic EAE mice. *Magn. Reson. Med.* **57**, 164–171 (2007)
29. Bjørnerud, A., et al.: Assessment of T₁ and T₂* effects in vivo and ex vivo using iron oxide nanoparticles in steady state—dependence on blood volume and water exchange. *Magn. Reson. Med.* **47**, 461–471 (2002)
30. Bonnemain, B.: Superparamagnetic agents in magnetic resonance imaging. Physicochemical characteristics and clinical application. A review. *J. Drug Target.* **6**, 167–174 (1998)
31. Bos, C., et al.: In vivo MR imaging of intravascularly injected magnetically labeled stem cells in rat kidney and liver. *Radiology* **233**, 781–789 (2004)
32. Boudghène, F.P., et al.: Contribution of oral magnetic particles in MR imaging of the abdomen with spin-echo and gradient-echo sequences. *J. Magn. Reson. Imaging* **3**, 107–112 (1993)
33. Brusentsov, N.A., et al.: Evaluation of ferromagnetic fluids and suspensions for the site-specific radiofrequency-induced hyperthermia of MX11 sarcoma cells in vitro. *J. Magn. Magn. Mater.* **225**, 113–117 (2001)
34. Bulte, J.W.M., et al.: Neurotransplantation of magnetically labeled oligodendrocytes progenitors: magnetic resonance tracking of cell migration and myelination. *Proc. Natl. Acad. Sci.* **96**, 15256–15261 (1999)
35. Bulte, J.W.M. and Kraitchman, D.L.: Iron oxide MR contrast agents for molecular and cellular imaging. *NMR Biomed.* **17**, 484–499 (2004)
36. Butle, J.W., et al.: Specific MR imaging of human lymphocytes by monoclonal antibody-guided dextran-magnetite particles. *Magn. Reson. Med.* **25**, 148–157 (1992)
37. Cahill, K.S., et al.: Noninvasive monitoring and tracking of muscle stem cell transplant. *Transplantation* **78**, 1626–1633 (2004)
38. Carreño, T.G., et al.: Preparation of homogeneous Zn/Co mixed oxides by spray pyrolysis. *Mater. Chem. Phys.* **27**, 287–296 (1991)
39. Cerdan, S., et al.: Monoclonal antibody-coated magnetite particles as contrast agents in magnetic resonance imaging of tumors. *Magn. Reson. Med.* **12**, 151–163 (1989)
40. Cheng, F.-Y., et al.: Characterization of aqueous dispersions of Fe₃O₄ nanoparticles and their biomedical applications. *Biomaterials* **26**, 729–738 (2005)
41. Choi, H.S., et al.: Renal clearance of quantum dots. *Nat. Biotechnol.* **25**, 1165–1170 (2007)
42. Choi, J.-S., et al.: Biocompatible heterostructured nanoparticles for multimodal biological detection. *J. Am. Chem. Soc.* **128**, 15982–15983 (2006)
43. Corot, C., et al.: Recent advances in iron oxide nanocrystal technology for medical imaging. *Adv. Drug Del. Rev.* **58**, 1471–1504 (2006)
44. Daldrup-Link, H.E., et al.: Macromolecular contrast medium (Feruglose) versus small molecular contrast medium (Gadopentetate) enhanced magnetic resonance imaging: differentiation of benign and malignant breast lesions. *Acad. Radiol.* **10**, 1237–1246 (2003)
45. Damadian, R.: Tumor detection by nuclear magnetic resonance. *Science* **171**, 1151–1153 (1971)
46. Damadian, R.: Apparatus and method for detecting cancer in tissue. US Patent 3,789,832: February 5, 1974

47. Dandamudi, S. and Campbell, R.B.: The drug loading, cytotoxicity and tumor vascular targeting characteristics of magnetite in magnetic drug targeting. *Biomaterials* **28**, 4673–4683 (2007)
48. Decher, G.: Fuzzy nanoassemblies: toward layered polymeric multicomposites. *Science* **277**, 1232–1237 (1997)
49. Deng, Y., et al.: Preparation of magnetic polymeric particles via inverse microemulsion polymerization process. *J. Magn. Magn. Mater.* **257**, 69–78 (2003)
50. Duterloo, H.S.: Historic publication on the first use of magnets in orthodontics. *Am. J. Orthod. Dentofacial Orthop.* **108**, 15A–16A (1995)
51. Dutton, A.H., et al.: Iron-dextran antibody conjugates: general method for simultaneous staining of two components in high-resolution immunoelectron microscopy. *Proc. Natl. Acad. Sci.* **76**, 3392–3396 (1979)
52. Fajardo, L.F.: Pathological effects of hyperthermia in normal tissues. *Cancer Res.* **44(suppl.)**, 4826s–4835s (1984)
53. Fauconnier, N., et al.: Thiolation of maghemite nanoparticles by dimercaptosuccinic acid. *J. Colloid Interface Sci.* **194**, 427–433 (1997)
54. Fishbane, S., et al.: The safety of intravenous iron dextran in hemodialysis patients. *Am. J. Kidney Dis.* **28**, 529–534 (1996)
55. Forbes, Z.G., et al.: An approach to targeted drug delivery based on uniform magnetic fields. *IEEE Trans. Magn.* **39**, 3372–3377 (2003)
56. Funovics, M.A., et al.: MR imaging of the her2/neu and 9.2.27 tumor antigens using immunospecific contrast agents. *Magn. Reson. Imaging* **22**, 843–850 (2004)
57. Gallo, J.M., et al.: Targeting anticancer drugs to the brain: II. Physiological pharmacokinetic model of oxantazole following intraarterial administration to rat glioma-2 (RG-2) bearing rats. *J. Pharmacokin. Biopharm.* **21**, 575–592 (1993)
58. Gittins, D.I. and Caruso, F.: Spontaneous phase transfer of nanoparticulate metals from organic to aqueous media. *Angew. Chem. Int. Ed.* **40**, 3001–3004 (2001)
59. Glöckl, G., et al.: The effect of field parameters, nanoparticle properties and immobilization on the specific heating power in magnetic particle hyperthermia. *J. Phys.: Condens. Matter* **18**, S2935–S2949 (2006)
60. Gomi, T., et al.: Evaluation of the changes in signals from the spleen using ferucarbotran. *Radiat. Med.* **25**, 135–138 (2007)
61. Goya, F.G., et al.: Static and dynamic magnetic properties of spherical magnetite nanoparticles. *J. Appl. Phys.* **94**, 3520–3528 (2003)
62. Grief, A.D. and Richardson, G.: Mathematical modelling of magnetically targeted drug delivery. *J. Magn. Magn. Mater.* **293**, 455–463 (2005)
63. Groman, E.V.: Biologically degradable superparamagnetic materials for use in clinical applications. US Patent 4,827,945: May 9, 1989
64. Gupta, A.K. and Wells, S.: Surface-modified superparamagnetic nanoparticles for drug delivery: preparation, characterization, and cytotoxicity. *IEEE Trans. Nanobiosci.* **3**, 66–73 (2004)
65. Gupta, A.K. and Curtis, A.S.G.: Surface modified superparamagnetic nanoparticles for drug delivery: interaction studies with human fibroblasts in culture. *J. Mater. Sci.: Mater. Med.* **15**, 493–496 (2004)
66. Gupta, A.K. and Gupta, M.: Cytotoxicity suppression and cellular uptake enhancement of surface modified magnetic nanoparticles. *Biomaterials* **26**, 1565–1573 (2005)
67. Gupta, A.K. and Gupta, M.: Synthesis and surface engineering of iron oxide nanoparticles for biomedical applications. *Biomaterials* **26**, 3995–4021 (2005)
68. Guzman, R., et al.: Long-term monitoring of transplanted human neural stem cells in developmental and pathological contexts with MRI. *Proc. Natl. Acad. Sci.* **104**, 10211–10216 (2007)
69. Häfeli, U.: The History of Magnetism in Medicine. In: Andrä, W. and Nowak, H. (eds.) *Magnetism in Medicine: A Handbook*, Second Edition, pp. 1–25. Wiley-VCH Verlag GmbH & Co. KGaA, Weinheim (2007)

70. Hahn, P.F., et al.: First clinical trials of a new superparamagnetic iron oxide for the use as an oral gastrointestinal contrast agent in MR imaging. *Radiology* **175**, 695–700 (1990)
71. Harisinghani, M.G., et al.: Splenic imaging with ultrasmall superparamagnetic iron oxide ferumoxtran-10 (AMI-7227): preliminary observations. *J. Comput. Assist. Tomogr.* **25**, 770–776 (2001)
72. Harisinghani, M.G., et al.: Noninvasive detection of clinically occult lymph-node metastases in prostate cancer. *N. Engl. J. Med.* **348**, 2491–2499 (2003)
73. Hasegawa, M. and Hokkoku, S.: Magnetic iron oxide-dextran complex and process for its production. US Patent 4,101,435: July 18, 1978
74. Hergt, R., et al.: Magnetic particle hyperthermia: nanoparticle magnetism and materials development for cancer therapy. *J. Phys.: Condens. Matter* **18**, S2919–S2934 (2006)
75. Hill, J.M., et al.: Serial cardiac magnetic resonance imaging of injected mesenchymal stem cells. *Circulation* **108**, 1009–1014 (2003)
76. Himes, N., et al.: In vivo MRI of embryonic stem cells in a mouse model of myocardial infarction. *Magn. Reson. Med.* **52**, 1214–1219 (2004)
77. Hogemann, D., et al.: High throughput magnetic resonance imaging for evaluating targeted nanoparticle probes. *Bioconjug. Chem.* **13**, 116–121 (2002)
78. Hong, R., et al.: Comparison of schemes for preparing magnetic Fe₃O₄ nanoparticles. *China Particuology* **5**, 186–191 (2007)
79. Hu, D.E., et al.: Monitoring T-lymphocyte trafficking in tumors undergoing immune rejection. *Magn. Reson. Med.* **54**, 1473–1479 (2005)
80. Hyeon, T., et al.: Synthesis of highly crystalline and monodisperse maghemite nanocrystallites without a size-selection process. *J. Am. Chem. Soc.* **123**, 12798–12801 (2001)
81. Hyeon, T., et al.: Synthesis of highly crystalline and monodisperse cobalt ferrite nanocrystals. *J. Phys. Chem. B* **106**, 6831–6833 (2002)
82. Ichikawa, T., et al.: MRI of transgene expression: correlation to therapeutic gene expression. *Neoplasia* **4**, 523–530 (2002)
83. Igartua, M., et al.: Development and characterization of solid lipid nanoparticles loaded with magnetite. *Int. J. Pharm.* **233**, 149–157 (2002)
84. Ittrich, H., et al.: In vivo magnetic resonance imaging of iron oxide-labeled, arterially-injected mesenchymal stem cells in kidneys of rats with acute ischemic kidney injury: detection and monitoring at 3T. *J. Magn. Reson. Imag.* **25**, 1179–1191 (2007)
85. Jacobsen, T.F., et al.: Oral magnetic particles (ferristene) as a contrast medium in abdominal magnetic resonance imaging. *Acad. Radiol.* **3**, 571–580 (1996)
86. Jendelova, P., et al.: Magnetic resonance tracking of transplanted bone marrow and embryonic stem cells labeled by iron oxide nanoparticles in rat brain and spinal cord. *J. Neurosci. Res.* **76**, 232–243 (2004)
87. Johannsen, M., et al.: Clinical hyperthermia of prostate cancer using magnetic nanoparticles: presentation of a new interstitial technique. *Int. J. Hyperthermia* **21**, 637–647 (2005)
88. Johansson, L.O., et al.: A targeted contrast agent for magnetic resonance imaging of thrombus: implications of spatial resolution. *J. Magn. Reson. Imaging* **13**, 615–618 (2001)
89. Josephson, L., et al.: High-efficiency intracellular magnetic labeling with novel superparamagnetic-tat peptide conjugates. *Bioconjug. Chem.* **10**, 186–191 (1999)
90. Ju, S., et al.: In Vivo MR tracking of mesenchymal stem cells in rat liver after intrasplenic transplantation. *Radiology* **245**, 206–215 (2007)
91. Jun, Y.-W., et al.: Nanoscale size effect of magnetic nanocrystals and their utilization for cancer diagnosis via magnetic resonance imaging. *J. Am. Chem. Soc.* **127**, 5732–5733 (2005)
92. Jung, C.W. and Jacobs, P.: Physical and chemical properties of superparamagnetic iron oxide MR contrast agents: ferumoxides, ferumoxtran, ferumoxsil. *Magn. Reson. Imaging* **13**, 661–674 (1995)
93. Jurgons, R., et al.: Drug loaded magnetic nanoparticles for cancer therapy. *J. Phys.: Condens. Matter* **18**, S2893–S2902 (2006)
94. Kanematsu, M., et al.: Imaging liver metastases: review and update. *Eur. J. Radiol.* **58**, 217–228 (2006)

95. Kang, E., et al.: Direct synthesis of highly crystalline and monodisperse manganese ferrite nanocrystals. *J. Phys. Chem. B* **108**, 13932–13935 (2004)
96. Kang, H.W., et al.: Magnetic resonance imaging of inducible E-selectin expression in human endothelial cell culture. *Bioconjug. Chem.* **13**, 122–127 (2002)
97. Kang, Y.S., et al.: Synthesis and characterization of nanometer-size Fe_3O_4 and $\gamma\text{-Fe}_2\text{O}_3$ particles. *Chem. Mater.* **8**, 2209–2211 (1996)
98. Kato, H., et al.: Ferumoxide-enhanced MR imaging of hepatocellular carcinoma: correlation with histologic tumor grade and tumor vascularity. *J. Magn. Reson. Imaging* **19**, 76–81 (2004)
99. Kehagias, D.T., et al.: Diagnostic efficacy and safety of MRI of the liver with superparamagnetic iron oxide particles (SH U 555 A). *J. Magn. Reson. Imaging* **14**, 595–601 (2001)
100. Kelly, K.A., et al.: Detection of vascular adhesion molecule-1 expression using a novel multimodal nanoparticle. *Circ. Res.* **96**, 327–336 (2005)
101. Kim, D.K., et al.: Synthesis and characterization of surfactant-coated superparamagnetic monodispersed iron oxide nanoparticles. *J. Magn. Magn. Mater.* **225**, 30–36 (2001)
102. Kim, S.-H., et al.: Fabrication and estimation of Au-coated Fe_3O_4 nanocomposite powders for the separation and purification of biomolecules. *Mater. Sci. Eng. A* **449–451**, 386–388 (2007)
103. Kim, Y.K., et al.: Detection of liver metastases: gadobenate dimeglumine-enhanced three-dimensional dynamic phases and one-hour delayed phase MR imaging versus superparamagnetic iron oxide-enhanced MR imaging. *Eur. Radiol.* **15**, 220–228 (2005)
104. Kircher, M.F., et al.: In vivo high resolution three-dimensional imaging of antigen-specific cytotoxic T-lymphocyte trafficking to tumors. *Cancer Res.* **63**, 6838–6846 (2003)
105. Koh, D.-M., et al.: New horizons in oncologic imaging. *N. Engl. J. Med.* **348**, 2487–2488 (2003)
106. Kopp, A., et al.: MR imaging of the liver with resovist: safety, efficacy, and pharmacodynamic properties. *Radiology* **204**, 749–756 (1997)
107. Kraitchman, D.L., et al.: In vivo magnetic resonance imaging of mesenchymal stem cells in myocardial infarction. *Circulation* **107**, 2290–2293 (2003)
108. Kresse, M., et al.: Targeting of ultrasmall superparamagnetic iron oxide (USPIO) particles to tumor cells in vivo by using transferrin receptor pathways. *Magn. Reson. Med.* **40**, 236–242 (1998)
109. Kullberg, M., et al.: Improved drug delivery to cancer cells: a method using magnetoliposomes that target epidermal growth factor receptors. *Med. Hypoth.* **64**, 468–470 (2005)
110. Laghi, A., et al.: Oral contrast agents for magnetic resonance imaging of the bowel. *Top. Magn. Reson. Imaging* **13**, 389–396 (2002)
111. Lawaczeck, R., et al.: Superparamagnetic iron oxide particles: contrast media for magnetic resonance imaging. *Appl. Organometal. Chem.* **18**, 506–513 (2004)
112. Lee, H., et al.: Thermally cross-linked superparamagnetic iron oxide nanoparticles: synthesis and application as a dual imaging probe for cancer in vivo. *J. Am. Chem. Soc.* **129**, 12739–12745 (2007)
113. Lee, J.-H., et al.: Dual-mode nanoparticle probes for high-performance magnetic resonance and fluorescence imaging of neuroblastoma. *Angew. Chem. Int. Ed.* **45**, 8160–8162 (2006)
114. Lee, J.-H., et al.: Artificially engineered magnetic nanoparticles for ultra-sensitive molecular imaging. *Nat. Med.* **13**, 95–99 (2007)
115. Lee, S.-J., et al.: Synthesis and characterization of superparamagnetic maghemite nanoparticles prepared by coprecipitation technique. *J. Magn. Magn. Mater.* **282**, 147–150 (2004)
116. Lee, Y., et al.: Large-scale synthesis of uniform and crystalline magnetite nanoparticles using reverse micelles as nanoreactors under reflux conditions. *Adv. Funct. Mater.* **15**, 503–509 (2005)
117. Lefebure, S., et al.: Monodisperse magnetic nanoparticles: preparation and dispersion in water and oils. *J. Mater. Res.* **13**, 2975–2981 (1998)

118. Lemke, A.-J., et al.: MRI after magnetic drug targeting in patients with advanced solid malignant tumors. *Eur. Radiol.* **14**, 1949–1955 (2004)
119. Lewin, M., et al.: Tat peptide-derivatized magnetic nanoparticles allow in vivo tracking and recovery of progenitor cells. *Nat. Biotechnol.* **18**, 410–414 (2000)
120. Li, S., et al.: Structured materials syntheses in a self-assembled surfactant mesophase. *Colloids Surf. A* **174**, 275–281 (2000)
121. Livesay, B.R.: 9th International Conference on rare earth magnets and their applications. (1987)
122. López, A., et al.: Magnetic properties of γ -Fe₂O₃ small particles prepared by spray pyrolysis. *J. Magn. Magn. Mater.* **140–144**, 383–384 (1995)
123. Lübke, A.S., et al.: Clinical applications of magnetic drug targeting. *J. Surg. Res.* **95**, 200–206 (2001)
124. MacVicar, D., et al.: Phase III trial of oral magnetic particles in MRI of abdomen and pelvis. *Clin. Radiol.* **47**, 183–188 (1993)
125. Matuszewski, L., et al.: Cell tagging with clinically approved iron oxides: feasibility and effect of lipofection, particle size, and surface coating on labeling efficiency. *Radiology* **235**, 155–161 (2005)
126. McLachlan, S.J., et al.: Phase I clinical evaluation of a new iron oxide MR contrast agent. *J. Magn. Reson. Imaging* **43**, 301–307 (1994)
127. Metz, S., et al.: Capacity of human monocytes to phagocytose approved iron oxide MR contrast agents in vitro. *Eur. Radiol.* **14**, 1851–1858 (2004)
128. Moore, A., et al.: Measuring transferrin receptor gene expression by NMR imaging. *Biochim. Biophys. Acta* **1402**, 239–249 (1998)
129. Moore, A., et al.: In vivo targeting of underglycosylated MUC-1 tumor antigen using a multimodal imaging probe. *Cancer Res.* **64**, 1821–1827 (2004)
130. Mykhaylyk, O., et al.: Doxorubicin magnetic conjugate targeting upon intravenous injection into mice: high gradient magnetic field inhibits the clearance of nanoparticles from the blood. *J. Magn. Magn. Mater.* **293**, 473–482 (2005)
131. Namkung, S., et al.: Superparamagnetic iron oxide (SPIO)-enhanced liver MRI with ferucarbotran: efficacy for characterization of focal liver lesions. *J. Magn. Reson. Imaging* **25**, 755–765 (2007)
132. Nedkov, I., et al.: Surface oxidation, size and shape of nano-sized magnetite obtained by co-precipitation. *J. Magn. Magn. Mater.* **300**, 358–367 (2006)
133. Nishijima, S., et al.: A study on magnetically targeted drug delivery system using superconducting magnet. *Physica C* **463–465**, 1311–1314 (2007)
134. Nishimura, H., et al.: Preoperative esophageal cancer staging: magnetic resonance imaging of lymph node with ferumoxtran-10, an ultrasmall superparamagnetic iron oxide. *J. Am. Coll. Surg.* **202**, 604–611 (2006)
135. Oude Engberink, R.D., et al.: Comparison of SPIO and USPIO for in vitro labeling of human monocytes: MR detection and cell function. *Radiology* **243**, 467–474 (2007)
136. Papell, S.S.: Low viscosity magnetic fluid obtained by the colloidal suspension of magnetic particles. US Patent 3,215,572: November 2, 1965
137. Park, H.-Y., et al.: Fabrication of magnetic core@shell Fe oxide@Au nanoparticles for interfacial bioactivity and bio-separation. *Langmuir* **23**, 9050–9056 (2007)
138. Park, J., et al.: Ultra-large-scale syntheses of monodisperse nanocrystals. *Nat. Mater.* **3**, 891–895 (2004)
139. Park, J., et al.: One-nanometer-scale size-controlled synthesis of monodisperse magnetic iron oxide nanoparticles. *Angew. Chem. Int. Ed.* **44**, 2872–2877 (2005)
140. Pellegrino, T., et al.: Hydrophobic nanocrystals coated with an amphiphilic polymer shell: a general route to water soluble nanocrystals. *Nano Lett.* **4**, 703–707 (2004)
141. Pillai, V., et al.: Preparation of nanoparticles of silver halides, superconductors and magnetic materials using water-in-oil microemulsions as nano-reactors. *Adv. Colloid Interface Sci.* **55**, 241–269 (1995)

142. Pirko, I., et al.: In vivo magnetic resonance imaging of immune cells in the central nervous system with superparamagnetic antibodies. *FASEB* **18**, 179–181 (2004)
143. Qin, J., et al.: A high-performance magnetic resonance imaging T₂ contrast agent. *Adv. Mater.* **19**, 1874–1878 (2007)
144. Raaphorst, G.P.: Fundamental aspects of hyperthermic biology. In: Field, S.B. and Hand, J.W. (eds.) *An Introduction to the Practical Aspects of Clinical Hyperthermia*, pp. 10–54. Taylor and Francis, London (1990)
145. Rad, A.M., et al.: Quantification of superparamagnetic iron oxide (SPIO)-labeled cells using MRI. *J. Magn. Reson. Imag.* **26**, 366–374 (2007)
146. Reimer, P., et al.: Receptor imaging: application to MR imaging of liver cancer. *Radiology* **177**, 729–734 (1990)
147. Reimer, P., et al.: Receptor-directed contrast agents for MR imaging: preclinical evaluation with affinity assays. *Radiology* **182**, 565–569 (1992)
148. Reimer, P., et al.: Pancreatic receptors: initial feasibility studies with a targeted contrast agent for MR imaging. *Radiology* **193**, 527–531 (1994)
149. Reimer, P. and Tombach, B.: Hepatic MRI with SPIO: detection and characterization of focal liver lesions. *Eur. Radiol.* **8**, 1198–1204 (1998)
150. Reimer, P. and Balzer, T.: Ferucarbotran (Resovist): a new clinically approved RES-specific contrast agent for contrast-enhanced MRI of the liver: properties, clinical development, and applications. *Eur. Radiol.* **13**, 1266–1276 (2003)
151. Remsen, L.G., et al.: MR of carcinoma-specific monoclonal antibody conjugated to monocrystalline iron oxide nanoparticles: the potential for noninvasive diagnosis. *Am. J. Neuroradiol.* **17**, 411–418 (1996)
152. Renshaw, P.F., et al.: Immunospecific NMR contrast agents. *Magn. Reson. Imaging* **4**, 351–357 (1986)
153. Ritter, J.A., et al.: Application of high gradient magnetic separation principles to magnetic drug targeting. *J. Magn. Magn. Mater.* **280**, 184–201 (2004)
154. Rockenberger, J., et al.: A new nonhydrolytic single-precursor approach to surfactant-capped nanocrystals of transition metal oxides. *J. Am. Chem. Soc.* **121**, 11595–11596 (1999)
155. Roger, J., et al.: Behavior of aqueous ferrofluids in presence of amino acids. *Eur. J. Solid State Inorg. Chem.* **26**, 475–488 (1989)
156. Rohrer, M., et al.: Comparison of magnetic properties of MRI contrast media solutions at different magnetic field strengths. *Invest. Radiol.* **40**, 715–724 (2005)
157. Rudge, S.R., et al.: Preparation, characterization, and performance of magnetic iron-carbon composite microparticles for chemotherapy. *Biomaterials* **21**, 1411–1420 (2000)
158. Sanderson, C.J. and Wilson, D.V.: A simple method for coupling proteins to insoluble polysaccharides. *Immunology* **20**, 1061–1065 (1971)
159. Savellano, M.D. and Hasan, T.: Targeting cells that overexpress the epidermal growth factor receptor with polyethylene glycolated BPD verteporfin photosensitizer immunoconjugates. *Photochem. Photobiol.* **77**, 431–439 (2003)
160. Schellenberger, E.A., et al.: Surface-functionalized nanoparticle library yields probes for apoptotic cells. *Chem. Bio. Chem.* **5**, 275–279 (2004)
161. Schulze, E., et al.: Cellular uptake and trafficking of a prototypical magnetic iron oxide label in vitro. *Invest. Radiol.* **30**, 604–610 (1995)
162. Seip, C.T., et al.: Magnetic properties of a series of ferrite nanoparticles synthesized in reverse micelles. *IEEE Trans. Magn.* **34**, 1111–1113 (1998)
163. Semelka, R.C. and Helmberger, T.K.: Contrast agents for MR imaging of the liver. *Radiology* **218**, 27–38 (2001)
164. Seo, W.S., et al.: FeCo/graphitic-shell nanocrystals as advanced magnetic-resonance-imaging and near-infrared agents. *Nat. Mater.* **5**, 971–976 (2006)
165. Shen, T., et al.: Monocrystalline iron oxide nanocompounds (MION): physicochemical properties. *MRM* **29**, 599–604 (1993)
166. Shen, T.T., et al.: Magnetically labeled secretin retains receptor affinity to pancreas acinar cells. *Bioconjug. Chem.* **7**, 311–316 (1996)

167. Simon, G.H., et al.: Ultrasmall superparamagnetic iron oxide-enhanced magnetic resonance imaging of antigen-induced arthritis. A comparative study between SHU 555 C, Ferumoxtran-10, and Ferumoxytol. *Invest. Radiol.* **41**, 45–51 (2006)
168. Sminia, P., et al.: Effect of hyperthermia on the central nervous system. *Int. J. Hyperthermia* **10**, 1–130 (1994)
169. Stark, D.D., et al.: Superparamagnetic iron oxide: clinical application as a contrast agent for MR imaging of the liver. *Radiology* **168**, 297–301 (1988)
170. Stolnik, S., et al.: Long circulating microparticulate drug carriers. *Adv. Drug Del. Rev.* **16**, 195–214 (1995)
171. Sun, R., et al.: Physical and biological characterization of superparamagnetic iron oxide- and ultrasmall superparamagnetic iron oxide-labeled cells. *Invest. Radiol.* **40**, 504–513 (2005)
172. Sun, S. and Zeng, H.: Size-controlled synthesis of magnetite nanoparticles. *J. Am. Chem. Soc.* **124**, 8204–8205 (2002)
173. Sun, S., et al.: Monodisperse MFe_2O_4 ($M=Fe, Co, Mn$) nanoparticles. *J. Am. Chem. Soc.* **126**, 273–279 (2004)
174. Suslick, K.S., et al.: Sonochemical synthesis of iron colloids. *J. Am. Chem. Soc.* **118**, 11960–11961 (1996)
175. Suwa, T., et al.: Magnetic Resonance imaging of esophageal squamous cell carcinoma using magnetite particles coated with anti-epidermal growth factor receptor antibody. *Int. J. Cancer* **75**, 626–634 (1998)
176. Takeda, S., et al.: Development of magnetically targeted drug delivery system using superconducting magnet. *J. Magn. Magn. Mater.* **311**, 367–371 (2007)
177. Tang, J., et al.: Magnetite Fe_3O_4 nanocrystals: spectroscopic observation of aqueous oxidation kinetics. *J. Phys. Chem. B* **107**, 7501–7506 (2003)
178. Taupitz, M., et al.: Phase I clinical evaluation of citrate-coated monocrystalline very small superparamagnetic iron oxide particles as a new contrast medium for magnetic resonance imaging. *Invest. Radiol.* **39**, 394–405 (2004)
179. Thorek, D.L.J., et al.: Superparamagnetic iron oxide nanoparticle probes for molecular imaging. *Ann. Biomed. Eng.* **34**, 23–38 (2006)
180. Tiefenauer, L.X., et al.: Antibody-magnetite nanoparticles: in vitro characterization of a potential tumor-specific contrast agent for magnetic resonance imaging. *Bioconjug. Chem.* **4**, 347–352 (1993)
181. Tiefenauer, L.X., et al.: In vivo evaluation of magnetite nanoparticles for use as a tumor contrast agent in MRI. *Magn. Reson. Imaging* **14**, 391–402 (1996)
182. Toma, A., et al.: Monoclonal antibody A7-superparamagnetic iron oxide as contrast agent of MR imaging of rectal carcinoma. *Br. J. Cancer* **93**, 131–136 (2005)
183. Torchilin, V.P.: Drug targeting. *Eur. J. Pharm. Sci.* **11(Suppl. 2)**, S81–S91 (2000)
184. Treleaven, J.G., et al.: Removal of neuroblastoma cells from bone marrow with monoclonal antibodies conjugated to magnetic microspheres. *The Lancet* **14**, 70–73 (1984)
185. Treleaven, J.G.: Bone marrow purging: an appraisal of immunological and non-immunological methods. *Adv. Drug Del. Rev.* **2/3**, 253–269 (1988)
186. Udrea, L.E., et al.: An in vitro study of magnetic particle targeting in small blood vessels. *Phys. Med. Biol.* **51**, 4869–4881 (2006)
187. van der Zee, J.: Heating the patient: a promising approach? *Ann. Oncol.* **13**, 1173–1184 (2002)
188. Veintemillas-Verdaguer, S., et al.: Effect of the oxidation conditions on the maghemites production by laser pyrolysis. *J. Appl. Organometal. Chem.* **15**, 365–372 (2001)
189. Vlahos, L., et al.: A comparative study between Gd-DTPA and oral magnetic particles (OMP) as gastrointestinal (GI) contrast agents for MRI of the abdomen. *Magn. Reson. Imaging* **12**, 719–726 (1994)
190. Wadghiri, Y.Z., et al.: Detection of alzheimer's amyloid in transgenic mice using magnetic resonance microimaging. *Magn. Reson. Med.* **50**, 293–302 (2003)
191. Walter, G.A., et al.: Noninvasive monitoring of stem cell transfer for muscle disorders. *Magn. Reson. Med.* **51**, 273–277 (2004)

192. Wang, F.H., et al.: Magnetic resonance tracking of nanoparticle labelled neural stem cells in a rat's spinal cord. *Nanotechnol.* **17**, 1911–1915 (2006)
193. Wang, J., et al.: Stepwise directing of nanocrystals to self-assemble at water/oil interfaces. *Angew. Chem. Int. Ed.* **45**, 7963–7966 (2006)
194. Wang, X., et al.: The heating effect of magnetic fluids in an alternating magnetic field. *J. Magn. Mater.* **293**, 334–340 (2005)
195. Wang, Y.-X.J., et al.: Superparamagnetic iron oxide contrast agents: physicochemical characteristics and applications in MR imaging. *Eur. Radiol.* **11**, 2319–2331 (2001)
196. Wang, Y., et al.: “Pulling” nanoparticles into water: phase transfer of oleic acid stabilized monodisperse nanoparticles into aqueous solutions of α -cyclodextrin. *Nano Lett.* **3**, 1555–1559 (2003)
197. Weissleder, R., et al.: Superparamagnetic iron oxide: pharmacokinetics and toxicity. *AJR* **152**, 167–173 (1989)
198. Weissleder, R., et al.: Ultrasmall superparamagnetic iron oxide: characterization of a new class of contrast agents for MR imaging. *Radiology* **175**, 489–493 (1990)
199. Weissleder, R., et al.: MR receptor imaging: ultrasmall iron oxide particles targeted to asialoglycoprotein receptors. *AJR* **155**, 1161–1167 (1990)
200. Weissleder, R., et al.: Polyclonal human immunoglobulin G labeled with polymeric iron oxide: antibody MR imaging. *Radiology* **181**, 245–249 (1991)
201. Weissleder, R., et al.: Antimyosin-labeled monocrystalline iron oxide allows detection of myocardial infarct: MR antibody imaging. *Radiology* **182**, 381–385 (1992)
202. Weissleder, R., et al.: Long-circulating iron oxides for MR imaging. *Adv. Drug Del. Rev.* **16**, 321–334 (1995)
203. Weissleder, R., et al.: In vivo magnetic resonance imaging of transgene expression. *Nat. Med.* **6**, 351–355 (2000)
204. Weissleder, R., et al.: Cell-specific targeting of nanoparticles by multivalent attachment of small molecules. *Nat. Biotechnol.* **23**, 1418–1423 (2005)
205. Whitehead, R.A.: Magnetic particles for use in separations. US Patent 4,554,088: November 19, 1985
206. Wondergem, J., et al.: Effects of local hyperthermia on the motor function of the rat sciatic nerve. *Int. J. Radiat. Biol.* **53**, 429–439 (1988)
207. Wunderbaldinger, P., et al.: Crosslinked iron oxides (CLIO): a new platform for the development of targeted MR contrast agents. *Acad. Radiol.* **9(suppl. 2)**, S304–S306 (2002)
208. Xia, H., et al.: Hyperthermia combined with intra-thoracic chemotherapy and radiotherapy for malignant pleural mesothelioma. *Int. J. Hyperthermia* **22**, 613–621 (2006)
209. Xu, Z., et al.: Magnetic core/shell $\text{Fe}_3\text{O}_4/\text{Au}$ and $\text{Fe}_3\text{O}_4/\text{Au}/\text{Ag}$ nanoparticles with tunable plasmonic properties. *J. Am. Chem. Soc.* **129**, 8698–8699 (2007)
210. Zeng, H., et al.: Shape-controlled synthesis and shape-induced texture of MnFe_2O_4 nanoparticles. *J. Am. Chem. Soc.* **126**, 11458–11459 (2004)
211. Zhang, C., et al.: Silica- and alkoxysilane-coated ultrasmall superparamagnetic iron oxide particles: a promising tool to label cells for magnetic resonance imaging. *Langmuir* **23**, 1427–1434 (2007)
212. Zhang, Y., et al.: Surface modification of superparamagnetic magnetite nanoparticles and their intracellular uptake. *Biomaterials* **23**, 1553–1561 (2002)
213. Zhang, Y. and Zhang, J.: Surface modification of monodisperse magnetite nanoparticles for improved intracellular uptake to breast cancer cells. *J. Colloid Interface Sci.* **283**, 352–357 (2005)
214. Zhao, M., et al.: Non-invasive detection of apoptosis using magnetic resonance imaging and a targeted contrast agent. *Nat. Med.* **7**, 1241–1244 (2001)
215. Zhao, M., et al.: Differential conjugation of tat peptide to superparamagnetic nanoparticles and its effect on cellular uptake. *Bioconjug. Chem.* **13**, 840–844 (2002)
216. Zinderman, C.E., et al.: Anaphylactoid reactions to dextran 40 and 70: reports to the United States Food and Drug Administration, 1969 to 2004. *J. Vasc. Surg.* **43**, 1004–1009 (2006)

Chapter 21

Nano-Magnetophotonics

Mitsuteru Inoue, Alexander Khanikaev, and Alexander Baryshev

Abstract Data-processing and optical communication systems that allow controlling intensity and polarization state of light via external magnetic fields require compact, efficient, and low-cost magnetic materials. It is these properties of magnetic materials that are the subject of the present chapter. Owing to their strong linear and nonlinear magneto-optical responses along with unique optical characteristics, magnetophotonic crystals have already found applications in electronics. As a particular example, film-type optical isolator/circulator devices have been proposed. Recent renewed interest in magneto-optical spatial light modulators has resulted from the development of optical volumetric recording using holography, particularly, collinear holography. Here we focus on reviewing experimental and theoretical studies of light coupling to various artificial magnetic nanostructured media and nanocomposites providing strong magneto-optical responses and having miniature dimensions. We first examine properties of different types of MPCs. Then, the magnetorefractive effect of various materials is considered, an enhancement of the magnetorefractive response is demonstrated for structures fabricated in the use of the magnetophotonic crystals' concept. Finally, the influence of localized surface plasmon resonances on optical and magneto-optical properties of bismuth-substituted yttrium iron garnet films impregnated with nanoparticles of noble metals is discussed. Another promising way to enhance Faraday rotation is to exploit the regime of extraordinary transmission for systems comprising a perforated noble-metal film supporting transmission resonances and a magnetic material.

21.1 Introduction

Up-to-date methods of microfabrication allow us to create inhomogeneous structures, for example, photonic crystals (PCs), with high accuracy. PCs with

A. Baryshev (✉)
Toyohashi University of Technology, Toyohashi, Aichi, Japan
e-mail: baryshev@eee.tut.ac.jp

periodically modulated dielectric properties attract an ever-growing interest since the early paper where they were considered [1]. Prediction on microscopic distribution of fields inside the primitive cell of a photonic structure can be used for optimizing their responses. When having a proper design, periodic structures made of repetitions of active materials exhibit significantly higher responses compared to that of the materials used for fabrication. For example, the magneto-optical quality factor of MPCs – the performance ratio showing the relation of Faraday rotation and transmissivity – is found to be substantially greater than that achieved for a homogeneous magneto-optical (MO) material. MPCs are certainly considered as next-generation fast and miniature elements for use in integrated optical circuits. The large MO response is particularly attractive for constructing micro-sized film-type optical isolator/circulator elements for optical communication systems [2] and ultra-high speed MO spatial light modulators for high density holographic data storage [3]. Large angles of Faraday rotation, wide working spectral ranges, and nano- (or micro-) sized dimensions of MO structures are essential properties demanded by applications. This has motivated scientists to explore new possibilities and principles in this field.

In this chapter, most of experimental and theoretical studies of light coupling to various magnetic nanostructured media and nanocomposites are briefly reviewed. Unique optical and magneto-optical properties are shown to exist for MPCs with different designs. The magnetorefractive effect (MRE) of different media is considered along with the possibility to enhance the MRE by the use of MPCs containing a nanocomposite or manganite film as a defect layer. Influence of localized surface plasmon resonances on optical and magneto-optical properties of bismuth-substituted yttrium iron garnet (Bi:YIG) films impregnated with Au nanoparticles are discussed. The regime of extraordinary transmission for the systems comprising a perforated metal film supporting transmission resonance excitations and a magnetic material is found to be responsible for the large, anomalous Faraday rotation.

21.2 Magnetophotonic Crystals

Artificial structures composed of alternating dielectric materials with different refractive indices, known as photonic crystals, have been shown to affect the propagation of light, providing a new mechanism to control and manipulate the flow of light. Following the concept of photonic band gaps originating in light coupling to the spatially periodic structure and localization of light in the vicinity of defects introduced into the periodic structure [4, 5], various one-, two-, and three-dimensional PCs, photonic crystal fibers and waveguides, wave plates have been designed, and new fabrication technologies have been developed within the last two decades [6, 7].

For a magnetophotonic crystal (or magneto-optical Bragg structure), in which the constitutive elements are magnetic (or even only a defect introduced into the periodic structure is magnetic), there exists an additional degree of freedom to operate

the photonic band structure, diffraction patterns, and the direction and state of polarization of light, i.e., these characteristics can be controlled by the external magnetic field [8–34]. Of primary importance is that MPCs enhance responses of known MO materials. Different designs, technologies, and experimental techniques have been involved in fabrication and studies of MPCs. In fact, the large enhancement of Faraday rotation is demonstrated for one-dimensional (1D) MPCs grown using sputtering where periodic multilayers were composed of thin magnetic garnet films and films of different dielectric materials deposited [11, 26]. All-garnet 1D MPCs fabricated by pulsed laser deposition are demonstrated and shown to exhibit good functional performance [15, 28]. So-called Bragg grating magnetic photonic crystal waveguides are shown to enhance polarization rotation [18, 19]. Three-port circulators with complete isolation and high transmission, which are the circulators formed of a magneto-optical cavity in a 2D MPC, are proposed [21, 22]. Surface state peculiarities in photonic structures composed of adjoining (interfacing) magnetic and nonmagnetic photonic crystals are shown to give rise to giant Faraday and Kerr effects [24]. Recently, full analytical treatment has been demonstrated for a layered-stack photonic crystal; the photonic band structure and Bloch states in birefringent 1D MPCs are studied [27]. MO waveguides operating in near-infrared with responses governed by the magnetostatic forward volume waves are experimentally studied [33]. Theoretical consideration of chirped Bragg gratings generated due to refractive-index perturbations and working as transmission windows is reported in [34].

MPCs are certainly considered as next-generation fast and miniature elements for use in integrated optics. The large MO enhancement is particularly attractive for constructing nano-sized film-type optical isolator/circulator elements for optical communication systems as theoretically predicted in [15], and ultra-high speed MO spatial light modulators for high density holographic data storage as examined experimentally [3].

This section focuses on functional performances of the film-type 1D MPCs with different designs: 1D MPCs composed of alternating magnetic and dielectric layers, and 1D MPCs with the localized states in photonic band gaps (PBGs). Results of theoretical consideration of 2D and 3D MPCs are presented, and their magneto-optical responses are discussed.

21.2.1 1D MPCs Composed of Alternating Magnetic and Dielectric Layers

A series of studies on MPCs dates back to 1995, where the light propagation in discontinuous magnetic media with a 1D array structure is discussed [8]. In the subsequent theoretical studies [11, 12], light propagation in bismuth-substituted yttrium iron garnet (Bi:YIG) films stacked into random multilayer structures was analyzed using the matrix approach, where enhancement of the MO effects associated with the localization of light was predicted. Starting 1D structures were the multilayer

films composed of N_M layers of Bi:YIG and N_S layers of SiO₂, which were piled up in an arbitrary sequence; each of Bi:YIG and SiO₂ layers had thickness of d_M and d_S , respectively. For such structures, the enhancement in both transmissivity and the Faraday rotation angle, θ_F , was shown to originate from the weak localization of light caused by the multiple interference [35, 36]. Results indicate that enhancement of θ_F becomes larger as the degree of light localization rises. In fact, the theoretical computations show that the large enhancement of θ_F can be obtained in the 1D MPCs with microcavity-type structures [11], in which a magnetic planar defect is introduced between two Bragg reflectors, and also in structures with periodical multilayered structure. Following these predictions, the magnetic multilayer- and microcavity-type 1D MPCs were fabricated and their experimental evaluation was performed.

Let us consider the Faraday rotation enhancement in magnetic multilayer-type 1D MPC shown in Fig. 21.1. This idea utilizes the spatial localization of light within magnetic layers for the wavelengths corresponding to the PBG edge. Figure 21.1(a)

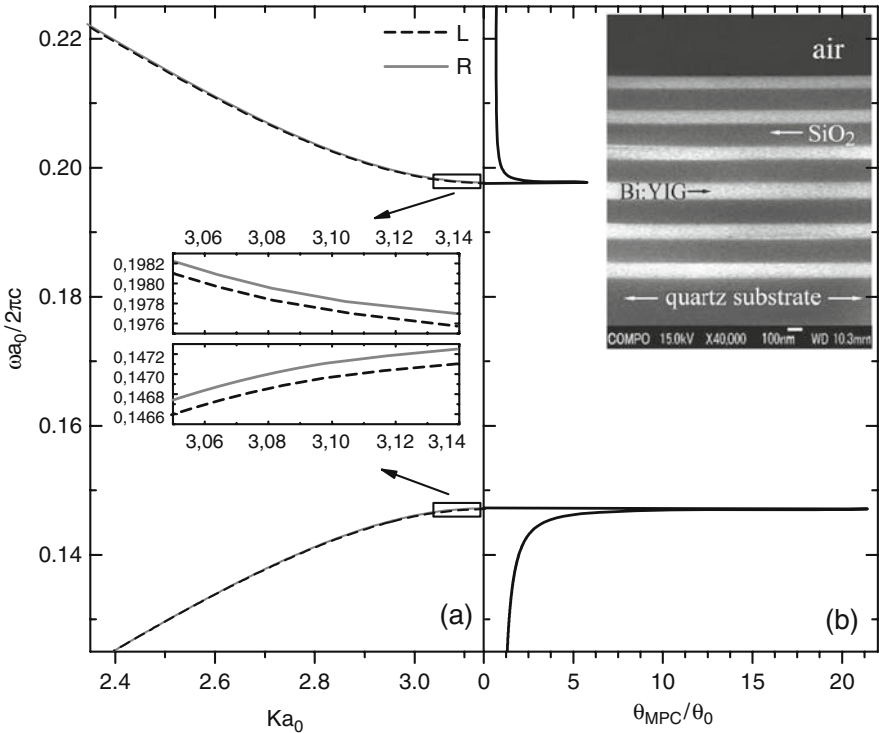


Fig. 21.1 (a) Photonic band structure for the circular-polarized waves calculated for normal incidence onto a 1D MPC consisted of layers of the nonmagnetic (SiO₂) and the magnetic (Bi:YIG) materials; dispersion is taken into account while absorption and dichroism are neglected. (b) Faraday rotation in the 1D MPC normalized to that of homogeneous (Bi:YIG) film of the same thickness; inset shows SEM image of a cleavage face of the sample under study

shows a photonic band structure [or the dispersion relations $\omega(\mathbf{k}_L)$ and $\omega(\mathbf{k}_R)$] calculated from the four-by-four matrix approach [9, 37–39] for the left- and right-circular-polarized waves propagating in a 1D MPC comprising magnetic and nonmagnetic quarter-wavelength-thick layers [see inset to Fig. 21.1(b)].

Note that Faraday rotation is expressed through the magnitude of wave vectors \mathbf{k}_L and \mathbf{k}_R , $\theta_F(\omega) = [\mathbf{k}_R(\omega) - \mathbf{k}_L(\omega)]d/2$, where d is the path length of light beam in the medium. As \mathbf{k}_L and \mathbf{k}_R approach the boundary of the Brillouin zone (the PBG edges), dispersion curves flatten. This indicates decrease of the group velocity or slowing down the electromagnetic energy propagation velocity which relates directly to the localization of light inside the MPC. Wave vectors \mathbf{k}_L and \mathbf{k}_R corresponding to the same frequency at the PBG edge differ significantly. This is a fingerprint of the expected strengthening of the effective circular birefringence and the enhancement of magneto-optical Faraday rotation for light with wavelength tuned across the PBG edge. The experimental sample was composed of microcrystalline Bi:YIG ($N_M=6$) and amorphous SiO₂ ($N_S=5$); note that both materials are characterized by low optical losses in red (and infrared) spectral range, and Bi:YIG has large Faraday rotation. This (Bi:YIG/SiO₂)⁵/Bi:YIG stack of alternating the $\lambda/4$ -thick layers of Bi:YIG and SiO₂ was fabricated by RF-magnetron sputtering onto the fused quartz substrate. The cleavage of the MPC is presented in Fig. 21.1(b) and shows abrupt interfaces between layers as well as reproducible thicknesses of layers throughout the sample; the thicknesses were $d_M = 98$ nm and $d_S = 147$ nm, the refractive indices were $n_{\text{SiO}_2} = 1.45$ and $n_{\text{Bi:YIG}} = 2.36$.

Optical and magneto-optical spectra of the sample are shown in Fig. 21.2. The MO response was measured in the Faraday geometry when the saturating external magnetic field of 2 kOe was applied (all the Faraday rotation spectra presented below were measured at this condition). One can see the first PBG ranging from 720 to 1,070 nm where transmission is strongly suppressed. The Faraday rotation

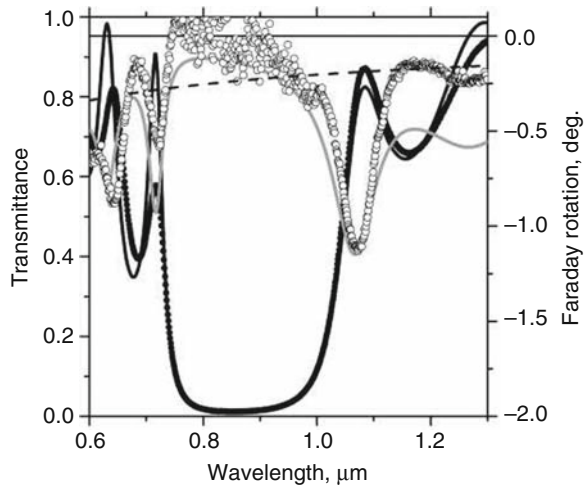


Fig. 21.2 Transmission (solid circles) and Faraday rotation spectra (open circles) of the 1D MPC are shown in Fig. 21.1 (at normal incidence). Solid curves show the fitting of the experimental data by the four-by-four matrix approach. Dashed line is for the interference-subtracted spectrum of the Faraday rotation for the Bi:YIG film with the thickness equal to the total Bi:YIG thickness in the 1D MPC under study

angle is found to decrease up to zero in this spectral range. Contrary, outside PBG transmittance rises and shows interference fringes, and the Faraday rotation angle θ_F oscillates and has the local maxima at 640 and 720 nm that correspond to the maxima in the transmission spectrum. The largest θ_F is observed at the long-wavelength edge of PBG, which is at 1,070 nm. The calculated interference-subtracted spectrum of Faraday rotation for a Bi:YIG film, whose thickness equals the total Bi:YIG thickness in the sample under study, is given for comparison by the dashed line. The θ_F enhancement at the long-wavelength PBG edge is of ~ 6 times. Calculations show that one can obtain larger Faraday rotation in the structures with a larger number of the N_M and N_S layers due to the stronger field localization for the waves corresponding to the PBG edges.

Both experimental spectra are matched using the four-by-four matrix technique with account of refractive index and absorption coefficients dispersions (see solid lines). This technique is generalization of the well-known transfer matrix method developed for studies of the optical properties of multilayered structures, but extended to the case of structures consisting of magneto-optical materials with permittivity tensor of the form:

$$\hat{\varepsilon} = \begin{pmatrix} \varepsilon_{xx} & i\varepsilon_{xy} & 0 \\ -i\varepsilon_{xy} & \varepsilon_{xx} & 0 \\ 0 & 0 & \varepsilon_{zz} \end{pmatrix}. \quad (21.1)$$

Following Ref. [8], we introduce a four-by-four transfer matrix $\hat{\Phi}_n$, which matches amplitudes of the electric and magnetic fields at the opposite boundaries of the n th layer:

$$\begin{bmatrix} E_x \\ E_y \\ H_x \\ H_y \end{bmatrix}^n = \hat{\Phi}^n \begin{bmatrix} E_x \\ E_y \\ H_x \\ H_y \end{bmatrix}^{n-1}, \quad (21.2)$$

where E_x (E_y) and H_x (H_y) are the amplitudes of the x - (y -) projection of the electric and magnetic fields, respectively, and the electromagnetic wave propagates along the z -direction chosen to coincide with the cross-section axis of the layered structure. In the case of multilayer-type MPCs representing N repetitions of the unit cell consisting of the pair of SiO_2 and Bi:YIG layers, the total transfer matrix can be written in the form:

$$\hat{\Phi} = (\hat{\Phi}^{\text{Bi:YIG}} \hat{\Phi}^{\text{SiO}_2})^N, \quad (21.3)$$

and, for the case of the microcavity-type MPC (see the next subsection),

$$\hat{\Phi} = (\hat{\Phi}^{\text{Ta}_2\text{O}_5} \hat{\Phi}^{\text{SiO}_2})^N \hat{\Phi}^{\text{Bi:YIG}} (\hat{\Phi}^{\text{SiO}_2} \hat{\Phi}^{\text{Ta}_2\text{O}_5})^N. \quad (21.4)$$

Since the transfer matrix $\hat{\Phi}$ relates the amplitudes at the two opposite boundaries of an MPC, the relation between the amplitudes of the transmitted and reflected waves with that of the incident wave can be found. Thus, the transfer matrix completely determines optical and magneto-optical properties of the MPC. When these amplitudes are determined from Eqs. (21.1) and (21.2), the well-known equation for evaluation of the Faraday rotation angle can be used:

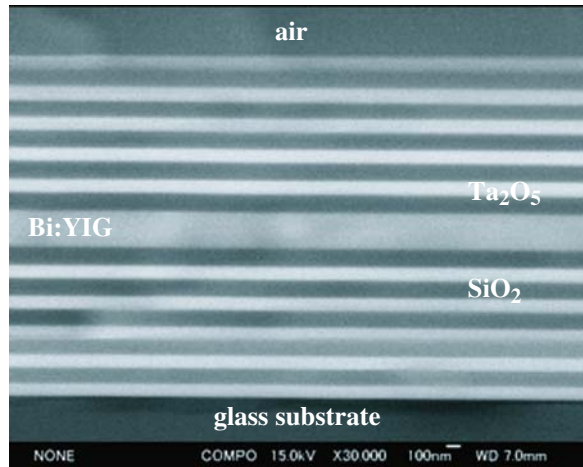
$$\theta_F = \frac{1}{2} \arctan \left(\frac{2\text{Re}(\chi)}{1 - |\chi|^2} \right), \quad (21.5)$$

where $\chi = E_y/E_x$ is the ratio of the y - and x -components of the electric (or magnetic) fields at the condition that the direction of polarization of the incident wave is along the x -direction.

21.2.2 Microcavity-Type 1D MPCs

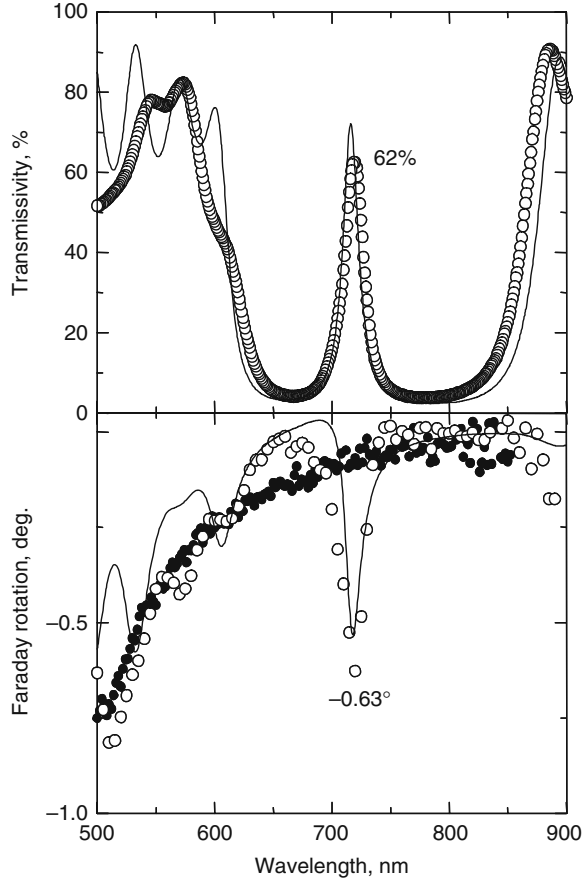
The theoretical predictions on existence of the enhancement of Faraday rotation in the microcavity structure composed of two dielectric Bragg reflectors and a Bi:YIG defect layer incorporated between them, $(\text{Ta}_2\text{O}_5/\text{SiO}_2)^5/\text{Bi:YIG}/(\text{SiO}_2/\text{Ta}_2\text{O}_5)^5$, were experimentally confirmed [11]. Figure 21.3 shows a representative of such microcavity-type 1D MPCs.

Fig. 21.3 Cross-sectional FESEM image of a 1D MPC – a microcavity with $(\text{Ta}_2\text{O}_5/\text{SiO}_2)^5/\text{Bi:YIG}/(\text{SiO}_2/\text{Ta}_2\text{O}_5)^5$ structure



As shown in Fig. 21.3, the sample has good layered structure in which interfaces are well defined. The thicknesses of layers were 167 nm (Bi:YIG), 111 nm (SiO_2), and 92 nm (Ta_2O_5). Refractive indices were $n_{\text{Ta}_2\text{O}_5} = 2.05$, $n_{\text{SiO}_2} = 1.45$, and $n_{\text{Bi:YIG}} = 2.36$. Figure 21.4 shows the transmission T and Faraday rotation spectra of the 1D magnetophotonic microcavity at normal incidence; the solid curves are the

Fig. 21.4 Transmission and Faraday rotation spectra of the 1D magnetophotonic microcavity shown in Fig. 21.3



theoretical ones calculated within the matrix approach [13], while open and closed circles present the experimental spectra for the sample. Good quantitative agreement between the observed and the calculated values is seen. Within a photonic band gap (600–850 nm), the resonant transmissivity ($T = 62\%$) occurred at $\lambda = 720$ nm due to light localization, and the rotation angle θ_F reached the value of -0.63° . It worth mentioning that mechanism of this enhancement is similar to that discussed in Section 21.2.1 (Fig. 21.1). Namely, the difference of magnitudes of the wave vectors \mathbf{k}_L and \mathbf{k}_R for left- and right-circular-polarized localized modes, multiple propagation of these modes within the defect layer, and the nonreciprocal character of the Faraday rotation enhance significantly the polarization rotation. The presented data show that the magnetophotonic microcavity provides high transmissivity and large enhancement of θ_F simultaneously that is very useful for various magnetophotonic applications. Another important feature of the microcavity-type 1D MPCs is controllability of the spectral positions of localized modes via change in the thickness of the spacer Bi:YIG layer [26].

21.2.3 Photonic Band Structure and Eigenmodes of 2D MPCs

It is well known that, due to a mirror symmetry of 2D PCs, the vector wave equation for nonmagnetic PCs (or nonmagnetized MPCs) can be reduced to two independent scalar eigenvalue problems for two modes: the transverse electric (TE) and transverse magnetic (TM) modes with the electric field vector parallel or perpendicular to the basal plane of the 2D structure, respectively [4, 40]. However, if one of the constituents of a PC is magneto-optical one, the TE–TM notation is not longer possible. In this case, we are forced to solve the fully vectorial eigenvalue problem of the form:

$$-\sum_{\mathbf{G}'} \kappa(\mathbf{G} - \mathbf{G}')(\mathbf{k} + \mathbf{G}') \times \{(\mathbf{k} + \mathbf{G}') \times \mathbf{E}_{\mathbf{k}n}(\mathbf{G}')\} = \frac{\omega_{\mathbf{k}n}^2}{c^2} \left(\mathbf{E}_{\mathbf{k}n}(\mathbf{G}) + i \sum_{\mathbf{G}'} \eta(\mathbf{G} - \mathbf{G}') \{\mathbf{m} \times \mathbf{E}_{\mathbf{k}n}(\mathbf{G}')\} \right). \quad (21.6)$$

The standard notations are used in here: $\mathbf{E}(\mathbf{r}, t)$ – the electric field, $\varepsilon(\mathbf{r})$ and $\mathbf{g}(\mathbf{r})$ – permittivity and gyration vector of constituents of an MPC, and c – the velocity of light in vacuum. As usual, $\omega_{\mathbf{k}n}$ denotes in Eq. (21.6) the eigenfrequency corresponding to the $\mathbf{E}_{\mathbf{k}n}(\mathbf{G})$ eigenmode of an MPC. \square and η are the coefficients of the Fourier expansion of the inverse permittivity $\varepsilon(\mathbf{r})^{-1}$ and the gyration vector, respectively. \mathbf{m} is the unit vector in the direction of magnetization, and \mathbf{G} is and the reciprocal lattice vector. Since the propagation of electromagnetic waves in periodical structures is considered, both the permittivity and the gyration vector have the same periodicity:

$$\varepsilon(\mathbf{r}) = \varepsilon(\mathbf{r} + \mathbf{a}_i), \mathbf{g}(\mathbf{r}) = \mathbf{g}(\mathbf{r} + \mathbf{a}_i), \quad (21.7)$$

where \mathbf{a}_i ($i=1,2,3$) is the elementary vectors of the lattice. Spatial periodicity of the MPC allows us to expand the inverse permittivity $\varepsilon(\mathbf{r})^{-1}$, the gyration vector, and the amplitude of the electric field in the Fourier series:

$$\varepsilon(\mathbf{r})^{-1} = \sum_{\mathbf{G}} \kappa(\mathbf{G}) \exp \{i\mathbf{G} \cdot \mathbf{r}\}, \quad (21.8)$$

$$\mathbf{g}(\mathbf{r}) = \mathbf{m} \sum_{\mathbf{G}} \eta(\mathbf{G}) \exp \{i\mathbf{G} \cdot \mathbf{r}\}, \quad (21.9)$$

$$\mathbf{E}(\mathbf{r}) = \sum_{\mathbf{G}} \mathbf{E}_{\mathbf{k}n}(\mathbf{G}) \exp \{i(\mathbf{k} + \mathbf{G}) \cdot \mathbf{r}\}. \quad (21.10)$$

By solving Eq. (21.6) numerically, one can find the photonic band structure (PBS) as well as eigenmodes of an MPC allowing analysis of its MO properties.

The system (21.6) represents the generalized eigenvalue problem in the following form, $\hat{\mathbf{A}}\mathbf{E}_{\mathbf{k}n} = \omega_{\mathbf{k}n}\hat{\mathbf{B}}\mathbf{E}_{\mathbf{k}n}$. For PCs composed of nonmagnetic materials, it simplifies to the common eigenvalue problem, $\hat{\mathbf{A}}\mathbf{E}_{\mathbf{k}n} = \omega_{\mathbf{k}n}\mathbf{E}_{\mathbf{k}n}$, because $\hat{\mathbf{B}}$ reduces to the identity matrix. This form of the eigenvalue problem makes physical consequences

of the MO activity on eigenmodes rather transparent. Existence of the nondiagonal elements in Eq. (21.1) introduces conversion (mixing) of the different Bloch waves of a nonmagnetic PC. However, these nondiagonal elements are small in comparison with the diagonal ones because of the natural weakness of the MO activity. As a result, the mode mixing is weak and direct correspondence between solutions of the nonmagnetic and magnetic problems can be ascertained in most cases. Moreover, the solutions of the generalized problem for MPCs, in general, share some features with solutions of the common eigenvalue problem for nonmagnetic PCs. Exceptions are the vicinities of the high-symmetry points of the Brillouin zone where the TE and TM modes are degenerate. Analysis based on the perturbation theory [41, 42] shows that even an infinitesimally weak MO activity leads to an effect of hybridization and causes strong coupling of the TE and TM modes along with notable alteration of PBS [43].

Example of the PBS of the square lattice of dielectric rods, when the lattice is magnetized and nonmagnetized, is shown in Fig. 21.5(a). Plot (b) shows that the alteration is maximal in the vicinities of the high-symmetry points where degeneracies occur (the M-point in this particular example) and brings tunability of PBSs of MPCs. This manifests as a splitting of the frequency branches and the complete removal of the degeneracies.

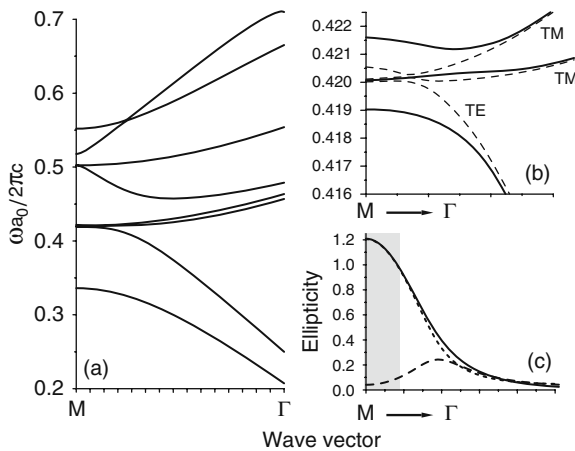


Fig. 21.5 (a) PBS of a 2D MPC with the square lattice composed of MO rods in air. The following parameters of the MO rods were assumed for the numerical calculation the diagonal component of the dielectric constant of $\epsilon_{xx} = 5.6$ and the off-diagonal component of $\epsilon_{xy} = -0.01$, the ratio of the lattice constant to the radius of the rods of 1:0.4. (b) Part of the PBS shown in plot (a); the vicinity of the M-point degeneracy between second, third, and fourth branches. Solid lines correspond to the MPC; dashed lines correspond to the nonmagnetic PC. (c) Ellipticity of Bloch eigenmodes of the MPC in the vicinity of M-point. Solid line corresponds to the second branch of the PBS (the TE mode of nonmagnetic PC); the ellipticity was calculated as E_{TE}/E_{TM} . Dashed and dotted lines correspond to the third and fourth branches (both are the TM modes of the nonmagnetic PC), respectively; the ellipticity was calculated as E_{TM}/E_{TE} . Gray square shows the same range of wave vectors as that in plot (b)

Note that the alteration of eigenmodes of 2D MPCs is even more profound. By projection of the eigenmodes of an MPC on those of the nonmagnetized MPC, we have found that the eigenmodes of the MPC are intermixed and form strongly elliptically polarized Bloch waves in the vicinities of the points of degeneracy [see Fig. 21.5(c). Here the ellipticity is the ratio between the TE- (TM-) and TM- (TE-) projections for branches corresponding to the TE (TM) modes of nonmagnetic PC]. The polarization state of the eigenmodes gradually transforms when moving apart from these points. Passing the regime of the elliptical polarization with the main axes in and out of the basal plane, eigenmodes tend to be the TE and TM modes of the nonmagnetic PC. This alteration of eigenmodes may therefore provide a possibility to manipulate the propagation direction of light beams in MPCs and control the intensities of transmitted and reflected waves [43].

21.2.4 Faraday Rotation of Three-Dimensional Magnetophotonic Crystals

The Korringa–Kohn–Rostoker (KKR) method as well as its modification for layered systems (LKRR) has been extensively and very successfully used in the study of the electronic structure and electronic properties of various materials. Recently, several groups have also developed the KKR [44–46] and LKRR formalism for electromagnetic (EM) waves [47]. The advantage of the LKRR is that one can calculate the PBS together with transmission and reflection spectra.

The LKRR formalism requires knowledge of the scattering properties of the elemental scatterer of the PC. Therefore, at first stage, we need to deal with the scattering of an EM wave of wave number $k_b = \sqrt{\varepsilon_b \mu_b} \omega / c$ by a MO active sphere having permittivity tensor $\hat{\varepsilon}$, permeability μ , and radius R , which is embedded in a optically inactive isotropic host medium defined by ε_b and μ_b . Assuming a time dependence of $\exp(-i\omega t)$, we express the EM field outside the sphere as follows [47]:

$$\begin{aligned} \vec{E}(\vec{r}) &= \vec{E}_{in}(\vec{r}) + \vec{E}_{sc}(\vec{r}) \\ &= \sum_{l,m} \left\{ \left[a_{lm}^{0E} \frac{i}{k_b} \nabla \times j_l(k_b r) \mathbf{X}_{lm}(\hat{\mathbf{r}}) + a_{lm}^{0H} j_l(k_b r) \mathbf{X}_{lm}(\hat{\mathbf{r}}) \right] \right. \\ &\quad \left. + \left[a_{lm}^{+E} \frac{i}{k_b} \nabla \times h_l^+(k_b r) \mathbf{X}_{lm}(\hat{\mathbf{r}}) + a_{lm}^{+H} h_l^+(k_b r) \mathbf{X}_{lm}(\hat{\mathbf{r}}) \right] \right\}, \end{aligned} \quad (21.11)$$

where j_l and h_l^+ are the spherical Bessel and Hankel functions, respectively, and $\mathbf{X}_{lm}(\hat{\mathbf{r}})$ are vector spherical harmonics. The coefficients a_{lm}^{0E} and a_{lm}^{0H} refer to the incident wave (\mathbf{E}_{in}), whereas a_{lm}^{+E} and a_{lm}^{+H} to the scattered wave (\mathbf{E}_{sc}). These coefficients are related to each other via the scattering matrix as follows:

$$a_{lm}^{+P} = \sum_{l',m',P'} T_{lm,l'm'}^{PP'} a_{l'm'}^{0P'}, \quad (P = E, H), \quad (21.12)$$

where the scattering matrix $T_{l_m, l_m'}^{PP'}$ can be found with use of an exact Mie technique solving the problem of EM wave scattering by a MO active sphere [48]. Although the KKR formalism can deal with situations in which the parameters of the problem depend on the frequency, for simplicity and to not obscure the MO response, we assumed in our calculations that $\hat{\epsilon}$ is constant over the considered frequency range and $\mu = 1$.

Let us consider MPC with the sc and fcc lattices (with the lattice constant of a_0) which consist of nonoverlapping spheres (one per the unit cell) and view the crystal as a sequence of the (001) and (111) planes, respectively. Having obtained the scattering matrix for a single MO active sphere, we can apply LKKR technique to calculate the PBS for the EM modes associated with a given crystallographic plane of crystals under study and the transmittance through a slab, in which the basal facets are parallel to the chosen crystallographic plane. The first question we have to answer is how the MO activity of the spheres affects the PBS of magnetophotonic crystals. Figure 21.6 shows sections of the PBS of sc photonic crystals, the slab with thicknesses of 16 layers, along the normal to the (001) surface. The direction

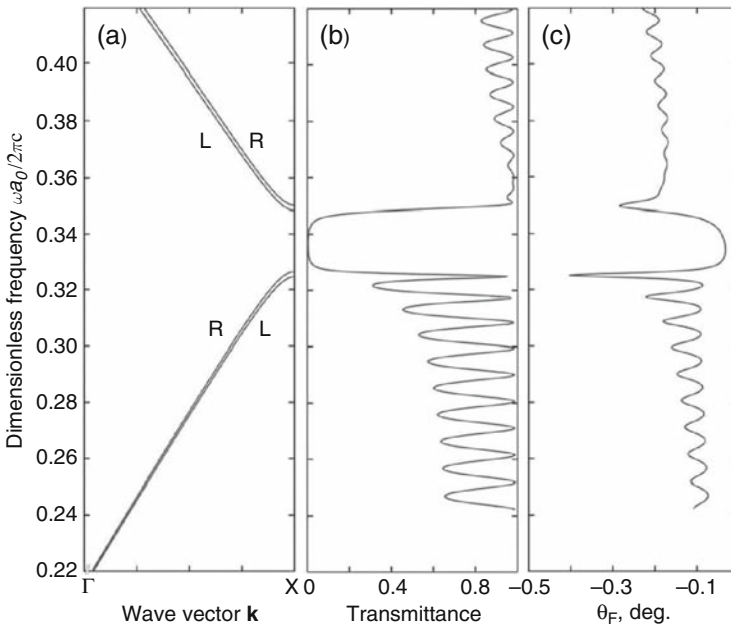


Fig. 21.6 (a) Band structure for the EM wave propagating along the normal to the (001) surface of a simple cubic photonic crystal. The photonic crystal consists of MO spheres with $\epsilon = 5.59$, $g = -3.69 \times 10^{-3}$, and the radius-to-lattice constant ratio of $R_s/a_0 = 0.5$ in air. Absorption and dichroism are neglected. The transmittance (b) and Faraday rotation (c) were calculated for the normal incidence of light onto a slab composed of 16 layers of the (001) planes of MO spheres with $\epsilon = 5.59 + i5.42 \times 10^{-3}$, $g = -3.69 \times 10^{-3}$ (Bi:YIG at $\lambda = 700$ nm), and $R_s/a_0 = 0.5$ in the air background

of light propagation and the magnetization direction in the slab coincide with the $\Gamma \rightarrow X$ direction. When MO activity is switched on, the degeneracy of the band structure of the nonmagnetic PC is removed and two splitted bands appear. These bands correspond to the circularly polarized light of R and L handedness.

Apart from this splitting of the bands, the changes in the dispersion curves and transmission spectra brought about by the MO activity of the spheres are marginal. At the same time our results show that PBSs of MPCs are richer than that obtained for PCs composed of nonmagnetic isotropic spheres. This is due to reduction of the crystal symmetry by the MO activity. Although the MO activity of the spheres does not affect significantly the PBS and transmission spectra of MPCs, it renders them to exhibit the MO response [Fig. 21.6(c)]. A linearly polarized plane wave incident normally on a slab of the crystal excites two Bloch waves, denoted by R and L, which propagate through the slab with different phase velocities; the transmission spectrum is given in Fig. 21.6(b). If, as it appears to be the case (except the small frequency range in the proximity of the band edges), the R and L components of the transmitted wave have the same amplitude, the transmitted wave will be linearly polarized one with the plane of polarization turned by an angle θ_F .

Finally, let us consider a magnetophotonic heterostructure consisted of an MO defect layer sandwiched in between fcc PC slabs composed of silica spheres in air. It will be instructive to analyze properties of the 3D magnetophotonic heterostructures in the qualitative comparison with its 1D counterpart, namely, the 1D PC with the incorporated MO defect. Simulations showed inapplicability of the relation for the resonant transmission wavelength for 1D structures $m\lambda_0 =$

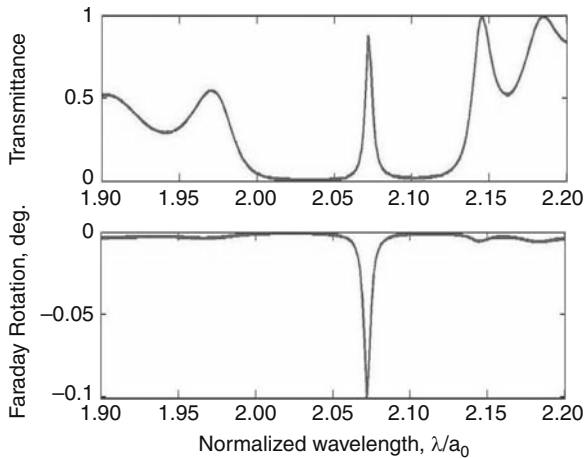


Fig. 21.7 Transmittance and Faraday rotation for the normal incidence on a heterostructure composed of a Bi:YIG layer sandwiched between two fcc PC slabs. Each PC slab consists of 24 planes of close-packed silica spheres (amorphous silica, $\epsilon = 1.9$) in air. The (111) planes are parallel to the basal surface of the slab. The thickness of the defect layer is $da_0 = 0.56$, while the permittivity is the same as for calculations presented in Fig. 21.6

$2nd$, where $m = 1, 2, 3 \dots$ is the positive integer, n is the refractive index of the defect layer and d is its thickness. This expression is based on the phase difference gained by the wave during its propagation through the defect layer. However, in the 3D heterostructures complicated light scattering at the interfaces between the 3D PCs and the defect layer results in impossibility to find any analytical expression similar to $m\lambda_0 = 2nd$. Therefore the problem in the 3D case can be treated only numerically.

Figure 21.7 shows the transmission and Faraday rotation spectra of the heterostructure under study. In analogy with 1D magnetophotonic crystals, the strong enhancement of the Faraday rotation appears at the resonance transmission and in its proximity. However, because of the lower quality factor for the defect mode in the heterostructure, values of the Faraday rotation angle are significantly smaller than that of microcavity-type 1D MPCs (Section 21.2.2).

21.2.5 Nonlinear Optical and Magneto-Optical Properties

To study nonlinear optical and MO properties of MPCs, tunable laser systems with broad tuning ranges are needed to cover the spectral intervals of photonic band gaps and microcavity modes. Nd:YAG laser pumped Optical Parametric Oscillators can be used for these studies [49–56] (for example, Spectra Physics MOPO 710) with the tuning spectral range of 430–1,500 nm, the pulse duration of 4 ns, and the pulse energy of 10 mJ. In the Kerr geometry (NOMOKE), magnetization-induced modulation of the intensity of the second-harmonic generation (SHG) was observed for the multilayer-type MPCs in the spectral range of PBG edges and for microcavity-type MPCs at wavelengths of the resonant localization modes. In both cases, the large enhancement of the SHG intensity (Fig. 21.8) was observed

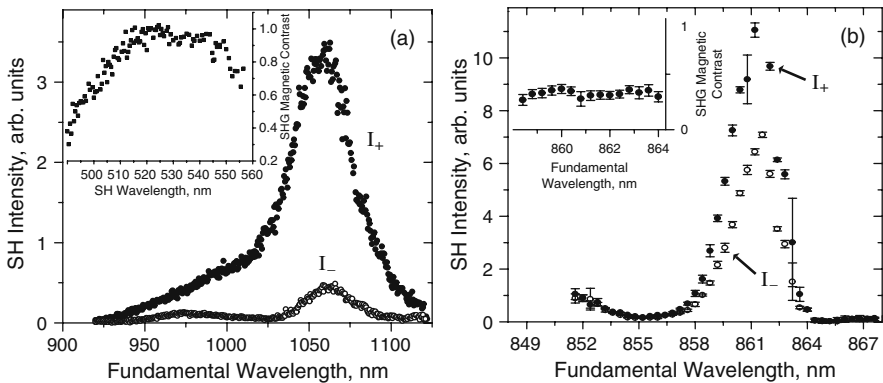


Fig. 21.8 The SHG spectra measured in the transversal NOMOKE configuration for the p -in, p -out polarization combination: (a) the multilayer-type MPCs shown in Fig. 21.1; the SHG enhancement is observed at the long-wavelength edge of the band gap. (b) A microcavity-type MPC; the maximum of SH intensity is observed at pumping the sample with the fundamental wavelength corresponding to the localized state of $\lambda \approx 860$ nm. I_+ and I_- denote the SH intensities for the opposite directions of magnetization, and the magnetic contrast is shown in the insets

and attributed to the localization of resonant fundamental radiation in Bi:YIG layers.

It has been predicted theoretically and then proven experimentally that in MPCs, as the magnetic and photonic properties are combined, magnetization-induced rotation of the polarization plane can reach dozens of degrees, and the SHG magnetic contrast dozens of percents. Figure 21.8 shows that, when the fundamental wavelength is tuned in the vicinity of the PGB edge, the enhancement factor of SHG becomes more than 10^2 , whereas the magnetic contrast reaches unity. Magnetization-induced shift of phase and rotation of polarization of the SHG wave were also observed in proper transversal, longitudinal, and polar NOMOKE configurations. Note that the SHG wave is linearly polarized, and the application of a magnetic field leads to the rotation of the polarization plane of the SH wave. The magnetization-induced intensity variations as well as the magnetization-induced shift of phase and rotation of polarization of SHG and third harmonic generation waves are discussed in detail in [36–43].

21.2.6 Conclusion

MPCs composed of sequences of magnetic and dielectric layers permit to enhance the MO responses of known materials. MPCs with PBGs in the visible and infrared spectral ranges and that exhibiting the localized states illustrate the advantages of adopting MPCs to optical integrated devices. Implementation of 1D, 2D, and 3D MPCs promises high-response, multi-mode and multi-directional control of light flow in these miniature magnetic media.

21.3 Magnetorefractive Effect in Nanostructures

The magnetorefractive effect (MRE), which is a high-frequency analogue of giant magnetic resistivity, consists in the variation of the permittivity of materials:

$$\epsilon(\omega) = \epsilon_r(\omega) - i4\pi\sigma(\omega)/\omega, \quad (21.13)$$

where $\epsilon_r(\omega)$ is the permittivity with allowance for the contribution of displacement currents, and $\sigma(\omega)$ is the conductivity at frequency ω . This variation leads to change in the coefficients of electromagnetic radiation reflection (R), transmission (T), and absorption (A) of magnetized samples with a significant magnetic resistance (MR) (see [57–59] and the references therein). The term MRE means that the refraction indexes n and k [$\epsilon = (n - ik)^2$] change in the presence of an external magnetic field (H). Therefore, initially, the MRE was considered for only the optical wavelengths but the usage of this term was later extended to a broader frequency range (see,

for example, [60–62]). The MRE parameters for reflection $\Delta R/R$ and transmission $\Delta T/T$ are defined as

$$\frac{\Delta R}{R} = \frac{R(H=0) - R(H)}{R(H=0)} \text{ and } \frac{\Delta T}{T} = \frac{T(H=0) - T(H)}{T(H=0)}. \quad (21.14)$$

The effects of magnetoreflexion and magnetotransmission in impermeable and magnetic semiconductors and metals are related to the change in (i) their electronic structure, (ii) the Fermi level shift, and (iii) the displacement of the mobility edge in the magnetic field. All this eventually leads to changes in the conductivity and the permittivity. In a strict sense, the mentioned phenomena are not manifestations of the MRE and are usually observed at low temperatures and in strong fields [63]; in some manganite-type complex compositions or in semiconductor systems they may compete with the MRE.

Common magneto-optic (MO) phenomena that are even and odd with respect to magnetization are related to the effect of the spin–orbital coupling on optical intraband transitions (within the IR spectral range) or interband transitions (in optics). The MRE is not related with the spin–orbital coupling and is due to spin-dependent scattering or tunneling. Hence, the MRE in systems characterized with a giant magnetic resistance significantly exceeds standard MO effects, such as the equatorial Kerr effect. Contributions to magnetoreflexion and magnetoabsorption due to the magnetic linear dichroism and the orientation MO effect can be separated via analysis of their interrelations in the angle- and polarization-resolved spectra [58, 64].

During the decade after the discovery of the MRE, many theoretical and experimental studies of the MRE were carried out for multilayers and granulated films with a giant MR, nanocomposites with a tunnel MR, and manganites with a colossal MR. Here, we briefly review studies of the MRE in the optical range. Simple scheme for description of the MRE for manganites is discussed along with an approach to enhance the MRE in 1D MPCs containing, as a defect, a thin film of a material exhibiting the MRE [65].

21.3.1 Magnetorefractive Effect in Nanostructures and Manganites

The MRE was theoretically studied and experimentally observed for the first time in NiFe/Cu/Co/Cu multilayers in the transmission geometry [66]. The theory of the MRE for metal multilayers was developed in [67–69]. The effect is reproducibly observed in the near infrared range. For multilayers, spin-gate NiFe/Cu and Fe/Cr structures in the case of reflection, it is about 0.10–0.15% (according to [66, 68]). For the Co/Cu multilayers exhibiting a 65% MR, the MRE at room temperature is as large as 5.4% [70].

The theory of the MRE in granulated metal/metal alloys was proposed in [71] and was later developed in [59, 72]. This theory is based on the Drude–Lorentz model for the frequency-dependent conductivity and the theory of spin-dependent scattering

for the giant MR in granulated alloys. The MRE was experimentally measured for granulated Co/Ag alloys [59, 72, 73], and, in sufficiently strong magnetic fields, it was less than 1% [59, 73]. The simplest expression for the MRE in metal systems was derived in [71] for the Hagen–Rubens spectral range ($\omega\tau \ll 1$, where τ is the relaxation time of electrons) for the normal incidence of light:

$$\frac{\Delta R}{R} = -\frac{1}{2}(1 - R)\frac{\rho(H = 0) - \rho(H)}{\rho(H = 0)} = -\frac{1}{2}(1 - R)\frac{\Delta\rho}{\rho}. \quad (21.15)$$

Here, $\rho(H = 0)$ and $\rho(H)$ are the electric resistivity in the absence and presence of magnetic field, respectively, and $\Delta\rho/\rho$ is the absolute value of the MR. This expression is in agreement with experiments and shows that larger MRE responses should be expected for systems with a large MR and a small reflection coefficient. Detailed analysis of the MRE dependence on microscopic parameters of granulated alloys is given in [59]. Significant (up to 1.5%) MRE is found for nanocomposites, i.e., granulated metal–dielectric films, such as Co–Al–O, SoFe–MgF, (SoFeZr)–SiO_n, Fe–SiO₂ [57, 58, 74], SoFe–Al₂O₃ [75]. The effect is observed only for compositions that are close to the percolation threshold and that are characterized by a significant tunnel MR. The theory of the MRE in magnetic nanocomposites [57, 58, 74] is built upon the mechanism of spin-dependent tunneling at optical frequencies. The tunnel contact between single-domain granules is described with a model of a capacitor and a tunnel resistance connected in parallel. It is assumed that the capacitance of the capacitor does not depend on the relative orientation of the magnetic moments of granules. It is also assumed that the same tunnel contact is responsible for both static and high-frequency MRs and that the tunnel MR does not depend on the light frequency over the range extending up to the near infrared one. This simple model yields results that agree with the experiment not only qualitatively [57, 58] but also quantitatively [74]. The same model was used to calculate the angle- and polarization-resolved dependences of the MRE in the reflection and transmission geometries [76, 77].

The effect of magnetotransmission in manganites with a colossal MR was discovered in 1997; La_{0.9}Sr_{0.1}MnO₃ single crystals were studied at low temperatures [78]. Experimental studies on many other manganites can be found in [79–82] and references therein. Important advance was that, for La_{0.67}Sr_{0.33}MnO₃ films, the value of magnetotransmission at room temperature and in a field of 8 kOe was as large as 6% [79]. The corresponding quantity for the composition of La_{0.8}Ag_{0.1}MnO_{3- δ} was as large as 15% [81] that was the record magnitude for room temperatures. Stronger magnetotransmission effects ($\sim 30\%$) were observed for LaSrMnO single crystals at T_c at 140 K when the concentration of strontium was lower than the percolation threshold [78]. Magnetoreflexion in manganite films was studied in [83]. Currently, there is no theoretical description of these effects. It is natural to assume that these effects are manifestations of the MRE, since they are observed in systems with a colossal or tunnel MR. Such assumption implies a strong correlation between the MRE and the MR, however, this correlation is violated for temperature

and concentration dependences of magnetotransmission and MR in the studied materials.

With allowance for the foregoing, let us note the following. In complex systems with separated phases whose optical properties and MR strongly depend on the composition and temperature, the correlation between the temperature and the concentration dependences of the MRE and MR is not indispensable (see, for example, [59]). Moreover, if the MR is large, simple estimates (see, for example, [71]) show that in the case of the MRE neither magnetoreflexion nor magnetotransmission depends linearly on the MR. The dependences of these effects and of the MR are not necessarily the same. These circumstances, as well as the absence of a consistent theory of the high-frequency conductivity and MR of manganites, hinder the consistent description of the MRE in such systems.

21.3.2 Enhancement of the MRE in Magnetophotonic Crystals

For MRE applications, it is very important to increase the magnitude of the effect in saturating fields or, equivalently, to diminish control fields. Since the enhancement of MO effects are demonstrated in magnetophotonic crystals (MPC_s) [84–86], one can expect that the MRE can be enhanced by in much the same way. The authors of [57] proposed to enhance the MRE utilizing 1D MPCs with a built-in magnetic layer made of a material with the MRE, i.e., a structure resembling a Fabry–Perot resonator (considered in Section 21.2.2). However, the permittivity of materials with the MRE changes in the magnetic field more strongly than that of magneto-optically active materials, such as bismuth-substituted yttrium garnet. Use of materials with the MRE as structural materials for an MPC can be promising from the standpoint of development of field-controlled optical elements. Therefore, this section is devoted to the analysis of the possibility of usage of thin magnetic films–nanocomposites and manganites–as structural materials for MPCs intended for both the enhancement of the MRE and the control of the MPCs' optical spectra by external magnetic fields.

Studies were conducted with finite samples of microcavity-type 1D MPCs $(\text{SiO}_2/\text{Ta}_2\text{O}_5)^l/\text{F}/(\text{Ta}_2\text{O}_5/\text{SiO}_2)^m$ containing a built-in defect layer (F) that might be a thin film of nanocomposite Co–(Al–O) or manganite $\text{La}_{0.67}\text{Sr}_{0.33}\text{MnO}_3$. Both in the reflection and in the transmission geometries, a symmetric structure with the same number of bilayers, $l = m = 6$, was considered. An antisymmetric scheme with $l = 6$ and $m = 12$ was considered only in the case of light reflection since the transmission coefficient is small in this case. The parameters of the MPC are presented in the table. The optical parameters of nanocomposites Co–(Al–O) and manganites $\text{La}_{0.67}\text{Sr}_{0.33}\text{MnO}_3$ were calculated from the experimental data [82, 87, 88], and their variation with the magnitude of the external magnetic field was calculated according to the MRE theory presented in [58, 62, 76]. The thickness of the SiO_2 and Ta_2O_5 dielectric layers was selected such that to create band gaps in the studied spectral ranges (see Table 21.1). Structural parameters of samples were optimized with the idea to determine the conditions for the maximal MRE and, at the same

Table 21.1 MPC parameters

Parameter	MPC with a Co-(Al-O) nanocomposite defect layer	MPC with a manganite (La _{0.67} Sr _{0.33} MnO ₃) defect layer	
External parameters			
Wavelength corresponding to the center of the PC's band gap (nm)	2,625	2,480	4,130
External magnetic field, (kOe)	8.0	8.0	
Parameters of the material of which the built-in defect layer is made			
Magnetoresistance (%)	8	7	
Magneto refractive effect for a 300-nm-thick film (%)			
Reflection transmission	-0.96	6.00	
Optical parameters in the absence of magnetic field:			
$n(H = 0)$	3.0000	2.4797	2.5927
$k(H = 0)$	0.5000	1.7744	1.9287
Optical parameters in the magnetic field of $H = 8$ kOe			
$n(H)$	3.0065	2.5271	2.63865
$k(H)$	0.5389	1.83307	1.9907
Variation range of the defect thickness (nm)	50–400	50–450	
PC parameters			
Thickness of the dielectric layers (nm)			
SiO ₂	500	300	600
Ta ₂ O ₅	300	420	580

time, to keep the maximal possible reflection or transmission for working wavelengths. It is evident that the change in the optical thickness of the defect layer shifts the spectral position of the defect mode (00) inside the band gap. This phenomenon is manifested as the shift of the peak of the MRE spectral dependence with respect to the center of the band gap. The reflection coefficient R was calculated through the transfer matrix method [89–91]; the light incidence angle was $\varphi = 20^\circ$.

Inside an MPC, owing to the presence of Bragg mirrors located on both sides of the magnetic layer, light is localized in the vicinity of this layer, i.e., light passes many times through this layer. As a result, the MRE is enhanced by more than an order of magnitude as compared to a thin film on a substrate and by two orders of magnitude as compared to thick films (Figs. 21.9 and 21.10). In the studied structures, magnetoreflexion (the relative change in the reflection factor when a field is applied) was over 60% for $R = 1.0\%$ for an MPC with a nanocomposite used as a 150-nm-thick defect (Fig. 21.10), 47% for $R = 1.5\%$ for a symmetric MPC scheme with a manganite used as a defect, and 25% in an antisymmetric MPC scheme with a manganite (Fig. 21.9). These values may significantly increase, first, if the reflection factor is diminished (for example, for an MPC with a manganite used as a defect, the MRE reaches 95% for the 0.1% reflection) and, second, if manganites with a larger MR and a weaker absorption are used.

Fig. 21.9 Magnetorefractive effect in a magnetophotonic crystal with manganite as a defect: calculated for reflection. The defect is 300 nm thick; the band-gap center corresponds to a wavelength of 4,130 nm. The *dotted curve* corresponds to an antisymmetric scheme; the *solid curve*, to a symmetric scheme. The responses are shown for the localized states, which are spectrally shifted to short wavelengths from to the bad-gap center

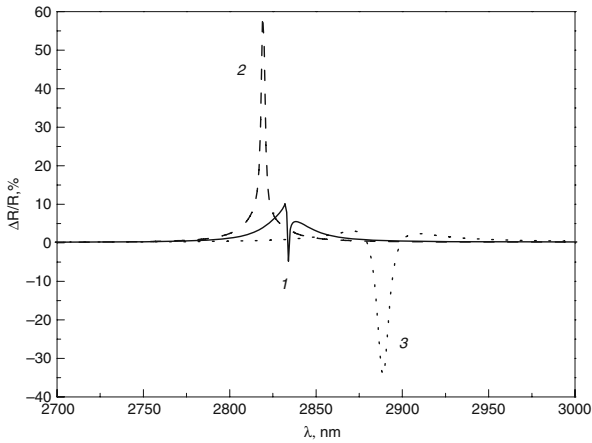
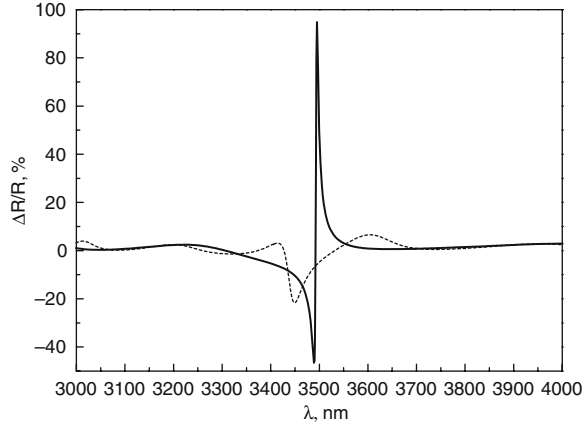


Fig. 21.10 Magnetorefractive effect in the magnetophotonic crystals with a nanocomposite as a defect: calculated for reflection for defect thicknesses of (1) 160, (2) 150, and (3) 200 nm

The MRE for an MPC may be positive or negative at different wavelengths (Figs. 21.9 and 21.10). This phenomenon was studied in detail in [90]. With the increase of the thickness of the magnetic layer, the role of the interference between the waves reflected from the front and the back boundaries of the defect layer diminishes because of losses in the defect layer. This results in that the MRE tends to the value corresponding to that for the single magnetic layer. The presence of losses in a magnetic layer is apparently a disadvantage of both nanocomposites and manganites used as structural materials for MPCs. However, the calculations show that light absorption is not an obstacle for the enhancement of the MRE and the development of optical elements controlled with a magnetic field.

21.3.3 Conclusion

Our studies have shown that the MRE can be successfully used in magnetophotonics, in particular, for contactless measurements of the MR in nanostructures, optical magnetic field sensors, high-speed modulators, and field-controlled optical elements. However, despite significant progress in studies of the MRE for different nanostructures, many problems need to be studied further. The list of important problems includes the following: (1) the development of the theory of spin-dependent tunneling in magnetically nonuniform media at high frequencies and of the theory of the MRE in manganites, (2) the search for materials characterized simultaneously with weak absorption and a high MR, (3) the development of a technology for forming multilayer structures and MPCs containing manganite and nanocomposite films, and (4) the extension of the frequency range involved in studies to both the visible range and the microwave range of the spectrum.

21.4 Plasmon-Enhanced Magneto-Optical Responses

Studies on electromagnetic scattering from various artificial nanometer-scale media supporting surface plasmon resonances (SPRs) and localized SPRs (LSPRs) [108] are currently attractive due to existence of the novel near-field effects and their contribution to anomalous transmission, surface-enhanced Raman scattering, propagation in electromagnetic waveguides, lithography overcoming diffraction limit and, what is of our interest in the present work, magneto-optical (MO) effects. Cooperation between the effect of the bulk plasma resonance and the Kerr effect was analyzed for metallic magnetic compounds in 1987 by Feil and Haas [92]. Theoretical treatment of Faraday rotation in granular magnetic materials is discussed by Xia et al. [93]. The experimental studies on the amplification of the MO effects by the surface plasmon resonances are presented for magnetic materials adjoining noble-metal films [94–97] or nanoparticles [98–100]. There are theoretical works on the Kerr and Faraday effects for the mentioned magnetic material–noble-metal systems, showing that the presence of noble-metal particles (or films) supporting LSPRs (or SPRs) in close proximity to a magnetic material results in enhancement of the MO response [101–104].

However, experiments show that the spectral position of a peak in the optical absorption spectrum [99], this peak is due to LSPR in silver nanoparticles, does not coincide with the wavelength of maximal difference between the measured Faraday rotation spectra for cobalt ferrite nanoparticles (CoFe_2O_4) and one with attached silver nanoparticles ($\text{CoFe}_2\text{O}_4\text{-Ag}$). The same structure, the $\text{CoFe}_2\text{O}_4\text{-Ag}$ binary nanoparticle system, is analyzed in work [102] showing a disagreement between the experimental [99] and the calculated Faraday rotation. As for studies on garnet–noble-metal nanoplasmonic composites, there is only a recent report by Tomita et al. [105] where the reversal of the Kerr rotation has been observed for yttrium–iron garnet thin films incorporating Au nanoparticles. It is shown that sign of the Kerr

rotation changes at the spectral range of LSPRs, but any apparent enhancement of the Kerr rotation has not been seen. This is controversial to theoretical predictions and experimental results [96–102, 106, 107] suggesting enhancements of MO effects for magnetic material–noble-metal structures. Thus, the up-to-date available experimental data are limited and their interpretation remains ambiguous.

Recently, there was significant interest in structured metallic materials exhibiting the extraordinary optical transmittance [111] originating from surface plasmon-like excitations [112]. Obviously, the possibility of dynamical control of this characteristic by inclusion of optically active components may endow future devices based on metallic metamaterials with additional functionality and flexibility. It has been theoretically demonstrated that metamaterials that are nonlinear media embedded into the slits of subwavelength apertures display changes in the transmission spectra and the optical bistability [113]. These features are explained as a result of the electric field enhancement associated with the excitation of the transmission resonances appearing in this type of structures.

Another possible way to achieve ultrafast dynamical controllability of the structured metallic materials is the usage of MO materials which optical response depends on an external magnetic field. One can expect that the extraordinary transmittance will be altered by properties of an MO material incorporated into (or adjoined to) structured metals. For light of resonant frequencies, this alteration may bring efficient control of the transmitted or reflected intensities. On the other hand, resonances appearing in these structures may bring huge enhancement of the MO response similar to that found in MPCs (Section 21.2).

This section highlights recent experimental and theoretical results of studies of garnet–noble-metal structures.

21.4.1 Garnet–Noble Metal Nanocomposites

The samples under experimental consideration were fabricated as follows. RF-magnetron sputtering system was used to deposit an 80-nm-thick bismuth-substituted yttrium iron garnet (Bi:YIG) film on the glass substrate. Next, an Au film with thickness of 5 nm was deposited using a DC-magnetron sputterer onto a part of the Bi:YIG film (the remaining part was used for fabrication of a reference Bi:YIG film), then this Bi:YIG–Au binary film was subjected to annealing at temperature of 750°C in air. Such treatment allow (i) to get crystalline phase of Bi:YIG and (ii) to form a planar array of Au nano-sized drops atop the Bi:YIG film [Fig. 21.11(a,b)] via melting of the Au film. Observations using a field emission scanning electron microscope show that Au particles have the surface extent from 10 to < 100 nm. According to our estimations, the prevailing surface extent is of 60 nm, and the spacing between Au drops varies from 10 nm to more than 100 nm. Finally, the second 80-nm-thick Bi:YIG film was deposited and annealed so that the array of Au nanoparticles got implanted into the 160-nm-thick Bi:YIG film [Fig. 21.11(c)]. Together with the Bi:YIG–Au film, the reference 160-nm-thick Bi:YIG film was

fabricated on the same substrate. FESEM observations [Fig. 21.11(c)] show that there is a Bi:YIG coat of different thickness (from bottom, top and sides) throughout the planar array of Au particles. Note that the seed thickness of Au films sputtered on the first Bi:YIG film strongly governs quality of LSPRs. By analyzing the experimental data, we found that better LSPRs are observed for the Bi:YIG–Au structures fabricated through melting of the 5-nm-thick Au film.

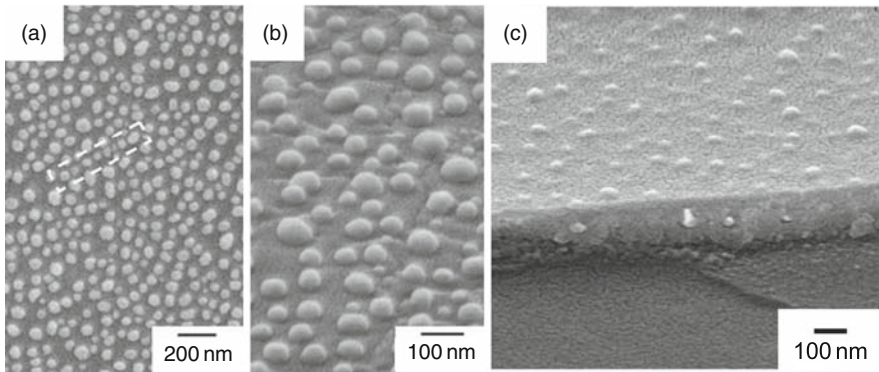


Fig. 21.11 (a, b) Top and side FESEM views of a planar array of Au nano-sized drops atop the Bi:YIG film; (c) 160-nm-thick Bi:YIG film impregnated with nano-sized Au particles

Figure 21.12 presents the transmission and Faraday rotation spectra of the Bi:YIG–Au film shown in Fig. 21.11(c) and of the reference Bi:YIG film; the spectra were measured at normal incidence. Clearly, the transmission spectrum of the Bi:YIG–Au film [plot (a)] illustrates an overall decrease in the intensity of transmitted light and a band centered at ~ 690 nm which is addressed to LSPRs in Au particles. As for the Faraday rotation spectra [plot (b)], we have found that the angles of rotation for wavelengths far from LSPRs have close values. Contrary, an enhancement of Faraday rotation is obvious for wavelengths corresponding to LSPRs (see also [114]). One can see that the angles of rotation increase as the probing wavelength reaches the minimum of the LSPR band. It is worth mentioning that this result contradicts to [99] and [105]. In these works, plasmon-assisted transformations of MO responses have been found either throughout all the investigated spectral range or for the wavelengths far from LSPRs. Note also that the enhancement shown in Fig. 21.12 qualitatively agrees with calculations presented by Smith and Stokes [102]. It is rather interesting that the ellipticity of transmitted light measured with high precision was found to be not influenced by LSPRs and was negligibly small (the inset to Fig. 21.12).

To further analyze the relationship between the observed features, spectra treatment was made and quantitative data were extracted. Figure 21.13 nicely illustrates presence of Au nanoparticles in Bi:YIG via the spectra of the Bi:YIG–Au film, which are normalized with respect to the spectra of the reference Bi:YIG film. For absorption of about 35% at 690 nm, the angle of rotation is two times amplified. Spectral positions of peaks in the absorption (691.5 ± 0.5 nm) and Faraday rotation

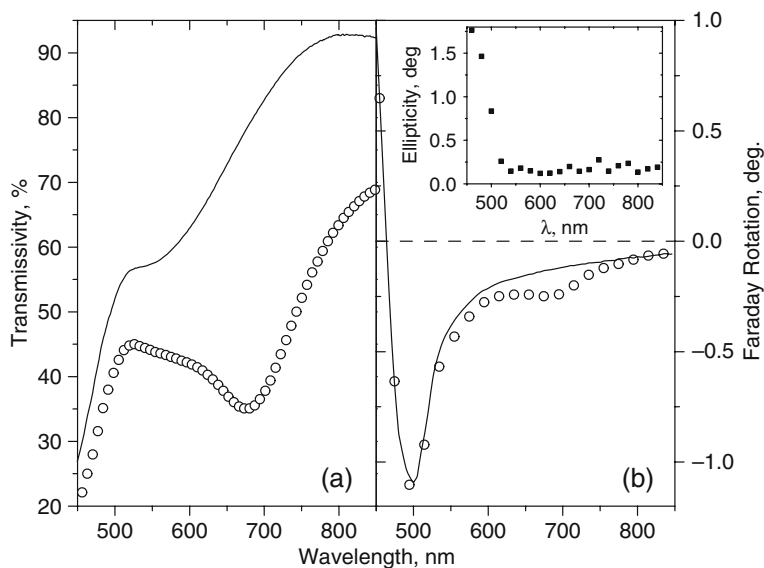


Fig. 21.12 (a) Transmission and (b) Faraday rotation spectra measured at normal incidence: *open circles*, the Bi:YIG–Au film shown in Fig. 21.11(b); a reference Bi:YIG film (*solid lines*). Inset: the ellipticity for the Bi:YIG–Au film. External magnetic field was 2 kOe

spectra (690.4 ± 2.8 nm) coincide. Remarkable difference in widths (full width at half maximum) of the bands is seen: 175 nm, for the LSPRs' band; and 105 nm, for the band in the Faraday rotation spectrum. What makes the peak in the Faraday rotation spectrum to be narrower? It is most likely that LSPRs in Au particles of various sizes, that are also randomly distributed, broaden the absorption band. But, as for the enhanced Faraday rotation, only limited collection of Au particles with certain sizes and spacings between them contributes to processes involved into amplification

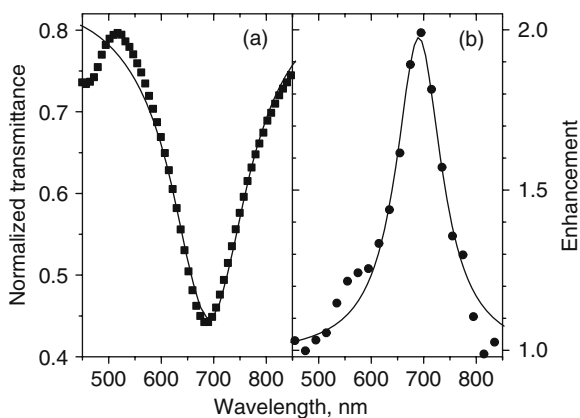


Fig. 21.13 (a) Normalized transmittance associated with presence of Au nanoparticles in the Bi:YIG–Au film. (b) Amplification of the angle of rotation for the Bi:YIG–Au film. *Solid squares* and circles are for experiment, *solid lines* are Lorentzians

of the rotation. Light of particular wavelengths generate a stronger near field which is maximally bound to whole array of different-in-size (and shape) Au particles [115].

It is known that the magnetically induced circular birefringence, the differential contribution of left- and right-circularly polarized light to electronic transitions in a magnetic material subjected to an external magnetic field, originates the MO effects. When considering artificial magnetic structures comprising known magnetic materials and summoned to increase the MO responses, the understanding of a mechanism responsible for the enhancement is based on the knowledge of light coupling to the bulk of the structure under study. It is believed that Faraday rotation measures the time of light interaction with a magnetic material [109]. In fact, multiple propagation of light or its slowing down, for example, in magnetophotonic crystals increases the interaction time and results in the strong enhancement of Faraday rotation [110].

Ideology suggested above can be used in the case of the considered Bi:YIG–Au nanostructures where the lifetime of LSPRs in the array of Au particles gears up the time of light interaction with Bi:YIG. Near field of resonant wavelengths is strongly bound to the interfaces between Au particles and surrounding Bi:YIG, providing the additional occurrence for transitions in the electronic system of Bi:YIG by interaction with circularly polarized light. This results in accumulation of the phase shift between waves with different helicity, i.e., in the enhancement of Faraday rotation.

Note that the suggested nanocomposite structures interact in the similar way with any chosen linear polarization and at any geometry of experiment, breaking the limit for magnetic material–noble-metal film structures (or multilayers) supporting SPRs when excitation happens only in the Kretschmann–Raether configuration (or using attached diffraction grating).

21.4.2 Metal–Garnet Structures Supporting Transmission Resonances

To demonstrate another possibility of enhancement of MO response, let us consider the structure composed of a perforated perfect conductor film with holes filled with an MO material (Fig. 21.14); silica glass was chosen as a background medium. The structure is designed so that to possess extraordinary transmittance at the optical communication wavelength of 1,550 nm. For calculations cerium-substituted yttrium iron garnet (Ce:YIG) was chosen to be a MO material filling the holes. Ce:YIG has negligible absorption, and dielectric constants are $\epsilon_{xx}=4.71$ and $\epsilon_{xy}=0.009$ at 1,550 nm. It is worth mentioning that the hole filler/background optical contrast determines the quality of the resonance – the extraordinary transmission through the hole arrays, i.e., it determines the MO response of the structure together with the transmission bandwidth.

Figure 21.14 shows the calculated transmittance and the Faraday rotation spectrum for the film with the holes size of $a = 350$ nm, the lattice constant of

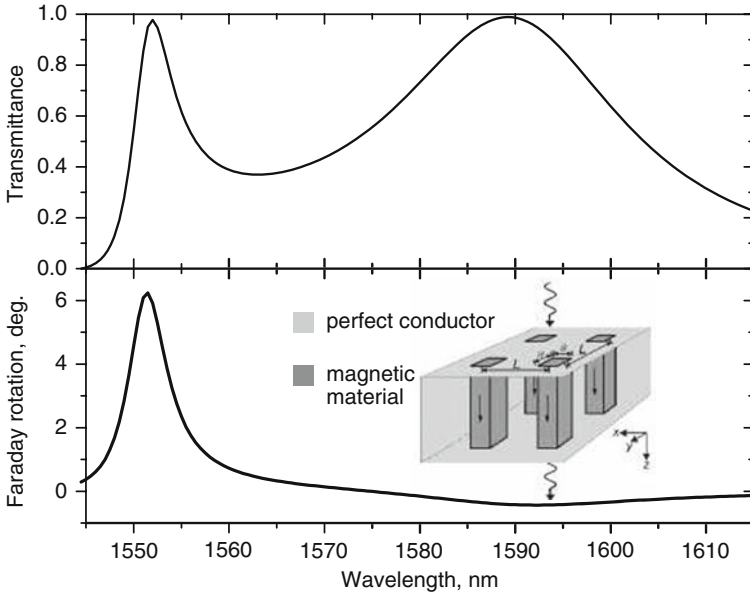


Fig. 21.14 Transmission and Faraday rotation spectra of the perforated perfect conductor film impregnated with Ce:YIG and embedded in the silica background. Inset, a schematic representation of the structure under study; the *arrows* show the magnetization direction of the MO component

$L = 1,069$ nm, and the thickness of $h = 350$ nm. Extraordinary transmittance occurs at around 1,550 nm and has double peak structure explained in details earlier [116, 117]. Width of the transmission peaks is about 2 and 10 nm for the first and second peaks, respectively. Note that the MO response of the homogeneous 350-nm-thick Ce:YIG film does not exceed a value of 0.5° . The enhancement of Faraday rotation of Ce:YIG by two orders of magnitude is evident.

Observed enhancement of the MO response is qualitatively explained as the result of interplay of the extraordinary transmission and the MO activity of the holes filler [117, 119]. 2D array of holes transfers via diffraction the incident light of resonant wavelengths into evanescent modes existing within the holes. And the accumulation of the polarization rotation occurs due to surface plasmon-like excitations [112] accompanied by localization the electromagnetic field within MO holes.

Another unique property of the structure under study is that the Faraday and Kerr rotations have opposite signs at two transmission peaks [117, 119], while in homogeneous MO film the sign of the rotation is retained. This reversal of the rotation is inherent in MO response of the systems with resonant excitation of the evanescent field. For example, for the composites of small metal particles embedded into a MO background such behavior is shown theoretically [118] and confirmed experimentally [105]; the rotation changes its sign when localized surface plasmon modes of small particles are excited.

It worth of mentioning that calculations results presented here were done in the perfect conductor approximation by method described in [119]. Obviously, the finite conductivity of the real metals will affect both optical and MO properties of the structure under study.

21.4.3 Conclusion

Subwavelength-thick artificial MO media supporting LSPRs, Bi:YIG–Au plasmonic nanostructures, are experimentally shown to exhibit the larger Faraday rotation. Two-times enhancement for the 160-nm-thick Bi:YIG–Au film was demonstrated, suggesting approach to achieve the next level of miniaturization of MO media. Studies on the figure of merit for these structures, which is a trade-off between the losses due to LSPR and the angle of polarization rotation, are getting of growing interest. It is evident that such attributes as the size and volume fraction of noble-metal nanoparticles, their shape and size deviations, and their arrangement are responsible for MO functionality of plasmonic nanocomposites.

The huge enhancement of the Faraday and Kerr rotations was found for frequencies corresponding to excitation of the resonances responsible for the extraordinary optical transmittance through optically thick perforated metal film with holes filled with a magneto-optically active material. Transmission bandwidth and polarization conversion are strongly sensitive to the resonance quality controllable by the optical contrast between MO holes filler and surrounding medium. Appropriate choice of the materials brings possibility to find a trade off between the transmission bandwidth and the polarization conversion optimal for particular applications. The considered structures provide flexibility in designing media with MO characteristics tailored for use in specific spectral regions via choice of spectral positions of LSPRs or the extraordinary optical transmittance.

Acknowledgments We thank O. A. Aktsipetrov, A. P. Vinogradov, A. B. Granovskii, A. A. Fedyanin, R. Fujikawa, A. M. Merzlikin, and H. Uchida for many discussions on the topics covered here and for their collaboration.

References

1. Yablonovitch, E., *Phys. Rev. Lett.* **58**, 2059–2062 (1987)
2. Kato, H., Matsushita, T., Takayama, A., et al.: Properties of one-dimensional magnetophotonic crystals for use in optical isolator devices, *IEEE Trans. Magn.* **38**, 3246–3248 (2002)
3. Park, H. J., Cho, J. K., Nishimura, K., Inoue, M.: Magneto-optic spatial light modulator for volumetric digital recording system, *Jpn. J. Appl. Phys.* **41**, 1813–1816 (2002)
4. Joannopoulos, J. D., Meade, R., Winn, J.: *Photonic Crystals*. Princeton University Press, Princeton (1995)
5. Fujii, T., Inoue, M.: *Photonic Kessho* (Japanese translation version). Corona Publishing Inc., Tokyo (2000)
6. Lopes, C.: Materials aspects of photonic crystals. *Adv. Mater.* **15**, 1679–1704 (2003)
7. Lourtioz, J.-M., Benisty, H., Berger, V., Gerard, J.-M., Maystre, D., Tcheltnokov, A.: *Photonic Crystals: Towards Nanoscale Photonic Devices*. Springer, Berlin (2005)

8. Inoue, M., Yamamoto, T., Isamoto, K., Fujii, T.: Effect of structural irregularity on propagation properties of optical waves in discontinuous magneto-optical media with one-dimensional quasirandom array structures. *J. Appl. Phys.* **79**, 5988–5990 (1996)
9. Inoue, M., Fujii, T.: A theoretical analysis of magneto-optical Faraday effect of YIG films with random multilayer structures. *J. Appl. Phys.* **81**, 5659–5661 (1997)
10. Kavokin, A. V., Vladimirova, M. R., Kaliteevski, M. A., Lyngnes, O., Berger, J. D., Gibbs, H. M., Khitrova G.: Resonant Faraday rotation in a semiconductor microcavity. *Phys. Rev. B* **56**, 1087–1090 (1997)
11. Inoue, M., Arai, K. I., Fujii, T., Abe, M.: Magneto-optical properties of one-dimensional photonic crystals composed of magnetic and dielectric layers. *J. Appl. Phys.* **83**, 6768–6770 (1998)
12. Inoue, M., Fujii, T., Arai, K. I., Abe, M.: Huge enhancement of magneto-optical Faraday effect in YIG films with disordered multilayer structures. *J. Magn. Soc. Jpn.* **22**, 141–143 (1998)
13. Steel, M. J., Levy, M., Osgood, R. M.: Photonic bandgaps with defects and the enhancement of Faraday rotation. *J. Lightwave Technol.* **18**, 1297–1308 (2000)
14. Gates, B., Xia, Y.: Photonic crystals that can be addressed with an external magnetic field. *Adv. Mater* **13**, 1605–1608 (2001)
15. Kato, H., Matsushita, T., Takayama, A., Egawa, M., Nishimura, K., Inoue, M.: Theoretical analysis of optical and magneto-optical properties of one-dimensional magnetophotonic crystals. *J. Appl. Phys.* **93**, 3906–3911 (2003)
16. Kahl, S., Grishin, A. M.: Enhanced Faraday rotation in all-garnet magneto-optical photonic crystal. *Appl. Phys. Lett.* **84**, 1438–1440 (2004)
17. Lyubchanskii, I. L., Dadoenkova, N. N., Lyubchanskii, M. I., Shapovalov, E. A., Lakhtakia, A., Rasing, T.: Bigyrotropic photonic crystals. *Proc. SPIE* **5508**, 184 (2004)
18. Jalali, A. A., Friberg, A. T.: Faraday rotation in two-dimensional magneto-optic photonic crystal. *Opt. Com.* **253**, 145–150 (2005)
19. Li, R., Levy, M.: Bragg grating magnetic photonic crystal waveguides. *Appl. Phys. Lett.* **86**, 251102 (2005); Erratum: Bragg grating magnetic photonic crystal waveguides [*Appl. Phys. Lett.* **86**, 251102 (2005)]. *App. Phys. Lett.* **87**, 269901/1 (2005)
20. Levy, M., Li, R.: Polarization rotation enhancement and scattering mechanisms in waveguide magnetophotonic crystals. *Appl. Phys. Lett.* **89**, 121113/3 (2006)
21. Wang, Z., Fan, S.: Optical circulators in two-dimensional magneto-optical photonic crystals. *Opt. Lett.* **30**, 1989–1991 (2005)
22. Wang, Z., Fan, S.: Magneto-optical defects in two-dimensional photonic crystals. *Appl. Phys. B* **81**, 369–375 (2005)
23. Kim, J. B., Lee, G. J., Lee, Y. P., Rhee, J. Y., Kim, K. W., Yoon, C. S.: One-dimensional magnetic grating structure made easy. *Appl. Phys. Lett.* **89**, 151111 (2006)
24. Vinogradov, A. P., Dorofeenko, A. V., Erokhin, S. G., et al.: Surface state peculiarities in one-dimensional photonic crystal interfaces. *Phys. Rev. B* **74**, 045128/8 (2006)
25. Khanikaev, A. B., Baryshev, A. V., Inoue, M., et al.: Two-dimensional magnetophotonic crystal: Exactly solvable model. *Phys. Rev. B* **72**, 035123/9 (2005)
26. Inoue, M., Fujikawa, R., Baryshev, A., et al.: Magnetophotonic crystals. *J. Phys. D: Appl. Phys.* **39**, R151–R161 (2006)
27. Merzlikin, A. M., Vinogradov, A. P., Inoue, M., et al.: The Faraday effect in two-dimensional magneto-photonic crystals. *J. Magn. Magn. Mater.* **300**, 108–111 (2006)
28. Merzlikin, A. M., Vinogradov, A. P.: Superprism effect in 1D photonic crystal. *Opt. Commun.* **259**, 700–703 (2006)
29. Merzlikin, A. M., Vinogradov, A. P., Dorofeenko, A. V., et al.: Controllable Tamm states in magnetophotonic crystal. *Physica B: Phys. Condens. Mat.* **394**, 277–280 (2007)
30. Levy, M., Jalali, A. A.: Band structure and Bloch states in birefringent one-dimensional magnetophotonic crystals: An analytical approach. *J. Opt. Soc. Am. B* **24**, 1603–1609 (2007)
31. Khartsev, S. I., Grishin A. M.: High performance $[\text{Bi}_3\text{Fe}_5\text{O}_{12}/\text{Sm}_3\text{Ga}_5\text{O}_{12}]^m$ magneto-optical photonic Crystals. *J. Appl. Phys.* **101**, 053906/6 (2007)

32. Lyubchanskii, I. L., Dadoenkova, N. N., Lyubchanskii, M. I., et al.: Response of two-defect magnetic photonic crystals to oblique incidence of light: Effect of defect layer variation. *J. Appl. Phys.* **100**, 096110/3 (2006)
33. Young, D., Tsai, C.S.: Bismuth-doped yttrium iron garnet guided-wave magneto-optic Bragg cells and applications. *Ultrasonics Symp. Proc. IEEE* **1**, 521–523 (1989)
34. Jonsson, F., Flytzanis, C.: Spectral windowing with chirped magneto-optical Bragg gratings. *J. Opt. Soc. Am. B* **22**, 293–298 (2005)
35. van Albada, M. P., Lagendijk, A.: Observation of weak localization of light in a random medium. *Phys. Rev. Lett.* **55**, 2692–2695 (1985)
36. Wolf, P. E., Maret, G.: Weak localization and coherent backscattering of photons in disordered media. *Phys. Rev. Lett.* **55**, 2696–2699 (1985)
37. Atkinson, R., Lissberger, P. H.: Correct formulation of first-order magneto-optical effects in multilayer thin films in terms of characteristic matrices and derivation of a related superposition principle. *J. Mag. Magn. Mat.* **118**, 271–277 (1993)
38. Schubert, M., Tiwald, T. E., Woollam, J.A.: Explicit solutions for the optical properties of arbitrary magneto-optic materials in generalized ellipsometry. *Appl. Opt.* **38**, 177–187 (1999)
39. Yeh, P.: *Optical waves in layered media*. J. Wiley & Sons, New York (1988)
40. Sakoda, K.: *Optical properties of Photonic Crystals*. Springer, Berlin (2001)
41. Nishizawa, H., Nakayama, T.: Magneto-optic anisotropy effect on photonic band structure. *J. Phys. Soc. Jpn.* **66**, 613–617 (1997)
42. Zvezdin, A. K., Belotelov, V. I.: Magneto-optical properties of two dimensional photonic crystals. *Eur. Phys. J. B* **37**, 479–487 (2004)
43. Khanikaev, A. B., Inoue, M., Granovsky, A. B.: TM-TE hybridization and tunable refraction in magnetophotonic crystals. *J. Magn. Magn. Mat.* **300**, 104–107 (2006)
44. Ohtaka, K.: Energy-band of photons and low-energy photon diffraction. *Phys. Rev. B* **19**, 5057–5067 (1979)
45. Lamb, W., Wood, D. M., Ashcroft, N. W.: Long-wavelength electromagnetic propagation in heterogeneous media. *Phys. Rev. B* **21**, 2248–2266 (1980)
46. Wang, X., Zang, X.-G., Yu, Q., Harmon, B. N.: Multiple-scattering theory for electromagnetic waves. *Phys. Rev. B* **47**, 4161–4167 (1992)
47. Stefanou, N., Yannopapas, V., Modinos, A.: Heterostructures of photonic crystals: Frequency bands and transmission coefficients. *Comput. Phys. Commun.* **113**, 49–77 (1998); Stefanou, N., Yannopapas, V., Modinos, A.: MULTEM2: A new version of a program for transmission and band-structure calculations of photonic crystals. *ibid.* **132**, 189–196 (2000)
48. Lin, Z., Chui, S. T.: Electromagnetic scattering by optically anisotropic magnetic particle. *Phys. Rev. E* **69**, 056614 (2004)
49. Fedyanin, A. A., Yoshida, T., Nishimura, K. et al.: Magnetization-induced second harmonic generation in magnetophotonic microcavities based on ferrite garnets. *JETP* **76**, 527–531 (2002)
50. Dolgova, T. V., Fedyanin, A. A., Aktsipetrov, O. A. et al.: Nonlinear magneto-optical Kerr effect in garnet magnetophotonic crystals. *J. Appl. Phys.* **95**, 7330–7332 (2004)
51. Fedyanin, A. A., Aktsipetrov, O. A., Kobayashi, D. et al.: Enhanced Faraday and nonlinear magneto-optical Kerr effects in magnetophotonic crystals. *J. Magn. Magn. Mater.* **282**, 256–259 (2004)
52. Fedyanin, A. A., Yoshida, T., Nishimura, K. et al.: Nonlinear magneto-optical Kerr effect in gyrotropic photonic band gap structures: Magneto-photonic microcavities. *J. Magn. Magn. Mater.* **258**, 96–98 (2003)
53. Murzina, T. V., Kapra, R. V., Dolgova, T. V. et al.: Magnetization-induced second-harmonic generation in magnetophotonic crystals. *Phys. Rev. B* **70**, 012407/4 (2004)
54. Aktsipetrov, O. A., Murzina, T. V., Kim, E. M. et al.: Magnetization-induced second- and third-harmonic generation in magnetic thin films and nanoparticles. *J. Opt. Soc. Am. B* **22**, 138–147 (2005)

55. Aktsipetrov, O. A., Dolgova, T. V., Fedyanin, A. A. et al.: Magnetization-induced second- and third-harmonic generation in magnetophotonic crystals. *J. Opt. Soc. Am. B* **22**, 176–186 (2005)
56. Murzina, T. V., Kim, E. M., Kapra, R. V., et al.: Magnetophotonic crystals based on yttrium-iron-garnet infiltrated opals: Magnetization-induced second-harmonic generation. *J. Appl. Phys.* **88**, 022501/3 (2006)
57. Granovsky, A. B., Inoue, M.: Spin-dependent tunnelling at infrared frequencies: Magneto-refractive effect in magnetic nanocomposites. *J. Magn. Magn. Mater.* **272–276**(Suppl. 1), E1601–E1605 (2004)
58. Granovsky, A. B., Bykov, I. V., Gan'shina, E. A., et al.: Magneto-refractive effect in magnetic nanocomposites. *JETP* **96**, 1104–1112 (2003)
59. Mennicke, R. T., Bozec, D., Kravets, V. G., et al.: Modelling the magneto-refractive effect in giant magnetoresistive granular and layered materials. *J. Magn. Magn. Mater.* **303**, 92–110 (2006)
60. Rinkevich, A. B., Romashev, L. N., Ustinov, V. V.: Radiofrequency magnetoresistance of Fe/Cr superlattices. *JETP* **90**, 834–841 (2000)
61. Ustinov, V. V., Rinkevich, A. B., Romashev, L. N., et al.: Giant magnetoresistive effect in Fe/Cr multilayers in a wide range of frequencies. *Phys. Met. Metallogr.* **96**, 291–297 (2003)
62. Yurasov, A. N., Granovsky, A. B., Tarapov, S. P., Clerc, J. P.: High-frequency magneto-impedance in nanocomposites. *J. Magn. Magn. Mater.* **300**, E52–E54 (2006)
63. Auslender, M. I., Barsukova, E. V., Bebenin, N. G., et al.: Absorption spectrum of n- and p-type single crystals of ferromagnetic semiconductor HgCr_2Se_4 in a magnetic field. *JETP* **68**, 139–142 (1989)
64. van Driel, J., de Boer, F. R., Coehoorn, R., et al.: Magneto-refractive and magnetic-linear-dichroism effect in exchange-biased spin valves. *Phys. Rev.* **61**, 15321/6 (2000)
65. Granovskii, A. B., Gan'shina, E. A., Yurasov, A. N., et al.: Magneto-refractive effect in nanostructures, manganites, and magnetophotonic crystals based on these materials. *J. Comm. Tech. and Electronics* **52**, 1065–1071 (2007)
66. Jacquet, J. C., Valet, T.: A new magneto-optical effect discovered on magnetic multilayers: The magneto-refractive effect. In: Marinero, E. (ed.) *Magnetic Ultrathin Films, Multilayers and Surfaces*. Pittsburgh, PA: Mat. Res. Soc. Symp. Proc. **384**, pp. 477–490 (1995)
67. Kubrakov, N. F., Zvezdin, A. K., Zvezdin, K. A., et al.: New intensity magneto-optical effect in materials exhibiting giant magnetoresistance. *JETP* **87**, 600–607 (1998)
68. Uran, S., Grimsditch, M., Fullerton, E., Bader, S. D.: Infrared spectra of giant magnetoresistance Fe/Cr/Fe trilayers. *Phys. Rev.* **57**, 2705/4 (1998)
69. Baxter, R. X., Pettifor, D. G., Tsymbal, E. Y., et al.: Importance of the interband contribution to the magneto-refractive effect in Co/Cu multilayers. *J. Phys.: Cond. Mat.* **15**, L695–L702 (2003)
70. Vopsaroiu, M., Bozec, D., Matthew, J. A. D., et al.: Contactless magnetoresistance studies of Co/Cu multilayers using the infrared magneto-refractive effect. *Phys. Rev. B* **70**, 214423/7 (2004).
71. Granovskii, A. B., Kuz'michev, M. V., Klerk, J. P.: Optical and magneto-optical properties of granular alloys with giant magnetoresistance in the IR region of the spectrum. *JETP* **89**, 955–959 (1999)
72. Kravets, V. G., Bozec, D., Matthew, J. A. D., et al.: Correlation between the magneto-refractive effect, giant magnetoresistance, and optical properties of Co-Ag granular magnetic films. *Phys. Rev. B* **65**, 054415/9 (2002)
73. Gester, M., Schlapka, A., Pickford, R. A., et al.: Contactless measurement of giant magnetoresistance in CoAg granular films using infrared transmission spectroscopy. *J. Appl. Phys.* **85**, 5045–5047 (1999)
74. Bykov, I. V., Gan'shina, E. A., Granovskii, A. B., et al.: Magneto-refractive effect in granular alloys with tunneling magnetoresistance. *Phys. Solid State* **47**, 281–286 (2005)

75. Bozec, D., Kravets, V. G., Matthew, J. A. D., et al.: Infrared reflectance and magnetorefractive effects in metal-insulator CoFe-Al₂O₃ granular films. *J. Appl. Phys.* **91**, 8795–8797 (2002)
76. Granovsky, A. B., Inoue, M., Clerk, J. P., Yurasov, A. N.: Magnetorefractive effect in nanocomposites: Dependence on the angle of incidence and on light polarization. *Phys. Solid State* **46**, 498–501 (2004)
77. Granovsky, A., Kozlov, A., Yurasov, A., et al.: Magnetorefractive effect in magnetic nanocomposites in reflection: Dependencies on incident angle and polarization of light. In: Aktas, B., Tagirov, L., Mikailov, F. (eds.) *Nanostructured Magnetic Materials and Their Applications*, pp. 433–440. Kluwer Academic Pub., London (2004)
78. Loshkareva, N. N., Sukhorukov, Yu., P., Gizhevskii, B. A., et al.: Red shift of absorption edge and nonmetal-metal transition in single crystals La_{1-x}Sr_xMnO₃ ($x = 0.1, 0.2, 0.3$). *Phys. Stat. Solidi A* **164**, 863–867 (1997)
79. Sukhorukov, Yu., P., Nosov, A. P., Loshkareva, N. N., et al.: The influence of magnetic and electronic inhomogeneities on magnetotransmission and magnetoresistance of La_{0.67}Sr_{0.33}MnO₃ films. *J. Appl. Phys.* **97**, 103710/5 (2004)
80. Melnikov, O. V., Sukhorukov, Yu., P., Telegin, A. V., et al.: The evolution of magnetotransport and magneto-optical properties of thin La_{0.8}Ag_{0.1}MnO_{3+δ} films possessing the in-plane variant structure as a function of the film thickness. *J. Phys.: Cond. Mat.* **18**, 3753–3765 (2006)
81. Sukhorukov, Yu., P., Telegin, A. V., Gan'shina, E. A., et al.: Tunneling of spin-polarized charge carriers in La_{0.8}Ag_{0.1}MnO_{3+δ} film with variant structure: Magnetotransport and magneto-optical data. *Tech. Phys. Lett.* **31**, 484–487 (2005)
82. Sukhorukov, Yu., P., Gan'shina, E. A., Belevtsev, B. I., et al.: Giant change in infrared light transmission in La_{0.67}Ca_{0.33}MnO₃ film near the Curie temperature. *J. Appl. Phys.* **91**, 4403–4408 (2002)
83. Marques, R. F. C., Abernethy, P. R., Matthew, J. A. D., et al.: Contactless measurement of colossal magnetoresistance in La_{1-x}Sr_xMnO₃ using the infrared magnetorefractive effect. *J. Magn. Magn. Mater.* **272–276**, 1740–1741 (2004)
84. Inoue, M., Fujikawa, R., Baryshev, A., et al.: Magnetophotonic crystals. *J. Phys. D: Appl. Phys.* **39**, R151–R161 (2006)
85. Vinogradov, A. P., Erokhin, S. G., Granovskii, A. B., Inoue, M.: The polar Kerr effect in multilayer systems (magnetophotonic crystals). *J. Commun. Technol. Electron.* **49**, 682–685 (2004)
86. Vinogradov, A. P., Erokhin, S. G., Granovskii, A. B., Inoue, M.: Investigation of the Faraday effect in multilayer one-dimensional structures. *J. Commun. Technol. Electron.* **49**, 88–90 (2004)
87. Okimoto, Y., Katsufuji, T., Ishikawa, T., et al.: Variation of electronic structure in La_{1-x}Sr_xMnO₃ ($0 < x < 0.3$) as investigated by optical conductivity spectra. *Phys. Rev. B* **55**, 4206–4214 (1997)
88. Nomerovannaya, L. V., Makhnev, A. A., Romyantsev, A. Yu.: Evolution of the optical properties of single-crystal La_{1-x}Sr_xMnO₃. *Phys. Solid State* **41**, 1322–1326 (1999)
89. Boriskina, Yu., V., Erokhin, S. G., Vinogradov, A. P., et al.: Enhancement of the magnetorefractive effect in magnetophotonic crystals. *Phys. Solid State* **48**, 717–721 (2006)
90. Zvezdin, A. K., Belotelov, V. I.: Magneto-optical properties of two dimensional photonic crystals. *Eur. Phys. J. B* **37**, 479–487 (2004)
91. Vinogradov A. P., Merzlikin, A. M.: Frequency dependence of localization length of an electromagnetic wave in a one-dimensional system. *Physica B* **338**, 126–131 (2003)
92. Feil, H., Haas, C.: Magneto-optical Kerr effect, enhanced by the plasma resonance of charge carriers. *Phys. Rev. Lett.* **58**, 65–68 (1987)
93. Xia, T. K., Hui, P. M., Stroud, D.: Theory of Faraday rotation by magnetic composites. *J. Appl. Phys.* **67**, 2736–2741 (1990)

94. Katayama, T., Suzuki, Y., Awano, H., Nishihara, Y., Koshizuka, N.: Enhancement of the magneto-optical Kerr rotation in Fe/Cu bilayered films. *Phys. Rev. Lett.* **60**, 1426–1429 (1988)
95. Safarov, V. I., Kosobukin, V. A., Hermann, C., Lampel, G., Peretti, J.: Magneto-optical effects enhanced by surface plasmons in metallic multilayer films. *Phys. Rev. Lett.* **73**, 3584–3587 (1994).
96. Hermann, C., Kosobukin, V. A., Lampel, G., Peretti, J., Safarov, V. I., Bertrand, P.: Surface-enhanced magneto-optics in metallic multilayer films. *Phys. Rev. B* **64**, 235422/11 (2001)
97. Kochergin, V. E., Toporov, A. Yu., Valeiko, M.: Polariton enhancement of the Faraday magneto-optic effect. *JETP Lett.* **68**, 400–403 (1998)
98. Pufall, M. R., Berger, A., Schultz, S.: Measurement of the scattered light magneto-optical Kerr effect from plasmon-resonant Ag particles near a magnetic film. *J. Appl. Phys.* **81**, 5689–5691 (1997)
99. Li, Y., Zhang, Q., Nurmikko, A. V., Sun, S.: Enhanced magneto-optical response in Dumbbell-like Ag-CoFe₂O₄ nanoparticle pairs. *Nano Lett.* **5**, 1689–1692 (2005)
100. Shemer, G., Markovich, G.: Enhancement of magneto-optical effects in magnetite nanocrystals near gold surfaces. *J. Phys. Chem. B* **106**, 9195–9197 (2002)
101. Kosobukin, V. A.: Magneto-optics via the near field. *Surf. Science* **406**, 32–47 (1998)
102. Smith, D. A., Stokes, K. L.: Discrete dipole approximation for magneto-optical scattering calculations. *Opt. Exp.* **14**, 5746–5754 (2006)
103. Belotelov, V. I., Doskolovich, L. L., Zvezdin, A. K.: Extraordinary magneto-optical effects and transmission through metal-dielectric plasmonic systems. *Phys. Rev. Lett.* **98**, 077401/4 (2007)
104. Battula, A., Chen, S., Lu, Y., Knize, R. J., Reinhardt, K.: Tuning the extraordinary optical transmission through subwavelength hole array by applying a magnetic field. *Opt. Lett.* **32**, 2692–2694 (2007)
105. Tomita, S., Kato, T., Tsunashima, S., et al.: Magneto-optical Kerr effects of Yttrium-Iron Garnet thin films incorporating gold nanoparticles. *Phys. Rev. Lett.* **96**, 167402/4 (2006)
106. Kosobukin, V. A.: Surface-enhanced magneto-optical effects in ferromagnetic superlattices. *Solid State Com.* **101**, 497–501 (1997)
107. Jen, S. U., Chen, K. C.: Enhancement of polar Kerr effect by forming Au nanoparticles on Ni surface. *J. Appl. Phys.* **97**, 10M311/3 (2005)
108. Bohrein, C. F., Huffman, D. R.: *Absorption and Scattering of Light by Small Particles*. John Wiley & Sons, New York (1983)
109. Gasparian, V., Ortuno, M., Ruiz, J., Cuevas, E.: Faraday rotation and complex-valued traversal time for classical light waves. *Phys. Rev. Lett.* **75**, 2312–2315 (1995)
110. Inoue, M., Fujikawa, R., Baryshev, A., Khanikaev, A., Lim, P. B., Uchida, H., Aktsipetrov, O., Fedyanin, A., Murzina, T., Granovsky, A.: Magnetophotonic crystals. *J. Phys. V: Appl. Phys.* **39**, R151–R161 (2006)
111. Ebbesen, T. W., Lezec, H. J., Ghaemi, H. F., et al.: Extraordinary optical transmission through sub-wavelength hole arrays. *Nature* **391**, 667–669 (1998)
112. Pendry, J. B., Martin-Moreno, L., Garcia-Vidal, F. J.: Mimicking surface plasmons with structured surfaces. *Science* **305**, 847–848 (2004)
113. Porto, J. A., Martin-Moreno, L., Garcia-Vidal, F. J.: Optical bistability in subwavelength slit apertures containing nonlinear media. *Phys. Rev. B* **70**, 081402(R)/4 (2004)
114. Fujikawa, R., Baryshev, A. V., Kim, J., et al.: Contribution of the surface plasmon resonance to optical and magneto-optical properties of a Bi:YIG–Au nanostructure. *J. Appl. Phys.* **103**, 07D301/3 (2008)
115. Rechberger, W., Hohenau, A., Leitner, A., et al.: Optical properties of two interacting gold nanoparticles. *Opt. Comm.* **220**, 137–141 (2003)
116. Martin-Moreno, L., Garcia-Vidal, F. J., Lezec, H. J., et al.: Theory of extraordinary optical transmission through subwavelength hole arrays. *Phys. Rev. Lett.* **86**, 1114–1117 (2001)

117. Khanikaev, A. B., Baryshev, A. V., Fedyanin, A. A., et al.: Anomalous Faraday effect of a system with extraordinary optical transmittance. *Opt. Exp.* **15**, 6612–6622 (2007)
118. Hui, P. M., Stroud, D.: Theory of Faraday rotation by dilute suspensions of small particles. *Appl. Phys. Lett.* **50**, 950–952 (1987)
119. Khanikaev, A. B., Baryshev, A. V., Fedyanin, A. A., et al.: Optical properties of nanostructured metallic films containing magnetic media. *Proc. SPIE* **6641**, 66411H/8 (2007)

Chapter 22

Hard Magnetic Materials for MEMS Applications

Nora M. Dempsey

Abstract Micro-magnets of thickness in the range 1–500 μm have many potential applications in micro-electro-mechanical-systems (MEMS) because of favorable downscaling laws and their unique ability to produce long range bi-directional forces. The advantages and disadvantages of a number of “top-down” routes, which use bulk processed precursors (magnets or magnetic powders), to produce μ -magnets of thickness in the range 10–500 μm will be discussed. Progress in the fabrication and patterning of thick film magnets (1–100 μm) using “bottom-up” deposition techniques will be reviewed. In particular, recent results concerning high-rate triode sputtering and micro-patterning of high-performance NdFeB and SmCo films will be presented.

22.1 An Introduction to MEMS

22.1.1 What Are MEMS?

Micro-electromechanical-systems (MEMS) are machines which range in size from a few micrometers to a few millimeters. They may operate as actuators, motors, generators, or switches and have applications in fields as diverse as telecommunications, automotive, aerospace, astronomy, ophthalmometry, biotechnology, and logistics. Some common examples of MEMS-based devices include inkjet printers, accelerometers for airbag deployment, and DLP projectors. Many different physical principles are exploited in MEMS. Owing to the fact that MEMS are an off-shoot of the microelectronics industry, the first MEMS were based on *electrostatic* principles. Following this, *differential thermal expansion* was exploited in bimorph actuators. Today’s MEMS also exploit *piezoelectricity*, *electromagnetism*,

N.M. Dempsey (✉)
Institut Néel, CNRS-UJF, 38042, Grenoble, France
e-mail: nora.dempsey@grenoble.cnrs.fr

ferromagnetism, magnetostriction, shape memory effects, etc. MEMS is a fast evolving domain and it is expected that other physical effects may also be exploited.

MEMS are of interest for the following reasons. Batch processing of MEMS using techniques developed by the microelectronics industry means that the price of an individual system may be very low. Their small size means that they do not take up much space and weigh little, with obvious benefits for portable applications (mobile phones, aerospace devices, etc.) or applications with space limitations (implantable devices, micro-surgery, etc.). MEMS hold great potential for the environment: they already increase fuel efficiency in modern cars and houses of the future will intelligently control energy consumption, by exploiting MEMS to regulate temperature and lighting in accordance with need. As MEMS are made using microelectronics technology, electromechanical elements can be integrated with electronics onto one substrate, the former acting as the arms and legs of the machine, the latter as the brain. Finally, MEMS challenge traditional engineering concepts, as gravity and inertia are of reduced importance and atomic forces and surface science effects may dominate. Scaling laws demonstrate that effects not exploitable at the macro-scale (e.g., electrostatic and van der Waal's forces) can become of interest at the micron scale.

22.1.2 How Are MEMS Made?

MEMS are made using a number of different technologies. *Bulk Micromachining* creates devices by wet etching into a wafer, typically Si. *Surface Micromachining* builds devices up from the wafer layer by layer. It requires more fabrication steps than bulk micromachining, and thus it is more expensive. However, it enables the creation of more sophisticated devices of higher functionality. *LIGA (Lithographie–Galvanoformung–Abformung)* is a relatively inexpensive fabrication technology which uses x-ray lithography to create small, but relatively high aspect ratio devices. Finally, *Deep Reactive Ion Etching* is a type of micromachining which uses a plasma to etch features. It is more expensive but also more flexible than traditional bulk micromachining based on wet etching. These different fabrication technologies use three basic building blocks, namely (1) deposition (e.g., chemical vapor deposition, electrodeposition, sputtering, evaporation, etc.) (2) lithography, and (3) etching. The emergence of MEMS based on active materials other than Si depends on the ability to produce these materials with existing or modified MEMS technologies, while maintaining the material's functional properties.

22.2 Magnetic MEMS

Magnetism has intrigued humans for millennia and has developed into a rich field of science with many important technological applications. The first and still most widely known magnetic materials are permanent magnets. They find many applica-

tions in electromagnetic devices which exploit the relationship between electricity and magnetism. There is great potential for the use of permanent magnets in MEMS, and this chapter deals specifically with this type of material. However, other classes of magnetic materials, such as soft magnetic materials, magnetostrictive materials, and magnetic shape memory materials are also studied for use in MEMS. For a review see [64].

Magnets can be exploited in different ways in an electromagnetic system through interactions with current carrying coils, other magnets, or soft magnetic materials. The movement of a magnet relative to a coil can be used to induce a voltage which in turn produces an electric current in the coil (generator, position sensor, etc.), and inversely, the passage of a current through a coil can be used to move a magnet and whatever mobile parts it is attached to (rotors, pumps, etc.). The interactions between two magnets or between a magnet and a soft magnetic material can be used to produce forces or torques (switches, bi-stable cantilevers, etc.). In the case of two magnets, the interaction force may be repulsive (levitation, bearings, suspensions). Action at a distance allows for contactless actuation through sealed membranes. Magnets may also be used to simply magnetize other magnetic materials such as soft or magnetostrictive materials. As a source of magnetic field, magnets have the advantage of not consuming power and consequently not being susceptible to power cuts. For all these reasons, permanent magnets are used extensively in macroscopic applications.

The use of permanent magnet-based electromagnetism in microscopic applications can greatly benefit from both down scaling laws and higher current density tolerances in micro-coils [18]. The principle arguments of Cugat et al. will now be recalled.

22.2.1 Downscaling Magnetic Systems

A magnet of volume v and magnetic polarization J generates a scalar potential V at any point P located at a distance r . The magnetic field H is the local gradient of the scalar potential V :

$$V(P) = \frac{v}{4\pi\mu_0} \frac{\vec{J} \cdot \vec{r}}{r^3} \quad (22.1)$$

$$\vec{H} = \overrightarrow{\text{grad}V} \quad (22.2)$$

Homothetic miniaturization (all dimensions reduced by the same factor $k = 10, 100, 1000, \text{etc.}$) of a given magnet, the magnet's polarization remaining constant, conserves the magnetic field H generated by the magnet while the scalar potential $V(P)$ is divided by k . The relative geometrical distribution and the magnitude of the field map around a magnet are conserved after a scale reduction and thus field gradients are multiplied by k .

The torque experienced by a magnet of polarization J and volume v immersed in a homogeneous magnetic field H is proportional to M and H , where $M = vJ$. During the homothetic $1/k$ reduction, both H and J remain constant, thus the torque-to-volume ratio also remains constant.

The magnetic interaction energy W_i and magnetic force F , between two magnets, each of volume v , or a magnet of volume v and a soft material are given by

$$W_i = -\vec{J} \cdot v \vec{H} \quad (22.3)$$

$$\vec{F} = -\overrightarrow{\text{grad}W_i} \quad (22.4)$$

If we scale the system down by a factor k , while the interaction energy W_i decreases by k^3 , the force F decreases by just k^2 . This results in a relative increase of the force/volume ratio by k . This implies that systems exploiting the attractive or repulsive forces between magnets and soft materials benefit greatly from downscaling.

The Lorentz force per unit volume exerted by a magnet on a current carrying conductor is proportional to the magnetic field produced by the magnet and thus remains unchanged as we scale down the size of the system. At the same time, the volume forces produced by current-carrying conductors on magnets, as described by the Biot–Savart law, also remain unchanged. This implies that, at constant current density, there is no particular advantage in scaling down a system which exploits interactions between a magnet and a current carrying conductor. However, the admissible current density in a conductor can be increased as we scale down the size of the conductor, and thus the size of the magnetic field produced by the coil, and the resultant forces, can be increased. This is because heating due to Joule losses scales as k^3 while cooling through heat flow, which is proportional to the area of the heat exchange surface and inversely proportional to the distance through which the heat flows, scales as k^2/k . Thus as we scale down, volume Joule losses increase by a factor $k^3/(k^2/k) = k^2$. The admissible current density is proportional to the square root of the Joule losses, and thus can be increased by a factor k . The admissible current density is further increased because of lower volume-to-surface ratios in micro-coils which are planar, more efficient cooling because of direct contact between the micro-coil and the substrate on which it is deposited (typically Si, which is a good conductor of heat), and the use of pulsed currents. Thus, while the maximum admissible current density in macroscopic systems is of the order of 5–50 A/mm², it increases to values of the order of 10³–10⁵ A/mm² in microscopic systems.

The influence of scaling down on magnetic interactions involving magnets, current carrying coils, and soft magnetic materials, allowing for increased maximum admissible current densities, is schematized in Fig. 22.1. In summary, scaling down is most beneficial for interactions between two magnets or between a magnet and a soft material, while interactions involving current carrying coils can gain from a consequent increase in the maximum admissible current density. Induc-

tive effects may benefit from the very high speeds and frequencies achievable in microsystems.



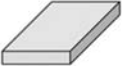
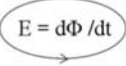










<i>Reduction factor</i> $1/k$	magnet 	current 	iron 	induction $E = d\Phi / dt$ 
magnet 	$\times k$ 	$\times k_1$ 	$\times k$ 	$/k$ \times frequency 
current 	$\times k_1$ 	$\times k_{i1} \times k_{i2} / k$ 	$\times k_1 / k$ 	$\times k_1 / k^2$ \times frequency 

Fig. 22.1 Effect of scale reduction $1/k$ on magnetic interactions, taking into account increased admissible current densities as well as high speeds and frequencies achievable in Microsystems [18]

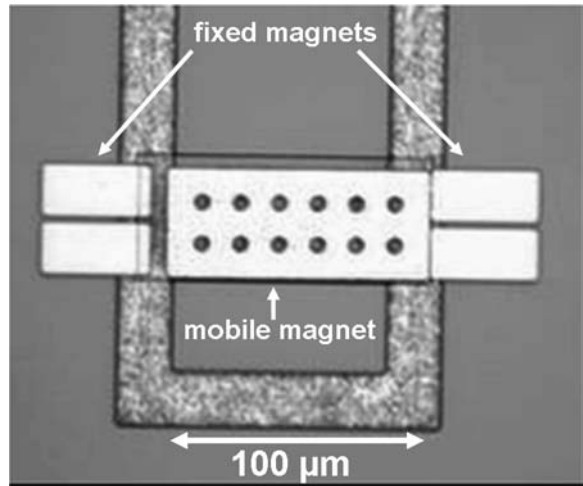
Finally, two other specific features favor the use of permanent magnets in MEMS. They produce magnetic fields and gradients which are effective over long distances allowing for large-throw and/or wide-angular actuation, for which electrostatic actuators would need unrealistically high voltages. Magnet-based systems are characterized by much higher energy densities than electrostatic systems.

22.2.2 Prototype Magnetic MEMS

Despite their great potential, magnetic MEMS based on magnets are much less developed than systems based on electrostatic or bimorph principles (thermal or piezoelectric) and have not gone beyond the prototype stage. Prototype magnetic MEMS include milli-motors [65], planar synchronous μ -motors [1], μ -generators [3, 32, 49], μ -switches (Fig. 22.2) [21, 55], deformable magnetic mirrors for astronomy and ophthalmology [17], mirror arrays for use in 3D optical switching [5], scanners [66], and linear microactuators [8]. A major bottleneck for the industrial emergence of such systems has been the challenge in producing high-quality magnets of the appropriate dimensions (1–500 μm) which can be prepared using techniques compatible with MEMS technology. Permanent magnets will be briefly described in the next section, while the following two sections will deal with the

“top-down” and “bottom-up” routes used to produce magnets in the thickness range 10–500 μm and 1–100 μm , respectively.

Fig. 22.2 Image of a magnetic bistable micro-switch based on electrodeposited CoPtP magnets [21]



22.3 Permanent Magnets

Permanent magnets, also known as “hard magnets” or simply “magnets”, are distinguished from soft magnetic materials because of their ability to remain magnetized in the absence of an external magnetic field. The quality of a magnet is measured by saturating it in an external magnetic field and then measuring its magnetization as a function of the value of the reduced and then reversed external magnetic field. The remanent magnetization (M_r) corresponds to the value of magnetization measured when the external field is reduced to zero while the coercivity (H_c) corresponds to the value of reversed external magnetic field needed to reduce the magnetization to zero. Both remanent magnetization and coercivity are extrinsic magnetic properties which depend on the material’s intrinsic magnetic properties and its micro-structure. The intrinsic magnetic properties (Curie temperature T_C , saturation magnetization $\mu_0 M_s$, anisotropy field $\mu_0 H_A$ and theoretical maximum energy product $(BH)_{\max,th}$) of a number of hard magnetic materials is given in Table 22.1. The saturation magnetization and anisotropy field define the upper limits to the remanence and coercivity (i.e. $M_r \leq M_s$, $H_c \leq H_A$). The energy product of a magnet quantifies the amount of magnetostatic energy stored in the magnet and is thus a good figure of merit for comparing different magnets. For magnets in which the coercivity is at least half the value of the remanent magnetization, the maximum energy product of the magnet is given by

$$(BH)_{\max} = \mu_0 M_r^2 / 4 \quad (22.5)$$

Thus to maximize the energy product, a magnet needs a sufficiently high coercivity ($\mu_0 H_c > 0.5 \mu_0 M_r$) and a maximum value of remanence. Coercivity may be induced at the atomic scale, through magneto-crystalline anisotropy, or at the macroscopic scale, through shape anisotropy [56]. The former gives rise to the high and mid-range values of coercivity achieved in rare earth transition metal (RE-TM), $L1_0$, hexagonal ferrites, and hexagonal close packed (hcp) Co-based alloys, while the latter gives rise to the low values of coercivity achieved in Alnico magnets. In all cases, the inducement of a particular microstructure is essential. The key to maximizing the magnet's remanence is to maximize the volume fraction of the hard magnetic phase and to crystallographically texture the particles so as to align their easy directions of magnetization.

Much work has been done on the nanostructuring of hard magnetic materials. A grain size refinement to the nanoscale has proved very useful in developing high coercivities while nanocomposite magnets, which combine the benefits of high coercivity hard grains and high magnetization soft grains, have the highest theoretical energy product values [56]. For a review of the techniques used to produce nanostructured bulk materials, and on the range of microstructures exploited in high-performance bulk magnets, the reader is referred to [28, 29].

When choosing a magnet, one must also consider the operating temperature and environmental conditions under which the magnet will be used. SmCo-based magnets are suitable for high-temperature applications, while RE-free magnets are less susceptible to oxidation than RE-TM alloys, and thus may be best suited to corrosive environments.

22.4 Fabrication of μ -Magnets: Top-Down Routes

The “top-down” approaches which have been used to prepare magnets of thickness in the range 10–500 μm can be classified according to whether they concern *magnets* or *hard magnetic powders* produced by bulk processing techniques (Fig. 22.3).

Table 22.1 Intrinsic magnetic properties (Curie temperature T_C , saturation magnetization $\mu_0 M_s$, anisotropy field $\mu_0 H_A$, and theoretical maximum energy product $(BH)_{\text{max,th}}$) of the most important hard magnetic materials

Material	T_C (K)	$\mu_0 M_s$ (T)	$\mu_0 H_A$ (T)	$(BH)_{\text{max,th}}$ kJ/m ³
Nd ₂ Fe ₁₄ B	585	1.61	7.6	514
SmCo ₅	1,000	1.05	40	220
Sm ₂ Co ₁₇	1,173	1.30	6.4	333
FePt – L1 ₀	750	1.43	11.6	407
CoPt – L1 ₀	840	1.00	4.9	200
hcp Co	1,394	1.72	0.77	–
BaFe ₁₂ O ₁₉	742	0.48	1.8	46

22.4.1 Bulk Processed Magnets

Sub-millimeter-sized bulk processed magnets can be used in the micro-assembly of magnetic MEMS. Though the micro-assembly of individual magnets can be time consuming (not a problem for proto-typing, but important for industrial processing), it may be worth the effort when the micro-magnets are of very high quality (i.e., high-energy product). This is the case for fully dense magnets made without non-magnetic binders, as the remanent magnetization is not reduced by dilution and may approach the saturation magnetization if the sample is textured. Such μ -magnets can be produced by machining of bigger magnets or by mechanical deformation routes.

22.4.1.1 Machining of Sintered Magnets

Machining of bulk magnets is presently used to prepare magnets for application in milli-systems (wrist watches, flip-dot displays, heart catheters, etc.) and has been used to prepare some large-sized prototype magnetic MEMS. Spark-cut 0.5 mm thick high-quality NdFeB magnets ($\mu_0 H_c = 1.2$ T; $\mu_0 M_r = 1.47$ T; $(BH)_{\max} = 424$ kJ/m³) are used in heart catheters [58]. However, the use of such magnets in MEMS is restricted as there is a lower limit to the magnet thickness achievable by machining (ca. 150 μ m for RE-TM magnets). What is more, high-quality RE-TM magnets suffer surface-degradation during machining, resulting in the loss of coercivity of the surface layer, and thus the overall magnet remanence. The problem is most critical for coarse grained sintered magnets (NdFeB and to a lesser extent SmCo₅) and least critical for nanostructured pinning type Sm₂Co₁₇ magnets [35].

22.4.1.2 Mechanical Deformation

A novel mechanical deformation process, involving the extensive co-deformation of elemental Fe and Pt foils by rolling, was recently developed to produce FePt (L1₀) foil magnets of typical thickness 100 μ m [30]. The weakly out-of-plane textured foils have the following magnetic properties: $\mu_0 H_c = 0.8$ T, $\mu_0 M_r = 0.75$ T, $(BH)_{\max} = 76$ kJ/m³. Some improvement in texture and thus energy product was achieved by annealing under magnetic field ($\mu_0 M_r = 0.82$ T, $(BH)_{\max} = 90$ kJ/m³) [19]. Though adapted to the production of thin foils, it may prove difficult to produce magnets of very small surface area. Another approach is the hot-deformation, essentially die-upsetting, of NdFeB-type powders down to thicknesses of several hundreds of microns [31]. Though these magnets have excellent magnetic properties ($\mu_0 H_c = 1.3$ T, $\mu_0 M_r = 1.25$ T, $(BH)_{\max} = 290$ kJ/m³), the fabrication process is quite laborious.

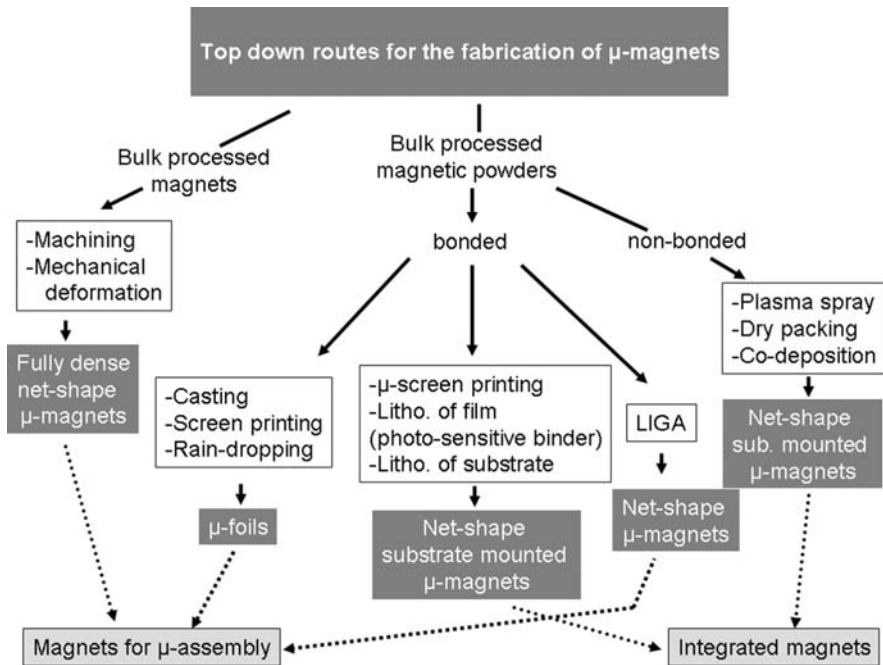


Fig. 22.3 Schematic flow chart for the production of μ -magnets using top down approaches

22.4.2 Bulk Processed Hard Magnetic Powders

A number of techniques have been used to produce μ -magnets using hard magnetic powders prepared by conventional bulk processing routes. These powders are used in both bonded and in non-bonded form. When choosing a powder for a given application, one needs to consider not only its magnetic properties but also the particle sizes available and the ease of handling/processing the powders. Ferrite powders are stable with respect to oxidation and are available as very fine particles ($\approx 1 \mu\text{m}$). SmCo powders are less susceptible to oxidation than NdFeB powders and are available in smaller particle sizes ($\text{SmCo} \geq 5 \mu\text{m}$; $\text{NdFeB} \geq 10 \mu\text{m}$). The different techniques which use hard magnetic powders to produce μ -magnets will now be discussed.

22.4.2.1 Bonded Powder Techniques

Composite magnets can be prepared by mixing hard magnetic powders with a non-magnetic binder (e.g. epoxy). The advantages of powder bonding include the relative ease of magnet shaping and the conferral of good mechanical properties

(fully dense magnets are brittle). When an appropriate binder is used, flexible hard magnetic foils can be produced. Nevertheless, these advantages come at the cost of the energy product which is reduced due to dilution of the magnetic phase and in many cases the isotropic nature of the bonded magnet. Sub-millimeter thick bonded magnet foils have been produced by casting [47, 53], screen printing [37, 46], and rain-dropping [54]. Net-shape substrate-mounted bonded μ -magnets have been produced by screen printing through screens containing sub-millimeter features [37], photo-lithography of spin-coated composite films made with a photo-sensitive binder [22], and the filling of lithographically defined patterns [15, 63]. LIGA processing (deep x-ray lithography + electroplating) has been used to produce individual high aspect ratio μ -magnets destined for micro-assembly [16]. The size and magnetic characteristics of different types of bonded μ -magnets are compared in Table 22.2.

Table 22.2 The size (t: thickness; w: width) and magnetic characteristics of bonded μ -magnets prepared by different techniques

Fab. Techn.	Magnet size	Mag. powder	$\mu_0 H_C$ (T)	$\mu_0 M_r$ (T)	$(BH)_{max}$ (kJ/m ³)	References
Casting	100–400 μm foils	$\text{Sm}_2\text{Co}_{17}$	1.1	0.27	13.6	[53]
	100–400 μm foils	$\text{Sm}_2\text{Co}_{17}$	0.9	0.45	40.3	[53]
	100–400 μm foils	NdFeB	1	0.41	28.8	[53]
	100–800 μm foils	NdFeB	0.4–1	0.35–0.45	–	[47]
Screen printing	9 μm films glass substrates	$\text{SrFe}_{12}\text{O}_{19}$	0.4	0.3	–	[37]
	20–100 μm films Fe substrates	NdFeB	–	0.5	–	[46]
Rain-dropping	500 μm foils	NdFeB	1.3	0.47	–	[54]
Litho-binder	t: 15 μm w: 1,250 μm	$\text{Sm}_2\text{Co}_{17}$	0.2	0.34	22	[22]
Litho-substrate	t: 65 μm w: 50–200 μm	$\text{SrFe}_{12}\text{O}_{19}$	0.4	0.03	2.7	[15]
	t: 40–200 μm	$\text{BaFe}_{12}\text{O}_{19}$	0.4	–	–	[63]
	t: 40–200 μm	NdFeB	0.2	–	–	[63]
LIGA	t: 500 μm w: $\geq 5 \mu\text{m}$	NdFeB	1.4	0.63	64	[16]

22.4.2.2 Non-Bonded Powder Techniques

SmCo particles (5–10 μm) have been *dry packed* into cavities in Si wafers (width: 150–600 μm ; thickness 15–500 μm) produced by deep reactive ion etching [6]. The particles were fixed in place and protected from oxidation by the deposition of a 6 μm polyimide capping layer. The thus structured magnets had the following characteristics: $\mu_0 H_c = 0.18 \text{ T}$, $\mu_0 M_r = 0.52 \text{ T}$, $(BH)_{\text{max}} = 23 \text{ kJ/m}^3$.

Plasma spraying, a rapid solidification technique in which alloy powder is injected into a very high-temperature plasma flame and then projected onto a surface, has been used to prepare 1 mm thick high coercivity SmCo films ($\mu_0 H_c = 6.7 \text{ T}$) with energy products of up to 56 kJ/m^3 [36]. More recently, it was used to prepare NdFeB films with energy products of up to 60 kJ/m^3 [45, 52]. Limited energy product values in plasma sprayed films are attributed to limited texture development, film porosity and degradation of the precursor magnetic powder. Finally, hard magnetic powders have been used in a *co-deposition* process, in which the powder is added to a solution used to electrochemically deposit a ferromagnetic alloy film: BaFeO powder + CoNiMnP [25], NdFeB powder + NiMnP [26]. Though the process lends itself to integration, its use may be limited by the very low-energy products achieved so far ($\leq 8 \text{ kJ/m}^3$).

The use of the techniques described above has not yet led to the emergence of commercially produced magnetic MEMS. This may be attributed to a play-off in the relative importance of the magnet's performance and its ease of integration: the highest energy products are achieved in the fully dense RE-TM magnets of limited lower size which are integrated through a time consuming and costly micro-assembly process. On the other hand, the fabrication techniques which use powders to produce smaller magnets and which are more favorable for magnet integration are characterized by much lower energy products. The film fabrication techniques described in the following section may hold the key to fulfilling the promise of magnetic MEMS.

22.5 Fabrication of Thick Hard Magnetic Films

A pre-requisite for MEMS applications is that the thick hard magnetic films can be produced at high deposition rates ($> 1 \mu\text{m/h}$) and over relatively large surface areas to allow for batch processing on acceptable time scales. These criteria being fulfilled, the challenge is to prepare coercive, mechanically intact films on substrates which are compatible with MEMS technology. The build up of stress in thick films can cause film deformation and fracture. RE-TM and $L1_0$ alloy films, which need to be heated during and/or after deposition so as to crystallize (i.e. RE-TM films) or order (i.e. $L1_0$ films) the hard magnetic phase, are susceptible to high thermal stresses. The build up of stress may dictate the maximum film thickness achievable as well as the choice of substrate and buffer layer, which could be chosen to minimize the difference in thermal expansion coefficients of the film and the substrate.

The three film preparation techniques which have been used to prepare thick film magnets, electrodeposition, sputtering and pulsed laser deposition (PLD) will now be discussed.

22.5.1 Electrodeposition

Electrodeposition, a film preparation technique widely used in MEMS processing, has been demonstrated to be suitable for the preparation of RE-free magnet alloys. A range of hcp Co-based alloys have been prepared in continuous film form without the need for high temperature processing: 5 μm CoNiMnP with $\mu_0 H_c = 0.17$ T on Si [27], 20 μm thick Co₈₀Pt₂₀ with $\mu_0 H_c \approx 0.25$ T on polycrystalline Cu sheets [11] and 1 μm thick Co₈₀Pt₂₀ with $\mu_0 H_c \approx 0.6$ T on Si with a Cu (111) seed layer [67]. The latter films have a strong out-of-plane texture and their relatively high values of coercivity are attributed to a combination of magnetocrystalline anisotropy and shape anisotropy due to columnar grain growth. Residual stress reduction in continuous 5 μm CoNiMnP films was achieved by the use of Ni sandwiching layers (the Ni layers are under compressive stress while the CoNiMnP layers are under tensile stress) [41] and a hybrid stress relieving addition in the electrolyte [27]. Electrodeposition followed by annealing at temperatures in the range 400–600°C has been used to produce L1₀ continuous films: CoPt on glass with $\mu_0 H_c \approx 1.1$ T [23]; FePt on polycrystalline Cu sheets with $\mu_0 H_c \approx 0.3$ T [50], and FePt on Si/Cu with $\mu_0 H_c \approx 1.1$ T [38]. The relatively high values of coercivity of the latter FePt films are achieved by annealing in an H₂ atmosphere. Deposition of FePt into nanoporous Al₂O₃ membranes (pores constitute 50 vol%) produced a coercivity of 1.3 T (the individual nanowires have a diameter of 200 nm and a length of 30 μm) [51]. A very recent paper reports on the deposition of 16 μm thick FePt films, however, the films are two phased (hard+soft), have micro-cracks in the as-deposited state and peel off when annealed [4].

22.5.2 Sputtering

Sputtering, like electrodeposition, is a technique which, in principle, can be upscaled to allow for large area deposition. Much of the pioneering work on sputtering of RE-TM thin films was done by Cadieu and co-workers, for a review see [10] (note that the highest deposition rates reported by Cadieu were of the order of 0.7 $\mu\text{m}/\text{h}$, which may be considered too low for MEMS applications). The highest deposition rates for RE-TM alloys (20–30 $\mu\text{m}/\text{h}$) have been reported for films prepared by DC triode sputtering {NdFeB: [20, 34], SmCo: [61]}, while rates as high as 5–10 $\mu\text{m}/\text{h}$ have been reported for magnetron sputtering {NdFeB: [33], SmCo: [8, 57]} and RF sputtering {NdFeB: [40]}. Rates of 2.5 $\mu\text{m}/\text{h}$ have been achieved for FePt films ($t \leq 10$ μm) prepared by triode sputtering of targets of relatively small surface area [43]. Higher deposition rates can be expected if the target size is upscaled [61]. Substrate heating during deposition can produce textured thick RE-TM films: NdFeB can be

prepared with out-of-plane texture [20, 34], while SmCo alloys can be prepared with in-plane texture [2, 61].

The build up of thermal stress during high-temperature deposition and/or annealing is a major issue to be addressed when preparing thick films of SmCo, NdFeB, or $L1_0$ Fe(Co)Pt, which have thermal expansion coefficients [12] very different to those of Si, the most commonly used substrate material for MEMS. While some groups working on the deposition of films of up to 5 μm in thickness have used Si substrates [48, 57], those working with thicker films (>5 μm) have used metallic substrates [34, 40] or insulating substrates {NdFeB: [33], SmCo: [8]} to minimize differential thermal expansion. Very thick (≈ 100 μm) mechanically intact SmCo films were made on Al_2O_3 substrates on which a 0.5 μm buffer layer of Al was deposited [10]. The even thicker NdFeB films (300 μm) prepared by triode sputtering onto metallic substrates were removed from the substrates prior to annealing [34]. A benefit of working with triode sputtering is that the target size can be easily varied. Maximizing the target size maximizes both the deposition rate and the area of the zone of homogeneous film thickness on the substrate. At the same time, smaller targets can be used for optimizing the target composition and/or for targets with high raw material costs (e.g., Pt). For these reasons, we at Institut Néel selected this technique and we use Si substrates so as to facilitate the structuring and integration of the hard magnetic films with existing MEMS technologies. Some of our principle results will now be recalled, for more details, the reader is referred to some recent publications [20, 60, 61].

22.5.2.1 High-Rate Triode Sputtering of NdFeB Films

NdFeB films were deposited at a rate of approximately 18 $\mu\text{m}/\text{h}$ (target size: 10×10 cm^2). A first study concerned the structural and magnetic characterization of {Ta (100 nm)/NdFeB(5 μm)/Ta (100 nm)} films deposited at temperatures in the range 230–500°C and then annealed at 750°C for 10 min (Fig. 22.4). The size of the equiaxed $\text{Nd}_2\text{Fe}_{14}\text{B}$ grains decreases with increasing deposition temperature and then the grain morphology changes from equiaxed to columnar on increasing the deposition temperature above 450°C. All films show out-of-plane crystallographic c -axis texture, with a progressive increase in the degree of texture with increasing deposition temperature, as evidenced by a significant sharpening of the (006) x-ray diffraction pole figures. Correspondingly, an increase in out-of-plane magnetic anisotropy is clearly identified. The maximum energy product (400 kJ/m^3), which was achieved for the films deposited at 500°C, is comparable to that of high-quality sintered magnets [28]. When the post-deposition annealing was carried out on an entire 100 mm wafer, it was found that the central region (diameter ≈ 30 mm) of all films peeled off during annealing. However, no peel off occurs in similar films deposited onto 100 mm wafers through a mask with millimeter-sized holes or onto 100 mm wafers which are topographically patterned (see next section). What is more, mechanically intact, out-of-plane textured 50 μm thick NdFeB films ($\mu_0 H_c \approx 1.6$ T, $\mu_0 M_r = 1.1$ T and $(\text{BH})_{\text{max}} = 234$ kJ/m^3) have been produced on Si wafers by depositing through a mask with millimeter-sized holes (diameter = 8 mm) and

using a 1-step procedure in which the films are directly deposited in the crystalline state (deposition temperature = 550°C).

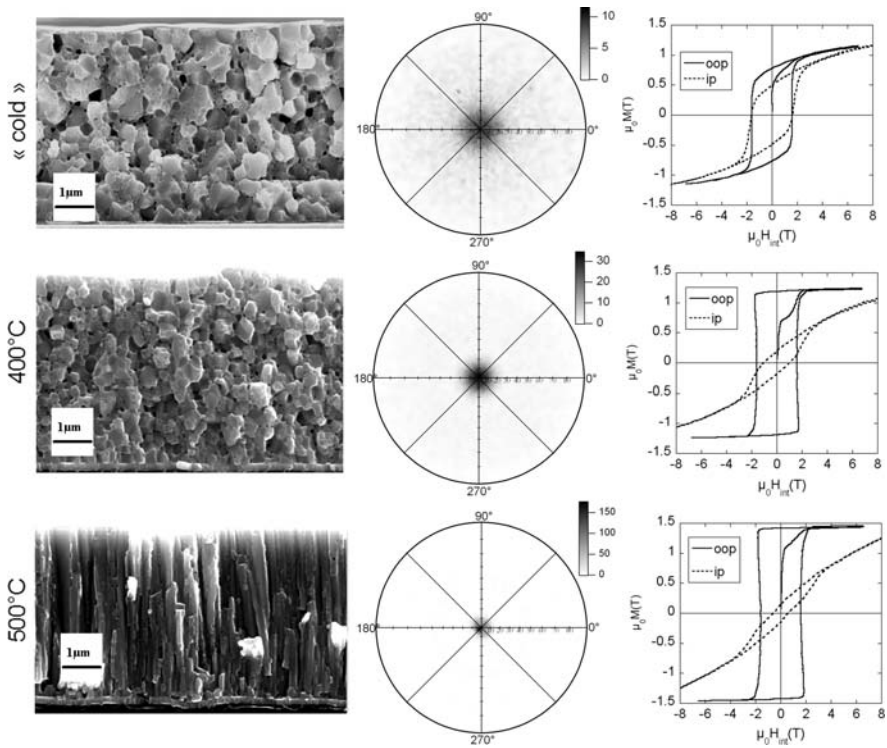


Fig. 22.4 Comparison of the evolution in structural and magnetic properties of sputtered 5 μm thick NdFeB films as a function of deposition temperature (all films annealed at 750°C for 10 min). Column 1: fractured cross sections imaged with a SEM (in-lens detector), Column 2: XRD pole figure of (006) diffraction peak of $\text{Nd}_2\text{Fe}_{14}\text{B}$, Column 3: in-plane (ip) and out-of-plane (oop) hysteresis loops (oop loops corrected with a demag. factor $N = 1$)

22.5.2.2 High-Rate Triode Sputtering of SmCo Films

A first study involved the characterization of Cr (50 nm)/SmCo (5 μm)/Cr (50 nm) films deposited at substrate temperatures up to 600°C using a target of diameter 3 cm which gave a deposition rate of 3.6 $\mu\text{m}/\text{h}$. These films crystallize in the TbCu_7 structure at temperature $\geq 350^\circ\text{C}$ and they show in-plane texture, the degree of which decreases with increasing deposition temperature. The deposition temperature of 350°C was found to be optimum as it gives the maximum values of coercivity, remanence, and energy product, 1.3 T, 0.8 T, and 112 kJ/m^3 , respectively (Fig. 22.5). An increase in target surface area (from 7 to 81 cm^2) raised the deposition rate from 3.6 to 18 $\mu\text{m}/\text{h}$ while a re-optimization of the deposition temperature (400°C) gave an in-plane energy product of 140 kJ/m^3 . The mechanical properties of the as-deposited films were found to depend on the substrate temperature during film

deposition. While films deposited at temperatures of up to 400°C remained entirely adhered to the Si substrate, small pieces (typically a few mm²) of those deposited at 500°C peeled off, and finally films deposited at 600°C almost entirely peeled off. All as-deposited films were found to be under tensile stress, the value of which increased with deposition temperature up to a maximum value of about 450 MPa for the films deposited at 500°C. Post-deposition annealing of non-patterned films led to peeling for all deposition temperatures. As was observed for the NdFeB system, the occurrence of peeling was found to be related to the lateral dimensions of the film. When 5 μm thick SmCo films were deposited onto pre-patterned wafers (see next section), peel off did not occur from film sections of reduced surface area. Furthermore, films of thickness up to 20 μm deposited onto heated Si (400°C) through a mask with 4 mm-sized holes remained adhered to the substrate and were crack free.

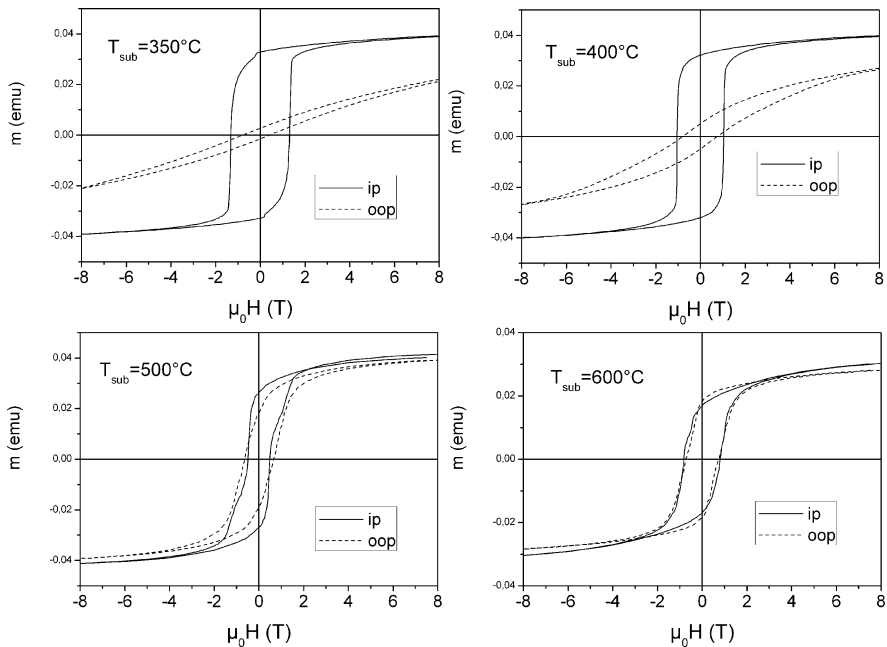


Fig. 22.5 In-plane (ip) and out-of-plane (oop) hysteresis loops of SmCo films as a function of deposition temperature

22.5.3 Pulsed Laser Deposition (PLD)

The vast majority of papers dealing with the PLD of RE-TM and L1₀ alloy films concern thin films (<1 μm) produced at low deposition rates. An exception is the work of Nakano and co-workers [42], in which high deposition rates (≤ 72 μm/h)

were used to prepare NdFeB films of up to 120 μm in thickness. However, such rates were only achieved over small surface areas (1 cm^2) and the maximum energy products were rather limited (77 kJ/m^3). The eventual use of PLD in MEMS processing of thick films will depend on the ability to increase the surface area over which high deposition rates can be achieved.

Before proceeding to the next section, which deals with the micro-patterning of hard magnetic films, it should be noted that the high-processing temperatures needed for producing NdFeB ($550\text{--}750^\circ\text{C}$) and L1_0 ($400\text{--}600^\circ\text{C}$) films dictate that these films need to be integrated onto a given wafer before other temperature sensitive components. On the other hand, the hcp Co-based alloys which can be produced at room temperature, and possibly the SmCo alloys which are produced at relatively low temperatures ($350\text{--}400^\circ\text{C}$), can be processed “above IC” (above integrated circuit).

22.6 Micro-Patterning of Thick Hard Magnetic Films

The integration of high-performance hard magnetic films into MEMS requires their patterning at the micron scale. The use of Si substrates greatly facilitates lateral structuring using standard micro-technology processes, though other substrates (e.g., glass, Al_2O_3) may also be used. The use of standard processes for the structuring of hard magnetic films, in particular steps based on chemical attack, is particularly challenging for rare earth-based alloys because of their poor resistance to oxidation. A number of different routes which have been used to pattern permanent magnet films are schematized in Fig. 22.6. The patterns produced can be categorized as (i) topographic or (ii) crystallographic.

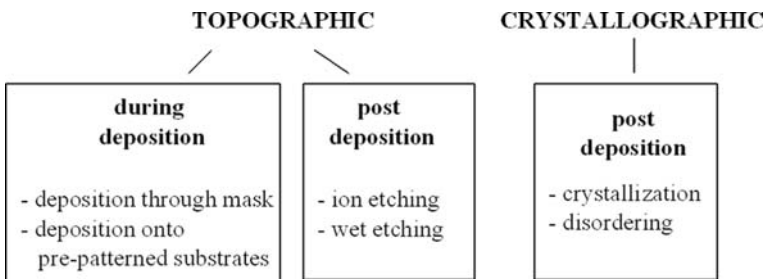


Fig. 22.6 Overview of different routes used to pattern permanent magnet films

22.6.1 Topographically Patterned Films

Topographic patterning can be achieved in the as-deposited state (deposition through a mask or onto a pre-patterned substrate) or by post-deposition film patterning. Lithographically defined photo-resist masks on Si wafers have been used

for the patterning of Co-rich films which need no high-temperature processing. This approach was used to prepare electrodeposited magnet arrays of CoMnNiP {thickness $\approx 20 \mu\text{m}$, minimum feature size $30 \times 30 \mu\text{m}$, $\mu_0 H_c = 0.1 \text{ T}$, $\mu_0 M_r = 0.19 \text{ T}$, $(BH)_{\text{max}} = 2.3 \text{ kJ/m}^3$ [14]}, $\text{Co}_{80}\text{Pt}_{20}$ {cylinders of height $2 \mu\text{m}$ and diameter 5 or $10 \mu\text{m}$, $\mu_0 H_c = 0.5 \text{ T}$, $(BH)_{\text{max}} = 52 \text{ kJ/m}^3$ [68]}, and CoPtP {thickness $\approx 5 \mu\text{m}$, feature size in the range $200\text{--}500 \mu\text{m}$, $\mu_0 H_c = 0.3 \text{ T}$, $\mu_0 M_r = 0.3 \text{ T}$ } [21, 59]. To allow for high-temperature ($400\text{--}500^\circ\text{C}$) processing, Cu masks have been used for the direct patterning of $5\text{--}20 \mu\text{m}$ thick SmCo films sputtered onto Si wafers [7]. Features of size $5 \times 5 \mu\text{m}$ up to $100 \times 100 \mu\text{m}$ were etched into $1 \mu\text{m}$ thick NdFeB films sputtered onto Al_2O_3 substrates using salpetric acid [39]. Post-deposition patterning of $30 \mu\text{m}$ thick $\text{Sm}_2\text{Co}_{17}$ films sputtered onto Al_2O_3 substrates has been carried out with ion beam etching and wet chemical etching at film removal rates of 1 and $750 \mu\text{m/h}$, respectively [8].

As explained in a previous section, the extrinsic properties of a permanent magnet depend on both the material's intrinsic magnetic properties and its microstructure. As the latter may be influenced by how the magnet is prepared, micro-patterning may be expected to influence the μ -magnet's extrinsic properties. Thus, beyond establishing the application of a given micro-patterning process to a given material, it is essential to study the magnetic properties of the thus produced μ -magnets.

The application of three different micro-patterning processes (*film deposition onto patterned substrates*, *wet etching*, and *planarization*) to the structuring of RE-TM films will now be presented.

22.6.1.1 Deposition of RE-TM Films onto Patterned Substrates

Patterned Si/SiO₂ substrates containing trench motifs with individual trenches of depth $6 \mu\text{m}$, length $500 \mu\text{m}$, and trench/wall widths on the scale of $5\text{--}100 \mu\text{m}$ were prepared by standard micro-fabrication processes: deposition of $6 \mu\text{m}$ of SiO₂ on Si followed by photo-lithography through a mask containing the trench motif and finally dry etching of the SiO₂. The magnetic (NdFeB, SmCo) and buffer/capping (Ta, Cr) layers were deposited using triode sputtering at rates of the order of $18 \mu\text{m/h}$ (see previous section). It was found that trench filling worked much better for NdFeB than SmCo, the latter deposits being characterized by trench corners which appear granular and less dense than the rest of the film, even when the films are deposited in the amorphous state (Fig. 22.7). As mentioned above, deposition onto patterned substrates improves the mechanical properties of RE-TM films. Post-deposition annealing (750°C for 10 min) of the entire 100 mm patterned wafers with NdFeB layers did not lead to film fracture or peel-off. For the case of SmCo deposits, when deposited directly in the crystallized state ($T_{\text{sub}} = 400^\circ\text{C}$), peel-off from patterned films does not occur in the trenched regions, but only in the continuous (i.e., non-patterned) regions between different motifs. However, post-deposition annealing of amorphous SmCo films deposited on patterned wafers does lead to film peel-off. The fact that the NdFeB films have distinctly less tendency to peel-off than

SmCo_7 films may be attributed to two particular features. The first is that $\text{Nd}_2\text{Fe}_{14}\text{B}$ has a lower thermal expansion anisotropy than SmCo_5 (SmCo_7 is closely related to the SmCo_5 phase) [12] at the annealing temperatures used. The second is the fact that $\text{Nd}_2\text{Fe}_{14}\text{B}$ is an Invar system. A large positive magnetovolume anomaly develops in the ferromagnetic state, below 585 K, which reduces very significantly the material's thermal expansion.

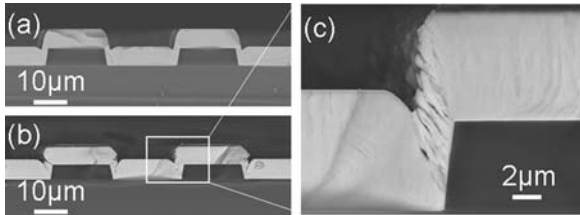


Fig. 22.7 SEM cross sectional images of amorphous RE-TM films deposited onto patterned wafers (this particular section has trench and wall widths of $20\ \mu\text{m}$): (a) NdFeB, (b) SmCo, and (c) zoom of a trench corner for the SmCo film [62]

The extrinsic magnetic properties of the RE-TM films, as characterized by their hysteresis loops, were little influenced by the use of patterned substrates. A polar Kerr image of a uniaxial magneto-optic-indicator-film or MOIF [24], placed on top of a patterned NdFeB film magnetized out of plane, is shown in Fig. 22.8. This image reveals that the patterned sections of the film produce micron-scaled multipolar magnetic field patterns at the position of the MOIF with a pole pitch approximately equal to the pitch of the trench walls (the non-patterned sections of film between motifs do not produce enough stray field to saturate the MOIF). Though

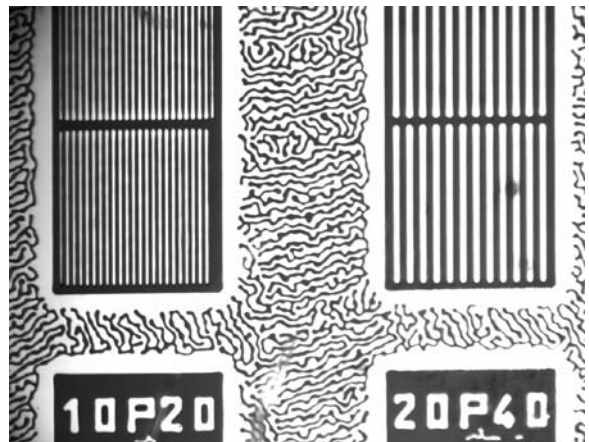


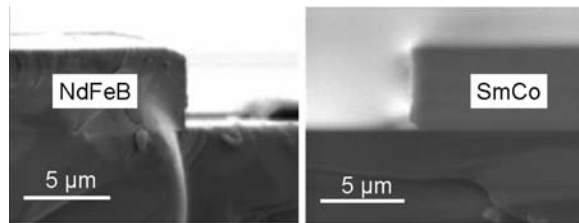
Fig. 22.8 Polar Kerr optical image of a Magneto-Optic-Indicator-Film placed on top of a patterned NdFeB film (this particular section contains two motifs, one with trench and wall widths of $10\ \mu\text{m}$ and one with trench and wall widths of $20\ \mu\text{m}$) [62]

only qualitative, this image shows that a simple fabrication procedure (deposition + annealing + unidirectional magnetization) can be used to produce a micron-scaled multi-polar field pattern. These micro-patterned films have been used to levitate diamagnetic beads [13] and have potential applications in lab-on-chip experiments.

22.6.1.2 Wet Etching of RE-TM Films

Wet etching trials were carried out on 5 μm thick RE-TM films in the amorphous state, as it is expected that such films should be less prone to oxidation than crystallized films because of the absence of grain boundaries which could act as paths for oxygen diffusion. Optical lithography was used to define millimeter-sized patterns in a resist layer deposited on the RE-TM film. Removal rates of approximately 1.25 $\mu\text{m}/\text{min}$ were achieved for both the NdFeB and the SmCo films wet etched at room temperature in an acidic bath containing $(\text{NH}_4)_2\text{S}_2\text{O}_8$, H_2O and H_2SO_4 . A large lateral over-etch of typically 20 μm occurred in both materials and the side walls of the etched films are relatively vertical (Fig. 22.9).

Fig. 22.9 SEM cross sectional images of a fracture surface of wet etched RE-TM films [62]



22.6.1.3 Planarization of NdFeB Films

Chemical–mechanical–planarization (CMP) was developed for NdFeB only, as the poor quality of the trench corners of SmCo deposited on patterned substrates, as well as stress issues, renders them unsuitable for planarization. 5 μm thick NdFeB films were topographically patterned by wet etching and then planarized at rates of up to 3 $\mu\text{m}/\text{min}$ by CMP to a final thickness of 1 μm . It was found that good magnetic properties (single-phase behavior, high coercivity [$\mu_0 H_C = 1.5 \text{ T}$], good squareness for an isotropic sample) could be achieved in wet-etched/planarized films if the exposed surface is cleaned by dry etching and then capped with Ta prior to being annealed.

22.6.2 Crystallographically Patterned Films

The second, and less conventional type of patterning featured in Fig. 22.6, involves the local modification of the film's magnetic properties through a change in its

crystallographic state. In this case, a modulation in the magnetic properties is achieved without a modulation in the film's surface height. A first example concerns the local crystallization of 2 μm thick amorphous NdFeB-sputtered films by laser annealing through a mask [44]. This technique was used to produce 100 μm wide strips of hard magnetic NdFeB (crystallized) in a soft magnetic (amorphous) matrix. The irradiated strips showed out-of-plane magnetic anisotropy and coercivities of at least 1.5 T. A second example concerns the local disordering of 40 nm thick $L1_0$ FePt by pulsed laser annealing [9]. This technique was used to produce 10 μm disks of soft magnetic FePt ($A1$ – disordered) in a hard magnetic ($L1_0$ – ordered) matrix ($\mu_0H_c = 5.5$ T). The applicability of this technique to thicker films is questionable.

22.7 Conclusions and Perspectives

Magnets have many potential applications in MEMS because of favorable down scaling laws and their unique ability to produce long range bi-directional forces. The emergence of magnetic MEMS at the industrial scale has been hindered by the challenge of integrating high-quality magnets using techniques compatible with today's MEMS technologies. The majority of prototype devices have been made using micro-assembled high-quality μ -magnets produced by machining of bulk RE-TM magnets or integrated low- to medium-quality magnets (bonded RE-TM and hexagonal ferrites or electroplated hcp Co-based alloys). Recent developments in the fabrication of high-energy product RE-TM magnets (NdFeB and SmCo) in thick film form are very promising and the micro-patterning of such films is now being studied. The successful integration of such high-performance magnets into devices should provide a boost for the field of magnetic MEMS.

Acknowledgments Some of the results presented here were achieved during the thesis of A. Walther (Institut Néel+CEA Léti + G2Elab) and in the framework of the ANR (French National Research Agency) “Nanomag2” project. They are the fruit of collaboration with a number of colleagues including D. Givord (Institut Néel), O. Cugat, J. Delamare, and G. Reyne (G2Elab), C. Marcoux and B. Desloges (CEA Léti), O. Gutfleisch (IFW Dresden) and R. Grechishkin (Tver State University). N. Kornilov is thanked for many fruitful discussions and his invaluable contribution to setting up the triode sputtering system at Institut Néel.

References

1. Achotte, N., Gilles, P.-A., Cugat, O., Delamare, J., Gaud, P., Dieppedale, C.: Planar brushless magnetic μ -motors. *J. MEMS* **15**(4), 1001–1014 (2006)
2. Allen, R.P., Dahlgren, S.D., Arrowsmith, H.W., Heinrich, J.P.: Research in the Production of Rare-Earth-Cobalt Permanent Magnet Material by Sputter Deposition. Technical report AFML TR-74-87 (1974)
3. Arnold, D.P., Das, S., Cros, F., Zana, I., Allen, M.G., Lang, J.H.: Magnetic induction machines integrated into bulk-micromachined silicon. *J. MEMS* **15**(2), 406–414 (2006)
4. Berkh, O., Rosenberg, Yu., Shacham-Diamand, Y., Gileadi, E.: Electrodeposited near Equiatomic CoPt thick films. *Electrochem. Solid-State Lett.* **11**(4), D38–D41 (2008)

5. Bernstein, J., Taylor, W., Brazzle, J.D., Corcoran, C.J., Kirkos, G., Odhner, J.E., Pareek, A., Waelti, M., Zai, M.: Electromagnetically actuated mirror arrays for use in 3D optical switching applications. *J. MEMS* **13**(3), 526–535 (2004)
6. Bowers, B.J., Agashe, J.S., Arnold, D.P.: method to form bonded micromagnets embedded in silicon. Solid-State Sensors, Actuators and Microsystems Conference, 2007. TRANSDUCERS'07, 1585–1588 (2007)
7. Budde T., Gatzen, H.H.: Patterned sputter deposited SmCo-films for MEMS Applications. *J. Magn. Magn. Mat.* **242–245**, 1146–1148 (2002)
8. Budde T., Gatzen, H.H.: Thin film SmCo magnets for use in electromagnetic microactuators. *J. Appl. Phys.* **99**, 08N304-3 (2006)
9. Buschbeck, J., Fähler, S., Weisheit, M., Leistner, K., McCord, J., Rellinghaus, B., Schultz, L.: Thermodynamics and kinetics during pulsed laser annealing and patterning of FePt films. *J. Appl. Phys.* **100**, 123901-7 (2006)
10. Cadieu, F.J.: Permanent magnet thin films: A review of Film Synthesis and Properties. In: Francombe, M., Vossen, J. (eds.) *Physics of Thin Films*, vol. 16. Academic Press Inc., (1992)
11. Cavallotti, P.L., Lecis, N., Fauser, H., Zielonka, A., Celis, J.P., Wouters, G., Machado da Silva, J., Brochado Oliveira, J.M., Sa, M.A.: Electrodeposition of magnetic multilayers. *Surface and Coatings Technology* **105**, 232–239 (1998)
12. Chen, C.H., Walmer, M.S., Walmer, M.H., Gong, W., Ma, B.-M.: The relationship of thermal expansion to magnetocrystalline anisotropy, spontaneous magnetization, and T_c for permanent magnets. *J. Appl. Phys.* **85**, 5669–5671 (1999)
13. Chetouani, H., Haguët, V., Jeandey, C., Pigot, C., Walther, A., Dempsey, N.M., Chatelain, F., Delinchant, B., Reyne, G.: Diamagnetic levitation of beads and cells above permanent magnets. Solid-State Sensors, Actuators and Microsystems Conference, 2007. TRANSDUCERS'07, 715–718 (2007)
14. Cho, H.J., Bhansali, S., Ahn, C.H.: Electroplated thick permanent magnet arrays with controlled direction of magnetization for MEMS application. *J. Appl. Phys.* **87**, 6340–6343 (2000)
15. Cho H.J., Ahn, C.H.: Microscale resin-bonded permanent magnets for magnetic micro-electro-mechanical systems applications. *J. Appl. Phys.* **93**, 8674–8676 (2003)
16. Christenson, T.R., Garino, T.J., Venturini, E.L., Berry, D.M.: Application of deep x-ray lithography fabricated rare earth permanent magnets to multipole magnetic microactuators. *Electrochem. Soc. Proc.* **98–20**, 312–323 (1999)
17. Cugat, O., Basrour, S., Divoux, C., Mounaix, P., Reyne, G.: Deformable magnetic mirror for adaptive optics: Technological aspects. *Sensors & Actuators A* **89**, 1–9 (2001)
18. Cugat, O., Delamare, J., Reyne, G.: Magnetic micro-actuators and systems (MAGMAS). *IEEE Trans. Mag.* **39**, 3607–3612 (2003)
19. Cui, B.Z., Han, K., Li, D.S., Garmestani, H., Liu, J.P., Dempsey, N.M., Schneider-Muntau, H.J.: Magnetic-field-induced crystallographic texture enhancement in cold-deformed FePt nanostructured magnets. *J. Appl. Phys.* **100**, 013902-4 (2006)
20. Dempsey, N.M., Walther, A., May, F., Givord, D., Khlopkov, K., Gutfleisch, O.: High performance hard magnetic NdFeB thick films for integration into Micro-Electro-Mechanical Systems. *Appl. Phys. Lett.* **90**, 092509-3 (2007)
21. Dieppedale, C., Desloges, B., Rostaing, H., Delamare, J., Cugat, O., Meunier-Carus, J.: Magnetic bistable μ -actuator with integrated permanent magnets. *Proc. IEEE Sensors* **1**, 493–496 (2004)
22. Dutoit, B., Besse, P.A., Blanchard, H., Guérin, L., Popovic, R.S.: High performance micro-machined $\text{Sm}_2\text{Co}_{17}$ polymer bonded magnets. *Sensors Actuators A* **77**, 178–182 (1999).
23. Fujita, N., Maeda, S., Yoshida, S., Takase, M., Nakano, M., Fukunaga, H.: Preparation of Co–Pt alloy film magnets by electrodeposition. *J. Magn. Magn. Mater.* **272–276**, e1895–e1897 (2004)
24. Grechishkin, R., Chigirinsky, S., Gusev, M., Cugat, O., Dempsey, N.M.: Magnetic imaging films. In: G. Asti, L. Pareti, and M. Ghidini (eds.) *Magnetic Nanostructures in Modern Technology*, pp. 195–224. Springer, Netherlands (2007)

25. Guan S., Nelson, B.J., Vollmers, K.: Electrochemical codeposition of magnetic particle ferromagnetic matrix composites for magnetic MEMS actuator applications. *J. Electrochem. Soc.* **151**(9), C545–C549 (2004)
26. Guan, S., Nelson, B.J.: Fabrication of hard magnetic microarrays by electroless codeposition for MEMS actuators. *Sensors Actuators A* **118**, 307–312 (2005)
27. Guan, S., Nelson, B.J.: Electrodeposition of low residual stress CoNiMnPt hard magnetic thin films for magnetic MEMS actuators. *J. Magn. Magn. Mater.* **292**, 49–58 (2005)
28. Gutfleisch, O.: Controlling the properties of high density permanent magnetic materials. *J. Phys. D: Appl. Phys.* **33**, R157–R172 (2000)
29. Gutfleisch, O., Dempsey, N.M.: High performance μ -Magnets for Microelectromechanical Systems (MEMS). In: G. Asti, L. Pareti, and M. Ghidini (eds.) *Magnetic Nanostructures in Modern Technology*, pp. 167–194. Springer, Netherlands (2007)
30. Hai, N.H., Dempsey, N.M., Veron, M., Verdier, M., Givord, D.: An original route for the preparation of hard FePt. *J. Magn. Magn. Mater.* **257**, 139–145 (2003)
31. Hinz, D., Gutfleisch, O., Müller, K.-H.: High performance NdFeB magnets with a thickness of some 100 μ m for MEMS applications. *Proceedings of the 18th International Workshop on High Performance Magnets and their Applications*, 797 (2004)
32. Holmes, A.S., Guodong, H., Pullen, K.R.: Axial-flux permanent magnet machines for μ power generation. *J. MEMS* **14**, 54–62 (2005)
33. Homburg, H., Sinnemann, Th., Methfessel, S., Rosenberg, M., Gu, B.X.: Sputtered NdFeB films of high coercivity. *J. Magn. Magn. Mater.* **83**, 231–233 (1990)
34. Kapitanov, B.A., Kornilov, N.V., Linetsky, Ya. L., Tsvetkov, V. Yu.: Sputtered permanent Nd-Fe-B magnets. *J. Magn. Magn. Mater.* **127**, 289–297 (1993).
35. Katter, M., Üstüner, K., Blank, R.: Model for calculating J(H) curves of Ni coated Nd-Fe-B magnets. *Proceedings of the 19th International Workshop on Rare Earth Magnets and their Applications*, 87–91 (2006)
36. Kumar, K., Das, D., Wettstein, E.: High coercivity, isotropic plasma sprayed Sm-Co magnets. *J. Appl. Phys.* **49**, 2052–2054 (1978)
37. Lagorce, L.K., Allen, M.G.: Micromachined polymer magnets. *Proceedings of the Ninth Annual International Workshop on Micro Electro Mechanical Systems*, 85–90 (1996).
38. Leistner, K., Thomas, J., Schlörb, H., Weisheit, M., Schultz, L., Fähler, S.: Highly coercive electrodeposited FePt films by postannealing in hydrogen. *Appl. Phys. Lett.* **85**, 3498–3500 (2004)
39. Lemke, H., Lang, T., Giiddehenrich, T., Heiden, C.: Micro patterning of thin Nd-Fe-B films. *J. Magn. Magn. Mater.* **148**, 426–432 (1995)
40. Liu, W.F., Suzuki, S., Machida, K.: Magnetic properties of Nd–Fe–B film magnets prepared by RF sputtering. *J. Magn. Magn. Mater.* **308**, 126–130 (2007)
41. Myung, N.V., Park, D.-Y., Yoob, B.-Y., Sumodjob, P.T.A.: Development of electroplated magnetic materials for MEMS. *J. Magn. Magn. Mater.* **265**, 189–198(2003)
42. Nakano, M., Katoh, R., Fukunaga, H.: Fabrication of Nd–Fe–B thick-film magnets by high-speed PLD method. *IEEE Trans. Magn.* **39**, 2863–2865 (2003)
43. Ndao, C.B., Givord, D., Dempsey, N.M.: (2009, in preparation)
44. Okuda, T., Sugimura, A., Eryu, O., Serrona, L.K.E.B., Adachi, N., Sakamoto I., Nakanishi, A.: Nd–Fe–B thin films with perpendicular magnetic anisotropy and high coercivity prepared by pulsed laser annealing. *Jpn. J. Appl. Phys.* **42**, 6859–6864 (2003)
45. Overfelt, R.A., Anderson, C.D., Flanagan, W.F.: Plasma sprayed Fe₇₆Nd₁₆B₈ permanent magnets. *Appl. Phys. Lett.* **49**, 1799–1801 (1986)
46. Pawlowski, B., Rahmig, A., Töpfer, J.: Preparation and properties of NdFeB thick films. *15th International Workshop on Rare Earth Magnets and their Applications* 1045 (1998)
47. Pawlowski, B., Scharzer, S., Rahmig, A., Töpfer, J.: NdFeB thick films prepared by tape casting. *J. Magn. Magn. Mat.* **265**, 337–344 (2003)

48. Pina, E., Palomares, F.J., Garcia, M.A., Cebollada, de Hoyos, F.A., Romero, J.J., Hernando, A., Gonzalez, J.M.: Coercivity in SmCo hard magnetic films for MEMS applications. *J. Magn. Magn. Mat.* **290–291**, 1234–1236 (2005)
49. Raisigel, H., Cugat, O., Delamare, J.: Permanent magnet planar μ -generators. *Sensors Actuators A* **130–131**, 438–444 (2006)
50. Rhen, F.M.F., Hinds, G., O'Reilly, C. Coey, J.M.D.: Electrodeposited FePt films. *IEEE Trans. Magn.* **39**, 2699–2701 (2003)
51. Rhen, F.M.F., Backen, E., Coey, J.M.D.: Thick-film permanent magnets by membrane electrodeposition. *J. Appl. Phys.* **97**, 113908-4 (2005)
52. Rieger, G., Wecker, J., Rodewald, W., Sattler, W., Bach, Fr.-W., Duda, T., Unterberg, W.: Nd–Fe–B permanent magnets (thick films) produced by a vacuum-plasma-spraying process. *J. Appl. Phys.* **87**, 5329–5331 (2000)
53. Rodewald, W., Wall, B., Fernengel, W., Katter, M.: Production of thin flexible RE magnet-foils. *Proceedings of the 15th International Workshop on Rare Earth Magnets and their Applications*, 1021 (1998)
54. Romero, J.J., Cuadrado, R., Pina, E., de Hoyos, A., Pigazo, F., Palomares F.J., Hernando, A., Sastre, R., Gonzalez, J.M.: Anisotropic polymer bonded hard-magnetic films. *J. Appl. Phys.* **99**, 08N303-3 (2006)
55. Rostaing, H., Stepanek, J., Cugat, O., Dieppedale, C., Delamare, J.: Magnetic, out-of-plane, totally integrated bistable μ -actuator. *Proc. TRANSDUCERS '05* **2**, 1366–1370 (2005)
56. Skomski, R., Coey, J.M.D.: Permanent Magnetism. Institute of Physics, Bristol (1999)
57. Speliotis, T., Niarchos, D.: Microstructure and magnetic properties of SmCo films. *J. Mag. Mag. Mat.* **290**, 1195–1197 (2005)
58. Vacuumschmelze GmbH, private communication (2006).
59. Vieux-Rochaz, L., Dieppedale, C., Desloges, B., Gamet, D., Barragatti, C., Rostaing, H., Meunier-Carus, J.: Electrodeposition of hard magnetic CoPtP material and integration into magnetic MEMS. *J. Micromech. Microeng.* **16**, 219–224 (2006)
60. Walther, A., Khlopkov, K., Gutfleisch, O., Givord, D., Dempsey, N.M.: Evolution of magnetic and microstructural properties of thick sputtered NdFeB films with processing temperature. *J. Magn. Magn. Mat.* **316**, 174–176 (2007)
61. Walther, A., Givord, D., Dempsey, N.M., Khlopkov, K., Gutfleisch, O.: Structural, magnetic and mechanical properties of 5 μ m thick SmCo films suitable for use in Micro-Electro-Mechanical-Systems. *J. Appl. Phys.* **103**, 043911-043911-5 (2008)
62. Walther, A., Marcoux, C., Desloges, B., Grechishkin, R., Givord, D., Dempsey, N.M.: Micro-patterning of NdFeB and SmCo magnet films for integration into Micro-Electro-Mechanical-Systems. *J. Magn. Magn. Mater.* (Accepted)
63. Wang, W., Yao, Z., Chen, J.C., Fang, J.: Composite elastic magnet films with hard magnetic feature. *J. Micromech. Microeng.* **14**, 1321–1327 (2004)
64. Wilson, S.A. et al.: New materials for micro-scale sensors and actuators, an engineering review. *Materials Science and Engineering R* **56**, 1–129 (2007)
65. Yamashita, S., Yamasaki, J., Ikeda, M., Iwabuchi, N.: Anisotropic Nd-Fe-B thin-film magnets for milli-size motor. *J. Appl. Phys.* **70**, 6627–6629 (1991)
66. Yan, J., Luanava, S., Casasanta, V.: Magnetic actuation for MEMS scanners for retinal scanning displays. *SPIE Proc.* 4985 MOEMS Displays and Imaging Systems, July 1–6 (2004)
67. Zana, I., Zangari, G.: Electrodeposition of Co-Pt films with high perpendicular anisotropy. *Electrochem. Solid-State Lett.* **6**(12), C153–C156 (2003)
68. Zana, I., Zangari, G., Park, J.-W., Allen, M.G.: Electrodeposited Co–Pt micron-size magnets with strong perpendicular magnetic anisotropy for MEMS applications. *J. Magn. Magn. Mat.* **272–276**, e1775–e1776 (2004)

Chapter 23

Solid-State Magnetic Sensors for Bioapplications

Goran Mihajlović and Stephan von Molnár

Abstract During the last decade, intensive research efforts have been expended to develop solid-state magnetic sensors for applications such as biomolecular sensing and single molecule detection. This chapter reviews sensors proposed thus far, including (a) GMR and spin valve sensors based on the giant magnetoresistance (GMR) effect; (b) magnetic tunnel junction (MTJ) sensors based on tunneling magnetoresistance (TMR); (c) anisotropic magnetoresistance (AMR) ring sensors and planar Hall effect sensors based on the AMR effect; (d) Hall sensors based on the classical Hall effect; and (e) giant magnetoimpedance (GMI) sensors based on the frequency-dependent variation of the skin depth in magnetic wires with field. Two different types of sensors are highlighted: the ones with large sensing areas (hundreds of μm^2) intended to provide statistical counting of a large number of magnetic micro- or nanoparticles and the others with micro- or submicrometer-sized sensing areas that focus on single particle detection.

23.1 Introduction

Integration of biology and solid-state physics at the micro- and nanoscale has become, in recent years, one of the most exciting and fruitful areas of multidisciplinary research and development in the natural sciences. The research efforts are expected to bring a new dimension to fundamental studies of biomolecular systems and their interactions. They will also lead to development of novel devices for utilization in bioanalysis and biomedical applications. Particularly promising, in this regard, is the recently proposed concept of biomolecular sensing based on magnetic microbeads or nanoparticles as biomolecular labels, and solid-state magnetic sensors as sensing elements. The concept is schematically depicted in Fig. 23.1. The idea is to functionalize the surface of the sensor with molecules (called the probes)

G. Mihajlović (✉)

Materials Science Division, Argonne National Laboratory, Argonne, IL 60439, USA
e-mail: mihajlovic@anl.gov

that would bind specifically to the target molecules to be detected. The specificity can be achieved through a biomolecular recognition mechanism, such as antigen–antibody affinity or ligand–receptor binding. In addition, the labels will be magnetic particles functionalized with molecules complementary to the target. In the presence of the target molecules, magnetic particles will settle on the sensor surface, since specific binding of their biofunctional coating to the probe molecules will be mediated by the target molecules. Ideally, the specificity of the coating will ensure that no magnetic particle will be present on the sensor if the target molecules are absent from the sample. The sensor therefore will detect the presence of the target molecules by detecting the presence of the magnetic particles on its surface, which is achieved by sensing the stray magnetic field signal from the particles.

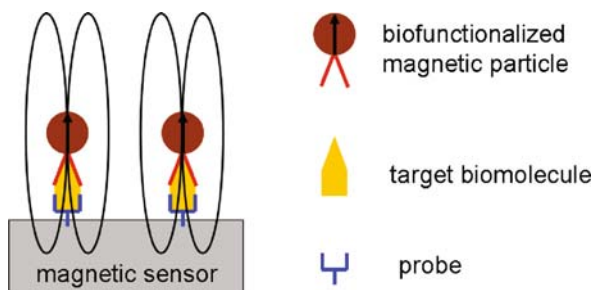


Fig. 23.1 Schematic depiction of the principle of on-chip magnetic biosensing. The target molecules are sandwiched between the complementary probe molecules on the sensor surface and magnetic particles coated with other complementary molecules. The sensor detects the stray magnetic field from the particles

This biosensing scheme, introduced in a pioneering work of the research group from Naval Research Laboratory (NRL) [3], has attracted significant interest due to several potential advantages over more traditional methods based on, for example, fluorescent labeling and optical detection. Some of these are direct consequence of magnetism of the labels themselves; for example, the fact that the magnetic properties are very stable over time and are generally not affected by reagent chemistry or subject to photo bleaching. Also, the magnetic background in biological samples is minimal, since these are composed predominantly of diamagnetic chemical elements. Finally, the stray magnetic fields from the labels as well as an externally imposed field gradients that can be used to generate forces on labels to remotely manipulate them are not screened in an aqueous biological environment. As for magnetic sensors, the advantages include possibility to achieve direct and fast electronic readout of the biomolecular recognition events as well as to integrate densely packed arrays of multiple sensors on a single chip. In addition, this detection scheme allows for single molecule detection as long as the sensor is sensitive enough to detect the stray magnetic field from the single label, if one can ensure that a single molecule is bound to a single label. Such sensors could also be utilized in the investigation of binding forces or mechanical properties of single molecules to provide direct electronic measurement of, for example, the extension length of the molecules

when these are pulled by magnetic tweezers [1]. These attractive properties have triggered intensive research efforts beginning in the late nineties to develop the core technologies for on-chip integration of micro- and nanoscale magnetics with molecular biology. The final goal is to produce highly sensitive, fast, reliable, cost-effective, portable, and easy-to-use biomolecular sensors, the so-called *magnetic biochips*.

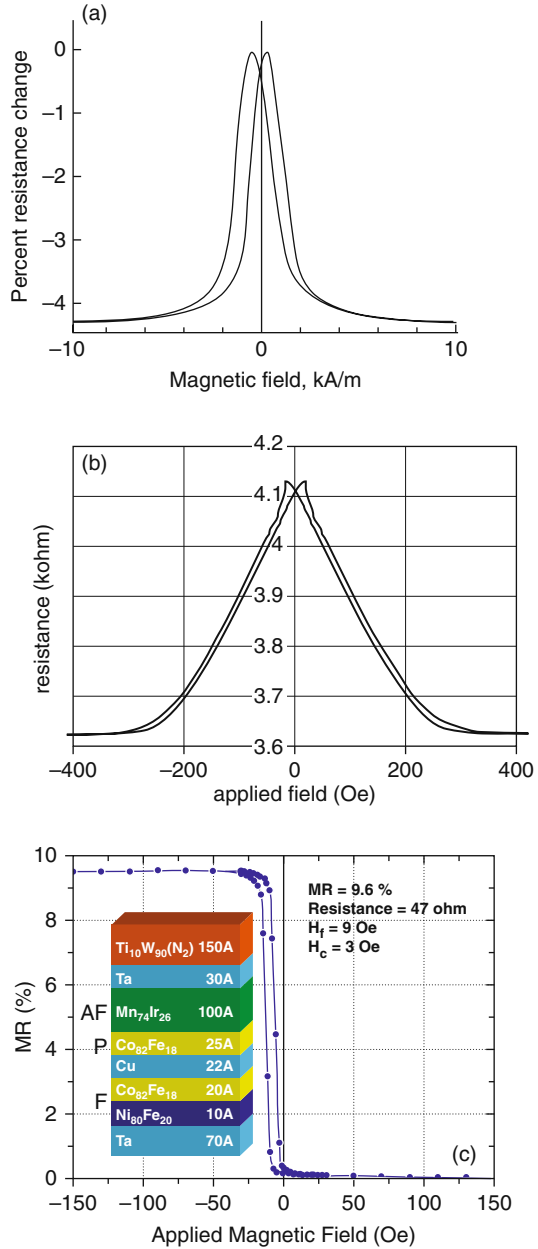
In this chapter, we will review solid-state magnetic sensors proposed thus far for applications in magnetic biomolecular sensing. Those will include (a) GMR and spin valve sensors based on giant magnetoresistance (GMR) effect; (b) magnetic tunnel junction (MTJ) sensors based on tunneling magnetoresistance (TMR) effect; (c) anisotropic magnetoresistance (AMR) ring sensors and planar Hall effect sensors based on AMR effect; (d) Hall sensors based on classical Hall effect; and (f) giant magnetoimpedance (GMI) sensors based on the frequency-dependent variation of the skin depth in magnetic wires with field. Two different types of sensors will be highlighted: the ones with large sensing areas (hundreds of μm^2) intended to provide statistical counting of a large number of magnetic micro- or nanoparticles and the others with micro- or submicrometer-sized sensing areas that focus on single particle detection.

23.2 Magnetic Sensors Based on GMR Effect

The GMR effect, discovered in 1988 [2, 5] and awarded the Nobel Prize in physics in 2007, pertains to a large change in electrical resistance of a layered structure consisting of thin magnetic and normal metal layers when it is exposed to an external magnetic field. The physical mechanism responsible for the effect is spin-dependent interfacial scattering of electrons carrying electrical current. When the respective magnetizations of the two magnetic layers are oriented parallel to each other, the electrons having the same spin orientation can pass through with much less scattering than those with the opposite spin. Thus one spin channel of the current is “shorted” and the sensor has a minimum resistance. On the other hand, the maximum resistance occurs for antiparallel magnetization orientations when both spin channels experience equal amount of scattering. The difference between the two resistances divided by one of them is called magnetoresistance (MR) ratio and is typically quoted in percents.

Different types of sensors based on the GMR effect have been utilized in experiments involving magnetic label detection. These include (a) devices based on unpinned sandwich GMR materials which consist of a nonmagnetic metal layer sandwiched between two soft magnetic layers; (b) antiferromagnetically coupled multilayer GMR devices consisting of multiple repetitions of magnetic and nonmagnetic metal layers; and (c) spin valves, in which the top or the bottom magnetic layer of the sandwich GMR material is antiferromagnetically pinned by insertion of an adjacent antiferromagnetic layer. Typical MR response curves of these devices are shown in Fig. 23.2.

Fig. 23.2 Typical MR response curves for sensors based on GMR effect: (a) unpinned sandwich GMR¹; (b) antiferromagnetically coupled multilayer GMR²; (c) spin valve³.



¹Reprinted with permission from Baselt et al. [3]. © 1998 Elsevier.

²Reprinted with permission from Tondra et al. [54]. © 2000 American Institute of Physics.

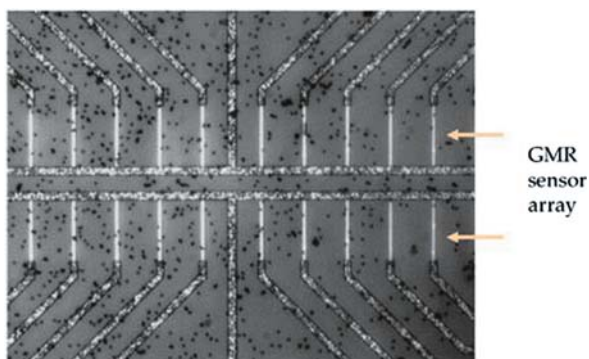
³Reprinted with permission from Freitas et al. [18]. © 2007 IOP Publishing.

In general, the sensors based on antiferromagnetically coupled multilayers show higher MR ratios than unpinned sandwich structures (typically 12–16% compared to 4–9%) and higher saturation fields than the other two sensor types (typically 25–30 mT compared to 3–6 mT in GMR sandwiches and 1–8 mT in spin valves). They also exhibit better linearity and lower hysteresis than unpinned sandwich GMRs although the response of the spin valves typically shows the best linearity and the lowest hysteresis. The values of MR ratio in spin valves can vary between 4 and 20% [50].

23.2.1 GMR Sensors

The sensor chip used in the original work of NRL group [3] was made in the form of an array of sandwich GMR strips shown on Fig. 23.3 with MR ratio of about 5% (Fig. 23.2a). It was named bead array counter (BARC). The sensor was fabricated in rectangular strip geometry so that the strips were sensitive only to an in-plane field component directed along their long axis. Their sensitivity was tested with commercial magnetic beads, Dynabeads M-280, 2.8 μm in diameter.

Fig. 23.3 The first BARC chip. The image shows an array of rectangular GMR strips with magnetic microbeads distributed over the chip surface⁴



Such beads were recently thoroughly characterized [17] using X-ray diffraction, SEM analysis, Mössbauer spectroscopy, and magnetic measurements. They were found to consist of large number of mostly maghemite ($\gamma\text{-Fe}_2\text{O}_3$) nanoparticles dispersed in a polymer matrix (Fig. 23.4), with non-uniform size distribution and average diameter ~ 8 nm. Being this small, the nanoparticles, and consequently the bead as a whole, exhibit superparamagnetic behavior. Superparamagnetic means that the beads acquire nonzero magnetization only in the presence of an external magnetic field, otherwise they are practically nonmagnetic. This way the mutual magnetic interactions between the beads that may lead to their agglomeration and eventually prevent them from binding to the target molecules in real bioassays are eliminated.

⁴Reprinted with permission from Baselt et al. [3]. © 1998 Elsevier.

The necessity for using superparamagnetic particles as magnetic labels in on-chip magnetic biosensing is, for this reason, now generally accepted. As a consequence, in detection experiments one usually needs to apply an external magnetic field to induce nonzero magnetization in the beads⁵.

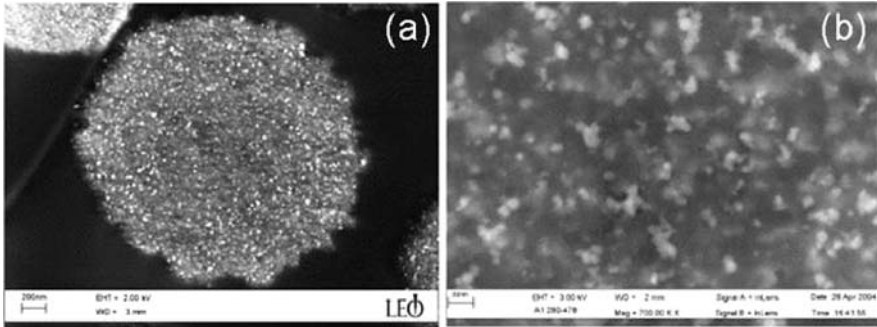


Fig. 23.4 (a) A scanning electron microscope (SEM) image of a Dynabeads M-280 bead (as used in the original experiments of the NRL group); (b) A closer look at the bead's structure. The nanoparticles in the bead are visualized as bright points⁶

The BARC sensor was biased with a dc current, and the bead was magnetized with an ac magnetic field of 5 mT perpendicular to the sensor plane which was modulated at a frequency of 200 Hz to enable lock-in detection. The output voltage of the sensor was measured at a second harmonic frequency due to an even sensor response to the magnetic field, with a time constant of the lock-in amplifier $\tau = 1$ s. Under these experimental conditions, the authors were able to detect the presence of a single bead on one $5 \times 20 \mu\text{m}^2$ strip with a signal-to-noise ratio (S/N) ~ 6 . The detection experiments performed in the same configuration with GMR strips having larger sensing areas have yielded $S/N \sim 4$ ($5 \times 80 \mu\text{m}^2$) and $S/N \sim 2$ ($10 \times 160 \mu\text{m}^2$) for the single bead.

The original BARC sensor design has been advanced in the later years leading to improved performance in several aspects. The later BARC-III sensor chips (Fig. 23.5a) [43] contain antiferromagnetically coupled GMR multilayer sensors. The improved composition resulted in a larger saturation field (~ 30 mT compared to ~ 5 mT) and a larger GMR effect ($\sim 15\%$ compared to $\sim 5\%$). In addition, the strip geometry shown in Fig. 23.3 has been replaced with a serpentine trace geometry (Fig. 23.5b) which increased the sensing area ~ 10 times (totaling $3.1 \times 10^4 \mu\text{m}^2$) while keeping the same area for biomolecular functionalization. This, however, led to somewhat lower sensitivity for bead detection, ~ 10 beads per sensor which, based on the most recent reports, has been overcome by providing GMR sensors with ~ 30 times better sensitivity [41]. Also, the sensors in BARC-III chips did not require a bias current for operation which led to significant improvements in reducing power dissipation and heat generation.

⁵We will see in Section 23.6 that this does not need to be the case for detection with GMI sensors.

⁶Reprinted with permission from Fønnum et al. [17]. © 2005 Elsevier.

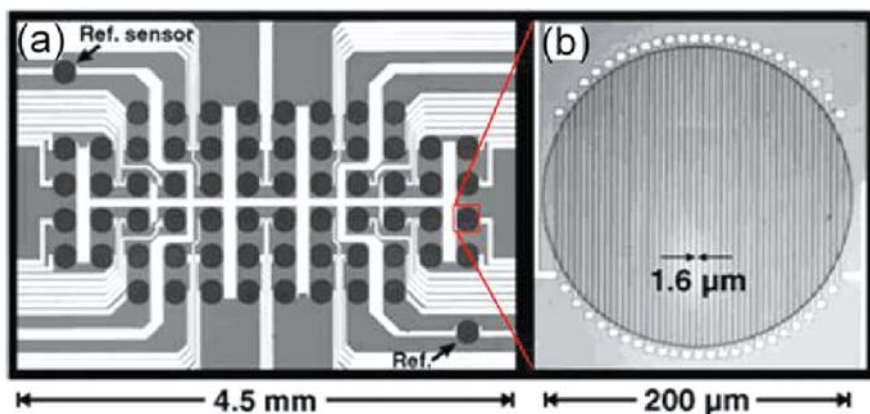


Fig. 23.5 (a) Optical image of the central sensing area of a BARC-III sensor chip. (b) Closer view of one serpentine GMR sensor trace encompassing a 200- μm -diameter sensing zone⁷

Although it was suggested already in the original article [3] that BARC chips could be used to perform DNA hybridization assays, it was not until three years later that the results of such experiments were first reported by the group [39]. The BARC chips used in the DNA hybridization assay contained 64 GMR sensor strips, $5 \times 80 \mu\text{m}^2$ in size, grouped in eight sensing zones, each containing the eight-sensor array (Fig. 23.6a). In order to demonstrate the selectivity of hybridization and magnetoelectronic detection, pairs of eight-sensor arrays were functionalized with four different single-stranded DNA probes (one of them serving as a control). Biotinylated target DNA strands, complementary to the control DNA and only one of the remaining DNA probes, were then introduced followed by streptavidin-coated M-280 beads. The chip response is shown in Fig. 23.6b. It was highest for the control zones, almost zero for the zones functionalized with non-complementary DNA probes, and a clear signal has been obtained from the zones with complementary DNA probes.

This experiment unambiguously showed that the concept of solid-state magnetic biosensing could provide selectivity in the detection response. It, however, did not show any quantitative dependence of the measured sensor response on concentration of the target DNA. The first step toward this goal, i.e. the quantitative relation between the sensor's output signal and the number of magnetic beads in the sensing area, was demonstrated more recently [43]. The dependence tends to be more linear the higher the ratio of the sensor size vs. the bead size. The situation is much more challenging when it comes to the quantitative dependence of the measured sensor response on concentration of the target biomolecules. The first work that addressed this problem experimentally was published by the group from the University of Bielefeld, Germany [46]. Their chips consisted of 206 spiral-shaped GMR lines, each covering a circular area 70 μm in diameter (Fig. 23.7a). In their

⁷Reprinted with permission from Rife et al. [43]. © 2003 Elsevier.

Fig. 23.6 (a) Optical image of BARC sensor chip used in the experiments of Miller et al. (b) The signal output of the BARC sensor chip from DNA hybridization assay. The data points show the signal from each individual sensor and the hatched rectangles correspond to the total signal from the sensing zone⁸

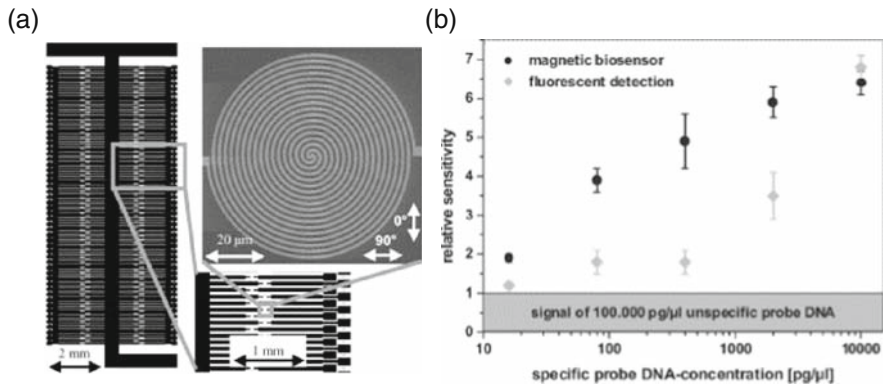
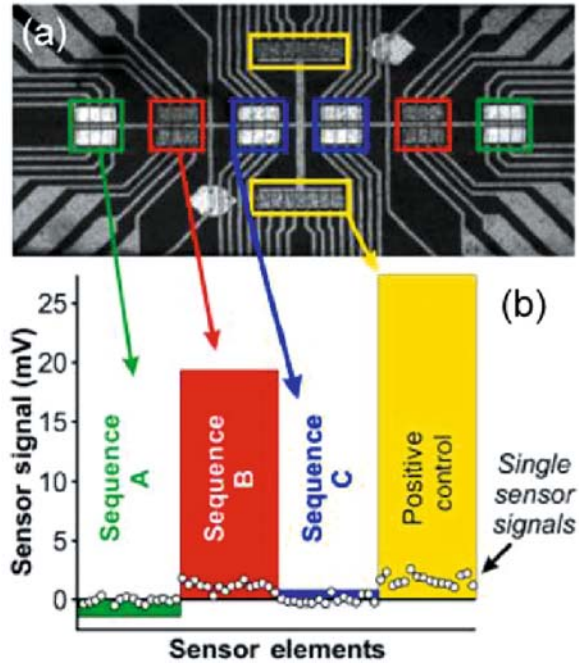


Fig. 23.7 (a) A magneto-resistive sensor array used in the experiments of Schotter et al. (b) Sensitivity of the magnetic biosensor and that obtained in a comparable fluorescent detection experiment. The magnetic biosensor sensitivity is defined as the maximum output signal at a magnetizing field of 40 kA/m relative to the average signal of the non-functionalized sensor element⁹

⁸Reprinted with permission from Tamanaha and Whitman [51]. © 2004 Elsevier.

⁹Reprinted with permission from Schotter et al. [46]. © 2004 Elsevier.

experiments, the same volume of probe DNA with five different concentrations, ranging from 16 pg/ μL to 10 ng/ μL , has been spotted on the sensor surface. After covalent attachment and washing, the sensor was incubated with 10 ng/ μL of biotinylated complementary DNA, after which 0.35- μm -diameter streptavidin-coated superparamagnetic beads were introduced and allowed to react with the target DNA. The results are shown in Fig. 23.7b along with those of the same assay where fluorescent, instead of the magnetic labels, were used for comparison. It can be seen that the output signal of a magnetic sensor increased only three times, with a clear tendency for saturation, when the probe DNA was increased by almost three orders of magnitude. The results were also significantly different from the corresponding fluorescent assay. This was not surprising considering that it was more an assay of the likelihood of the DNA attachment than of the concentration in a test sample, since the concentration of probe DNA was varied, not the concentration of target DNA in the sample [33]. It did, however, represent the first reported attempt at establishing a quantitative bioassay with GMR magnetic sensors.

Most recently, relation between the density of the beads bound to the sensor and the concentration of target molecules, the so-called dose-response curve, has been demonstrated by the NRL group [41]. In their experiments Dynal M-280 superparamagnetic beads were used (2.8 μm in diameter) with BARC-III magnetic chips incorporated into a flow cell. After target molecules, labeled by beads, had been captured on the chip surface, a controlled laminar flow was used to apply microfluidic forces and preferentially remove labels that were bound nonspecifically. The method, called fluidic force discrimination (FFD), dramatically reduced the background label density, giving rise to dose-response curves that follow a logarithmic dependence of the sensor signal (which is linearly proportional to the number of beads) on analyte concentration. The authors achieved femtomolar detection of DNA and proteins in complex matrices such as whole blood, serum, plasma, and milk and verified that an assay performed on a magnetic sensor chip is equivalent to the one performed in the same flow cell geometry on a similarly functionalized slide with optical bead counting. However, they also emphasized that for any practical microfluidic flow rates, the sensing scheme is limited to micrometer-size beads due to rapidly diminishing fluidic forces with decreasing bead radius.

23.2.2 Spin Valve Sensors

Spin valve sensors for detection of magnetic biomolecular labels were introduced by the group from INESC-MN, Portugal [19]. Their chips consisted of a series of $2 \times 6 \mu\text{m}^2$ rectangular spin valve strips exhibiting $\sim 5\%$ MR ratio. By performing a dc measurement with a bias current of 8 mA and external in-plane magnetizing dc field of 1.5 mT, the authors were able to detect the presence of a Micromer-M 2- μm -diameter bead, situated on the edge of the strip, with $S/N \sim 10$. They estimated that approximately 4 times better value would have been obtained if the beads were centered on the strip. In addition, the authors reported detection of large numbers of 400-nm-diameter beads with the same spin valve sensors.

Following the initial work, the group has focused on detecting binding of streptavidin-functionalized superparamagnetic beads to surface-biotinylated spin valve sensors [14, 20]. For this purpose, the $2 \times 6 \mu\text{m}^2$ sensing strips (Fig. 23.8a) were covered by 200-nm thick SiO_2 film to provide surface for biochemical procedures involved in biotin functionalization as well as to serve as an electrical insulating layer. The solution of streptavidin-functionalized magnetic beads was dropped on the sensor, allowed several minutes to react and then washed away while the sensor signal response was monitored in real time. The residual signals (Fig. 23.8b) were observed only in the case of surface-biotinylated sensors, demonstrating that the real-time magnetic detection of biotin-streptavidin binding through the mechanism of biomolecular recognition is possible. This detection, however, was not achieved for beads smaller than 250 nm in diameter.

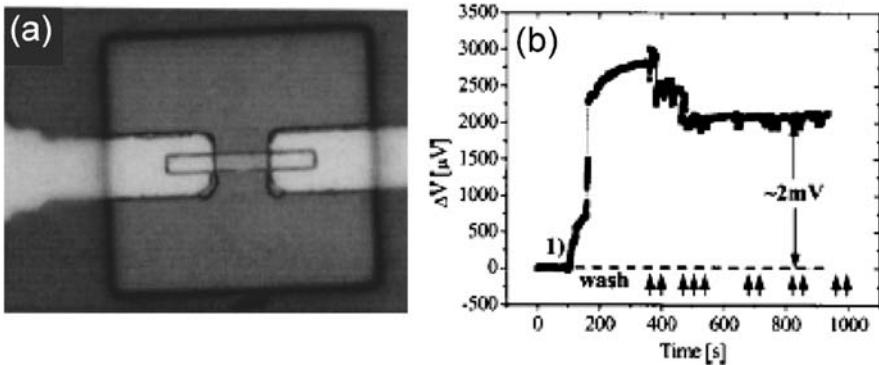


Fig. 23.8 (a) An optical image of a $2 \times 6 \mu\text{m}^2$ spin valve sensor from Ferreira et al. A $25 \times 25 \mu\text{m}^2$ biotinylated SiO_2 surface on top of the sensor is also visible. (b) Real-time detection of binding of 250-nm Nanomag[®]-D streptavidin-functionalized magnetic labels to a biotinylated SiO_2 surface. The residual 2-mV signal that remained after washing is due to the bound beads¹⁰

Most recently, the group has developed on-chip current lines for focusing of magnetic labels to the sensing zone [16]. Previously, they showed that such U-shaped current lines can increase the speed of hybridization between the surface-bound probe DNA and magnetically labeled target DNA [15]. Their integrated chip was comprised of an array of $2.5 \times 80 \mu\text{m}^2$ U-shaped spin valve sensors (MR ratio of $\sim 7\%$, sensitivity $\sim 25 \Omega/(\text{kA/m})$ in the linear range from -1.2 to 0.1 kA/m ; see Fig. 23.9a) that were integrated within current line structures for magnetic label manipulation (Fig. 23.9a, inset). The authors used streptavidin-coated superparamagnetic beads, Nanomag[®]-D 250 nm in diameter as well as Micromer[®]-M 2 μm in diameter. ac field focusing of these labels was accomplished by applying currents of 30 mA rms at a frequency of 0.2 Hz through the U-shaped current lines, in combination with the 0.8 kA/m dc bias field. Lock-in detection was carried out

¹⁰Reprinted with permission from Ferreira et al. [14]. © 2003 American Institute of Physics.

(1 mA dc bias, an in-plane ac magnetizing field of ~ 1 kA/m rms at 30 Hz and the equivalent noise bandwidth $\Delta f \sim 0.83$ Hz) ~ 10 min after ~ 10 μ l solutions of different label concentrations were dispersed over the chip and focused at the sensor sites. The obtained signals increased linearly with the label concentration (Fig. 23.9b). The demonstrated detection limit was below 1 pM for 250-nm beads (~ 12 beads per U-shaped sensor) and ~ 10 fM for 2- μ m ones (single-bead sensitivity). By considering that ~ 500 streptavidin molecules are bound to a 250-nm label and $\sim 77,000$ to a 2- μ m one, and assuming that 1 DNA strand can bind to each molecule, the authors concluded that these detection limits correspond to DNA concentrations of less than 500 pM and ~ 770 pM respectively. These numbers were already much smaller than in conventional DNA assays (μ M concentrations) but, according to the authors, could be improved further by varying magnetizing fields at higher frequencies, closer to the sensor's thermal noise limit.

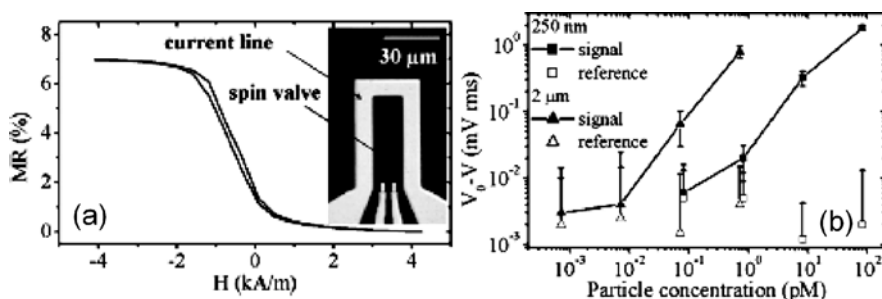


Fig. 23.9 (a) MR response curve of a $2.5 \times 80 \mu\text{m}^2$ spin valve sensor shown in the inset within an U-shaped aluminum current line. (b) An output signal of an 11 spin valve sensor array as a function of concentration of 250 nm beads (filled squares), and 2 μm beads (filled triangles) concentrations. Empty symbols correspond to the reference 5 sensor array not sensitive to the presence of the labels¹¹

23.2.3 GMR and Spin Valve Sensors for Detection of Nanoparticles

In the experiments described so far, the magnetic labels used had diameters ranging from 250 nm to 2.8 μm . However, some authors have pointed out [38, 56] that such beads cannot provide reliable quantitative detection when it comes to biomolecules that are significantly smaller in size (single DNA strand or a protein, for example, only few nanometers) because one cannot reliably know how many molecules are bound per bead. In addition, to achieve single molecule detection of nanosized molecules, one should be able to develop sensors capable of detecting nanometer-scale particles, ideally with single particle sensitivity [54].

¹¹ Reprinted with permission from Ferreira et al. [16]. © 2006 American Institute of Physics.

The most extensive efforts in this direction have been made by the group at Stanford University [29, 30, 56]. Following their initial detection of single Dynabeads M-280 bead with a $3 \times 4.1 \mu\text{m}^2$ spin valve sensor and a $S/N \sim 12$ [28], the group has turned its focus to detection of very small magnetite (Fe_3O_4) nanoparticles, only 16 nm in diameter. For this purpose, they fabricated submicrometer spin valve sensors with sensing area $1 \times 0.3 \mu\text{m}^2$ and MR ratio of 10.3%. Such miniaturized sensors provide higher average stray field fluxes generated by the particles and therefore increase the measurable signals. In their initial experiments, lock-in detection was used with magnetizing ac field of 10 mT rms at 208 Hz (applied in plane but transversal to the sensor longitudinal axis which was dc field biased to its linear point) and $\Delta f = 1$ Hz. They succeeded in detecting, under these conditions, the presence of a monolayer of such nanoparticles completely covering the sensor's active area (Fig. 23.10a). The best signal obtained was, however, only 3 times higher than the noise level (Fig. 23.10b) indicating that detection of low number of the nanoparticles, let alone a single nanoparticle, would not be possible in this configuration. Surprisingly, by performing the detection experiments in a much simpler dc configuration and further reducing the sensor width to $0.2 \mu\text{m}$, they were able to reach better S/N and demonstrate the detection of just 23 nanoparticles (Fig. 23.11). By fitting the dependence of the measured signals on the number of beads on the sensor to a linear curve, the authors determined that the minimum detection limit of their sensors is 14 nanoparticles. It is important to point out that this result represents experimental detection of the lowest numbers of nanoparticles reported up to now¹².

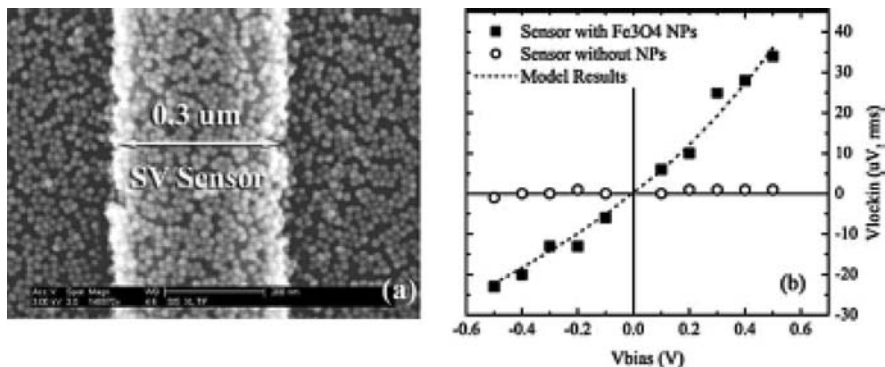


Fig. 23.10 (a) 16-nm Fe_3O_4 nanoparticle monolayer on a $1 \times 0.3 \mu\text{m}^2$ spin valve sensor. (b) Voltage signals for the spin valve sensor with (solid squares) and without (open circles) Fe_3O_4 nanoparticle monolayer. The dashed line is calculation model prediction of the signal¹³

¹²The potential of submicrometer GMR sensor strips for single nanoparticle detection was also examined by researchers from the University of California at Santa Barbara [57] through magnetoresistance and electrical noise measurements combined with numerical calculations. They obtained magnetic field resolution of $12 \mu\text{T}/\text{Hz}^{1/2}$ for $2 \times 0.15 \mu\text{m}^2$ GMR strip in a thermal noise range > 50 Hz, and estimated that such sensor could resolve $2.2 \times 10^4 \mu_B/\text{Hz}^{1/2}$ and be capable of detecting a 100-nm particle. They however did not perform detection experiments.

¹³Reprinted with permission from Li et al. [29]. © 2004 IEEE.

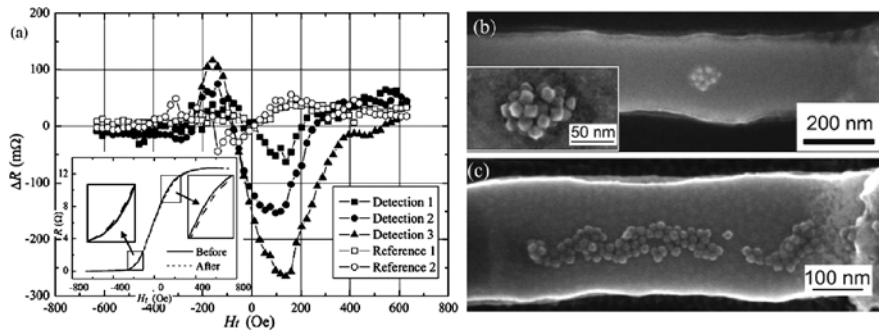


Fig. 23.11 (a) The resistance differences before and after depositing 16-nm Fe_3O_4 nanoparticles for three sensors containing different numbers of nanoparticles (*filled symbols*) and two reference sensors without nanoparticles (*open symbols*). The inset shows the MR curves measured before (*solid line*) and after (*dashed line*) the nanoparticle deposition for the detection sensor 3, containing ~ 630 nanoparticles. The three detection sensors have different numbers of the Fe_3O_4 nanoparticles. SEM images of (b) the detection sensor 1 with ~ 23 deposited Fe_3O_4 nanoparticles that are also shown in the inset at a higher magnification and (c) the detection sensor 2 with ~ 108 nanoparticles¹⁴

23.3 MTJ Sensors

The operation of MTJ sensors is based on the effect of tunneling magnetoresistance in sandwich structures similar to spin valves with the exception that a normal layer is not a metal but an insulator. Another difference is that the bias current in MTJ sensors is always oriented perpendicular to the film plane (CPP geometry) so that the electrons have to tunnel across an insulating barrier between two magnetic electrodes. The tunneling current depends strongly on relative orientation of magnetizations of the ferromagnetic layers and is maximal (minimal) for parallel (antiparallel) orientation configurations [26].

The physical mechanism responsible for this behavior is the difference in the density of states at the Fermi level for two spin populations [34]. When majority spin electrons carrying the current have to tunnel from one ferromagnetic electrode to another, they may find large (minimal resistance) or small (maximum resistance) density of available energy states at the Fermi level depending on whether the other electrode is oriented parallel or antiparallel to the first one.

The relative resistance changes of the MTJ structures are significantly higher than those of GMR and spin valve devices. For amorphous AlO_x insulating barriers, MR ratios up to 70% have been reported [55]. Replacing this with a crystalline MgO barriers has yielded values above 200% [11, 42]. Theoretical analysis, however, predicts that values higher than 1000% are possible to realize with current technologies [7, 32].

¹⁴Reprinted with permission from Li et al. [30]. © 2004 Elsevier.

Potential of MTJ sensors for detection of superparamagnetic biolabels has been examined by several groups. The group at Brown University [47] fabricated MTJ sensors in the form of $2 \times 6 \mu\text{m}^2$ ellipses with Al_2O_3 barrier and MR ratio of 15.3%. In their experiments, the Dynabeads M-280 beads were flowed through a $600\text{-}\mu\text{m}$ wide and $50\text{-}\mu\text{m}$ deep microfluidic channel fabricated in PDMS and sealed with the sensor chip from below (Fig. 23.12a). The sensor was ac biased at frequency of 8 kHz while dc magnetic field of 1.5 mT was applied to magnetize the beads. The signal was measured by a lock in amplifier in a bridge configuration. Whenever a bead would cross over an active region of an MTJ sensor (Fig. 23.12b), dips in the sensor output voltage response were observed (Fig. 23.12c). The obtained S/N in these measurements was ~ 16 (24 dB) per single bead.

In their efforts to eventually reach a single nanoparticle detection, the group at Stanford University [56] has also reported fabrication of MTJ strips based on Al–O barriers with MR ratio of 50%. The authors examined the potential of these devices for single nanoparticle detection by carrying analytical calculations. They found that when reduced to the same area of $1 \times 0.3 \mu\text{m}^2$ as previously described spin valve sensors, the devices should provide about 10 times higher signals, thus making single nanoparticle detection more feasible.

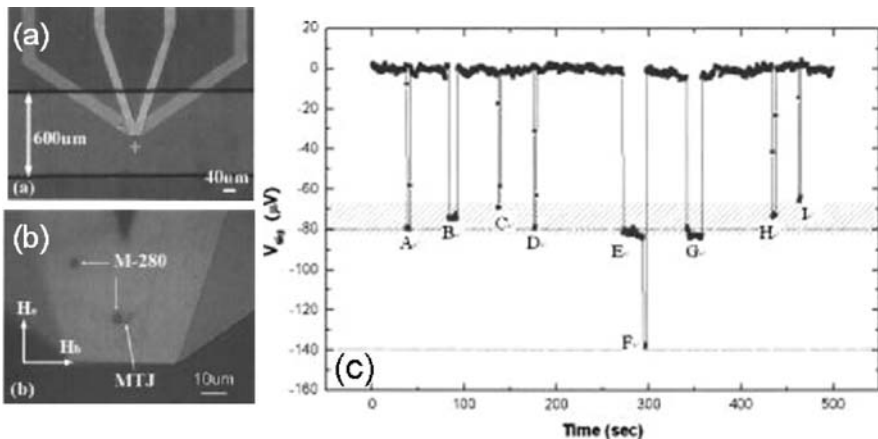


Fig. 23.12 Optical images of (a) a single $2 \times 6 \mu\text{m}$ MTJ sensor sealed inside a $600 \mu\text{m}$ wide microfluidic channel, and (b) an identical sensor with two single M-280 beads in close proximity. The orientation of the two external fields used in the experiment H_c and H_b is also shown; (c) Real-time voltage data demonstrating single-bead detection. When a single bead passes by the sensor, a sharp signal drop is observed (points A, C, D, H, and I). When a bead becomes stuck on the sensor area for an extended length of time, a plateau signal is obtained (points B and G). Two-step signals (points E and F) correspond to a situation where two beads are attached to the junction at the same time. The shadowed band indicates the typical signal range measured for a single bead¹⁵

¹⁵Reprinted with permission from Shen et al. [47]. © 2005 American Institute of Physics.

More recently the group at INESC-MN, Portugal, reported MTJ sensors with AlO_x tunnel barriers which showed a TMR ratio of 27% [8]. The devices with sensing area of $2 \times 10 \mu\text{m}^2$ were tested with Nanomag-D 250-nm-diameter beads. ac lock-in detection was used, with a bias field of 1.5 mT rms at 30 Hz applied in plane and bias current of $30 \mu\text{A}$. Clear signals, with magnitudes proportional to the concentration of the beads in the solution, were recorded upon dropping the bead solutions on the sensor. However, the reported signal per single bead was lower than the sensor noise level.

The first realization of MTJ sensors for bioapplications that contains MgO tunnel barriers has been recently reported by the group from Brown [48]. These devices exhibit significantly higher MR ratio of 97% (sensitivity of 0.91%/G over the field range of ± 10 G; see Fig. 23.13a) than those based on Al_2O_3 barriers. The performance of the devices was examined in DNA hybridization assays. Detection of target DNA molecules was carried out with a serial array of 64 MTJ sensors with lateral dimensions of $6 \times 18 \mu\text{m}^2$ (a similar array of 256 sensors is shown in the inset of Fig. 23.13a). The sensor array surface was first treated with $40 \mu\text{M}$ probe DNA, followed by hybridization with a $2.5 \mu\text{M}$ complementary target DNA. Ten microliter solution of 16-nm-diameter Fe_3O_4 nanoparticles or commercial MACSTM nanoparticles (50 nm in diameter) was then introduced to the sensor area, allowed to react for 10 min and then washed with PBS buffer to remove nonspecifically bound nanoparticles. Magnetic response curves were measured before and after the binding of nanoparticles on the sensor surface. The differences in the two recorded transfer curves are plotted in Fig. 23.13(b) along with that of the reference array that was not treated with probe DNA molecules. Clear signals with peak S/N of approximately 25 and 12 were obtained for Fe_3O_4 and MACSTM nanoparticles respectively while no signal was measured for a reference sensor.

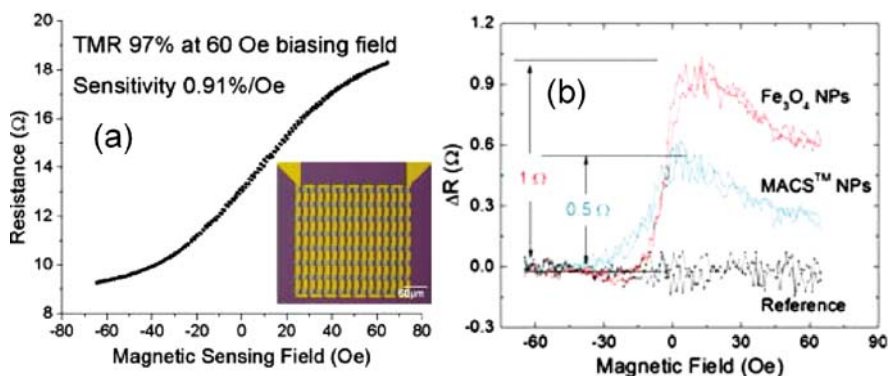


Fig. 23.13 (a) An MR response curve of a single MTJ sensor ($3 \times 6 \mu\text{m}^2$) in a 60 Oe external bias field. Inset: an optical image of 256 MTJ sensors in a serial array. (b) Differences in the measured resistance before and after binding of Fe_3O_4 and MACSTM nanoparticle to the sensor surface. The reference sensor without bound particles shows a zero signal¹⁶

¹⁶Reprinted with permission from Shen et al. [48]. © 2008 American Institute of Physics.

23.4 Sensors Based on AMR Effect

AMR is a dependence of electrical resistance of a magnetic conductor on the angle between the direction of electrical current and the magnetization orientation [52]. The effect originates from the anisotropy of electron scattering produced by the spin-orbit interaction. The stronger scattering is expected when electrons travel parallel to magnetization than perpendicular to it [49]. The net effect is that the electrical resistance has maximum value when the direction of current is parallel or antiparallel to the magnetization and minimum when it is perpendicular to it. The difference is typically 1–3% of the material's zero field resistance.

23.4.1 AMR Ring Sensors

Anisotropic magnetoresistance (AMR) ring sensors for applications in magnetic biosensing have been introduced in 2001 [39]¹⁷. The principle of sensor operation is sketched in Fig. 23.14. In the absence of an external magnetic field, the magnetization of an AMR ring, typically fabricated from a soft ferromagnetic material such as permalloy, forms a closed loop, the so-called onion state. In this state, electrical current passed through the ring experiences maximum resistance since magnetization is oriented along the current direction (Fig. 23.14a). When the ring is exposed to a radial magnetic field, the magnetization rotates to the radial direction and the resistance of the ring decreases (Fig. 23.14b). The relative difference between the resistances in the two ultimate states is usually 1–2%.

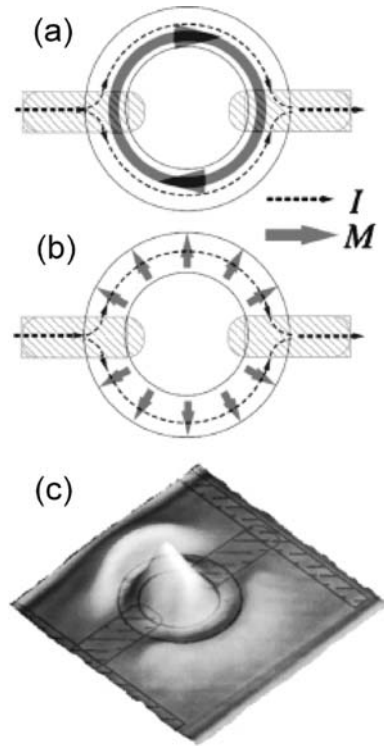
The AMR ring sensor in this original work was fabricated from permalloy (Py) and had outer and inner diameters of 5 and 3.2 μm respectively. By using lock-in detection in a Wheatstone bridge configuration at 200 Hz and applying a magnetizing field of 3.5 mT (amplitude value) to magnetize the 4.3- μm -diameter NiFe bead, the authors showed that S/N of nearly 100 can be obtained when the bead is situated in the center of the ring and a distance 300 nm above it. By attaching the bead to atomic force microscope cantilever, the authors were even able to map out the sensor signal as a function of the lateral position of the bead (Fig. 23.14c).

23.4.2 Planar Hall Effect Sensors

Planar Hall effect (PHE) sensors are Hall crosses made of thin ferromagnetic films in which the transverse voltage V_{PH} depends on the relative orientation between the material's magnetization and the direction of the bias current (see Fig. 23.15a).

¹⁷Micrometer-sized ring sensors for bioapplications have been also reported more recently by the group from University of Cambridge [31]. Although these devices are geometrically similar, they are fabricated from a sandwich structure containing hard ferromagnet/normal metal/soft ferromagnet (Co/Cu/Py, for example) so that their operation is based on the GMR effect rather than AMR.

Fig. 23.14 (a–b) Schematic diagram of the operation of the AMR ring sensor. The hatched areas represent the contact fingers. Maximum resistance state in which the current I is mostly parallel or antiparallel to the circumferential magnetization M (a). Minimum resistance state in which I is mostly normal to M (b). (c) Surface plot of the sensor signal with respect to the position of the bead¹⁸



Formally, this voltage is given as $V_{PH} = \Delta R I \sin \theta \cos \theta$, where $\Delta R = (\rho_{pl} - \rho_{pp})/t$ is change in the resistance of the material when magnetization is oriented parallel ρ_{pl} and perpendicular ρ_{pp} to the direction of the current giving rise to different resistivities respectively (AMR effect), and t is the film thickness.

Typically the direction of the magnetization of the film in zero external magnetic field is set along the current direction by exchange coupling to an antiferromagnetic material. A small external magnetic field with non-zero component perpendicular to this direction can rotate magnetization and give rise to measurable V_{PH} . As long as this field is small compared to the anisotropy field of the film, the sensor response is linear. For permalloy-based planar Hall cross devices, this linear region was determined to be within about ± 2 mT (see Fig. 23.15b).

The potential of the PHE sensors for detection of superparamagnetic beads was investigated by collaborative research of the groups from Technical University of Denmark, Denmark and INESC-MN, Portugal [12, 13]. In their experiments, the sensing Hall cross area was $10 \times 10 \mu\text{m}$ and detection was performed with Micrometer-M and Nanomag-D beads with diameters of $2 \mu\text{m}$ and 250 nm respectively. When the sensor was dc biased with $I = 10 \text{ mA}$ and the particles were

¹⁸Reprinted with permission from Miller et al. [40]. © 2002 American Institute of Physics.

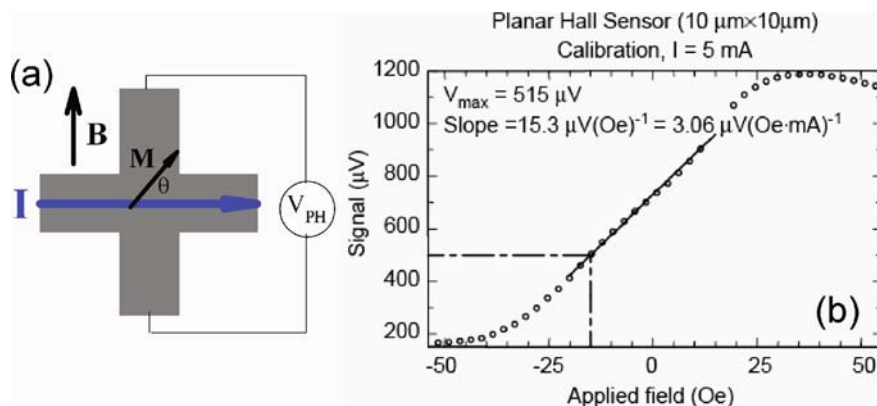


Fig. 23.15 (a) Schematic diagram describing the operation of the planar Hall effect sensor. (b) Typical response of the planar Hall effect sensor to an in-plane magnetic field¹⁹

magnetized with 1.5 mT (the magnetizing field had to be kept low to avoid the sensor saturation which occurs at about 3 mT), a signal-to-noise ratio, $S/N \sim 1$ per bead, was obtained for 2 μm beads. The authors have also predicted single-bead sensitivity for 250 nm beads if efficient noise reduction can be achieved by utilizing lock-in detection.

Most recently the group has investigated exchange-biased permalloy planar Hall effect sensors of different thicknesses (20–50 nm) and a fixed Hall cross area of $40 \times 40 \mu\text{m}^2$ [10]. They showed that sensors made of the thickest film exhibit the highest signal as well as the lowest noise. An $S/N = 6$ was estimated for single Dynabeads M-280 bead by analytical calculations.

23.5 Hall Effect Sensors

Performance of Hall effect sensors in the detection of superparamagnetic micro- and nanobeads has been examined by several groups as a potentially advantageous alternative to magnetoresistive devices for magnetic biosensing applications. The operation of these sensors is based on the classical Hall effect [6, 21], i.e., the fact that a measurable voltage, called the Hall voltage, develops in thin conducting films along the direction transversal to the current flow when they are exposed to an external magnetic field perpendicular to the film plane. The Hall voltage depends linearly on the magnetic field. At room temperature, this dependence is usually satisfied in a broad magnetic field range, of the order of teslas (see Fig. 23.16a). Due to the already mentioned superparamagnetic behavior of magnetic biolabels, this is an important characteristic potentially advantageous compared to most

¹⁹Reprinted with permission from Ejsing et al. [13]. © 2002 Elsevier.

magnetoresistive devices. It means that high external fields can be used to excite the particle’s magnetization without compromising the sensor sensitivity. In addition the linearity allows for a rather elegant detection method which gives definite information, from one measurement, on both the presence and the absence of the beads from the sensor.

The detection method is described schematically in Fig. 23.16b. It is based on the nonlinear response of the magnetization of the beads to the applied field and was first used by a group at the Swiss Federal Institute of Technology for detection of single Dynabead M-280 bead with a cross-shaped silicon Hall sensor [4]²⁰. Magnetization of the bead was first excited by an ac excitation magnetic field \tilde{B}_0 yielding an initial value $\tilde{M}_0 \sim (\chi_0/\mu_0)\tilde{B}_0$, where χ_0 is the magnetic susceptibility of the bead in zero external magnetic field and $\mu_0 = 4\pi \times 10^{-7}$ H/m is the permeability of free space. The induced ac magnetization generates a stray ac magnetic field distribution in the Hall cross region which is converted into an ac Hall voltage, $\tilde{V}_{H0} \propto \tilde{M}_0$, with the same frequency as that of the excitation field.

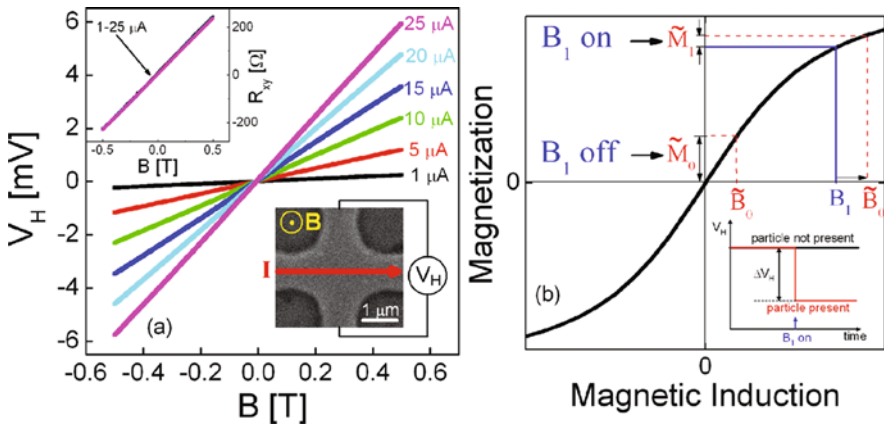


Fig. 23.16 (a) Hall voltage output of the micro-Hall sensor (*lower right inset*) as a function of externally applied perpendicular magnetic field for several dc bias currents. *Upper inset*: The Hall resistance as a function of the magnetic field for different dc bias currents. (b) A sketch of the physical principle underlying the detection method described in the text. Inset shows the expected Hall voltage signal upon applying the dc field B_1 when the bead is (*red*) and is not (*black*) present on the Hall cross²¹

When an additional dc magnetic field, B_1 , is applied, the magnetic state of the bead shifts toward a lower susceptibility χ_1 , and the induced ac magnetization of the bead, $\tilde{M}_0 \sim (\chi_0/\mu_0)\tilde{B}_0$, decreases. This drop leads to a decrease in the average stray magnetic field over the Hall cross, which manifests itself as a drop in

²⁰Variation of this detection method with B_0 applied in plane and detection at the second harmonic frequency has been also demonstrated in this original work and further used by the group from Tokyo Institute of Technology, Japan [44, 45, 53].

²¹Reprinted with permission from Mihajlović et al. [37]. © 2007 American Institute of Physics.

the measured ac Hall voltage (inset of Fig. 23.16b). Due to the linearity of the Hall sensor response, a definitive signal indicating the presence of a bead on the Hall cross can be obtained from just one measurement. The magnitude of the drop in the ac Hall voltage can be expressed as $\Delta \tilde{V}_H = R_H I \Delta \tilde{B}$, where $\Delta \tilde{B} \propto \Delta \tilde{M} = \tilde{M}_0 - \tilde{M}_1$ is the difference between the detected ac stray magnetic fields generated by the induced ac magnetizations of the bead before and after B_1 has been applied (see Fig. 23.16b). It is important to note that $\Delta \tilde{M}$ depends on both \tilde{B}_0 and B_1 ; increasing these fields leads to increases in $\Delta \tilde{M}$ and hence $\Delta \tilde{B}$ [37].

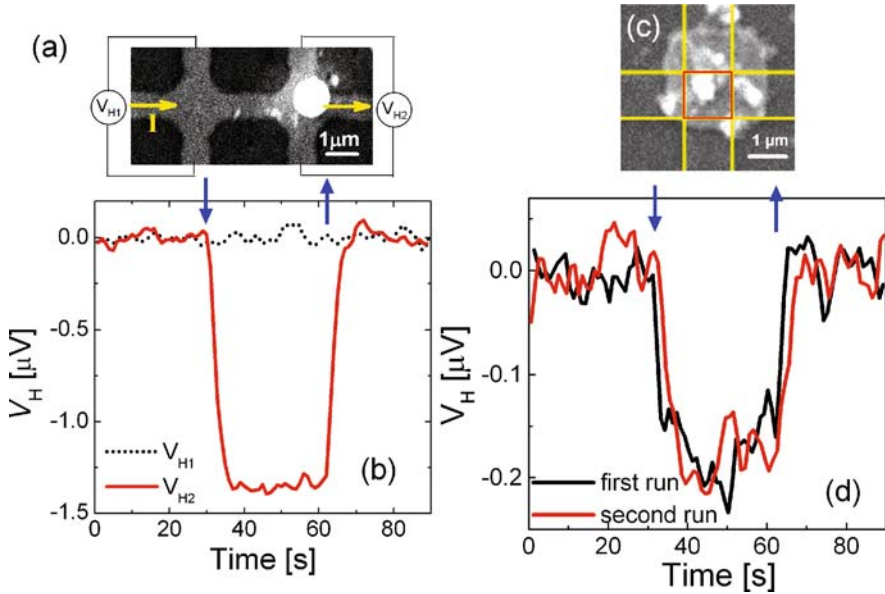


Fig. 23.17 (a) A SEM image of two adjacent Hall crosses with a 1.2- μm diameter superparamagnetic bead positioned on one of them. The image was adapted to show the actual detection measurement configuration. (b) ac Hall voltage as a function of time for the two crosses shown in part (a) of the figure. (c) A SEM image of the Hall cross with Nanomag D-250 superparamagnetic beads. Six beads are located in the Hall cross area (marked as a *square* for clarity). (d) Hall voltage signal as a function of time from the Hall cross shown in part (c) of the figure. The arrows on parts (b) and (d) of the figure indicate the moments of time when B_1 was applied and removed, respectively²²

The Hall sensor used in the original work was fabricated in CMOS technology and had an active area $2.4 \times 2.4 \mu\text{m}^2$. Due to the sensor design, the bead had to be situated at a distance $5.4 \mu\text{m}$ above the sensitive region, which was significantly further than in the previously described experiments with MR sensors (typically hundreds of nanometers). This had a deteriorating effect on the magnetic signal from the bead, since the magnitude of the stray magnetic field in the sensitive region was significantly reduced. Nevertheless, the obtained S/N was comparable to those

²²Reprinted with permission from Mihajlović et al. [37]. © 2007 American Institute of Physics.

obtained with MR sensors indicating that more appropriately designed Hall sensor devices with comparable, or possibly even better sensitivity, may provide single magnetic particle detection of even smaller particles with high-enough S/N.

Such predictions were soon demonstrated by researchers from Florida State University [35, 37] with smaller, $1 \times 1 \mu\text{m}^2$ Hall cross sensors fabricated from InAs/AlSb semiconductor heterostructures [23] containing two-dimensional electron gas (2DEG)²³. In these devices, the sensitive 2DEG layer was significantly closer to the bead, and the smaller Hall cross area provided a higher sensitivity to the bead's induced magnetic moment. The authors have demonstrated detection of a single superparamagnetic bead with diameter of $1.2 \mu\text{m}$ with S/N up to ~ 46.5 , as well as detection of 6 Nanomag D-250 beads, 250 nm in diameter. Because the total S/N in the latter experiment was 7.8, the S/N per single bead was larger than one. Therefore, the experiment demonstrated single 250-nm bead sensitivity of these sensors.

The group has recently also reported results on fabrication and characterization of submicrometer Hall sensors from the same material with a Hall cross area of only $250 \times 250 \text{ nm}^2$ [36] (Fig. 23.18a). By combining experimentally determined magnetic field resolution of the devices with analytical calculations, they showed that they can reach detection limit of the order of $10^4 \mu_B / \sqrt{\text{Hz}}$ above $\sim 1 \text{ kHz}$ (see Fig. 23.18b), with a possibility for single nanoparticle detection in a phase-sensitive Hall detection experiment described above.

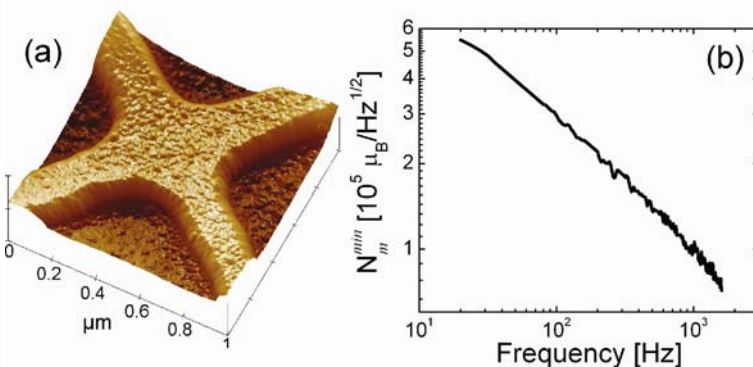


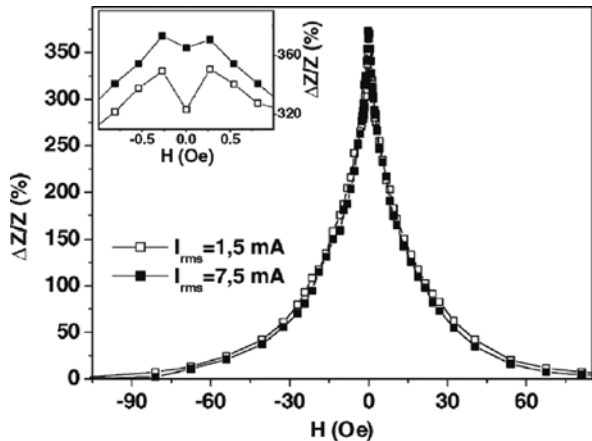
Fig. 23.18 (a) The $250 \times 250 \text{ nm}^2$ Hall cross sensor fabricated from InAs/AlSb quantum well. (b) Room-temperature noise-equivalent magnetic moment resolution of the 250-nm Hall sensor, as a function of frequency

²³Similar sensors were also examined by the group from NRL [27].

23.6 GMI Sensors

The GMI effect is an abrupt change of the impedance of a magnetic conductor biased by a radio frequency (RF) current in a dc magnetic field. Physically, the effect originates from magnetic field dependence of the magnetic permeability which causes variation of the skin depth of the magnetic conductor, thus changing the density of the RF current sent through it [22]. For sensing applications, mostly soft magnetic metals are used due to their high permeability which also exhibits strong dependence on external magnetic field. Typical MI ratios of such devices are of the order of several hundred percents over the field range of tens of militeslas.

Fig. 23.19 MI response curves of a $\text{Co}_{67}\text{Fe}_4\text{Mo}_{1.5}\text{Si}_{16.5}\text{B}_{11}$ amorphous ribbon measured for two different values of the driving ac current. Inset: Closer look at the low field GMI peaks²⁴



Several groups have tested the performance of GMI sensors in detection of magnetic particles suitable for bioapplications. The group at the University of Oviedo, Spain, has utilized commercial Vitrovac[®] 6025 amorphous ribbons with composition $\text{Co}_{67}\text{Fe}_4\text{Mo}_{1.5}\text{Si}_{16.5}\text{B}_{11}$ [24]. The MI response curves of these devices measured at room temperature are shown in Fig. 23.19. They exhibit $\sim 360\%$ change for magnetic fields of ~ 10 mT and are particularly sensitive in the low field range: about $35\%/G$ for $0.3\text{ G} < B < 1.75\text{ G}$ [25].

Figure 23.20a shows the conditions and the measurement results for detection of a suspension of Dynabeads M-450 beads ($4.5\ \mu\text{m}$ in diameter) in phosphate buffered saline (PBS) by these sensors. About 2.7 ml of solution containing approximately 4×10^5 beads/ml was used with a $28\text{-}\mu\text{m}$ thick ribbon having a sensing area of $90 \times 0.8\text{ mm}^2$. The MI values for the bead-free and the bead-present PBS solutions differed by approximately 25%.

Another class of GMI sensors for bioapplications was developed at the National Institute of Research and Development for Technical Physics, Romania [9]. The sensors were arrays of Co–Fe–Si–B glass-coated GMI microwires, $39\ \mu\text{m}$ in

²⁴Reprinted with permission from Kurlyandskaya et al. [25]. © 2005 Elsevier.

diameter and 70 mm in length, with a glass layer thickness of about 7 μm . They were tested in detection of 2- μl suspensions of Estapor beads (1.9 μm in diameter) of different concentrations that were uniformly dispersed over the array surface. The relative changes in MI response of the devices as a function of bead concentration and the number of microwires in the array were found to increase with increasing bead concentration and the number of microwires, as expected. A maximum $\sim 35\%$ change was reached for an array of 10 microwires and 2.4×10^9 beads/ml. A measured field dependence of the MI, from GMI sensor with 10 microwires in the array, with and without Estapor beads is shown on Fig. 23.20b.

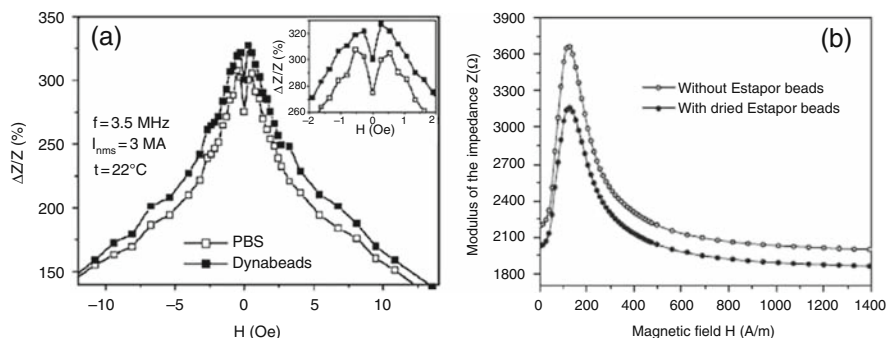


Fig. 23.20 (a) Field dependence of the GMI sensor signal for PBS solution (*empty squares*) and the PBS solution containing Dynabeads® M-450 (*filled squares*)²⁵. (b) Field dependence of the MI, from GMI sensor with 10 active microwires in the array, with and without Estapor beads²⁶

An interesting fact in these results is that significant signals have been measured even in the absence of an external magnetic field (Fig. 23.20). In the described experiments, these values were $\sim 25\%$ and $\sim 8\%$ respectively. Chiriac et al. attributed these signals to the ac magnetic field generated by the RF bias currents which induces measurable magnetic moments in superparamagnetic beads to be detected. The fact that it is not necessary to apply external magnetic fields to detect the presence of the particles on the sensor might be attractive for implementation of these sensors in practical biosensing devices.

23.7 Conclusions

We have reviewed the concerted efforts of many research groups to develop solid-state magnetic sensors and on-chip detection platforms based on magnetic labeling that can be utilized in biomolecular sensing, single molecule detection, or fundamental biophysical studies on individual molecules. Two different approaches have been highlighted. The first one relies on sensors with large

²⁵ Reprinted with permission from Kurlyandskaya et al. [25]. © 2005 Elsevier.

²⁶ Reprinted with permission from Chiriac et al. [9]. © 2007 Elsevier.

active areas (hundreds of μm^2) and micrometer-sized beads and intends to provide dose-response curves between the sensor's particle coverage and concentration of target molecules in the sample. The second approach utilizes smaller sensors with micro- or submicrometer-sized active areas and submicrometer beads or nanoparticles where, ideally, one magnetic label should correspond to one target molecule. Due to its promise for single molecule detection, the latter approach has triggered significant research efforts toward single magnetic particle detection.

Referring to large area detectors, the most advanced have been those based on GMR sensors. The research gradually progressed from early experiments focusing only on sensor sensitivity with respect to detection of various magnetic labels to the more advanced ones involving biofunctionalization of sensor surfaces and integration of sensor chips with microfluidics that eventually led to demonstration of a complete bioassay.

On the other hand, single magnetic microbead detection has been demonstrated with several types of MR sensors, but detection of the nanoparticles still presents a challenge. This is expected to be overcome by utilizing MTJ sensors since they offer larger MR ratios and higher sensitivities.

Hall effect sensors can provide suitable alternatives to MR ones. They offer the advantage of using higher magnetic fields to magnetize the beads as well as detection methods which give information on both the presence and the absence of the bead in a single measurement. The reported signal-to-noise ratios in experiments on single microbead detection have been higher than those for MR sensors, and the detection of 250 nm beads with single particle sensitivity was also demonstrated.

Finally, GMI sensors were described. They offer high MI ratios and advantage of not having to use external magnetic fields for magnetizing the beads.

References

1. Abels, J. A., et al.: Single-molecule measurements of the persistence length of double-stranded RNA. *Biophys. J.* **88**, 2737–2744 (2005)
2. Baibich, M. N., et al.: Giant magnetoresistance of (001)Fe/(001)Cr magnetic superlattices. *Phys. Rev. Lett.* **61**, 2472–2475 (1988)
3. Baselt, D. R., et al.: A biosensor based on magnetoresistance technology. *Biosens. Bioelectron.* **13**, 731–739 (1998)
4. Besse, P. A., et al.: Detection of single magnetic microbead using using a miniaturized silicon Hall sensor. *Appl. Phys. Lett.* **80**, 4199–4201 (2002)
5. Binasch, G., et al.: Enhanced magnetoresistance in layered magnetic structures with antiferromagnetic interlayer exchange. *Phys. Rev. B* **39**, 4828–4830 (1989)
6. Boero, G., et al.: Micro-Hall devices: performances, technologies and applications. *Sens. Actuators A* **106**, 314–320 (2003)
7. Butler, W. H., et al.: Spin-dependent tunneling conductance of Fe|MgO|Fe sandwiches. *Phys. Rev. B* **63**, 054416–054427 (2001)
8. Cardoso, F. A., et al.: Diode/magnetic tunnel junction cell for fully scalable matrix based biochip. *J. Appl. Phys.* **99**, 08B307–08B309 (2006)
9. Chiriac, H., et al.: Microwire array for giant magneto-impedance detection of magnetic particles for biosensor prototype. *J. Magn. Mater.* **311**, 425–428 (2007)

10. Damsgaard, C. D., et al.: Exchange-biased planar Hall effect sensor optimized for biosensor applications. *J. Appl. Phys.* **103**, 07A302 (2008)
11. Djayaprawira, D. D., et al.: 230% room-temperature magnetoresistance in CoFeB/MgO/CoFeB magnetic tunnel junctions. *Appl. Phys. Lett.* **86**, 092502 (2005)
12. Ejsing, L., et al.: Planar Hall effect sensors for magnetic micro- and nanobead detection. *Appl. Phys. Lett.* **84**, 4729–4731 (2004)
13. Ejsing, L., et al.: Magnetic micro-bead detection using the planar Hall effect. *J. Magn. Magn. Mater.* **293**, 677–684 (2005)
14. Ferreira, H. A., et al.: Biodetection using magnetically labeled biomolecules and arrays of spin valve sensors (invited). *J. Appl. Phys.* **93**, 7281–7286 (2003)
15. Ferreira, H. A., et al.: Rapid DNA hybridization based on ac field focusing of magnetically labeled target DNA. *Appl. Phys. Lett.* **87**, 013901 (2005)
16. Ferreira, H. A., et al.: Magnetoresistive DNA-chips based on ac field focusing of magnetic labels. *J. Appl. Phys.* **99**, 08P105–08P107 (2006)
17. Fonnum, G., et al.: Characterization of Dynabeads[®] by magnetization measurements and Mössbauer spectroscopy. *J. Magn. Magn. Mater.* **293**, 41–47 (2005)
18. Freitas, P. P., et al.: Magnetoresistive sensors. *J. Phys.: Condens. Mat.* **19**, 165221 (2007)
19. Graham, D. L., et al.: Single magnetic microsphere placement and detection on-chip using current line designs with integrated spin valve sensors: *Biotechnol. Appl. J. Appl. Phys.* **91**, 7786–7788 (2002)
20. Graham, D. L., et al.: High sensitivity detection of molecular recognition using magnetically labelled biomolecules and magnetoresistive sensors. *Biosens. Bioelectron.* **18**, 483–488 (2003)
21. Hall, E. D.: On a new action of the magnet on electric currents. *Am. J. Math.* **2**, 287–292 (1879)
22. Hauser, H., et al.: Giant magnetoimpedance sensors. *IEEE Instrum. Meas. Mag.* **4**, 28–32 (2001)
23. Kroemer, H.: The 6.1 Å family (InAs, GaSb, AlSb) and its heterostructures: a selective review. *Physica E* **20**, 196–203 (2004)
24. Kurlyandskaya, G. V., et al.: Giant magnetoimpedance-based sensitive element as a model for biosensor. *Appl. Phys. Lett.* **82**, 3053–3055 (2003)
25. Kurlyandskaya, G. and Levit, V.: Magnetic Dynabeads detection by sensitive element based on giant magnetoimpedance. *Biosens. Bioelectron.* **20**, 1611–1616 (2005)
26. Julliere, M.: Tunneling between ferromagnetic films. *Phys. Lett. A* **54**, 225–226 (1975)
27. Landry, G., et al.: Characterization of single magnetic particles with In As quantum-well Hall devices. *Appl. Phys. Lett.* **85**, 4693–4695 (2004)
28. Li, G., et al.: Detection of single micron-sized magnetic bead and magnetic nanoparticles using spin valve sensors for biological applications. *J. Appl. Phys.* **93**, 7557–7559 (2003)
29. Li, G., et al.: Model and experiment of detecting multiple magnetic nanoparticles as biomolecular labels by spin valve sensors. *IEEE Trans. Magn.* **40**, 3000–3002 (2004)
30. Li, G., et al.: Spin valve sensors for ultrasensitive detection of superparamagnetic nanoparticles for biological applications. *Sens. Actuators A* **126**, 98–106 (2006)
31. Liandro, J., et al.: Quantitative digital detection of magnetic beads using pseudo-spin valve rings for multiplexed bioassays. *Appl. Phys. Lett.* **91**, 203904 (2007)
32. Mathon, J. and Umerski, A.: Theory of tunneling magnetoresistance of an epitaxial Fe/MgO/Fe(001) junction. *Phys. Rev. B* **63**, 220403–220406 (2001)
33. Megens, M. and Prins, M.: Magnetic biochips: a new option for sensitive diagnostics. *J. Magn. Magn. Mater.* **293**, 702–708 (2005)
34. Meservey, R. and Tedrow, P. M.: Spin-polarized electron tunneling. *Phys. Rep.* **238**, 173–243 (1994)
35. Mihajlović, G., et al.: Detection of single magnetic bead for biological applications using an InAs quantum-well micro-Hall sensor. *Appl. Phys. Lett.* **87**, 112502 (2005)

36. Mihajlović, G., et al.: Submicrometer hall sensors for superparamagnetic nanoparticle detection. *IEEE Trans. Magn.* **43**, 2400–2402 (2007a)
37. Mihajlović, G., et al.: InAs quantum well Hall devices for room-temperature detection of single magnetic biomolecular labels. *J. Appl. Phys.* **102**, 034506 (2007b)
38. Millen, R. L., et al.: Giant magnetoresistive sensors and superparamagnetic nanoparticles: a chip scale detection strategy for immunosorbent assays. *Anal. Chem.* **77**, 6581–6587 (2005)
39. Miller, M. M., et al.: A DNA Array sensor utilizing magnetic microbeads and magnetoelectronic detection. *J. Magn. Magn. Mater.* **225**, 138–144 (2001)
40. Miller, M. M., et al.: Detection of a micron-sized magnetic sphere using a ring-shaped anisotropic magnetoresistance-based sensor: A mode; for a magnetoresistance-based biosensor. *Appl. Phys. Lett.* **81**, 2211–2213 (2002)
41. Mulvaney, S. P., et al.: Rapid, femtomolar bioassays in complex matrices combining microfluidics and magnetoelectronics. *Biosens. Bioelectron.* **23**, 191–200 (2007)
42. Parkin, S. S. P., et al.: Giant tunneling magnetoresistance at room temperature with MgO (100) tunnel barriers. *Nat. Mater.* **3**, 862–867 (2004)
43. Rife, J. C., et al: A design and performance of GMR sensors for the detection of magnetic microbeads in biosensors. *Sens. Actuators A* **107**, 209–218 (2003)
44. Sandhu, A., et al.: High sensitivity InSb ultra-thin film micro-hall sensors for bioscreening applications. *Jpn. J. Appl. Phys.* **43**, L868–L870 (2004)
45. Sandhu, A. and Handa, H.: Practical Hall sensors for biomedical instrumentation. *IEEE Trans. Magn.* **41**, 4123–4127 (2005)
46. Schotter, J., et al.: Comparison of a prototype magnetoresistive biosensor to standard fluorescent DNA detection. *Biosens. Bioelectron.* **19**, 1149–1156 (2004)
47. Shen, W., et al.: In situ detection of single micron-sized magnetic beads using magnetic tunnel junction sensors. *Appl. Phys. Lett.* **86**, 253901 (2005)
48. Shen, W., et al.: Detection of DNA labeled with magnetic nanoparticles using MgO-based magnetic tunnel junction sensors. *J. Appl. Phys.* **103**, 07A306 (2008)
49. Smit, J.: Magnetoresistance of ferromagnetic metals and alloys at low temperatures. *Physica (Amsterdam)* **17**, 612–627 (1951)
50. Smith, C. H. and Schneider, R. W.: Low-field magnetic sensing with GMR sensors. NVE Research and Development Papers & Presentations. <http://www.nve.com/Downloads/lowfield.pdf> (1999). Accessed 10 January 2008
51. Tamanaha, C. R. and Whitman, L. J.: Magnetic labeling and detection of biomolecules. In: Buschow, K. H. J. (ed.) *Encyclopedia of Materials: Science and Technology*. Elsevier, Amsterdam (2004)
52. Thomson, W.: On the electro-dynamic qualities of metals: effects of magnetization on the electric conductivity of nickel and of iron. *Proc. R. Soc London* **8**, 546 (1857)
53. Togawa, K., et al.: Detection of magnetically labeled DNA using pseudomorphic AlGaAs/InGaAs/GaAs heterostructure micro-Hall biosensors. *J. Appl. Phys.* **99**, 08P103 (2006)
54. Tondra, M., et al.: Model for detection of immobilized superparamagnetic nanosphere assay labels using giant magnetoresistive sensors. *J. Vac. Sci. Technol. A* **18**, 1125–1129 (2000)
55. Wang, D., et al.: 70% TMR at room temperature for SDT sandwich junctions with CoFeB as free and reference layers. *IEEE Trans. Magn.* **40**, 2269–2271 (2004)
56. Wang, S. X., et al.: Towards a magnetic microarray for sensitive diagnostics. *J. Magn. Magn. Mater.* **225**, 731–736 (2005)
57. Wood, D. K., et al.: Submicron giant magnetoresistive sensors for biological applications. *Sens. Actuators A* **120**, 1–6 (2005)

Index

A

Activation energy, 381, 494
Activation volume, 191, 204, 212, 351
Agglomeration, 324, 331, 542, 689
Aggregation, 61, 78, 567, 583, 584, 593, 596, 597
 gas aggregation, 78
Amorphous structures, 285
Anisotropic exchange, 79–81, 83–85
Anisotropy
 annealing-induced anisotropy, 79, 143
 interface anisotropy, 70, 80–81, 82, 188, 190, 204, 248, 252
 magnetocrystalline, 80, 81, 129, 139, 143, 275, 276, 279, 281, 282, 283, 285, 286, 287, 288, 290, 291, 292, 296, 298, 299, 300, 301, 304, 311, 317, 338, 339, 362, 376, 378, 383, 384, 385, 386, 387, 402, 476, 518, 538, 548, 556, 557, 672
 magnetoelastic, 169, 170, 287, 418, 426
 origin, 413
 perpendicular, 81, 165, 185–214, 237, 248, 252, 254, 256
 random anisotropy, 80, 275, 282, 283–287, 288, 290, 291, 292, 293, 296, 297, 300, 304, 312, 383, 384, 387
 shape anisotropy, 80, 82, 188, 204, 223, 227, 287, 301, 324, 331, 515, 567, 576, 667, 672
 surface anisotropy, 80, 81, 515
 temperature dependence, 85, 87, 413, 516
 unidirectional, 160, 170
Anisotropy constant, 78, 79, 283, 284, 285, 286, 288, 291, 312, 313, 343, 344, 346, 354, 357, 359, 383, 413, 420, 539, 556
Anisotropy energy, 9, 69, 81, 82, 163, 190, 284, 285, 286, 312, 383, 412, 418, 516, 517, 518, 519, 520, 522, 556, 566

Anisotropy field, 79, 245, 248, 364, 366, 406, 414, 420, 422, 424, 516, 520, 534, 666, 667, 701
Annealing
 flash annealing, 537, 549–550, 558
 salt-matrix annealing, 309, 324–325, 331, 552
Antiferromagnetism, 124
Areal density, 68, 69, 73, 78, 83, 238, 240, 242, 243, 246, 256

B

Bacteria, magnetotactic, 376
Ballistic transport, 11
Ball milling
 magnetic-field assisted ball milling, 332
 surfactant-assisted ball milling, 309, 325, 326
Band structure, 43, 68, 81, 90, 110, 139, 455, 629, 630, 631, 635–637, 638, 639
Biocompatibility, 609, 616
Biomagnetism, 95
Biomaterials, 38, 599
Biomolecular recognition, 616, 686, 694
Biomolecules, 599, 691, 695
Biosensors, 586
Biotechnology, 36, 661
Biotoxity, 600–603
Bit-patterned media (BPM), 68, 237, 238, 256–259, 264, 265, 268, 270, 271
Bloch equation, 6–7
Boron oxide, 279
Brillouin zone, 631, 636
Brownian-dominated particle systems, 565

C

Carbon, 78–79, 106, 115, 119, 126, 140, 148, 328, 469, 475, 542, 544

- Chemical methods, vapor deposition, 70, 491, 512, 531, 599, 662
- Chemotherapy, 611, 614, 615
- Clathrates, 105–119
- Clearance time, 601–602
- Cluster-assembled nanocomposites, 72
- Cluster gun, 329, 331
- Clusters
 - alloy clusters, 38, 42, 44–46
 - atomic clusters, 36, 41, 43, 59, 60
 - cluster deposition, 70, 72, 75
 - cluster source, 72
 - isolated clusters, 71, 78, 79, 89
 - molecular clusters, 35, 36, 46, 52, 54, 57
 - nanoclusters, 35–62
- Cluster source, 72
- Co–Al, 643
- Coatings, polysaccharide, 592
- Cobalt, 37, 44–50, 53–59, 125, 279, 291, 296, 297, 298, 299, 300, 337–367, 496, 565, 583, 585, 586, 592, 647
- CoCrPt, 176, 177
- Coercivity, mechanism, 316, 343–349, 355
- Co ferrite, 647, 680
- Colloidal particles, 38, 49, 563–587
- Compaction
 - shock compaction, 310, 329, 330, 331
 - spark plasma sintering, 327, 329
 - warm compaction, 309, 310, 327–329
- Computational nanoscience, 36
- Conduction electrons, 87, 88, 92, 139, 195
- Contrast agents, 591, 592, 599, 600, 603, 604, 605, 608, 609, 616
- CoO, 85, 86, 170, 178
- Cooling, field cooled (FC), 49, 179
- Cooperativity, 71, 83, 303, 360, 401
- CoPt, 83, 164, 165, 166, 167, 173, 667, 672
- CoPtCr, 248
- Co_x·Ti_{1-x}O₂, 496–499
- Cr_x·V_{1-x}O₂, 491–496
- CrO₂, 491, 511–534
- Coulomb repulsion, 5
- Crystal-field interactions, 80, 81
- Curie temperature, 74, 85, 87, 129, 280, 290, 311, 314, 338, 339, 343, 356, 376, 377, 384, 386, 389, 403, 409, 412, 430, 442, 444, 448–449, 452, 453, 454, 456, 458, 460, 462, 465, 467, 468, 469, 470, 478, 488, 497, 500, 502, 505, 507, 516, 521, 538, 566, 666, 667
- Current perpendicular to the plane (CPP), 531, 697
- Cyclic mechanical deformation, 332
- D**
- Decoherence, 3, 6, 489
- Delocalized states, 93
- Demagnetizing field, 220, 298, 318, 352, 515, 576, 577, 578
- Density of states, 90, 105, 109, 110, 111, 113, 511–513, 697
- Deposition, 49, 55, 57, 69, 70, 72, 73, 75, 85, 98, 220, 237, 248, 249, 256, 296, 310, 326, 376, 429, 489–499, 512, 514, 521, 523, 526, 528, 530, 531, 532, 596, 599, 629, 661, 662, 671, 672, 673, 674, 675–676, 677–679, 697
- Diffraction, 38, 42, 50, 123, 124, 125, 126–133, 135–138, 140, 144, 149, 379, 380, 417, 429, 456, 469, 492, 498, 501, 502, 593, 629, 647, 651, 652, 674, 689
- Diffusion barriers, 71–72, 255, 526, 527
- Direct patterning, 677
- DNA, 691, 692, 693, 694, 695, 699
- Domains
 - domain in nanocrystalline films, 296–300
 - interaction domains, 282–296, 388
- Domain wall logic, 224, 226, 227, 233–234, 235
- Domain wall motion, in wires, 185–214, 250, 251, 255, 292
- Domain walls
 - constricted walls, 200
 - narrow walls, 187, 209, 210, 212, 286
 - pinning, 186, 187, 279, 316, 343–344, 349, 352, 354, 375
 - wall energy, 343, 349, 352, 354
 - width, 276, 277, 282, 302, 312, 352
- Drug delivery, 567, 591, 615–616
- Dynamic viscosity, 580, 603–604
- E**
- Eddy current losses, 293, 294, 295, 388, 390, 392
- Electromagnets, 376, 387, 631, 632, 635, 637, 641, 647, 652, 661, 663
- Electron energy-loss spectroscopy (EELS), 41, 493, 532, 533
- Electron holography, 298
- Electronic structure
 - density functional theory (DFT), 51, 55, 57
 - first-principle calculations, 315, 453
 - full-potential methods, 616, 662
 - green-function methods, 106
 - Korringa–Kohn–Rostoker method (KKR), 637, 638
 - local spin-density approximation (LSDA), 87, 94

- pseudopotential, 110
- supercell, 410
- Electron microscopy
 - High-resolution (HREM), 189, 263, 264, 277, 283, 286, 288, 289, 293, 359, 528
 - high resolution transmission (HRTEM), 39, 43, 46, 47, 50, 346, 347, 387, 388, 530, 555
 - scanning transmission (STEM), 41, 189, 346, 347, 350, 525, 532, 533
 - transmission (TEM), 38, 39, 41, 50, 78, 249, 255, 256, 323, 324, 325, 327, 328, 329, 342, 346, 357, 360, 361, 363, 493, 496, 498, 499, 500, 501, 506, 507, 523, 525, 529, 530, 544, 546, 547, 548, 549, 554, 555
- Energy barriers, 71, 79, 186, 190, 204, 213, 243, 248, 516, 539, 540, 584
 - activation energy, 381, 494
- Energy product, 68, 71, 309, 310, 311, 312, 315, 316, 321, 322, 325, 327, 328, 331, 366, 666, 667, 668, 670, 671, 673, 674, 676, 680
- Entanglement, 67, 70, 93, 94, 489
- Epitaxial growth, 71, 72, 74, 160, 429, 513, 518, 521, 532
- Exchange, 159–179, 309–332
 - Intergranular, 79
- Exchange bias, tunable, 159–179
- Exchange constant, 187, 357
 - see also* Exchange stiffness
- Exchange-coupled nanostructures, 275, 285, 291, 304
- Exchange-coupled permanent magnets, 309–332
- Exchange interaction
 - anisotropic exchange, 87
 - exchange bias, 159–179
 - Heisenberg, 87
 - interatomic, 87, 89
 - RKKY, 87, 88, 89
- Exchange length, 186, 275, 285, 286, 288, 304, 317
- Exchange spring magnets, 310
- Exchange stiffness, 74, 79, 199, 283, 284, 312, 344, 357, 383, 520
- Exposure dose, 257–258
- Extrinsic properties, 338, 667
- F**
- Fe-8 (magnetic molecule), 92
- Fe-B, 131, 142, 288, 376, 377, 378, 384, 389, 467
- Fe-Co, 85, 348, 374, 376, 378
- FeN, 300
- FePt, 68, 74, 77, 78, 79, 83, 129, 310, 312, 319, 322, 323, 324, 325, 326, 327, 329, 331, 537, 538, 539, 541, 542, 543, 544, 545, 546, 547, 548, 549, 550, 551, 552, 553, 554, 555, 556, 557, 558, 592, 667, 668, 672, 680
- FeRh, 68–69
- Fermi level, 86, 90, 511, 512, 513, 642, 697
- Ferrites, 286, 337, 376, 390, 392, 393, 592, 603, 614, 667, 680
 - Hexaferrites, 301
- Ferritin, 600, 601
- Ferrofluids, 144, 567, 585, 593, 616
- Ferromagnetic seeding, 595
- Ferromagnetism, 45, 74, 80, 88, 90, 220, 455, 486, 488, 496, 498, 499, 500, 502, 662
- Fe-Si-B-Nb-Cu, 375, 376
- Fe-Zr-B-(Cu), 376
- Field sensors, 160, 486, 647
- Finite element method, 312
- Fluctuation field, 6
- Fluorescence, 320, 491, 599
- Flux closure state, 280
- Focused ion beam (FIB), 17, 219
- Focused ion beam milling (FIB), 70
- Foucault imaging, 302
- Four-probe method, free energy, 176, 177, 261, 443, 444, 518
- G**
- GaAs, 429, 546, 549, 558
- Garnet–noble metal nanocomposites, 648, 649, 650, 651
- Gas aggregation, 78
- Gaussian distribution, 242, 250
- Gd₅(Ge, Si)₄, 472–476
- Ge_{1-x}Mn_x, 500–507
- Giant magnetoresistance (GMR), 160, 168, 193, 194, 195, 196, 201, 203, 210, 486, 487, 490, 511, 517, 529, 530, 531, 685, 687, 688, 689, 690, 691, 693, 695, 696, 697, 700, 708
- Gilbert, 2, 5, 6, 7, 79
- Grain boundaries, 142, 279, 281, 285, 296, 297, 302, 357, 375, 411, 418, 427, 679
 - exchange, 2, 4, 52, 69, 74, 78, 79, 81, 83, 85, 87, 88, 89, 90, 91, 92, 93, 94, 95, 130, 140, 143, 144, 146, 147, 148, 159, 160, 161–178, 186, 187, 190, 199, 220, 238, 241, 244, 248, 250, 255, 271, 275, 282, 284, 285, 286–291, 296, 297, 300,

- Grain boundaries (*cont.*)
 301, 303, 304, 309–323, 325–329, 331, 332, 338, 339, 356, 357, 360, 362, 364, 366, 375, 383–387, 406, 445, 446, 470, 476, 496, 505, 511, 512, 520, 523, 529, 534, 546, 547, 597, 664, 701, 702
 layer-resolved calculations, 679
- Grain growth, 300, 322, 325, 327, 329, 332, 366, 375, 537, 538, 545, 546, 548, 549, 550, 551, 554, 557, 558, 672
- Granular nanostructures, 85
See also Magnetic nanostructures; Grain boundaries
- H**
- Hall effect, 188, 193, 194, 196, 204, 210, 496, 506, 685, 687, 700, 702, 708
 Hall sensors, 685, 687, 705
- Hard disk drives (HDDs), 160
- Hard disks, 160, 186, 234, 238, 259, 485, 541
- Hard-magnetic nanostructures, 70, 77, 80, 81
- Hard magnets, 68, 142, 666
See also Permanent magnets
- HDDR, 131, 132, 301, 362, 364, 365, 366, 367
- Heat-assisted magnetic recording (HAMR), 541
- Heat of formation, 142
- Heavy transition metals, 83, 84, 85
- Heusler alloys, 399, 408, 412, 476, 477, 478
- Hyperthermia, 591, 612, 614, 615
- Hysteresis, 41, 45, 48, 49, 67, 71, 78, 79, 80, 81, 82, 85, 160, 161, 163, 164, 167, 169, 171, 172, 173, 174, 175, 176, 177, 178, 188, 219, 220, 275, 276, 281, 290, 291, 294, 295, 311, 317, 318, 320, 321, 349, 353, 361, 362, 364, 365, 374, 382, 386, 387, 388, 391, 392, 403, 405, 406, 411, 414, 423, 424, 430, 443, 446, 452, 454, 460, 465, 466, 470, 471, 473, 474, 475, 478, 479, 495, 497, 499, 502, 503, 504, 516, 518, 520, 522, 524, 533, 540, 547, 550, 553, 554, 556, 558, 566, 612, 674, 675, 678, 689
- Hysteretic losses, 386, 387, 388
- I**
- Icosahedron, 52, 453
- Imaging
 bright field image, 342, 346, 493, 498, 500, 501, 502
 Foucault imaging, 302
- Immiscible, 259, 262, 594
- Imprint technology, 239, 249, 257, 258, 271
- Inert gas condensation, 377, 490, 491, 542, 593
- Information technology, 489, 511
See also Magnetic recording; Quantum computing
- Interaction plots (delta-M), 145
- Interface, 36, 50, 51, 56, 57, 70, 80, 81, 82, 84, 85, 91, 159, 160, 161, 162, 163, 164, 165, 166, 168
 interface anisotropy, 70, 80, 82, 188, 190, 204, 248, 252
- Interface diffusion, 195, 315
- Interfaces, 36, 50, 51, 56, 57, 70, 80, 81, 82, 84, 85, 91, 159, 160–166, 168–179, 185, 187, 188, 189, 190, 195, 197, 202, 204, 205, 210, 226, 248, 252, 254, 255, 262, 309, 314, 315, 316, 321, 350, 352, 354, 361, 490, 491, 493, 496, 501, 517, 519, 520, 523, 525, 526, 527, 528, 529, 530, 533, 558, 631, 633, 640, 651
- Intramultiplet excitations, 146–147
- Intrinsic, 3, 4, 81, 109, 129, 161, 164, 165, 186, 187, 189, 196, 198, 200, 201, 203, 204, 208, 213, 220, 235, 252, 253, 254, 262, 338, 343, 346, 351, 355, 356, 357, 359, 360, 384, 486, 496, 499, 511, 513, 517, 551, 552, 556, 558, 666, 667, 677
- Intrinsic properties, 129, 169, 198, 220, 262, 351, 360, 513
- Ion etching, 258, 260
- Ion irradiation, 204
- Iron oxide, 38, 39, 43, 591, 592, 593, 594, 595, 598, 599, 600, 601, 606, 610, 617
- Irradiation, 42, 133, 203, 204, 205, 206, 207, 232
- Irreversible susceptibility, 567
- J**
- Jitter noise, 261
- K**
- Kerr measurements, 208
- Kondo effect, 92, 93
- L**
- $L1_0$ magnets, 90, 668
- $\text{LaFe}_{3-x}\text{M}_x$, 452–471
- Landau–Lifshitz equation, 6–9
- Landau–Lifshitz–Gilbert equation, 2, 6–9, 79
- Langevin equation, 442, 539, 569
- Laser-assisted direct imprint (LADI), 138
- Laser interference, 489
 interferometric laser annealing, 680

- Length scales
 correlation length, 143, 204, 205, 276, 279, 281, 285, 288, 304, 373, 375, 383, 384, 387
 domain-wall width, 189
 exchange length, 186, 275, 285, 286, 288, 304, 317
- Linear response theory, 703
- Lithography
 electron beam lithography (EBL), 193, 219, 220, 237, 249, 273
 nanoimprint technology, 237, 239, 249, 257, 258, 259, 271
 X-ray lithography, 662, 670
- Localized states, 93, 629, 640, 641, 646
- M**
- Magnetic beads, 567, 573, 687, 691, 694
- Magnetic capsule, 612
- Magnetic circular dichroism, 321
- Magnetic clusters, 37–50, 61, 142
- Magnetic dichroism, 321
- Magnetic domains
 multidomain state, 287
 single-domain particles, 298, 301, 361
 stripe domain structure, 360
- Magnetic excitation, 124, 125, 146–148
- Magnetic fluids, 38
- Magnetic imaging, contrast enhancement, 599, 604, 611
- Magnetic logic devices, 233, 490
See also Quantum computing
- Magnetic marker, 265, 266, 597, 616
- Magnetic materials, 11, 30, 43, 71, 73, 81, 93, 118, 123–150, 160, 220, 233, 235, 242, 248–256, 258, 259, 265, 271, 275, 277, 282, 293, 309, 310, 316, 325, 329, 338, 373–394, 402, 403, 407, 425, 441, 443, 444, 445, 446, 449, 451, 485–507, 565, 612, 627, 628, 647, 648, 651, 652, 661–680
- Magnetic molecules, 93
See also Molecular nanomagnets, single molecule
- Magnetic moment, 2, 3–4, 36, 39, 41–42, 51, 52, 53, 54, 57–58, 59, 60, 69, 82, 83–84, 90, 93, 117, 118, 125, 127, 130, 134–135, 136, 138, 139–140, 148, 149–150, 163–164, 165, 244, 250, 254, 256, 297–298, 312, 313, 338–339, 383, 384, 402, 403–404, 406, 412–413, 441, 447, 453, 476, 486, 497, 498–499, 506, 534, 567, 592, 643, 705, 707
- Magnetic nanostructures
 elements, 67–68, 83–84, 90
 granular, 79, 85
 nanoclusters, 78, 85
 nanodots, 70–71, 93–94
 nanoparticles, 68, 70, 78, 80, 81, 86, 88, 92, 95
 nanorods, 331
 nanowires, 68
- Magnetic oxides, 75, 489–499
- Magnetic random access memory (MRAM), 2, 209–210, 226, 485, 487, 488, 489–490
- Magnetic recording
 bit-patterned media (BPM), 237, 238, 239, 240, 241, 242–243, 244–245, 246–248, 249, 250, 251, 252, 254, 255, 256–259, 264, 265–266, 268–269, 270, 271
 hard disks, 238, 259
 high densities, 239, 262
 jitter noise, 239, 242, 260, 261, 263, 264, 268
 noise, 238, 239, 241, 248, 255–256, 266, 270, 271
 perpendicular (PMR), 82
 read heads, 246, 252, 254, 270
 recording media, 248, 254
 single-particle-per-bit, 252, 259
 ultrahigh densities, 538
 writability, 239, 270–271
- Magnetic resonance, 6, 338, 489, 592, 603–612
- Magnetic resonance imaging (MRI), 338, 592, 599, 603–612, 613, 616
- Magnetic sensors, 60–61, 685–708
- Magnetic separation, 38, 46, 564, 568, 570, 587
- Magnetic shape memory, 477, 663
- Magnetic switches, 239, 252–254, 387, 391, 517, 522–525
- Magnetic targeting, 613, 615–616
- Magnetic thin films, patterned, 248, 270–271
- Magnetic tunnel junction (MTJ), 226, 486, 491, 523–525, 527–528, 529, 531, 532, 533, 687, 697–700, 708
- Magnetic viscosity, 351
See also Magnetization dynamics
- Magnetite, 68, 376, 591, 592, 593, 595, 603, 611, 696
- Magnetization
 reversal, 238, 249–252
 saturation, 141, 406
 spontaneous, 288, 504, 506, 507

- Magnetization dynamics
 blocking temperature, 38, 173
 damping, 3, 7, 10, 11–12, 13–15, 16–17, 19–20, 21, 24–25, 26, 27, 28, 30–32
 Langevin equation, 539, 569
 magnetic viscosity, 351
 stochastic LLG equation, 7
 sweep-rate dependence, 540
 thermally activated, 71, 189, 190, 191, 192, 200, 205, 206, 208, 212, 213
- Magnetization reversal
 coherent rotation, 2
 curling, 2
 nucleation, 2
 pinning, 161–162
 Stoner–Wohlfarth model, 161–162
- Magnetization ringing, 2, 3, 10, 13, 17, 19
- Magnetocaloric effect, 430, 441–479
- Magnetophotonics, 627–653
 magnetophotonic crystals (MPC), 628–641, 642, 644–645, 646, 647, 648
- Magnetorefractive effect, 628, 641–647
- Magnetoresistance, anisotropic magnetoresistance (AMR), 687, 700–702
- Magnetostatic interactions, stray field, 266, 276, 277–278, 279, 285, 297, 298
- Mask-less patterning, 193
- Masks
 patterning with masks, 70, 193, 254, 260, 264, 413, 586, 673, 675, 676, 677, 680
- Mean-field approximation, 74, 77, 444
- Mechanical alloying, 129–130, 301, 310, 322, 362
- Melt spinning, 70, 362–363, 376, 377
- MEMS, 310, 661–680
- MFM, 161, 252–253, 255–256, 358–359, 360
- Micromagnetic free energy, 455
- Micromagnetism, 361–362
- Microscopy
 conventional transmission electron microscope (CTEM), 38, 41, 42, 607
 electron microscopy, 38, 39, 41, 194, 282, 343
 Lorentz microscopy, 296, 301, 357, 361
- Microstructure, 275–304, 315, 322, 338–339, 340–341, 342, 343–345, 349, 351–352, 357–358, 359, 360, 361, 362, 363, 373, 374–375, 376, 377, 378, 379, 380–381, 382, 384, 387–388, 400, 402, 403, 405, 406, 416, 417, 418, 493, 496, 498, 667, 677
- Molecular beam epitaxy (MBE), 70, 72, 145, 500
- Molecular nanomagnets, single molecule, 2
- Monodisperse nanoparticles, 324–325, 545
- Multilayers, 8, 67–68, 140–141, 144–145, 166, 188–189, 195, 196, 201–203, 204, 210, 248, 249–250, 259, 300, 312, 322, 490–491, 629–631, 632, 640–641, 642, 647, 651, 687, 688, 689, 690
- N**
- Nanobead, 702, 703
- Nanocomposites, arrays, 538, 542, 544, 552
- Nanodots, 70–71, 93–95, 145
- Nanofabrication, 193–194, 256–259
- Nanojunctions, 68
- Nanoparticles, 537
 arrays, 538, 542, 544, 552
 core-shell, 546–548
 monodisperse, 538, 544, 545, 546
 synthesis, 541–545
- Nanostructures
 chains, 68
 materials, 68, 71
 nanotubes, 67, 68
 nanowires, 68
 patterned, 68, 69, 70
- Nanotubes, 67–68, 69, 95
- Nd–Fe–B, 131, 142
- Neel model, 187, 209, 567
- Neel walls, 212, 213
- Neutron scattering (diffraction)
 Polarized, 124, 125, 132
 In situ, 128–133
 Small angle, 124, 131, 141–144
- NiFe, 186, 276, 279, 282, 287, 304, 642, 700
- Ni–Mn–Ga, 400, 401, 403, 405, 407, 408–416, 417, 425, 426, 427, 428, 429, 430, 476–477
- Noncollinearity, 18, 95
- Non-epitaxial growth, 296
- Nonequilibrium, 174, 175, 176
- Nonmagnetic matrix, 142
- Nuclear magnetization decay, 442
- O**
- Opsonization, 598
- Ordering temperature, 75, 76, 144–145, 408, 505, 507, 550–551, 558
- Oxidation resistance, 43
- P**
- Paramagnetism, 90, 503, 566
- Patterned bits, 255
- Patterned nanostructures, 68, 69, 70, 277, 278, 280

- Patterned thin films, 187
 Permalloy, 68, 219–220, 221, 223, 232,
 276, 282, 286, 296–297, 298–300,
 375, 702
 Permanent magnets
 bonded magnets, 301, 669–671
 exchange-coupled permanent magnets,
 309–332
 high-temperature permanent magnets,
 337–367
 Phase transformation, 124, 332, 378–381, 401,
 402, 403, 404–405, 408, 409, 472,
 550, 586
 Photoresist, 676
 Piezoelectric, 169–170, 400–401, 661–662,
 665–666
 Piezomagnetic, 169–170
 Pinning, 160–161, 162, 163, 164, 165,
 166–168, 169, 170–171, 173–176, 177,
 178, 186, 187, 189–190, 191, 192, 196,
 198, 200–203, 204–206, 207–208, 209,
 210–213, 250, 279, 281, 303, 316,
 343–344, 349–356, 361, 363, 375,
 417–418, 668
 Plasmon-enhanced magneto-optical responses,
 647–653
 Polycrystalline, 124, 134, 147, 150, 170, 279,
 281, 285, 297–298, 299, 301, 331,
 357–358, 373, 403, 411–412, 415, 418,
 421, 427, 428–429, 473, 475, 477,
 478, 672
 Polyethylenamine, 50–51
 Polymers
 block copolymers, 259–264
 copolymers, 598
 Precursor, 50, 319, 341, 376, 377, 378–379,
 381–382, 409, 513, 525, 529, 531,
 532, 671
 Precursors, 301, 377, 529, 530, 543, 595,
 596, 612
 Propagation, 2, 144–145, 186, 188, 189–190,
 192, 194, 196–197, 200, 201–203, 204,
 206–208, 213, 219–221, 222, 223, 224,
 225, 229, 231, 235, 514–515, 628,
 629–630, 631, 634, 635, 637, 639, 640,
 647, 651
 Pulsed laser deposition (PLD), 70, 629, 672,
 675–676
- Q**
 Quantum bits or qubits, 489
 Quantum computing, 93–94, 486, 489
 Quantum dots, 489
 Quantum effects, 9, 36, 86, 95, 489
 Quantum entanglement, 93–94
 Quantum interference, 38, 250, 386–387,
 489, 495
 Quantum tunneling, 592
 Quenching (orbital moment), 51, 159, 178,
 280, 282, 301, 339–340, 341, 349, 350,
 355, 356, 358, 359, 381, 408, 412
- R**
 Radiotherapy, 614–615
 Random anisotropy, 80, 282, 283–288, 290,
 291–293, 296–298, 300, 304, 312, 383,
 384, 387
 Rare-earth containing magnets,
 146, 303
 Receptor ligands, 686
 Recording media, 69, 80, 248
 self-organized magnetic arrays, 70, 249
 Relaxivity, 595, 600, 602, 604, 605,
 607–608
 Remanence
 remanence enhancement, 301
 remanence ratio, 392
 Replication, 239, 257, 271
 Rhombohedral, 136–137, 339–341, 364
 Rings, 67, 223, 224, 225, 227–228, 290,
 293–294, 295, 554, 577, 587, 687,
 700, 701
 Ruthenium, 529
- S**
 Schrödinger equation, 87
 Self-assembly, 38–39, 70, 73, 239, 249, 257,
 259–264, 271, 322, 326, 570–571
 SEM, 199, 202–203, 229, 231, 249, 264, 346,
 347, 415, 416, 630, 633, 649, 674, 678,
 679, 689, 690, 697, 704
 Semiconductors, magnetic, 76, 88, 90, 488,
 498, 642
 Sensors, 36, 60–61, 95, 160, 186, 208–210,
 234, 254, 266, 339, 376, 387, 393, 399,
 430, 446, 486–487, 489–490, 491, 496,
 586, 647, 663, 685–708
 Signal-to-noise ratio (SNR), 78, 238, 239, 241,
 266, 270, 690, 702, 708
 Simulations, micromagnetic, 297, 301, 312
 Single crystals, 50, 78, 108, 124, 126–128,
 132–133, 134, 137–138, 139, 140–141,
 150, 167–168, 170, 331, 359, 399–400,
 403, 405, 406, 408, 412, 413, 414–415,
 416, 417, 421, 426, 429, 430, 476, 477,
 512, 513, 522–523, 555, 592, 643–644
 Single-domain state, critical
 radius, 166

- Single-ion magnetic anisotropies, 166
- Size distribution, 49, 72–73, 78, 260–262, 263, 264, 322–323, 325, 326, 328, 331, 541, 554, 556, 557–558, 594, 689
- Size effect, 51, 69, 93, 537, 538, 556–557, 592
- Sm–Co, 67–68, 342–343
- Soft magnets
- FINEMETS, 142, 375, 376, 380, 389
 - HITPERM, 376, 378, 379, 380, 384, 385, 387
 - NANOPERM, 142, 376, 378, 379, 380, 384, 385, 387, 389
- Soft nanoparticles, 322
- Spatial resolution, 195–196, 201–203, 609
- Spin-dependent transport, 160, 167–168, 486, 489
- Spin injection, 496
- Spin LEDs, 486
- Spin-orbit coupling, 80–81, 83–84, 86, 90, 195–196, 201, 506, 527
- Spin transistor, 487
- Spintronics, 5, 93, 164, 167–168, 174, 179, 186–187, 213, 222, 234–235, 485–507, 517, 529
- Spin valves, spin valve sensors, 693–697
- Spin waves, 9, 125, 146, 148, 213, 222
- Spirals, 10, 11, 134, 137, 691–693
- Sputtering, 188–189, 204, 296, 299, 322, 326, 376, 490–491, 629, 631, 648–649, 662, 672–675, 677–678
- SQUID, 38, 41, 43, 47, 48, 176, 250, 489, 495
- STM image, 72, 73–74, 81–82
- Stoner criterion, 90–91
- Stoner theory, 2–3, 32
- Substrates, 57, 69, 71–73, 74, 75, 82–83, 84, 92, 93, 95, 188–189, 204, 210–212, 240, 248–249, 250, 252, 255, 256, 258, 259, 260, 263–264, 429, 491, 492, 493, 494, 495, 496, 498, 500, 503, 504, 512, 513, 514–523, 525, 531, 532–533, 544–545, 550–551, 553, 565, 570–573, 586, 587, 596, 631, 633, 645, 648–649, 662, 664, 670, 671, 672–673, 674–675, 676–679
- Superconductivity, 105–119
- Superparamagnetic iron oxides (SPIO), 592, 593–599, 600–601, 603–606, 607, 608, 609, 610, 611, 613, 615, 616
- Superparamagnetism, 36
- blocking temperature, 38, 45, 46, 47, 48, 49, 50, 51
- Surface charge, 568
- Surfaces, 17, 36, 39, 41–42, 43, 46, 47, 50, 51, 53, 55, 57, 59, 60, 68, 69–75, 77, 80–81, 82, 88, 89, 91, 92, 93, 95, 124, 141, 144–146, 161, 169, 173, 195–196, 199, 202–203, 207, 220, 240, 249, 256, 258, 259, 260, 263, 265, 275–278, 279, 280, 281, 286, 287, 301, 324–325, 328, 329, 348–349, 357–358, 362–363, 376, 377, 393, 401, 415, 416, 418, 421, 453, 490–491, 492, 493, 498, 500, 501–502, 507, 515–517, 521–525, 530, 532–533, 538, 539, 547–548, 564, 565, 567, 568–569, 570, 571–573, 576, 578, 586, 587, 592, 594, 596–599, 600, 608, 610, 611, 615, 616, 627, 628, 629, 638–639, 647, 648–649, 652, 662, 664, 668, 671, 672–673, 674–675, 676, 679, 680, 685–686, 689, 693, 694–695, 699, 701, 707, 708
- Symmetry
- cubic, 401
 - hexagonal, 139
 - monoclinic, 472
 - orthorhombic, 410, 414, 416, 429, 472, 478
 - tetragonal, 492, 493, 494, 513
 - uniaxials, 11, 14, 17, 21, 25, 28, 30, 138–141
 - unidirectional, 160, 170, 229, 679
- T**
- Targeting, 597, 598, 608–609, 613, 615–616
- Texture, c-axis alignment, 144, 673
- Therapeutic applications, 612–616
- Thermal activation, 186, 189, 190, 201, 202, 426
- See also* Magnetization dynamics
- Thermal constraint, 243–245
- Thermal stability, 69–70, 78, 80, 83, 93–94, 186, 207, 213, 238, 239, 241, 244–245, 270–271, 547, 553, 557–558
- Training effect, 164, 174–178, 179, 534
- Transformers, 286, 294, 387
- Tunnel magnetoresistance (TMR), 160, 168, 517, 526, 527–528, 531, 532–533, 534, 687, 699
- V**
- Valence electrons, 113–115, 384, 476, 512–513
- Vortex states, 186
- W**
- Wall energy, 198–199, 278, 293, 343, 349, 352, 353–354, 355, 356, 361

X

X-ray diffraction, 38, 42, 77, 124, 329,
379–380, 429, 455, 456, 469–470,
491–493, 593, 689
X-ray lithography, 662, 670

Z

Zeeman energy, 162–163, 171, 172–173, 174,
198–199, 404, 418, 419
Zintl concept and vacancies,
115–116